OpenFOAM 2018 SHANGHAI

PROCEEDINGS

of The 13th OpenFOAM® Workshop

June 24-29, 2018, Shanghai, China
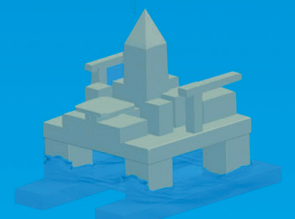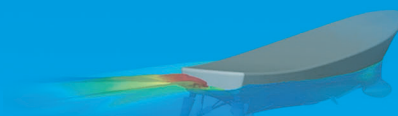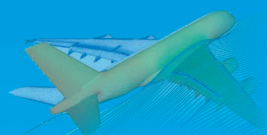
Editor-in-Chief
D.C. Wan

Editors
J.H. Wang W.W. Zhao D. Deng Z. Wang

上海交通大学船海计算水动力学研究中心

CMHL COMPUTATIONAL MARINE HYDRODYNAMICS LAB
SHANGHAI JIAO TONG UNIVERSITY

June 25, 2018

Preface

Welcome to OpenFOAM 2018! Welcome to Shanghai! On behalf of the OpenFOAM® Workshop Committee, I would like to welcome all delegates from all of the world to Shanghai Jiao Tong University to attend the 13th OpenFOAM® Workshop (OFW13). We are honored and proud to host this annual OpenFOAM® Workshop which is the most important and influential forum for researchers and users from universities, institutes as well as industries to promote collaborative activities and share recent advances on OpenFOAM® in many areas.

OpenFOAM® is the leading free, open source software for computational fluid dynamics, and other computational science and engineering. It is an attractive community event opening to scientists, scholars, engineers, students, users and contributors, regardless of their background and avocations. In 2006, the 1st OpenFOAM® Workshop (OFW1) was held in Zagreb, Croatia. Since then it was held every year successively in Zagreb, Milan, Montréal, Gothenburg, Pennsylvania, Darmstadt, Jeju, Zagreb, Ann Arbor, Guimarães and Exeter, respectively. The workshop series provide a forum to promote scientific advancement, technological progress, information exchange, and cooperation among engineers and researchers in computational fluid dynamics and other related fields. It is no doubt that the achievements obtained in the past 12 years are admirable.
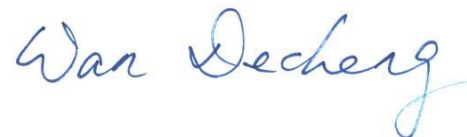
OFW13 has accepted 133 extended abstracts for the collection in the proceedings from a total of 138 abstracts received from 22 countries and regions. Among these 133 abstracts, 123 abstracts including 5 keynote lectures, 15 training lessons and 4 mini-symposiums of community day have been scheduled for oral presentations in 11 sessions of different topics over four days. In addition, 14 abstracts have been selected for poster session during the workshop. All abstracts have been peer reviewed and the accepted abstracts have been included in the OFW13 proceedings. Selected abstracts will be recommended their full papers for publication in special issues or columns of the following five journals: Ocean Engineering, Computers & Fluids, China Ocean Engineering, Journal of Hydrodynamics, Journal of Ocean Engineering and Science based on the regular journal review after the workshop.

I sincerely wish to acknowledge the help we received from our colleagues in the local organizing committee and the international scientific committee. I appreciate all contributors for their care in preparing their manuscripts according to the prescribed guidelines. Special thanks go to Prof. Hrvoje Jasak (Wikki, UK, University of Zagreb,

Croatia), Prof. Francois Guibault (Ecole Polytechnique de Montreal, Canada), Prof. Gavin Tabor (University of Exeter, UK), Prof. Xinhai Xu (National University of Defense Technology, China) and Dr. Jianhua Wang (Shanghai Jiao Tong University, China) who will deliver the invited keynote lectures at the plenary sessions of OFW13. I would like to express sincere thanks to all staff and students of the conference secretariat for their efforts to make this event a successful one. I also wish to thank the generous support of Journal of Hydrodynamics, Shanghai Key Laboratory of Ship Engineering, State Key Laboratory of Navigation and Safety Technology, Shanghai Jiao Tong University, and ENGYS, CALCNEXT, and CAESolution. Finally, millions of thanks go to you for your participation and sharing of your exciting research developments.

As the host and organizer of the Workshop, Shanghai Jiao Tong University(SJTU) invites you to enjoy perfect facilities, beautiful environment and densely academic atmosphere at Minhang Campus of Shanghai Jiao Tong University. The beautiful environment creates a unique academic atmosphere. In addition, Shanghai is also a place with plenty of areas of interest to visit. The city's Cultural Center with its public activities and community facilities and finally the main Entertainment and Holiday Tourism area is located at Mt. Sheshan, Chongming Island, Dingshan Lake and Shenshuigang Area. Known as "the Oriental Paris", Shanghai is a shopper's paradise. One of the musts for tourists is Nanjing Road. Huaihai Road intrigues those with modern and fashionable tastes, while Sichuan North Road meets the demands of ordinary folks. In addition, Xujiahui Shopping Center, Yuyuan Shopping City, Jiali Sleepless City are thriving and popular destinations for those who are seeking to buy something special as a memento of their visit.

I do wish you a rewarding experience in participating in the 13th OpenFOAM® Workshop. Enjoy your stay in Shanghai.

Wan Decheng

Prof. Decheng Wan
Chair of the 13th OpenFOAM Workshop
June 25, 2018, Shanghai

CONTENTS

Aerodynamics / Civil Engineering / Atmospheric Flows

General CFD

Porous Media / Complex Materials

Heat Transfer / Phase Change / Reacting Flows / Compressible Flows

Disperse Multiphase Flows / Free Surface Flows

Fluid-Structure Interaction / Structural Analysis

Fuel Cells / Sprays and Injection / Turbomachinery

Naval Hydrodynamics / Coastal / Offshore

Optimization and Control

Pre-Processing / Post-Processing / Meshing / User Environments

Turbulence Modelling

Poster

ENHANCING COMPUTATIONAL AERO-ACOUSTIC PROCESSES FOR GROUND VEHICLES RESOLVING OPEN SOURCE CFD

TORBJÖRN LARSSON[1], JOHAN HAMMAR[1], JING GONG[2], MICHAELA BARTH[2], LILIT AXNER[2]

[1]*Creo Dynamics AB, Sweden, [torbjorn.larsson, johan.hammar]@creodynamics.com*
[2]*PDC-HPC, KTH Royal Institute of Technology, Sweden, [gongjing, caela, lilit]@kth.se*

Keywords: *Scalability, High Performance Computing, CAA*

Introduction

The aerodynamic drag on a heavy-duty truck-trailer equipage is significant and, with new stringent legislations on fuel efficiency and CO_2 reductions in the pipeline, substantial development to improve the aerodynamic efficiency of such ground vehicles is required. Furthermore, the trend towards electrification and hybrid technologies for vehicles means that now, more than ever, there is a need for the aerodynamic drag to be decreased in order to increase the range of electric vehicles (EVs). With EVs expected to dominate the road car market in the near future, there is also renewed interest in topics relating to airborne noise.

Experimental aerodynamic testing of full-size trucks is challenging, particularly as there are only very few facilities in the world where it is possible to do such tests. Highly accurate predictions of the aerodynamic (and acoustic) properties of these large vehicles via physical testing are immensely expensive, and consequently often not justifiable in a repetitive manner, especially in the fast-paced development that is paving a route to sustainable transportation. Instead, further investments in dedicated virtual testing techniques are required with a firm commitment to large-scale high-performance computing (HPC). In this paper, we are aiming for high fidelity scale-resolving simulations to enable us to make accurate predictions, not only of the airflow distribution, but also of the aeroacoustic noise generation and propagation. For these reasons all the steps in the simulation processes need to be made efficient for parallel computation with scalability to many thousands of computational cores.

Herein, we set up and analyse an automated process that, using prepared CAD surfaces as input, generates a high resolution CFD mesh fulfilling predefined quality metrics. The process also performs a steady state RANS (Reynolds-averaged Navier-Stokes) simulation, and extracts results and post-processing data. All these steps are implemented in parallel on distributed compute nodes without the need for any intermediate input/output (I/O) or data transfers.

Open Source CFD Workflow

Parallel performance of all steps of the simulation process, as well as efficient I/O and data extraction, are becoming vital as the size of models and the complexity of simulations increases. Building a fully parallelized simulation process that removes serial bottlenecks, time consuming I/O operations, and labor intensive manual work is a quest that is being actively pursued in the automotive industry due to the significant benefits such a process will bring.

Here, in this project, the basic idea is to derive a (semi-) automated and fully scripted simulation process for a chosen application (truck-trailer) starting from prepared CAD data. The automation, along with the possibility to perform the mesh generation in parallel on distributed compute nodes where the same nodes are also used for subsequent CFD simulations, are central features of the work. These features mean that all the steps in the process can be executed in a homogeneous Linux-based computer environment thus avoiding serial bottlenecks, time-consuming I/O, and additional data transfers. The main steps of this process, illustrated in Figure 1, are based entirely on the *OpenFoam* toolbox [1].
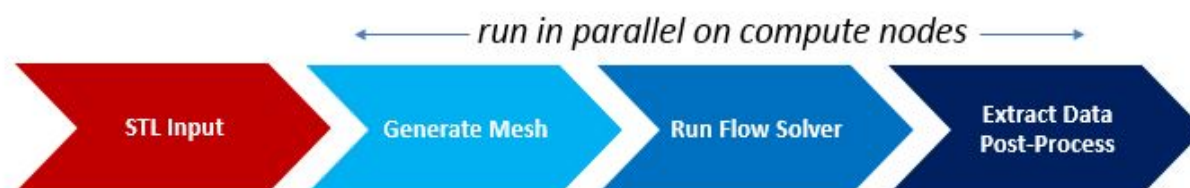
Figure 1: OpenFoam Workflow

The OpenFoam Utilities and Solvers

The pre-processing phase (that is, the Generate Mesh phase in Figure 1 is based on the *OpenFoam* meshing utility *snappyHexMesh,* which relies on a geometry description in STL file format. Before executing *snappyHexMesh* (in parallel) though, a couple of serial steps are performed to create and decompose an initial background hexahedral mesh and to extract geometrical feature edges. These operations only require a few seconds of computational time running on a single core, and consequently will not be described here. In this study, the three steps in the mesh generation process have been monitored in terms of memory usage and parallel run-time performance.

Creating high quality meshes on complex configurations with *snappyHexMesh* is far from trivial and finding suitable "meshing recipes" often requires a sound understanding of the various steps in the mesh generation algorithms, as well as rigorous knowledge of the model configuration and the predominant flow physics involved. Often a good deal of iterative testing and parameter tuning may be needed before a mesh of acceptable quality can be generated. In the *meshQualityControls* section of the *snappyHexMeshDict,* we define relatively strict criteria for the final mesh quality, with face skewness and face orthogonality being two very important quality metrics (see Figure 4 for the definition of these metrics).

Face skewness is calculated as the distance from the face centre to the cell-centre to cell-centre face intersection point normalised by the distance from centroid of the cell to centroid of the adjacent cell

$$metric_{face,skewness} = \frac{|\vec{d_i}|}{|\vec{c_i}|}$$

Face orthogonality is calculated as the normalised dot product of the face area vector with a vector from the centroid of the cell to centroid of the adjacent cell

$$metric_{face,orthogonaliy} = \frac{\vec{A_i}.\vec{c_i}}{|\vec{A_i}||\vec{c_i}|}$$

Figure 2: Skewness and orthogonality quality metrics

Since *snappyHexMesh* can run in parallel on distributed cluster nodes by using dynamic load balancing, it is well suited to become an integrated part of a fully scripted CFD process running in batch on a large parallel cluster.

Since the solutions for the coupled equations are not straightforward, the viscous and pressure sub-steps require solving a Poisson-equation subject to various boundary conditions. Within the project, the *simpleFoam* solver [2] is employed to address the large simulations. The Semi-implicit methods for Pressure-Linked Equations (SIMPLE) algorithm is implemented in the solver *simpleFoam* and couples the Navier-Stokes equations in an iterative procedure following [3].

Results and Discussions

The simulations were performed on the Cray XC40 system Beskow [4] at PDC, KTH Royal Institute of Technology, Sweden, and on MareNostrum [5] at BSC, Spain. Beskow is based on Intel Haswell processors and the Cray Aries interconnect technology. During the simulations it consists of 1676 compute nodes, each of which consists of 32 Intel Xeon E5-2698v3 cores. MareNostrum has 36 racks dedicated to calculations. These racks have a total of 48,448 Intel SandyBridge cores with a frequency of 2.6 GHz and 94.625 TB of total memory.

Before proceeding with the large-scale distributed parallel meshing, the parallel scalability of *snappyHexMesh* was first evaluated on a couple of thin compute nodes at PDC where each node has 24 cores and 512 GB RAM. Different releases of *snappyHexMesh* (2.3.x, 2.4, 3.0+, 1606+) were tested. Although there were some performance differences observed between the various releases, unfortunately all the releases were suffering from poor parallel scalability. For these tests, an intermediate sized mesh of 160 million cells was constructed to make the mesh generation possible on a single core. Figure 3 below shows the run-time performance and scalability obtained for this intermediate test case.
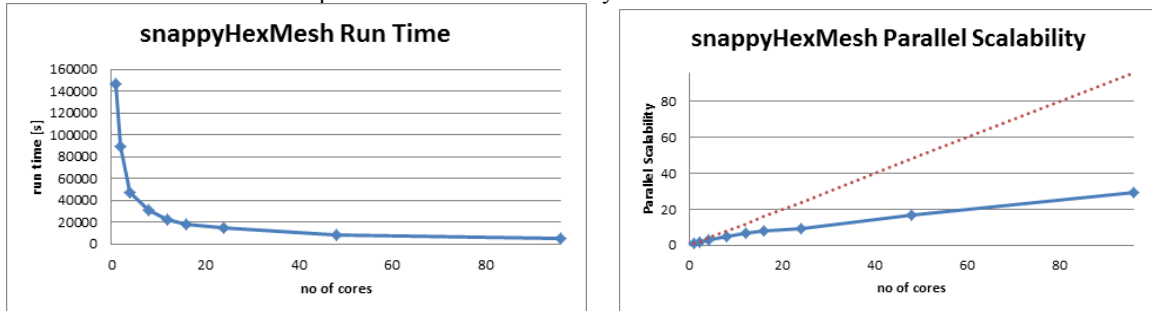
Figure 3: Run-time and scalability test of snappyHexMesh, intermediate case using OpenFoam v3.0+

Next, larger meshes of around 350 million cells were generated in parallel on a sequence of 512, 1024, 2048, 4096 and 8192 cores, respectively. The run-time performance and scalability of the entire meshing process, as well as the timings for each meshing step. *snappyHexMesh* also suffers from relatively high memory consumption. This may lead to performance implications if the computational nodes have limited RAM. Often separate (fat) nodes or another shared memory compute architecture must be brought in for the mesh generation for large and complex cases. This not only creates additional bottlenecks and performance deficits in the overall simulation process but it also increases the cost and complexity of the necessary compute infrastructure. Using distributed STL input can reduce the memory consumption of *snappyHexMesh* and may provide opportunities to generate larger meshes by using less overall memory. In the more recent versions of *snappyHexMesh* this functionality has been improved. Herein we present results obtained while using version 1606+. Using a distributed STL input we save close to 300 GB in total accumulated memory while meshing in parallel on 1024 cores. This represents about a 30% reduction in the overall memory consumption. However, this saving in RAM comes with a significant penalty in mesh generation time. Performance degradation in all steps in the mesh generation process is observed.

Assessments of the total run-times for the *simpleFoam* solver using the two mesh generation strategies, i.e. based on the standard and distributed STL input, are presented below. Figure 4 shows the flow solver scalability for a case containing 110 million cells on MareNostrum and Beskow, respectively. For each run we average the timings over 500 time steps.

An almost linear speed-up can be observed from 64 to 1024 cores on MareNostrum for the standard STL input. A scalability of 74.4% is achieved using 2048 cores compared with 64 cores for the standard STL input. Due to memory limitations, the minimum number of cores that can be used for this case on MareNostrum is 64.
Here we use the definition of the parallel efficiency as

$$\eta(\%) = \frac{T_{min}}{T_{max}} \cdot \frac{N_{min}}{N_{max}} \cdot 100$$

where is T_{min} the execution time per step for the minimum number of cores N_{min}, while T_{max} is the execution time per step using the maximum number of cores N_{max}. The performance and scalability for the Distributed STL input is a bit worse than those for the Standard STL, see Figure 4. A partial reason for this deficit is that the more efficient partition tool *Scotch* [6] is employed for the Standard STL. Currently only simple partition methods, such as *hierarchical,* are implemented for the Distributed STL input. On Beskow we can obtain almost linear speed-up from 128 to 2048 cores for the Standard STL, see Figure 4. The efficiency is 82.9% with 4096 cores compared with 128 cores. Using the Distributed STL, the performance is worse, but this allows us to run on as little as just two nodes. Beyond 3072 cores the performance degrades significantly. Due to the limit of memory on Beskow (32G RAM per node), the minimum requirement for the Standard STL is four nodes (128 cores).

We have presented a complete CFD simulation process that runs in parallel on large Linux clusters. The entire workflow, from prepared CAD input to the output of results, is executed in batches without the need for any intermediate I/0, data transfer or human interventions in between. All the steps in this process rely exclusively on open source software. Although the scalability of *snappyHexMesh* is rather mediocre, we demonstrated that fairly large and complex CFD meshes could be successfully generated on distributed compute clusters in a limited period of time. Mesh generation of a detailed semi-trailer configuration comprising 350 million cells was completed in less than 25 minutes using 4096 compute cores. On the same number of cores, the *simpleFoam* solver was shown to perform well. Hence, for this size of problem, the presented process performs well.
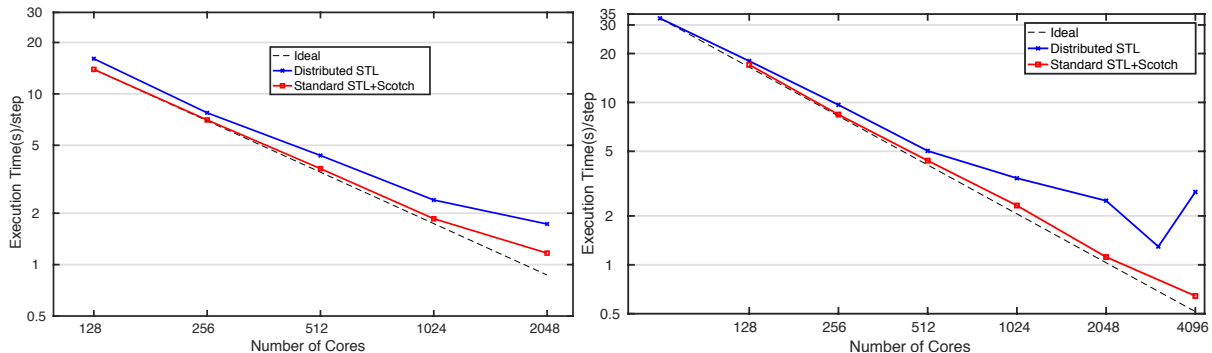
Figure 4: The performance results on MareNostrum and Beskow

However, while scaling beyond a few thousand computational cores and with model sizes above a few hundred million cells, a variety of problems and performance deficits arise. In particular, the mesh generation phase (*snappyHexMesh*) revealed weaknesses and several software issues have been reported.
Below are a few snapshots from a steady state Reynolds Averaged Navier Stokes (RANS) simulation.
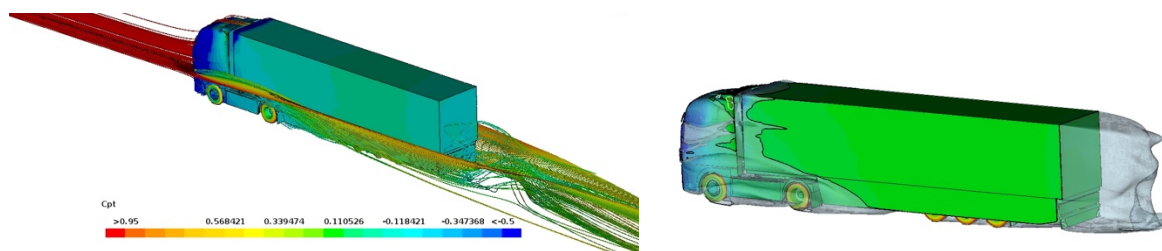
Figure 5: (left) Flow path lines rendered by total pressure (right) Iso-contours rendered by total pressure
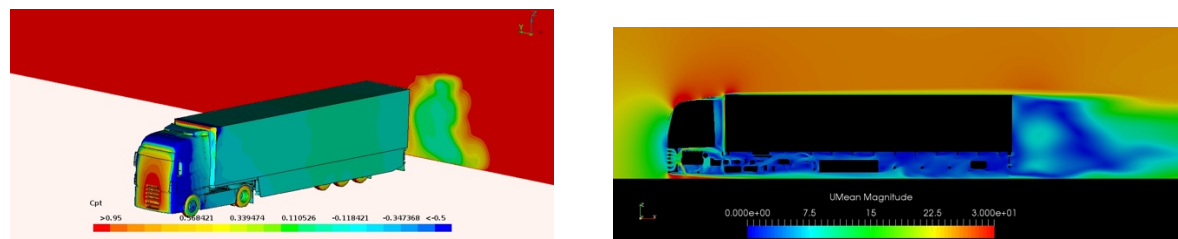
Figure 6: (left) Vehicle surfaces rendered by static pressure and plane rendered by total pressure (right) Vehicle centreline plane rendered by mean velocity magnitude

Conclusion

During the project a (semi) automated CFD simulation process tailored towards aerodynamics predictions for heavy duty semi-trailers was developed. A variety of benchmarks related to parallel meshing and flow solving using *OpenFoam* were performed. The memory usage and parallel scalability were monitored revealing performance deficits and weaknesses, particularly related to parallel mesh generation on many cores. For efficient simulations of large problems requiring many thousands of computational cores there are still critical bottlenecks and deficiencies in current *OpenFoam* distributions that need to be addressed.

References

[1] OpenFoam, http://www.openfoam.com/

[2] simpleFoam, https://openfoamwiki.net/index.php/OpenFOAM_guide/The_SIMPLE_algorithm_in_OpenFOAM

[3] J. H. Ferziger, M. Peric, Computational Methods for Fluid Dynamics, Springer, 3rd Edition, 2001

[3] Beskow, https://www.pdc.kth.se/hpc-services/computing-systems/beskow-1.737436

[4] MareNostrum, https://www.bsc.es/innovation-and-services/supercomputers-and-facilities/marenostrum

[5] Scotch, http://www.labri.fr/perso/pelegrin/scotch/

Acknowledgements

WAKE MAP OF FLAPPING AIRFOIL AND DMD ANALYSIS

HONGYU ZHENG[1], FANGFANG XIE[*], YAO ZHENG[2]

Center for Engineering and Scientific Computation, and School of Aeronautics and Astronautics,
Zhejiang University, Zhejiang 310027, China, fangfang_xie@zju.edu.cn

Keywords: *Flapping airfoil, Radial basis function(RBF) interpolation, Wake map, Dynamic mode decomposition(DMD).*

1.Introduction

The mysterious aerodynamics mechanisms behind flapping wings always draw a great deal of attention of engineering scientists for a long time. Although some progress has been achieved, there are still some unsteady effects undiscovered. Understanding the flapping mechanism may enable the development of more effective flapping wing micro air vehicles.
In 2008, Ramiro and Jean-Luc[1] studied the vortex streets produced by a flapping foil in a hydrodynamic tunnel, using two-dimensional particle image velocimetry, and got the transition points between Bénard-von Kármán (BvK) wake to the reverse BvK(RBvK) vortex street in the flapping frequency-amplitude phase space. On this basis, Anders et al.[2] mapped out the wake types in a phase diagram spanned by the width-based the Strouhal number and the dimensionless amplitude and investigated the relationship between the wake types and aerodynamic forces. In these studies, only the effect of heaving amplitudes is involved. In the current study, we will consider the effect of pitching amplitude, which might enrich the wake types around the flapping foil and bring more interesting phenomena.
More recently, in the postprocessing, there has been more and more emphases on modal decomposition techniques, because these tools are able to extract dynamic information from transient snapshots generated by either experiments or numericial simulations. Shervin[3] decomposed the flow past a cylinder into a sequense of Koopman-modes to analyze the first Hopf bifurcation. Arvind[4] applied the DMD to the plunging airfoil to analyze the deep dynamic stall. All these attempts give us new inspirations to explore the underlying physical mechanisms around the flapping foil.
In the current study, we use the dynamic mesh method based on the radial basis function interpolation to simulate the 2D NACA0012 foil harmoniclly oscillating by varying the flapping frequency and pitching-heaving amplitudes. Accroding to the vortex patterns per oscillation period, we divide the wake flow into six typical types and draw the wake map and lift-drag contour map. Moreover, we apply the DMD to the transient results in one period and obtain the dominant coherent structure of the shedding vortex street.

2.Numercial methods

2.1 Dynamic mesh based on radial basis function interpolation

In the current study, the open-source code OpenFOAM is used for the simulations of the fluid flow around the flapping foil. Here we adopt the RBF interpolation[5] to the dynamic mesh in the OpenFOAM to improve the accuracy and efficiency of meshes since the rotation of boundary is high around the flapping foil. Besides, unlike the classical spring analogy formulations, the dynamic mesh based on RBF interpolation leaves out the grid adjacency relationship and the displacement of each point can be obtained by the interpolation of the movements of the boundary points.

2.2 Dynamic mode decomposition

Compared to the wildly used proper orthogonal decomposition(POD) whose modes are ranked by their energy, DMD ranks the decomposed modes by their mode frequency. Moreover, we use the DMD[6] algorithm to analyze the wake flow around the flapping foil since it can not only extract the coherent structures in the wake flow, also obtain some signicant information such as the growth/decay rate and frequency of each mode.

2.3 Simulation setup and parameters

The sinusoidal motion of the airfoil is defined as:

$$y(t)/c = h\sin(2\pi ft) \qquad (1)$$

$$\theta(t) = \theta_0 \sin(2\pi ft + \phi) \qquad (2)$$

where h is the maximum heaving amplitude, θ_0 is the maximum pitching amplitude, and f is the frequency which is the same in heaving and pitching. The Reynolds number is 1100, and the initial phase $\phi = \pi/2$. The chord length of the foil

c is 1 and the pivoting point is located at the chord line of the foil with a distance 0.3 from the leading edge.

The values of parameters are shown in table 1. All the cases are divided into two groups. Here the heaving amplitude and frequency is kept constant respectively in group 1 and 2 while the values of other two parameters are freely combined.

Table 1: Parameters

Parameters	Group 1	Group 2
Frequency	0.06, 0.08, 0.10, 0.12, 0.14, 0.16 0.18, 0.20, 0.225, 0.25	0.2
Pitching amplitude (°)	5, 10, 20, 30, 40, 50	10, 20, 30
Heaving amplitude (h/c)	1	0.25, 0.375, 0.5, 0.625, 0.75, 0.875, 1

3.Results

3.1 Wake map

The observed wake is divided into six categories, including Bvk wake, vortex string, transition vortex street, RBvK wake, chaotic RBvK and the asymmetry vortex street, as shown in Figure 1. As you can see in Figure 1(a), BvK-type wake appears at a quite small Strouhal number, and the drag is dominant. As the Strouhal number increases, in Figure 1(b), every vortex shedding from the tail of airfoil quickly pairs with another vortex rotating in the opposite direction and then the wake flow becomes a local RBvK vortex street, which we call vortex string. The transient wake can be observed if the Strouhal number continues to increase, as shown in Figure 1(c), where in every half circle, a counter-rotating vortex pair and a series of single vortices are generated. The vortex pair gradually merges with the nearest single vortex as the Strouhal number increases and eventually a wake with the features which resemble a typical RBvK will be emmerged as shown in Figure 1(d). Furthermore, if we keep the Strouhal number fixed and further increase the pitching amplitude, as you can see in Figure 1(e), the RBvK wake will suddenly plunge into chaos with some features of the RBvK wake, which we call chaostic RBvK wake. And when the Strouhal number further increases, in Figure 1(f), a symmetry breaking occurs and this kind of deflected wake is first observed by Bratt[7].

Based on further simulations, we have draw the wake map of the flapping foil in terms of two group of parameters: the width-based frequency with the pitching amplitude in Figure 1(g), and the width-based the heaving with the pitching amplitude in Figure 1(h). BvK is the typical wake type when the heaving amplitude is quite small, while at a low frequency the typical type is vortex string. And then by further increasing the frequency or the heaving amplitude, it will lead the the wake flow transforming into the RBvK wake, and eventually to the asymmetry wake. More notably, as pitching amplitude increases, the transiton point between every two types of wake flow is delayed, that is, the higher the pitching amplitude, the higher the frequency or heaving amplitude of trasition point. And for all the cases the critical pitching amplitude between the RBvK wake and chaotic RBvK wake is approximately $45°$.

3.2 Aerodynamic force contour map

Since the flapping form in the current study is symmetric, the positive lift component generated within the upstroke of the airfoil approximates to the negetive component within the downstroke. So compared with drag or thrust, the value of lift is quite small as shown in Figure 2. When the flapping frequency is small, there is no bound vortex generated, which makes the lift either zero or negetive. As the frequency increases, the vortices begin to attach to the leading edge of the airfoil and the vorticity of bound vortices increases, which results in the increase of lift. Moreover, the increase of pitching amplitude will delay the generation of the bound vortex, hence the lift decreases as the pitching amplitude increases.

The thrust increases as the frequency increases because of the transition from the BvK wake to the RBvK wake[1]. Moreover, in the transition wake or RBvK wake, there is a dominant vortex in the vortex pair, and as the pitching amplitude increases, the vorticity of another vortex whose revoling direction is opposite with the dominant vortex decreases. Therefore, the vorticity of the combined vortex increases, which leads to stronger RBvK vortex street and higher thrust. However, when the pitching amplitude is beyond the critical value $45°$, the chaotic RBvk has a sudden drop of thrust compared with the RBvk wake. As for the cases with the frequency fixed, the effect of the heaving and pitching amplitudes on the aerodynamic forces behaves in a similar way.

3.3 DMD analysis

In this section, DMD is applied for the wake flow of three cases, with the frequency 0.2 and the heaving amplitude 1, and the pitching amplitudes from $20°$ to $40°$. The corresponding Ritz values and mode amplitre spectrum are shown in Figure 3. The four most energetic modes correspond to mode 0-3, where the mode 0 is the average flow and the mode 1 has the same frequency with the flapping foil and the peak of normalized vector energy. Moreover, the Ritz value of all these modes lies on or in the unit circle on the complex plane, which indicates that these modes are stable.

As the pitching amplitude increases, the vorticity of the wake vortex street in all four modes decreases. However, in

(a) $\theta_0 = 10°, h = 0.25, f = 0.20$ (b) $\theta_0 = 10°, h = 1, f = 0.06$ (c) $\theta_0 = 20°, h = 1, f = 0.14$

(d) $\theta_0 = 20°, h = 1, f = 0.20$ (e) $\theta_0 = 50°, h = 1, f = 0.18$ (f) $\theta_0 = 5°, h = 1, f = 0.25$

(g)   (h)
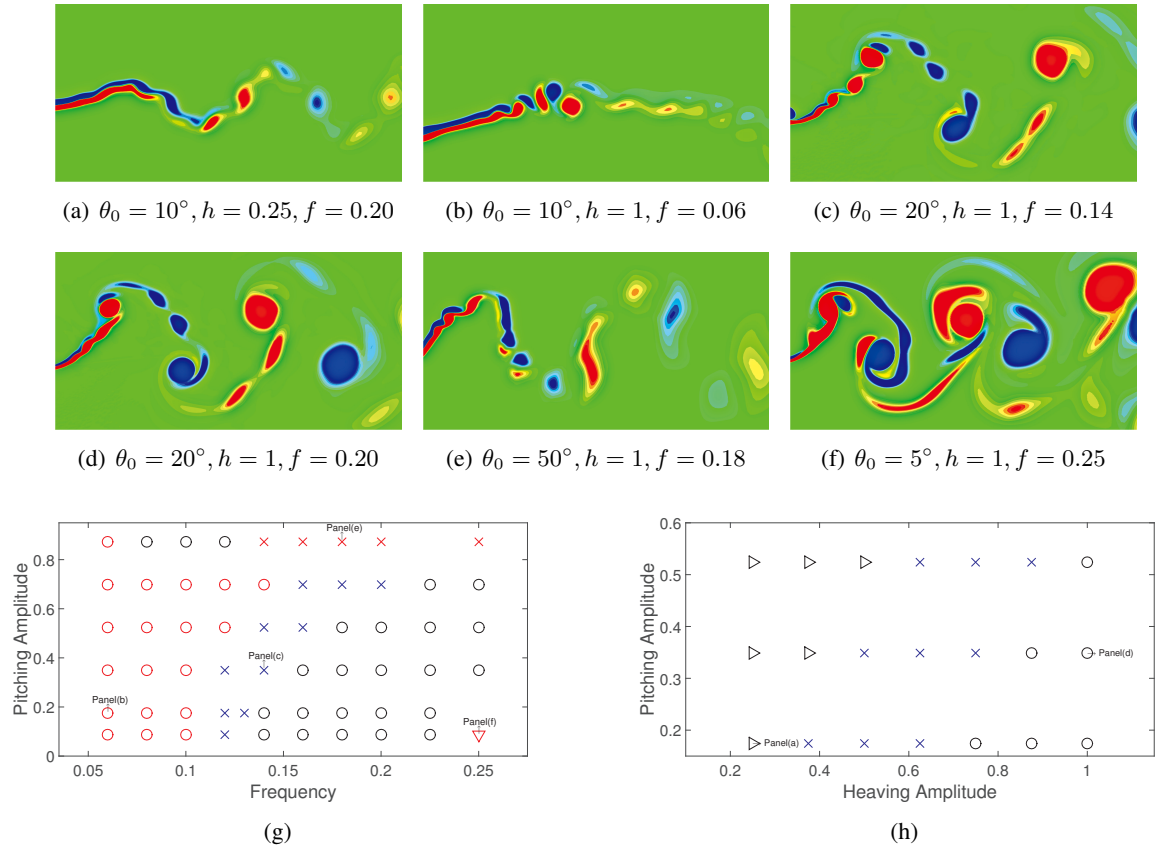
Figure 1: Wake types and wake map. Panel (a) BvK; (b) Vortex string; (c) Transition wake; (d) RBvK; (e) Chaotic RBvK; (f) Asymmetry wake; (g) the wake map of group 1; (h) the wake map of group 2. The simulation points are labeled as: ◯: vortex string; ×: transition wake; ◯: RBvK; ▽: asymmetry wake; ×: chaotic RBvK; ▷: Bvk.

(a)   (b)
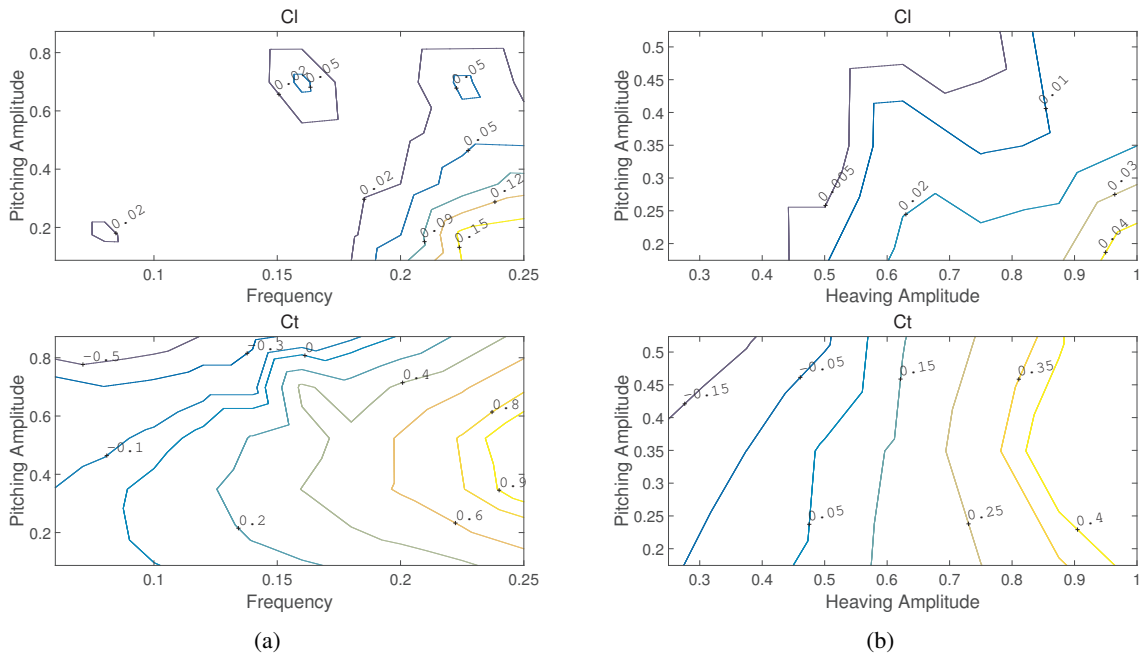
Figure 2: Panel (a) the lift and thrust contour map of gourp 1; (b) the lift and thrust contour map of group 2.

all these modes, there are two series of vortices symmetrically located above and below the equilibrium position of the oscillating motion, as shown in the right column of figure 3. And when the pitching amplitude is 20°, a few vortices will be close to the equilibrium position and even merge with near vortices, which results in a greater loss of vorticity. Moreover, the higher the pitching amplitude, the less this phenomenon appears. And after the pitching amplitude reaches

$30°$, this phenomenon barely appears. Therefore, as the pitching amplitude increases, the vorticity of these modes firstly increases and then decreases and reaches the peak when the pitching amplitude is approximately $30°$, which corresponds with the thrust contour map in Figure 2(a), that is, the corresponding pitching amplitude of the maximum thrust is $30°$.
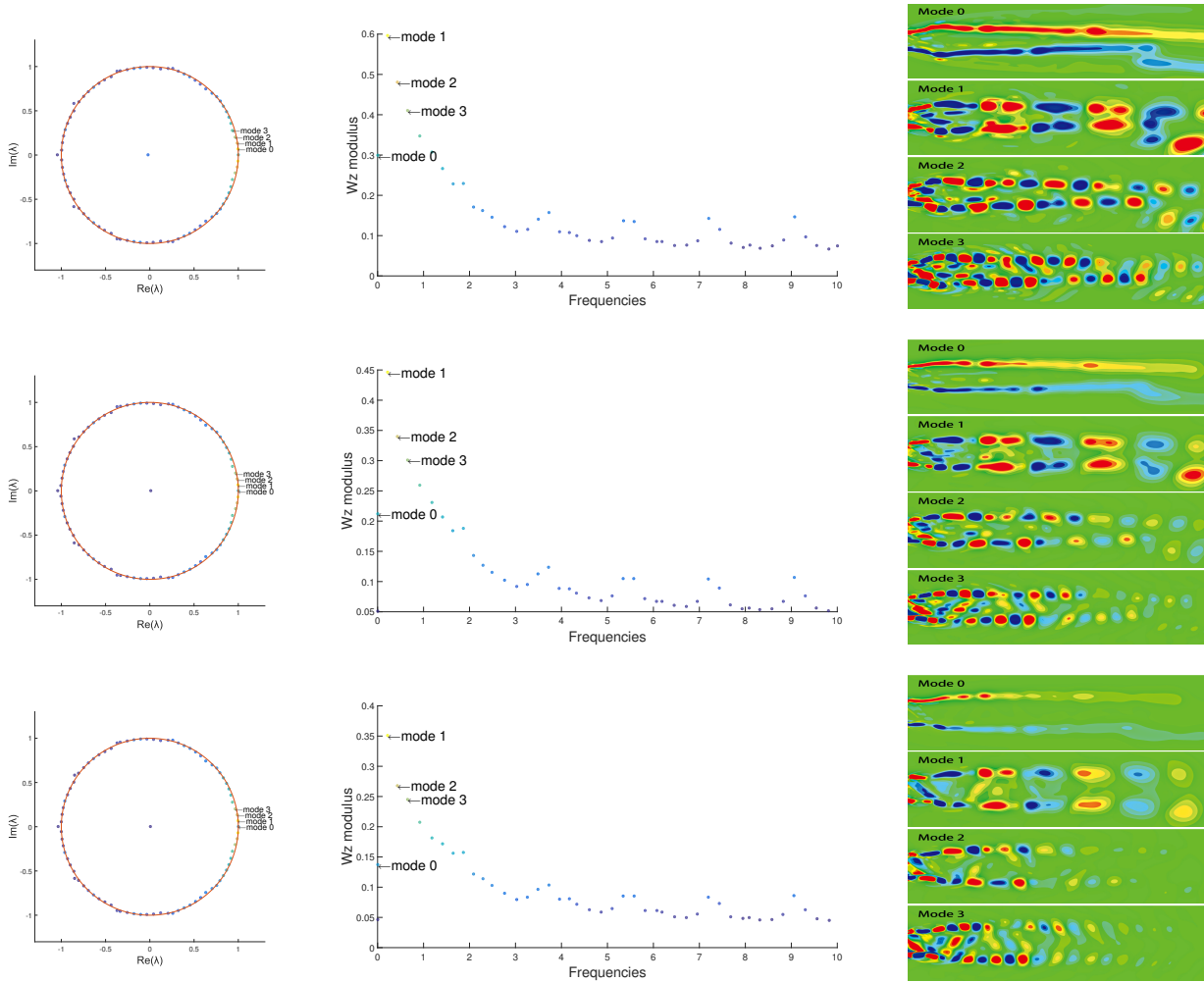
Figure 3: Ritz values computed from the DMD and the dynamic modes are visualized by contours of the vorticity. The pitching amplitudes are respectively $20°$, $30°$, $40°$ from top row to bottom row.

References

[1] R. Godoy-Diana, J.-L. Aider, and J. E. Wesfreid, "Transitions in the wake of a flapping foil," *Physical Review E*, vol. 77, no. 1, p. 016308, 2008.

[2] T. Schnipper, A. Andersen, and T. Bohr, "Vortex wakes of a flapping foil," *Journal of Fluid Mechanics*, vol. 633, pp. 411–423, 2009.

[3] S. Bagheri, "Koopman-mode decomposition of the cylinder wake," *Journal of Fluid Mechanics*, vol. 726, pp. 596–623, 2013.

[4] A. T. Mohan, M. R. Visbal, and D. V. Gaitonde, "Model reduction and analysis of deep dynamic stall on a plunging airfoil using dynamic mode decomposition," in *53rd AIAA Aerospace Sciences Meeting*, 2015, p. 1058.

[5] F. M. Bos, "Numerical simulations of flapping foil and wing aerodynamics: Mesh deformation using radial basis functions," Ph.D. dissertation, Technische Universiteit Delft, 2010.

[6] P. J. Schmid, "Dynamic mode decomposition of numerical and experimental data," *Journal of fluid mechanics*, vol. 656, pp. 5–28, 2010.

[7] J. Bratt, *Flow patterns in the wake of an oscillating aerofoil*. HM Stationery Office UK, 1953, no. 2773.

AERODYNAMIC INVESTIGATION OF A 2D AIRFOIL IN GROUND EFFECT ABOVE WATER USING OPENFOAM

DUAN XUPENG[1], WEI MENG[2], YANG YONG[3]

[1] *School of Aeronautics, Northwestern Polytechnical University, dxpmiller@126.com,*
[2] *AVIC General Aircraft Research Institute, weimeng16092@126.com*
[3] *School of Aeronautics, Northwestern Polytechnical University, yyang@nwpu.edu.cn,*

Based on the OpenFOAM two-phase flow solver, the ground effect of a two-dimensional airfoil above the water surface is studied. The ground effect is intense during the surface taxiing of a seaplane. In order to verify the adaptability of OpenFOAM to this type of problem, the aerodynamic calculation of a simple two-dimensional airfoil above the water surface is investigated. Considering the subsequent need to simultaneously study the two-phase flow of water and gas, the interFoam solver is specifically used to calculate the problem. And both the results of the single-phase and two-phase flow calculation are compared with the experimental data as well. The results show that the ground effect will induce the separation of the airfoil upper wing surface. And also the two-phase flow calculation results of OpenFOAM are different from those of the single-phase flow calculation, but the magnitude of the difference is not very significant in a strong ground effect area close to the water surface.

Introduction

The high-speed taxxing along the surface of amphibious aircraft is a complex process of mechanical phenomena, involving the large-scale high-speed incompressible gas-liquid two-phase flow. To the scope of the author's knowledge, however, research on two-phase flow of amphibious aircraft is quite few. Qu Qiulin of Beihang [1] calculates the problem of the water landing of regional passenger aircraft. Using VOF, 6DOF, and global dynamic grid technology, the ditch landing performance of the upper single wing and high horizontal tail aircraft is studied. Liangjun Qiu [2] of Shanghai Jiaotong University uses the decoupled algorithm to carry out the dynamic simulation of the takeoff process of amphibious aircraft based on commercial software. Besides the complex two-phase flow hydrodynamic computaion, it is also very import to calculate the aerodynamic force accurately using two-phase slover during the taxiing of amphibious aircraft. On this point, this paper will investigate the 2D airfoil gliding on water to reveal the ground effect above the water level using two-phase slover of OpenFOAM.
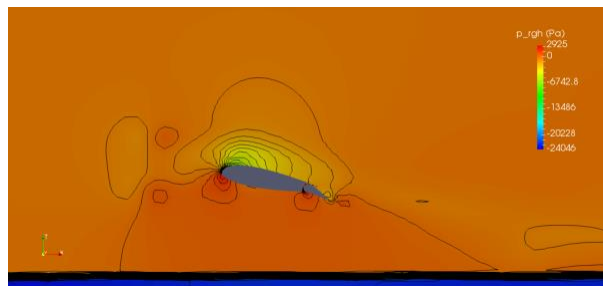
Figure 1: Pressure distribution on a section of the wing and flap
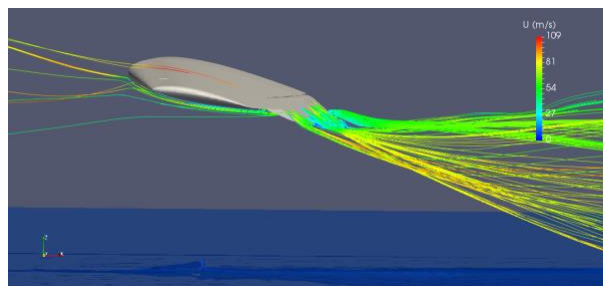
Fig. 2 Streamline passing through flaps at AoA=5 degree

When the angle of attack comes to 5°, there is a small area of separation at the trailing edge of the flap. As shown in Fig. 2, this phenomenon of early occurrence of separation is typical for ground effect. As shown in Figures 1, because of the coexistence of slipstream and ground effect, there is a clear airflow obstruction below the wing, which causes the speed of the airflow above the water surface to slow down and the pressure in the corresponding area to increase.

References

[1] QU Q L, LIU C S, LIU P Q. Numerical Simulation of Water-Landing Performance of a Regional Aircraft, JOURNAL OF AIRCRAFT [J], Vol. 53, No. 6, November-December, 2016.

[2] QIU L J, SONG W B. Efficient Decoupled Hydrodynamic and Aerodynamic Analysis of Amphibious Aircraft Water Takeoff Process [J], JOURNAL OF

COUPLED AERO-HYDRODYNAMIC SIMULATIONS OF TWO FLOATING OFFSHORE WIND TURBINES

YANG HUANG, PING CHENG, DECHENG WAN

State Key Laboratory of Ocean Engineering, School of Naval Architecture, Ocean and Civil Engineering, Shanghai Jiao Tong University, Collaborative Innovation Centre for Advanced Ship and Deep-Sea Exploration, Shanghai, China

Keywords: Floating offshore wind turbines; Tandem layout; Wake interaction phenomenon; Coupled aero-hydrodynamic simulations; FOWT-UALM-SJTU solver.

INTRODUCTION

The floating offshore wind turbines (FOWTs) play a vital role in the development of offshore wind power. It is necessary to study the coupled aero-hydrodynamic characteristics of FOWT in the floating wind farms. However, the complicated environment loads and the coupling effects between wind turbine and floating platform make it difficult to accurately predict the FOWT's coupled aero-hydrodynamic responses under variable wind and wave conditions. Along with the success of the emerging offshore wind industry, floating wind farms are planned for huge amount of clean electricity. In wind farms, wind turbines are usually clustered to decrease the overall installation and maintenance expenses, causing an adverse effect that the wind turbines generally experience a significant increased turbulence because of wake interaction from surrounding wind turbines [1]. Considering the fact that the wake interaction between FOWTs has significant effect on the power output, system dynamic responses and structural loadings, the wake interaction phenomenon in floating wind farms should be paid enough attention.

Based on the open source platform OpenFOAM, our research team developed the CFD solver naoe-FOAM-SJTU to investigate hydrodynamic problems in the field of ship and ocean engineering. And the unsteady actuator line model (UALM) is developed to study the unsteady aerodynamic characteristics of FOWTs. To achieve coupled aero-hydrodynamic simulations of FOWTs, the UALM is embedded into the naoe-FOAM-SJTU to establish a fully coupled CFD analysis tool named FOWT-UALM-SJTU. By using the solver, the validation of unsteady aerodynamic loads is conducted compared to different numerical methods. Moreover, Coupled aero-hydrodynamic simulations of two OC3 Hywindspar FOWT models in tandem layout under shear wind and regular wave conditions are performed.

NUMERICAL METHOD

The actuator line model (ALM) [2] is an effective way to displace the real blade surfaces with virtual actuator lines. In consequence, it acquires a benefit of not requiring to solve the blade geometry layer. In the present work, the unsteady actuator line model (UALM) is used to simulate the unsteady aerodynamics of FOWTs, which is accomplished by modifying the initial ALM to consider the influence of the platform motions on the blades.
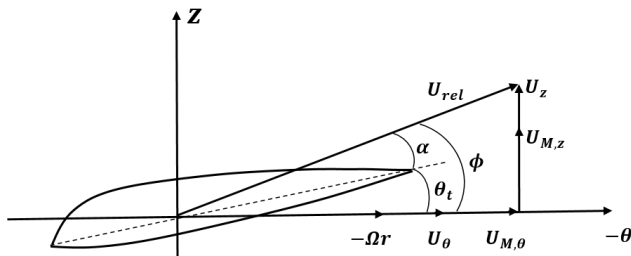
Figure 1: Velocity triangle seen locally on a blade section
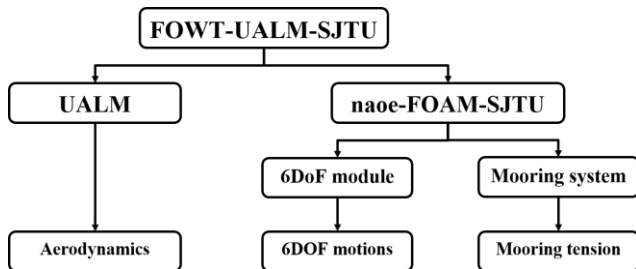
Figure 2: Frame diagram of FOWT-UALM-SJTU
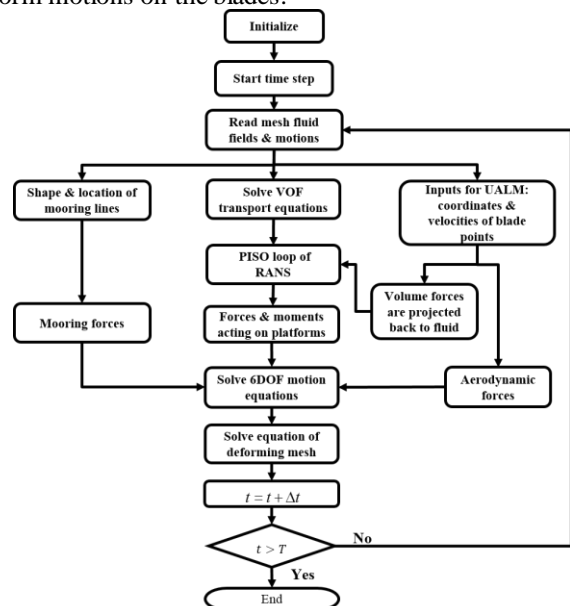
Figure 3: Solving procedure of coupled simulation

To determine the body forces distributed along the actuator lines, a blade element approach combined with two-dimensional airfoil characteristics is used. In Fig.1, a cross-sectional element at radius r defines the airfoil at the (θ, z) plane. Denoting the tangential and axial velocity in the inertial frame of reference as U_θ and U_z, respectively. The relative wind velocity $\vec{U}_{rel}$ seen from the blade section is determined as follows.

$$U_{rel} = U_\theta - \Omega r + U_z + U_M \tag{1}$$

Where Ω is the angular velocity of the rotor, U_M is the six degree of freedoms (DOFs) motion velocity of the actuator point induced by the platform motions.

The attack angle is defined as:

$$\alpha = \varphi - \gamma \tag{2}$$

Where $\varphi = \tan^{-1}\left(\frac{U_z + U_{M,z}}{U_\theta - \Omega r + U_{M,\theta}}\right)$ is the inflow angle with respect to rotor plane. θ_t is the local twist angle. $U_{M,\theta}$ and $U_{M,Z}$ are the projections of U_M on (θ, z) plane. After getting the attack angle, the body forces distributed along the actuator lines are calculated from the local attack angle and a look-up table of airfoil data. And the calculated body forces need to be distributed smoothly on the mesh points near the actuator point by using a 3D Gaussian function, which is the same as the traditional actuator line model.

The frame diagram of FOWT-UALM-SJTU is shown in Fig. 2. The aerodynamic forces can be got by the UALM. And the hydrodynamic responses including six-degree-of-freedom motions and mooring tensions are predicted by the naoe-FOAM-SJTU. In the coupled aero-hydrodynamics simulation code, the governing equations need some modification: a source term f_ε is added on the right side of the N-S equations for the flow field simulation (shown in Eqn (3)). And the solving procedure of coupled aero-hydro simulation for the FOWT system is shown in Fig. 3.

$$\frac{\partial \rho U}{\partial t} + \nabla \cdot (\rho U U) = -\nabla p - g \cdot x \nabla \rho + \nabla \cdot (\mu_{eff} \nabla U) + (\nabla U) \cdot \nabla \mu_{eff} + f_\sigma + f_\varepsilon \tag{3}$$

RESULTS AND DISCUSSIONS

Aerodynamic Validation

The FOWT-UALM-SJTU solver is employed for the aerodynamic validation. And the results of power and thrust are compared with results obtained with FAST-BEM by Jonkman and OVERFLOW2. In Fig. 3, thrust and power results from aerodynamic numerical with FOWT-UALM-SJTU solver show good agreement with other results, which certifies that the FOWT-UALM-SJTU solver is reliable in aerodynamic simulation. Considering the wind turbine in the whole FOWT system experiences six DOF motion , another aerodynamic simulation for turbine rotor with periodic surge motion is conducted for validation . The results are compared with those calculated with overset grid technique [3], and the curves in Fig. 4 show good agreement in both thrust and power of the wind turbine, and the difference between the two curves is no more than 7%. With these validations above, the FOWT-UALM-SJTU solver is proved to be a reliable solver for both steady aerodynamic simulation and unsteady aerodynamic calculations.
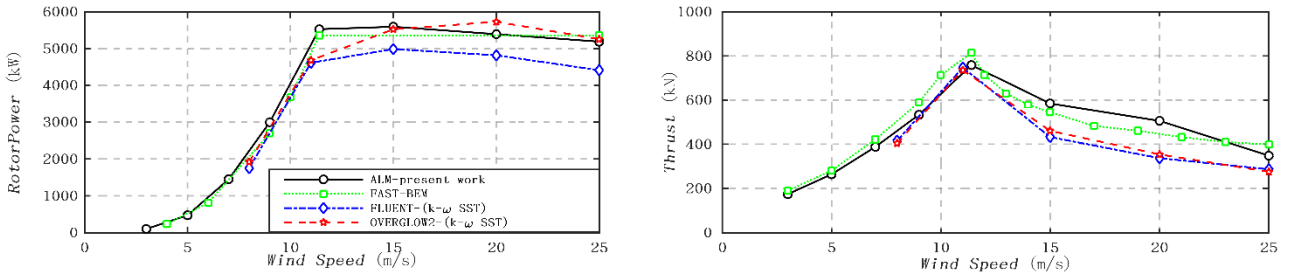
Figure 4: Aerodynamic Simulation Results with Different Numerical Methods
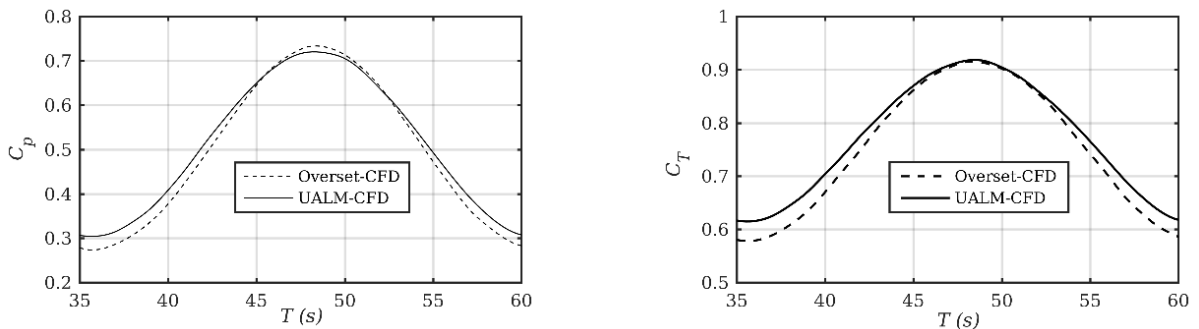
Figure 5: aerodynamic thrust and power of the NREL-5MW baseline wind turbine with periodic surge motion ($s = 8sin(0.246t)$) of platform.

Coupled Aero-hydrodynamic Simulation

Coupled aero-hydrodynamic simulations for two OC3 Hywindspar FOWT models in tandem layout under shear wind and regular wave conditions are carried out based on in-house CFD solver FOWT-UALM-SJTU. To investigate the

influence of motion response of floating support platform on the wake interaction, both the platforms are fixed and the platforms are free to move are taken into consideration: *a*) Fixed case: the platforms are fixed; *b*) Coupled case: the platforms are free to move. Wind and wave conditions are kept in the same in these two cases. Steady wind velocity U=5m/s is adopted. The rotating speed is a fixed value 7.45rpm. Wave period and wave length are $T = 10s$ and $\lambda = 156m$, respectively. And the wave height is $H = 4m$.

The time history curves of the rotor power and the thrust under different simulation conditions are shown in Fig. 6 and Fig. 7. The unsteady aerodynamic loads including the rotor power and thrust of the FOWTs in coupled case both fluctuate greatly and change periodically. The oscillation is believed to be caused by the motion of platform shown in Fig. 8, which makes the relative wind speed changes with the platform motion. Compared with aerodynamic loads in coupled case, the rotor power and thrust in parked case change little over time. It suggests that the aerodynamic loads of the FOWT are greatly influenced by the motions of floating support platform.

Affected by the wake from upstream FOWT, the incoming wind velocity for downstream FOWT is lower than that for upstream FOWT, which leads to the aerodynamic loads of downstream FOWT are much smaller than those of upstream FOWT. The rotor power and the thrust of the downstream FOWTs in fixed case are 94% and 99% compared with those in coupled case, respectively. And the rotor power and the thrust of the upstream FOWTs in fixed case are 85% and 97% compared with those in coupled case, respectively. It indicates that the rotor power and the thrust of FOWTs in coupled case are slightly larger than those of FOWTs in fixed case, which indicates that the motions of floating support platform may have beneficial effects on the aerodynamic loads of the FOWTs. And the influence of platform motions on rotor power is more significant than that on the thrust.
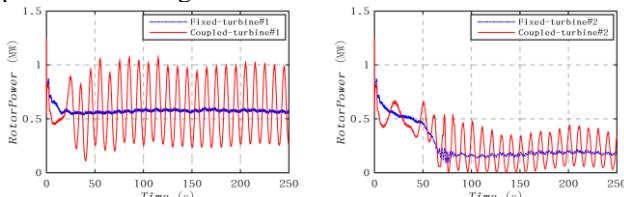
(a) Upstream FOWT	*(b)* Downstream FOWT

Figure 6: Power output of the FOWTs
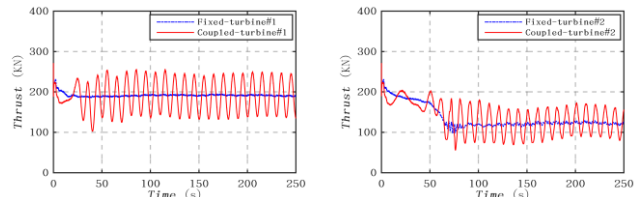
(a) Upstream FOWT	*(b)* Downstream FOWT

Figure 7: Thrust of the FOWTs

The motion responses of floating support platform in coupled case are presented in Fig. 8. The amplitude of surge motion of the upstream platform is larger than that of the downstream platform, resulted from the aerodynamic loads of upstream FOWT are larger than those of downstream FOWT. And the average value of pitch motion of upstream platform is greater than that of downstream platform for the same reason. In addition, the heave motion amplitudes of two platforms are almost the same. It suggests that the aerodynamic loads derived from the wind turbine have remarkable impact on the motion responses of floating support platform, especially for surge motion and pitch motion. While the heave motion is much less influenced by the aerodynamic loads.
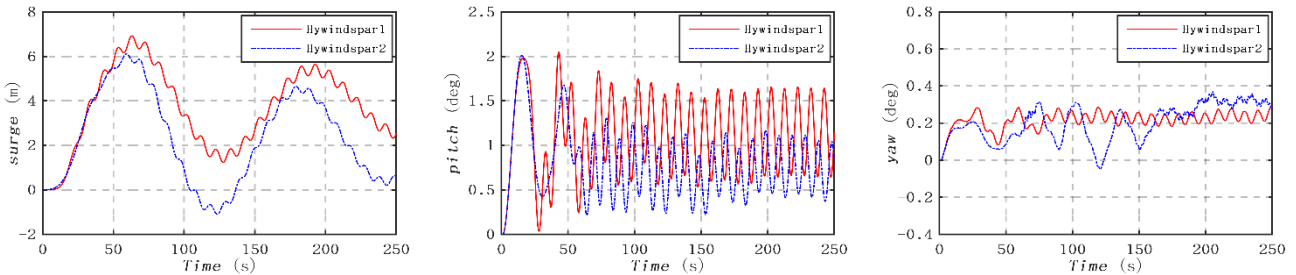
(a) Upstream FOWT	*(b)* Downstream FOWT	*(a)* Upstream FOWT

Figure 8: Platform motion responses in coupled case

The evolution of wake vortex at different times of an entire wave circle in coupled case is illustrated in Fig. 8. The wake vortex of the rotor is visualized by the second-order invariant of velocity gradient, Q, and the free surface is contoured by elevation. Clearly spiral tip vortex from the upstream FOWT is captured, while this vorticity is quickly diffused in the downstream. While the tip vortex of downstream FOWT is not clear. The vorticity diffuses more quickly, and the vortex distance is much smaller compared with that of vortex from upstream FOWT. Due to the wake effect of the upstream FOWT, the axial direction incoming wind speed to the downstream FOWT decreases and the instability of flow field increases. This leads to the instability of the vortex from the downstream FOWT. Moreover, the vortices structures lean backward obviously resulting from the motions of floating support platform.
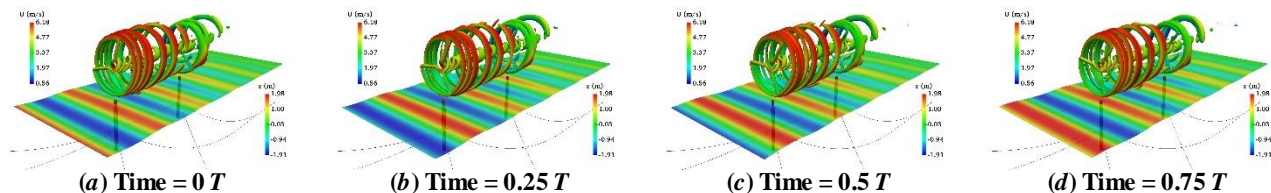
(a) Time = 0 *T*	*(b)* Time = 0.25 *T*	*(c)* Time = 0.5 *T*	*(d)* Time = 0.75 *T*

Figure 9: Instantaneous vortex structure of the rotor and wave height counter in coupled case

CONCLUSIONS

The unsteady actuator line model (UALM) is built up by modifying the traditional ALM based on OpenFOAM. By implementing the UALM into naoe-FOAM-SJTU, the fully coupled aero-hydrodynamic solver named FOWT-UALM-SJTU for the whole FOWT system is developed. Proper fundamental validations for the FOWT-UALM-SJTU solver are carried out, which show that it is reliable on unsteady aerodynamic performance research of wind turbine and on coupled aero-hydrodynamic simulation for the whole FOWT system containing the wind turbine, platform and mooring system respectively. Coupled aero-hydrodynamic simulations of two OC3 Hywindspar FOWT models in tandem layout under shear wind and regular wave conditions are performed with FOWT-UALM-SJTU. Both the platforms are fixed and the platforms are free to move are considered in the simulations. It can be found that the aerodynamic loads of downstream FOWT are much smaller than those of upstream FOWT due to wake interaction. And the platform motions have a bigger effect on the rotor power than that on the thrust. The blade tip vortex from the downstream FOWT become more unsteady owing to the wake interaction. And the platform motions increase the instability of the vortices in the wake. Furthermore, the aerodynamic loads affected greatly by the wake interaction have remarkable impact on the platform motion responses, especially for surge motion and pitch motion. The motion responses of floating support platform increase with the aerodynamic loads.

References

[1] N. Troldborg, GC. Larsen, HA. Madsen, KS. Hansen, JN. Sørensen, and R. Mikkelsen, "Numerical Simulations of Wake Interaction between Two Wind Turbines at Various Inflow Conditions," Wind Energ, vol. 14, no.7, pp. 859-876, 2011

[2] J. N. Sorensen and W. Z. Shen, "Numerical Modeling of Wind Turbine Wakes," J. Fluid Eng., vol. 124, no. June 2002, pp. 393–399, 2002.

[3] T. T. Tran and D. Kim, "Fully coupled aero-hydrodynamic analysis of a semi-submersible FOWT using a dynamic fluid body interaction approach," Renew. Energy, vol. 92, pp. 244–261, 2016.

RESEARCH OF GAS FLOWING CHARACTERISTICS IN KNUDSEN PUMP

XIAOWEI WANG, ZHIJUN ZHANG, PIAOPIAO ZHANG, SHIWEI ZHANG

Northeastern University, 345567074@qq.com

Abstract: Micro Electro Mechanical System(MEMS) is a hot interdisciplinary study, with its miniaturization, low-cost mass production, highly integration, easy expansion and other advantages, which can be widely used in information, electronics, communication, military, biomedical, aerospace and other fields. Therefore, the drive and control of fluid in MEMS is one of the problems that must be solved when researching microfluidic devices. For developing and improving the microfluidic devices, micro-pumps, the drive control engine, are the most important point. The Knudsen pump was first proposed by Danish physicist Martin Knudsen in 1909. Compared to other micro-pumps, it is highly favored in the microfluidic devices application because of the advantages: no complex moving parts, simple structure, long service life, easy mass production, easy expansion, wide energy sources and low energy consumption.

Gas can flow in the channel since the gradient temperature field in the dilute gas, and the functional mechanism of the Knudsen pump is thermal induction flow. The classic Knudsen pump consists of a series of connecting fat and thin channels. Thermal creep effect is based on the gradient temperature which parallels to the wall of channel, which can drive gas flow from the low temperature to the high temperature side. In this paper, the classical Knudsen Pump in rectangular channel model is studied. We analyze the flow characteristics of single gas (Ar, N_2, O_2) respectively and mixed gas (N_2 and O_2) in the pump channels by using Direct Simulation Monte Carlo (DSMC) method based on dsmcFoam solver of OpenFOAM . In addition, how these three different molecular models (Hard-Sphere (HS) model, Variable Hard Sphere (VHS) model, and Variable Soft Sphere (VSS) model) affect the gas flow is also researched by applying self compiling code of Binary Collision Model.

The results indicate that changes in gas compositions, species, and molecular models do not affect the overall distribution and variation of the gas flow in the channels. Under the same parameters, the lighter the molecular mass is, the stronger thermal creep effect (volume flow is larger) becomes, mass flow increases with the mass of the molecules; the thermal creep effect shows a trend of increasing first and then decreasing as the increasing gas pressure, and the smaller the molecular diameter is, the greater the pressure which for the best thermal creep effect is (the smaller the Kn number is). When the proportion of the lighter molecular increases in the mixed gas, it can not only enhance the thermal creep effect but also promote the forward movement of the heavier gas. That is to say, gas with the lighter molecule mass can help the heavier one move forward. Compared with the VSS model that can more practically reflect the movement of gas, the HS model will underestimate the actual performance of the pump, while the VHS model will overestimate the actual performance. While the gas pressure is lower, the movement rule of the VSS model is more consistent with that of HS model. On the contrary, while the pressure is higher, the VSS model movement rule is closer to that of VHS model. In conclusion, the performance of thermal creep flow effect increases with the increase of the gas molecular diameter under the same condition.
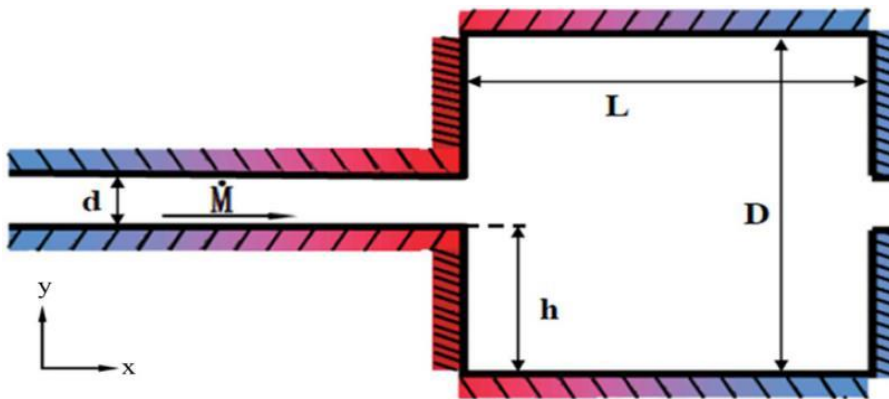
Figure 1: Knudsen pump in rectangular channel model

Table 1: Size and temperature of the model

parameter	d(um)	h(um)	L(um)	D(um)	Tc(K)	Th(K)
value	1	1	4	3	225	375
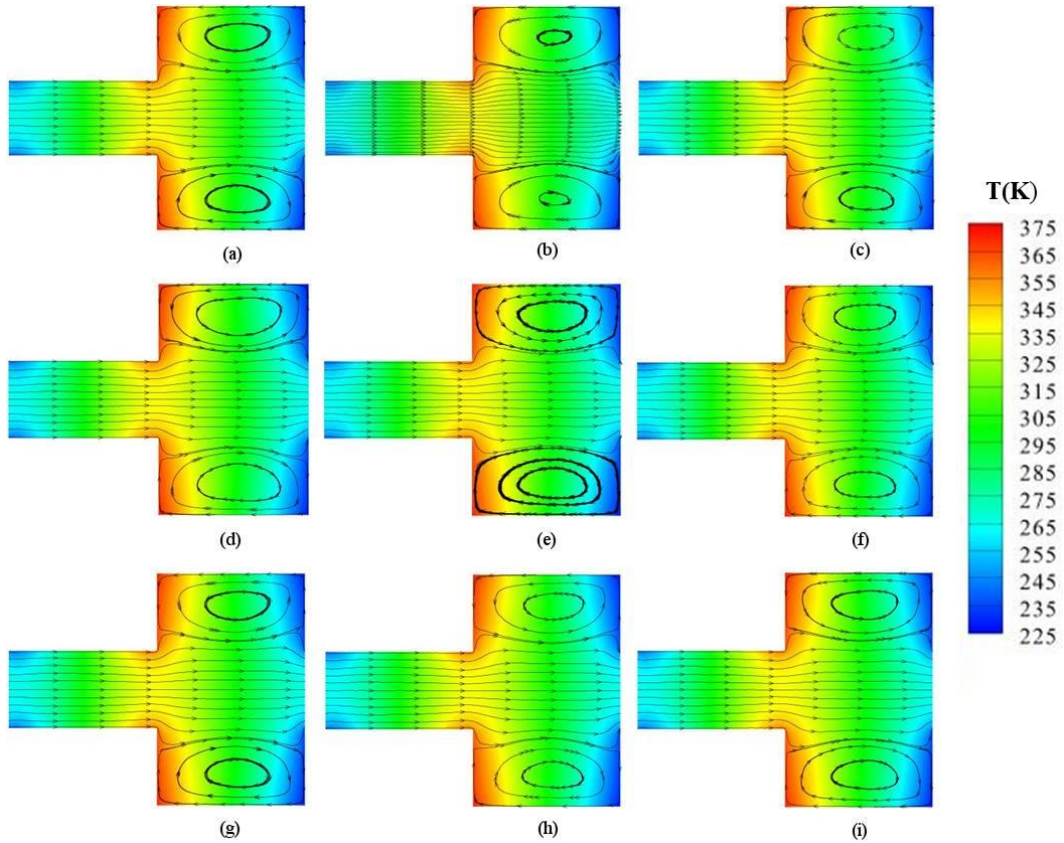
Figure 2: Streamlines and temperature contours for different gas compositions : (a)Ar; (b)N₂; (c)O₂; (d)N₂&O₂=4:1; (e)N₂&O₂=1:1; (f)N₂&O₂=1:4 and different molecular models: (g)HS model; (h)VHS model; (i)VSS model corresponding to case 1.

Table 2: Pressures for different cases

case	1	2	3	4	5	6	7	8	9
Pressure(Kpa)	101.325	71.495	35.747	14.2989	10.214	7.149	3.575	1.430	0.715
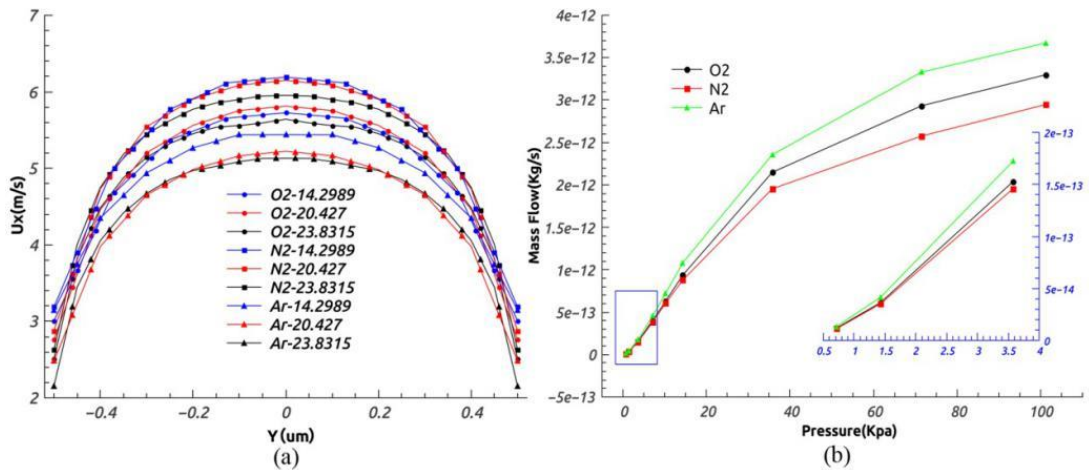
Figure 3: Under different pressures(14.2989,20.427,23.8315), (a)velocity Ux of three different gases for the reference case at X=1. (b) mass flow for three different gas at different pressures.
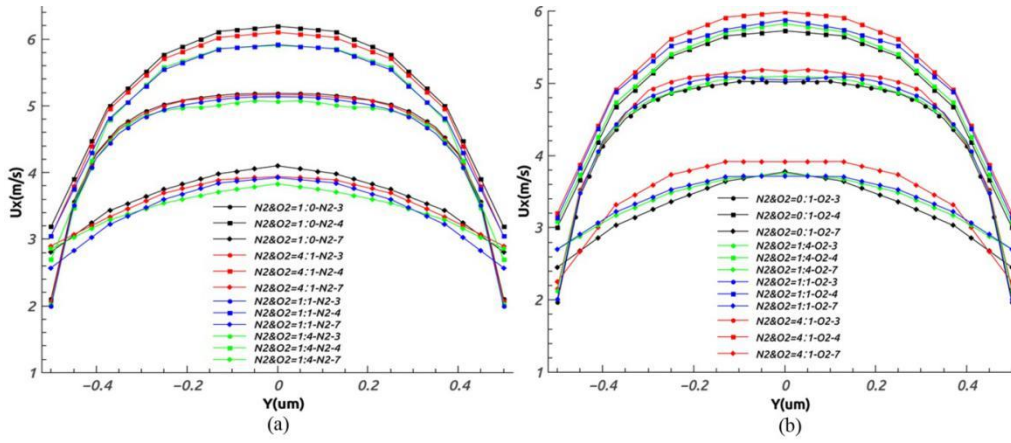
Figure 4: Velocity of three different gases for the reference case at X=1 in cases 3, 4 , and 5.
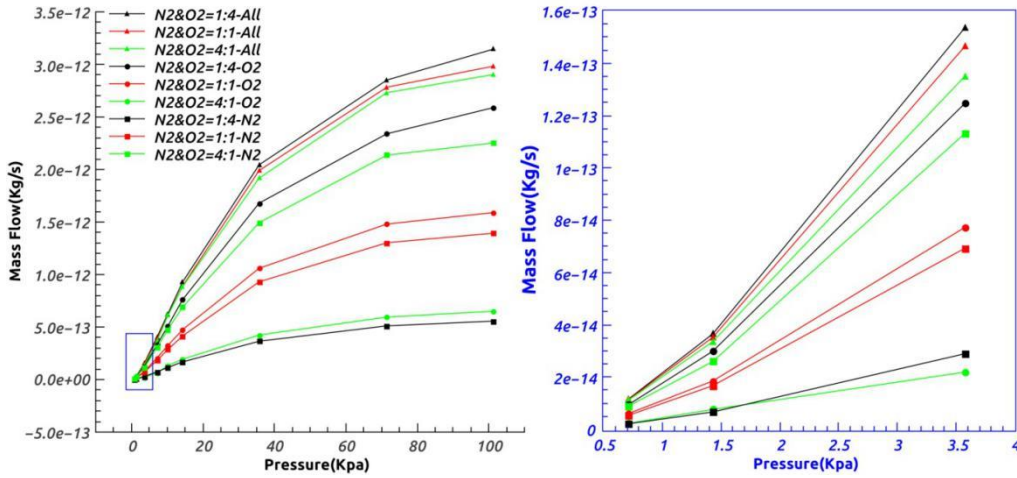
Figure 5: Mass flow and gross mass flow for three mixed gases compositions with the changes of pressure.
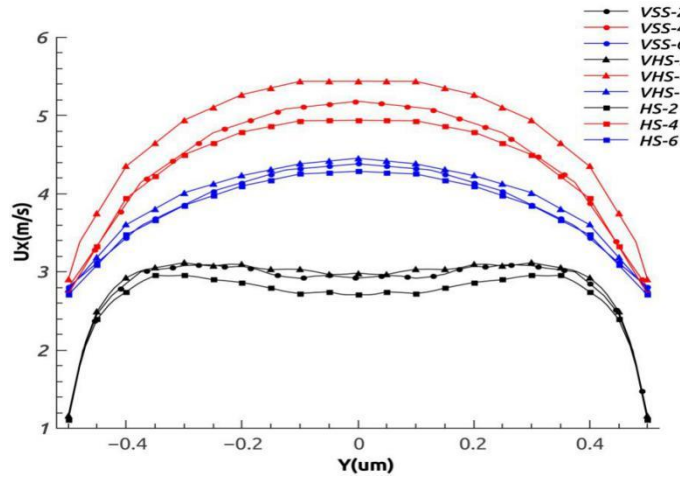
Figure 6: Velocity of three molecular models for X=1 at 2,4,6 case respectively.
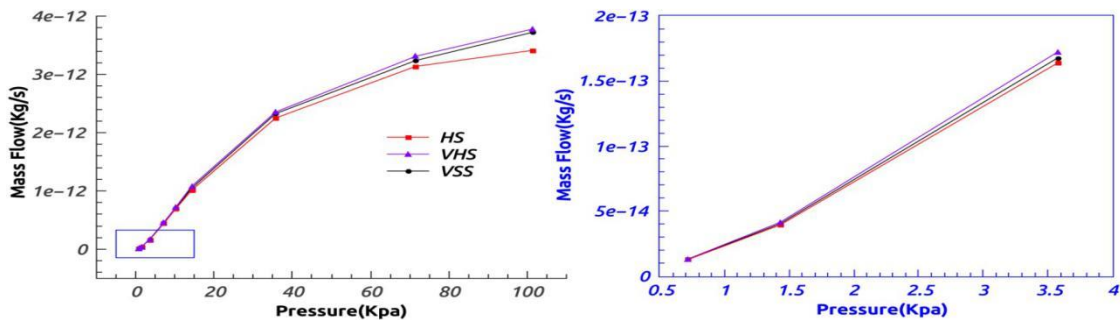
Figure 7: Mass flow changes with the the pressure for three molecular models.

References

[1] M.Knudsen, Eine revision der gleichgewichtsbedingung der gase. Thermische Molekularströmung, Ann. Phys. 336 (1) (1909) 205–229.

[2] Scanlon T J, Roohi E, White C, et al. An open source, parallel DSMC code for rarefied gas flows in arbitrary geometries[J]. Computers & Fluids, 2010, 39(10):2078-2089.

[3] Nakaye S, Sugimoto H, Gupta N K, et al. Thermal method of gas separation with micro-pores[C]// Sensors. IEEE, 2014:815-818.

[4] Szalmas L, Valougeorgis D, Colin S. DSMC Simulation of Pressure Driven Binary Rarefied Gas Flows Through Short Microtubes[C]// ASME 2011, International Conference on Nanochannels, Microchannels, and Minichannels. 2011:279-288.

[5] Vargas M, Naris S, Valougeorgis D, et al. Time-dependent rarefied gas flow of single gases and binary gas mixtures into vacuum[J]. Vacuum, 2014, 109(2):385-396.

[6] Bird G A. Monte Carlo Simulation of Gas Flows[J]. Annual Review of Fluid Mechanics, 2003, 10(8):11-31.

[7] G.A. Bird, Molecular Gas Dynamics and the Direct Simulation of Gas Flows,Clarendon Press, Oxford, 1994.

[8] Han Y L. Thermal-Creep-Driven Flows in Knudsen Compressors and Related Nano/Microscale Gas Transport Channels[J]. Journal of Microelectromechanical Systems, 2008, 17(4):984-997.

Comparison of the strong- and the weak-imposition approach for boundary condition treatments in density-based solvers

Yidao Dong[1], Xiaogang Deng[2], Xiang Gao[3], Min Xiong[4], Guangxue Wang[5]

[1]*National University of Defense Technology, tianyatingxiao@163.com*
[2]*National University of Defense Technology, xgdeng2000@vip.sina.com*
[3]*National University of Defense Technology, gaoxiang12@nudt.edu.cn*
[4]*National University of Defense Technology, xiongmin08@nudt.edu.cn*
[5]*Sun Yat-sen University, wgx111@sina.com*

The imposition of boundary conditions can be classified into two types: the strong- and the weak-imposition approach. The strong approach is to determine the state vectors at the boundary. This approach is generally based on the characteristic theory, where the hyperbolic governing equations are considered to represent the propagation of waves. At the boundary, there are waves propagating into or out of the computational domain. For those outgoing waves, their behaviour is determined entirely by the interior flowfields. While for the ingoing waves, it is often necessary to formulate an approximation of the wave evolution equations at the boundary through the derivation of the Local One-Dimensional Inviscid (LODI) relations. Corresponding researches can be originated from Thompson [1]. Poinsot and Lele [2] proposed a new formulation using characteristic wave relations through boundaries. Kim and Lee [3] generalized the characteristic boundary conditions in curvilinear coordinates for computational aeroacoustics. To account for the multi-dimensional flow effect as well as the viscous and reaction effects, Yoo et al. [4, 5] improved the characteristic boundary condition. Lodato et al. [6] incorporated transverse terms and carried out direct and large-eddy simulation for three dimensional viscous flows. It should be pointed out that for the edge and corner boundaries, special treatments were proposed [6]. Actually, when considering the influence of transverse terms, this complicated procedure is unavoidable. Apart from these, Gross and Fasel [7] introduced additional ghost cells to apply the characteristic boundary condition. Recently, Motheau et al. [8] extended the characteristic ghost-cell boundary condition to include the transverse terms. All the above-mentioned research is conducted on the structured grid. Granet et al. [9] applied the characteristic boundary condition to cell-vertexed schemes and compare different nonreflective outlet boundary conditions.

In comparison, the weak imposition approach aims at constructing the numerical flux, rather than obtaining the boundary state vectors directly. Approximate Riemann solvers are utilized to calculate the numerical flux at the boundary. Therefore, the left and the right state vectors need to be specified. This approach is widely applied in the framework of Finite Volume [10] and Discontinuous Finite Element methods [11]. It should be noted that recent researches for Discontinuous Galerkin methods [12, 13, 14, 15] are concentrating on the high-order representation of the curved boundary instead of the method for the acquisition of the numerical flux. However, for the treatment of boundary conditions like the subsonic inlet and outlet, it is always very complicated to obtain the left and the right state vectors, where isentropic relations as well as Riemann invariants are often utilized. To avoid the complexity, some new techniques are required. Actually, as early as 1994, Atkins and Casper [16] proposed an approach based on the finite wave model to nonreflective boundary conditions, including the subsonic inlet and outlet, for high-order methods on the structured grid. This approach employed the exact solution to finite waves to relate interior state vectors and ambient conditions to boundary values. And the high-order convergence was preserved independent of wave amplitude.

In [17], we compared the weak-imposition approach named as the Riemann method with the simple ghost-cell method. In this paper, the Riemann method is compared with the characteristic ghost-cell method. For convenience, in the following, the Riemann method and the Characteristic ghost-cell method are denoted as "Riemann" and "Characteristic" respectively. First of all, the circular explosion is simulated in the square domain $x \times y = [-0.05, 0.05] \times [-0.15, 0.15]$ with triangular grid. All boundary conditions are defined as outlet. This case is to test the non-reflecting characteristics of methods for boundary condition treatments. The pressure is initialized as

$$p - p_\infty = \begin{cases} 1, & if \ r < 0.0015 \\ 0, & otherwise \end{cases} \tag{1}$$

where $r^2 = x^2 + y^2$. Other flow variables are initialized as $u = v = 0$, $T = 1$ and $p_\infty = 1/\left(\gamma M^2\right)$ with $M = 0.1$. The time step for the numerical simulation is set as $\Delta t = 3 \times 10^{-5}$. The simulation ends at $t = 0.048$
In figure 1, the root mean square of the pressure perturbation is displayed. With both methods for the boundary condition treatment, the pressure fluctuation converges to 0. In figure 1, the pressure perturbation at $t = 0.012$ is illustrated. It
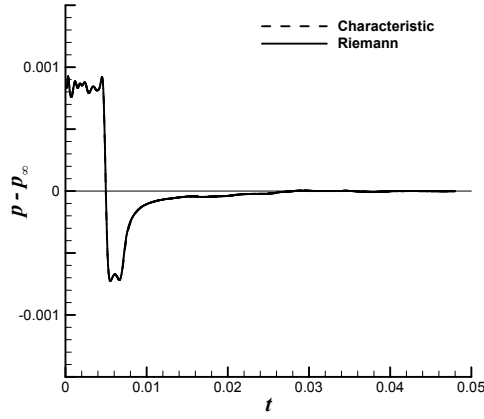
Figure 1: Root mean square of pressure perturbation for circular explosion

(a) Characteristic   (b) Riemann
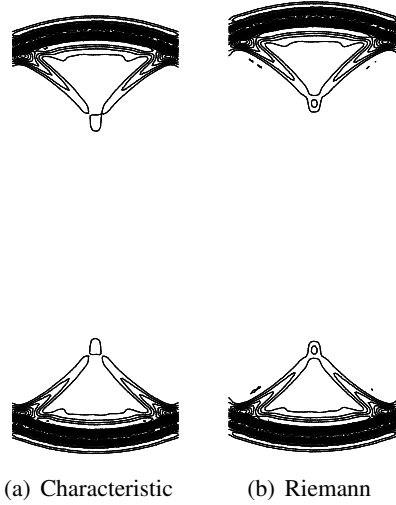
Figure 2: Pressure perturbation at $t = 0.012$ on triangular grid for the circular explosion

can be seen that no big difference exists for these two methods. Only slight reflection is observed at the outlet. In this section, the isentropic supersonic flow is simulated and the analytical solution is given. The computational domain is two concentric circular arcs of radius $r_i = 1$ and $r_o = 1.384$ in the first quadrant. These two circular arcs represent the inviscid wall boundary, and the flow in the inlet and the outlet are supersonic. The exact solution of this case can be found in [12] and is given below,

$$\rho = \rho_i \left(1 + \frac{\gamma - 1}{2} M_i^2 \left(1 - \left(\frac{r_i}{r}\right)^2\right)\right)^{(1/(\gamma-1))},$$
$$P = \frac{\rho^\gamma}{\gamma}, \tag{2}$$
$$||\vec{v}|| = \frac{c_i M_i}{r}.$$

where the Mach number in the inner radius is $M_i = 2.25$ and the density is $\rho_i = 1$. The sound speed is calculated as,

$$c_i = \sqrt{\gamma \frac{p_i}{\rho_i}} = 1. \tag{3}$$

In Fig. 3, the triangular grid is shown, along with the pressure contour. Obviously, the contour calculated with the Riemann method is more similar to the analytical solution.

In Fig. 4, the pressure error is illustrated. Second order of accuracy is achieved in both the global and the wall region for the Riemann method. While for the Characteristic method, only first-order of accuracy is obtained.

(a) The triangular grid   (b) Riemann   (c) Characteristic
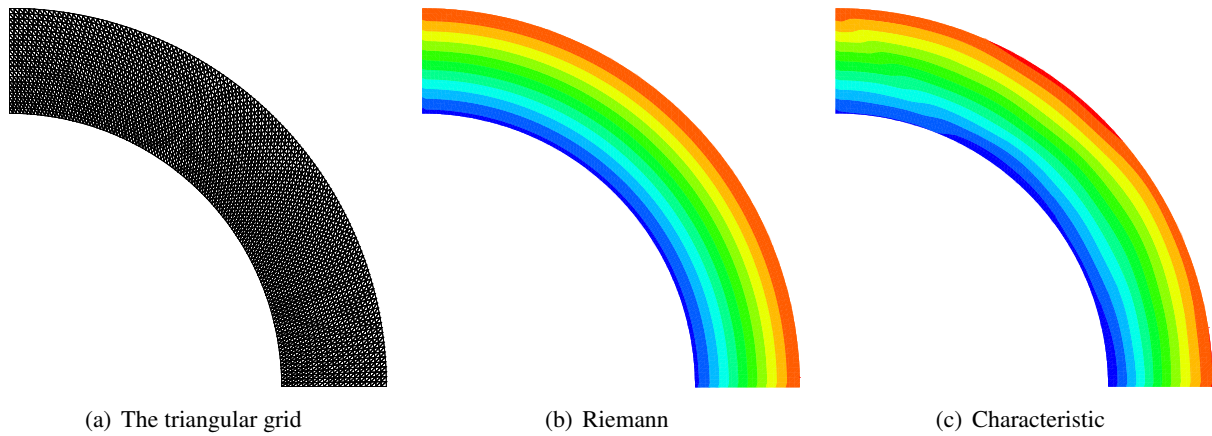
Figure 3: The triangular grid and corresponding pressure contour of the supersonic vortex flow

(a) Global error   (b) Wall error
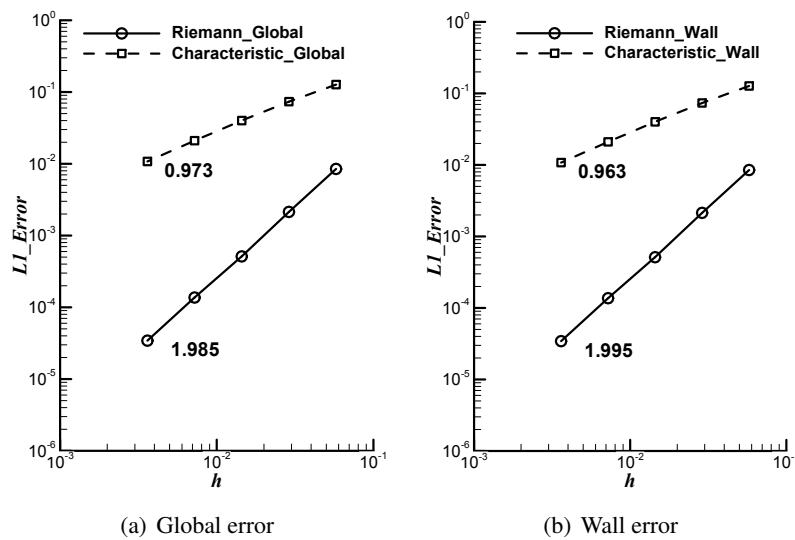
Figure 4: The pressure error of the supersonic vortex flow

References

[1] K. W. Thompson, "Time-dependent boundary conditions for hyperbolic systems," *J Comput Phys*, vol. 68, pp. 1–24, 1987.

[2] T. J. Poinsot and S. K. Lele, "Boundary conditions for direct simulations of compressible viscous flows," *J Comput Phys*, vol. 101, pp. 104–129, 1992.

[3] J. W. Kim and D. J. Lee, "Generalized characteristic boundary conditions for computational aeroacoustics," *AIAA J*, vol. 38, pp. 2040–2049, 2000.

[4] C. S. Yoo, Y. Wang, A. Trouvé, and H. G. Im, "Characteristic boundary conditions for direct simulations of turbulent counterflow flames," *Combust Theor and Modell*, vol. 9, pp. 617–646, 2005.

[5] C. S. Yoo and H. G. Im, "Characteristic boundary conditions for simulations of compressible reacting flows with multi-dimensional, viscous and reaction effects," *Combust Theor Modell*, vol. 11, pp. 259–586, 2007.

[6] G. Lodato, P. Domingo, and L. Vervisch, "Three-dimensional boundary conditions for direct and large-eddy simulation of compressible viscous flows," *J Comput Phys*, vol. 227, pp. 5105–5143, 2008.

[7] A. Gross and H. F. Fasel, "Characteristic ghost-cell boundary condition," *AIAA J*, vol. 45, pp. 302–306, 2007.

[8] E. Motheau, A. Almgren, and J. B. Bell, "Navier-Stokes characteristic boundary conditions using ghost cells," in *AIAA-2017-3625*, 2017.

[9] V. Granet, O. Vermorel, T. Lonard, and L. Gicquel, "Comparison of nonreflecting outlet boundary conditions for compressible solvers on unstructured grids," *AIAA J*, vol. 48, pp. 2348–2364, 2010.

[10] J.-R. Carlson, "Inflow/outflow boundary conditions with application to FUN3D," NASA/TM-2011-217181, Tech. Rep., 2011.

[11] F. Bassi and S. Rebay, "High-order accurate discontinuous finite element solution of the 2D euler equations," *J Comput Phys*, vol. 138, pp. 251–285, 1997.

[12] L. Krivodonova and M. Berger, "High-order accurate implementation of solid wall boundary conditions in curved geometries," *J Comput Phys*, vol. 211, pp. 492–512, 2006.

[13] T. Toulorge and W. Desmet, "Curved boundary treatments for the discontinuous galerkin method applied to aeroacoustic propagation," in *AIAA 2009-3176*, 2009.

[14] H. Gao, Z. J. Wang, and Y. Liu, "A study of curved boundary representations for 2D high order euler solvers," *J Sci Comput*, vol. 44, pp. 323–336, 2010.

[15] X. Zhang, "A curved boundary treatment for discontinuous galerkin schemes solving time dependent problems," *J Comput Phys*, vol. 308, pp. 153–170, 2016.

[16] H. Atkins and J. Casper, "Nonreflective boundary conditions for high-order methods," *AIAA J*, vol. 32, pp. 512–518, 1994.

[17] Y. Dong, X. Deng, X. Gao, M. Xiong, and G. Wang, "A comparative study of boundary conditions for the density-based solvers in the framework of openfoam," *Comput Fluids*, in Press, 2018.

A COMPUTATIONAL FLUID DYNAMICS STUDY OF STREET-LEVEL VENTILATION IN URBAN AREAS

CHUN-HO LIU[1], WAI-CHI CHENG[2], WENYE LI[3], ZIWEI MO[4], ZHANGQUAN WU[5],
LILIAN Y.L. CHAN[6], W.K. KWAN[7], Hing Tuen YAU[8]

[1]*Department of Mechanical Engineering, The University of Hong Kong, liuchunho@graduate.hku.hk*
[2]*Department of Mechanical Engineering, The University of Hong Kong, wccheng2007@yahoo.com.hk*
[3]*Department of Mechanical Engineering, The University of Hong Kong, liwenye@connect.hku.hk*
[4]*Department of Mechanical Engineering, The University of Hong Kong, ziwei.mo@gmail.com*
[5]*Department of Mechanical Engineering, The University of Hong Kong, wzqmec@gmail.com*
[6]*Information Technology Services, The University of Hong Kong, lilianyl@hku.hk*
[7]*Information Technology Services, The University of Hong Kong, hcxckwk@hku.hk*
[8]*Information Technology Services, The University of Hong Kong, billyau_hpc@hku.hk*

Introduction

Economic activities and industrialization unavoidably lead to degrading street-level ventilation and elevating pollutant concentrations in urban areas. Buildings, skyscrapers and infrastructures in metropolises collectively form complicated urban morphology in which the dynamics is different from that in the atmospheric boundary layer (ABL) aloft. Under this circumstance, the conventional (meso-scale) meteorology models would not be fully applicable to diagnose the problems in details [1, 2, 3]. Engineering computational fluid dynamics (CFD), such as OpenFOAM [4], is commonly used to tackle the problems in refined micro-scale. The protocol of using building information for OpenFOAM CFD studies in the city ventilation perspective is reported in this paper.

Methodology

Detailed information of buildings and terrain is collected from the Lands Department, The Hong Kong Special Administrative Region (HKSAR) [5]. The digital maps are three-dimensional (3D) spatial data of the HKSAR territory that include buildings (commercial and residential), infrastructure (roads and bridges) and natural terrain (mountains and slopes) for land assessment, engineering visualization and air ventilation analysis, etc. The 3D geometric models are available in virtual reality modeling language (VRML) format. In this paper, we use one of the HKSAR downtown areas as an example to demonstrate the solution protocol (Figure 1 (a)). The digital models in the files are divided into tile basis so MeshLab [6] is used to assemble and convert the VRML files to STL format for subsequent input into CFD and discretization. The STL files of building information are then merged with the OpenFOAM mesh generation utility *blockMesh* and are discretized by *snappyHexMesh* to 3D unstructured meshes. The mesh generator *snappyHexMesh* uses the triangulated surface geometries in the STL files to generate 3D meshes, approximating the solid surfaces. It also refines the surfaces iteratively to morph the buildings by split-hex meshes to the facades and ground in high spatial resolution. Additional layers of refined spatial resolution are fabricated as well to improve the accuracy of near-wall-flow calculation. The STL model of downtown HKSAR areas, which is reduced in scale approximately 1:300, is discretized into over 5 million hexahedral cells for subsequent CFD calculation (Figure 1 (b)).

Mathematical Models and Numerical Methods

Reynolds-averaged Navier-Stokes (RANS) k-ϵ turbulence model of OpenFOAM version 4.1 is used in this paper. It is assumed that the flows are isothermal and incompressible that are calculated by the continuity and the momentum conservation. Turbulence is modeled by the standard RANS k-ϵ model with the conservation equations of turbulence kinetic energy (TKE) k and TKE dissipation rate ϵ. The CFD spatial domain (1:300 reduced scale) sizes 14 m (length) $\times$ 2.7 m (width) $\times$ 4 m (height), covering one of the downtown areas in HKSAR. No-slip boundary conditions (BCs) are applied on all the solid boundary and a shear-free BC along the top. Neumann BCs of flows are applied on the spanwise boundaries. The prevailing wind is prescribed by an inflow boundary at the upstream inlet together with an outflow
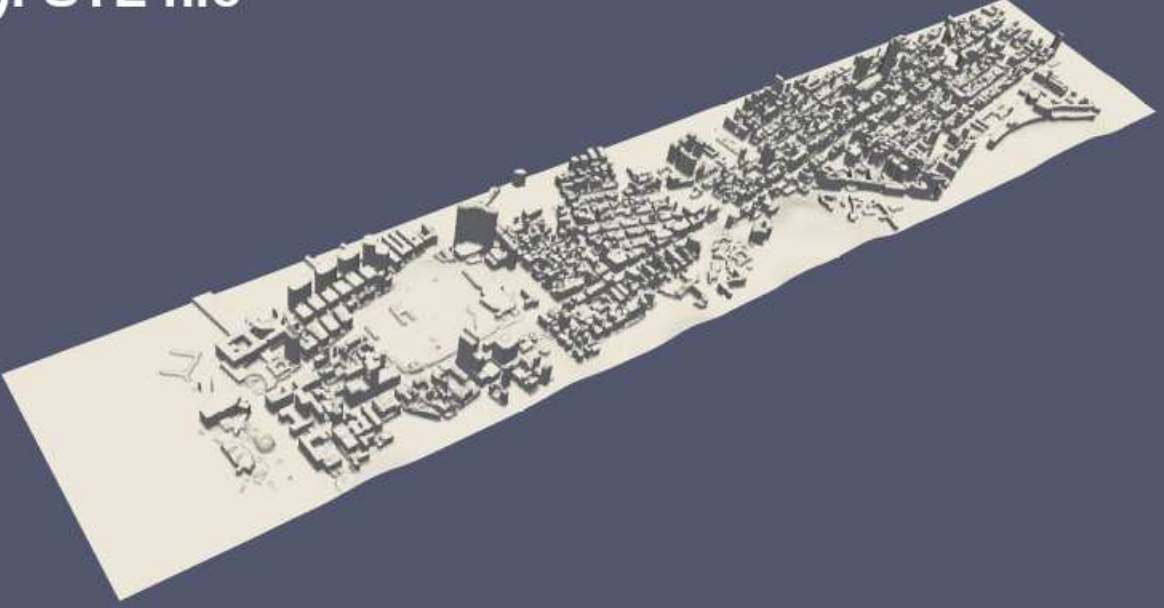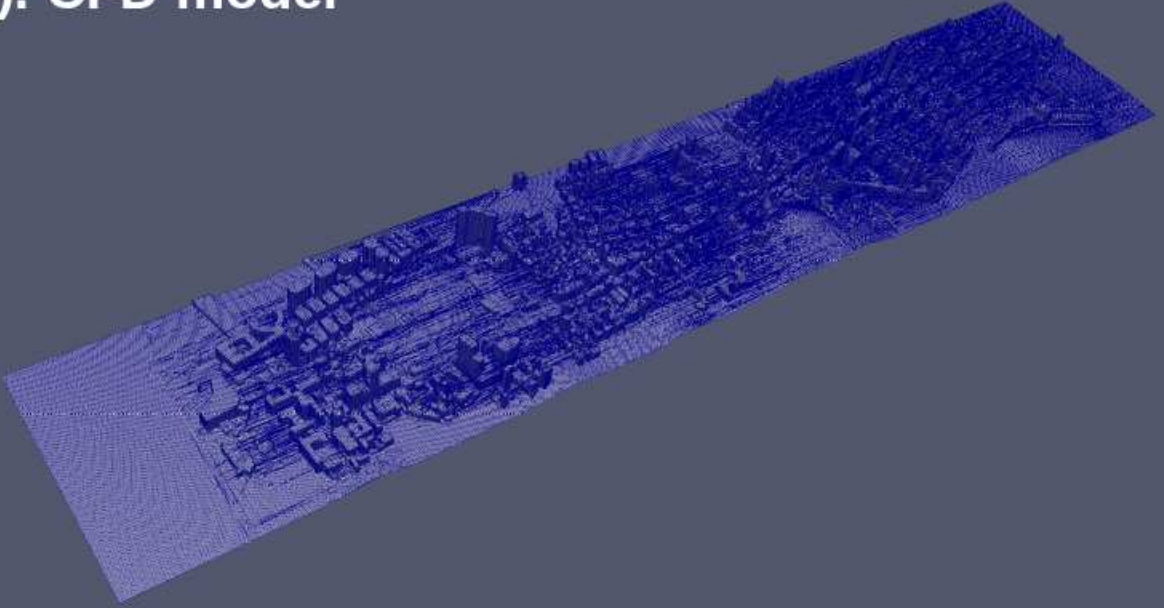
Figure 1: Preprocessing of building information from (a). STL file to (b). CFD model of downtown HKSAR.

boundary at the downstream outflow [7]. The inflow wind profile is given by the power law

$$U(z) = U_s (z/z_s)^\alpha \tag{1}$$

where U_s is the wind speed at reference height z_s (= 1 m) and α (= 0.2) the power-law exponent. The BCs of k and ϵ are

$$k(z) = 0.01 \times U_s^2 \times (z/z_s)^{-0.1} \tag{2}$$

(10% turbulence intensity) and

$$\epsilon(z) = C_\mu^{1/2} k(z) \times U_s/z_s \times (z/z_s)^{\alpha-1} \tag{3}$$

(TKE production equal to dissipation), respectively, where C_μ (= 0.09) is a modeling constant. The prevailing wind enters the spatial domain from the upstream inflow is free of pollutant ($\phi = 0$). An area source of tracer with constant concentration Φ_0 is placed on the ground right after the upstream inflow. Neumann BCs of tracer are applied on the

domain top, spanwise extent and all the solid boundaries. An open BC is prescribed at the downstream outflow so the tracer are removed from the computational domain without any reflection.

Over 5 million finite volume (FV) cells are used to discretize the spatial domain. Trial runs based on approximately 1 million and 3 million FV cells have been performed to check the grid dependence. The minimum and maximum cell volume is about 8×10^{-8} m^{-3} and 4×10^{-5} m^{-3}, respectively. The OpenFOAM standard solver *simpleFoam* is used to solve the steady-state problem. The first-order upwind scheme is employed for all the CFD variables. Successive overrelaxation method is adopted to solve the equation systems. The residuals of all the results presented in this paper are less than 10^{-6}. The Reynolds number (Re) based on free-stream wind speed and domain height is almost 3×10^{6} that is sufficiently large for turbulent flows in neighborhood scale.

Preliminary Findings

Figure 2 (a) shows the wind flows over the urban-area model of downtown HKSAR. A turbulent boundary layer (TBL) is clearly developed in which the wind speed U increases in the wall-normal direction z. The reduction in wind speed in the vicinity of buildings (less than 50% of free-stream wind speed) is clearly depicted, signifying the drag induced by (rough) urban areas and the impact on street-level ventilation. It is clearly shown that the wake behind one of the high-rise buildings, whose size extends almost to the domain outflow, substantially slows down the flows so the potential impact from individual high-rise buildings (on the entire neighborhood) should be assessed. The pressure on the windward facade of that building is large so we also need to pay attention to the turbulence and gust upwind (wind hazard). The domain inflow a harbor so the impingement on the coastal buildings are notable. A zone of low pressure is clearly observed after the coastal buildings, implying the formation of recirculating flows (i.e. weakened aged air removal) at the canopy level. The streamlines help illustrate how the background flows are modified by the buildings. Similarly, the influence of individual high-rise buildings is substantial. The flows in their wakes slow down (or even reverse flows), leading to weakened wind breeze even the local building density is not high. Under this circumstance, the (adverse) environmental impact of buildings could be beyond their length scale.

A hypothetical ground-level line source of tracer is included in the computational domain to examine the tracer transport. It is placed in crossflows so the dispersion is essentially two-dimensional (2D) on the streamwise-vertical (x-z) plane. Figure 2 (b) depicts the tracer distribution over the urban-area model of downtown HKSAR. Ground-level concentration ϕ decreases exponentially in the streamwise direction that is similar to behavior of the conventional plume dispersion over smooth surfaces. It thus arouses our interest of developing a Gaussian dispersion model for urban setting. Isosurfaces of tracer concentration illustrate an interesting finding of the enhanced mixing in the wakes after high-rise buildings. The building blockage diverts the flows, initiating eddies in the wake region. Those eddies are large in size in which the scales of both the velocity and length are substantially enlarged that collectively strengthen the plume dispersion and mixing processes. Hence, the ground-level tracer concentrations in the wakes of high-rise buildings could be (unreasonably) low that cannot be estimated accurately by the current tracer transport models.

Concluding Remark

The protocol of using OpenFOAM modeling urban-area street-level ventilation is briefly introduced. The complicated building morphology is digitized by *snappyHexMesh* to 3D unstructured hexhedrons. Preliminary findings highlight the importance of high-rise buildings on street-level wind environment that could be beyond their length scale. Moreover, large-scale eddies are generated in the wakes after high-rise buildings that could enhance the tracer dispersion. Additional CFD sensitivity tests are being undertaken to examine the roles of buildings in a city in the environmental perspective. More results and findings will be reported in the workshop.

Acknowledgments

References

[1] W. C. Cheng and C.-H. Liu, "Large-eddy simulation of flow and pollutant transports in and above two-dimensional idealized street canyons," *Boundary-Layer Meteorol.*, vol. 139, no. 3, pp. 411–437, 2011.

[2] Z. Wu and C.-H. Liu, "Time scale analysis of chemically reactive pollutants over urban roughness in the atmospheric boundary layer," *Int. J. Environment and Pollution*, vol. 62, no. 2/3/4, pp. 264–273, 2017.

[3] Z. Mo and C.-H. Liu, "Wind tunnel measurements of pollutant plume dispersion over hypothetical urban areas," *Build. Environ.*, vol. 132, pp. 357–366, 2018.

[4] H. G. Weller, G. Tabor, H. Jasak, and C. Fureby, "A tensorial approach to computational continuum mechanics using object-oriented techniques," *Comput. Phys.*, vol. 12, no. 6, pp. 620–631, Nov/Dec 1998.

[5] "Lands Department, the Government of the Hong Kong Special Administrative Region of the People's Republic China," https://www.landsd.gov.hk/, accessed: March 31, 2018.

[6] "Meshlab," https://www.meshlab.net/, accessed: March 31, 2018.

[7] Y. Tominaga, A. Mochida, R. Yoshie, H. Kataoka, T. Nozu, M. Yoshikawa, and T. Shirasawa, "AIJ guidelines for practical applications of CFD to pedestrian wind environment around buildings," *J. Wind Eng. Ind. Aerodyn.*, vol. 96, pp. 1749–1761, 2008.
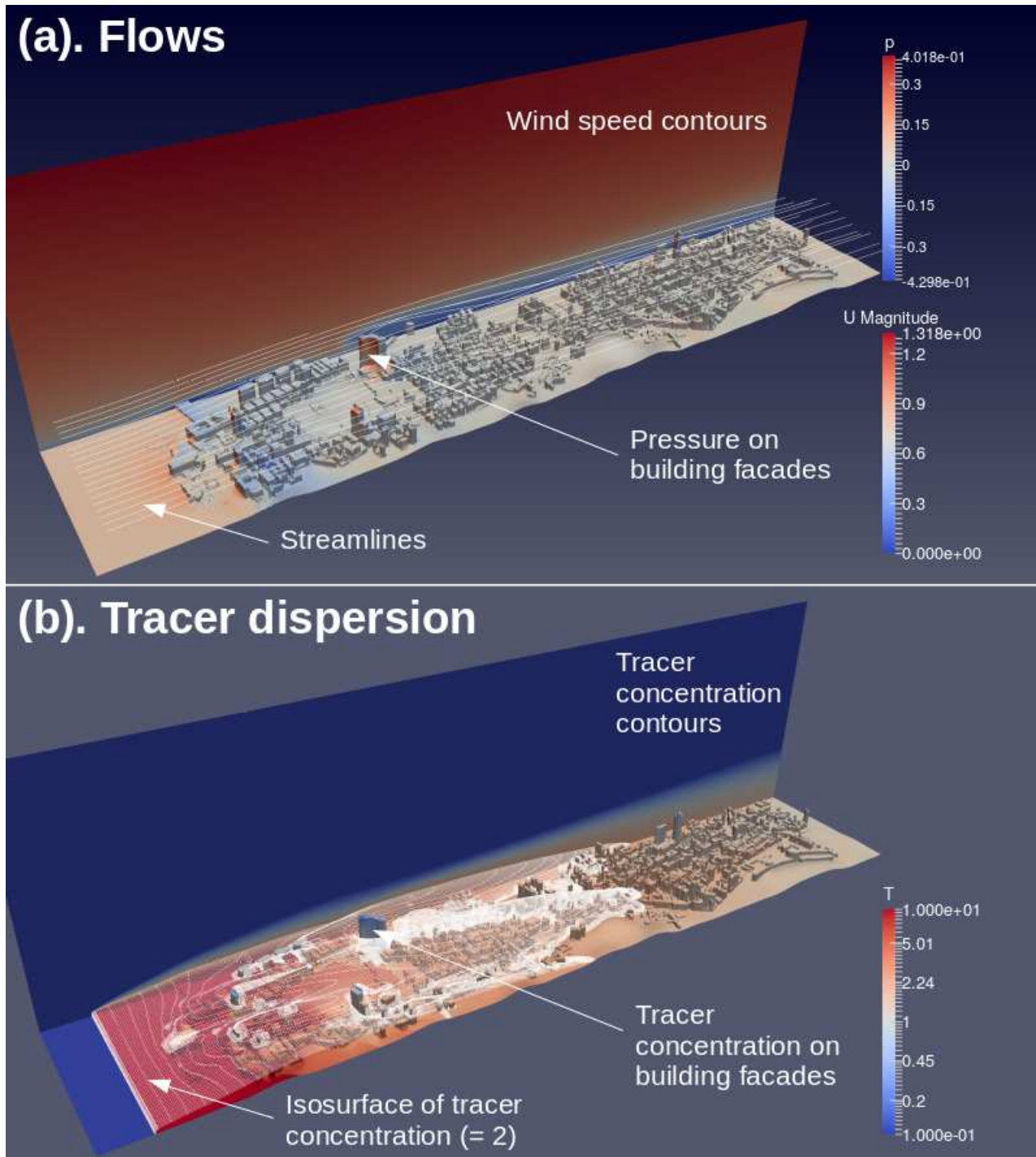
Figure 2: Preliminary CFD results of (a). flows and (b). tracer dispersion over the urban-area model of downtown HKSAR.

TOWARDS FIRE DYNAMICS SIMULATION IN HELYX

DANIEL DEISING[1], SALVATORE RENDA[2], EUGENE DE VILLIERS[3]

[1]Engys GmbH, d.deising@engys.com
[2]Engys Ltd, s.renda@engys.com
[3]Engys Ltd, e.devilliers@engys.com

Keywords: HELYX, Fire Dynamics Simulator, Fire Modelling, HVAC

Introduction

Over the last decade, the use of CFD methods for fire safety design has received increasing attention from the Architecture, Engineering and Construction (AEC) industry, leading to an urgent demand for accurate and efficient tools, capable to easily handle complex geometries and physics. The key ingredients for a fire simulation framework are mainly the capability of modelling in a simplified fashion the flame and smoke propagation through buildings, and a set of components such as water sprinklers for fire suppression, ventilation units, extractors and doors, whose operating conditions can be modified by a sensor logic, based on external or internal inputs, e.g. temperature at monitoring location, visibility of the area etc.

Nowadays, the standard tool for fire analysis in industry is the open-source Fire Dynamics Simulator (FDS) software, developed by the National Institute of Standards and Technology (NIST) and the VTT Technical Research Centre of Finland. Despite FDS being a widely used, well-established and validated code, to the best knowledge of the authors it exhibits several drawbacks:

- the use of simple cartesian meshes which are incapable to capture the complex geometric features of buildings
- an inherently transient solver with no possibility to run steady state analyses
- poor scalability and a non-user-friendly pre- and post-processing environment.

Furthermore, FDS is a stand-alone simulation platform, which means it cannot be easily integrated with other CFD tools and/or workflows generally used by the AEC industry. On the other hand, other commercial codes can today still be used to cope with fire-driven flow applications, however these are almost exclusively available as close source software.

Motivated by the limitations mentioned above, by the fact that HELYX already constitutes a successful framework in the ACE industry and because integrating new features for fire analysis is relatively straightforward in the existing code, we decided to carry out a research and development project on this topic which is in high demand.

In this work, we present an innovative fire dynamics modelling framework, designed for the solution of fire security problems and the development of fire control strategies. Due to the large scale of the geometries, which often represent floors, carparks or even entire buildings, the use of detailed physical models and numerical techniques is infeasible. Therefore, our proposed method is based on detail-reduced modelling approaches, i.e. averaging, loose coupling between smoke and air and a certain number of model simplifications. We remark that the proposed framework is not intended to be a replacement of other fire solvers already included into OpenFOAM such as FireFOAM, it is rather to be considered as an additional simplified modelling tool for large-scale fire dynamics simulations.

Modelling strategy

Main modelling components for a fire dynamics environment are:

- Fire source
- Smoke and visibility index
- Coolant spray
- Air humidity
- Sensor logic
- Fans
- Doors and windows

The simulation framework is based on a pressure-based, compressible, single-specie, buoyant thermal solver. Turbulence is modelled by means of RANS equations plus a two-equation turbulence model. Support for DES and LES is also included. All the heat transfer mechanisms, i.e. conduction, natural and forced convection and radiation are taken into account. Specifically, the radiation component is modelled by means of an improved version of the discrete order (DO) method, along with a constant absorption-emission model to include the interaction of radiation with fumes and air. This last aspect was found to be crucial for the accuracy of the plume development and shape. Furthermore, two additional transport equations are solved to model the smoke and humidity concentration transport. The solver can run both as steady-state or transient.

Within this modelling approach, smoke, coolant (water) and humidity are only loosely coupled to the primary air phase [1]. Smoke and humidity are solely acting as passive scalars regarding the hydrodynamics, while the coolant spray affects the air via the standard momentum exchange terms [3]. Moreover, thermal and mass coupling between air humidity, coolant spray and the primary air phase is accounted for. Within the context of fire simulation, the coupling of coolant mass and air humidity due to thermal phase change is modelled via simplified closures. The air temperature is affected by heat transfer from the coolant as well as phase change due to evaporation. Unlike common practice in other tools, the coolant spray is herein simulated as an Eulerian phase, as are all other participating phases. The fire itself is modelled as time-dependent heat and smoke release from boundary patches or sub-domains. To enable the simulation of realistic fire scenarios with fire suppression systems, the modelling of opening and closing doors, as well as the activation and deactivation of sprinklers and fans, are required. Specifically, we propose to model the opening and closing of doors by switching between boundary conditions, while fans are modelled as momentum sources with prescribed target velocity or fan curve. The control of the fire suppression systems and doors status is coordinated by means of the sensor logic which monitors solution parameter such has flow temperature and visibility index and makes decisions based on these.

Implementation

The presented modelling approach is accomplished via a newly developed class of solverObjects. These solvers are registered mesh objects for which wrappers for functionObjects and fvOptions as well as direct access functions within solvers have been created. The presented implementation utilizes the capabilities of fvOptions and adds hooks for the solverObjects to each of the fvOptions function call, which allows automatic execution of a solverObject at all fvOption calls within the top-level solver. Thus, the user can control at which stage of the top-level solver passive scalar transport equations or other solverObjects are executed. Within this framework, passive scalar transport equations can be modified to interact with the solver - and thus becoming active scalars - without modifying the source code, only by case setup. This is made possible by allowing the solverObject in turn to access any fvOption. Thus, solverObject and top-level solver or even different solverObjects can directly interact by fvOptions, e.g. source terms.

This functionality is extensively used to compute different transport quantities on demand, whenever fvOption-based source terms which need these quantities are evaluated. The primary goal of this framework is to introduce a new level of user flexibility in manipulating and adding new functionality to existing solvers without having to resort to code customisation.

Other user-interactions, like the switching of boundary conditions (e.g. opening and closing of doors) or activation and deactivation of sprinklers, are enabled via a new sensor class which allows users to perform algebraic and logical operations on fields, coupled with the available Function1 as a lookup table for the sensor output value. With this functionality, the user obtains a large amount of control over the setup of dynamically changing cases. Currently, this functionality is only available within a generic boundary condition that allows the switching between two user-specified boundary conditions based on sensor operations and the Function1 lookup table.

Results

Initial results for two test cases, a sprinkler water jet and flame development in a building, are shown to prove the capabilities of the proposed modelling framework.
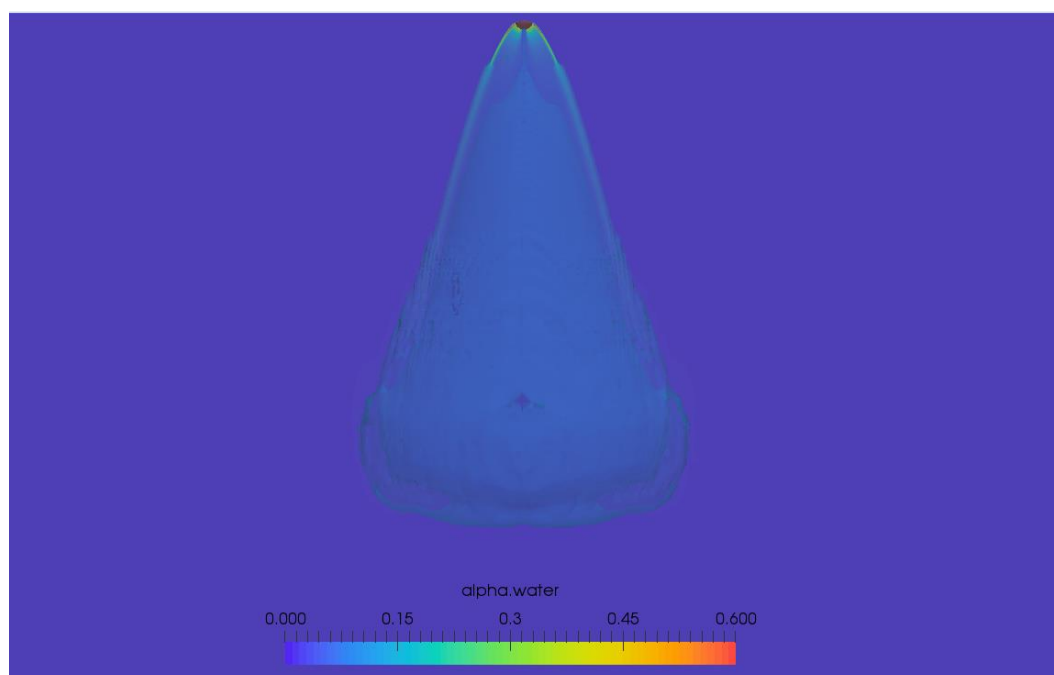
Figure 1. Water sprinkler modelled with uncoupled Eulerian spray.

Figure 1 shows contours of the water volume fraction for the sprinkler case. At the top, the sprinkler can be seen, coloured in red and modelled as a sphere sector. The aim of this test case was the verification of the droplet spray path and the cooling of the air due to heat transfer and evaporation.

Figure 2 presents the contours of the temperature field of the second test case. The case aims to reproduce experiments carried out at the Murcia fire test facility [2]. In this test case, which is specified in [2], a fire is modelled as a heat source originated in a pool located at the centre of the atrium. In the picture, the plume formation and development, with air stratification at different temperatures is displayed.
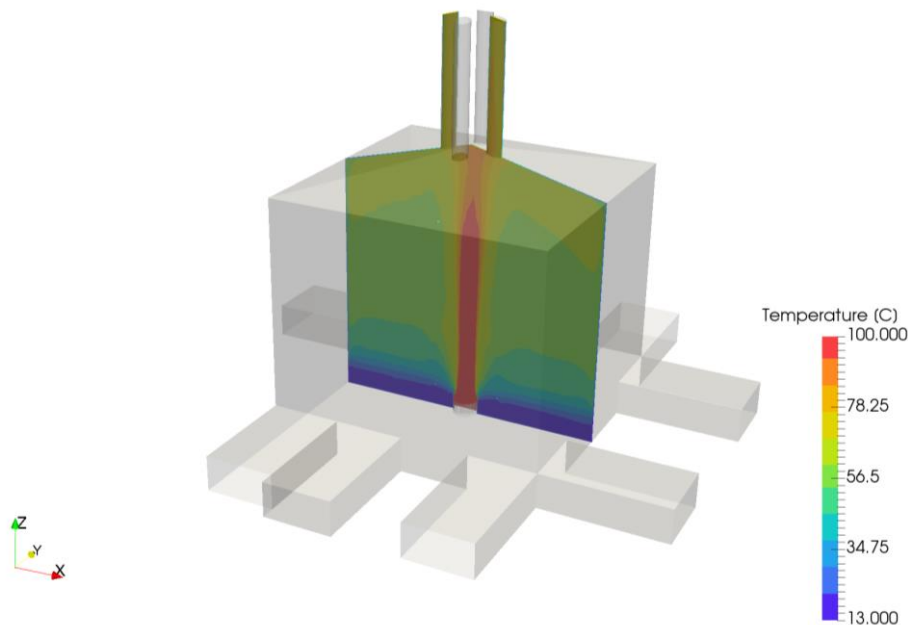
Figure 2 Temperature plume developed for the Mercia facility case

Acknowledgements

References
[1] Kubilay A, Derome D, Blocken B, Carmeliet J. Wind-driven rain on two parallel wide buildings: field measurements and CFD simulations. Journal of Wind Engineering & Industrial Aerodynamics; 146:11-28, 2015

[2] Gutierrez-Montes C, Sanmiguel-Rojas E, Viedma A, Rein G, Experimental Data and Numerical Modelling of 1.3 and 2.3 MW Fires in a 20 m Cubic Atrium, Building and Environment 44, pp. 1827-1839, 2009.

[3] Wörner M, A compact introduction to the Numerical Modeling of Multiphase Flows, FZKA 6932, 2003.

DETACHED-EDDY SIMULATIONS OF ATMOSPHERIC FLOW OVER COMPLEX TERRAINS

GUOLEI WANG[1], PANKAJ JHA[1], GREGORY OXLEY[1]

[1]*Envision Energy, guolei.wang@envisioncn.com*
[1]*Envision Energy, pankaj.jha@envision-energy.com*
[1]*Envision Energy,gregory.s.oxley@envision-energy.com*

Keywords: *Wind farm simulation, hybrid RANS/LES, atmospheric boundary layer*

Introduction

As the growing requirement from renewable energy, especially for wind energy, more and more on-shore wind farms has been constructed on the mountain ridges and plateaus. In contrast to the off-shore or flat terrain wind farms, reliably modelling the atmospheric flow over the complex terrains is a big challenge. A separation bubble, induced by the rolling hills includes low wind speed and high turbulence intensity. If the wind turbine happened to be located in this region, a low annual energy production (AEP) and fatigue failure of the wind turbine will be caused. Negative wind shear, which means the wind speed in the lower part of the turbine is higher than that in the higher part, will cause the turbine blade collide with the turbine tower, resulting the broken of the blade. Such unfavourable wind conditions will cause a finance loss, resulting a big risk of the project.

Currently, Reynolds-Averaged Navier Stokes (RANS) with two-equation turbulence model (k-ε model) is a standard process for the wind resource assessment and the siting optimization. By considering the measured met mast data and a standard post-processing form IEC, the wind resource file can be obtained and will be used to represent a 20 years mean value for the siting engineers. A following siting optimization and AEP calculation can be done to evaluate the risk of the project. However, it has been reported that steady RANS failed to accurately predict the flow features when flow separation occurs [1]. Large-Eddy Simulation, which only model the sub-grid scale turbulence, is a promising method to increase the accuracy when solving the wind farm. But due to the consuming of the calculation, it usually used to simulate the turbine-scale flows, such as SOWFA [2]. Detached-Eddy Simulation (DES), which will use RANS method in the near wall region and switches to LES method in the turbine region, can provide us more information than the traditional RANS method. It can be used to investigate the unsteady features in the wind farm, such as the possibility of the negative turbine wind shear and wind veer [3]. Compared with RANS method, DES method shows better performance when solving the hill induced separation [4].

Greenwich CFD (GWCFD), is a wind resource assessment CFD software developed by Envision Energy based on OpenFOAM. It integrates the pre-processing of the wind farm engineering, such as map and mast data clean, mesh generation and the post-processing, like cross-checking and the annual energy production (AEP). The primary workhorse of Greenwich CFD is the neutral RANS solver with k-ε closure, which carries 90% of the internal workload from the operational siting engineers in Envision Energy. In addition, Greenwich CFD has developed advanced models, such as thermal stratification model of atmosphere boundary layer, forest model, actuator line/disk model, as well as meso/micro scale coupling model.

Description of the case

In this paper, a wind farm in China is selected to investigate as shown in Figure 1. Wind turbines with hub height of 44m are located along the hill. The length of the plateau is about 1000m from southeast to northwest and about 10km from southwest to northeast. The hill elevation ranges from 1100m to 1700m. A met mast is located on the northeast of the wind farm. The wind rose at the measured met mast is shown in Figure 2, with the main wind direction of about 135degree (The direction of the wind from north is defined as 0 degree). The hill slope is about 30deg in the windward side. Based on the result from RANS, the predicted wind speed (or AEP) on the upwind side of the turbine group is higher than that on the downwind side. While the operating data from Year 2012 to Year 2015 shows the AEP on the upwind side is 30% lower than predicted. A detached-eddy simulation method with the standard K-Omega SST model [5] is used to review this case. Parameters in the turbulence model are carefully selected to make them consistent with the RANS k-Epsilon model [6]. Wind conditions at the problematic turbines will be fully considered.

Results and Discussion

The computational domain is 20km*20km, with the horizontal mesh resolution of 12.5m and the first wall normal mesh of 1m, resulting a total mesh size of about 70million. A log law inflow profile is used to simulate the neutral atmosphere boundary layer[1,3]. A rough wall function is used to model the near wall roughness effect [7]. Flow features in the dominant wind direction (135 degree) is simulated and analysed in this paper.

Figure 3 shows the flow pattern along the main wind direction near the problematic wind turbine. A separation bubble is observed in the leeside of the hill. The flow is disturbed on the plateau. The zoomed-in result at four time steps are shown in Figure 4. The turbine suffers unsteady wind conditions during the operation. The history of the wind speed variation at the upwind and downwind turbines is recorded during the simulation. Two probes at turbine bottom (H=20m) and turbine top (H=60m) are used to check the wind speed difference on the turbine disk as shown in Figure 5. The wind shear defined as (dU/dz), is analysed based on the probe data. It is found that the possibility of the negative wind shear is 65% for the upwind turbine and only 19% for the downwind turbine. Since large negative wind shear can cause the turbine blade collide with turbine tower, It is a high risk for the wind turbine in the upwind side.
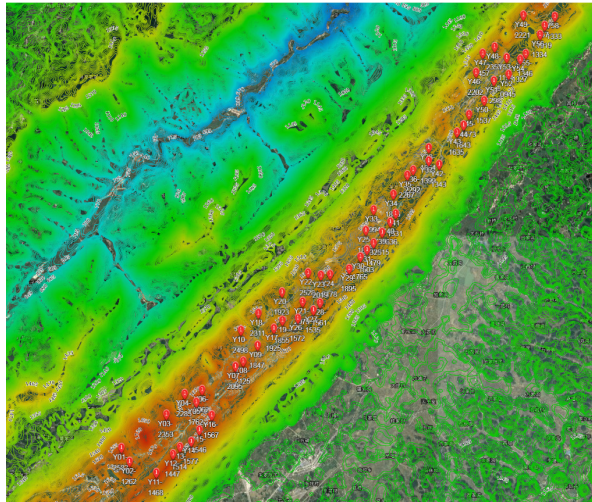
Figure 1. Terrain information of the site
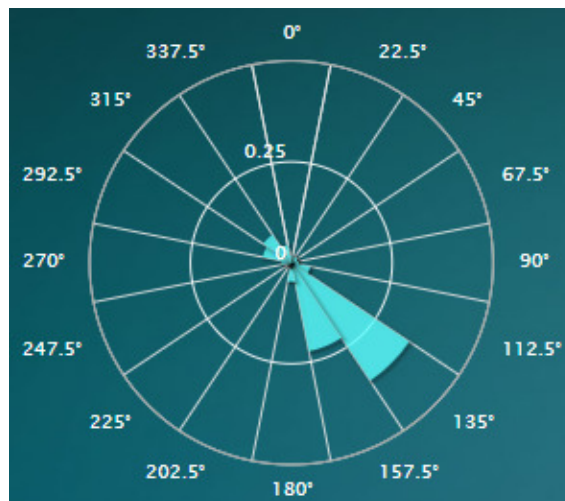
Figure 2. Wind rose of the Met mast
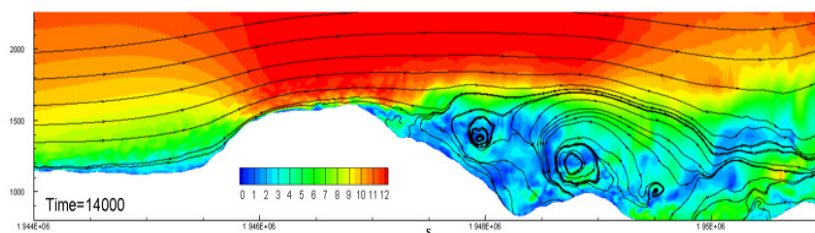
Figure 3. Flow pattern along the problematic wind turbine plane.
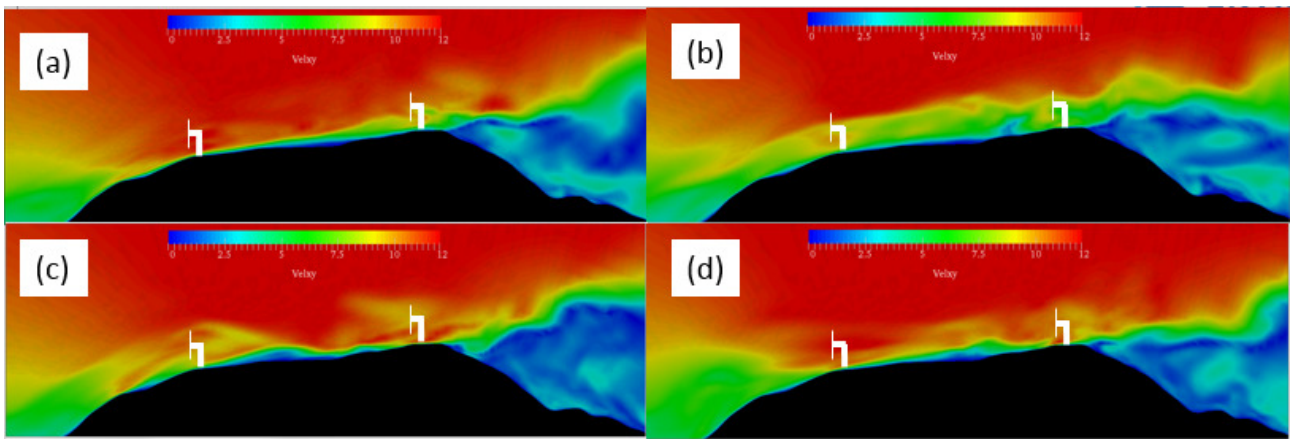
Figure 4. Zoomed-in flow patterns at different time near the problematic turbines.
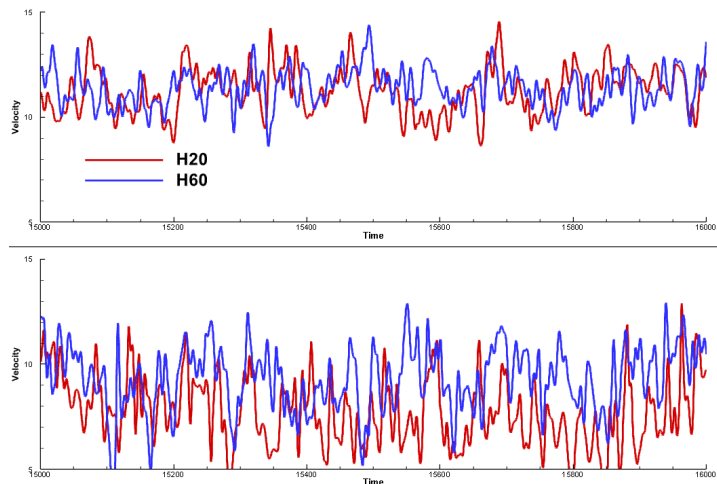
Figure 4. Time history of the wind speed variation at the upwind and downwind turbines.

References

[1] Bechmann A, Sørensen N N, Berg J, et al. The Bolund experiment, part II: blind comparison of microscale flow models[J]. Boundary-Layer Meteorology, 2011, 141(2): 245

[2] Churchfield M, Lee S, Moriarty P, et al. A large-eddy simulation of wind-plant aerodynamics[C]//50th AIAA Aerospace Sciences Meeting including the New Horizons Forum and Aerospace Exposition. 2012: 537

[3] Hu C H. Investigation of unfavorable winds associated with complex terrain using Detached Eddy Simulation[J]

[4] Bechmann A, Sørensen N N. Hybrid RANS/LES method for wind flow over complex terrain[J]. Wind Energy, 2010, 13(1): 36-50

[5] Menter F R, Kuntz M, Langtry R. Ten years of industrial experience with the SST turbulence model[J]. Turbulence, heat and mass transfer, 2003, 4(1): 625-632

[6] Sogachev A, Kelly M, Leclerc M Y. Consistent two-equation closure modelling for atmospheric research: buoyancy and vegetation implementations[J]. Boundary-layer meteorology, 2012, 145(2): 307-327

[7] Richards P J, Hoxey R P. Appropriate boundary conditions for computational wind engineering models using the k-ε turbulence model[M]//Computational Wind Engineering 1. 1993: 145-153

VERIFICATION OF OPENFOAM TO SIMULATE TANGENTIAL VORTEX INTAKE FOR CIVIL ENGINEERING APPLICATION

LAU YAU FU, EDDY

AECOM Asia Company Limited, eddy.lau@aecom.com

Abstract

In urban drainage/sewerage design, it is common to encounter water flow with large drop in elevation, such as intercepting stream flow to deep drainage tunnel for urban flood protection in Hong Kong. Tangential vortex intake is an efficient way to convey flow with large drop due to its good energy dissipation and large air core in drop shaft to release entrained air. Physical modelling is the conventional way to design vortex intake but it is timely and expensive to build. Commercial CFD software, e.g. Flow 3D, is increasingly used by civil engineering industry in Hong Kong to design/review hydraulic performance of vortex intake and other complex hydraulic structures. However, there is no known study which has examined accuracy of CFD in modelling flow in such complex hydraulic structures in detail. This study aims at validating OpenFOAM using comprehensive measurements on tangential intake physical model by Qiao et al. (2013) on: (i) head-discharge (Q-H) relation; and (ii) flow structure at approach channel and drop shaft. The results show that OpenFOAM is capable of giving good prediction of Q-H relation, and resolving flow structure of the swirling flow in drop shaft. This demonstrates the potential of CFD software, particularly OpenFOAM which is free and open source, as a tool to advance design of complex hydraulic structures in civil engineering industry in a more efficient and cost effective way.

Keywords: Tangential Vortex Intake, Drop Shaft, Vortex Flow, Swirling Flow, Air Core

Introduction

Tangential vortex intakes are commonly used to convey flow with large drop in elevation in drainage system. A tangential intake is a compact hydraulic structure which is composed of: (i) a rectangular approach channel with horizontal bottom; (ii) steep taping channel; (iii) a narrow slot at the junction; and (iv) drop shaft. Yu and Lee (2009) proposed a stable design criterion for tangential intake based on 1D model assuming circular vortex flow in drop shaft and constant streamwise velocity in the junction. Yet these assumptions were not verified until the work of Qiao et al. (2013). They carried out detailed velocity measurements on the structure of a tangential intake vortex flow for the first time. The works of Qiao et al. form the basis of this study to verify capability of OpenFOAM to simulate tangential vortex intake for civil engineering application.

Experimental Study by Qiao et al. (2013)

Detailed velocity field measurement with Laser Doppler Anemometry was carried out Qiao et al. (2013) for the first time for a steady tangential vortex intake. The experimental setup for measuring vortex flow field with LDA is shown in **Figure 1** below.
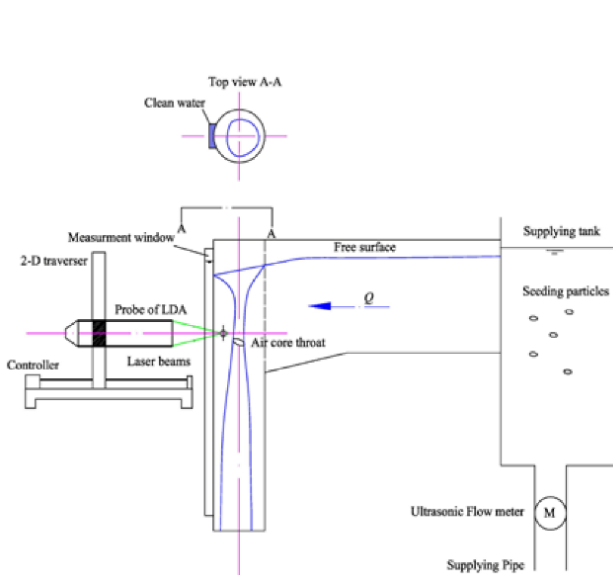
Figure 1: Experimental setup for measuring vortex flow field with LDA (Extracted from Qiao et al. (2013))
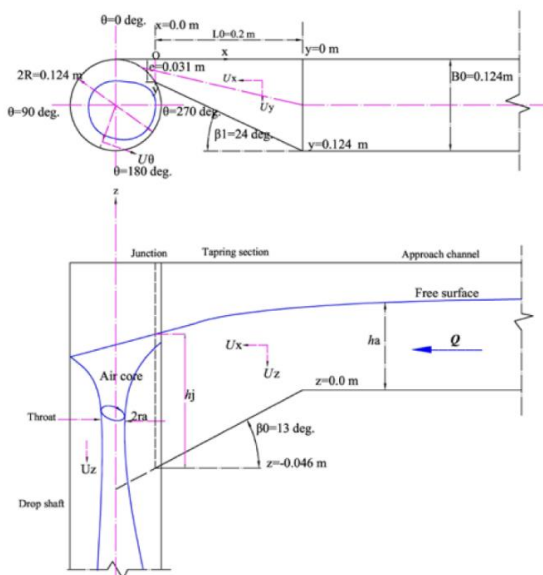
Figure 2: Main geometric parameters and measured vortex flow variables (Extracted from Qiao et al. (2013))

The geometry of tangential intake is shown in **Figure 2** and is determined by the following parameters: junction width (e), approach channel width (B0), drop shaft radius (R), bottom slope of tapering section (β0) and tapering angle of tapering section (β1).

The flow depth in the approach channel (ha) and the flow depth at the junction (hj) in the tapering channel were measured by point gauge. The local horizontal velocity Ux, the transverse velocity Uy perpendicular to the vertical boundary wall and the vertical velocity Uz are measured in a Cartesian coordinate system for Q = 2.0, 4.0, 6.0, 8.0 and 10.0L/s. The local vertical velocity Uz and the tangential velocity Uθ are also measured for the swirling flow velocity field in the drop shaft in a cylindrical polar coordinate system.

Model Setup & Description of Flow
Tangential intake in **Figure 2** was setup in OpenFOAM v4.1 using the standard solver, interFoam, for 2 incompressible, isothermal immiscible using volume of fluid phase-fraction based interface capturing approach. Parameters used are summarized in **Table 1** below. Overview of the model and water surface profile are shown in **Figures 3 and 4**.

Table 1: Parameters of the Model Setup

Parameters	Values
Meshing	blockMesh & snappyHexMesh
Number of Cells	1,485,577
Mesh Size	0.01m in approach channel, 0.0025m in drop shaft
Turbulence Model	kOmegaSST
Inlet patch	Flow rate boundary condition (variableHeightFlowRate)
Outlet & atmosphere patches	Atmospheric boundary condition (totalPressure)

For the range of flow simulated (Q=2L/s to 10L/s), flow regime in the approach channel is subcritical with smooth and flat water surface. The flow accelerates in the tapering and sloping section of approach channel, and it passes through critical depth at the junction before entering into the drop shaft horizontally. In the drop shaft, the flow attaches to the wall surface and the initial thickness of the flow is approximately equal to the width of junction. The swirling flow follows a helical path down the shaft and leaves the outlet patch at the bottom.
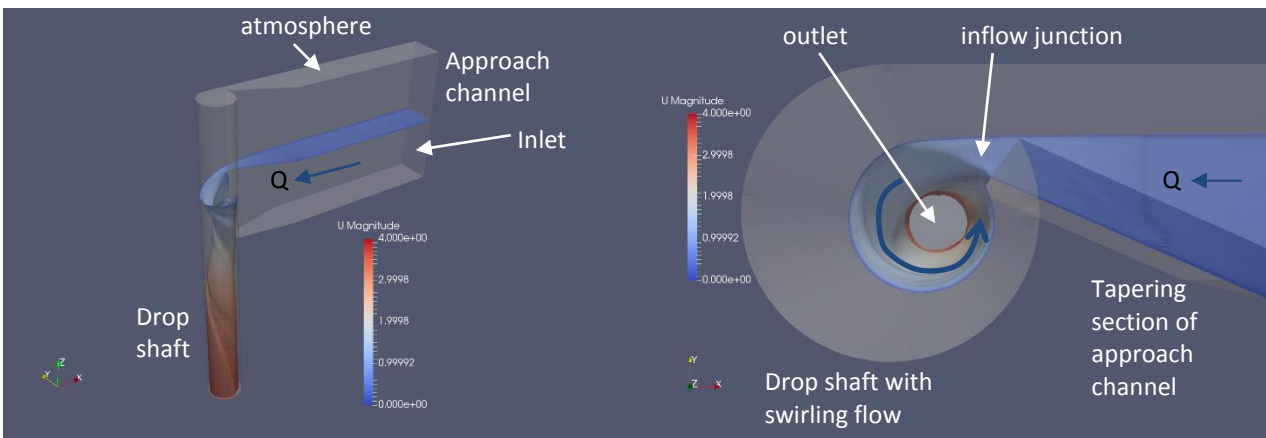
Figure 3: Isometric View of Water Surface Profile at Q=10L/s

Figure 4: Top View of Swirling Flow in Drop Shaft at Q=10L/s

Depth Discharge (Q-H) Relation
Water depth (ha) at approach channel of vortex intake is important as it affects hydraulic profile of its upstream drainage system. Therefore, accurate prediction of Q-H relation is essential for proper design of vortex intake to avoid water overtopping at upstream. Based on the measurements by Qiao et al. (2013), discharge and depth at approach channel (blue dots) show a close to linear relation as shown in **Figure 5**. Results of OpenFOAM (orange dots) show the same linear trend and the water depths (ha) in approach channel are reasonably well predicted. At the largest discharge of 10L/s, the difference is less than 10%. Q-H relation of tangential intake can be estimated with reasonably good accuracy for practical use.
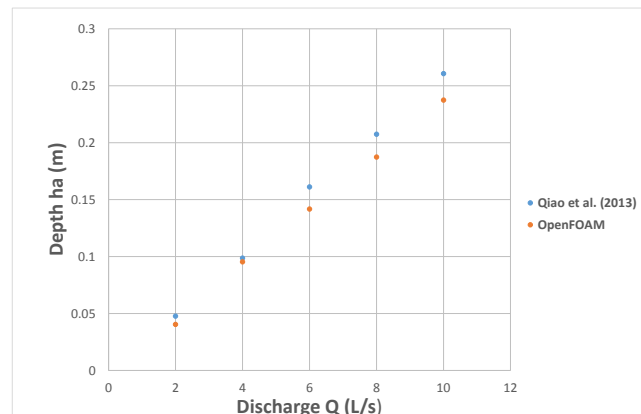
Figure 5: Comparison of depth-discharge relation

Minimum Air Core Area Ratio

The air core size decreases with discharge. Yu and Lee (2009) defined a key parameter λ as the ratio of air core area to the drop shaft cross-sectional area, $\lambda = b^2/a^2$ where a, b=radius of drop shaft and air core, respectively. The value of λ must be sufficiently large to allow free passage of air and ensure stable operation of the vortex intake. A typical criterion is $\lambda \geq 0.25$ for the design discharge. Yu and Lee (2009) assume circular air core in order to derive an analytical equation to calculate air core area ratio from a given discharge Q.

In **Figure 6**, the air core shapes from physical measurement (blue lines) and numerical model (orange lines) are compared at z=-0.04m at Q=4L/s and 8L/s. It is clearly seen that the actual air core is of D-shape and is asymmetrical about the axis of the drop shaft. The thickness of the flow layer being almost minimum at swirling angle $\theta=270^{\circ}$. The shape of simulated air core agrees reasonably well with the measured one.

In **Figure 7**, the variation of air core area ratio (λ) down the drop shaft at different flow rates are compared. Results of OpenFOAM are consistent with the measurements in general. The physical measurements show that the throat, i.e. the critical section of vortex flow with minimum air core area ratio, is located at z=0m to -0.05m. Elevations of throat are depicted by OpenFOAM correctly under different flow rates. The minimum air core area ratio (λ) predicted by OpenFOAM is reasonably accurate, taking into account of the possible human measurement errors in using specially designed ruler in measuring air core size in drop shaft.
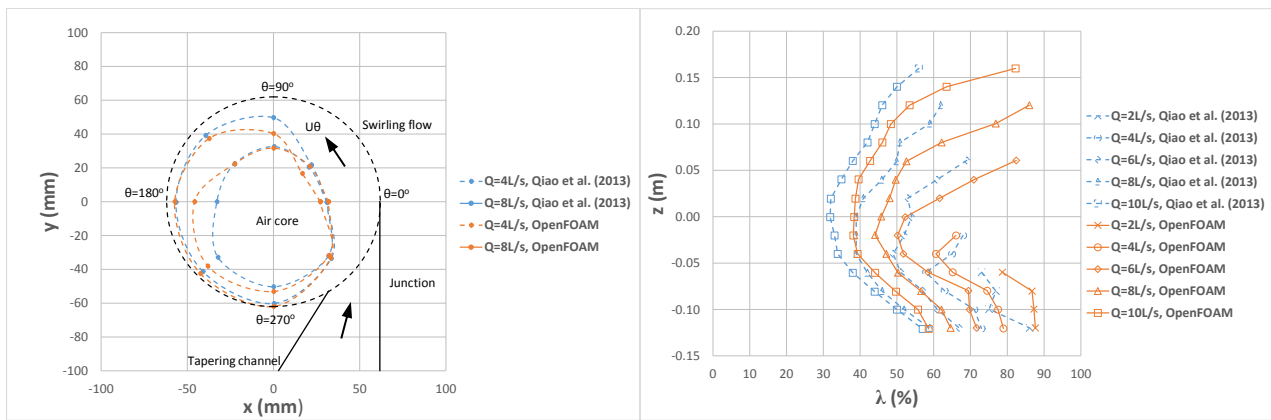
Figure 6: Comparison of air core shape at z=-0.04m

Figure 7: Comparison of air core area ratio

Velocity Distribution at Inflow Junction

Before the measurement by Qiao et al. (2013), the actual inflow pattern from the tapering channel into the drop shaft was unknown. Yu and Lee (2009) assumed a constant horizontal velocity U_x at the inflow junction in deriving an analytical equation to predict the free drainage discharge, i.e. the maximum discharge at which the vortex flow, after turning 360° in the drop shaft, doesn't disturb the parallel inflow jet at the junction. This is an important criterion to ensure formation of smooth and stable vortex flow.

In **Figure 8**, velocity distribution of U_x at inflow junction along depth of flow at different flow rates are compared. The physical measurements show that U_x varies linearly in the vertical direction for Q=2L/s to 6L/s. For larger discharge, U_x close to the bottom of inflow junction is affected by the swirling flow in the drop shaft after turning 360°, and the velocity profile of U_x starts to deviate from linear. Results of OpenFOAM give very good agreement with the measurements.
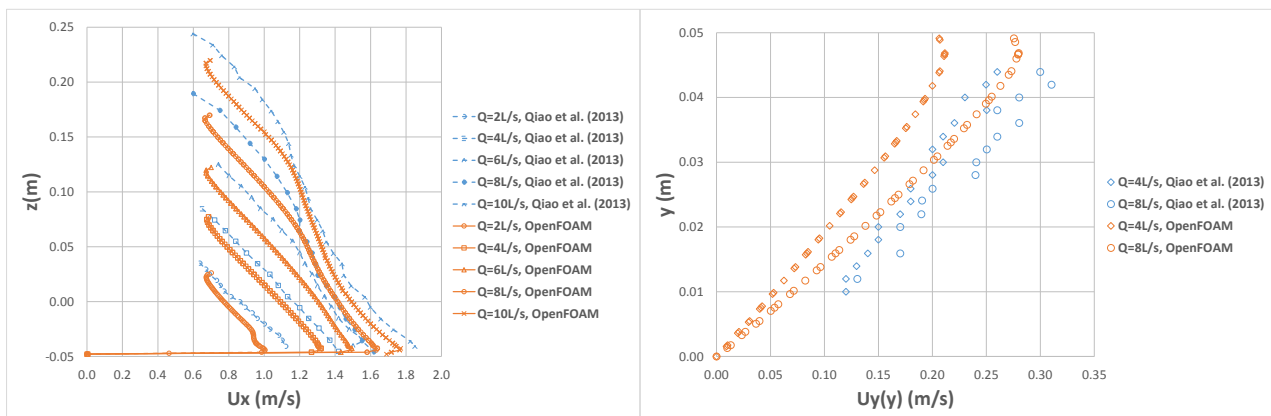
Figure 8: Comparison of velocity distribution $U_x(z)$ at the junction (y=0.009m, x=0.0m)

Figure 9: Comparison of velocity distribution $U_y(y)$ at the junction (x=0.045m, z=0.05m)

In **Figure 9**, there is small transverse velocity Uy at the junction due to tapering of the approach channel. All these detailed flow structures at the junction are very well predicted by the CFD model.

Velocity Distribution of Swirling Flow near to the Throat

Yu and Lee (2009) made another two assumptions in deriving an analytical equation for predicting minimum air core area ratio (λ) at the throat of swirling flow for tangential intake, they are: (i) horizontal tangential velocity Uθ of the swirling flow is inversely proportional to the radial position; and (ii) vertical velocity Uz is uniformly distributed in the radial direction.

In **Figure 10**, horizontal tangential velocity Uθ of swirling flow near throat of drop shaft is plotted against its radial distance (r) from centre of drop shaft at θ=45° for Q=4L/s. From the measurement, there is clearly an inverse relationship between Uθ and r. Results of OpenFOAM can resolve this distribution of Uθ to a high degree, and the velocity drops rapidly to zero at drop shaft wall surface (r=62mm) due to no slip condition.

In **Figure 11**, vertical velocity Uz of swirling flow near throat of drop shaft is also plotted again its radial distance (r) at θ=45° for Q=4L/s. From the measurement, the assumption of uniform distribution of Uz in the radial direction is obviously justifiable. Results of OpenFOAM not only show uniform vertical velocity Uz distribution in radial direction, but also correctly predicts increase in vertical velocities down the drop shaft. Results of OpenFOAM give good prediction of the distribution of Uθ and Uz, despite the flow in drop shaft is highly three-dimensional helical flow.
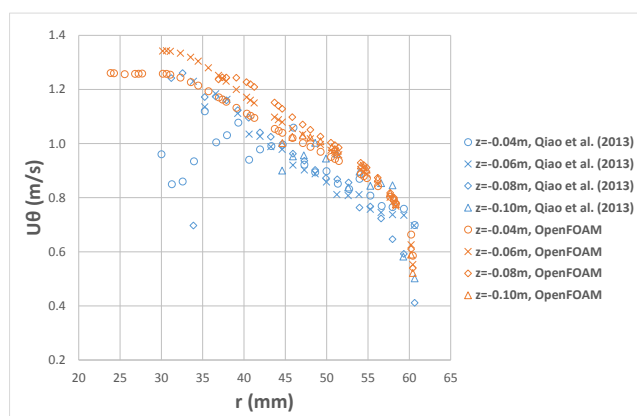
Figure 10: Comparison of tangential velocity (Uθ) of vortex flow at θ=45° for Q=4L/s
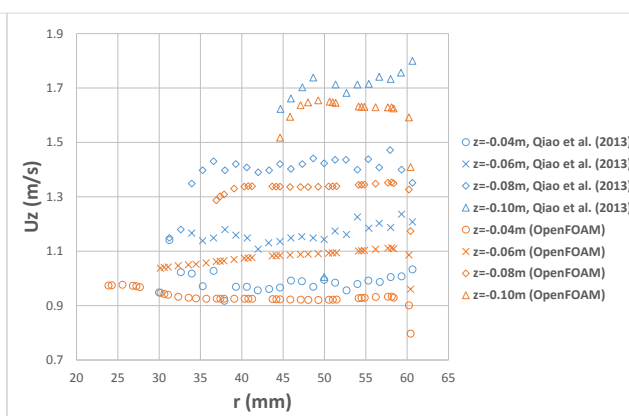
Figure 11: Comparison of vertical velocity (Uz) of vortex flow at θ=45° for Q=4L/s

Conclusions

With the detailed measurements by Qiao et al. (2013) on physical model of tangential intake, comprehensive insight can be gained and the results provide solid basis to verify capability of OpenFOAM to simulate such complex flow. The results presented here have demonstrated the capability of OpenFOAM to predict two important parameters to civil engineers in designing tangential intake: (i) Q-H relation; and (ii) minimum air core area ratio.

More than that, OpenFOAM can also resolve complex flow structures of: (i) the accelerating inflow into the drop shaft at the junction, together with the effects of swirling flow in the drop shaft after turning 360° at large discharge; and (ii) tangential and vertical velocity distribution along the radial direction of the swirling flow. It is of more interest to academics who develop theory for the hydraulics of tangential intake/complex hydraulic structures.

Findings in this study clearly illustrate the potential of this free and open source OpenFOAM to be used as: (i) an efficient and cost effective tool to supplement conventional physical model which is timely and expensive to build; (ii) a design tool for complex hydraulic structure for civil engineering application, as a cost effective alternative to the commonly used commercial software; and (iii) a research tool for academics to gain insight into complex flow problems to develop better hydraulic theory.

Acknowledgements

References

[1] D.Y. Yu and J.H.W. Lee, "Hydraulics of Tangential Vortex Intake for Urban Drainage," *Journal of Hydraulic Engineering*, vol. 135, no. 3, pp. 164-174, 2009.

[2] Q.S. Qiao, J.H.W. Lee and K.M. Lam, "Steady Vortex Flow in Tangential Intake," *IAHR World Congress Proceedings: 35th IAHR Congress*, pp. 1254-1261, 2013.

UPPER BOUND LIMIT ANALYSIS OF THE UPLIFT BEARING CAPACITY OF SUCTION CAISSON FOUNDATION BASED ON REVERSE PRANDTL MECHANISM

Zhu Wen-bo[1] Dai Guo-liang[1,2] Gong Wei-ming[1,2] Zhao Xue-liang[1,2]

(*1 School of Civil Engineering, Southeast University, Nanjing 210096, China)*
(*2 Key Laboratory of Concrete and Prestressed Concrete Structure of Ministry of Education, Southeast University, Nanjing 210096, China*)
E-mail: First author:763566305@qq.com / Corresponding author: daigl@seu.edu.cn

Abstract: In order to study the upper bound solution of bearing capacity of suction caisson foundation under vertical uplift load, a reverse Prandtl failure mechanism is constructed. On the basis of upper bound theorem of limit analysis, this paper introduces the viewpoint of reverse bearing capacity and the Prandtl failure mode for study. The reverse Prandtl failure mechanism means that the active area under the foundation becomes the passive area and the logarithmic spiral direction is opposite. Accordingly, the upper bound solution of bearing capacity of suction caisson foundation is derived by establish the corresponding kinematically admissible velocity field. At the same time, the upper bound solution is calculated by using the Matlab program and compared with the previous experimental data and other upper bound solution. The results show that the error between the upper bound solution and the experimental value is basically around 20% and it can prove that the reverse Prandtl failure mode is reasonable.

Key words: *suction caisson foundation; Prandtl failure mode; ultimate bearing capacity; upper bound theorem*

Introduction

Suction caissons have been widely used in as foundations in offshore oil and gas industry and have recently extended to offshore wind turbines. However, there are still no wide spread engineering specifications on design and calculation of uplift bearing capacity for the suction caisson foundation. Existing methods for estimating the pullout capacity of suction are mainly based on experiments or finite element analysis (Rao et al.1997, Deng and Carter 2002, Feng 2016, Zhai 2017 and Du et al. 2017). Andersen et al.(1993) carried out four field tests to study the pullout behavior of suction caissons in soft clay and concluded that the ultimate capacity may be calculated by assuming a reverse bearing capacity failure. They also suggested that an upper limit could be solved by assuming a failure mechanism which is similar to the approach to compute the bearing capacity of the shallow foundation as introduced by Terzaghi (1943). The upper bound theorem have been proved to be a powerful tool for the analysis of the plastic collapse associated with shallow foundations, buried caissons and circular foundations (Chen 1975, Yang 2001 and Wang 2008). However, limited attempts have been reported to estimate the pullout capacity of the suction caisson foundation using the upper bound solution.

In this paper, the reverse Prandtl failure mode was adopted to represent the failure mechanism of suction caisson subjected to pullout loading. An upper bound method for calculating uplift bearing capacity of suction caisson foundation based on the reverse Prandtl failure mode. The proposed equation was verified using the experimental data from published literatures and it shows that the results from proposed equations agree well with the experimental results.

Theory

The distinct failure mechanism, referred to as the M1, is utilized in the analysis. M1 is the reverse Prandtl failure mechanism. The Prandtl reverse failure mechanism means that the active wedge under the caisson becomes the passive wedge at the vertical pullout loads, at the same time, the direction of the principal stress is horizontal and the minor principal stress is vertical. The angle between the direction of horizontal plane and the failure surface is $45°-\phi/2$, so it is different from Prandtl failure mechanism(The angle is $45°+\phi/2$), and the logarithmic spiral direction is opposite. The upper bound theorems, which assumes a perfectly plastic soil model with an associated flow rule, states that the internal

power dissipated by any kinematically admissible velocity field can be equated to the power dissipated by the external loads and so enables a strict upper bound on the true limit load to be deduced.

Reverse Prandtl Failure Mechanism

The configuration of the suction caisson foundation here was described through two parameters-the radius R, the Caisson buried depth L. An overall schematic illustration of M1 is shown in Fig.1, the kinematic mechanism and the associated velocity field is shown in Fig.2. Since the movement is symmetrical about the footing, it is only necessary to consider the movement on the left-side of M1.The wedge ABC, with weight G_1, move with velocities v_0 but making an angle ϕ, the friction angle of soil, with the linear failure surfaces AC. The Logarithmic spiral ACD, with weight G_2, move with velocity v but making an angle ϕ, with the curved failure surfaces CD. The wedge ADE, with weights G_3, moves with velocity v_1. The suction caisson foundation moves vertically with velocity v_p. Soil may slide either along the foundation surface, referred to as interface shear with limiting shear stress $a \cdot c$. At the same time, the soil weight above the bottom of caisson was considered in the upper bound solution of M1. And the soil weight above the bottom of caisson equivalent to q.
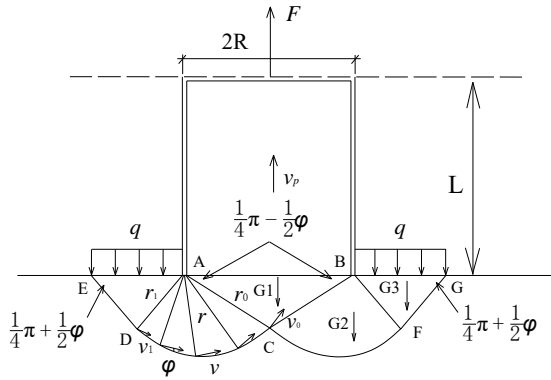
Fig.1 Reverse Prandtl failure mechanism   **Fig.2 velocity hodographs**
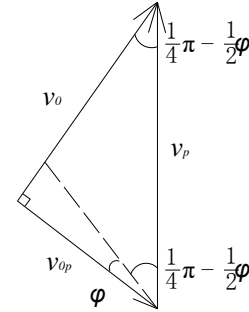
Formulation of Upper Bound Solution

Equating the work rates of external loads to the total internal energy dissipation rates, we can obtain the general equation of the ultimate bearing capacity using upper bound method, which is

$$
\begin{aligned}
F = &-2f_6 e^{-\pi\tan\phi}\left[f_7+1\right]q+\frac{1}{3}\gamma\pi R^3\tan\left(\frac{\pi}{4}-\frac{\phi}{2}\right) \\
&-\frac{1}{2}\gamma R f_5\left\{\begin{array}{l}-f_1+\tan\left(\dfrac{\pi}{4}-\dfrac{\phi}{2}\right)f_2+\dfrac{1}{3}\sec^2\left(\dfrac{\pi}{4}-\dfrac{\phi}{2}\right)* \\ \left[\dfrac{1-e^{-2\pi\tan\phi}}{4\tan\phi}+\cos 2\left(\dfrac{\pi}{4}-\dfrac{\phi}{2}\right)f_3-\sin 2\left(\dfrac{\pi}{4}-\dfrac{\phi}{2}\right)f_4\right]\end{array}\right\} \\
&-\frac{2}{3}\gamma R f_6 e^{-\frac{3}{2}\pi\tan\phi}\left[f_7+1\right]+\gamma\pi R^2 L+\frac{1}{2}c\cos\phi f_5+cf_5\left(\frac{1-e^{-\pi\tan\phi}}{2\tan\phi}-f_1+\tan\left(\frac{\pi}{4}-\frac{\phi}{2}\right)f_2\right) \\
&+\frac{1}{2}c\cos\phi f_5 e^{-\pi\tan\phi}\left[3f_7+2\right]+cf_5\left(\frac{1-e^{-\pi\tan\phi}}{2\tan\phi}-\frac{1}{2}f_1+\frac{1}{2}\tan\left(\frac{\pi}{4}-\frac{\phi}{2}\right)f_2\right)+2\pi RLac
\end{aligned}
\tag{1}
$$

Comparison with experimental values

Singh et al.(1991), Shi et al.(2003), Jiao et al.(2006), El-Gharbawy and Olson(1998) and Chen and Cassidy(2012) have performed the vertical uplift tests for suction caisson foundations under the undrained condition. The results of these tests and the upper bound solutions for the ultimate uplift force are shown on Fig.3. It can be seen from Fig.3 that the M1 solutions agree reasonably well with the test results, with differences in the range from 3% to 44%. The upper bound solution used in this paper are less than the upper bound solution of completely Prandtl failure mechanism of Wang(2008) and closer to the test results. The comparisons presented that the suggested upper bound solutions can be applied to suction caissons for estimating the uplift bearing capacity under the undrained condition.
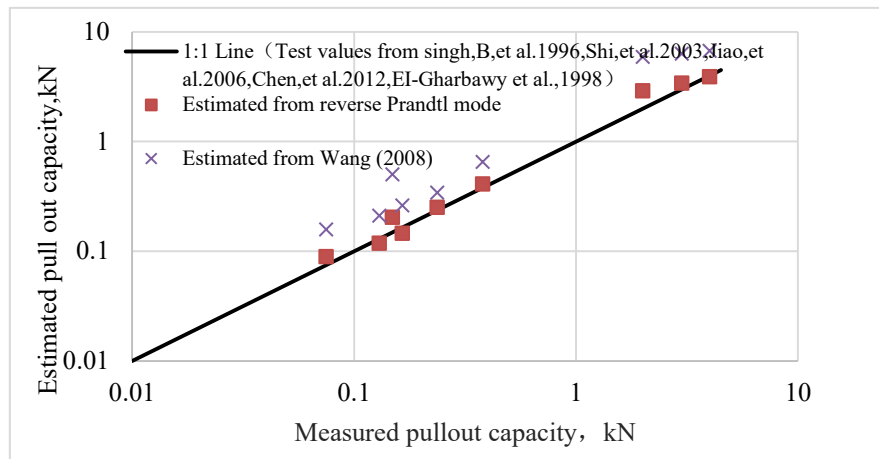
Fig.3 Verification of upper bound solutions for undrained vertical uplift capacity

Conclusions

In this paper, the reverse Prandtl failure mode was adopted to represent the failure mechanism of suction caisson subjected to pullout loading. And the upper bound solution agrees reasonably well with the test results, with differences in the range from 3% to 44%. The upper bound solution used in this paper is less than the upper bound solution of completely Prandtl failure mechanism of Wang（2008） and closer to the experimental value. It can be proved that both failure mechanisms are reasonably and more consistent with the actual force condition.

Acknowledgement

References

[1] Rao SN, Ravi R and Prasad BS(1997). "Pullout behavior of suction anchors in soft marine clays", Marine georesources & geotechnology, 15(2):95–114.

[2] Deng W and Carter J P.(2002). "A theoretical study of the vertical uplift capacity of suction caissons", International Offshore and Polar Engineering Conference. International Society of Offshore and Polar Engineers, Seattle, Vol.12, No.2, 89–97.

[3] Feng X., Pi X., Feng S. and Bian C.(2016). "Research on the Uplift Bearing Capacity of Suction Caisson Foundation under Local Tensile Failure", Procedia engineering, 166:61–68.

[4] Zhai H and Li D (2017). "Experimental Studies on Modified Suction Caissons in Fine Sand Subject to Uplift Loading", Transactions of Tianjin University, 23(6): 562–569.

[5] Du J.Q., Du S.J., Shen S.L. and Ma X.F.(2017), "Centrifuge evaluation of the influential factors in the uplift capacity of suction foundations in clay", Marine Georesources & Geotechnology, 35(4): 456–465.

[6] Andersen, KH, Dyvik, R, Schrøder, K, Hansteen, OE, and Bysveen, S (1993). "Field Tests of Anchors in Clay. II: Predictions and Interpretation," J Geotech Eng, ASCE, Vol 119,GT10, pp 1532–1549.

[7] Terzaghi, K. (1943). Theoretical soil mechanics. John Wiley and Sons Inc., New York.

[8] Wang Z.Y.(2008), "A Study on Uplift Bearing Characteristics of Suction Caisson Foundation in Soft. Dalian: Dalian University of Technology".

[9] Chen H.F.(1975), Limit Analysis and Soil Plasticity. Elsevier Scientific Publishing Company, London.

[10] Yang X.L. (2002), "Method and application of rock and soil limit analysis under linear and nonlinear failure criteria". Changsha: Central South University.

[11] Singh, B, Datta, M, and Gulhati, SK (1996), "Pullout Behaviour of Superpile Anchors in Soft Clay Under Static Loading", Marine Georesources and Geotech, Vol 14, pp 217–236.

[12] El-Gharbawy, SL, and Olson, RE (1998), "Pullout Capacity of Suction Caisson Foundation for Tension Leg

Platforms", Proc 8th Int Offshore and Polar Eng Conf, Montréal, ISOPE, Vol 1,pp 531–536.

[13] Shi X.C., Gong X.N., Yu J.L. and Chen G.X.(2003), "Study on buckling resistance of bucket foundation". Building Structure, 33(8): 49–51.

[14] Jiao B.T., Lu X.B., Zhao J. and Shi Z. M.(2006),"Experimental study on the uplift bearing capacity of suction bucket foundation". China Ocean Platform, 21(3): 27–29.

[15] Chen R, Gaudin C, Cassidy M J.(2012), Investigation of the vertical uplift capacity of deep water mudmats in clay. Revue Canadienne De Géotechnique, 49(49):853-865.

Appendix A

$$f_1 = \int_0^{\frac{\pi}{2}} e^{-3\theta \tan\phi} \cos\theta \mathrm{d}\theta = \frac{e^{-\frac{3}{2}\pi \tan\phi} + 3\tan\phi}{1 + (3\tan\phi)^2} \tag{A.1}$$

$$f_2 = \int_0^{\frac{\pi}{2}} e^{-3\theta \tan\phi} \sin\theta \mathrm{d}\theta = \frac{1 - 3\tan\phi\, e^{-\frac{3}{2}\pi \tan\phi}}{1 + (3\tan\phi)^2} \tag{A.2}$$

$$f_3 = \int_0^{\frac{\pi}{2}} e^{-4\theta \tan\phi} \cos 2\theta \mathrm{d}\theta = \tan\phi \frac{e^{-2\pi \tan\phi} + 1}{1 + (2\tan\phi)^2} \tag{A.3}$$

$$f_4 = \int_0^{\frac{\pi}{2}} e^{-4\theta \tan\phi} \sin 2\theta \mathrm{d}\theta = \frac{1}{2} \frac{1 + e^{-2\pi \tan\phi}}{1 + (2\tan\phi)^2} \tag{A.4}$$

$$f_5 = \pi R^2 \sec^2\left(\frac{\pi}{4} - \frac{\phi}{2}\right) \tag{A.5}$$

$$f_6 = \pi R^2 \tan^2\left(\frac{\pi}{4} - \frac{\phi}{2}\right) \tag{A.6}$$

$$f_7 = \tan\left(\frac{\pi}{4} - \frac{\phi}{2}\right) e^{-\frac{\pi}{2}\tan\phi} \tag{A.7}$$

MULTIPHASE MODELING OF LOCAL SCOUR IN LONG CONTRACTION

JOONGCHEOL PAIK[1]

[1]*Department of Civil Engineering, Gangneung-Wonju National University, paik@gwnu.ac.kr*

Keywords: Multiphase flow, Local scour, Contraction, Open channel

The contraction of a watercourse is typically induced by hydraulic structures, such as bridge piers, abutment and barrages. The channel contraction leads to the increase of flow velocity and free surface deformation due to the reduction of cross-section which may result in local scouring in the contracted zone of the open channel. The increase in depth in an a long contraction can be calculated from the equations of motion and continuithy for sediment and water[1]. In this study, a local scour in a long contraction is numerically invesitygated through multiphase computational fluid dynamics (CFD) modeling with rheological model for non-Newtonain sediment layer.

A Multi-phase flow model for simulation of the interaction of water flow and sediment bottom in the channel contraction was developed, which is based on three-dimensional Navier-Stokes equations incorporated with multiphase transport equations and employed a viscoplastic models for water-saturated sediment flows. The governing equations for the flow are the unsteady, incompressible filtered Navier-Stokes equations. The interfaces of water, air and water-solid mixture fluids are captured by means of the multiphase volume of fluid (VOF) method which is capable of modeling flows in complex free surface geometries. The location of the free-surface and interface of fluids are obtained by the VOF variable. The contribution of three fluid velocities to the evolution of the free surface and interface is proportional to the corresponding phase fraction, and the volume fraction is used to determine the fluid properties.

The governing equations are solved numerically by the finite volume method. Overall fully second-order-accurate setup both in time and in space is used for the simulation. The generalized second-order-accurate backward, implicit, differencing scheme is used to evaluate the time derivatives. Spatial discretization for the convective term is achieved using the central differencing schemes. One of the major difficulties in the VOF method is ensuring the transport of sharp interfaces without artificial numerical diffusion or dispersion. In the VOF model, the boundedness of volume faction is maintained by utilizing a bounded central differencing scheme combined with a solution procedure referred to as multi-dimensional universal limiter for explicit solution. The rheological behavior of the water and sediment mixture is approximated by a modified Herschel-Bulkley model. The delayed detached eddy simulation is used to compute subgrid-scale eddy viscosity of turbulent flow. Sufficiently refined computational mesh and appropriate boundary conditions are essential to accurately reproduce the dynamical interaction of water phase and solid-water mixture phase in the multiphase, turbulent modeling.

A series of laboratory experiments had been carreid out by Dey and Raikar [2] in a 12 m long, 0.6 m wide and 0.7 m deep rectangular flume. In the experiemnt, a 3 m long, 0.3 m deep, rectangular contraction model containing sediment is installed at 6 m downstream of the flume inlet as seen in Fig. 1. A numerical flume, of which the configurations are identical to the experimental ones, is generated to reproduce the experimental measurements. Among a series of experiments with different contraction ratios, sediments and flow conditions [1], a measurement observed for the contration ratio $\tilde{b}$ $(= b_2/b_1)$ of 0.4, median diameter of sediment d_{50} of 2.54 mm, approaching bulk mean velocity of 0.568 m/s and the upstream flow depth of 0.1286 m. The Reynolds number and Froude number based on the approaching velocity and flow depth are 71,000 and 0.506, respectively.

Numerical results show that the multiphase CFD model is successfully applied to resolve propagation of sediments wave and local scour in a long contraction of the open channel. Fig. 2 shows snapshots of free surface and bed deformation at three different instants. Numerical solutions well reproduce the experimental measurements in terms of overall shape of free surface and the bed evolution.

References
[1] A. J. Raudkivi, Loose Boundary Hydraulics, A.A. Balkema, Rotterdam, Netherlands, 1998.
[2] S. Dey and R. V. Raikar, Scour in Long Contractions, Journal of Hydraulic Engineering, Vol. 131, No. 12, pp. 1036-1049, 2005.
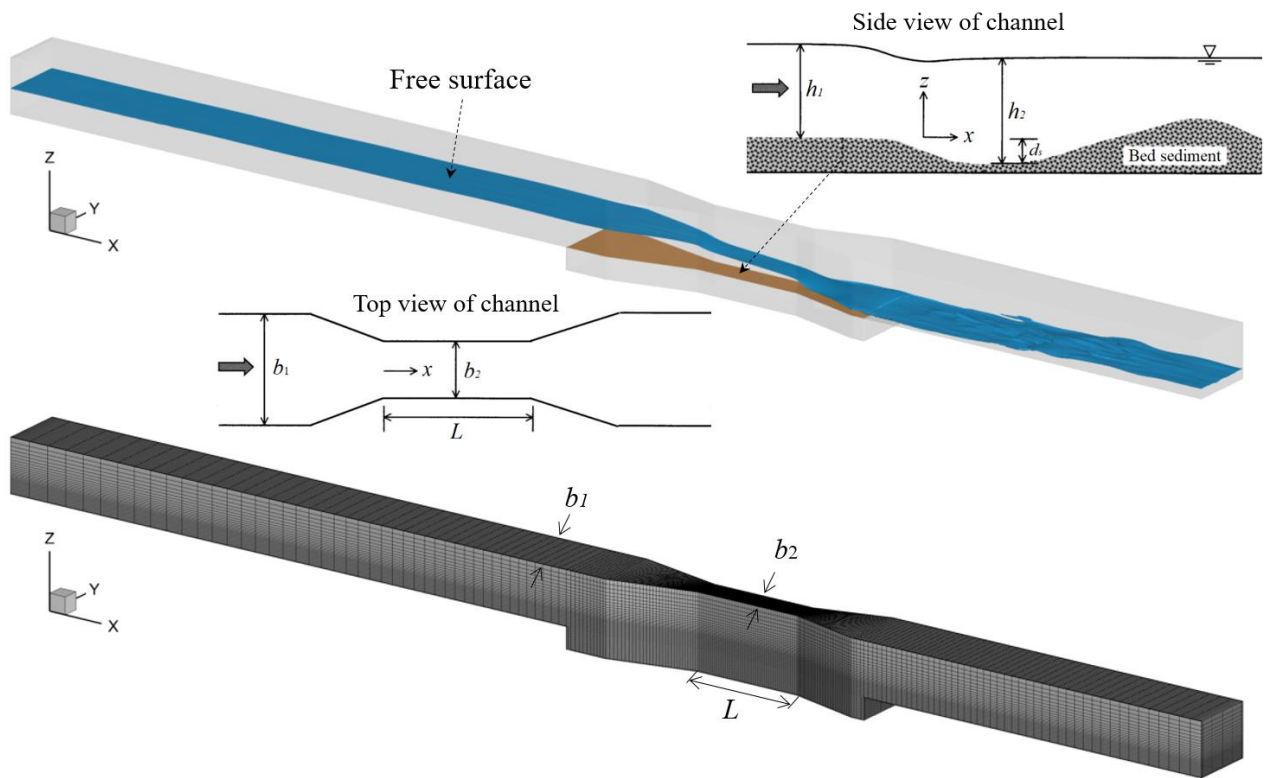
Figure 1: Schematic of a long rectangular channel contraction experimentally investigated by (Dey and Raikar, 2005) and computational mesh
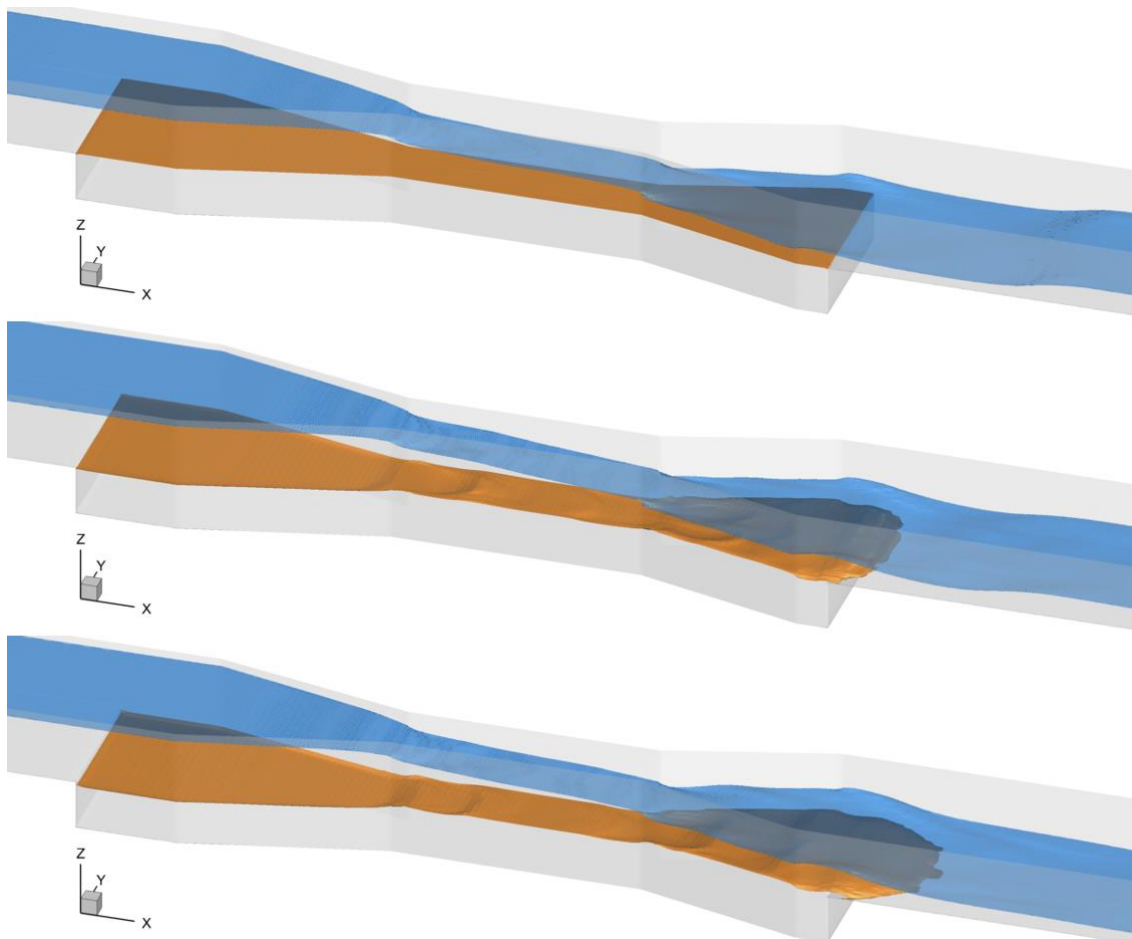
Figure 2: Computed free surface and sand bed deformation at subsequent three time instants: $t = 0$ s (*upper*), $t = 120$ s and $t = 300$ s (*lower*)

DEVELOPMENT OF A COUPLED INCOMPRESSIBLE VISCOELASTIC FLUID FLOW SOLVER BASED ON FOAM-EXTEND

C. FERNANDES[1], V. VUKČEVIĆ[2], T. UROIĆ[2], O.S. CARNEIRO[1], H. JASAK[2,3] AND J.M. NÓBREGA[1]

[1]*Institute for Polymers and Composites/i3N, University of Minho, Campus de Azurém, 4800-058 Guimarães, Portugal, cbpf@dep.uminho.pt*
[2]*Faculty of Mechanical Engineering and Naval Architecture, Ivana Lučića 5, 10000 Zagreb, Croatia*
[3]*Wikki Ltd, 459 Southbank House, SE1 7SJ, London, United Kingdom*

Keywords: *coupled pressure-velocity-extra stress tensor, block solver, foam-extend*

To help designing polymer processing tools it is essential to use efficient computational fluid dynamics numerical codes, which can save time and resources when compared to those usually spent on experimental trial-and-error processes. The design tasks are even more difficult to undertake, both experimentally and numerically, when dealing with complex rheology materials, as happens with the viscoelastic fluids, which present some counter intuitive phenomena. On the computational side, for this type of fluids a non-linear constitutive equation that includes elastic effects must be considered. In this framework, for an isothermal problem, the set of highly coupled governing equations, consisting of the continuity, the momentum and the constitutive equations, has to be solved.

The usual approaches employed are based on segregated algorithms, in which all the equations are solved iteratively and sequentially [1]. Due to the strong coupling between the governing equations, this sequential iterative process is quite sensitive and prone to divergence. Additionally, the segregated approach is known to present slow convergence (due to the requirement of using high relaxation factors), and limit substantially the Deborah number (a measure of the elasticity relevance) that can be achieved in the numerical calculation.

This work describes a new numerical code, in the context of the finite-volume method, which follows a coupled approach to compute the flow of viscoelastic fluids. The code was implemented in the open-source computational library foam-extend [2], a community driven fork of the OpenFOAM® software. The solution of the enlarged system of equations, composed by continuity, momentum and extra-stress constitutive equations, is obtained using an algebraic multigrid solver. The performance of the coupled viscoelastic solver is assessed with two case studies, namely the Oldroyd-B Poiseuille and the UCM lid-driven cavity flows, targeting to evaluate the advantages in terms of the number of iterations and CPU time, with increasing mesh density and Deborah number. Additionally, for verification purposes, the results obtained with the developed code are compared with analytical solutions and results obtained with the segregated version of the viscoelastic modelling code [1].

Acknowledgements

References
[1] C. Fernandes, M. S. B. Araujo, L. L. Ferrás, and J. M. Nóbrega. Improved Both Sides Diffusion (iBSD): a new and straightforward stabilization approach for viscoelastic fluids flows. J. of Non-Newtonian Fluid Mech., 249:63-78, 2017.

[2] foam-extend. Open Source CFD Toolbox, 2013. URL https://sourceforge.net/projects/foam-extend/

NEW OPENFOAM SOLVERS FOR TRANSONIC AND INCOMPRESSIBLE FLOW SIMULATIONS

MATVEY V. KRAPOSHIN[1,2], DANIIL A. RYAZANOV[1,3], KIRILL A. VATUTIN[1,3], TATIANA G. ELIZAROVA[4]

[1]*Ivannikov Institute for System Programming of the RAS*
[2]*The Department of Aeromechanics and Flight Engineering of Moscow Institute of Physics and Technology*
[3]*Lomonosov Moscow State University*
[4]*Keldysh Institute of Applied Mathematics RAS*

Keywords: *Regularized gas dynamic equations, Quasi hydrodynamic equations, transonic flows, incompressible flows, Finite Volume Method, QGDFoam, QHDFoam*

Introduction

Regularized or quasi-gas dynamics equations (QGD) and their extensions for transonic and incompressible flows have found applications for numerical simulations of different types of viscous flows [1]: subsonic, transonic, super- and hypersonic flows of viscous perfect gas, flows of binary mixtures, low-compressible fluids flows, etc. Our implementation of QGD numerical algorithm as OpenFOAM solver *QGDFoam* has proved to operate properly in wide range of Mach and Reynolds numbers for several prominent practical 1D & 2D cases, such as laminar subsonic flows in channels, subsonic flows with separation, compressible jet flows, supersonic inviscid flows and others [2]. Perfect scalability for medium-sized High Performance Computing clusters (HPC) with number of computational cores up to 96 has been achieved.

In this work we continue to develop OpenFOAM implementations of numerical algorithms for regularised gas and hydrodynamic equations for the next particular cases:

- *TQGDFoam* — a solver for transonic and subsonic viscous gas flow with possibility of extension to arbitrary equation of state;

- *QHDFoam* — a solver for incompressible viscous fluid simulation.

Developed solvers are tested for well-known 2D and 3D cases on large HPC cluster with the number of used computational cores up to 1500.

Quasi hydrodynamic equations for TQGDFoam and QHDFoam solvers

Quasi hydrodynamic (QHD) equations were proposed by Yu. V. Sheretov in 1996 as a special variant of QGD system e.g., [3]. This system has more simple mathematical form comparing to QGD system that simplifies its numerical implementation. It allows directly usage of arbitrary equation of state $p = p(\rho, T)$. Compared with QGD system, QHD equations have a limited range of applicability in terms of Mach numbers, namely, from subsonic to transonic regimes. QHD system of equations includes continuity(1), momentum (2) and total energy equations (3), accomplished with closure relations for Navier-Stokes viscous stress tensor Π_{NS} and heat flux vector q_{NS}.

$$\frac{\partial \rho}{\partial t} + div\,(\rho \vec{u}) = div\,(\rho \vec{w}) \tag{1}$$

$$\frac{\partial(\rho \vec{u})}{\partial t} + div\,(\rho \vec{u} \otimes \vec{u}) + \vec{\nabla} p = \rho \vec{F} + div\,\Pi_{NS} + div\,[(\rho \vec{w} \otimes \vec{u}) + (\rho \vec{u} \otimes \vec{w})] \tag{2}$$

$$\frac{\partial}{\partial t}\left[\rho\left(\frac{\vec{u}^2}{2} + \varepsilon\right)\right] + div\left[\rho \vec{u}\left(\frac{\vec{u}^2}{2} + \varepsilon\right) + p\vec{u}\right] + div\,\vec{q}_{NS} = \rho \vec{F} \cdot (\vec{u} - \vec{w}) +$$
$$div\,(\Pi_{NS} \cdot \vec{u}) + div\left[\rho \vec{w}\left(\frac{\vec{u}^2}{2} + \varepsilon\right) + p\vec{w} + \rho \vec{u}(\vec{w} \cdot \vec{u})\right] \tag{3}$$

with

$$\vec{w} = \tau\left[(\vec{u} \cdot \vec{\nabla})\vec{u} + \frac{1}{\rho}\vec{\nabla} p - \vec{F}\right] \tag{4}$$

In numerical algorithms the regularisation parameter τ has the form $\tau = \alpha \Delta_h / C_s$, where α is a tuning parameter, Δ_h is a local computational grid step and C_s is the speed of sound.

Similarly to Navier-Stokes system, it is possible to construct QHD system for incompressible flows. If the density changes can be neglected, the QHD system of equations reduces to its incompressible form, which can be used for deep subsonic flows simulation: (5) — (7). This system of equations can also be used for stratified flows simulation within Boussinesq assumption with $\vec{F} = -\beta \vec{g} T$.

$$div\ \vec{u} = div\ \vec{w}, \tag{5}$$

$$\frac{\partial \vec{u}}{\partial t} + div\ (\vec{u} \otimes \vec{u}) + \frac{1}{\rho}\vec{\nabla}p = \frac{1}{\rho}div\ \Pi_{NS} + div\ [(\vec{w} \otimes \vec{u}) + (\vec{u} \otimes \vec{w})] - \beta \vec{g} T, \tag{6}$$

$$\frac{\partial T}{\partial t} + div\ (\vec{u}T) = div\ (\vec{w}T) + \chi \Delta T, \tag{7}$$

where $\rho = const > 0$ — average value of density, $\vec{u} = \vec{u}(\vec{x}, t)$ - hydrodynamic velocity, $p = p(\vec{x}, t)$ - static pressure, $T = T(\vec{x}, t)$ - deviation of temperature from its average value T_0, $\vec{g}$ — acceleration due to gravity, β — temperature coefficient of expansion, coefficients of dynamic viscosity μ and thermal diffusivity χ are assumed to be constant and $\nu = \mu/\rho$ is kinematic viscosity. In contrast to compressible simulations, the smoothing parameter can be calculated using system Re number, e.g.: $\tau = \alpha \cdot \Delta_h^2 / \nu$, or $\tau = \alpha \Delta_h / U_0$, where U_0 is the characteristic flow velocity.

The approximations of the both systems were implemented in OpenFOAM as *TQGDFoam* and *QHDFoam* solvers. For demonstration purposes here *TQGDFoam* uses only perfect gas equation of state, but it can be modified effortless to use in conjunction with arbitrary EoS.

Conclusion

Several cases were selected for assessing developed solvers properties:

1. Laminar unsteady flow over cylinder.

2. Laminar flow in the quadrangular cavity.

3. Laminar and transitional flow over bacward-facing step.

Numerical solution was compared with the standard OpenFOAM solvers. The solvers was tested in parallel regime using HPC cluster with up to 1500 cores. Preliminary results of comparison between *QHDFoam* solver and *icoFOam* solver are presented on figures below.
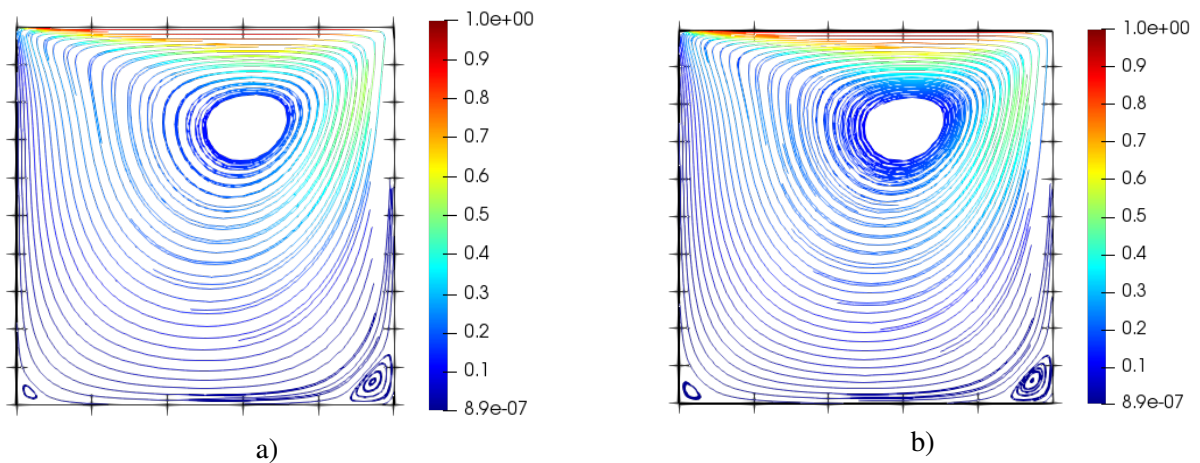
Figure 1: Visualization of streamlines and the velocity field magnitude for the cavity case at Re=100 calculated on 100x100 grid using a) icoFoam solver and b) *QHDFoam* solver

Two new solvers based on regularized hydro-dynamic equations for viscous subsonic (*TQGDFoam*) and incompressible *QHDFoam* flows have been implemented in OpenFOAM library. First order Euler scheme for time derivatives and second order scheme for spatial derivatives are used in the implementation. Solvers were tested on classical 2D and 3D cases.
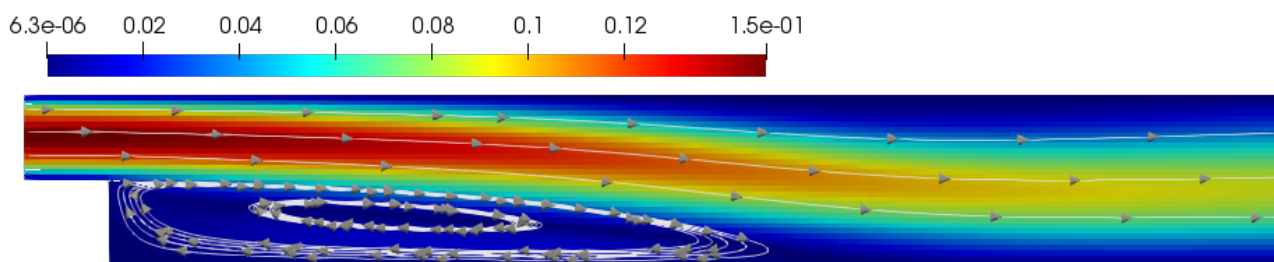
Figure 2: Visualization of velocity field and streamlines for backward step case at Re=100 calculated on 100x100 grid using *QHDFoam*

Acknowledgments

References

[1] Tatiana G. Elizarova. *Quasi Gas Dynamic equations*. Springer; 2009 . ISBN 978364200295.

[2] Matvey V. Kraposhin,Elena V. Smirnova, Tatiana G. Elizarova, Maria A. Istomina. Development of a new OpenFOAM solver using regularized gas dynamic equations, *Computers and Fluids*, 166(2018), pp. 163175

[3] T. G. Elizarova, Y. V. Sheretov. Theoretical and numerical analysis of quasi-gasdynamic and quasi-hydrodynamic equations, *J. Computational Mathematics and Mathematical Physics* 41 (2) (2001) 219234.

VLES OF DRAG REDUCTION FOR A SQUARE CYLINDER WITH SHAPED CORNER BASED ON OPENFOAM

ZHONGYU CHENG[1], ZHAOYANG XIA[1], XINGSI HAN[1,2], JUNKUI MAO[1], FENG JIN[1]

[1] *College of Energy and Power Engineering, Nanjing University of Aeronautics and Astronautics,*
Aero-engine Thermal Environment and Structure Key Laboratory of Ministry of Industry and
Information Technology, Nanjing 210016, China
[2] *Corresponding author, email: xshan@nuaa.edu.cn*

1. Introduction

The drag reduction of high Re number turbulent flow past a bluff body has attracted extensive interests in both academia and industry for decades. For industrial applications, it can reduce the fuel consumption and improve the performance of the vehicles. In academic research, the flow configuration provides abundant fundamental problems, such as massive separated flow, unsteady vortex evolution, flow control strategies, etc.

Generally, the flow control strategies can be divided into two main groups [1]: passive flow control and active flow control. The present study focuses on the passive flow control method which mainly adopts to modify the geometry for reducing the drag. Turbulent flow around a square cylinder has been a classic flow test case [2] for various problems. It was also used for drag reduction studies [3-5]. Previous experiments have found that by shaping the corner of the square cylinder, the drag can be reduced by 50% for some conditions. Although the significant drag reduction result has been observed in the experiments, the underlying physical mechanism has not been well understood. On the basis, the current study aims to reveal some of the key flow mechanics based on high-fidelity numerical simulation.
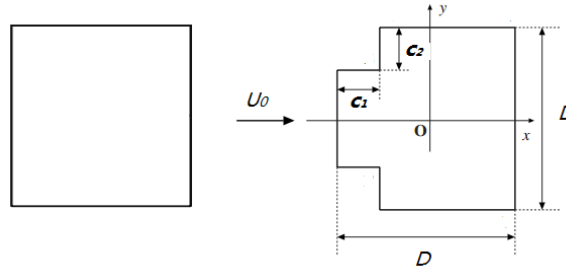
Figure 1: Square cylinder and a shaped-corner square cylinder (a cut plane).

High fidelity simulation, such as Large Eddy Simulation (LES) has been applied for various flow control studies. It shows high potential to investigate the involved flow mechanics. However, LES suffers from the high computation cost for high Re number turbulent flow. In recent years, hybrid turbulence modeling method [6] has been developed rapidely as it combies the advantages of different turbulence modeling approaches, such as hybrid RANS-LES method. One of the hybrid method is VLES method (Very-Large Eddy Simulation) [7, 8], which has been validated in some classic flow cases and performs very well. It is found that the VLES method can provide accurate predictions using quite coarse numrical mesh, and thus suitable for complex high Reynolds turbulent flow. The other objective of the present study is to assess the VLES method for flow control problems.

2. Numerical methods

The VLES method [7] based on the standard k-ε turbulence model is applied. The governing equations of turbulent kinetic energy k and its dissipation rate ε is the same as in the standard k-ε turbulence model. The turbulent viscosity is modelled by introducing a new resolution control function Fr. It has the form shown in Eq. (4), where L_c, L_i and L_k are the cut-off length scale, integral length scale and Kolmogorov length scale, respectively.

$$D\rho k / Dt = P_k - \rho\varepsilon + \partial\left[\left(\mu + \mu_t / \sigma_k\right)\partial k / \partial x_j\right] / \partial x_j \tag{1}$$

$$D\rho\varepsilon / Dt = (\varepsilon / k)\left(C_{\varepsilon 1}P_k - C_{\varepsilon 2}\rho\varepsilon\right) + \partial\left[\left(\mu + \mu_t / \sigma_\varepsilon\right)\partial\varepsilon / \partial x_j\right] / \partial x_j \tag{2}$$

$$\mu_t = Fr \cdot \rho C_\mu k^2 / \varepsilon \tag{3}$$

$$Fr = \min\left[1.0, \left(\left(1.0 - \exp(-\beta L_c / L_k)\right) / \left(1.0 - \exp(-\beta L_i / L_k)\right)\right)^2\right] \tag{4}$$

With the mesh resolution changing, the resolution control function *Fr* changes and then it determines how much of the turbulence is modelled. Thus, with different mesh resolution, the VLES method can work in different modelling modes, ranging from the RANS, LES to DNS. More details about the VLES method can be found in refs. [7-9].

The present VLES method has been implemented in the OpenFOAM toolbox [10]. The unsteady simulations are performed using the pimpleFOAM solver. The convective terms are discretized using a second-order central differencing scheme coupled with a small fraction of first order upwind scheme. The temporal advancement was approximated using a second-order implicit Crank-Nicolson scheme.

3. Results and discussions

Firstly, the classic turbulent flow around a square cylinder at Re=22000 is carried out to assess the performance of the VLES turbulence modelling using OpenFOAM toolbox. Two meshes with around 0.7 million and 1.2 million cells are used in the present simulations. The mean and RMS velocities at the central line downstream the square cylinder are shown in Fig. 2, with the experimental data [2] included. It can be seen that the present VLES model gives quite good predictions compared with experimental data for both the mean and RMS velocities. Also, with decreasing the mesh resolution, the results changes slightly, which demonstrates that the present VLES method is not sensitive to the mesh resolutions, and coarse meshes can be used for VLES studies.
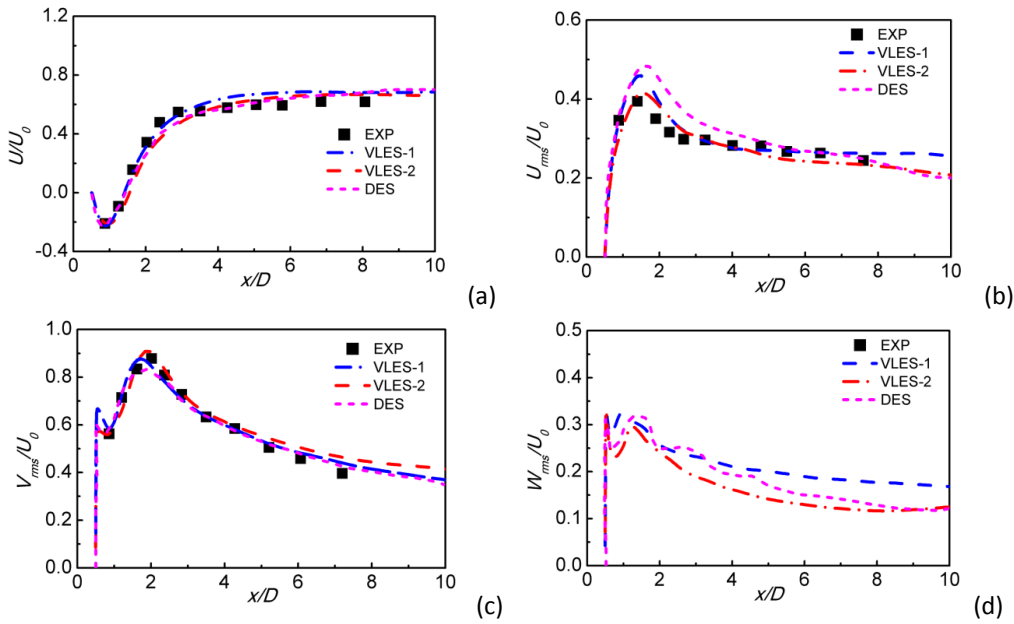
Figure 2: Comparisons of mean and RMS velocities along the central line in the middle plane of the square cylinder. (a) mean velocity in the x direction; (b) RMS velocity in the x direction; (c) RMS velocity in the y direction and (d) RMS velocity in the z direction. Experimental data is from ref. [2] and DES results from ref. [9].

The comparisons in Fig. 2 demonstrate that the present simulations with VLES modelling can give satisfactory results for the flow around a square cylinder. On the basis, the simulations are applied for the flow around the shaped-corner square cylinder, where the two corners at the front (as in Fig. 1) are cut-off. In the present study, two test cases are applied, i.e., case F1 with cut-corner scales of c_1/D=0.15 and c_2/D=0.15, case F2 with c_1/D=0.20 and c_2/D=0.15.

Table 1: The global flow parameters for turbulent flow around a square cylinder

		St	Cd_mean	Cd_rms	Cl_rms	ΔCd%
Square cylinder (F0) c_1/D=0, c_2/D=0	VLES	0.12	2.3	0.26	1.03	—
	Exp. [2]	0.13	2.2	—	—	—
	LES [11]	0.12-0.13	2.0-2.3	0.16-0.20	1.2-1.5	—
Shaped cylinder (F1) c_1/D=0.15, c_2/D=0.15	VLES	0.14	1.4	0.20	0.48	-39%
	Exp. [3]	0.16	1.3	—	—	-41%
Shaped cylinder (F2) c_1/D=0.20, c_2/D=0.15	VLES	0.17	1.2	0.18	0.37	-48%
	Exp. [3]	0.22	1.1	—	—	-50%

The global flow parameters for the baseline case F0 and two shaped corner cases, F1 and F2, are summarized in Table 1 with experimental data and previous simulation results. The comparisons show that the present VLES method generally gives good predictions compared with experimental data for all the three cases. The present simulation predicts a significant drag reduction of around 39% for case F1 and 48% for case F2, which are quite close to

experimental data. The results show that with the drag reduction, the Strouhal number is increasing and the RMS drag and RMS lift decreasing.
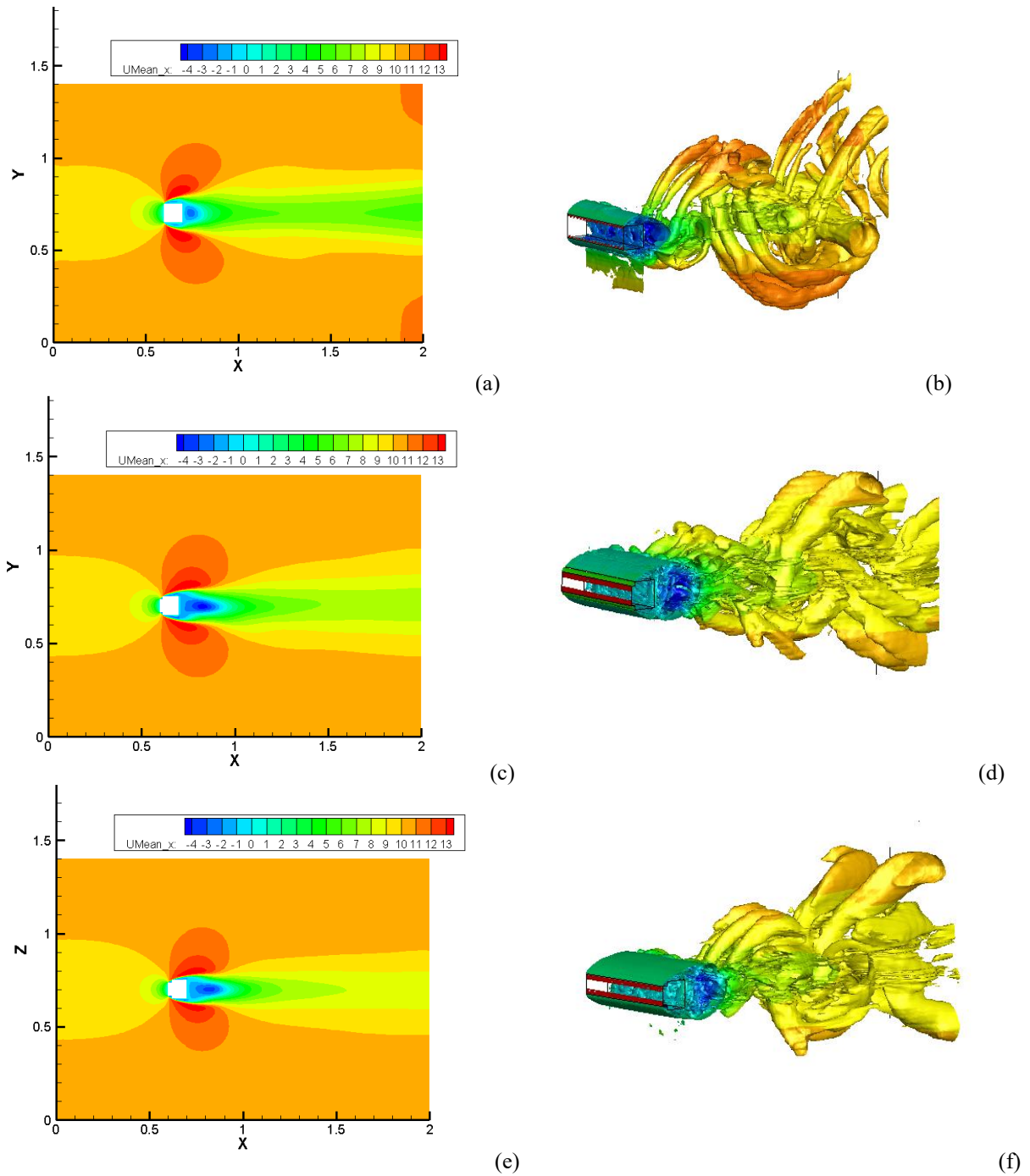
Figure 3: Results of the mean velocity (*Ux*) and the iso-surface of the second invariant of the velocity gradient (*Q*=100) for different cases: (a) *Ux* for case F0; (b) *Q* for case F0; (c) *Ux* for case F1; (d) *Q* for case F1; (e) *Ux* for case F2; (f) *Q* for case F2.

The mean velocity and the second invariant of the velocity gradient (Q) for different cases are shown in Fig. 3, where case F0 is the baseline case, F1 and F2 are the shaped corner cases. The mean velocity shows that cases F1 and F2 give a longer recirculation region compared with the baseline F0, which are consistent with previous observations. For the cases F1 and F2, a larger drag reduction is observed in case F2. However, the recirculation region behind the cylinder is not bigger than the case F1, while the width of the flow around the cylinder seems become narrow in case F2. The results imply that the drag reduction mechanisms of the case F1 and F2 are not the same. Detailed analysis will be carried out in the full length paper. The results of Q in Fig. 3 show that with the drag reduction, the wake region seems to become narrow and more stable. It also shows that bigger vortex structures can be observed in cases F1 and F2 compared with the baseline F0.

The results show that the present VLES modelling can give satisfactory results for the passive flow drag reduction simulations. The physical mechanism can be explored with the obtained simulation results. The study demonstrates that the OpenFOAM toolbox provides a very good platform for perform such kind of high-fidelity simulation studies.

More simulation results, comparisons and detailed analysis will be given in the full length paper.

References

[1] M. Gad-El-Hak, A. Pollard, J.P. Bonnet, Flow Control: Fundamentals and Practices, Assembly Automation, 42(2): 118 – 124, 1998.

[2] D.A. Lyn, S. Einav, W. Rodi, et al. A laser-Doppler velocimetry study of ensemble-averaged characteristics of the turbulent near wake of a square cylinder, Journal of Fluid Mechanics, 304: 285–319, 1995.

[3] M. Kurata, Y. Ueda, T. Kida, et al., Drag Reduction Due to Cut-Corners at the Front-Edge of a Rectangular Cylinder With the Length-to-Breadth Ratio Being Less Than or Equal to Unity, ASME Journal of Fluids Engineering, 131: 064501, 2009.

[4] G.S. He, N. Li, J.J. Wang, Drag reduction of square cylinders with cut-corners at the front edges, Experiments in Fluids, 55: 1745, 2014.

[5] A. Sohankar, M. Khodadadi, E. Rangraz, Control of fluid flow and heat transfer around a square cylinder by uniform suction and blowing at low Reynolds numbers, Computers & Fluids, 109:155-167, 2015.

[6] P. Sagaut, S. Deck, M. Terracol, Multiscale and Multiresolution Approaches in Turbulence, LES, DES and Hybrid RANS/LES Methods: Applications and Guidelines, 2nd ed., Imperial College Press, London, 2013.

[7] X. Han, S. Krajnovic, An efficient very large eddy simulation model for simulation of turbulent flow, International Journal for Numerical Methods in Fluids, 71(11):1341-1360, 2013.

[8] X. Han, S. Krajnovic, Very-Large Eddy Simulation Based on k-ω Model. AIAA Journal, 53: 1103-1108, 2015.

[9] X. Han, T. Ye, Y. Chen, Calibration of a new very large eddy simulation (VLES) methodology for turbulent flow simulation, Science China: Physics, Mechanics and Astronomy, 55: 1905-1914, 2012.

[10] OpenFOAM: The Open Source CFD Toolbox. User Guide Version 4.0, the OpenFOAM Foundation, 2017.

[11] A. Sohankar, L. Davidson, Large eddy simulation of flow past a square cylinder: comparison of different subgrid scale models, ASME Journal of Fluids Engineering, 122:39–47, 2000.

A CFD-PBE SOLVER FOR BUBBLE COLUMNS OPERATING AT HIGH PRESSURE

QIAN LI[1,2], YANLI QU[1,3], MUHAMMAD TAMOOR[1,2], JINGCAI CHENG[1*], CHAO YANG[1,2*], ZAI-SHA MAO[1]

[1] CAS Key Laboratory of Green Process and Engineering, Institute of Process Engineering, Chinese Academy of Sciences, Beijing 100190, China

[2] University of Chinese Academy of Sciences, Beijing 100049, China

[3] Sichuan University, Chengdu, Sichuan 610065, China

[*] Corresponding authors: jccheng@ipe.ac.cn (J.C. Cheng); chaoyang@ipe.ac.cn (C. Yang)

Keywords: OpenFOAM, high pressure, bubble column, population balance equation.

1. Introduction

OpenFOAM (open-source field operation and manipulation) is a free source CFD (computational fluid dynamics) package written in C++, which uses classes and templates to manipulate and operate scalar, vectorial and tensorial fields [1]. Its open-source characteristics facilitate the implementation of any addition or modification in the source code, which is very suitable for the purposes of research [2]. Recently, our group has developed several solvers and carried out simulations in the framework of OpenFOAM. Cheng et al. [3] developed a CFD-PBE (population balance equation) solver for gas-liquid flows. To validate this solver, a bubble column was simulated, and the simulation results showed generally reasonable agreement with the published experimental data. The coupling of pressure and velocity is resolved with the PIMPLE algorithm, which is a combination of the PISO (Pressure-Implicit with Splitting of Operators) and the SIMPLE (Semi-Implicit Method for Pressure-Linked Equations) algorithms. They found the PBE could be solved outside the PIMPLE loop to save much computation time, while still preserving the temporal information on variables. On this basis, a CFD-PBE-PBE solver for the reactive crystallization in airlift loop reactors was developed then [4]. PBE describing bubble coalescence and breakage was solved by the cell average method. Primary nucleation, secondary nucleation and particle growth were considered in the PBE describing the crystallization process, and solved using the standard moment method. The solver is validated with the formation of calcium carbonate via the reaction of CO_2 gas with $Ca(OH)_2$ solution in an airlift loop crystallizer. Effects of the crystallization kinetics and operation parameters were investigated. In addition, the primary KT high-resolution finite-volume central scheme [5] for uniform grids is extended to a general form and validated for pure growth in homogeneous systems [2]. With the extended KT scheme, a solver coupling the multiphase mixture model with a micromixing model and the general discretized PBE in OpenFOAM was used for simulating the antisolvent crystallization of lovastatin from a methanol-water mixture in a confined impinging jet [2]. The shapes of crystal size distribution (CSD) at various jet velocities were consistent with experimental observations.

Gas-liquid bubble columns are encountered in many industrial processes. Most industrial bubble columns are operated at high pressure [6]. The pressure has significant influence on the hydrodynamic parameters, such as gas holdup and bubble diameter. With the increase of pressure, the gas holdup increases and the bubble diameter and bubble rising velocity decrease significantly. The simulation investigations about the ambient pressure bubble columns have been carried out by many researchers. However, the simulation about high pressure bubble columns is very limited. Based on our previous works, a CFD-PBE solver for high pressure bubble columns is developed in this work. The effects of pressure on the gas holdup, bubble diameter and bubble size distribution (BSD) are investigated.

2. Mathematical models

The gas-liquid Eulerian two-fluid model is used to simulate the flow field. Mixture k-ε equations proposed by Behzadi et al. [7] are employed to model the turbulence. The interphase momentum transfer includes drag, lift, virtual mass, wall lubrication and turbulent dispersion terms. The drag force coefficient is calculated by the model of Tomiyama et al. [8]. In order to consider the effect of bubble swarm, the drag force is modified by the model of Rampure et al. [9]. The lift coefficient model of Fank et al. [10] and a constant virtual mass coefficient $C_{VM} = 0.25$ are used. The turbulent dispersion force is modeled by the formula of Burns et al. [11], and the wall lubrication is by the model of Tomiyama [12]. To describe the effect of pressure, a factor of $(\rho_g/\rho_{g,atm})^{0.25}$ is employed to modify the drag force [13]:

$$\mathbf{F}_{D,g} = -\frac{3C_D}{4d_b}\rho_l\alpha_g\alpha_l\left(\frac{\rho_g}{\rho_{g,atm}}\right)^{0.25}\left|\mathbf{u}_g - \mathbf{u}_l\right|(\mathbf{u}_g - \mathbf{u}_l) \tag{1}$$

It is found that the bubble diameter is decreased with the increase of pressure. The higher pressure enhances the breakup of large bubbles [14-16]. In order to describe the influence of the pressure on the bubble breakage rate, a factor B is used to modify the bubble breakage rate according to Yang et al. [6] as shown below:

$$B = \begin{cases} \rho_g^{70d-2800d^2} & d < 0.018 \\ \rho_g^{0.35} & d \geq 0.018 \end{cases} \tag{2}$$

The PBE is solved using the cell average method, which is an extension of the widely used fixed pivot method and has been proved more accurate in predicting the BSD. The bubble aggregation model of Prince and Blanch [17] and breakage model of Lehr et al. [18] are employed.

3. Results

Figure 1 shows the comparison of the simulated radial profiles of gas holdup with the published experimental results [19] at different pressures. It can be seen that, the simulated gas holdup increases with the increasing pressure. At the superficial gas velocity of 0.08 m/s, the variation of gas holdup with the pressure in the experiment is not very obvious. When the superficial gas velocity increased to 0.14 m/s, the distinction between the gas holdup measurements is significant, and the simulated results are in good agreement with the experimental data.

(a)   (b)
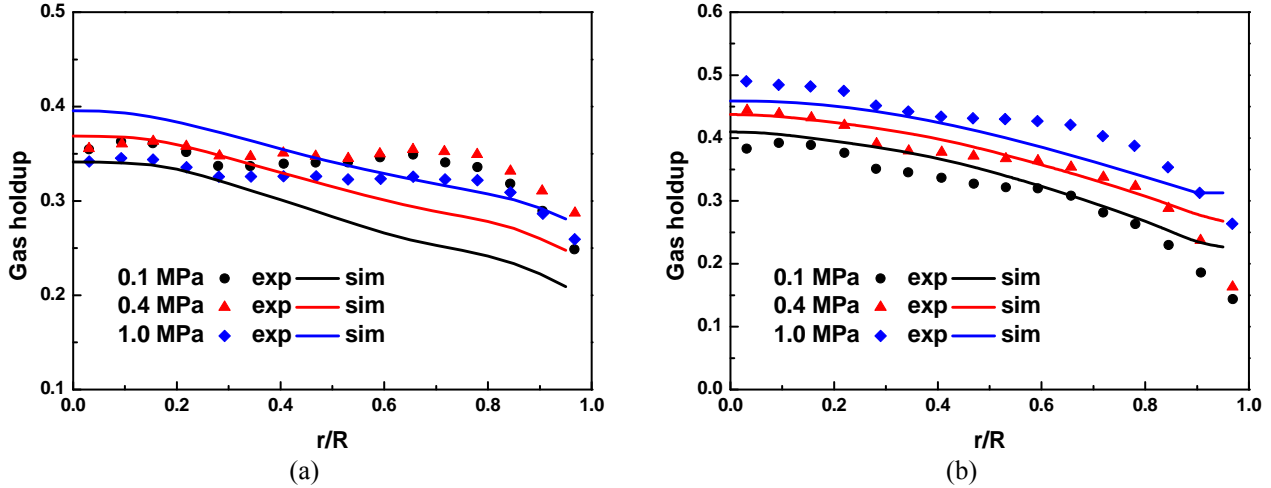
Figure 1: Comparison of simulated radial profiles of gas holdup with the reported experimental data [19] at different superficial gas velocities: (a) Vg = 0.08 m/s; (b) Vg = 0.14 m/s.

Figure 2 shows the variation of the radial profiles of the bubble mean diameter with the pressure at the superficial gas velocities of 0.08 and 0.14 m/s. It is obvious that, at the constant superficial gas velocity, the bubble diameter decreases when the pressure is changed from 0.1 to 1.0 MPa. A decrease of bubble diameter from the center of the reactor to the wall is captured by the simulation, which is consistent with the experimental observations.

(a)   (b)
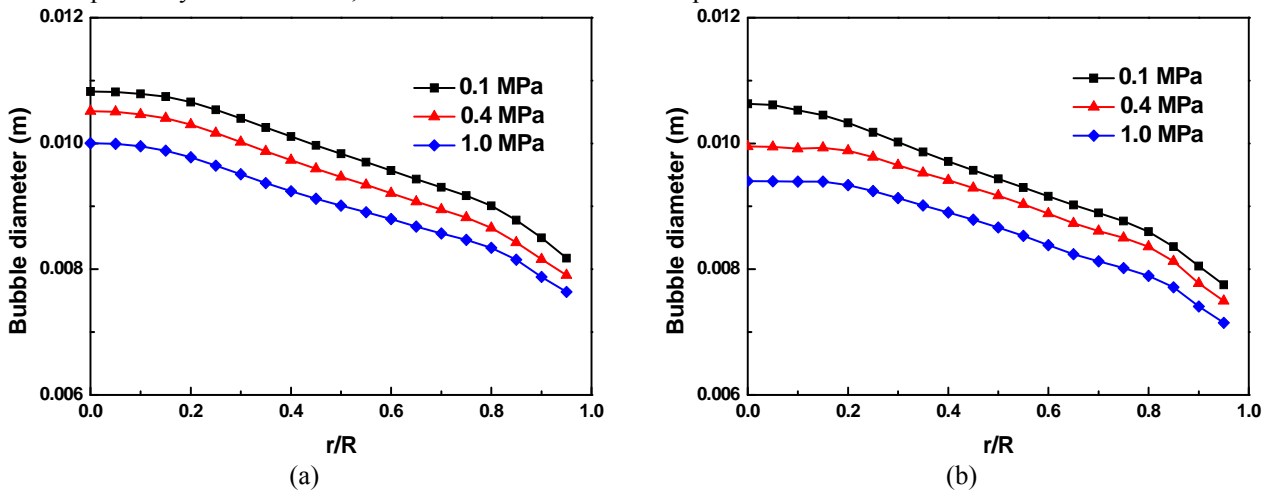
Figure 2: The effect of pressure on the radial profiles of bubble mean diameter at different superficial gas velocities: (a) Vg = 0.08 m/s; (b) Vg = 0.14 m/s.

Figure 3 is the variation of the bubble size distribution with the pressure at different superficial gas velocities. From the simulation results, one can found that the bubble size distribution becomes narrower when the pressure increases. Meanwhile, the number of large bubbles decreases obviously with the increase of pressure, implying that the bubble breakage rate increases.

(a)   (b)
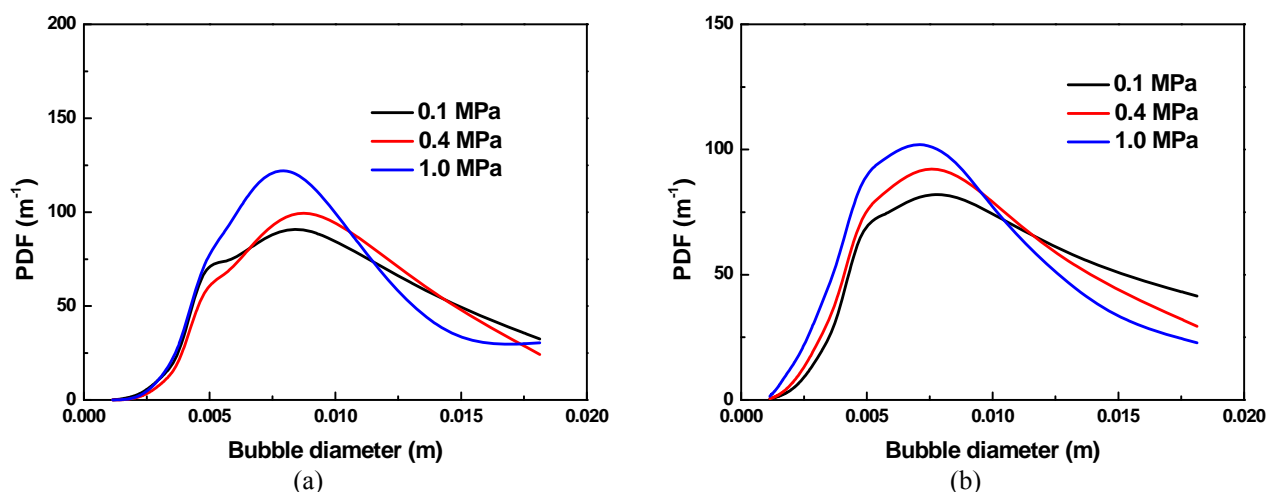
Figure 3: Effect of pressure on the bubble size distribution at different superficial gas velocities: (a) Vg = 0.08 m/s; (b) Vg = 0.14 m/s.

4. Conclusion

A CFD-PBE solver for high pressure gas-liquid bubble column is developed in the framework of OpenFOAM in this work. The predicted bubble diameter is larger in the center and smaller in the wall region, indicating that large bubbles are tend to gathering in the center region. With the increase of pressure, the bubble diameter decreases and the BSD is narrower, and the number of large bubbles decreases and that of small bubbles increases. These results show the feasibility of this solver in simulating the high pressure bubble columns.

References

[1] H. Jasak, H.G. Weller, A.D. Gosman. High resolution NVD differencing scheme for arbitrarilly unstructured meshes. Int. J. Numer. Meth. Fluids, 1999 (31), 431-449.

[2] J. Cheng, C. Yang, M. Jiang, Q. Li, Z.-S. Mao. Simulation of antisolvent crystallization in impinging jets with coupled multiphase flow-micromixing-PBE. Chem. Eng. Sci., 2017 (171), 500-512.

[3] J. Cheng, Q. Li, C. Yang, Z.-S. Mao. CFD-PBE simulation of a bubble column in OpenFOAM. Chinese J. Chem. Eng., 2018, in press.

[4] Q. Li, J. Cheng, C. Yang, Z.-S. Mao. CFD-PBE-PBE Simulation of an Airlift Loop Crystallizer. Can. J. Chem. Eng., 2018, in press.

[5] A. Kurganov, E. Tadmor. New high-resolution central schemes for nonlinear conservation laws and convection–diffusion equations. J. Comput. Phys., 2000 (160), 241–282.

[6] G. Yang, K. Guo, T. Wang. Numerical simulation of the bubble column at elevated pressure with a CFD-PBM coupled model. Chem. Eng. Sci., 2017 (170), 251-262.

[7] A. Behzadi, R. I. Issa, H. Rusche. Modelling of dispersed bubble and droplet flow at high phase fractions. Chem. Eng. Sci., 2004 (59), 759-770.

[8] A. Tomiyama, H. Tamai, I. Zun, et al. Transverse migration of single bubbles in simple shear flows. Chem. Eng. Sci., 2002 (57), 1849-1858

[9] M. R. Rampure, A. A. Kulkarni, V. V. Ranade. Hydrodynamics of bubble column reactors at high gas velocity: experiments and computational fluid dynamics (CFD) simulations. Ind. Eng. Chem. Res., 2007 (46), 8431-8447.

[10] T. Frank, J. M. Shi, A. D. Burns. Validation of Eulerian multiphase flow models for nuclear safety application. 3rd International Symposium on Two-Phase Flow Modelling and Experimentation. Pisa. 2004.

[11] A. D. Burns, T. Frank, I. Hamill, et al. The favre averaged drag model for turbulent dispersion in Eulerian multi-phase flows. 5th international conference on multiphase flow. Yokohama, Japan. 2004: No. 392.

[12] A. Tomiyama. Struggle with computational bubble dynamics. Multiphase Science and Technology, 1998 (10), 369-405.

[13] P. Chen, M. P. Dudukovic, J. Sanyal. Three-dimensional simulation of bubble column flows with bubble coalescence and breakup. AIChE J., 2005, 51(3), 696-712.

[14] V. Parisien, A. Farrell, D. Pjontek, et al. Bubble swarm characteristics in a bubble column under high gas holdup conditions. Chem. Eng. Sci., 2017 (157), 88-98.

[15] P. M. Wilkinson, L. L. V. Dierendonck. Pressure and gas density effects on bubble break-up and gas hold-up in bubble columns. Chem. Eng. Sci., 1990 (45), 2309-2315.

[16] S. Kumar, P. Munshi, A. Khanna. High pressure experiments and simulations in cocurrent bubble columns. Procedia Engineering, 2012 (42), 842-853.

[17] M. J. Prince, H. W. Blanch. Bubble coalescence and break-up in air-sparged bubble-columns. AIChE J., 1990 (36), 1485-1499.

[18] F. Lehr, M. Millies, D. Mewes. Bubble-size distributions and flow fields in bubble columns. AIChE J., 2002 (48), 2426-2443.

[19] B. Ong. Experimental investigation of bubble column hydrodynamics: Effect of elevated pressure and superficial gas velocity. Saint Louis, Missouri, USA. Sever Institute of Washington University, 2003.

IMMERSED BOUNDARY SURFACE METHOD IN FOAM-EXTEND

HRVOJE JASAK[1,2]

[1]*Wikki Ltd, United Kingdom, h.jasak@wikki.co.uk*
[2]*University of Zagreb, Croatia,hrvoje.jasak@fsb.hr*

This paper describes a new method of handling non-conforming immersed boundaries within the background mesh with minimal level of approximation. The immersed boundary surface is represented by a triangulated surface mesh which interacts with the polyhedral background body-fitted mesh only at the level of implicit and explicit discretisation operators. While no new cells or faces are introduced in the geometry, the Immersed Boundary Surface method accounts for the presence of a non-conforming patch in the manner consistent with the "cut cell" approach. Surface data such as pressure or viscous stress is evaluated on an adaptively coarsened representation of the triangulated surface, created via intersection with the background mesh. The immersed boundary surface method is validated against body-fitted meshes for laminar, turbulent and free surface flows on static and moving mesh/surface cases and deployed with a new implementation of adaptive mesh refinement.

Introduction

The existing implementation of the Immersed Boundary Method (IBM) In `foam-extend-4.0` [1] has proven to be versatile, but with some drawbacks. The most significant are loss of accuracy in the vicinity of the Immersed Boundary (IB), handling of Neumann boundary conditions which cannot be fully implicit, wall function implementation with sampling of turbulence variables beyond a single-cell depth and others.
In free surface flows, the IBM solver exhibits strong instability next to the IB surface, which has proven to be particularly cumbersome. The crux of the problem is the inability of the IBM to match gradients of different variables at the IB, and polynomial fitting of the Volume of Fluid (VoF) field which contains a step-function.
Having failed to stabilise the IBM sufficiently for industrial-grade CFD simulations, our objective is to provide a robust and efficient Immersed Boundary capability for naval hydrodynamics simulations, specifically for motion of floating objects in confined spaces. To achieve this, handling of IB patches is re-examined from first principles.

Existing Immersed Boundary Method

Existing implementation of the Immersed Boundary Method (IBM) is based on polynomial fitting of the solution with respect to the boundary condition and the internal field supporting stencil:

$$\phi_P = \phi_{ib} + C_0(x_P - x_{ib}) + C_1(y_P - y_{ib}) \\ + C_2(x_P - x_{ib})(y_P - y_{ib}) + C_3(x_P - x_{ib})^2 + C_4(y_P - y_{ib})^2, \tag{1}$$

where P and ib denote the cell centre and the IB point, respectively (see Figure 1). Equation 1 requires sufficient resolution in front of the IB point, matching of the IB patch and background mesh resolution and *a-priori* assumption that a variable can be fitted by a polynomial In general none of these hold.
The IBM implementation relies on the imposition of the boundary condition in the bulk of the mesh: this is built into the discretisation matrix at the location of the IB cell centre. While this standard manner of handling IB boundaries may sound adequate, the implementation loses information in the cut cell: reduction in cell volume; loss of precision at the intersection, choice of the supporting stencil for polynomial fitting, handling of the mesh motion fluxes *etc.*
While functionally correct, the idea of polynomial fitting is only adequate for smoothly varying solution variables, but clearly fails for *e.g.*. turbulent wall functions or a a step-profile variables such as the volume fraction α in free surface flows. Attempts to use the Level Set free surface capturing and the Ghost Fluid Method for interface handling [2] proved superior over the original method, but not completely satisfactory.
Further issues with the existing IBM have come to the fore. The most notable is related to evaluation of forces on IB surfaces, as required eg. by a 6-DOF floating body simulation in a free surface flow, which is the main objective of this work. The IB force data can only be correctly evaluated on a continuous and closed STL surface, but whose resolution may vary substantially from the background mesh. Under such conditions, inaccuracy in interpolation from volumetric background mesh data to the IB surface mesh may be significant and further degrade the solution.

Finally, the problem of a moving IB surface is more severe than previously thought. It is necessary to consistently handle the moving wall boundary condition, requiring a manner inconsistent with the conventional moving deforming Finite Volume Method (FVM) [3].

In conclusion: further improvement in robustness and accuracy is sought regarding the precision and stability of discretisation at the IB surface via a completely new approach: The Immersed Boundary Surface (IBS) Method.

New Algorithm: Immersed Boundary Surface

Starting from first principles, we shall discard the idea of polynomial interpolation into IB points which is the basis of existing IBM. Instead, we shall account for the influence of the IB within the mesh as if the mesh is body-fitted, similar to the way a GGI patch imitates the presence of actual cut faces via interpolation factors [4]. The procedure consists of the following steps:

- Introduce the "new" IB face in the cut cell;

- Account for the partial cell volume and face area of affected cells / faces without loss of accuracy; and

- Perform conventional body-fitted FVM discretisation on a partial cell / partial face geometry,

but without changing the geometric mesh at all!

The conventional body-fitted FVM method operates on the following geometrical data:

- Cell-to-face connectivity: owner/neighbour addressing;

- Cell volumes and face area vectors;

- Face interpolation factors and delta-coefficients (1/distance).

For static mesh cases, no further geometrical data is required.

For cells that are unaffected by the IBM or located within the IB surface, conventional discretisation applies without correction. Inactive cells/faces are removed from the matrix by setting their volume/area to zero, without the need for interpolation or stabilisation, as they are completely detached from the region of interest. A cell which intersects with the IB surface is recognised by the fact that some part of it remains on the "live side" of the surface. While this cell is modified, its (topological) connectivity with the rest of the mesh remains unchanged. It however, yields an extra boundary face, representing the IB surface cut.

A schematic approach of the existing IBM and new IBS implementation is shown in Figure 1.
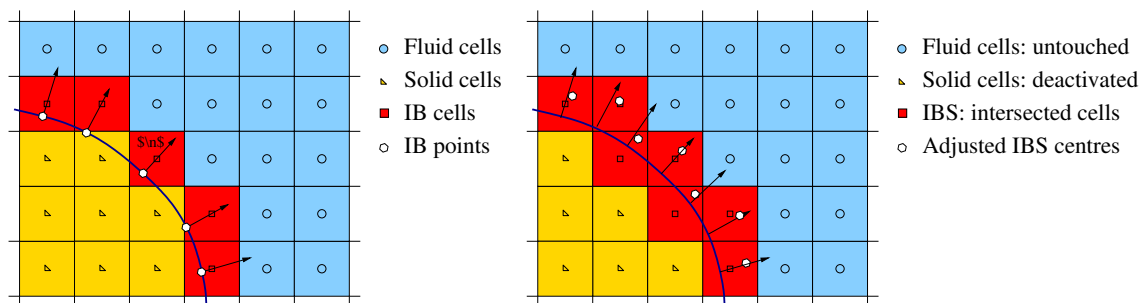
Figure 1: Comparison of the old and new Immersed Boundary Algorithm: dead, interpolated and live cells.

Such an approach has numerous advantages. Firstly, the IB patch is included into the mesh via the distance function: all cells that straddle the immersed boundary remain active and their cell volume and face areas are adjusted using the exact geometrical operations. Secondly, the resolution of the IB STL patch or its quality are unimportant: only the nearest distance data is used. Thirdly, underlying mesh connectivity remains the same after cutting and cut cell re-uses discretisation matrix slot of the original cell. Finally, new faces are created as 1-per-cut-cell and contained in the immersed patch: IB patch face-cell addressing identifies cut cells. In such an arrangement, conventional FVM discretisation can be used without modification or polynomial fitting. The topological connectivity and the sparseness pattern of the background mesh are preserved.

Implementation of the Immersed Boundary Surface Algorithm

The matrix entry for the cut (IB) cell shall represent a geometry which is significantly different from the background cell, and which shall be calculated by cutting with the IB surface. For the cut cell we shall introduce a new IBS face. Cell volume, centroid, face centres, area and interpolation factors for intersected faces are calculated by intersecting the cell and its faces with the IB, via a distance functions, yielding perfect intersection.

The original cell volume and face area entries in the `fvMesh` class for intersected cell/face elements of the background mesh shall be adjusted by intersection and represent the "live" part of cell/face, with appropriate adjustment in the cell/face centroid and norm.

Imposition of boundary conditions on the IB patch is straightforward and consistent with the body-fitted FVM. Immersed boundary is represented in the mesh by STL intersection with cells and its resolution is adjusted "automatically": by intersection with the background mesh. In other words, the STL IB surface is automatically refined/coarsened to comply with the background mesh without intervention.

On static meshes, the IB patch supports regular boundary conditions without change. For moving mesh / moving IB surface cases, the IB cut shall be re-calculated in response to mesh motion, yielding a different number of cut cells (equal to the number of IB patch faces) and different face-cell connectivity. In such cases, the definition of the IB boundary shall be attached to the IB STL surface and interpolated to currently live cut faces. This requires a custom `immersedBoundaryFvPatchField` boundary condition, which also handles data I/O and evaluation of IB patch field data.

Some degenerate cases need to be handled. A "regular intersection" occurs between a cell and the IB surface when there are no exact point-to-point hits between the IB and background mesh, which cannot be assumed. Due to finite accuracy, STL regularly coincides with background mesh points or faces, or does not provide accurate intersection. An example would be a direct face intersection between a Dry and a Wet cell, where the background mesh face in fact becomes the IB face.

Degenerate Intersections

Inaccurate intersection of STL feature edges/points may yield a geometrically open cell, with possible robustness issues. This is resolved using the trick known as the Marooney Manoeuvre [5] to guarantee a closed cell after cutting:

$$\sum_C \mathbf{s}_f = \mathbf{0} \qquad \text{for a regular cell,} \qquad (2)$$

$$\sum_C \gamma_f \mathbf{s}_f + \mathbf{s}_{f\,IB} = \mathbf{0} \qquad \text{for an intersected cell,} \qquad (3)$$

where γ_f is the area correction, obtained by cutting. The corrected IB face area $\mathbf{s}_{f\,IB}$ is:

$$\mathbf{s}_{f\,IB} = -\sum_C \gamma_f \mathbf{s}_f. \qquad (4)$$

Moving Immersed Boundary Surface

Moving mesh Finite Volume Method uses a compensated form of the transport equation for the arbitrary moving/deforming volume, introducing mesh motion fluxes $F_b = \oint_f \mathbf{u}_b$, where U_b is the mesh velocity calculated directly from the deforming geometry. The motion is deemed correct, if the Space Conservation law is satisfied:

$$\int_V \frac{\partial V}{\partial t} - \oint_S (\mathbf{n} \cdot \mathbf{u}_b)\, dS = 0. \qquad (5)$$

On body-fitted meshes, its first-order accurate discretised form reads:

$$\frac{V^n - V^o}{\Delta t} - \sum_f F_b = 0. \qquad (6)$$

For moving IB surface cases (assuming either static or moving background mesh), the volume swept by the immersed face needs to be evaluated consistently. However, since the IB-to-cell connectivity is no longer clear, a special practice, consistent with the moving mesh FVM is needed.

Volume swept by immersed face is calculated from the new IB face geometry and motion distance Figure 2 and distributed into the affected cells:

$$V_b = \mathbf{x}_b \cdot \mathbf{s}_f{}^n \quad \text{volume swept in red,} \qquad (7)$$

where $\mathbf{x}_b$ is geometrical motion distance from old to new STL As the intersected area changes, swept volume must be distributed, Figure 2:

- Cell A: expand from cut volume to full volume: no IB face in new configuration;

- Cell B: cut both at new and old configuration: IB face present;

- Cell C: expand from zero volume to partial volume: IB face present;
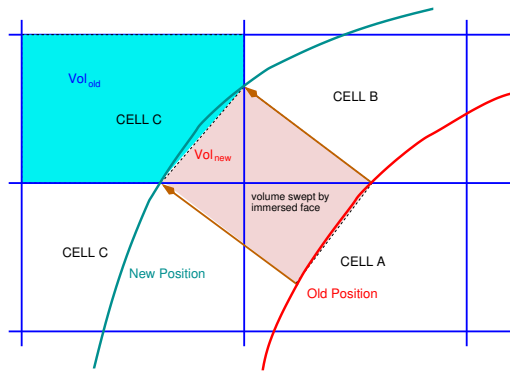
Figure 2: Moving Immersed Boundary Surface: mesh motion fluxes.

- (Cell D): expand from zero to full volume (cell fully swept by IB): no IB face.

To guarantee that the Space Conservation Law, Equation 5 is satisfied, the "Motion Flux manoeuvre" is performed, following the idea of the original Marooney Manoeuvre:

1. If the cell is "dead" at new level, no compensation is needed: $V^n = 0$

2. If the cell is "live" at new level, compensate by adjusting cell volume to keep both V^o and V^n positive: **Cell B, Cell C**

    - Perform virtual re-meshing at old time-level

$$V^o = V^n - \Delta t \sum_f V_b \; if \; V^o >= 0$$

    - Otherwise, perform virtual re-meshing at new time level:

$$V^n = V^o + \Delta t \sum_f V_b \; if \; V^n >= 0$$

This yields a consistent and conservative mesh motion fluxes for all cases.

Validation on Turbulent and Free Surface Flows

A number of laminar and turbulent flow cases has been studied with excellent results, some of which are shown in Figure 3.

Conclusion and Future Work

A new method for handling non-conformal Immersed Boundary interfaces has been implemented and validated. The Immersed Boundary Surface method accounts for the presence of the non-conforming boundary by directly changing the discretisation matrix to mimic the form it would have if the IB faces were included directly into the background mesh. The method has been implemented in `foam-extend-4.1`, parallelised and validated in laminar and turbulent flow and multi-phase free surface simulations. It is regularly used with the IB-sensitised polyhedral adaptive mesh refinement, which locally enriches the background mesh in the vicinity of the IB surface to the required level

References

[1] U. Senturk, D. Brunner, H. Jasak, N. Herzog, C. Wodled, and A. Smits, "Benchmark simulations of flow past rigid bodies using an open-source, sharp interface immersed boundary method," *Progress oin CFD*, 2018.

[2] V. Vukčević, H. Jasak, and I. Gatin, "Implementation of the Ghost Fluid Method for Free Surface Flows in Polyhedral Finite Volume Framework," *Comput. Fluids*, vol. 153, pp. 1–19, 2017.

[3] v. Tuković and H. Jasak, "A moving mesh finite volume interface tracking method for surface tension-dominated interfacial fluid flow," *Computers and Fluids*, vol. 55, pp. 70–84, 2012.

[4] M. Beaudoin and J. H., "Development of a generalized grid mesh interface for turbomachinery simulations with openfoam," in *Open Source CFD International Conference, Berlin*, December 2008.

[5] C. Marooney, "The Marooney Manoeuvre," Private Communication.
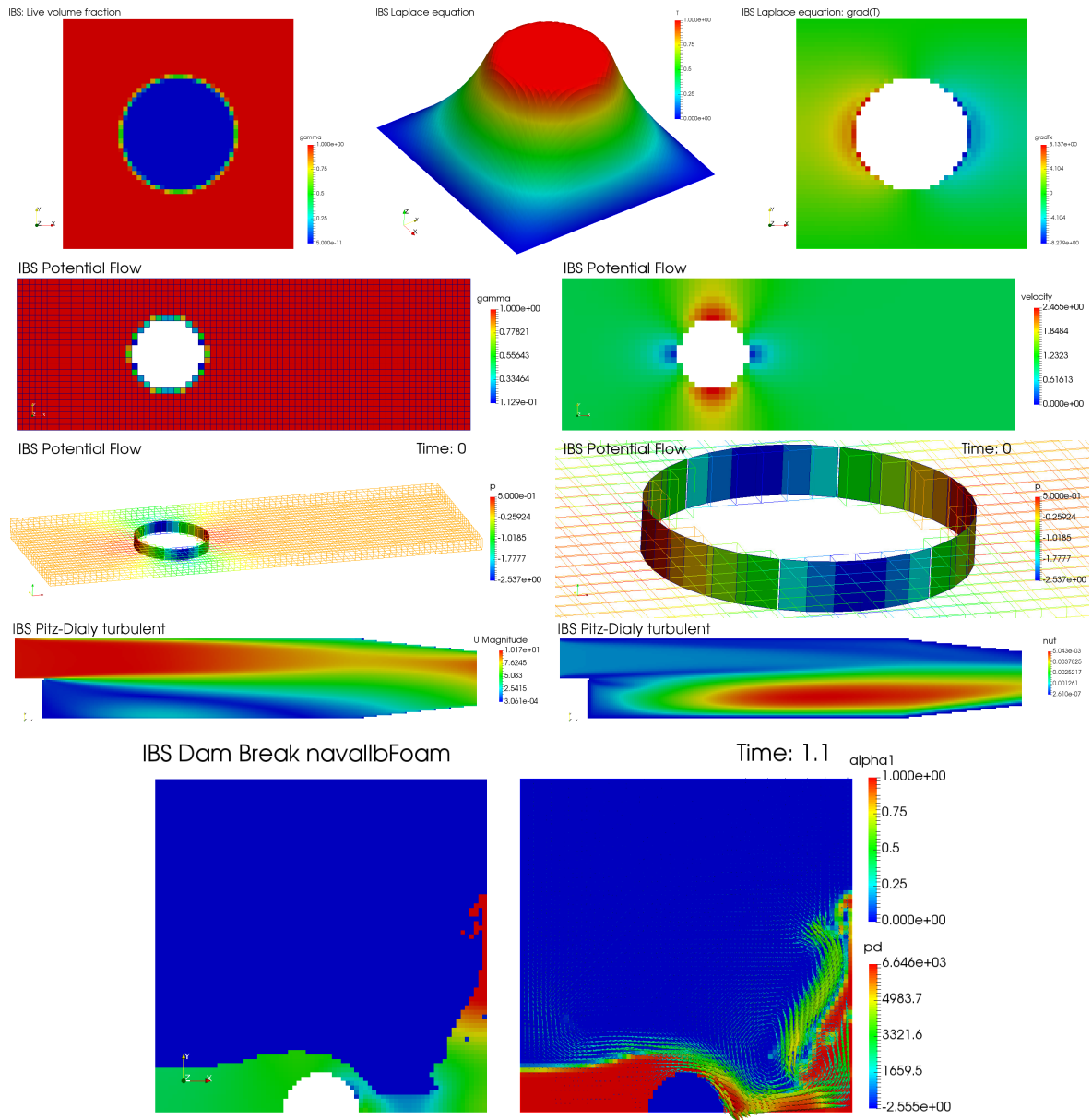
Figure 3: **Validation of the Immersed Boundary Surface method for laminar, turbulent and free surface flows.**

NUMERICAL VALIDATION OF WAKE INTERACTION BETWEEN TWO OFFSET MODEL WIND TURBINES BASED ON ACTUATOR LINE MODEL

XINZE DUAN[1], PING CHENG[2], DECHENG WAN*

State Key Laboratory of Ocean Engineering, School of Naval Architecture, Ocean and Civil Engineering, Shanghai Jiao Tong University, Collaborative Innovation Center for Advanced Ship and Deep-Sea Exploration, Shanghai 200240
*Corresponding Author: dcwan@sjtu.edu.cn

In large wind farms, some wind turbines are disturbed by the wake of other turbines. The wake interaction phenomenon among wind turbines has a great influence on aerodynamic power output, wind speed deficit turbulence stress and wake vortex structure, which indicates that more attention should be placed on the wake interaction for the optimal arrangement of wind farm. In this paper, the actuator line model combined with CFD technique will be applied to study the wake interaction between two offset wind turbines. The results obtained from the present simulations are compared to the data from the experiment "Blind Test 3" and other simulation models. From the comparison, the results from the present study show a good agreement with the experimental results especially for the aerodynamic loads prediction, whose error is not over 3% for the upstream wind turbine. Although the simulations for two offset wind turbines model exist some difference in wake prediction compared to the "Blind Test 3", the overall change trend is consistent with the experiment. Based on the results, the actuator line model can simulation the aerodynamic loads of the two offset model wind turbines and basic features of the wake, including the distribution characteristics of the mean wake velocity and mean turbulent stress.

Introduction

The wake interaction among wind turbines will lead to the decreased inflow wind velocity and increased turbulence intensity. Decreased total production of power and increased levels of fatigue loads are imposed on the turbines in the wind farm due to the phenomenon of wake interaction[1]. Therefore, how to accurately simulate the wake interaction among multiple wind turbines is becoming the key problem to improve the efficiency of the wind farm.

In order to study the complex phenomenon of wake interaction in wind farms, some scholars attempt to model the flow field in wind farms are based on CFD approach. Frandsen[2] pointed out that the advantage of using CFD approach is that they, besides avoiding the scale effect in the model experiment and handling the large Reynolds number problem well, also provide necessary information about the wake characteristics. A mixed method named actuator line model (ALM) combined with CFD technique was developed by Sørensen and Shen[3] is an extensively used method to model the rotor as force field. Some researchers have done lots of work about the wind farm simulation using actuator line model. Churchfield[4][5] have done a large-eddy simulation of the Lillgrund wind plant which contains 48 multi-megawatt turbines, and turbines were modeled using actuator line representation. Ai Yong[6] presented numerical simulations of the effects of inter-turbines spacing changed from three to nine times of rotor diameter on aerodynamics for wind farms contained two NERL 5MW baseline wind turbines in tandem layout.

In this present study, a numerical validation of CFD combined with actuator line methods for modeling the rotors is conducted. The results obtained from the present simulations are compared to the data from the experiment "Blind Test 3" and other simulation models including the aerodynamic loads, the mean wake velocity and mean turbulent stress.

Numerical modelling

The actuator line model (ALM) was firstly developed by Sørensen and Shen[7]. The rotating blades are virtualized into span wise sections of constant airfoil, chord and twist and the forces are distributed over them. Hence, there is not requirement to build the actual blades model. The local velocity U_{rel} relative to the rotating blade is calculated as:

$$|U_{rel}| = \sqrt{(U_{in})^2 + (\Omega r - U_{rot})^2} \tag{1}$$

where U_{in} represents the inflow wind velocity, Ω is the angular velocity of the rotor. The inflow angle is determined as:

$$\phi = tan^{-1}\left(\frac{U_{in}}{\Omega r - U_{rot}}\right) \tag{2}$$

The local angle of attack is given by $\alpha = \phi - \theta_t$, where the θ_t is the local twist angle. Having determined the angle of attack and relative velocity, the lift and drag force per span wise length can be got:

$$f = (L, D) = \frac{\rho |U_{rel}|^2 c N_b}{2 r d\theta dz}(C_L e_L + C_D e_D) \tag{3}$$

where c is the chord length; N_b is the number of blades; C_L and C_D are the lift and drag coefficient, respectively; The aerodynamic blade force that cannot be directly applied to the flow field, it need to be distributed smoothly on the flow field volume in order to avoid singular behaviour. In practice, a 3D Gaussian function is made to smooth the force over the blade by taking the convolution of the force with a regularization kernel.

$$f_\varepsilon = f \otimes \eta_\varepsilon \tag{4}$$

$$\eta_\varepsilon(d) = \frac{1}{\varepsilon^3 \pi^{3/2}} exp\left[-\left(\frac{d}{\varepsilon}\right)^2\right] \tag{5}$$

where d is distance between cell-centered grid points and the actuator line point, and ε is parameter that serves to control the width of Gaussian and to adjust the concentration of the regularized loads.

The k-ω SST turbulence model is applied to solve the RANS equation. And the governing equations can be written as:

$$\nabla \cdot U = 0 \tag{6}$$

$$\frac{\partial U_i}{\partial t} + \frac{\partial}{\partial t}(U_i U_j) = -\frac{1}{\rho}\frac{\partial p}{\partial x_i} + \frac{\partial}{\partial x_j}(v\frac{\partial U_i}{\partial x_j} - \overline{u_i' u_j'}) + \frac{1}{\rho}f_\sigma \tag{7}$$

where U is the velocity of flow; ρ is the density of the fluid; p is the pressure; v is the kinematic viscosity, f_σ denotes the body forces, which represent the loading on the rotating blades. The body force acting on the blades are determined using a blade element method combined with tabulated two-dimensional airfoil characteristics.

Experiment Description and Simulation Setup

The Blind test 3 was organized by Norcowe and Nowitech in Bergen, 10 and 11 December, 2013. The wake development behind two model wind turbines that have been extensively tested in the large close-loop wind tunnel facility at NTNU. The two turbines were arranged offset so that downstream wind turbine was affected by the partial impingement of the wake developed by the upstream turbine. Sketches of the layout are given in Fig. 1 shows a picture of the turbines mounted in the tunnel. The wind tunnel has a rectangle test section, whose dimensions at the inlet are W=2.72 m and H=1.80m (W means width and H means height). In addition, a large scale bi-planar grid was mounted at the entrance to the test section in order to make the conditions more similar to the atmospheric conditions. The reference velocity was set to U_∞ = 10 m/s. At this velocity, the turbulence intensity is TI =10% at the inlet. More detail about the "Blind Test 3" can be found in reference[8][9].

Figure 1: wind tunnel

Furthermore, the two wind turbines have the same blade geometry, but slightly different hub size, thus leading to different rotor diameter. The diameters of upstream and downstream wind turbine are 0.944 m and 0.894 m, respectively. Table 1 gives some specification of the two wind turbines used in this present study. Where WT1 represents the upstream wind turbine and WT2 is the downstream wind turbine.

Table 1. Parameters of two wind turbines

Items	WT1	WT2
Airfoil	S826	S826
Rotor Diameter	0.944 m	0.894 m
Nacelle Diameter	0.13 m	0.08 m
Height of tower	0.817 m	0.817 m
Pitch Angle	0	0
Tip Speed Ratio	6	4.75

In order to compared to "Blind test 3", the computation of the numerical study is stayed as the same dimensions with the wind tunnel in NTNU. Meanwhile, the wind turbines maintain the same layout. Furthermore, the mesh has been densified in order to fully resolve the strong gradients in the vicinity of the actuator lines and carefully observe significant meandering of the wake. Finally, the total mesh is controlled about 14.5 million for the numerical case.

(a) Grid in cross section   (b) Grid in lengthwise section
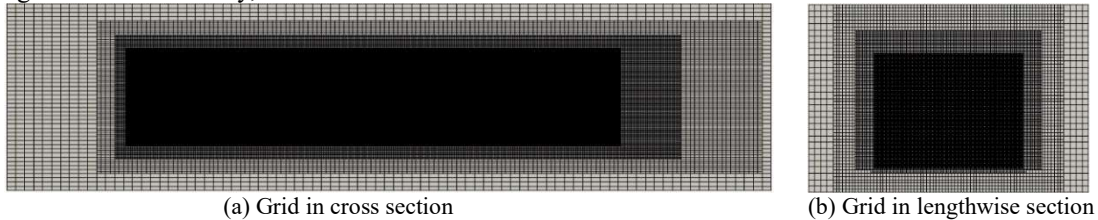
Fig. 2 The grid in lengthwise section and cross section

In this study, the uniform free-stream flow condition whose values is 10 m/s at the reference height of hub is applied to the inlet. A relative pressure of 0 Pa based on the atmospheric pressure is chosen for outlet boundary. Considering the blockage effects, the wall condition is applied to the top, bottom and sidewall boundary.

Results of Validation

The upstream wind turbine operates at tip speed ratio 6 and the downstream wind turbine runs at lower tip speed ratio 4.75. The experimental value from the "Blind Test 3" and the numerical value are summarized in table 2. From the validation of aerodynamic loads against the results from "Blind Test 3", it can be concluded that there is quite well prediction of aerodynamic load including the aerodynamic power and thrust for the upstream wind turbine when simulation for two offset wind turbines by using CFD technique the actuator line model. There is reasonable error for the engineering application, whose error is not over 5% for the both wind turbines.

Table 2. Summary of numerical and experimental results for aerodynamic power and thrust coefficient

Items		Numerical value	Experiment	Relative error
C_P	WT1	0.440	0.430	+2.326%
	WT2	0.292	0.299	-2.341%
C_T	WT1	0.801	0.771	+3.891%
	WT2	0.570	0.547	+4.205%

The time history curves of aerodynamic loads are shown in Figure 3. The most noticeable feature of these time history curves of aerodynamic loads, aside from the difference in loads levels, is that there is obvious oscillation in the loads curves of the downstream wind turbines. The loads curves of the wind turbine in the middle with the offset layout have a periodic variation that the frequency of oscillation equals to three times the rotor rotation frequency on these three-bladed turbines roughly. The reason of this interesting phenomenon may be that the middle turbine in the offset model is affected by the partial impingement of the wake developed by the upstream turbine.

(a) aerodynamic power	(b) aerodynamic thrust
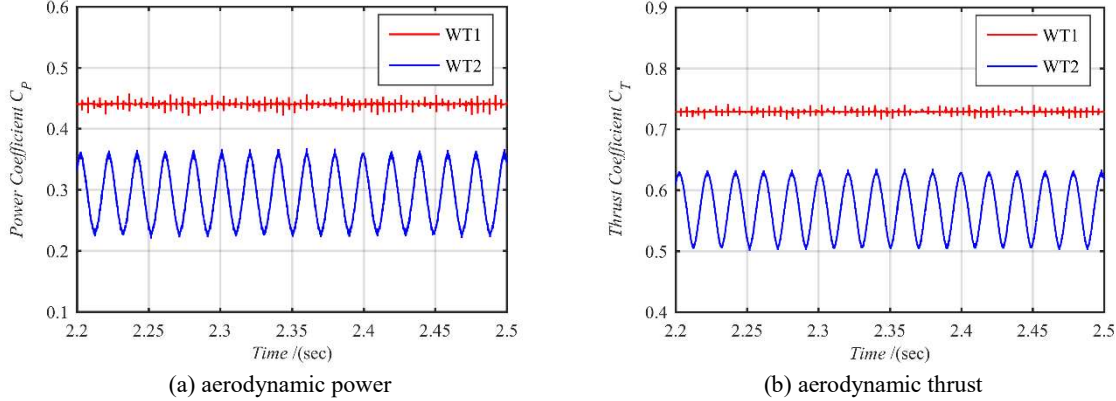
Figure 3: Time-history curve of aerodynamic loads.

Meanwhile, Figures. 4~5 show the wake prediction including the mean wake velocity and mean turbulent stress at two positions (X=1D, 3D; D is the rotor diameter of the downstream turbine) behind the downstream wind turbine along the width direction. Furthermore, the effect of hub, nacelle and tower are not included in present simulation.

(a) Mean wake velocity	(b) Mean turbulent stress
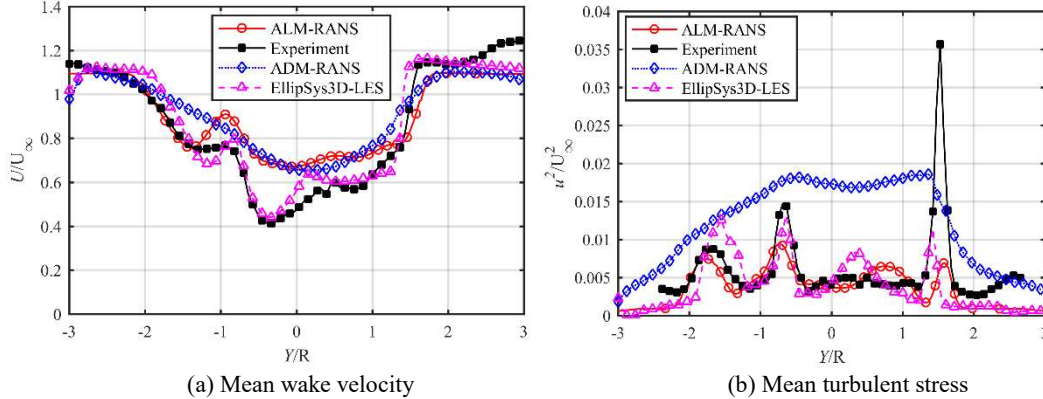
Figure 4: Wake prediction at X/D=1 behind the downstream wind turbine

(a) Mean wake velocity	(b) Mean turbulent stress
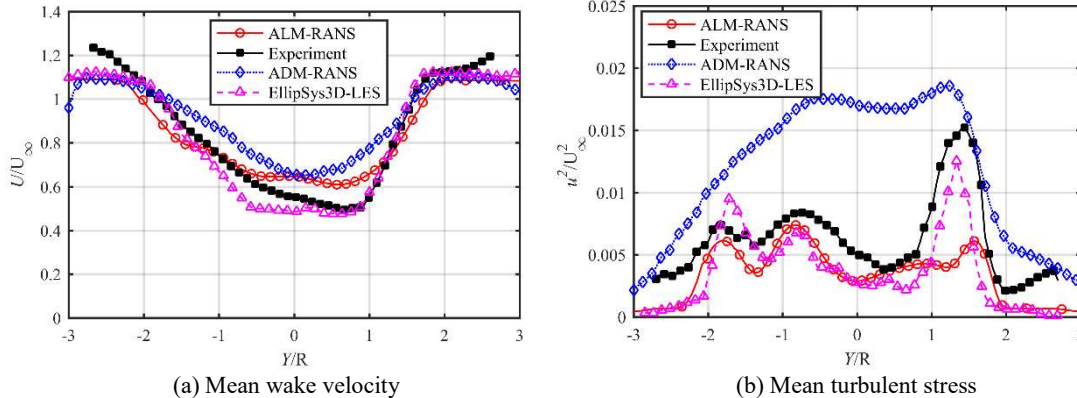
Figure 5: Wake prediction at X/D=3 behind the downstream wind turbine

From the figures, the numerical value by using the ALM is marked with solid red circles, there are a few obvious observations that may be made immediately. The mean wake velocity profile calculated from the simulation using actuator line model is higher compared to the experimental results marked in filled black squares. Since the current simulations don't take into account the effect of the nacelle and tower, the wake generated by the tower is ignored, which leading to the prediction for the wind velocity deficit is some lower. Furthermore, to a certain extent, the mean turbulent stress profile also has a good agreement with the experiment. Though the present study underestimates the turbulent stress magnitude especially in the peaks, whose value is much lower than the "Blind Test 3".
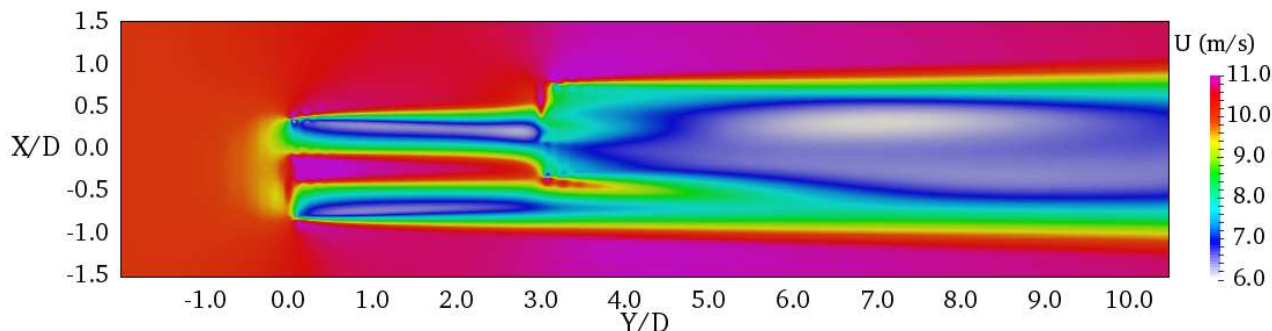
Figure 6: Axial velocity contour

Figure 6 shows contours of instantaneous streamwise velocity in horizontal plane through the center of wind turbine rotor, these figures are meaningful to understand overall wake flow regions. There is a higher speed region of flow near the center of the rotor. The reason for this phenomenon is that the effect of the hub, nacelle and tower are not considered in present simulation. It can also imply that the influence of upstream wind turbine on wake is significant, so there is still strong wake interference which is the main reason that causes the serious decrease in velocity of wake flow.

Conclusion

From above discussion, in actuator line simulations, the boundary layers are not explicitly simulated, but their effect is taken into account via the lift and drag coefficients. Although there is a certain error in wake prediction between the numerical simulation and the experiment "Blind Test 3", the overall change trend is consistent with the experiment. The actuator line model still can result the aerodynamic loads of the two offset model wind turbines and basic features of the wake.

Acknowledgements

References

[1] Abderrazzaq M A, Hahn B (2006). Analysis of the turbine standstill for a grid connected wind farm (case study) [J]. Renewable energy, 2006, 31(1): 89-104.

[2] Frandsen S T, Jørgensen H E, BARTHELMIE R, et al. The making of a second-generation wind farm efficiency model complex[J]. Wind Energy, 2009, 12(5): 445-458.

[3] Sørensen J N, Shen W Z. Computation of wind turbine wakes using combined Navier-Stokes/actuator-line Methodology[C]//1999 European Wind Energy Conference and Exhibition. 1999: 156-159.

[4] Churchfield M J, Lee S, Moriarty P, et al. A large-eddy simulation of wind-plant aerodynamics[C]// 50th AIAA Aerospace Sciences Meeting including the New Horizons Forum and Aerospace Exposition. 2012: 537.

[5] Churchfield M J, Lee S, Michalakes J, et al. A numerical study of the effects of atmospheric and wake turbulence on wind turbine dynamics[J]. Journal of turbulence, 2012 (13): N14.

[6] Ai Y, Wan D, Hu C. Effects of Inter-Turbines Spacing on Aerodynamics for Wind Farms Based on Actuator Line Model[C]//The 27th International Ocean and Polar Engineering Conference. International Society of Offshore and Polar Engineers, 2017.

[7] Sørensen J N, Shen W Z. Numerical modelling of wind turbine wakes[J]. Journal of fluids engineering, 2002, 124(2): 393-399.

[8] Pierella F, Eriksen P E, Sætran L, et al. Invitation to the 2012" Blind test 2" Workshop Calculations for two wind turbines in line[J]. Dept. Energy and Process Eng., NTNU, Trondheim, Norway, 2012.

[9] Krogstad P Å, Sætran L, Adaramola M S. "Blind Test 3" calculations of the performance and wake development behind two in-line and offset model wind turbines[J]. Journal of Fluids and Structures, 2015, 52: 65-80.

A 3D NUMERICAL STUDY ON TADPOLE SWIMMING

LI TINGTING[1, 2, 3], HU WENRONG[1, 2, 3,*]

1 Department of Engineering Mechanics, Shanghai Jiaotong University, China (200240)

2 Shanghai Jiaotong University and Chiba University International Cooperative Research Center, Shanghai Jiaotong University, China (200240)

3 MOE Key Laboratory of Hydrodynamics, Shanghai Jiaotong University, China (200240)

*wrhu@sjtu.edu.cn

Keywords: three-dimensional, tadpole, school swimming, in-phase, numerical simulation

1. Introduction

The morphology of tadpoles is quite different from that of fish. As the larva of the frogs and toads, the abrupt transition from their globose bodies to the laterally compressed tails makes them seem less 'streamlined' [1].This may relate to their high-frequency and large-amplitude undulation. In fact, tadpoles are good at swimming. Wassersug [2-3] measured the propulsive efficiency of a tadpole and found that the efficiency is as high as that of a fish.

On the other hand, group living is a widespread behavior, observed in many aquatic animals. Fish school swimming is also a common behavior in nature. In general, schooling is considered to be a social behavior to reduce predatory risks and increase foraging success. Recently, numerical simulations and experimental studies on fish schooling discovered that fish can take advantage of the adjacent vortices shed by neighbors to save energy in swimming [4]. Inspired by schooling from hydrodynamic perspective, a group of aquatic animals can be modelled as a collection of individuals arranged in tandem or side-by-side. Compared to the fish which have streamlined bodies, less attention was paid to tadpole school swimming.

The study on school swimming of blunt bodies could provide new ideas for the vibration resistance and drag reduction of underwater structures. Apart from this, it's helpful to design the best locomotion pattern for the biomimetic underwater vehicles.

In this paper, a numerical study on the tadpole swimming including a single tadpole swimming and schooling side-by-side is carried out. The hydrodynamics and vortex structures in the flow field are analyzed.

2. Materials and methods

2.1 Physical model
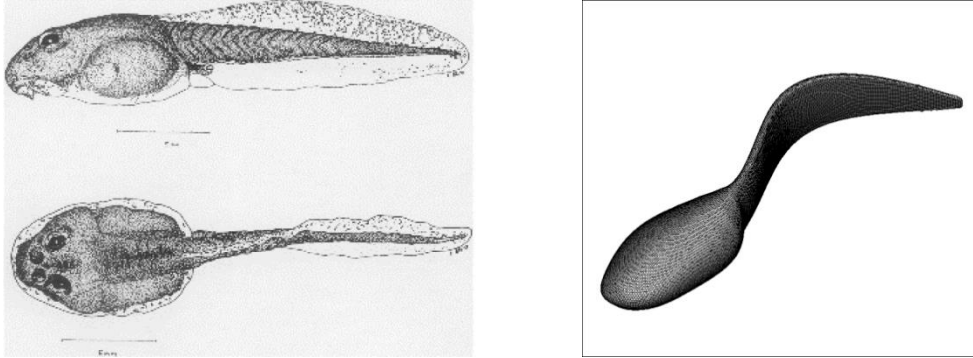
(a)The tadpole model by Köhler G[5]   (b) The cross section of tadpole model used in this article

Figure.1 Side view and top view of the tadpole of American toad (a) and the cross section of simplified tadpole model (b)

According to the observed data [5], the tadpole of American toad is built as seen in Figure 1(a).The head of the tadpole is similar to one ellipse which the widest part equals 24% of body length and the highest part accounts for 17% of body length. In this paper, the tadpole model is simplified as Figure 1(b).

In this paper, the motion of the tadpole can be described by the following function:

$$y(x,t) = A(x)\sin(2\pi x/\lambda - 2\pi ft) \tag{1}$$

Here λ is the wave-length which is set to be $0.87L$ (L representing the body length of tadpole) in the study according to the observation[3]. t is time and f is the frequency of the tadpole undulation. It is noted that the undulating mode of the tadpole is much different from that of the fish. The undulating amplitude of a tadpole is much larger than that of fish. Additionally, the head of a tadpole usually oscillates in swimming while fish's head has no oscillation. The amplitude of the tadpole along the length, $A(x)$, is calculated by spline interpolation from original data [3].

2.2 Numerical method

In this paper, open source software OpenFOAM is used to simulate hydrodynamic performance of tadpole swimming.

The motions of the unsteady incompressible viscous fluid flow are governed by the Navier-Stokes and continuity equations. The equations could be expressed by the following forms:

$$\nabla \bullet \boldsymbol{u} = 0 \tag{2}$$

$$\frac{\partial \boldsymbol{u}}{\partial t} + (\boldsymbol{u} \bullet \nabla)\boldsymbol{u} = \boldsymbol{f} - \frac{1}{\rho}\nabla p + \nu\nabla^2\boldsymbol{u} \tag{3}$$

Where ρ denotes the fluid density, ν represents the kinematic viscosity of fluid.

The finite volume method is used to solve the Navier-Stokes equations for the unsteady incompressible viscous flow. In this study, TFI-transfinite interpolation is employed to solver the dynamic mesh. It means that when the tadpole undulates in a specific pattern, the boundary of the computational domain remains fixed with the grid deformation passing smoothly and no mesh quality problem. The PIMPLE method, which is the combination of the SIMPLE (Semi-Implicit Method for Pressure-Linked Equations) method and the PISO (Pressure Implicit with Splitting of Operators) method, is specially introduced to solve the unsteady flow. The SIMPLE method is used to solve the N-S equations within each iteration step, while the PISO method is used in the time marching.

2.3 Force coefficients

In this study, the hydrodynamic performance of the undulating tadpole in side-by-side pattern is studied based on the numerical results. The lift coefficient C_L, the net thrust coefficient C_T, the net thrust coefficient C_T^*, the pressure coefficient C_p, the lateral power coefficient C_{P_S} and the propulsive efficiency η is calculated.

$$C_L = \frac{F_L}{0.5\rho U^2 A}, C_T = \frac{F_T}{0.5\rho U^2 A} = -C_D, C_T^* = \frac{F_T^*}{0.5\rho U^2 A}, C_p = \frac{p}{0.5\rho U^2},$$

$$C_{P_S} = \frac{Ps}{0.5\rho U^3 A}, \eta = \frac{\overline{C_T^*} U}{C_{P_S}}, Q = \frac{1}{2}(\Omega_{ij}\Omega_{ji} - S_{ij}S_{ji}), \Omega_{ij} = \frac{1}{2}(\frac{\partial u_i}{\partial x_j} - \frac{\partial u_j}{\partial x_i}), S_{ij} = \frac{1}{2}(\frac{\partial u_i}{\partial x_j} + \frac{\partial u_j}{\partial x_i})$$

(4)

Here F_L is the tadpole's resultant lift force in the y-axis direction, F_T is the net thrust which is the resultant force in the swimming direction, Ps is the power to produce the lateral undulating swimming of tadpole, F_T^* denotes the thrust, U is the free-stream velocity and A is the reference area, s_{ij} represents the symmetric tensor of the velocity and Ω_{ij} represents the anti-symmetric tensor of the velocity.

3. Numerical validation
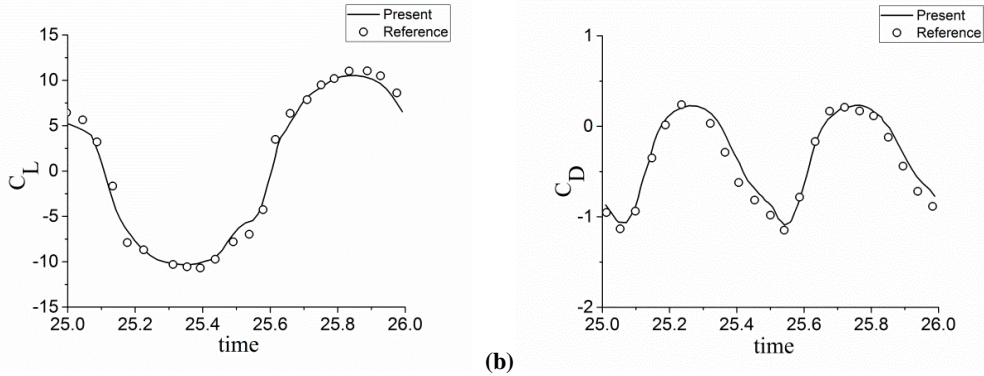
Figure 2: Comparison of (a) the lifting coefficient and (b) the drag coefficient against time in one period

In this work, the dynamic mesh code is validated to ensure the reliability of the numerical method. An eiilptic foil undergoing a plunging motion is simulated at Reynolds number of 1000.As plotted in Figure 2, the comparison of the lift force coefficient and the drag force coefficient exhibit good agreement with the numerical results of Lu et al[6] (Fig.3) with the approximate oscillating frequency, the maximum magnitude and the minimum magnitude.

4. Results and discussion

4.1 a single tadpole swimming

The Reynolds number based on the tadpole body length is 800 in this study, which matches the experimental observation [3]. In this subsection, a single tadpole undulates at the non-dimensional frequencies $f^* = 1.8, 2.4, 4.0$, respectively. As presented in Figure 3, the resultant force on the tadpole is drag force at the undulatory frequency $f^* = 1.8$ while at the frequency $f^* = 4.0$, the net thrust force coefficient is large enough($\overline{C_T} = 0.2888$).As a result, the non-dimensional frequency is set to 4.0 to investigate the side-by-side school swimming. It's also found that the net thrust coefficient and the power coefficient increase with the increasing undulating frequency which is consistent with the general swimming law of aquatic animals.

Figure 4 presents the contours of vorticity in z-direction(Ω_z), velocity in x-direction(U_x) at plate z=0 for a single tadpole swimming at different undulating frequencies. As showed in Figure 4(b), four vortices are formed in one undulating period. It can be observed that the wake shedding associated with the force production is characterized by counter rotating vortex pairs. It is interesting that two reverse Kármán vortex streets are formed and deflect away from the symmetric line. Hence, two strong backward jets are formed which contribute to the thrust generation (Figure 4(b)). In additional to the vortices shed from the tail of tadpole, one vortex pair is formed behind the head of the tadpole.
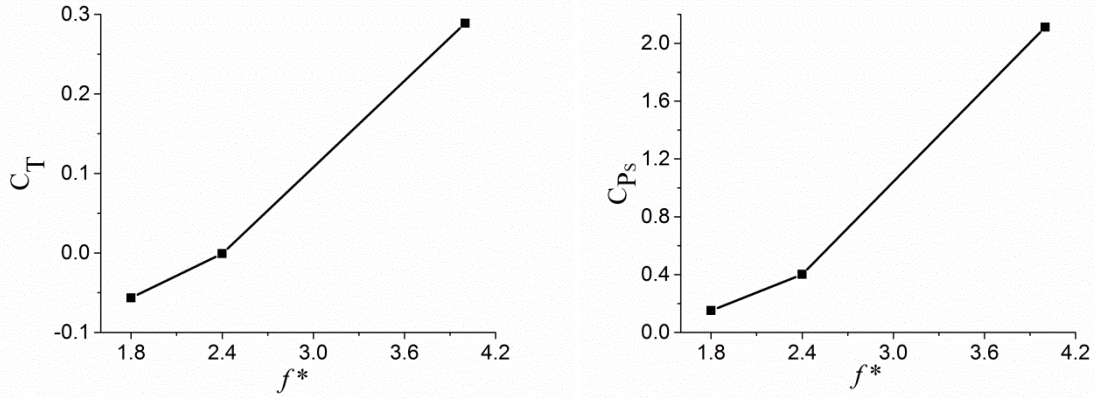
(a)Thrust coefficient of a single tadpole   (b) total power consumption coefficient of a single tadpole

Figure 3: (a) Net thrust coefficient and (b) the transverse power consumption coefficient of a single tadpole swimming under different frequency

(b)
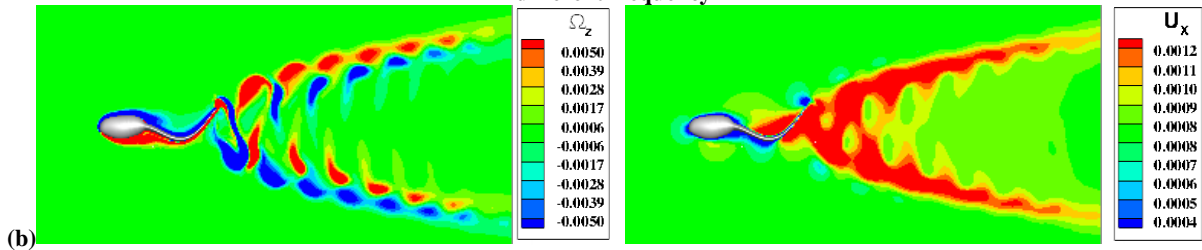
Figure 4: Contour of z vorticity at plate z=0 of a tadpole undulating at time 0.5T (a) $f^* = 1.8$ and (b) $f^* = 4.0$

4.2 Paralleled tadpoles swimming in an in-inphase pattern

(a)

(b)

(c)

(d)
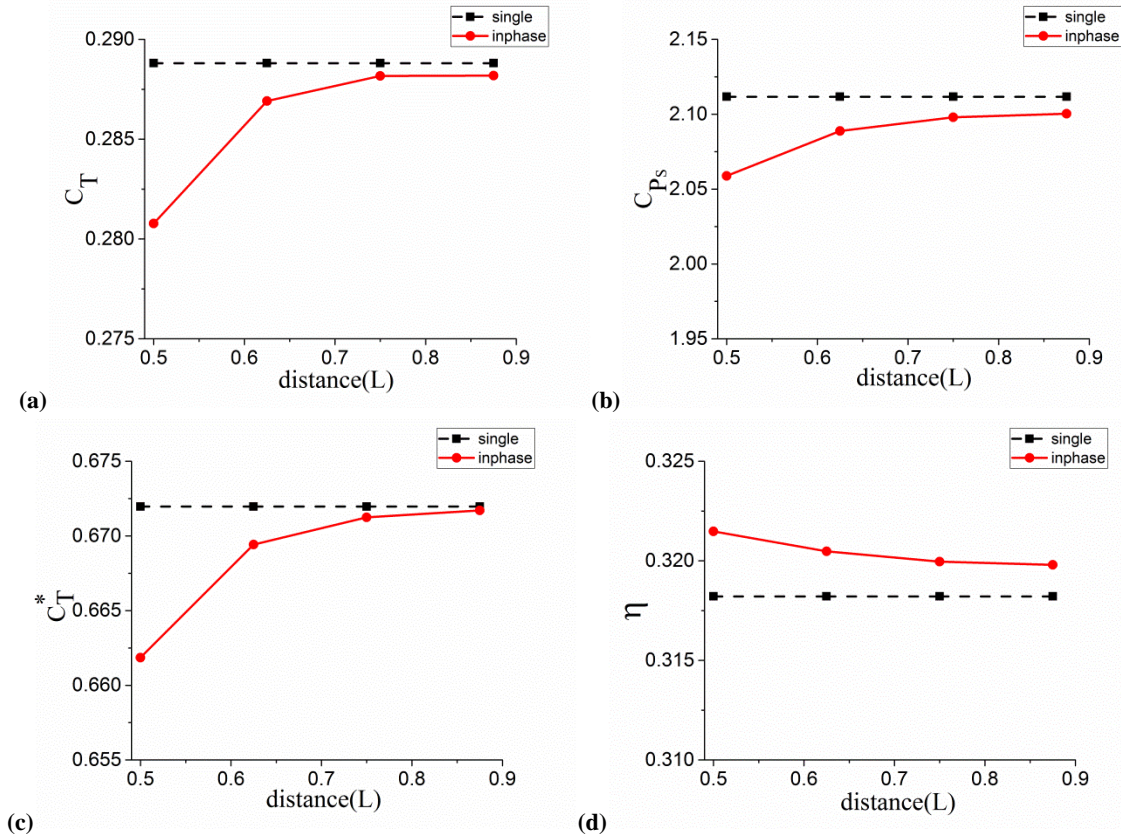
Figure 5:(a)Net thrust coefficient,(b) transverse power consumption coefficient,(c) thrust coefficient,(d) propulsive efficiency of tadpoles in in-phase mode with different lateral distance at $f^* = 4.0$

As seen from Figure 5(a)-(b), the smaller lateral distance between tadpoles always leads to the smaller net thrust and the lower lateral power consumption. The propulsive efficiency is defined as the ratio of useful power to input power which is plotted against the lateral distance in Figure 5(d).The efficiency is maximized at s=0.5L with a value of $\eta = 0.3215$ .For the lateral distance of s=0.875L, the power consumption of this case is quite lower as compared to the single tadpole while the thrust generation of the two cases likely approaches. This suggests that tadpole schooling

experiences energy-saving benefits.

For the lateral distance s=0.5L, the net thrust force is smaller than that of a single tadpole. The closer the tadpoles approach, the smaller the spacing around the tadpole becomes. As a consequence, the flow passes the tadpole more quickly. According to the wavy plate theory, the net thrust force decreases while the wave velocity decreases relate to the flow velocity. Meanwhile, the lower pressure region behind the head becomes larger resulting in increasing the pressure drag and the viscous drag force also gets larger.

(a)

(b)

(c)

(d)
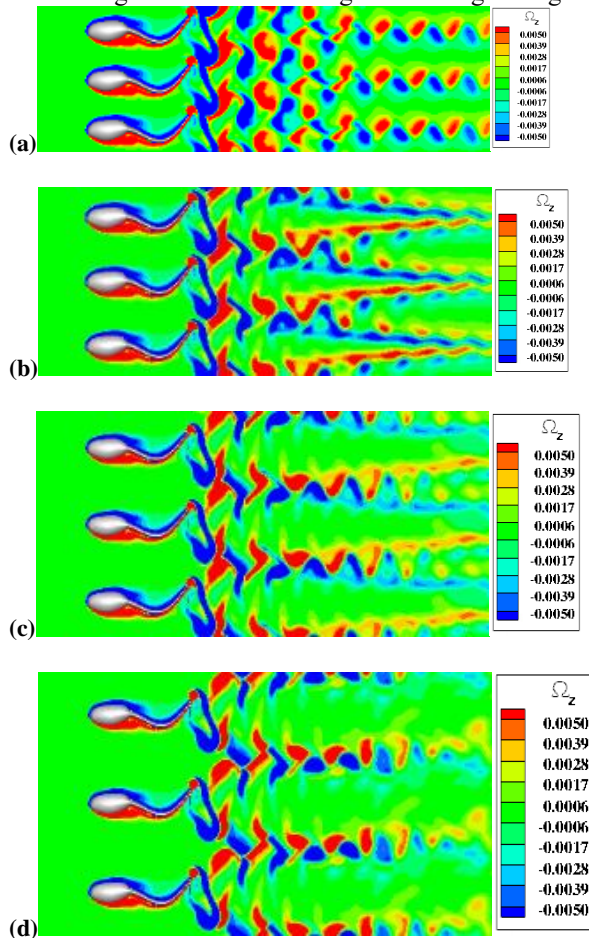
Figure 6:Contour of z vorticity at plate z=0 of tadpoles swimming in in-phase mode at time 0.5T, $f^* = 4.0$,with lateral distance:(a)0.5L;(b) 0.625L;(c)0.75L;(d)0.875L

Figure 6(a)-(d) exhibits the instantaneous wake flow at the representative moment 0.5T for different lateral distance at the frequency $f^* = 4.0$. In each undulating period, four vortices shed from the tail tip and pairs of positive and negative vortices form on the head of tail. Owing to adjacent tadpoles undulating in an in-phase mode, columns of positive and negative vortices appear alternately at s=0.5L showed in Figure 6(a).When the lateral distance becomes larger, the formation of two reverse Kármán vortex streets behind each tadpole is observed according to Figure 6(b)-(d). At s=0.625L, the two reverse Kármán vortex streets evolved in inward shape while at s=0.875L, vortices with the same direction between adjacnt tadpoles merge together and reverse Kármán vortex streets are strengthened and become parallel in relevant to the wake centerline.

5. Conclusions

In this study, three-dimensional simulations have been performed to investigate the tadpole undulating swimming, including swimming alone and side-by-side swimming. The hydrodynamic performance of the tadpole and the vortex structure of the flow filed are studied.

When a single tadpole swims at different undulating frequency, the transition from the drag force to thrust force occurs. The net thrust force and the lateral power consumption increase with the increasing undulating frequency. It's found that pairs of positive and negative vortices are formed on the head of tadpole. Two reverse Kármán vortex streets are observed in the wake where in the condition where thrust generation is involved.

For a fixed undulating frequency, tadpoles swimming in side-by-side arrangement at different lateral distances are simulated. The net thrust force and the lateral power consumption show an increasing trend against varying lateral distance. The highest efficiency is maximized at s=0.5L with a value of $\eta = 0.3215$ .Compared to the single case, tadpole schooling experiences energetic advantages and higher propulsive efficiency. On the base of single tadpole, three kinds of the wake structure are observed at different lateral distances: columns of positive and negative vortices appearing alternately, inward-shape reverse Kármán vortex streets and parallel and strengthened reverse Kármán vortex streets.

References

[1] Videler J J. Fish swimming [M]. Springer Science & Business Media, 2012.

[2] Wassersug R J. Locomotion in amphibian larvae (or "Why aren't tadpoles built like fishes?")[J]. American Zoologist, 1989, 29(1): 65-84.

[3] Wassersug R J, HOFF K. The kinematics of swimming in anuran larvae [J]. Journal of Experimental Biology, 1985, 119(1): 1-30.

[4] Chen Szu-Yung, Fei Yueh-Han J, Chen Yi-Cheng, et al. The swimming patterns and energy-saving mechanism revealed from three fish in a school [J]. Ocean Engineering, 2016, 122:22-31.

[5] Köhler G, Lehr E, McCranie J R. The tadpole of the Central American toad Bufo luetkenii Boulenger[J]. Journal of Herpetology, 2000: 303-306.

[6] LU X Y, YANG J M, YIN X Z. Propulsive performance and vortex shedding of a foil in flapping flight[J]. Acta Mechanica, 2003, 165(3-4): 189-206.

SIMULATIONS FOR SOME LOW AND MEDIUM REYNOLDS NUMBER PROBLEMS USING IMMERSED BOUNDARY METHOD IN FOAM-EXTEND

DONG ZHANG[1,5], JIANZHEN ZHAO[2,5], PAN GUANG[3,5], LIMING CHAO[4,5]

[1] *Dong Zhang School of Marine Science and Technology, Northwestern Polytechnical University, Xi'an 710072,P.R.China, zhang_dong@mail.nwpu.edu.cn*

[2] *JianZhen Zhao School of Marine Science and Technology, Northwestern Polytechnical University, Xi'an 710072,P.R.China, 1024454625@qq.com*

[3] *Guang Pan School of Marine Science and Technology, Northwestern Polytechnical University, Xi'an 710072,P.R.China, panguang@nwpu.edu.cn*

[4] *Liming Chao School of Marine Science and Technology, Northwestern Polytechnical University, Xi'an 710072,P.R.China, clm@mail.nwpu.edu.cn*

[5]*Key Laboratory for Unmanned Underwater Vehicle, Northwestern Polytechnical University, Xi'an 710072,P.R.China*

Key words: numerical simulation; immersed boundary method; dynamic boundary

Immersed boundary method was first proposed by Peskin[1,2] for the simulation of human heart. The method was later extended to many fields[3,4]. By using cartesian grids, the immersed boundary method has some advantages in the simulation of complex boundary and moving boundary problems. In this paper, the method employs a discrete force approach which uses two polynomial interpolation combined with weighted least squares method[5,6] for the reconstruction of the flow variables. Space domain was discretized using the finite volume method and time was discretized using Euler method. PISO algorithm was utilized for the couple of velocity and pressure field. Simulations of flow around a two-dimensional cylinder, an oscillating cylinder, a three-dimensional sphere and a two-dimensional fish were conducted to verify the accuracy and fidelity of the solver over low and medium Reynolds numbers covering static and dynamic boundary problems. It can establish foundations for the future handling of more complex problems in the field of naval and bionic hydrodynamics. Results show that those simulations have a high fit degree with relevant references.

Flow around a cylinder

Simulations of flow around a two-dimension cylinder were conducted and compared with the result of Chiu[7] and Xu[8].The Reynolds numbers are 100 and 200 respectively, and the characteristic length is defined as the radius of the cylinder, *d*. The computational domain is 50×25 *d*.
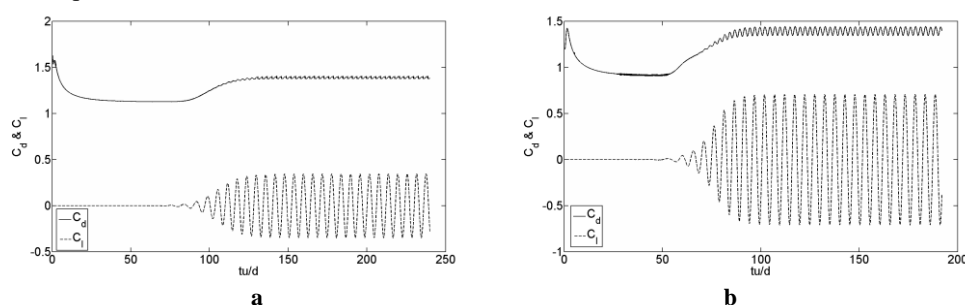
Figure 1: The evolution of drag and lift coefficient at (a): Re =100, (b): Re=200
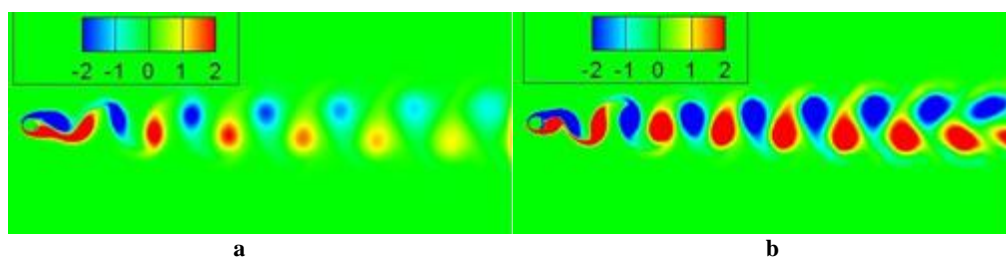
Figure 2: Vortical structures of flow over a cylinder at (a): Re =100, (b): Re=200

Table 1: Comparison of present results and literature results

	Re	C_d
Current	100	1.38
	200	1.39
Chiu[7]	100	1.35
	200	1.37
Xu S[8]	100	1.42
	200	1.42

Flow over an oscillating cylinder

Simulations of an oscillating cylinder were computed under the Re = 185. The amplitude (Ae) was 0.2d , and the oscillation frequency (fe) are $1f_0$, $1.2f_0$, where f_0 is the vortex shedding frequency. The computational domain was the same as the flow around the stational cylinder.

| a | b |
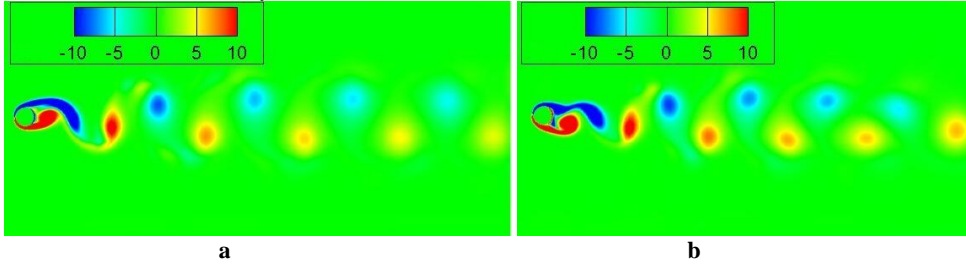
Figure 3: Vortical structures of flow over an oscillating cylinder. (a): fe/f0=1, (b): fe/f0=1.2

| a | b |
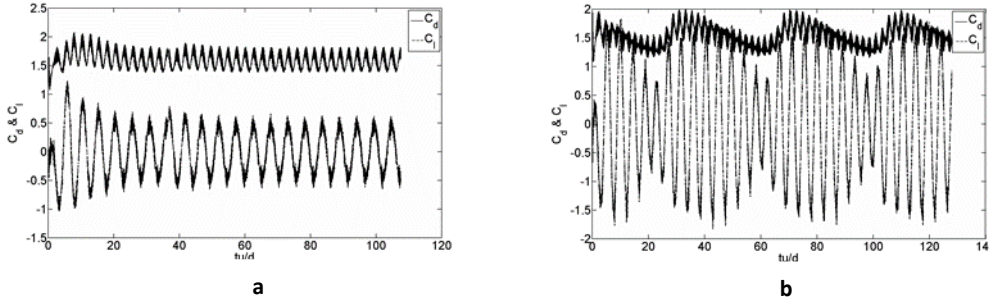
Figure 4: The evolution of drag and lift coefficient for the cylinder oscillation. (a): fe/f0=1, (b): fe/f0=1.2

Flow over a 3D sphere

The 3D sphere simulations were conducted under the condition of Re = 100 and 300. The computational domain was 33d×16d×16d(d is the diameter of the sphere) .

| a | b |
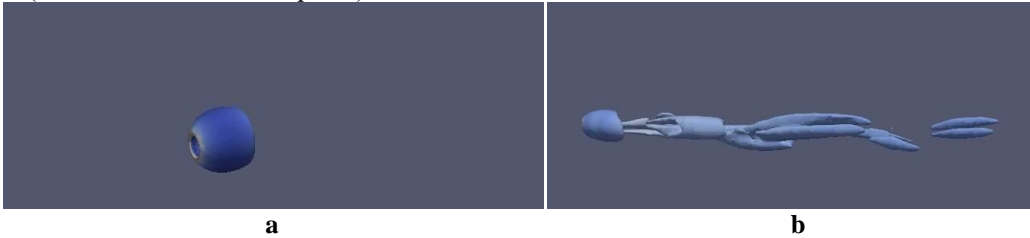
Figure 5: Vortical structures of flow over a 3D sphere. (a): Re=100, (b): Re=300

Table 2: Comparison of drag coefficient

	Re	C_d
Current	100	1.071
	300	0.692
JungwooKim[9]	100	1.087
	300	0.657
Fornberg[10]	100	1.085
Constantinescu[11]	300	0.655

Simulation of undulatory swimming

The fish body is represented by a NACA 0012 foil, the following motion is selected to resemble the fish-swimming motion observed in nature. The movement equation[12] is described as:

$$h(x,t) = a(x) \sin \left[2\pi \left(\frac{x}{\lambda} - \frac{t}{T} \right) \right] \qquad (1)$$

$$a(x) = L\left[0.351\,sin\left(\frac{x}{L} - 1.796\right) + 0.359\right] \qquad (2)$$

whrerλ is the wavelength, L is the body length, and the Strouhal number is defined by

$$St = \frac{fA}{U} \qquad\qquad (3)$$

The simulations were carried out under the condition of Re=45000, St = 0.23 , 1.18.
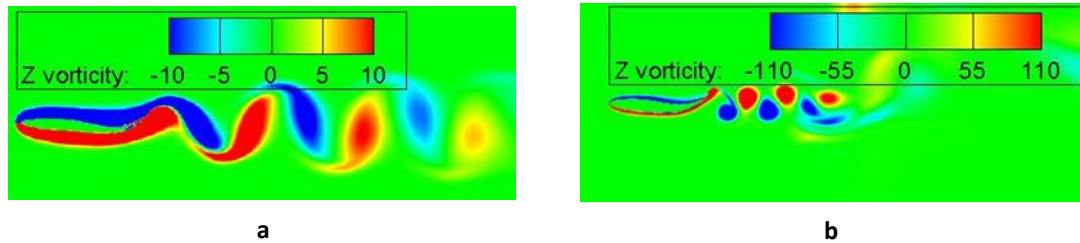
Figure 6: Vortical structures of the fish-like movement. (a):St=0.23, (b):St=1.18

Reference

[1] Peskin C S. Flow patterns around heart valves: A numerical method[J]. Journal of Computational Physics, 1972, 10(2):252-271.

[2] Fogelson A L, Peskin C S. A fast numerical method for solving the three-dimensional Stokes' equations in the presence of suspended particles[J]. Journal of Computational Physics, 1988, 79(1):50-69.

[3] Mohd–Yusof. Combined immersed–boundary/B–Spline methods for simulations of flow in complex Geometries [C].CTR Annual Research Briefs, Center for Turbulence Research, NASA Ames/Stanford Univ, 1997, 317–27

[4] Fadlun E A, Verzicco R, Orlandi P, et al. Combined Immersed-Boundary Finite-Difference Methods for Three-Dimensional Complex Flow Simulations[J]. Journal of Computational Physics, 2000, 161(1):35-60.

[5] Mittal R, Dong H, Bozkurttas M, et al. A versatile sharp interface immersed boundary method for incompressible flows with complex boundaries [J]. Journal of Computational Physics, 2008, 227(10):4825-4852.

[6] Seo J H, Mittal R. A high-order immersed boundary method for acoustic wave scattering and low-Mach number flow-induced sound in complex geometries[J]. Journal of Computational Physics, 2011, 230(4):1000.

[7] Chiu P H, Lin R K, Sheu T W H. A differentially interpolated direct forcing immersed boundary method for predicting incompressible Navier-Stokes equations in time-varying complex geometries[J]. Journal of Computational Physics, 2010, 229(12):4476-4500.

[8] Xu S, Wang Z J. An immersed interface method for simulating the interaction of a fluid with moving boundaries[J]. Journal of Computational Physics, 2006, 216(216):454-493.

[9] Kim J, Kim D, Choi H. An Immersed-Boundary Finite-Volume Method for Simulations of Flow in Complex Geometries[J]. Journal of Computational Physics, 2001, 171(1):132-150.

[10] B F. Steady viscous flow past a sphere at high Reynolds numbers[J]. Journal of Fluid Mechanics, 1988, 190(-1):471-489.

[11] Constantinescu G, Squires K. LES and DES investigations of turbulent flow over a sphere[J]. Aiaa, 2013, 70(1-4):267-298(32).

[12] Xiao Q, Sun K, Liu H, et al. Computational study on near wake interaction between undulation body and a D-section cylinder[J]. Ocean Engineering, 2011, 38(38):673-683.

INVESTIGATION OF RAIN EFFECTS ON NACA0012 AIRFOIL WITH OPENFOAM

LIU NINGYU, ZHAO XIANG, SHAO JIANGYAN, SHU CHANG

National University of Singapore, tslln@nus.edu.sg

Keywords: rain effects, NACA0012 airfoil, DPM model, surface film model

1. Introduction

Heavy rain can cause severe aerodynamic performance degradation to airfoil, particularly during take-off and landing stage. It has been deemed as a critical cause to many aviation accidents [1]. Rain condition can lead to aircraft aerodynamic penalties in several ways. For instance, raindrops can stick on and roughen the surface of wings. This phenomenon can induce changes in critical aerodynamic performance indicators such as pressure distribution as well as drag and lift force [2][3]. Thus, rainfall is considered as an important aircraft safety hazard. Nevertheless, accurate assessment of rain effect on aerodynamic performance poses many difficulties to both experimental and numerical study and it is still an open topic.

To analyse this problem numerically, it is noticed that OpenFOAM provides a powerful platform for simulation of fluid mechanics [4]. On the other hand, it was found that there is no built-in application in OpenFOAM for simulation of rain effect on airfoil that involves complex interactions among droplets, air flow and the structures, which is the focus of the present work. To achieve this aim, we developed an incompressible Eulerian-Lagrangian solver within OpenFOAM framework, named parcelFilmFoam. This solver integrates several OpenFOAM built-in libraries and applications. It is validated against benchmark data first, and then used to investigate aerodynamic performance of NACA0012 airfoil with dry air and heavy rain conditions.

2. Methodology

The main part of the solver for continuous phase is based on the OpenFOAM built-in solver named pisoFoam. Meanwhile, the Lagrangian library is linked to the main solver to implement Discrete Particle Model (DPM). Additionally, a thin film model is applied. DPM interacts with continuous phase and thin film through the source terms in the corresponding equations of main solver and surface film solver. They are introduced respectively in the following subsections.

2.1 Main Solver

To simulate incompressible viscous flow, there are semi-implicit method for pressure-linked equations (SIMPLE), pressure-implicit split-operator algorithms [5] (PISO) and a combination of SIMPLE and PISO algorithms (PIMPLE). In OpenFOAM, the corresponding built-in incompressible solvers are simpleFoam, pisoFoam and pimpleFoam. Among them, simpleFoam is steady-state solver, while both pisoFoam and pimpleFoam are transient solvers. pimpleFoam is featured as a large time-step transient solver for incompressible, turbulent flow. However, the Eulerian-Lagrangian solver we are developing needs to couple the detailed dynamics of DPM and thin film models with the flow field, and it requires small time-step. Thus, instead of using pimpleFoam, pisoFoam is adopted as the reference to build the solver for continuous phase.

2.2 DPM Model

The standard Lagrangian DPM is based on a translational force balance that is formulated for an individual particle. In this model, each particle represents a parcel of particles, and a DPM parcel is subject to gravity, drag force, and other forces when more complicated physics is considered. The particle trajectory is calculated by integrating the particle force balance equation. In this work, the drag force and gravity play the most important role.

$$\frac{du_p}{dt} = \frac{3\mu C_d Re_p}{4\rho_p D_p^2}(u - u_p) + g \tag{1}$$

Here, u and u_p are the air and particle velocity respectively; g denotes the gravity acceleration; ρ_p and D_p are the density and diameter of the particle; Re_p is the particle Reynolds number and C_d is drag coefficient. Literature on similar approaches can be found in [6].

In Eulerian-Lagrangian approach, there are one-way coupled model [7] and two-way coupled model [8]. The one-way coupled model assumes that the motion of particles is affected by the continuous phase, while the continuous phase is not affected by the presence of particles. A two-way coupled model assumes that there is a two-way exchange of mass and momentum between the continuous phase and the particles. In the developed solver, the dynamics of the particle and the flow field are two-way coupled.

2.3 Surface Film Model

In order to model film layers with OpenFOAM, a dedicated mesh region for surface film needs to be extruded from the airfoil surface. The surface film is modelled inside the extruded mesh region. In this work, a thin film assumption is used, namely the velocity normal to the mesh wall is assumed to be zero and the wall-tangential diffusion is considered negligible compared to wall-normal diffusion. The surface film flow is solved with the continuity equation and the momentum equation, with a film layer thickness δ_f included.

$$\frac{\partial \rho \delta_f}{\partial t} + \nabla \cdot \left(\rho \delta_f U \right) = S_{imp} + S_{splash} + S_{sep} \tag{2}$$

$$\frac{\partial \rho \delta_f U}{\partial t} + \nabla \cdot \left(\rho \delta_f U U \right) = -\delta \nabla p + S_{\rho \delta_f U} \tag{3}$$

The continuity equation contains several source terms as shown in Eqn. (2). They include the mass added to the film layer due to impinging particles, as well as the mass deducted from the film layer due to rebounding, splashing particles, and separation of the film layer [9].

In the present case, the Weber number (We), which is defined as a measure of fluid's inertia to its surface tension, is used to decide the type of particle-film interaction. The particle-film interaction is classified as "stick" if We<5, "rebound" for 5<We<10, and "splash" when We>10.

3. Validation of Numerical Modelling

The parcelFilmFoam is used to simulate rain effects on NACA0012 airfoil. In this solver, the rain effects are investigated by simulation of the coupled dynamics between the particle, film and the flow field. The results will be validated by the measurement data from Hansman and Craig [10], as well as the numerical simulation results from Ismail et al. [11].

A 2D mesh model is built. The chord of airfoil is 1, and the calculation domain is 250×200×1 in meter. The total cell number is about 64,000. The inlet flow velocity is 18m/s. The angle of attack (AOA) is varied between 0° to 12°, and SA turbulent model is used.

3.1 Validation of Results without Rain

For the NACA0012 airfoil, there are many reliable benchmark data under dry air condition at various Reynolds number, (Re). Here, Re is defined as a ratio of fluid's inertial force to its viscous force. At high Re (Re=3.E6), the results have been verified based on the well-known benchmark data from Abbott and von Doenhoff [12]. The results indicate that, with the current setup, Cd (drag coefficient) is slightly overestimated, while Cl (lift coefficient) agrees well with the benchmark data, as shown in Figure 1. The results at a lower Re (Re=3.E5) are also included in the same plots, to illustrate the variation of force coefficients versus Reynolds number. It can be observed that the lower Re can lead to higher Cd and lower Cl.
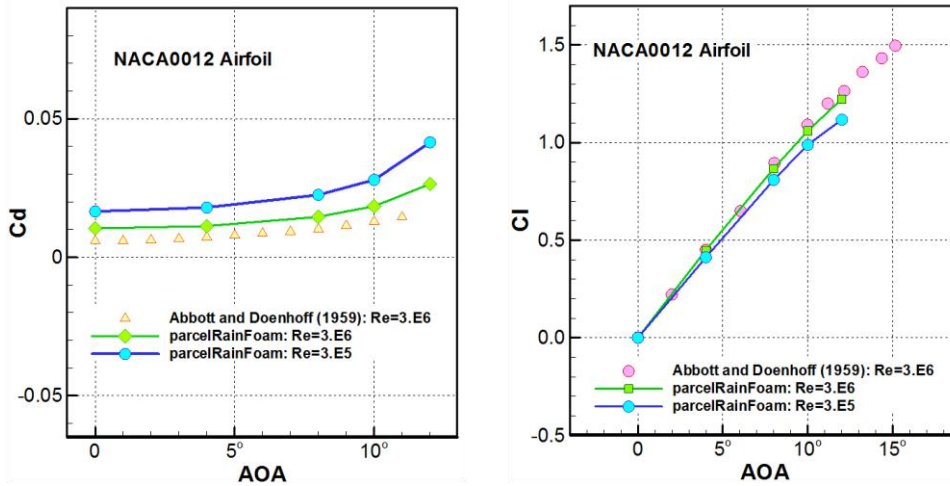
Figure 1: Validation of force coefficients for NACA0012 without particle injection

3.2 Validation of Results with Rain

To consider rain effects, the particle properties and the particle injection setting are needed. The particle properties are: density is 1000kg/m³ and diameter is 0.5mm. The particle injection settings are: the particle velocity is $u_p = 18m/s$ and $v_p = -3m/s$ in horizontal and vertical directions, and the liquid water content (LWC) is 30 g/m³. The results considering rain effects simulated by parcelFilmFoam are compared with the experimental data from Hansman and Craig [10], and the numerical results from Ismail et al. [11], as shown in Figure 2.

The experimental data provided a lower Cl and a much higher Cd even for the dry air cases. As Hansman and Craig [10] claimed, their experimental data are the raw data and no correction was made. To demonstrate the difference, the experimental results with necessary corrections at low Re for dry air from Eastman et al. [13] are presented in the figures. In addition, the numerical simulation by ANSYS Fluent from Ismail et al. [11], with scale-down model (chord= 0.14m) and both the particle (diameter of 0.46mm) and the film effects are also shown. It can be seen that the present results of Cd and Cl by parcelFilmFoam are comparative to those of Ismail et al. [11] (The present simulation using normal scale, chord= 1m, and particle diameter 0.5mm). The "in-house Fortran Code" and the "Fluent" data in Figure 2 are obtained by using the same setting as that in parcelFilmFoam. They are included in plots for cross-comparison.
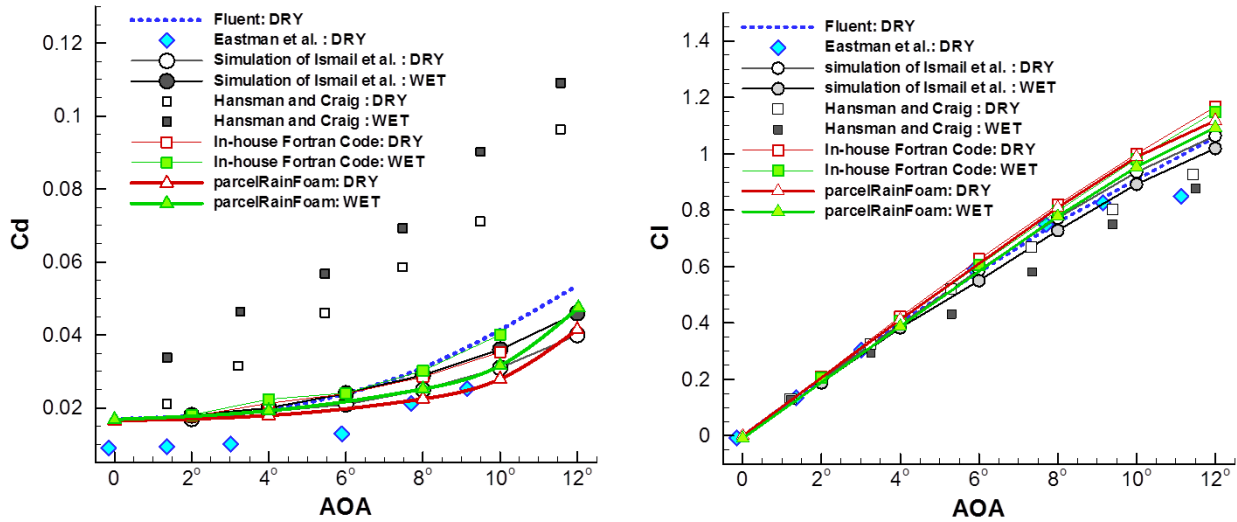
Figure 2: Validation of force coefficients with particle injection at Re=3.E5

4. Results and Discussion

A direct application of the unsteady solvers, such as pisoFoam, or parcelFilmFoam, may lead to obvious oscillation and even diverging of the simulation, especially for high AOA cases. To overcome this problem, a three-step simulation procedure is designed. It includes: i) obtain the steady flow field using simpleFoam; ii) obtain the unsteady flow without rain by parcelFilmFoam; iii) run parcelFilmFoam with DPM model and film model.

4.1 Results of DPM Model
To investigate the rain effects (with particle inject) on NACA0012 airfoil, the force coefficients with AOA=4° is recorded at each time step, as shown in Figure 3.
The particle injection starts at t=2s, and the particles start to hit the airfoil at t=2.17s. It can be seen that before the particles hitting the wing, there is a slight drag decrease and lift rising. The plot shows that rain (upon impact of particles) can cause the drag increase and lift decrease. At a later stage, raindrops (modelled as particles) can surround the airfoil and also present in its wake region. In this phase, the drag and lift coefficient become stable, and the final force coefficients can be obtained by averaging their value in this phase.
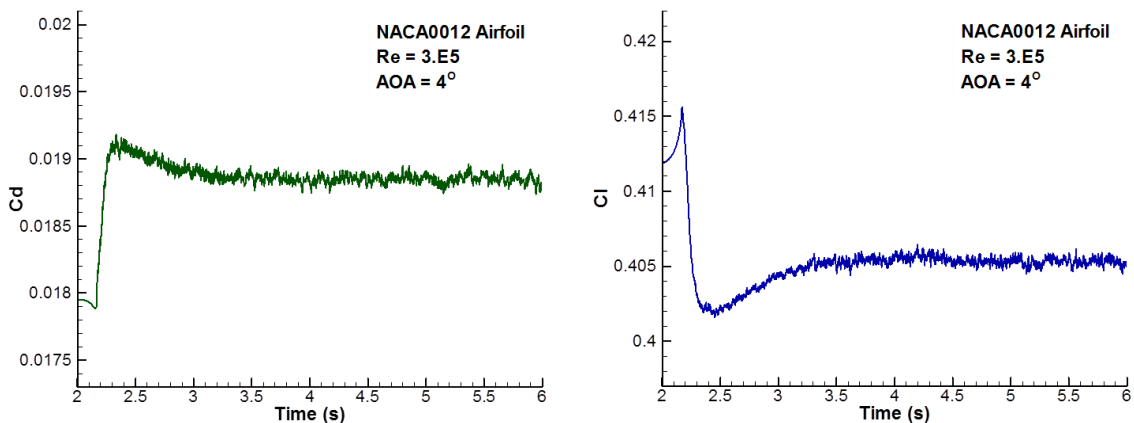
Figure 3: Force Coefficient profiles at Re=3.E5 and AOA=4°

4.2 Results of Surface Film

Two-dimensional flow is considered here. This means that the wall film velocity will be along the surface according to the thin film assumption. The film results are presented in term of the film velocity, u_f and the film thickness, δ_f as shown in Figure 4. The raindrops exchange mass and momentum with the surface film during impact. When there is thin film on airfoil, it can in turn affect the motion of the impacting particles in several ways. For example, raindrops can stick on the surface of airfoil, and they can become part of the film and contribute to its mass and momentum. On the other hand, when the film is too thick or the curvature of film is too sharp at certain place (such as the place around the trailing edge), the water film can break into drops, and the drops will leave the film layer.
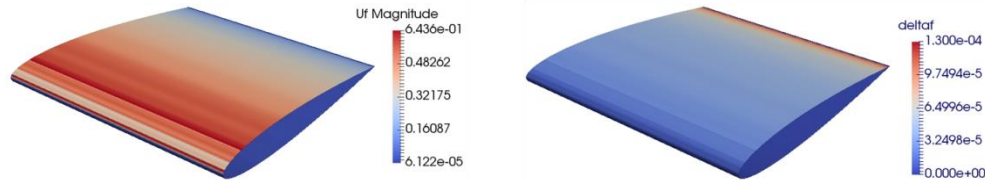
Figure 4: Film velocity and film thickness at Re=3.E5, AOA=4° and t=4.8s

5. Conclusions

In this work, based on OpenFOAM platform, a new incompressible Eulerian-Lagrangian solver, parcelFilmFoam, is developed. It is applied to simulate the aerodynamic performances of NACA0012 airfoil under rain conditions. Firstly, the solver is validated against the benchmark data from both experiments and numerical simulations. The aerodynamic efficiency degradation of NACA0012 airfoil in the rain is then investigated by parcelFilmFoam. Quantitative variations in drag and lift coefficients of the airfoil under rain condition are presented in this work. For the future work, we will keep on investigating the underlying physics as well as the influence of the interactions among raindrops, water film, air flow and the wing surface. In the meantime, we will also further explore the potential of OpenFOAM, to optimize the new solver, and to extend its applications to different types of airfoils, wings, and aircrafts.

References

[1] Y. Cao, Z. Wu and Z. Xu, Effects of rainfall on aircraft aerodynamics. Progress in Aerospace Sciences, 71 (2014) 85-127.

[2] J. Valentine and R. Decker, A Lagrangian-Eulerian scheme for flow around an airfoil in rain. International journal of multiphase flow, 21 (1995) 639-648.

[3] R. Zhang and Y.-H. Cao, Study of aerodynamic characteristics of an airfoil in rain. Journal of Aerospace Power, 25 (2010) 2064-2069.

[4] C.J. Greenshields, OpenFOAM: The OpenFOAM foundation user guide version 5.0. OpenFOAM Foundation Ltd. 24th July 2017.

[5] R.I. Issa, Solution of the implicitly discretised fluid flow equations by operator-splitting. Journal of Computational Physics, 62 (1986) 40-65.

[6] A.B. Yu, B. Wright, Z.Y. Zhou, H.P. Zhu and P. Zulli, Discrete particle simulation of gassolids flow in a blast-furnace. Computers & Chemical Engineering, 32 (2008)1760-1772.

[7] J.R. Valentine and R.A. Decker, Tracking of raindrops in flow over an airfoil. Journal of Aircraft, 32 (1995) 100-105.

[8] J.R. Valentine and R.A. Decker, A Lagrangian-Eulerian scheme for flow around an airfoil in rain. International journal of multiphase flow, 21 (1995) 639-648.

[9] D.W. Stanton and C. Rutland, Multidimensional modeling of thin liquid films and spray-wall interactions resulting from impinging sprays. International Journal of Heat and Mass Transfer, 41 (1998) 3037-3054.

[10] R.J. Hansman and A.P. Craig, Low Reynolds number tests of NACA 64-210, NACA 0012, and Wortmann FX67-K170 airfoils in rain. Journal of Aircraft, 24 (1987) 559-566.

[11] M. Ismail, Z. Wu, A. Bakar and S. Tariq, Aerodynamic characteristics of airfoil cruise landing and high lift configurations in simulated rain environment. Journal of Aerospace Engineering, 28 (2014) 04014131.

[12] I.H. Abbott and A.E. von Doenhoff, Theory of wing section: including a summary of airfoil data. New York: Dover Publication, (1959).

[13] N. Eastman, N. Jacobs and A. Sherman, Airfoil section characteristics as affected by variations of the Reynolds number. NACA TR-586 (1937) 231.

A PRACTICAL METHOD FOR HYDRODYNAMIC COEFFICIENT CALCULATION WITH OPENFOAM

JI ZHAO[1], RENCHUAN ZHU[2], YANG CAO[3]
[1] Shanghai Jiaotong University, zjdedongxi@sjtu.edu.cn
[2] Shanghai Jiaotong University, renchuan @ sjtu.edu.cn
[3] AECC Commercial Aircraft Engine Company, 531389523@qq.com

In the procedure of predicting ship motions in waves, the hydrodynamic coefficient should be obtained in advance for solving ship's motion equation. The added mass and damping is usually computed with potential method [1], however the potential theory is based on the hypothesis of potential flow, and its result can not include the viscous effect and failed to obtain the nonlinear component. In this work, we proposed a method to obtain hydrodynamic coefficient and non-linear hydrodynamic coefficient by analysing the force-time curve of ship hull, and the force-time curve is obtained by simulating forced oscillations of ships in OpenFOAM[2]. Meanwhile, an efficient mesh manipulation model specific for simulating ship oscillation is put forward in this work. The hydrodynamic coefficient computed by the present method is compared with the result obtained by potential method, which shows the accuracy of the present method.

1. Hydrodynamic coefficient computation method

For a ship hull forced oscillation with specified degree of freedom (DOF), the total hydrodynamic force can be discomposed as follow [3],

$$F_{i,j} = F_{i,j}^C + C_{i,j}\xi_i + A_{i,j1}\ddot{\xi_\iota} + A_{i,j2}(\ddot{\xi_\iota})^2 + B_{i,j1}\dot{\xi_\iota} + B_{i,j2}(\dot{\xi_\iota})^2 \quad (i,j = 1,2,\dots,6) \quad (1)$$

where the $F_{i,j}^C$ is the constant force which including the ship gravity and wave making resistance, $A_{i,j1}$ and $B_{i,j1}$ are the added mass and damping respectively, $A_{i,j2}$ and $B_{i,j2}$ are the nonlinear added mass and damping, $C_{i,j}$ is the hydrostatic recovery force and can be expressed as follow

$$C_{i,j} = \begin{pmatrix} 0 & 0 & & \cdots & & 0 \\ 0 & 0 & & & & 0 \\ & & \rho g A_w & 0 & \rho g A_w x_f & \\ \vdots & & 0 & \rho g(A_w d_1^2 + z_B\nabla) & 0 & \vdots \\ & & \rho g A_w x_f & 0 & \rho g(A_w d_2^2 + z_B\nabla) & \\ 0 & 0 & & \cdots & & 0 \end{pmatrix} \quad (2)$$

where the A_w is the water plane area, d_1 is the inertial radius around the X axis and d_2 is the inertial radius around the Y axis. z_B is the Vertical coordinate of buoyant centre, x_f is the x coordinate of floatation centre, ∇ is the volume of displacement.

In case of oscillation motion, the displacement ξ_i can be expressed in harmonic form. The displacement, velocity and acceleration can be expressed as follow

$$\begin{cases} \xi_i = \xi_{i0}sin(\omega t) \\ \dot{\xi}_i = \xi_{i0}\omega cos(\omega t) \quad (i = 1,2\dots,6) \\ \ddot{\xi}_i = -\xi_{i0}\omega^2 sin(\omega t) \end{cases} \quad (3)$$

Substituting Eq. 3 into Eq. 1 gives

$$F_{i,j} = \left(F_{i,j}^C + A_{i,j2}\frac{\xi_{i0}^2\omega^4}{2} + B_{i,j2}\frac{\xi_{i0}^2\omega^2}{2}\right) + \left(C_{i,j}\xi_{i0} - A_{i,j1}\omega^2\xi_{i0}\right)sin(\omega t) +$$
$$\left(B_{i,j1}\omega\xi_{i0}\right)cos(\omega t) + \left(-A_{i,j2}\frac{\xi_{i0}^2\omega^4}{2} + B_{i,j2}\frac{\xi_{i0}^2\omega^2}{2}\right)cos(2\omega t) \quad (4)$$

By monitor the force of ship oscillation movement, the force-time curve can be obtained, and which curve can be fitted in Fourier series form.

$$F_{i,j} = F_{i,j0} + F_{i,ja1}sin(\omega t) + F_{i,jb1}cos(\omega t) + F_{i,ja2}sin(2\omega t) + F_{i,jb2}cos(2\omega t)\dots\dots \quad (5)$$

Comparing the Eq.4 and Eq.5, it's easy to obtain the added mass, damping, nonlinear added mass and nonlinear damping, the expression are showed as Eq.6.

$$\begin{cases} A_{i,j1} = \dfrac{-F_{i,ja1}+C_{i,j}\xi_{i0}}{\omega^2\xi_{i0}} \\[2mm] B_{i,j1} = \dfrac{F_{i,jb1}}{\omega\xi_{i0}} \\[2mm] A_{i,j2} = \dfrac{F_{i,jo}-F_{i,jb2}-F_{i,j}^C}{\omega^4\xi_{i0}^2} \\[2mm] B_{i,j2} = \dfrac{F_{i,jo}+F_{i,jb2}-F_{i,j}^C}{\omega^2\xi_{i0}^2} \end{cases} \qquad (i,j = 1,2,\dots,6) \qquad (6)$$

It is worth to mention that the movement amplitude ξ_{i0} is displacement in the motion modality of i=1,2,3, while in the motion modality of i=4,5,6, the ξ_{i0} is the rotational amplitude with the dimension of radian. The Eqn.6 is suitable for the hydrodynamic calculation of all motion modality.

2. Mesh manipulation model in OpenFOAM

To simulate the simple harmonic motion of ship hull, a suitable mesh manipulation model is necessary for an efficient computation. Considering that each motion is just with one Degree of Freedom, and moving amplitude is rather small compared to the mesh size in the far field, we give out a dynamic mesh model named smallOscillationFvMesh. The smallOscillationFvMesh is originated from the mesh manipulation model of movingConeTopoFvMesh, and the process of the present method are showed in the figure below.
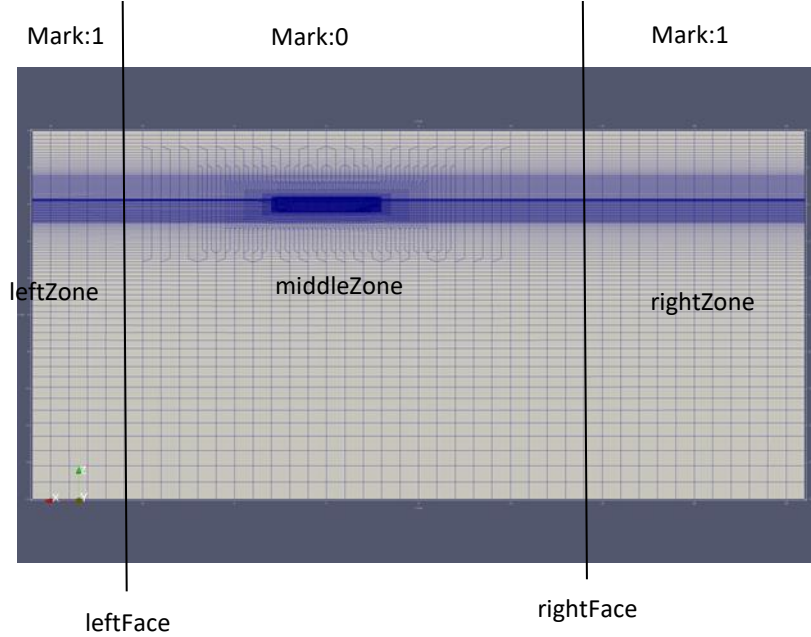
Figure 1: Mesh setting for surge motion

Figure 1 gives the mesh manipulation for ship surge simulation. As the mesh for ship motion simulation is trend to be coarse and regular in the far field, so it is easy to find two sets of faces that the trance grid scale between which is far larger than the motion amplitude. Then, the zone that between the two face is marked 0 which means the point in this part shall moving according to the given expression, the other part we marked 1 to keep the point in which zone steady. The motion amplitude of ship surge is set 0.05m which is far smaller than the transverse scale of the grid adjacent to the leftface and rightface which is 1.0m, so the topology needn't to be changed, and all the manipulation that preparing for changing topology is discarded to minimize the time cost on mesh moving. For the motion of heave and sway, the method is still working by adjusting the direction and position of the two faces shown in the figure

It should point out that the original movingConeTopoFvMesh is not suitable for ship motion simulation, because there exists large grid aspect ratio grid near the free surface, and the topology changing manipulate may cause bad mesh quality.

smallOscillationFvMesh   movingConeTopoFvMesh
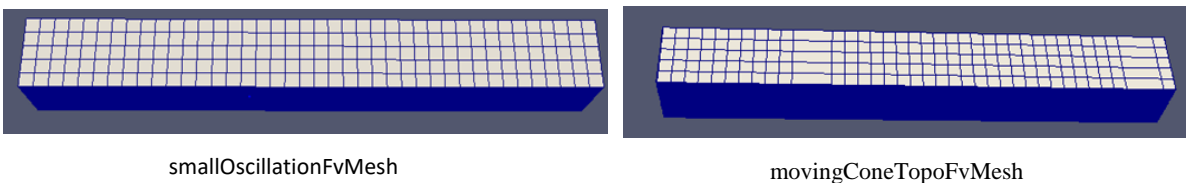
Figure 2: Mesh after a period

The Fig.2 gives the mesh scene after a period with the present method and the original movingConeTopoFvMesh to handle the mesh with large aspect ratio with same setting, and which proves the present smallOscillationFvMesh model can keep high quality of meshes, besides it is convenient to use and efficient when comparing with overset mesh or other dynamic mesh model.

3.   Some results and conclusion
3.1 model and mesh
The forced oscillation of KVLCC2 ship hull is simulated in this work. The performance of KVLCC2 ship hull has been wildly studied by many researchers [4] as a standard ship hull, and there exist plenty of experiment data of this ship hull. The length of the hull is 5.5172m, the other main dimensions can be fined in reference 5. The main motion parameters are shown in Table 1.

Table 1: Motion parameters

Parameter	value
Advancing velocity	0.1047m/s
Motion amplitude (surge, heave, sway)	0.05m
Motion amplitude (roll, yaw, pitch)	0.01 radian
Motion frequency (dimensionless)	1.0; 2.0;2.75;3.75;5;10

The mesh used for simulation is generated by snappyHexMesh[6] tool, and the grid quantity is about 770,000 for half domain. The near wall mesh is shown in Fig. 3. The turbulence model chooses KomegaSST[7].
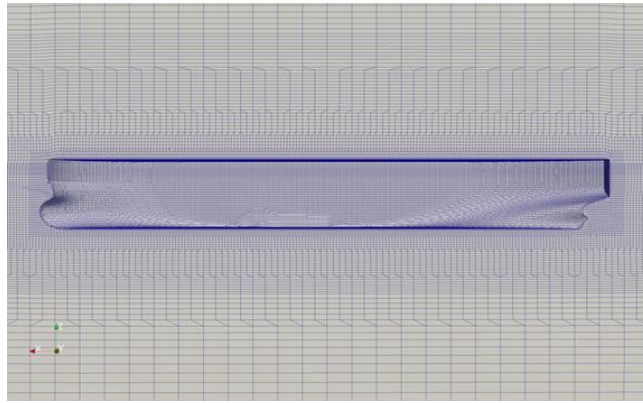
Figure 3: Mesh near ship hull

3.2 Data processing
 For each advancing velocity, motion frequency and motion modality, a set of time-force and time-moment curves can be obtained by interDyMFoam solver in OpenFOAM.
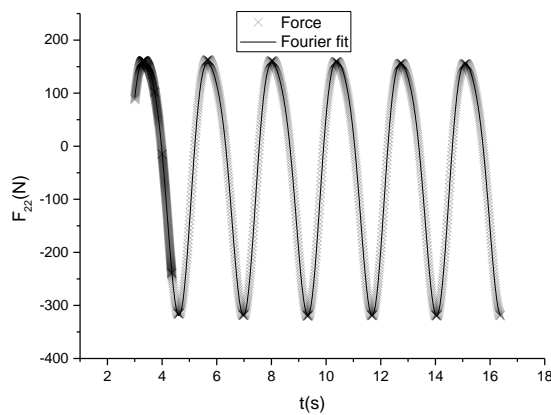
Figure 4: F_{22}-t curve and Fourier fit

The figure 4 gives the F_{22}-t curve at advancing velocity is 0.142 and omega is 2.6676, and which curve is fixed with a 6-expansion Fourier expression. The fit curve can be expressed as follow.

$$F_{2,2} = -48.41 + 75.32sin(\omega t) - 223.4F_{i,jb1}cos(\omega t) + 7.723sin(2\omega t) - 35.96F_{i,jb2}cos(2\omega t)$$
$$-1.05sin(\omega t/3) - 1.396F_{i,jb1}cos(\omega t/3) + 0.2179sin(2\omega t/3) + 1.501F_{i,jb2}cos(2\omega t/3)$$
$$+0.3912sin(4\omega t/3) + 0.8571F_{i,jb1}cos(4\omega t/3) - 0.9586sin(5\omega t/3) - 1.243F_{i,jb2}cos(5\omega t/3) \quad (7)$$

Comparing the Eq. 7 and Eq. 5, it is easy to obtain the needed $F_{i,j0}, F_{i,ja1}, F_{i,jb1}$ and $F_{i,jb2}$. Form the expression of Eq. 7, it is obvious that the parameter what we needed is much larger than the others, which means the present force

decomposition model contains almost all force component and the remaining high-order hydrodynamic coefficient can be ignored.

3.3 Part of hydrodynamic results
   The obtained hydrodynamic coefficient results are shown in the figure below.
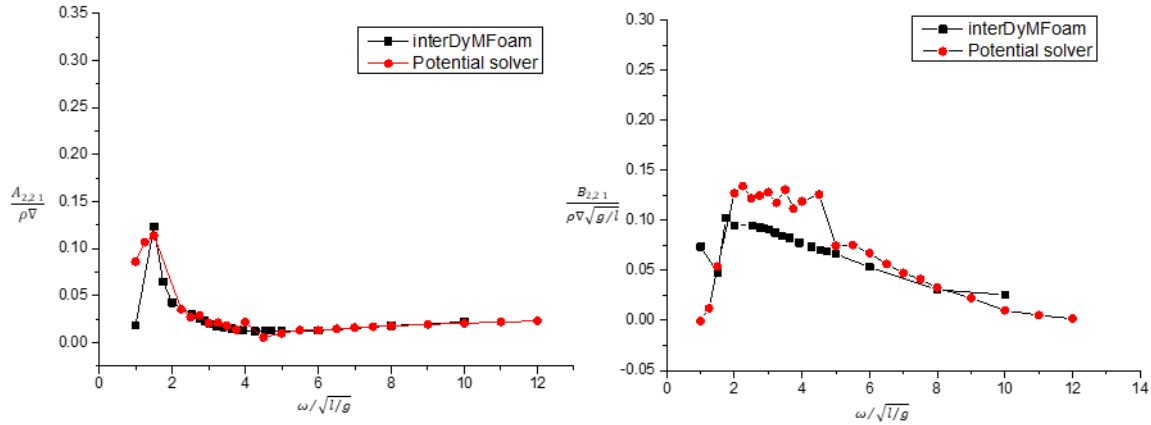
Figure 5: Added mass and damping result

   Fig. 5 give out the added mass and damping result calculated with the present method and a translating–pulsating source potential solver [1]. The added mass coefficient results coincide with the potential result very well, while there exists some gap between in the comparing of the damping coefficient, and this phenomenon is caused by the inviscid hypothesis in the potential method. The results show that the present method can make full use of the result to obtain each component hydrodynamic force, and suitable for hydrodynamic coefficient calculation with the considering of viscous and nonlinear effects.

References

[1] Hong L, Zhu R C, Miao G P, et al. Study on Havelock form translating–pulsating source Green's function distributing on horizontal line segments and its applications [J]. Ocean Engineering, 2016, 124:306-323.

[2] OpenCFD, OpenFOAM: The Open Source CFD Toolbox. User Guide Version 5.0, OpenCFD Limited. Reading UK, Jul. 2017.

[3] Zhu R C, Guo H Q, Miao G P, et al. Computational method for evaluation of added mass and damping of ship based on CFD theory[J]. Journal of Shanghai Jiaotong University, 2009, 43(2):198-203.

[4] Cao Y, Zhu R C, Jiang Y, et al. The computation and analysis of KVLCC2's motion and added resistance in waves [J]. Journal of Harbin Engineering University, 2017, 38(12):1828-1835.

[5] SIMMAN. MOERI Tanker KVLCC2[C]. Workshop on Verification and Validation of Ship Manoeuvring Simulation Methods (SIMMAN 2008). Copenhagen, Denmark, 2008.

[6] Jackson A. A comprehensive tour of snappyHexMesh[C]//7th OpenFOAM Workshop Lecture, Darmstadt. 2012.

[7] Hellsten A. Some improvements in Menter's k-omega SST turbulence model[C]//29th AIAA, Fluid Dynamics Conference. 1998: 2554

LES AND ACTUATOR LINE METHOD FOR MODELING THE TIDAL POWER PLANT DEEP GREEN, USING OPENFOAM

SAM T. FREDRIKSSON[1], GÖRAN BROSTRÖM[2], BJÖRN BERGQVIST[3], JOHAN LENNBLAD[4], HÅKAN NILSSON[5]

[1]*Department of Marine Sciences, University of Gothenburg, Sweden, sam.fredriksson@gu.se*
[2]*Department of Marine Sciences, University of Gothenburg, Sweden, goran.brostrom@marine.gu.se*
[3]*Minesto AB Gothenburg, Sweden, bjorn.bergqvist@minesto.com*
[4]*Minesto AB Gothenburg, Sweden, johan.lennblad@minesto.com*
[5] *Department of Mechanics and Maritime Sciences, Chalmers University of Technology, Gothenburg, Sweden, hakan.nilsson@chalmers.se*

Keywords: Tidal energy, Turbulence, LES, Actuator Line Model (ALM)

Tidal energy has a great potential as a renewable electric energy source, following the sustainable development goals of the UN. Tidal energy can be harvested in different ways, of which one way is to directly extract the energy from the flowing water. The tidal stream is special in the sense that it is oscillating back and forth, with rather low velocities. The turbulence behaves differently in the accelerating and decelerating phases of the tidal cycle. Furthermore, the marine environment is particularly harsh for technical equipment, and tidal power plants must co-exist with other marine activities. A tidal energy plant must be able to handle such situations with a high efficiency, and with low environmental and social impacts. The tidal power plant Deep Green, developed by Minesto AB uses a novel technology with a 'flying' wing with an attached turbine that sweeps the tidal stream with a velocity several times faster than the mean flow, see Figure 1. The trajectory of the wing is controlled by an advanced control system and forms a sideways figure eight that is almost perpendicular to the tidal flow. The trajectory is fully submerged during operation, but the wing can reach the surface for maintenance. The wing is attached to the seabed by a tether, through which the electric power from the turbine is transmitted to a local distribution network that connects a number of Deep Green plants in a farm to the land-based electric grid. A farm of Deep Green power plants must be designed so that the individual power plants have a minimum negative impact on the other power plants in the farm. The distance must be large enough to avoid collision, both at full tidal stream and when the flow reverses. Most of the energy can be extracted during full tidal stream, and then it is important that the farm is designed to minimize any negative effects of the wakes on downstream power plants. The aim of the present work is to accurately model the influence of the Deep Green power plant on the turbulent tidal flow. The results can be used to increase the knowledge of the Deep Green wake, which in turn can be used to design optimized Deep Green farms. The results can also be used as input to models of the dynamics of the wings, to determine how the control systems should be designed to safely consider both the tidal turbulence and wakes from upstream wings.
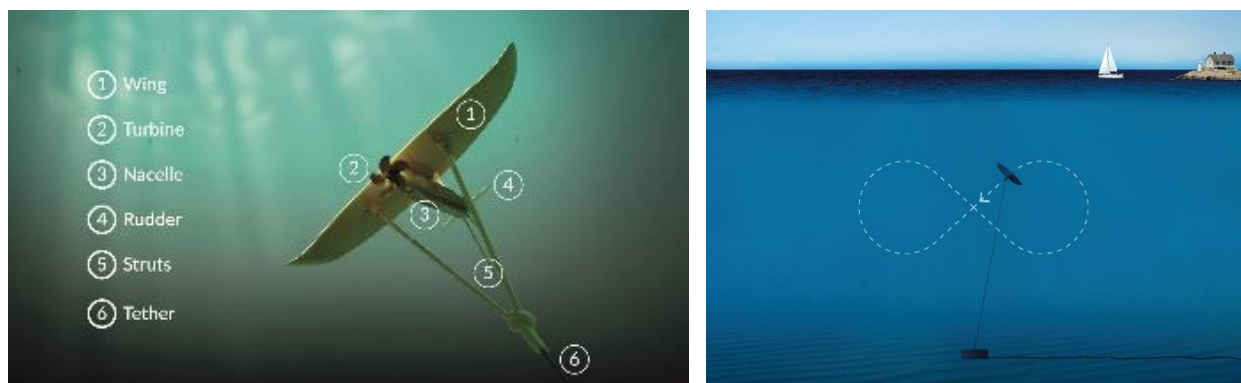
Figure 1: The tidal power plant Deep Green, with its components and operating procedure.

The conditions of the tidal flow are in the present study resembling those at a test site west of Holy Island, along the west coast of Wales. The depth is 80m, with a rather smooth seabed with individual boulders of about 2x2x2m. A bottom roughness is introduced in the simulations to give mean velocity profiles in accordance with field measurements. The Coriolis force and any surface shear forces are neglected. A precursor cyclic one-equation eddy-viscosity LES simulation of two full tidal cycles is used to set initial conditions for the Deep Green simulation. An additional half tidal cycle proved that the oscillating flow is fully developed. The tidal flow of the precursor simulation

is obtained by a sinusoidal varying body force, adjusted to fit the tidal peaks at the test site. The simulation with the Deep Green power plant is started at a condition with accelerating flow at approximately 1.6m/s, close to the tidal flow peak (at 2.0m/s). The initial condition is taken from the precursor simulation, and the inlet boundary condition that drives the flow in this simulation is mapped from the precursor simulation each time step. The Deep Green power plant is modelled using the Actuator Line Method (ALM) [1, 2] from the turbinesFoam [3] package, adapted to the particular trajectory of the Deep Green wing. The lift and drag along the wing profile for different angles of attack are taken from a separate RANS simulation of the Deep Green wing, using the k-ω turbulence model. A momentum sink is added to take the turbine into consideration [4].

Figure 2 shows the results of the Deep Green simulation. The wing is visualized by a green iso-surface of the force field from the ALM. Grey iso-surfaces of the Q-criterion is used to visualize the turbulent vortices at the seabed and the wing wake in the form of tip vortices. The domain boundaries and five cross-sections are coloured by the velocity magnitude. The cross-sections are located at the centre of the wing trajectory, and at 1-4 trajectory widths downstream the centre of the wing trajectory. A single wing is considered in the simulation, but since cyclic conditions are used at the sides of the domain the results resemble an infinite number of wings side-by-side. The plots show the time-averaged vertical and horizontal velocity profiles, going through the centre of the trajectory of the wing at the different downstream positions. It can be seen that the wake of the wing influences the flow throughout the computational domain. The wake is asymmetric in the vertical direction, due to the vertical shear in the main flow. The horizontal width of the wake and its number of peaks decrease with distance to the wing. The wake tends to stabilize its shape at about $3D_y$ downstream the wing.
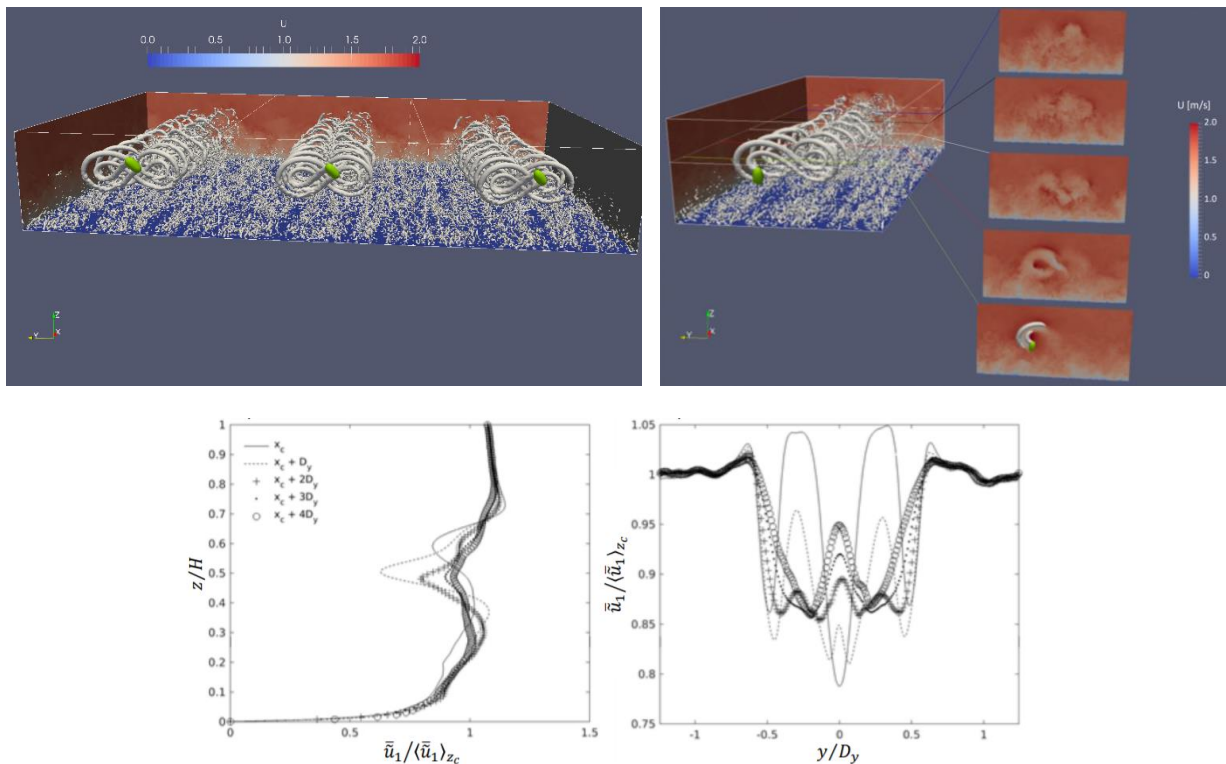
Figure 2: Wake of the Deep Green power plant, visualized by iso-surfaces of the Q-criterion and velocity plots.

Acknowledgements

References

[1] N. Troldborg, Actuator line modeling of wind turbine wakes (2009).

[2] M.J. Churchfield, Y.Li and P.J. Moriarty, A large-eddy simulation study of wake propagation and power production in an array of tidal-current turbines, Philos. Trans. R. Soc. A 317.1985 (2013): 20120421.

[3] P. Bachant, A. Goude and M. Wosnik, Actuator line modeling of vertical-axis turbine, 2016.

[4] S.T. Fredrikson, G. Broström, M. Jansson, H. Nilsson and B. Bergqvist, Large eddy simulation of the tidal power plant deep green using the actuator line method, IOP Conference Series: Material Science and Engineering, 276 (2017), doi 10.1088/1757-899X/276/1/012014.

PARALLEL LOAD BALANCING CAPABILITIES IN FOAM-EXTEND

Henrik Rusche[1], Hrvoje Jasak[2]

[1]*Wikki GmbH, Braunschweig, Germany, h.rusche@wikki-gmbh.de*
[2]*Wikki Ltd., London, United Kingdom, h.jasak@wikki.co.uk*

Keywords: *Parallel Load Balancing, Dynamic Load Balancing, Multi Physics Simulations*

The majority of todays simulations using FOAM are run in parallel. In order to use, the allocated computational nodes efficiently, it is important that the computational load is distributed equally across the computational nodes while minimising the communication overhead. This process is known as partioning. For an Eulerian problem on a static mesh, it is usually sufficient to partition the mesh before starting the solver application using METIS or SCOTCH by running decomposePar.

However, the initial partioning may become inadequate during the simulation when the simulation involves features such as topologically changing meshes (for example adaptive mesh refinement, layer-addition and removal), multi-physics (for example Lagrangian particles, reaction kinetics) or expensive search and/or geometric algorithmns (immersed boundary, generalised grid interface, sliding interfaces, geometric VOF).

In these applications, it can be beneficial to re-partition the computational domain according to the actual dynamic load during the simulation. While the repartitioning (colouring the cells using METIS or SCOTCH) itself is computationally cheap, writing the computational state to disk is in most cases prohibitively expensive. It is therefore important that the full re-balancing machinery is executed within the solver process.

In this presentation, the new parallel load balancing capabilities in foam-extend are presented and examples of their productive use are shown.
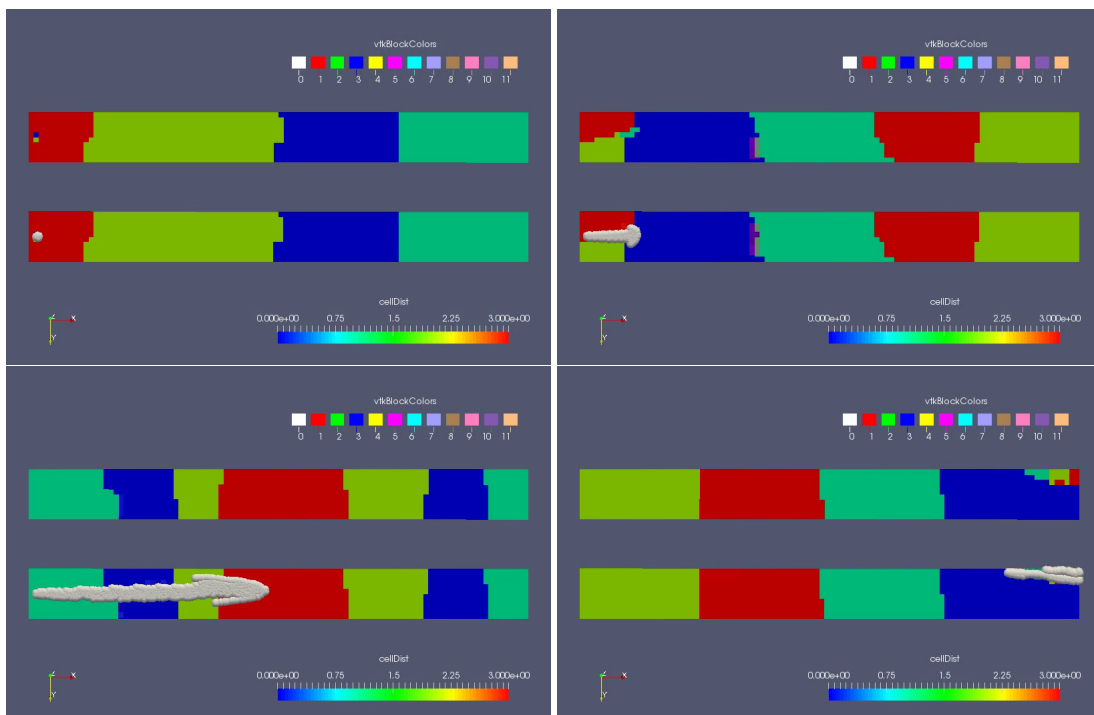
Figure 1: Dynamic load balancing of a Lagrangian particles simulation running on four nodes. The four pictures show charateristics time instances as the Lagragian particles injected on the left cross the computational domain. The computational domains are coloured by their partition ID and are shown twice in each picture: without particles (top), with particles (bottom).

AN IMMERSED BOUNDARY WALL FUNCTION FOR SMOOTH WALL SHEAR STRESS

XIAOFENG LIU[1], YUNCHENG XU[2]

[1]*Dept. of Civil and Environmental Engineering, Pennsylvania State Univ., xliu@engr.psu.edu*
[2]*Dept. of Civil and Environmental Engineering, Pennsylvania State Univ., ycxu1990@gmail.com*

Keywords: immersed boundary method, wall function, wall shear stress

An immersed boundary (IB) wall function for turbulent flows using the $k - \epsilon$ model is developed in this work. The IB method is based on the existing method in foam-extend-3.0 and foam-extend-4.0 [1, 2]. In this method the whole computational mesh is classified into three categories, i.e., live cells, IB cells, and dead cells. No-slip boundary condition on the IB surface is imposed through manipulating the values in IB cells. The coefficient matrices of the resulted linear equation system are manipulated by eliminating the corresponding off-diagonal elements and modifying the relevant diagonal elements and source term. Thus, the values in IB cells are prescribed. The values in dead cells are fixed (usually as zero) and not included in the computation. In essence, the key of this IB method is imposing boundary conditions through IB cells.

However, we found that the current implementation of turbulence models and in particular the wall functions sometime cause issues in the simulation results. An important quantify for many fields is the wall shear stress. In man y cases, current implementation gives noisy wall shear stress distribution on the immersed boundary, which makes further calculation based on the wall shear not reliable. Examples of such further calculation include heat transfer, sediment transport, and surface wear.

To address this problem, we developed a new wall function with the use of the $k - \epsilon$ model. It is modified from the method introduced in previous work [1, 2]. It enforces the wall law by changing the values in IB cells. However, the original wall function implemented does not behave well when y^+ is in the buffer layer or the viscous sublayer range.

As shown in Fig. 1a, in order to evaluate the value at the IB cell center, an image point, which is further away from the immersed wall and into the fluid region, is defined to reconstruct the flow information from surrounding live cells. For the image point and the IB cell center, y^+ is calculated respectively according to

$$y_{\text{IP}}^+ = \frac{C_\mu^{1/4}\sqrt{k_{\text{IP}}}y_{\text{IP}}}{\nu}, \quad y_{\text{IB}}^+ = y_{\text{IP}}^+ \frac{y_{\text{IB}}}{y_{\text{IP}}} \tag{1}$$

where y_{IP} denotes the distance from image point to IB surface. y_{IB} denotes the distance from IB cell center to IB surface. In the original implementation, the ratio of $y_{\text{IP}}/y_{\text{IB}}$ is usually set as 2. Shear velocity (u_τ) for the image point, which is assumed to be equal to the shear velocity calculated at IB cell center since both are on the same velocity profile, is calculated as

$$u_\tau = \begin{cases} C_\mu^{1/4}\sqrt{k_{\text{IP}}} & \text{if } y_{\text{IP}}^+ > y_{\text{Laminar}}^+ \\ \sqrt{\nu|u_{\text{tan,IP}}^{old}|/y_{\text{IP}}} & \text{if } y_{\text{IP}}^+ \leqslant y_{\text{Laminar}}^+ \end{cases} \tag{2}$$

where $u_{\text{tan,IP}}^{old}$ denotes the interpolated tangential velocity at image point, $|\ |$ denotes its magnitude. $y_{\text{Laminar}}^+ = 11$. Thus, wall shear stress can be calculated as

$$\tau_w = u_\tau^2 \tag{3}$$

Then, based on the wall law, new tangential velocity at IB cell center can be evaluated as

$$u_{\text{tan,IB}}^{\text{new}} = \begin{cases} \dfrac{u_\tau \kappa}{\log\left(E y_{\text{IB}}^+\right)} & \text{if } y_{\text{IB}}^+ > y_{\text{Laminar}}^+ \\ u_\tau y_{\text{IB}}^+ & \text{if } y_{\text{IB}}^+ \leqslant y_{\text{Laminar}}^+ \end{cases} \tag{4}$$

where E is the roughness coefficient, usually set as 9.8 for smooth wall. Afterwards, the eddy viscosity ν_t, k, and ϵ at IB cell center can be calculated respectively as follows

$$\nu_t = \begin{cases} \dfrac{y_{\text{IB}}^+ \kappa}{\log\left(E y_{\text{IB}}^+\right)}\nu & \text{if } y_{\text{IB}}^+ > y_{\text{Laminar}}^+ \\ 0 & \text{if } y_{\text{IB}}^+ \leqslant y_{\text{Laminar}}^+ \end{cases} \tag{5}$$

$$k_{\text{IB}}^{\text{new}} = \begin{cases} (\nu_T + \nu)\dfrac{u_{\text{tan,IP}}^{\text{old}}}{y_{\text{IP}}}C_\mu^{-0.5} & \text{if } y_{\text{IB}}^+ > y_{\text{Laminar}}^+ \\ k_{\text{IP}} & \text{if } y_{\text{IB}}^+ \leqslant y_{\text{Laminar}}^+ \end{cases} \tag{6}$$

$$\epsilon_{\text{IB}}^{\text{new}} = \begin{cases} \dfrac{C_\mu^{0.75}(k_{\text{IB}}^{\text{new}})^{1.5}}{\kappa y_{\text{IB}}} & \text{if } y_{\text{IB}}^+ > y_{\text{Laminar}}^+ \\[2ex] \epsilon_{\text{IP}} & \text{if } y_{\text{IB}}^+ \leqslant y_{\text{Laminar}}^+ \end{cases} \tag{7}$$

where in the laminar region, k_{IB} is treated as the same value as at image point.

As seen in Fig. 2a, when the IB wall distance (y_{IB}^+) falls in the laminar region, the original wall function can not reproduce the log-law. Unfortunately, in immersed boundary method, it is hard to control the distance between the IB cells and the immersed surface. This distance can even change when the immersed boundary is moving. In order to overcome this, a new algorithm is developed. The key idea is to adaptively increase y^+ by changing the IB cells (see Fig. 1). For any IB cell, if y_{IB}^+ falls in the laminar region, the IB cell will be replaced by an adjacent live cell slightly away from the IB surface to ensure the new IB cell is located in the log-law layer. This replacement of IB cell will not have significant impact on the accuracy since the mesh around the immersed boundary is usually refined. After all, the immersed boundary method is only an approximation of the wall effect to the flow.

(a) before y^+ adaptation   **(b) after y^+ adaptation**
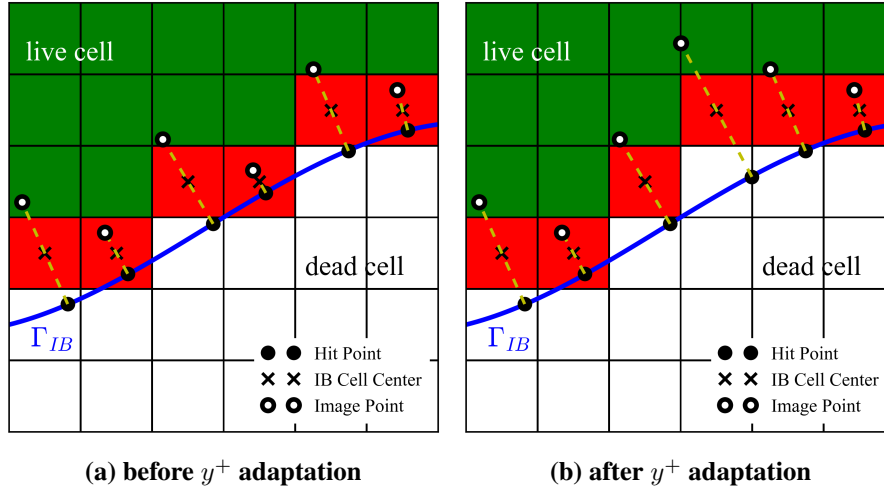
Figure 1: 2D schematic of y^+ adaptation process. **Red-filled cells are IB cells. Green-filled cells are live cells. White-filled cells are dead cells.**

As shown in Fig. 2 (b), the result of 1D channel flow validation case shows the new y^+ adaptation algorithm captures the wall law regardless the IB wall distances. One can also observe that the new algorithm makes sure y_{IB}^+ is always in the log-law region (> 11).

To further demonstrate the new algorithm, Fig. 3 shows the wall shear stress distribution over a dune-like bathymetry

(a) before y^+ adaptation (original method)   **(b) after y^+ adaptation**
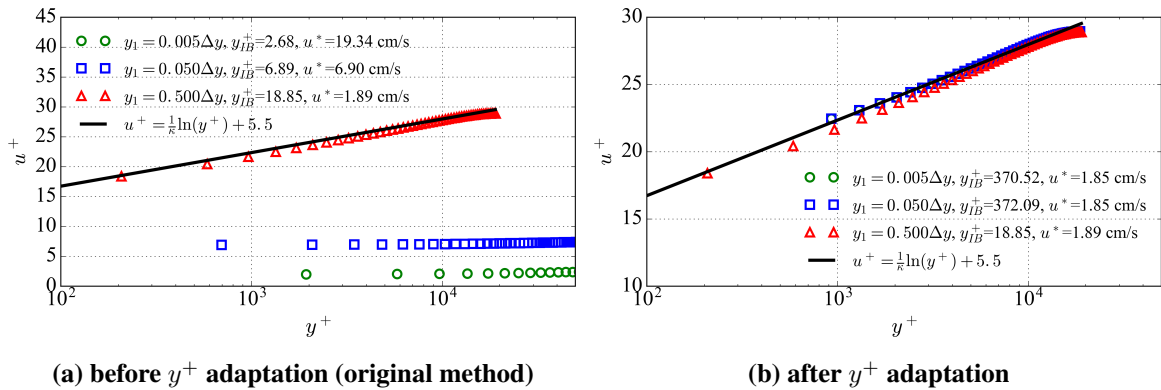
Figure 2: **Log-law results for 1D validation case with different y_1.**

using immersed method. In this case, the background 3D mesh is structured and the immersed interface is dune-like. It can be observed that without y^+ adaptation, the wall shear stress is not smooth as it should be. In the back of the dune, there are some "hot" spots of high wall shear caused by the small IB wall distance. By applying the new algorithm, the wall shear stress distribution is much smoother and more reasonable.
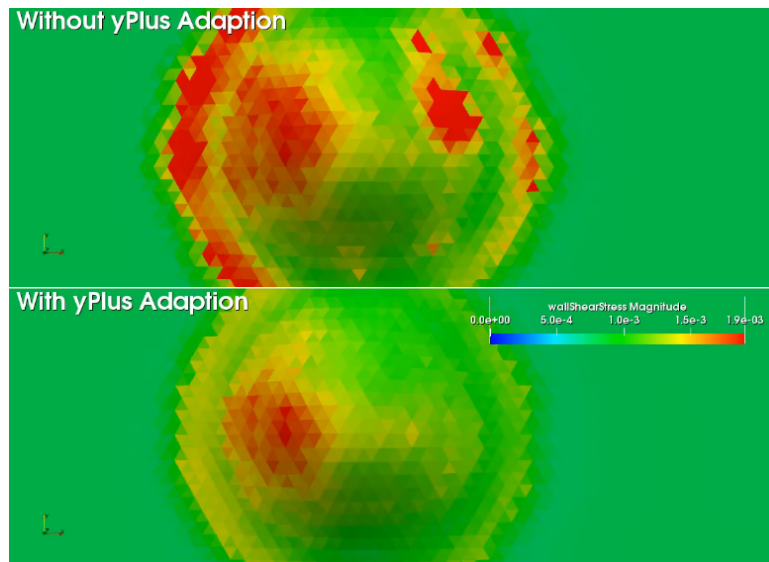
Figure 3: Wall shear stress distribution over a dune-like bathymetry. Flow is from left to right.

Acknowledgments

The authors wish to thank Dr. Hrvoje Jasak for his discussions with us on the topic of this paper.

References

[1] H. Jasak, D. Rigler, and Ž. Tuković, "Design and implementation of Immersed Boundary Method with discrete forcing approach for boundary conditions," 2014.

[2] H. Jasak and Ž. Tuković, "Immersed Boundary Method in FOAM," CFD with OpenSource Software Course, Chalmers University 2015, pp. 1–36, 2015.

AFEPACK SOLVER CONSTRUCTION BASED ON OPENFOAM

CAO YUAN[1], YAO CHENGBAO[2], SU JUNWEI[3]

[1]Northwest Institute of Nuclear Technology, caoyuan@nint.ac.cn
[2]Northwest Institute of Nuclear Technology, yaochengbao@nint.ac.cn
[3]Xi'an Jiaotong University, sujunwei@mail.xjtu.edu.cn

As the strongest open source CFD package now, OpenFOAM[1] has open and complete upper layer. It also provides a lot of compiled solvers, so it gets widespread applications. Especially, its dictionary and hash table function make parameter queries faster and more convenient than before. Its runtime selection mechanism uses virtual function of C++, which makes program dynamically selecting different models during runtime without compiling the program again. It is useful to build solvers and expand functions.

AFEPack[2] is an adaptive finite element package developed by professor Li Ruo of Beijing University with C++ language. It provides basic and general support to finite element method and finite volume method. It helps AFEPack users to achieve finite element program and finite volume program with parallel and adaptive function very conveniently. Unfortunately, AFEPack doesn't has model selection mechanism, so programs based on AFEPack can't form solvers, which goes against for function expansion of AFEPack programs.

Based on the dictionary, hash table and runtime selection mechanism of OpenFOAM, we reconstruct AFEPack program to applicable solver. Specifically, aiming at the characteristics and flow of numerical simulation using AFEPack finite element and finite volume methods, selectors are provided for links needed selections, then parameter dictionary and flow controller are formulated for parameter and flow control, finally the conversion from program to solver is achieved. The specific modification plan is shown in Figure 1.
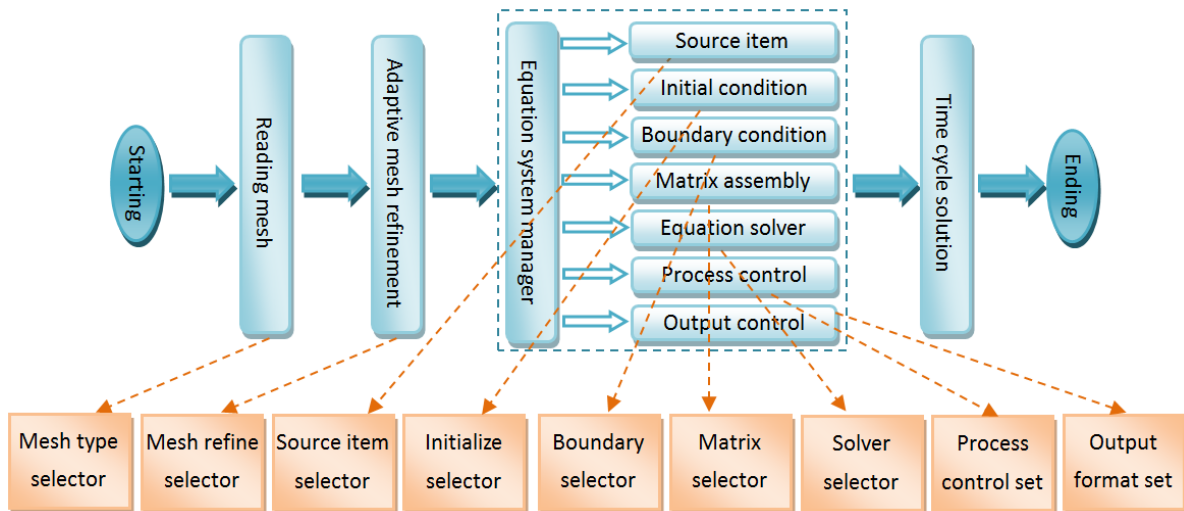
Figure 1: Modification scheme of AFEPack program to solver

There are nine modules in specific programming, such as mesh reading module, mesh refinement module, source item handling module, initialize module, boundary handing module, matrix assembly/flux calculation module, algebraic equations solving module, flow control module, output format setting module. Here we take mesh reading module as an example to explain its implementation process.

Mesh reading module is used to select the way to generate mesh for users. Mesh dictionary shown in Figure 2 is read to get key word after meshType.

```
MESH
{
    Mesh_data_file        "data/D.mesh";
    Mesh_data_directory   "data/D";
    meshType        internal;
}
```

Figure 2: Mesh dictionary

The code call structure of mesh reading module is shown in Figrue 3.
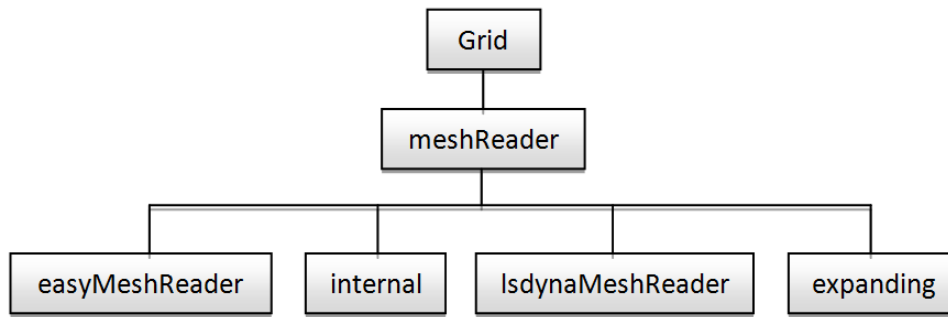
Figure 3: Code call structure of mesh reading module

First meshreader object is used in Grid class, then the way of building meshReader is select by runtime selection table. There are three format to build meshReader now, such as easyMeshReader，internal and lsdynaMeshReader. Other formats can be expanded too, which is only need to add subclasses, without modifications of existing codes. The main code files and their functions is shown in Table 1.

Table 1: Main code file and their functions of mesh reading module

Code file	functions
meshReader.C	Definite hash table, read mesh from string information flow and generate file.
meshReader.H	Declare hash table, and select different mesh type during runtime.
meshReaderNew.H	Read mesh type string after meshType.
internal.C	Add internal subclass to hash table.
internal.H	Achieve virtual function of mesh reading，and read mesh file of internal format to string information flow.
easyMeshReader.C	Add easyMeshReader subclass to hash table.
easyMeshReader.H	Achieve virtual function of mesh reading，and read mesh file of easymesh format to string information flow.
lsdynaMeshReader.C	Add lsdynaMeshReader subclass to hash table.
lsdynaMeshReader.H	Achieve virtual function of mesh reading，and read mesh file of lsdyna format to string information flow.

The realization principle of other modules are similar to mesh reading module, here omitted. Then the AFEPack solver is formed.

At last we use an example to validate the correctness of the reconstruction, which is an AFEPack program to simulate strong explosion shock wave. The conditions are even atmosphere and 1kt TNT equivalent. We use dictionary file of args.txt to set selector options, which can be specified on demand by users, here omitted. The shock wave pressure of flow field on different time are shown in Figure 4.

(a) (b)
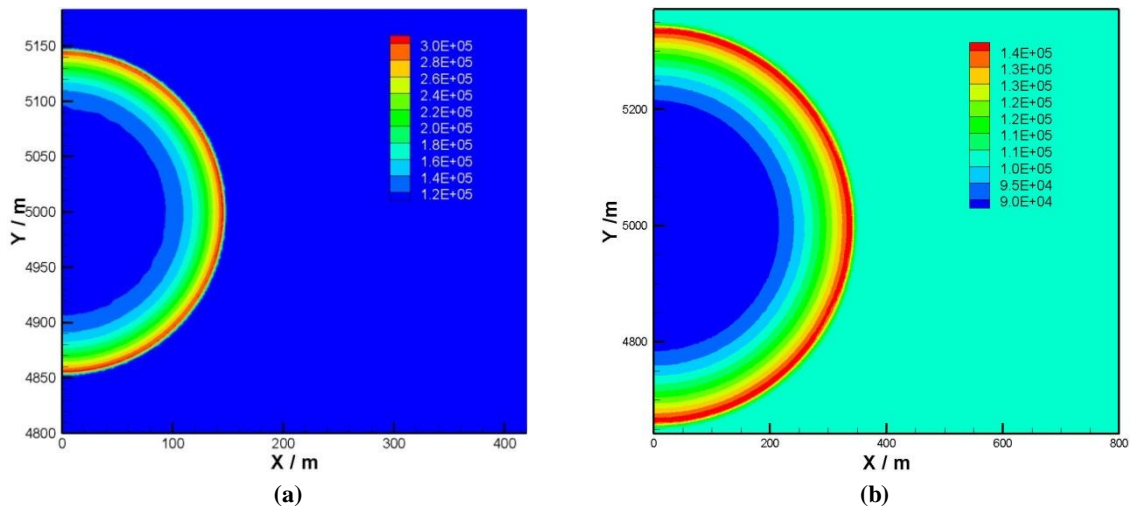
Figure 4: Flow field cloud of shock wave pressure on different time

Shock wave over pressure history curve at different distance to burst heart by calculation shown in Figure 5 can correctly describe shock wave positive pressure, negative pressure and secondary shock at certain positions in strong explosion. It shows the calculation is reasonable and the result is reliable.

(a) 200m   (b) 300m
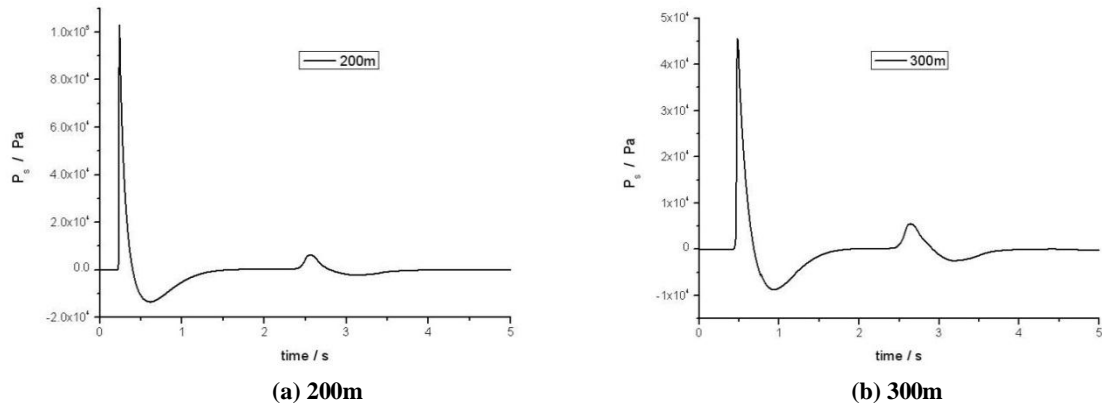
Figure 5: Shock wave over pressure history curve at different distance to burst heart

Shock wave overpressure peak, positive pressure impulse, shock wave arrival time and positive pressure action time of solver result are all same with that of the program before. It shows the correctness of the program is not changing in the solver reconstruction. At the same time, the selection functions of the selectors, such as mesh file, initial condition, boundary condition and solution algorithm are all achieve scheduled goals.

As a solver, it has more selectivity and applicability than the program before. Users only need to assignment parameters by dictionary file, then different solution functions can be implemented dynamically. So the solver has stronger functions than before.

Based on the dictionary, hash table and runtime selection mechanism of OpenFOAM, we reconstruct AFEPack program to applicable solver, which expanding dynamical selection functions of program largely. It shows the feasibility and correctness of the reconstruction through example validation. The reconstruction ideas and technologies are universal, and can be applied to the reconstruction from programs based on other open source package to solvers.

References

[1] OpenCFD, OpenFOAM: The Open Source CFD Toolbox. User Guide Version 1.4, OpenCFD Limited. Reading UK, Apr. 2007.

[2] Li R., Liu W. B.. http://circus.math.pku.edu.cn/AFEPack, 2013-08-12.

NUMERICAL SIMULATIONS OF ELECTRICAL DOUBLE LAYER AND ELECTROOSMOTIC FLOW IN A NANOPORE BY OPENFOAM

JIE LI，JIAN YE，DILIN CHEN, LI XU

Mail：yejianjerry@163.com, school of Energy and Power Engineering，Wuhan University of

Technology, 1040 Heping Road,Wuhan 430063, PR China

Keywords: EDL，EOF，OpenFOAM

The microfluidic chip transfers the pretreatment, chemical reaction, separation, detection, and other functions of the sample to a chip of several square centimeters, which embodies the characteristics of miniaturization, integration, automation, and simplicity. The drive and control of microfluidic have become the key problems in the research of microfluidic chip. In this work, numerical simulation of the electrical double layer (EDL) formed next to a charged planar surface and an electroosmotic flow (EOF) in a nanopore is demonstrated using OpenFOAM. The electrostatics and the ionic mass transport are governed by the Poisson–Nernst –Planck (PNP) equations without considering fluid motion in the model for EDL. The numerical predictions of the electric field and ionic concentrations are in good agreement with the analytical solution. The model for EOF includes the modified Stokes equations for the flow field, the Poisson equation for the electrostatics, and the Nernst–Planck equations with the convective term for the ionic mass transport. The predicted EOF velocity quantitatively agrees with the analytical solution.

IMPLEMENTATION OF ADVANCED PLASTICITY MODELS IN OPENFOAM

MICHAEL CLANCY[1], PHILIP CARDIFF[1], PETER DE JAEGER[1,2], ALOJZ IVANKOVÍC[1]

[1]*University College Dublin, School of Mechanical and Materials Engineering, Ireland, michael.clancy@ucdconnect.ie*

[2] *N.V. Bekaert S.A., Belgium*

Keywords: solid mechanics, plasticity, distortional hardening

The use of the finite-volume method, in particular the segregated approach advocated in [1], has been proven to be a viable approach in the solution of solid mechanics problems. The implementation of a large-strain Lagrangian solution methodology and its application to metal forming has now been carried out by [2]. The extension of this suite of tools to handle advanced plasticity models has been carried out by the present authors. The overall aim of the work is to more accurately describe the deformation behaviour of steel wire products during forming processes.

Need for advanced material models

The availability of robust and fast numerical methods, such as radial-return map for the Von-Mises yield criterion, has led to widespread use of computational plasticity models in mechanical forming applications for the prediction of geometry and mechanical properties. All major finite-element codes now contain one of the standard implementations of this plasticity model.

The need for models with the ability to describe anisotropic yield strengths was found for forming simulations in [3][4]. During processing the reorientation of material leads to the formation of a crystalline texture. In the case of pearlitic steel, a large portion of which finds its use in ultra-high strength wire, this texture takes the form of regularly spaced cementite lamellae in a ferrite matrix. The cementite lamellae are hard and brittle, compared to the relatively softer ferrite. With geometric inhomogenity comes expected anisotropic behaviour. Confirmation of the yield-anisotropy of pearlitic microstructures is found in [5]. A failure of basic material models in the prediction of wire geometry is seen, which creates difficulty in the production of novel wire products. An example of such a geometry is seen in Figure 1. The use of anisotropic material models, which can accurately capture the initial and evolved yield-strength in all directions is required.
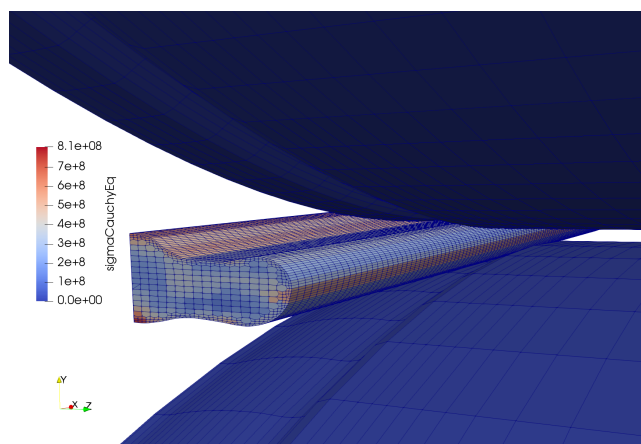
Figure 1: An example of special wire geometry where advanced material models find application.

Implemented material models

From the vast array of advanced material models that exist, three were selected and implemented within OpenFOAM. The choice of these models were made due to the original authors appreciation for numerical efficiency, which is often secondary to model development. The models selected for implementation are given in the works of [6][7][8]. The most advanced model studied being that of distortional hardening, with the ability to predict evolving anisotropy of the yield-locus as seen in Figure 2b. This model was used to predict the geometry of flat-rolled wire in Figure 3b.

Additionally, a material model with some basis in the physical characteristics of pearlitic steel was developed and implemented by the current authors. This plasticity model was inspired from existing works such as [9][10][11], which
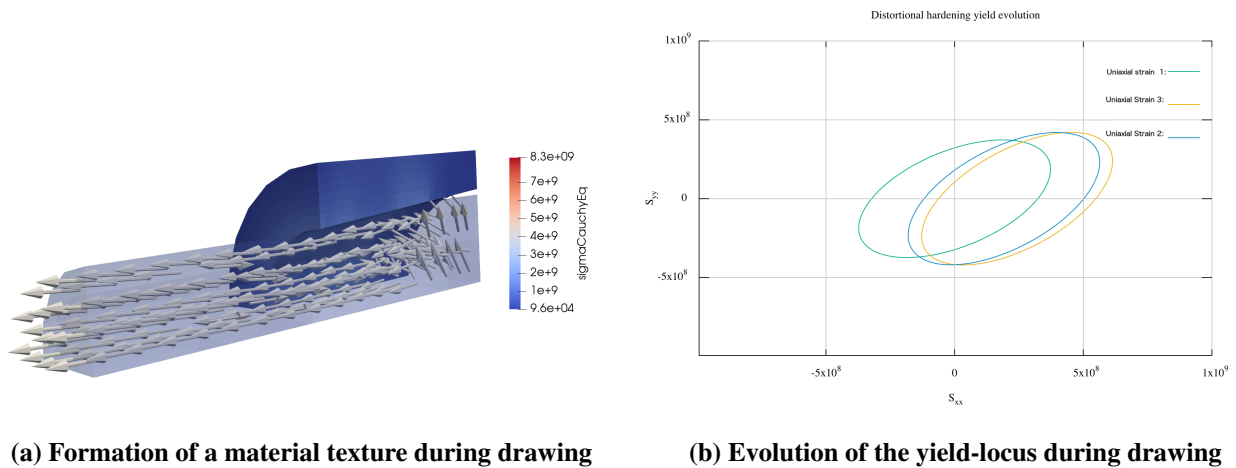
(a) Formation of a material texture during drawing

(b) Evolution of the yield-locus during drawing

Figure 2: Advanced material models
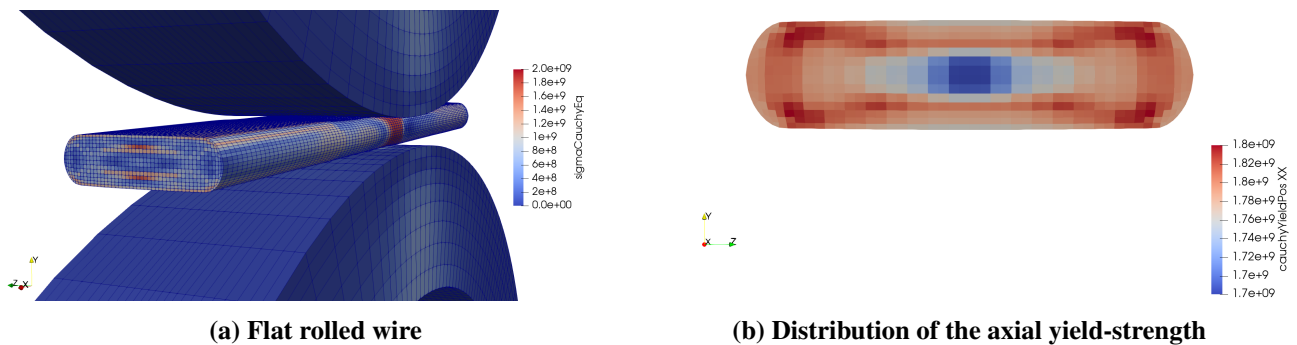
(a) Flat rolled wire

(b) Distribution of the axial yield-strength

Figure 3: Simulation of flat-rolling with an advanced material model

aim to capture the material reorientation of the crystal microstructure. A simulation of this material reorientation for wire drawing can be seen in Figure 2a.

The numerical implementation of plasticity models almost always requires the solution of a differential-algebraic system. The differential equations describing the material history parameter evolution must be integrated whilst maintaining the condition that the stress-state either lies upon the yield-surface (indicating plastic flow) or within its boundary (indicating elastic deformation). The use of a backwards Euler integration scheme for the history variable evolution results in the solution of a system of non-linear equations.

Automatic differentiation (AD) was found to be a useful tool that enabled the quick calculation of the Jacobian for each material model implemented. The AD library Fadbad [12] was used for this purpose. The use of templated tensor types in OpenFOAM allowed easy integration with this package.

Acknowledgments

References

[1] K. Maneeratana, "Development of the finite volume method for non-linear structural applications," Ph.D. dissertation, Imperial College London, 2000.

[2] P. Cardiff, Ž. Tuković, P. D. Jaeger, M. Clancy, and A. Ivanković, "A lagrangian cell-centred finite volume method for metal forming simulation," *International journal for numerical methods in engineering*, vol. 109, no. 13, pp. 1777–1803, 2017.

[3] T. Massé, Y. Chastel, P. Montmitonnet, C. Bobadilla, N. Persem, and S. Foissey, "Impact of mechanical anisotropy on the geometry of flat-rolled fully pearlitic steel wires," *Journal of Materials Processing Technology*, vol. 211, no. 1, pp. 103–112, 2011.

[4] B. Plunkett, O. Cazacu, and F. Barlat, "Orthotropic yield criteria for description of the anisotropy in tension and compression of sheet metals," *International Journal of Plasticity*, vol. 24, no. 5, pp. 847–866, 2008.

[5] M. Kapp, A. Hohenwarter, S. Wurster, B. Yang, and R. Pippan, "Anisotropic deformation characteristics of an ultrafine-and nanolamellar pearlitic steel," *Acta Materialia*, vol. 106, pp. 239–248, 2016.

[6] A. Bartels and J. Mosler, "On the numerical implementation of thermomechanically coupled distortional hardening," *International Journal of Plasticity*, vol. 96, pp. 182–209, 2017.

[7] P. Papadopoulos and J. Lu, "On the formulation and numerical solution of problems in anisotropic finite plasticity," *Computer Methods in Applied Mechanics and Engineering*, vol. 190, no. 37, pp. 4889–4910, 2001.

[8] M. Á. Caminero, F. J. Montáns, and K.-J. Bathe, "Modeling large strain anisotropic elasto-plasticity with logarithmic strain and stress measures," *Computers & Structures*, vol. 89, no. 11, pp. 826–843, 2011.

[9] J. G. Sevillano, "On the yield and flow stress of lamellar pearlite," *Pergamon Press Ltd,*, pp. 819–824, 1980.

[10] G. Johansson, A. Menzel, and K. Runesson, "Modeling of anisotropic inelasticity in pearlitic steel at large strains due to deformation induced substructure evolution," *European Journal of Mechanics-A/Solids*, vol. 24, no. 6, pp. 899–918, 2005.

[11] J. Alkorta, J. Martínez-Esnaola, P. de Jaeger, and J. G. Sevillano, "New mesoscopic constitutive model for deformation of pearlitic steels up to moderate strains," in *IOP Conference Series: Materials Science and Engineering*, vol. 219, no. 1. IOP Publishing, 2017, p. 012010.

[12] C. Bendtsen and O. Stauning, "Fadbad, a flexible c++ package for automatic differentiation," Tech. Rep., 1996.

[13] Irish Centre for High End Computing (ICHEC), "Fionn supercomputer," http://www.ichec.ie, 2012.

SYSTEMATIC SIMULATION COMBINING CFD AND 1-D DRIVE SYSTEM OF HIGH-VISCOSITY FLUID DISPENSING JET IN MICRO-ELECTRONICS PACKAGING

RUN DU[1], YONGJIE ZHOU, XIAO YE

School of Mechanical Engineering, Southwest Jiaotong University, Chengdu, China
[1]*rdu@swjtu.edu.cn*

Keywords: *Dispensing Jet; High Viscosity; CFD*

Adhesives are used extensively in the assembly and packaging of micro-electronics and MEMS, especially in the current mass production of electronic hardware, e.g., computers, cell phones, smart cards, and sensors. They are used both in single-chip packages and multichip assemblies.[1] Adhesives, as a kind of fluid, are used to produce dots, lines, or patterns, and has been dispensed on the substrate. The process is called fluid dispensing. Stencil printing, screen printing, pin transfer, daub transfer, and stamping are examples of mass-transfer types.[1] In comparison, selective dispensing methods are computer data driven, dispensing adhesives where it is necessary. One of the selective dispensing type is contact dispensing, in which the dispensing tools have a short time of contact to the substrate, e.g., syringe-needle dispensing. The other one is jet dispensing, a direct-dispensing process where the adhesive is forced through a fine nozzle and programmed to flow at selected position controlled from a computer database, which is not required to contact the surface. Currently, the selective dispensing used in very large portion of all production processes. As a sketch, Figure 1 shows the basic components of a pneumatic-driven jet dispensing pump. The compressed air pushes the piston up, when the pneumatic valve is triggered. the adhesive is pressurized to fill the void left when the piston retracts from the seat. When the pneumatic valve is closed, the spring-driven ball returns, the force pushes the fluid through the nozzle. Once the ball impacts on the seat, it breaks the stream of adhesive, which is then jetted in precisely controlled amounts onto the substrate.
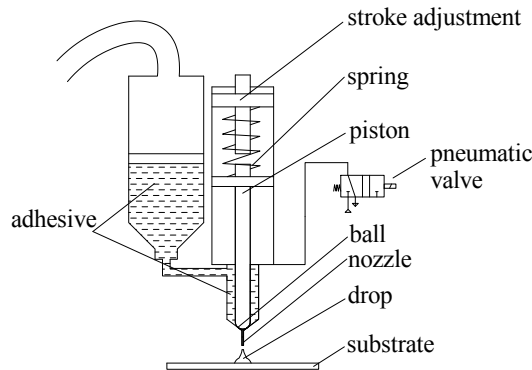
Figure 1: Sketch of a pneumatic-driven jet dispensing pump

This is a kind of drop-on-demand (DOD). The differences to DOD inkjet includes: relatively high viscosity fluids, relatively large nozzle size, and mechanical-driven in jet dispensing.

Currently, many reserachers build one-dimensional model to analyze the perfomance of whole system[2, 3, 4, 5], in which the nozzle part is simplified as a 1-D nozzle; While others build detailed model of ball-seat mechanism[6, 7, 8], in which the ball velocity is pre-determined. Both need improvements. The 1-D models need ball-seat mechanism detailed data, such as pressure, flow, and considering fluid properties. And the ball-seat mechanism needs accurate drive force and needle (or piston) position. Therefore, Combination of 1-D model of drive system and detailed ball-seat mechanism can help to acquire more accurate analysis.

In this paper, the systematic model combining CFD and 1-D drive system has been built. The CFD model is built in OpenFOAM, and 1-D drive system model is embedded to couple the CFD model. Thus, the ball-seat mechanism and the 1-d drive system is coupled in one application, which can be more easily applied, and extra interface with other simulation tools, such as AMESim, is not necessary.

1 Model

The CFD geometric model of ball-seat mechanism is shown in Figure 2. The ball is moving up and down according to the force calculated with 1-D drive system model as

$$F_{\mathrm{p}} = m_{\mathrm{p}} a_{\mathrm{p}} \tag{1}$$

where, F_p is the total force acting on the piston, m_p is the mass of the piston assembly, and a_p is the acceleration of the piston.
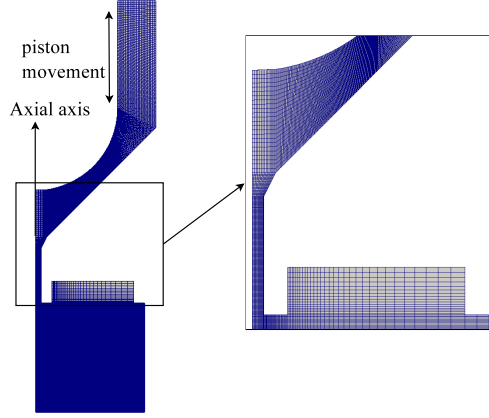
Figure 2: CFD geometric model of ball-seat mechanism

$$F_p = F_a + F_s + F_g + F_f + F_\nu \tag{2}$$

$$F_s = ky + F_d \tag{3}$$

$$\dot{y} = \int_0^t a_p dt \tag{4}$$

where, F_a is the force generated by compressed air, F_s is the spring force, F_g is the gravity force, F_f is the friction force acting on the piston, F_ν is the shear force due to fluid flow in the annulus, k is the spring coefficient, F_d is the pre-compressed spring force, y is the displacement of the piston, and t is the time.

The compressed air charges into or releases from the chamber under piston as adiabatic process because of the very short period in several milliseconds. The mass flow rate of air charging and releasing is [9]

$$q'_m = 0.04 \frac{p_{a1}}{\sqrt{T}} S, \; (p_{a2}/p_{a1} \le b) \tag{5}$$

$$q_m = q'_m \sqrt{1 - \left(\frac{p_{a2}/p_{a1} - b}{1 - b} \right)^2}, \; (b < p_{a2}/p_{a1} \le 1) \tag{6}$$

where, q_m is the mass flow rate of air charging into or releasing from the chamber, T is the temperature of air inside the chamber, S and $b = 0.528$, respectively, are the effective area and the critical pressure ration of the pneumatic valve orifice, p_{a1} and p_{a2} are the pressure at up- and down-streams of the valve orifice.

The laminar fluid system can be described as continuity equation

$$\frac{\partial \rho}{\partial t} + \nabla \cdot (\rho \mathbf{U}) = 0, \tag{7}$$

momentum equation

$$\frac{\partial \rho \mathbf{U}}{\partial t} + \nabla (\rho \mathbf{U} \mathbf{U}) = -\nabla p - \nabla \cdot \tau, \tag{8}$$

where U is the velocity of fluid, ρ is the density of the fluid, p is the pressure, and τ is the stress.

To track the interface of fluid-air, the two-phase VOF (Volume of Fluid) model is used

$$\rho = \alpha_2 \rho_2 + (1 - \alpha_2) \rho_1 \tag{9}$$

where ρ_2 is the fluid density, α_2 is the fraction of fluid, ρ_1 is the air density.

One adhesive is modelled as a Cross-Power-Law fluid,

$$\eta_1 = \eta_\infty + \frac{\eta_0 - \eta_\infty}{1 + (m\dot{\gamma})^n}, \tag{10}$$

where η_0 and η_∞ are the zero-shear-rate and infinite-shear-rate kinematic viscosity respectively, m is relaxation time, n is the power index.

The other adhesive is modeled as a Newtonian fluid,

$$\eta_2 = \eta_0, \tag{11}$$

Because of the high pressure in the ball-seat chamber, the fluid compressibility is considered. The density can be well approximated by a linear relation,

$$\rho_2 = \rho_{20}(\beta(p - p_0) + 1), \tag{12}$$

where ρ_{20} is the density at the reference pressure p_0, β is the isothermal compressibility of the fluid. The computation procedure is as follows:

1. start;
2. according to force acting on the piston to calculate the piston position and velocity using the 1-D drive model;
3. update the boundary condition;
4. calculate the CFD model;
5. collect the pressure acting on the piston, and the viscous stress;
6. go to step 2 to calculate the piston position of next time step;
7. end.

2 Results

Results will be presented in the workshop.

Acknowledgments

References

[1] J. J. Licari and D. W. Swanson, *Adhesives Technology for Electronic Application: Materials, Processing, Reliability*, 2nd ed. Waltham: William Andrew, 2011.

[2] J. Jeon, S.-M. Hong, M. Choi, and S.-B. Choi, "Design and performance evaluation of a new jetting dispenser system using two piezostack actuators," *Smart Materials and Structures*, vol. 24, no. 1, p. 015020, 2015.

[3] S. LU, Y. LIU, Y. YAO, and L. Sun, "Bond graph modeling of needle typed jet dispensing system driven by piezoelectric actuator," *Journal of Xi'an Jiaotong University*, vol. 48, no. 1, pp. 133–138, 2014.

[4] C. Zhou, J. Li, J. Duan, and G. Deng, "The principle and physical models of novel jetting dispenser with giant magnetostrictive and a magnifier," *Scientific Reports*, vol. 5, no. 18294, 2015.

[5] F. Tan and X. Shan, "Modeling and control of jetting dispensing processes in microelectronics packaging," *Chinese Mechanical Engineering*, vol. 28, no. 6, pp. 656–660,668, 2017.

[6] H. Quinones, A. Babiarz, C. Deck, and L. Fang, "Jet dispense for electronic packaging applications," in *SEMICON China 2004 SEMI Technology Symposium*, 2004.

[7] X.-M. WEI, P. SHEN, X.-Y. SHAN, and W.-S. LI, "Optimization of the backflow gap of pneumatic jetting valve based on numerical simulation," *Chinese Journal of Engineering Design*, vol. 23, no. 3, pp. 244–250, 2016. [Online]. Available: http://www.zjujournals.com/gcsjxb/CN/abstract/article_1507.shtml

[8] S. Lu, H. Jiang, M. Li, J. Liu, S. Gu, X. Jiao, and X. Liu, "Nozzle and needle during high viscosity adhesive jetting based on piezoelectric jet dispensing," *Smart Materials and Structures*, vol. 24, no. 10, p. 105023, 2015. [Online]. Available: http://stacks.iop.org/0964-1726/24/i=10/a=105023

[9] SMC China, *Modern Practical Pneumatics Technology*, 3rd ed. Beijing: China Machine Press, 2008.

MULTI-SPECIES TRANSPORT AND PH MODELING IN POROUS MEDIA

ROMAIN GUIBERT[1], PIERRE HORGUE[1], TORSTEN CLEMENS[2], GERALD DEBENEST[1]

[1]*Institut de Mécanique des Fluides de Toulouse (IMFT) - Université de Toulouse, CNRS-INPT-UPS*

[2]*OMV*

Chemical flooding (such as Alkali-Surfactant-Polymer flooding) is an efficient way for enhancing oil production in reservoirs modifying locally fluid properties and reducing surface tension between oil and water. The recovery factor (recovery factor = cumulative oil produced / oil originally in place) can be increased by up to 20% applying chemical flooding. Understanding the coupling between transport and phase properties remains still an important issue at both scales, pore- or reservoir-scale. Alkali, which are widely used in enhanced oil recovery processes, modify significantly the pH of the flowing solution inside porous media and this is of major importance because the modifications of phase properties induced by the injection of polymers depend strongly on the pH.

The objective on this work is to simulate alkali/tracer flooding at pore- and Darcy-scale in real porous media to

(i) compare the simulated results with core experiments (Darcy-scale)

(ii) understand the local phenomena of pH and species concentration on macroscopic flow properties (pore-scale).

The chemical model describing pH evolution involves four distinct acid/base couples (plus water autoprotolysis) and two of them are related to the bicarbonate anion which is amphoteric, *i.e.* it can react both as an acid and a base depending on the pH of the solution. The resulting model, not detailed here, consists in solving a set of two non-linear equations (which the Jacobian is easy to determine) in each cell of the domain.

The flow and transport modeling depends on the scale considered. At the micro-scale, the flow is modeled using the real pore-scale geometry solving Stokes equations whereas at the macro-scale the flow follows Darcy's equation using effective properties (porosity, permeability). Moreover, the transport equations for species are different according to the considered scale. The transport reads at the micro-scale as

$$\frac{\partial X_m}{\partial t} + \mathbf{u}\nabla X_m - D_m\nabla\mathbf{u} = 0$$

with $\mathbf{u}$ the local flow velocity and D_m the molecular diffusion.
At the macro-scale (involving macroscopic effective properties), the transport reads

$$\varepsilon\frac{\partial X_M}{\partial t} + \mathbf{u}_D\nabla X_M - \varepsilon D_M\nabla\mathbf{u}_D = 0$$

with ε the porosity, $\mathbf{u}_D$ the Darcy velocity and D_M the effective dispersion coefficient.

Both micro- and macro- scales solvers have been implemented in foam-extend 4.0. At each time step, pH is computed in each cell solving a non-linear system using a Newton's algorithm. In order to validate implementation and numerical settings, a comparison has been performed using an idealized porous medium (simulation results are illustrated on figure 1 at two different times).

(a)   (b)
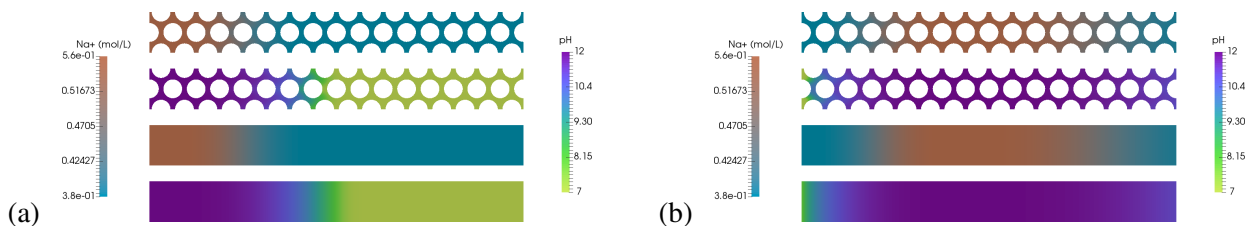
Figure 1: Comparisons of micro- and macro-scales simulations at different times

The macro-scale solver allows direct comparisons with core experiments and measurements and can be used to determine effective dispersion of solute species. These comparisons suggest that the chemical model is well described by this simple model and we also show the benefit of pH measurements for the characterization of the effective dispersion. The micro-scale solver, deployed on small volumes imaged by computed micro-tomography, allows to observe localized phenomena that modify the pH solution as illustrated on figure 2.
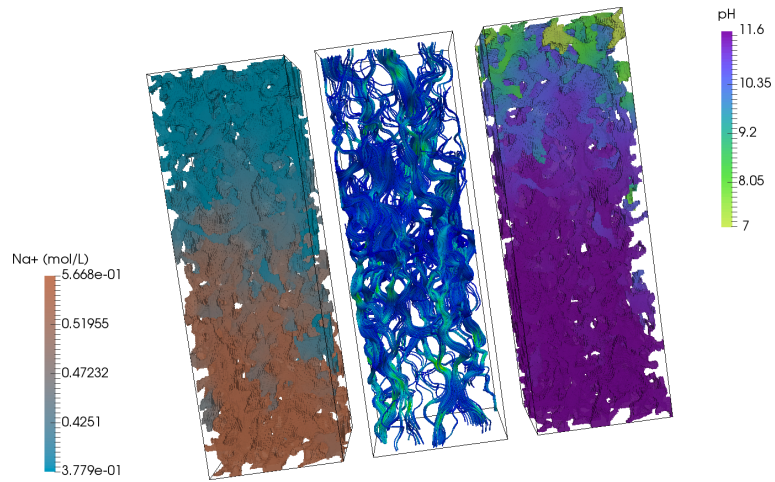
Figure 2: Snapshot of Na^+ concentration and pH computed over a parallelipipedic volume of 3 mm

RECENT DEVELOPMENTS OF THE POROUSMULTIPHASEFOAM TOOLBOX

PIERRE HORGUE[1], ROMAIN GUIBERT[1], JACQUES FRANC[1], GERALD DEBENEST[1]

[1]*Institut de Mécanique des Fluides de Toulouse (IMFT) - Université de Toulouse, CNRS-INPT-UPS*

Keywords: *porous media, multiphase flow, groundwater*

Understanding and modeling multiphase flow in porous media is a major point of interest for various applications, from hydrological issues (flow in aquifer for example) to industrial process (oil production, filtration processes). The native/original implementation of porous media flows in OpenFOAM is handled as a penalization term included in the momentum equations which cannot handle the main features of multiphase flow in porous media. Based on this observation, the porousMultiphaseFoam toolbox [1, 2] has been developed and proposed to the community for the first time in 2014 (OpenFOAM workshop 9). Its first release contained two solvers (for iso- and anisotropic porous media) using the two most known relationships for modeling capillary pressure and relative permeabilities Brooks and Corey [3] and Van Genuchten[4]) and two boundary conditions for imposing Darcy velocity (all compiled as external libraries). In recent years, several new features has been developed and included in the toolbox.

Developments have been made both on the existing solvers and towards new physics. In a first stage to improve both the stability and the efficiency of simulations, we implement some characteristic numbers (Todd and Coats) more suitable to for porous multiphase flow to compute stable time step than the classical Courant Numbers. We also evaluate their performance according to the type of the flow (gravity, viscous or capillary-driven flows) in order to provide some practical advices to the toolbox's users [5].

In a second part, the toolbox has been extended to the specific cases of groundwater flows solving the Richards' equation. In this approach, the pressure gradient of the non-wetting phase is neglected which allows to solve only the liquid phase mass conservation. This approach is particularly useful when studying groundwater flows at the scale of the watershed. Each time iteration is solved using a Picard's algorithm to allow larger time-steps. A new boundary condition has been developed for that case in order to impose the water height on the lateral boundaries. This dedicated solver has been tested on a real case (with topographic dataset and infiltration data overtime) as illustrated on figure 1.
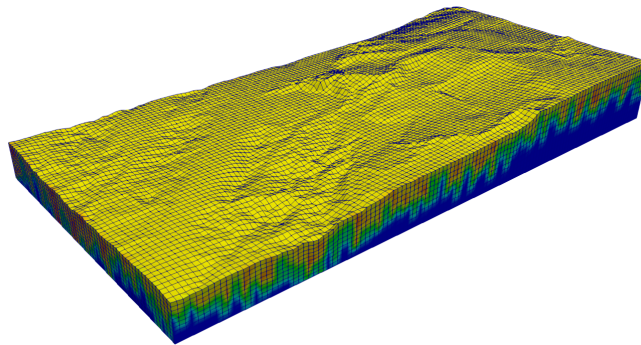
Figure 1: groundWaterFoam – Water saturation field of groundwater flow with infiltration on real topographic dataset.

In a third part, the impesFoam solver initially dedicated to two-phase flow has been extend to three-phase flow (triImpesFoam) to simulate a hydrocarbon pollution scenario. New three-phase capillary and relative permeability model (Parker and Lenhard [6]) have been implemented to handle the oil-water-air system. The application case was to study the contamination of a groundwater flow by a leak of gasoline (figure 2).
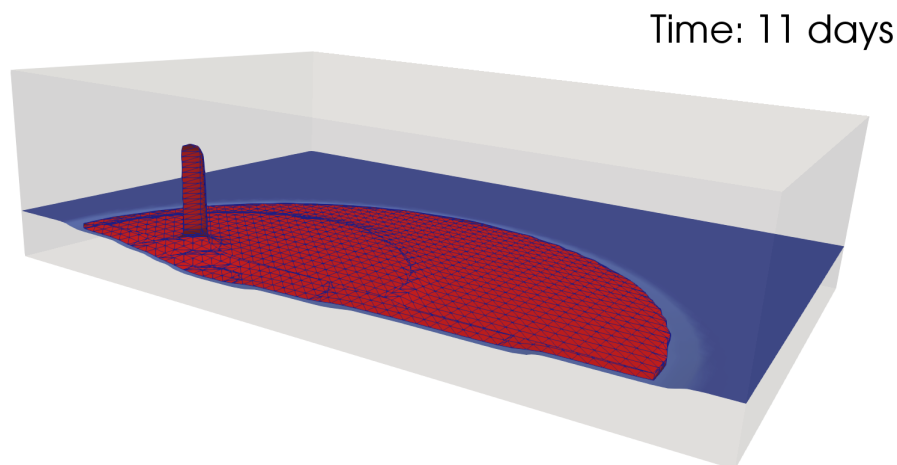
Figure 2: triImpesFoam – Oil leak over groundwater flows (oil-saturated area in red, water-saturated area in blue).

References

[1] P. Horgue, C. Soulaine, J. Franc, R. Guibert, and G. Debenest, "An open-source toolbox for multiphase flow in porous media," Computer Physics Communications, vol. 187, pp. 217–226, oct 2015.

[2] https://github.com/phorgue/porousMultiphaseFoam.

[3] A. Corey and R. Brooks, "Drainage characteristics of soils," Soil Science Society of America Journal, 1975.

[4] M. T. Van Genuchten, "A closed-form equation for predicting the hydraulic conductivity of unsaturated soils," Soil Science Society of America Journal, 1980.

[5] J. Franc, P. Horgue, R. Guibert, and G. Debenest, "Benchmark of different CFL conditions for IMPES," Comptes Rendus Mécanique, vol. 344, no. 1, pp. 715–724, 2016.

[6] J. C. Parker and R. J. Lenhard, "Determining three-phase permeability-saturation-pressure relations from two-phase system measurements," Journal of Petroleum Science and Engineering, vol. 4, no. 1, pp. 57–65, 1990.

NUMERCIAL WAVE FLUME FOR THE STUDY OF SCOUR PROTECTION AROUND OFFSHORE MONOPILE FOUNDATIONS UNDER CURRENTS LOADING

CARLOS EMILIO ARBOLEDA CHAVEZ[1], PETER TROCH[2], VASILIKI STRATIGAKI[3]
[1]Ghent University, CarlosEmilio.ArboledaChavez@UGent.be
[2]Ghent University, Peter.Troch@UGent.be
[3]Ghent University, Vicky.Stratigaki@UGent.be

Keywords: Free surface flows, porous media, Computational fluid dynamics

Introduction

Offshore Wind Farms are a growing technology in the energy generation market. On one hand, the competitiveness of the energy market, driven by cheap hydrocarbons, is asking from offshore wind turbines for better energetic and economic yields. On the other, climate change, driven by polluting hydrocarbons, is harshening environmental conditions, thus increasing the cost and risks of such turbines. In this context, a better knowledge of the behaviour of offshore wind turbines foundations, can reduce the installations cost, increase/extend its lifetime and prevent failure under extreme weather events. Scour around monopiles has been widely studied, while, scour protection - made of stones - around monopiles has not. De Vos et al. [1] distinguish three main failure modes for scour protection:

- Disintegration
- Edge scour
- Sinking.

Sinking has been studied experimentally in Nielsen et al. [2] for currents, waves and breaking waves. The latter paper hypothesizes that the main reason for the sinking of the scour protection in the case of Horns Rev 1 wind farm, is the pick-up of seabed sediment by the horseshoe vortex - induced by currents - penetrating in the scour protection. Following this hypothesis, a numerical model - based on the Flow 3D software [3]- for the study of current's action on the scour protection was developed. The paper concludes that a porous medium approach of scour protection can be used to determine the bed shear stresses underneath the scour protection, although calibration is needed.

Research objectives

The main objectives of this research is to develop a numerical model able to describe the full depth - from free surface to sand bed - flow characteristics and model the bed shear stresses for a variety of hydrodynamic conditions - current, waves and their combined action - around monopiles and around/inside their scour protection. To the author's knowledge, such a model is not available. This study will try, therefore, to cover this knowledge gap. The current paper focuses on the action of currents on the fluid motion inside the scour protection, the first step in the development of the complete hydrodynamic model. Approaches for macroscopic porous medium and free surface modelling are features readily available in the OpenFOAM framework [4]. These approaches are discussed further later in this paper and have successfully been used by Nielsen et al. [2]. Thus, this study aims to provide a better understanding of the processes involved in the sinking failure of riprap scour protections around monopoles through the use of numerical tools.

Numerical Model

The numerical model used for the study of scour protection around monopile structures is developed in the OpenFOAM framework and uses the foam-extend 4.0 package. In order to model the behaviour of water around the monopile and inside the scour protection, the Volume Averaged Reynolds Averaged Navier Stokes (VARANS) equations are used:

$$\nabla \cdot \boldsymbol{u} = 0 \tag{1}$$

$$\frac{\partial}{\partial t}\frac{\rho \boldsymbol{u}}{n} + \frac{1}{n}\nabla \cdot \left(\frac{\rho}{n}\boldsymbol{u}\boldsymbol{u}\right) - \nabla \cdot \left(\frac{\mu}{n}\nabla \boldsymbol{u}\right) - \frac{1}{n}(\nabla \boldsymbol{u}) \cdot \nabla \mu + \boldsymbol{F_p} = -\nabla p_d - (\boldsymbol{g} \cdot \boldsymbol{x})\nabla \rho + \sigma \kappa \nabla \gamma \tag{2}$$

Vectorial quantities are shown in bold characters. The derivation and implementation in the OpenFOAM framework of the VARANS equations was done at IH Cantabria [5]. Here, the VARANS equation include a porous media flow model in the last term of the left hand side of eq. (2). The macroscopic porous media flow approach considers the bulk properties of a material by adding drag and inertial terms to the Navier Stokes equations rather than solving the flow in every single pore. The resulting velocity depicts the mean fluid motion in a control volume by averaging the individual interstitial flows. The extended Darcy-Forchheimer equation models inertial and drag forces inside a porous material, and is widely used in the study of coastal structures. The formulation proposed in Higuera et al. [5] for the inclusion of the extended Darcy-Forchheimer equation in the Navier Stokes equations is followed:

$$\boldsymbol{F_p} = A\frac{\boldsymbol{u}}{n} + B\left|\frac{\boldsymbol{u}}{n}\right|\frac{\boldsymbol{u}}{n} + C\frac{\partial}{\partial t}\frac{\rho \boldsymbol{u}}{n} \tag{3}$$

A, B and C are coefficients that need to be determined. A variety of formulations exist to determine their values, thus, the reader is referred to Higuera et al. [5], Losada et al. [6], Jensen et al. [7] for more information about their derivation and formulation. For this work, the implementation done by Higuera et al. [5] is used:

$$A = \alpha \frac{(1-n)^3}{n^2} \frac{\mu}{D_{50}^2} \tag{4}$$

$$B = \beta (1 - \frac{7.5}{KC}) \frac{1-n}{n^2} \frac{\rho}{D_{50}} \tag{5}$$

As the flow considered is a steady current, then eq.(5) is reduced to:

$$B = \beta \frac{1-n}{n^2} \frac{\rho}{D_{50}} \tag{6}$$

Coefficient C in equation (3) is set to 0 in order to have a similar formulation of the porous medium to Nielsen et al. [2]. Here again, for coefficient α and β, in equations (4) and (6), a large variety of values can be found in literature and consensus has not been reached upon their values. Nielsen et al.[2] set α to 180 and calibrate β to 2.9, those values will be used in this paper. Eq.(2) is an equation solving multiphase incompressible flow where the Volume of Fluid Method is used. This method has the advantage of allowing the use of a sole set of equations for the water and the air phase and is implemented as depicted by Berberović et al. [8]. If the volume fraction of liquid is $\gamma_l = \gamma$ and the volume fraction of gas is $\gamma_g = \gamma - 1$, then the fluid properties are determined as a weighted average of γ:

Averaged density:

$$\rho = \rho_l \gamma + \rho_g (1 - \gamma) \tag{4}$$

Averaged viscosity:

$$\mu = \mu_l \gamma + \mu_g (1 - \gamma) \tag{5}$$

The transport of the volume fraction γ is defined as:

$$\frac{\partial \gamma}{\partial t} + \nabla \cdot (\gamma \boldsymbol{u}) + \nabla \cdot (\boldsymbol{u_r} \gamma (1 - \gamma)) = 0 \tag{6}$$

Where $\mathbf{u_r}$ is defined as the "compression velocity". The velocity is active at the interface of the two fluid and reduces numerical dissipation.

Experimental set up and model parameters

Nielsen et al. [2] present velocity measurements inside the scour protection. During these experiments, a plastic plate was placed at the bottom of the flume, this was done in order to obtain a rigid smooth bottom. For a more detailed description of the experimental setup, the reader is referred to Nielsen et al. [2]. Hereafter, are presented some of the key parameter for the test and modelling of scour protections under currents.

Table 1: Experimental and numerical parameters

Physical parameters	Value
Flume Width [m]	2
Flume Length [m]	23
Flume Heigth [m]	0.5
Pile diameter (D_p) [m]	0.14
Scour protection diameter (W)[m]	0.8
Mean armour layer stone diameter (D_{50})[cm]	4.3
Number of armour layers [-]	4
α[-]	180
β[-]	2.9
Porosity (n)	0.5 (Numerical model) 0.43 (Measured for experiments)
Water depth (d) [m]	0.45
Current velocity (U) [m/s]	0.4
Water density (ρ_w) [kg/m^3]	1000
Air density (ρ_a) [kg/m^3]	1
Kinematic viscosity of water (ν_w) [m^2/s^{-1}]	1e-6
Kinematic viscosity of air (ν_a) [m^2/s^{-1}]	1.48e-5
Numerical domain parameters	
Length [m]	4.5
Width [m]	2.0
Height [m]	0.65
Number of cells [-]	~1.3 * 10^6
Δt [s]	0.001

Computational domain
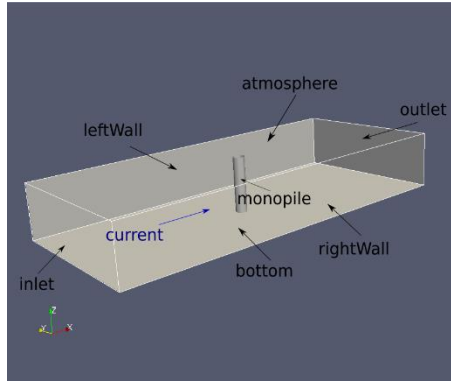
Figure 1:Numerical domain, boundaries and direction of propagation of current

In Figure 1 are presented the boundaries and the numerical domain. The monopile, the bottom and the sides of the computation domain are treated as non-slip wall boundary conditions. For the inlet, outlet and atmosphere (upper boundary) conditions, it is make use of the generation, absorption and atmospheric boundary conditions provided by ihFoam, see Higuera et al. [6]. At t=0, the velocity of the liquid phase in the interior of the domain is set to the current velocity - $u\,[m/s] = (0.4, 0, 0)$ - except in the porous medium where the velocity is set to 0 - $u[m/s] = (0, 0, 0)$. These initial condition are clearly not divergence free, the solver reaches a quasi-steady state and the results are taken at t = 50s.
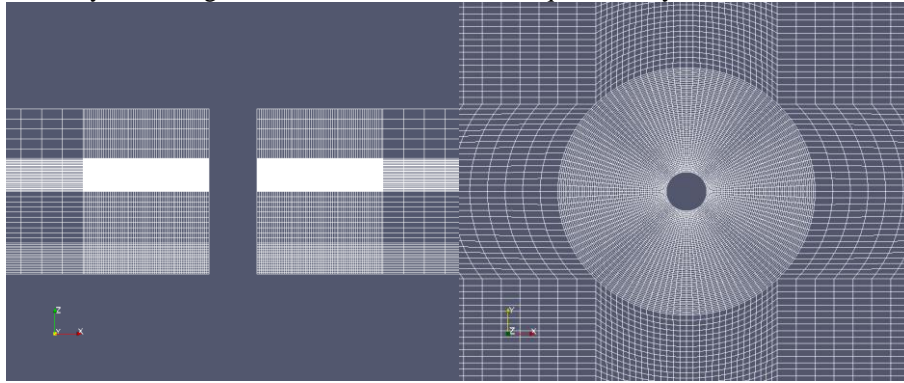
Figure 2: Side (left) and top (right) view of the meshing strategy

As can be seen in Figure 2, the mesh chosen to solve the flow around the monopile and the scour protection is an hexahedral structured grid around the monopile. Special consideration to the free surface, the zone close to the sea bed and around the monopile is given. Those zones are object of a refinement of the control volumes. Mesh generation is performed using the blockMesh utility provided along with the foam-extend 4.0 package. In order to parse the blockMeshDict file, the Python library PyFOAM is used, providing the versatility needed for the comparison to a large variety of test setups.

Results discussion
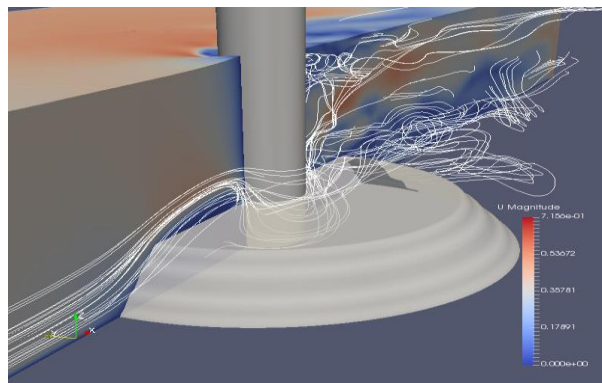
Figure 3: Velocity magnitude and streamlines around a monopile and scour protection for a 4 layer scour protection with a mean stone diameter of 4.3 cm

Figure 3 shows the velocity magnitude and streamlines of water; upstream, around and downstream of the monopile and its scour protection at t=50s. Upstream (left of Figure 3) of the monopile, the streamlines are parallel to each other with a constant velocity. At the approach of the scour protection, the flow is directed upwards as this is the path with least hydraulic resistance. In front of the monopile, inside the scour protection, water is 'hitting' the monopile with a lower velocity than outside the scour protection. A pressure gradient is created leading to a downward flow penetrating the scour protection. The latter phenomenon can be seen by the streamlines entering the scour protection in front of the monopile. Downstream the monopile, streamlines become chaotic showing evidence of turbulent structures produce by the

disturbance of the flow by the monopile. In fact, the Reynolds number of this experiment is 56000, therefore, a fully turbulent behaviour of the fluid at the wake of the monopile is expected. At the sides of the monopile, higher tonalities of red indicate an acceleration of the fluid due to the presence of the monopile. Finally, a slight set up of the fluid can be seen in front of the monopile.
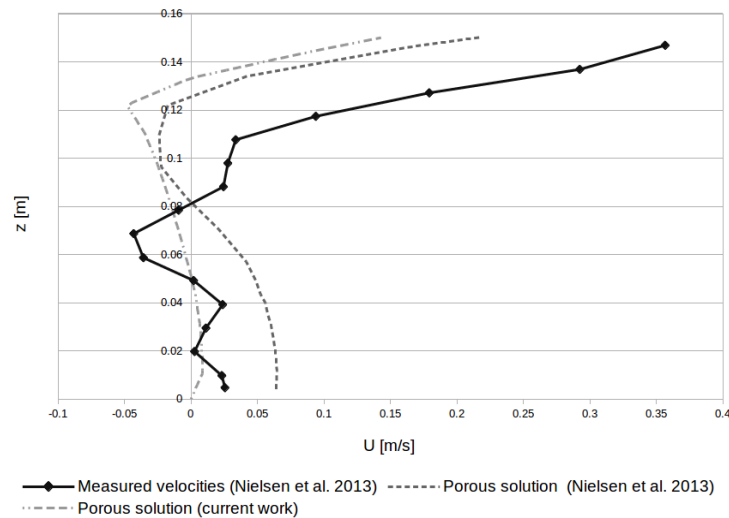
Figure 4: Comparison between measured and numerical solution from Nielsen et al.[2] and current work for a 4 layer scour protection, with a d_{50} of 4.3 cm, 12cm upstream the monopile centre.

In Figure 4 are plotted the velocity measurements (black solid marked line) and numerical model's results (dark grey dashed line) presented in Nielsen et al. [2], 12cm upstream the monopile centre. Also in Figure 4, the numerical results from our developed model are plotted at the same location (light grey dot dashed line). The sea bed is located at z=0m. The scour protection composed of four armour layers has a measured height of z = 12.3cm in the experiments. The current model shows a good agreement with the measurements until 8 cm above the sea bed. From z=8cm to z=12cm, the two numerical models (not marked grey lines) deviate from the measurements. From there on, with increasing z, the three lines seem to become parallel. The difference in the formulation of the porous medium between Higuera et al. [5] and Nielsen et al. [2] certainly plays a role in de difference between the two numerical results. This will be studied further and updated results will be presented at the 13th OpenFOAM Workshop.

Further work

In order to expand the present model, waves and a combination of waves and current will be implemented. Furthermore, a mesh analysis is on the way to quantify the mesh size impact on the results. An approach to model the disintegration failure mode of the scour protection is under study.

Acknowledgements

References

[1] De Vos, L., De Rouck, J., Troch, P., Frigaard P., Empirical design of scour protections around monopile foundations. Part 2: Dynamic approach. Coastal Engineering 60:286-298, 2012.

[2] Nielsen A. W., Liu X, Sumer B. M., Fredsoe J., Flow and bed shear stresses in scour protections around a pile in a current, Coastal Engineering 72:20-38, 2013.

[3] Flow3D User Manual, Flow3D User Manual, v9.4.2, Flow Science, Inc., Santa Fe, N.M., 2011.

[4] H. G. Weller, G. Tabor, H. Jasak, C. Fureby, A tensorial approach to computational continuum mechanics using object-oriented techniques, Computers in Physics, vol.. 12, no. 6, Nov/Dec 1998.

[5] Higuera P., Lara J. L., Losada I. J., Three-dimensional interaction of waves and porous coastal structures using OpenFOAM®. Part I: Formulation and validation, Coastal Engineering 83:243-258, 2014.

[6] Losada I. J., Lara J. L., del Jesus M., Modeling the interaction of water waves with porous coastal structures, Journal of Waterway Port Coastal and Ocean Engineering 142(6):03116003, August 2016.

[7] Jensen B., Jacobsen N. G., Christensen E. D., Investigation on the porous media equations and resistance coefficients for coastal structures, Coastal Engineering 84:56-72, 2014.

[8] Berberović E., van Hinsberg N. P., Jakirlić S., Roisman I. V., Tropea C., Drop impact onto a liquid layer of finite thickness: Dynamics of the cavity evolution. Physical Review E79, 036306, 2009.

IMPROVED PRESSURE-VELOCITY COUPLED ALGORITHM FOR COMPRESSIBLE FLOW

TAEWOO KIM[1], JAEHEUNG GILL[2], JAERYUL SHIN[3]
[1]NEXTfoam Co., LTD., truepray@nextfoam.co.kr
[2]NEXTfoam Co., LTD., jhgill@nextfoam.co.kr
[3]NEXTfoam Co., LTD., jrshin@nextfoam.co.kr

Keywords: Compressible Flow, Coupled Solver, Algorithm

In this paper, an improved pressure-velocity coupled computational fluid dynamics algorithm for numerical analysis of compressible flow with the discontinuous phenomena as like shock waves was described.

The pressure-velocity coupled algorithm to analyse at various flow speeds was studied by Drawish[1]. In that paper, they demonstrated that the developed algorithm works well in flow fields at various speeds. The other hand, the pressure-enthalpy coupling scheme for the simulation with high change of enthalpy was performed Emans[2]. This algorithm was adapted to analyse for engine flow problems.

Kraposhin[3] has applied the Kurganov-Tadmor flux splitting scheme, which is mainly used in density-based solvers, to the pressure-based algorithm of OpenFOAM. In that study, they proved that flux splitting schemes are appropriate to interpret the discontinuous flow phenomena as a pressure-based algorithm.

In this study, the Kurganov-Tadmor flux splitting scheme, developed by Kraposhin[3], was applied to a developed coupled algorithms and a verification analysis of compressible flow problems were performed using the developed solver. It was confirmed that the developed solver had the similar analytical ability with that of the other numerical codes through the analysis of the shock wave induced problems in the supersonic flow region. In order to verify the analytical ability for the transonic flow region of the developed solver, the external flow problems were analyzed and compared with results of experiments and other numerical analysis codes. It is confirmed that the analytical ability of developed solver in the high speed flow region such as supersonic and transonic is somewhat improved than the commercial analysis package and is similar to the density based in-house CFD code.
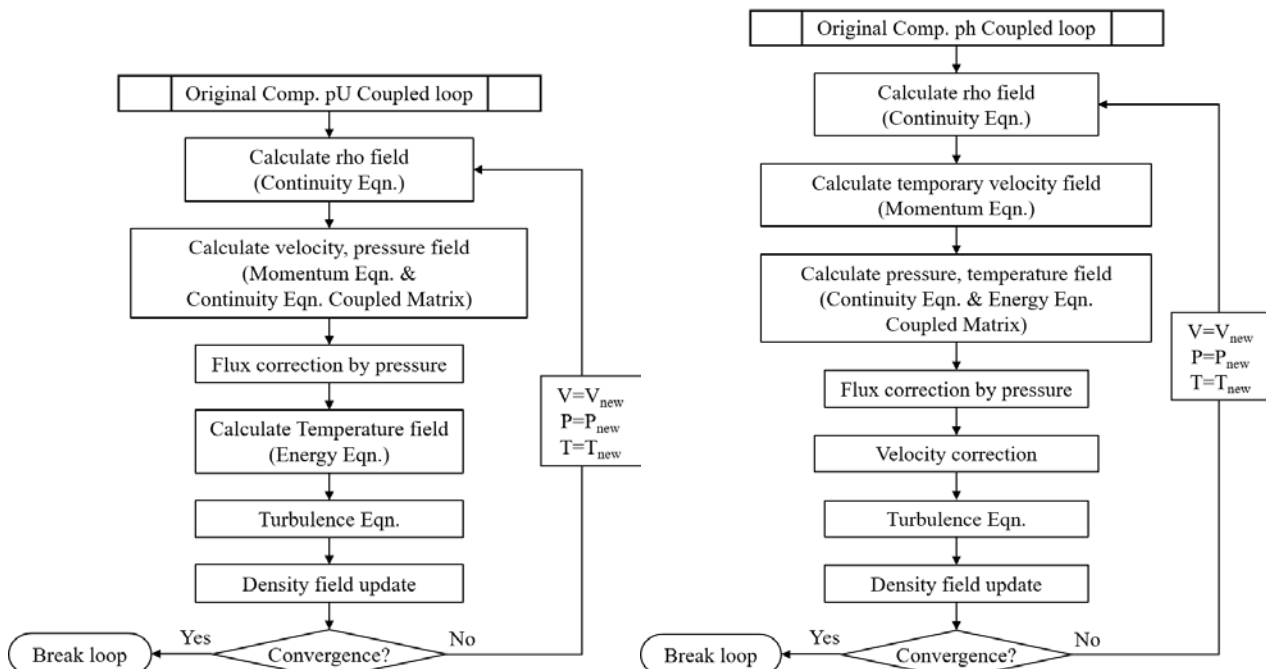
Figure 1: The original algorithms of coupled numerical analysis
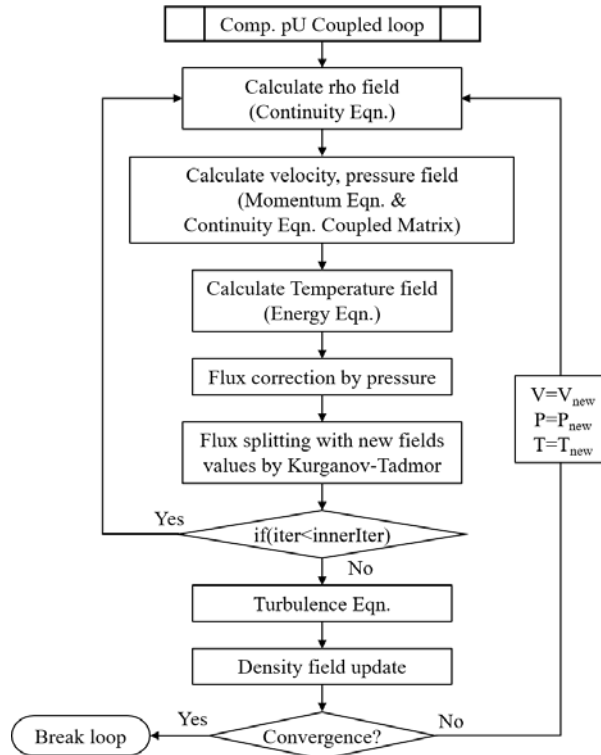
Figure 2: The developed algorithm of coupled numerical analysis
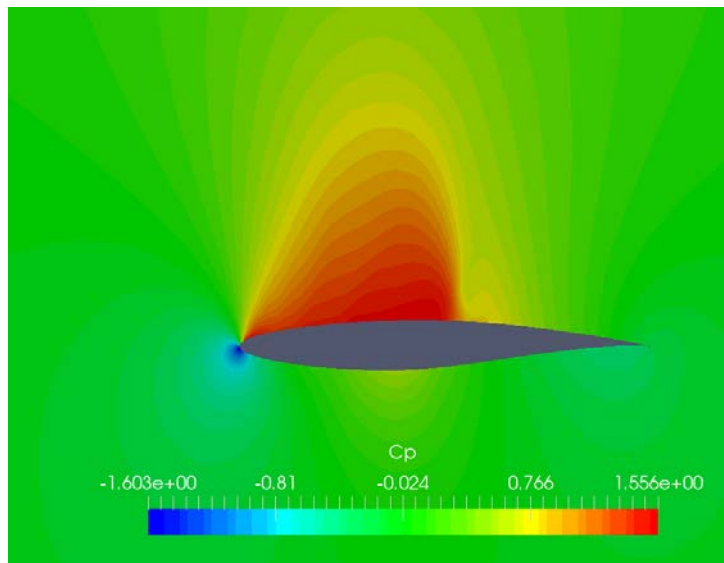
Figure 3: pressure contour results around RAE 2822

References

[1] M. Drawish and F. Moukalled, OpenCFD, A Fully Coupled Navier-Stokes Solver For Fluid Flow at All Speeds, Numerical Heat Transfer, Part B, 45: 410-444, 2014.

[2] M. Emans, Z. Zunic, B. Basara, S. Frolov, A Novel SIMPLE-Based Pressure-Enthalpy Coupling Scheme for Engine Flow Problems, Mathematical Modelling and Aanalysis, Vol. 17, No. 1, pp. 1-20, 2012.

[3] M. Kraposhin, A. Bovtrikova, S. Strijhak, Adaptation of Kurganov-Tadmor Numerical Scheme For Applying in Combination With the PISO Methodin Numerical Simulation of Flows in a Wide Range of Mach Numbers, Procedia Computer Science, Vol. 66, pp. 43-52, 2015.

NUMERICAL MODELING OF A SINGLE CAVITATION BUBBLE NEAR THE SOLID WALL WITH A COUPLED LEVEL SET AND VOLUME OF FLUID METHOD

JIANYONG YIN[1], YONGXUE ZHANG[2], YUNING ZHANG[3*]

[1] *China University of Petroleum-Beijing, China, jianyongyin@foxmail.com*
[2] *China University of Petroleum-Beijing, China, zhyx@cup.edu.cn*
[3] *China University of Petroleum-Beijing, China, zynlzyn.100@163.com*
* Corresponding Author

Keywords: *cavitation bubbles; volume of fluid; level set; compressible flows*

For the simulation of the growth and collapse of the cavitation bubble near the solid wall, the open source package OpenFOAM [1] is used and the source code of two-phase solver compressibleInterFoam is modified for inclusion of equation of state for the gas and the liquid [2]. A coupled level set and volume of fluid (CLSVOF) [3, 4] method is established to track the movement of the gas-liquid interface, to improve the accuracy of the simulation of interface curvature and surface tension force. All the numerical results are well consistent with the experimental data, which demonstrates the correctness and reliability of the model.

Figure 1 shows that the comparison of the evolution of the bubble radius of the CLSVOF and VOF with the experiment data. In experiment, A high-power laser pulse (wavelength532nm, duration 6ns) of the Q-switch Nd:YAG laser is focused into a plexiglass container filled with deionized water in order to generate a single cavitation bubble. The stand-off distance (γ, where $\gamma = L / R_{max}$, L is the diatance between the solid wall and the bubble centre, R_{max} is the maximum bubble radius) is equal to 2.0. In numerical simulation, both the initial pressure inside the bubble and the initial bubble radius are almost impossible to be exactly specified, and therefore are assumed to be 9×10^7Pa and 0.072 mm, respectively. The distance between the initial bubble centre and the solid wall is 1.58mm, which is same as the experiment. It's worth noting that the numerical interfaces are captured by both compressible VOF and CLSVOF. When the cavitation bubble reaches the maximum radius, there is a relative error of radius of 1.53% between the numerical results by the method of VOF and experiment data. What's more, the relative error of radius is 1.24% between the numerical results by the method of CLSVOF and experiment data. Meanwhile, compared with the results by using the VOF method, the CLSVOF has a smaller bubble radius during the bubble collapse. As shown in Figure 1, the CLSVOF results are better consistent with the experimental data.
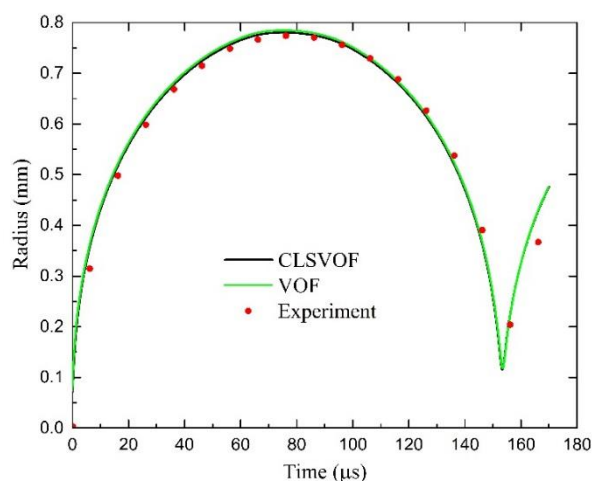
Fig. 1. The comparison of the numerical results with the experimental data with $\gamma = 2.0$

Acknowledgements

References

[1]   Greenshields, C.J., Openfoam user guide. OpenFOAM Foundation Ltd, version, 2015. **3**(1).

[2]   Koch, M., et al., Numerical modeling of laser generated cavitation bubbles with the finite volume and volume of fluid method, using OpenFOAM. Computers & Fluids, 2016. **126**: p. 71-90.

[3]   Albadawi, A., et al., Influence of surface tension implementation in volume of fluid and coupled volume of fluid with level set methods for bubble growth and detachment. International Journal of Multiphase Flow, 2013. **53**: p. 11-28.

[4]   Jadidi, M., et al. A coupled level set and volume of fluid method with application to compressible two-phase flow. in Proceedings of the 22nd Annual Conference of the CFD Society of Canada, Toronto, ON, Canada. 2014.

HIGH-PERFORMANCE IMPLEMENTATION OF MATRIX-FREE RUNGE-KUTTA DISCONTINUOUS GALERKIN METHOD FOR EULER EQUATIONS BASED ON OPENFOAM

LIYANG XU1*, YONGQUAN FENG1, SHUAI YE1, YANZHANG CHEN2, YUNRUI GUO1, XIAOGUANG REN3, XINHAI XU3

1 State key Labratory of High Performance Computing, NUDT, Changsha, China
2 Advanced Institute of Engineering Science for Intelligent Manufacturing, Guangzhou University, China
3 National Innovation Institute of Defense Technology
*xuliyang08@nudt.edu.cn

1. Introduction

The high-order methods have received considerable attention from research communities during the past several decades in that they offer the potential to significantly improve solution accuracy and efficiency[1, 2]. The Discontinuous Galerkin(DG) method is one of the high-order finite element methods using completely discontinuous basis functions[3]. It is locally conservative and stable, and can easily handle complex geometries and irregular meshes. These properties bring it into the mainstream of the CFD and prompt its application to a wide variety of problems. Our research group have developed DG discretization framework on HopeFOAM[4] which is based on OpenFOAM-4.0[5].

[6] has pointed that relying on the coefficient matrix limits the efficiency of high-order finite element discretization and the combination of the matrix-free and the Continuous Galerkin(CG) method can effectively improve the performance of its numerical simulation. Recently, the idea of matrix-free has been used to improve the performance of the DG implicit numerical simulations and achieved significant optimization[7]. However, DG explicit numerical simulations have not received proper attention that they deserve. Our research group have combined the matrix-free with Runge-Kutta Discontinuous Galerkin(RKDG) method[8] on HopeFOAM and dramatically speed-up the numerical simulation of Euler equations.

2. Major Work

This paper focuses on the matrix-free RKDG implementation for the compressible Euler equations on HopeFOAM. The inviscid compressible Euler equations in conservative form can be written in Eqn.1

$$\frac{\partial u}{\partial t} + \nabla \cdot F(u) = 0 \tag{1}$$

The RKDG numerical solution of the above equations consists of two parts: temporal discretization and spatial discretization. For temporal discretization, we use Runge-Kutta explicit time stepping method and in this paper, we use 2nd order Runge-Kutta which can be detailed as Eqn.2, where L is the spatial discretization operator for $\left(-\nabla \cdot F(u)\right)$ in Eqn. 1

$$\begin{cases} K_1 = L\left(U^n\right) \\ K_2 = L\left(U^n + \Delta t K_1\right) \\ U^{n+1} = U^n + \Delta t \frac{\left(K_1 + K_2\right)}{2} \end{cases} \tag{2}$$

For spacial discretization, we use DG discretization and Eqn.3 can be get from Eqn.1.

$$M\frac{dU}{dt} + R(U) = 0 \tag{3}$$

The matrix-free implementation includes two stages. First, the data structures of two- and three-dimensional space construct from tensor products of one-dimensional objects. In this stage, there is no coefficient matrix, so both the arithmetic operations and the memory cost during numerical simulation decrease. In the second stage, we implement vectorization explicitly to improve the gain by Single Instruction Multiple Data(SIMD) instruction. As we all know, most modern CPU designs include SIMD instructions to improve performance and offers a third level of parallelism. However,

SIMD vectorization is left to compilers to take optimization in most CFD simulation code, which brings the cost of data alignment and decreases the gain of vectorization. Therefore, we design and implement the data SIMD vectorization to make the most of CPU's multiple processing elements.

3. Results and Conclusions

We verify the correctness and efficiency of matrix-free implementation on Euler equations with several benchmark test cases. First, we consider a two-dimensional isentropic vortex whose exact solution given by Eqn.4.

$$
\begin{cases}
u = 1 - \beta e^{(1-r^2)} \dfrac{y - y_0}{2\pi} \\
v = \beta e^{(1-r^2)} \dfrac{x - x_0}{2\pi} \\
\rho = \left(1 - \dfrac{\gamma - 1}{16\gamma\pi^2} \beta^2 e^{2(1-r^2)}\right)^{\frac{1}{\gamma-1}} \\
p = \rho^\gamma
\end{cases}
\tag{4}
$$

where, x0 = 5 y0 = 0, β = 5, and γ = 1.4. To verify the correctness and high-order effectiveness of matrix=free implementation, the case are run on a sequence of meshes with different scale. Table.1 shows convergence results, where matrix-free implementation obtains nearly theoretically optimal convergence rate.

Table 1: 2D isentropic vortex pressure field error and convergence rate

Order	h	0.5h	0.25h	Rate
1	7.5534E-03	2.0602E-03	5.2704E-04	1.92
2	2.3543E-03	2.6309E-04	3.1887E-05	3.10
3	4.2271E-04	3.0372E-05	1.7986E-06	3.94
4	1.0954E-04	3.7670E-06	1.0757E-07	4.99
5	2.7787E-05	4.3644E-07	7.2526E-09	5.95
6	6.1963E-06	7.0940E-08	5.3634E-10	6.85
7	2.1034E-06	7.2805E-09	1.2982E-10	7.00

Based on the correctness and high-order effectiveness of our implementation, we have tested the performance by measuring the wall-clock time needed for different orders. Fig.1(a) shows the wall time of numerical simulation(1000 time steps) for various orders of DG, comparing the traditional matrix-vector multiplication implementation in serial with the matrix-free. Fig.1(b) details the wall time of simulation for three-dimensional isentropic vortex whose exact solution can be listed as Eqn.5.

$$
\begin{cases}
u = 1 - \beta e^{(1-r^2)} \dfrac{y - y_0}{2\pi} \\
v = \beta e^{(1-r^2)} \dfrac{x - x_0}{2\pi} \\
w = 0 \\
\rho = \left(1 - \dfrac{\gamma - 1}{16\gamma\pi^2} \beta^2 e^{2(1-r^2)}\right)^{\frac{1}{\gamma-1}} \\
p = \rho^\gamma
\end{cases}
\tag{5}
$$

Compared the result of original matrix-vector multiplication with the matrix-free's, we can get that the matrix-free RKDG effectively speed up the simulation. Typically, when the polynomial order is 8th, the performance speed-up ratioof matrix-free is 8.278 higher than the original matrix-vector multiplication in two-dimensional space, and 26.287 times higher than for the 6th polynomial order in three-dimensions.

Moreover, we test the parallel scalability of matrix-free RKDG implementation on two-dimensional isentropic vortex problem with 4 million DoFs. Fig.2 describes the corresponding parallel speed-up ratio on different number of cores. From 1 to 192 cores, the parallel speed-up ratio of matrix-free implementation is approximately the same as original, which means the matrix-free does not decrease the parallel speed-up ratio of HopeFOAM.

Finally, we test the complex double mach problem with reflective boundary conditions using the detector and the limiter. The temporal integration is conducted by RKDG, coupled with matrix free. The numerical results reveal excellent accuracy and efficiency. Fig.3 shows the density of double mach problem.

(a) 2D case result

(b) 3D case result
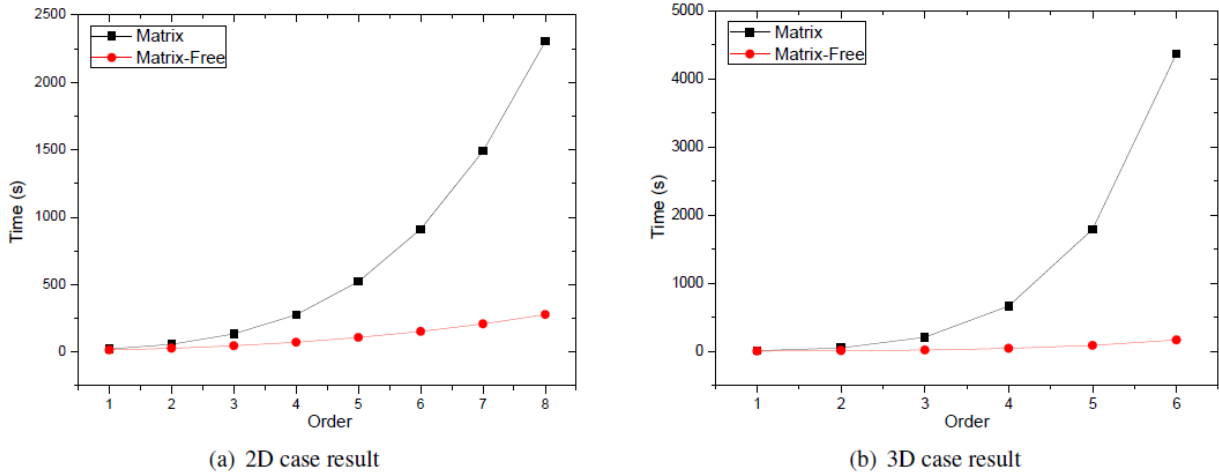
Figure 1: Wall-clock time
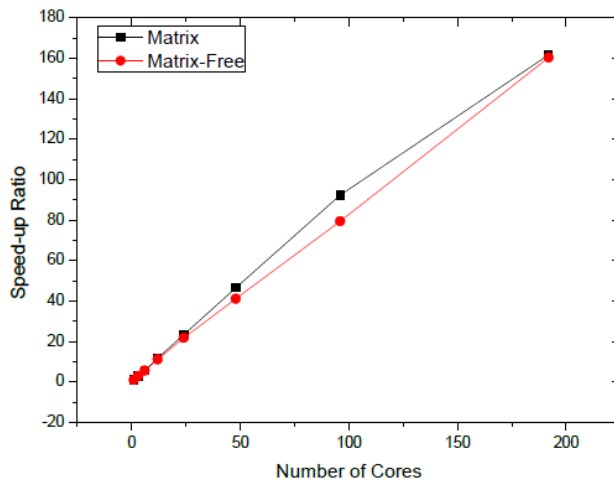
Figure 2: The parallel speed-up ratio of 2D isentropic vortex test on HopeFOAM

Figure 3: The contour plot for density of double mach

Acknowledgments

References

[1] Z. J. Wang, K. Fidkowski, R. Abgrall, F. Bassi, D. Caraeni, A. Cary, H. Deconinck, R. Hartmann, K. Hillewaert, H. T. Huynh et al., "High-order cfd methods: current status and perspective," *International Journal for Numerical Methods in Fluids*, vol. 72, no. 8, pp. 811–845, 2013.

[2] Z. Wang, "A perspective on high-order methods in computational fluid dynamics," *Science China Physics, Mechanics & Astronomy*, vol. 59, no. 1, p. 614701, 2016.

[3] C.-W. Shu, "Discontinuous galerkin methods: general approach and stability," *Numerical solutions of partial differential equations*, vol. 201, 2009.

[4] T. E. Group, "Hopefoam: High order parallel extensible cfd software," https://github.com/HopeFOAM/HopeFOAM, accessed January 2, 2018.

[5] H. Jasak, A. Jemcov, Z. Tukovic et al., "Openfoam: A c++ library for complex physics simulations," in *International workshop on coupled methods in numerical dynamics*, vol. 1000. IUC Dubrovnik, Croatia, 2007, pp. 1–20.

[6] M. Kronbichler and K. Kormann, "A generic interface for parallel cell-based finite element operator application," *Computers & Fluids*, vol. 63, pp. 135–147, 2012.

[7] M. Kronbichler, B. Krank, N. Fehn, S. Legat, and W. A. Wall, "A new high-order discontinuous galerkin solver for dns and les of turbulent incompressible flow," in *New Results in Numerical and Experimental Fluid Mechanics XI. Springer*, 2018, pp. 467–477.

[8] B. Cockburn and C.-W. Shu, "Tvb runge-kutta local projection discontinuous galerkin finite element method for conservation laws. ii. general framework," *Mathematics of computation*, vol. 52, no. 186, pp. 411–435, 1989.

SIMULATION OF BUBBLE EXPANSION AND COLLAPSE BETWEEN A FREE SURFACE AND A RIGID WALL

MENG YI[1], ZHANG DUO[1]

[1]College of Liberal Arts and Sciences, National University of Defense Technology, 2634310621@qq.com
[2] College of Liberal Arts and Sciences, National University of Defense Technology, zhangduo@nudt.edu.cn

Keywords: shallow water; bubble; dimensionless distance

I.SIMULATION SETUP

The computational domain is positioned in such a way that the point (0, 0) corresponds to the axis of symmetry at the initial free surface level (see Figure 1). No-slip wall boundary condition[1] is placed at the bottom of the domain and fixed pressure at the open top of the domain (see Figure 2). The 2D rectangular domain spans in the x-direction from 0 to 10 mm and in y-direction from −18/-12/-6 to 20 mm.
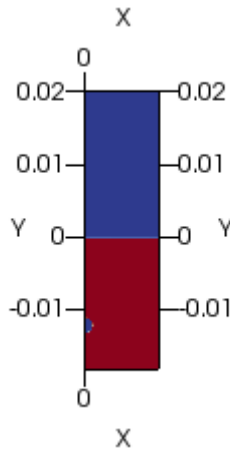
Figure 1: The 2D computational domain used
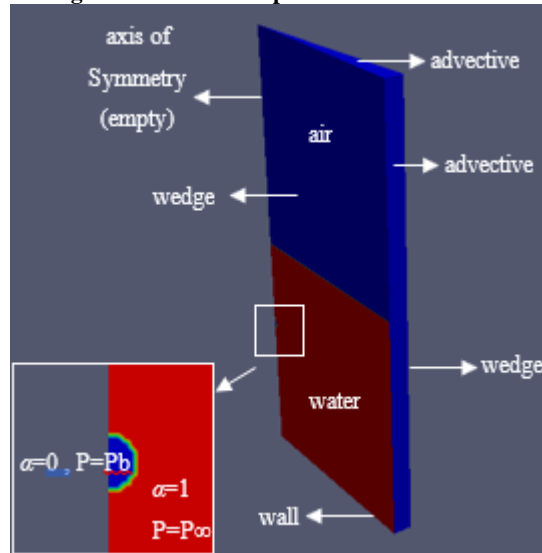
Figure 2: Boundary patches for CFD of single bubble pulsation in a free field

Initial conditions of the bubble pressure were estimated through the traditional Rayleigh-Plesset equation. The standard Rayleigh-Plesset equation[2] was used in the form

$$\rho \left[R\ddot{R} + \frac{3}{2}\dot{R}^2 \right] = p_v - p_\infty + p_0 \left(\frac{R_0}{R} \right)^{3n} - \frac{2\sigma}{R} - 4\mu\frac{\dot{R}}{R} \tag{1}$$

The Volume Of Fluid method was employed for tracking liquid and gas phases while compressibility effects were introduced with appropriate equations of state for each phase. Compressibility effects in both gas and liquid phases are included. Volume fraction equation[3] was in the form

$$\frac{\partial \alpha \rho_1}{\partial t} + \nabla \cdot (\alpha \rho_1 \boldsymbol{u}) = 0 \tag{2}$$

where α represents the volume fraction and ρ_1 the density of the gas phase. In the interface, where α varies from zero to unity, volume fraction averaging is performed for determining the value of viscosity and density.

II.RESULTS

First, simulation results of TNT spherical charge detonation in free field were compared with empirical values. Related data of maximum radius and period can be seen in table 1. Simulations were successful in the prediction of bubble expansion and collapse.

Table 1: The comparison of the bubble radius and the period

W(g)	R_m(cm)			T(ms)		
	Empirical value	Simulation value	Deviation	Empirical value	Simulation value	Deviation
0.055	6.0	6.3	6.18%	11.5	11.2	-2.8%
0.184	8.9	8.3	-6.6%	17.2	14.6	-15.3%
0.437	11.9	10.6	-10.1%	23.0	18.5	-19.5%

Second, simulations were conducted where the underwater bubble expands in shallow water, between two boundaries, a free surface and a horizontal rigid wall. The motion features of both the bubble and the free surface were investigated, via the consideration of two key factors, i.e., the non-dimensional distances from the bubble to the two boundaries. There are two length parameters[4] in the current work, namely

1. the non-dimensional standoff distance from the free surface, defined as $\gamma_f = df /R_{eq.}$

2. the non-dimensional standoff distance from the rigid wall, defined as $\gamma_w = dw /R_{eq.}$

where df and dw are the vertical distances from the initial center of the bubble to the free surface and the rigid bottom respectively. The two parameters are found to be the major factors affecting the motion features of the bubble and the free surface. An equivalent maximum radius R_{eq} is adopted since in many cases the bubbles develop into non-spherical shapes.

Keep non-dimensional standoff distance from the free surface, defined as γ_f=0.91, γ_w=0, 0.91 and 1.82 have been selected to study the effect of rigid wall on bubble motion.
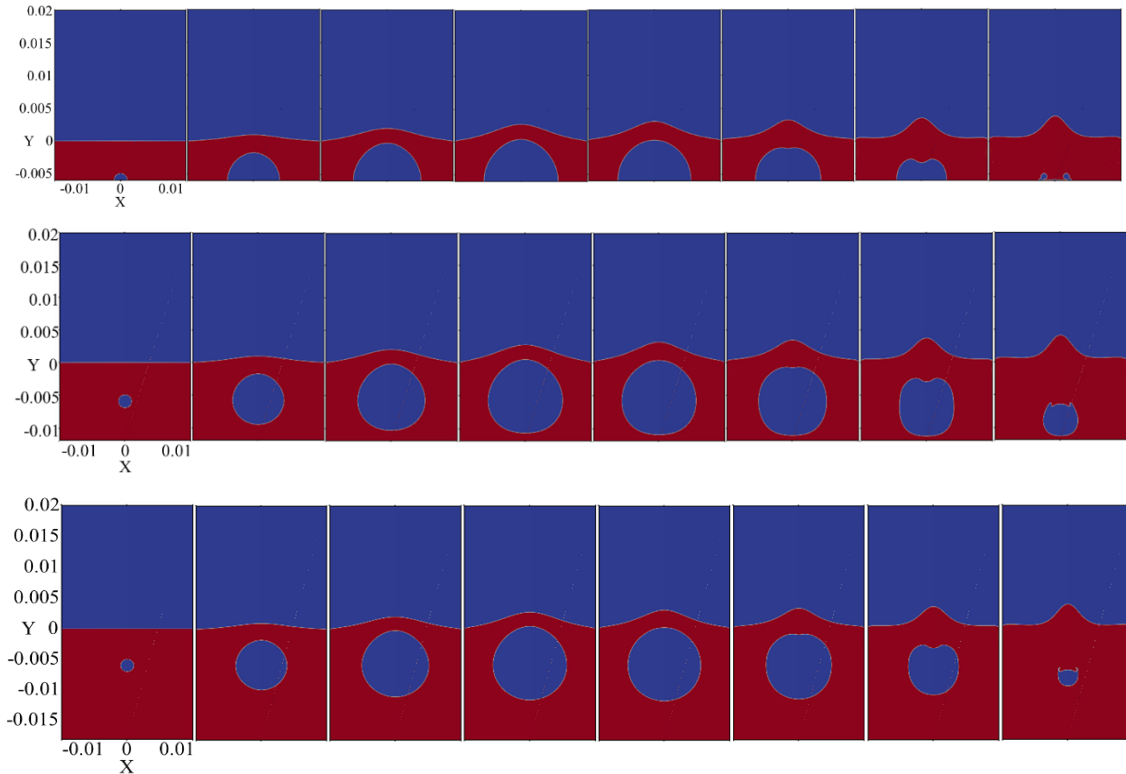
Figure 3: Evolution of single bubble between a free surface and a solid wall, γ_f=0.91, (a) γ_w=0; (b) γ_w=0.91; (c) γ_w=1.82

Keep non-dimensional standoff distance from the free surface, defined as γ_w =0.31, γ_f =0.63, 1.54 and 2.26 have been selected to study the effect of free surface on bubble motion.
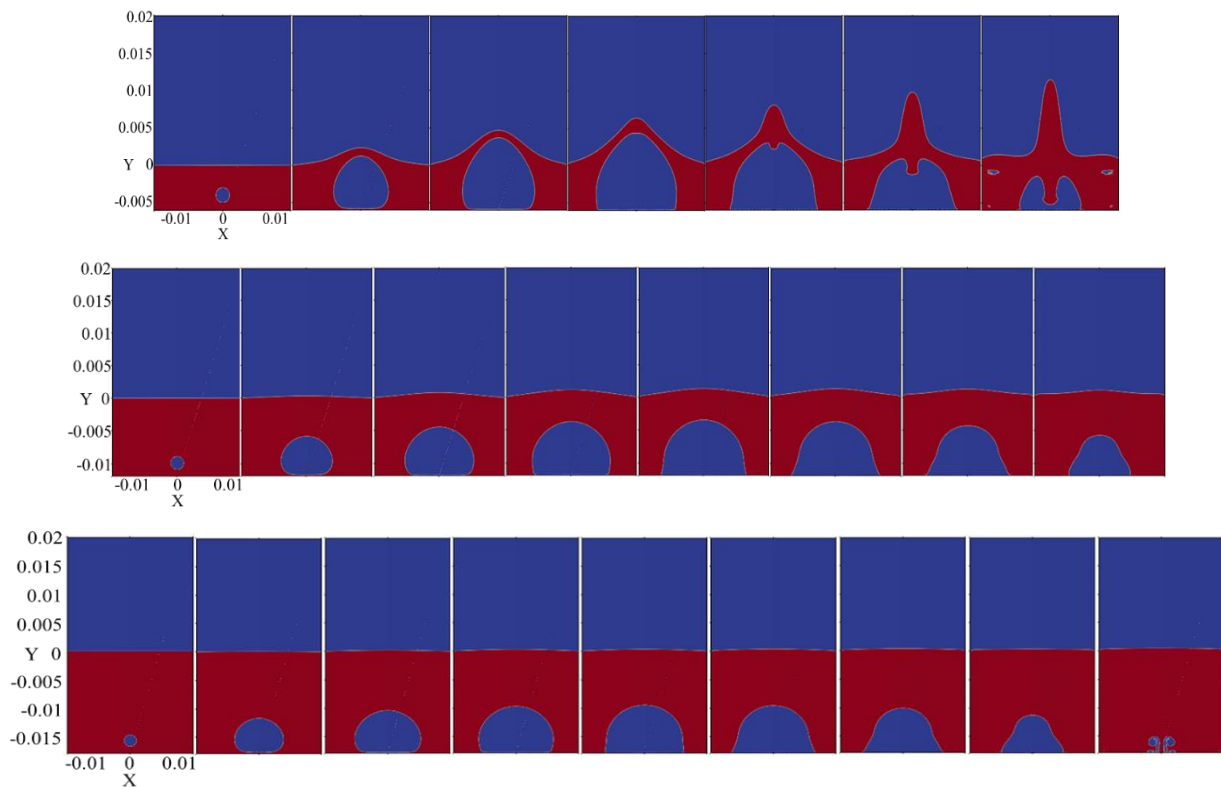
Figure 4: Evolution of single bubble between a free surface and a solid wall, γ_w =0.31, (a) γ_f=0.63; (b) γ_f =1.54; (c) γ_f =2.26

The dynamics of the bubble and the free surface have been experimentally studied using high-speed photography. The bubbles are generated by underwater electric discharge and pulsate in the vicinity of the free surface and/or a horizontal rigid boundary, with varying bubble-boundary distances (γ_f and γ_w). Intriguing motion features have been found with both single and double boundaries. Most of the motion features observed in the double boundary cases are inherited from the single-boundary cases but change in speed, height, etc. Therefore, additional considerations are required in bubble applications with multiple boundaries, especially those of different nature.

Acknowledgements

References

[1] C. M. Christian, E. G. Paterson, A. A. Fontaine, "Modeling Laser-Generated Cavitation Bubbles", M.S. Thesis, Dept. Mech. Eng., Penn State Univ., PA, 2012.

[2] J. P. Franc, J. M. Michel, "Fundamentals of Cavitation", Springer Netherlands, 2005.

[3] A. Prosperetti, G. Tryggvason, "Computational methods for multiphase flows", *International Journal of Multiphase Flow*, vol. 34(11), pp. 1096-1097, 2008.

[4] A. M. Zhang, P. Cui, Y. Wang, "Experiments on bubble dynamics between a free surface and a rigid wall", *Experiments in Fluids*, vol.54(10), pp. 1602, 2013.

THE OPENFOAM CALCULATION OF SUBSONIC-SUPERSONIC SHEAR MIXING LAYER

LIU YANG, FU BEN-SHUAI

Corresponding author: liuyang802@nwpu.edu.cn

Science and Technology on Combustion, Internal Flow and Thermo-structure Laboratory,
Northwestern Polytechnical University, Xi'an 710072

1   Introduction

Subsonic-Supersonic shear mixing layer flow is one of the important flow types. In the combustion chamber of the rocket-ramjet combined propulsion system, the rocket jet flow and inflow air is a typical subsonic-supersonic shear mixing layer flow. To achieve the high efficient mixing in a finite length combustion chamber and improve the performance of the propulsion system, it is very essential to carry out research on the development rule of the subsonic-supersonic shear mixing layer.

OpenFOAM (Open Field Operation and Manipulation) is an open source CFD software under Linux platform, and its essence is a C++ library based on object-oriented programming. The software has many advantages of using finite volume method, many kinds of schemes, the superior design architecture, excellent portability, containing abundant physical model and numerical solver, good interface with other software, can and it can write specialized for specific problem solver. Its computing power has got the recognition and application, so it is widely popular with the CFD developers, and gets the wide attention from researchers. The numerical simulation work of subsonic-supersonic shear mixing flow is carried out based on OpenFOAM computing platform, and using rhoCentralFoam compressible solver, which is a compressible density solver, based on Kurganov&Tadmor center windward format, and has good adaptability for compressible flow.

2   Main results

In this paper, three groups of large eddy simulation were carried out, and the range of convection Mach number (Mc) was 0.39-0.69. The subsonic-supersonic shear mixing flow of normal temperature and normal pressure state is studied. The numerical calculation parameters are shown in table 1.

Table 1: Numerical calculation parameters.

	U1(m/s)	U2(m/s)	Ma1	Ma2	Mc
Case1	517.61	103.24	2	0.3	0.69
Case2	517.61	201.22	2	0.6	0.53
Case3	517.61	289.90	2	0.9	0.39

Keeping the total temperature constant and changing Ma of the secondary flow of Case1-Case3, study the effect of Mc on compressibility of shear mixing layer.

In this paper, the classical plane shear flow configuration is adopted, as shown in figure 1. In the flow area of the cube, the upper part is supersonic flow (primary flow), and the lower part is subsonic flow (secondary flow). The left side is the entrance, and the right side is the exit. The upper and lower surfaces are walls.
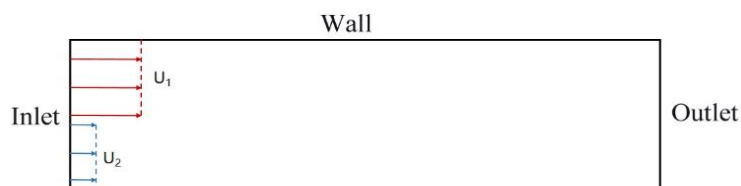
Figure 1: Schematic diagram of flow area.

The length of the flow area is 300mm, the height is 80mm, and each of the primary and secondary flow is 39.75mm, the thickness of the split board is 0.5mm. The minimum grid scale is 0.1mm and the grid amount is about 170,000.

Velocity and static temperature are given at high speed and low speed inlet. Given static pressure at the high speed inlet, the low speed inlet pressure is obtained by extrapolation. The export condition is zero-gradient boundary condition. The split board is non-slip boundary condition, and the upper and lower wall is sliding wall surface.

In the calculation process, when the shear mixing flow reaches the quasi-steady state, the data of a certain moment is selected to obtain the temperature contour. Figure 2 (a) - (c) is the temperature contour of each group of Case1-Case3.
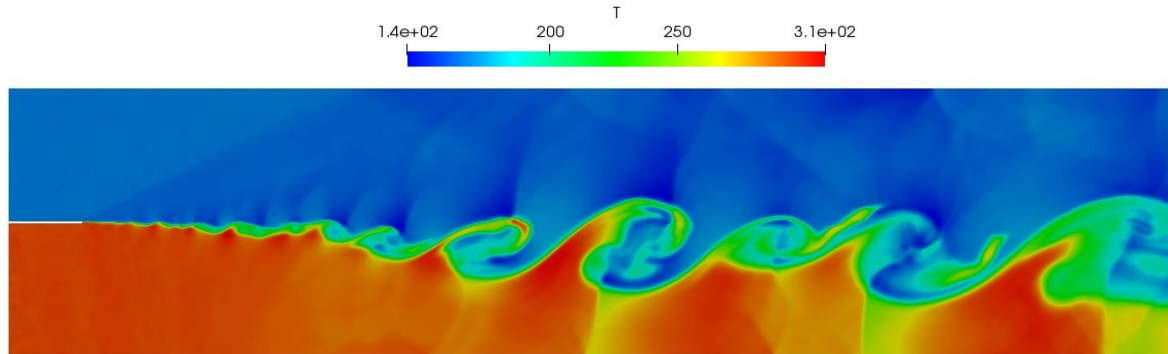
(a)Static temperature distribution contour of Case1.
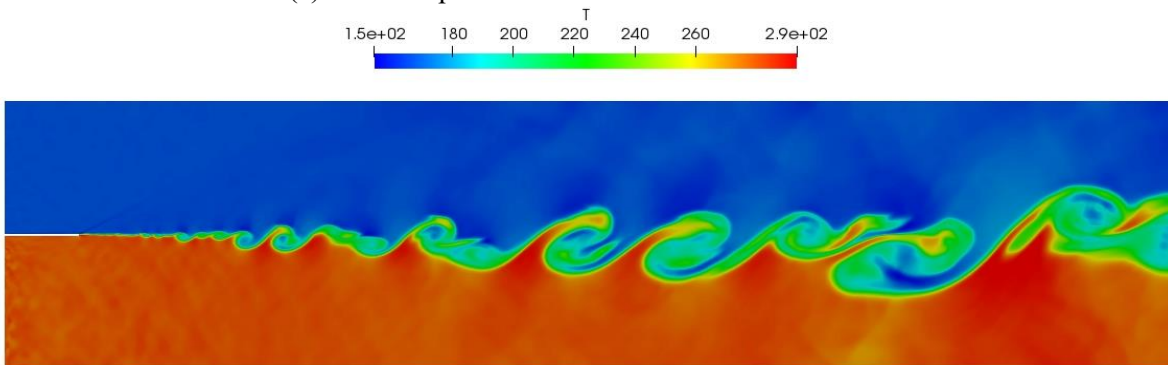
(b)Static temperature distribution contour of Case2.
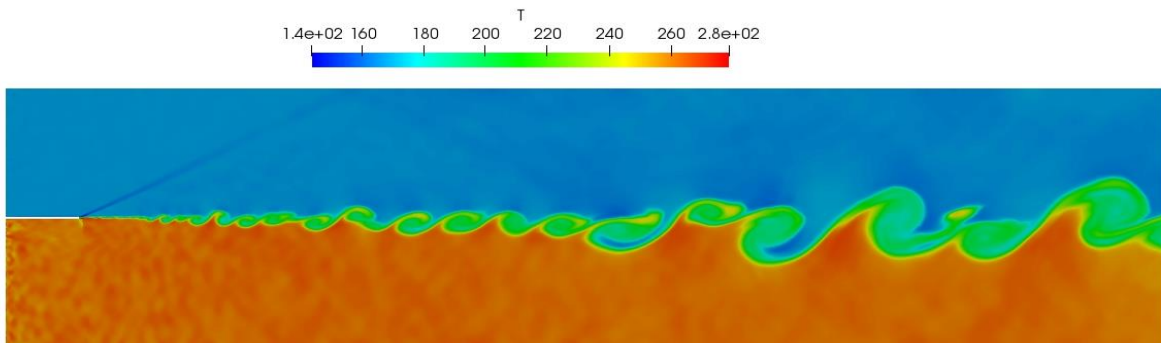
(c)Static temperature distribution contours of Case3.
Figure 2: Static temperature distribution contour of Case1-Case3.

The density distribution contour can be obtained as the temperature distribution contour does, then get the gradient of the density distribution, and numerical schlieren contour can be obtained, as shown in figure 2.
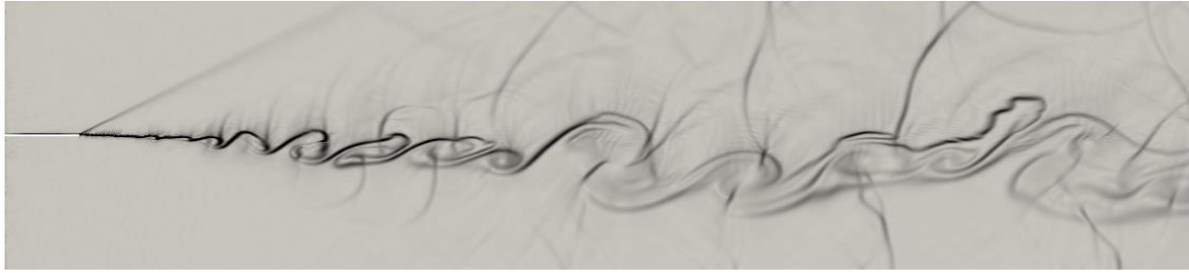
(a)Numerical schlieren contour of Case 1.

(b) Numerical schlieren contour of Case 2.
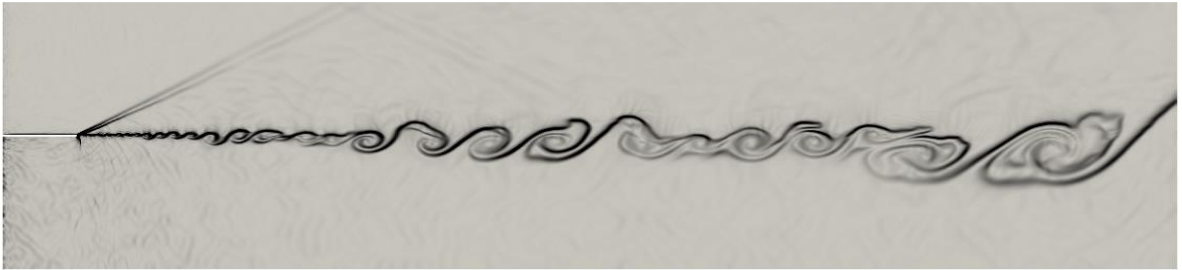
(c) Numerical schlieren contour of Case 3.

Figure 3: Numerical schlieren contours of Case1-Case3.

It can be seen from figure 2 and figure 3 that the compressibility of shear mixing layer is weak, and large scale coherent structures can be observed, and coherent structure is very clear and regular, while the Mc is low.

For shear mixing layer thickness, the average velocity thickness is used here. The average velocity thickness can be defined as the longitudinal distance of the normalized velocity of 0.1 and 0.9. And the normalized velocity is defined as:

$$U^*(y) = \frac{U(y) - U_2}{U_1 - U_2} \tag{1}$$

Then: $\delta_v = y_{U_1 - 0.1\Delta U} - y_{U_2 + 0.1\Delta U}$.

Figure 4 shows the thickness of shear mixing layer along the flow direction of Case1-Case3. The points are the original data, and the lines are the linear fitting data. It can be found that the original data is very close to the linear fitting data and the thickness of shear mixing layer varies greatly in the calculated working conditions.
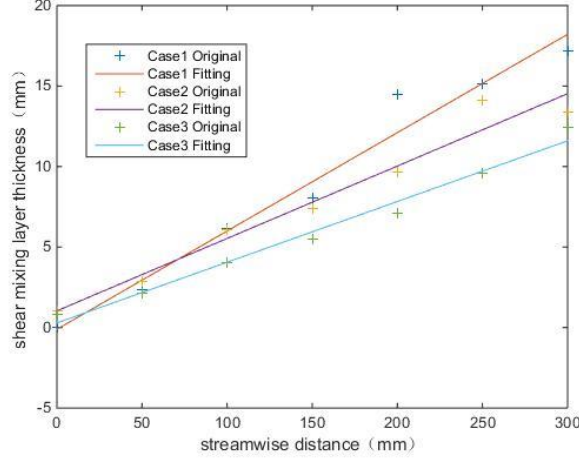
Figure 4: Thickness of shear mixing layer of Case1-Case3.

For decoupling the effect of compressibility, speed ratio and density ratio on the shear mixing layer growth rate, the growth rate of the normalized compressible shear mixing layer concept is put forward, which is the ratio of compressible shear mixing layer with the incompressible shear mixing layer growth rate under the condition of same speed ratio and density ratio under, as shown in equation (2).

$$\delta_{nor} = \frac{(d\delta/dx)}{(d\delta/dx)_{inc}} = f(M_c) \tag{2}$$

Dimotakis (1986) proposed the calculation formula for the incompressible shear mixing layer growth rate:

$$\left(\frac{d\delta}{dx}\right)_{inc} = C_\delta \frac{(1-r)(1+\sqrt{s})}{2(1+r\sqrt{s})}\{1 - \frac{(1-\sqrt{s})/(1+\sqrt{s})}{1+2.9(1+r)/(1-r)}\} \tag{3}$$

Here: $0.25 < C_\delta < 0.45$, $r = U_2/U_1$, $s = \rho_2/\rho_1$.

Using the incompressible shear layer thickness growth rate δ_0' to make the compressible shear layer thickness growth rate δ' nondimensionalize, then get the shear layer thickness growth rate δ'/δ_0', and give the corresponding Mc, shown in the following table.

Table 2: Shear layer thickness growth rate and corresponding Mc of Case1-Case3.

	Case1	Case2	Case3
δ'	0.0611	0.0450	0.0377
δ_0'	0.2078	0.1433	0.0948
δ'/δ_0'	0.2940	0.3138	0.3977
Mc	0.69	0.53	0.39

It can be seen from the above table, the dimensionless thickness growth rate of shear mixing layer decreases with the increase of Mc.

3 Conclusions

In view of the subsonic-supersonic shear mixing flow, this paper uses the software of OpenFOAM to carry out large eddy simulation study, and the results show that the development process of the subsonic-supersonic shear mixing layer has the following rules:

(1) With the increase of compressibility, the dimensionless thickness growth rate of the shear mixing layer decreases.

(2) The shear mixing flow with weak compressibility and the incompressible shear flow have similar rules in the shear mixing layer growth rate et al. It shows that the flow rules of the two kinds of shear mixing flow are similar.

RIPPLE FORMATION AND WHOLE-PROCESS MODELLING OF SELECTIVE LASER MELTING

ZEKUN WANG[1], KHURAM WALAYAT[2], MOUBIN LIU[3]

[1] *BIC-ESAT & State Key Laboratory for Turbulence and Complex Systems, College of Engineering, Peking University, Beijing 100187, China, zekunwang@pku.edu.cn*

[2] *BIC-ESAT & State Key Laboratory for Turbulence and Complex Systems, College of Engineering, Peking University, Beijing 100187, China, khuram_walayat@yahoo.com*

[3] *BIC-ESAT & State Key Laboratory for Turbulence and Complex Systems, College of Engineering, Peking University, Beijing 100187, China, mbliu@pku.edu.cn*

Keywords: *Ripples, Selective laser melting, Phase change, Marangoni flow, Whole-process modelling, OpenFOAM*

[Abstract] In this paper, we present the development of a modelling framework to simulate the powder deposition and powder melting with multiple tracks and multiple layers in selective laser melting (SLM). The framework is implemented through coupling the Finite Volume Method (FVM) and the Discrete Element Method (DEM). The framework is further used to investigate the ripple formation in SLM and a dimensionless number is then given to characterize the strength of ripple effects.

Introduction

Selective laser melting (SLM) based on metal powders is a promising additive manufacturing technology which has already drawn attention in many industrial fields, e.g., aerospace engineering, bio-implants, smart materials and even architectures. However, the extremely intense laser hinders direct observation of the laser-powder interaction, making numerical simulation a powerful tool to explore the underlying physics like melting, balling, splashing and rippling.

During past decades, many researchers conducted numerical study on the melting process of the powder bed. Qiu et al. [1] and Panwisawas et al. [2] established a VOF-based frame to reproduce the melting process and the evolution of a single molten track. Khairallah et al. [3, 4] also provided comparable simulations results of the melting process in SLM and the formation mechanisms of pores, spatter, and denudation zones were also studied. Yan et al. [5] used Flow3D, EDEM and other commercial software and established a framework to reproduce the whole-process of electron beam selective melting (EBSM).

Surface roughness and the ripples that occur in SLM play important roles in product quality and reflectivity. Due to limited experimental conditions, it is difficult to figure out the detailed formation process of the surficial cavities and ripples, therefore, relevant studies are also conducted. Gečys et al. [6] studied the influence of laser frequency on the ripple formation. Besides, when laser power increases, the temperature gradient becomes lager, and the difference in surface tension drives the molten metal to a certain direction, namely, Marangoni effect. Kou et. al [7] studied this thermo-capillary force in welding and found that the content of surface-active agents will change the temperature dependence of the surface tension coefficient, thus affects the surface deformation. When the content of surface-active agent is low, the surface tension coefficient tends to be negative, and Marangoni force drives the molten liquid outward, and ripples occur where disturbance exists. However, the heat source in this study is fixed, thus ripples form a series of homocentric circles.

In this study, we coupled the Finite Volume Method (FVM) in *OpenFOAM* with Discrete Element Method (DEM) in *LIGGGHTS* to reproduce powder deposition. Thus the radii of the powders can be controlled as wished, e.g., Gaussian distribution. Then we modified the Volume of Fluid (VOF) solvers in *OpenFOAM* to reproduce the melting process during SLM, and the two-phase interface is reconstructed using a sharp interface capturing method, iso-Advector. Combining these two steps, we can simulate multi-track and multi-layer SLM with different powder distribution. In this paper, we also proposed a dimensionless number judging whether the ripples can occur, which considers the physical parameter of the material and laser beam, temperature gradient and powder bed morphology. Several simulations are performed and comparable results are obtained.

Formulations and modelling processes

Deposition of the metallic powders are simulated by coupling *OpenFOAM* with *LIGGGHTS*, the governing equations for the powders are:

$$m_{pj}\frac{d\mathbf{V}_j}{dt}=-V_{pj}\nabla p+\mathbf{F}_{drag}+m_{pj}\mathbf{g}+\Sigma\mathbf{F}_{p-p}+\Sigma\mathbf{F}_{p-w} \tag{1}$$

$$\mathbf{I}_{pj}\frac{d\boldsymbol{\omega}_j}{dt}=\Sigma\mathbf{M}_t+\mathbf{M}_r \tag{2}$$

where $\mathbf{V}_j$, m_{pj}, V_{pj} and $\mathbf{I}_{pj}$ are the velocity, mass, volume and rotational inertia of Particle j, respectively. p is the ambient pressure of air, and $\mathbf{g}$ is the gravitational acceleration. $\mathbf{F}_{drag}$ is the drag force exerted on the particle by surrounding air [8]. $\mathbf{F}_{p-p}$ is the particle-particle interaction force, and $\mathbf{F}_{p-w}$ is the particle-wall interaction forces while relevant details can be found in [9, 10]; $\mathbf{M}_t$ is the moment generated by tangential forces exerted by other particles and $\mathbf{M}_r$ is the rolling friction toque [11].

During the former DEM step, the drag force, position and velocity of a powder particle are calculated, and the information is sent to the CFD solver to calculate the momentum exchange. The governing equations for the CFD solver are the continuity equation and N-S equation:

$$\frac{\partial\alpha_I}{\partial t}+\nabla\cdot(\alpha_I\mathbf{V}_I)=0 \tag{3}$$

$$\frac{\partial}{\partial t}(\alpha_I\rho_2\mathbf{V}_I)+\nabla\cdot(\alpha_I\rho_2\mathbf{V}_I\otimes\mathbf{V}_I)=-\alpha_I\nabla p-\nabla\cdot(\alpha_I\mu_2(\nabla\mathbf{V}_I))+\alpha_I\rho_2\mathbf{g}-\frac{1}{V_{\text{Cell}I}}\sum_{\forall j\in\text{Cell}I}\frac{V_{pj}\beta(\mathbf{V}_I-\mathbf{V}_j)}{\alpha_{pj}}D(\mathbf{r}_I-\mathbf{r}_j) \tag{4}$$

where $\mathbf{V}_I$ and α_I are the velocity and volume fraction of air in cell I. ρ_2 and μ_2 are the density and dynamic viscosity of air as the second phase. The last term is the source term that governs the momentum exchanges, in which $V_{\text{Cell}I}$ is the volume of the air cell, β is an empirical coefficient related to the particle void fraction α_{pj} of Cell I and Reynolds number, $\mathbf{r}_j$ is the position vector of the particles, $\mathbf{r}_I$ is that of air cell I, D is a distribution function that distributes the reaction forces on fluid phase at the velocity nodes in staggered Eulerian grids [12].

By now, the deposition of the powders can be reproduced. In order to simulate the melting process of the powder bed, the particles have to be 'moved' to FVM cells, and then we use VOF to distinguish metal phase from air phase, use iso-Advector [13] to reconstruct the interface. In VOF, metal phase is defined as the first phase α_1, and the air as the second α_2, $\alpha_1+\alpha_2=1$. Physical parameters are also weighed by the volume fractions, e.g., the viscosity $\mu=\alpha_1\mu_1+\alpha_2\mu_2$, where μ_1 is the metallic viscosity, subscript 1 denotes the first phase, as with other parameters, which are not listed here. For convenience, α_1 is just denoted as α. Particle positions and theirs radii are obtained from the DEM solver, then we use *funkySetFields* tool in *swak4foam* to set the volume fraction according to the positions and radii. In the modified VOF solver, the governing equations are continuity equation, like Eqn.3, N-S equation and energy equation. N-S equation is written as:

$$\frac{d}{dt}(\rho\mathbf{U})+\nabla\cdot(\rho\mathbf{U}\otimes\mathbf{U})=\nabla\cdot(\mu\nabla\mathbf{U})+c\kappa\nabla\alpha-\nabla p+\rho\mathbf{g}+\left|\nabla\alpha\right|\frac{\partial\kappa}{\partial T}(\nabla T-\mathbf{n}(\mathbf{n}\cdot\nabla T)) \tag{5}$$

where $\mathbf{U}$ is velocity, t is time, ρ is density, μ is viscosity, in particular, the viscosity of the molten metal μ_1 is approximated by: $\ln\mu_1=\frac{1}{2}\text{erfc}[\frac{4}{\ln T_l-\ln T_s}\cdot(\ln T-\frac{\ln T_s+\ln T_l}{2})](\ln\mu_s-\ln\mu_l)+\ln\mu_l$, where T_l and T_s are the liquidus and solidus point, μ_s and μ_l are the viscosity of solid and liquid metal. And c is the curvature, κ is the coefficient of surface tension, p is pressure, $\mathbf{g}$ is gravitational acceleration, T is temperature.

Energy equation is:

$$\frac{d}{dt}(\rho CT+\rho L\alpha_m)+\nabla\cdot(\rho CT\mathbf{U}+\rho L\alpha_m\mathbf{U})-\nabla\cdot(kT)=-\left|\nabla\alpha\right|[h_c(T-T_{ref})-\frac{2\eta P}{\pi R^2}\exp(\frac{-2\left|\mathbf{x}-\mathbf{X}_I(t)\right|^2}{R^2})]+\Phi, \tag{6}$$

where C is thermal capacity, L is latent heat of fusion, α_m is melting degree, $\alpha_m=\frac{1}{2}[1+\text{erf}(\frac{4}{T_l-T_s}(T-\frac{T_l+T_s}{2}))]$, k is thermal conductivity, h_c is heat transfer coefficient, T_{ref} is the reference temperature, P is the laser power, η is

laser absorption coefficient, R is the effective laser beam radius, **x** is the position vector of a FVM cell, **X** is the laser scanning path and Φ is the dissipation.

Last but not the least, we use iso-Advector to reconstruct the surface of the first layer of powder bed and export it using *Paraview* in *stl* files. The *stl* files are then imported to *LIGGGHTS* and set as boundary condition for another round of powder deposition. Accordingly, the SLM process of the succeeding layer of powder bed can again be reproduced by the aforementioned steps. Figure 1 shows the simulation results of the molten track on the first layer of powder bed, and Figure 2 shows the deposition of the succeeding layer on the original layer.
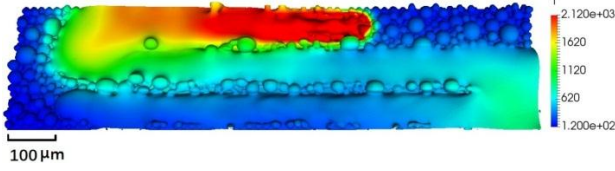
Figure 1: Molten track on the first layer of powders.
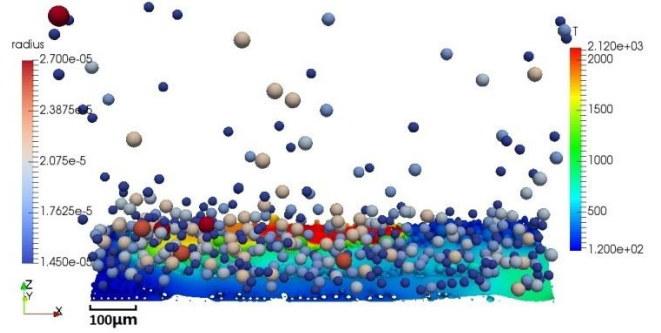
Figure 2: Deposition of powders for the succeeding layer.

Ripple formation

Ripples that formed during SLM has great influence on the surface structure and reflectivity of the product, and the ripple marks between layers could evolve into cracks and break the structure under fatigue loading. Hence, studies on rippling and its wavelength should claim more attention.

There are several characteristic velocities in SLM process: Molecular diffusion velocity $\dfrac{v_1}{R}$, where v_1 is the metallic kinematic viscosity; Thermal diffusion velocity $\dfrac{\alpha_1}{R}$, where α_1 is the metallic thermal diffusivity; Characteristic velocities of surface tension and Marangoni force, $\sqrt{\dfrac{\kappa}{\rho_1 r}}$ and $\sqrt{\dfrac{\frac{\partial \kappa}{\partial T}(T_v - T_s)}{\rho_1 L_{v-s}}}$, respectively, where r is the mean radius of particle, which is the distance for surface tension to smooth the surface, T_v is the evaporation point and L_{v-s} is the distance between laser spot and solidus line along the scanning path, where Marangoni flow exists. By comparison, it is easy to find that the last two velocities are pre-dominant during melting. In order to see whether the gaps between particles will be smoothed by the uniform part of surface tension or be stretched by Marangoni force and forms ripples, a ratio of these two characteristic velocities is given as $\theta = \sqrt{\dfrac{\kappa}{\frac{\partial \kappa}{\partial T}(T_v - T_s)} \dfrac{L_{v-s}}{r}}$.

Several simulations are conducted to see how the relevant physical parameters can influence this ratio. As shown in Figure 3 (a), (b) and (c), the particle radius is 9.8 μm, and temperature gradient or $\dfrac{\partial \kappa}{\partial T}$ increases. The particle radius in figure (d), (e) and (f) is 14 μm, and other parameters corresponds to (a), (b) and (c).
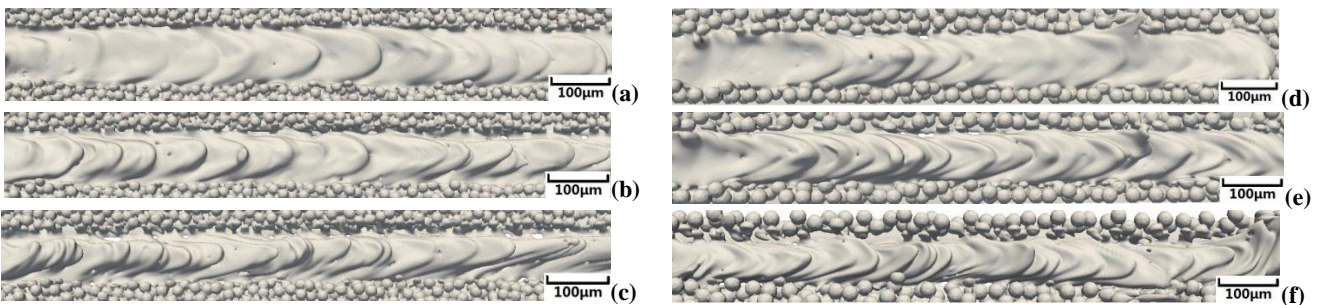
Figure 3: Simulation results for different physical parameters. θ for figure (a), (b), (c) and (d), (e), (f) are 8.25, 5.04, 3.52, and 6.90, 3.43, 2.94..

According to simulation results, if θ is larger than 8.25, rippling is very weak, and even vanishes as θ continue to grow. If θ is lower than 8.25, there exist two kinds of ripples. Ripples with long wavelength are dominant in Figure 3 (a), (b) and (d), where θ is larger than 5.04. However, in Figure 3 (c), (e) and (f), both ripples with short wavelength and long wavelength exist, where θ is lower than 5.04, and the ripples with short wavelength is believed to be caused by the gaps between particles.

Conclusion

In this work, we developed a modelling framework based on *OpenFOAM* and *LIGGGHTS* to reproduce the powder deposition and melting process of SLM. In industry, it is not easy to manipulate the material properties of the metals used in SLM, and this poses challenges to the study of many crucial physics inherent in SLM. However, with this modelling framework, we can freely change the physical parameters to study crucial physics in SLM like rippling, balling, splashing and so on. Additionally, both *OpenFOAM* and *LIGGGHTS* are open source codes, allowing us to develop more reliable physical models for better understanding and optimizing the manufacturing process in SLM.

Acknowledgements

References

[1]   C. L. Qiu, C. Panwisawas, M. Ward, H. C. Basoalto, J. W. Brooks, and M. M. Attallah, "On the role of melt flow into the surface structure and porosity development during selective laser melting," *Acta Mater.,* vol. 96, pp. 72-79, 2015.

[2]   C. Panwisawas, C. L. Qiu, Y. Sovani, J. W. Brooks, M. M. Attallah, and H. C. Basoalto, "On the role of thermal fluid dynamics into the evolution of porosity during selective laser melting," *Scripta Mater. ,* vol. 105, pp. 14-17, 2015.

[3]   S. A. Khairallah, A. T. Anderson, A. Rubenchik, and W. E. King, "Laser powder-bed fusion additive manufacturing: Physics of complex melt flow and formation mechanisms of pores, spatter, and denudation zones," *Acta Mater.,* vol. 108, pp. 36-45, 2016.

[4]   W. King, A. T. Anderson, R. M. Ferencz, N. E. Hodge, C. Kamath, and S. A. Khairallah, "Overview of modelling and simulation of metal powder bed fusion process at Lawrence Livermore National Laboratory," *Mater. Sci. & Tech.,* vol. 31, no. 8, pp. 957-968, 2015.

[5]   W. T. Yan *et al.*, "Multi-physics modeling of single/multiple-track defect mechanisms in electron beam selective melting," *Acta Mater.,* vol. 134, pp. 324-333, 2017.

[6]   P. Gečys, "Ripple Formation by Femtosecond Laser Pulses for Enhanced Absorptance of Stainless Steel," *J Laser Micro Nanoen,* vol. 10, no. 2, pp. 129-133, 2015.

[7]   S. Kou, C. Limmaneevichitr, and P. S. Wei, "Oscillatory Marangoni flow: A fundamental study by conduction-mode laser spot welding," *Weld. J.,* vol. 90, no. 12, pp. 229-240, 2011.

[8]   S. Benyahia, M. Syamlal, and T. J. O'Brien, "Extension of Hill Koch Ladd drag correlation over all ranges of Reynolds number and solids volume fractions," *Powder. Technol.,* no. 162, pp. 166-174, 2006.

[9]   A. D. Renzo and F. P. D. Maio, "Comparison Of Contact Force Models For The Simulation Of Collisions In DEM Based Granular Flow Codes," *Chem. Eng. Sci.,* vol. 59, no. 3, pp. 525-541, 2004.

[10]   A. B. Stevens and C. M. Hrenya, "Comparison of soft-sphere models to measurements of collision properties during normal impacts," *Powder. Technol.,* vol. 154, no. 2-3, pp. 99–109, 2005.

[11]   H. P. Zhu, Z. Y. Zhou, R. Y. Yang, and A. B. Yu, "Discrete particle simulation of particulate systems: Theoretical developments," *Chem. Eng. Sci.,* vol. 62, no. 13, pp. 3378-3396, 2007.

[12]   R. J. Hill, D. L. Koch, and A. J. C. Ladd, "The first effects of fluid inertia on flows in ordered and random arrays of spheres," *J. Fluid Mech.,* vol. 448, pp. 213-241, 2001.

[13]   J. Roenby, H. Bredmose, and H. Jasak, "A computational method for sharp interface advection," *R. Soc. open sci.,* vol. 3, p. 160405, 2016.

DEVELOPMENT AND ASSESSMENT OF A NUMERICAL MODELLING CODE FOR THE THERMOPLASTIC PROFILE EXTRUSION COOLING STAGE

O.S. Carneiro[1], A. Rajkumar[1], C. Fernandes[1], L.L. Ferrás[1], F. Habla[2], J.M. Nóbrega[1]

[1]*IPC/i3N-Institute for Polymers and Composites, Department of Polymer Engineering, University of Minho, Guimarães, Portugal*
[2]*Technische Universitat Munchen, Catalysis Research Center and Chemistry Department, Munchen, Germany*

Keywords: profile extrusion, cooling tools, experimental assessment, OpenFOAM

On the extrusion of thermoplastic profiles, upon the forming stage that takes place in the extrusion die, the profile must be cooled at a high rate to assure increased productivity, but avoiding high temperature gradients, to minimize the level of induced thermal residual stresses. These objectives are conflicting, since the increase of the cooling rate usually promotes higher temperature gradients. Due to the non-linear nature of the material behaviour and the large number of processing conditions involved, the employment of numerical modelling tools is mandatory to properly understand the system behaviour and to support its design. To model the profile extrusion cooling system, the temperature distribution must be computed both at the metallic calibrator and at the polymeric profile, which are in contact through a common interface. The traditional computational tools available for this purpose, start by assuming a certain temperature distribution in both domains, which are used to compute the interface heat fluxes. Subsequently, these new heat fluxes are used to update again the temperature distribution in both domains. This gives rise to an iterative process, which must be substantially relaxed to assure convergence. This relaxation as the direct impact on the computational time consumed to achieve a converged solution. In this work, we present the development a new coupled numerical solver, developed in the framework of the OpenFOAM® computational library, that computes the temperature distribution in both domains simultaneously, aiming to minimize the requied computational time. The solver was verified by comparison of its predictions with analytical solutions (for simple problems), through the Method of Manufactured Solutions and with results published in the literature [1]. In this work, the solver was experimentally assessed with an industrial case study. Subsequently, to evidence the novel numerical tool potential, the same industrial case study is employed in a sensitivity analysis, aiming to quantify the importance and effect of the main process variables.

References

[1] F. Habla, C. Fernandes, M. Maier, L. Densky, L. Ferrás, O. S. Carneiro, O. Hinrichsen and J. M. Nóbrega, Appl. Thermal Eng. 100, 538-552 (2016).

NUMERICAL STUDY OF THE TURBULENT SLOT JET IMPINGEMENT HEAT TRANSFER USING THE MODIFIED SST K-W MODEL BASED ON OPENFOAM

HUAKUN HUANG[1], GUIYONG ZHANG[1,2,3*], ZHI ZONG[1,2,3]

[1]*Liaoning Engineering Laboratory for Deep-Sea Floating Structures, School of Naval Architecture, Dalian University of Technology, huanghuakun@mail.dlut.edu.cn*

[2]*State Key Laboratory of Structural Analysis for Industrial Equipment, Dalian University of Technology, gyzhang@dlut.edu.cn*

[3]*Collaborative Innovation Center for Advanced Ship and Deep-Sea Exploration, zongzhi@dlut.edu.cn*

Keywords: jet impingement, heat transfer, Nusselt number, transition, modified SST k-ω model

Abstract: Jet impingement heat transfer has been applied in many industry fields due to its high heat and mass transfer rate. A numerical simulation about the turbulent slot steady jets has been carried out using the modified SST- k-ω model based on OpenFOAM. The cases studied are of nozzle-plate spacing of 4 and 9.2, respectively, and the Reynolds number is 20,000. The modified SST k-ω turbulence model is constructed based on the Kato-Launder mode. To test the modified SST k-ω model's validation for jet impingement, the velocity profiles, skin friction and Nusselt number distribution are investigated in detail. By comparing with both experimental data and other numerical results, the good agreement between the present model and the experimental data has indicated the model's ability for predicting the transition in slot impinging jets.

1 Introduction

The SST k-ω model proposed by Menter [1] which blends the standard k-ε model and k-ω model is very popular in many applications. However, the complex impinging jet flows are also challenges for various turbulence models, due to the complex phenomena including the vortex developing, separation and high adverse pressure gradient [2, 3]. For a typical impinging jet, there are a dip and second peak of the Nusselt number along the impinging plane at low nozzle-plate spacing ($H/B \leq 4$), which disappear at high nozzle-plate spacing. This phenomenon is affected by the laminar to turbulence transition [2]. Thus, the turbulence models with the ability of predicting the transition have been carried out to investigate the jet impingement problems in recent years [3-5]. Based on earlier studies, the SST k-ω model has been recommended due to its appropriate performances [6]. And the SST k-ω model has been used in many studies, which shows good performances in jet impingements [7-10]. However, the SST k-ω model predicted the second peak and dip of Nusselt number earlier than the experiment and provided a false secondary peak of the Nusselt number at high nozzle-plate spacing [3, 11]. These findings imply that there is not a single turbulence model which shows best for different conditions, which leads to the importance of studying the new modifications using the same framework to assess their relative performances.

The work of this paper modifies the SST k-ω model based on the Kato-Launder model to the available reference data [3, 12-14] for different nozzle-plate spacing of 4 and 9.2. The Kato-Launder modification has been succeeded in improving the flow structures not only in the stagnation region but also in the wall jet region [15]. Various comparisons against the experimental data and numerical results in terms of velocity profiles, skin friction and Nusselt number distribution are presented in this work.

Section 2 describes the modified work for SST k-ω model. Section 3 shows the results of the velocity profiles, skin friction and Nusselt Number distribution. Section 4 presents the conclusions draw from the present study.

2 The modified SST k-ω model

The modifications based on the Kato-Launder model are carried out using the open software OpenFOAM platform to ensure the codes' accuracy and robustness. The eddy viscosity for modified SST k-ω model is defined as:

$$\mu_t = a_1 k \frac{1}{\max\left(a_1\omega, b_1\sqrt{S}F_2\right)} \tag{1}$$

where a_1 is 0.31, b_1 is 1.0, k is the turbulent kinetic energy, ω is the specific dissipation rate, S is the strain rate and F_2 is the blending function.

The equation k and ω are modified as following:

$$\frac{\partial k}{\partial t} + U_j \frac{\partial k}{\partial x_j} = \min\left(P_k, 10\beta^* k\omega\right) - \beta^* k\omega + \frac{\partial}{\partial x_j}\left[\left(\mu + \sigma_k \mu_t\right)\frac{\partial k}{\partial x_j}\right] \tag{2}$$

$$\frac{\partial \omega}{\partial t}+U_i \frac{\partial \omega}{\partial x_i}=\alpha \frac{\omega}{k}\min\left(Gu,\frac{c_1\beta^*\omega}{a_1}\max\left(a_1\omega,b_1 F_{23}\sqrt{S}\right)\right)$$

$$-\beta\omega^2+\frac{\partial}{\partial x_j}\left[\left(\mu+\frac{\mu_t}{\sigma_\omega}\right)\frac{\partial \omega}{\partial x_j}\right]+2\left(1-F_1\right)\frac{\sigma_{\omega2}}{\omega}\frac{\partial k}{\partial x_j}\frac{\partial \omega}{\partial x_j}$$

(3)

where $P_k=2S\Omega$, Ω is the vorticity rate, β_0^* is 0.09, $Gu=\left(\frac{\partial u_i}{\partial x_j}+\frac{\partial u_j}{\partial x_i}\right)-\frac{2}{3}\frac{\partial u_k}{\partial x_k}\delta_{ij}$, $\beta^*=0.09$.

3 Results and discussion
3.1 The velocity profiles

(a) x/B=1   (b) x/B=7
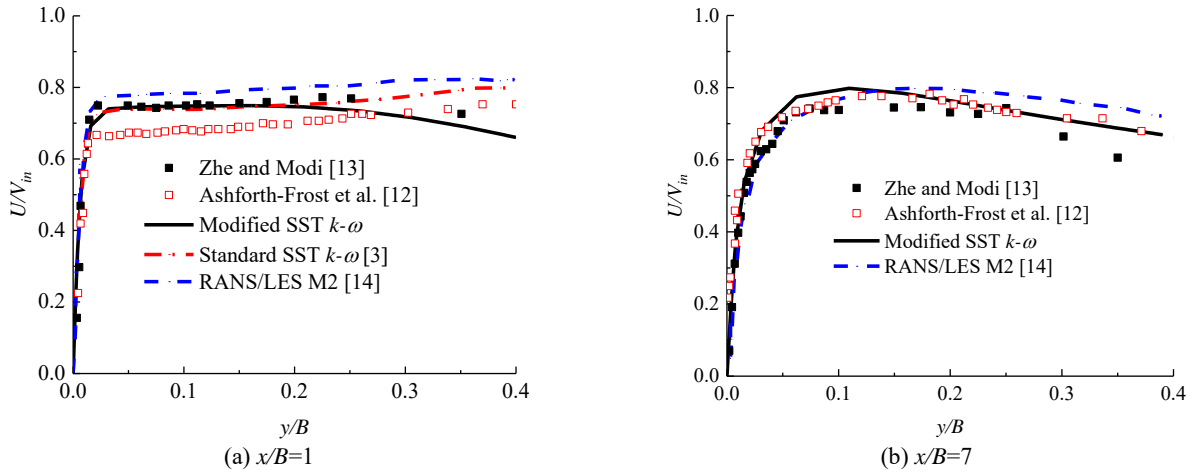
Figure 1. The comparison of velocity profiles against the experimental data and numerical results for H/B = 4
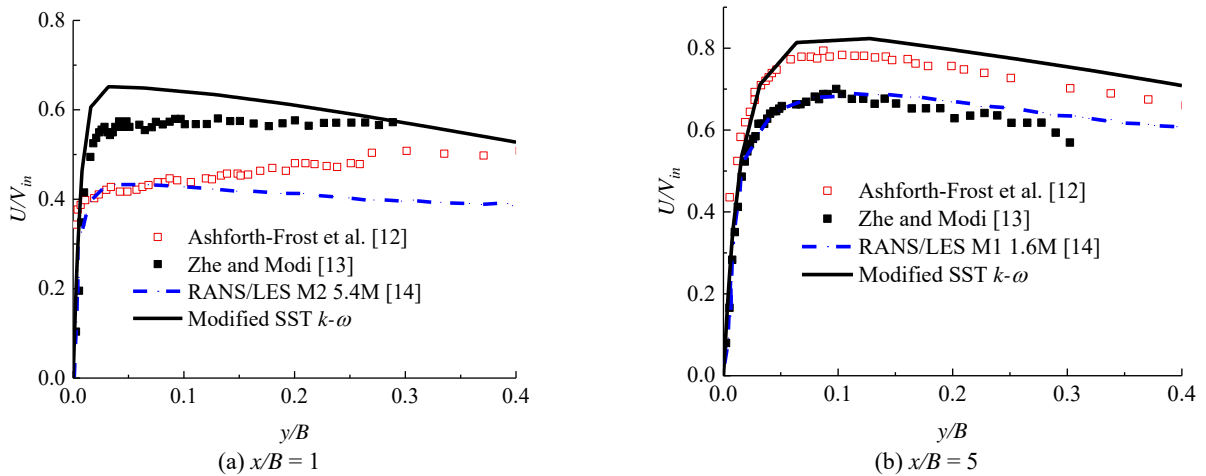
(a) x/B = 1   (b) x/B = 5

Figure 2. The comparison of velocity profiles against the experimental data and numerical results for H/B = 9.2

3.2 The skin friction
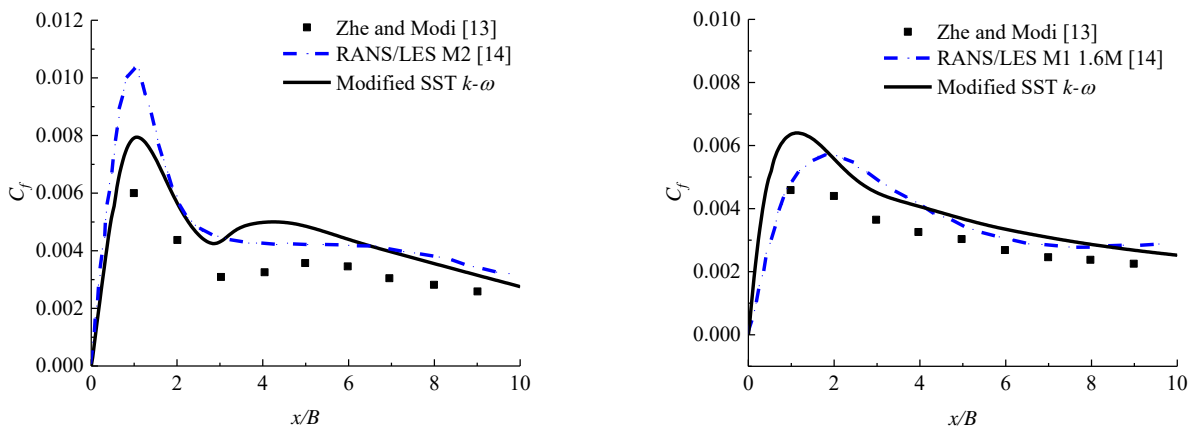
(a) $H/B = 4$ (b) $H/B = 9.2$
Figure 3. The comparison of skin friction against the experimental data and numerical results

3.3 The Nusselt Number distribution
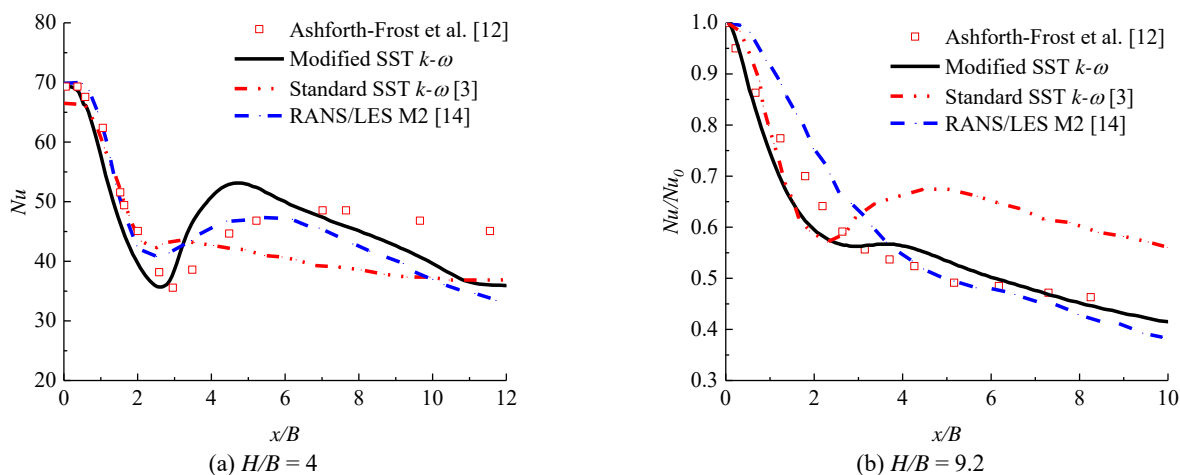
(a) $H/B = 4$ (b) $H/B = 9.2$
Figure 2. The comparison of Nusselt Number against the experimental data and numerical results

4 Conclusions

The modified SST k-ω model has been assessed in this work for turbulent slot impinging jet with two different nozzle-plate spacing of 4 and 9.2. The results are compared with the standard SST k-ω model, the RANS/LES model and the experimental data in terms of fluid structures including the velocity profiles, skin friction and Nusselt number distribution. It is observed that the modified SST k-ω model improves the ability of predicting the transition process and overcomes the false secondary peak of the Nusselt number at high nozzle-plate spacing ($H/B = 9.2$) which is predicted by the standard SST k-ω model. In general, the modified SST k-ω model provides fair performances using low computational resources comparing with the RANS/LES model.

Acknowledgements

Reference

[1]   F. R. Menter, "Two-equation eddy-viscosity turbulence models for engineering applications," *Aiaa Journal,* vol. 32, pp. 1598-1605, 1994.

[2]   E. Khalaji, M. R. Nazari, and Z. Seifi, "2D numerical simulation of impinging jet to the flat surface by k-ω-v2-f   turbulence model," *Heat and Mass Transfer,* vol. 52, pp. 127-140, 2015.

[3]   R. Dutta, A. Dewan, and B. Srinivasan, "Comparison of various integration to wall (ITW) RANS models for predicting turbulent slot jet impingement heat transfer," *International Journal of Heat and Mass Transfer,* vol. 65, pp. 750-764, 2013.

[4]   S. Alimohammadi, D. B. Murray, and T. Persoons, "Experimental Validation of a Computational Fluid Dynamics Methodology for Transitional Flow Heat Transfer Characteristics of a Steady Impinging Jet," *Journal of Heat Transfer,* vol. 136, p. 091703, 2014.

[5]   S. Pramanik and M. K. Das, "Numerical characterization of a planar turbulent offset jet over an oblique wall," *Computers & Fluids,* vol. 77, pp. 36-55, 2013.

[6]   N. Zuckerman and N. Lior, "Jet Impingement Heat Transfer: Physics, Correlations, and Numerical Modeling," vol. 39, pp. 565-631, 2006.

[7]   J. Ortega-Casanova and S. I. Castillo-Sanchez, "On using axisymmetric turbulent impinging jets swirling as Burger's vortex for heat transfer applications. Single and multi-objective vortex parameters optimization," *Applied Thermal Engineering,* vol. 121, pp. 103-114, 2017.

[8]   M. Papadrakakis, V. Papadopoulos, and G. Stefanou, "Uncertainty Quantification and Modelling og CFD Simulations of Swirling Turbulent Jet Created by A Rotating Pipe for Application to Heat Transfer from A

Heated Solid Flat Plate," presented at the Proceedings of the 1st International Conference on Uncertainty Quantification in Computational Sciences and Engineering, Crete, Greece, 2015.

[9]   A. Dewan, R. Dutta, and B. Srinivasan, "Recent Trends in Computation of Turbulent Jet Impingement Heat Transfer," *Heat Transfer Engineering,* vol. 33, pp. 447-460, 2012.

[10]   M. Wae-hayee, P. Tekasakul, S. Eiamsa-ard, and C. Nuntadusit, "Effect of cross-flow velocity on flow and heat transfer characteristics of impinging jet with low jet-to-plate distance," *Journal of Mechanical Science and Technology,* vol. 28, pp. 2909-2917, 2014.

[11]   M. A. R. Sharif and K. K. Mothe, "Evaluation of Turbulence Models in the Prediction of Heat Transfer Due to Slot Jet Impingement on Plane and Concave Surfaces," *Numerical Heat Transfer, Part B: Fundamentals,* vol. 55, pp. 273-294, 2009.

[12]   S. Ashforth-Frost, K. Jambunathan, and C. F. Whitney, "Velocity and Turbulence Characteristics of a Semiconfined Orthogonally Impinging Slot Jet," *Experimental Thermal and Fluid Science,* vol. 14, pp. 60-67, 1997.

[13]   J. Zhe and V. Modi, "Near Wall Measurements for a Turbulent Impinging Slot Jet " *Journal of Fluids Engineering,* vol. 123, pp. 112-120, 2000.

[14]   S. Kubacki and E. Dick, "Simulation of plane impinging jets with k–ω based hybrid RANS/LES models," *International Journal of Heat and Fluid Flow,* vol. 31, pp. 862-878, 2010.

[15]   J. Wienand, A. Riedelsheimer, and B. Weigand, "Numerical study of a turbulent impinging jet for different jet-to-plate distances using two-equation turbulence models," *European Journal of Mechanics - B/Fluids,* vol. 61, pp. 210-217, 2017.

MESH TOPOLOGY MODIFICATION METHOD FOR SOLVING MULTI-REGION COUPLING PROBLEMS WITH PHASE CHANGE

XUDONG NA[1], ZHIXUN XIA[1], LIKUN MA[1] , XIAOTING YAN[1]

[1]*College of Aerospace Science and Engineering, National University of Defense Technology, Changsha, China, ngvjai@126.com, zxxia@nudt.edu.cn, malikun1987@163.com, yxt0322@foxmail.com*

Keywords: multi-region coupling, phase change, mesh topology modification, Neumann-Dirichlet partitioning, cartesian mesh

Introduction

The aim of the present work is to develop a mesh topology modification method for solving the multi-region coupling problems with phase change. A lot of phenomenons involving coupled multi-region problems with phase change, such as liquid frozen/melting, machining, nozzle erosion and solid fuel combusiton etc. The ultimate goal of the work is to investigate variety of effects on the dynamic evolving process of this type problems, such as the effects on the combustion rate of solid propellant combustion. The method was developed using the foam-extend 3.2 version.

The main techniques under developing this method involve: multi-region conjugate heat/mass transfer[1], interface tracking[2] and mesh topology changes[3, 4, 5]. For multi-region coupling problems, the fully-coupled model using a Dirichlet-Neumann partitioned method is adopted. The region's interface is tracked using the method of clsvof with phase change. A new RegionMeshTopoFvMesh class and a new mesh modifier cellAdditionRemoval for handling the dynamic change of the mesh topology have been implemented. The cells can add or remove from one region to another region by the rules of interface tracking or the variables assigned, for example, when the cells temperature of solid region larger than some value , those cells will be removed from solid region and add into fluid region, shown as in figure 1.
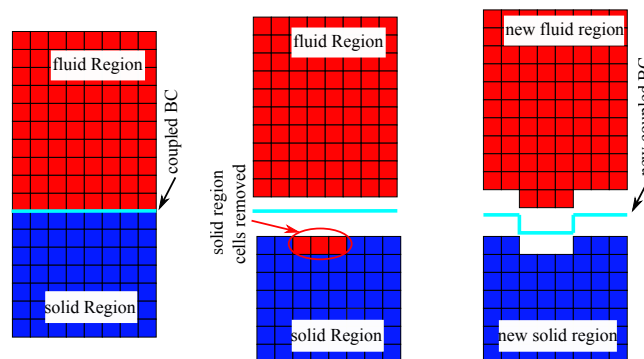
Figure 1: mesh topology modification

Overview of Implemented Technology

The entire computational domain is discretized into Cartesian mesh. Each region has its own mesh and governing equations. The matrix equation systems of each region solved individaully and coupled at the multi-region interface boundaries. The coupled boundaries are imposed by the Dirichlet-Neumann conditions. The governing equations describing fluid systems comprise equations for mass continuity, species continuity, momentum and energy. The governing equations for the solid regions comprise the energy equation and interface tracking equations. When phase change of regions happened, the mesh topology will update. The solution algorithm implemented for mesh topology modification method of solving the multi-region coupling problems with phase change is as follow:

1. Define multiple meshes, one for each region.

2. Create field variables on each mesh.

3. Judge if the mesh topology needed to change by tracking the interface of the regions or comparing with the assigned some field value. If mesh topology needed to change, then update the mesh topology and mapped the fileds of regions.

4. Set up separate governing equations for each region considered.

5. Solve the separate matrix equation systems.

6. Couple the solution obtained in Step 5 at the boundary interface among the regions.

7. Sub-iterate on the coupled solution until convergence is obtained.

8. Go to next time step.

Applications

Two cases finished by this work shown in this part. The geometry configuration of the first case comes from paper[1]. There are two regions, the one above is fluid region and the one below is solid region, as shown in figure 2.

Figure 2: Geometry configuration in case one

Compare with the case in paper [1], the mesh topology change method developed by this work is added in this case. The rule of removing cells in this case is by assigning a temperature value, when the temperature of solid region cells is larger than the value assigned, the cell will removed from solid region and added into the fluid region. Figures 3-5 show the topology change, velocity and temperature filed separately in local part. From the results, it can be seen that the solid region becomes smaller with the temperature that comes from fluid region increment. The whole dynamic process simulated by this case can be used to study the phenomenon with simple phase change, such as the melting of ice.

Figure 3: The topology structure change
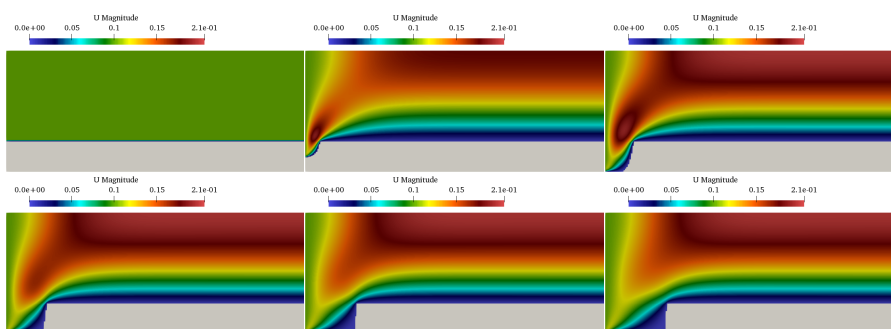
Figure 4: The velocity field

Figure 6 shows another case computed by the present work, it demonstrates the dynamic combustion process of some kind of solid propellant in the temperature filed. Compared with case above, the fluid region contains chemical reactions and the solid region contains the clsvof with phase change mehods in this case. With the help of the method developed in this work, some effects on the combustion of solid fuel can be investgated, such as ambient pressure, the initial temperature of solid region and even the formula of the propellant.
Development of the adaptive mesh refinement technique nearby the coupled interface and a parallel implementation model is still in progress.
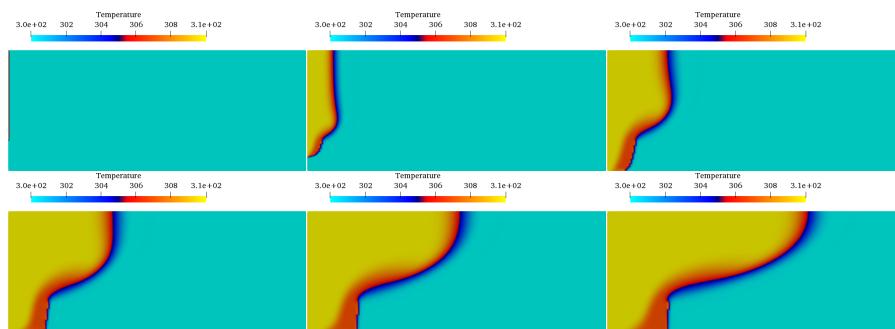
Figure 5: The temperature field
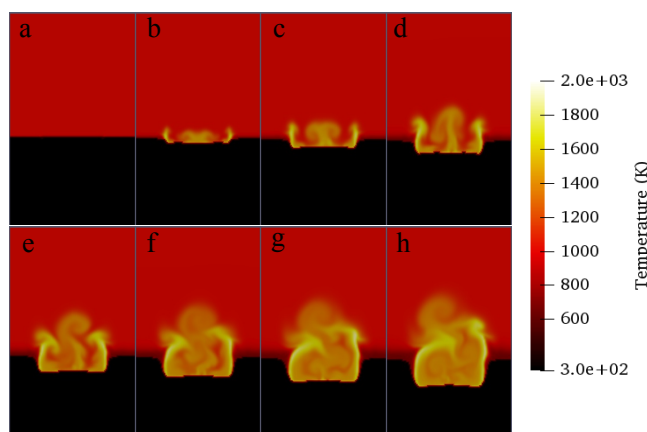
Figure 6: The temperature field of dynamic combustion processing of solid propellant

References

[1] B. A. Craven and R. L. Campbell, "Multi-Region Conjugate Heat/Mass Transfer MRconjugateheatfoam: A Dirichlet-Neumann partitioned multi-region conjugate heat transfer solver," in *6th OpenFOAM Workshop*, Jun. 2011. [Online]. Available: http://www.personal.psu.edu/dab143/OFW6/Training/craven_slides.pdf

[2] A. Albadawi, D. Donoghue, A. Robinson, D. Murray, and Y. Delaur, "Influence of surface tension implementation in Volume of Fluid and coupled Volume of Fluid with Level Set methods for bubble growth and detachment," *International Journal of Multiphase Flow*, vol. 53, pp. 11 – 28, 2013. [Online]. Available: http://www.sciencedirect.com/science/article/pii/S0301932213000190

[3] E. Bjerklund, "OpenFOAM project: A modification of the movingConeTopoFvMesh library," Tech. Rep., 2009. [Online]. Available: http://www.tfd.chalmers.se/~hani/kurser/OS_CFD_2008/ErikBjerklund/OpenFoamBjerklundE3.pdf

[4] J. H. Tomislav Marić and Kyle Mooney, *The OpenFOAM Technology Primer*. sourceflux, 2014.

[5] F. Nozaki, "Dynamic Mesh in OpenFOAM," Dec. 2015. [Online]. Available: https://www.cfd-online.com/Forums/openfoam-community-contributions/164712-slide-dynamic-mesh-openfoam.html

NUMERICAL STUDY OF CAVITATING FLOWS AROUND A HYDROFOIL

DEZHI DAI* and ALBERT Y. TONG

Department of Mechanical and Aerospace Engineering, University of Texas at Arlington, Arlington, TX 76019, USA, dezhi.dai@mavs.uta.edu, tong@uta.edu

1 Introduction

Cavitation appears when local static pressure drops below the vapor pressure of water and usually causes significant impacts on the performance of many hydraulic devices, especially marine propeller blades. For efficiency reasons, the propeller usually operates in cavitating conditions whereas the cavitation may cause blade surface erosion, noise, vibration and performance breakdown [1]. Accurate prediction of the cavitating flows around a hydrofoil is essential in the design of modern marine propellers.

The Transport Equation based Model (TEM) has been extensively employed in the numerical study of cavitating flows around a hydrofoil [1]. In the TEM model, the interface between water and its vapor is captured by the Volume of Fluid (VOF) method and a source term regarding the mass transfer is added to the standard VOF equation. Four important factors should be considered for the TEM model: an appropriate mass transfer rate evaluation method, turbulent effect of cavitating flows, computational domain discretization and a numerical algorithm to solve the VOF equation.

The mass transfer rate between the liquid and gas phases is evaluated by cavitation models. A detailed developing history of the cavitation models can be found in [2]. Schnerr and Sauer [3] presented the first model without any empirical constants and it is employed in the present study.

Most of the applications of cavitation are based on Reynolds-Averaged NavierStokes (RANS) equations [3–7]. In the present study, the Spalart-Allmaras (SA) one-equation model is employed for the sake of computational efficiency and several studies [5, 7] have already confirmed that the SA turbulence model can ensure the accuracy for the cavitating flow simulations.

The applications with structured meshes are restrained to a very simple domain. Polygonal unstructured meshes with superior flexibility for complex geometries are employed in the present study for the sake of computation efficiency and gradient evaluation accuracy [8].

The discontinuity property of the VOF function near the interface makes it unable to be solved like other flow variables by using standard advection schemes. In OpenFOAM, the Multidimensional Universal Limiter with Explicit Solution (MULES) scheme [9] is employed to capture the interface. However, MULES scheme suffers from numerical diffusion at the interface cells [10]. The Piecewise Linear Interface Calculation (PLIC) method [11] can keep the interface sharp while maintaining mass conservation at the expense of an extra reconstruction step and few papers [12] have employed this method.

The present study focuses on verification of the PLIC-VOF method on a polygonal unstructured mesh with RANS flow solver, SA turbulent and SchnerrSauer cavitation models in cavitating flow simulations and the influence of cavitation on the dynamics of the two-dimensional hydrofoil used in [13].

2 Methodology

The RANS equations with phase-change are given by:

$$\nabla \cdot \vec{U} = \left(\frac{1}{\rho_1} - \frac{1}{\rho_2} \right) \dot{m} \tag{1a}$$

$$\frac{\partial}{\partial t} \left(\rho \vec{U} \right) + \nabla \cdot \left(\rho \vec{U} \vec{U} \right) = -\nabla p + \nabla \cdot \left(\left(\mu + \mu_t \right) \left(\nabla \vec{U} + \left(\nabla \vec{U} \right)^T - \frac{2}{3} \left(\nabla \cdot \vec{U} \right) \bar{\bar{I}} \right) \right) \tag{1b}$$

$$\frac{\partial \alpha}{\partial t} + \nabla \cdot \left(\alpha \vec{U} \right) = \frac{\dot{m}}{\rho_1} \tag{1c}$$

where ρ_1 and ρ_2 are the density of the liquid and vapor phases, respectively, $\dot{m}$ the mass transfer rate due to cavitation, μ_t the turbulent eddy viscosity, $\bar{\bar{I}}$ the unit tensor and α the VOF function. Both the liquid and vapor phases are considered

incompressible and share the same mixture velocity field $\dot{U}$. Also, the turbulent eddy viscosity μ_t and the mass transfer rate $\dot{m}$ are solved by the SA turbulence and SchnerrSauer cavitation models built in OpenFOAM, respectively.

The RANS equations are solved by a modified cavitating flow solver based on interPhaseChangeFoam (details can be found in [14]) which is a standard for two incompressible, isothermal immiscible fluids with phase-change. The MULES-VOF scheme is replaced by a PLIC-VOF scheme developed in the present study and the source code will be released once the full paper is published.

On an unstructured mesh, Eq.(1c) is discretized as

$$\left(\alpha^{n+1} - \alpha^{n}\right) + \frac{1}{\Omega}\sum_{f=1}^{NF}\left(\phi_f^n \int_t^{t+\Delta t}\alpha_f dt\right) = \frac{\dot{m}}{\rho_1}\Delta t \tag{2}$$

where t is the time, Δt the time step, Ω the cell volume, NF the number of cell faces, ϕ_f the volumetric flux through cell face f and superscripts n+1 and n represent $t + \Delta t$, respectively. The liquid fraction flux $L_f = \left(\phi_f^n \int_t^{t+\Delta t}\alpha_f dt\right)$ is calculated by using the PLIC-VOF method. As shown in Figure 1, the reconstructed interface is given by:

$$\vec{n}\cdot\vec{X} + D_0 = 0 \tag{3}$$

where $\vec{n}\left(=-\dfrac{\nabla\alpha}{\|\nabla\alpha\|}\right)$ is the unit outward normal vector of the interface, $\vec{X}$ the position vector of the interface and D_0 the signed distance from the origin. D_0 is calculated by an analytical algorithm developed by the authors recently. The interface moved from D_0^n to a new position D_0^{n+1} in the time interval $[t, t + \Delta t]$ with interface normal velocity U_0 and $D_0^{n+1} = D_0^n - U_0\Delta t$. In the PLIC-VOF method, the liquid fraction flux L_f is evaluated by using the trapezoidal rule, i.e.

$$L_f = \phi_f^n \int_t^{t+\Delta t}\alpha_f dt = \frac{\phi_f^n}{A_f}\int_t^{t+\Delta t}A_{l,f} dt = \frac{\phi_f^n \Delta t\left(A_{l,f}^n + A_{l,f}^{n+1}\right)}{2A_f} \tag{4}$$

where A_f and $A_{l,f}$ are the area of face f and the area below the interface, respectively

Figure 1: Illustration of the interface line in a mixed cell

3 Preliminary Results

The numerical simulations are performed on a polygonal unstructured grid with a body-fitted boundary layer mesh as shown in Figure 2. The numerical models, that is the combination of the PLIC-VOF method, SchnerrSauer cavitation model, RANS solver and SA turbulent model, are verified by comparing the numerical results in cavitating conditions with the experimental data [13] and other numerical results available in the literature [15]. All of the simulations are performed at $AOA = 6°$ and $Re = 7.5 \times 10^5$ with different cavitation numbers. The time-averaged c_p distribution on the suction side of the hydrofoil and water volume fraction contours at $\sigma = 1.622, 1.541$ and 1.495 are shown in Figures 3 - 5. The agreement between the present numerical results and measured c_p values is very good. Compared with the numerical results in [15], the c_p distributions in the present study are closer to the experimental data, especially near the cavity closure region. This suggests that the numerical models employed in the present study could adequately simulate the fluid dynamics of cavitating flows around a hydrofoil.

The influence of various parameters on the dynamics of the hydrofoil is currently being studied. The results will be reported in the conference.
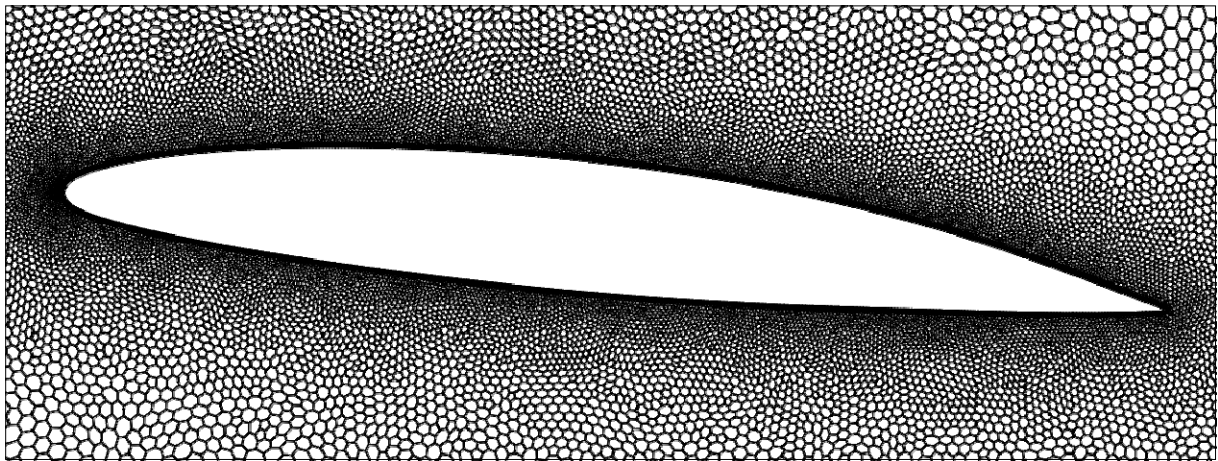
(a) Mesh around the hydrofoil
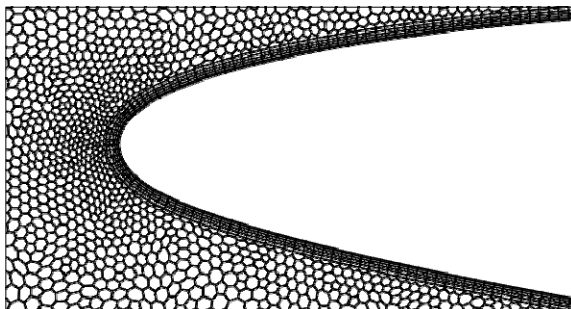
(b) Close-up view of mesh near the leading edge
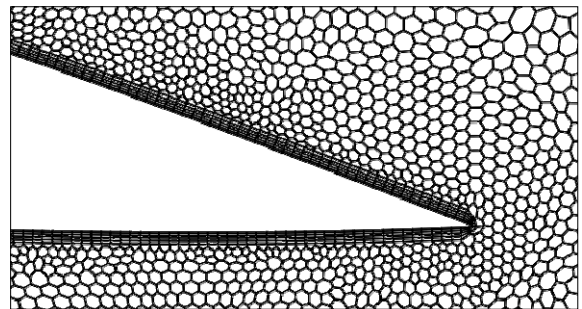
(c) Close-up view of mesh near the trailing edge

Figure 2: Employed polygonal mesh with 22359 cells at $AOA = 6°$**.**

Figure 3: Time-averaged c_p **distribution and water volume fraction contours at** $\sigma = 1.622$**.**

Figure 4: Time-averaged c_p **distribution and water volume fraction contours at** $\sigma = 1.544$**.**

Figure 5: Time-averaged c_p distribution and water volume fraction contours at $\sigma = 1.495$.

Acknowledgments

References

[1] E. Roohi, A. P. Zahiri, and M. Passandideh-Fard, "Numerical simulation of cavitation around a two-dimensional hydrofoil using vof method and les turbulence model," *Applied Mathematical Modelling*, vol. 37, no. 9, pp. 6469–6488, 2013.

[2] A. Nied źwiedzka, G. H. Schnerr, and W. Sobieski, "Review of numerical models of cavitating flows with the use of the homogeneous approach," *Archives of Thermodynamics*, vol. 37, no. 2, pp. 71–88, 2016.

[3] G. H. Schnerr and J. Sauer, "Physical and numerical modeling of unsteady cavitation dynamics," in *Fourth international conference on multiphase flow, New Orleans, USA*, vol. 1, 2001.

[4] S. H. Rhee, T. Kawamura, and H. Li, "Propeller cavitation study using an unstructured grid based navier-stoker solver," *Journal of Fluids Engineering*, vol. 127, no. 5, pp. 986–994, 2005.

[5] J. Seo and S. Lele, "Numerical investigation of cloud cavitation and cavitation noise on a hydrofoil section," 2009.

[6] M. Morgut, E. Nobile, and I. Biluš, "Comparison of mass transfer models for the numerical prediction of sheet cavitation around a hydrofoil," *International Journal of Multiphase Flow*, vol. 37, no. 6, pp. 620–626, 2011.

[7] S. J. Ahn and O. J. Kwon, "Numerical investigation of cavitating flows for marine propulsors using an unstructured mesh technique," *International Journal of Heat and Fluid Flow*, vol. 43, pp. 259–267, 2013.

[8] M. Peric and S. Ferguson, "The advantage of polyhedral meshes," *Dynamics*, vol. 24, p. 45, 2012.

[9] S. S. Deshpande, L. Anumolu, and M. F. Trujillo, "Evaluating the performance of the two-phase flow solver interfoam," *Computational science & discovery*, vol. 5, no. 1, p. 014016, 2012.

[10] J. Roenby, H. Bredmose, and H. Jasak, "A computational method for sharp interface advection," *Open Science*, vol. 3, no. 11, p. 160405, 2016.

[11] D. L. Youngs, "Time-dependent multi-material flow with large fluid distortion," *Numerical methods for fluid dynamics*, vol. 24, no. 2, pp. 273–285, 1982.

[12] M. Passandideh-Fard and E. Roohi, "Transient simulations of cavitating flows using a modified volume-of-fluid (vof) technique," *International Journal of Computational Fluid Dynamics*, vol. 22, no. 1-2, pp. 97–114, 2008.

[13] J.-B. Leroux, J. A. Astolfi, and J. Y. Billard, "An experimental study of unsteady partial cavitation," *Journal of fluids engineering*, vol. 126, no. 1, pp. 94–101, 2004.

[14] M. Andersen, E. Yasari, C. J ärpner, and A. Zarmehri, "A interphasechangefoam tutorial," *MSc/PhD course in CFD with OpenSource software*, 2011.

[15] S. Phoemsapthawee, J.-B. Leroux, J.-M. Laurens, ENSIETA, F. Deniset, and E. Navale, "A transpiration velocities based sheet cavitation model," *Ship Technology Research*, vol. 56, no. 4, pp. 161–176, 2009.

OPENFOAM SIMULATIONS OF ISOTHERMAL PHASE-CHANGE IN THE ABSENCE AND PRESENCE OF SHRINKAGE

T. YAMAMOTO[1], R. HELLMUTH[2], J. ZHANG[3], AND M. TORABI RAD[4]

[1]*Tohoku University, Aoba-ku, Sendai City, Miyagi, Japan, t-yamamoto@tohoku.ac.jp*
[2] *Vascular Flow Technologies, Dundee, UK, rudolf.hellmuth@vascular-flow.com*
[3]*School of Aeronautic Science and Engineering, Beihang University, Beijing 100191, China, jun.zhang@buaa.edu.cn*
[4]*The University of Iowa, Iowa City, IA, USA mahdi-torabirad@uiowa.edu*

Keywords: Isothermal Phase-Change, Macro-Shrinkage, Enthalpy-Porosity Method, Volume of Fluid Method

Introduction

Solidification and melting of metals are phase-change phenomena, which take place at a single temperature for pure metals, or at a range of temperatures for metal alloys. In this work, we focused only on phase-change of pure metals, i.e. isothermal phase change. Most metals have higher density in the solid phase than in the liquid phase. Therefore, during their solidification, their overall volume shrinks. This phenomenon is refereed to macro-shrinkage.

In this paper, we present our most recent results in simulating phase-change problems using OpenFOAM. We have studied two different problems involving isothermal phase change. The first one is a benchmark melting problem of pure gallium, and the second one is a solidification simulation of pure aluminium in the presence of macro-shrinkage.

Isothermal Melting Models

The model that we used to simulate the isothermal melting problem consists of continuity and energy equations, whose details can be found elsewhere [1], and the energy equation reads

$$\rho_0 c_p \frac{\partial T}{\partial t} + \rho_0 c_p \nabla \cdot (\boldsymbol{v} T) = \nabla \cdot (k \nabla T) + S_h \tag{1}$$

where ρ_0, c_p, T, $\boldsymbol{v}$, and k are the density, specific heat, temperature, liquid velocity, and thermal conductivity, respectively. The last term, S_h, represents the latent heat release due to melting. We have explored two different methods to calculate S_h. In the first method, which is referred to as the linear method, S_h is calculated as

$$S_h = -\rho_0 L_f \frac{\partial g_l}{\partial t} \tag{2}$$

where L_f is the latent heat and g_l is the liquid fraction. We define $g_l = 1$ in cells filled solely with liquid, and $g_l = 0$ in cells filled solely with solid. The liquid fraction is calculated from

$$T < T_f \quad : \quad g_l = 0$$
$$T > T_f \quad : \quad g_l = g_l^n + \alpha \frac{c_p}{L_f} (T - T_f) \tag{3}$$

where T_f and g_l^n are the melting point of a pure material and the most recent liquid fraction, respectively. In the second method, which is referred to as the error-function method developed by Rösler and Brüggemann [2], S_h is calculated as

$$S_h = -\rho_0 L_f \frac{4 \exp\left\{-\left[\frac{4(T - T_m)}{T_l - T_s}\right]^2\right\}}{(T_l - T_s)} \left(\frac{\partial T}{\partial t} + \boldsymbol{v} \cdot \nabla T\right) \tag{4}$$

where T_l and T_s are liquidus and solidus temperatures and T_m is the arithmetic mean between T_l and T_s.

Macro-Shrinkage Model

To simulate isothermal solidification in the presence of macro-shrinkage, we used the following model. The continuity equation reads

$$\nabla \cdot \boldsymbol{v} = S_s \tag{5}$$

where S_S is the shrinkage source and is calculated from

$$S_s^{i+1} = S_s^i - \left| \frac{\partial (\alpha_1 \rho_0)}{\partial t} + \nabla \cdot (\rho_0 \boldsymbol{v}) \right| \tag{6}$$

where α_1 is the volume fraction of melt. The advection equation of volume fraction (VOF method) is expressed as

$$\frac{\partial \alpha_1}{\partial t} + \nabla \cdot (\alpha_1 \boldsymbol{v}) + \nabla \cdot \left[(1 - \alpha_1) \alpha_1 \boldsymbol{v}_r \right] = S_s \tag{7}$$

where $\boldsymbol{v}_r$ is relative velocity.

Implementation

To simulate the above model in OpenFOAM we used buoyantBoussinesqPimpleFoam solver. The linear method is already implemented in OpenFOAM as solidificationMeltingSource fvOption. In this study, we implemented the error-function method by hard-coding equation (4) into the energy equation of buoyantBoussinesqPimpleFoam.

In the simulations, if solidificationMeltingSource is used with the original form of buoyantBoussinesqPimpleFoam, the solution algorithm is as follows: First, equation (1) is solved for a new temperature field using the liquid fraction field from the *previous* time step; and then, equation (4) is used to update the liquid fraction field. Here, we propose a revision to this solution algorithm by adding an inner iteration loop to repeat solving equations (1) and (4) at every time step until the solid fraction and temperature fields converge, i.e. don't change with further iterations. Our revision improves the computational efficiency of the algorithm as it allows one to use significantly larger time steps.

The details about the implementation of multiphase flow are in Yamamoto *et al.* [3]. Steep density variation around the melting point causes macro-shrinkage. We also validate the shrinkage model, while it is not implemented in OpenFOAM originally. In addition to the above model, the advection equation of liquid fraction with source term have to be solved. OpenFOAM originally provides a solver for multiphase flow as *interFoam*. This macro-shrinkage solver is developed by combining *interFoam* and *buoyantBoussinesqPimpleFoam* based on Bounds *et al.* [4].

Problem Statement

We have studied two different problems involving isothermal phase-change. The first problem is a benchmark problem for melting of pure Gallium [5]. The schematic of the problem is shown in Figure 1(a). It consists of a rectangular cavity initially filled with pure Gallium. The cavity is heated from the left wall and is insulated from the top and bottom. The temperature of the right wall is equal to the initial temperature. The initial and boundary conditions are also shown in the figure. The width and height of the cavity are 8.89 and 6.35 cm, respectively. The material properties were taken from Bounds *at al.* [5].

The second problem is a test case for solidification of pure aluminium in the presence of macro-shrinkage. The schematic of the problem is shown in Figure 3. It consists of a cavity partially filled with pure aluminium melt at 943 K in temperature. The solidification of two ingots of different aspect ratios were simulated. The width and height of ingot cavity for the first and second cases are 10 and 5 mm (aspect ratio of 2) and 40 and 5 mm (aspect ratio of 8), respectively. The physical properties were taken from Leitner *at al.* [6].

Results and Discussion

Simulation results for the melting problem are shown in Figure 2, where snapshots of the temperature field (colour) along with the velocity vectors (the black arrows) and the melting front (the while line) are plotted at: (a) 240, (b) 480, (c) 960, and (d) 1200 seconds after the start of melting. In the figure, the top and bottom rows show the results obtained using the linear and error-function methods, i.e. equations (2) and (3), respectively. Predictions of the two models, including temperature distributions, flow patterns, and the locations of the melting front are very similar. This provides confidence

in the accuracy of these results. Due to the upwards thermal buoyancy forces the hot liquid Gallium moves upwards which results in higher temperatures, and consequently faster melting at the upper parts of the cavity.

For the macro-shrinkage problem, simulation results are shown in Figure 3 where snapshots of the temperature field (colour) along with the melting front (the white line) and the liquid-melt interface (the black line) are shown for the low and high aspect ratio ingots at the top and bottom rows, respectively, at 0.1 and 2.5 seconds after the start of solidification. For the low aspect ratio ingot, i.e. the top row, the size of the shrinkage cavity is small relative to the overall size of the ingot; while, for the high aspect ratio ingot, i.e. the bottom row, the size of this cavity is large relative to the overall size of the ingot. The calculation results qualitatively express the generally observed experimental results. More detailed simulations, including quantitative comparisons with the available experimental data are ongoing.

References

[1] Rad, M.T., *solidificationMeltingSource: A Built-in fvOption in OpenFOAM to Simulate Isothermal Solidification*, in *OpenFOAM - Selected papers of the 11th Workshop*, J.M. Nobrega, Jasak, H., Editor. 2018, Springer International Publishing.

[2] Rösler, F. and D. Brüggemann, *Shell-and-tube type latent heat thermal energy storage: numerical analysis and comparison with experiments.* Heat and mass transfer, 2011. **47**(8): p. 1027-1033.

[3] Yamamoto, T., Y. Okano, and S. Dost, *Validation of the S-CLSVOF method with the density-scaled balanced continuum surface force model in multiphase systems coupled with thermocapillary flows.* International Journal for Numerical Methods in Fluids, 2017. **83**(3): p. 223-244.

[4] Bounds, S., K. Moran, K. Pericleous, M. Cross, and T.N. Croft, *A computational model for defect prediction in shape castings based on the interaction of free surface flow, heat transfer, and solidification phenomena.* Metallurgical and Materials Transactions B, 2000. **31**(3): p. 515-527.

[5] Brent, A., V. Voller, and K. Reid, *Enthalpy-porosity technique for modeling convection-diffusion phase change: application to the melting of a pure metal.* Numerical Heat Transfer, Part A Applications, 1988. **13**(3): p. 297-318.

[6] Leitner, M., T. Leitner, A. Schmon, K. Aziz, G. Pottlacher, *Thermophysical properties of liquid aluminum.* Metallurgical and Materials Transactions A, 2017. **48A**: p. 3036-3045.
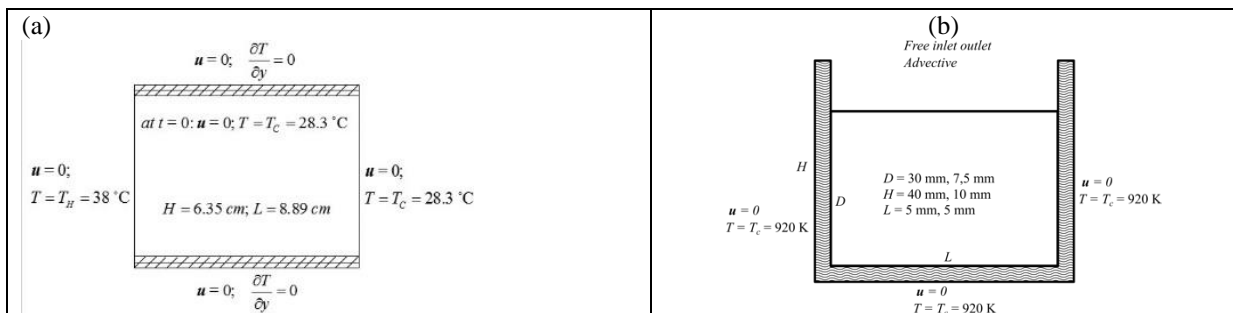
Figure 1: Schematics of the benchmark melting experiment (a) and the macro-shrinkage test problem simulated in this study (b)
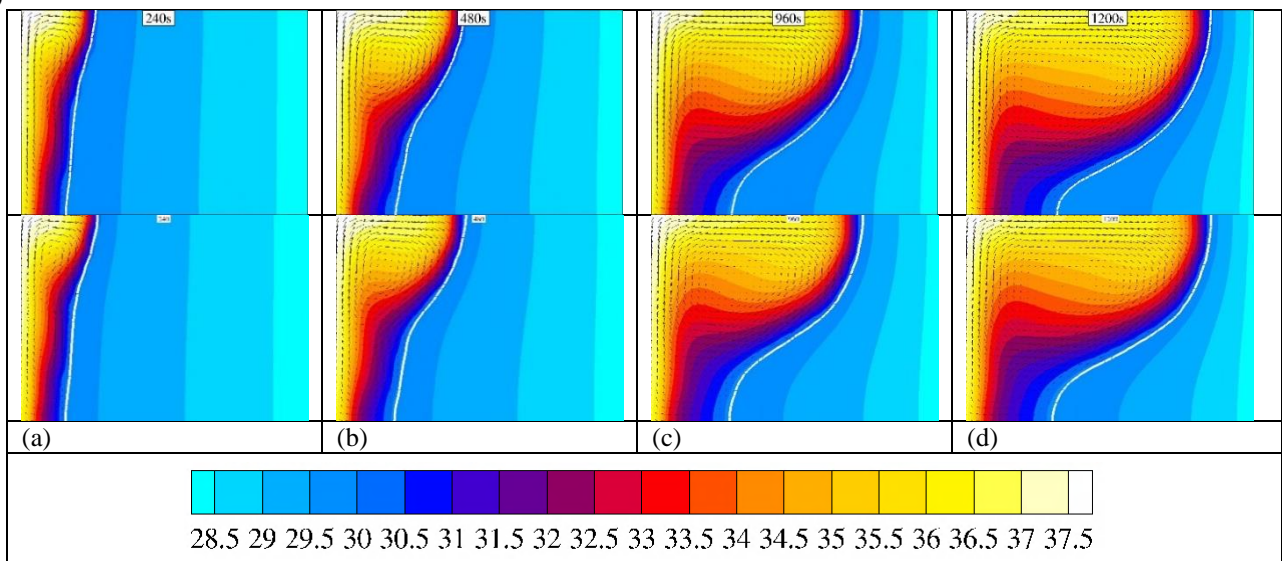
Figure 2: Snapshots after the start of melting obtained using the linear model (top row) and the error-function model (bottom row) at (a) 240, (b) 480, (c) 960, and (d) 1200 s. Each snapshot shows the temperature field (colour map), the velocity field (black arrows), and the melting front (white line)
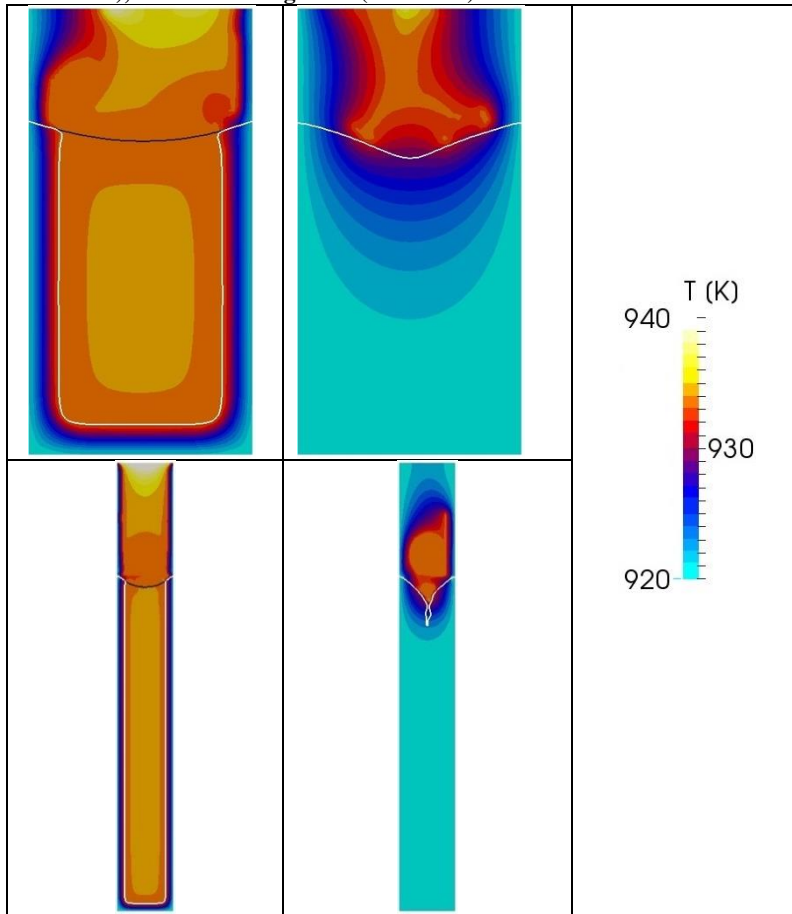
Figure 3: Snapshots after the start of solidification of the 10x5 mm ingot (top) and of the 40x5 mm ingot (bottom) at 0.1 (left) and 2.5 s (right). Each snapshot shows the temperature field (colour map), the solidification front (white line), and the liquid-melt interface (black line).

A NUMERICAL STUDY OF CAVITATING FLOWS AROUND A HYDROFOIL USING OVERSET MESHES

DEZHI DAI[1] and ALBERT Y. TONG[2]

[1]*Department of Mechanical and Aerospace Engineering, University of Texas at Arlington, Arlington, TX 76019, USA, dezhi.dai@mavs.uta.edu*

[2]*Department of Mechanical and Aerospace Engineering, University of Texas at Arlington, Arlington, TX 76019, USA, tong@uta.edu*

1 Introduction

Cavitation appears when local static pressure drops below the water vapor pressure and causes significant impacts on marine propeller blades. For efficiency reasons, marine propellers usually operate under cavitating conditions and may suffer blade surface erosion, noise, vibration and performance breakdown [1]. As hydrofoil is the radial section of propeller blades, an accurate prediction of cavitating flows around a hydrofoil is essential in the design of marine propellers.

The Transport Equation-based Model (TEM) has been extensively employed in the numerical study of cavitating flows [1]. In the TEM model, the interface between liquid and vapor is captured by the Volume of Fluid (VOF) method and a source term regarding the mass transfer is added to the standard homogeneous VOF equation. Four important elements are considered in the TEM model: computational domain discretization, numerical algorithm for the VOF equation, mass transfer rate evaluation for phase change and the turbulent modeling of cavitating flows.

The use of stationary meshes is restrained to unmoving parts in the computational domain. Also, a common difficulty in simulating complex fluid flows is that some geometries cannot be well-represented by using a single mesh [2]. Representing distinct geometries by different mesh parts is a better choice in general. It is also complicated and time-consuming to prepare a single stationary mesh with complex geometries. Dynamic overset mesh [3] can be especially useful in applications involving component motion and is supported in the latest version of OpenFOAM. However, overset mesh cannot be used in the standard cavitation solver, *interPhaseChangeFoam*, in OpenFOAM.

Furthermore, *interPhaseChangeFoam* employs an algebraic method, the Multidimensional Universal Limiter with Explicit Solution (MULES) scheme [4], to solve the VOF equation which suffers from numerical diffusion at interface cells [5]. Piecewise Linear Interface Calculation (PLIC) method [6] can keep the interface sharp while maintaining mass conservation at the expense of an extra reconstruction step and has been employed in the study of cavitation [7].

The mass transfer rate between the liquid and gas phases is evaluated by cavitation models. A detailed developing history of the cavitation models can be found in [8]. Schnerr and Sauer [9] presented the first model without any empirical constants and is employed in the present study.

Most of the applications on cavitation are based on the Reynolds-Averaged Navier-Stokes (RANS) equations [9–13]. In the present study, the Spalart-Allmaras (SA) one-equation model is employed for the sake of computational efficiency. Several studies [11, 13] have already confirmed that the SA turbulence model can ensure accuracy for the cavitating flow simulations.

The cavitation solver *overInterPlicPhaseChangeDyMFoam*, recently developed by the authors, implements the dynamic overset mesh technique in conjunction with an analytical PLIC interface reconstruction algorithm to perform interface flow simulations. The present study focuses on the applications of the solver on an overset mesh along with the RANS equation, SA turbulent and SchnerrSauer cavitation models in cavitating flow simulations over a hydrofoil.

2 Methodology

The VOF equation phase-change is given by:

$$\nabla \cdot \vec{U} = \left(\frac{1}{\rho_1} - \frac{1}{\rho_2} \right) \dot{m} \tag{1}$$

where ρ_1 and ρ_2 are the density of the liquid and vapor phases, respectively, $\dot{m}$ the mass transfer rate due to phase change and α the VOF function. Both the liquid and vapor phases are considered incompressible and share the same

mixture velocity field $\vec{U}$. Also, the mass transfer rate $\dot{m}$ is solved by the SchnerrSauer cavitation models built in the OpenFOAM.

On a general unstructured mesh, Eq.(1) is discretized as

$$\left(\alpha^{n+1} - \alpha^{n}\right) + \frac{1}{\Omega}\sum_{f=1}^{NF}\left(\phi_f^n \int_t^{t+\Delta t} \alpha_f dt\right) = \frac{\dot{m}}{\rho_l}\Delta t \tag{2}$$

where t is the time, Δt the time step, Ω the cell volume, NF the number of cell faces, ϕ_f the volumetric flux through cell face f and superscripts $n+1$ and n represent $t + \Delta t$, respectively. The liquid fraction flux $L_f = \left(\phi_f^n \int_t^{t+\Delta t} \alpha_f dt\right)$ is calculated by using the PLIC-VOF method. As shown in Figure 1, the reconstructed interface is given by:

$$\vec{n} \cdot \vec{X} + D_0 = 0 \tag{3}$$

where $\vec{n}\left(= -\dfrac{\nabla \alpha}{\|\nabla \alpha\|}\right)$ is the unit outward normal vector of the interface, $\vec{X}$ the position vector of the interface and D_0 the signed distance from the origin. D_0 is calculated by an analytical algorithm developed by the authors recently. The interface moved from D_0^n to a new position D_0^{n+1} in the time interval $[t, t+\Delta t]$ with interface normal velocity U_0 and $D_0^{n+1} = D_0^n - U_0\Delta t$. In the PLIC-VOF method, the liquid fraction flux L_f is evaluated by using the trapezoidal rule, i.e.

$$L_f = \phi_f^n \int_t^{t+\Delta t} \alpha_f dt = \frac{\phi_f^n}{A_f}\int_t^{t+\Delta t} A_{l,f} dt = \frac{\phi_f^n \Delta t \left(A_{l,f}^n + A_{l,f}^{n+1}\right)}{2A_f} \tag{4}$$

where A_f and $A_{l,f}$ are the area of face f and the area below the interface, respectively

Figure 1: Illustration of the interface line in a mixed cell

The overset interpolation of the VOF function α as well as the other variables are implemented by using the inverse distance scheme.

3 Preliminary Results

The numerical simulations are performed on an overset mesh as shown in Figure 2. The numerical models, based on the combination of the PLIC-VOF method in overset mesh, SchnerrSauer cavitation model, RANS solver and SA turbulent model, are verified by comparing the numerical results in cavitating conditions with the experimental data [14] and other numerical results available in the literature [15]. All of the simulations are performed at AOA = 6◦ and Re = 7.5 105 with different cavitation numbers. The time-averaged cp distribution on the suction side of the hydrofoil and water volume fraction contours at σ = 1.622, 1.541 and 1.495 are shown in Figures 3 - 5. The present numerical results for cp are in good agreement with the experimental values. Compared with the numerical results in [15], the cp distributions in the present study are closer to the experimental data, especially near the cavity closure region. This suggests that the overset mesh and numerical models employed in the present study could adequately simulate the fluid dynamics of cavitating flows around a hydrofoil.

The influence of various parameters on the dynamics of the hydrofoil is currently being studied. The results will be reported in the conference.
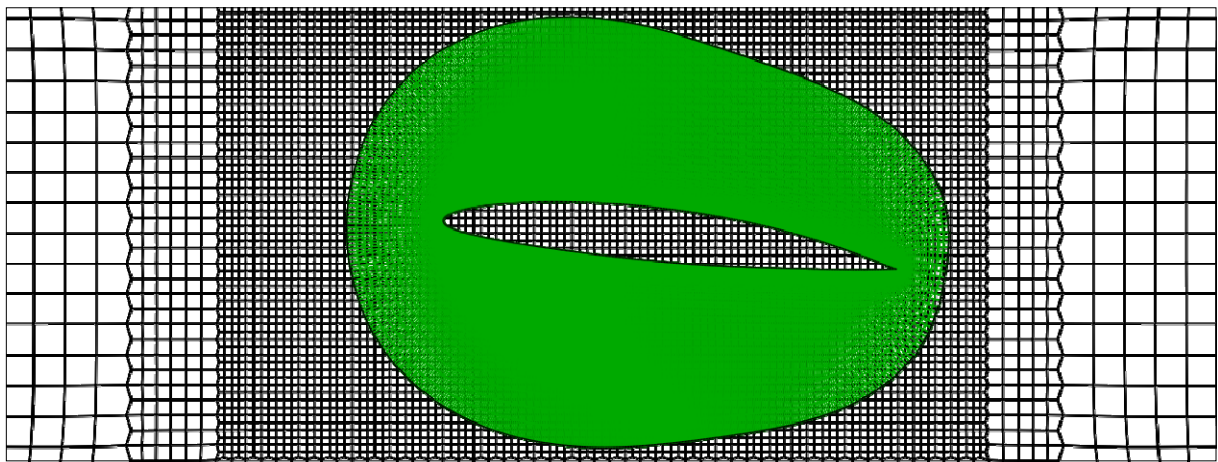
(a) Overset around the hydrofoil
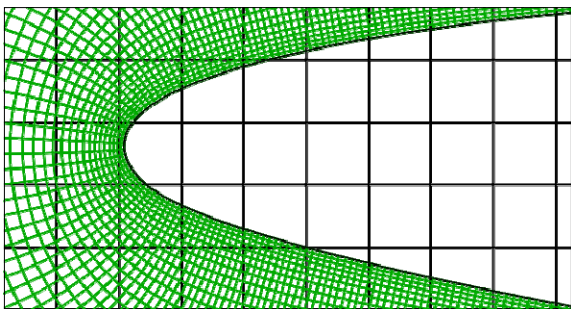
(b) Close-up view of mesh near the leading edge
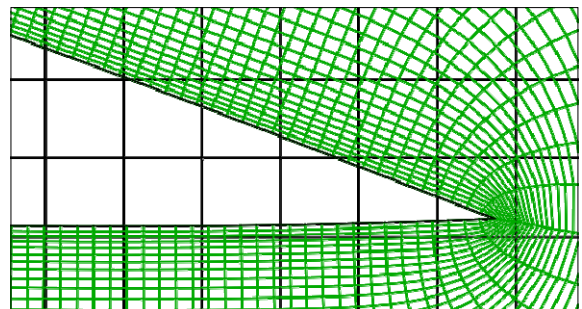
(c) Close-up view of mesh near the trailing edge

Figure 2: Employed overset mesh with 30665 cells at $AOA = 6°$**.**

Figure 3: Time-averaged c_p **distribution and water volume fraction contours at** $\sigma = 1.622$**.**

Figure 4: Time-averaged c_p **distribution and water volume fraction contours at** $\sigma = 1.544$**.**

Figure 5: Time-averaged c_p distribution and water volume fraction contours at $\sigma = 1.495$.

References

[1] E. Roohi, A. P. Zahiri, and M. Passandideh-Fard, "Numerical simulation of cavitation around a two-dimensional hydrofoil using vof method and les turbulence model," *Applied Mathematical Modelling*, vol. 37, no. 9, pp. 6469–6488, 2013.

[2] A. Fluent, "Fluent 12. theory guide," 2017.

[3] Z. Shen, D. Wan, and P. M. Carrica, "Rans simulations of free maneuvers with moving rudders and propellers using overset grids in openfoam," in *SIMMAN workshop on Verification and Validation of Ship Maneuvering Simulation Methods. Presented at the SIMMAN workshop on Verification and Validation of Ship Maneuvering Simulation Methods, Lyngby, Denmark*, 2014.

[4] S. S. Deshpande, L. Anumolu, and M. F. Trujillo, "Evaluating the performance of the two-phase flow solver interfoam," *Computational science & discovery*, vol. 5, no. 1, p. 014016, 2012.

[5] J. Roenby, H. Bredmose, and H. Jasak, "A computational method for sharp interface advection," *Open Science*, vol. 3, no. 11, p. 160405, 2016.

[6] D. L. Youngs, "Time-dependent multi-material flow with large fluid distortion," *Numerical methods for fluid dynamics*, vol. 24, no. 2, pp. 273–285, 1982.

[7] M. Passandideh-Fard and E. Roohi, "Transient simulations of cavitating flows using a modified volume-of-fluid (vof) technique," *International Journal of Computational Fluid Dynamics*, vol. 22, no. 1-2, pp. 97–114, 2008.

[8] A. Nied źwiedzka, G. H. Schnerr, and W. Sobieski, "Review of numerical models of cavitating flows with the use of the homogeneous approach," *Archives of Thermodynamics*, vol. 37, no. 2, pp. 71–88, 2016.

[9] G. H. Schnerr and J. Sauer, "Physical and numerical modeling of unsteady cavitation dynamics," in *Fourth international conference on multiphase flow, New Orleans, USA*, vol. 1, 2001.

[10] S. H. Rhee, T. Kawamura, and H. Li, "Propeller cavitation study using an unstructured grid based navier-stoker solver," *Journal of Fluids Engineering*, vol. 127, no. 5, pp. 986–994, 2005.

[11] J. Seo and S. Lele, "Numerical investigation of cloud cavitation and cavitation noise on a hydrofoil section," 2009.

[12] M. Morgut, E. Nobile, and I. Bilu sˇ, "Comparison of mass transfer models for the numerical prediction of sheet cavitation around a hydrofoil," *International Journal of Multiphase Flow*, vol. 37, no. 6, pp. 620–626, 2011.

[13] S. J. Ahn and O. J. Kwon, "Numerical investigation of cavitating flows for marine propulsors using an unstructured mesh technique," *International Journal of Heat and Fluid Flow*, vol. 43, pp. 259–267, 2013.

[14] J.-B. Leroux, J. A. Astolfi, and J. Y. Billard, "An experimental study of unsteady partial cavitation," *Journal of fluids engineering*, vol. 126, no. 1, pp. 94–101, 2004.

[15] S. Phoemsapthawee, J.-B. Leroux, J.-M. Laurens, ENSIETA, F. Deniset, and E. Navale, "A transpiration velocities based sheet cavitation model," *Ship Technology Research*, vol. 56, no. 4, pp. 161–176, 2009.

DETAILED TRANSPORT AND PERFORMANCE OPTIMIZATION FOR MASSIVELY PARALLEL SIMULATIONS OF TURBULENT COMBUSTION WITH OPENFOAM

THORSTEN ZIRWES[1,2], FEICHI ZHANG[2], JORDAN A. DENEV[1], PETER HABISREUTHER[2]
HENNING BOCKHORN[2], DIMOSTHENIS TRIMIS[2]

[1]*Karlsruhe Institute of Technology, Steinbuch Centre for Computing, [thorsten.zirwes, jordan.denev]@kit.edu*
[2]*Karlsruhe Institute of Technology, Engler-Bunte-Institute, Combustion Technology,*
[thorsten.zirwes, feichi.zhang, peter.habisreuther, henning.bockhorn, dimosthenis.trimis]@kit.edu

This work describes the implementation of two key features for enabling high performance computing (HPC) of highly resolved turbulent combustion simulations: detailed molecular transport for chemical species and efficient computation of chemical reaction rates. The transport model is based on an implementation of the thermo-chemical library Cantera [1] and is necessary to resolve the inner structure of flames. The chemical reaction rates are computed from automatically generated chemistry-model classes [2], which contain highly optimized code for a specific reaction mechanism. In combination with Sundials' [3] ODE solver, this leads to drastic reductions in computing time. The new features are validated and applied to a turbulent flame with inhomogeneous mixing conditions on a grid with 150 million cells. The simulation is performed on Germany's fastest supercomputer "Hazel Hen" [4] on 28,800 CPU cores, showing very good scalability. The good agreement with experimental data shows that the proposed implementations combined with the capabilities of OpenFOAM are able to accurately and efficiently simulate even challenging flame setups.

1 Detailed Molecular Transport Coefficients

Although many transport models are available in OpenFOAM for standard solvers like `reactingFoam`, they all have in common that each chemical species in the fluid has the same diffusion coefficient. This assumption is justified if turbulent transport is more important than molecular transport. In highly resolved simulations however, where no turbulence models are used as shown in Sect. 3, detailed diffusion coefficients for each species are necessary in order to correctly capture the flame structure. Therefore, a coupling interface [5] between OpenFOAM's thermo classes and Cantera [1] was created, following an idea by Gschaider and Rhem [6], where Cantera was used as an external library to compute the transport coefficients and chemical reaction rates. Since then, the relevant parts of the Cantera code have been extracted and directly compiled into a thermo-physical model for OpenFOAM 5.x and 1712+. This eliminates indirections leading to better performance and making the new solver independent of Cantera as a third-party library.

In the detailed thermo-physical model, the transport of each chemical species is described by six gas kinetic properties: Lennard-Jones collision diameter and energy well depth, polarizability, dipole moment, rotational relaxation collision number and molecule geometry. These information are usually provided as part of the chemical reaction mechanism in CHEMKIN format which can easily be converted into Cantera's xml format. The xml file then serves as input for the thermo-physical model. OpenFOAM provides a similar utility `chemkinToFoam` which converts reaction mechanisms from CHEMKIN format to OpenFOAM format, but ignores the aforementioned transport properties. In the detailed transport model, the gas kinetic properties are used to compute binary diffusion coefficients $\mathcal{D}_{k,i}$, viscosity μ_k and heat conductivity λ_k for each species k from the Chapman-Enskog solution of the Boltzmann equation. Mixing laws are applied to compute mixture-averaged properties, like Wilke's mixing law for viscosity, or the Hirschfelder-Curtiss approximation for the mass diffusion coefficient $\frac{1}{D_k} = \sum_{i \neq k} \frac{X_i}{\mathcal{D}_{k,i}} + \frac{X_k}{1-Y_k} \sum_{i \neq k} \frac{Y_i}{\mathcal{D}_{k,i}}$ [7], where X_k is the mole fraction and Y_k the mass fraction of the k-th species. Because every species has its own diffusion coefficient D_k and molecular mass diffusion flux $\vec{j}_k$, the governing equations for the species masses and energy have to be adapted:

$$\frac{\partial (\rho Y_k)}{\partial t} + \nabla \cdot (\rho(\vec{u} + \vec{u}_c)Y_k) = \dot{\omega}_k - \nabla \cdot \vec{j}_k, \qquad \vec{j}_k = -\rho D_k \nabla Y_k, \qquad k = 1 \dots N-1 \tag{1}$$

$$\frac{\partial (\rho h_{s,t})}{\partial t} + \nabla \cdot (\rho \vec{u} h_{s,t}) = \nabla \cdot (\alpha \nabla h_s) + \frac{\partial p}{\partial t} - \sum_k h_k^\circ \dot{\omega}_k - \nabla \cdot \sum_k h_{s,k} \left(\left(\vec{j}_k + \rho Y_k \vec{u}_c \right) + \alpha \nabla Y_k \right) \tag{2}$$

Here, ρ is the density, t time, $\vec{u}$ the fluid velocity, $\dot{\omega}$ the chemical reaction rate, N the number of species, $h_{s,t} = h_s + \frac{1}{2}\vec{u} \cdot \vec{u}$ the total sensible enthalpy of the mixture, T the temperature, p the pressure, α the ratio of thermal conductivity to isobaric heat capacity, h_k° the enthalpy of formation and $h_{s,k}$ the sensible enthalpy of species k. Both equations are the same as
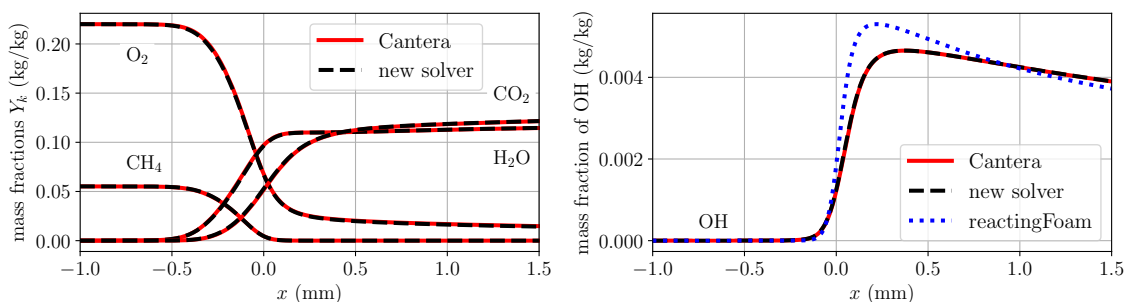
Figure 1: Spatial profiles of species mass fractions in a one-dimensional flame. Computed with Cantera [1], the new solver including detailed transport and the standard `reactingFoam` solver with the Sutherland transport model in OpenFOAM 5.x.

in the standard `reactingFoam` family of solvers, with the exception of the correction velocity $\vec{u}_c = -\frac{1}{\rho} \sum_k \vec{j}_k$ in the convective term of Eq. (1), which is necessary in order to ensure overall mass conservation, and the last term on the r.h.s. of Eq. (2), which is a consequence of nonequidiffusion or non-unity Lewis number.

Figure 1 on the left shows the main species profiles for a canonical flame setup, the one-dimensional premixed flame. The domain consists of 10,000 cells spanning 10 cm. The left boundary is an inlet with an unburnt methane-air mixture at an equivalence ratio of $\phi = 1$, $T = 300$ K and $u = 0.37$ m/s, and the right side is an outlet. The chemistry is described by the GRI 3.0 [8] reaction mechanism. The domain is initialized with cold, unburnt gas in the left half, and hot burnt gas in the right half. After some time, a stationary flame develops. The same setup is simulated in Cantera. The comparison on the left of Fig. 1 validates the implementation of the new solver by comparing spatial species profiles in the flame with Cantera. On the right of Fig. 1, results for the profile of the intermediate radical species OH from the new solver and the standard `reactingFoam` solver are compared. Again, Cantera's reference solution coincides with the new solver. The simulation with `reactingFoam` uses the exact same numerical and physical settings as the new solver except for the transport model. As in many of the standard OpenFOAM tutorial cases, the Sutherland transport model is used for the GRI 3.0 mechanism in `reactingFoam`, which shows large deviation for the intermediate species profiles. This demonstrates that detailed transport coefficients for each species are necessary to correctly predict the flame properties.

2   Performance Optimization for Chemical Reaction Rates

Combustion processes are governed by a large number of intermediate species and chemical reactions. The computation of chemical reaction rates is therefore often the performance bottleneck. Because of this, a new approach has been introduced in order to speed up the chemistry computations. When preparing a new case with standard solvers like `reactingFoam`, OpenFOAM's `chemkinToFoam` utility can be used to convert a reaction mechanism in CHEMKIN format to a new set of files in OpenFOAM's format, which serve as input files for the general chemistry model. In the new approach [2], instead of using `chemkinToFoam`, a self-developed converter tool can be used which takes a reaction mechanism in CHEMKIN or Cantera format as input and creates a directory containing C++ source code for a new chemistry model class specifically for that mechanism. For example, applying the converter tool to the GRI 3.0 mechanism would generate code for a new chemistry model class named `optimizedChemistryModel_GRI`. Compiling this class results in a chemistry model which can directly be used in the simulation through OpenFOAM's runtime selection mechanism and is compatible to the general chemistry implementation, for example it can be combined with OpenFOAM's TDAC model. The code in the generated class contains all information for computing the chemical reaction rates from detailed Arrhenius and other reaction type formulations without simplification, in the same way that OpenFOAM and Cantera do. This approach has several advantages: it requires little effort by the user because all steps of the conversion are performed automatically. During the conversion, species and reactions are reordered by their type in order to allow auto-vectorization of critical loops by the compiler. Redundant operations are eliminated and more compiler optimizations are enabled because otherwise unknown parameters for the species and reactions are known at compile time. The data is laid out in a cache-friendly way and is explicitly aligned. The resulting code has been shown to perform significantly faster and to reduce cache misses by up to a factor of 30. For more information, see [2].

Figure 2 shows results for another canonical flame setup, the zero-dimensional auto-ignition of a hydrogen-air mixture using the reaction mechanism by Li et al. [9]. The computational domain consists of only one cell, similar to `chemFoam`. Therefore, transport processes are irrelevant in this setup. The domain is initially filled with hot hydrogen and air, which then auto-ignite. On the left of Fig. 2, the mass fraction profile of H_2O_2 is depicted over time, which is an intermediate species during ignition. The simulation has been performed with the first order `Euler` time discretization with the standard `reactingFoam` solver and the new solver. For the `Euler` scheme, the chemical reaction rates are computed from the linear approximation $\dot{\omega}_k \approx M_k(C_k^{n+1} - C_k^n)/\Delta t$ in all solvers, where M_k is the molar mass of the species, Δt the time step and C_k^n the species concentration at the current time step n. C_k^{n+1} is an estimate for the concentration at the next time step obtained from an operator splitting approach, where the concentrations in each cell are integrated over the time step by an ODE integrator, allowing to use adaptive sub-time stepping. The results coincide with the reference
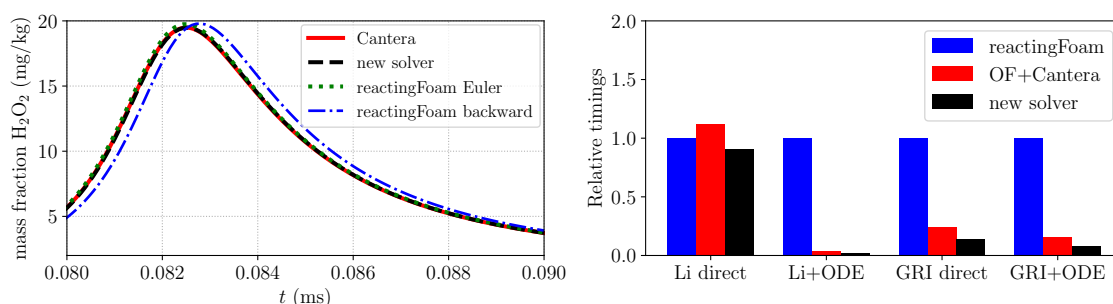
Figure 2: Left: Mass fraction of H_2O_2 over time during ignition of hydrogen. Right: Time spent computing chemical reaction rates for the auto-ignition case normalized to the time of `reactingFoam`. Measurements are done for two reaction mechanism (GRI 3.0 [8] and Li [9]) using either the operator splitting approach ("ODE") or direct computation.

solution obtained from Cantera. In the case of the three-point `backward` time discretization, the new solver also gives accurate results while `reactingFoam` deviates from the reference solution. The reason is that the chemistry model in `reactingFoam` always computes the chemical reaction rates from the linear approximation above, while the new solver switches to the more consistent formulation $\dot{\omega}_k \approx M_k \left(\frac{3}{2} C_k^{n+1} - 2C_k^n + \frac{1}{2} C_k^{n-1} \right) / \Delta t$ for the `backward` scheme.

In Fig. 2 on the right, the time spent on computing chemical reaction rates, which corresponds to the call of `reaction->correct()` in `YEqn.H`, is plotted normalized to the respective time needed by `reactingFoam` for the auto-ignition simulations. All codes have been compiled with the Intel compiler icpc 18 with `-fast`. In general, the reaction rates can either be computed directly (corresponds to combustion model setting `integrateRates false;`) denoted by "direct", or from the operator splitting approach which requires an ODE integrator. In the timings denoted with "ODE", seulex is used as the ODE integrator in `reactingFoam`. In the new solver containing the automatically generated optimized code ("new solver") and in the solver which is coupled to Cantera as an external library for computing the reaction rates ("OF+Cantera"), Sundials' [3] CVODE integrator is available and has been used in the measurements. The times needed to compute the reaction rates from the mechanism by Li directly ("Li direct") is about 10 % slower with `reactingFoam` and 20 % slower with Cantera compared to the optimized code in the new solver. This is due to Li being a relatively small mechanism with only 9 species and 21 reactions. As the mechanisms become larger, the performance benefit of the optimized code becomes larger as well. With the GRI 3.0 mechanism, which contains 53 species and 325 reactions, direct computation of reaction rates with `reactingFoam` takes seven times longer and Cantera's implementation twice as long compared to the optimized code. There is also a large difference in runtime which stems from the choice of ODE integrator. In the measurements, the initial time step and absolute and relative tolerances are the same for seulex and CVODE, and have been chosen to keep errors below 1 % compared to the reference solution by Cantera. With these strict tolerances, CVODE combined with the optimized chemistry code is by an order of magnitude faster than the standard OpenFOAM implementation while still giving the same simulation results. Similar performance results have been obtained for the Rosenbrock integrator instead of seulex.

3 Massively Parallel Simulation of a Turbulent Flame

This section describes an application of the new solver where both implementations are required—detailed transport and efficient chemistry computations. Subject of the simulation is the Sandia/Sydney burner [10]. This burner is experimentally well investigated and is operated with methane-air, but due to very inhomogeneous mixing conditions at the burner nozzle most combustion models are not able to correctly predict the flame properties. Therefore, this simulation utilizes the detailed transport model and fully resolves the flame, allowing a model free simulation. The computational grid consists of 150 mil. cells, uses `backward` time discretization, `cubic` for spatial discretizations and a complex reaction mechanism with 19 species [2]. Due to the optimized chemistry code and the use of the CVODE integrator, the total simulation time can be reduced by 50 % compared to the Cantera implementation [2]. This makes it possible to run the simulation on Germany's fastest supercomputer [4] on 28,800 CPU cores. The total simulation required about 15 mil. core hours and produced 15 TB of data, which includes transient fields of flow variables and chemical scalars.

Figure 3 depicts the temperature profile of the flame where the inner fuel-air jet is ignited by a hot pilot gas and leads to a high-temperature combustion zone along the shear layer. Fig. 4 on the left shows a snapshot from the simulation. Depicted is an iso-surface of vorticity near the burner nozzle. It illustrates the turbulent flow structures which are formed by the inner unburnt jet and become destroyed due to increasing viscosity when the flame begins to burn at larger radii. Parallel
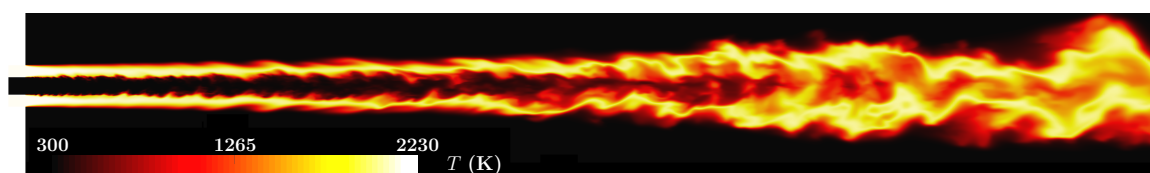
Figure 3: 2D cut of the temperature profile from the 3D simulation of the Sandia/Sydney flame [10].
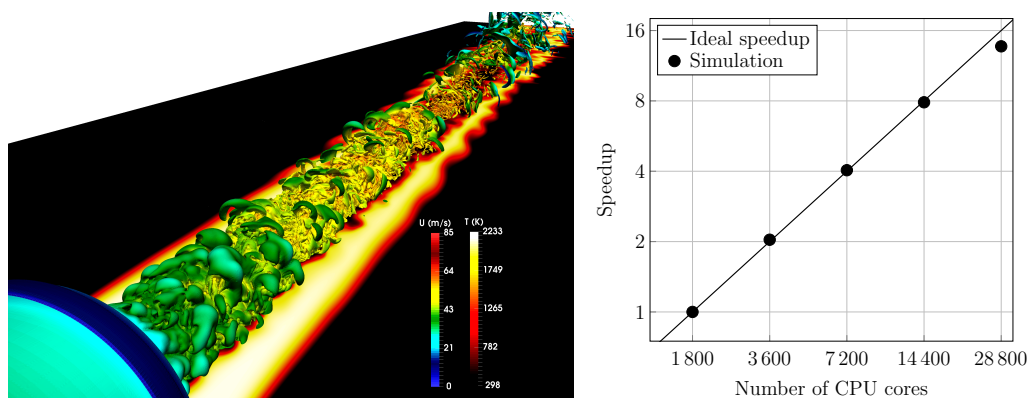
Figure 4: Left: Iso-surface of vorticity near the inlet nozzle colored by fluid velocity U and a 2D cutting plane of the temperature, illustrating the turbulent flow structures in the inner jet region. Right: Parallel speedup for a strong scaling case with 175 million cells and optimized chemistry performed with OpenFOAM 5.x on the Hazel Hen supercomputer at HLRS [4].
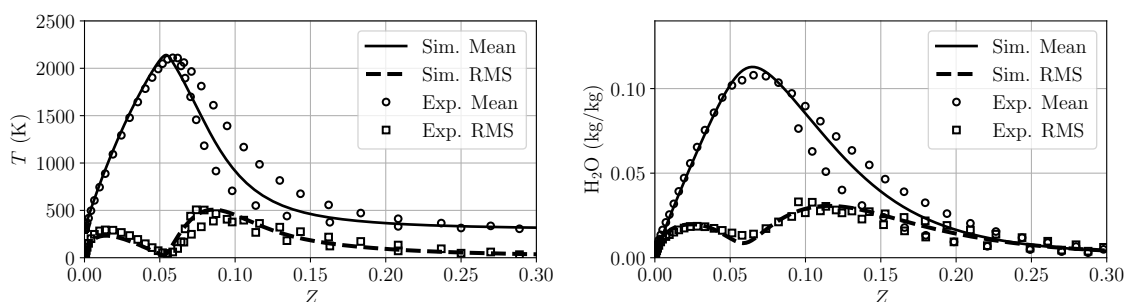
Figure 5: Comparison of radial temperature (left) and water mass fraction (right) profiles of time averaged and RMS values at fixed axial positions plotted against radial mixture fraction Z profiles with experimental measurements [10].

scaling on the right of Fig. 4 is almost linear up to 14,400 cores and still has an efficiency of 86 % at 28,800 CPU cores. The good scaling results are achieved because a large part of the simulation time is spent on computing chemical reaction rates, which does not require MPI communication. In Fig. 5, the simulation results are compared with experimental measurements. Time averaged and RMS values show very good quantitative agreement, e.g. the temperature and water mass fraction profiles lie well within the experimental uncertainties. Due to the highly resolved results, this simulation will be published as a reference database for the development of new combustion models.

Acknowledgments

References

[1] D. Goodwin, H. Moffat, and R. Speth, "Cantera: An object-oriented software toolkit for chemical kinetics, thermodynamics, and transport processes. version 2.3.0b," 2017, software available at www.cantera.org.

[2] T. Zirwes, F. Zhang, J. Denev, P. Habisreuther, and H. Bockhorn, "Automated code generation for maximizing performance of detailed chemistry calculations in OpenFOAM," in *High Performance Computing in Science and Engineering '17*, W. Nagel, D. Kröner, and M. Resch, Eds. Springer, 2017, pp. 189–204.

[3] "Suite of nonlinear and differential/algebraic equation solvers," http://computation.llnl.gov/casc/sundials.

[4] "High performance computing center stuttgart," www.hlrs.de/systems/cray-xc40-hazel-hen, 2018.

[5] H. Bonart, "Implementation and validation of a solver for direct numerical simulations of turbulent reacting flows in OpenFOAM," Bachelor's Thesis, Karlsruhe Institute of Technology, Germany, 2012.

[6] B. Gschaider, M. Rhem, P. Seifert, and B. Meyer, "Implementation of an alternative chemistry library into OpenFOAM," http://powerlab.fsb.hr/ped/kturbo/openfoam/Berlin2008/SessionVA/OSCIC-08_GschaiderRehm.pdf.

[7] R. Kee, M. Coltrin, and P. Glarborg, *Chemically reacting flow: theory and practice*. John Wiley & Sons, 2005.

[8] G. Smith, D. Golden, M. Frenklach, N. Moriarty, B. Eiteneer, M. Goldenberg *et al.*, "Gri 3.0 reaction mechanism."

[9] J. Li, Z. Zhao, A. Kazakov, and F. L. Dryer, "An updated comprehensive kinetic model of hydrogen combustion," *International journal of chemical kinetics*, vol. 36, no. 10, pp. 566–575, 2004.

[10] R. Barlow, S. Meares, G. Magnotti, H. Cutcher, and A. Masri, "Local extinction and near-field structure in piloted turbulent CH4/air jet flames with inhomogeneous inlets," *Combust. Flame*, vol. 162, no. 10, pp. 3516–3540, 2015.

SIMULATION OF COMBUSTION AND CHARGED PARTICLE TRANSPORT UNDER DC ELECTRIC FIELD

YEONGDO PARK[1] , KANG Y. HUH[2]

[1] *Pohang University of Science and Technology (POSTECH) , yeongdo.park@postech.ac.kr*
[2] *Pohang University of Science and Technology (POSTECH) , huh@postech.ac.kr*

Keywords: *Ionic wind, Electric field assisted combustion, Laminar counterflow diffusion flame*

Applying electric field to flame is regarded as a promising technique to enhancing combustion characteristics. A flame applied electric field having better stability[1] and a sooting diffusion flame subject to electric field emitting less amount of soot[2] have been reported.

Ions and electrons generated in hydrocarbon flames are usually not considered in combustion simulations since they are very small in numbers and have little effect unless external electric field is applied. Therefore, eReactingFoam is written based on reactingFoam, one of OpenFOAM's basic solvers for reacting flows, to simulate flames under DC electric field. Models implemented in eReactingFoam and required data are briefly introduced here.

Drift-diffusion approximation is adopted to calculate charged species' drift flux in species transport equation (eq. 1, the last term of its left hand side).

$$\rho\partial_t Y_i + \nabla \cdot \left(\rho\vec{U}Y_i\right) + \nabla \cdot \left(\rho\mu_i\vec{E}Y_i\right) = \nabla \cdot (\rho D_i \nabla Y_i) + \dot{\omega}_i \tag{1}$$

Electric drift of charged species induces net space charge ρ_q. Space charge in applied electric field create momentum source by Lorentz force (See eq. 2, the last term of its right hand side).

$$\rho\partial_t\vec{U} + \nabla \cdot \left(\rho\vec{U}\vec{U}\right) = \nabla \cdot \left(\mu\nabla\vec{U}\right) + \nabla \cdot \left(\mu\left(\nabla\vec{U}^T - \frac{2}{3}\mathrm{tr}\left(\nabla\vec{U}\right)I\right)\right) + \nabla p + \rho_q\vec{E} \tag{2}$$

Electric field $\vec{E}$ is calculated from electro-static potential Φ (eq. 3) and Φ is obtained by solving Poisson's equation (eq. 4). ϵ_0, e, n_i and z_i are repspectively vacuum permittivity, elementary charge, number density of ith species and charge number of ith species.

$$\vec{E} = -\nabla\Phi \tag{3}$$

$$\nabla^2\Phi = -\frac{\rho_q}{\epsilon_0} = -\frac{e}{\epsilon_0}\sum_{i=1}^{N} n_i z_i \tag{4}$$

Hydrocarbon flames generate ions via chemi-ionization reactions [3, 4]. Those reactions should be included in the reaction mechanism to be used. The reaction mechanism consists of GRI-Mech 3.0[5] gas combustion mechanism and 3 chemi-ionization reactions [4] were used for the following results.

Diffusivity and mobility of electrons are calculated using electron scattering cross section data. [6]

Diffusivities of ions are calculated assuming they have the same diffusivity of their parent neutral species. Cantera[7] is coupled with the solver to calculate species diffusivities. Binary diffusivities are calculated using Stockmayer interaction potential and mixture-average formula is used to caculate diffusion coefficients of species transport equations. Mobilities of ions are calculated from their diffusivities using Einstein relation (eq. 5).

$$\frac{D_i}{\mu_i} = \frac{k_B T_i}{q_i} \tag{5}$$

A counterflow diffusion flame under DC electric field [8] was simulated. Figure 1 shows that two perforated metal plates are placed at the ends of two nozzles (for fuel and oxidizer streams) to provide uniform electric field parallel to nozzle axis.

2D-axisymmetric simulation was conducted using wedge type mesh. Dimensions and boudary conditions of the computational domain are described in Figure 2 and Table 1 .

Figure 3 shows overlays of streamlines and CH mass fraction image for simulation cases with and without externally applied electric field. Streamlines show flow modification by ionic wind and CH images imply blue flame position. The figure clearly shows flame position displacement toward the lower nozzle, which agrees with the experiment. However, the model should be impoved to obtain quantitative prediction.

Currently implementation of $(n, 6, 4)$ potential which models ion-neutral interaction and screened Coulomb potential which models interaction between charged particles [9] is in progress to calculate transport properties more accurately.
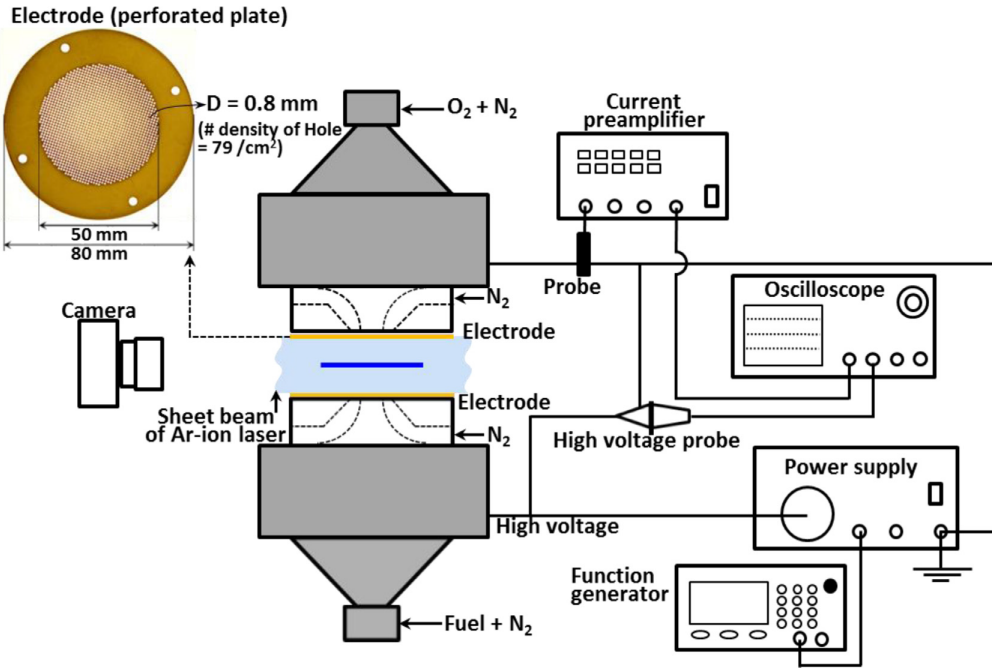
Figure 1: Schematic of experimental setup, taken from [8]
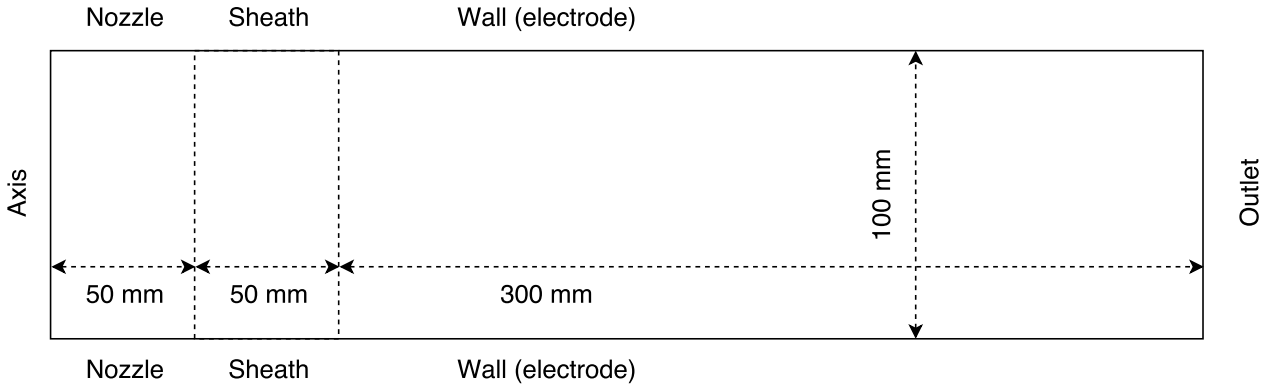
Figure 2: 2D-Axisymmetric simulation domain

Table 1: Boundary conditions

	Upper			Lower		
	Nozzle	**Sheath**	**Wall**	**Nozzle**	**Sheath**	**Wall**
U	20 cm/s	20 cm/s	Slip	20 cm/s	20 cm/s	Slip
T	300 K	300 K	$\frac{\partial}{\partial \vec{n}} = 0$	300 K	300 K	$\frac{\partial}{\partial \vec{n}} = 0$
Y_{CH_4}	0	0	$\frac{\partial}{\partial \vec{n}} = 0$	0.14046	0	$\frac{\partial}{\partial \vec{n}} = 0$
Y_{O2}	0.559989	0	$\frac{\partial}{\partial \vec{n}} = 0$	0	0	$\frac{\partial}{\partial \vec{n}} = 0$
Y_{N_2}	0.440011	1	$\frac{\partial}{\partial \vec{n}} = 0$	0.85954	1	$\frac{\partial}{\partial \vec{n}} = 0$
Y_i (neutral)	0	0	$\frac{\partial}{\partial \vec{n}} = 0$	0	0	$\frac{\partial}{\partial \vec{n}} = 0$
Y_i (charged, +)	0	0	$\frac{\partial}{\partial \vec{n}} = 0$	$\frac{\partial}{\partial \vec{n}} = 0$	$\frac{\partial}{\partial \vec{n}} = 0$	$\frac{\partial}{\partial \vec{n}} = 0$
Y_i (charged, -)	$\frac{\partial}{\partial \vec{n}} = 0$	$\frac{\partial}{\partial \vec{n}} = 0$	$\frac{\partial}{\partial \vec{n}} = 0$	0	0	$\frac{\partial}{\partial \vec{n}} = 0$
Φ	0	0	0	-2400	-2400	-2400

147

Figure 3: Flow modification due to ionic wind induced by DC electric field. Upper electrode at 0 kV in all cases. Left: Lower electrode at 0 kV; Right: Lower electrode at -2.4 kV

References

[1] M. Belhi, P. Domingo, and P. Vervisch, "Direct numerical simulation of the effect of an electric field on flame stability," *Combustion and Flame*, vol. 157, no. 12, pp. 2286–2297, dec 2010. [Online]. Available: http://dx.doi.org/10.1016/j.combustflame.2010.07.007http://linkinghub.elsevier.com/retrieve/pii/S0010218010001951

[2] D. G. Park, B. C. Choi, M. S. Cha, and S. H. Chung, "Soot Reduction Under DC Electric Fields in Counterflow Non-Premixed Laminar Ethylene Flames," *Combustion Science and Technology*, vol. 186, no. 4-5, pp. 644–656, 2014. [Online]. Available: http://www.tandfonline.com/doi/abs/10.1080/00102202.2014.883794

[3] J. Prager, H. Najm, M. Valorani, and D. Goussis, "Structure of n-heptane/air triple flames in partially-premixed mixing layers," *Combustion and Flame*, vol. 158, no. 11, pp. 2128–2144, nov 2011. [Online]. Available: http://linkinghub.elsevier.com/retrieve/pii/S0010218011001039

[4] N. Speelman, M. Kiefer, D. Markus, U. Maas, L. de Goey, and J. van Oijen, "Validation of a novel numerical model for the electric currents in burner-stabilized methaneair flames," *Proceedings of the Combustion Institute*, vol. 35, no. 1, pp. 847–854, 2015. [Online]. Available: http://dx.doi.org/10.1016/j.proci.2014.05.067http://linkinghub.elsevier.com/retrieve/pii/S1540748914000704

[5] G. P. Smith, D. M. Golden, M. Frenklach, N. W. Moriarty, B. Eiteneer, M. Goldenberg, C. T. Bowman, R. K. Hanson, S. Song, J. Gardiner, William C., V. V. Lissianski, and Z. Qin, "GRI-Mech 3.0." [Online]. Available: http://www.me.berkeley.edu/gri{_}mech/

[6] F. Bisetti and M. El Morsli, "Calculation and analysis of the mobility and diffusion coefficient of thermal electrons in methane/air premixed flames," *Combustion and Flame*, vol. 159, no. 12, pp. 3518–3521, dec 2012. [Online]. Available: http://linkinghub.elsevier.com/retrieve/pii/S0010218012002295

[7] D. G. Goodwin, H. K. Moffat, and R. L. Speth, "Cantera: An object-oriented software toolkit for chemical kinetics, thermodynamics, and transport processes," http://www.cantera.org, 2017, version 2.3.0.

[8] D. G. Park, S. H. Chung, and M. S. Cha, "Bidirectional ionic wind in nonpremixed counterflow flames with DC electric fields," *Combustion and Flame*, vol. 168, pp. 138–146, jun 2016. [Online]. Available: http://linkinghub.elsevier.com/retrieve/pii/S0010218016300426

[9] J. Han, M. Belhi, and F. Bisetti, "Numerical modeling of ion transport in flames," *Combustion Theory and Modelling*, vol. 19, no. 6, pp. 744–772, 2015. [Online]. Available: http://www.tandfonline.com/doi/abs/10.1080/13647830.2015.1090018?journalCode=tctm20{&}instName=Cranfield+University

ANALYSIS OF STANDING AND TRAVELING TANGENTIAL WAVE IN A LOX/KEROSENE LIQUID ROCKET ENGINE BASED ON OpenFOAM

GUO KANG-KANG[1],NIE WAN-SHENG[2],LIU YU[3],CHEN PENG[4],SHI TIAN-YI[5]

[1]*Guo Kang-kang, Department of Aerospace Science and Technology, Space Engineering University,*
guokangkang@sjtu.edu.cn

[2]*Nie Wan-sheng, Department of Aerospace Science and Technology, Space Engineering University,*
nws1969@126.com

[3]*Liu Yu, Department of Aerospace Science and Technology, Space Engineering University,*
liuyu@nudt.edu.cn

[4]*Chen Peng, Department of Aerospace Science and Technology, Space Engineering University,*
chenpengxiao@sjtu.edu.cn

[5]*Shi Tian-Yi, Department of Aerospace Science and Technology, Space Engineering University,*
13810980707@163.com

Self-excited first-order tangential (1T) high frequency combustion instability is captured in a high-staged combustion LOX/Kerosene liquid rocket engine based on sprayFOAM solver. The 1T mode combustion instability behaves two different patterns: standing wave and traveling wave. In the design operation condition, the value of oxygen-fuel ratio (O/F) is 2.5, all injectors share the same propellant mass flow, and there is no oscillatory combustion in the numerical calculation results. The chamber pressure between numerical calculation and experiment shows a good agreement, which validate the numerical model. When the fuel mass flow of two injectors which are along the same diameter and locate at the edge of injector face is changed, severe unstable combustion occurs and nodal diameter remains consistent, which is a standing 1T wave mode. When the value of O/F increases to 4.4 and the propellant distribution is completely uniform, there is also a high frequency combustion instability whose nodal diameter is spinning, demonstrating a traveling 1T wave mode. Once the combustion instability occurs, no matter what kind of wave modes, thermo-acoustic coupling forms, and the pressure and heat release oscillate totally in phase temporally and couples spatially. It is the coupling process between heat release and combustion that results in the combustion instability.

A PRESSURE-BASED SOLVER FOR COMPRESSIBLE THREE-PHASE FLOW WITH PHASE CHANGE

BINGSHENG YE[1,2], YIWEI WANG*[1,2], CHENGUANG HUANG[1],JIAN HUANG[1]

[1] *Institute of Mechanics, Chinese Academy of Sciences, Beijing, 100190, China*

{yebingsheng, wangyw , huangcg , huangjian }@imech.ac.cn

[2] *School of Engineering Science, University of Chinese Academy of Sciences, Beijing, 100049, China*

Keywords: *Cavitating Flow, Shedding Mechanism, Shock Propagation*

Introduction

Cavitation is a common phenomenon capturing the attention of industry and academia. In general, it results in negative and undesirable effect on structure, like erosion on structure. To reduce or avoid damage caused by cavitation, research works have been carried out for a long period of time, establishing several theories. Since a few practical solvers which consider the effect of phase change are available in OpenFOAM, most problems involving cavitation can be investigated through numerical method. However, recent research progress and difficulty in engineering introduce new requirements. On the one hand, cavitation near free surface has become a heat topic in the field of high speed hydrodynamics, requiring a solver able to deal with three phases, including liquid(water) and other two kinds of gas (vapor and non-condensable gas), as well as considering effect of phase change. On the other hand, in the interesting work of Genesh et al [1] a high temporal resolution X-ray device was used to investigate the shedding mechanism of cavity by measuring density inside, which proposes the concept of cavity shedding induced by shock, quite different from previous agreement that re-entry jet dominates the process of cavity shedding. To reflect the propagation of shock in numerical simulation, compressibility should be taken into consideration. Since none solver available can satisfy the demands above, a new useable one is in urgent need.

Method

A pressure-based solver for compressible three-phase flow with phase change is developed based on the utility of *interPhaseChangeFoam* and *compressibleInterFoam*. Besides the effect of free surface and shock propagation in cavitating flow mentioned above, many other relevant research can be also conducted with this new solver.

Solvers can be density-based or pressure-based. The density-based solvers were widely used in hypersonic problems in aviation. But they would have difficulty when Mach number is not that high. Within the frame of OpenFOAM, *cavitatingFoam* is a density-based solver which consider phase change, but quite unstable in subsonic condition. In several cases tested iteration cannot obtain convergence unless a tiny time step is adopted which however leads to another trouble that calculation will never be finished. This situation is due to stiffness of matrix given by density-based algorithm when Mach number is low. Although it can be overcome with some specialized solvers implementing pre-conditioning approach [2], we still prefer to pressure-based solvers which are much more stable itself in many tests. Pressure-base method is firstly designed to deal with incompressible flows. But recent research has expanded their application to flows at all speeds [3]. Fortunately, most solvers considering compressibility in OpenFOAM are pressure-base, providing convenience to establishing a new solver for our requirement.

A few solvers in OpenFOAM are able to deal with a system of more than two phases. A member function named *MULES:correct* is first called to calculate the flux of volume fraction of each phase, followed by use of *MULES:limitSum* to adjust that flux so that in the next step where the volume fraction transport equation of each phase is solved by *MULES:explicitSolve* the sum can be ensured to be nearly 1. Some tests indicate that this method will encounter some difficulties if phase change is involved, e.g. much less cavity than experimental observation. So in our solver only two phases, water and non-condensable gas, are consider to have independent volume fraction, namely α_{vapor} is obtained through the constraint $\sum \alpha_i = 1$.

Results and discussion

A case about cavitating flow around an axisymmetric projectile is conducted by this new solver, also compared with the numerical result from *interPhaseChangeFoam* as well as the experimental result based on the SHPB (Split Hopkinson Pressure Bar) technology and high-speed photography. The inflow velocity is 18.5m/s with a cavitation number about 0.572. A 2D axisymmetric mesh is used. Figure 1 shows the comparison of variety of cavity shape over time，reflecting good agreement with each other, especially in the first half cycle. The length of cavity versus time is also

measured, indicating that whether the compressibility is considered or not, the numerical results almost coincide but a shift exists when they are compared with the experimental result.
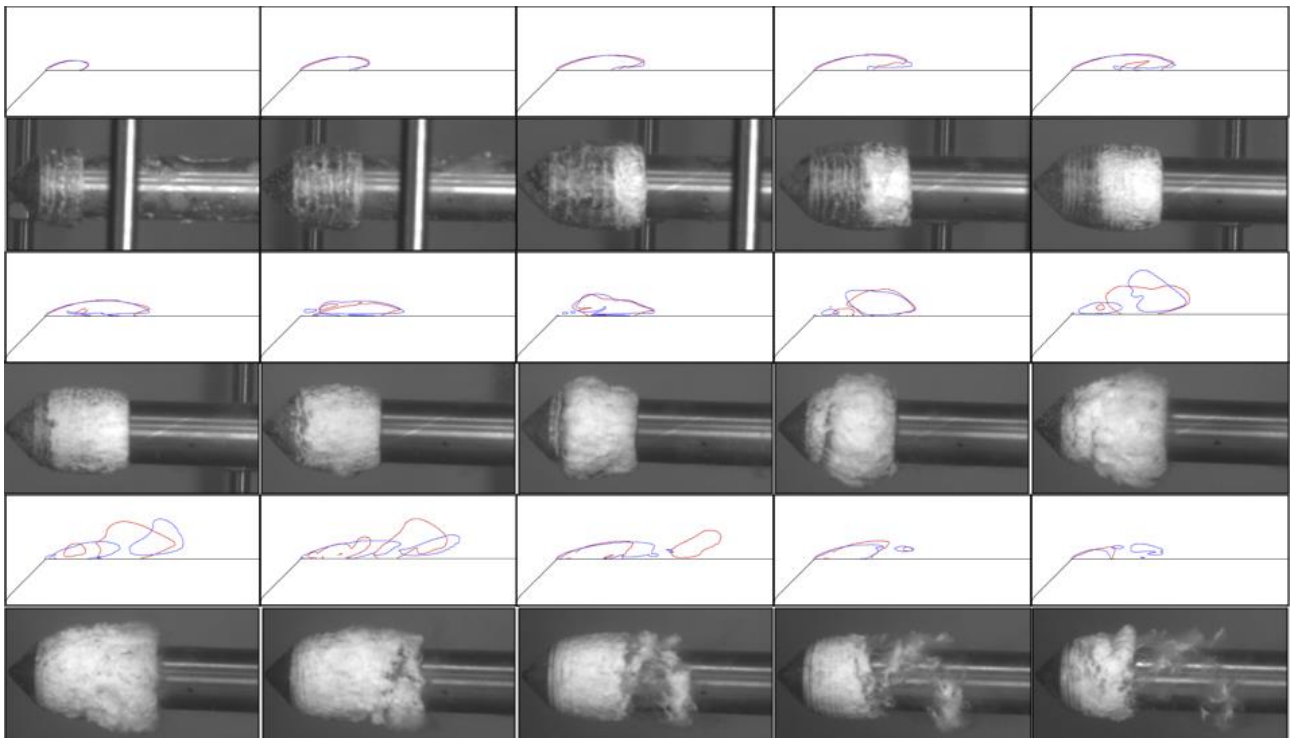
Figure 1: Time sequences of cavity shape obtained from a new solver (red lines), *interPhaseChangeFoam* **(blue), compared with experimental observation**
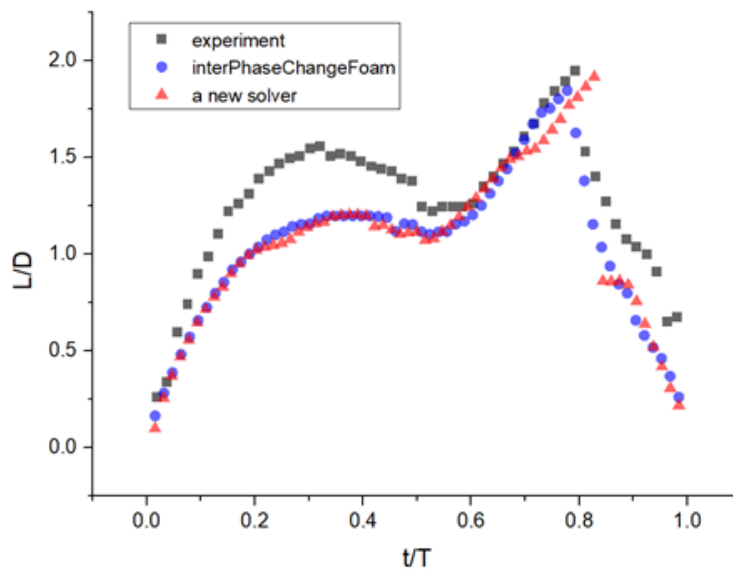
Figure 2: Comparison of cavity length

Most previous research works were focused on the shedding mechanism induced by the re-entry jet, which is usually considered as the most important factor on the transition [4]. Recently proposed concept of shedding induced by shock propagation has impelled academia to reassess the mechanism in cavitation instability. In our results, different mechanisms above is found. In the first half cycle, the re-entry jet whose formation is promoted by the inverse pressure gradient afterwards is attached to trailing edge of the cavity and finally cut it off. However, the last half cycle seems to be quite different. A part of the cavity shedding previously collapses, leading to formation and propagation of a shock. When intersected by high pressure of the shock, the rest part also begins to collapse from its closure as shown by high condensation rate in Figure 3. The velocity field indicates that although the re-entry jet still generates, its head has a distance from trailing edge of the cavity therefore contribute little in shedding process. So it is more believable that the last half is dominated by effect of shock.

(a)

(b)
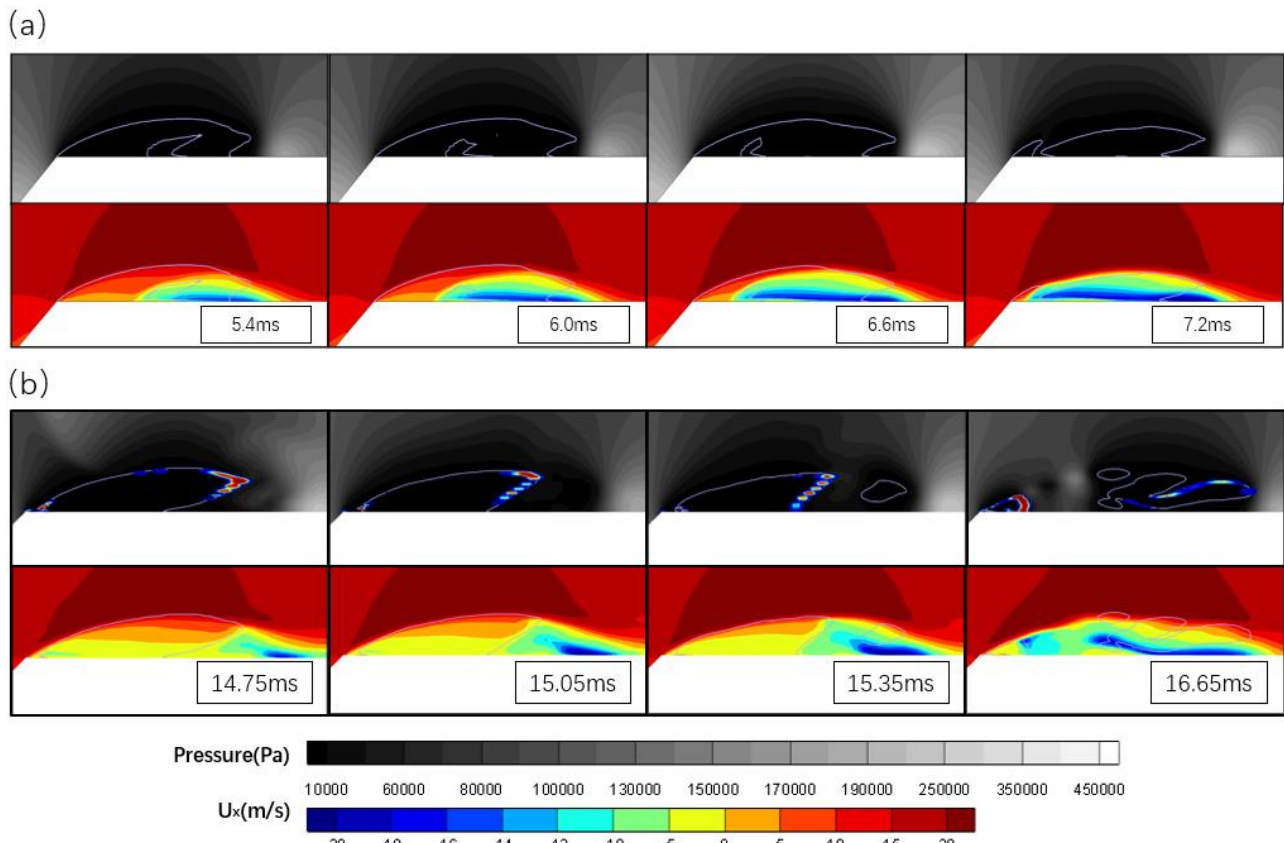
Figure 3: Pressure fields with condensation rate and velocity fields: (a)the first half cycle, (b)the last half cycle

Acknowledgements

References

[1] H. Ganesh. Bubbly shock propagation as a cause of sheet to cloud transition of partial cavitationand stationary cavitation bubbles forming on a delta wing vorte. PhD thesis, University of Michigan, 2015.

[2] A. Gnanaskandan, K. Mahesh, A numerical method to simulate turbulent cavitating flows, International Journal of Multiphase Flow, Volume 70, 2015.

[3] F. Moukalled, M. Darwish, A High-Resolution Pressure-Based Algorithm for Fluid Flow at All Speeds, Journal of Computational Physics, Volume 168, Issue 1, 2001.

[4] C. E. Brennen. Cavitation and Bubble Dynamics, USA:Oxford University Press, 1995.

[5] Arndt, Song et al. Instability of partial cavitation- A numerical & experimental approach. Symposium on Naval Hydrodynamics, 599-615, 2001.

VERIFICATION OF IMMERSED BOUNDARY METHOD AND NUMERICAL SIMULATION OF NEWTONIAN FLUID IN MICROCHANNELS BY OPENFOAM

DI-LIN CHEN*, JIE LI , LI XU, XIN KANG, YI ZHOU

[1] *School of Energy and Power Engineering, Wuhan University of Technology, No.1040 Heping Ave, Wuchang District, Wuhan 430063, China,chen326540039@163.com*

Research on Microfluidics and Nanofluidics has advanced rapidly over the past two decades, which is a cutting-edge subject and has great application potential in biochemistry, human health, new energy, advanced materials, and so forth. The IBM (immersed boundary method) allows for a precise representation of fixed and moving solid obstacles embedded in the physical domain, using uniform or stretched Cartesian meshes. We recall that the IBM formulation chosen in this work is the discrete forcing approach. The motion of particles suspended in fluid in straight and curved microchannels was simulated by immersed boundary method, and several laws of particle in flow, including the distribution and velocity variation characteristics were obtained. In addition, various 2D and 3D well-documented test cases were carried out to validate IBM solver, based on simulated results of different ratios of Re to viscosity. In summary, the mathematical model of microfluid, in the movement of straight and curved microchannels, is established and further explored in theoretically and experimentally, leading a foundation for the optimal design of microfluidic control.

AN OPTIMIZED CHEBYSHEV SMOOTHER IN GAMG SOLVER OF OPENFOAM ON SUNWAY TAIHULIGHT SUPERCOMPUTER

HANFENG GU[1], HU REN[1], CHANGXI LIU[1,2], WEI XUE[1,3], XIN LIU[1,4]

[1]*National Supercomputing Center in Wuxi, Wuxi 214072, China, hanfenggu@gmail.com*
[2]*Beihang University, Beijing 100191, China*
[3]*TsingHua University, Beijing 100084, China*
[4]*Wuxi Jiangnan Institute of Computing Technology, Wuxi 214000, China*

Abstract

The Sunway TaihuLight supercomputer is the first system with a peak performance greater than 100 PFlop/s and has been the fastest computer in the world since June 2016[1, 2]. The computer node of Sunway system is based on a homegrown heterogeneous many-core processor called SW26010, which consists of 260 processing elements that including both the 4 management processing elements (MPEs) and 256 computing processing elements (CPEs). OpenFOAM is a leading open source software for Computational Fluid Dynamics(CFD) but not fully compatible with processor SW26010 since its heterogeneity. Each CPE has its own local device memory (LDM) space and one needs control manually the data on each CPE's LDM to take advantage of powerful accelerating ability provided by these CPEs. Some efforts have been paid to optimize the hot-spots of OpenFOAM on SW26010 and achieve significant performance improvement. In some cases, the performance of the CPE cluster on SW26010 is better than that on a single core of Intel(R) Xeon(R) CPU E5-2695 v3.[3].

GAMG solver in OpenFOAM

GAMG (Geometric agglomerated Algebraic MultiGrid) algorithm (see Figure 1) is the main solver in OpenFOAM, which is usually used to solve the pressure correction Poisson equation. According to the profiling results, the smoother usually takes more than half in GAMG solving time. The only default smoother in the latest OpenFOAM version 5.0 is Gauss-Seidel, which is difficult to maintain good parallel efficiency in the context of unstructured meshes due to its natural sequentiality.[4]. In OpenFOAM, the Gauss-Seidel smoother is designed to be as the hybrid of Jacobi-type iteration for processor boundary points and real Gauss-Seidel-type iteration for processor inner points, which make its convergence path depend on the participation of the matrix and even to diverge if the problem size per processor is not large enough[5]. The worse situation can be found on SW26010 if we want to take advantage of powerful accelerating ability provided by the CPEs. The data have to be assigned to CPEs and thus the communication between CPEs become very complicated.

Chebyshev smoother in OpenFOAM

Polynomial smoothers become the nature choice in modern heterogeneous parallel computing system for a couple of reasons. Firstly, they don't need to compute communication-intensive inner products for the determination of the recurrence coefficients, and they only need the matrix-vector multiplication, which is often highly-optimized. Secondly, they are unaffected by the parallel partitioning of the matrix, the number of parallel processes, and the ordering of the unknowns[5]. The main drawback is the cost of computing the upper and lower bounds of eigenvalues of the matrix.

To the authors' knowledge, the polynomial type smoother in OpenFOAM has not been implemented. In this paper, we present an implementation of a polynomial smoother in OpenFOAM: the Chebyshev smoother[6] combined with the Preconditioned Conjugate Gradient (PCG) solver. Figure 2 shows the algorithm, where the PCG loops are used to obtain the largest eigenvalues since it has same upper bound as for the Chebyshev iteration in the symmetric case[7, 8]. While the lower bound of eigenvalues in Chebyshev iteration is not so important since the smoother of MultiGrid in each level only eliminates the errors compared to the local mesh size. One can simply divide the largest eigenvalue by a constant value to obtain the lower bound of eigenvalue in that MultiGrid level. The MultiGird convergence does not seem very sensitive to this estimate[4].

pre-smoothing: $A^h \tilde{u}^h = b^h$
scaling: $\tilde{u}^h = sf * \tilde{u}^h$
residuals: $r^h = b^h - A^h \tilde{u}^h$

scaling: $\tilde{v}^h = sf * \tilde{v}^h$
approximation corrected: $\bar{u}^h = \tilde{u}^h + \tilde{v}^h$
post-smoothing: $A^h \bar{u}^h = b^h$

Ω^h :

restriction:
$r^H = I_h^H r^h$

interpolation:
$\tilde{v}^h = I_H^h \tilde{v}^H$

Ω^H :

solving(smoothing): $A^H \tilde{v}^H = r^H$
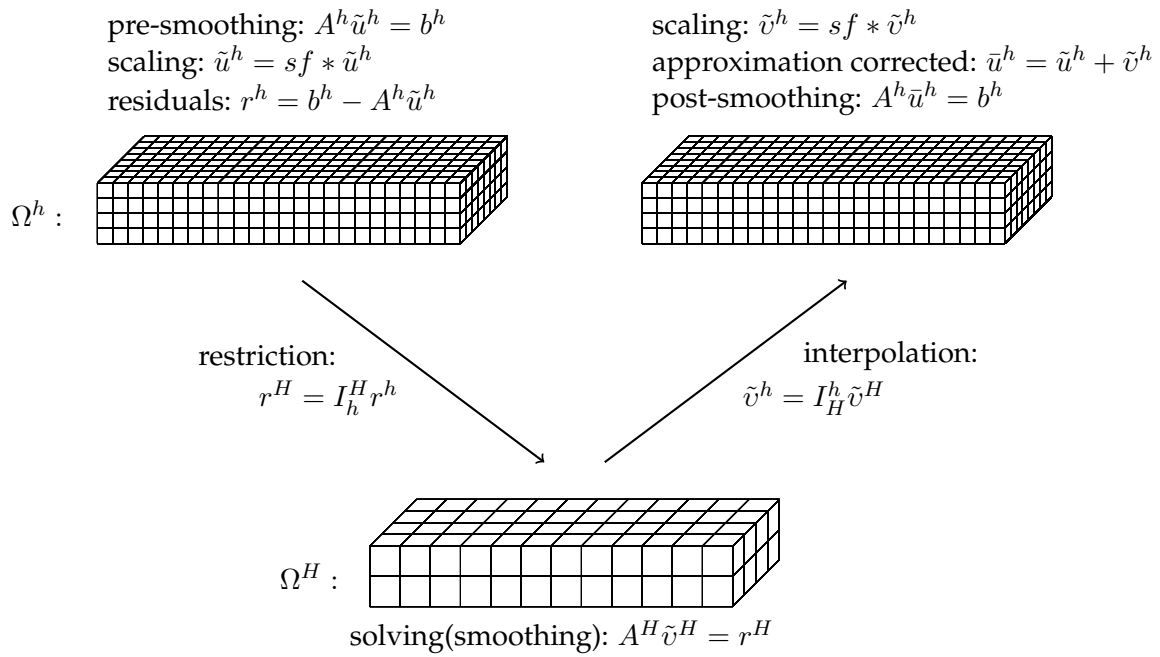
Figure 1: A two-level GAMG example in OpenFOAM.

smooth::new

start

if A keeps same? — no → PCG loops

yes

if λ_{max} computed? — no →

yes

λ_{max}

Cheby loops

check residuals

no

if converged? ← check residuals

yes

exit
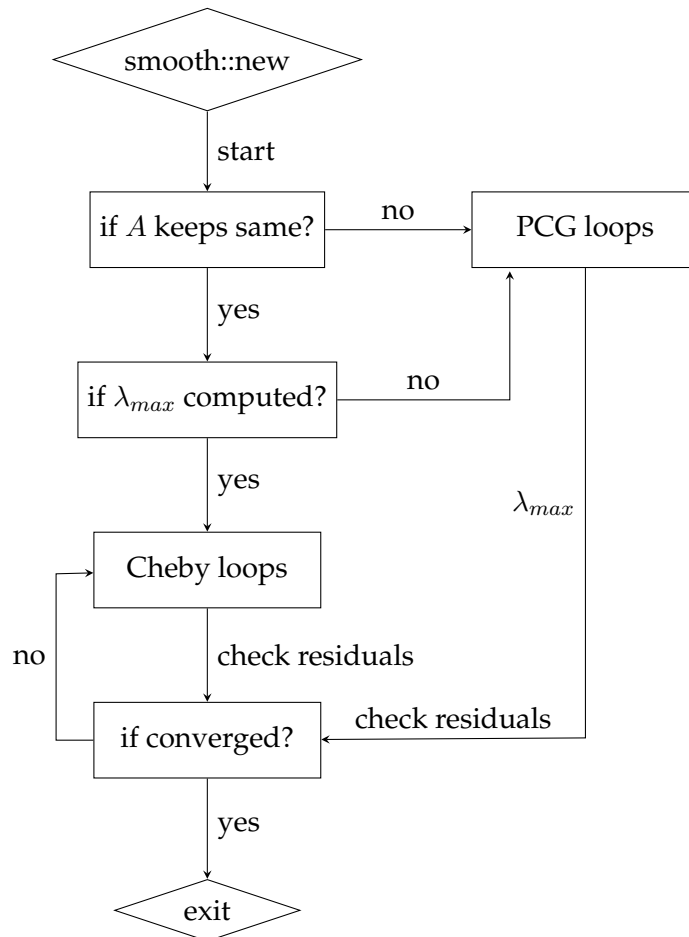
Figure 2: Chebyshev smoother combined with PCG in OpenFOAM.

Implementations and Results

The advantages of Chebyshev smoother make it easier to be fully parallelized compared to Gauss-Seidel smoother. The kernel in Chebyshev smoother is the matrix-vector multiplication, which has been already fully

accelerated in previous work done by C. Chang[9]. For the rest of continuous vector operations, we proposed a unified accelerating interface to involve all of the rest kernels. To improve the efficiency of obtaining the largest eigenvalue, we also modified the implementation of PCG to reduce the global synchronization according the algorithm proposed in[10]. The Table 1 shows that the optimized Chebyshev smoother is 3.55x faster the Gauss-Seidel smoother.

Table 1: Results comparison between Gauss-Seldel and Chebyshev smoother in a simpleFOAM case

	Gauss-Seidel	Chebyshev
Mesh	50 million, unstructured	
MPIs	256	256
time (seconds)	70.49s	19.88s

References

[1] H. Fu, J. Liao, J. Yang, L. Wang, Z. Song, X. Huang, C. Yang, W. Xue, F. Liu, F. Qiao *et al.*, "The sunway taihulight supercomputer: system and applications," *Science China Information Sciences*, vol. 59, no. 7, p. 072001, 2016.

[2] J. Dongarra, "Sunway taihulight supercomputer makes its appearance," *National Science Review*, vol. 3, no. 3, pp. 265–266, 2016.

[3] D. Meng, M. Wen, J. Wei, and J. Lin, "Hybrid implementation and optimization of openfoam on the sw26010 many-core processor," 2016.

[4] M. Adams, M. Brezina, J. Hu, and R. Tuminaro, "Parallel multigrid smoothing: polynomial versus gauss–seidel," *Journal of Computational Physics*, vol. 188, no. 2, pp. 593–610, 2003.

[5] A. H. Baker, R. D. Falgout, T. V. Kolev, and U. M. Yang, "Multigrid smoothers for ultraparallel computing," *SIAM Journal on Scientific Computing*, vol. 33, no. 5, pp. 2864–2887, 2011.

[6] M. H. Gutknecht and S. Röllin, "The chebyshev iteration revisited," *Parallel Computing*, vol. 28, no. 2, pp. 263–283, 2002.

[7] R. Barrett, M. W. Berry, T. F. Chan, J. Demmel, J. Donato, J. Dongarra, V. Eijkhout, R. Pozo, C. Romine, and H. Van der Vorst, *Templates for the solution of linear systems: building blocks for iterative methods*. Siam, 1994, vol. 43.

[8] J. A. Scales, "On the use of conjugate gradient to calculate the eigenvalues and singular values of large, sparse matrices," *Geophysical Journal International*, vol. 97, no. 1, pp. 179–183, 1989.

[9] C. Liu, B. Xie, X. Liu, W. Xue, H. Yang, and X. Liu, "Towards efficient spmv on sunway many-core architectures," in *Proceedings of the 32th ACM on International Conference on Supercomputing, ICS'18, Beijing, China, June 12 - 15, 2018*, 2018.

[10] E. D'Azevedo, V. Eijkhout, and C. Romine, "Conjugate gradient algorithms with reduced synchronization overhead on distributed memory multiprocessors," 1999.

SIMULATION OF GAS-SOLID FLOW IN A TRANSFER CHUTE BASED ON CFD-DEM COUPLING METHOD

SHAN ZHANG[1], XIAOLING CHEN[2*], FANHAO DENG[3] ,ZEKUN WANG[4*]

[1]*Beijing Key Laboratory of Process Fluid Filtration and Separation, China University of Petroleum - Beijing, Beijing, China , Hky_shan@163.com*

[2]*Beijing Key Laboratory of Process Fluid Filtration and Separation, China University of Petroleum - Beijing, Beijing, China ,cxling612@126.com*

[3]*Beijing Key Laboratory of Process Fluid Filtration and Separation, China University of Petroleum - Beijing, Beijing, China ,dengfanhao1119@163.com*

[4] *BIC-ESAT & State Key Laboratory for Turbulence and Complex Systems, College of Engineering, Peking University, Beijing , China, zekunwang@pku.edu.cn*

[Abstract] This paper focuses on the simulation of gas-solid two-phase flow in the transfer chute based on the coupled CFD-DEM method. The Computational Fluid Dynamics (CFD) is used to solve the gas phase through the open source software OpenFOAM. Discrete Element Method (DEM) is used to solve the particulate flow, through the open source software LIGGGHTS. This method can simulate the complex gas-particle, particle-particle and particle-wall interaction in the transfer chute at mesoscopic scale. Compared with the previous experimental results, the maximum error is 13%. It proves that the method can be used to analyze the gas-solid two-phase flow in the transfer chute .

Introduction

Bulk solids handling is a crucial stage during coal, ore processing and chemical engineering in various industrial fields. Typically, dust is generated when the bulk materials loaded, dumped and transferred. Since belt conveyors typically operate with the lowest overall transport and maintenance cost per ton, they are extensively employed to transport bulk materials in a great many industries, particularly those associated with mining and mineral processing. In the case of belt conveyors, an area of particular concern for dust control occurs during transfer of bulk material from one conveyor to another, namely, transfer point. Usually, a chute is employed at a transfer point to make sure that the loads be discharged in a centralized stream and in the same direction as the receiving conveyor. Therefore, the performance of transfer chutes has a significant impact on not only the efficiency of conveyor belt systems, but also on the level of fugitive dust emissions. In view of the current stringent standards concerning the environment, occupational health and safety, the study of the dust generation and discharge in a transfer chute is a matter of high importance to control dust emission during bulk material handling.

At present, the main methods to elimination dusts are emission and blockage. Many dust removal devices are designed to control dust emission to a certain extent, but produce higher economic costs. Practice shows that the a reasonable design of the transfer chute can not only reduce the amount of dusts produced, but also greatly reduce the energy consumption generated by the use of dust removal equipments [1,2]. However, it is difficult to further improve the design of transfer chutes for lack of the understanding of the mechanism of dust generation and the dust dissipation law in the transfer chute. Moreover, due to the existing experimental conditions and test level limitations, experimental research is expensive and time-consuming, and is difficult to obtain particle movement information at the meso scale such as particle velocity, concentration and interacting force.

With the rapid development of computer technology, numerical simulation has become another important method in gas-solid two-phase flow research, which serves as a powerful supplement to experimental research. Wang [3] had applied DEM method to simulate and optimize the bulk material transfer system by using the EDEM, but he did not consider the influence of the gas on the bulk material delivery process. Chen [4] used two-fluid model to simulate the gas-solid flow in the transfer chute, and evaluated the dust-removal effect of different transfer chutes. However, due to the limitation of the model per se, we cannot analyze the issue at particle scale. In this paper, the CFD-DEM coupling method is used to study the mechanism of gas-solid two-phase flow at meso-scale. The airflow in the transfer chute entrains particles, and the effect of gas on the entrainment of particles is different under different gas velocities. In this paper, the mechanism of dust generation is analyzed numerically by the obtained gas velocity and volume fraction at the bottom of the transfer chute.

There are two different substances in the flow of the transfer chute, air and particles. From a mesoscopic point of view, the gas can be treated as a continuous medium, and its physical and mechanical properties, such as velocity, pressure, temperature, density, etc., also experience continuous changes with the position. The motion and energy laws are described by mass conservation equation, Navier-stokes equation and energy equation. The particles flow are composed of a large number of discrete particles as discrete phase, and its velocity, position, motion and force are

described by Newton's third law and constitutive relation, respectively [5]. Therefore, this paper uses the CFD method to solve the gas phase through the open source codes OpenFOAM. and uses DEM method to solve the particle through open source codes LIGGGHTS. This method not only considers the complex flow of gas, but also simulates the complex interaction between gas-particle, particle-particle and particle-wall.

The step-by-step CFD-DEM implementation route is shown as follows:

(1) Predict momentum exchange in CFD

(2) Obtain particle velocity position information by solving Newton's Law in DEM

(3) Obtain the particle information in the DEM, identify the grid ID of the particle and set the porosity in CFD

(4) Select the reasonable force model in CFD to carry out momentum exchange and transfer to DEM to continue solving

(5) Solve the whole flow field based on the Finite Volume Method (FVM) in CFD

Simulation

The gas-solid two-phase flow mechanism in the transfer chute is studied based on the CFD-DEM coupling method. According to the previous experimental results, the iron ore particles with diameter of 4mm were selected, and the shape of the particles was assumed to be spherical. The geometry of the transfer chute is shown in Figure 1, and its height is 2.05m. Hertz-Mindlin soft sphere model is adopted as the contact model, and the particle physical parameters required in the simulation are shown in table 1. Potapov verified the influence of different turbulence models on gas-solid two-phase flow, the results show that the turbulence model has no great effects on the simulation result [6]. In this simulation, the k-ε turbulence model and the Gidaspow drag model were adopted to conduct the simulation study.

Table1: Particle Physical Property Parameters

Parameters	Units	Value
Particle density	Kg/m^3	3948
Sliding friction coefficient		0.48
Rolling friction coefficient		0.21
Recovery coefficient		0.48
Mass flow rate	Kg/s	4.19

First, the CFD-DEM simulation of a single particle is carried out to verify its feasibility and the grid independence of the grid in CFD. Su[5] compared the effects of different grid scales on particle settling velocity in regular rectangular geometry, results show that the particle settling velocity does not change with the increase of ratio, when the ratio of mesh size to particle diameter is greater than 5 for large scale particles. Multiple grids are employed to conduct mesh independence study, the results show that when the number of grids reaches around 18000, both the accuracy and efficiency can be obtained. Thus, this grid with 18426 grids was used in subsequent simulations. The grid partitioning is shown in Figure 2.
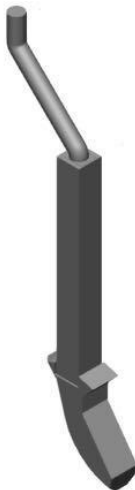
Figure 1: The geometry of the chute
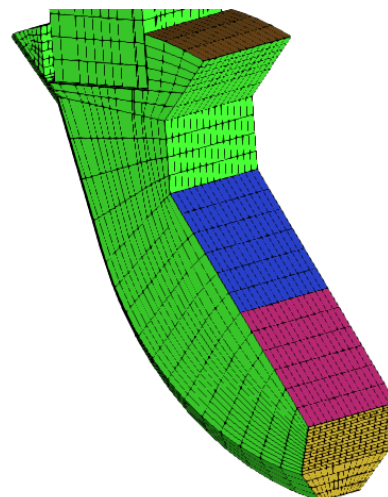
Figure 2: Grid Partitioning

Results and discussion

Through the CFD-DEM coupling simulation we obtained the gas velocity in the transfer chute. In addition, We used PIV measurement technology to measure the gas velocity at the bottom of the transfer chute.Comparing the simulation results with the experimental data, as shown in Figure 3, it shows that the simulation result is comparable

with the experimental result and the maximum error is 13%. It is proved that the gas-solid two-phase flow in the transfer chute can be well predicted by using the CFD-DEM coupling method. It can be used as a powerful tool to evaluate the effect of transfer chute on the particulate flow.
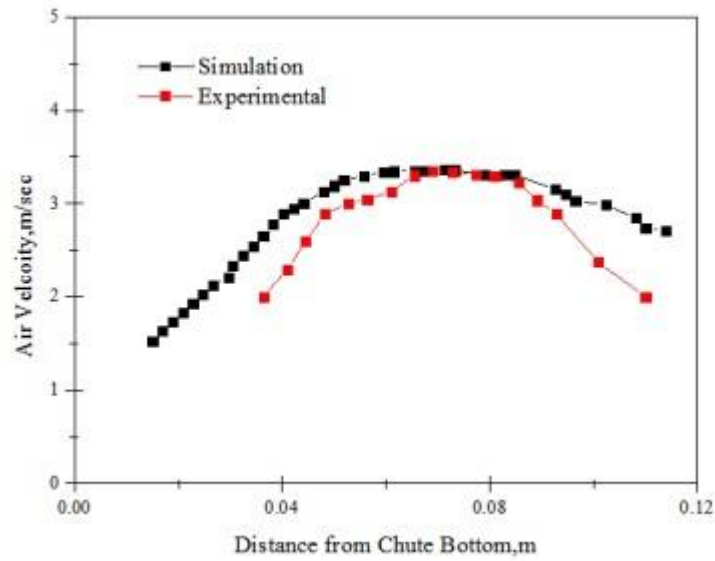
Figure 3: comparison between simulated and experimental

In addition, some other were also obtained through simulation, which are illustrated in the figures4-5. Figure 4 is the gas phase and the particle phase velocity. We can not only obtain the continuous change of gas velocity, but also the velocity and position information of each particle. Figure 5 is the gas volume fraction. These data can help to predict the dust generation in transfer chute dust.
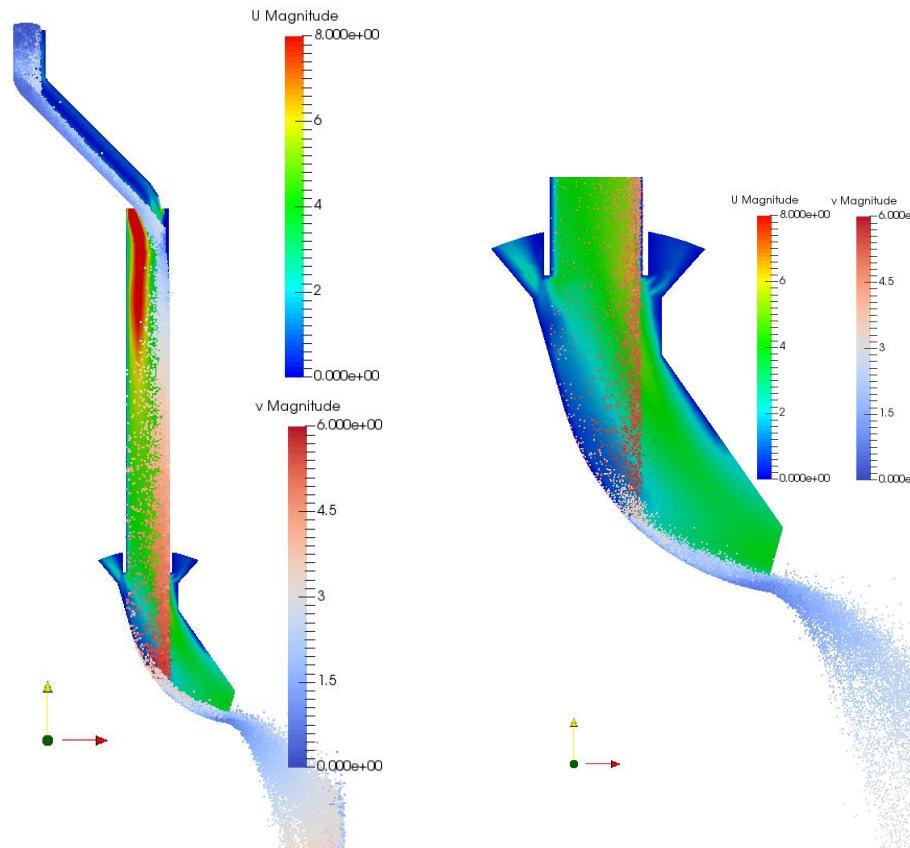
Figure 4: gas phase and particle phase velocity (U-gas velocity; V-phase velocity)
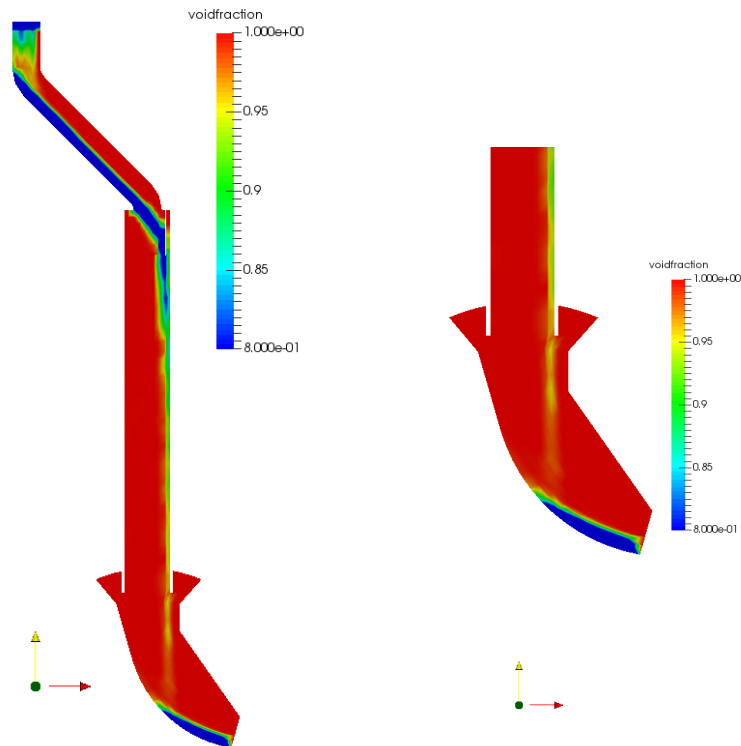
Figure 5: Gas volume fraction

Conclusion

From the above, the gas-solid two-phase flow simulation in the transfer chute can be used to obtain the internal flow parameters on the mesoscopic scale based on the CFD-DEM coupling method. Compared with the two-fluid model, it not only reduces the model hypothesis, but also can obtain more information on the mesoscopic scale, such as the speed, position and force of each particle, which can make the results more accurate. Using this method, different parameters can be changed to simulate the flow mechanism in the transfer chute, which can provide possible optimizations for dust emission controllong.

Acknowledgements

References

[1] Maynard, E.P., Designing Transfer Chutes to Eliminate Spillage and Dusting. Bulk Solids Handling,2003. 23(SPECIAL): p. 28-34.

[2] Petro, G., Baxter, T. and Cabrejos, F., Chutes: The ultimate dust control. Powder and Bulk Engineering, 2004. 18(7): p. 36-46.

[3] Wang, K.L. Study on DEM simulation of unloading trajectory and reprint process of belt conveyor [D]. Northeastern University, 2014..

[4] Chen, X.L., Wheeler, C.A., Donohue, T.J., et al., Evaluation of dust emissions from conveyor transfer chutes using experimental and CFD simulation. International Journal of Mineral Processing, 2012.110-111: p. 101-108..

[5] Su, D.S. Study on flow and sediment movement based on CFD-DEM coupling simulation method [D]. Tianjin University, 2015.

[6] Potapov, A., Chen, X., Donohue, T., et al. Computer simulation of airflow around transfer chutes via linked discrete element method - Computational fluid dynamics approach. in 11th International Conference on Bulk Materials Storage, Handling and Transportation, ICBMH 2013, July 2, 2013 - July 4,2013. 2013. Newcastle, NSW, Australia: Centre for Bulk Solids and Particulate Technologies (CBSPT).

NUMERICAL INVESTIGATION OF AIR BUBBLES EVOLUTION AND COALESCE FROM SUBMERGED ORIFICES BASED ON OPENFOAM

FENG PAN, YING HE[*], LI-ZHONG MU

* School of Energy and Power Engineering, Dalian University of Technology, heying@dlut.edu.cn

Summary

With the help of the Volume of Fluid (VOF) model in OpenFOAM framework, the air bubbles evolution and coalescence behaviours from submerged orifices has been investigated. First, the air bubble formation and rising process from a submerged orifice with different air flow rate has been simulated according to Zhang's experiments. Results show that, with the increase of the air flow rate, collision and vertical coalescence occur as a result of the reinforced wake flow. The numerical experiment of the different spacing of the twin orifice shows that, horizontal coalescence only occur in the range when S/D<1.5. The results can provide useful reference for the mechanism of coalescence in boiling process.

1 Introduction

Due to the vast majority of nucleation sites with high randomness on the boiling surface and the complex interactions of the multiple sub-processes, the heat transfer mechanism during boiling process is still challenging. A single bubble on an active nucleation site eliminates the interaction of the surrounding bubbles, thus offering clearer insight into the details of bubble nucleation, growth and departure processes than natural surfaces with many cavities. Shoji and Zhang [1] [2] manufactured isolated cavity on copper and silicon surface, investigating the effect of cavity's shape, size and depth on bubble growth and departure processes. Further investigation was conducted by arranging twin or triple artificial cavities with different spacing and arrangement to make clear the thermal interaction between nucleation sites and the hydrodynamic interaction between vapour bubbles. Three kinds of coalescence were found near the boiling surface: horizontal coalescence, vertical coalescence and declining coalescence. A dimensionless indicator, S/D was introduced as the ratio of the active sites spacing to the single bubble departure diameter. It is shown that the horizontal and declining coalescence only occur in the range when S/D<1.5 in the artificial surface. Similar experiment has been conducted on natural copper surfaces, recently. It is found that in the horizontal coalescence cases, the distances between the adjacent actives sites are less than 1.5 times of the single bubble departure diameter, which is consistent with Shoji's results on artificial surfaces. Besides, it can been also observed that, vertical coalescence only occurs in high heat flux region, with horizontal coalescence and declining coalescence accompanied at the same time.

In fact, the bubble behaviour is not only influenced by the phase change phenomenon on the boiling surface but also the two-phase fluid flow pattern. Zhang [3] investigated successive air bubbles formation, coalescence and departure behaviours from a submerged orifice, whose air flow rate was in the regime 100 cc/min ~ 2000 cc/min. As an effect of the wake flow, the interaction between air bubbles in vertical leads to multiple periods on the growing bubble. In Zhang's work, a force balance model was developed to describe the bubble's evolution in isothermal flow without phase change, including formation, interference, collision and coalescence. In current work, a series of numerical experiments based on OpenFOAM have been carried out to investigate the bubble behaviour from single submerged orifice. Subsequently, the coalescence processes of bubbles from two orifices are simulated. The criteria that horizontal coalescence occurs in isothermal system has been demonstrated. Current work can reveal the mechanism in the horizontal coalescence during boiling process from the perspective of hydrodynamic factor.

2 Numerical Model

interFoam is a standard isothermal two-phase flow solver based on Volume of Fluid (VOF) method in OpenFOAM. It is assumed that the physical properties of single phases are independent with local temperature. The two-phase fluid is treated as a mixture with homogeneous but not constant properties in a certain cell. In the VOF method, fluid volume function α (the volume fraction of the liquid phase in a cell in case of air-liquid two phase flow) is introduced as an indicator to distinguish the two phases and interface. The mixture density is defined as:

$$\rho = \left(1-\alpha_1\right)\rho_g + \alpha_1\rho_l \tag{1}$$

The Navier-Stokes equations of incompressible, Newtonian fluids are given as

$$\frac{\partial \rho}{\partial t} + \nabla \cdot \left(\rho u\right) = 0 \tag{2}$$

$$\frac{\partial \left(\rho u\right)}{\partial t} + \nabla \cdot \left(\rho u u\right) = -\nabla p + \nabla \cdot \tau + \rho g + f_\sigma \tag{3}$$

The fluid volume function equation (4) can be derived from (1) and (2), as

$$\frac{\partial \alpha}{\partial t} + \nabla \cdot (\alpha u) = 0 \tag{4}$$

In the above equations, f_σ is surface tension term. Through the Continuum surface Force (CSF) model embedded in the solver, the surface tension in the two-phase interface is turned into the adjacent control volumes as a body force expressed in equation (5):

$$f_\sigma = \sigma \kappa \nabla \alpha \tag{5}$$

Where κ is the curvature in the two-phase interface. It can be calculated as follows,

$$\kappa = -\nabla \cdot \frac{\nabla \alpha}{|\nabla \alpha|} \tag{6}$$

The governing equations are discretized by finite volume method. At each time step, PIMPLE algorithm embedded in OpenFOAM is called to deal with the pressure–velocity solution loop. The two-phase fluid mixture properties is updated first. Then the fluid volume function equation is solved employing MULES (multidimensional universal limiter with explicit solution) limiter to guarantee the boundedness of fluid volume function. Next, the velocity field and the pressure field are corrected for several iterative steps. Then the turbulence model is updated and next time step will begin.

3   Results and discussions
3.1   Single bubble behaviour
The air bubble formation and rising process from a submerged orifice with different air flow rate has been simulated according to Zhang's experiments [3] at first. The system is supposed at a uniform temperature system and the liquid is water, with the kinematic viscosity of 1.05×10^6 m^2/s. The calculated area is 3cm×6cm and 100×200 uniform grids has been divided in the case. An air inlet with a diameter of 2mm has been set in the bottom and there is an air space (3cm×1cm) above the mixture. The effect of the air flow rate on bubble departure diameter has been investigated in current simulation. The present prediction obtains a good agreement with Zhang's experiment [3]. As the air flow rate increases from 100cc/min to 2000cc/min, the bubble departure diameter climbs from 5.4mm to 14.0mm, as show in Figure 1.
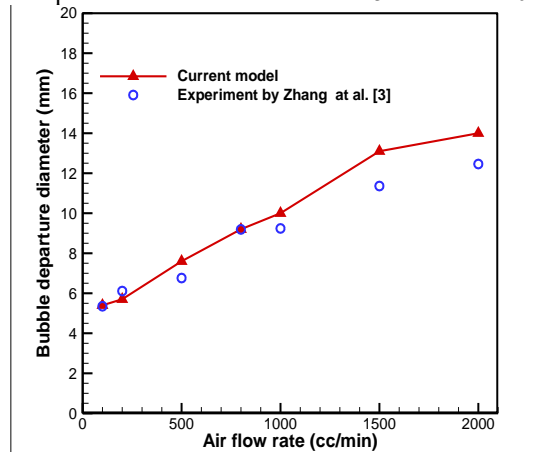
Figure 1: Variation of bubble departure diameter with the increase of air flow rate

Figure 2 shows the formation, departure, and rising process of single bubble when the air flow rate is 100cc/min. The red represents liquid and the blue represents air. There are two stages during the bubble generation. From the initial time to the 100ms, the bubble expands in both vertical and horizontal simultaneously, during which period, the surface tension force keeps balance with the buoyancy. As the bubble grows larger, once the bubble buoyancy is large enough to conquer the surface tension force, the bubble centre raises remarkably and neck forms in the bottom. As can be seen, the bubble departures at 235ms and 460ms respectively, with the same diameter 5.4mm. As the distance between the bubbles is far enough, the influence of the wake flow of the previous bubble seems negligible. In current model, the contact angle between the two-phase flow and the bottom wall is set to 90°, which represents a hydrophobic surface. This may lead to deviation in the simulated bubble growth periods compared with Zhang's experiment at al. [3].

When the air flow rate increases to 500cc/min, the bubble departures with a diameter of 7.6mm, as shown in Figure 3. The bubble departures at 85ms and rises up into bulk liquid. Meanwhile a new bobble forms, and departures at 155ms in the end. For the sake of the closer distance between the two bubbles, the wake flow induced by the rising bubble is much more intense than lower flow rate case. Therefore, the following bubble elongates obviously and departures with a slimmer shape. Consequently, the rising process of this bubble is accelerated rapidly and collides with the previous bubble at 195ms in the height about 2cm above the orifice. The collision finishes at 215ms and the double bubbles rise as a whole. In the case that the air flow rate is 800cc/min, the collision occurs at a lower position about 1.5cm and there is another bubble collides with the former double bubbles.

When the air flow rate is up to 1500cc/min, vertical coalescence occurs between two successive bubbles. The first bubble leaves the orifice at 65ms. From 65ms, a little bubble begins to grow and at 80ms coalesces with the former bubble during

the growth process. Within a very short time interval of 20ms, the following bubble elongates quickly in vertical and is pulled up and absorbed into the upper bubble rapidly.
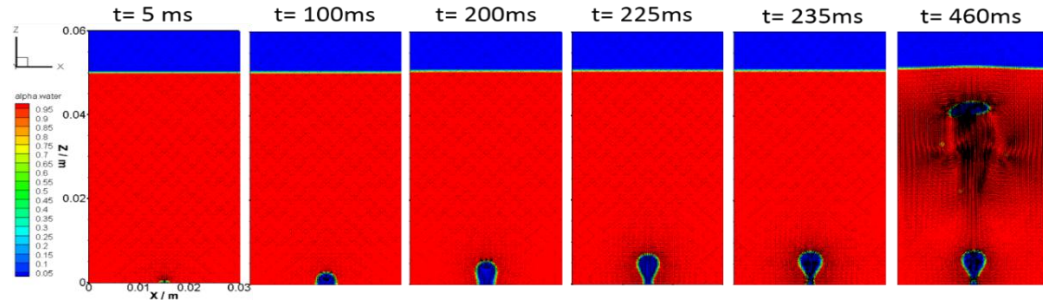
Figure 2: Single bubble behaviour from a submerged orifice when the air flow rate is 100 cc/min
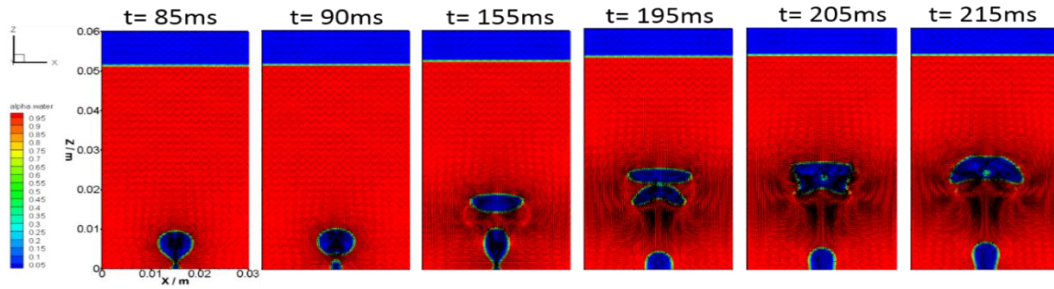
Figure 3: Bubbles collision from a submerged orifice when the air flow rate is 500 cc/min
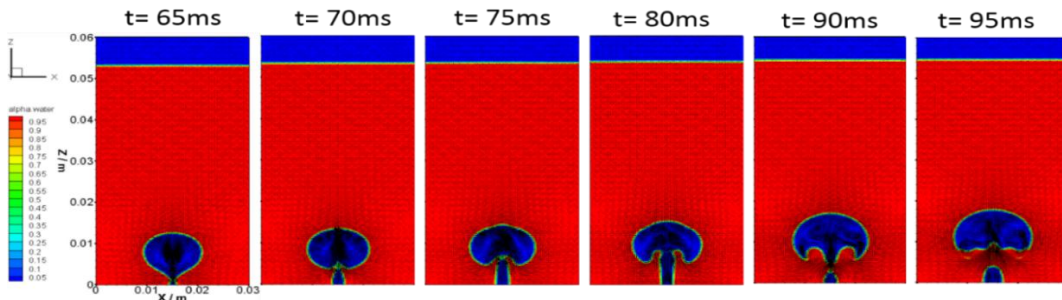
Figure 4: Bubbles coalescence in vertical from a submerged orifice when the air flow rate is 1500 cc/min

Table 1: Evolution of bubble behaviours with the increase of air flow rate

Air flow rate (cc/min)	Without interaction	Bubble collision	Vertical coalescence
100	○	×	×
200	○	×	×
500	○	○	×
800	○	○	×
1000	○	○	×
1500	○	○	○
2000	○	○	○

○: existent in the case; ×: non-existent in the case.

The evolution of bubbles behaviour from single submerged orifice can be summarized in Table.1. From above analysis, conclusion can been drawn that, in lower air flow rate cases (less than 200cc/min), the air bubble grows and rises as a single bubble without interactions with each other. Owing to the strong influence of the wake flow from the rising bubble, when the air flow rate is higher (larger then 500cc/min), bubble collision will occur between two or several successive bubbles. If the air flow is up to 1500cc/min, vertical coalescence will bring about near the bottom orifice. This is analogical with the boiling experiment results that, the vertical coalescence will only occur at high heat flux cases.

3.2 Bubble coalescences in horizontal direction

Based on Shoji's boiling experiments, the active sites spacing plays a decisive role in horizontal coalescence process. In current numerical experiments, double orifices has been set with three different spacing as shown in Figure 5. S/D is defined as the distance between the orifices divided by the single bubble departure diameter, as depicts in Figure 1. The

bubbles grow and rise as isolated bubbles when S/D=1.67 without coalescence, which are similar to the bubbles in two single orifices, as shown in Figure 5(a). When S/D is 1.48 (Figure 5(b)) and 1.67 (Figure 5(c)), horizontal coalescence occurs at 625ms and 200ms, respectively. The results is consistent with the conclusion al. [2] that horizontal coalescence couldn't occur if S/D>1.5. As coalescence occurs, two bubbles merged into one bigger bubble and departures form the orifices as a whole. However, it should been noted that, when S/D=1.48, after the coalescence bubble departure at 635ms, new bubble grows from each orifice as shown 670ms and 720ms in Figure 5(b). While in the case of S/D=0.93, coalesced bubble leaves the orifices at 215ms. After that, only one new bubble forms from two orifices as seen in Figure 5(c). The two inlets cooperate and offer air for the single bubble. The bubble grows for 170ms and departures at 385ms. The bubble growth period is less than the former coalesced bubble.

(a): S=9mm, S/D=1.67

(b): S=8mm, S/D=1.48

(c): S=5mm, S/D=0.93
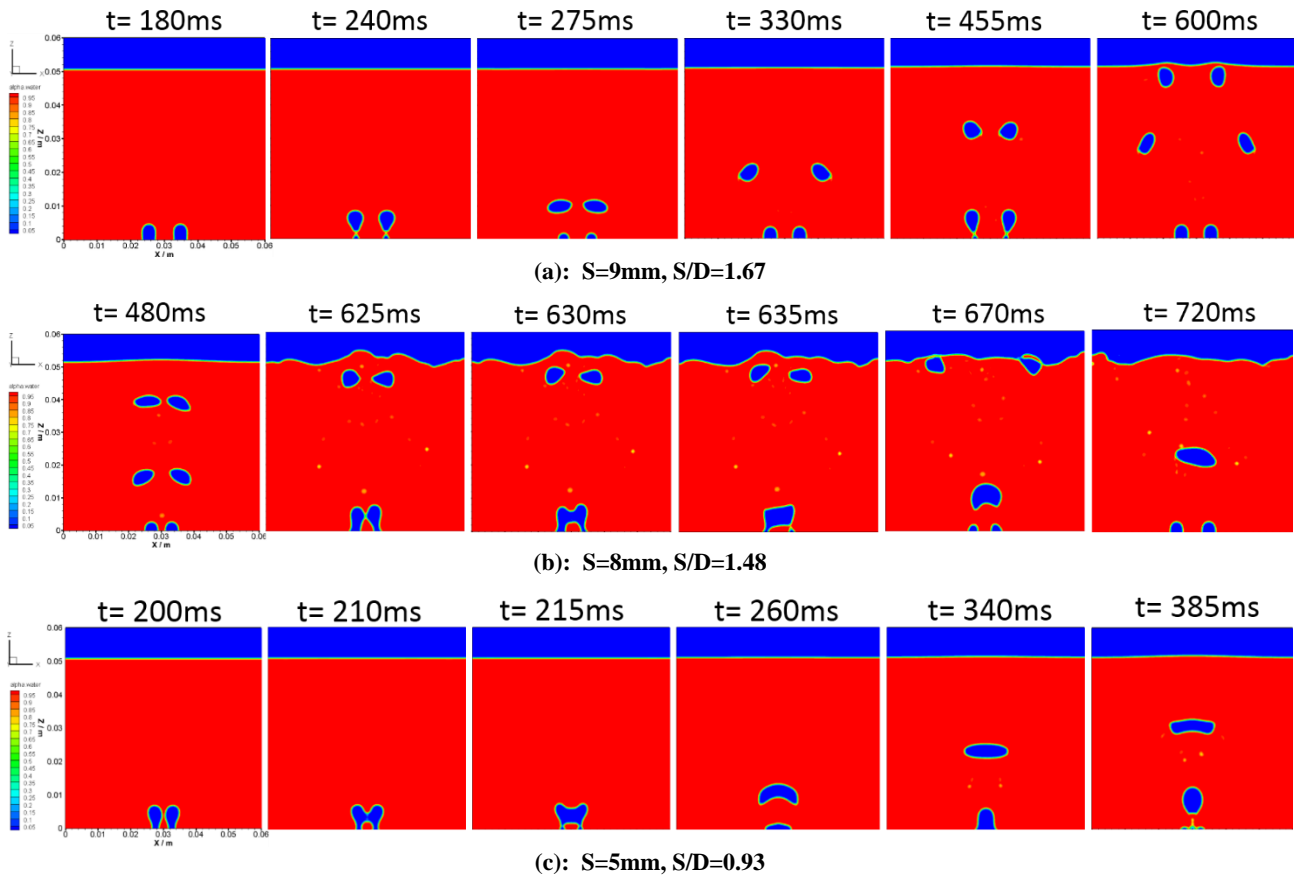
Figure 5: The bubbles behaviour from double submerged orifices with different spacing

4 Conclusions

A numerical simulation has been presented with VOF model based on OpenFOAM to reveal the evolution mechanisms of bubble behaviours. Single bubble behaviours from one orifice with different air flow rate has been investigated first. Results show that, vertical coalescence and collision between successive bubbles only occurs in cases with larger air flow rate, which should been owing to the strong wake flow from the previous bubble. The effect of the spacing between two orifices on the air bubbles behaviour has been investigated subsequently. The conclusion can been drawn that, horizontal coalescence will not occur when S/D >1.5, supporting the results of boiling experiments recently. Although the current research is based on isothermal system without phase change, the results may be helpful to reveal the mechanism of the coalescence during boiling process.

Acknowledgements

References

[1] M. Shoji, R. Mosdorf, L. Zhang, Y. Takagi, K. Yasui, and M. Yokota, "Features of Boiling on an Artificial Surface—Bubble Formation, Wall Temperature Fluctuation and Nucleation Site Interaction," *J. Therm. Sci.*, vol. 11, no. 3, pp. 226-234, 2002.

[2] L. Zhang and M. Shoji, "Nucleation site interaction in pool boiling on the artificial surface," *Int. J. Heat Mass Transf.*, vol. 46, no. 3, pp. 513–522, 2003.

[3] L. Zhang and M. Shoji, "Aperiodic bubble formation from a submerged orifice," *Chem. Eng. Sci.*, vol. 56, no. 18, pp. 5371–5381, 2001.

A TWO-PHASE MODEL FOR SATURATED GRANULAR-WATER INCLINED FLOWS

PENGFEI SI[1], XIPING YU[2]

[1] *State Key Laboratory of Hydroscience and Engineering, Department of Hydraulic Engineering,*
Tsinghua University, spf14@mails.tsinghua.edu.cn
[2] *yuxiping@tsinghua.edu.cn*

1 Introduction

Gravity-driven flows of highly concentrated mixtures of granular material and water are involved in a wide variety of geophysical processes. Among them, natural flows such as debris flows, snow avalanches and submarine landslides have caused serious disasters worldwide. As compared to the relatively abundant studies of dry granular flows, study of granular-water mixture flows is more challenging due to the complex interactions between granular particles and the ambient water. The existence of ambient water has a great effect on the dynamic characteristics of dense granular flows.

This paper presents a comprehensive two-dimensional two-phase model for inclined flows of saturated granular and water mixtures over erodible and rigid beds (see Figure 1). The model is based on a general collisional-frictional law for the granular stresses. The buoyancy and drag force are considered to represent the two-phase interactions. The effects of sidewall and bottom wall are also taken into account in this model.

The present numerical model is developed via OpenFOAM® based on the solver called twoPhaseEulerFoam. The two-phase model is further applied to simulate the laboratory experiments of fully-developed granular-water mixture flows over an inclined erodible and a rigid bed. The good agreements with the measured distribution of the concentration, velocity and granular temperature confirm the capability of the model to capture the dynamic features of saturated granular-water mixture flows under different regimes.
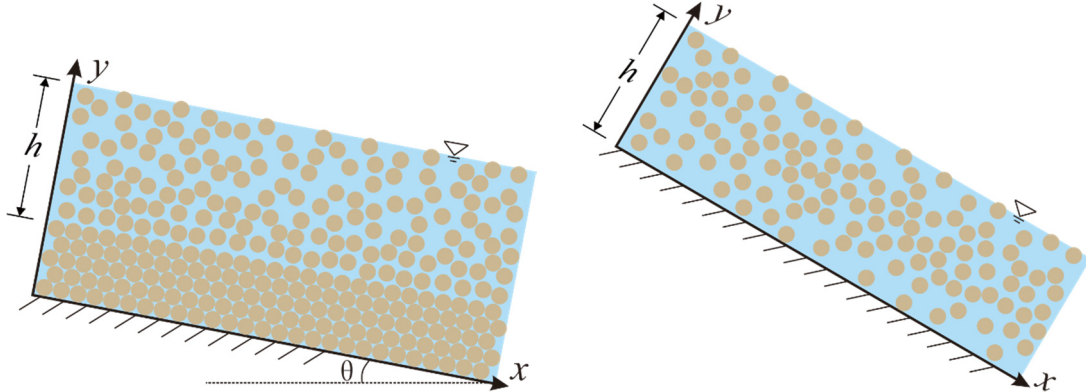
Figure 1: Sketches of saturated granular-water inclined flows over erodible (left panel) or rigid bed (right panel).

2 Model formulation

In an Eulerian-Eulerian two-phase model, the granular phase and the fluid phase are described as two interpenetrating continuums. The phase-averaged basic equations can thus be derived from an average of the mass and momentum conservation laws for the granular material and the fluid over a control volume. To consider the effects of the sidewall, through further averaging along transversal direction, the governing equations for the fluid and granular phase can be written as

$$\frac{\partial\left(\alpha_f\rho_f\right)}{\partial t}+\frac{\partial\left(\alpha_f\rho_f U_{f,i}\right)}{\partial x_i}=0 \tag{1}$$

$$\frac{\partial\left(\alpha_s\rho_s\right)}{\partial t}+\frac{\partial\left(\alpha_s\rho_s U_{s,i}\right)}{\partial x_i}=0 \tag{2}$$

$$\frac{\partial\left(\alpha_f\rho_f U_{f,i}\right)}{\partial t}+\frac{\partial\left(\alpha_f\rho_f U_{f,i}U_{f,j}\right)}{\partial x_j}=-\alpha_f\frac{\partial p_f}{\partial x_i}+\frac{\partial\tau_{f,ij}}{\partial x_j}-F_i+\alpha_f\rho_f g_i \tag{3}$$

$$\frac{\partial\left(\alpha_s\rho_s U_{s,i}\right)}{\partial t}+\frac{\partial\left(\alpha_s\rho_s U_{s,i}U_{s,j}\right)}{\partial x_j}=-\alpha_s\frac{\partial p_f}{\partial x_i}-\frac{\partial p_s}{\partial x_i}+\frac{\partial\tau_{s,ij}}{\partial x_j}+F_i+\alpha_s\rho_s g_i+\frac{2p_s\mu_w}{W}\frac{U_{s,i}}{|\mathbf{U}_s|} \tag{4}$$

where, the subscripts f and s denote quantities of fluid and granular phases, respectively; the subscripts $i, j = 1, 2$ denote streamwise and vertical directions. α is the volume fraction and satisfies $\alpha_s + \alpha_f = 1$; U is the velocity and ρ is the material density of the relevant phase; p is the pressure and τ is the deviatoric stress; F represents the granular-fluid interactive force; g is the gravitational acceleration; W is the width of channel and μ_w is the frictional coefficient between granular material and the channel sidewall.

The interaction term F_i in Eqs. (3) and (4) governs the momentum exchange between the fluid and granular phases. In dense granular problems, the lift and virtual-mass forces are insignificant when compared to the drag force. Thus, we consider only drag force in F_i, as

$$F_i = K\left(U_{f,i} - U_{s,i}\right) \tag{5}$$

where K is a generalized drag coefficient. Considering the particle group effect, the Gidaspow's (1994) formula is employed

$$K = \begin{cases} \dfrac{3}{4} C_D \dfrac{\rho_f \alpha_s \left|\mathbf{U}_f - \mathbf{U}_s\right|}{d_s} \alpha_f^{-1.65} & (\alpha_s \leq 0.2) \\[4mm] \dfrac{150\alpha_s^2 \mu_f}{\alpha_f^2 d_s^2} + \dfrac{1.75\rho_f \alpha_s \left|\mathbf{U}_f - \mathbf{U}_s\right|}{\alpha_f d_s} & (\alpha_s > 0.2) \end{cases} \tag{6}$$

where d_s is the particle diameter and the drag coefficient C_D is given by

$$C_D = \begin{cases} \dfrac{24}{\mathrm{Re}_s}\left(1 + 0.15\,\mathrm{Re}_s^{0.687}\right) & (\mathrm{Re}_s < 1000) \\[4mm] 0.44 & (\mathrm{Re}_s \geq 1000) \end{cases} \tag{7}$$

in which, $\mathrm{Re}_s = \rho_f \left|\mathbf{U}_f - \mathbf{U}_s\right| d_s / \mu_f$ is the particle Reynolds number and μ_f is the viscosity of the fluid.

Ignoring the fluid turbulence for dense granular problems, the shear stress of the fluid phase can be expressed as

$$\tau_{f,ij} = 2\alpha_f \mu_f S_{f,ij} \tag{8}$$

with $S_{f,ij} = 1/2\left(\partial U_{f,i}/\partial x_j + \partial U_{f,j}/\partial x_i\right) - 1/3\left(\partial U_{f,k}/\partial x_k\right)\delta_{ij}$ being the tensor of the deviatoric rate of fluid strain.

Flows of granular material generally cover two contrasting regimes: the rapid regime in which intense collisions occur among granular particles, and the quasi-static regime when enduring inter-particle contacts are predominant. To accurately describe the granular stresses in various regimes, a general collisional-frictional law is adopted, including a rate-dependent collisional part and a rate-independent frictional part

$$p_s = p_s^c + p_s^f, \qquad \tau_{s,ij} = \tau_{s,ij}^c + \tau_{s,ij}^f \tag{9}$$

where the superscripts c and f represent the collisional and frictional components of the granular stress, respectively. The collisional pressure can be formulated by the kinetic theory of Lun et al. [1],

$$p_s^c = \alpha_s \rho_s \Theta\left(1 + 4\eta\alpha_s R\right) \tag{10}$$

where, Θ is so-called granular temperature, representing the kinetic energy of the granular material due to velocity fluctuations; $R = (2 - \alpha_s)/\left[2(1-\alpha_s)^3\right]$ is the particle radial distribution function; $\eta = (1+e)/2$ with e is the restitution coefficient of particle collisions, defined as

$$e = e_d - 2.85\mathrm{St}^{-0.5} \tag{11}$$

which has proved effective for various types of granular material. e_d is the restitution coefficient of dry granular particles, which is often suggested to be 0.9 for glass beads. The Stokes number adopted here is a function of the granular temperature: $\mathrm{St} = \rho_s d_s \Theta^{0.5}/\left(18\mu_f\right)$.

The governing equation for the granular temperature Θ, taking into account the effect of the fluid phase [2], can be written as

$$\frac{3}{2}\left[\frac{\partial\left(\alpha_s\rho_s\Theta\right)}{\partial t} + \frac{\partial\left(\alpha_s\rho_s U_{s,i}\Theta\right)}{\partial x_i}\right] = \frac{\partial}{\partial x_i}\left(\kappa_s\frac{\partial\Theta}{\partial x_i}\right) + \left(-p_s^c\delta_{ij} + \tau_{s,ij}^c\right)\frac{\partial U_{s,i}}{\partial x_j} - \alpha_s\rho_s J_s + \Gamma \tag{12}$$

where, the first term on the right side represents the diffusion of fluctuating energy with κ_s being a diffusion coefficient; the second term is the production of fluctuating energy due to shear in the granular material; J_s is the energy dissipation due to inelastic particle collisions; and Γ represents the production or dissipation due to interaction between the granular particles and the fluid. Based on the kinetic theory of Lun et al. [1] and Gidaspow [2],

$$\kappa_s = \frac{75\rho_s d_s\sqrt{\pi\Theta}}{48\eta\left(41 - 33\eta\right)R}\left[\left(1 + \frac{12}{5}\eta\alpha_s R\right)\left(1 + \frac{12}{5}\eta^2\left(4\eta - 3\right)\alpha_s R\right) + \frac{64}{25\pi}\left(41 - 33\eta\right)\eta^2\alpha_s^2 R^2\right] \tag{13}$$

$$J_s = \frac{48}{\sqrt{\pi}} \eta(1-\eta) \frac{\alpha_s R}{d_s} \Theta^{3/2}, \qquad \Gamma = -3K\Theta + \frac{81\alpha_s \mu_f^2 \left| \mathbf{u}_f - \mathbf{u}_s \right|^2}{R d_s^3 \rho_s \sqrt{\pi\Theta}} \tag{14}$$

Following Lun et al. [1], the collisional shear stress for granular material can be written as

$$\tau_{s,ij}^c = 2\mu_s^c S_{s,ij} \tag{15}$$

with $S_{s,ij} = 1/2\left(\partial U_{s,i}/\partial x_j + \partial U_{s,j}/\partial x_i\right) - 1/3\left(\partial U_{s,k}/\partial x_k\right)\delta_{ij}$ being the tensor of the deviatoric rate of granular strain. The granular viscosity μ_s^c can be determined as

$$\mu_s^c = \rho_s d_s \sqrt{\Theta} \left[\frac{5\sqrt{\pi}}{96\eta(2-\eta)R} \left(1 + \frac{8}{5}\eta\alpha_s R\right)\left(1 + \frac{8}{5}\eta(3\eta-2)\alpha_s R\right) + \frac{8}{5\sqrt{\pi}}\eta\alpha_s^2 R \right] \tag{16}$$

Frictional stress develops when contacts between granular particles become long-lasting and form a granular skeleton. For cohesionless granular material, the frictional stress may be generally expressed as

$$\tau_{s,ij}^f = 2\mu_s^f S_{s,ij} \tag{17}$$

where μ_s^f is the viscosity due to inter-particle friction, formulated as

$$\mu_s^f = \frac{p_s^f}{\hat{S}} \left(\sqrt{\sin^2\phi + \left(\frac{\partial U_{s,k}}{\partial x_k}\frac{\cos^2\phi}{2\hat{S}}\right)^2} + \frac{\partial U_{s,k}}{\partial x_k}\frac{\cos^2\phi}{2\hat{S}} \right) \tag{18}$$

in which, p_s^f is the frictional normal stress; $\hat{S} = \sqrt{2S_{s,ij}S_{s,ij}}$; and ϕ is the internal friction angle of the granular material. p_s^f is evaluated using an empirical relation

$$p_s^f = \begin{cases} \eta\rho_s g d_s \dfrac{(\alpha_s - \alpha_{\min})^{\gamma_1}}{(\alpha_{\max} - \alpha_s)^{\gamma_2}} & (\alpha_{\max} > \alpha_s > \alpha_{\min}) \\ 0 & (\alpha_s < \alpha_{\min}) \end{cases} \tag{19}$$

where $\alpha_{\max}$ is the close-packed volume fraction and $\alpha_{\min}$ is the loose-packed volume fraction. The frictional pressure vanishes when the volume fraction α_s is less than $\alpha_{\min}$. The values of $\alpha_{\max}$ and $\alpha_{\min}$ depend on the arrangement pattern and size distribution of the granular particles. η, γ_1 and γ_2 are empirical constants.

3 Validation and results

Saturated granular-water inclined flows over an inclined erodible and a rigid bed [3, 4], as ideal configurations of fully developed debris flows, are tested and performed in this work. The slope inclination, granular properties and other parameters used in our model are summarized in Table 1. To obtain a steady uniform flow condition observed in experiments, periodic boundaries are used for the left and right boundaries of the computation domain (see Figure 1). A non-slip boundary condition is applied on the bottom for the erodible bed case, due to the presence of a static layer beneath the flow layer. However, for the rigid bed case, intense collisions occur between the granular particles and the bottom wall. To describe the collisional mechanism near the wall, a collisional boundary condition is employed

$$U_{s,i}\tau_{s,ij}n_j + \frac{\psi\sqrt{3}\pi\rho_s\alpha_s R\Theta^{1/2}\left|\mathbf{U}_f - \mathbf{U}_s\right|}{6\alpha_{\max}} + p_s^f \tan\phi = 0 \tag{20}$$

$$-\kappa_s n_i \frac{\partial\Theta}{\partial x_i} = \frac{\sqrt{3}\pi}{4\alpha_{\max}}\left(1 - e_w^2\right)\rho_s\alpha_s R\Theta^{3/2} + \frac{\psi\sqrt{3}\pi\rho_s\Theta^{1/2}\left|\mathbf{U}_f - \mathbf{U}_s\right|^2}{6\alpha_{\max}} \tag{21}$$

Here, ψ is the roughness of the wall; e_w is the restitution coefficient between granular particles and the wall; $\mathbf{n} = (n_1, n_2)$ is the unit normal vector of the wall.

Figure 2 shows the comparisons between the numerical results and the experimental data, in terms of the concentration, velocity and granular temperature distributions. The distribution profiles appear a significant difference between erodible and rigid bed cases. For saturated granular-water flows over an erodible bed, the granular concentration decreases monotonically over depth, with maximum values close to the packed bed. The velocity profile is convex, with maximum gradients close to the free surface. The granular temperature, i.e., the fluctuation energy of the granular phase, remains nearly zero close to the bed and increases linearly over depth, reaching its maximum at the free surface. In the case of the granular-water flows over a rigid bed, the distribution profiles become quite different. The granular concentration is minimum at the bed, reaches a maximum towards the centre and reduces again near the free surface. The velocity profile is slightly concave, with its steepest gradients near the bed. The granular temperature is maximum near the bed and decreases towards the free surface, presenting a contrary variation compared to the counterpart in the erodible bed case. The overall agreements between the numerical results and experiments demonstrate the capability of our model to simulate the gravity-driven granular-water mixture flows.

Table1: Parameters for numerical simulations

Parameter	Erodible bed	Rigid bed	Parameter	Erodible bed	Rigid bed
θ	8°	22°	α_{max}	0.7	0.7
h	62 mm	31 mm	α_{min}	0.5	0.5
ρ_s	2210 kg/m³	1540 kg/m³	η	4×10^{-4}	4×10^{-4}
ρ_f	1000 kg/m³	1000 kg/m³	γ_1	2	2
d_s	6 mm	3.7 mm	γ_2	5	5
e_d	0.9	0.9	μ_w	0.4	0.4
ϕ	20°	35°	ψ	--	0.9
α_0	0.56	0.545	e_w	--	0.7

Figure 2: Depth profiles of concentration, velocity and granular temperature of the granular phase over erodible (top panel) and rigid bed (bottom panel).

4 Conclusions

An Eulerian-Eulerian two-phase model based on a general formulation of the granular stress is developed for granular-water mixture flows. In the model, the kinetic theory is extended to consider the influences of the ambient fluid and employed to compute the collisional stress in the granular phase. For the frictional stress, an improved formula derived by statistically averaging the individual contact forces among cohesionless particles is employed. The proposed two-phase model is successfully applied to the saturated granular-water inclined flows over both erodible and rigid bed. The various distribution profiles of granular concentration, velocity and granular temperature are well captured by the model.

Acknowledgements

References

[1] C.K.K. Lun et al., "Kinetic theories for granular flow: inelastic particles in Couette flow and slightly inelastic particles in a general flowfield," J. Fluid Mech., vol. 140, 223–256, Mar. 1984.

[2] D. Gidaspow, (1994) Multiphase flow and fluidization: continuum and kinetic theory descriptions, Academic press, San Diego, 1994.

[3] A. Armanini et al., "Rheological stratification in experimental free-surface flows of granular-liquid mixtures," J. Fluid Mech., vol. 532, 269–319, Jun. 2005.

[4] A. Armanini et al., "Submerged granular channel flows driven by gravity," Adv. Water Resour., vol. 63, 1–10, Jan. 2014.

TWO-WAY COUPLED EULER-EULER SIMULATIONS OF PARTICLE-LADEN FLOWS

ZIAD BOUTANIOS[1], HRVOJE JASAK[2]

[1]*FAMENA, University of Zagreb ziad.boutanios@fsb.hr*
[2]*FAMENA, University of Zagreb hrvoje.jasak@fsb.hr*

Keywords: drifting snow, euler-euler, suspension, saltation, sediment, two-way coupling

A novel two-way coupled Eulerian-Eulerian CFD formulation for simulating particle-laden flows is presented. It is based on a new viscous model of the particle phase, and turbulent dispersion through a turbulent drag term in the phase-averaged momentum equations as detailed by [1]. This approach allows explicit resolution of both saltation and suspension layers without resorting to empiricism, unlike other one-way coupled Eulerian-Eulerian approaches based on mixture formulations using the convection-diffusion particle transport equation, or the Volume of Fluid method. Successful validations are carried out against detailed measurements from controlled experiments of drifting snow and sediment suspension, by [2]. The present two-way coupled approach is found capable of accurately predicting snowflux and airflow profiles as shown in Figure 1. Comparison is also made to the results of a one-way coupled method by [3] based on the convection-diffusion equation for transport of solid sediment. Both approaches are used for simulating an experiment by [4] of sediment suspension in a laboratory flume. The two-way coupled approach is shown capable of accurately predicting both sediment concentration and water velocity profiles, more accurately than the one-way coupled approach as shown in Figure 2. In Figure 3, the present two-way coupled approach is also shown capable of accurately predicting the sediment fall velocity and wall effect, without the need for the empirical relationships used for the one-way coupled approach that predict a constant sediment fall velocity throughout the entire computational domain.
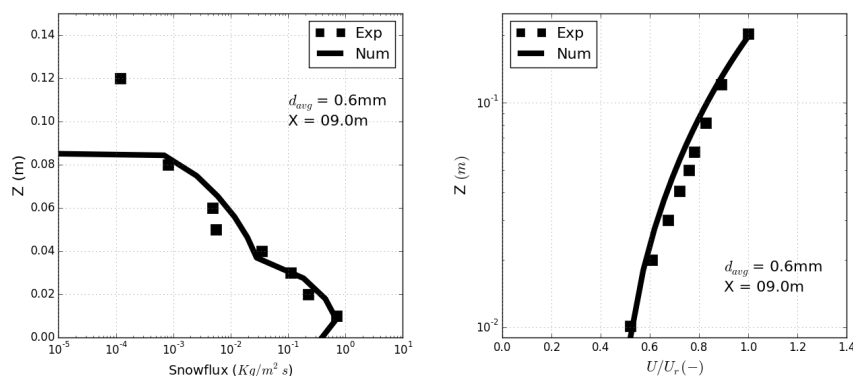
Figure 1: Comparison of the two-way coupled approach numerical profiles of snowflux (left) and non-dimensional airflow velocity (right), to the experimental measurement at the X = 9m measurement station, for an average particle size of 0.6mm.

Acknowledgments

References

[1] Z. Boutanios and H. Jasak, "Two-way coupled eulerian-eulerian simulations of drifting snow with viscous treatment of the snow phase," *Journal of Wind Engineering and Industrial Aerodynamics*, vol. 169, 10 2017.

[2] T. Okaze, A. Mochida, Y. Tominaga, M. Nemoto, T. Sato, Y.Sasaki, and K. Ichinohe, "Wind tunnel investigation of drifting snow development in a boundary layer," *J. Wind Eng. Ind. Aerodyn.*, vol. 104-106, pp. 532–539, 2012.

[3] A. Sattar, H. Jasak, and V. Skuric, "Three dimensional modeling of free surface flow and sediment transport with bed deformation using automatic mesh motion," *Environmental Modelling & Software*, vol. 97, 11 2017.

[4] Z. Wang and J. Ribberink, "The validity of a depth-integrated model for suspended sediment transport," *J. Hydr. Res.*, vol. 24, no. 1, pp. 53–66, 1986.
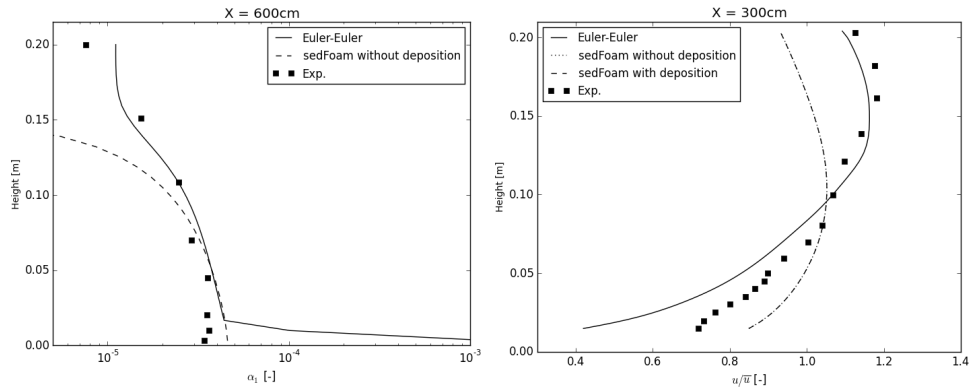
Figure 2: Comparison of the numerical profiles of sediment volume fraction (left) and non-dimensional water velocity (right), of the two-way coupled approach (Euler-Euler) numerical profiles to the one-way coupled approach numerical profiles (sedFoam), and the experimental measurement at the X = 600cm and X = 300cm measurement stations.
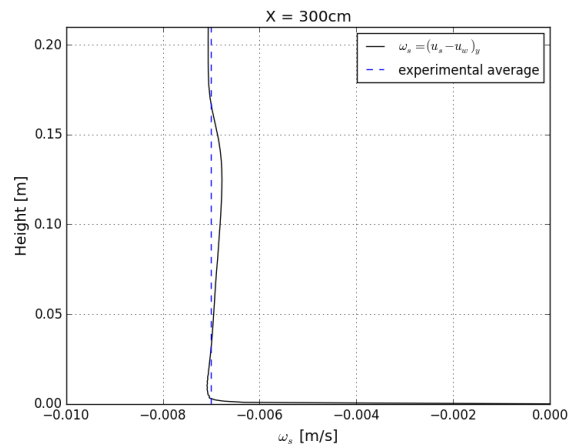
Figure 3: Comparison of the numerical profile of sediment fall velocity as calculated using the two-way coupled approach, to the average of the experimental fall velocity at the X = 300 cm measurement station.

NUMERICAL INVESTIGATION OF TURBULENCE MODELS FOR SIMULATION OF A GAS-LIQUID STIRRED TANK

YEFEI LIU

College of Chemical Engineering, Nanjing Tech University, yefei.liu@njtech.edu.cn

1. Introduction

Gas-liquid stirred tank reactors are widely used in chemical, biochemical and petrochemical industries. The interaction between stationary baffles and rotating impellers produces complicated and highly turbulent flow, which in turn has substantial influence on gas holdup, bubble size distribution and interphase transfer efficiency. It is very important to understand the gas-liquid turbulence in stirred tanks for successful reactor design and scale-up.

During last decades computational fluid dynamics (CFD) methods have been developed for resolving turbulent hydrodynamics in gas-liquid stirred tanks. In the simulation of gas-liquid stirred tanks, due to the simplicity, the k-ε model is usually the preferable choice to simulate the liquid turbulence. Among the various formulations of the k-ε models (standard, RNG and realizable), the standard model has been most widely used. The realizable k-ε model was also employed for simulating the gas-liquid hydrodynamics and mass transfer in stirred tanks. The predictions of liquid velocity, local bubble sizes and dissolved oxygen concentration were in good agreement with experimental data reported in the literature. However, there is currently no clear justification on the choice of different formulations of k-ε models for simulating gas-liquid stirred tanks.

The purpose of this work is to provide detailed investigation on the turbulence modelling in simulating of a gas-liquid stirred tank. Also, the previous studies in the literature are performed in different commercial CFD tools. The other objective of this work is to make the validation of the open source CFD tool OpenFOAM, which has been not done until the date for gas-liquid stirred tanks. The simulation results are compared with the data in the literature. The different formulations of k-ε models are more specifically investigated and the influence of bubble-induced turbulence is also evaluated by the comparison with the liquid turbulent kinetic energy.

2. Mathematical models

The CFD simulation is performed with the two-fluid model. The continuity and momentum equations of the gas and liquid phases are written as

$$\frac{\partial(\alpha_k\rho_k)}{\partial t} + \nabla\cdot(\alpha_k\rho_k\mathbf{U}_k) = 0 \tag{1}$$

$$\frac{\partial(\alpha_k\rho_k\mathbf{U}_k)}{\partial t} + \nabla\cdot(\alpha_k\rho_k\mathbf{U}_k\mathbf{U}_k) = -\alpha_k\nabla p + \nabla\cdot(\alpha_k\tau_k) + \alpha_k\rho_k\mathbf{g} + \mathbf{F}_k + \mathbf{M}_k \tag{2}$$

where k refers to the phase (l for liquid and g for gas), $\mathbf{U}$ is the phase velocity, α is the volume fraction of each phase, τ is the effective stress tensor, $\mathbf{M}_k$ is the interfacial momentum transfer term due to various interphase forces. The term $\mathbf{F}$ represents the Coriolis and centrifugal forces expressed in the MRF method for rotating flows and it is calculated as

$$\mathbf{F}_k = -\mathbf{\Omega}\times\left(\alpha_k\rho_k\mathbf{U}_k\right) \tag{3}$$

where $\mathbf{\Omega}$ is the angular velocity vector.

In this study the only drag is considered, while the other forces are neglected since they have little effect on the flows. The momentum interfacial transfer term due to the drag force is calculated as

$$\mathbf{M}_{D,g} = -\mathbf{M}_{D,l} = \frac{3}{4}\alpha_g\rho_l\frac{C_D}{d_b}\left|\mathbf{U}_g\text{ - }\mathbf{U}_l\right|\left(\mathbf{U}_l\text{ - }\mathbf{U}_g\right) \tag{4}$$

where d_b is the mean bubble size and C_D is the drag coefficient determined by the flow regime and the liquid property. Here the drag coefficient follows the model proposed by Khopkar et al. [8] as

$$\frac{C_D-C_{D0}}{C_{D0}} = K\left(\frac{d_b}{\lambda}\right)^3 \tag{5}$$

where λ is the Kolmogorov scale, K is an empirical constant, $K = 6.5\times 10^{-6}$, C_{D0} is drag coefficient for a single bubble rising in a stagnant liquid and it is estimated as

$$C_{D0} = \max\left[\frac{24}{\text{Re}}\left(1+0.15\,\text{Re}^{0.687}\right),\ \frac{8}{3}\frac{\text{Eo}}{\text{Eo}+4}\right] \tag{6}$$

where the bubble Reynolds number Re and Eötvös number Eo are defined as

$$\mathrm{Re} = \frac{\rho_l d_b |\mathbf{U}_g - \mathbf{U}_l|}{\mu_l} \tag{7}$$

$$\mathrm{Eo} = \frac{g(\rho_l - \rho_g) d_b^2}{\sigma} \tag{8}$$

The k-ε models with three formulations (standard, RNG, and realizable) are implemented with the two-fluid model.

3. Numerical simulation

Nowadays the open source CFD tool OpenFOAM gains some success in the multiphase flow simulation. The OpenFOAM package offers the possibility to have insight into the source codes and hence it is of great convenience to implement various physical models. In this work, the two-phase flow solver is developed based on the `twoPhaseEulerFoam` solver in OpenFOAM-2.3.1. Our solver is rewritten into the incompressible version, since the compressibility is quite small in the simulation. The effect of phase inversion has been treated using the blending methods. The different formulations of k-ε turbulence models for liquid turbulence are implemented into the solver.

The linear equation systems resulting from the finite volume discretization are solved in a segregated fashion. The pressure-velocity coupling is handled using the PISO solution algorithm. The interphase coupling terms in the phase momentum equations are treated using the semi-implicit method. First, the gas phase fraction equation is solved. Second, the pressure equation is constructed from the continuity equations and solved. Third, the predicted phase velocities are corrected by the new pressure fields.

The gas-liquid flow generated by the six-bladed down-pumping pitched-blade turbine in a stirred tank is simulated. The diameter of the cylindrical vessel is $T = 0.19$ m. More details of the configuration can be found in Aubin et al.[1]. The vessel is filled with water and air is supplied at the volumetric gas flow rate of 4.29×10^{-5} m^3/s. The mean bubble size of 4 mm is used in this work. The impeller rotational speed is equal to 300 rpm. Differently from the work of Khopkar et al. [2], the whole geometry of the stirred vessel is considered as the computational domain. By using the MRF method, the computational domain is divided into two cell zones, one for the rotating reference frame and the other for the stationary reference frame.

Initially, the static water exists in the stirred tank and the gas holdup is set to be zero within the static water. The gas distributor is treated as a uniform inlet with the gas volume fraction of 1.0. The liquid inlet velocity is set to zero for all test cases because of no water supply into the stirred tank. The pressure at the inlet is specified using the zero gradient boundary condition. At the outlet, the pressure is specified as atmospheric pressure. The no-slip boundary condition is applied at the wall for the velocities of gas and liquid phases. The standard wall function is used to specify the turbulence quantities. The transient solutions are performed for 20 s and the time-averaged results are obtained using the field averaging utility.

4. Results and discussion

Figure 1 shows the predicted profiles of liquid axial velocity using three k-ε models. The three models give very close results at the axial position $z/T = 0.31$, but the agreement with experimental data is still not obtained. The flow fields predicted using the three k-ε models are shown in Figure 2. It can be seen that similar results are found between the standard and RNG models. Differently, in the upper region of the vessel, the higher liquid velocity is predicted using the realizable model.
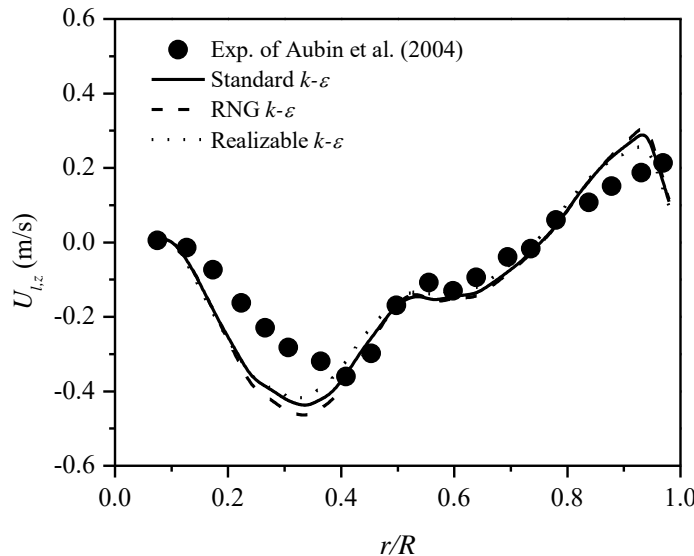
Figure 1: Comparison of liquid axial velocity predicted using three k-ε models.

|U$_l$| (m/s)

Standard k-ε RNG k-ε Realizable k-ε
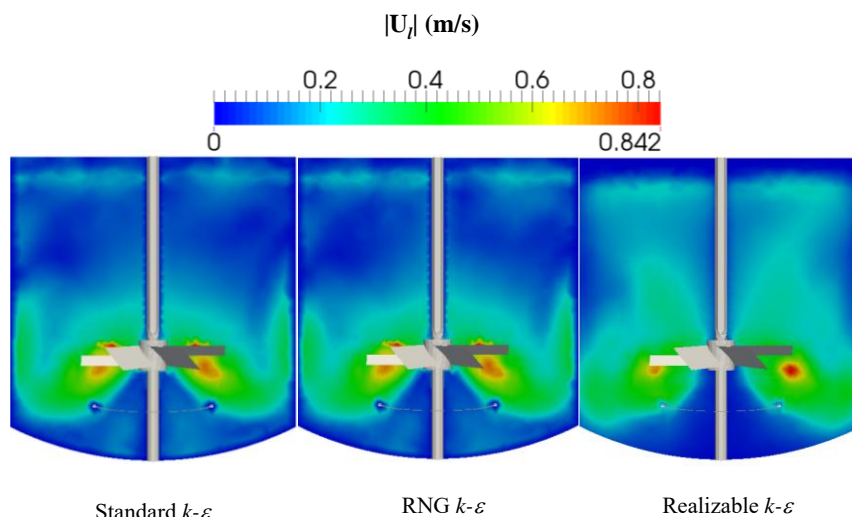
Figure 2: Comparison of liquid velocity fields predicted using three k-ε models.

Figure 3 gives the profiles of liquid turbulence quantities predicted using the three k-ε models. In Figure 3(a), the overprediction on turbulent kinetic energy is also provided by the realizable model. Although the peak in turbulent kinetic energy is underpredicted by the RNG model, good agreement with experimental data is found at the other radial positions. Comparing with the standard and realizable models, the RNG model gives smaller values of turbulent kinetic energy. The RNG model is more responsive to the effects of rapid strain than the standard model. In the rapid strained flows, the RNG model predicts a lower turbulent viscosity than the standard model, as shown in Figure 3(c).The turbulence production term becomes smaller and thus the turbulent kinetic energy is reduced.

In Figure 3(b), the smaller values of the dissipation rate of turbulent kinetic energy are also observed for the RNG model, which is due to the smaller turbulence production term in the transport equation of dissipation rate. In Figure 3(c), a different profile of liquid turbulent kinematic viscosity is predicted using the realizable model and the largest value is observed near the impeller blade tip (r/R = 0.5). It was reported that the realizable model has a limitation that it produces non-physical turbulent viscosity in the situations when the computational domain is composed of both rotating and stationary zones. Therefore, great caution should be given when using the realizable model to predict the turbulent viscosity.
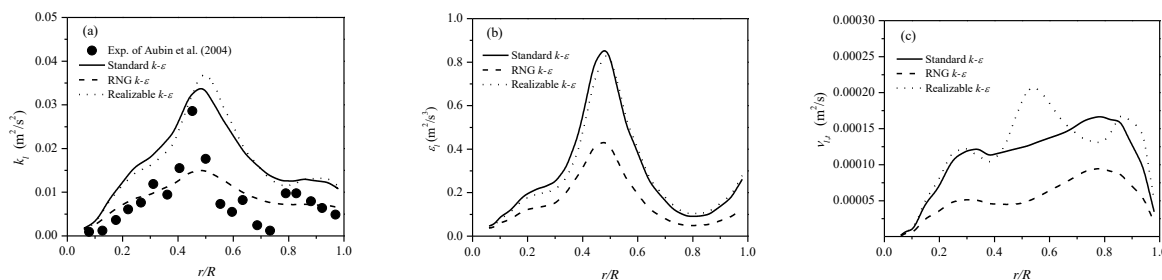
Figure 3: Comparison of liquid turbulent kinetic energy (a), dissipation rate (b) and turbulent kinematic viscosity (c) predicted using three k-ε models.

Acknowledgements

References

[1] Aubin, J., Le Sauze, N., Bertrand, J., Fletcher, D. F., Xuereb, C., 2004. PIV measurements of flow in an aerated tank stirred by a down- and an up-pumping axial flow impeller. Exp. Therm. Fluid Sci. 28, 447-456.

[2] Khopkar, A. R., Aubin, J., Xuereb, C., Le Sauze, N., Bertrand, J., Ranade, V. V., 2003. Gas-liquid flow generated by a pitched-blade turbine: Particle image velocimetry measurements and computational fluid dynamics simulations. Ind. Eng. Chem. Res. 42, 5318-5332.

NUMERICAL SIMULATION OF BUBBLE DYNAMICS NEAR THE FREE SURFACE

TONG LI[1], SHIPING WANG[2], A-MAN ZHANG[3]

[1]*Harbin Engineering University, litong123sss@163.com*
[2]*Harbin Engineering University, wangshiping@hrbeu.edu.cn*
[3]*Harbin Engineering University, zhangaman@hrbeu.edu.cn*

Keywords: Bubble dynamics, Free surface, Bursting

The strong interaction between the submerged oscillating bubble and the free surface will cause complex phenomena [1]. The dynamics of the collapsing bubble and the free surface is severely dependent on γ_f, which stands for the non-dimensional bubble-free surface distance scaled with the maximum bubble radius. When γ_f is sufficiently small, the bubble will burst at the free surface [2]. The present study performs the simulation using the compressible two-phase flow solver implemented in OpenFOAM. OpenFOAM is now a popular tool utilized for simulating bubble dynamics. The excellent examples are the work of Han *et al* [3] studying the dynamics of the laser-induced bubble pairs, the work of Koch *et al* [4] calculating the growth and collapse of the bubble with mass conservation improved, the work of Moezzi-Rafie *et al* [5] investigating the flow physics of the bubble implosion and the work of Lechner *et al* [6] researching on the pressure and tension waves from bubble collapse near a solid boundary. VOF method is utilized and it allows to simulate the complex physical phenomena, like splitting and coalescence of the bubble, smoothly without artificial interference. The adiabatic equation of state for the gas and the Tait equation for the water are adopted, which leads to the closure of the Navier-Stokes equations with energy equation omitted. Complex dynamic behaviors of the bubble and free surface are well predicted.
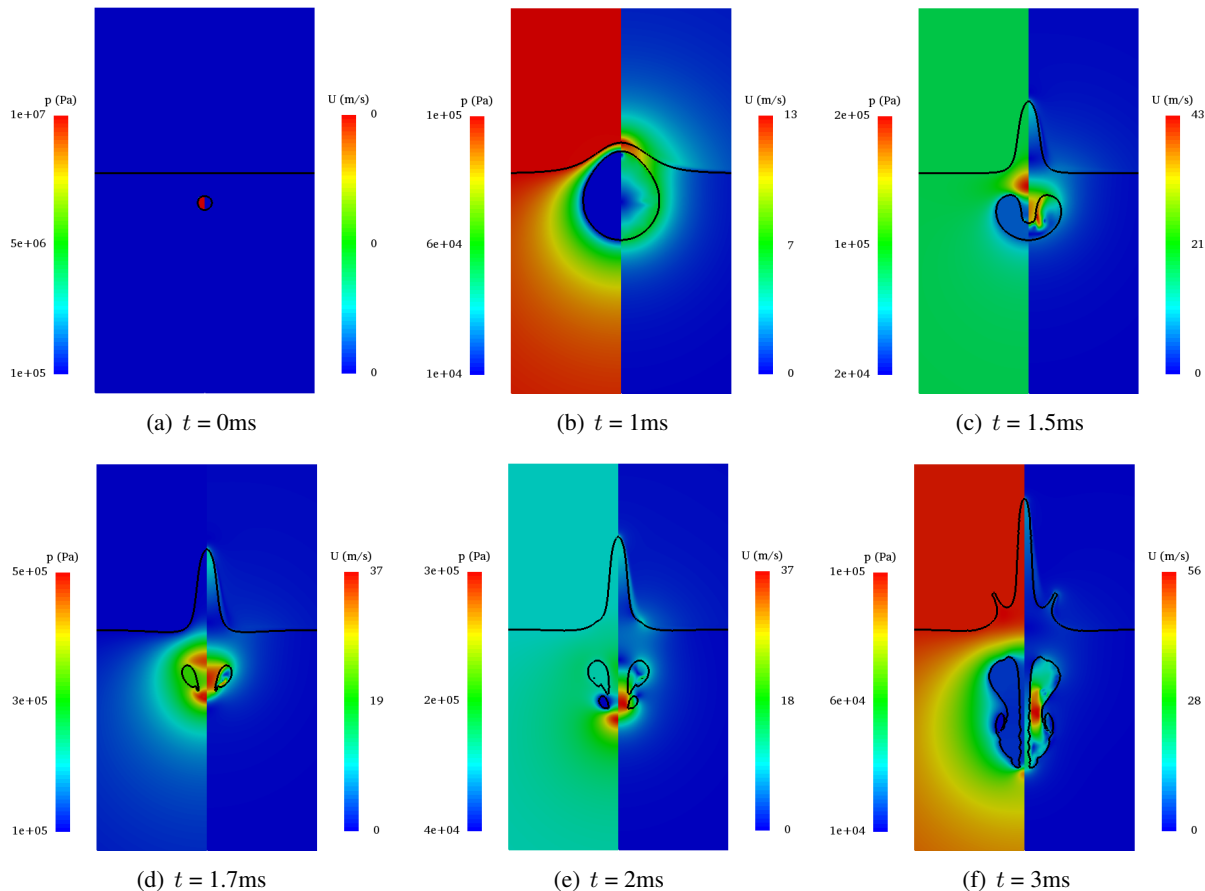
Figure 1: Bubble oscillating near the free surface

Fig. 1 shows the dynamic behaviors of a bubble initially located 8.1mm below the free surface. The initial bubble radius is 1.9mm and the initial bubble pressure is 10MPa in Fig. 1(a). The free surface is pushed upward by the expanding bubble.

174

The bubble cannot maintain its spherical shape due to the attraction by the free surface, as shown in Fig. 1(b). When the bubble starts to collapse, a high pressure region is induced between the top of the bubble and free surface. The bubble is repelled by the free surface, leading to a downward liquid jet, as shown in Fig. 1(c). The liquid jet impacts on the opposite side and a toroidal bubble is generated. The toroidal bubble goes through splitting and coalescence during its rebounding phase, as shown in Fig. 1(d) and Fig. 1(e). The water spike grows continuously along with the oscillation of the bubble. An interesting phenomenon called "crown spike" can be observed in Fig. 1(f).

Fig. 2 shows the case of the bursting of the bubble near the free surface. In Fig. 2(a), the initial radius of the bubble radius is 5mm and the initial bubble pressure is 20MPa. The initial bubble-free surface distance is 10mm. As shown in Fig. 2(b), there is still a free surface hump as the bubble expands. The water layer between the top of the bubble and the free surface breaks up when it is thin enough, as shown in Fig. 2(c). The cavity generated by the bursting continues to expand with inertial effect, as shown in Fig. 2(d).

(a) $t = 0$ms

(b) $t = 0.1$ms

(c) $t = 0.2$ms

(d) $t = 0.3$ms
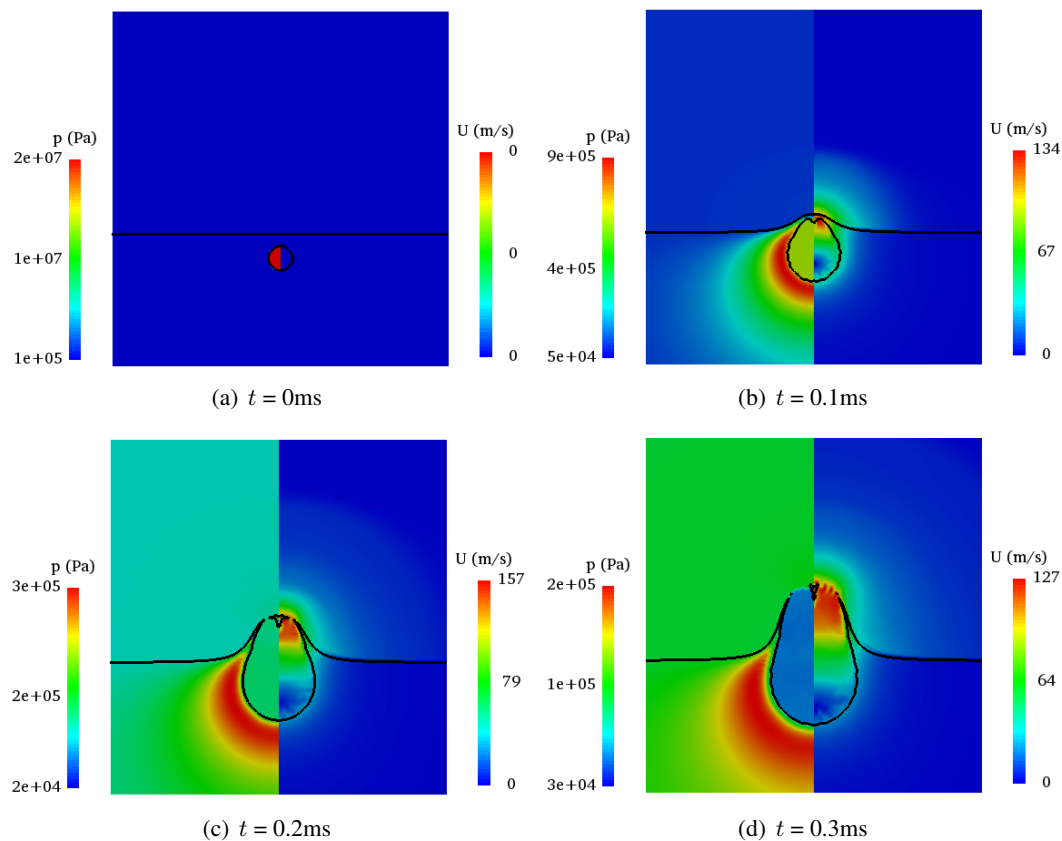
Figure 2: Bubble bursting at the free surface

Acknowledgments

References

[1] S. Zhang, S. P. Wang, and A. M. Zhang, "Experimental study on the interaction between bubble and free surface using a high-voltage spark generator," *Physics of Fluids*, vol. 28, no. 3, p. 032109, 2016.

[2] S. P. Wang, W. Y. Duan, and Q. X. Wang, "The bursting of a toroidal bubble at a free surface," *Ocean Engineering*, vol. 109, pp. 611–622, 2015.

[3] B. Han, K. Khler, K. Jungnickel, R. Mettin, W. Lauterborn, and A. Vogel, "Dynamics of laser-induced bubble pairs," *Journal of Fluid Mechanics*, vol. 771, pp. 706–742.

[4] M. Koch, C. Lechner, F. Reuter, K. Khler, R. Mettin, and W. Lauterborn, "Numerical modeling of laser generated cavitation bubbles with the finite volume and volume of fluid method, using OpenFOAM," *Computers and Fluids*, vol. 126, pp. 71–90.

[5] H. Moezzi-Rafie and M. M. Nasiri, "An investigation on the flow physics of bubble implosion using numerical techniques," *Ocean Engineering*, vol. 153, pp. 185–192.

[6] C. Lechner, M. Koch, W. Lauterborn, and R. Mettin, "Pressure and tension waves from bubble collapse near a solid boundary: A numerical approach," *The Journal of the Acoustical Society of America*, vol. 142, no. 6, pp. 3649–3659.

[7] OpenCFD, *OpenFOAM: The Open Source CFD Toolbox. User Guide Version 1.4, OpenCFD Limited.* Reading UK, Apr. 2007.

QUANTITATIVE BENCHMARK OF A SINGLE RISING BUBBLE USING VOF METHODS

LIONEL GAMET[1], JOHAN ROENBY[2], MARCO SCALA[1],HAMZA ZEHARA[1]

[1]*IFPEN, Process Experimentation Division,*
Lionel.Gamet@ifpen.fr, Marco.Scala@ifpen.fr, Hamza.Zehara@ifpen.fr
[2]*STROMNING, johan@stromning.com*

1   Introduction

Gas-liquid flow systems are often encountered in the chemical process industry, with various scales ranging from large bubble columns, plate columns, agitated vessels, surface aerators, jets, static mixers or micro-reactors. Their applications are generally reactive flow systems, mixing, stripping or saturation systems. Complex phenomena of turbulent hydrodynamics involving breakup and coalescence, coupled with gas-liquid mass and heat transfers, appear in such systems. Thanks to the increase of computing resources, highly resolved simulations gain more and more interest to analyze in detail the physics of such multiphase flows. Many numerical methods have emerged to attempt to simulate gas-liquid flows. Among these, implicit interface capturing approaches like volume of fluid (VoF) [1] and level set (LS) [2] have proven to be efficient in simulating multiphase flows.

Before running into complex geometries, elementary quantitative benchmark configurations are essential for validation and comparison of interfacial flow solvers. Hysing et al. [3] have proposed a 2D benchmark consisting in a single rising bubble in a quiescent liquid. Two different cases are described in [3], corresponding to different density, viscosity and surface tension ratios. More recently, Adelsberger et al. [4] have published a 3D equivalent of the same benchmark. For both these benchmarks, result data was made available online by the authors at the URLs mentioned in the bibliography.

Roenby et al. [5] have recently developed a new geometric VoF method, called isoAdvector, for advecting the interface between two incompressible fluids. This method was implemented in OpenFOAM-v1706 in the new solver `interIsoFoam`. IsoAdvector gives a sharper interface, but validation data for this new method is still sparse, especially for surface tension dominated flows. Following the single rising bubble benchmarks [3, 4], the objective of this paper is to perform quantitative comparisons of the isoAdvector method with the benchmark data. Furthermore, the isoAdvector results are compared with results from OpenFOAM's original interfacial flow solver, `interFoam`.

2   Numerical methods

We consider here an unsteady, laminar and incompressible two-phase flow. The governing equations are the continuity equation for the fluid-wise constant mass density field, the Navier-Stokes equations for the momentum evolution, and the incompressibility condition for the velocity field.

In the VoF method, the continuity equation is converted into an evolution equation for the volume fraction field α, representing for each cell the fraction of its volume, which is occupied by one of the two fluids. Special care must be taken in the numerics to prevent smearing of the α-field and at the same time keeping it bounded ($0 \leq \alpha \leq 1$). In the `interFoam` solver, sharpness is obtained by introducing an artificial interface compression term in the α-equation [6], and boundedness is ensured by employing the MULES limiter (Multidimensional Universal Limiter with Explicit Solution). More details can be found in Deshpande [7].

The solver `interFoam` has been widely used and validated [8, 9, 10, 11], but under some conditions the described method may fail in keeping the interface sufficiently sharp. Furthermore, the heuristic nature of the added compression term can lead to inaccurate interface advection and undesirable features such as unphysical ripples on the interface [12, 13]. This motivated the developmed of the isoAdvector geometric VoF method, which was first presented by Roenby et al. [5]. Here it was tested with a variety of pure advection cases yielding very good results in terms of volume conservation, interface sharpness, boundedness and shape preservation. With recent improvements, the method has been made consistently second order for all mesh types (See Scheufler and Roenby [14]). The isoAdvector method implements new ideas in both the interface reconstruction step and the interface advection step. The reconstruction step uses efficient isosurface calculations to compute the distribution of fluids in a grid cell. The interface advection step uses a novel division of a physical time step into sub-time steps on which the volume fraction flux through a cell face can be calculated analytically under the assumption that the interface is moving steadily across the face during the interval. In

the development of this procedure, no assumptions are made on the shape of a cell face, which makes the advection step applicable on arbitrary meshes.

Except for the interface advection step, the `interIsoFoam` (isoAdvector) solver is identical to the `interFoam` (MULES) solver. They both solve the governing system of equations in a seggregated manner using the PIMPLE algorithm (a combination of the SIMPLE and PISO algorithms) for pressure-velocity coupling. Strictly speaking, isoAdvector and MULES also differ in the way `rhoPhi` (used in the momentum convection term) is calculated, which is described in [13].

3   Definition of test case

The test case number 2 as described by Hysing et al. [3] has been used here. We have used only this second test case as it is more representative of final industrial applications. The 2D case setup is schematized in Figure 1. First phase (liquid) properties are $\rho_1 = 1000$ kg/m^3, $\mu_1 = 10$ kg/(ms), while second phase (gas) takes $\rho_2 = 1$ kg/m^3, $\mu_2 = 0.1$ kg/(ms) as physical parameters. The surface tension is $\sigma = 1.96$ kg/s^2. Gravity is taken as $g = 0.98$ m/s^2. Extension of the case to 3D is straightforward.

Square/cubic cells were used for all simulations in 2D/3D. Six grid resolutions have been used ranging from 20 to 640 cells along the x direction, with the cell size halfed in each refinement. The bubble was initialized as a cylinder in 2D and as a sphere in 3D using the `setFields` utility. The Crank-Nicolson second order time scheme with blending coefficient 0.9 has been used for all computations. The convective term was treated with `Gauss limited linearV 1`, and in the MULES simulations `Gauss vanLeer` was used for the α convection. The `Gauss linear` scheme was used for gradient terms. The GAMG implicit solver was used for pressure terms, while the smooth solver was used for the velocity. Constant time steps have been used, starting at $\Delta t = 0.002$ s for the coarsest level and reduced for finer grids to keep the maximum CFL number below 0.05. The PIMPLE algorithm was run in PISO mode (`nOuterCorretors` set to 1) with 3 PISO correctors. Setting `momentumPredictor` to `true` was important for accuracy with isoAdvector. Computations were run up to time $t = 3$ s in 2D and $t = 3.5$ s in 3D.

4   Results

Post-processing quantities of interest are described in details in [3, 4]. These are the vertical position of the bubble centroid, the bubble rise velocity, the bubble circularity/sphericity, bubble area/volume and surface perimeter/area in 2D/3D. The circularity/sphericity is the inverse ratio of the bubble surface perimeter/area to the area/volume-equivalent circle/sphere in 2D/3D. It takes the value 1 at the beginning of the computation and decreases as the bubble deforms.

Figure 1: Configuration and boundary conditions for 2D bubble benchmark.

The Figure 2 shows the bubble shape obtained with MULES and isoAdvector for the finest 2D simulation at time $t = 3$ s together with results from the reference data from [3]. Slight differences appear in the prediction of the front and back main interface positions (see zooms 1 and 2), with the most noticable difference being isoAdvector falling slightly behind the other methods. All the codes predict rather different trains of detached bubbles (see zoom 3 frame). The time evolution of Figure 3 shows a comparison between MULES and isoAdvector at grid resolution 160, and for the 2D calculations. Again results are very similar, especially for the main bubble shape, and we see a small retardation of the isoAdvector bubble compared with the MULES bubble towards the end of the simulation.

Figure 4 shows 3D results for the rise velocity and sphericity. MULES and isoAdvector results are almost identical. When compared with the available reference data, the bubble rise velocity is, however, overpredicted by both solvers. This discrepancy will require further investigation, as the results obtained in reference [4] using `interFoam` version 2.2.2 differ from the currently used version taken from OpenFOAM-v1712. The right hand side of Figure 4 shows that sphericity results start to differ between MULES and isoAdvector at times larger than roughly 2.5 s. This is mainly explained by the presence of small trains of detached bubbles in the isoAdvector run. The available reference data shows that the scatter between all the different solvers is important at large times. This is again explained by the prediction of different structures in the bubble queue, as observed in 2D (see also Figure 2).

3D computations have been run on the Occigen supercomputer at CINES, on Intel Xeon E5-2690V3. The largest computation with $320 \times 640 \times 320 = 65536000$ cells was run on 504 cores for 29.25 hours for MULES versus 26.78 hours for isoAdvector (so about 10% faster).
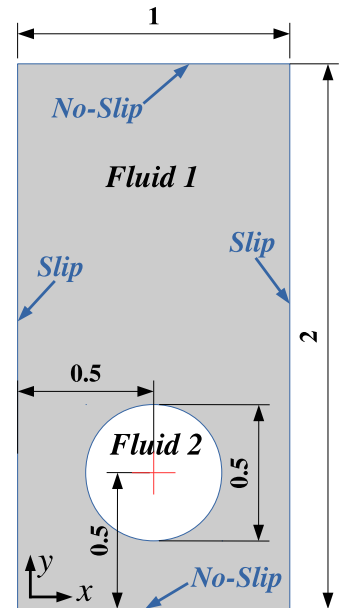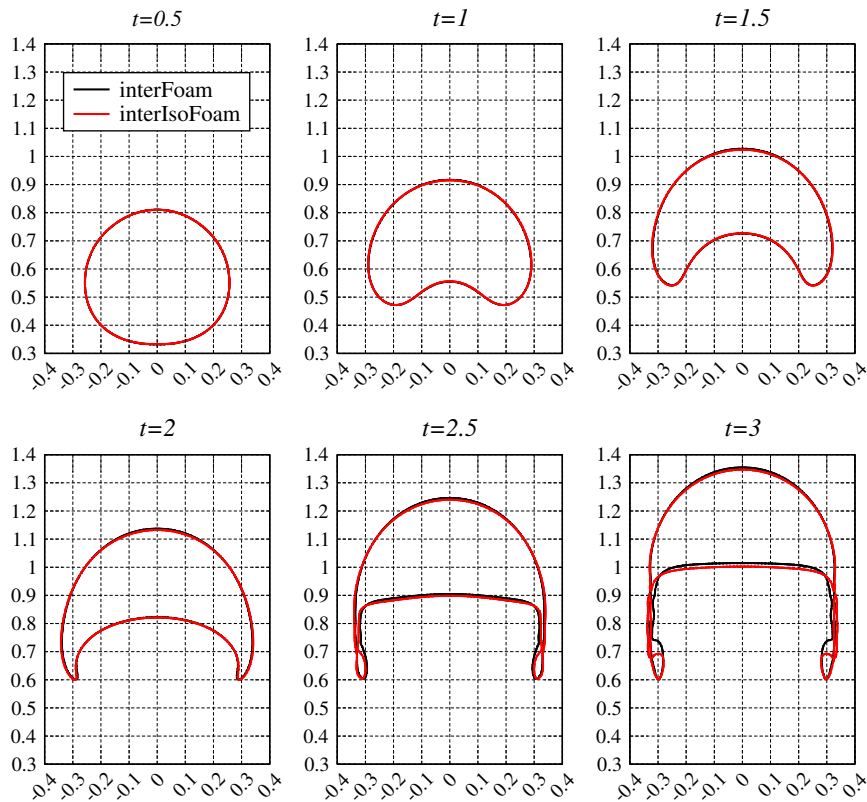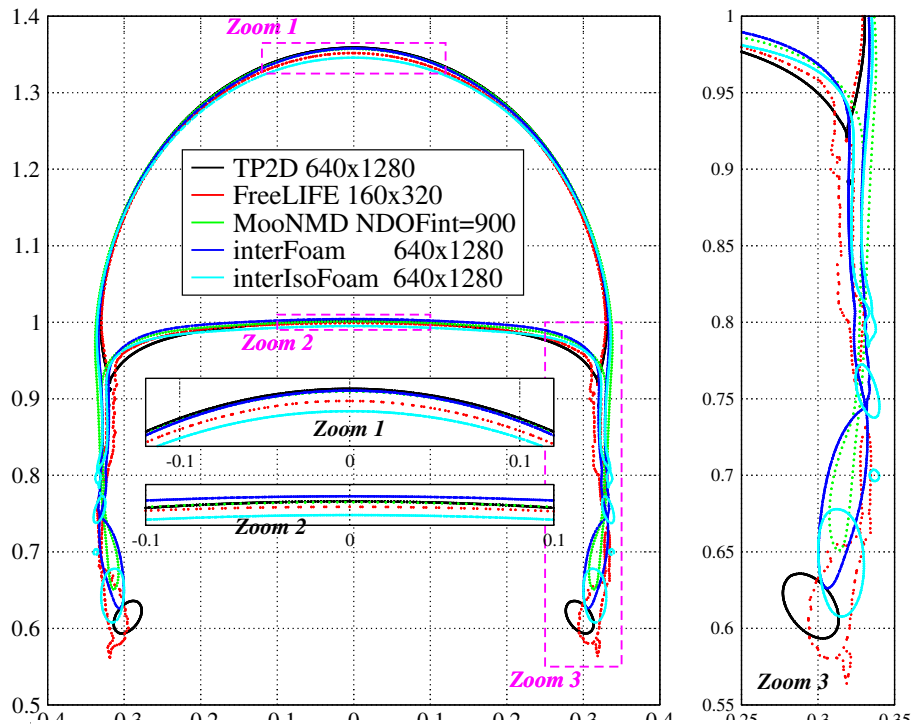
Figure 3: Time evolution of bubble shapes for 2D test case at resolution 160×320. **Comparison of MULES with isoAdvector.**

5 Summary

This paper has shown a quantitative validation of the isoAdvector method against MULES and other codes. The test case used is the Hysing benchmark, both in 2D and 3D. isoAdvector has been verified to work for rising bubble simulation with similar accuracy as MULES and with a sharper interface and slightly smaller calculation times. This reference case will be contributed to the OpenFOAM® tutorial wiki.
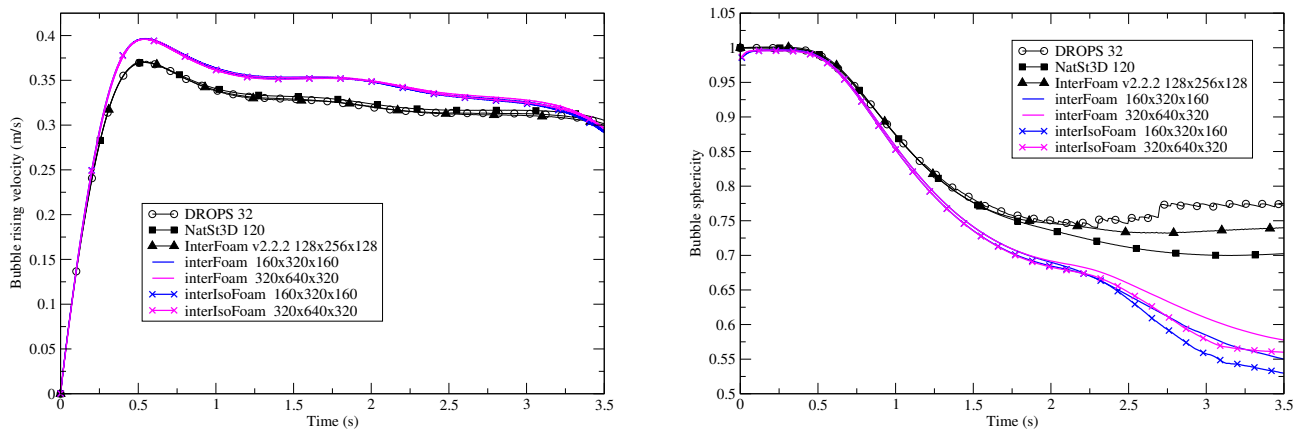
Figure 4: Time evolution of rise velocity (left) and sphericity (right) for 3D test case.

References

[1] C. Hirt and B. Nichols, "Volume of fluid (VOF) method for the dynamics of free boundaries," J. Comp. Phys., vol. 39, no. 1, pp. 201 – 225, 1981.

[2] S. Osher and J. A. Sethian, "Fronts propagating with curvature-dependent speed: Algorithms based on Hamilton-Jacobi formulations," J. Comp. Phys., vol. 79, no. 1, pp. 12 – 49, 1988.

[3] S. Hysing, S. Turek, D. Kuzmin, N. Parolini, E. Burman, S. Ganesan, and L. Tobiska, "Quantitative benchmark computations of two-dimensional bubble dynamics," I.J.N.M.F., vol. 60, no. 11, pp. 1259–1288, 2009. [Online]. Available: http://www.featflow.de/en/benchmarks/cfdbenchmarking/bubble.html

[4] J. Adelsberger, P. Esser, M. Griebel, S. Groß, M. Klitz, and A. Rüttgers, "3D incompressible two-phase flow benchmark computations for rising droplets," 2014, proceedings of the 11th World Congress on Computational Mechanics (WCCM XI), Barcelona, Spain, also available as INS Preprint No. 1401 and as IGPM Preprint No. 393. [Online]. Available: http://wissrech.ins.uni-bonn.de/research/projects/risingbubblebenchmark/

[5] J. Roenby, H. Bredmose, and H. Jasak, "A computational method for sharp interface advection," Royal Society Open Science, vol. 3, no. 11, 2016.

[6] H. G. Weller, "A new approach to vof-based interface capturing methods for incompressible and compressible flow," OpenCFD Ltd., Report TR/HGW/04, 2008.

[7] S. S. Deshpande, L. Anumolu, and M. F. Trujillo, "Evaluating the performance of the two-phase flow solver interfoam," Comp. Sc. & Discovery, vol. 5, no. 1, p. 014016, 2012. [Online]. Available: http://stacks.iop.org/1749-4699/5/i=1/a=014016

[8] H. Marschall, K. Hinterberger, C. Schler, F. Habla, and O. Hinrichsen, "Numerical simulation of species transfer across fluid interfaces in free-surface flows using openfoam," Ch. Eng. Sc., vol. 78, pp. 111 – 127, 2012.

[9] A. Q. Raeini, M. J. Blunt, and B. Bijeljic, "Modelling two-phase flow in porous media at the pore scale using the volume-of-fluid method," J. Comp. Phys., vol. 231, no. 17, pp. 5653 – 5668, 2012.

[10] D. A. Hoang, V. van Steijn, L. M. Portela, M. T. Kreutzer, and C. R. Kleijn, "Benchmark numerical simulations of segmented two-phase flows in microchannels using the volume of fluid method," Computers & Fluids, vol. 86, pp. 28 – 36, 2013.

[11] C. Bilger, M. Aboukhedr, K. Vogiatzaki, and R. Cant, "Evaluation of two-phase flow solvers using level set and volume of fluid methods," J. Comp. Phys., vol. 345, pp. 665 – 686, 2017.

[12] J. Roenby, B. E. Larsen, H. Bredmose, and H. Jasak, "A new Volume-of-Fluid method in OpenFOAM," in VII International Conference on Computational Methods in Marine Engineering, MARINE 2017, 2017.

[13] J. Roenby, H. Bredmose, and H. Jasak, "IsoAdvector: Geometric VOF on general meshes," in OpenFOAM - Selected papers of the 11th Workshop. Springer, 2018.

[14] H. Scheufler and J. Roenby, "Accurate and efficient surface reconstruction from volume fraction data on general meshes," arXiv, Jan. 2018. [Online]. Available: http://arxiv.org/abs/1801.05382

WETTING PHENOMENA WITH ALE INTERFACE TRACKING

DIRK GRÜNDING[1], DIETER BOTHE[2], HOLGER MARSCHALL[3]

[1][2][3]*Technical University Darmstadt, Institute for Mathematical Modeling and Analysis*
[1]*gruending@mma.tu-darmstadt.de*, [2]*bothe@mma.tu-darmstadt.de*, [3]*marschall@mma.tu-darmstadt.de*

Keywords: multiphase flows, free surface flows, interface tracking, mesh movement, wetting, dynamic contact angles, growing droplet

Introduction

Multiphase flows are present in numerous situations in our daily live, may it be the droplet on a window while it is raining, or the liquids that we drink. They are relevant in a wide variety of industrial processes e.g. rain drops on the windshield of a car or a drop of blood in a micro fluidic device.

Within such applications, only few situations arise where there is no relevant interaction with a solid boundary as e.g. with free flow of a bubble in a column reactor. In most devices, wall boundaries are a relevant factor, as these may e.g. give the shape of the product or can cause undesired inclusions reducing the product's quality and mechanical stability. Consequently, it is crucial to provide CFD tools that can be used within the development process of products that deal with wetting phenomena in their application or during their production.

Multiphase flow phenomena on the drop or bubble scale are usually modeled via a continuum mechanical approach which is followed in this work. Here, an incompressible, immiscible, Newtonian fluid with constant fluid properties in each phase is considered. In this work, the multiphase flow is modeled as a free surface flow, where the gaseous phase is neglected. Additionally, Marangoni effects are neglected. This leads to solving the Navier-Stokes equations in combination with the mass and momentum transmission conditions at liquid free surface on a deforming domain $\Omega_-(t)$. In addition to the constitutive equation for the Cauchy stresses $\mathbf{S}$ and a relation for the dynamic contact angle is required. As boundary conditions on the wall, a generalized slip boundary condition with slip coefficient β is assumed. This yields the following analytical model:

Mass & momentum conservation
for $t > 0$, $x \in \Omega_\pm(t)$

$$\operatorname{div} \mathbf{v} = 0$$
$$\rho \partial_t \mathbf{v} + \rho \operatorname{div}(\mathbf{v} \otimes \mathbf{v}) = \operatorname{div} \mathbf{S} + \rho \mathbf{g}$$

Boundary conditions
for $t > 0$, $x \in \mathcal{S}(t)$

$$\mathbf{v} \cdot \mathbf{n}_\mathcal{S} = 0$$
$$\mathbf{P}_\mathcal{S} \mathbf{v} + \beta \mathbf{P}_\mathcal{S} \mathbf{S} \mathbf{n}_\mathcal{S} = 0$$

Mass & momentum transmission
for $t > 0$, $x \in \Sigma(t)$

$$[\![\mathbf{v}]\!] = 0$$
$$-[\![\mathbf{S}]\!] \mathbf{n}_\Sigma = \sigma \kappa \mathbf{n}_\Sigma$$

Constitutive equations

$$\mathbf{S} = -p\mathbf{I} + \mu(\nabla \mathbf{v} + \nabla \mathbf{v}^\mathrm{T})$$
$$\theta = f(\mathrm{Ca}), \quad \mathrm{Ca} = \mu v_\Gamma / \sigma$$

Jump brackets:

$$[\![\phi]\!] := \lim_{h \to 0} (\phi(\mathbf{x}_\Sigma + h\mathbf{n}_\Sigma) - \phi(\mathbf{x}_\Sigma - h\mathbf{n}_\Sigma))$$
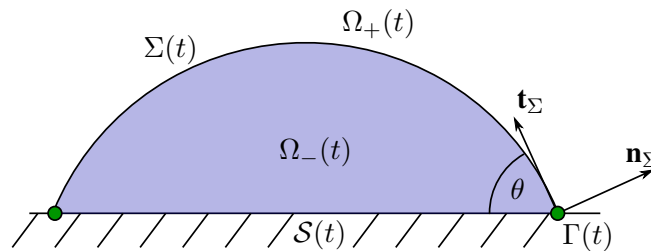
Figure 1: Illustration of bulk phases for the gaseous and liquid phases $\Omega_+(t)$ and $\Omega_-(t)$ that are separated by the liquid gas interface $\Sigma(t)$. The droplet wets a planar solid wall on the area $\mathcal{S}(t)$ and forms a contact line $\Gamma(t)$ where surface normal and tangent vectors n_Σ and t_Σ are depicted. As the domain changes over time, all illustrated quantities depend on time t.

Here, μ and ρ are the dynamic viscosity and density of the liquid, v_Γ is the contact line velocity, κ is twice the mean curvature of the free surface, σ is the surface tension coefficient, $\mathbf{g}$ is the vector of gravitational acceleration, and Ca is the capillary number. The relevant sets are the gaseous and liquid phases $\Omega_-(t)$ and $\Omega_+(t)$, the interface $\Sigma(t)$, the contact line $\Gamma(t)$ and wetted wall $\mathcal{S}(t)$, all illustrated in figure 1. Furthermore, $\mathbf{P}_\mathcal{S}$ is the projector onto the wall boundary.

While multiphase flows are undoubtedly relevant in various phenomena in nature and industry, it is still under debate what models are needed to resolve certain hydrodynamic phenomena. Simpler models are of the form $\theta = f(\text{Ca})$. In the simplest way, the contact angle is modeled constant or via a advancing and receding contact angle. Experimental results can provide a functional relation, e.g. [1, 2, 3]. More sophisticated models e.g. [4] addresses the moving contact line paradox, see [5] however, they require the solution of coupled partial differential equations on the boundaries of the moving liquid domain.

ALE - Interface Tracking

The wetting problem described above is solved with OpenFOAM's arbitrary Lagrangian Eulerian (ALE) interface tracking method [6, 7]. With this approach a subset of the mesh boundary coincides with the interface allowing to accurately track its deformation. This means that when the interface is moving, the interface mesh is following this change. Aiming for mass conservation, the interface is moved using a control-point based algorithm [8]. To maintain overall mesh quality, the bulk mesh has to adapt to this deformation by mesh motion (controlled by mesh modifiers) or remeshing. While the effort to move the mesh is extensive and does also limit the capability to capture highly deforming domains without remeshing, it provides a consistent surface mesh. This outstanding feature of the interface tracking method can be used to simulate the evolution of surface active species (surfactants) usually present on the liquid gas interface by means of a finite area method. This is an important feature to model actual physical systems, as even a small contaminations by surfactants can significantly influence the surface tension coefficient and thereby the hydrodynamics of flow [9, 10, 11].

Results

The ALE interface tracking method has been extended to handle wetting phenomena and provides a library for dynamic contact angle models. Boundary conditions have been added to allow the simulation of wetting of planar surfaces. These simulations include among others the verification case where a drop is spreading on a planar surface for varying Eötvös numbers. A more complex validation is performed by comparison to experimental data. This allows to compare results for varying wall boundary conditions where the contact line of a drop with increasing volume is modeled.

Stationary Droplet

To validate the wetting models that have been implemented into the existing ALE interface tracking framework, the test from [12] is used. This setup can be used in 2D or 3D and consists of a droplet that is initialized as e.g. a hemisphere. Then, the simulation is started to obtain the stationary state of the system. When varying the Eötvös number e.g. by varying the magnitude of the gravitational acceleration, the stationary state of the drop is flattening with increasing Eötvös number. Analytic reference solutions are available for one regime where gravitation is the dominant effect and the other where surface tension is the relevant influence on the drop shape. In addition simulation results from a volume of fluid approach are available for the full spectrum of Eötvös numbers including the transition region between the two regimes mentioned before. Results for this test case are given in figure 2. It can be seen that the ALE simulation results show an overall excellent agreement with the analytic reference solutions as much as with the simulation results from [12].
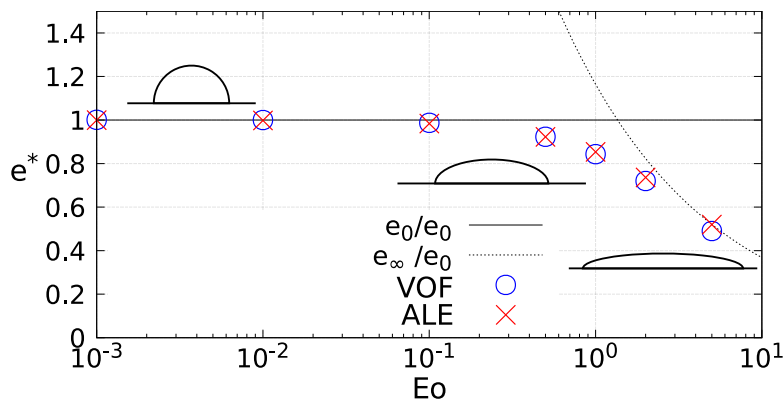
Figure 2: Comparison of non-dimensional stationary drop height e^* over varying Eötvös numbers. The straight horizontal line at $e^* = 1$ shows the limit vanishing Eötvös number. The dotted line indicates the limiting case for a gravity dominated regime. Reference data from a volume of fluid method (VOF) obtained from [12] is (blue circles) compared to ALE interface tracking results from OpenFOAM (red crosses).

Growing Droplet

In order to evaluate the implemented wetting model in comparison to experimental data, a spherical cap shaped drop is initialized. Here, the initial contact angle depends on the equilibrium contact angle of the fluid-surface combination. To achieve a moving contact line situation, liquid is pumped into the droplet from an opening on the surface. This setup is illustrated in figure 3. It shows the clipped region of a liquid drop on a planar surface. The colored mesh indicates the magnitude of the velocity inside the liquid bulk phase. The light blue stream lines illustrate the inflow of liquid from the bottom. The inflow region can be identified by a higher velocity magnitude marked in red. A coarse mesh is shown to illustrate the structure of the mesh. Here, a constant contact angle model with $\theta = 70°$ is used. This experimental setup allows to compare a variety of properties such as e.g. interface shape, dynamic contact angles, etc.
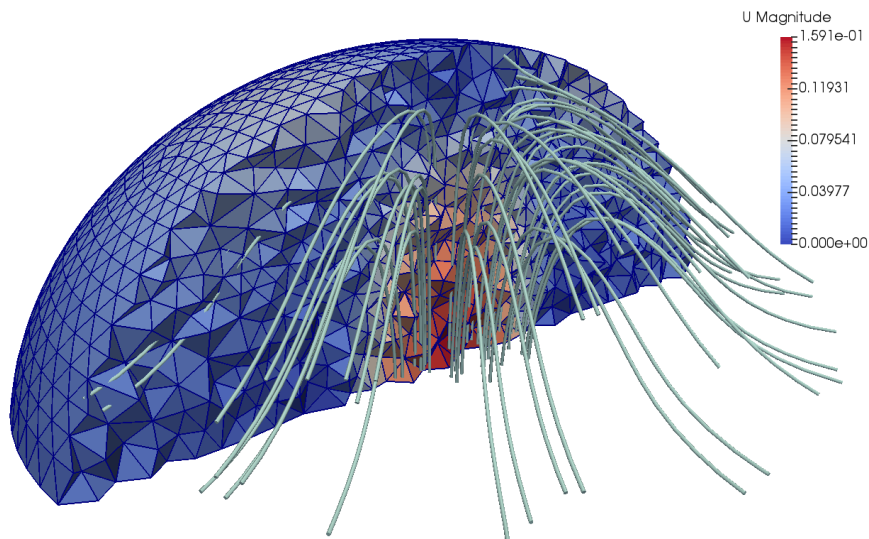
Figure 3: Clipped part of a hemispherical droplet with a radius of $5\,\mathrm{mm}$ for a preliminary study for comparison to experiments. Constant contact angle model with $\theta = 70°$. Inflow of liquid with Poiseuille flow profile and volume flux of $10^{-6}\,\mathrm{m^3\,s^{-1}}$ through pipe with radius of $2\,\mathrm{mm}$. Mesh color signifies the magnitude of the bulk velocity. The stream lines are indicated with light blue lines.

Relevance

Wetting phenomena are relevant for a wide variety of phenomena in nature and countless technical applications. Especially for technologies where high resolution of the interface is of importance when surfactants come into play the interface tracking method can provide detailed local information. With the implemented contact angle models, it is possible to capture basic wetting phenomena and to evaluate the models performance in comparison to experiments. In addition, the influence of the wall boundary conditions on the flow field can be investigated. The presence of OpenFOAM's finite area method promises an extension and hence a direct comparison to Shikhmurzaev's interface formation model. Furthermore, the incorporation of wetting models into the existing ALE framework will allow to investigate the influence of surfactants on the wetting behavior in the future.

References

[1] R. L. Hoffman, "A Study of the Advancing Interface. I. Interface Shape in Liquid-Gas Systems," Journal of Colloid and Interface Science, vol. 50, no. 2, pp. 228–241, Feb 1975. [Online]. Available: http://dx.doi.org/10.1016/0021-9797(75)90225-8

[2] S. Kistler, "Hydrodynamics of wetting," in Wettability, ser. surfactant science series, J. Berg, Ed. Dekker, M., 1993, vol. 49.

[3] M. Bracke, F. Voeght, and P. Joos, "The kinetics of wetting: the dynamic contact angle," Trends in Colloid and Interface Science III, pp. 142–149, 1989. [Online]. Available: http://dx.doi.org/10.1007/BFb0116200

[4] Y. Shikhmurzaev, "The moving contact line on a smooth solid surface," International Journal of Multiphase Flow, vol. 19, no. 4, pp. 589–610, Aug 1993. [Online]. Available: http://dx.doi.org/10.1016/0301-9322(93)90090-H

[5] J. H. Snoeijer and B. Andreotti, "Moving contact lines: Scales, regimes, and dynamical transitions," Annual Review of Fluid Mechanics, vol. 45, no. 1, pp. 269–292, Jan 2013. [Online]. Available: http://dx.doi.org/10.1146/annurev-fluid-011212-140734

[6] Ž. Tuković, "Metoda kontrolnih volumena na domenama promjenjivog oblika," Ph.D. dissertation, University of Zagreb, 2005. [Online]. Available: http://ara.srce.hr/index.php/record/view/144806

[7] Ž. Tuković and H. Jasak, "A moving mesh finite volume interface tracking method for surface tension dominated interfacial fluid flow," Computers & Fluids, vol. 55, pp. 70–84, 2012. [Online]. Available: http://www.sciencedirect.com/science/article/pii/S0045793011003380

[8] S. Muzaferija and M. Perić, "Computation of free-surface flows using the finite-volume method and moving grids," Numerical Heat Transfer, Part B: Fundamentals, vol. 32, no. 4, pp. 369–384, Dec 1997. [Online]. Available: http://dx.doi.org/10.1080/10407799708915014

[9] K. Dieter-Kissling, H. Marschall, and D. Bothe, "Direct numerical simulation of droplet formation processes under the influence of soluble surfactant mixtures," Computers & Fluids, vol. 113, pp. 93–105, May 2015. [Online]. Available: http://dx.doi.org/10.1016/j.compfluid.2015.01.017

[10] C. Pesci, K. Dieter-Kissling, H. Marschall, and D. Bothe, "Finite Volume/Finite Area Interface Tracking method for two-phase flows with fluid interfaces influenced by surfactant," in Progress in colloid and interface science, M. T. Rahni, M. Karbaschi, and R. Miller, Eds. CRC Press, Taylor & Francis Group, 2015, ch. 18, pp. 373–409.

[11] C. Pesci, A. Weiner, H. Marschall, and D. Bothe, "Computational analysis of single rising bubbles influenced by soluble surfactant," ArXiv e-prints, Dec. 2017.

[12] J.-B. Dupont and D. Legendre, "Numerical simulation of static and sliding drop with contact angle hysteresis," Journal of Computational Physics, vol. 229, no. 7, pp. 2453–2478, Apr 2010. [Online]. Available: http://dx.doi.org/10.1016/j.jcp.2009.07.034

A HIGH FIDELITY WAVE MAKER BASED ON MULTI-MOMENT FINITE VOLUME FORMULATION AND THINC METHOD

ZHIHANG ZHANG[1], XIZENG ZHAO[2], BIN XIE[3]

[1]*Ocean college, Zhejiang University, lokikerry@zju.edu.cn*
[2]*Ocean college, Zhejiang University, xizengzhao@zju.edu.cn*
[3]*School of Naval Architecture, Shanghai Jiaotong University, xie.b.aa@sjtu.edu.cn*

Second-order accurate numerical methods underpin the majority of industrial CFD solvers as well as the open-source CFD library OpenFOAM. Based on these methods, wave makers are expected to suffer from excessive numerical viscosity, resulting in notable dissipation and reduction in wave energy even for zero physical viscosity. Commercial software STAR-CCM+ and open-source solver interFoam(a multiphase solver within OpenFOAM) are widely used for simulations of free-surface waves in oceanographic engineering and coastal engineering. Simulations of regular-wave propagation with these two solvers show that the results are sensitive to temporal and spatial discretizations [1] [2], indicating that satisfactory results are promised merely when grids and time steps are refined enough using these numerical solvers. But refining grids and time steps leads to increase in computational cost. The increase could be unaffordable for some cases, e.g. those involve short-period waves as the relatively higher frequency causes greater numerical dissipation.

To overcome this problem in numerical investigations, a wave maker based on third-order accurate VPM(volume-average/point-value multi-moment) scheme [3] and THINC/QQ method(the THINC method with quadratic surface representation and Gaussian quadrature) [4] is presented in this study. A mass source function [5] and a sponge layer [6] are embedded into this two-dimensional Navier-Stokes model for wave generation and absorption respectively. Numerical simulations of regular waves with different time steps and grid resolutions are carried out with the present model and interFoam solver for comparison. It is demonstrated that with interFoam solver, generated wave trains encounter a significant loss of wave hight along the propagation direction, in addition, a phase shift is produced due to a change in wave period and wavelength. While the wave maker based on the present model produces high-fidelity results, which show a fairly trifling loss of wave height and negligible phase shift.

The rest of this abstract is organized as follows. After a brief description of governing equations, the solution procedures for both solvers and the numerical setups are given. The simulation results with both solvers are presented and compared to verify the performance of the present solver. This abstract is ended with conclusion remarks and future work.

In this study, the incompressible two-fluid flows with moving interface are solved based on the one-fluid model. The Navier-Stokes equations containing the effects of surface tension and gravity are used for both fluids in the same form,

$$\nabla \cdot \mathbf{u} = s(t), \tag{1}$$

$$\frac{\partial \rho \mathbf{u}}{\partial t} + \nabla \cdot (\rho \mathbf{u} \otimes \mathbf{u}) = -\nabla p + (\nabla \cdot (\mu \nabla \mathbf{u}) + \nabla \mathbf{u} \cdot \nabla \mu) + \mathbf{F}_s - \mathbf{g} \cdot \mathbf{x} \nabla \rho + \mathbf{F}_d, \tag{2}$$

$$\frac{\partial \phi}{\partial t} + \nabla \cdot (\mathbf{u}\phi) = \phi \nabla \cdot \mathbf{u}. \tag{3}$$

where $\mathbf{u} = (u, v)$ is the velocity vector with components u and v in x and y directions respectively, p is the pressure in excess of the hydrostatic part, $\mathbf{g}$ is the gravity acceleration, ρ the density and μ the dynamic viscosity coefficient. $\mathbf{F}_s$ is the surface tension force formulated by $\mathbf{F}_s = \sigma \kappa \nabla \phi$ with σ being the surface tension coefficient and κ the interface curvature. A volume-of-fluid(VOF) function is used with an indicator function $\phi(\mathbf{x}, t)(0 \le \phi \le 1)$ distinguishing two kinds of fluids and the intrinsic fluid properties, such as density and viscosity, are updated based on the VOF function. It is noted that the mass source $s(t)$ and momentum source $\mathbf{F}_d$ are employed for wave generation and absorption respectively, the specific forms of which are given in following sections.

The solution of the momentum equation in interFoam is performed by constructing a predicted velocity field and then correcting it using the "Pressure Implicit with Splitting of Operators"(PISO) procedures to update the numerical solution from time level n($t = t^n$) to n+1($t = t^n + \Delta t$). To evaluate the fluxes on cell boundaries, a central differencing flux and a non-oscillatory upwind flux are adopted. When using a so-called limitedLinearV scheme, a TVD conforming flux limiter of $\psi(r) = max[0, min(2r, 1)]$ is applied to switch between two flux schemes. A numerical interface compression method is applied in interFoam to keep the interface sharp and the compression is obtained by adding a heuristic term to VOF transport equation, such that it attains,

$$\frac{\partial \phi}{\partial t} + \nabla \cdot (\mathbf{u}\phi) + \nabla \cdot [\mathbf{u}_r \phi(1 - \phi)] = \phi \nabla \cdot \mathbf{u} \tag{4}$$

And the "Multidimensional universal limiter with explicit solution"(MULES) limiter is used to limit the phase fluxes in solving VOF function. It is noted that, in this study, the divergence term $\phi\nabla \cdot \mathbf{u}$ in Eq. (4) is included in view of the fact that the mass source function turns it into a non-zero value within the source region.

The numerical framework of the present model is constructed by combining VPM and THINC/QQ schemes, which are for solving momentum equation and VOF function respectively. The projection solution procedure is employed to time advance the pressure and velocity fields and the detailed solution procedures can be found in [7]. The VPM method is applied to discretize the momentum equation, which includes the point values(PV) at cell vertices as new degrees of freedom(DOFs) in addition to the volume integrated average(VIA) and the two kinds of variables are updated separately in each time step. By adding additional DOFs, high-order reconstructions are realized over compact mesh stencil to make a significant improvement in accuracy and robustness on unstructured grids with a mild increase in computation cost. The interested readers are referred to Xie et al.(2014) [3] for more details on numerical implementation. The VOF function is computed with THINC/QQ scheme, in which a hyperbolic tangent function in the local coordinate (ξ, η, ζ) is used to approximate the indicator function $H(\mathbf{x}, t)$ for the target cell Ω_i at each time step,

$$H_i(\xi, \eta, \zeta) = \frac{1}{2}(1 + tanh(\beta(P_i(\xi, \eta, \zeta) + d_i))), \tag{5}$$

where β determines the steepness of the jump in the interpolation function and has a constant value of 1.5 in this study. $P_i(\xi, \eta, \zeta) = 0$ represents the interface surface in the standard element, which is approximated as a curved surface by using fully quadratic polynomial that includes the geometric information. See Xie and Xiao(2017) [4] for details.

For this study, a simple base case of regular wave trains on a constant water depth $d = 0.35m$ will be simulated with
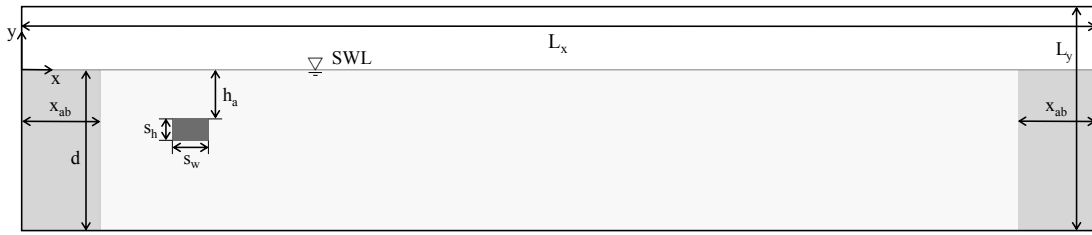
Figure 1: 2D computational domain filled with water(ivory white) and air(white), with source region(dark grey) and sponge layers(light grey).

wavelength and 10 cells per wave height in the vicinity of the SWL. The grid remains uniform in the horizontal direction but nonuniform in the vertical direction, which is coarsened gradually from the SWL to the tank bottom. The time step for reference simulation is set as $\Delta t = 0.004s$, which corresponds to 250 time steps per wave period. For the generation of linear monochromatic wave trains, $\eta(t) = Hsin(\sigma t)/2$, a mass source function field will be given as,

$$s(t) = \begin{cases} \frac{CHk}{A}sin(\sigma t) & within\ source\ region \\ 0 & elsewhere \end{cases} \tag{6}$$

where C stands for the phase velocity and A is the area of the source region. A magnification factor k is applied to the mass source function for the fact that not all the momentum introduced into the system contributes to the wave generation. And according to our observation, the amplitudes of generated waves highly depend on the location of the source region relative to the SWL, so the value of factor k will be determined by making the observed wave amplitudes close enough to the desired value in this study. To prevent undesirable wave reflections from the domain boundaries, absorbing regions are employed by adding damping force $\mathbf{F}_d$ into the momentum equation, which has a form as,

$$\mathbf{F}_d = \rho\mathbf{u}A_b, \tag{7}$$

where A_b is the absorption coefficient, a commonly used form proposed by Wei and Kirby(1995) [6] is applied,

$$A_b = \begin{cases} c_\alpha\dfrac{e^{\left[\left(\frac{|x-x_{st}|}{x_{ab}}\right)^{n_c}\right]}-1}{e^1-1} & x_{st} < x < x_{st} + x_{ab} \\ 0 & elsewhere \end{cases} \tag{8}$$

where x_{st} and x_{ab} are the starting position and length of the absorbing regions, respectively, c_α and n_c are the empirical damping coefficients to be determined via the numerical tests, which in this study are taken as $c_\alpha = 100$ and $n_c = 3.5$.

It is noted that, with the present model, the steepness parameter β from the THINC function is reduced to 0.5 within the absorbing regions to enhance the absorption efficiency. Numerical experiments are conducted with both interFoam solver and the present solver, the simulated results will be compared and discussed in this section.

First, linear monochromatic wave trains which have the same setup with the base case are performed for 60 wave periods. The surface elevations along the horizontal direction after 60 wave periods are shown in Fig. 2, distinct differences between interFoam simulation and the results with the present model can be seen from this figure. This figure intuitively illustrates that the wave amplitudes in interFoam simulation diminish as the wave trains propagate farther and a nonnegligible phase shift is produced at the same time. It is noted that, though the mass source function has a form of a linear wave, the generated wave trains show nonlinearity due to the intermediate water depth condition. So the 2nd-order Stokes theory is treated as the analytical results as well as what follows.
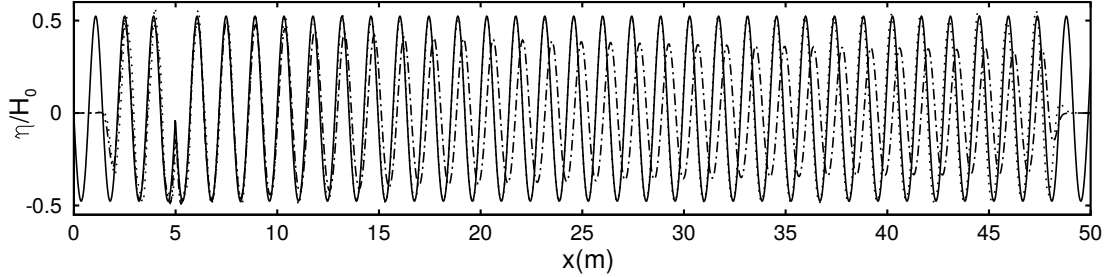
Figure 2: Surface elevations over x-location at t/T=60 with: ———, 2nd-order Stokes theory; – – – – –, interFoam solver; ⋯⋯⋯⋯, the present solver.

Simulations are performed with different time steps and with otherwise the identical setup as the base case. A close-up view of the surface elevations recorded $10\lambda_0$ away from the source region are presented in Fig. 3a. The interFoam simulation shows that, after propagating a distance of $10\lambda_0$, significant amplitude loss and phase antedisplacement are produced in the 0.008s case. The wave profiles approach the analytical result as the time step reduces, but there is still noticeable discrepancy even with a time step of 0.0002s which roughly corresponds to a maximum Courant number of 0.01. Snapshots of the wave tank at $t/T = 60$ presented in Fig. 3b shows that interFoam simulation brings phase retrodisplacement simultaneously, which is attributed to wavelength expansion. While the present solver produces highly consistent results and the insensitivity of the present solver to time step is supposed to be attributed to the use of third-order Runge-Kutta time-integration scheme instead of first-order Euler scheme.

For the grid study, simulations are performed on two other sets of grid, one coarser grid, and one finer grid. The time steps are modified in the light of the grid size to synchronize the Courant number of the simulations. As shown in Fig. 4a and Fig. 4b, with interFoam solver, the wave amplitudes diminish, the time series of the wave profile shift forward and the wave profiles over x-location shift backward. The disparities aggravate as the coarser grid is employed. And the height loss of the simulated wave trains at the location of $10\lambda_0$ away from the source region is up to 28% of the primitive wave height H_0 on the coarsest grid. While slight differences are produced with the present solver merely when the coarsest grid is used. Something needs to be clarified is that the phase shift with the present solver is not caused by a change in wave period or wavelength as it can be observed from the start of the time series and the snapshots.

Numerical simulations of free-surface waves are carried out with both open-source code interFoam and the present model based on VPM and THINC/QQ methods. A mass source function and a sponge layer are employed to generate wave trains from the inner field and absorb the generated waves near the tank boundaries. Main attention has been paid to the numerical dissipation along the propagation direction of the wave trains. By examining the surface elevations at the location of several wavelengths away from the source region, numerical dissipation is evaluated in the terms of wave amplitude and phase consistency. It has been shown that great numerical dissipation is produced with interFoam solver as wave amplitude loss and phase shift can be observed in interFoam simulations. And the dissipation enlarges as coarser grid solutions and larger time steps are adopted. On the other hand, the results obtained by the present model are insensitive to the temporal and spatial discretization in our time step and grid studies which show a great advantage in wave energy preservation. Future research will focus on the simulation performance of surface-waves with different wave periods and wave steepness in light of that the relatively higher-frequency waves and steeper waves are supposed to suffer from greater numerical dissipation. Although only structured grids are employed in this study, the present numerical framework can be straightly applied on unstructured grids with arbitrary and hybrid elements, which makes it potentially useful and efficient for applications involving complex geometrical configurations such as wave-structure interactions and wave deformation.

(a) over time recorded $10\lambda_0$ away from source region

(b) over x-location at $t/T = 60$
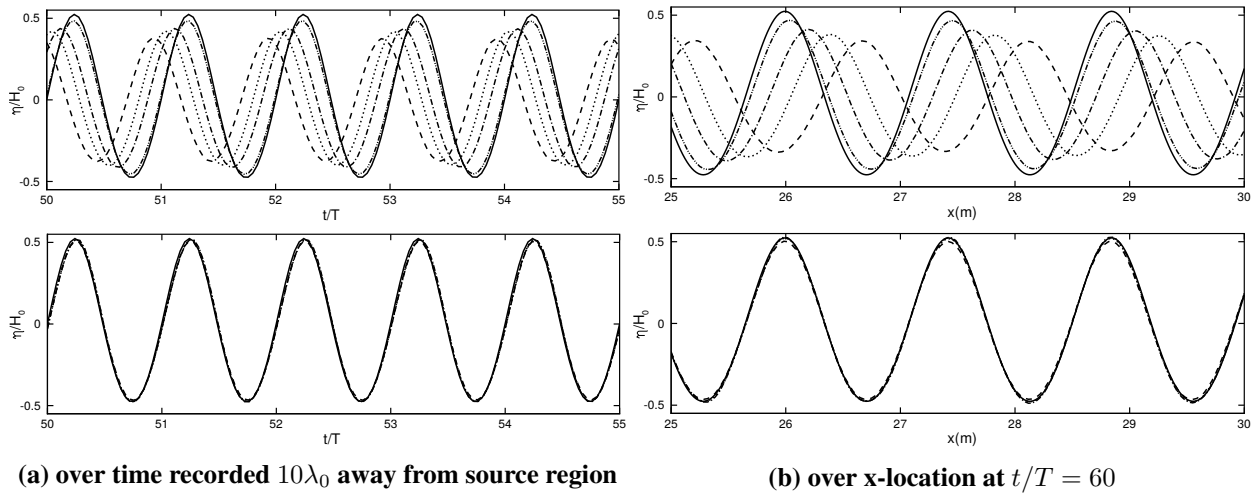
Figure 3: Surface elevations for different time steps: ———, 2nd-order Stokes theory; - - - - -, 0.008s; ·············, 0.004s; - · - · -, 0.002s; - ·· - ·· -, 0.0002s, with interFoam solver(top) and the present solver(bottom)

(a) over time recorded $10\lambda_0$ away from source region

(b) over x-location at $t/T = 60$
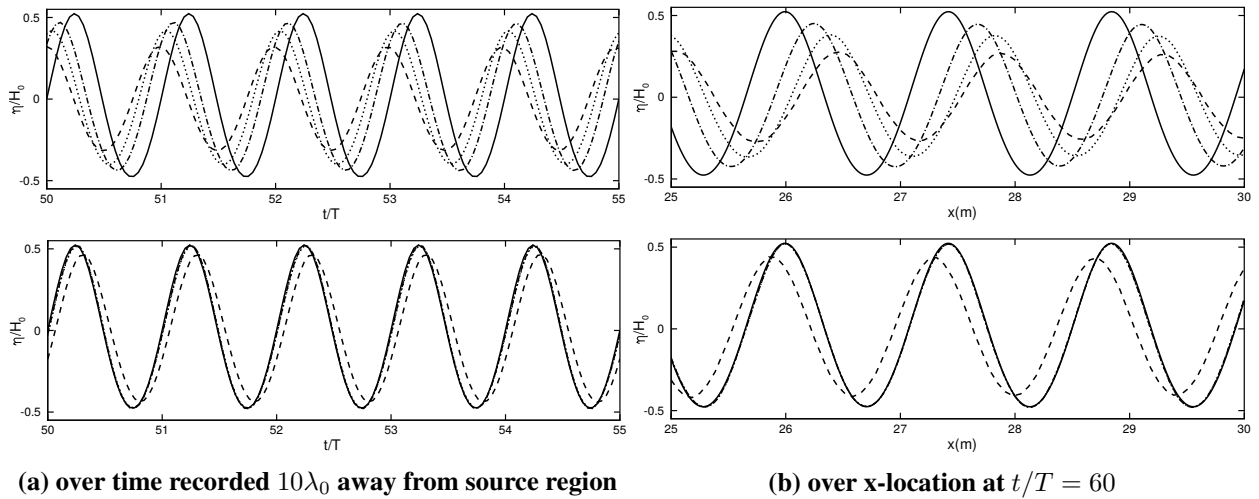
Figure 4: Surface elevations for different grid resolutions: ———, 2nd-order Stokes theory; - - - - -, 2 times coarser grid; ·············, reference grid; - · - · -, 2 times finer grid, with interFoam solver(top) and the present solver(bottom).

References

[1] J.-J. Cha and D.-C. Wan, "Numerical wave generation and absorption based on openfoam," *Ocean Engineering(Haiyang Gongcheng)*, vol. 29, no. 3, pp. 1–12, 2011.

[2] R. Perić and M. Abdel-Maksoud, "Generation of free-surface waves by localized source terms in the continuity equation," *Ocean Engineering*, vol. 109, pp. 567–579, 2015.

[3] B. Xie, S. Ii, A. Ikebata, and F. Xiao, "A multi-moment finite volume method for incompressible navier–stokes equations on unstructured grids: volume-average/point-value formulation," *Journal of Computational Physics*, vol. 277, pp. 138–162, 2014.

[4] B. Xie and F. Xiao, "Toward efficient and accurate interface capturing on arbitrary hybrid unstructured grids: The thinc method with quadratic surface representation and gaussian quadrature," *Journal of Computational Physics*, vol. 349, pp. 415–440, 2017.

[5] P. Lin and P. L.-F. Liu, "Internal wave-maker for navier-stokes equations models," *Journal of waterway, port, coastal, and ocean engineering*, vol. 125, no. 4, pp. 207–215, 1999.

[6] G. Wei and J. T. Kirby, "Time-dependent numerical code for extended boussinesq equations," *Journal of Waterway, Port, Coastal, and Ocean Engineering*, vol. 121, no. 5, pp. 251–261, 1995.

[7] B. Xie, P. Jin, and F. Xiao, "An unstructured-grid numerical model for interfacial multiphase fluids based on multi-moment finite volume formulation and thinc method," *International Journal of Multiphase Flow*, vol. 89, pp. 375–398, 2017.

REGULAR AND IRREGULAR WAVE GENERATION IN OPENFOAM USING HIGH ORDER SPECTRAL METHOD

YUAN ZHUANG[1], DECHENG WAN[1], BENJAMIN BOUSCASSE[2], PIERRE FERRANT[2]

[1] *Collaborative Innovation Center for Advanced Ship and Deep-Sea Exploration, State Key Laboratory of Ocean Engineering, School of Naval Architecture, Ocean and Civil Engineering, Shanghai Jiao Tong University, Shanghai, China. dcwan@sjtu.edu.cn*

2 Ecole Centrale de Nantes, LHEEA Lab. (ECN) Nantes, France

Keywords: *Computational fluid dynamics, High order spectral, waves2Foam*

Introduction

On a number of engineering applications involving wave-structure interactions [1], the use of CFD is essential in order to account for viscous effects and non-linear deformations and breaking of the free surface. Solving Navier-Stokes equations in a viscous numerical wave tank is of low efficiency, in particular is the target is a fully developed sea state. The High Order Spectral (HOS) method [2], [3] solving the nonlinear inviscid problem is therefore applied for outer field wave generation. This reduces the computational cost, by reducing the size of the viscous domain. HOS method has been validated and developed [4], [5], [6] into two open source solvers available on github, nonlinear wave propagation in open sea (HOS-Ocean) [6] and in numerical wave tank (HOS-NWT) [7].

The spatial discretization needed for the solution of the Euler equations with HOS and the Navier-Stokes equations with OpenFOAM is very different. Grid2Grid [8] is a wrapper program of HOS (also available on github) developed to exchange the information between the two solvers. The plug-in toolbox of OpenFOAM waves2Foam [9] can generate fully developed wave fields in arbitrary time and space. In this paper we aim to combine these two methods and this new method is implemented to do the simulations.

Major Work

Inlet and outlet can be imposed in waves2Foam through the relaxation zones which can be seen as coupling zones. At each time step the flow velocity (u,v,w) and the volume fraction of the fluid (α) in coupling zone is computed with equation 1. The value of $\Phi_{t\,arg\,et}$ is obtained from HOS results. Through the relaxation zone, the values of wave fields such as wave elevation and velocity from HOS can be transfered into inner CFD zone and the scattered wave in CFD zone can be mapped in target (incident) wave components when spreading outside. The sketch of the coupling method is shown in Figure 1.

$$\Phi = \alpha_R \Phi_{computed} + [1 - \alpha_R]\Phi_{t\,arg\,et} \tag{1}$$
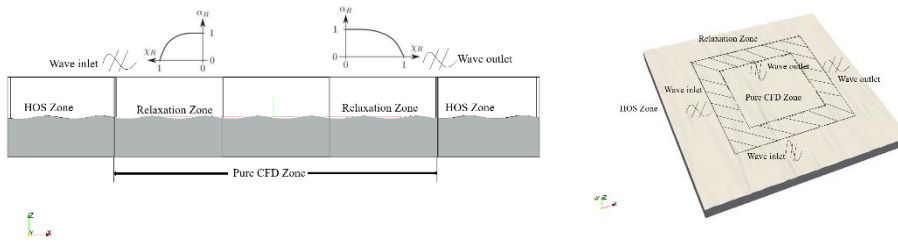
Figure 1 Sketch of the coupling method to compute the propagation wave in 2D and 3D

Results and Conclusions

To validate the effectiveness and accuracy of the coupling method, 6 cases are considered to compare the HOS solution to the CFD solution, shown in table 1. These tests have been computed [8], [10] in coupled method with HOS and foamStar, which is developed by Bureau Veritas and based on OpenFOAM. Therefore, we include the results from foamStar to compare.

Table 1 HOS wave conditions

Wave type	Value	HOS-Ocean		HOS-NWT	
		2D	3D	2D	3D
Regular wave	T (s)	-	-	0.702	0.702
	H (m)	-	-	0.0431	0.0288
Irregular wave	Tp (s)	0.702	1.0	1.0	0.702
	Hs (m)	0.0288	0.10	0.05	0.0384
	γ	3.3	3.3	3.3	3.3

The mesh generation is shown in Figure 2. The 2D cases are 1.14M grid numbers ($\lambda / \Delta x = 95$, $H / \Delta z = 17$ $T / \Delta t = 400$) and 3D cases are 3.2M grid numbers ($\lambda / \Delta x = 32$, $H / \Delta z = 20$ $T / \Delta t = 400$). [10] The wave elevation is analyzed based on the wave probe. The wave probe is put in the middle of the computational domain, see in figure 3. The wave probe is set in the same place both in HOS zone and in CFD zone. Figure 4 shows the comparison of wave elevation results from three methods.
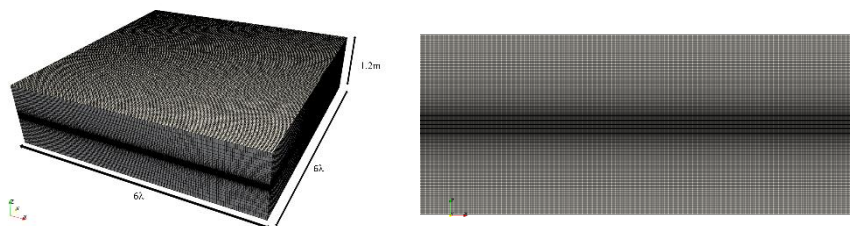
Figure 2 Mesh generation

The time history of wave elevation from CFD zone fairly agree with that from HOS zone, which shows the coupling method has the ability to simulate identical wave elevation which is generated by HOS. The contour of wave elevation indicates that the CFD zone can simulate in arbitrary space. The coupling method can do the simulation in naval and offshore wave-structure interaction effectively in the future.
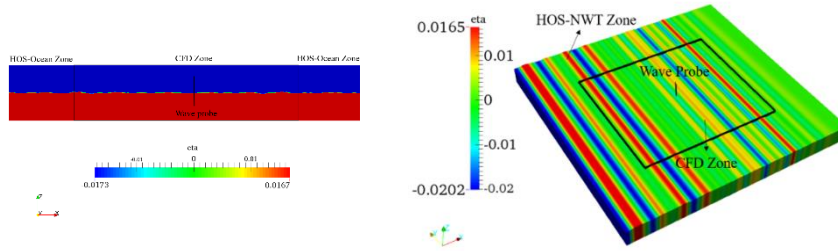
(a) HOS-Ocean 2D irregular wave   (b) HOS-NWT 3D irregular wave

Figure 3 Wave elevation of coupled methods with HOS and waves2Foam.
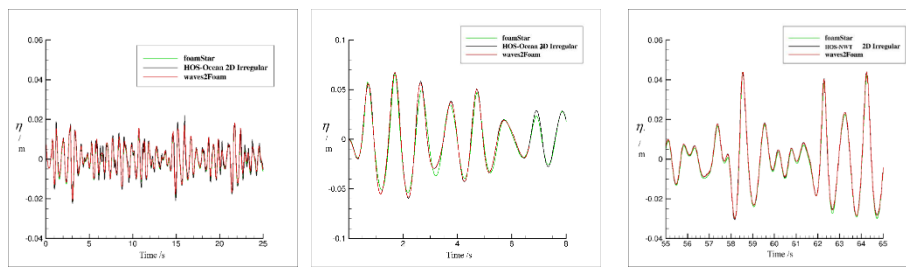
(a) HOS-Ocean 2D irregular wave   (b) HOS-Ocean 3D irregular wave   (c) HOS-NWT 2D irregular wave
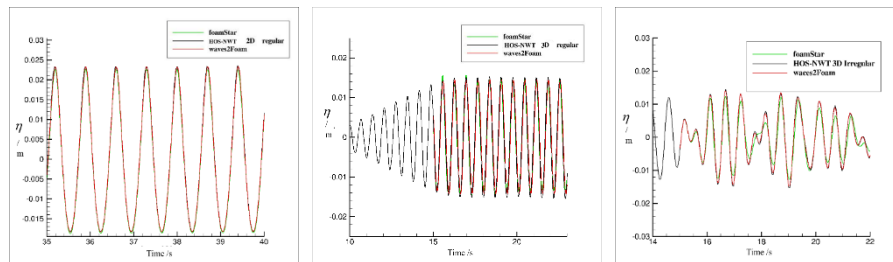
(d) HOS-NWT 2D regular wave   (e) HOS-NWT 3D regular wave   (f) HOS-NWT 3D irregular wave

Figure 4 Validation and comparison of coupled methods with HOS and waves2Foam.

Reference

[1]. Y. Zhuang, D. C. Wan, Numerical study on coupling effects of FPSO ship motion and LNG

tank sloshing in low-filling condition, Applied Mathematics and Mechanics, vol. 37, pp. 1378-1393, 2016.

[2]. B. J. West, K. Brueckner, R. Janda, M. Milder, R. Milton, A new numerical method for surface hydrodynamics. Journal of Geophysical Research, vol. 92, pp. 11803-11824, 1987.

[3]. D. Dommermuth, D. Yue. A high-order spectral method for the study of nonlinear gravity waves. Journal of Fluid Mechanics, vol. 184, pp. 267-288, 1987.

[4]. G. Ducrozet, F. Bonnefoy, D. L. Touzé, P. Ferrant. 3-d hos simulations of extreme waves in open seas. Natural Hazards and Earth System Sciences, vol. 7, pp. 109-122, 2007.

[5]. G. Ducrozet, F. Bonnefoy, D. L. Touzé, P. Ferrant. A modified high-order spectral method for wavemaker modeling in a numerical wave tank. European Journal of Mechanics - B/Fluids, vol. 34, pp.19-34, 2012.

[6]. G. Ducrozet, F. Bonnefoy, D. L. Touzé, P. Ferrant. Hos-ocean: Opensource solver for nonlinear waves in open ocean based on high-order spectral method. Computer Physics Communications, vol. 203, pp.245-254, 2016.

[7]. G. Ducrozet, F. Bonnefoy, D. L. Touzé, P. Ferrant. Implementation and validation of nonlinear wavemaker models in a HOS numerical wave tank. International Journal of Offshore and Polar Engineering, vol. 16, 2006.

[8]. Y. M. Choi, M. Gouin, G. Ducrozet, B. Bouscasse, P. Ferrant. Grid2Grid: HOS Wrapper Program for CFD solvers. arXiv preprint arXiv:1801.00026, 2017.

[9]. N. G. Jacobsen, D. R. Fuhrman, J. Fredsøe. A wave generation toolbox for the open-source CFD library: OpenFoam®. International Journal for Numerical Methods in Fluids, vol. 70, pp.1073-1088, 2012.

[10]. Y. M. Choi, B. Bouscasse, S. Seng, G. Ducrozet, L.Gentaz, P. Ferrant. Generation of regular and irregular waves in Navier-Stokes CFD solvers by matching with the nonlinear potential wave solution at the boundaries. In Proceedings of the ASME International Conference on Ocean, Offshore and Arctic Engineering, Madrid, 2018. (Accepted)

A ONE-WAY COUPLING STRATEGY OF THE GREEN-NAGHDI EQUATIONS AND THE OPENFOAM

W.Y. DUAN[1], K. ZHENG[1], B.B. ZHAO[1*] and J.T. XIE[1]

1 *College of Shipbuilding Engineering, Harbin Engineering University, 150001 Harbin, China*
Email: zhaobinbinheu@hotmail.com

Keywords: OpenFOAM, Green-Naghdi equations, One-way Coupling strategy
Highlights:
- A numerical wave tank is built based on the one-way coupling of the fully nonlinear Green-Naghdi equations and the OpenFOAM.
- The regular waves and Freak waves are simulated to give a comparative study between the Green-Naghdi equations and the one-way coupling strategy.

1. Introduction

The viscous effects usually need not to be considered on the free surface in a numerical wave tank. This has a great benefit for decreasing the computing cost. However, it could not be ignored on a solid boundary and for breaking waves because of the existence of vortex. The Navier-Stokes equations are most commonly used for a viscous numerical wave tank. It is usually accompanied with an expensive computing cost. So it should be attractive to develop a coupling method for the viscous and non-viscous flow. There are two methodologies to achieve the coupling work. One is "Velocity decomposition" and the other is "Domain decomposition".

An exhaustively description on the "velocity decomposition" strategy is given in Edmund (2012). He divides the velocity to irrotational and rotational parts. On the other hand, Ferrant et al. (2002) propose another "velocity decomposition" strategy named Spectral Wave Explicit Navier-Stokes Equations (SWENSE). It avoids the computational cost of refining the mesh on the free surface.

Campana et al (1992) propose a "domain decomposition" strategy to calculate the wing in steady flow. They state that the information exchanging is mainly problem for this strategy. Hamilton and Yeung (2011) used a cylindrical surface to separate the viscous domain from the potential domain. The prediction-correction scheme is utilized to solve the pressure discontinues on the match surface. Kim et al. (2012) develop an Euler Overlay Method (EOM) to analysis the ringing loads on a vertical cylinder in the Ocean wave. In the overlay zone, an added source term related with the outer Euler solution is introduced in the Navier-Stokes equations. Moreover, a damping function is utilized to avoid reflecting effect to the CFD boundary. Paulsen et al. (2014) developed a one-way coupling strategy by using relaxation zone. A fully nonlinear potential flow solver combined with a Navier-Stokes solver is carried out.

Herein, we provided a coupling strategy of the fully nonlinear Green-Naghdi (GN) equations and OpenFOAM. The GN equations (see e.g., Demirbilek and Webster, 1992) have different levels for representation of the horizontal and vertical variations in the wave kinematics. This level theory is subject to degree of polynomial representation. The free surface boundary conditions are always satisfied and the irrotationality assumption is not required in the derivation of the GN equations. So the GN equations are derived from Euler Equation. Owing to the assumption on the velocity variation in the vertical direction across the fluid sheet, the GN equations can be easily utilized in deep water (Zheng et al., 2016) and wave-current interactions (Duan et al., 2016).

In this paper, a couple work of GN equations and OpenFOAM is carried out. The governing equations and coupling strategy are described in Section 2, test cases are in Section 3 and some conclusions are in Section 4.

2. Numerical model and coupling strategy

2.1 The Green Naghdi Equations

The governing equations of GN theory are developed from the continuity equation and the Euler's equations for an incompressible fluid:

$$\frac{\partial u}{\partial x} + \frac{\partial w}{\partial z} = 0 \tag{1}$$

$$\frac{\partial u}{\partial t} + u \cdot \frac{\partial u}{\partial x} + w \frac{\partial u}{\partial z} = -\frac{1}{\rho} \cdot \frac{\partial p}{\partial x}$$

$$\frac{\partial w}{\partial t} + u \cdot \frac{\partial w}{\partial x} + w \frac{\partial w}{\partial z} = -\frac{1}{\rho} \cdot (\frac{\partial p}{\partial z} + \rho \cdot g) \tag{2}$$

The fully nonlinear free surface conditions are always satisfied. The shape function in the finite depth GN equations is a polynomial depends upon z only:

$$u(x, z, t) = \sum_{n=0}^{K-1} u_n(x, t) \cdot z^n \quad ; \quad w(x, z, t) = \sum_{n=0}^{K} w_n(x, t) \cdot z^n \tag{3}$$

For more details, the reader is referred to Zhao et al. (2014). The Green-Naghdi equations are used as the solver of non-viscous domain.

2.2 The OpenFOAM

In OpenFOAM, each application implements has a specific mathematical model. For the water wave issues, the momentum and continuity equations as well as the Volume of Fluid (VOF) scheme are solved in a standard implementation in OpenFOAM.

$$\nabla \cdot \vec{u} = 0 \tag{4}$$

$$\frac{\partial(\rho\vec{u})}{\partial t} + \nabla \cdot (\rho\vec{u} \cdot \vec{u}^T) = -\nabla p + g(x - x_r) \cdot \nabla\rho + \nabla \cdot (\mu_{tot}\nabla\vec{u}) \tag{5}$$

A Finite Volume Method (FVM) is used in OpenFOAM to discretize the computational domain.

2.3 Coupling Strategy
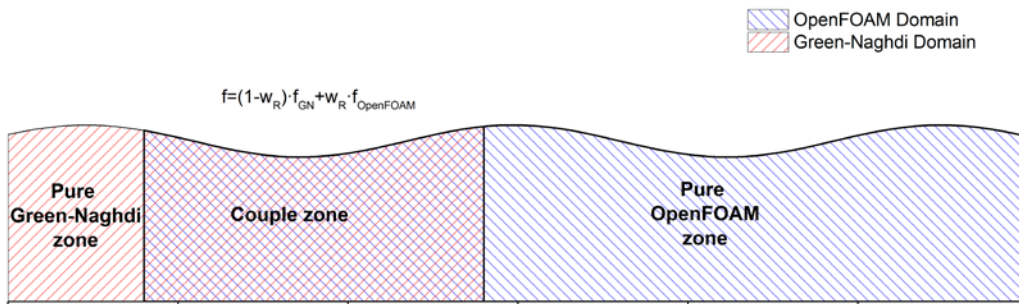
Figure 1. The sketch of computational domain

The strategy introduced here can be classified as the domain decompositions. An open-source toolbox named Waves2Foam is used as the solver of CFD domain. We use the relaxation scheme developed by Jacobsen et al. (2012) to achieve a one-way coupling strategy. In Fig. 1 the computational domain is presented. The relaxation scheme is used in the coupling zone shown in Fig. 1. The target quantities denoted by f_{GN} are obtained from the Green-Naghdi equations. w_R is the weighting function.

3. Test cases

3.1 Regular waves

Regular wave is simulated by using the Green-Naghdi results as target information. The description of the regular wave is displayed in Table 1. The length of coupling zone is 2λ. The time history of two wave probe (x/λ=2, x/λ=4) are shown in Fig. 2. The CFD wave agrees with the target Green-Naghdi wave. However, significant decreasing is observed in wave elevation during the propagation. We have to state that more exhaustively convergence study will be given in the workshop.

Table 1: Case description

Items	Water depth (d)	Wave period (T)	Wave length (λ)	Wave amplitude (A)
Values	0.6 m	0.7018 s	0.808 m	0.0288 m
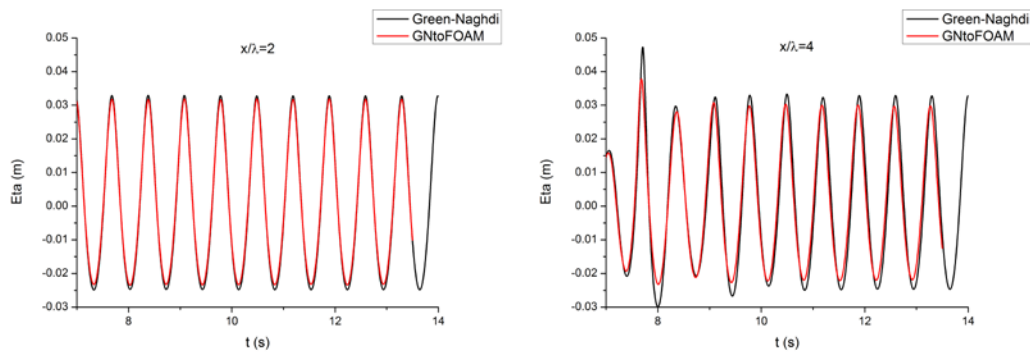
Figure 2. Time history of two wave probes (x/λ=2, x/λ=4)
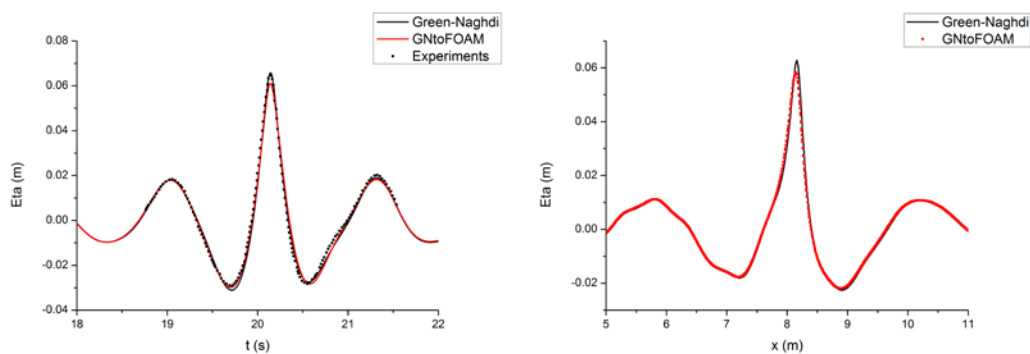
3.2 Freak waves

Figure 3. Time history (8.32 m) and snapshot (20 s) of focusing freak wave

In Fig. 3, the freak wave generated from wave focusing is simulated. The period ranges are (0.6 s, 1.4 s) and the wave group consisted of 29 individual wave components which has equal amplitude and equal period spacing. The input amplitude A is 55 mm. The focus location and time is set as 8.0 m and 20 s, respectively. This focus time is long enough for the high frequency component go through the focus location. The same focusing wave group is generated in a physical wave flume by Baldock et al. (1996). In the numerical simulation, the focus location and time is shifted to 8.32 m and 20.14 s because of the

nonlinearity. It is shown that the target Green-Naghdi wave has better agreement with the experimental data than the focusing CFD wave even though the later has finer mesh in the horizontal direction. The computational cost is 111 s for GN and 489560 s for GNtoFOAM. Similarly, we have to states that more convergence studies will be presented in the workshop.

4. Conclusions

This paper provided a one-way coupling strategy of the fully nonlinear Green-Naghdi equations and the OpenFOAM. Two cases including the regular wave and focusing freak wave are shown in this work. In both of them, the waves generated from the coupling strategy agree with the target Green-Naghdi waves. This one-way coupling strategy provides a probability to shorten the computational domain and has good performance in accuracy. However, it is shown that the Green-Naghdi equations do well in efficiency. More exhaustively convergence studies will be presented in the workshop. A study on the two-way coupling strategy of Green-Naghdi equations and OpenFOAM is undergoing.

Acknowledgments

Reference

[1] D.O. Edmund, A Velocity Decomposition Method for Efficient Numerical Computation of Steady External Flows, Ph.D. Thesis, University of Michigan, 2012.

[2] P. Ferrant, L. Gentaz & D.L. Touzé, A New Potential & RANSE Approach For Water Wave Diffraction, Proceedings of 5th NuTTS, 2002.

[3] E.F. Campana, A.D. Mascio, P.G. Esposito & F. Lalli, Viscous-Inviscid Coupling in Ship Hydrodynamics, 11th Australasian Fluid Mech. Conf., Australia, 1992.

[4] J.A. Hamilton & R.W. Yeung, Viscous and Inviscid Matching of three-dimensional free-surface flows utilizing shell functions, J. Eng. Math., Vol 70: 43-66, 2011.

[5] J.W. Kim, J.O'. Sullivan & A. Read, Ringing Analysis of a Vertical Cylinder by Euler Overlay Method, 31st of OMAE, OMAE2012-84091, 2012.

[6] B.T. Paulsen, H. Bredmose & H.B. Bingham, An efficient domain decomposition strategy for wave loads on surface piercing circular cylinders, Coastal Engineering, Vol 86: 57-76, 2014.

[7] Z. Demirbilek, & W.C. Webster, Application of the Green-Naghdi theory of fluid sheets to shallow-water wave problems, US Army Corps. of Eng. Waterways Experiment Station, Rep. No. CERC-92-11, Vicksburg, MS, 1992.

[8] W.Y. Duan, K. Zheng, B.B. Zhao, Z. Demirbilek, R.C. Ertekin & W.C. Webster, On wave–current interaction by the Green–Naghdi equations in shallow water. Natural Hazards, 84(2): 567-583, 2016.

[9] K. Zheng, B.B. Zhao, W.Y. Duan, R.C. Ertekin & X.B. Chen, Simulation of evolution of gravity wave groups with moderate steepness. Ocean Modelling, 98: 1-11, 2016.

[10] B.B. Zhao, W.Y. Duan, & R.C. Ertekin, Application of higher-level GN theory to some wave transformation problems. Coastal Engineering, 83: 177-189, 2014.

[11] N.G. Jacobsen, , D.R. Fuhrman, & J. Fredsøe, A wave generation toolbox for the open source CFD library: OpenFoam. Int. J. Numer. Methods Fluids 70, 1073–1088, 2012.

[12] T.E. Baldock, C. Swan & P.H. Taylor, A Laboratory Study of Nonlinear Surface Waves on Water, 354(1707):649-676, 1996.

DECIDING OPTIMAL PARAMETER FOR INTERNAL WAVEMAKER USING COUPLING OF DAKOTA AND OPENFOAM

WOONG-HYOUN LEE[1], SANG-HO OH[2], SANG DON LEE[3]
[1]NEXTfoam Co., LTD., Korea, whlee@nextfoam.ac.kr
[2]Coastal Engineering Research Department, KIOST, Korea, ohsangho@kiost.ac.kr
[3]NEXTfoam Co., LTD., Korea, sdlee@nextfoam.ac.kr

Keywords: Navier-Stokes model, Internal wavemaker, Mass source functions, OpenFOAM, DAKOTA

In order to generate a water wave adequately in numerical simulation, several specialized techniques have been developed: internal wavemaker, static boundary method and moving boundary method. For internal wavemaker, especially, geometry of mass source region needs to be decided minimizing numerical error. Chen and Hsiao [1] suggested the method to set the dimension of wavemaker, deriving height from linear wave theory and constructing empirical formula about wavenumber and width of wavemaker, with FLOW-3D code. The procedure, however, required hundreds of trial calculations, followed by excessive computational cost. In this paper, automated process to find optimal geometry for given relative water depth is proposed, introducing coupling of DAKOTA and OpenFOAM. The waves2Foam utility had been modified to simulate the generation of second-order stokes wave and linked with DAKOTA to control the input file and observe the output file.

The continuity equation and the Navier-stokes equation were adopted as governing equation to describe incompressible viscous flow. The continuity equation which includes wavemaker as following:

$$\nabla \cdot \vec{\mathbf{U}} = \begin{cases} s(t) \text{ for } \vec{x} \in \Omega \\ 0 \quad \text{for } \vec{x} \notin \Omega \end{cases} \tag{1}$$

$$s(t) = \frac{2C\eta W}{l_x l_y l_z} \tag{2}$$

where $\vec{U}$ is velocity vector of flow, $s(t)$ represents mass source function for corresponding target wave and Ω is mass source region. The mass source function is defined in the form of (2), where C is phase velocity, η is surface elevation, W is width along span and l represents the dimension of mass source region in each direction.

The momentum equation for incompressible viscous flow can be written as following:

$$\frac{\partial \rho \mathbf{U}}{\partial t} + \nabla \cdot (\rho \mathbf{U}\mathbf{U}^T) = -\nabla p + \nabla \cdot \mathbf{T} + \rho \mathbf{f}_b \tag{3}$$

where p is pressure, $\mathbf{T}$ is viscous stress tensor and $\mathbf{f}_b$ is body force vector. In the momentum equation, velocity and pressure are calculated using PIMPLE algorithm of OpenFOAM. The water surface elevation was tracked using volume of fluid scheme, represented as following:

$$\frac{\partial \alpha}{\partial t} + \nabla \cdot (\alpha \mathbf{U}) = 0 \tag{4}$$

$$\rho = \rho_l \alpha + \rho_g (1 - \alpha) \tag{5}$$

$$\mu = \mu_l \alpha + \mu_g (1 - \alpha) \tag{6}$$

Where α represents specific volume of fluid and subscript l and g indicates liquid and gas respectively.
The regular 3D wave was generated with following mass source function.

$$s_x(x, t) = \frac{2C\sin}{l_y l_z} \frac{H}{2} \sin\big((k \cos \theta)\,|x - x_c| - wt\big) \tag{7}$$

$$s_y(y, t) = \frac{2C\cos}{l_x l_z} \frac{H}{2} \sin\big((k \sin \theta)\,|y - y_c| - wt\big) \tag{8}$$

In order to exclude effect of unwanted reflection wave from boundary, numerical sponge layer is allocated to the edge of computational domain. In the sponge layer, the following additive term is implemented to momentum equation, dissipating kinetic energy of fluid.

$$D_x = \theta_{xy}\sqrt{\frac{g}{h}}(N+1)\left(\frac{max(|x-x_0|,|y-y_0|)}{l}\right)^N \tag{9}$$

$$D_y = \theta_{xy}\sqrt{\frac{g}{h}}(N+1)\left(\frac{max(|x-x_0|,|y-y_0|)}{l}\right)^N \tag{10}$$

$$D_z = \theta_z\sqrt{\frac{g}{h}}(N+1)\left(\frac{max(|x-x_0|,|y-y_0|)}{l}\right)^N \tag{11}$$

The parameter x_0, y_0 indicate the starting position of sponge layer, while N and θ are adjusted for intensity of dissipation.

The schematic design of numerical setup and an example of calculated surface elevation are shown in figure 1 and 2 respectively.
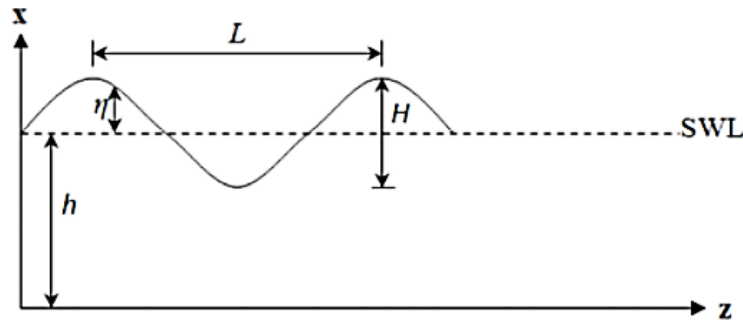
Figure 1: Schematic drawing of computational domain
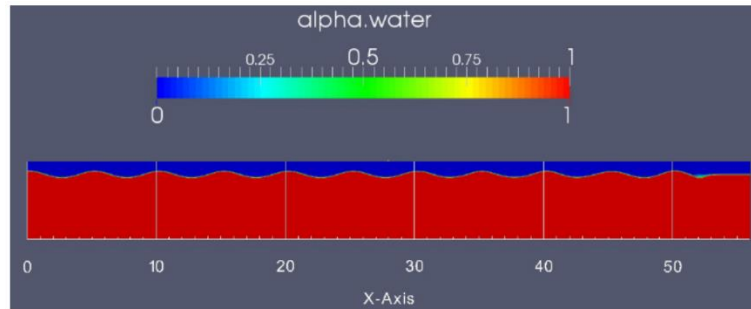
Figure 2: Example of visualized surface elevation by numerically generated wave

The numerical model is validated comparing generated wave and expected target wave, computing root-mean-square error between them with following formula, where N is the number of observation point.

$$RMS = \frac{1}{\eta_{ref,max}-\eta_{ref,min}}\sqrt{\frac{\sum_{i=1}^{N}(n_{ref,i}-\eta_{m,i})^2}{N}} \tag{12}$$

For coupling of DAKOTA and OpenFOAM, the input and output files of OpenFOAM solver was directly connected to DAKOTA, regarding OpenFOAM as block-box. DAKOTA directly control the file 'waveProperties.input', which define the parameters for wave generation in mass source region. The result of calculation is evaluated with the output file, 'surfaceElevation.dat', which contains surface elevation by numerically generated wave according to time. The calculation is started with trial parameters and automatically repeated until optimal parameters were found by DAKOTA, using its own optimization algorithm. The overall routine is described in Figure 3.

The modified OpenFOAM solver with mass source function, numerical sponge layer, and DAKOTA optimization successfully generated target waves, finding optimal geometry of mass source region with fewer trial calculation and computational cost.
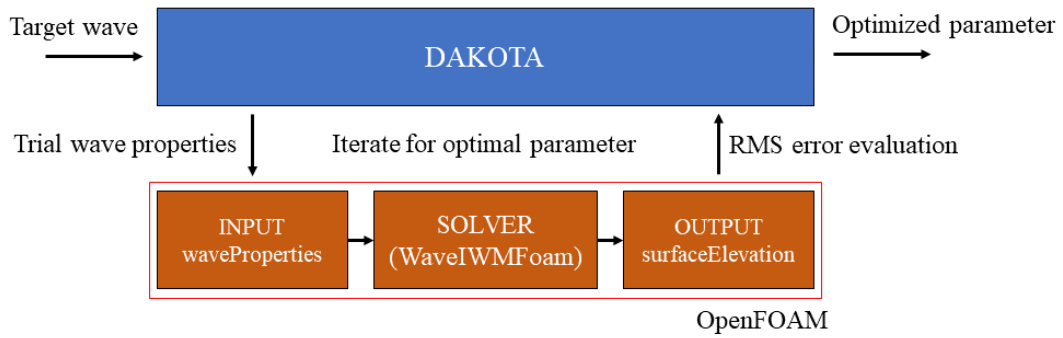
Figure 3: Parameter optimization routine for coupling DAKOTA and OpenFOAM
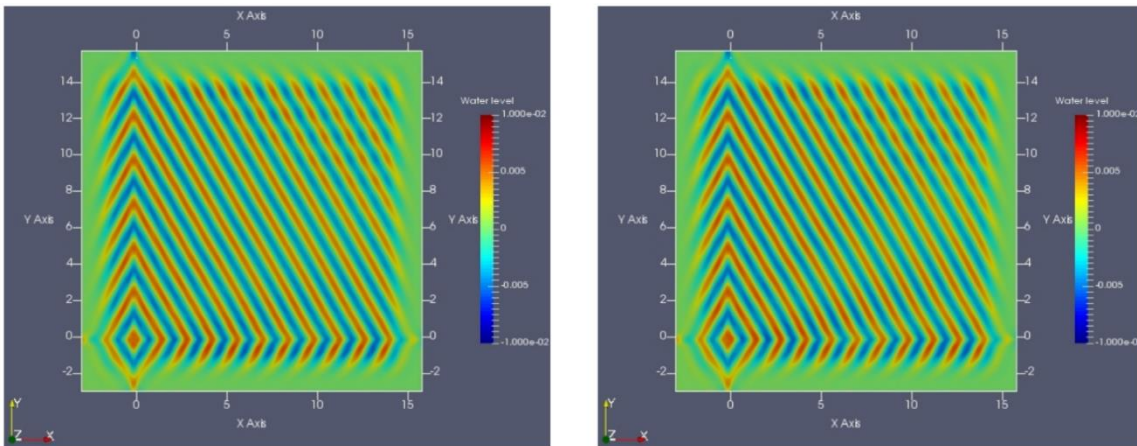
Figure 4: Surface elevation by directional Stokes 2nd wave at 30T(left) and 60T(right)
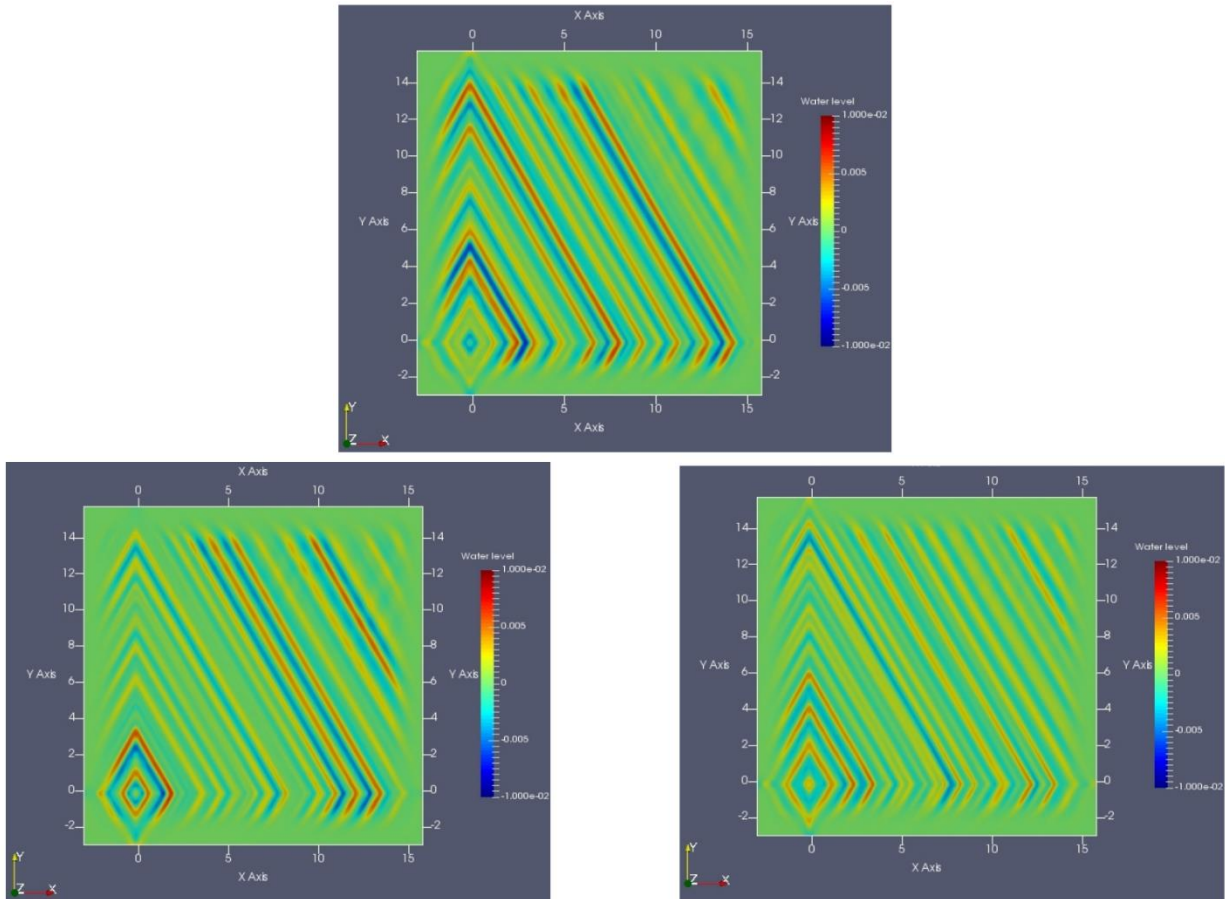
Figure 5: Surface elevation by TMA spectrum at t=30T(up), 40T(left) and 60T(right)

References

[1] Y.-L. Chen and S.-C. Hsiao, "Generation of 3D water waves using mass source wavemaker applied to Navier–Stokes model," Coastal Engineering, vol. 109, pp. 76-95, 2016.

[2] N. G. Jacobsen, D. R. Fuhrman, and J. Fredsoe, "A wave generation toolbox for the open- source CFD library: OpenFoam[R]," International Journal for Numerical Methods in Fluids, p. 1073, 2012.

[3] P. Lin and P. L. F. Liu, "Internal wave-maker for Navier-Stokes equations models," Journal of Waterway, Port, Coastal and Ocean Engineering, vol. 125, no. 4, p. 207, 1999.

[4] G. Kim, C. Lee, and K.-D. Suh, "Internal generation of waves: Delta source function method and source term addition method," 2007.

DEVELOPMENT OF A MULTIPHASE SOLVER FOR CAVITATION FLOW NEAR FREE SURFACE

HOUCUN ZHOU[1], MIN XIANG[2], SHIWEI ZHAO[3], WEIHUA ZHANG[4]

[1]*National University of Defense Technology, zhouhoucun09@nudt.edu.cn* [2]*National University of Defense Technology, xiangmin333@hotmail.com* [3]*National University of Defense Technology, 15211122522@163.com* [4]*National University of Defense Technology, zhangweihua@nudt.edu.cn*

1 Introduction

Cavitation is a common phenomenon in fluid machinery, which oftentimes negatively affects the performance of most fluid machinery applications, therefore leading to problems such as undue vibrations, noise and material erosion [1]. In more recent years, cavitation has attracted intensive attention due to its potentials in drag reduction for underwater vehicles [2]. When vehicles run near or across the free surface, ventilated cavitation happens, which is complicated issue and may provide new inspiration on high-speed surface cruising. Researchers have done a lot of investigation on this topic up to now[3][4][5]. In order to fully studies this problem, a multiphase cavitation solver is developed based on the OpenFOAM open source platform. And a fully investigation of the free surface flow will be carried out with the developed solver.

2 Mathematical Method

2.1 Governing Equation

In this paper, the flow described is treated as a homogeneous mixture, therefore only one set of equations is needed. The governing equations basically consist of the conservation of mass, momentum. The continuity equation of the mixture flow can be written as

$$\frac{\partial \rho}{\partial t} + \nabla \cdot (\rho U) = 0 \tag{1}$$

Neglecting the gravity and surface tension term, the conservation of momentum for the mixture flow can be expressed as,

$$\frac{\partial (\rho U)}{\partial t} + \nabla \cdot (\rho U \otimes U) = -\nabla p + \nabla \cdot \tau \tag{2}$$

Where ρ is the density of the mixture, which is related to the volume of fractions of all phases as

$$\rho = \alpha_l \rho_l + \alpha_v \rho_v + \alpha_g \rho_g \tag{3}$$

For a three phases system, the basic form of transport equations for the volume fraction of each phase could write as:

$$\frac{\partial (\rho_l \alpha_l)}{\partial t} + \nabla \cdot (\rho_l \alpha_l U) = \dot{m} \tag{4}$$

$$\frac{\partial (\rho_v \alpha_v)}{\partial t} + \nabla \cdot (\rho_v \alpha_v U) = -\dot{m} \tag{5}$$

$$\frac{\partial (\rho_g \alpha_g)}{\partial t} + \nabla \cdot (\rho_g \alpha_g U) = 0 \tag{6}$$

Where the subscript l and v are for the liquid and vapour phases respectively. While g represents gas. Note that the velocity vector U in the above equations should be expressed as the averaged velocity, and $U = \alpha_l U_l + \alpha_v U_v + \alpha_g U_g$. And the $\dot{m}$ term on the RHS of the equations is donates the mass transfer rate caused by cavitation between the liquid and vapour phase, which is $\dot{m} = \dot{m}^+ + \dot{m}^-$.

Considering that the volume fraction of these phases obey the conservation law,

$$\alpha_l + \alpha_v + \alpha_g = 1 \tag{7}$$

The divergence of the velocity can be,

$$\nabla \cdot U = \left(\frac{1}{\rho_l} - \frac{1}{\rho_v} \right) \dot{m} \tag{8}$$

Neglecting the compressibility of the phases, and take the divergence term into consideration, the final form of the transport equation is:

$$\frac{\partial \alpha_l}{\partial t} + \nabla \cdot (\alpha_l U) = \alpha_l (\nabla \cdot U) + \left(\frac{1}{\rho_l} - \alpha_l \left(\frac{1}{\rho_l} - \frac{1}{\rho_v} \right) \right) \dot{m} \tag{9}$$

$$\frac{\partial \alpha_v}{\partial t} + \nabla \cdot (\alpha_v U) = \alpha_v (\nabla \cdot U) - \left(\frac{1}{\rho_v} + \alpha_v \left(\frac{1}{\rho_l} - \frac{1}{\rho_v} \right) \right) \dot{m} \tag{10}$$

$$\frac{\partial \alpha_g}{\partial t} + \nabla \cdot (\alpha_g U) = \alpha_g (\nabla \cdot U) - \alpha_g \left(\frac{1}{\rho_l} - \frac{1}{\rho_v} \right) \dot{m} \tag{11}$$

Given that the interface disperses due to numerical diffusion it might appear that a good approach to limit or reverse this effect would be to include a diffusion operator into the phase-fraction equation with a negative diffusion coefficient. While this approach would be conservative it would also be unbounded and unstable; negative diffusion is always problematic. An alternative to negative diffusion which is also conservative is to apply some kind of additional convection-based term which compresses the interface, maintains boundedness and reduces to zero (at least the integrated effect of it reduces to zero) as the mesh is refined. A "Counter-gradient" term, which is clearly conservative and maintains boundedness, has a general form of $\nabla \cdot (U_r \alpha \beta)$, U_r is the relative velocity between the two phases across the interface.

$$\frac{\partial \alpha_l}{\partial t} + \nabla \cdot (\alpha_l U) + + \nabla \cdot (\alpha_l \alpha_v (U_l - U_v) + \alpha_l \alpha_g (U_l - U_g)) = \alpha_l (\nabla \cdot U) + \left(\frac{1}{\rho_l} - \alpha_l \left(\frac{1}{\rho_l} - \frac{1}{\rho_v} \right) \right) \dot{m} \tag{12}$$

$$\frac{\partial \alpha_v}{\partial t} + \nabla \cdot (\alpha_v U) + \nabla \cdot (\alpha_v \alpha_l (U_v - U_l) + \alpha_v \alpha_g (U_v - U_g)) = \alpha_v (\nabla \cdot U) - \left(\frac{1}{\rho_v} + \alpha_v \left(\frac{1}{\rho_l} - \frac{1}{\rho_v} \right) \right) \dot{m} \tag{13}$$

$$\frac{\partial \alpha_g}{\partial t} + \nabla \cdot (\alpha_g U) + \nabla \cdot (\alpha_g \alpha_l (U_g - U_l) + \alpha_g \alpha_v (U_g - U_v)) = \alpha_g (\nabla \cdot U) - \alpha_g \left(\frac{1}{\rho_l} - \frac{1}{\rho_v} \right) \dot{m} \tag{14}$$

However, in this study, the homogeneous multiphase model which adopts an incompressible Navier-Stokes equations and the compressive volume of fluid (VOF) approach are adopted for flow simulation. Phases in the multiphase system share the velocity and pressure fields. So the relative velocity term should be reconstructed. Here we just adopt the following form which is also used by some other multiphase solver in OpenFOAM.

$$U_c = \min (c_\alpha |U|, \max (|U|)) \frac{\nabla \alpha}{\|\nabla \alpha\|} \tag{15}$$

where c_α is a compressive factor, expression $\max (|U|)$ returns the largest value of $|U|$ anywhere in the domain.

2.2 Flux Corrected Transport Theory

In OpenFOAM, the volume fraction transport equation of the multiphase system is solved by the MULES tool kit. For the given equation below

$$\frac{\partial (\rho \alpha)}{\partial t} + \nabla \cdot (\rho \alpha U) = \alpha \text{Sp} + \text{Su} \tag{16}$$

We have the following discretization equation

$$\rho \frac{\alpha^{n+1} - \alpha^n}{\Delta t} + F = \alpha^{n+1} \text{Sp} + \text{Su} \tag{17}$$

$$\alpha^{n+1} \left(1 - \frac{\Delta t \text{Sp}}{\rho} \right) = \frac{\Delta t}{\rho} \left(\frac{\alpha^n \rho}{\Delta t} + \text{Su} - F \right) \tag{18}$$

$$\alpha^{n+1} = \frac{\alpha^n \rho / \Delta t + \text{Su} - F}{\rho / (\Delta t) - \text{Sp}} \tag{19}$$

Usually, the density is set to unity in MULES correction. Therefore, the Sp term is an implicity volumetric source term due to cavitation, the Su is an explicit term in Eq.19. And F is the total volume fraction flux due to transportive effect of a velocity. The values of the flux depend on many variables but particularly on the values of α at faces. Boundedness of the temporal solution can be achieved via face value limiting, such as in TVD/NVD schemes, or by limiting the face fluxes. The values of F are obtained by a lower order and bounded method and a limited portion of the values obtained
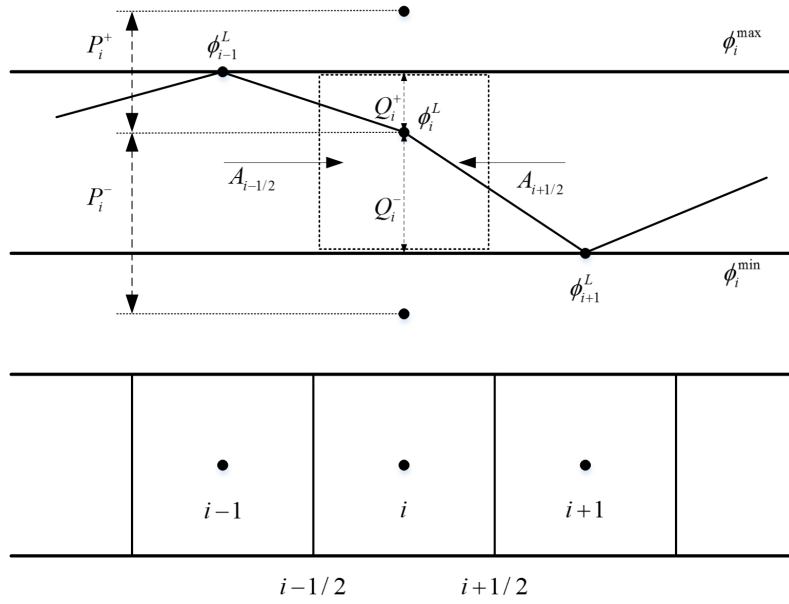
Figure 1: Schematic diagram of limiter for one dimensional geometry.

by a high order and possible unbounded method. This technique is Flux Corrected Transport (FCT). The sequence of this theory could be described as below[6]:

1. Compute F^L, the transportive flux given by some low order scheme which guarantees to give monotonic results.
2. Compute F^H, the transportive flux given by some high order scheme.
3. Define the anti-diffusive flux $A = F^H - F^L$.
4. Compute the corrected flux $F^C = F^L + \lambda A$, with $0 \le \lambda \le 1$.
5. Solve the equation by the given temporal scheme using corrected fluxes.

The critical step is clearly the fourth, where it is necessary to find the λ weighting factors.

The implementation of FCT theory is called MULES (Multidimensional Universal Limiter for Explicit Solution)[6] in OpenFOAM. Illustrated by Fig.1, the whole procedure is presented in Algorithm 1.

Algorithm 1 Procedure for MULES limiter

1: Calculate local extrema as
$$\alpha_i^a = max(\alpha_i^n, \alpha_{i,N}^n)$$
$$\alpha_i^b = min(\alpha_i^n, \alpha_{i,N}^n)$$
where $\alpha_{i,N}^n$ are all the neighbors by face for the i-th cell. In addition the inflows and outflows for each cell have to be calculated as $P^+ = -\sum_f A_f^-$ and $P^- = -\sum_f A_f^+$, where A_f^- are the inflows and A_f^+ the outflows;

2: Correct the local extrema by the limits imposed by user's defined global extrema α^{maxG} and α^{minG}
$$\alpha_i^a = max(\alpha^{maxG}, \alpha_i^a)$$
$$\alpha_i^b = min(\alpha^{minG}, \alpha_i^b)$$

3: Find $Q_i^\pm$ as
$$Q_i^+ = \frac{V}{\Delta t}(\alpha_i^a - \alpha_i^n) + \sum_f F_f^L$$
$$Q_i^- = \frac{V}{\Delta t}(\alpha_i^n - \alpha_i^b) - \sum_f F_f^L$$

4: Set $\lambda_f^{v=1} = 1$ for all faces. Do the following loop $nLimiterIter$ times to find the final λ_f's
$$\lambda_i^{\mp, v+1} = max \left[min \left(\frac{\pm \sum_f \lambda_f^v A_f^\pm + Q_i^\pm}{P_i^\pm}, 1 \right), 0 \right]$$
$$\lambda_f^{v+1} = \begin{cases} min\{\lambda_P^{+,v+1}, \lambda_N^{-,v+1}\}, \text{if} A_{i+1/2} \ge 0, \\ min\{\lambda_P^{-,v+1}, \lambda_N^{+,v+1}\}, \text{if} A_{i+1/2} < 0 \end{cases}$$
where λ_P and λ_N represent the λ's for the owner and neighbor cell of a given face f.
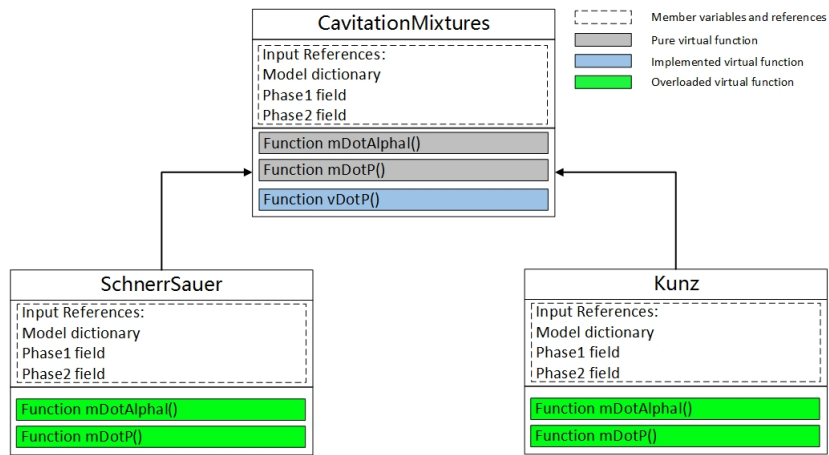
Figure 2: Block diagram of the mass transfer model framework and implemented models.
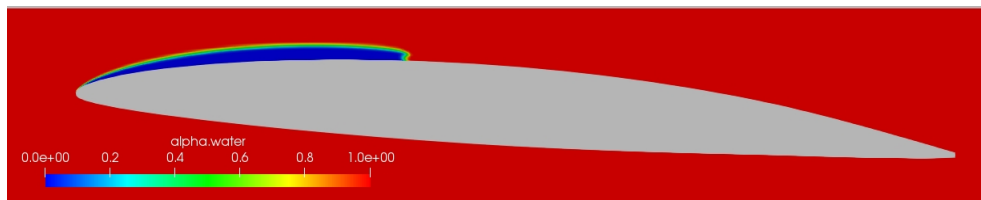
Figure 3: Sheet cavitation on the suction side of the hydrofoil

2.3 Mass Transfer Model

In order to calculate the mass transfer rate within multiphase systems, a framework of cavitation model is developed. All models inherit from a abstract class, which accepts a dictionary reference to look up parameters needed by the model and two reference of phase fraction field object. Additionally, the Kunz model[7] and Schnerr Sauer model[8] are also implemented to return the mass transfer rate. A UML block diagram of the mass transfer model framework is presented in Fig.2.

3 Validation

3.1 2D hydrofoil case

In this section, the two dimensional NACA66(MOD) hydrofoil is adopted. The main purpose of this case is validating the performance of two phase flow simulation. So only water and vapour phase are involved in this validation case. Results calculated by the new solver will compare with experimental results[9] and those calculated by the interPhaseChangeFoam solver. Some of the primary results are shown in Fig.3 and Fig.4.

3.2 2D throttle case

This 2D throttle case is copied form cavitatingFoam tutorials.In this case, three phases are involved, i.e. the water, vapour phase and gas. Two different flow condition are considered. Numerical simulation results are shown in Fig.5 and Fig.6, which validate the developed solver.

3.3 3D underwater projectile

The effect of the free surface has a great effect on high-speed surface vehicles. Wang et. al [3] carried out a typical launching experiment around an axisymmetric projectile to investigate the free surface effect. In this study, the established numerical approach is adopted to study this case. The numerical methods are validated by comparing results with underwater launching experiments. Results are shown in Fig.7 and Fig.8.

4 Conclusion

The new developed multiphase cavitation solver shows good performance in two phases and three phases cavitating flow simulation. It could also be applied to analyse the cavitating flow near free surface.
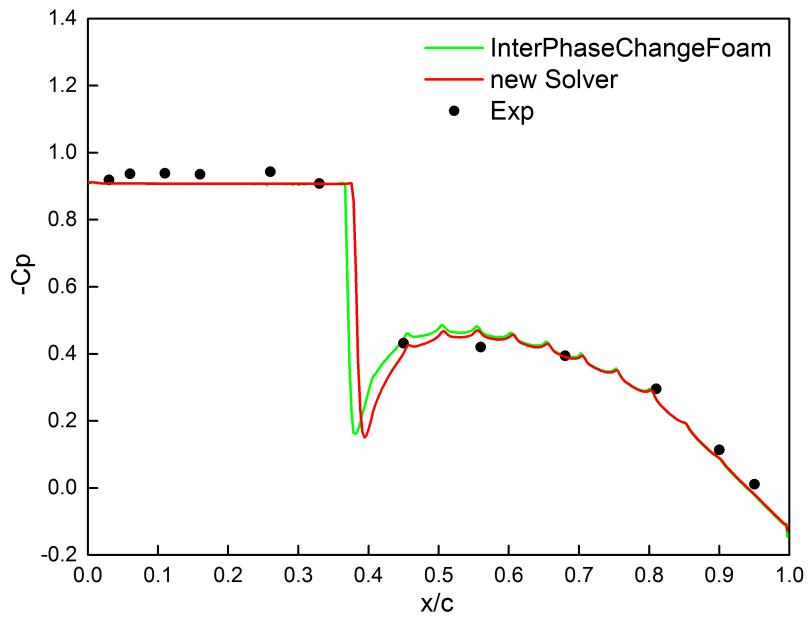
Figure 4: Pressure coefficient distribution on the suction side of the hydrofoil
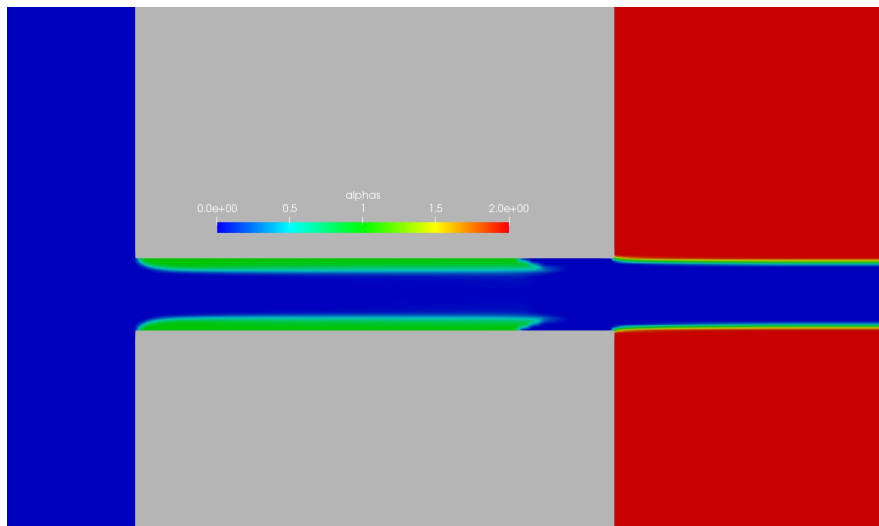
Figure 5: Volume fraction distribution in the throttle($P_{out} = 15$atm)
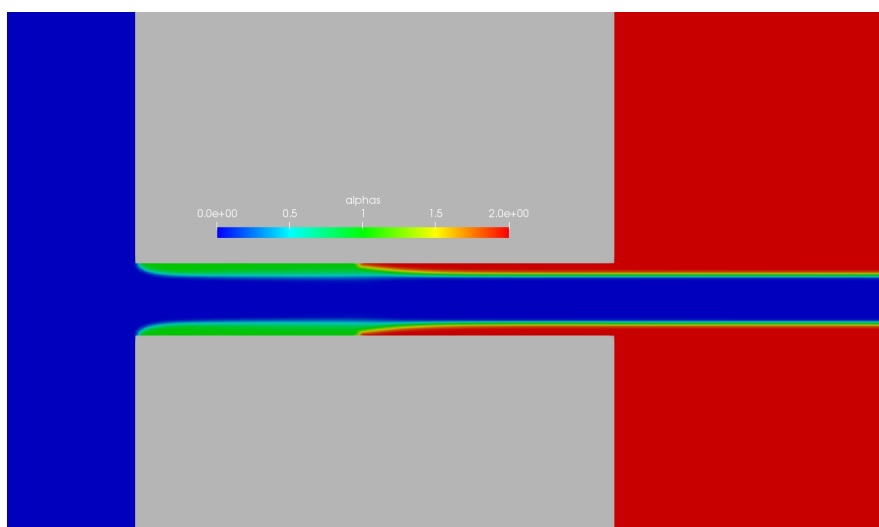
Figure 6: Volume fraction distribution in the throttle($P_{out} = 10$atm)

t=3ms

t=4ms

t=5ms
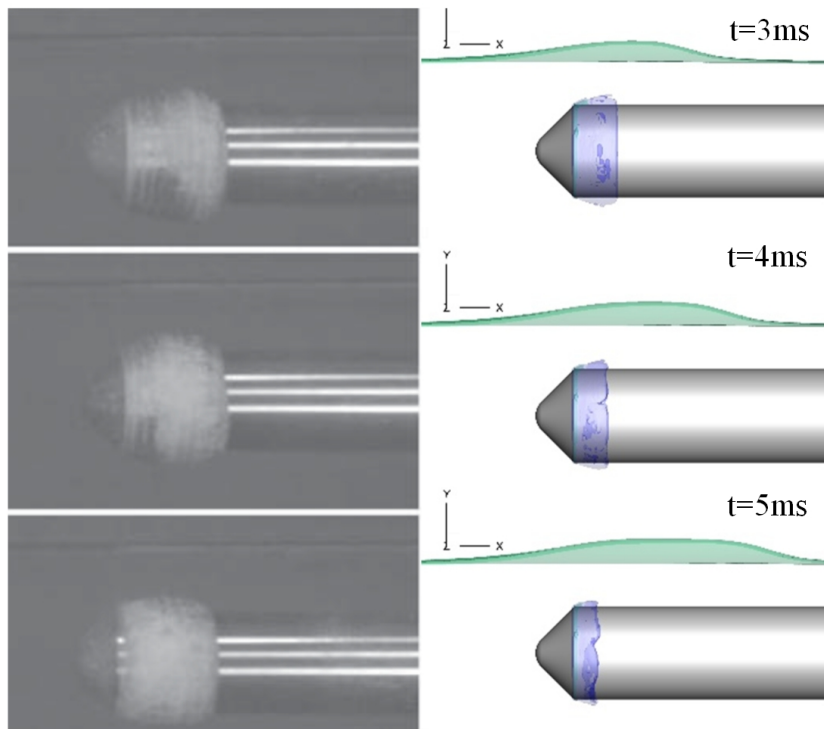
Figure 7: Evolutions of the cavity and free surface

Relative Error 1.5%
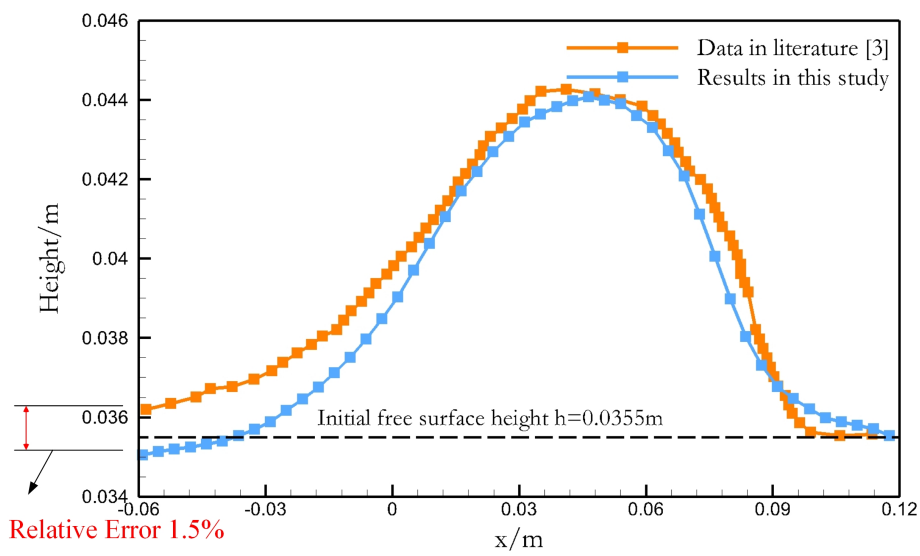
Figure 8: Wave profiles on the upper side of the projectile

Acknowledgments

References

[1] J.-P. Franc, J.-P. Franc, J.-M. Michel, and J.-M. Michel, *Fundamentals of cavitation*, 2004.

[2] B.-K. Ahn, C.-S. Lee, and H.-T. Kim, "Experimental and numerical studies on super-cavitating flow of axisymmetric cavitators," *International Journal of Naval Architecture and Ocean Engineering*, vol. 2, no. 1, pp. 39–44, mar 2010. [Online]. Available: http://linkinghub.elsevier.com/retrieve/pii/S2092678216302308

[3] Y. Wang, X. Wu, C. Huang, and X. Wu, "Unsteady characteristics of cloud cavitating flow near the free surface around an axisymmetric projectile," *International Journal of Multiphase Flow*, vol. 85, pp. 48 – 56, 2016. [Online]. Available: http://www.sciencedirect.com/science/article/pii/S0301932215300999

[4] M.-S. Jin, C.-T. Ha, and W.-G. Park, "Numerical study of ventilated cavitating flows with free surface effects," *Journal of Mechanical Science and Technology*, vol. 27, no. 12, pp. 3683–3691, Dec 2013. [Online]. Available: https://doi.org/10.1007/s12206-013-0914-0

[5] C. Xu, J. Huang, Y. Wang, X. Wu, C. Huang, and X. Wu, "Supercavitating flow around high-speed underwater projectile near free surface induced by air entrainment," *AIP Advances*, vol. 8, no. 3, p. 035016, 2018. [Online]. Available: https://doi.org/10.1063/1.5017182

[6] S. M. Damian, "An extended mixture model for the simultaneous treatment of short and long scale interfaces," 2013.

[7] R. F. Kunz, D. A. Boger, T. S. Chyczewski, D. R. Stinebring, H. J. Gibeling, and T. R. Govindan, "Multi-Phase Cfd Analysis of Natural and Ventilated Cavitation About Submerged Bodies," *FEDSM 99 1999 ASME/JSME Joint Fluids Engineering Conference*, pp. 1–9, 1999.

[8] G. H. Schnerr and J. Sauer, "Physical and numerical modeling of unsteady cavitation dynamics," in *Proceedings of the 4th International Conference on Multiphase Flow*, New Orleans, La, USA, 2001.

[9] P. E. Dimotakis, H. F. Gaebler, and H. T. Hamaguchi, "Two Dimentional NACA 66(MOD) Hydrofoil High Speed Water Tunnel Tests," GALCIT Report HSWT 1142, Tech. Rep., 1987.

DEVELOPMENTS THE 'ESPER' FOR ESTIMATING SHIP PERFORMANCE

HYUN-SIK KIM[1], KWANG-LEOL JEONG[2], JAE-HEUNG GILL[3]
[1]Research Centre, NEXTfoam co.,LTD, hskim@nextfoam.co.kr
[2]Research Centre, NEXTfoam co.,LTD, kl.jeong@nextfoam.co.kr
[3]Research Centre, NEXTfoam co.,LTD, jhgill@nextfoam.co.kr

The methods for estimating the ship performance are mainly the model test in the towing tank and the method using CFD. Using CFD to estimate the ship performance has recently been actively pursued because it has advantages over the model test not only reduction of the cost but also duration of the estimation of ship performance. Many articles such as [1], [2] and [3] shows that numerical methods are effective and accurate by comparing the calculation results to experimental data of towing tank.

The estimation of ship performance using CFD was conducted with commercial CFD programs such as 'Fluent' and 'starCCM+' that are mainly used in the shipyard. The versatile commercial programs are developed for various kinds of fluid flow simulation like compressible flow, heat transfer, chemical reaction, non-Newtonian fluids, therefore it is too expensive to calculate ship resistance and population calculation. Many Korean ship building companies are examining OpenFOAM to replace the commercial CFD programs with OpenFOAM solvers.

'ESPER' is an OpenFOAM package including libraries and solvers for Propeller Open-Water (POW), ship resistance and self-propulsion analysis developed by NEXTfoam. 'ESPER' puts emphasis on the development of unique analysis technique and numerical model to stabilize the solution and reduce calculation time. 'ESPER' uses the RANS equation as the governing equations and can optionally use the turbulence model provided by OpenFOAM. 'ESPER' computes the pressure Poisson equation using Rhie-Chow interpolation and linearizes source term in k-omegaSST turbulence model for stability of the solution.

In this paper, the numerical methods of ESPER are introduced briefly and verified by comparing the results with other experimental data. Validation cases consist of ship resistance case, POW case and self-propulsion case. Target hulls are KRISO Container Ship(KCS) and Japan Bulk Carrier(JBC) and target propellers for POW Test are KP505 and MP687. ESPER's calculation results were compared to the Towing tank experiment data.

Numerical Method

ESPER is developed by improving simpleFoam for POW and interDyMFoam for resistance and self-propulsion. OpenFOAM standard solver simpleFoam and interDyMFoam is not as stable as commercial code. To increase the stability, Rhie-Chow interpolation is employed to calculation of the flux of Poisson equation source term.

	original	modified
1. solve momentum equation and get $\vec{U}^*$	$a_P \vec{U}_P = H(\vec{U}) - V_P (\nabla p)_P$	$a_P \vec{U}_P = H(\vec{U}) - V_P (\nabla p)_P$
2. interpolate pseudo-velocity to get mass flow rate	$F^* = \left\{ \dfrac{H(\vec{U}^*)}{a} \right\}_f \cdot \vec{S}_f$	$F^* = \left\{ \vec{U}^* + \dfrac{V_P}{a_P}(\nabla p)_P \right\}_f \cdot \vec{S}_f$
3. solve pressure equation and get p^*	$\nabla \cdot \left(\dfrac{V}{a} \nabla p \right) = \sum_f F^*$	$\nabla \cdot \left(\dfrac{V}{a} \nabla p \right) = \sum_f F^*$
4. correct mass flow rate	$F^{new} = F^* - \left(\dfrac{V}{a} \right)_f \|\vec{S}_f\| \vec{n} \cdot (\nabla p^*)_f$	$F^{new} = F^* - \left(\dfrac{V}{a} \right)_f \|\vec{S}_f\| \vec{n} \cdot (\nabla p^*)_f$
5. original: under-relax pressure modified: correct velocity	$p^{new} = p^{old} + \alpha_p (p^* - p^{old})$	$\vec{U}_P^{new} = \vec{U}_P^* - \dfrac{V_P}{a_P}(\nabla p')_P$
6. original: correct velocity modified: under-relax pressure	$\vec{U}_P^{new} = \dfrac{H(\vec{U}^*)}{a_P} - \dfrac{V_P}{a_P}(\nabla p^{new})_P$	$p^{new} = p^{old} + \alpha_p (p^* - p^{old})$

Figure 1 comparison of solution procedure between standard OpenFOAM and ESPER

The pseudo velocity $\vec{U}^*$ is calculated with pressure gradient of old time step. And the mass flow rate of grid face is calculated by interpolating the pseudo velocity subtracting pressure gradient. The pressure Poisson equation is composed with the mass flow rate of grid face. The mass flow rate is corrected with the unrelaxed pressure gradient ∇p^* from the Poisson equation. The new velocity is obtained by correcting the pseudo velocity with unrelaxed pressure correction $p' = p^* - p^{old}$. The new pressure is calculated by adding the relaxed pressure correction to old pressure. The solution procedures are compared in Figure 1. The Single Rotational Frame model is employed to POW cases for propeller rotation for steady calculation. In the resistance and self-propulsion calculations, the ship speed is increased gradually to avoid spurious free-surface disturbance in initial stage. The acceleration and the derivative of the acceleration are set zero at the end of the acceleration to remove the abrupt pressure change in time. The running attitude is also controlled for smooth variation. The acceleration of the ship motion is damped. The damping coefficient is set one in initial stage and the coefficient is decreased to zero as time goes on.

POW cases

The POW test of KP505 of KCS and MP687 of JBC has calculated. The thickness of the first prism layer of a propeller is set Y^+=50 at 0.7R. The total number of the grid is about 2.0million. The results of the calculations are in good agreement with the results of the experiments, especially the error of η_0 is about 1% and error of K_T and K_Q is smaller than 3% at advance ratio 0.6 or less. The comparison results are shown in the Figure 1.
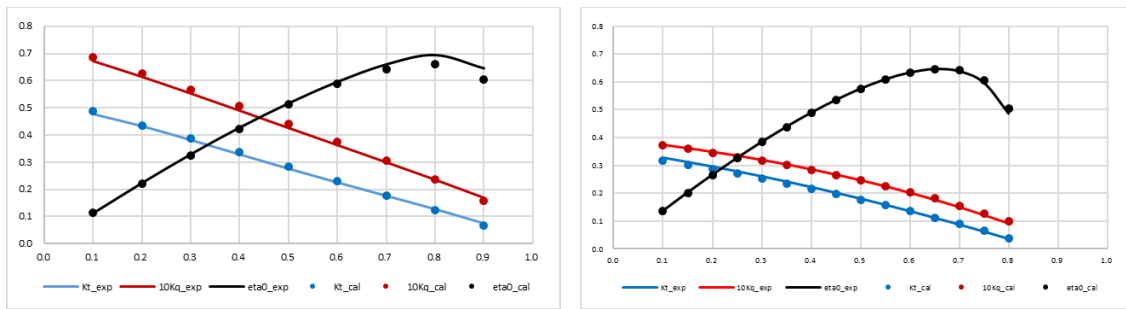
Figure 1 Comparison of thrust, torque and efficiency coefficients of KP505(left) propeller and MP687(right)

Resistance

To verify the performance of ESPER, the resistance results of KCS and JBC were compared with the experimental result [3] and [5]. The simulation conditions of the calculations are the same with experiment conditions, Froude number and Reynolds number of KCS are 0.260 and 1.40 X 10^7, respectively. In JBC case, Froude number and Reynolds number are 0.142 and 7.46 X 10^6.

The thickness of the first prism layer of KCS and JBC hull are set Y^+=30. The number of prism layers is 6 and the total number of the grid is about 1 million in KCS case and 2 million in JBC case. The calculations progressed 0s to 80s and took about 4.5 hours in KCS case and 18 hours in JBC case using 64 cores that is 2.3Ghz clock individually.
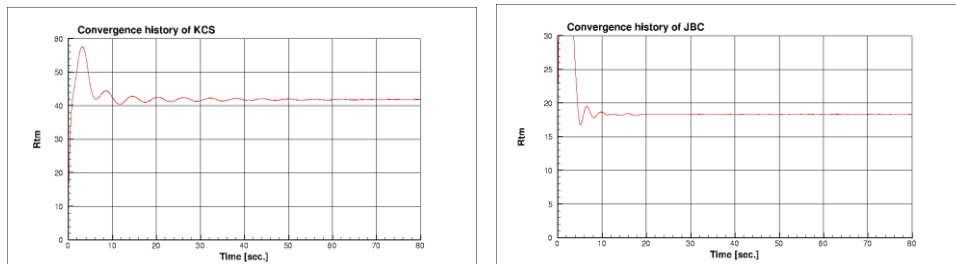
Figure 2: Convergence history of KCS(left) and JBC(right)

Table 1 shows the comparison results between the present calculation results and experimental data. The differences in total resistance between present calculations and experimental data is smaller than 2%. Wake fractions from the present calculations are also acceptable.

The wave height contours of KCS and JBC are compared in Figure 3. Divergence and transverse waves of KCS are well simulated and the agreement with experimental date is good. In JBC case, the wave height is too small to simulate the wave patterns by calculation. To observe the wave pattern of such a slow full ship, more small grids are arranged around the hull. The waves around the stem and stern are similar to experimental data due to enough wave height. Figure 4 shows the wave profiles along the KCS and JBC. The black line or dots of Figure 4 is experiment data and the red line is a wave profile of the present calculation. Figure 4 also shows good agreement. The wake distributions on the propeller planes of

KCS and JBC are shown in Figure 5. Qualitative and quantative agreements of wake distributions are enough to apply to hull form design.

Table 1: Comparison of computed resistance of the model ship of the KCS & JBC

	KCS			JBC		
	Exp.[3]	Present	Error	Exp.[5]	Present	Error
Total resistance (N)	41.170	41.847	1.64%	18.206	18.500	1.62%
Frictional resistance (N)	32.777	33.346	1.74%	13.409	13.691	2.10%
Pressure resistance (N)	8.393	8.501	1.28%	4.797	4.809	0.26%
Wake fraction	0.208	0.224	7.80%	0.61	0.59	-2.81%
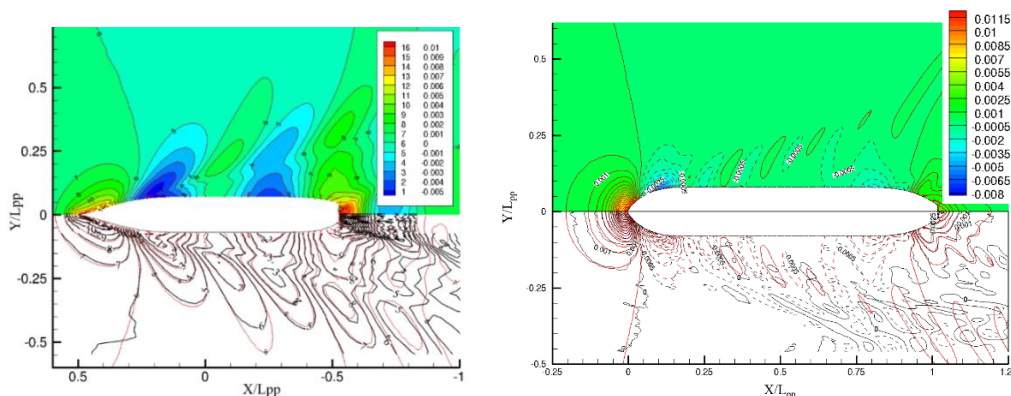
Figure 3 Wave pattern of KCS(left) and JBC(right)
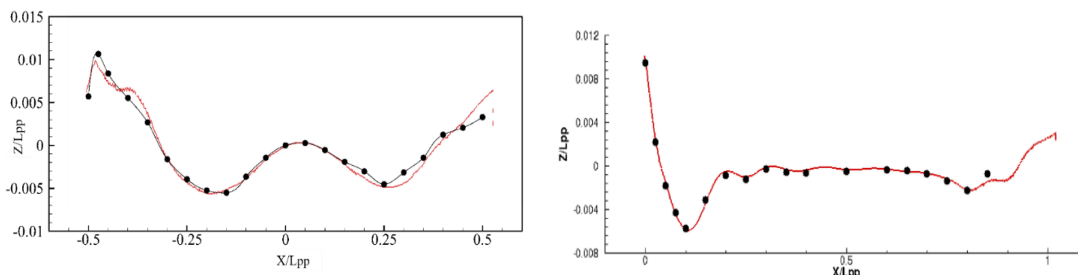
Figure 4 Wave profile along the KCS(left) and JBC(right)
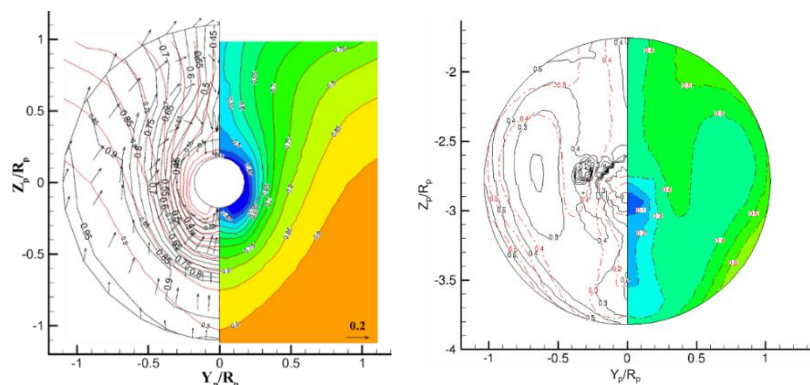
Figure 5 Wake distribution on propeller plane [KCS, X/L$_{pp}$ =-0.4825] (left), [JBC, X/L$_{pp}$ = -0.4843](right)

Self propulsion – JBC case

The self-propulsion performance of JBC is calculated with present numerical method. In this case, the propeller rotation speed is 7.8 RPS. The propulsive force is imposed as body force instead of propeller rotation to reduce the calculation time. The axial and circumferential forces are calculated with POW data. The inflow velocity of the propeller is obtained by averaging the velocity on the 2.857%LBP ahead of propeller plane. It is assumed that the propeller force is distributed following [10]. The grid for the self-propulsion simulation was generated by mirroring the grid for the resistance calculation with 'mirrorMesh' utility.

The Froude number of the calculation is the same with resistance case 0.142. The calculation results, K_T, K_Q and SFC are shown in Table 2. The errors of total resistance, thrust coefficient, torque coefficient and SFC are about 1.22%, -0.24%, 1.23% and 4.24%, respectively. The velocity contour at the stern of JBC has shown in Figure 6. The velocity increment due to the body forces around propeller plane is observed. The JBC hull surface has represents the pressure distribution and the free surface has represents the Z coordinate value. The contour lines around the stern represent the dimensionless velocity it is the velocity of x-axis divided by the reference velocity.

Table 2: Comparison of calculation data of the model ship of the JBC

	Exp.[5]	Present	Error
Total resistance (N)	40.844	41.344	1.22%
Frictional resistance (N)	26.818	26.783	-0.13%
Pressure resistance (N)	14.025	14.561	3.82%
Thrust Coefficient, K_T	0.217	0.216	-0.24%
Torque Coefficient, K_Q	0.0279	0.0282	1.23%
Skin Friction Correction (N)	18.2	19.0	4.24%
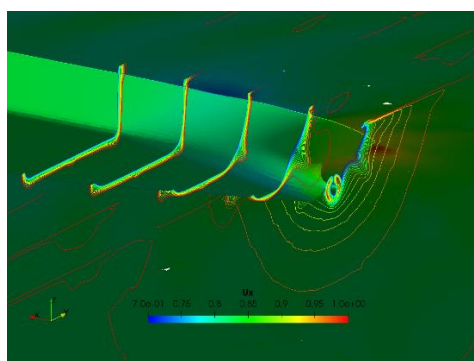
Figure 6 Velocity contour at the stern of JBC

Acknowledgements

References

[1] Jin Kim, Il-Ryong Park, Kwang-Soo Kim, Suak-Ho Van & Yoo-Chul Kim : Development of a Numerical Method for the Evaluation of Ship Resistance and Self-Propulsion Performances : Journal of the Society of Naval Architects of Korea. Vol. 48, No.2, pp.147-157, April 2011.

[2] W. J. Kim, S. H. Van & D. H. Kim : Measurement of flows around modern commercial ship models : Experiments in Fluids 31 (2001), pp.567-578.

[3] Kadir Burak Korkmaz : CFD predictions of resistance and propulsion for the JAPAN Bulk Carrier(JBC) with and without an energy saving device : Master's Thesis, Department of Shipping and Marine Technology, Division of Marine Technology, CHALMERS University of Technology, Gothenburg, Sweden 2015.

[4] 대한조선학회 선박유체역학연구회 : 선박의 저항과 추진, Chapter 9, 1st ed., 2009.

[5] A Workshop on CFD in Ship Hydrodynamics, Tokyo 2015, www.t2015.nmri.go.jp

[6] Workshop on Verification and Validation of Ship Manoeuvering Simulation Methods, SIMMAN 2008, www.simman2008.dk/KCS/container.html

[7] Workshop on Verification and Validation of Ship Manoeuvering Simulation Methods, SIMMAN 2019, www.simman2019.kr

[8] Byoung-Nam Kim, Jong-Hwan Park & Wu-Joan Kim : Calculation of Flows around Container Ship Models with Different Reynolds Numbers : Journal of the Society of Naval Architects of Korea. Vol. 44, No. 3, pp.258-266, June 2007.

[9] Hyun-sik Kim, Sangmook Shin : Computation of flow around a ship using a surface integrated from station lines : J. Comput. Fluids Eng., Vol. 20, No. 4, pp.21-27, 2015.

[10] Goldstein, s. : On the vortex theory of screw propellers : Proc. Of the Royal Society (A) 123, 440, 1929.

NUMERICAL SIMULATION OF OVERTOPPING OF SLOPING BREAKWATER UNDER IRREGULAR WAVE

LI JINGYUAN[1], ZHANG QINGHE[2]
[1]Tianjin University , jingyuan1i@tju.edu.cn
[2]Tianjin University , qhzhang@tju.edu.cn

Keywords: Irregular wave; armour block; seepage equation; wave overtopping; prototype–scale simulation

Abstract: Based on the open source software OpenFOAM, a three-dimensional wave model is developed to generate irregular waves. The Volume-Averaged RANS equation and the seepage equation containing nonlinear term are used to describe the water flow under the amour layer of the sloping breakwater. The full-scale simulation of the accropode blocks as armour layer of sloping breakwater is realized through mesh generation tool. The interaction between the normally-incident irregular waves and the sloping breakwater armored by accropode blocks is investigated through numerical simulation. The results indicate reasonably good agreement both between the simulated mean overtopping rates and physical model results and between the simulated overtopping rates for full-size prototype breakwater and the prototype results converted from the model test based on the gravity similarity. It is concluded that the developed numerical model can be used to describe the overtopping process of sloping breakwater armored by accropode blocks under working conditions.

SIMULATION OF THE HYDROELASTIC RESPONSE OF A FLOATING ICE SHEET

LUOFENG HUANG[1], MINGHAO LI[2], ŽELJKO TUKOVIĆ[3], GILES THOMAS[4]

[1]*University College London, UK, ucemlhu@ucl.ac.uk*
[2]*Chalmers University of Technology, Sweden, limi@student.chalmers.se*
[3]*University of Zagreb, Croatia, Zeljko.Tukovic@fsb.hr*
[4]*University College London, UK, giles.thomas@ucl.ac.uk*

Keywords: Fluid-Structure Interaction, Hydroelasticity, Sea Ice, Ocean Surface Wave, OpenFOAM

Introduction

In the polar region, ice sheets can be several kilometres long and subjected to the effects of ocean waves. As its thickness to length ratio is very small, an ice sheet may experience significant localised vibrations under continuous wave excitation. In such situations, the vibratory response of the large ice sheet is dominated by an elastic deformation rather than rigid body motions, which is also known as the hydroelastic response of sea ice. A review on this phenomenon has been given by Squire [1], indicating that understanding it fully will be a key challenge of polar engineering. The hydroelastic wave-ice interaction can induce wave reflection and transmission [2], which makes the wave field nearby very different from that in the open ocean and can lead to a considerable influence on any adjacent structures and/or passing vessels.

Previous studies on the hydroelasticity of sea ice have mainly been conducted analytically. Fox and Squire [2] considered the reflection and transmission of waves from open water to an ice sheet. They adopted the method of eigenfunction expansion for the velocity potentials of the water, and used the conjugate gradient method to impose continuity at the interface and edge condition. The reflection and transmission coefficients of the incident waves were obtained and found to be dependent on the wave period, ice thickness and water depth. A similar analytical study was also conducted by Chung and Fox [3] using the Wiener-Hopf method.

The analytical works have provided great insight into this problem. However, in order to formulate the case in mathematics, they were built upon specific ideal assumptions, where the fluid viscosity and non-linear behaviours were neglected. This limitation makes an analytic analysis insufficiently realistic and accurate, which motivates an improvement of developing a numerical model that has the ability to obtain a higher-order solution and capture the phenomena that have not been included in the analytical models.

Fluid-Structure Interaction (FSI) simulation through Computational Fluid Dynamics (CFD) is an advanced numerical method to model solid deformations induced by fluid, but has not to date been applied to ice hydroelasiticity. To develop a reliable CFD tool to fill this gap, Tukovic et al. [4] designed an FSI package using the opensource CFD platform OpenFOAM, and Huang [5] extended this package into multiphases so that it can model the hydroelastic problem where the floating structure is in contact with both air and water.

As shown in Figure 1, this work will use the the developed code [5] to simulate the hydroelastic response of a floating ice sheet, and assess its accuracy by comparing the computational results with the experimental data of Sree et al. [6]. The influence of environmental variables will also be investigated, including the incident wave period, ice thickness and water depth. Furthermore, the wave field affected by the ice sheet will be compared with its open water counterpart.
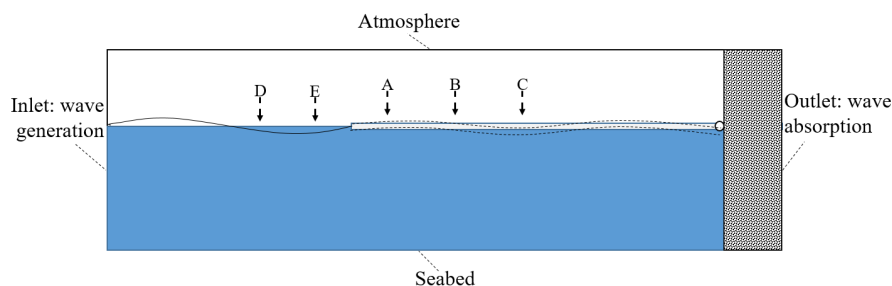
Figure 1: Schematic of the case: a thin ice sheet is floating on the water surface and subjected to incoming waves, with its elastic deformation induced. Three probes (A, B and C) are set at 0.1 m, 0.3 m, and 0.5 m inside the ice edge respectively to measure the local vertical vibration, and two other probes (D and E) are set at 0.1 m and 0.3 m outside the ice edge respectively to measure the free surface elevation.

Numerical Approach

A partitioned FSI scheme is applied to simulate the hydroelastic case, where the fluid and solid sides are solved separately and coupled via the fluid-solid interface. The fluid side is solved through the Reynolds-averaged Navier-Stokes (RANS) equations together with the Volume of Fluid (VOF) method. On the solid side, the ice deformation is solved according to the Saint-Venant Kirchoff constitutive model with the plane strain assumption. An extended introduction of this FSI scheme has been given by Tukovic et al. [7]. The solution procedure of this work is illustrated in Figure 2, with the details being explained in the steps outlined below:

- To start a new time step loop, the structural displacement is first updated according to the results of the previous time step. Then, to keep the fluid mesh in accordance with the solid mesh, the Aitken coupling scheme is employed, which introduces an Aitken Relaxation Factor (ARF), as defined in Equation (1).

$$ARF- = ARF \times \frac{\sum(Res_{t=n-1} \cdot \Delta Res)}{\sum(\Delta Res \cdot \Delta Res)} \tag{1}$$

Thus the ARF is updated according to the residual (Res), which is the difference between the structural interface displacement (SID) and the fluid interface displacement (FID), namely $Res = SID - FID$. Afterwards, the fluid mesh is adjusted with the updated ARF value, as in Equation (2).

$$FluidMesh+ = ARF \times Res \tag{2}$$

- The FID is extracted from the adjusted fluid mesh. Then its differential produces the velocity of the fluid interface and the mesh motion of the rest fluid region is obtained according to this interface velocity.

- Based on the moved mesh, the fluid solver calculates the velocity and pressure field. Meanwhile, the pressure and viscous force on the fluid interface can be obtained.

- The fluid load on the fluid interface is transferred to the solid interface, considered as the fluid load on the structure.

- According to the load on the interface, the structure solver calculates the displacement of the structure.

- The SID can be extracted from the structural displacement and then compared with the FID to obtain a new residual, Res. The solver switches to the next time step when either the residual criteria is satisfied or the pre-defined maximum FSI iteration time has been reached, otherwise it continues looping in the current time step.
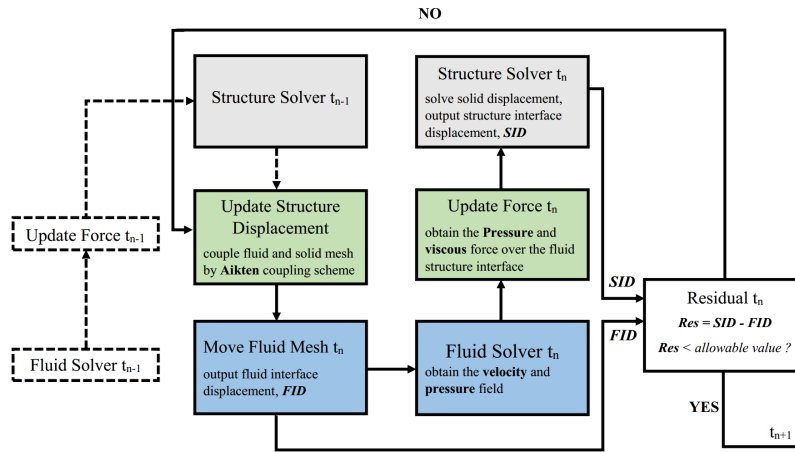
Figure 2: Flow chart of the FSI solution procedure.

Case setup

The general setup of the simulation case is shown in Figure 1. The case is set as a two-dimensional rectangular computational domain. It is filled with fresh water of density $\rho_w = 1000$ kg m^{-3} to a depth of $h = 0.3$ m. On the top of the domain, a static pressure boundary condition is applied to model the atmosphere. The bottom boundary is defined as a no-slip wall to account for the presence of the seabed. Using the waves2Foam tool [8], regular waves of amplitude $a = 0.0085$ m and period $T = 0.7$ s are constantly generated at the inlet boundary without any current speed, and a wave absorption zone is set up in front of the outlet boundary to avoid waves being reflected here.

A thin ice sheet is initialised as one side free floating on the water surface and the other side fixed, with its length L of 1 m and thickness t of 0.01 m. The ice rheology is set as density $\rho = 910$ kg m^{-3}, Young's modulus $E = 870$ MPa and

Poisson ratio $\nu = 0.3$. These properties may be varied to study their influence. Three probes (A, B and C) are set at 0.1 m, 0.3 m, and 0.5 m inside the ice edge respectively to measure the local vertical vibration, and two other probes (D and E) are set at 0.1 m and 0.3 m outside the ice edge respectively to measure the free surface elevation.

Results and discussion

To validate the proposed model, the vertical vibrations at the point A, B, C were computed and compared with the experimental data of Sree et al. [6]. In spectral analysis, both the computational results (CFD) and the experimental results (Exp.) are plotted in Figure 3, in which the proposed model reveals very good agreement with the experimental measurements at all the three points. The main oscillating frequency of the ice sheet (where the peaking amplitude occurs) equals to the frequency of the incident wave, which means the vertical oscillation of the ice has approached a steady state. Besides, the peaking amplitude gets smaller from the ice edge to the middle section of the ice (from point A to C).

To investigate the influence of environmental variables on the hydroelastic response of the ice sheet, the ratio of the local vertical oscillation amplitude (A) to the incident wave amplitude (a) was calculated and plotted out, as a function of different incident wave period, ice thickness and water depth, in Figure 4, 5 and 6 respectively. Generally, the deformation of the ice sheet is found to increase as the wave period is increased, and decrease with increasing ice thickness. However, the variation is undistinguished when the water depth is changed, with a slight increase in the shallow water situation and nearly constant in deep water.

Figure 4 shows the ice deformation reducing dramatically when the incident wave period is less than 0.5 s, which is because the waves become very short then, corresponding to a wavelength of less than 0.4 m. As the wave period increases, the vibration amplitude of the ice can approach the incident wave amplitude. Figure 5 shows the ice deformation becomes very weak when the ice thickness increases to a level of the incident wave height, and when the thickness keeps decreasing, the oscillating amplitude can be larger than the ice thickness.

The ice sheet is found to have a significant influence on the wave field, where there is a superposition of the ice-reflected waves and the incident waves. The free surface elevation at points D and E is plotted in Figure 7, alongside a comparison with the open water situation of no ice. It shows that the existence of the ice sheet weakened the waves at point D but induces stronger waves at point E, which suggests the ice sheet can influence the wave field to a large degree and the influence is dependent on the location.

Conclusions

This work provided an available CFD code to simulate the wave-induced FSI problems. After validation against experiments, the code reveals very good accuracy on predicting the hydroelastic response of a floating ice sheet. It can also be applied to other deformable floating bodies, not just the sea ice case.

Acknowledgments

References

[1] V. A. Squire, "Past, present and impendent hydroelastic challenges in the polar and subpolar seas," *Philosophical Transactions of the Royal Society of London A: Mathematical, Physical and Engineering Sciences*, vol. 369, no. 1947, pp. 2813–2831, 2011.

[2] C. Fox and V. A. Squire, "Reflection and transmission characteristics at the edge of shore fast sea ice," *Journal of Geophysical Research: Oceans*, vol. 95, no. C7, pp. 11 629–11 639, 1990.

[3] H. Chung and C. Fox, "Calculation of wave-ice interaction using the wiener-hopf technique," *New Zealand J. Math*, vol. 31, no. 1, pp. 1–18, 2002.

[4] Z. Tukovic, P. Cardiff, A. Karac, H. Jasak, and A. Ivankovic, "Openfoam library for fluid structure interaction," in *9th OpenFOAM Workshop*, vol. 2014, 2014.

[5] L. Huang, "An opensource solver for wave-induced fsi problems," In Proceedings of CFD withOpenSource Software, Tech. Rep., 2018.

[6] D. K. Sree, A. W.-K. Law, and H. H. Shen, "An experimental study on the interactions between surface waves and floating viscoelastic covers," *Wave Motion*, vol. 70, pp. 195–208, 2017.

[7] Z. Tukovic, A. Karac, P. Cardiff, H. Jasak, and A. Ivankovic, "Openfoam finite volume solver for fluid-solid interaction," *Tractions of FAMENA*, 2018.

[8] N. G. Jacobsen, D. R. Fuhrman, and J. Fredsøe, "A Wave Generation Toolbox for the Open-Source CFD Library: OpenFoam®," *International Journal for Numerical Methods in Fluids*, vol. 70, no. 9, pp. 1073–1088, 2012.

Figure 5: Local vibrations of the ice sheet, as a function of the ice sheet thickness (t).
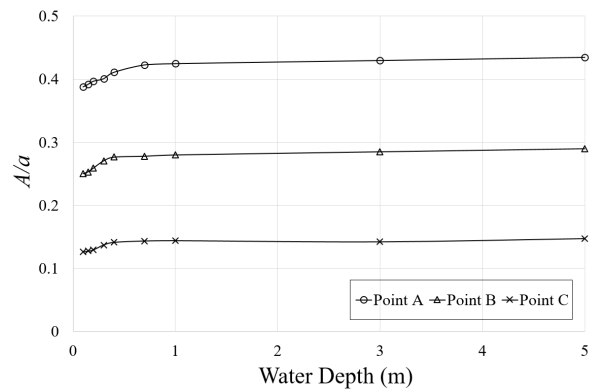
Figure 6: Local vibrations of the ice sheet, as a function of the water depth (h).

Figure 3: Spectral analysis (discrete Fourier transform, $| Y(\sigma) |$) of the vertical vibration at different locations along the ice sheet: a comparison between computational and experimental results.
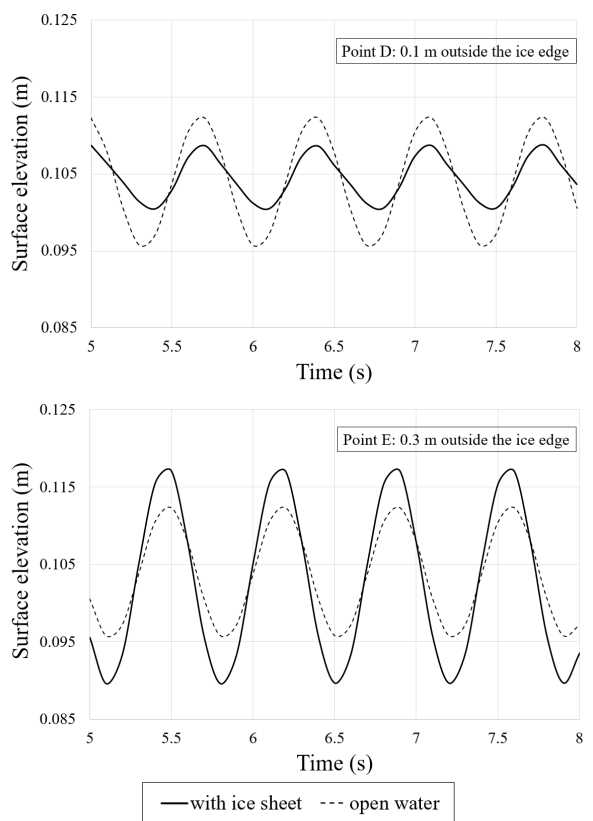
Figure 7: Free surface elevation at different locations outside the ice sheet: a comparison between the computational results and corresponding open water counterpart.

Figure 4: Local vibrations of the ice sheet, as a function of the incident wave period (T).

TOWARDS THE MODELING OF FLUID-STRUCTURE INTERACTIVE LOST CORE DEFORMATION IN HIGH-PRESSURE DIE CASTING

SEBASTIAN KOHLSTÄDT[1], MICHAEL VYNNYCKY[2], JAN JÄCKEL[3], LUDGER LOHRE[4]

[1]*KTH Royal Institute of Technology, Stockholm, Sweden, skoh@kth.se*
[2]*KTH Royal Institute of Technology, Stockholm, Sweden, michaelv@kth.se*
[3]*Volkswagen AG - Division of components manufacturing, Baunatal, Germany, jan.jaeckel@volkswagen.de*
[4]*Volkswagen AG - Division of components manufacturing, Baunatal, Germany, ludger.lohre@volkswagen.de*

1 Introduction

High-pressure die casting (HPDC) is an important process for manufacturing high volume and low cost automotive components, such as automatic transmission housings and gear box components [1, 2]. Liquid metal, generally aluminium or magnesium, is injected through complex gate and runner systems and into the die at high speed, typically between 50 and 100 ms^{-1}, and under very high pressures up to 100 MPa. However, it has up to date proven difficult to employ lost salt cores within the process [3]. The basic idea of using salt cores is to create undercuts or hollow sections with them, which may then later act as cooling or oil-flow channels [4, 5, 6]. Given this process constraint in design freedom for the CAD-engineer, the idea of using salt as the material for lost cores has been put forward by machine manufacturers, as well as automotive companies [7, 8]. One way to determine whether this is indeed viable is to employ numerical simulation [9].

2 Model equations

2.1 Fluid side

We model the two-phase flow of molten metal and air in high pressure die casting by using the VOF method [10], wherein a transport equation for the VOF function, γ, of each phase is solved simultaneously with a single set of continuity and Navier-Stokes equations for the whole flow field; note also that γ, which is advected by the fluids, can thus be interpreted as the liquid fraction. Considering the molten melt and the air as Newtonian, compressible and immiscible fluids, the governing equations can be written as [11, 12]

$$\frac{\partial \rho}{\partial t} + \nabla \cdot (\rho \mathbf{U}) = 0, \tag{1}$$

$$\frac{\partial}{\partial t}(\rho \mathbf{U}) + \nabla \cdot (\rho \mathbf{U}\mathbf{U}) = -\nabla p$$
$$+ \nabla \cdot \left\{ (\mu + \mu_{tur}) \left(\nabla \mathbf{U} + (\nabla \mathbf{U})^{\mathrm{T}} \right) \right\} + \rho \mathbf{g} + \mathbf{F}_s, \tag{2}$$

$$\frac{\partial \gamma}{\partial t} + \nabla \cdot (\gamma \mathbf{U}) + \nabla \cdot (\gamma (1 - \gamma) \mathbf{U}_r) =$$
$$- \frac{\gamma}{\rho_g} \left(\frac{\partial \rho_g}{\partial t} + \mathbf{U} \cdot \nabla \rho_g \right), \tag{3}$$

where t is the time, $\mathbf{U}$ the mean fluid velocity, p the pressure, $\mathbf{g}$ the gravity vector, $\mathbf{F}_s$ the volumetric representation of the surface tension force and $^{\mathrm{T}}$ denotes the transpose. In particular, $\mathbf{F}_s$ is modelled as a volumetric force by the Continuum Surface Force (CSF) method [13]. It is only active in the interfacial region and formulated as $\mathbf{F}_s = \sigma \kappa \nabla \gamma$, where σ is the interfacial tension and $\kappa = \nabla \cdot (\nabla \gamma / |\nabla \gamma|)$ is the curvature of the interface. The term $\mathbf{U}_r$ is a supplementary velocity field for compressing the phase-interface introduced by the solving scheme for the γ-field (MULES) [11, 14]. The material properties ρ and μ are the density and the dynamic viscosity, respectively, and are given by

$$\rho = \gamma \rho_l + (1 - \gamma) \rho_g, \tag{4}$$
$$\mu = \gamma \mu_l + (1 - \gamma) \mu_g, \tag{5}$$

where the subscripts g and l denote the gas and liquid phases, respectively. We take ρ_l, μ_g and μ_l to be constant, but use the approach to assume air as a barotropic fluid, i.e. its density changes linearly with pressure and the process to be isothermal and hence the equation of state for our model reads

$$\rho_g = \frac{p}{R_s T} = p\psi. \tag{6}$$

where R_s is the specific gas constant and T is the temperature. Since $\frac{1}{R_s T}$ is taken as constant, we introduce the constant compressibility factor ψ for the gaseous phase. Furthermore, μ_{tur} in equation (2) denotes the turbulent eddy viscosity, which will be calculated via the Menter k–ω-SST model [15]. The implementation of the Menter k–ω-SST model inside the OpenFOAM framework has shown to be robust and also in excellent agreement with experimental data [16].

2.2 Solid side

On the solid side only the stress equation is evaluated for calculating the displacement of the salt core in space. This process is physically governed by the following equation

$$\rho_s \frac{\partial^2 \mathbf{D}}{\partial t^2} - \nabla \cdot [(2\mu_s + \lambda_s)\nabla \mathbf{D}] = \nabla \cdot \mathbf{q}. \tag{7}$$

In equation (7) $\mathbf{D}$ represents the displacement vector, ρ_s denotes the density of the solid, λ_s and μ_s denote the solid's first and second Lamé parameters, respectively and $\mathbf{q}$ is the load per unit unit area. $\mathbf{q}$ consists of the pressure and viscous forces from the fluid side. There are no body forces taken into account for the selected approach.

3 Solver development and testing

Given the complexity of the physics involved and also the niche nature of the application, the C++ toolbox OpenFOAM [17, 18] was used to implement the model as it is freely available, rather suitable for being extended by the user and very well scalable for industrial application as extra cores in parallelisation do not require additional licenses. The solver that was used for the simulations in this paper does not yet exist in neither the OpenFOAM foundation release nor the foam-extend project. However, the foam-extend release offers a toolbox called the fsi library [19]. Inside the fsi library several solvers are available depending on the intensity of the coupling between the fluid and the solid. Here, as we expect to see rather large deformations, the solver *fsiFoam* was used. It follows a process chain depicted in figure 1. The names of the steps closely resemble the names given to the methods that are being called while the code is running. It may thus be easier to bridge between the code and the chart. One sees clearly that at first the displacement of the flow domain is evaluated, then the flow field according to the displacement and boundary conditions is evolved and then its eventual impact on the stress field in the solid is calculated. The blue loop indicates that this entire process is repeated until the specified residual is reached. After that the solver moves on to the next time step.
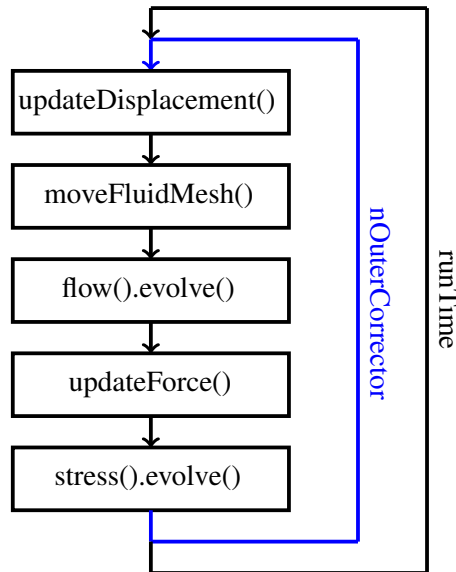
Figure 1: Solving process scheme of fsiFoam Solver

As outlined in the previous section, already the fluid side is a rather complex fluid flow problem. There was thus previously no solver class available that could solve such a problem within the framework of the fsi library. It however is available as a top level solver inside the normal OpenFOAM solver toolbox. The first step was therefore to implement the

same methodology of the solver *compressibleInterDyMFoam* into a class that fits the requirements of an fsi fluid solver class. The standard pimple algorithm was for this purpose modified and an additional step at the beginning was added that solved the transport equation (equation 3) at the beginning of the process chain, i.e. before the momentum predictor.

This newly coded solver class inside the fsi library was benchmarked against the standard version of the solver *compressibleInterDyMFoam* with the simple standard *damBreak* tutorial case (figure 2) with the coupling between the fluid and the solid as well as the mesh motion switched off. Figure 2 shows the result of this benchmark study. As the reader can easily see the results for the phase field are entirely identical in the two pictures indicating that both the standard *compressibleInterDyMFoam* as well as the newly developed solver class *FSI::compInterFluid* produce the same flow field result.

(a) compressibleInterDyMFoam   (b) FSI::compInterFluid

air $\leftarrow \gamma \rightarrow$ water

| 0 | 0.1 | 0.2 | 0.3 | 0.4 | 0.5 | 0.6 | 0.7 | 0.8 | 0.9 | 1 |
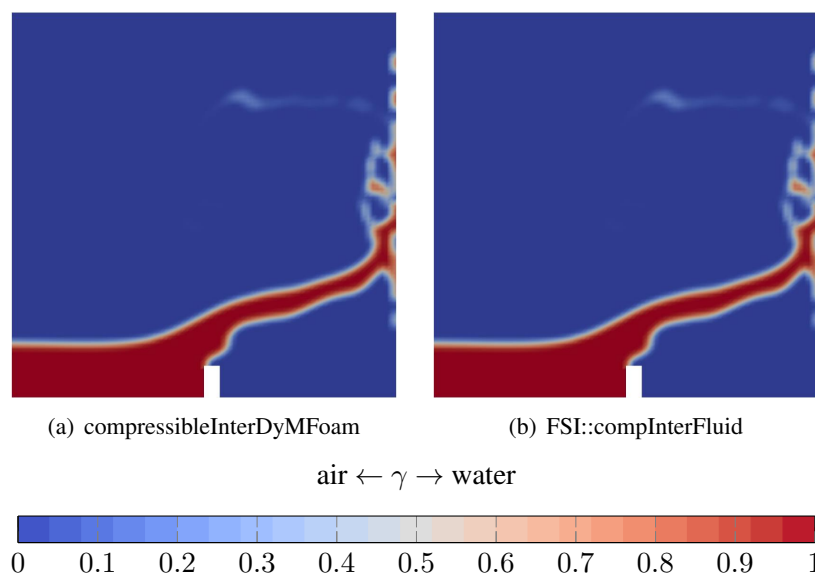
Figure 2: γ-field comparsion of compressibleInterDyMFoam and FSI::compInterFluid at 0,4 s

In addition to this graphical comparison the solver has also been tested for mass conservation, volume conservation and conservation of γ in the process on simple geometries and benchmarked with analytical models.

4   Results and validation

The ultimate goal is to simulate the deformation of lost cores during the high-pressure die casting process. A simple structured mesh was constructed for this purpose that resembles the setup of a three-point bending test within a casting mould. Figure 3 shows a picture of the produced casting without the core in the upper part and also a picture of the deformation of the core in the lower part. The result is written out for the time step of 0.1 s shortly after the first drops of melt hit the core. Note that the geometry does not have an outlet. The die is initially filled with air and melt is flowing in at a constant velocity from the inlet.

It can be observed in figure 3 that the salt core undergoes a deformation in the range of 2.5 mm as soon as the melt hits the core and hence the momentum of the melt gets redirected due to the core blocking the initial channel flow. The core vibrates initially due to an observable spike in the force when the interface hits the core and is then displaced constantly by the bypassing flow, when the flow pattern around it becomes stable.

For the sake of validating the solver an experimental die was constructed and manufactured that resembles the geometry of the meshed body shown in figure 3. The die was then tested on a high-pressure die casting machine with the same process parameters that had previously been used for the simulation. One result of the so cast prototypes is shown in its cross-section in figure 4. One sees in this picture that analogously to the shape that we saw in figure 3 the core also gets symmetrically bent by the inflowing melt. The displacement is also in the order of magnitude of more than 2 mm and thus produces a comparable result as previously seen in the CFD-simulation (figure 3). Previously so far unpublished research by the authors also shows that the highest expectable impact on the core also occurs at the transition from the air phase to the melt phase at the core interface.

References

[1] B. Nogowizin, *Theorie und Praxis des Druckgusses*, 1. Edition ed.   Berlin: Schiele und Schoen, 2010.

[2] E. Brunnhuber, *Praxis der Druckgussfertigung*.   Berlin: Schiele und Schoen, 1991.
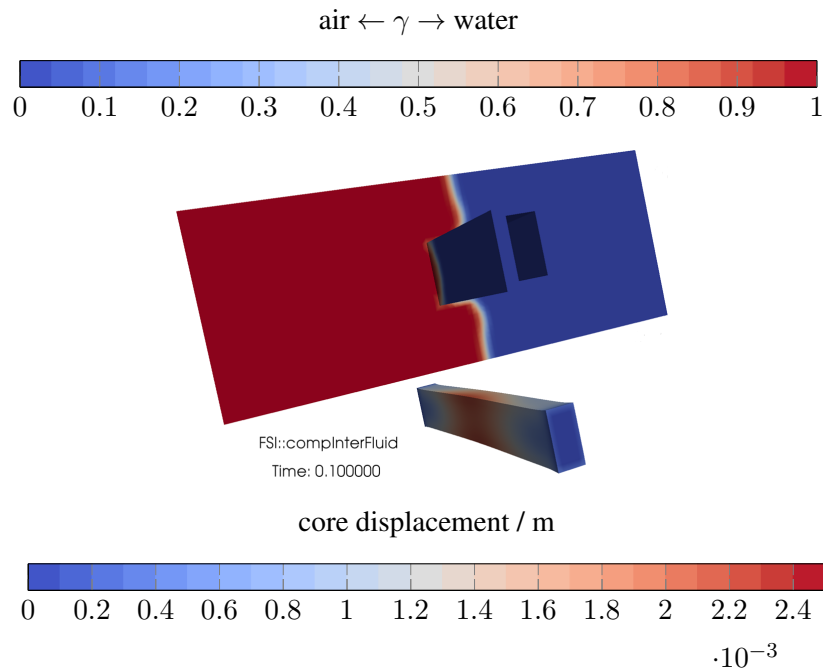
Figure 3: The deformation of the salt core as result of the CFD simulation.

Figure 4: The deformation of the salt core in a casting experiment.

[3] B. Fuchs, H. Eibisch, and C. Körner, "Core viability simulation for salt core technology in high-pressure die casting," *Int. J. Metalcasting*, vol. 7, pp. 39–45, 2013.

[4] E. Graf and G. Soell, "Vorrichtung zur Herstellung eines Druckgussbauteils mit einem Kern und einem Einlegeteil," 2003, dE Patent DE2,001,145,876.

[5] E. D. I. Graf and G. D. I. Söll, "Verfahren zur Herstellung eines Zylinderkurbelgehäuses," 2008, dE Patent DE200,710,023,060.

[6] S. Kohlstädt, U. Rabus, S. Goeke, and S. Kuckenburg, "Verfahren zur Herstellung eines metallischen Druckgussbauteils unter Verwendung eines Salzkerns mit integrierter Stützstruktur und hiermit hergestelltes Druckgussbauteil," 2016, dE Patent DE201,410,221,359.

[7] P. Jelínek and E. Adámková, "Lost cores for high-pressure die casting," *Archives of Foundry Engineering*, vol. 14, no. 2, pp. 101–104, 2014.

[8] T. Schneider, S. Kohlstädt, and U. Rabus, "Gehäuse mit Druckgussbauteil zur Anordnung eines elektrischen Fahrmotors in einem Kraftfahrzeug und Verfahren zur Herstellung eines Druckgussbauteils," 2016, dE Patent DE201,410,221,358.

[9] B. Fuchs and C. Körner, "Mesh resolution consideration for the viability prediction of lost salt cores in the high pressure die casting process," *Prog. Comp. Fluid Dyn.*, vol. 14, pp. 24–30, 2014.

[10] C. W. Hirt and B. D. Nichols, "Volume of fluid (VOF) method for the dynamics of free boundaries," *J. Comp. Phys.*, vol. 39, pp. 201–225, 1981.

[11] P. M. Ferrer, D. Causon, L. Qian, C. Mingham, and Z. Ma, "A multi-region coupling scheme for compressible and incompressible flow solvers for two-phase flow in a numerical wave tank," *Computers & Fluids*, vol. 125, pp. 116–129, 2016.

[12] R. Mayon, Z. Sabeur, M.-Y. Tan, and K. Djidjeli, "Free surface flow and wave impact at complex solid structures," in *12th International Conference on Hydrodynamics , Egmond aan Zee, NL, 18 - 23 Sep 2016*, 2016, p. 10pp.

[13] J. Brackbill, D. B. Kothe, and C. Zemach, "A continuum method for modeling surface tension," *Journal of computational physics*, vol. 100, no. 2, pp. 335–354, 1992.

[14] H. Rusche, "Computational fluid dynamics of dispersed two-phase flows at high phase fractions," Ph.D. dissertation, Imperial College London (University of London), 2003.

[15] F. R. Menter, "2-equation eddy-viscosity turbulence models for engineering applications," *AIAA J.*, vol. 32, pp. 1598–1605, 1994.

[16] E. Robertson, V. Choudhury, S. Bhushan, and D. Walters, "Validation of OpenFOAM numerical methods and turbulence models for incompressible bluff body flows," *Computers & Fluids*, vol. 123, pp. 122–145, 2015.

[17] H. Jasak, A. Jemcov, and Z. Tukovic, "OpenFOAM: A C++ Library for Complex Physics Simulations," in *International Workshop on Coupled Methods in Numerical Dynamics IUC*, 2007.

[18] H. G. Weller, G. Tabor, H. Jasak, and C. Fureby, "A tensorial approach to computational continuum mechanics using object-oriented techniques," *Computers in Physics*, vol. 12, no. 6, pp. 620–631, 1998.

[19] P. Cardiff, Ž. Tuković, H. Jasak, and A. Ivanković, "A block-coupled finite volume methodology for linear elasticity and unstructured meshes," *Computers & structures*, vol. 175, pp. 100–122, 2016.

CONTROL OF CYLINDER WAKE USING A FLEXIBLE FILAMENT

FANGFANG XIE[1], JIAN DENG[1]

[1]*School of Aeronautics and Astronautics,Zhejiang University,*
Hangzhou, Zhejiang, 310027, P.R. China, fangfang_xie@zju.edu.cn

Keywords: *Flexible filaments, suppression, penalty Immersed boundary method*

1 Inroduction

Controlling vortex-induced vibrations (VIV) is important in ocean structures, in designing robust heat exchangers, and especially in the offshore industry given the new emphasis on deep water drilling [1]. In deep water, immersed structures such as risers usually have low damping and over time VIV will weaken the risers and ultimately cause fatigue and fracture. Replacement of the pipelines is a very expensive and time consuming process, hence new suppression techniques are required.

Many flow-control techniques have been proposed to suppress VIV, such as splitter plates [2, 3], suction based flow control [4, 5], slits parallel to the incoming flow [6], stream-lining of the structural geometry [7, 8], helical strakes [9, 10], and other add-on devices for passive control [11, 12, 13]. Recently, flexible plates or filaments have attracted much attention for their role in passive flow control [12, 14], as they can self-adapt to direct flow without the input of energy.

In the current study, control of cylinder wake by using a flexible filament in the downstream stagnation point is numerically studied in the framework of OpenFoam. The cylinder is fixed, and the filament is attached to the base of the cylinder. Its leading end is fixed and its trailing end is free to flap. To execute the numerical simulation and deal with the fluid-structure interaction (FSI) of the filament as well, a penalty Immersed boundary method (IBM) is presented.

2 Numerical method

For the simulations, we adopt a penalty Immersed Boundary Method (IBM)[**?**]. The equations governing this fluid-structure coupling system are expressed as following:

$$\rho \left(\frac{\partial u}{\partial t} + u \cdot \nabla u \right) = -\nabla p + \mu \nabla^2 u + f, \tag{1}$$

$$\nabla \cdot u = 0, \tag{2}$$

$$f(x) = \int F(r,s)\delta(x - X(r,s))drds, \tag{3}$$

$$\frac{\partial X}{\partial t}(r,s) = U(r,s) = \int u(x,t)\delta(x - X(r,s))dx, \tag{4}$$

$$F = F_E + F_K + F_C, \tag{5}$$

$$F_E = -\frac{\partial E}{\partial X}, \tag{6}$$

$$F_K(r,s) = K[Y(r,s) - X(r,s)], \tag{7}$$

$$F_C(r,s) = \delta(X(r,s) - X'(s))\frac{X - X'}{|X - X'|}, \tag{8}$$

$$\rho_s(r,s)\frac{\partial^2 Y}{\partial^2 t} = -F_K(r,s) - \rho_s(r,s)Fr\frac{\mathbf{g}}{g}. \tag{9}$$

Equations 1 and 2 are the Navier-Stokes equations for a viscous incompressible fluid, which are solved by a finite-volume based solver OpenFOAM. Here, ρ, u, p are the density, velocity and pressure of the fluid, respectively. The term $F(r,s)$ in equation 3 include the elastic force induced by the deformation of the elastic boundary and the repulsive force between the filament and cylinder, and the term $f(x)$ represents the fluid body force density.

For the rigid cylinder, the F_E component can be ignored. For the flexible filament, it can be regarded as a 1-D massive boundaries, which are represented by a serial of one-dimensional rods. We impose two elasticities to these rods, one resists stretching and compression, and the other resists bending. The energy function $E[X(.)]$ can therefore be formalized as

$$E[\mathbf{X}(\cdot)] = \frac{1}{2}k_s \int \left(\left|\frac{\partial X}{\partial s}\right| - 1\right)^2 ds + \frac{1}{2}k_b \int \left|\frac{\partial^2 X}{\partial^2 s}\right|^2 ds, \tag{10}$$

where k_s and k_b denote the coefficients by resisting the stretching and bending respectively.

3 Numerical results

In the current work, we consider a fixed Reynolds number, Re = 100, for the following simulations. We define the Reynolds number $Re = U_\infty/\nu D$, where D is the diameter of the circular cylinder, U_∞ is the streamwise velocity far upstream and ν is the kinematic viscosity.

We firstly examine the effects of the filament on the flow control of the cylinder by varying the length (L) of the filament. Figure 1 shows the phase diagram of drag and lift coefficients for the cylinder-filament system under various length. The black line denotes the reference value for the cylinder without filaments. It is seen that the effect of the attached filament on the evolution of the forces acting on the cylinder is remarkable. With the attached filament, both the mean drag coefficient and the fluctuation of lift force can be suppressed effectively. The longer filament performs better since it can delay the vortex shedding in the cylinder wake to a further downstream, see figure 2.

For the case with the filament length of $L = 0.5D$ and $L = D$, the symmetry of lift fluctuation is broken and a positive net lift force is achieved. By looking at the flapping trajectory of the filament in figure 3, we see that the filament is flapping in the low half part of the cylinder wake, thus generating a positive lift force to the cylinder-filament system.

Moreover, as the effect of the bending stiffness, we see that in figure 4 a more rigid filament can achieve a lower drag coefficient and smaller lift fluctuation/ flapping amplitude . By checking the flow pattern, it is seen that the vortex is roll up back to the top surface of the filament tail for the rigid one (with $kb = 0.002$), therefore leading to the recovery of pressure in the wake of filament.
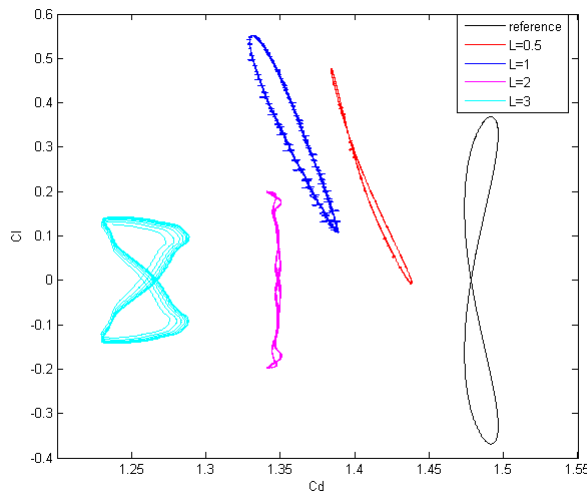
Figure 1: Effect of filament's length on the force of the cylinder-filament system.
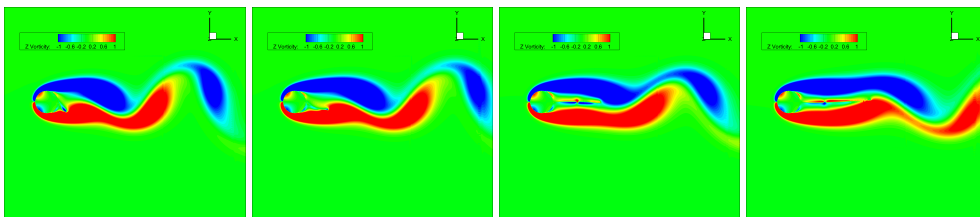
Figure 2: Vorticity plot for flow around a cylinder with a single filament attached to the downstream stagnation point under various length ($\rho_s = 1, kb = 0.01$).
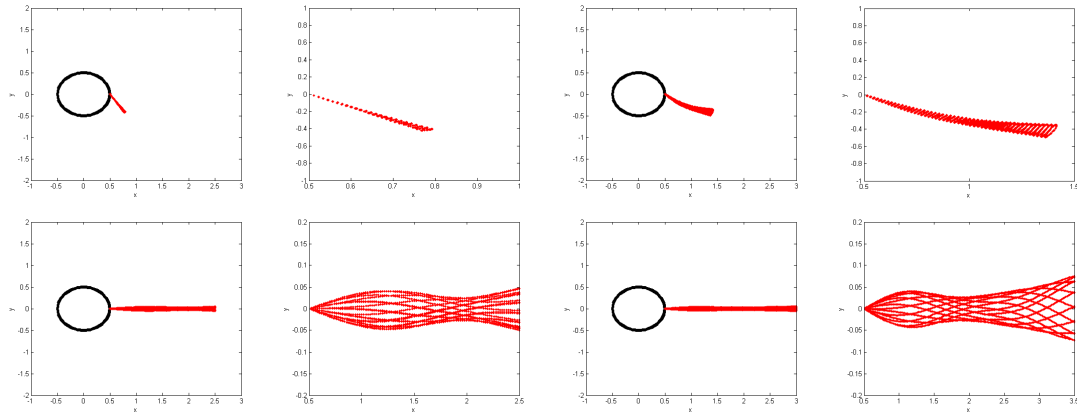
Figure 3: Ranges of motion of the filament attached on the cylinder under various length ($\rho_s = 1, kb = 0.01$).
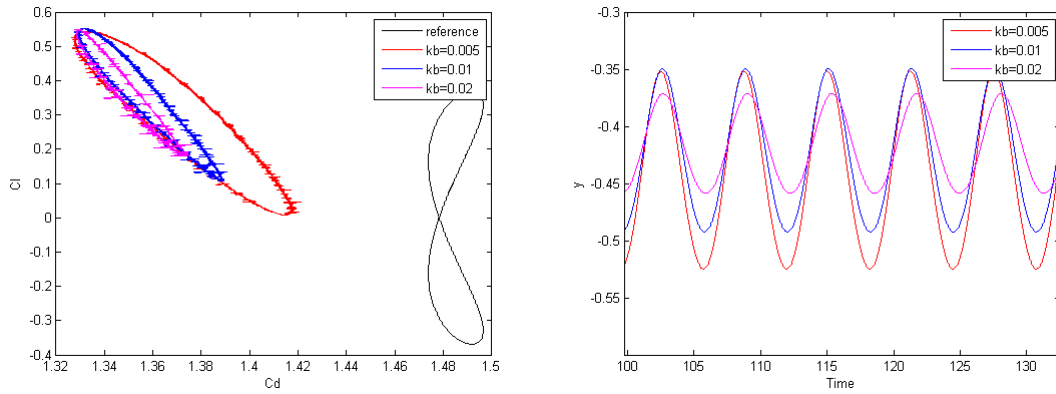
Figure 4: Effect of bending stiffness on the force and tail displacement of the cylinder-filament system.
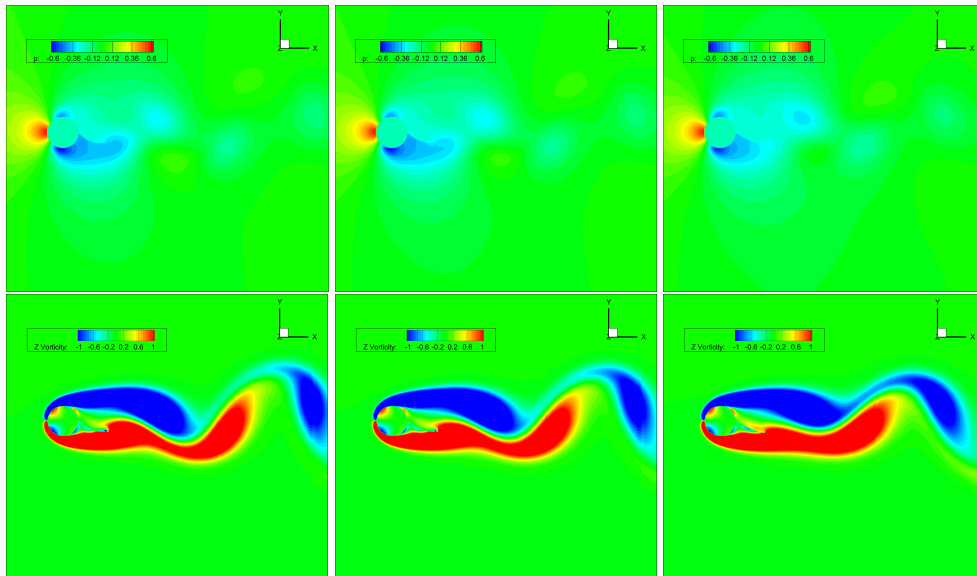
Figure 5: Effect of bending stiffness on the flow pattern of the cylinder-filament system. Left Column: $kb = 0.0005$, **Middle Column:** $kb = 0.001$, **Right Column:** $kb = 0.002$. **Top row: pressure contour, bottom row: vorticity contour.**

Acknowledgments

References

[1] C. H. K. Williamson and R. Govardhan, "Vortex-induced vibrations," *Annu. Rev. Fluid Mech.*, vol. 36, pp. 413–455, 2004.

[2] G. R. S. Assi, P. W. Bearman, and N. Kitney, "Low drag solutions for suppressing vortex-induced vibration of circular cylinders," *Journal of Fluids and Structures*, vol. 25, no. 4, pp. 666–675, 2009.

[3] Y. Bao and J. Tao, "The passive control of wake flow behind a circular cylinder by parallel dual plates," *Journal of Fluids and Structures*, vol. 37, pp. 201–219, 2013.

[4] S. Dong, G. S. Triantafyllou, and G. E. Karniadakis, "Elimination of vortex streets in bluff-body flows," *Physical review letters*, vol. 100, no. 20, p. 204501, 2008.

[5] W. Chen, D. Xin, F. Xu, H. Li, J. Ou, and H. Hu, "Suppression of vortex-induced vibration of a circular cylinder using suction-based flow control," *Journal of Fluids and Structures*, vol. 42, pp. 25–39, 2013.

[6] H. Baek and G. E. Karniadakis, "Suppressing vortex-induced vibrations via passive means," *Journal of Fluids and Structures*, vol. 25, no. 5, pp. 848–866, 2009.

[7] J. P. Pontaza and R. G. Menon, "Numerical simulations of flow past an aspirated fairing with three degree-of-freedom motion," in *ASME 2008 27th International Conference on Offshore Mechanics and Arctic Engineering*. American Society of Mechanical Engineers, 2008, pp. 799–807.

[8] D. Corson, S. Cosgrove, and Y. Constantinides, "Application of CFD to predict the hydrodynamic performance of offshore fairing designs," in *ASME 2014 33rd International Conference on Ocean, Offshore and Arctic Engineering*. American Society of Mechanical Engineers, 2014, pp. V002T08A079–V002T08A079.

[9] D. W. Allen, D. L. Henning, J. H. Haws, D. W. McMillan, and R. B. McDaniel, "Partial helical strake for vortex-induced-vibrationsuppression," May 13 2003, uS Patent 6,561,734.

[10] A. D. Trim, H. Braaten, H. Lie, and M. A. Tognarelli, "Experimental investigation of vortex-induced vibration of long marine risers," *Journal of fluids and structures*, vol. 21, no. 3, pp. 335–361, 2005.

[11] J. C. Owen, P. W. Bearman, and A. A. Szewczyk, "Passive control of VIV with drag reduction," *Journal of Fluids and Structures*, vol. 15, no. 3, pp. 597–605, 2001.

[12] J. Wu, Y. Qiu, C. Shu, and N. Zhao, "Flow control of a circular cylinder by using an attached flexible filament," *Physics of Fluids*, vol. 26, no. 10, p. 103601, 2014.

[13] F. Xie, Y. Yu, Y. Constantinides, M. S. Triantafyllou, and G. E. Karniadakis, "U-shaped fairings suppress vortex-induced vibrations for cylinders in cross-flow," *Journal of Fluid Mechanics*, vol. 782, pp. 300–332, 2015.

[14] J. Favier, A. Dauptain, D. Basso, and A. Bottaro, "Passive separation control using a self-adaptive hairy coating," *Journal of Fluid Mechanics*, vol. 627, pp. 451–483, 2009.

A NUMERICAL FRAMEWORK FOR SOLIDIFICATION AND RESIDUAL STRESS MODELLING IN METALLURGICAL APPLICATIONS

HRVOJE JASAK[1], SEBASTIAN, KOHLSTAEDT[2,3], MICHAEL VYNNYCKY[3]

[1]*Wikki Ltd, London, United Kingdom, h.jasak@wikki.co.uk*

[2]*, Volkswagen AG, Kassel, Germany, sebastian.kohlstaedt@volkswagen.de*

[3]*, KTH Royal Institute of Technology, Stockholm, Sweden, michaelv@kth.se*

Quality of foundry products depends on the control of the solidification process; if the phase change is not managed correctly, residual stresses and material shrinkage shall result in loss of product quality. Physical modelling of solidification is particularly challenging: it requires a unified fluid-solid model capable of simulating fluid flow, heat transfer, solidification phase change as well as solid mechanics aspects of the resulting material.

We shall present a physical model capable of following the progress of the melt from injection/pouring of the molten phase into a batch or a continuous casting system and resolving heat transfer, flow of the fluid component, phase change and accumulation of residual stresses in the solid. The model is implemented in OpenFOAM and used to simulate transient 3-D casting process. Such a model is capable of predicting shrinkage and solidification effects and can be used in optimisation of casting systems, mould pressurisation and heat transfer management in foundry applications.

The model is currently validated on fluid and solid mechanics cases and basic fluid-solid interaction with a fixed phase interface.

Introduction

This paper describes a framework for modelling of solidification and residual stress distribution in metallurgical applications. The challenge in the process is in the assembly of a unified model covering both the fluid and solid phase with sufficient fidelity to capture the thermal front and the stress state at the point of solidification, which is the main source of residual stresses, volumetric imperfections and other quality-degrading features of the cast.

The challenge in solidification modelling is its "atypical" model of Fluid-Solid Interaction (FSI), where it is necessary to deploy a single equation set covering the whole process and the complete domain. In essence, this is trivial: conservation laws for mass, momentum and energy readily serve this purpose. However, the problem lies in the chosen constitutive law which needs to cover both the fluid and solid phase. In solids, material accumulates stress with the gradient of displacement, while in fluids the stress is results from the velocity gradient. In consequence, the natural choice of a working variable in solids is displacement or displacement increment and the stress tensor (when accounting for material or geometrical non-linearity), while in fluids the working variable is regularly the velocity $\mathbf{u}$ and pressure p.

The primary objective of this study is the simulation of cast shrinkage and residual stresses. To achieve this, it is necessary to follow the development of stress history from the point of solidification to final state, accounting for thermal stresses in the solid and temperature-dependent material properties. In solidification, a *mushy region* is assumed, with material properties of the solid shell and liquid melt dependent on temperature, and the progress of solidification is followed by a liquid fraction variable.

In what follows, we shall present the choice of appropriate working variable, conservation laws and constitutive relations covering the full range of solidification physics. The new model is validated on canonical cases of solid mechanics, fluid flow and conventional fixed interface fluid-solid interaction, in preparation for solidification studies.

Model Formulation: Solid Phase

A trivial solid mechanics model is a linear elastic model with constant material properties and displacement $\mathbf{d}$ as the working variable [1]. This, however, is not applicable to solidification, due to the presence of material non-linearity (temperature and solidification-dependent material properties) and geometric non-linearity (large deformations and rotations). Thus, the stress model formulation used in this study is the Large Deformation Stress Model in the incremental form, with the displacement increment $\delta\mathbf{d}$ chosen as a working variable [2]. The model is formulated as follows.

Non-Linear Stress Model

The choice of the solid phase model is driven by the need to account for all non-linearities in the system and at the same time align the formulation with the fluid flow model. In fluids, the choice of working variables is naturally the $(p, \mathbf{u})$ pair and we shall aim to achieve the same.

Second Piola-Kirchoff stress tensor increment $\delta\mathbf{\Sigma}$ is defined as:

$$\delta\mathbf{\Sigma} = 2\mu_s\delta\mathbf{E} + \lambda\,tr(\delta\mathbf{E})\mathbf{I}, \tag{1}$$

where μ_s and λ are the Lamé's coefficients, defined in terms of the material modulus of elasticity E and is the Poisson's ratio ν.

Green-Lagrangian strain tensor increment $\delta\mathbf{E}$ is defined as:

$$\delta\mathbf{E} = \frac{1}{2}\left[\nabla\delta\mathbf{d} + (\nabla\delta\mathbf{d})^T + \nabla\delta\mathbf{d}{\scriptstyle\bullet}(\nabla\mathbf{d})^T + \nabla\mathbf{d}{\scriptstyle\bullet}(\nabla\delta\mathbf{d})^T + \nabla\delta\mathbf{d}{\scriptstyle\bullet}(\nabla\delta\mathbf{d})^T\right]. \tag{2}$$

In preparation to the model combination, introducing $\delta\mathbf{d} = \mathbf{u}\,\Delta t$ and writing $\delta\mathbf{\Sigma}$ the stress model can be rewritten in terms of $\mathbf{u}$, yielding the final form of the Green-Lagrangian strain tensor increment:

$$\begin{aligned}\delta\mathbf{\Sigma} = \mu_s\,\Delta t\left[\nabla\mathbf{u} + (\nabla\mathbf{u})^T + \nabla\mathbf{u}{\scriptstyle\bullet}(\nabla\mathbf{d})^T + \nabla\mathbf{d}{\scriptstyle\bullet}(\nabla\mathbf{u})^T + \Delta t\left(\nabla\mathbf{u}{\scriptstyle\bullet}(\nabla\mathbf{u})^T\right)\right]\\ + \lambda\,\Delta t\,tr\left[\nabla\mathbf{u} + (\nabla\mathbf{u})^T + \nabla\mathbf{u}{\scriptstyle\bullet}(\nabla\mathbf{d})^T + \nabla\mathbf{d}{\scriptstyle\bullet}(\nabla\mathbf{u})^T + \Delta t\left(\nabla\mathbf{u}{\scriptstyle\bullet}(\nabla\mathbf{u})^T\right)\right]\mathbf{I}.\end{aligned} \tag{3}$$

Integration formulas for displacement, strain and stress are used to accumulate the solid stress as a function of displacement (increment) and read:

$$\mathbf{d} = \mathbf{d}_0 + \int_0^t \mathbf{u}\,dt \approx \mathbf{d}_{old} + \mathbf{u}\Delta t \approx \mathbf{d}_{old} + \frac{1}{2}(\mathbf{u}_{old} + \mathbf{u})\Delta t, \tag{4}$$

$$\mathbf{E} = \mathbf{E}_0 + \int_0^t \delta\mathbf{E}, \tag{5}$$

$$\mathbf{\Sigma} = \mathbf{\Sigma}_0 + \int_0^t \delta\mathbf{\Sigma}, \tag{6}$$

where $\mathbf{d}_0$, $\mathbf{E}_0$ and $\mathbf{\Sigma}_0$ represent the initial displacement, strain and stress. At each time instance, the Cauchy stress $\boldsymbol{\sigma}$ can be recovered as:

$$\boldsymbol{\sigma} = \frac{1}{det(\mathbf{F})}\,\mathbf{F}{\scriptstyle\bullet}\mathbf{\Sigma}{\scriptstyle\bullet}\mathbf{F}^T, \tag{7}$$

where $\mathbf{F}$ is the deformation gradient tensor

$$\mathbf{F} = \mathbf{I} + (\nabla\mathbf{d})^T. \tag{8}$$

Linear momentum conservation law in the total Lagrangian formulation reads:

$$\int_{V_0} \rho_0 \frac{\partial\mathbf{u}}{\partial t}\,dV_0 = \oint_{S_0} \mathbf{n}_0{\scriptstyle\bullet}(\mathbf{\Sigma}{\scriptstyle\bullet}\mathbf{F}^T)\,dS_0 + \int_{V_0} \rho_0\mathbf{f}_b\,dV_0, \tag{9}$$

where V_0, S_0, $\mathbf{n}_0$ represent the initial configuration of the system. This is remarkably similar to the fluid formulation of the momentum equation, barring the absence of the pressure gradient term.

The standard stress formulation of the above equation uses the $\mathbf{I}$ part of the $\mathbf{F}$ tensor to create the implicit terms and treats the rest as an explicit correction, accounting for model non-linearities.

Papadakis Solid Pressure Term Formulation

The non-linear solid stress model suffers from a particular failure mode, where the Poisson's ratio ν reaches the value of 0.5: the second Lamé coefficient λ tends to infinity.

$$\lambda = \frac{E}{3(1-2\nu)};\ \ \nu = 0.5 \to \lambda \to \infty, \tag{10}$$

While $\nu = 0.5$ may be unrealistic for solids, in fluids it describes the state of incompressibility and the model failure for $\nu = 0.5$ must be circumvented. Note that realistic solids are never considered incompressible, meaning that λ remains bounded.

The following pressure manipulation is introduced by Papadakis into the $\nabla{\scriptstyle\bullet}[\Delta t\,\lambda tr(\nabla\mathbf{u})]$ term in Equation 3, recognising that the pressure p is related to the trace of the stress tensor and divergence of the velocity field $\nabla{\scriptstyle\bullet}\mathbf{u}$.

Introduction of the solid pressure term in the non-linear model yields a solid continuity equation, with the bulk modulus K:

$$K = \rho\frac{\partial p}{\partial\rho} = \frac{2}{3}\mu_s + \lambda = \frac{E}{3(1-2\nu)}, \tag{11}$$

defining the pressure (in the solid region!) as:

$$p = -\frac{1}{3} tr(\boldsymbol{\sigma}) = -K \nabla_\bullet \mathbf{d} \tag{12}$$

and yielding the final form of the linear stress equation

$$\boldsymbol{\sigma} = -\left(p + \frac{2}{3} \mu_s \nabla_\bullet \mathbf{d} \right) \mathbf{I} + \mu_s \left[\nabla \mathbf{d} + (\nabla \mathbf{d})^T \right] \tag{13}$$

The continuity equation is manipulated in terms of velocity $\mathbf{u}$. For a linear elastic material, the equation set reads:

$$\mathbf{u} = \frac{\partial \mathbf{d}}{\partial t}, \tag{14}$$

$$\frac{\partial(\rho\mathbf{u})}{\partial t} + \nabla_\bullet(\rho\mathbf{u}\mathbf{u}) - \nabla_\bullet\mu_s \left[\nabla \mathbf{d} + (\nabla \mathbf{d})^T \right] = -\left(1 + \frac{\mu_s}{3\,K} \right) \nabla p, \tag{15}$$

$$\nabla_\bullet(\rho\mathbf{u}) = -\frac{\rho}{K}\frac{\partial p}{\partial t}. \tag{16}$$

For the non-linear material, the starting form is somewhat more complex (Equation 9); manipulation of the divergence term reads:

$$\Delta t\, \lambda tr(\nabla \mathbf{u}) = -\Delta t \left(p + \frac{2}{3} \mu_s \nabla_\bullet \mathbf{u} \right), \tag{17}$$

whereas the solid continuity equation preserves the same form as in the linear case. With the above modification, the system is ready for the use in a blended solid-fluid model, using the $(p, \mathbf{u})$ as the primitive variables.

Thermal Stress Model

Curiously, within the same framework, thermal stresses can be handled in a straightforward manner. In linear elasticity, thermally induced stress is:

$$\boldsymbol{\sigma}_T = 3\,K\alpha_E(T - T_0)\mathbf{I}, \tag{18}$$

where α_E is the thermal expansion coefficient and T_0 the reference temperature. This is clearly inconvenient for the formulation of displacement increment. As the spherical stress is extracted into the solid pressure, thermal stress can be accounted for as a change-of-volume term:

$$\frac{\rho}{K}\frac{\partial p}{\partial t} + \nabla_\bullet(\rho\mathbf{u}) = 3\alpha_E\,\frac{\partial T}{\partial t}. \tag{19}$$

This is physically consistent and numerically convenient: any alternative formulation does not satisfy the integral volume increase in the solid. Physically, the *r.h.s.* of Equation 19 accounts for the volumetric expansion of a heated solid, as a part of the solid continuity equation.

Model Formulation: Fluid Phase

Fluid equations can assume the easiest form of the incompressible laminar flow with buoyancy effects, using the decomposition of the pressure into the dynamic and quasi-hydrostatic component [3]:

$$p_d = p - \rho\,\mathbf{g}_\bullet\mathbf{x}, \tag{20}$$

where ρ is the density, $\mathbf{g}$ is the gravitational acceleration and $\mathbf{x}$ is the position vector, yielding a reformulated balanced momentum source term:

$$-\nabla p + \rho\mathbf{g} = -\nabla p_d - (\mathbf{g}_\bullet\mathbf{x})\nabla\rho, \tag{21}$$

The final form of the fluid phase equation set reads:

$$\nabla_\bullet(\rho\mathbf{u}) = 0 \tag{22}$$

$$\frac{\partial(\rho\mathbf{u})}{\partial t} + \nabla_\bullet(\rho\mathbf{u}\mathbf{u}) - \nabla_\bullet(\mu\nabla\mathbf{u}) = -\nabla p_d + \mathbf{g}_\bullet\mathbf{x}\nabla\rho \tag{23}$$

Model Formulation: Unified Non-Linear FSI Model

Formulation of the solid and fluid models are now well aligned. The total Lagrangian formulation in the incremental approach used the pressure p and velocity $\mathbf{u}$ as the base variable and match perfectly with the fluid model both in working variables and model layout. Therefore, conventional "fluids solution techniques" should be applicable to both.

As the working variables match perfectly between the solid model (Equation 16, Equation 9) and the fluid model (Equation 22, Equation 23), it remains to derive the combined model. Blending is performed using the liquid fraction variable α, combining governing equations for the fluid and the solid phase. The fluid model is recovered for $\alpha = 1$, while the other extreme of $\alpha = 0$ indicates solid behaviour. Presence of a mushy region is indicated by $0 \leq \alpha \leq 1$, assuming a linear combination of the two.

Some Validation Cases

In the first instance, the combined model shall be tested for "pure" fluid flow and solid mechanics. As the formulation and solution algorithm originates from the fluids, the flow validation cases are omitted. For solid mechanics, basic tests have been performed for: linear and non-linear elasticity and linear thermo-elasticity for cases with analytical solutions. In parametric studies of mesh refinement, time-step size and discretisation settings, the model performs perfectly across all cases, with examples of thermal expansion of a heated solid shown in Figure 1.

Conventional fluid-solid interaction cases can also be modelled without difficulty. In such cases, there exists a step change in the fluid fraction indicator α, delimiting the boundary between the fluid and solid. Examples of a travelling pressure wave in an elastic pipe and a fluid jet hitting an elastic membrane are shown in Figure 2.
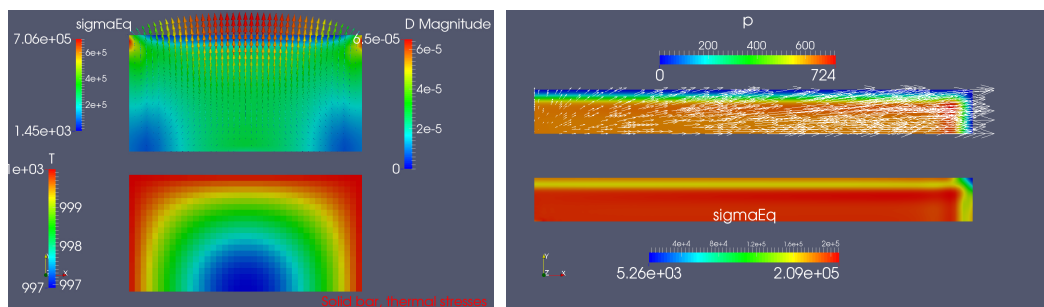
Figure 1: Combined FSI model for cases of thermal expansion of a solid brick and bar.
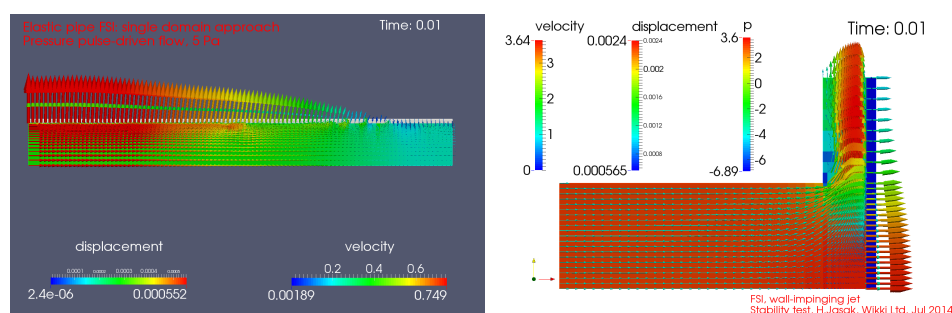
Figure 2: Conventional FSI cases: wave propagation in an elastic pipe and a jet impacting an elastic membrane.

The model can now be considered ready for solidification applications, with extensive validation and verification still in progress.

Conclusion and Future Work

This paper describes a combined model for fluid-solid interaction cases in the unified modelling approach, with the pressure p and velocity $\mathbf{u}$ chosen as the working set of variables. The solid model accounts for material and geometric non-linearities, include the novel handling of thermal stresses and is formulated in terms of the momentum and continuity equation to avoid the Lamé coefficient singularity at Poisson's ratio of $\nu = 0.5$. The fluid model is a conventional single-phase transient laminar non-Newtonian flow model.

The blended fluid-solid model uses a fluid fraction variable α to indicate the phase state and is capable of modelling the mushy zone solidification. At this stage the combined model is validated in the cases of pure fluid flow, various cases of linear and non-linear thermo-elasticity and simple fluid-solid interaction. The work towards a validated and verified solidification model continues and will be reported in further publications.

References

[1] H. Jasak and H. Weller, "Application of the finite volume method and unstructured meshes to linear elasticity," *Int. J. Num. Meth. Engineering*, vol. 48, no. 2, pp. 267–287, 2000.

[2] P. Cardiff, Ž. Tuković, P. D. Jaeger, M. Clancy, and A. Ivanković, "A Lagrangian cell-centred finite volume method for metal forming simulation," *International Journal for Numerical Methods in Engineering*, vol. 109, no. 13, pp. 1777–1803, Sep 2016. [Online]. Available: https://doi.org/10.1002/nme.5345

[3] H. Jasak, "CFD Analysis in Subsea and Marine Technology," in *IOP Conference Series: Materials Science and Engineering*, vol. 276, 2017. [Online]. Available: www.scopus.com

NUMERICAL STUDY OF VORTEX-INDUCED MOTIONS OF A BUOYANCY CAN IN CURRENTS

XIE KANGDI [1], ZHAO WEIWEN [2], WAN DECHENG [3]

[1,2,3]Collaborative Innovation Center for Advanced Ship and Deep-Sea Exploration, State Key Laboratory of Ocean Engineering, School of Naval Architecture, Ocean and Civil Engineering, Shanghai Jiao Tong University, Shanghai 201306, China [3]Corresponding Author: dcwan@sjtu.edu.cn

Keywords: *Buoyancy can, DDES, overset grid, vortex-induced motions.*

Buoyancy cans in typical cylindrical shape are widely applied in deep-water fields to tension a riser and keep it vertical[1]. Flow over a buoyancy can induces an alternating vortex shedding, which leads to the surge, sway and yaw motions. Recent studies concentrate on the motion characteristics of Spar platforms and semi-submersible platforms, while few researchers push forward the investigation into the VIM (vortex-induced motion) phenomenon especially the yaw motion of the typical cylindrical object. Therefore, the buoyancy can in typical cylindrical shape is a suitable object to reveal the mechanism of VIM phenomenon.

Numerical simulation is an effective method to investigate the VIM issues, and numerical tests have fit well with the experimental results in vortex-induced motion of the platform. Etienne and Fontaine [2] conducted a 2D (two-dimensional) numerical simulation to study the motion trajectory of the cylinder after releasing the rotational degree of freedom. Minguez et al. [3, 4] presented a slender buoyancy can flow-induced response at high Reynolds number and 2D CFD (computational fluid dynamic) model is built to investigate the yaw responses of the buoyancy can.

The aim of this paper is to present 3D CFD model to analyse the FIR (flow-induced response) especially the yaw motion of a buoyancy can and illustrate the relationship between the yaw motion and the motion in the inline and cross flow directions. Furthermore, the influence level of release in the degree of rotation is also illustrated in this paper.

In this paper, a DDES (delayed detached-eddy simulation) method based on the SST (shear-stress transport) model is used to simulate the turbulence detached flow during a large range of high Reynolds numbers [5]. SST-DDES is a hybrid RANS (Reynolds-Averaged Navier-Stokes)-LES (large eddy simulation) method. It utilizes sub-grid scale model to handle the flow in the free shear flow area far away from wall, and employs RANS's SST model to solve the flow in the boundary layer near wall and other areas. This can guarantee the accuracy of LES solution, and reduce the amount of calculation in the near-wall region of the boundary layer. For incompressible viscous fluids, the continuity equation and momentum equation can be expressed as:

$$\frac{\partial \overline{u}_i}{\partial x_i} = 0 \tag{1}$$

$$\frac{\partial \overline{u}_i}{\partial t} + \frac{\partial \overline{u}_j \overline{u}_i}{\partial x_j} = \frac{\partial \overline{P}}{\partial x_i} + \frac{\partial}{\partial x_j}\left[v\left(\frac{\partial \overline{u}_i}{\partial x_j} + \frac{\partial \overline{u}_j}{\partial x_i} \right) \right] - \frac{\partial \tau_{ij}}{\partial x_j} \tag{2}$$

where, v is the molecular viscosity, τ_{ij} is the Reynolds stress or sub-grid stress tensor. According to the Boussinesq hypothesis, τ_{ij} can be expressed as:

$$\tau_{ij} = \frac{2}{3}\delta_{ij}k - v_t\left(\frac{\partial \overline{u}_i}{\partial x_j} + \frac{\partial \overline{u}_j}{\partial x_i} \right) \tag{3}$$

SST-DDES turbulence model assumes that the turbulent viscosity v_t can be expressed as a function of turbulent kinetic energy k, turbulence dissipation rate ω and velocity strain S [6]:

$$v_t = \frac{a_1 k}{\max(a_1 \omega, SF_2)} \tag{4}$$

where, k and ω can be obtained by solving the corresponding transport equation:

$$\frac{\partial k}{\partial t} + \frac{\partial (u_j k)}{\partial x_j} = \tilde{G} - \frac{k^{\frac{2}{3}}}{l_{DDES}} + \frac{\partial}{\partial x_j}\left[(v + \alpha_k v_t)\frac{\partial k}{\partial x_j} \right] \tag{5}$$

$$\frac{\partial \omega}{\partial t} + \frac{\partial (u_j \omega)}{\partial x_j} = \gamma S^2 - \beta \omega^2 + \frac{\partial}{\partial x_j}\left[(v + \alpha_\omega v_t)\frac{\partial \omega}{\partial x_j} \right] - (1 - F_1)CD_{k\omega} \tag{6}$$

The l_{DDES} in Eq. (5) is the mixed length, which is the switch that controls the transformation between LES and RANS model [5].

The computational model in this paper is the model in the towing experiment delivered by KANG et al. [7] The model of the buoyancy can is in typical cylindrical shape and detail parameters of the buoyancy can are shown in Table 1.

As shown in Fig. 1, the overall buoyancy can is underwater regardless of the free surface issue. The buoyancy can is connected with a mooring line at the centre of the bottom of the model, fairlead point. And the anchor point is outside the computational domain.
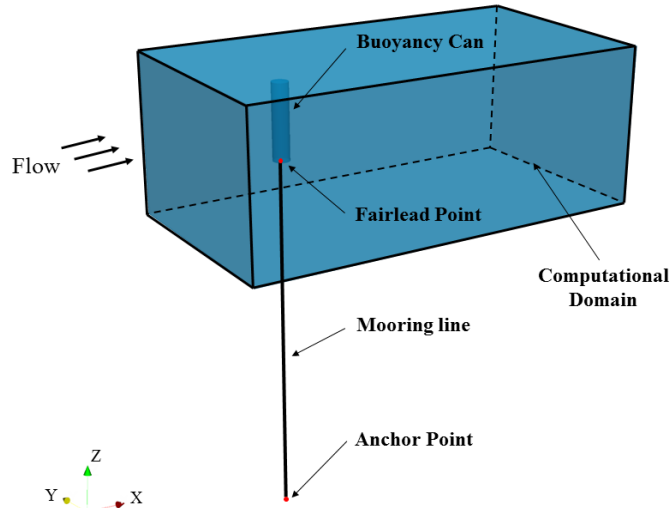
Figure 1: Schematic diagram of computational model

Table 1: Parameters of the buoyancy can

Parameter	Unit	Value
Outer diameter (D)	mm	150
Length (L)	mm	700
Displacement (△)	Kg	12.37
Weight (w)	Kg	4.24

Since the overset grid is applied in the cases, there are two kinds of mesh, one is cylinder grid, the other is background grid. Both grids are structured grid and the vicinity of the cylinder is locally refined as Fig. 3a shows. In cylinder grid region, the grid size near the wall is set to be small to obtain more accurate flow separation and y+ is about 5. And the grid number of background grid region is 0.71 million, while that of cylinder grid region is 1.62 million. Fig. 3b shows the local mesh distribution of cylinder at the z = 0 section. The boundary conditions of the computational domain are set as follow: free stream velocity for inlet, pressure equals zero for outlet, symmetry for top, slip for other side patches.
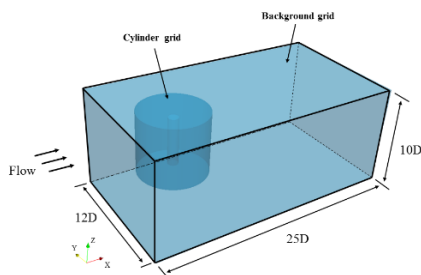
Fig. 2 Computational domain
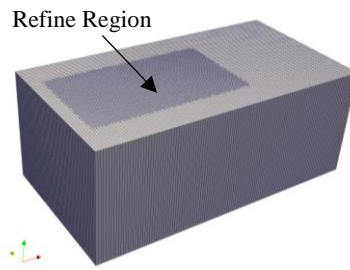
Fig.3 Overall computational mesh
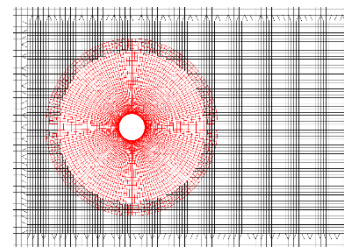
Fig.4 Local mesh

In free decay test case, the buoyancy can under no incoming flow is given an initial velocity and released to get the natural period of the mooring system. Since the consecutive VIM numerical tests are under the condition that the length of mooring line is 2.672 m, the numerical free decay test keeps the same length of the mooring line. After the Fourier transform, it shows that the CFD result fits well with the KANG et al.'s [6] experimental result as Fig. 5 presents:
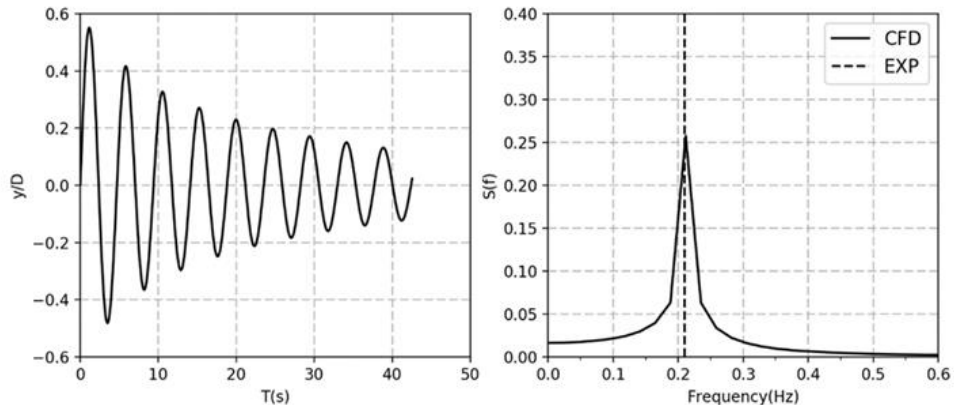
Fig. 5 Tether length L = 2.672 m free decay result

With the increase of reduced velocity, the average surge displacement and surge and sway frequency of the buoyancy can are increased significantly. In general, when the vortex shedding is stable, the motion trajectory becomes regular in "8" shape. The internal mechanism of the special shape is that the surge frequency is twice of the sway frequency just as Fig. 6 presents.
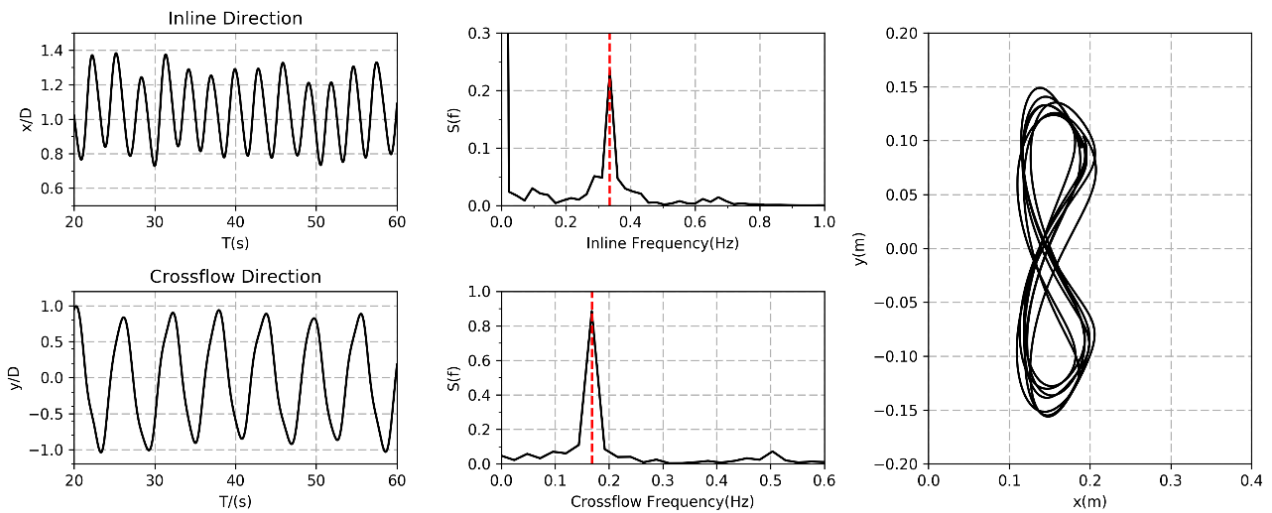
Fig. 6 Time-Displacement profile & Fourier transform profile & Motion trajectory ($U_r = 6$)

In this paper, this numerical method can obviously capture the rotation phenomenon of the buoyancy can in the uniform flow as Fig. 7 presents.
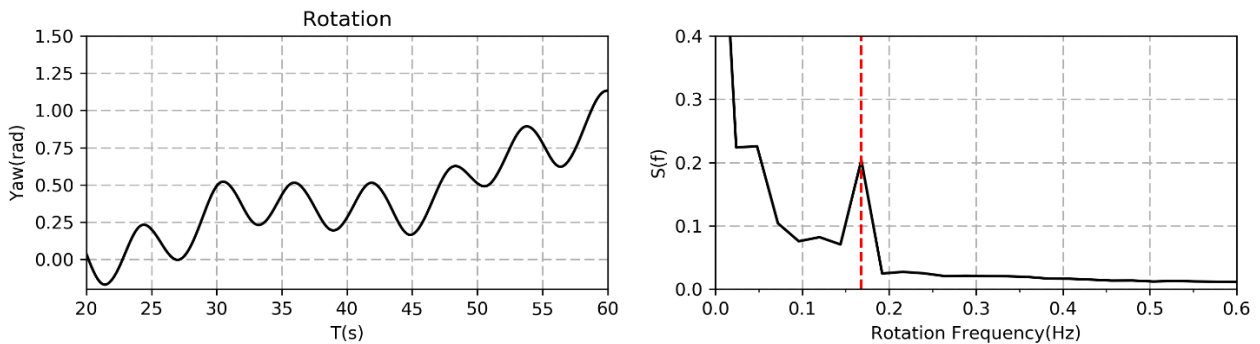
Fig. 7 Time-rotation profile & Fourier transform profile ($U_r = 6$)

According to Table 2, same as surge and sway frequency, the yaw frequency increases with the increase of reduced velocity. Secondly, yaw frequency is equal to the sway frequency, which is consistent with KANG et al.'s [6] experimental result. The reason for this circumstance is that the sway motion and yaw motion are both caused by the vortex shedding. It can infer that the sway motion and yaw motion share the same exciting force component.

Table 2: Surge frequency, sway frequency and yaw frequency

Reduced velocity (U_r)	Surge frequency/Hz	Sway frequency/Hz	Yaw frequency/Hz
4	0.303	0.151	-
6	0.336	0.168	0.168
7	0.376	0.182	0.182
8	0.428	0.214	0.214
10	0.498	0.249	0.249

Acknowledgements

References

[1] Karunakaran, D., Lee, D., and Mair, J. 2009. Qualification of the Grouped SLOR Riser System. In Proceedings of the Offshore Technology Conference, 4-7.

[2] Etienne, S., and Fontaine, E. 2010. Effect of Rotational Degree of Freedom on Vortex-Induced Vibrations of a Circular Cylinder in Cross-Flow. In Proceedings of the 20th International Offshore and Polar Engineering Conference, 20-5.

[3] Minguez, M., Luppi, A., and Berger, A. 2012. Slender Buoy FSHR Vortex Induced Rotations. In Proceedings of the ASME 31st International Conference on Ocean, Offshore and Arctic Engineering, 713-22.

[4] Minguez, M., Luppi, A., Pattedoie, S., and Maloberti, R. 2011. Slender Buoy VIM and VIR Analysis by CFD/FSI Approach. In Proceedings of the ASME 30th International Conference on Ocean, Offshore and Arctic Engineering, 1-9.

[5] ZHAO, W. W., and WAN, D. C. 2016. Detached-Eddy Simulation of Flow past Tandem Cylinders. Applied Mathematics and Mechanics 37 (12): 1272-81.

[6] Menter, F. R., Kuntz, M., and Langtry, R. 2003. Ten Years of Industrial Experience with the SST Turbulence Model. In Proceedings of the 4th International Symposium on Turbulence Heat and Mass Transfer, 625-32.

[7] KANG, Z., NI, W. C., MA, G., and XU, X. 2017. A Model Test Investigation on Vortex-Induced Motions of a Buoyancy Can. Marine Structures 53: 86-104.

DEVELOPMENT OF AN ARBITRARY LAGRANGIAN-EULERIAN FINITE VOLUME METHOD FOR METAL FORMING SIMULATION IN OPENFOAM

PHILIP CARDIFF[1], ŽELJKO TUKOVIĆ[2], ALOJZ IVANKOVIĆ[1], PETER DE JAEGER[1,3]

[1]*University College Dublin, School of Mechanical and Materials Engineering, Ireland, philip.cardiff@ucd.ie*
[2]*University of Zagreb, Faculty of Mechanical Engineering and Naval Architecture, Croatia*
[3]*NV Bekaert SA, Belgium*

Introduction

Modelling of metal forming pr

- Eulerian approach;

- Lagrangian approach;

- Arbitrary Lagrangian-Eu

As indicated schematically in Figu   t; whereas, the
Lagrangian approach follows materi   agrangian Eulerian
(ALE), is a hybrid method that attempt   ian methods, where the

(c) Arbitrary
Lagrangian-
Eulerian
formulation
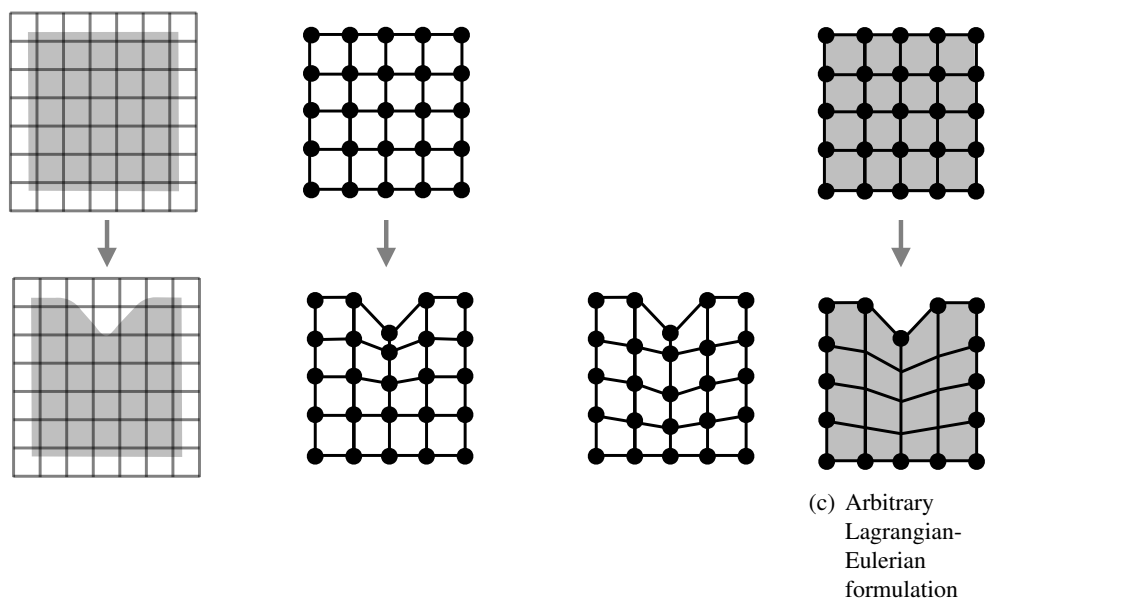
Figure 1: Approaches to describe the initial and deformed configurations (adapted from [1])

The current project builds on the previous developments of Lagrangian finite volume methods for solid mechanics [1, 2, 3, 4, 5] to propose an ALE approach suitable for metal forming problems.

Methodology

There are a number of variants of ALE methods; the approach adopted in the current work is a two step procedure:

1. an updated Lagrangian solution step,

2. followed by a mesh smoothing and field mapping step.

Updated Lagrangian solution step:

In the first step, an updated Lagrangian formulation is used to solve the governing momentum equation for the displacement field, as described recently [1]: this step provides the displacement/velocity of the deforming material, and as a Lagrangian step it also provides the motion of the mesh. To complete the updated Lagrangian step, the mesh is moved to the deformed configuration using the material displacement/velocity field.

Mesh smoothing and field remapping step:

In the second step, a mesh smoothing and field mapping procedure is applied to improve the overall mesh quality. A number of different mesh smoothing methods have been examined, including: (i) explicit point-based Laplacian smoothing with arithmetic-average weights (see Figure 2(b)); (ii) explicit point-based Laplacian smoothing with cell-volume weights (see Figure 2(c)); and (iii) implicit cell-based Laplacian smoothing method with cell-volume weights.

| (a) Mesh before smoothing | (b) Mesh after smoothing (arithmetic-average weights) | (c) Mesh after smoothing (cell-volume weights |
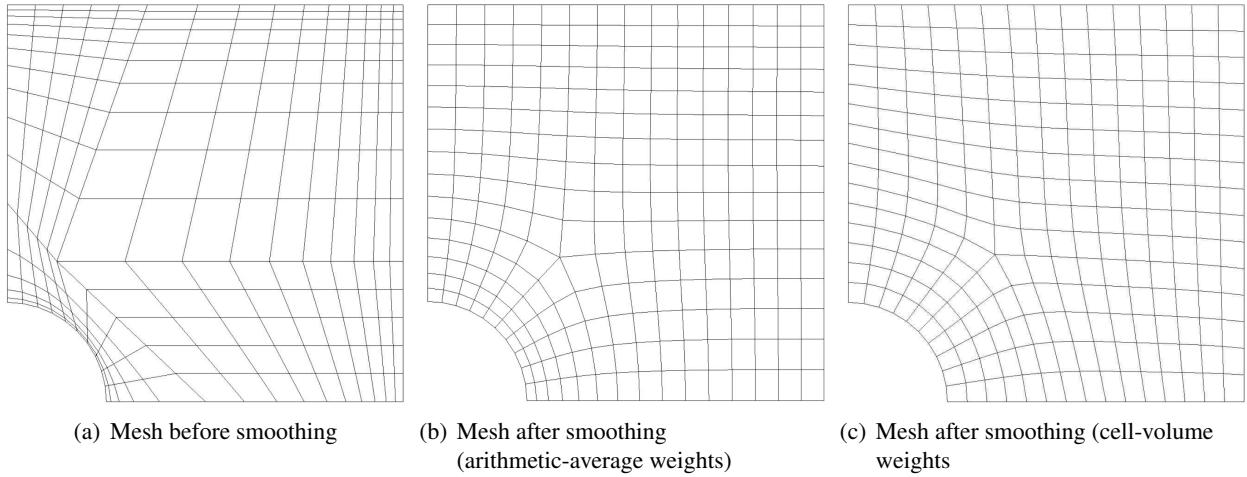
Figure 2: Point-based Laplacian smoothing method, comparing weight calculation method. The initial mesh is purposely distorted to examine the robustnesses of the mesh smoothing procedures.

Following mesh smoothing, the fields must be mapped to the new smoothed mesh. This field mapping can be performed in at least two ways: (a) interpolation from the initial mesh to the smoothed mesh; or (b) transport the fields using an advection equation approach. Both methods are considered here; however, the interpolation method is found to be much more expensive and difficult to efficiently parallelise. Consequently, focus is given here to the advection method. The advection mapping approach solves a conservation advection equation for each field to be mapped:

$$\frac{\partial \psi}{\partial t} + \boldsymbol{\nabla} \cdot \phi_{\mathrm{m}} \psi = 0 \tag{1}$$

where ψ represents the scalar/vector/tensor intrinsic field to be mapped, and ϕ_{m} is the mesh flux/velocity. By limiting the mesh motion to a fraction of the local cell size (*i.e.* a mesh Courant number less than unity), Equation 1 can be solved in an efficient explicit manner. The equation is discretised using the standard finite volume method, as implemented in OpenFOAM, where the temporal term employs a 1st order Euler method and the advection term interpolation is performed using a 2nd order van Leer scheme with Monotone Upstream-centered Schemes for Conservation Laws (MUSCL) limiter; the explicit update of a field cell value reduces to:

$$\psi^{[i+1]} = \frac{1}{\Omega^{[i+1]}} \left[\Omega^{[i]} \psi^{[i]} + \sum_f^{\mathrm{nfaces}} (\Delta \Omega)_f \; \psi_f^{[i]} \right] \tag{2}$$

where $\psi^{[i]}$ is the cell field value before smoothing, $\psi^{[i+1]}$ is the cell field value after smoothing, $\Omega^{[i]}$ is the cell volume before smoothing, $\Omega^{[i+1]}$ is the cell volume after smoothing, f represents a cell face, nfaces is the number of faces in the cell, $(\Delta \Omega)_f$ is the volume swept by face f, and $\psi_f^{[i]}$ is the value of the field at face f before smoothing.

Following details of the solution algorithm, mesh smoothing and field mapping, a number of steel wire metal forming test cases will be presented, and the new ALE method compared with a traditional fully Lagrangian approach.

Acknowledgments

Irish Centre for High-End Computing (ICHEC) for the provision of computational facilities and support.

References

[1] P. Cardiff, Ž. Tuković, P. D. Jaeger, M. Clancy, and A. Ivanković, "A Lagrangian cell-centred finite volume method for metal forming simulation," *International journal for numerical methods in engineering*, vol. 109, no. 13, pp. 1777–1803, 2016.

[2] P. Cardiff, Ž. Tuković, H. Jasak, and A. Ivanković, "A block-coupled finite volume methodology for linear elasticity and unstructured meshes," *Computers and Structures*, vol. 175, pp. 100–122, 2016.

[3] P. Cardiff, T. Tang, Ž. Tuković, H. Jasak, A. Ivankovic, and P. D. Jaeger, "An Eulerian-inspired Lagrangian finite volume method for wire drawing simulations," in *IUTAM Symposium on Multi-scale Fatigue, Fracture and Damage of Materials in Harsh Environments*. Galway, Ireland: National University of Ireland Galway, 2017.

[4] H. Jasak and H. G. Weller, "Application of the finite volume method and unstructured meshes to linear elasticity," *International Journal for Numerical Methods in Engineering*, pp. 267–287, 2000.

[5] H. G. Weller, G. Tabor, H. Jasak, and C. Fureby, "A tensorial approach to computational continuum mechanics using object orientated techniques," *Computers in Physics*, vol. 12, pp. 620–631, 1998.

SIMULATING THE INTERACTION BETWEEN WAVES AND A FIXED RECTANGLE WITH OPENFOAM

WEIYE DING, CONGFANG AI, YUXIANG MA, GUOHAI DONG

State Key Laboratory of Coastal and Offshore Engineering , Dalian University of Technology
tings@mail.dlut.edu.cn
aicongfang@dlue.edu.cn
yuxma@126.com
ghdong_dut@yeah.net

During the past few decades, two dimensional wave tank about the interaction of waves with cylinder [8, 12] or rectangular [4, 11, 13] structures have been studied. Numerical models provide a valuable tool to predict the wave-induced response of a fixed rectangle. Such a model should account for the interactions between the local wave field and the structure, such as the scattering of the waves by the structure, and the radiation of waves due to the structure motions. Furthermore, the model should account for the complex nearshore evolution of the waves as they propagate from relatively deep water to shallower water depths. This includes processes like shoaling refraction, diffraction, wave breaking, and nonlinear interactions. With the increase of computational powers, various detailed Computational Fluid Dynamics (CFD) models have been developed that can resolve the turbulent flow field in the vicinity of a floating body. Examples includes models that are based on the Reynolds-averaged Navier-Stokes (RANS) equations and models based on the Smoothed Particle Hydrodynamics (SPH) method. The use of RANS equations to model coastal engineering processes is growing in importance. One of their greatest features is the capability to obtain three dimensional pressure and velocity profiles, which allow for a more realistic treatment of all the dynamics, being capable of accurately simulating wave conditions along the while spectrum of relative water depth.

The central idea in this paper is to drive an open source CFD toolbox OpenFOAM○®[5, 7], which in Bredmose et al. [1~2] and Jasak et al.[6] has been successfully applied to calculations of waves flow over obstacles, resolves the waves around the fixed rectangle structure. The numerical solution is obtained by solving the incompressible Navier-Stokes equations in combination with volume of fluid (VOF) method [3], which is a famous surface tracking scheme. Advantages of VOF method are that it is very simple, allowing very complex free surface configurations to be represented easily and that it involves no mesh motion. In this study, the validity of the isotropic assumption is considered by using a nonlinear (NL) k-ε model developed by Shih et al. [10], which accounts for anisotropic effects by introducing a nonlinear Reynolds stress term into the standard NL k-ε model. A solitary wave pass a submerged, immersed, or floating fixed rectangle is firstly simulated (Figure 1). The numerical results are compared to the experimental data and very good agreements have been obtained for velocities in the vortex behind the structure (Figure 2). Then a three-dimensional regular wave flow over a rectangle also has been simulated and validated in this paper (Figure 3). Waves are found to be generated realistically and agreement between laboratory and numerical data is very high regarding wave breaking, run up and undertow currents (Figure 4).
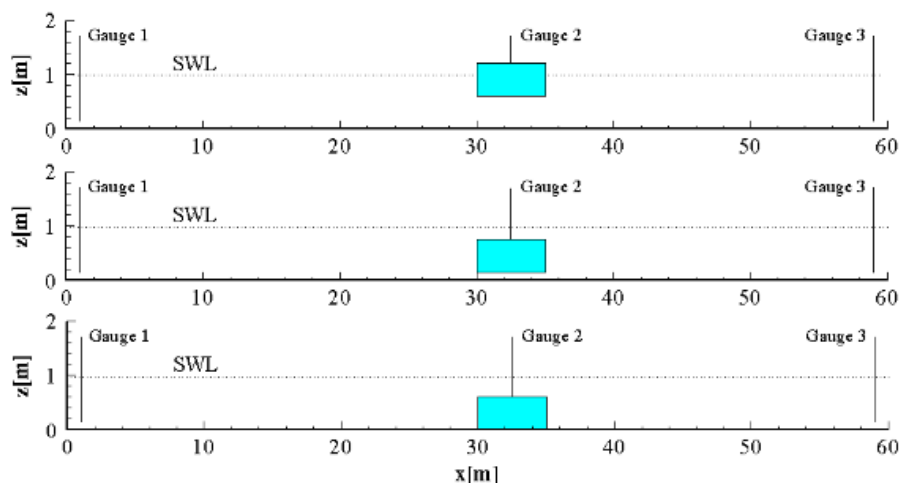
Figure 1: Schematic illustration of a solitary past a submerged, immersed, or floating rectangle
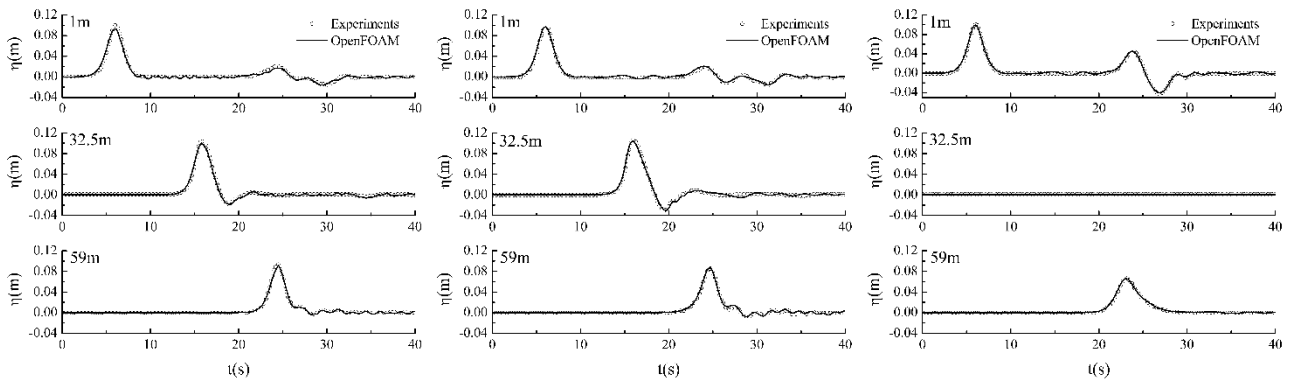
Figure 2: The comparisons of time histories of free surface displacement at x = 1 m, 32.5 m, and 59 m between experiments and OpenFOAM (left panel: submerged; middle panel: immersed; right panel: floating)
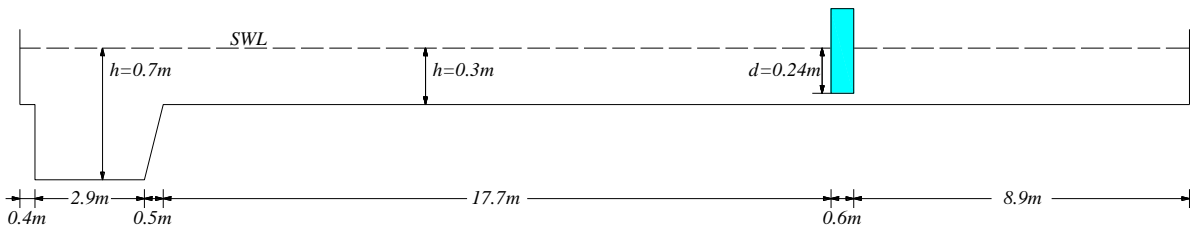
Figure 3: Schematic illustration of a regular wave past an immersed rectangle

Figure 5: Time series of wave elevations (left panel) and forces on rectangle (right panel)

References

[1] Bredmose, H., & Jacobsen, N. G. (2010). Breaking wave impacts on offshore wind turbine foundations: focused wave groups and cfd.

[2] Bredmose, H., & Jacobsen, N. G. (2011). Vertical Wave Impacts on Offshore Wind Turbine Inspection Platforms. ASME 2011, International Conference on Ocean, Offshore and Arctic Engineering (pp.645-654).

[3] Hirt, C. W., & Nichols, B. D. (1981). Volume of fluid (vof) method for the dynamics of free boundaries ☆. J.comput.phys, 39(1), 201-225.

[4] Huang, Z. (2006). Wave interaction with one or two rows of closely spaced rectangular cylinders. Ocean Engineering, 34(11), 1584-1591.

[5] http://www.openfoam.org/version2.3.0/multiphase.php.

[6] Jasak, H. and Vukčević, V. (2014). Simulation of Wave Impact Loads in OpenFOAM. 21st Symposium on Theory and Practice in Shipbuilding. Hrvatska znanstvena bibliografija i MZOS-Svibor.

[7] OpenCFD, OpenFOAM: The Open Source CFD Toolbox. User Guide Version 1.4, OpenCFD Limited. Reading UK, Apr. 2007.

[8] Paulsen, B. T., Bredmose, H., and Bingham, H. B. (2012). Accurate computation of wave loads on a bottom fixed circular cylinder.

[9] Pengzhi Lin. (2006). A multiple-layer σ-coordinate model for simulation of wave structure interaction. Computers & Fluids, 35, 147-167

[10] Shih, T. H., Zhu, J. and Lumley, John L. (1996). Calculation of wall-bounded complex flows and free shear flows. International Journal for Numerical Methods in Fluids, 23(11), 1133-1144.

[11] Sue, Y. C., Chern, M. J., & Hwang, R. R. (2005). Interaction of nonlinear progressive viscous waves with a submerged obstacle. Ocean Engineering, 32(8–9), 893-923.

[12] Teng, T. L., Pizer, D., Simmonds, D., Kyte, A., Greaves, D., & Teng, T. L., et al. (2017). Simulation and analysis of wave-structure interactions for a semi-immersed horizontal cylinder. Ocean Engineering.

[13] Venugopal, V., Varyani, K. S., & Barltrop, N. D. P. (2006). Wave force coefficients for horizontally submerged rectangular cylinders. Ocean Engineering, 33(11–12), 1669-1704.

[14] Wang Daguo. (2011). A 3D Time domain coupled model for nonlinear waves acting on a box-shaped ship fixed in a harbor. China Ocean Engineering, 25(3), 441-456.

WAVE AND CURRENT INTERACTION WITH MOORED FLOATING BODIES USING OVERSET METHOD

JAVIER L. LARA[1], B. DI PAOLO[2], G. BARAJAS[3], INIGO J. LOSADA[4]

[1] *Environmental Hydraulics Institute (IH Cantabria), Universidad de Cantabria, Isabel Torres 15, 39011 Santander, Spain, lopezjav@unican.es*

[2] *Environmental Hydraulics Institute (IH Cantabria), Universidad de Cantabria, Isabel Torres 15, 39011 Santander, Spain, benedetto.dipaolo@unican.es*

[3] *Environmental Hydraulics Institute (IH Cantabria), Universidad de Cantabria, Isabel Torres 15, 39011 Santander, Spain, gabriel.barajas@unican.es*

[4] *Environmental Hydraulics Institute (IH Cantabria), Universidad de Cantabria, Isabel Torres 15, 39011 Santander, Spain, losadai@unican.es*

Keywords: *Overset mesh, Wave-current interaction, mooring systems*

Introduction

Nowadays floating structures like breakwaters, floating wave energy converters, offshore platforms and floating wind turbine substructures are widely applied in coastal and offshore engineering because they offer many advantages over traditional solutions. For example, floating breakwaters can be installed in deep waters, limiting the environmental impact and offering a cheaper solution compared with traditional breakwaters (Chun-Yan Ji et al., 2016). Characterization of waves and current interaction with the floating structure is a complex issue due to the relevance of the non-linear physical processes involved that hinder the resolution of the problem in an analytical way. Therefore, the main methodology has been physical modeling. During the last decades, the improvements in hardware architecture have encouraged the development of numerical models, with the main goal of reducing the number of carried out physical model tests, as they are more expensive than the numerical ones.

Numerical modelling of floating bodies is still being a very challenging issue, especially for large body displacements. Despite of the good performance of potential flow models in predicting floating body dynamics, there are still physical processes which are not well reproduced with that approximation. Their strong assumptions yield into a lack of accuracy when high non-linear effects become predominant. In addition, the presence of restrictions to motion induced by mooring elements also introduces additional non-linear features which are sometimes out of the framework of the use of potential flow models. The use of Computational fluid dynamics (CFD) approach overcomes potential model limitations especially for non-linear effects. When CFD models are applied to solve waves and current interaction with floating bodies, several issues arise such as the numerical treatment of the floating element, mooring implementation and also the computational cost.

The main challenge regarding wave-floating structure interaction is how to handle the mesh motion to perfectly reproduce the complexity of body motion and the flux around it. Although several approaches are available in literature regarding the numerical implementation of the mesh motion as described in Jasak and Tukovic 2010, (also implemented in OpenFOAM enviroment), or in Liu et al. 2017, the implementation of the overset mesh grid (also called "Chimera grid") (Meakin Robert L., 1999, Petersson N. Anders, 1999, Suhs and Rogers, 2002) appears as the most accurate one for large body displacements. In a Chimera grid scheme, a complex geometry is decomposed into a system of geometrically simple overlapping grids (first step: grid generation). Boundary information is passed between these grids via interpolation of the flow variables, and many points may not be used (second step: interpolation, hole cutting and determination of interpolation weights).

In this work, we will present a numerical analysis of wave and current interaction with floating bodies. The objective of the work is to present a set of numerical implementations performed in OpenFOAM environment with the use of the overset mesh method to study moored floating body dynamics due to the combined action of waves and current. The implementations, included in IHFOAM (Higuera et al., 2013) (www.ihfoam.ihcantabria.com) are a new set of boundary conditions to generate waves and current without the use of relaxation zones. The main consequence is that the computational cost can be reduced due to the use of smaller domains. In addition, the implementation of mooring will be also presented in order to extend the use of the model to realistic conditions. Numerical model predictions compared with laboratory data of wave interaction with moored floating bodies have been performed showing a high degree of agreement. The combined effect of waves and current, traveling in the same direction than waves, and their interaction with floating bodiesand mooring will be also studied. Results will show the applicability of the new implementations to be included in real problems.

Wave – floating body interaction: validation cases

A numerical wave tank was developed in order to validate wave interaction with a floating breakwater as in Rhaman et al. (2006). The dimensions of wave tank were 2.8m long, 1.9 wide and 1.2 of high. It is shown in the figure 1. The floating

body is 30.4 cm long, 68 cm wide and 13.7 cm deep. The body is anchored to the bottom with linear spring devices. A simplified model of linear spring with damping was considered in the numerical models developed. This kind of device applies a dumping when the spring is at rest, avoiding the small numerical errors that could arise at the beginning of the simulation. This mechanism was implemented in OpenFOAM, modifying the existing linear spring model. More deatails about the implelentation will done during the presentation.

The mesh consisted of 2 grids, being the external one the global domain mesh. The internal mesh was used floating body. The overset mesh was performed between the two grids. The dimensions of the external grid were: $\Delta x = 3$cm, $\Delta y = 4$cm, $\Delta z = 4$ cm and $\Delta x = 2.5$ cm, $\Delta y = 4.5$ cm, $\Delta z = 1.5$ cm for the internal grid. Discretization around the floating body was refined up to: $\Delta x = 0.625$ cm, $\Delta y = 1.125$ cm, $\Delta z = 0.375$ cm. This discretization allowed to accurately generate all wave conditions and to validate the model.

Because of the tension of mooring lines was omitted in Rhaman et al. (2006), realistic values of the devices used to calibrate and validate the model developed were estimated based on literature. The equivalent stiffness and damping of the linear spring have been calibrated numerically yielding: k=323.47 N/m and c = 200 Kg/s, for the spring and damping coefficients. Additionally, k-epsilon model has been used for turbulence modeling. Wave generation and active absorption was defined as boundary condition on the left of domain while only active absorption was used at outlet on the other side of domain. A classical non-slip boundary condition was assigned to the bottom. The top was defined as atmosphere and the lateral walls have been defined as slip.

Two cases were considered:

- **Case A**:
  - Wave Height: 3.1cm, water depth: 65 cm, wave period: 1s
  - Mooring system: 4 inclined mooring chains ($\vartheta = 60$)

- **Case B**:
  - Wave Height: 7.3 cm, water depth: 65 cm, wave period: 1.3s
  - Mooring system: 4 vertical mooring chains ($\vartheta = 90$)
  - The results of the two cases and the comparison with laboratory data of Rhaman et al. (2006) are shown in the figures 3,4 and 5.
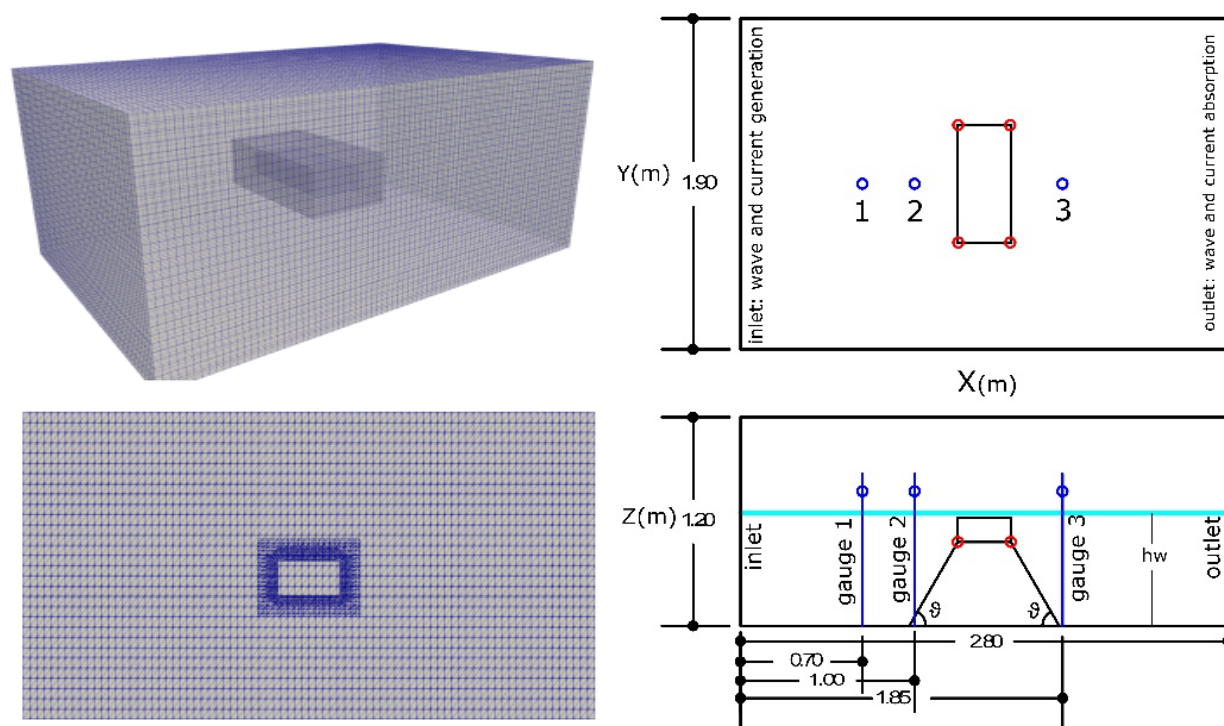
Figure 1: On the left: the global 3D mesh. On the bottom: a section of the mesh showing the two system of grids used to perform the overset mesh. On the right: Numerical wave tank developed.
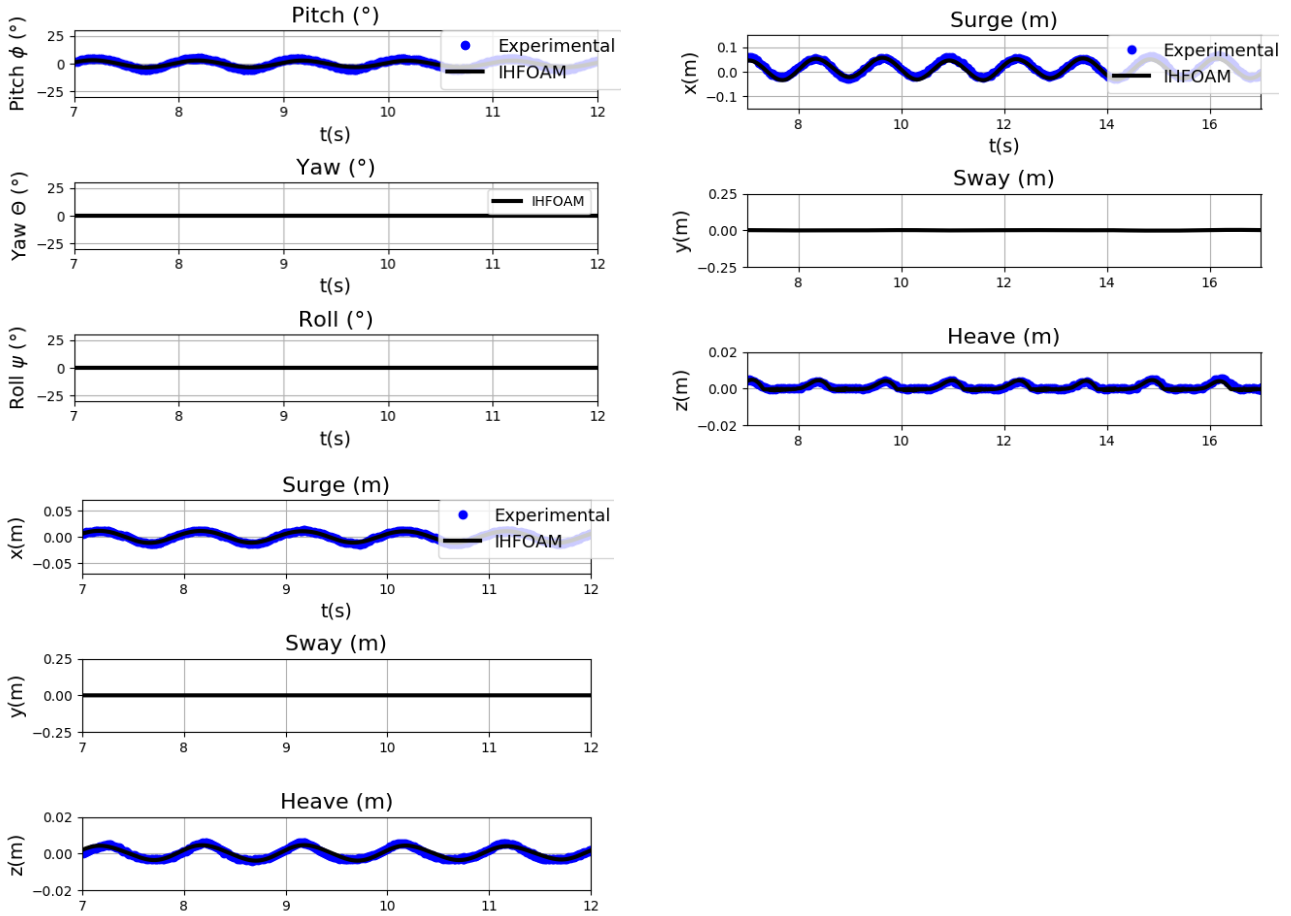
Figure 2: On the top: Case B: H = 3.1cm, T = 1s, h = 65cm. Pitch, Yaw and Roll (degrees) and Surge, Sway and Heave (m). On the bottom: Case A: H = 7.3cm, T = 1.3s, h = 65 cm . Surge, Sway and Heave (m).

Wave and current interaction

Once the model was calibrated and validated, the combined effects wave and current were analyzed. The new set of boundary conditions implemented in IHFOAM allow generating waves with a depth-uniform current. Uniform current was imposed at the patch inlet for current generation. In the present work we analyzed the effect of the interaction of current with regular second order Stokes waves. Firstly three simulations with three different values of current in horizontal direction were carried out for each of the cases above.

The case A (H = 7.3cm, T = 1.3s, h = 65cm) was selected to develop the numerical simulations of only current action and wave-current interaction. The following values of positive and negative current were considered:

- Ux current = + 0.25 m/s
- Ux current = + 0.5 m/s
- Ux current = + 0.75 m/s
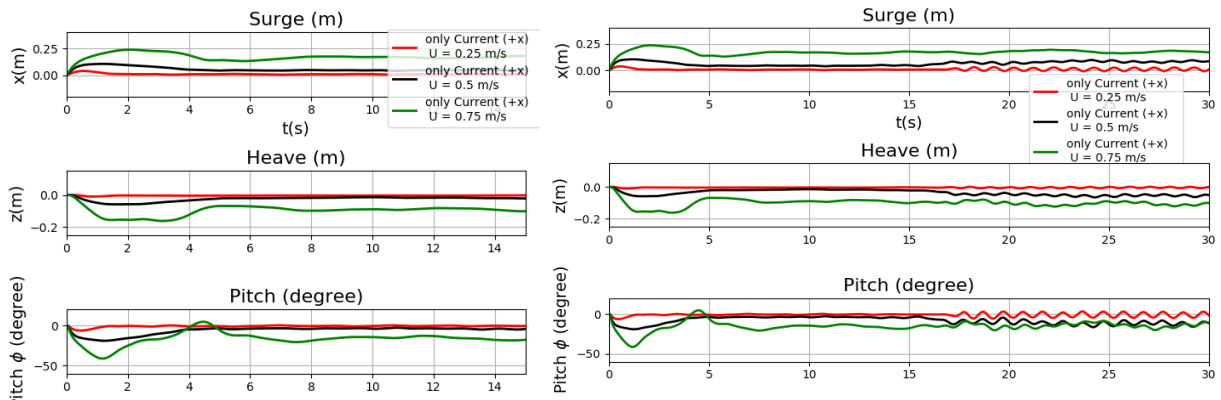
Figure 3: On the left: Only current interaction – Comparison of Surge, Heave and Pitch under the action of positive current. Positive current: U = 0.25 m/s, U = 0.5 m/s, U = 0.75 m/s, in red, black and green, respectively. On the right: Wave-current interaction – Comparison of Surge, Heave and Pitch under the action of wave and positive current of magnitudes 0.25, 0.5 and 0.75 m/s. The wave case considered is: Case A: H = 7.3cm, T = 1.3s, h = 65cm.
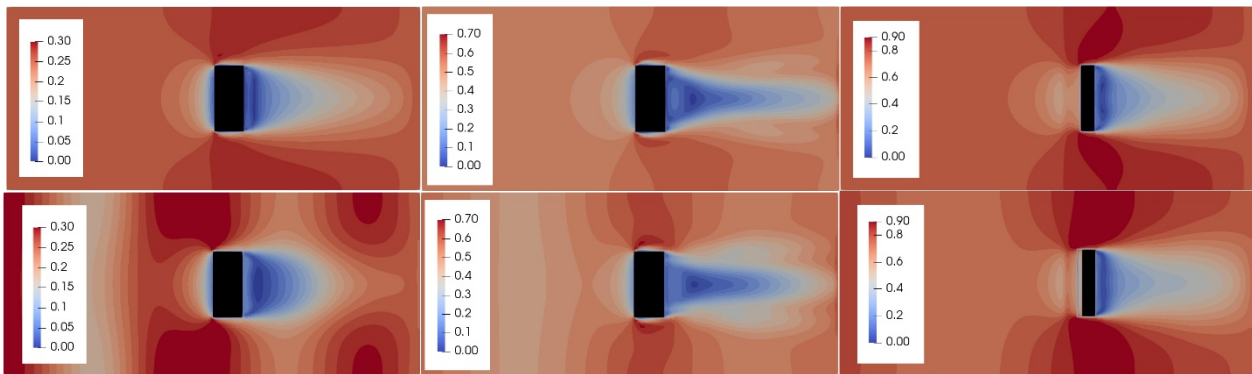
Figure 4: On the top, from the left to the right: velocity field magnitude U(m/s) induced by only current of 0.25 –0.5 –0.75 m/s, respectively. On the bottom, from the left to the right: wave-current interaction with current intensities of 0.25 –0.5 – 0.75 m/s, respectively. The wave case considered is: Case A: H = 7.3cm, T = 1.3s, h = 65cm.

Conclusions

A numerical model for wave-current interaction was carried out. The new implementations in IHFOAM, including a modified linear spring model and wave and current join generation, were used to demonstrate that this model could be used for all offshore and coastal engineering application of wave-current floating structure interaction. Numerical implementations were validated with existing experimental data in literature showing a good agreement in the reproduction of the six degrees of freedom of the floating body subjected to the action of waves. The new implementations were stressed to analyse the combined effects of waves and currents. When performing the overset mesh, high dynamic mesh motion stability was achieved for all the cases. Finally, the main goals were accomplished with a not so expensive computational grid. The computational time for wave and current case (the most expensive simulation) was 20 hours with 16 cores.

References

[1] JI, Chun-Yan, et al. Experimental study on configuration optimization of floating breakwaters. *Ocean Engineering*, 2016, vol. 117, p. 302-310.

[2] Jasak, Hrvoje; TUKOVIĆ, Željko. Dynamic mesh handling in OpenFOAM applied to fluid-structure interaction simulations. En *Proceedings of the V European Conference on Computational Fluid Dynamics ECCOMAS CFD 2010*.

[3] Meakin, Robert L. Composite overset structured grids. *Handbook of Grid Generation*, 1999, p. 1-20.

[4] Petersson, N. Anders. Hole-cutting for three-dimensional overlapping grids. *SIAM Journal on Scientific Computing*, 1999, vol. 21, no 2, p. 646-665.

[5] Suhs, Norman E., et al. PEGASUS 5: an automated pre-processor for overset-grid CFD. 2002.

[6] Higuera, Pablo; Lara, Javier L.; Losada, Inigo J. Realistic wave generation and active wave absorption for Navier–Stokes models: Application to OpenFOAM®. *Coastal Engineering*, 2013, vol. 71, p. 102-118.

[7] Rahman, Md Ataur; Mizutani, Norimi; Kawasaki, Koji. Numerical modeling of dynamic responses and mooring forces of submerged floating breakwater. *Coastal Engineering*, 2006, vol. 53, no 10, p. 799-815.

NUMERICAL INVESTIGATION ON THE PERFORMANCE OF A 'V' TYPE BREAKWATER

AO GANG, YUXIANG MA, GUOHAI DONG, TAO HANG

State Key Laboratory of Coastal and Offshore Engineering, Dalian University of Technology,
gangao@mail.dlut.edu.cn
yuxma@126.com
ghdong_dut@yeah.net
2393358795@qq.com

Introduction

Breakwater is a common structure in coastal region, which is used to dissipate the energy from the sea and protect the structure and vessel near shore. Traditional breakwaters are effective, such as rubble mount, upright concrete caissons and so on, but they are more expensive in materials. For less cost, permeable breakwaters are paid more attention in recent years. Therefore, more and more novel type structures have been proposed. Neelamani and Rajendran investigated the wave transmission, reflection and dissipation characteristics of 'T' and '⊥' type breakwaters[1][2]. Günaydın and Kabdaşlı analysed the characteristics of 'U' and 'Π' type breakwaters in 2004 and 2007 respectively[3][4].

Recently, Computational Fluid Dynamics (CFD) simulation, as a new method differing from theoretical analysis and experimental measurement, can provide a comprehensive information about the flow field. More and more CFD software applied to fluid calculation are developed, for example, FLUENT, COMSOL, STAR-CCM+ and so on. Compared with the above, Open Field Operation and Manipulation (OpenFOAM) is an open source code written by C++, having a broad range of application including CFD, heat transfer, computational chemistry, even finance. OpenFOAM provides a multi-phase solver called Waves2FOAM, which can simulate wave propagation effectively.

In this paper, the character of a 'V' type breakwater will be discussed. Using the VOF model in OpenFOAM, 2D numerical simulation of regular waves through a 'V' type breakwater is carried out. In the present research, the performance of the breakwater is evaluated by measuring reflection and transmission coefficient.

Government equations

The numerical model is based on OpenFOAM, simulating two-phase incompressible flow of air and water. By secondary development of the CFD toolbox OpenFOAM, Jacobsen developed the Waves2Foam, a new utility to simulate wave propagation. The free surface is captured by the VOF method, and the continuity and momentum equations are solved using the finite volume method. The detailed information can be seen in the manual of Waves2Foam[5].

The continuity equation is as follows:

$$\nabla \cdot \mathbf{u} = 0 \tag{1}$$

The momentum equation is as follows:

$$\frac{\partial \rho \mathbf{u}}{\partial t} + \nabla \cdot \rho \mathbf{u} \mathbf{u}^T = -\nabla p^* + g \cdot (\mathbf{x} - \mathbf{x}_r)\nabla \rho + \nabla \cdot \mu_{tot} \nabla \mathbf{u} \tag{2}$$

The meaning of the above variables can find in the manual of Waves2Foam.

Numerical simulations

1. Model scale

According to the research of Günaydın and Kabdaşlı[3][4], the way of absorbing wave energy by the new type structure is cutting the orbits of water particles, so the breakwater should be set at the free surface. The position of breakwater is demonstrated by Fig.1 in detail. To cut wave more effectively, Günaydın suggested the horizontal length α_h should be greater than the horizontal orbit of water particles ($\alpha_h > \alpha = (H/2)\coth(2\pi h/L)$) and the vertical length α_v should be greater than the vertical orbit ($\alpha_v > \beta = H/2$).
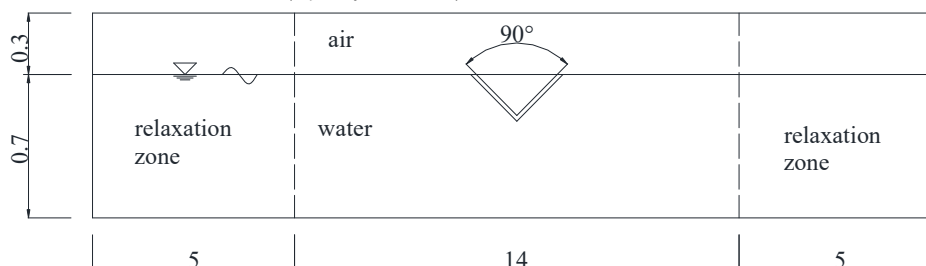
Figure 1: Sketch of the model

In the present study, the size of wave flume is 24m×1m×1m, and the characteristic of the regular wave is listed in the Table 1.

Table 1: The characteristic of wave

Height(m)	Period(s)	Depth(m)
0.05		
0.10	1	0.7
0.15		

Then, based on the wave parameters, the size of 'V' type breakwater can be calculated:

Table 2: The size of breakwater

Height(m)	$\alpha = (H/2)\coth(2\pi h/L)$(m)	$\beta = H/2$(m)
0.05	0.0252	0.025
0.10	0.0503	0.05
0.15	0.0755	0.075

The horizontal length of the breakwater is set to 20 cm. By varying the angle of the breakwater, the vertical length can be determined.

2. Wave characteristics

In order to evaluate the performance of the breakwater, it is indispensable to measure the reflection and transmission coefficients. According to the two coefficients, the dissipation coefficient of energy can be calculated. These parameters are given below.

Reflection coefficient:

$$C_r = \frac{H_r}{H_i} \tag{3}$$

Transmission coefficient:

$$C_t = \frac{H_t}{H_i} \tag{4}$$

Dissipation coefficient:

$$C_I = \sqrt{1 - C_r{}^2 - C_t{}^2} \tag{5}$$

where H_i is the incident wave height, H_r is the reflection wave height and H_t is the transmission wave height. The incident and transmission wave height can be separated by the method presented by Goda and Suzuki[6].

Results and Discussion

Three different angles are chosen in the study, 60°, 90° and 120°. In the simulation, the bubbles are generated between the two plates, causing wave energy dissipation of wave energy. At first, the surface is calm. When the first wave contacts the structure, a jet is generated front the structure. After a second, the wave reaches the back plate, and an inverted jet prevents the propagation of waves. Lasing for a while, some bubbles occur between two plates, and it is the main reason of energy dissipation. The following figure shows the generation of the bubbles.
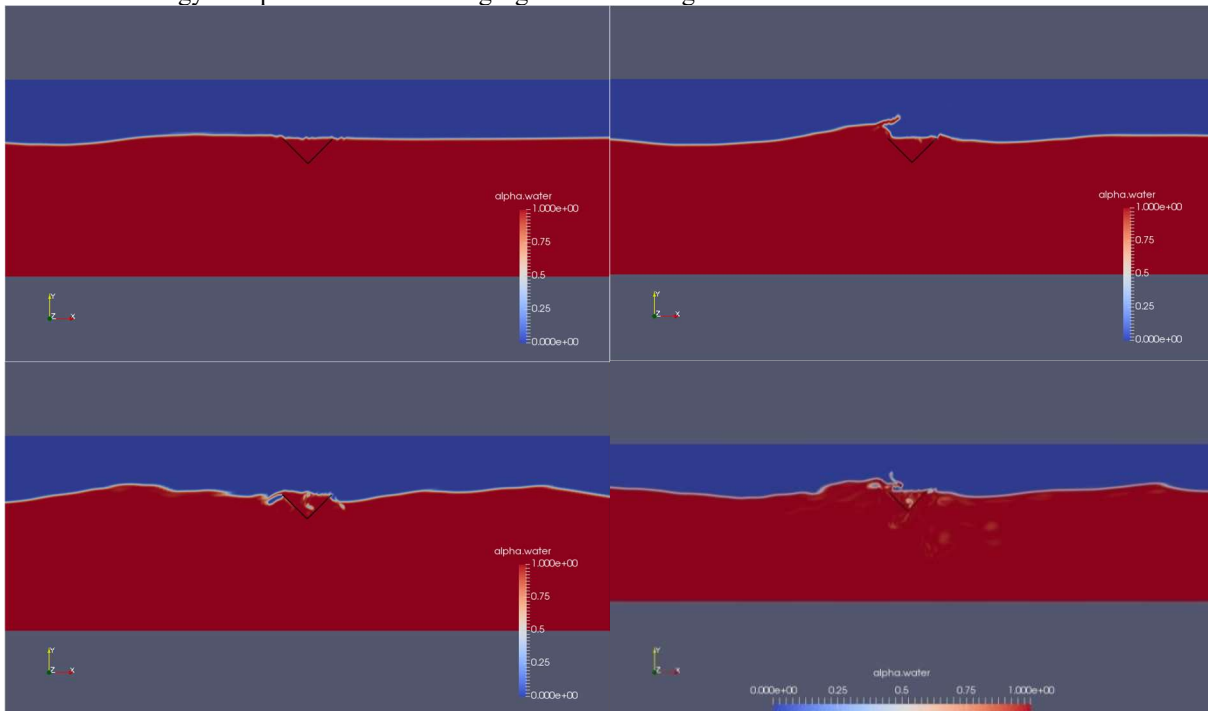
Figure 2: wave propagation between the two plates

Using the two-points separation method, the reflection and transmission coefficients can be calculated readily. After the simulation, the wave height of the front and back of the structure can be obtained by the Waves2Foam utility. On the basis of two-points separation method, the reflection wave and incident wave is separated through the wave height measured. Setting the inlet as origin, the breakwater is at 12 meters, so the wave height at 7, 8 and 16 meters is measured. The results of the case of angle 60° under wave height of 0.15m are as follows.
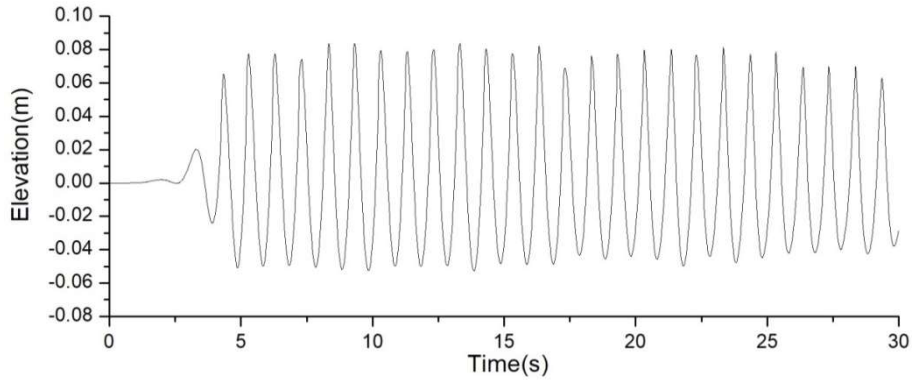
Figure 3: Surface Elevation (7m)
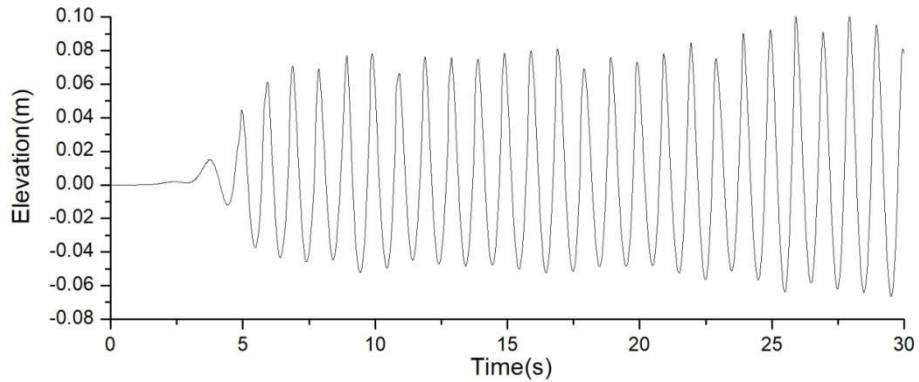
Figure 4: Surface Elevation (8m)
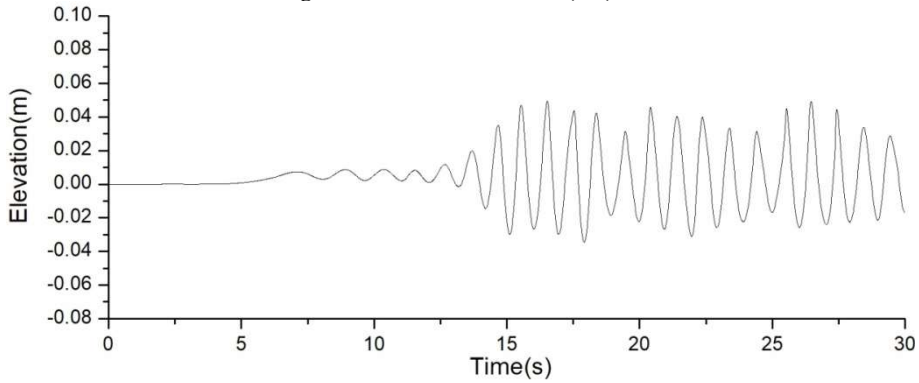
Figure 5: Surface Elevation (16m)

Table 3: The coefficients of simulations

	Angle(degree)	Reflection coefficient	Transmission coefficient	Dissipation coefficient
H=0.05m	60	0.732	0.261	0.629
	90	0.671	0.305	0.675
	120	0.713	0.386	0.621
H=0.10m	60	0.778	0.211	0.591
	90	0.784	0.264	0.561
	120	0.847	0.275	0.455
H=0.15m	60	0.509	0.222	0.832
	90	0.532	0.232	0.814
	120	0.559	0.184	0.809
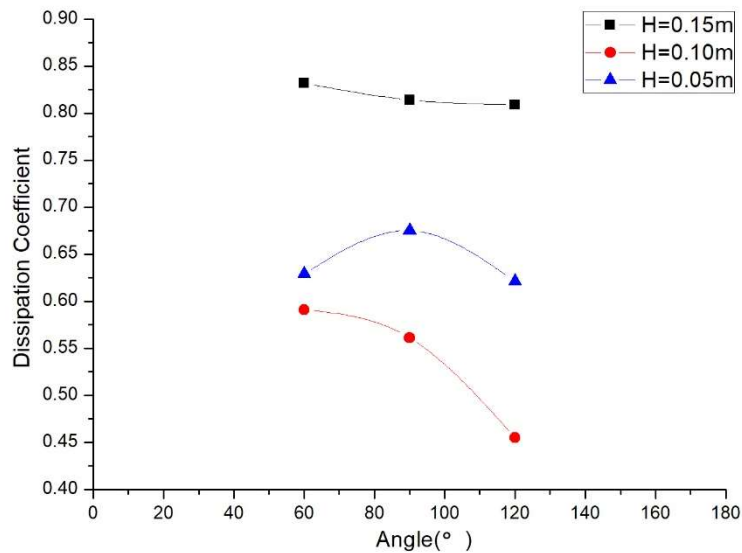
Figure 6: Dissipation coefficient

In the result, the dissipation coefficient of wave height of 0.05m and 0.1m is lower than 0.15m. With the angle of 90°, the vertical length of structure is 0.1m, which is double than β of the breakwater under the wave height of 0.1m. Between the two plates, two whole water orbits are remained. The structure cannot effectively cut the orbit of water particles, so the breakwater under the wave height of 0.1m has a poor performance. It is same under the wave height of 0.05m. The vertical length is 1.33 times than β under the wave height 0.15m, which is not integer times than β, so the dissipation coefficient is the larger than the other cases. The dissipation coefficient have the same property under other angles. The distance of two plates is shorter, namely the angle is smaller, the appearance of reverse jet is earlier and more frequent, so the dissipation coefficient is larger. With the increasing of angle, the dissipation coefficient decreases.

Acknowledgments

References

[1] Neelamani, S., Rajendran, R., 2002a. Wave interaction with T-type breakwaters. Ocean Engineering 29, 151–175.

[2] Neelamani, S., Rajendran, R., 2002b. Wave interaction with '⊥'-type breakwaters. Ocean Engineering 29, 561–589

[3] Günaydın, K., Kabdaşlı, M.S., 2006. Performance of solid and perforated U-type breakwaters under regular and irregular waves. Ocean Engineering 31, 1377–1405

[4] Günaydın, M.S. Kabdaşlı, 2007. Investigation of Π-type breakwaters performance under regular and irregular waves, Ocean Engineering 34, 1028-1043

[5] Jacobsen, Niels. (2017). waves2Foam Manual.

[6] Goda, Y., Suzuki, Y., 1976, Estimation of incident and reflected waves in random wave experiments, In Proceedings of the 15th Coastal Engineering Conference, Hawaii, 828-845

SIMULATION OF FLUID-STRUCTURE INTERACTION IN BIOMECHANICS USING FOAM-EXTEND

HUA-DONG YAO[1, A)], HÅKAN NILSSON[1, B)], MATS SVENSSON[1], HÅKAN ROOS[2]

[1] *Department of Mechanics and Maritime Sciences, Chalmers University of Technology, Sweden*
[2] *Department of Vascular Surgery, Sahlgrenska University Hospital, Gothenburg, Sweden*
a) huadong.yao@chalmers.se; b) hakan.nilsson@chalmers.se

Abstract

Fluid-structure interaction (FSI) occurring in two applications in biomechanics is investigated using numerical simulations. One application is the interaction between the dorsal root ganglion and the surrounding fluids (i.e., venous blood and cerebrospinal fluid), and the other application is for the forces and deformation of stent grafts caused by pulsatile blood pressure. In these applications the fluids dynamically interact with the deformable structures. The simulation tool is the FSI package distributed in the Extend-bazaar. The flow and structural deformation are simulated in a segregated way. A strongly coupled partitioned method is used to couple the fluid and structure simulations. The interaction processes of the applications are addressed qualitatively. New insights into the dorsal-root-ganglion injury, which could arise due to whiplash motion, and the forces on stent grafts are gained based on the results. The present FSI solver is considered an effective numerical tool for studying FSI subjects in biomechanics.

Methodology of FSI solver

The open source software FOAM-extend [4] is used together with the FSI package distributed in the Extend-bazaar. Refer to the studies by Jasak [4] and Tuković and Jasak [8] for the details of the governing equations of fluids and structures.

The flow equations are solved based on a second-order finite volume method (FVM) with automatic mesh motion. The PISO (Pressure Implicit Splitting of Operators) algorithm [2] is utilized in the method. A Laplace equation is adopted to govern the automatic mesh motion. A second-order finite element method (FEM) is used to solve this equation [8]. A second-order backward scheme is employed for the time marching.

The structure equations are solved using a second-order cell-centered scheme for the space discretization [8]. A segregated algorithm is used to separately solve the displacement increment vectors. The incomplete Cholesky conjugate gradient iterative solver (ICCG) [3] is employed to compute the system matrix. An implicit second-order three-stage backward scheme is used for the time-marching.

A strongly coupled partitioned method with a Picard iterative process is employed to couple the fluid and structure solvers [5]. The Aitken method [1] is applied to accelerate the convergence speed of the coupling.

Whiplash dorsal root ganglion injury

The dorsal root ganglion (DRG) can be injured during whiplash motion [9]. As shown in Figure 1, the DRG is embedded in the foramen of the cervical vertebra. A possible cause of the injury is that the DRG and dura mater (DM) can be significantly deformed due to impulsive pressure in the surround fluids, i.e., the venous blood and cerebrospinal fluid (CSF).

A geometrical model is established based on the anatomy illustrated in Figure 1. The fluid and structure geometries and corresponding boundary conditions are shown in Figure 2. The FSI is found including pulling and pressing processes, to which the DRG is subjected. The extreme statuses of the processes are shown in Figure 3. The maximum stretched deformation of the DRG is observed at 0.055 s during the pulling, and the maximum compression at 0.1s during the pressing. The deformation interacts with the flows inside and outside the spinal canal. The largest von Mises stress of the DRG is observed near its end. This indicates potential structural damage positions. In addition, the largest pressure gradient is found at the foramen, where the DRG is located at. The figure for this observation is not shown here for the sake of brevity.
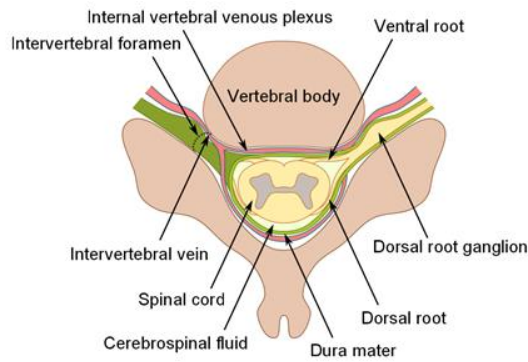
Figure 1: A schematic diagram showing a transverse slice of a vertebra in the mid cervical spine [9].
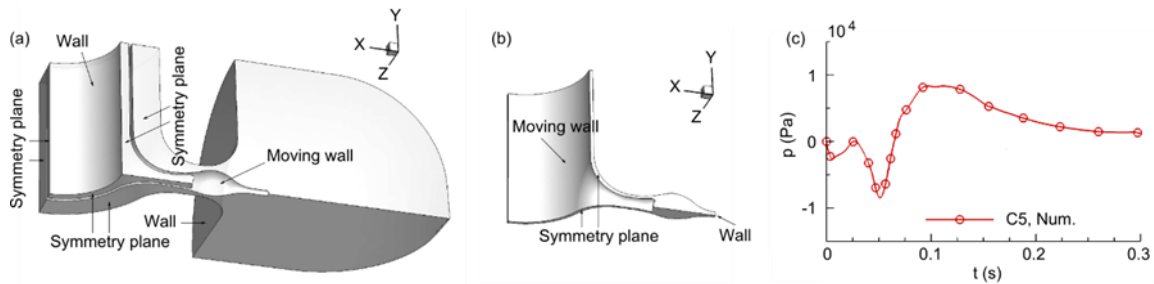
Figure 2: (a) The fluid domain and boundary conditions, (b) the structure domain and boundary conditions, and (c) the transient pressure in the cervical vertebra C5 [9], which is imposed at the inlets of the fluid domain.
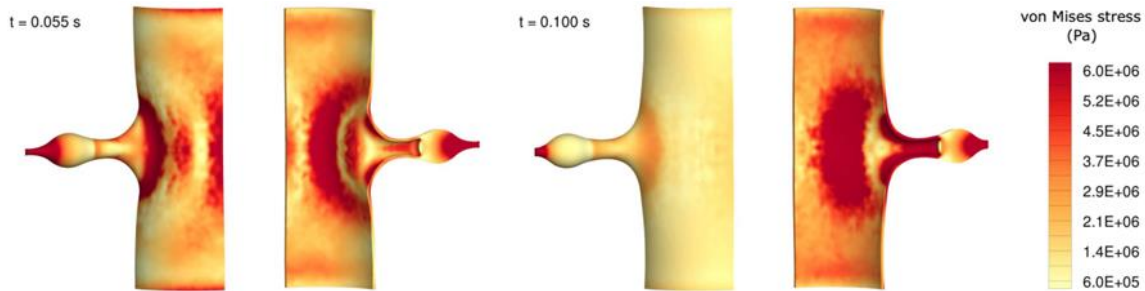
Figure 3: The deformation of the DRG and DM, which is the sheet part of the structure, at 0.055 s and 0.1 s. The contours of the von Mises stress are colored.

Flow-induced forces and deformation of stent grafts

Endovascular aortic repair (EVAR) is a minimal-invasive technique for treating abdominal aortic aneurysms. A stent graft is placed in the aorta through a sheath that is inserted into the aorta through the femoral arteries in the groin. As the sheath is slowly pulled back the stent graft is released and self-expands to fixate to the healthy artery walls at the proximal and distal ends of the aneurysm. An iliac limb stent graft is inserted into the contralateral iliac artery. It self-expands to fixate to the already inserted stent graft in the proximal end and to the iliac artery in the distal end. The stent graft is kept in place by the force exerted on the artery wall due to the self-expansion, and in some cases hooks at the proximal end but not in the connection and at the distal ends. The stent graft thus excludes the aneurysm from the circulation. Long-term EVAR durability is mainly compromised due to leakage into the aneurysm sac which is influenced by stent graft migration at the connections and distal ends, causing potentially lethal leakages. The flow-induced forces have experimentally been shown to have the potential to cause distal end iliac limb stent graft migration [6]. It was shown that the distal displacement forces increase with the magnitude of the pulsatile forces and the angulation, but not with stroke frequency. Roos et al. [7] showed in an extended experimental study that the forces are influenced by the distal stent graft diameter and the shape of the curvature. The experimental studies are however not sufficient to distinguish between the different mechanisms causing the forces, which is why numerical fluid-structure interaction studies are performed in the present work.

Figure 4 shows the tapered, tubular and bell-bottom iliac limb stent graft configurations and numerical results. The straight proximal and distal end sections are rigid fluid regions that separate the flexible stent graft region from the inlet (upper) and outlet (lower). The pulsatile velocity and pressure, determined from the experiments by Roos et al. [7], are set at the inlet and outlet, respectively. Each configuration shows the velocity magnitude (upper left) and the magnified iliac limb stent graft deformation and von Mises stress (lower right). It is shown that large deformations and high displacement forces occur at the distal end, in particular for the bell-bottom configuration. The main cause of the forces is determined

by a comparison with a case without flow, keeping only the pressure pulsations. It can be seen that less than 3% of the forces have their origin in the flow, and the pressure is thus the main cause of the forces. The 90-degree bend of the iliac limb stent graft separates the proximal and distal forces, and the forces are also estimated by calculating the instantaneous values of pressure times cross-section area. This shows that the flexibility of the graft absorbs up to 15% of the forces.
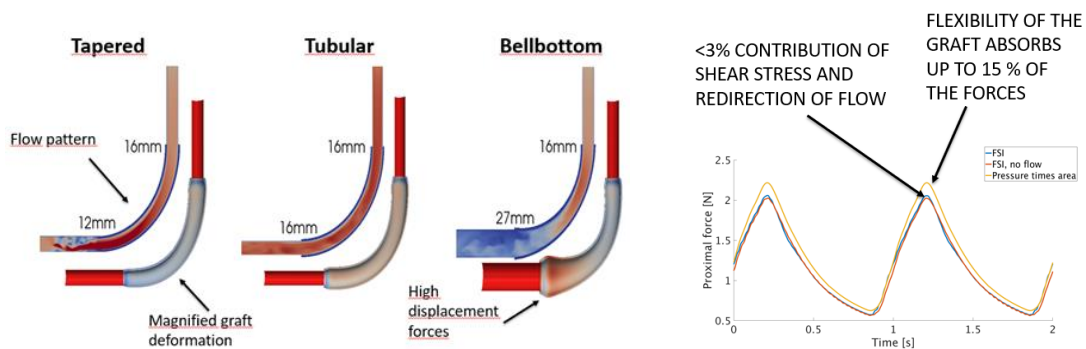
Figure 4: Iliac limb stent graft configurations and numerical results.

References

[1] Aitken, A., 1926. On bernoulli's numerical solution of algebraic equations. Proceedings of the Royal Society of Edinburgh 46, 289–305.

[2] Issa, R.I., 1986. Solution of the implicitly discretised fluid flow equations by operator-splitting. Journal of Computational Physics 62, 40.

[3] Jacobs, D.A.H., 1980. Preconditioned conjugate gradient methods for solving systems of algebraic equations. Technical Report RD/L/N193/80, Central Electricity Research Laboratories.

[4] Jasak, H., 1996. Error Analysis and Estimation for the Finite Volume Method with Applications to Fluid Flows. Phd thesis. Department of Mechanical Engineering, Imperial College of Science, Technology and Medicine.

[5] Matthies, H., Niekamp, R., Steindorf, J., 2006. Algorithms for strong coupling procedures. Computer Methods in Applied Mechanics and Engineering 195, 2028–2049.

[6] Roos, H., Ghaffari, M., Falkenberg, M., Chernoray, V., Jeppson, A., Nilsson, H., 2014. Eur J Vasc Endovasc Surg (2014) 47, 262-267

[7] Roos, H., Tokarev, M., Chernoray, V., Ghaffari, M., Falkenberg, M., Jeppson, A., Nilsson, H., 2016. Displacement Forces in Stent Grafts: Influence of Diameter Variation and Curvature Asymmetry. Eur J Vasc Endovasc Surg (2016) 52, 150-156

[8] Tuković Ž., Jasak, H., 2007. Updated lagrangian finite volume solver for large deformation dynamic response of elastic body. Transactions of FAMENA 31(1), 55.

[9] Yao, H.D., Svensson, M.Y., Nilsson, H., 2016. Transient pressure changes in the vertebral canal during whiplash motion a hydrodynamic modeling approach. Journal of Biomechanics 49 (3), 416–422.

FLUID-STRUCTURE INTERACTION OF INFLATABLE WING SECTION

M. A. M. FOLKERSMA[1], P. THEDENS[2], R. SCHMEHL[3]

[1]*TU Delft, PhD Candidate, m.a.m.folkersma@tudelft.nl*
[2]*TU Delft, PhD Candidate, p.thedens@tudelft.nl*
[3]*TU Delft, Associate Professor, r.schmehl@tudelft.nl*

Keywords: *Inflated wing, FSI, preCICE, OpenFOAM*

1 Introduction

Airborne wind energy (AWE) is a concept for harvesting wind energy using tethered flying devices. Compared to conventional wind turbines AWE systems require substantially less support structures like a tower [1]. The replacement of towers by tethers also allow accessing higher altitudes where winds blow stronger and more persistent [2]. Several configurations are currently pursued. Electricity can be generated with on-board propellers which are driven by the air flow and the power is transmitted to the ground through a conducting tether. Another configuration is the pumping cycle in which case the kite flies crosswind to pull a tether that is unreeled as it moves a ground-based electrical generator, and a retraction phase when the kite is reeled in. Next to electricity generation AWE can also be used for ship propulsion.
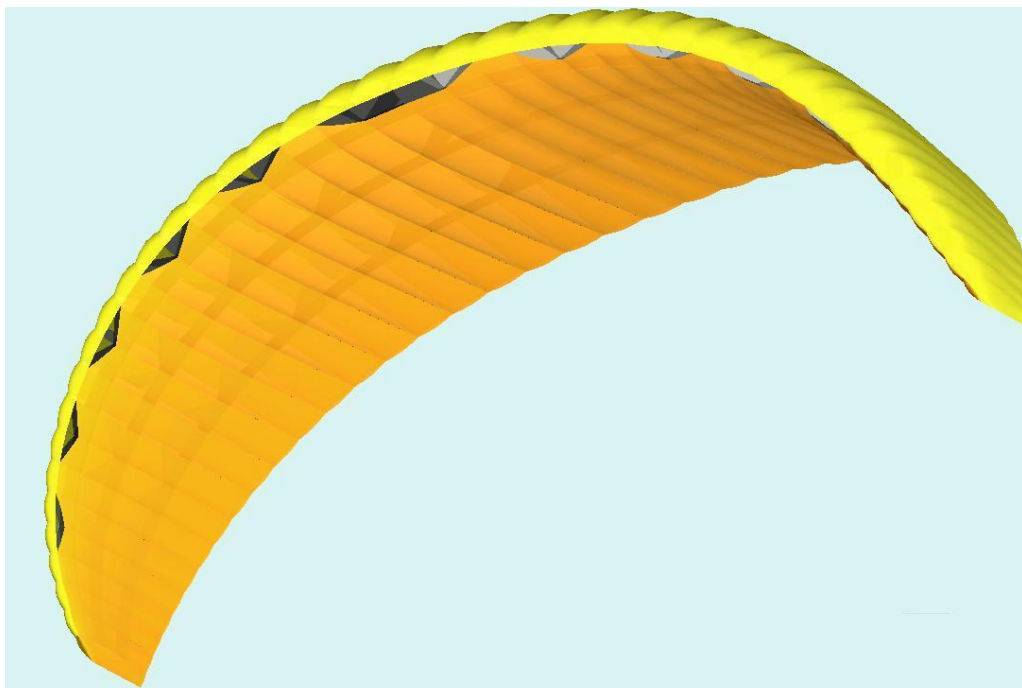
Figure 1: Ram-air kite layout [3]

We consider a single cell of a ram-air wing in our study which is based on an inflatable double skin design. As shown in Figure 1 ram-air wings are inflated by the stagnation pressure entering through inlets at the leading edge. The internal pressure provides structural stability and stiffness. The fully or partially inflated structure is flexible and can therefore exhibit large deformations during flight. This introduces a strong coupling between the structure and the air flow since the internal pressure in dependent on the wind speed, and a deformed kite will inevitably have a different pressure field caused by the flow compared to an un-deformed kite. Also, bridle system induces a significant additional drag to the wing drag and therefore the kites fly with high angle of attack to obtain high lift and to ultimately maximise power output. High angles of attack causes the flow to separate which cannot be simulated with fast inviscid methods and therefore a CFD analysis tool such as OpenFOAM is required.

The main challenge in analysis and design of these kites is the governing fluid-structure interaction (FSI) mechanism, which leads to a drastic increase in model complexity. On the other hand utilising FSI is crucial to obtain reliable results

on performance measures and structural integrity. We follow the partitioned coupling approach, where the fluid and structure domains are solved individually and coupled at their interface. In this work we couple OpenFOAM with our finite element (FE) solver *mem4py* by using the coupling tool preCICE. The coupled solver is then used to simulate a single ram-air wing section (cell) and its change in aerodynamic performance due to deformation.

2   Methodology

The FE solver *mem4py* is an in-house development for inflated membrane structures with large deformations. The fabric's thickness used for soft kites is thin and therefore its bending and compressive stiffness is negligibly small. This assumption simplifies the shell formulation but comes with difficulties in numerical convergence for static equilibrium. The remedy is a dynamic formulation which simulates the structure with inertia and viscous terms. In our study we focus on finding a static equilibrium between structure and fluid to analyse the change in airfoil profile in span-wise direction as a function of angle of attack. Therefore the mass and viscous terms can be arbitrary and usually are chosen such that the structure is critically damped to quickly arrive at steady state configuration. This method is called dynamic relaxation [4], and is often applied in form-finding. On the other hand, the real dynamic structural behaviour can also be simulated by using realistic mass and damping parameters. This flexibility of the approach comes in handy for soft-kites because both static and dynamic behaviours can be simulated.

The aerodynamic loads are determined by CFD simulations using the FOAM-FSI library [5] which is an extension to the foam-extend project [6]. The FOAM-FSI library comes with several strong coupling algorithms for partitioned FSI problems, efficient mesh deformation solvers based on radial basis function (RBF) and an adapter to the preCICE coupling tool. The transient pimpleFoam solver is used together with the Reynolds Averaged Navier-Stokes (RANS) based SST k-ω turbulence model. The boundary layer around the airfoil is resolved to capture the flow separation and therefore an O-type mesh is generated with hyperbolic extrusion.

The two solvers are coupled using preCICE. It is an open-source library that comes with an extensive set of tools to couple existing solvers for partitioned multi-physics simulations. The strong (implicit) coupling schemes include several quasi-Newton variants to accelerate the convergence. The exchanged data is mapped for non-conforming meshes by using either consistent or conservative RBF. Both the coupling and the execution of the solver modules can be run in parallel.

Setting up a multi-physics simulation with preCICE requires a configuration file and implementing an adapter for each solver. The configuration file defines the general coupling parameters such as the names of the participating solvers, the exchanged data sets and the desired mapping and coupling algorithms. The adapter is a minimal piece of code which interfaces the solver modules with preCICE. The adapters can be implemented by using any of supported languages: C++/C, Fortran and Python. The simulation begins by executing each adapter individually with either serial or parallel execution. In this work we use the preCICE adapter in FOAM-FSI library to couple OpenFOAM and preCICE and we show how to implement the adapter for the structural solver *mem4py*. The implemented adapter contains less than 100 lines of code. Both adapters are implemented in the same programming language as the solver thus C++ for OpenFOAM and Python/Cython for *mem4py*.

3   Results

The FSI simulation framework is used to study the static aeroelasticity of a common ram-air kite airfoil MH 92 (Figure 2). The airfoil is extruded in span-wise direction and clamped at both ends. For simplicity no opening at the leading edge is introduced. Instead, a uniform stagnation pressure p_t is assumed inside the airfoil, and by superimposing internal and external pressure loads, no compressive forces act on the wing. The membrane has a thickness t and isotropic linear elastic material properties with Young's modulus of E and Poisson's ratio of ν. Typical flight conditions for a kite used for AWE generation are assumed with a Reynolds number of $Re_c = 5 \times 10^6$ and turbulence intensity of $I = 2\%$.

Expected results are a strong coupling between inflow conditions such as angle of attack and the deformed airfoil shape. Especially for high angles of attack the nose section experiences large pressure forces which deform the wing and completely change its drag polar compared to the un-deformed wing. Figure 3 shows cross-sections of the deformed kite shape experiencing an angle of attack of $10°$. At mid span ($z = 0.5b$) the profile is considerably different than the initial shape ($z = 0b$). The nose section is dented inwards due to missing support from the ribs. The leading edge is pulled up and the whole section thickness is increased by nearly twofold.

4   Conclusions

Coupling existing solvers for partitioned multi-physics problems is straight-forward by using the preCICE tool. The implemented FSI framework is used to study a single cell of an inflated ram-air wing used in airborne wind energy. Drastic profile changes of the wing are observed and can only be resolved when incorporating a FSI routine into the analysis.
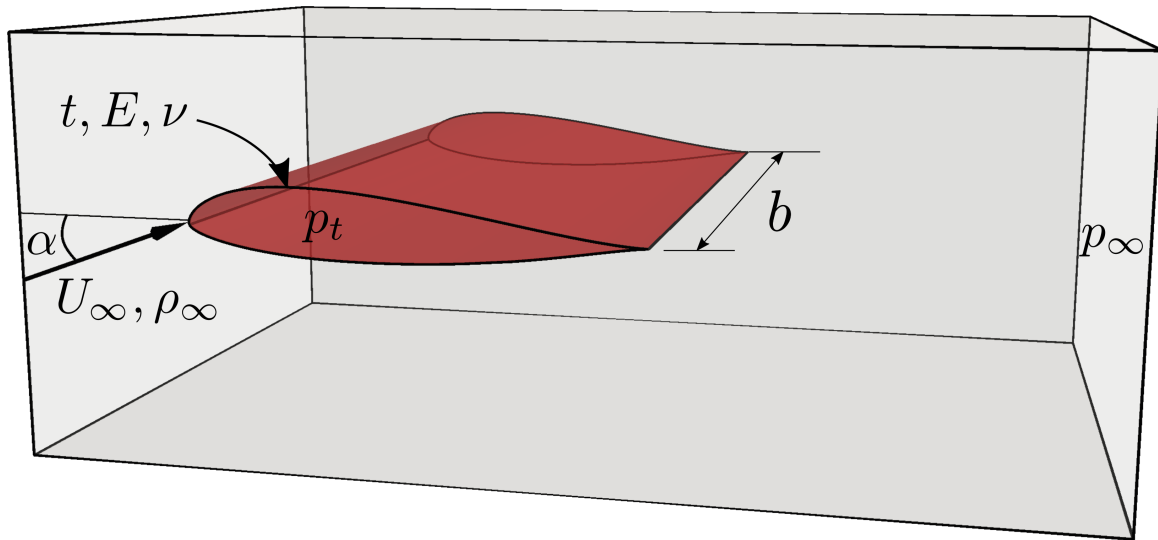
Figure 2: Inflated wing in virtual wind tunnel.
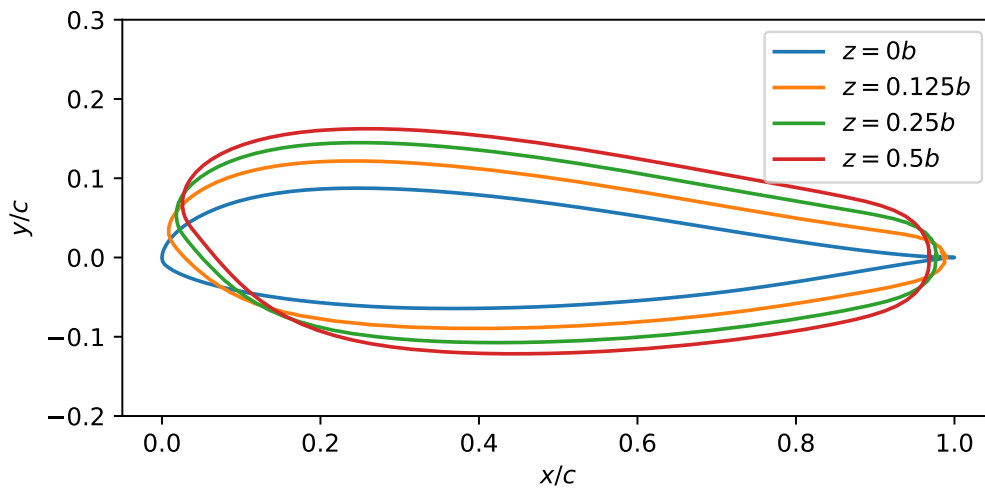
Figure 3: Cross-sections of the deformed inflated wing section at $10°$ angle of attack.

Acknowledgments

References

[1] R. Schmehl, Ed., *Preface. Airborne Wind Energy*, ser. Green Energy and Technology. Springer, 2018.

[2] A. Gambier, I. Bastigkeit, and E. Nippold, *Projekt OnKites II : Untersuchung zu den Potentialen von Flugwindenergieanlagen (FWEA) Phase II*. Final Project Report, Fraunhofer Institute for Wind Energy and Energy System Technology IWES Bremerhaven, Germany, 2017.

[3] Tools for inflatable kite design. Visited on 2018-04-12. [Online]. Available: http://www.wingdesignsoftware.net/indexEN.htm

[4] M. R. Barnes, "Form finding and analysis of tension structures by dynamic relaxation," *International journal of space structures*, vol. 14, no. 2, pp. 89–104, 1999.

[5] FOAM-FSI repository. Visited on 2018-05-18. [Online]. Available: https://github.com/davidsblom/FOAM-FSI

[6] foam-extend repository. Visited on 2018-05-18. [Online]. Available: https://sourceforge.net/projects/foam-extend/

[7] OpenCFD, *OpenFOAM: The Open Source CFD Toolbox. User Guide Version 1.4, OpenCFD Limited*. Reading UK, Apr. 2007.

NUMERICAL SIMULATION OF WAVE RUN-UP OF A SUBMERSIBLE PLATFORM USING OPENFOAM

YANG LIN[1], LIAO KANG PING[2], MA QING WEI[3]

[1] College of Shipbuilding Engineering, Harbin Engineering University, China,
yanglin205@163.com

[2] College of Shipbuilding Engineering, Harbin Engineering University, China,
liaokangping@hrbeu.edu.cn

[3] School of Engineering and Mathematical Sciences, City University London, United Kingdom
qw_ma2004@yahoo.co.uk

Abstract:

A numerical simulation of wave run-ups and wave loads on a model scale semi-submersible offshore platform was conducted using interFoam solver combining the wave module in openFOAM 5.0.For interFoam simulation, a high-quality block-based structured grid is generated by ANSYS-ICEM 17.0 and then exported to openFOAM. Grids between the inlet and the platform are carefully refined to minimize numerical dissipations avoiding unphysical wave height reductions. A vertical damping technique is adopted for wave relaxation which applying an explicit damping force to components of the vector field in the direction of gravity. Wave elevation at different locations are monitored by interfaceHeight utility in openFOAM 5.0 and the pressure loads are probed at target points lies on the columns and under deck of the platform.

0.introduction

The wave run-up is a complex nonlinear phenomenon due to the interactions between marine structures and waves, currents, which is widely encountered in offshore engineering applications. This paper tries to validate the suitability of the incompressible multiphase flow solver interFoam in openFOAM 5.0[1] with the newly added wave module to simulate wave run-up phenomenon.

Two extensively concerned physical index of wave run-up are wave elevations at specific positions and wave impacting loads on marine structures. These numerical results are obtained by using interfaceHeight utility and probe utility in OpenFOAM 5.0 with a properly positioned virtual monitoring points and wave gauge locations as can be seen in Fig.1(a).

1.Geometries and numerical set up

This model scale submersible platform has dimensions of 4.58×0.35×0.36×0.32[m](Length×Width×Height×Draft), and simulated in the numerical computational domain with the size of 25×2×2[m] of which inlet is approximately one wave length upstream the fixed platform. The platform geometries and the computational domain are illustrated in Fig.1.

A block based structured grids (depicted in Fig.2) generated by ANSYS ICEM 17.0 instead of snappyHexMesh are utilized in this paper.The incident wave is set to be 5th-stokes wave with wave length of 5.49 m and wave height of 0.4m. The length of wave relaxation zone is set to be 11m (approximately two wave length) in the outlet region to avoid reflections. The damping type and damping coefficient Lambda are set to be verticalDamping and 1.0, respectivrly.
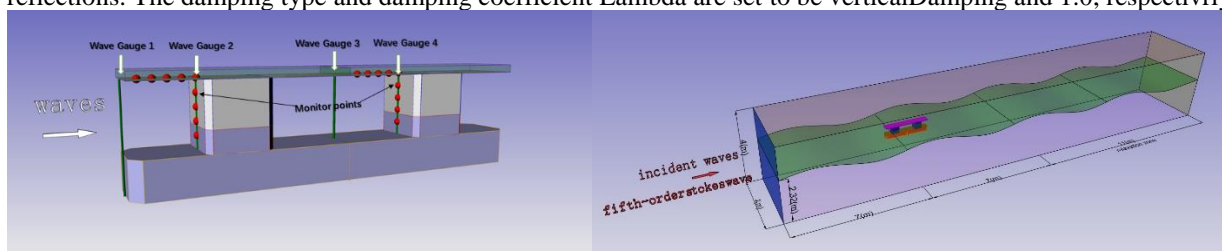
Fig.1 (a) Geometries and virtual monitoring points   (b) computational domain
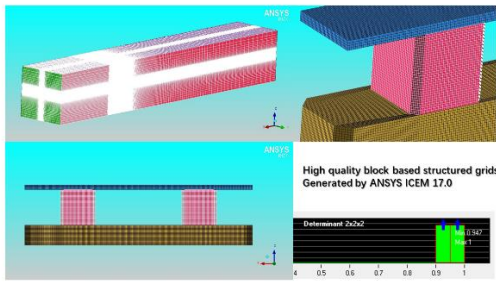
Fig.2   Computational mesh   Fig.3   wave impact and breaking waves
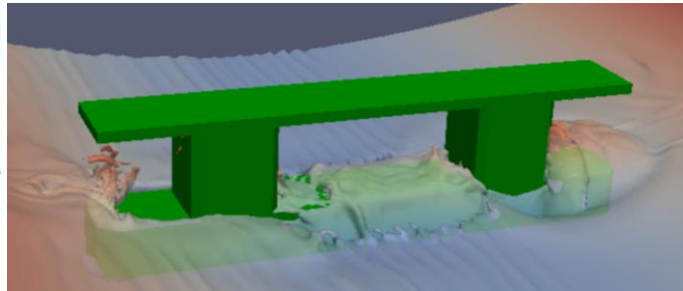
2.Numerical cases and results

2.1 grid convergent study

The numerical diffusion origins from low order discretization scheme of the convection term and insufficient grid size in the vicinity of the free surface can cause severe wave height reduction which is a major shortcoming compared with traditional potential solvers. For the discretization of convection terms, the Gauss linearUpwindV is used for momentum equations and Gauss vanleer for VOF equation. Numerical cases with different grids in a wave length and a wave height are conducted to investigate the relation between wave height reduction and grid size. The elevation at the position one wave length away from the inlet are monitored and illustrated in Fig 4 and Fig5. For a grid with 100 grids in a wave length and 10 grids in a wave amplitude (20 grids in a wave height) it is donated as X100A10 in this paper. Since the main purpose of this part is to exam the grid size's effect on wave height reduction, all cases are running without the submersible platform and the left/right patches are set to empty boundary condition to run the interFoam solver in 2D mode.

As can be seen from Fig.4 and Fig.5, given 100 grids in every wave length, refining the mesh in a wave amplitude from 10 to 40 brings little change to the wave height reduction and similar results are observed in refining the mesh in wave length direction from 100 to 300 with 40 grids in every wave amplitude, both of which all suffers severer wave height reduction. Specifically, the observed wave height for X100A40 and X300A40 are 0.245 (m) and 0.279(m), respectively, corresponding to wave height reductions of 38.75% and 30.28% since the initialized wave height is 0.4 (m). These results are actually unexpected and the reasons remained unclear since the wave module in openFOAM 5.0 is quite new. A screen shot of the wave profile at the end of the run time simulation of X100A10 is exhibited in Fig.6 showing that the wave is effectively relaxed with the explicit damping technique.
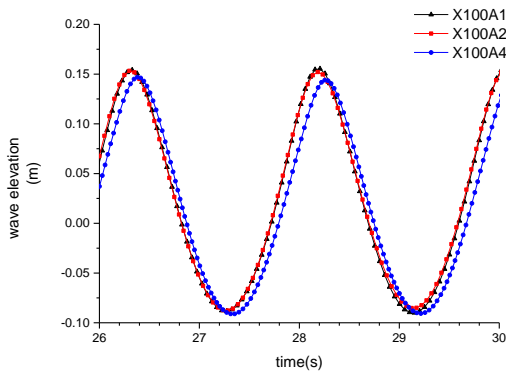
Fig.4 refining mesh in wave length direction   Fig.5 refining mesh in wave height direction
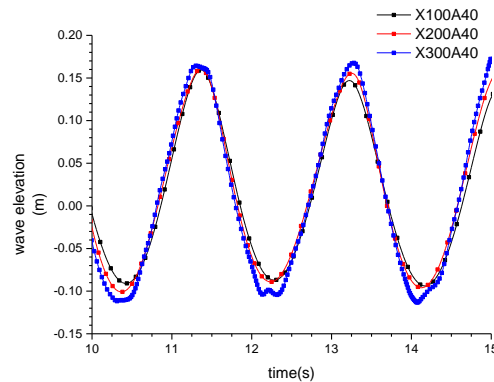
Fig.6 wave profile of X100A10

2.2 wave run-up results of openFOAM

In this submitted abstract, a numerical case with approximately 5 million hexahedrons is conducted to provides some tender results which definitely need further improvements either in mesh refinements or algorithm justification. The wave run-up and wave breaking phenomenon are observed in Fig.3. The wave elevation above the platform bottom at 4 gauges can be seen in Fig.7.

Fig.7 wave run up height above the bottom of the platform

Acknowledgements

References

[1] OpenCFD, OpenFOAM: The Open Source CFD Toolbox. User Gide Version 5.0, OpenCFD Limited. Reading UK, July. 2017.

NUMERICAL SIMULATION OF VORTEX-INDUCED VIBRATION FOR A REAL SIZE DRILLING RISER SYSTEM WITH AUXILIARY LINES

TENGTENG KONG[1, 2], WENBO WU[1, 2, 3], JIASONG WANG [1, 2*]

¹Department of Engineering Mechanics, School of Naval Architecture, Ocean and Civil Engineering,
Shanghai Jiao Tong University, 200240, China
*jswang@sjtu.edu.cn
²Key Laboratory of Hydrodynamics（Ministry of Education）, Shanghai Jiao Tong University
³School of civil engineering, Guangzhou University, 510006, China

Keywords: *riser system；auxiliary line；vortex-induced vibration；vortex shedding；numerical simulation*

In our recent study on the flow control modeling for a drilling riser system with auxiliary lines, it was shown that the auxiliary lines can suppress the vortex shedding on the main riser at all incidence angles [1]. This finding is of significance to the real engineering of drilling operation. Here we further simulate the vortex-induced vibration (VIV) response for this real-size drilling riser system in service in the South China Sea by the secondary development of OpenFOAM platform. By simulating the VIV of the riser system at various angles of attack under typical reduced velocity, the influence of the flow direction on the vortex shedding and response process of the riser system was analyzed. The obtained results indicate that the auxiliary lines can effectively suppress the vortex shedding on the main cylinder and reduce the amplitude due to the clamping of the downstream auxiliary lines, but the effect is greatly related to the angle of attack. The VIV of a real-size drilling riser system does not show an upper branch and the amplitude is much smaller than the amplitude of a single cylinder.

1. Introduction

The vortex-induced vibration of a circular cylinder has encountered in a lot of practical engineering fields, especially in the offshore engineering. As a consequence of significant interactions of vortex shedding and structural dynamics, VIV will cause fatigue damage and thus seriously affect the engineering operations and may even bring environmental accidents. In last several decades, the mechanism of VIV has been studied in detail, both experimentally and numerically. Zhao et al. [2,3] studied the vibration response of two cylinders at low Reynolds numbers for tandem and parallel rigid connections. Rahmanian et al. [4] studied the VIV characteristics of staggered rigidly mounted cylinders and found that there may be multiple locking zones in the vibration of the cylinder. Zhao & Yan [5] studied the characteristics of VIV when two cylinders with different diameters were staggered, and discussed the effects of gap and incoming angle of attack on the locking zone. The coupled motion of multiple cylinders (triple cylinders and above) is rarely seen in literature. This article starts from 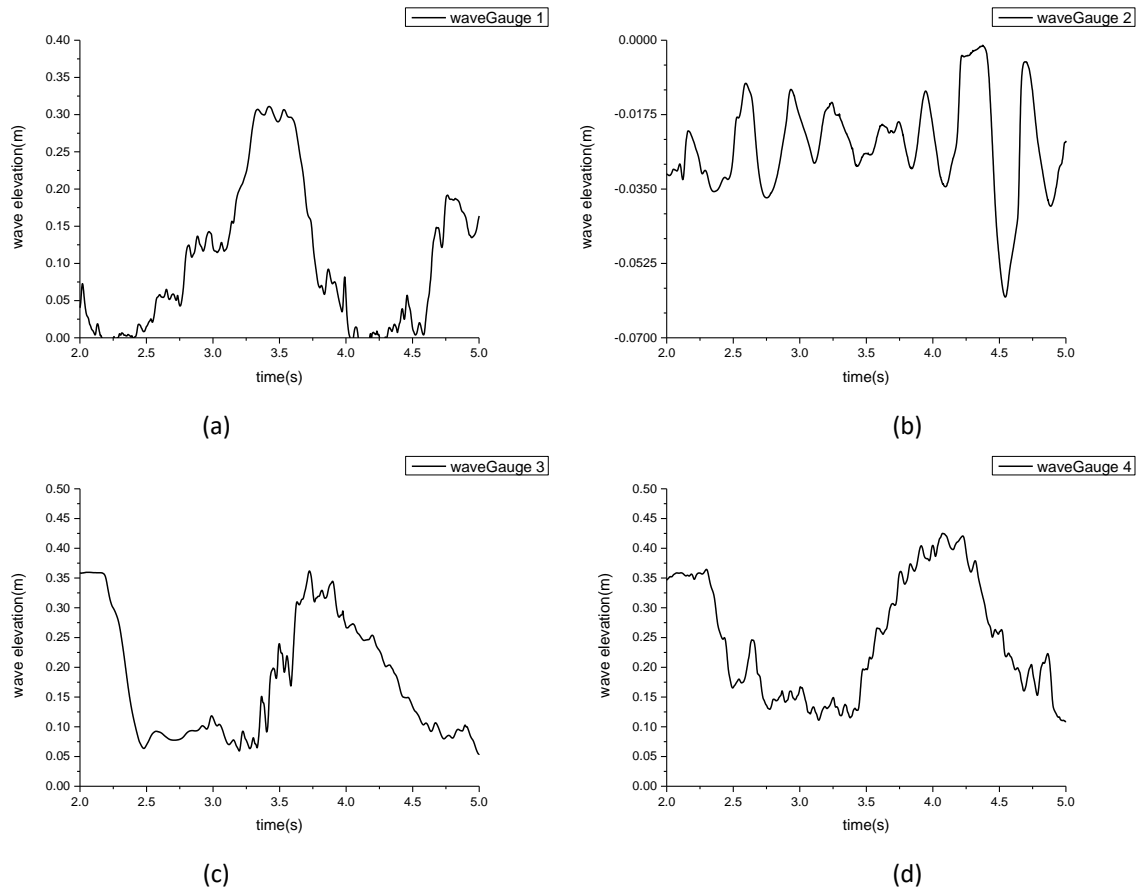the actual engineering background and simulates the vortex-induced vibration response of a real-size drilling riser system.

2. Problem description

Fig.1 is the sketch of the cross section of a real drilling riser system with auxiliary lines. In the riser system, the auxiliary lines had different diameters and distributed asymmetrically around the main line. The complicated flow was investigated based on the different incidence angles. In Fig.1, α represents the incidence angle of the flow, θ is the circumferential angle of the main line, U is the free stream velocity of the flow. The diameter of the main line is represented as D, the diameters of the auxiliary lines in the riser system and the geometrical parameters are shown in Fig.1. All the cylinders in the riser system were rigidly connected, i.e. the risers moved synchronously at any time.
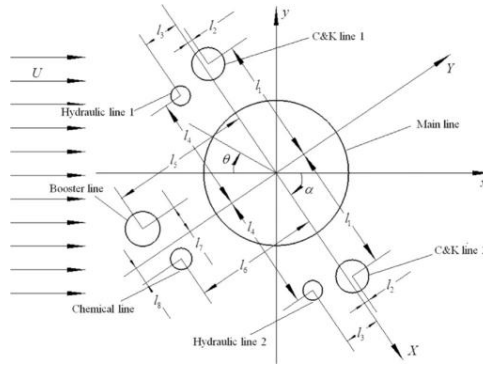
Fig.1 Sketch of the model for a real drilling riser system

Fig.2 shows that the risers can move in the in-line and cross flow directions simultaneously, and the stiffness coefficient and the damping coefficient are the same in both directions. The vortex-induced vibration of the drilling riser system at different angles of attack can be obtained by changing the angle of attack at the incoming flow.
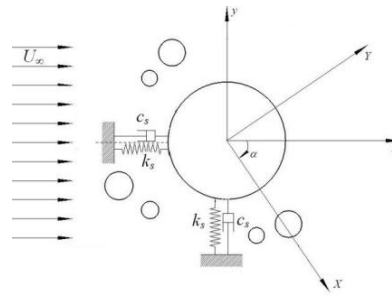
Fig.2 Sketch of the model for VIV of a real drilling riser system

3. Governing equations and computational model

In this paper, the secondary developed OpenFOAM was used to compute the VIV of the riser system by the finite volume method, and all cylinders moved synchronously and were modeled using a single spring oscillator model. The analytical form of the governing equations of unsteady flow of viscous incompressible fluid in Cartesian coordinates can be expressed as follows:

$$\frac{\partial U_i}{\partial x_i} = 0 \tag{1}$$

$$\rho \frac{\partial U_i}{\partial t} + \rho \frac{\partial}{\partial x_i}\left(U_j U_i\right) = \mu \frac{\partial^2 U_i}{\partial x_j \partial x_j} - \frac{\partial p}{\partial x_i} + \frac{\partial \tau_{ij}}{\partial x_j} \tag{2}$$

where μ is the molecular dynamic viscosity, U is the time-average velocity vector of the fluid, τ is the Reynolds stress tensor, p is the pressure, ρ is the density of the fluid. K-ω model was used here, and the Reynolds stresses were computed in two-equation models with the Boussinesq expression.

4. Validation of tandem cylinders

In order to validate the computational method in this paper, the results of VIV of single circular cylinder and tandem cylinders computed with OpenFOAM were compared with the results of other researchers. The non-dimensional transverse displacement (A^*_y) and non-dimensional transverse frequency (f^*_y) were defined as:

$$A^*_y = \frac{A_y}{D} \, , \, f^*_y = \frac{f_y}{f_n} \tag{3}$$

where A_y is the displacement in the cross-flow direction, D is the diameter of the cylinder, f_n is the natural frequency of the riser system, f_y is the frequency of the transverse vibration of the cylinder, which the value is equal to the vortex shedding frequency and calculated by the FFT of the lift coefficient.

Assi et al. [6] studied the wake-induced vibration(WIV) in a tandem arranged system. Two cylinders were placed in series, and the distance between the centers of the cylinders was P. The upstream cylinder was stationary, and the downstream cylinder could only vibrate in the cross-flow direction. Both cylinders had a diameter of D and a uniform flow velocity of U. It can be seen from Fig.3 that the RMS amplitude of the downstream cylinder agrees well with the results of Assi et al. [6] , and the numerical difference is not obvious; the variation trend of the amplitude with reduced velocity is the same as that of Assi et al. [6], which can reflect the WIV amplitude of the downstream cylinder continues to increase as the reduced velocity increases. Therefore, it can be considered that the error between the results of this paper and the results of Assi et al. [6] is within the experimentally acceptable error.
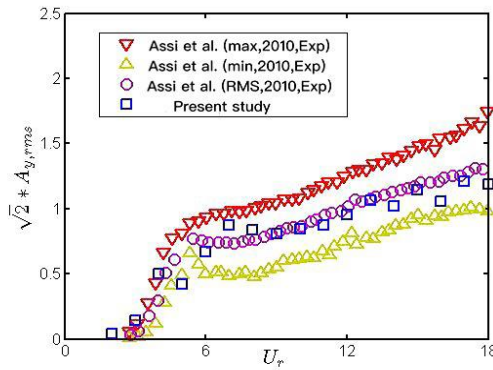
Fig.3 The vortex-induced vibration amplitude of the downstream cylinder

5. Results and discussions

In this section, the results and discussions about this simulation were given from the vibration amplitudes to flow fields. Fig.4 shows the amplitudes of VIV at various incoming angles of attack for a real-size drilling riser system. In order to more clearly show the variation at different angles, the amplitudes are shown in the different diagrams according to the flow patterns described in Wenbo Wu et al. [1]. CVP there represents the clamped vortices pair mode, and SVF is the single vortex forming mode.

As can be seen from Fig.4, the upper branch of the riser system does not appear at any angle of attack, and its amplitude is much smaller than that of a single cylinder, especially at 210°, 300° and 330°, the amplitudes are almost close to zero.

(a) CVP   (b) SVF
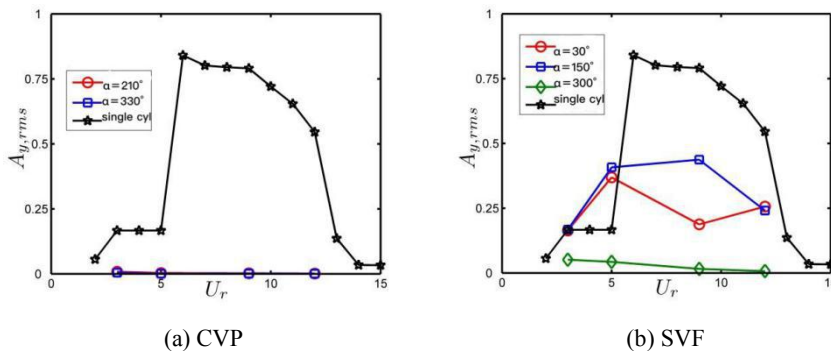
Fig.4 The vortex-induced vibration amplitude of the riser system at different incidence angles

From the analysis in the previous section, it can be known that the VIV of the drilling riser system is very weak at some angles of attack and can be considered as a static cylinder system. In practical conditions, the stability of the riser has a significant impact on the ease of drilling operations and the risk factor. Therefore, the flow field near the cylinder system during the vortex-induced vibration of the riser is further analyzed and studied.

Fig.5 shows the vorticity contour at the reduced velocity corresponding to the maximum amplitude of the cylinder system under different angles of attack. Each diagram corresponds to the time when the riser system is located at the valley value. It can be seen from Fig.5 that the vortices near the riser system are affected by multiple auxiliary lines and the vortices are irregularly distributed. As can be seen from Fig.4(a), almost no vortex-induced vibration occurs in the riser system at 210° and 330°. According to the vorticity contour, at 210° and 330°, the shear layer on the main line is

confined to a very small area by the downstream auxiliary lines, and disappears quickly due to the interaction, so obvious discrete vortices in the riser system wake cannot be observed.

(a) α=210° , Ur=3   (b) α =330° , Ur=3
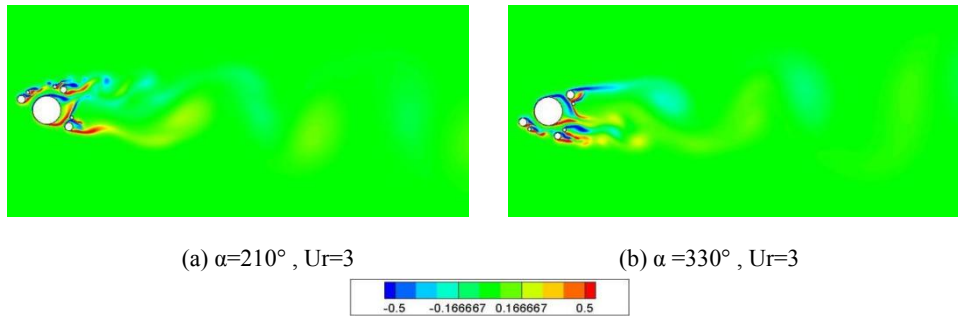
Fig.5 The vorticity contour near the riser system

6. Conclusions

In this paper, the vortex-induced vibration of a real-size drilling riser system under various attack angles was numerically simulated by the second developed OpenFOAM platform. The obtained results indicated that the auxiliary lines can effectively suppress the vortex shedding on the main cylinder and reduce the amplitude, but the effect is greatly related to the angle of attack. When auxiliary lines were located downstream of the main line, the VIV was so weak because the main line cannot shed vortex due to the clamping of the downstream auxiliary lines, especially at 210°, 300° and 330°, the amplitudes were almost close to zero. However, due to the characteristics of multi-cylinder, multi-size, irregular arrangement, etc., this article cannot analyze the role of each sub-cylinder in the riser system, nor can it discuss the effect of auxiliary lines in the joint action of the riser system to the main line. Therefore, it is necessary to simplify the model and conduct more in-depth research.

References

[1] Wenbo Wu, Jiasong Wang, Shiquan Jiang,et al. Flow and flow control modeling for a drilling riser system with auxiliary lines. Ocean Engineering, 2016, 123: 204-222.

[2] Zhao, M. Flow induced oscillation of two rigidly coupled circular cylinders intandem and side-by-side arrangements at a low Reynolds number of 150 [J]. Physics of Fluids, 2013, 25: 123601.

[3] Zhao, M., Murphy, J.M. and Kwok, K. Numerical simulation of vortex induced vibration of two rigidly connected cylinders in side-by-side and tandem arrangements using RANS model [J]. Journal of Fluids Engineering, 2016, 138: 021102.

[4] Rahmanian, M., Zhao, M. and Cheng, L. et al. Two degree of freedom vortex induced vibration of two mechanically coupled cylinders of different diameters in steady current [J]. Journal of Fluids and Structures, 2012, 35: 133-159.

[5] Zhao, M. and Yan, G. Numerical simulation of vortex induced vibration of two circular cylinders of different diameters at low Reynolds number [J]. Physics of Fluids, 2013, 25: 083601.

[6] Assi, G.R.S., Bearman, P.W. and Meneghini, J.R. On the wake-induced vibration of tandem circular cylinders: the vortex interaction excitation mechanism [J]. Journal of Fluid Mechanics, 2010, 661: 365-401.

NUMERICAL INVESTIGATIONS ON VORTEX-INDUCED VIBRATION OF A FLEXIBLE CYLINDER EXPERIENCING COMBINED FLOW

DI DENG[1], ZHE WANG[2], DECHENG WAN[*]

[1]*Collaborative Innovation Center for Advanced Ship and Deep-Sea Exploration, State Key Laboratory of Ocean Engineering, School of Naval Architecture, Ocean and Civil Engineering, Shanghai Jiao Tong University, Dengdi@sjtu.edu.cn*

[2] *Collaborative Innovation Center for Advanced Ship and Deep-Sea Exploration, State Key Laboratory of Ocean Engineering, School of Naval Architecture, Ocean and Civil Engineering, Shanghai Jiao Tong University, wangzhe2016@sjtu.edu.cn*

[*]*Corresponding author, dcwan@sjtu.edu.cn*

1.INTRODUCTION

Vortex-Induced Vibration (VIV) is the main source of risers' fatigue damage. In actual production, offshore floating structures subject to waves, currents or winds may cause the platform to move periodically in the water. Then relatively oscillatory flow is generated between the riser and the water. In recent decades, researches of the sinusoidal motion of a cylinder in viscous fluid have been extensively studied. Fu[3] has taken experimental studies on VIV of a flexible cylinder in oscillatory flow for different KC numbers and raise the VIV development process of build-up, lock-in and die-out. Zhao[2] has carried out numerical simulations of a circular cylinder in combined oscillatory and steady flow. In this paper, VIV of a flexible cylinder experiencing combined uniform and oscillatory flow is investigated numerically based on experiments of Fu[3]. The flow ratio α of the uniform flow in the total combined flow increase from 0 to 1 through an interval of 0.5.

2.METHOD
2.1 Hydrodynamics governing equations

The flow field is supposed to be incompressible, with constant dynamic viscosity μ and constant density ρ. The Reynolds-averaged Navier-Stokes equations are used as the hydrodynamics governing equations as follow:

$$\frac{\partial \overline{u}_i}{\partial x_i} = 0 \tag{1}$$

$$\frac{\partial}{\partial t}\left(\rho \overline{u}_i \right) + \frac{\partial}{\partial x_j}\left(\rho \overline{u}_i \overline{u}_j \right) = -\frac{\partial \overline{p}}{\partial x_i} + \frac{\partial}{\partial x_j}\left(2\mu \overline{S}_{ij} - \rho \overline{u_j' u_i'} \right) \tag{2}$$

where $\overline{S}_{ij} = \frac{1}{2}\left(\frac{\partial \overline{u}_i}{\partial x_j} + \frac{\partial \overline{u}_j}{\partial x_i} \right)$ is the mean rate of strain tensor, $-\rho \overline{u_j' u_i'}$ is referred as Reynolds stress τ_{ij} computed by

$\tau_{ij} = -\rho \overline{u_j' u_i'} = 2\mu_t \overline{S}_{ij} - \frac{2}{3}\rho k \delta_{ij}$, where μ_t is the turbulent viscosity and $k = (1/2)\overline{u_i' u_i'}$ is the turbulent energy, computing from the fluctuating velocity field.

2.2 Structural dynamics governing equations

In order to form the relatively oscillatory flow, the supporting frame was forced to oscillate harmonically. The oscillation can be expressed as:

$$x_s = A_m \cdot \sin(\frac{2\pi}{T}t) \tag{3}$$

$$U_s = \frac{2\pi \cdot A_m}{T} \cdot \cos(\frac{2\pi}{T}t) = U_m \cdot \cos(\frac{2\pi}{T}t) \tag{4}$$

$$KC = \frac{2\pi \cdot A_m}{D} = \frac{U_m \cdot T}{D} \tag{5}$$

where A denotes the oscillating amplitude，T is the oscillating period, x_s is the oscillating displacement，U_s is the oscillating velocity ，U_m is the amplitude of the oscillating velocity ，D is the diameter of the cylinder。
Fu[1] uses the support excitation method combined with the Bernoulli–Euler bending beam theory to obtain the structural response of the cylinder. The in-line displacement of the cylinder is the sum of support frame motion and the relative in-line vibration of the cylinder:

$$x_t = x_s + x \tag{6}$$

where x_t is the in-line displacement, x_s is the support motion and x is the relative in-line displacement.

The equilibrium of forces for this system can be written as follow:

$$f_I + f_D + f_S = f_H \tag{7}$$

where f_I, f_D, f_S, f_H are the inertial, the damping, the spring, and the hydrodynamic force, respectively.

Then the equilibrium of forces for the system can be written as:

$$m\ddot{x}_t + c\dot{x} + kx = f_H \tag{8}$$

$$m\ddot{x} + c\dot{x} + kx = f_H - m\ddot{x}_s \tag{9}$$

where m, c, k are the mass, the damping and the stiffness of the system.

In the finite element method(FEM), the equations can be discretized as:

$$\mathbf{M\ddot{x} + C\dot{x} + Kx = F_{Hx} - M\ddot{x}_s} \tag{10}$$

$$\mathbf{M\ddot{y} + C\dot{y} + Ky = F_{Hy}} \tag{11}$$

Where **M**, **C**, **K** are the mass, the damping and the stiffness matrices, while **x**, **x$_s$** and **y** are the relative in-line, the support and the cross-flow nodal displacement vectors. **F$_{Hx}$** and **F$_{Hy}$** are the hydrodynamic force in the in-line and cross-flow direction respectively.

2.3 Strip method

In this paper, numerical investigations are carried out by viv-FOAM-SJTU solver based on the strip method and the pimpDyMFOAM solver attached to the open source code OpenFOAM. The strip method is very appropriate for solving CFD investigations of supramaximal computational domain. It owns high computational efficiency and the computational accuracy is reliable, The reliability of the viv-FOAM-SJTU solver has been testified by Duan[4], in which the benchmark case has been verified in detail.

For a long flexible cylinder, a direct computation of the three dimensional flow field will cost too much resources. Instead of this, we simplify CFD model and obtain the two dimensional flow field on strips distributed equably along the cylinder. The hydrodynamic force is obtained from each strip, which is then applied to the structural field. The structural displacements of all nodes are interpolated to get the boundary motion of dynamic mesh of flow field. The strip theory is shown as figure 1.

During the numerical simulations, the RANS equations and SST k-ω turbulence model are adopted to solve the flow field in each strip, while the whole structure filed is solved through Bernoulli–Euler bending beam theory with the finite element method. The fluid-structure interaction is carried out by loose coupling strategy.
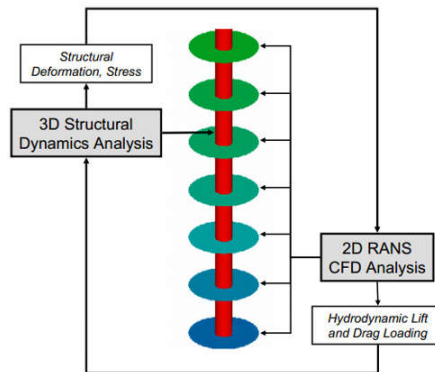
Figure 1: Schematic diagram of strip theory

3. PROBLEM DESCRIPTION

3.1 CFD model

The numerical model follows experiments of Fu[1] and the layout of the experiments is shown in figure 2. Detailed information about parameters of the cylinder is shown in Table 1. 20 strips located equidistantly along the cylinder. Figure 3 shows the distribution of strips. Figure 4 shows the entire computational domain and meshes of strips.
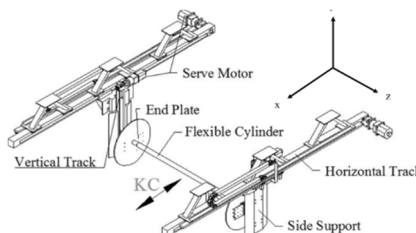
Figure 2: Layout of the experiments of Fu et al

Table 1: Main parameters of the cylinder

	Symbols	Values	Units
Mass ratio	m^*	1.53	–
Diameter	D	0.024	m
Length	L	4	m
Bending stiffness	EI	10.5	$N \cdot m^2$
Top tension	T_t	500	N
First natural frequency	f_n^1	2.68	Hz
Second natural frequency	f_n^2	5.46	Hz
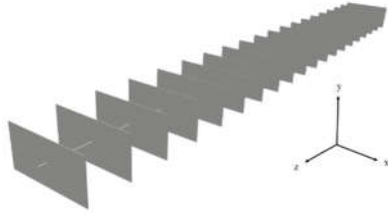
Figure 3: Illustration of multi-strip model
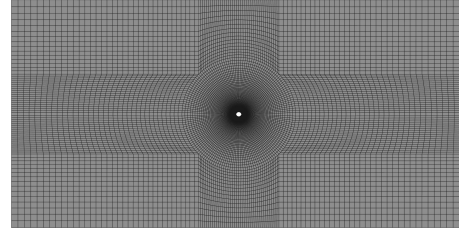
Figure 4: Computational domain and mesh of a strip

3.2 Computational conditions

According to equations (3) and (4), the total velocity and the flow ratio can be written as equations (12) and (13).

$$U_c\left(t\right) = U_s + U_m \cos(\frac{2\pi}{T}t) = U_s + A_m \frac{2\pi}{T}\cos(\frac{2\pi}{T}t) \tag{12}$$

$$\alpha = \frac{U_s}{U_s + U_m} = 1 - \frac{A_m}{U_c} \cdot \frac{2\pi}{T} \tag{13}$$

where U_s is the uniform flow velocity, U_c is the total velocity, A_m is the amplitude of the oscillation, T is the oscillating period.

4 RESULTS

Figure 5 shows subplots of non-dimensional cross-flow amplitude of the intermediate node of the cylinder between experiment and simulation. From comparison, it can be concluded: (i)the development process of "Building-up—Lock-in—Dying-out" of vortex-induced vibration is observed in both experiment and numerical simulation; (ii)the lock-in region is 17.3% of the half oscillating period in numerical simulation, which is close to the experiment result of 17%; (iii)the non-dimensional cross-flow amplitude is 0.37D in half oscillating period, which is close to the experiment result of 0.36D.
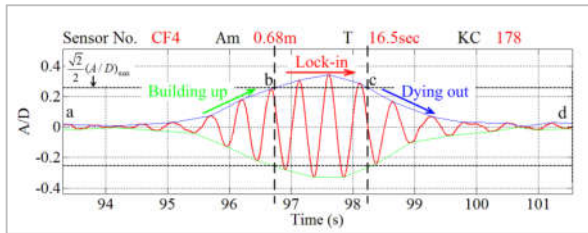
(a)Result of Fu et al.
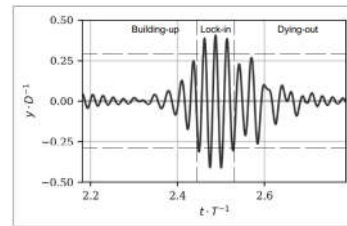
(b)The present simulation

Figure 5: Non-dimensional cross-flow amplitude of the intermediate node in half an oscillating period

Figure 6 shows subplots of non-dimensional cross-flow amplitude of the intermediate node of the cylinder in three flow ratios. It can be known that when flow ratio equals 0, the cylinder is in pure oscillatory flow. And two obvious VIV development processes can be observed in an oscillating period. When flow ratio equals 1, the cylinder is in pure uniform flow. And the obvious VIV phenomenon occurs through the whole computational process. While flow ratio equals 0.5, only one obvious VIV development process can be observed when the oscillatory flow and the uniform flow are in the same direction. Figure 7 shows subplots of Modal weights of each vibration mode of the cylinder for different flow ratios. We can know that the cylinder mainly vibrates in the 1st mode and the effects higher modes of 2nd and 3rd are relatively small. Figure 8 shows subplots of wavelet analysis of the cross-flow displacement. When flow ratio equals 0 and 1, the dominant vibration frequency of the cylinder is close to the first natural frequency of 2.68Hz. While flow ratio equals 0.5, the vibration frequency transition happens in each oscillating period. The dominant vibration frequency is approximately the 1st natural frequency when the oscillatory flow is in the same direction with the uniform flow. And the dominant vibration frequency turns to be approximately 0 when flows are in adverse direction.

(a)$\alpha=0$ (b)$\alpha=0.5$ (c)$\alpha=1.0$
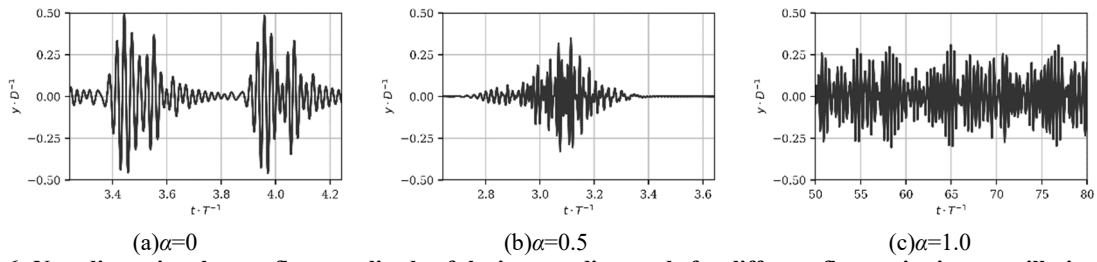
Figure 6: Non-dimensional cross-flow amplitude of the intermediate node for different flow ratios in an oscillating period

(a)$\alpha=0$ (b)$\alpha=0.5$ (c)$\alpha=1.0$
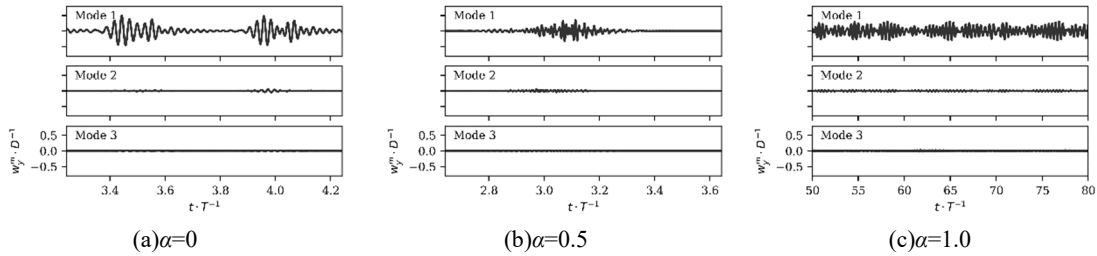
Figure 7: Modal weights of each vibration mode of the cylinder for different flow ratios

(a)$\alpha=0$ (b)$\alpha=0.5$ (c)$\alpha=1.0$
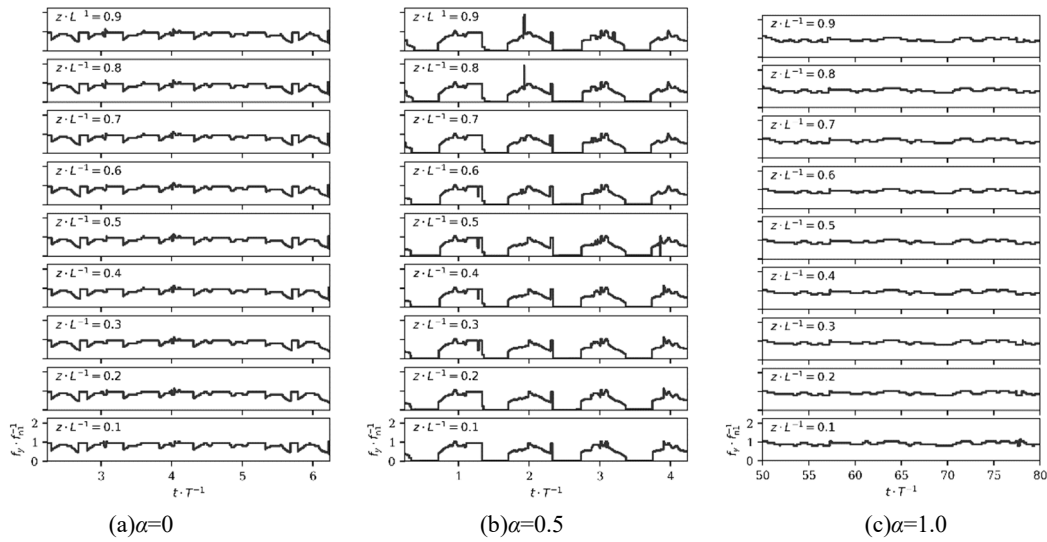
Figure 8: Cross-flow wavelet analysis of the cylinder for different flow ratios

Acknowledgements

References

[1] B. W. Fu et al. Numerical study of vortex-induced vibrations of a flexible cylinder in an oscillatory flow. Journal of Fluids and Structures, 2018, 77:170-181.

[2] M. Zhao et al. Vortex-induced vibration (VIV) of a circular cylinder in combined steady and oscillatory flow. Ocean Engineering, 2013, 73:83-95.

[3] S. X. Fu et al. VIV of Flexible Cylinder in Oscillatory Flow. Int Conf on Offshore Mech and Arctic Eng, OMAE, Nantes, France, June 9–14, 2013, pp. V007T08A021.

[4] Y. Duanmu et al. Prediction of Response for Vortex-Induced Vibrations of a Flexible Riser Pipe by using Multi-Strip Method. Proc 26th Int Offshore and Polar Eng Conf, ISOPE, Rhodes, Greece, 26 June-2 July, 2016, 65-1073.

ANALYSIS OF FLOW-INDUCED VIBRATION OF NUCLEAR STREAM GENERATOR F U-TUBES USING OPENFOAM

XIAO YE, RUN DU[*], XIAOYU ZHANG PINGDI REN

School of Mechanical Engineering, Southwest Jiaotong University, Chengdu 610031, China
[*]*Corresponding author: rdu@swjtu.edu.cn*

Keywords: OpenFoam; Flow-induce vibration; U-tube

Nowadays nuclear power is increasingly used in the occasion of energy supply. However some problem also might happen in nuclear power plant, especially the steam generator, which could lead to serious consequence and must be paid much attention to. In the steam generator(SG),the u-tubes will interactor with the support plant because of fluid induced vibration(FIV)caused by high-speed water in SG. At the first place, I give an introduction of SG structure and the mathematic model FSI(fluid structure interaction). Then I simulate this process by OpenFoam after modeling, meshing, initializing and FsiFoam programming, which is based on computational fluid dynamics (CFD)code. The simulation help us get the fluid-solid interaction details. How the fluid forces interact with U-tubes were explained. The flow region at the U-tube and fixure contact area has been detailed and analyzed, then the frequencies and amplitudes of vibration at the contact area were determined. This will lay the foundation for dynamic analysis of FSI in SG U-tubes and the reasons, and it also can help the scientists take more protection to avoid the negative effect of fluid induced vibration (FIV).

NUMERICAL SIMULATIONS OF VIV OF A FLEXIBLE CYLINDER WITH VARYING AXIAL TENSIONS

ZHE WANG[1], DI DENG[2], DECHENG WAN[3]

[1,2,3]*Shanghai Jiao Tong University, State Key Laboratory of Ocean Engineering, Collaborative Innovation Center for Advanced Ship and Deep-Sea Exploration, Shanghai 200240, China,*
[3]*Corresponding Author: dcwan@sjtu.edu.cn*

Keywords: *VIV, flexible cylinder, varying axial tension, viv-FOAM-SJTU solver*

Flexible cylindrical structures are widely used in the offshore scenario, such as deep-sea risers and tethers. Vortex-induced vibration of flexible cylinders has been extensively studied in the past decades. In actual production, the periodic heave motion of floating structures may generate a periodic impact towards the top-tensioned riser, which leads to a periodic tension. Because of the dynamic effect, the cylinder's natural characteristics change over time resulting in a continuous modal transition. Under the effect of time-varying tensions, the mechanism of vibration is different from the simple VIV problem. Previous researches have made great contributions on the stability problem [1] and vibration mode [2].

In this paper, numerical simulations are conducted by the in-house CFD code viv-FOAM-SJTU, which is developed based on the pimpeDyMFOAM solver attached to OpenFOAM. For a long flexible structure, a direct three-dimensional simulation of the flow field is accurate but cost too many resources. Instead, a simplified strip method is applied for solving CFD simulations of supramaximal computational domain. It owns high computational efficiency and the computational accuracy is reliable, which has been verified through related researches. The reliability of the viv-FOAM-SJTU solver has been validated by Duan and Wan [3] and Fu et al [4].

Several strips are distributed equally along the cylinder and simulations of fluid field are performed based on RANS equations and SST k-ω turbulence model. As for the structural field, the Euler-Bernoulli beam model and finite element method is used. Interpolation is used to realize the transformation of data between the fluid field and the structure field. The strip model and the procedure of fluid-structure interaction is shown in Fig. 1. The schematic diagram of the viv-FOAM-SJTU solver is shown in Fig. 2.
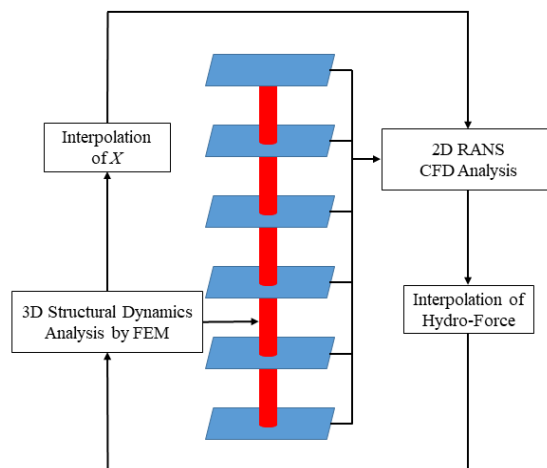
Fig 1: Schematic diagram of of the strip model and fluid-structure interaction
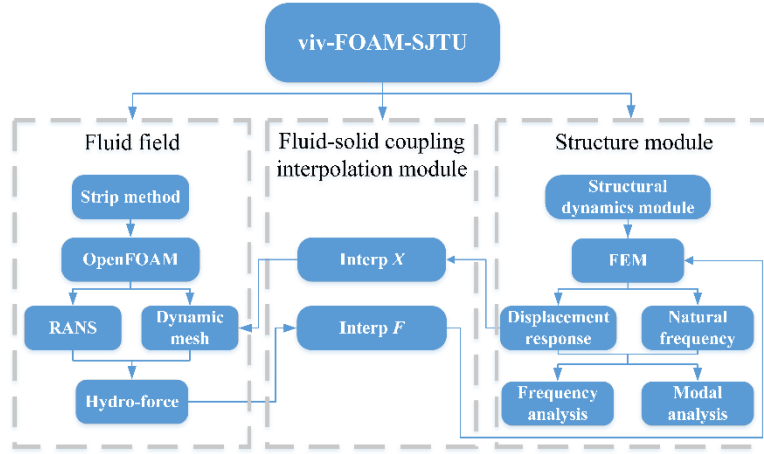
Fig 2: Schematic diagram of of the viv-FOAM-SJTU solver

In this paper, the flexible cylinder is simulated as a beam simply supported at both ends. The axial tension changes periodically and is a parametric excitation of the cylinder model. Twenty strips are set equidistantly along the cylinder with the same computational domain. The computational model and the initial mesh are shown in Fig. 3. The axial tension is assumed to change harmonically. Main parameters of the model and cases are listed in table1 and table 2. The first case is a VIV problem with constant tension and is chosen as a comparison. The second case is VIV of a flexible cylinder with time-varying tension. The frequency of the varying tension is 1.1410Hz, namely the first order natural frequency.
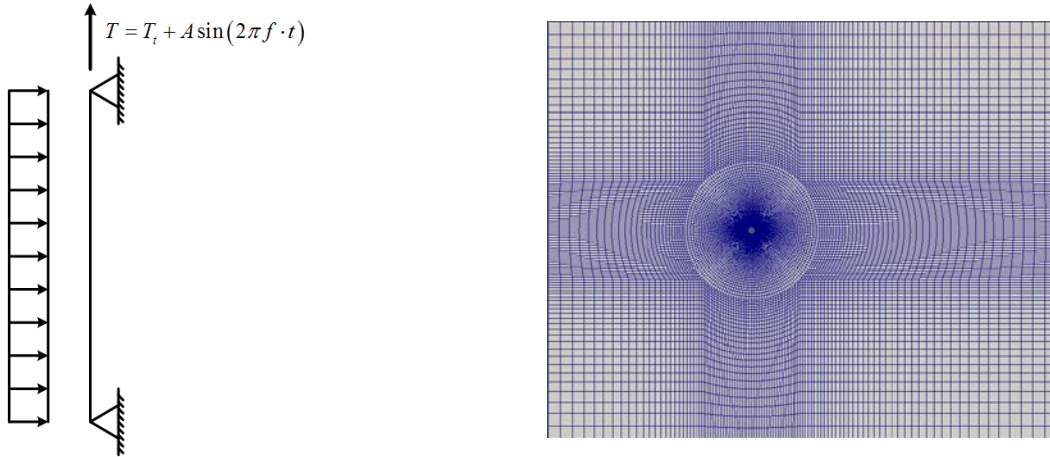
Fig 3: Strip model and the initial mesh on each strip

Table 1. Main parameters of the computational model

Parameter	Symbol	Value	Unit
Diameter	D	0.028	m
Length	L	14	m
Mass Ratio	m^*	2.4	-
Bending Stiffness	EI	29.88	$N \cdot m^2$
Flow Speed	U	0.4	m/s
Static Top Tension	Tt	1610	N
Varying Tension Amplitude	A	0/500	N
Varying Tension Frequency	f	1.14	Hz

Table 2. Main parameters of the cases

Case No.	Pre-Tension (N)	Varying Tension Amplitude (N)	Varying Tension Frequency (Hz)
Case 1	1610	0	0
Case 2	1610	500	1.14

Fig. 4 shows the vortex-shedding along the riser model. Vortices at different strips can be viewed clearly. Fig. 5 compares the standard deviation between the two cases in both in-line and cross-flow directions. The solid and dashed lines represent Case 1 and Case 2, respectively. For the in-line vibration, effect of the varying tension is obvious. The maximum STD displacements is about 0.1 for Case 1 and over 0.6 for Case 2, which is caused by internal resonances. In the in-line vibration, the cylinder appears as an arc under the effect of uniform flow, the shape of which is similar to the first mode

related to the first order natural frequency. When the tension varies at the first-order frequency at a relatively large amplitude, it inspires the internal resonances. Therefore, an obvious amplification is observed in the Fig. 5(a). For the cross-flow vibration, the amplification effect is little, as shown in Fig. 5(b). This is reasonable because there is no internal resonance for the cross-flow vibration.
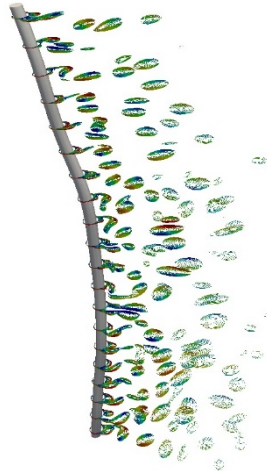
Fig 4: Vortex-shedding contour along the riser

(a)   **(b)**
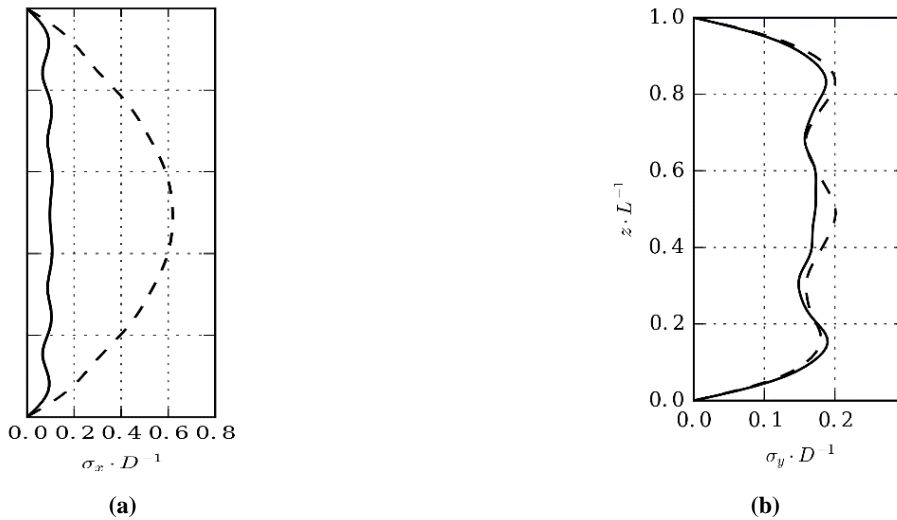
Fig 5: Standard Deviation of the displacements: (a) stands for the in-line vibration; (b) stands for the cross-flow vibration

Fig. 6 shows the comparisons of power spectral density of each mode and displacements at several places along the cylinder model in in-line direction. Under the effect of the varying tension, multi-modal vibrations are inspired. Previous researches have shown that a long flexible cylinder tends to vibrate at various modes (Willden and Graham [5] and Vandiver et al [6]). The time-varying tension changes the natural characteristics of the riser and inspires the multi-modal vibration of the cylinder model. The frequency component at the third mode equals to the frequency of the varying tension.

Fig. 7 shows the comparisons in cross-flow direction. Effects of the varying tension are not the same as the in-line vibration. The sub-harmonic vibration appears in the middle part of the cylinder (Fig. 7) which is a typical phenomenon in the parametric excitations caused by the nonlinearity of the system. Similar to the in-line vibration, more frequency components appear in the power spectral density figure. However, it is different that the varying tension do not dominate the vibration frequency and the original VIV frequency components are still obvious.

(a) Case1　　　　　　　　　　　　　　　　　　**(b) Case2**
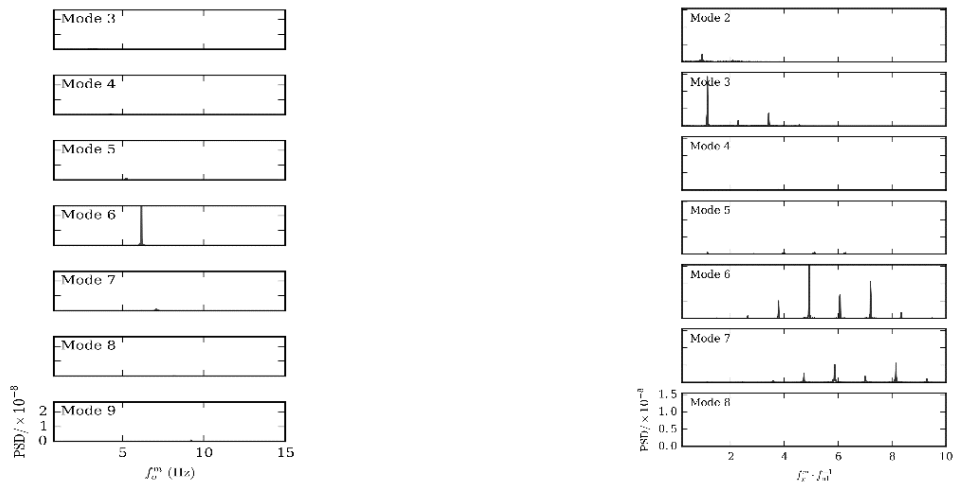
Fig 6: Comparison of modal power spectral density between case 1 and case 2 in the in-line direction

(a) Case1　　　　　　　　　　　　　　　　　　**(b) Case2**
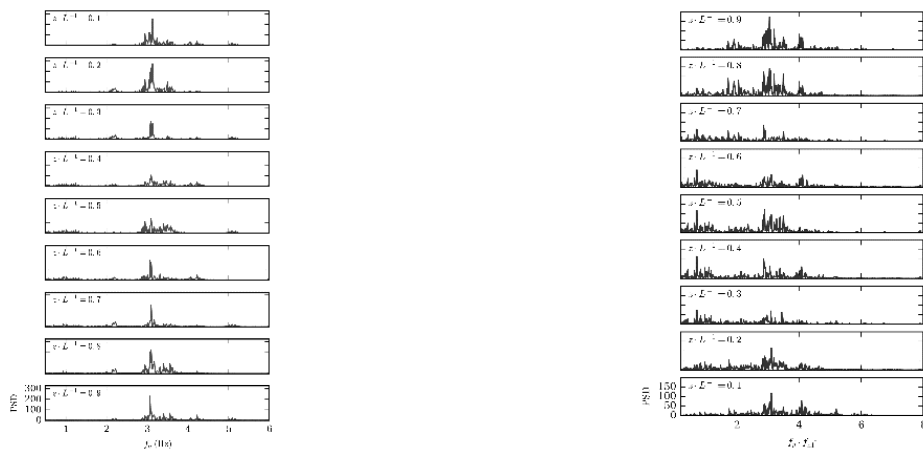
Fig 7: Comparison of power spectral density between case 1 and case 2 in the cross-flow direction

References

[1] J. Brugmans. Parametric instability of deep-water risers. Netherlands: Delft University of Technology, 2007.

[2] W.M. Chen, M. Li, S.X. Guo, and K. Gan. Dynamic analysis of coupling between floating top-end heave and riser's vortex-induced vibration by using finite element simulations[J]. Applied Ocean Research, 48, 2014: 1-9.

[3] M.Y. Duan, D.C. Wan, H.X. Xue. Prediction of response for vortex-induced vibrations of a flexible riser pipe by using multi-strip method. Proceedings of the Twenty-Sixth International Ocean and Polar Engineering Conference, Rhodes, Greece, June 26-July 1, 2016: 1065-1073.

[4] B. Fu, L. Zou, D.C. Wan. Numerical study of vortex-induced vibrations of a flexible cylinder in an oscillatory flow. Journal of Fluids and Structures, 77, 2018: 170-181.

[5] Richard H.J. Willden and J. Michael R. Graham. Multi-modal Vortex-Induced Vibrations of a vertical riser pipe subject to a uniform current profile. European Journal of Mechanics B/Fluids, 23(1), 2004: 209-218.

[6] J.K. Vandiver, V. Jaiswal, and V. Jhingran. Insights on vortex-induced, traveling waves on long risers. Journal of Fluids and Structures, 25(4), 2009: 641-653.

MODELING DIESEL ENGINE COMBUSTION USING FLAMELET/PROGRESS VARIABLE BASED ON OPENFOAM

QIYAN ZHOU[1], YONG QIAN[2], LIKUN MA[3], JIN XIA[4], XINGCAI LU[5]

[1] *Key Lab. for Power Machinery and Engineering of M. O. E, Shanghai Jiao Tong University, 200240 Shanghai, PR China, Zhou_qy@sjtu.edu.cn*

[2] *Key Lab. for Power Machinery and Engineering of M. O. E, Shanghai Jiao Tong University, 200240 Shanghai, PR China, qiany@sjtu.edu.cn*

[3]*Science and Technology on Scramjet Laboratory, National University of Defense Technology, Changsha 410073, China, malikun@nudt.edu.cn*

[4] *Key Lab. for Power Machinery and Engineering of M. O. E, Shanghai Jiao Tong University, 200240 Shanghai, PR China, xiajinhb@sjtu.edu.cn*

[5] *Key Lab. for Power Machinery and Engineering of M. O. E, Shanghai Jiao Tong University, 200240 Shanghai, PR China, lyuxc@sjtu.edu.cn*

Keywords: Spray Combustion; Flamelet/progress variable (FPV); Diesel engine; OpenFOAM

The flamelet/progress variable (FPV) approach was proposed as a model for non-premixed turbulent combustion and gave encouraging simulation results in several combustion environments [1, 2]. In present study, it was employed to model combustion process inside n-heptane fueling conventional compression ignition engine. The flamelet database was constructed on the basis of counter-flow flame configuration using published n-heptane mechanism [3]. The flame equations were solved by FlameMaster [4] in space of mixture fraction defined by Bilger [5] as follows:

$$Z = \frac{2\frac{Y_C - Y_{C,2}}{M_C} + 0.5\frac{Y_H - Y_{H,2}}{M_H} - \frac{Y_O - Y_{O,2}}{M_O}}{2\frac{Y_{C,1} - Y_{C,2}}{M_C} + 0.5\frac{Y_{H,1} - Y_{H,2}}{M_H} - \frac{Y_{O,1} - Y_{O,2}}{M_O}} \qquad (1)$$

where Y_i and M_i were correspondingly mass fraction and molar mass of elements carbon (C), hydrogen (H) and oxygen (O); and subscripts 1 and 2 respectively referred to mass fraction in fuel stream and oxidizer stream. Figure 1 presents temperature profiles in mixture fraction space obtained from flame solutions. The black lines representing fully burning illustrate that maximum temperature of fully burning flame increases as scalar dissipation rate decreasing, while blue lines describe unstable burning and mixing.
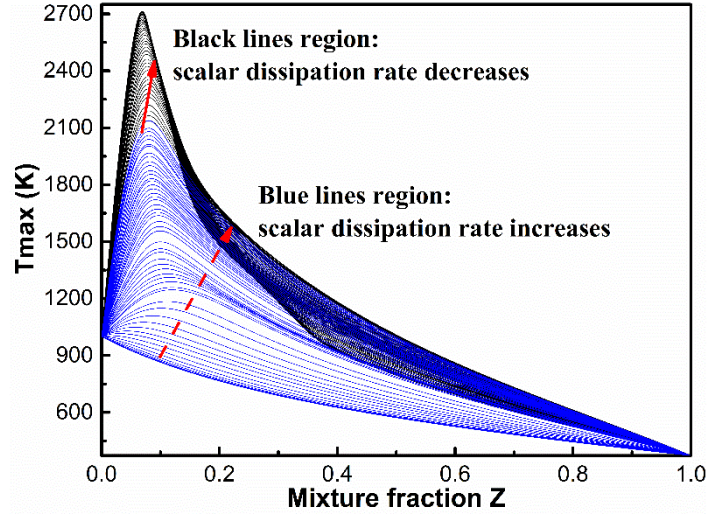
Figure 1: Temperature profile in mixture fraction space

In FPV approach, the flame solutions should be transferred to mixture fraction and progress variable spaces. The following definition of progress variable was used:

$$Y_c = Y_{H_2O} + Y_{CO_2} + Y_{H_2} + Y_{CO} \qquad (2)$$

where Y_i was the mass fraction of species. In order to simplify table look-up procedure, $C = \frac{Y_c - Y_c^u}{Y_c^b - Y_c^u}$ was introduced as a scaled progress variable to normalize Y_c. The laminar flame solutions were integrated with presumed probability density functions (PDF) to incorporate turbulence-chemistry interaction. For mixture fraction and progress variable, β-PDF and δ-PDF were applied, respectively. The average or filtered quantities were defined as:

$$\tilde{f} = \int_0^1 \int_0^1 f(Z, C) \, \tilde{P}\left(Z; \tilde{Z}, \widetilde{Z''^2}\right) \tilde{P}(C; \tilde{C}) \, dZ \, dC \qquad (3)$$

Besides, the table solution of FPV approach was set to $\tilde{Z} \times \widetilde{Z''^2} \times \tilde{C} = 101 \times 41 \times 101$.

The simulations in present work were carried out on basis of open source CFD package-OpenFOAM [6]. Reynolds Averaged Navier-Strokes (RANS) based k-ε model was used for three-dimensional (3-D) turbulent simulation and the Reitz-Diwakar model was chosen to mimic spray atomization and droplet break up. New libraries were created for FPV tabulated approach in framework of OpenFOAM. New solver referred as "sprayEngineFPVFoam" was developed to model diesel engine. The following additional transport equations were added:

$$\frac{\partial \bar{\rho}\tilde{Z}}{\partial t} + \frac{\partial(\bar{\rho}\widetilde{u_j}\tilde{Z})}{\partial x_j} = \frac{\partial}{\partial x_j}\left[\bar{\rho}(\widetilde{D} + D_t)\frac{\partial \tilde{Z}}{\partial x_j}\right] + \tilde{S}_Z \qquad (4)$$

$$\frac{\partial \bar{\rho}\tilde{Y}_c}{\partial t} + \frac{\partial(\bar{\rho}\widetilde{u_j}\tilde{Y}_c)}{\partial x_j} = \frac{\partial}{\partial x_j}\left[\bar{\rho}(\widetilde{D} + D_t)\frac{\partial \tilde{Y}_c}{\partial x_j}\right] + \bar{\dot{\omega}}_{Y_c} \qquad (5)$$

$$\frac{\partial \bar{\rho}\widetilde{Z''^2}}{\partial t} + \frac{\partial\left(\bar{\rho}\widetilde{u_j}\widetilde{Z''^2}\right)}{\partial x_j} = \frac{\partial}{\partial x_j}\left[\bar{\rho}(\widetilde{D} + D_t)\frac{\partial \widetilde{Z''^2}}{\partial x_j}\right] + 2\bar{\rho}D_t\left(\frac{\partial \tilde{Z}}{\partial x_j}\right)^2 - C_{d,Z_v}\bar{\rho}\frac{\varepsilon}{k}\widetilde{Z''^2} \qquad (6)$$

$$\tilde{\chi} = C_{d,\chi}\bar{\rho}(\varepsilon/k)\widetilde{Z''^2} \qquad (7)$$

where mean progress variable source term due to reaction was tabulated and mixture fraction source term $((\tilde{S}_Z = -\frac{1}{V_c}\sum_p \dot{m}_p N_p)$ introduced by liquid fuel evaporation was modeled referred to Baba et al. [7].

To investigate the capability of FPV approach, general computed combustion characteristics were compared and validated with experiments conducted by authors on a single-cylinder direct-injection and naturally aspirated diesel engine. Figure 2 presents comparison between experimental and calculated in-cylinder pressure trace. It demonstrates that FPV approach can well reproduce the pressure history of engine operating under different conditions. Besides, influence of injection pressure on in-cylinder pressure trend is also precisely predicted. Specifically, peak pressure goes higher as injection pressure increasing.
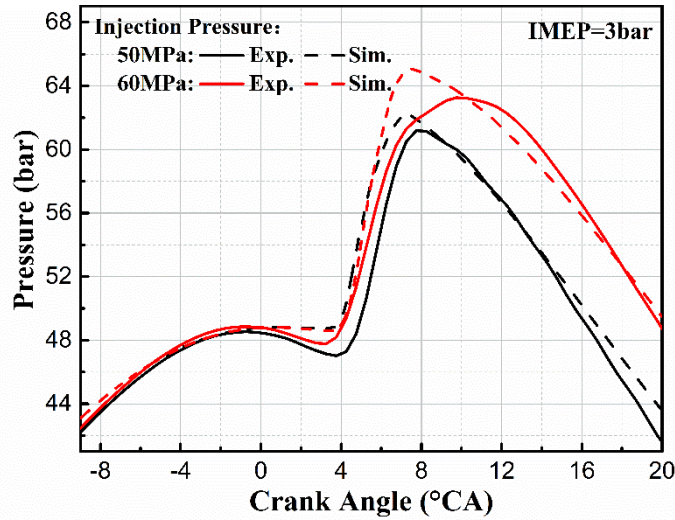
Figure 2: In-cylinder pressure trace

In Figure 3, comparisons of engine ignition delay are shown for all operation loads with injection pressure maintained at 50MPa and 60MPa, respectively. Although negligible ignition delay variations resulted from fixed injection timing, agreement between simulated and measured results is good, which proves the capability of FPV approach to predict the onset of combustion.
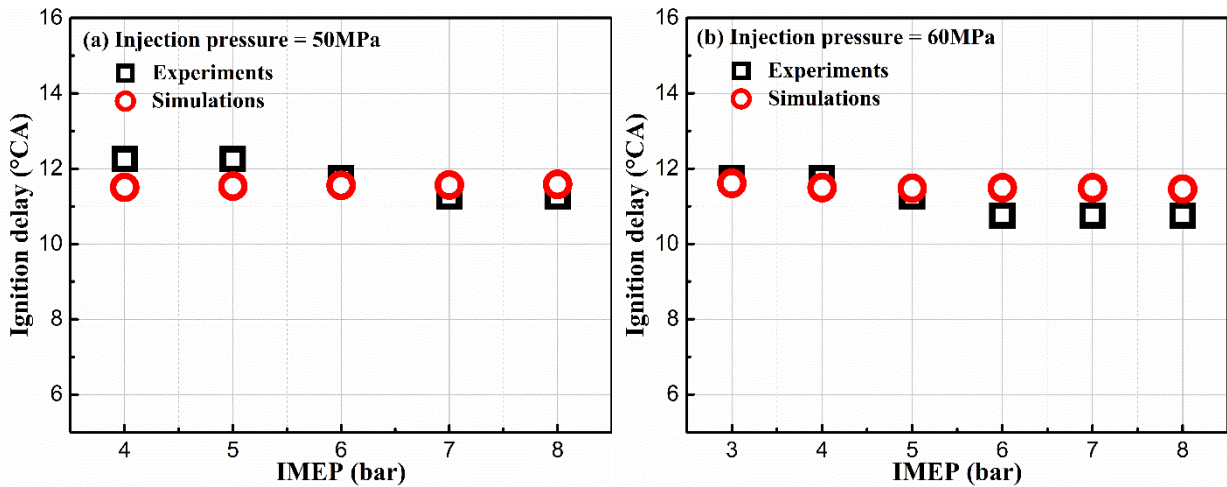
Figure 3: Ignition delay versus IMEP with injection pressure fixed at (a) 50MPa and (b) 60MPa

Figure 4 displays the distribution of progress variable reaction rates in space of scalar dissipation rate approaching ignition.

As time propagating towards ignition, progress variable reaction rate is intensified. In addition, it can also be observed from blue scatters on behalf of the onset of combustion, the ignition occurs in the region with extremely low scalar dissipation rate.
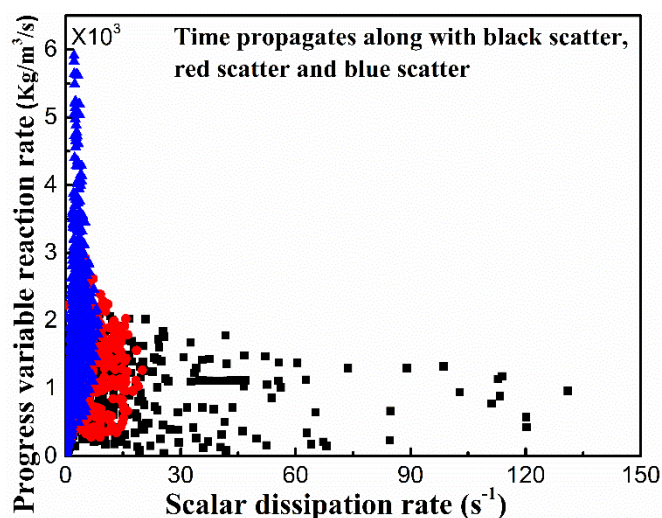
Figure 4: Distribution of progress variable reaction rates with scalar dissipation rates before ignition

References

[1]   Ihme M, Cha CM, Pitsch H. Prediction of local extinction and re-ignition effects in non-premixed turbulent combustion using a flamelet/progress variable approach. Proceedings of the Combustion Institute 2005;30(1):793-800.

[2]   Ihme M, Pitsch H. Prediction of extinction and reignition in nonpremixed turbulent flames using a flamelet/progress variable model: 2. Application in LES of Sandia flames D and E. Combustion and flame 2008;155(1):90-107.

[3]   Liu S, Hewson JC, Chen JH, Pitsch H. Effects of strain rate on high-pressure nonpremixed n-heptane autoignition in counterflow. Combustion and flame 2004;137(3):320-39.

[4]   FlameMaster. FlameMaster v3.3.10: A C++ Computer Program for 0D Combustion and 1D Laminar Flame Calculations; Available from: https://www.itv.rwth-aachen.de/index.php?id=flamemaster.

[5]   Bilger R, Stårner S, Kee R. On reduced mechanisms for methane   air combustion in nonpremixed flames. Combustion and Flame 1990;80(2):135-49.

[6]   Fundation O. OpenFOAM The Open Source CFD Toolbox. Programmer's Guide Version 2012;2(1).

[7]   Baba Y, Kurose R. Analysis and flamelet modelling for spray combustion. Journal of Fluid Mechanics 2008;612:45-79.

LARGE EDDY SIMULATION OF EVAPORATING SPRAYS UNDER DIESEL-LIKE CONDITIONS

RUITIAN HE, TIE LI, YUMENG GU

[1]Ruitian He, Collaborative Innovation Centre for Advanced Ship and Deep-Sea Exploration, State Key Laboratory of Ocean Engineering, Shanghai Jiao Tong University, heruitian@sjtu.edu.cn

[2]Tie Li, Collaborative Innovation Centre for Advanced Ship and Deep-Sea Exploration, State Key Laboratory of Ocean Engineering, Shanghai Jiao Tong University, litie@sjtu.edu.cn

[3]Yumeng Gu, Collaborative Innovation Centre for Advanced Ship and Deep-Sea Exploration, State Key Laboratory of Ocean Engineering, Shanghai Jiao Tong University, shirlingym@sjtu.edu.cn

Keywords: spray, LES, evaporation, diesel

Given that there are no black boxes and no limitations for detailed user-defined model development in the open source software OpenFOAM in contrast to other commercial computational fluid dynamics (CFD) codes, the long-term goal of this study is to establish an efficient 3-D evaporative spray model coupled with the Large-eddy Simulations (LES) over a wide range of diesel-like conditions through user-definition in OpenFOAM. This model coupled with LES not only minimizes the penalties in computational efficiency compared with Direct Numerical Simulations (DNS), but also has an insight into the vortex dynamics of the spray in contrast to Reynolds-averaged Navier-Stokes Simulations (RANS). The emphasis of this study is placed on the assessment of the predictive capability of vaporizing spray simulation under a specified high-temperature, high-pressure condition with experimental verifications.

The precise modelling of the spray is divided into three parts, which are the gas phase, vapor-liquid interface and the spray sub-models. Reasonable simplifications such as the quasi-steady state in gas phase, homogeneous distribution of temperature in the liquid phase as well as the vapor liquid equilibrium (VLE) are utilized in the numerical approach. The physicochemical properties of n-Dodecane, which acts as a substitute for the diesel fuel is employed in this model.

Experiments of diesel spray are conducted under the conditions of 3.96Mpa ambient pressure, 900K ambient temperature and 15kg/m^3 density (inertia gas N$_2$) in the constant-volume pre-combustion vessel (CVPV) equipped with the Z-type high-speed shadowgraph arrangement. Comparisons between experiments and simulations exhibit the feasibility of the model in predicting the temporal histories of both the liquid and vapor-phase spray penetrations.

The results reveal that with the lapse of time, the liquid penetration length elevates drastically attributed to the 120 MPa injection pressure and gradually shows a propensity to a constant value within 0.4 ms time after start-of-injection (ASI). The latter quasi-steady period is dominated by the exchange of momentum with the ambient inertia gas N$_2$ under the entrainment effect, which leads to the irregular periphery of the spray. In this study, the velocity field as well as the pressure field of the spray are also visualized by the post-processing ParaView. In addition, the effects of both the ambient temperature as well as the ambient pressure on the morphology and flow field of sprays are investigated respectively by means of extensive computational tests. Despite small discrepancies between the estimated and measured transient liquid penetration appear at the initial stage, the simulation of vaporizing spray gives a satisfactory agreement with experiments. The verification and universality of the spray model will be further examined over a wide range of diesel-like operating conditions using the multi-components fuels in the near future.

RESOLVING THE NEAR-FIELD FLOW PATTERNS OF AN IDEALIZED FIRE SPRINKLER WITH VOF MODELING AND ADAPTIVE MESH REFINEMENT

KARL V. MEREDITH[1], VUKO VUKČEVIĆ[2]

[1][1]*Research Division, FM Global, Norwood MA, U.S.A., karl.meredith@fmglobal.com*
[2][2]*Univ. of Zagreb, Faculty of Mech. Engineering and Naval Architecture, Ivana Lučića 5, Zagreb, Croatia, v.vukcevic@wikki.co.uk*

***Keywords:** Fire suppression, primary atomization, volume of fluid, adaptive mesh refinement*

The atomization of water by a fire sprinkler is of great interest to fire suppression research. The resulting droplet velocity, diameter, and liquid volume flux largely determine the suppression effectiveness. For example, large droplets can easily penetrate through a fire plume, while small droplets tend to be easily evaporated or carried away with the fire plume and have difficulty reaching the burning surfaces.

The goal of this work is to demonstrate the feasibility of using VOF modeling to adequately capture key aspects of sprinkler atomization in an idealized sprinkler geometry. Numerical modeling has been applied to understand the atomization behavior of an idealized sprinkler geometry consisting of a 9.5 mm inner-diameter cylindrical nozzle and a flat, 25.4 mm diameter disk with a liquid flow rate of 0.71 L/s. The simulations have been performed with *foam-extend-4.1* (a community driven fork of the OpenFOAM CFD software), using the ghost-fluid scheme and the isoAdvector scheme for interfacial reconstruction. In order to achieve efficient computations, a newly implemented adaptive-mesh-refinement (AMR) scheme has been used. Comparisons of atomization behavior (e.g. sheet-breakup length) and computational efficiency are made with previously measured results [1] and previous calculations [2] using static meshes. This study shows that using AMR coupled with VOF modeling can adequately obtain injection patterns in the near-field, and provides a path to subsequently simulate realistic sprinkler geometries.

Technical Approach

Numerical Model

The sprinkler simulations utilized a VOF solver, *navalFoam*, implemented in *foam-extend-4.1* [3], a community driven fork of the OpenFOAM [4] CFD software. The equations solved in *navalFoam* have been adequately documented elsewhere [5, 6], and portions of the model are reproduced here for reference purposes only. Equations (1-3) represent the continuity, momentum, and phase volume fraction transport equations, respectively,

$$\boldsymbol{\nabla} \cdot \mathbf{U} = 0 \qquad (1)$$

$$\frac{\partial(\mathbf{U})}{\partial t} + \boldsymbol{\nabla} \cdot (\mathbf{U}\mathbf{U}) - \boldsymbol{\nabla} \cdot \left(\nu_{eff}\boldsymbol{\nabla}\mathbf{U}\right) = -\frac{\boldsymbol{\nabla}p_d}{\rho} + \boldsymbol{\nabla}\mathbf{U} \cdot \boldsymbol{\nabla}\nu_{eff} \qquad (2)$$

$$\frac{\partial\alpha}{\partial t} + \boldsymbol{\nabla} \cdot (\mathbf{U}\alpha) = 0 \qquad (3)$$

where $\mathbf{U}$ represents the velocity vector, α represents the phase fraction, ρ is the density (assumes a combination of phase densities weighted by respective phase fractions), and ν_{eff} is the effective kinematic viscosity from turbulence modeling. The phase fraction, α, will only have values between 0 and 1 over the few cells spanning the interface between fluids.

The r.h.s. of Equation 2 represents the pressure body force and the variation of dynamic viscosity across the interface. The dynamic pressure is represented as

$$p_d = p - \rho\,\mathbf{g}\cdot\mathbf{x} \qquad (4)$$

where $\mathbf{g}$ is the gravity vector and $\mathbf{x}$ represents the position vector. The pressure gradient discontinuity and surface tension are included within the discretization using the ghost fluid method (GFM) [6].
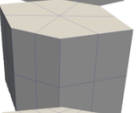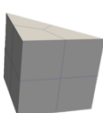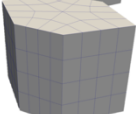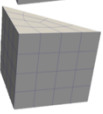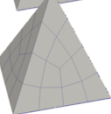
Rather than using typical interface compression schemes [18] to try to maintain a sharp interface, *navalFoam* includes the isoAdvector scheme [5] for approximating a geometric reconstruction of the interface. This scheme explicitly reconstructs a phase interface in each computational cell where $0<\alpha<1$ (i.e., at the intersection between the two phases). This interface is then advected through the cell at each time step. When calculating fluxes through cell faces, the interface information is used to determine the relative amounts of phase 1 or phase 2 to be advected out of the cell. This approach results in the ability to strongly limit numerical diffusion of the interface. A detailed description of the isoAdvector scheme is beyond the scope of this work, but additional details can be found in Ref. [5].

Large eddy simulation (LES) was used to treat turbulence, and the one-equation eddy model was used for simulating the turbulent kinetic energy. Additional details of the *navalFoam* model can be found in Refs. [6].

Adaptive Mesh Refinement

The recently implemented adaptive mesh refinement (AMR) scheme in *navalFoam* handles arbitrary polyhedra. The AMR algorithm operates by first identifying candidate cells for refinement. Through a composite process, multiple mesh refinement criteria can be used to precisely focus the candidate pool. For example, the mesh refinement criteria could be comprised of two conditions: 1) a minimum cell size (i.e., cube root of the cell volume), 2) a threshold for a scalar value (e.g. α), and a maximum refinement level. The user specifies the desired frequency (in terms of time steps) at which to perform the mesh refinement and unrefinemnt steps. These need not be the same frequency. Once the candidate pool is selected for refinement, the cells are then refined. Refinement proceeds by selecting the cell edges, splitting them, and creating a new node. A node is also placed at the centroid of each face, and at the centroid of the cell. New edges are then constructed to link the nodes together, forming the refined cells. Examples of this procedure for the various cell types are shown in Table 1. Unrefinemnt proceeds in reverse fashion.

Table 1: Polyhedral cell types covered by AMR implementation.

Simulated Geometry

The simulated geometry, shown in Figure 1, consists of a cylindrical nozzle, $r = 4.25\ mm$ and $l = 28\ mm$, where r is the inner radius and l is the length. The pipe flow inside the nozzle is simulated, having the nozzle inlet at the top of the domain. A disk with diameter $d = 12.7\ mm$ is placed 20 mm below the nozzle outlet. The disk thickness is set to 2 mm. The overall domain bounds are $x = [-30\ mm, 30\ mm]$, $y = [-30\ mm, 30\ mm]$, and $z = [-30\ mm, 48\ mm]$. The top, bottom, and sides of the domain are open.

The inlet velocity was held constant at 10 m/s, which is a flow rate of 0.71 L/s (corresponding to a pressure of 0.55 bar) entering the nozzle inlet. This is near the upper range of flow rates tested in Ref. [14]. The inlet was set to a phase fraction of one, and represents the only source of water inflow into the domain. The nozzle and disk wall boundaries consisted of a no-slip velocity condition. The initial conditions were stationary with a zero liquid volume fraction. For this study, no turbulent fluctuations were specified at the inlet boundary. This assumption warrants further investigation in future studies, as an operating sprinkler will likely have large fluctuations at the inlet due to pump frequencies, turbulent pipe flow, and flow turning effects from the feed line (typically oriented perpendicular to the nozzle).
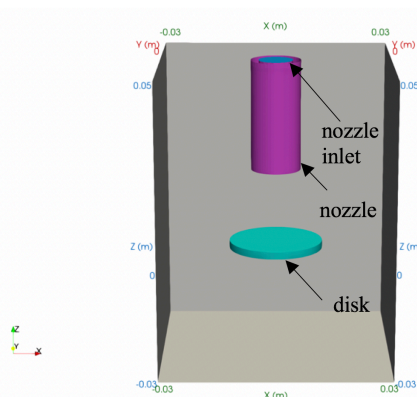
Figure 1: Simulated geometry showing the cylindrical nozzle oriented above the cylindrical disk with nozzle inlet, top, side, and bottom external boundaries shown.

Results and Discussion

The simulations were performed starting from a base mesh. The background mesh was 8 mm, and the finest mesh cells near the nozzle and the disk were ~ 1 mm, yielding approximately 40K cells. A portion of the base mesh is shown in Figure 2 as a triangulated slice on the x-z plane.
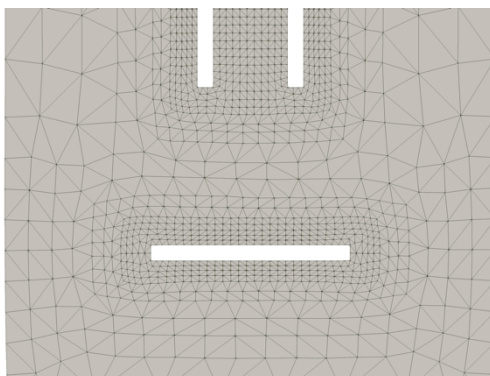
Figure 2: Base mesh for starting AMR simulations.

Five AMR criteria were simulated relating to minimum cell sizes of 1, 0.8, 0.6, 0.4, and 0.2 mm. In a previous study [2] using static meshes, it was shown that a mesh requirement of 0.5 mm and less is required to accurately predict the liquid film remaining in-tact in the vicinity of the deflector. The magnitude of the gradient of the phase fraction (α) was used as the refinement criterion, i.e., ($\mathrm{mag}(\nabla\alpha)$). A value of 100 was selected for this criterion. Any cells with a gradient magnitude greater than 100, with a cell volume greater than the minimum cell size, and a refinement level less than the maximum refinement level specified (10), were selected for refinement.

An example of the mesh refinement for the 0.4 mm case is shown in Figure 3 at a simulated time of 10 ms. Refinement can be observed at the interface between the liquid and gas. Figure 3-b shows the magnitude of the gradient of liquid phase fraction, which accurately captures the interface between liquid and gas. Refinement based on the gradient of α leads to a sharp interface.

a)   liquid phase fraction (α)

b)   magnitude of gradient of liquid phase fraction ($\mathrm{mag}(\nabla\alpha)$), clipped at a value of 100
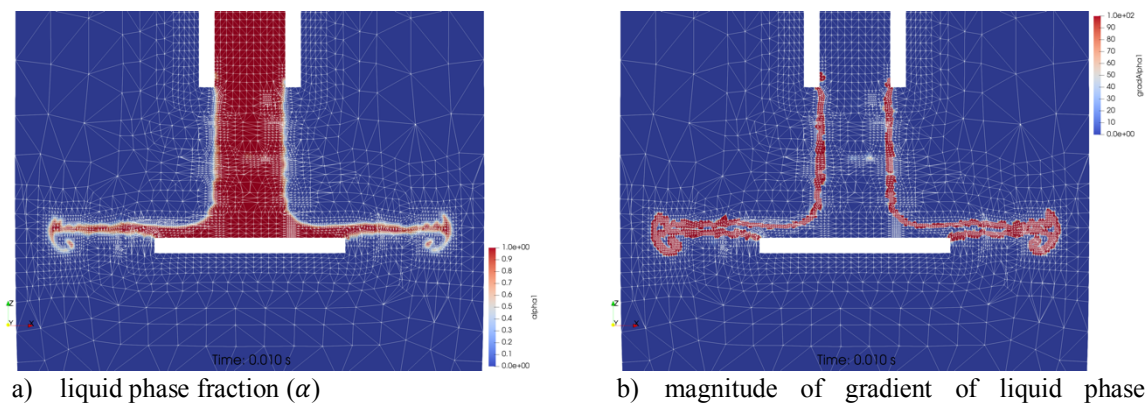
Figure 3: Liquid phase fraction and gradient used for grid refinement criterion shown for 0.4 mm case.

Near steady-state profiles for the various AMR cases are shown in Figure 4. The 1.0 mm mesh resolution clearly shows the liquid film breaking up within a few millimetres of the disk edge. The 0.6 mm mesh also shows, although difficult to make out from the figure, that the film breaks up along the edges of the film in the corners of the domain. The 0.4 mm mesh remains wholly intact. This behaviour matches previous static-mesh simulations [2], where the threshold for accurately predicting the sheet breakup distance (~160 mm for this case) was established for mesh resolutions of 0.5 mm and below. The 0.2 mm results, while only simulated out to 10 ms, are expected to yield similar results to the 0.4 mm mesh.

Summary and Conclusions

Simulating the atomization processes of a sprinkler has the potential to allow for enhanced insight into the key physics and controlling parameters. This approach also has the potential to be used as a predictive tool to estimate the spray injection profiles. In this study, the atomization of an idealized sprinkler geometry was simulated, and comparisons were made to experimental observations. The feasibility of using an adaptive mesh refinement scheme to reproduce flow features in the near-field region was demonstrated. Additionally, an innovative isoAdvector scheme allowed for maintaining a sharp interface even with relatively coarse mesh resolution. Computational cost of each simulation was quantified.

Similar to the previous static-mesh study, the AMR study revealed that mesh resolutions of 1.0, 0.8, and 0.6 mm provided insufficient refinement, as the sheet breakup distance was greatly under predicted due to numerical diffusion of the interface. Mesh resolutions of 0.4 and 0.2 mm yield results consistent with experimental observations. Ultimately, a mesh resolution of less than 0.2 mm or less will be required to resolve the flow features necessary to accurately predict atomization processes due to the anticipated drop size. Comparisons for film thickness predictions were also made, showing the simulated values fall within the expected range.

This study establishes the feasibility of using VOF modeling with AMR to adequately obtain injection patterns in the near-field. The numerical model can subsequently be used to predict atomization at locations beyond sheet breakup. This

work has provided a foundation for eventually to simulating realistic sprinkler geometries to obtain the atomization results necessary to initialize the sprinkler spray in fire suppression simulations.
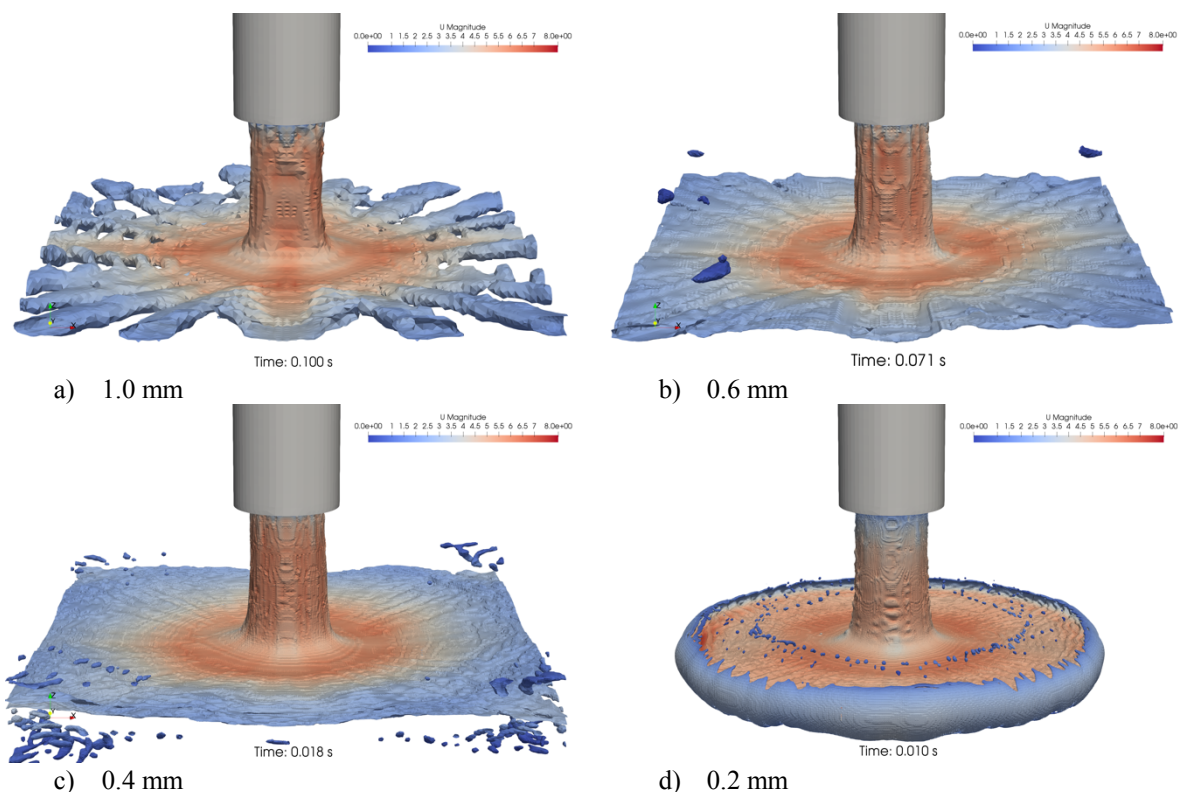
Figure 4: Isocontours of α=0.5 colored by velocity magnitude [m/s] for various minimum cell size criteria.

References
[1] Zhou, X. and H.-Z. Yu, *Experimental investigation of spray formation as affected by sprinkler geometry.* Fire Safety Journal, 2011. **46**: p. 140-150.
[2] Meredith, K.V., X. Zhou, and Y. Wang, *Towards Resolving the Atomization Process of an Idealized Fire Sprinkler with VOF Modeling*, in *ILAS-Europe 2017, 28th Conference on Liquid Atomization and Spray Systems.* 2017: Valencia, Spain.
[3] *foam-extend.* 2016 [cited 2017 June 13]; Available from: http://www.sourceforge.net/projects/foam-extend.
[4] Weller, H.G., et al., *A tensorial approach to computational continuum mechanics using object-oriented techniques.* Computers in Physics, 1998. **12**(6): p. 620-631.
[5] Roenby, J., H. Bredmose, and H. Jasak, *A computational method for sharp interface advection.* Royal Society Publishing open sci, 2016. **3**(160405).
[6] Vukcevic, V., H. Jasaka, and I. Gatina, *Implementation of the Ghost Fluid Method for free surface flows in polyhedral Finite Volume framework.* Computers and Fluids, 2017. **153**: p. 1-19.

PREDICTION OF FLOW PHYSICS IN TURBINE UNIT OF TURBOCHARGER BY DYNAMIC MESH MOTION

MANIMARAN RENGANATHAN[1]

[1]*Associate Professor, Thermal and Automotive Research Group, School of Mechanical and Building Sciences, Vellore Institute of Technology, Chennai, India 600127*

Keywords: *Turbocharger, Dynamic mesh, snappyHexMesh, rhoPimpleDymFOAM, Grid Independence, Performance.*

A turbocharger is a device composing turbine, compressor linked and connected by a shaft with bearings. The three dimensional drawing of the entire device is shown in Fig. 1. Energy is extracted using a turbine mounted in the device (shown as left) and the compressor is coupled to a turbine by a coupling shaft with bearings. The compressor supplies pressurised air to the engine for increasing the charge density during the suction stroke. An intercooler is usually present after the turbocharger for maintaining proper temperature.
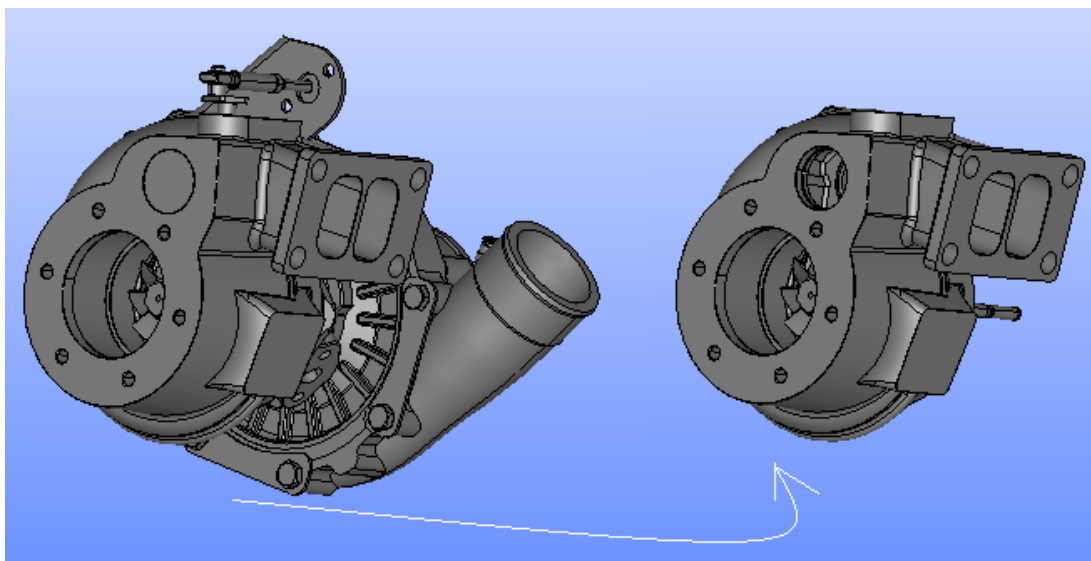
Fig. 1. Turbocharger (left) and turbine part of the turbocharger (right)
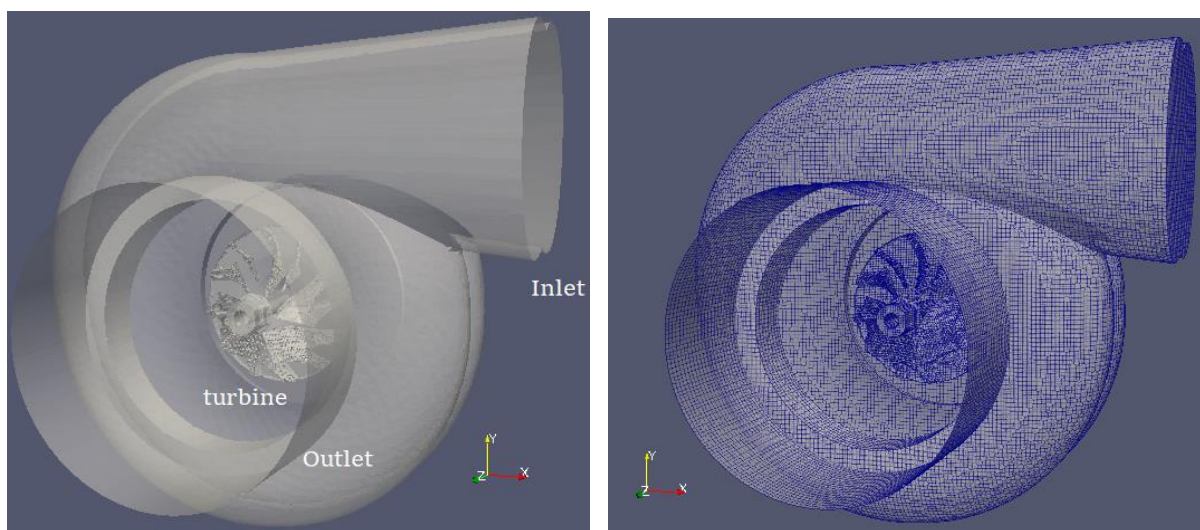
Fig.2. Fluid domain of the turbine (left), meshed model of turbine flow (right)

The objective of the present study is to simulate the flow field inside the turbine fluid domain with the rotation of turbine wheel imposed as dynamic mesh motion considered in the study. The geometry is created (Fig. 2) with the use

of Salome software and the meshing is completed using snappyhexmesh grid generator. One of the solvers in OpenFOAM [1] namely rhoPimpleDymfoam solver is used in this work. This solver takes care of the flow field with temperature variations in a dynamic mesh environment. The mesh elements are carefully selected such that grid convergence criteria is satisfied with the experimental study. Inlet conditions are maintained at 463 K and 123 m/s with a blade velocity of 20,000 rpm. A test section plane is created normal to +Z axis and the streamlines emanating at the outlet are colored with angular velocity as shown in Fig. 3.
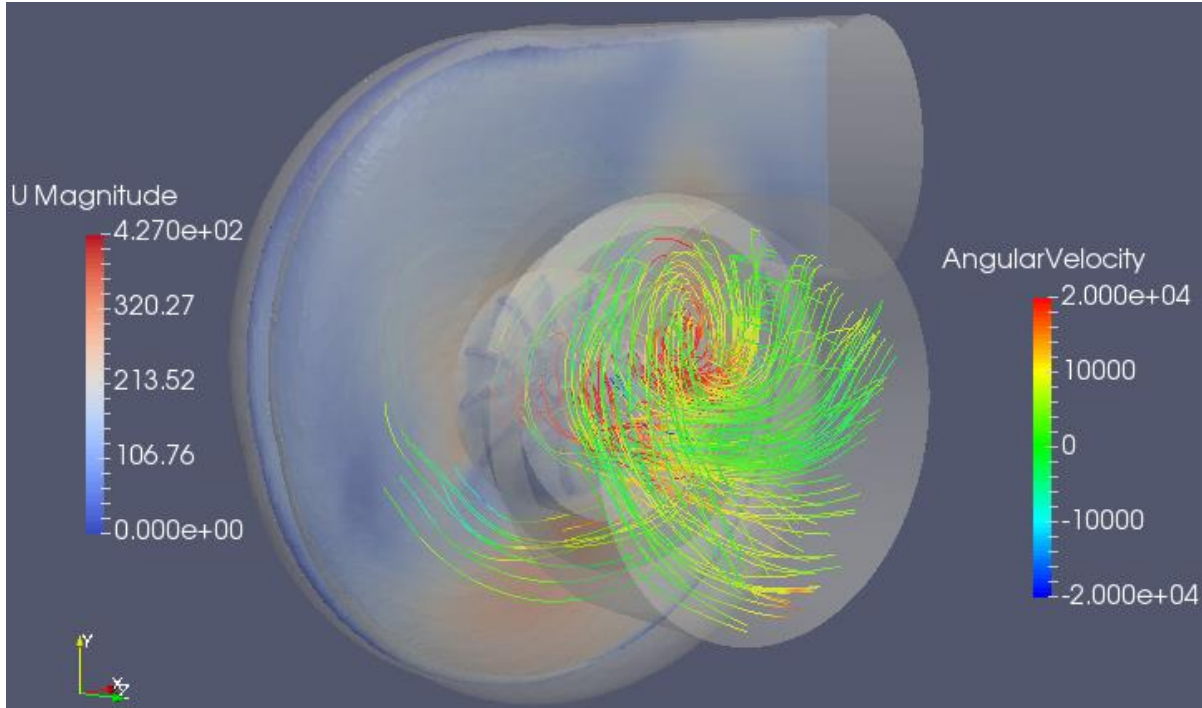
Fig. 3. Test section plane (shown in blue) with streamlines colored by angular velocity at the exit

Grid independence study is carried out at total mass flow parameter of 0.0105 kg/s.K$^{0.5}$kPa and the resulting non-dimensional mass flow rate parameter is compared as shown in Table 1. The convergence is reached as the number of elements increases beyond 2 million (in number) where the aspect ratio is almost close to 1.

Table 1: Grid Independence study

Grid Size (no. of elements)	Total pressure at inlet-to-exit static pressure ratio	
0.2 million	1.21	
0.5 million	1.29	
1.0 million	1.42	
2.0 million	1.47	
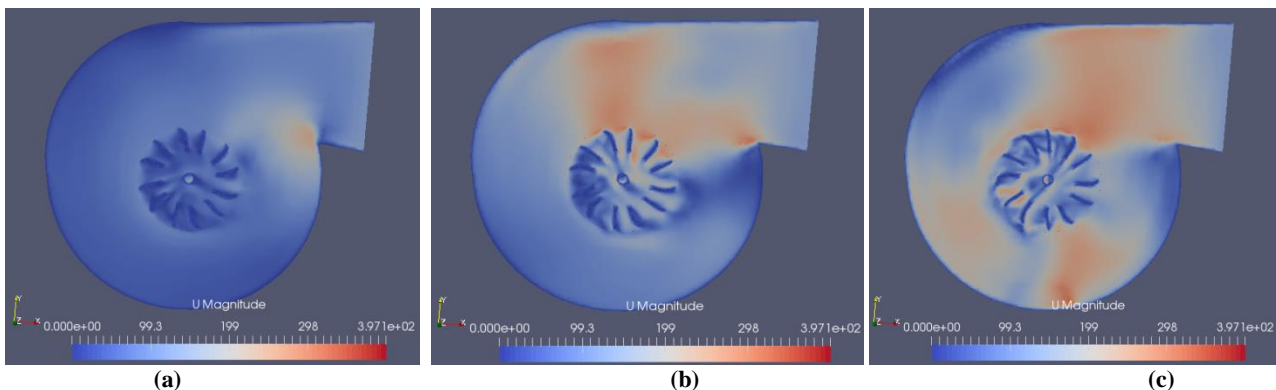
Fig. 4. Velocity magnitude in the test section at 15 mS (a), 30 mS (b) and 45 mS (c)
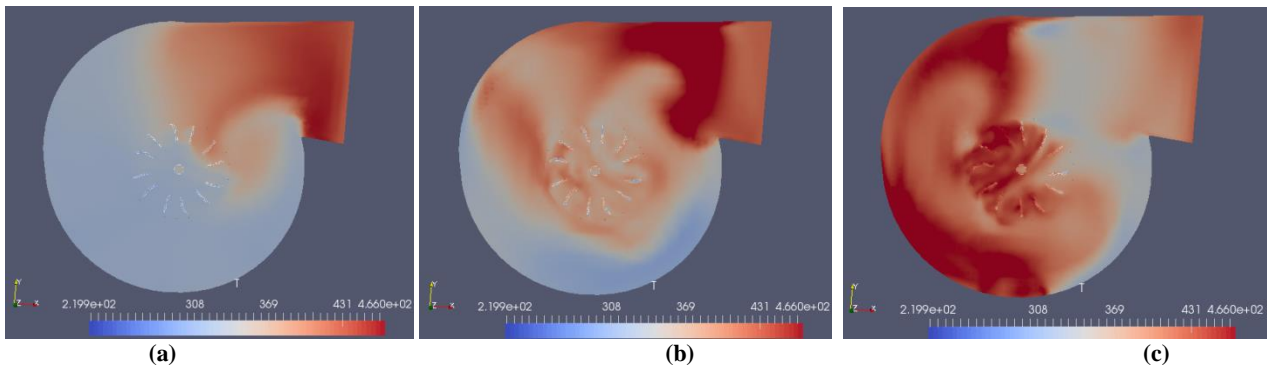
Fig. 5. Static Temperature contour in the test section at 15 mS (a), 30 mS (b) and 45 mS (c)
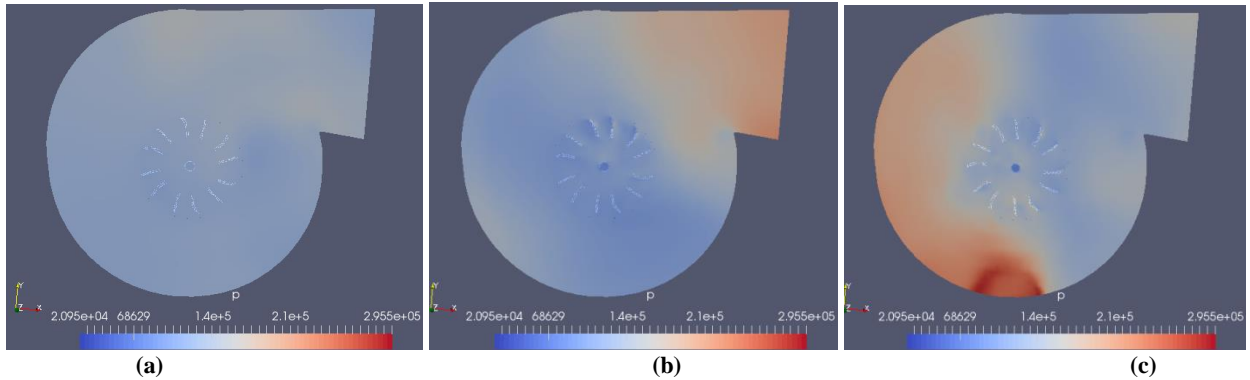
Fig. 6. Static Pressure magnitude in the test section at 15 mS (a), 30 mS (b) and 45 mS (c)

The contours of the velocity magnitude, static temperature and static pressure are presented in figures 4,5 and 6 respectively. It is clear that the flow motion from the inlet is influenced by the rotating turbine blade. The temperature distribution and flow expansion is also evident. The output parameters are compared against the experimental readings [2]. The output parameter from the study is compared and found to be within lower degree of variation with respect to experimental measurement as reported in literature[2]. The mass flow rate of the turbine is varied as per the following formula in equation (1) and the output parameter (pressure ratio in equation 2) is observed using Paraview.
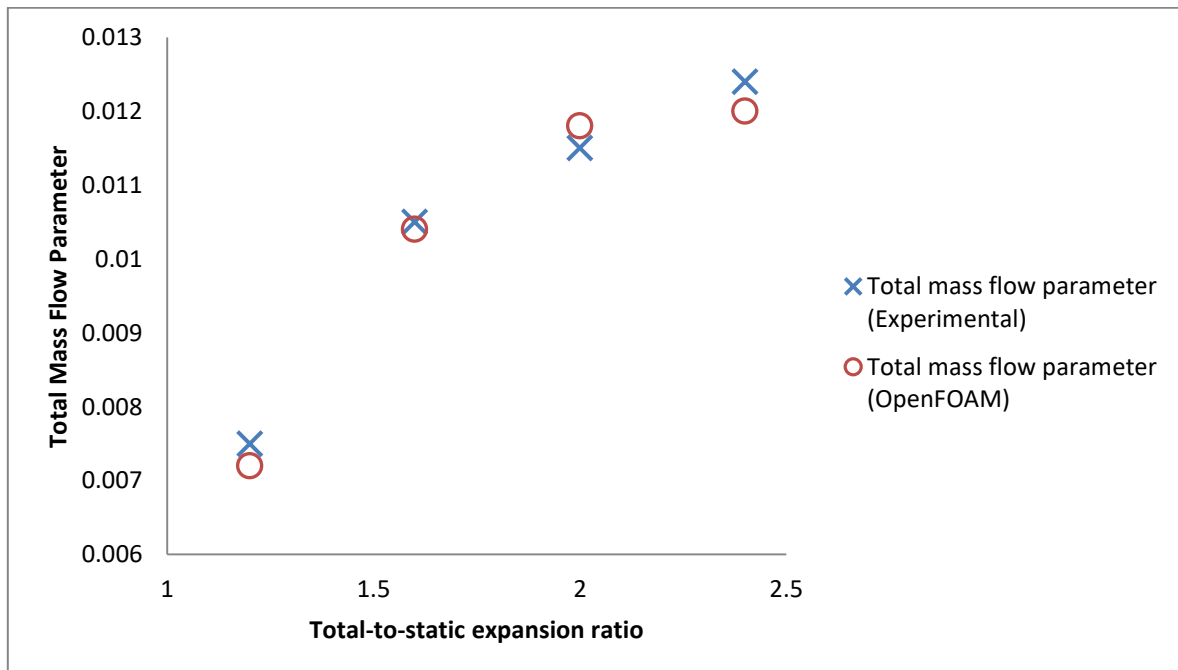
Fig. 7. Comparison of different cases by varying total-to-static expansion ratio

Total-to-static expansion ratio   : P_o/P_{exit} (1)
Total mass flow parameter   : $\dot{m}(T_o)^{0.5}/P_o$ (2)

T_o – Turbine inlet total temperature
P_o – Turbine inlet total pressure
P_{exit} – static pressure at the exit of turbocharger
$\dot{m}$ – mass flow rate in the turbine

This study is possible with the help of blueCFD software [3], an OpenFOAM source in windows distribution. The future of this work is aimed at coupling the turbine with the compressor fluid domain. Further, a realistic analysis is focussed on the fluid structure interaction by the expanding flow on the turbine blades.

Acknowledgements

References

[1] OpenCFD, OpenFOAM: The Open Source CFD Toolbox. User Guide Version 1.4, OpenCFD Limited. Reading UK, Apr. 2007.

[2] Kevin John Fogarty, Turbocharger turbines: An experimental study on the effects of wastegate size and flow passage design, M.S. Thesis, Mechanical Engineering, The Ohio State University, 2013.

[3] BlueCFD-core project, http://bluecfd.github.io/Core.

CFD FOR TURBOMACHINERY: METHODS AND APPLICATIONS

HRVOJE JASAK[1,2], GREGOR CVIJETIĆ[1], TESSA UROIĆ[1], LUKA ČULIĆ[1]

[1]*University of Zagreb, gregor.cvijetic@fsb.hr, tessa.uroic@fsb.hr, lukaculic1@gmail.com, hrvoje.jasak@fsb.hr*
[2]*Wikki Ltd., h.jasak@wikki.co.uk*

Abstract

Turbomachinery CFD has been extensively used for decades and variety of tools have been developed for dealing with specific phenomena appearing in these machines. The tools enable significant computational savings, or provide simplified models for preliminary evaluation, which resulted in establishing CFD as a common, efficient R&D technique in industry. In this paper we present the methods for modeling complex flows inside various types of turbomachinery. A general overview of tools for turbomachinery simulations available in `foam-extend` is given, with the application demonstrated for both incompressible and compressible flow problems. Appropriate methods should be chosen depending on the physics and geometry involved:

- steady-state or transient approach,
- single blade passage or full annulus configuration,
- type of rotor-stator interaction interface,
- compressible or incompressible problem,
- implicitly block–coupled or segregated pressure-velocity system, etc.

All options will be addressed for specific test cases presented in the paper. Furthermore, the mathematical and numerical model applied in the cases will be presented.

In the paper, three incompressible test cases will be considered: a Francis turbine, a centrifugal pump and a ship propeller. A comparison of steady-state multiple reference frames (MRF) approach [1], transient approach and Harmonic Balance method [2] (quasi–steady state) will be given and results will be validated against experimental data, where available. Compressible solvers described in [3, 4] will be evaluated for three test cases as well, each comprising of different flow regime: low compressibility Onera M6 wing, high compressibility Aachen turbine and transonic NASA Rotor 67 test case. Methods for treating the rotor–stator interface, mixing plane and general grid interface (GGI) [5], will be presented and tested in the Aachen turbine test case. Coupling of the pressure and velocity for both the compressible and incompressible flow equations will be presented in the segregated and implicitly coupled formulation.

Mathematical Model

Transient equations provide a solution with a fully resolved flow in time, compared to steady-state or Harmonic Balance methods, which introduce temporal simplifications or approximations to reduce the computational CPU time. The high cost of computational time make the transient approach less attractive for everyday use. To alleviate this problem, simplified methods are often used: multiple reference frame (MRF) which is a steady state approach and the Harmonic Balance (HB) method.

In MRF the rotation effects are modelled by solving the conventional steady–state equation set with terms accounting for rotation: the Coriolis force and centrifugal force, which are included in the momentum equation, either as a source term (segregated approach) or implicitly in the matrix (implicit approach).

Equations 1-6 represent the governing equations for transient, MRF and HB approach, respectively. As previously noted, the MRF equations do not include the temporal derivation term and have the additional term $-\omega \times (\rho \mathbf{u})$.

Transient equation set:

Steady-state equation set with MRF:

$$\frac{\partial \rho}{\partial t} + \nabla_{\bullet}\rho\mathbf{u} = 0\,, \qquad (1)$$

$$\nabla_{\bullet}\rho\mathbf{u} = 0\,, \qquad (3)$$

$$\frac{\partial \rho\mathbf{u}}{\partial t} + \nabla_{\bullet}(\rho\mathbf{u}\mathbf{u}) - \nabla_{\bullet}(\mu\nabla\mathbf{u}) = -\nabla p\,. \qquad (2)$$

$$\nabla_{\bullet}(\rho\mathbf{u}_{rel}\mathbf{u}) - \nabla_{\bullet}(\mu\nabla\mathbf{u}) = -\nabla p - \omega \times (\rho\mathbf{u})\,. \qquad (4)$$

Harmonic Balance equation set:

$$\nabla_{\bullet}\rho_{t_j}\mathbf{u}_{t_j} = -\frac{2\omega}{2n+1}\left(\sum_{i=1}^{2n} P_{i-j}\rho_{t_i}\right)\,, \qquad (5)$$

$$\nabla_{\bullet}(\rho_{t_j}\mathbf{u}_{t_j}\mathbf{u}_{t_j}) - \nabla_{\bullet}(\mu\nabla\mathbf{u}_{t_j}) = -\nabla p_{t_j} - \frac{2\omega}{2n+1}\left(\sum_{i=1}^{2n} P_{i-j}\rho_{t_i}\mathbf{u}_{t_i}\right)\,, \qquad (6)$$

$$\text{for } j = 1 \ldots 2n+1.$$

Index rel denotes the relative velocity while index t_j denotes the time instant for which the solution is sought. HB source term accounts for the temporal coupling between the time instants - the use of different indices t_i and t_j on the LH and RH side should be noticed.

HB is considered to be a quasi steady–state method as all the equations are steady-state, but mutually coupled by the right hand side term, obtained using the Fourier decomposition on a transient set of equations, which necessarily restricts the application of HB to periodic problems only. For details on the derivation, the reader is referred to [6, 7]. HB simulations can be computed with an arbitrary number of harmonics n, which affects the accuracy of the method. The number of equations scales with $2n + 1$, meaning that for $n = 1$ harmonic, three sets of velocity and pressure equations will be solved. Therefore, by increasing the number of harmonics, the CPU time is also increased. Depending on the problem, the optimal number of harmonics can change, as some transient flow features are more complex than others. The major benefit of HB compared to MRF is that although $2n + 1$ time instants are solved for, the solution can be reconstructed at any point in time, thus the solution for the whole period is available.

Numerical Model

In the first subsection of the numerical model, the segregated and block–coupled implicit approach for solving the Navier–Stokes equations will be analysed. In the second section, turbomachinery–specific boundary conditions will be presented.

Pressure–Velocity Coupling

The derivation of the pressure equation as a Schur complement from the continuity and momentum equations can be found in [4]. The final form of the incompressible, steady–state system can be written as:

$$\begin{bmatrix} [A_{\mathbf{u}}] & [\nabla(.)] \\ [\nabla_{\bullet}(.)] & [\nabla_{\bullet}(D_{\mathbf{u}}^{-1}\nabla(.))] \end{bmatrix}\begin{bmatrix} \mathbf{u} \\ p \end{bmatrix} = \begin{bmatrix} 0 \\ \nabla_{\bullet}(D_{\mathbf{u}}^{-1}\overline{\nabla(p^o)}) \end{bmatrix}\,, \qquad (7)$$

where $[A_{\mathbf{u}}]$ is the momentum matrix (convection and diffusion operators), $D_{\mathbf{u}}^{-1}$ is the inverse of the diagonal of the momentum matrix, p^o is the previously available pressure solution and is only used in the Rhie-Chow correction, [8]. Overline indicates face-interpolated cell-centred pressure gradient. The convection term is linearised by using the old available values of flux. The formulation is valid for both the segregated and implicit block–coupled approach, as the off–diagonal terms are treated explicitly in the segregated approach. As stated previously, the additional terms coming from the MRF method are treated as a source term in the segregated approach, while they are added into the matrix in the implicit approach. In implicitly coupled system, there is no need for underrelaxation (or very little) which leads to faster time–to–solution, and also more stability and robustness in converging the solution. The drawback is a high memory demand caused by the 4 times larger matrix dimension of the linear system and, due to the properties of the matrix, more complex linear solvers have to be used, such as the selective algebraic multigrid method, [9].

Boundary Conditions

Usually, the geometry of turbines, pumps and other machines with rotating parts is symmetric and it is beneficial to exploit the fact by applying special boundary conditions which will enable significant reduction in mesh cell count. Some will be presented in this work: periodic boundary conditions for single blade passage simulations, mixing plane [10] and general

grid interface [11] for inter–domain interpolation. In order to use the sliding mesh technique in a transient simulation with multiple domains (rotor and stator) which are not connected, a general grid interface (GGI) is used. GGI handles the interpolation between non–conformal boundaries (non–matching faces) of two domains. Common use of GGI is presented in [1]. If a single blade passage with both rotor and stator configuration is simulated, the two domains usually have a partial overlap which should be specially handled. This is done with the aid of `overlapGgi` in `foam-extend`, which mathematically creates the full annulus of the paired interfaces and than performs interpolation. In order to reduce the mesh size, spatially periodic flow can be assumed in turbomachinery, meaning that the same flow pattern appears in each blade passage. This allows the reduction of the simulation domain to a single blade passage with the aid of suitable periodic boundary condition on meridional boundaries. In `foam-extend` such boundary condition is called `cyclicGgi`, and it handles the transformation and interpolation from one meridional patch to its matching pair and vice versa. For more details, the reader is referred to [10].

Results

Several cases will be utilized for demonstration of turbomachinery capabilities, for both the incompressible and compressible flow.

Incompressible flow

For problems with low compressibility, the standard incompressible solver can be used, thus reducing the number of coupled governing equations solved and complexity of the problem.

Francis 99 is a water turbine test case available from the Francis–99 Workshop [12], with the experimental data available. The turbine consists of 28 stator and 30 rotor blades, followed by a draft tube outlet, Figure 1. The rotational velocity is 335 rpm and best efficiency is achieved at 0.2 m³/s flow rate. We compared the two steady–state methods: MRF and HB, for the best efficiency point. In the final paper, results for the high load and part load operating points will be presented as well. Integral values are compared in Table 1.
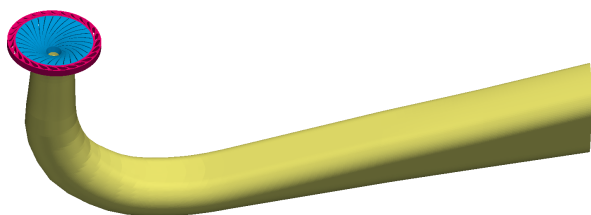
Figure 1: Stator (red), rotor (blue) and draft tube (yellow).

Table 1: Comparison of integral quantities.

	P [W]	H [m]	η [%]
Experiment	21 617	11.94	92.39
HB simulation	22 457	11.53	94.40
Error	3.74%	3.43%	2.13%

The second test case is a centrifugal pump, for which the geometry is shown in Figure 2. The flow will be simulated using the transient solver with sliding mesh rotor–stator interface and also using the steady–state approach. For steady–state, we will use a MRF and compare the results and convergence of the segregated and coupled approach.
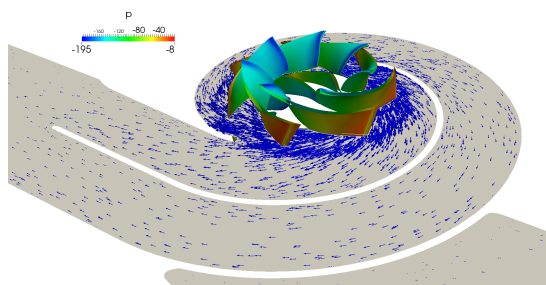
Figure 2: Centrifugal pump geometry with the pressure field on the rotor and velocity vectors.
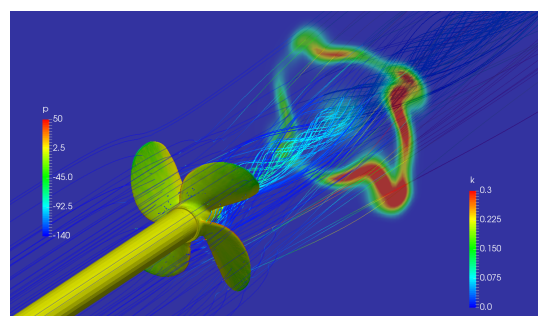
Figure 3: A ship propeller simulation results.

The third test case is a ship propeller, similar to the one shown in Figure 3, for which the transient and steady state approach will be compared (MRF with segregated and coupled solver, and HB solver).

Compressible flow

A low compressibility test case which will be presented is the flow around the Onera M6 wing at Mach number equal to 0.7, for which experimental data is available, [13]. A comparison of the segregated and implicitly coupled approach will

be given. Aachen test case, Figure 5, will be presented to demonstrate the use of rotor-stator interface treatment since the configuration of the test case is stator-rotor-stator, coupled with the MRF solver will be used. The final test case is a high compressibility transonic NASA rotor 67. The geometry is shown in Figure 4, for which MRF segregated and coupled compressible solver will be benchmarked against experimental data.

Figure 5: Aachen test case geometry and velocity field.

Figure 4: NASA rotor 67 geometry, full annulus.

References

[1] H. Jasak and M. Beaudoin, "OpenFOAM turbo tools: From general purpose cfd to turbomachinery simulations," in *Proceedings of ASME-JSME-KSME Joint Fluids Engineering Conference (AJK2011-FED)*, 2011.

[2] H. Jasak and G. Cvijetić, "Implementation and validation of the harmonic balance method for temporally periodic non–linear flows," in *ASME Turbo Expo 2016: Turbomachinery Technical Conference and Exposition*. American Society of Mechanical Engineers, 2016, pp. V02CT39A009–V02CT39A009.

[3] I. De Dominicis, G. Cvijetić, M. Willetts, and H. Jasak, "Enhanced turbomachinery capabilities for foam-extend: Development and validation," in *11th OpenFOAM Workshop*, 2016.

[4] T. Uroic and H. Jasak, "Implicitly coupled pressure-velocity solver," in *OpenFOAM Selected papers of the 11th Workshop*, 2016.

[5] M. Beaudoin and H. Jasak, "Development of a generalized grid interface for turbomachinery simulations with OpenFOAM," in *Open source CFD International conference*, vol. 2. Berlin, 2008.

[6] G. Cvijetic, H. Jasak, and V. Vukcevic, "Finite volume implementation of the harmonic balance method for periodic non–linear flows," in *54th AIAA Aerospace Sciences Meeting*, 2016, p. 0070.

[7] G. Cvijetic, I. Gatin, V. Vukcevic, and H. Jasak, "Harmonic Balance developments in OpenFOAM," *Computers & Fluids*, 2018. [Online]. Available: http://www.sciencedirect.com/science/article/pii/S0045793018300793

[8] C. Rhie and W. Chow, "A numerical study of the turbulent flow past an isolated airfoil with trailing edge separation," in *AIAA Journal*, vol. 21, 1983, pp. 1525–1532.

[9] T. Uroic and H. Jasak, "Block-selective algebraic multigrid for implicitly coupled pressure-velocity system," vol. 167, pp. 100–110, 2018.

[10] M. Beaudoin, H. Nilsson, M. Page, R. Magnan, and H. Jasak, "Evaluation of an improved mixing plane interface for OpenFOAM," in *IOP Conference Series: Earth and Environmental Science*, vol. 22, no. 2. IOP Publishing, 2014, p. 022004.

[11] M. Beaudoin and H. Jasak, "Development of a General Grid Interface for Turbomachinery simulations with OpenFOAM," in *Open Source CFD International Conference*. American Society of Mechanical Engineers, 2008.

[12] C. Trivedi, M. J. Cervantes, and O. G. Dahlhaug, "Experimental and numerical studies of a high-head francis turbine: A review of the francis-99 test case," *Energies*, vol. 9, no. 2, p. 74, 2016.

[13] "ONERA M6 Wing." [Online]. Available: https://www.grc.nasa.gov/www/wind/valid/m6wing/m6wing.html

LES OF TRANSIENTS IN THE FRANCIS-99 WATER TURBINE MODEL

Jonathan Fahlbeck[1], Ludvig Uppström[2], Eric Lillberg[3], Håkan Nilsson[4]

[1]*MSc student, Chalmers University of Technology, Mechanics and Martime Sciences,*
jonathan.fahlbeck@outlook.com

[2]*MSc student, Chalmers University of Technology, Mechanics and Martime Sciences,*
ludvig.uppstrom@gmail.com

[3]*Vattenfall AB Research and Development, eric.lillberg@vattenfall.com*

[4]*Chalmers University of Technology, Mechanics and Maritime Sciences, hakan.nilsson@chalmers.se*

Keywords: LES, Transients, Rotor-stator interaction, Mesh morphing, Francis-99, Hydropower

Due to the new intermittent electric energy sources, hydropower is forced to run more and more at off-design conditions to regulate the operating conditions. This causes flow instabilities with pressure fluctuations, and load variations that may deteriorate the machine. One effort to learn more about the flow in water turbines during transients is the Francis-99 workshops, organized at NTNU (https://www.ntnu.edu/nvks/francis-99). It is a series of three workshops, where geometrical and experimental data of a Francis turbine model is openly available for validation of CFD results. The first workshop was organized 2014, focusing on three steady operating conditions; the best efficiency point (BEP), a part load point and a high load point. The 14 papers presented at the first workshop [1] showed state-of-the art simulations of the three steady operating conditions using a wide range of CFD codes, including OpenFOAM. The second workshop was organized in 2016 and had a focus on transients between operating conditions. Most of the 10 papers presented at the workshop [2] did however not investigate the full experimental transients that were made available. The advanced investigations require dynamic meshes that both rotate the runner, using a coupling interface to the non-rotating part of the mesh, and morph the guide vane mesh due to the change in guide vane angle during the transient. Most codes and workshop participants were not ready for such simulations at the time of the workshop. The third workshop has not yet been organized. It should focus on FSI, including the deformation of the runner. That will require to also add deformation to the rotating mesh.

The present work addresses the scope of the second Francis-99 workshop, using OpenFOAM-2.3.x. The standard code has a class for dynamic mesh motion that can handle rotating regions coupled to stationary regions using the AMI interface. It also has a class for mesh morphing. Those two classes are combined in the present work, to allow simulations with both a rotating runner region and guide vanes that continuously change angle. Due to the large deformation of the guide vane mesh it is necessary to map the fields to new meshes of better quality a number of times during the procedure. Most of the meshes are generated using cfMesh, but snappyHexMesh is used when the distance between the guide vanes becomes too small. Turbulence is modelled by LES based on the dynamic one-equation eddy viscosity sub-grid model (dynOneEqEddy) [3] and the cube root volume filter width. The time term is discretized using CrankNicolson 0.5, and the convection term for velocity is discretized using linearUpwind Grad(U). The inlet and outlet boundary conditions are set using total pressure conditions. The outlet total pressure is taken from the experiment at BEP. The inlet total pressure is adjusted to yield the same flow rate as in the experiment at BEP. Those conditions are kept during the transient. We here present numerical results at BEP and when closing the guide vanes, comparing with the experimental data.

Figure 1 shows the geometry and the locations of the experimental measurements [4]. The flow enters through the spiral casing, through the stationary stay and guide vanes, through the rotating runner with full blades and splitter blades, continuing through the draft tube. A number of pressure transducers are mounted at different locations, named VL01 (Vane-Less space), VL2 (not shown in figure, but at a similar location as VL01), P42, P71 (Pressure side of runner blade), S51 (Suction side of runner blade), DT11 and DT21 (Draft Tube). DT5 and DT6 are located at similar positions as DT11 and DT21, but at different angles. It should in particular be noted that it is only the experimental data for the pressure at VL2, DT5 and DT6 that is obtained from the second workshop. The other pressure data is from the first workshop, at a slightly different operating condition. PIV measurements of the velocity distribution were made at the plane that is shown as a striped rectangle below the runner, at an angle shown with respect to the spiral casing (top view of spiral casing). Velocity distributions were extracted from the PIV data along Lines 1-3, to the extent of the PIV plane.
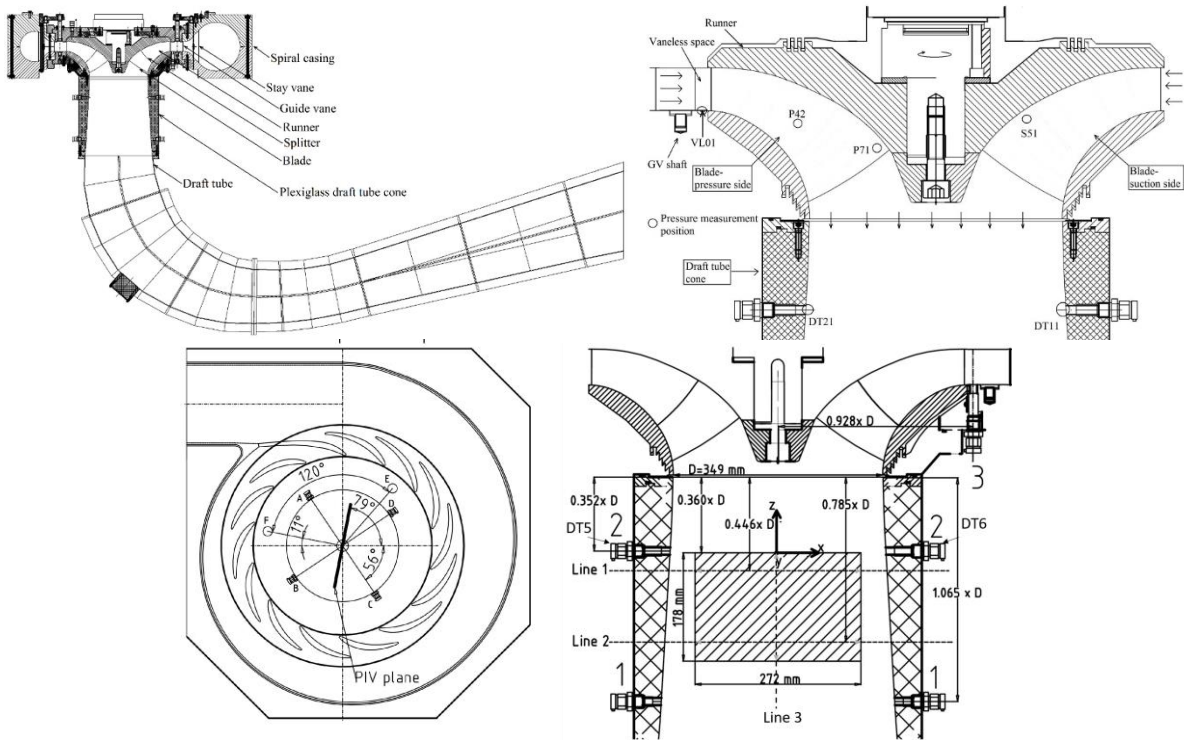
Figure 1: Geometry and locations of experimental measurements.

Figure 2 shows the mean and fluctuating experimental and numerical pressure at various probes, at the BEP operating condition. It can be seen that the mean pressure distribution through the machine is predicted qualitatively correct. It should be recalled that only the VL2 measurement was done at the same conditions as in the present simulation, which is why that point shows the best agreement. The fluctuating pressure at DT5 and DT6 show similar experimental and numerical behaviour, as well as standard deviation. The experimental data was here presented as deviation from the mean value of the sequence, as then also done for the numerical data.
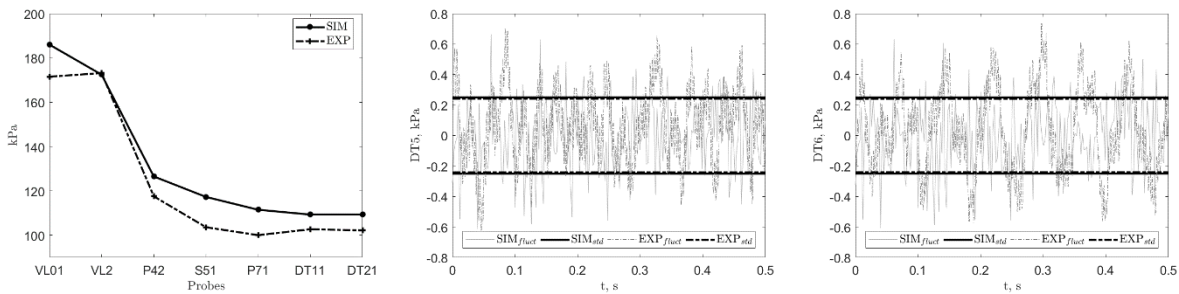
Figure 2: BEP experimental (EXP) and numerical (SIM) static pressure comparisons. Left: Mean data in various probes (see Figure 1). Center and right: Fluctuations and standard deviation at probes DT5 and DT6.

Figure 3 shows the mean axial and horizontal velocity components along Line 1, at BEP. The axial component is positive in the (0, 0, 1) direction and the horizontal component is positive in the (-0.191, -0.982, 0) direction, according to the workshop descriptions (i.e. along two perpendicular directions parallel to the PIV plane). The horizontal direction is thus a measure of the radial component, but with a change in sign at $r/R_{max}=0$. The axial component shows a very good agreement compared to the experimental data. The deviation close to $r/R_{max}=0$ is similar as for the better ones of the workshop contributions.
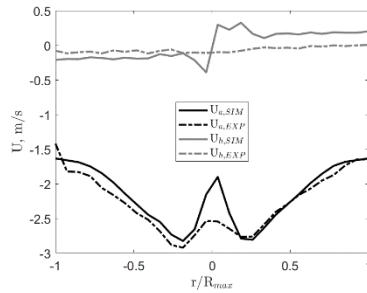
Figure 3: BEP experimental (EXP) and numerical (SIM) mean velocity profile comparisons at Line 1, where a =axial and h = horizontal. R_{max} is the largest radial position along the experimental line (i.e. extent of PIV plane, not draft tube wall).

Figure 4 shows a top view of the guide vane mesh at BEP, and while morphing it by changing the guide vane angle up to 2.6 degrees. At a 3 degree angle change it is necessary to generate a new mesh and map the fields to the new mesh in order to be able to continue the simulation. As the space between the guide vanes gets more narrow it is necessary to switch mesh and map field more frequently. In the lower part of each of the pictures it is possible to see a top view of the rotating runner mesh and the rotor-stator interface.
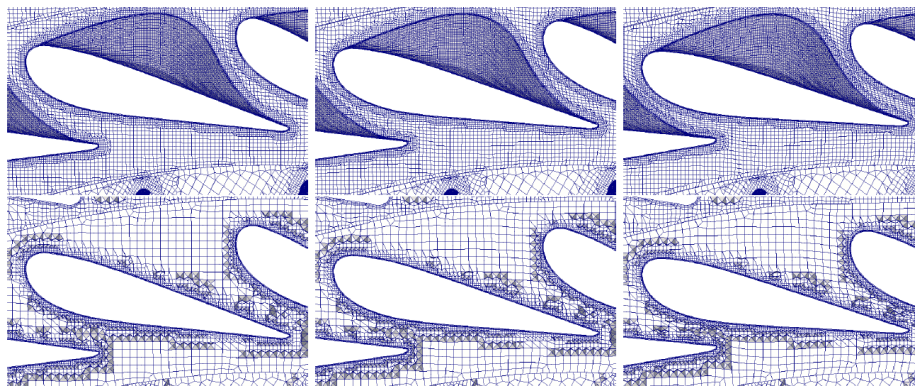
Figure 4: Guide vane mesh during a 2.6° guide vane angle change. Top: At upper cover (also showing a part of the special shape of the guide vane walls, at the densely meshed region above the guide vane). Bottom: Mid-plane. Left: 9.84° (BEP, and original mesh that the meshes at the other angels are morphed from), Center: 8.54°, Right: 7.24°

Figure 5 shows the experimental and numerical static pressure development at VL2, DT5 and DT6, as the guide vanes start closing at t=1s (at 9.84°) and change angle linearly during 7s (to 0.8°, where 0° is fully closed). The experimental data at DT5 and DT6 was presented as deviation from the mean value of each sequence, as then also done for the numerical data. It can be seen that both the general trend and the magnitude of the pressure fluctuations are similar. The major peaks in the numerical results are due to the switches between meshes.
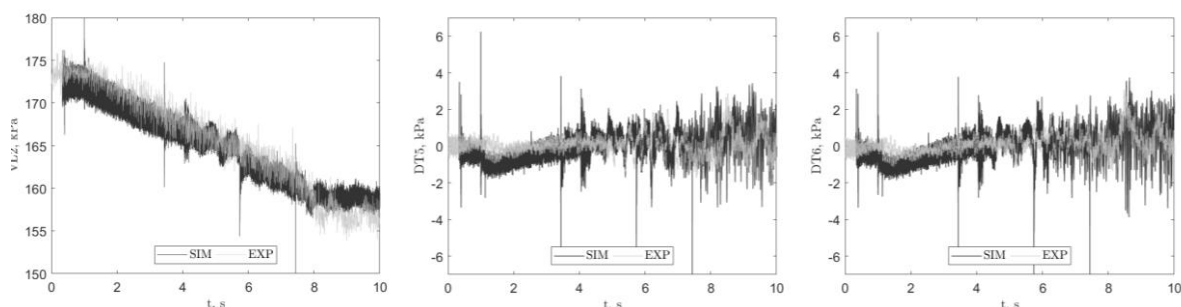
Figure 5: Transient experimental (EXP) and numerical (SIM) static pressure comparison at probes VL2 (left), DT5 (center), and DT6 (right), going from BEP and closing the guide vanes linearly from t=1s to t=8s.

Figure 6 shows contour plots of the velocity along Lines 1 and 2 during the shutdown sequence. The r/R_{max}-axis is along the measurement lines, and the t-axis is along the time (bottom to top). Both the experimental and numerical data is probed at 28 positions along the r/R_{max}-axis. The numerical data has been filtered using a filter width of 15 (using 7 time steps before and after the corresponding time step), and is presented every 50 time step to reduce the influence of the instantaneous turbulent fields. The experimental procedure must involve smoothing both in time and space, but it has not been described in detail in the Francis-99 workshop instructions.
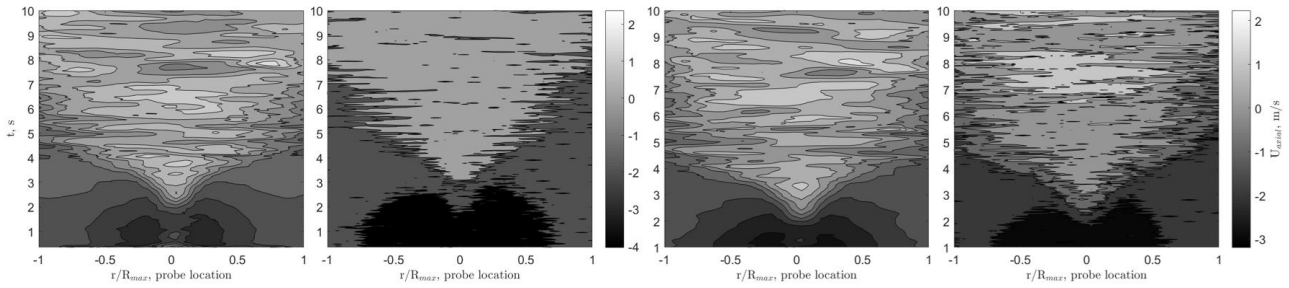
Figure 6: Velocity along line 1 (left pair) and line 2 (right pair) over time (vertical axis). In each pair, Left: simulation. Right: experiment. The guide vanes close linearly from t=1s to t=8s.

When looking at the central vortex rope using the Q-criterion one can see a significant change in flow behaviour during the transient, see Figure 7. The initial small central vortex indicates a relatively stable flow with a high axial and a moderate tangential velocity. As the velocity decreases, the flow is diverging towards the wall and the tangential velocity becomes dominant. This creates a wider vortex in the center of the draft tube that eventually breaks up in 2-3 processing vortices, which finally breaks up in several more chaotic vortices.
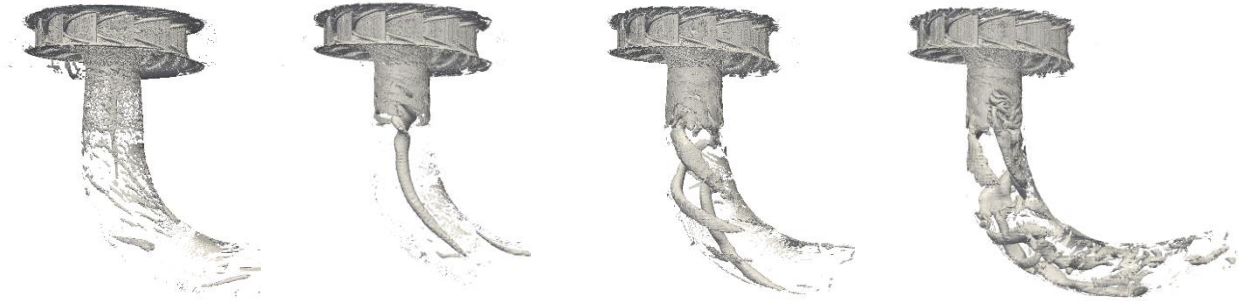
Figure 7: Iso-surface of the Q-criterion (iso-value 200). Left: BEP, at initiation of guide vane closing. Center left: guide vanes appr. 3.3° from BEP. Center right: guide vanes appr. 4.2° from BEP. Right: guide vanes appr. 6.2° from BEP.

Acknowledgements

References

[1] Cervantes, M.., Trivedi, C., Dahlhaug, O.G., Nielsen, T.K. (editors), 'Francis-99 Workshop 1: Steady operation of Francis turbines', IOP Conf. Series: Journal of Physics: Conf. Series 579 (2015) 011001, doi:10.1088/1742-6596/579/1/011001

[2] Cervantes, M.., Trivedi, C., Dahlhaug, O.G., Nielsen, T.K. (editors), 'Francis-99 Workshop 2: transient operation of Francis turbines', IOP Conf. Series: Journal of Physics: Conf. Series 782 (2017) 011001, doi:10.1088/1742-6596/782/1/011001

[3] Lillberg, E., Nilsson, P., 'Generic CFD for Vortex Induced Acoustic Resonance in Deep Cavities', ICONE16, 2008

[4] Trivedi, C., Cervantes M., Dahlhaug, O.G., 'Experimental and Numerical Studies of a High-Head Francis Turbine: A Review of the Francis-99 Test Case', Energies, vol. 9/no. 2, 2016, pp. 1-24.

NUMERICAL ANALYSIS ON THE REFLECTION COEFFICIENT OF A CURTAIN BREAKWATER USING OPENFOAM

SHENG-QIANG YIN[1], XIN-YU WANG[2], YONG LIU[3]

[1]*Shandong Provincial Key Laboratory of Ocean Engineering, Ocean University of China, Qingdao, China, yinshengqiang0214@163.com*

[2]*Shandong Provincial Key Laboratory of Ocean Engineering, Ocean University of China, Qingdao, China, wangxinyutykc@126.com*

[3]*Shandong Provincial Key Laboratory of Ocean Engineering, Ocean University of China, Qingdao, China, liuyong@ouc.edu.cn*

Abstract: This paper presents a two-dimensional numerical investigation on the reflection coefficient of a curtain breakwater including a seaside drooping plate and a leeside caisson. A numerical wave flume is developed based on the continuity equation and the Navier-Stokes equation where the VOF method is used to track and locate the free surface. Relaxation zone method is used to implement the generation and absorption of waves. The numerical results of the reflection coefficient for the curtain breakwater are in good agreement with experimental data in literature. The variations of the reflection coefficient versus factors of the wavelength, the wave chamber width, the immersed depth of the drooping plate and the angle at the bottom of the drooping plate are examined. It is found that for reaching lower reflection, the values of the wave chamber width should be around one tenth of the wavelength. The incident wave energy is dissipated by the vortex flows around the drooping plate effectively. The present numerical wave flume based on OpenFOAM can well estimate the hydrodynamic performance of the curtain breakwater for practical application.
Key Words: Reflection coefficient; Curtain breakwater; Numerical wave flume; OpenFOAM

1 Introduction

Research on the hydrodynamic performance of vertical plate-type breakwaters has been of great interest since the last century. Very important developments have been achieved thanks to the efforts of different researchers. Ursell and Dean (1947) studied the reflection coefficient of a vertical plate breakwater in deep water. Mei (1966) studied the effect of a vertical plate on the progressing waves. Evans (1970) analytically investigated the diffraction of water waves by a submerged vertical plate. Ikeda et al. (1985) studied the eddy's type and the energy dissipation near a vertical plate. Nakamura et al. (1999) experimentally studied the hydrodynamic performance of a curtain breakwater (a drooping plate in front of a vertical wall) and analyzed the effects of the chamber width and the immersed depth of the drooping plate on the reflection coefficient of the breakwater. Ono et al. (2003) analyzed the flow field around a vertical plate. Nakamura and Nakahashi (2005) experimentally investigated the effectiveness of a water exchanging curtain breakwater and analyzed its ability of wave power extractions by wave induced vortex flows.

As mentioned above, most of the existing research on the vertical plate-type breakwater is based on theoretical research or experimental tests. A numerical analysis may give more understanding in the hydrodynamic performance of the breakwater. In this paper, a numerical wave flume based on OpenFOAM is used to study the reflection coefficient of a curtain breakwater as shown in Figure 1. The curtain breakwater consists of a seaside drooping plate and a leeside vertical wall (caisson) providing a simple method to reduce the reflected waves. The drooping plate hanging in front of the vertical wall forms a wave chamber. With this structure, the reciprocating motion of wave resonance increases the phenomenon of eddy at the bottom of the plate. Vortex flow can be utilized to dissipate the incident wave energy effectively. Compared with the conventional vertical wall breakwater, the reflection coefficient of the curtain breakwater is significantly decreased.

In the following Section 2, the numerical method based on OpenFOAM for analyzing the present wave-structure interaction problem is introduced. In Section 3, the numerical results of the reflection coefficient for the curtain breakwater are presented and discussed. Finally, the main conclusions of this study are drawn.
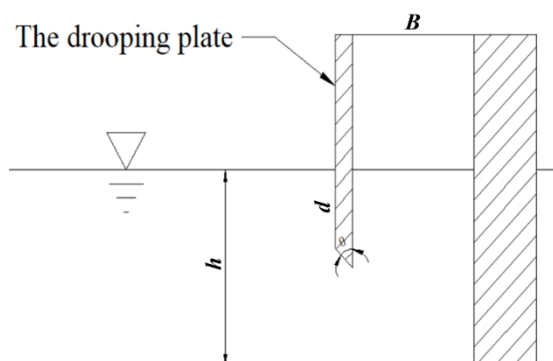
| Figure 1: Sketch of a curtain breakwater | Figure 2: The mesh near the curtain breakwater in numerical method |
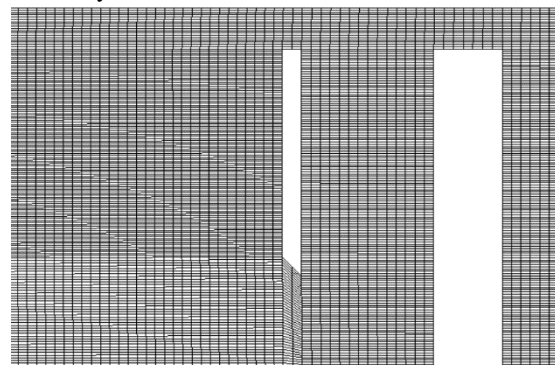
2 Numerical methods

2.1 Governing equations

In this study, both air and water are incompressible viscous fluid. The continuity equation and N-S equation for incompressible viscous fluid are expressed as below:

Continuity equation:

$$\frac{\partial u}{\partial x} + \frac{\partial v}{\partial y} = 0 \tag{1}$$

N-S equation：

$$\frac{\partial u}{\partial t} + u\frac{\partial u}{\partial x} + v\frac{\partial u}{\partial y} = -\frac{1}{\rho}\frac{\partial p}{\partial x} + \frac{\mu}{\rho}(\frac{\partial^2 u}{\partial x^2} + \frac{\partial^2 u}{\partial y^2}) \tag{2}$$

$$\frac{\partial v}{\partial t} + u\frac{\partial v}{\partial x} + v\frac{\partial v}{\partial y} = -\frac{1}{\rho}\frac{\partial p}{\partial y} + \frac{\mu}{\rho}(\frac{\partial^2 v}{\partial x^2} + \frac{\partial^2 v}{\partial y^2}) + g \tag{3}$$

where ρ represents density, t represents time, p represents pressure, μ represents dynamic viscosity, u and v represent respectively velocity components in x- and y-directions, g is the gravitational acceleration.

The above equations are solved based on interFoam solver. The second-order Stokes wave theory is adopted, and the relaxation zone method proposed by Jacobsen et al. (2012) is used to implement the generation and absorption of waves. The basic principle of the relaxation zone method can be expressed as

$$u = \alpha_R u_{\text{model}} + (1-\alpha_R)\,u_{\text{target}} \tag{4}$$

$$\alpha_R = 1 - \frac{\exp\left(X_R^{3.5}\right) - 1}{\exp(1) - 1} \qquad X_R \in [0,1] \tag{5}$$

where u_{model} is the velocity calculated by N-S equation and u_{target} is the target velocity that we expected.

Volume of fluid (VOF) is a numerical method for tracking and locating free surface which is the interface of air and water in the numerical wave flume. This method is used by OpenFOAM to specify the fraction of each fluid (air and water) in each cell. The phase fraction equation is given by

$$\frac{\partial \alpha}{\partial t} + \nabla \alpha U = 0 \tag{6}$$

where α represents the phase fraction and U refers to velocity. α is always between 0 and 1. $\alpha = 0$ means the cell is fully filled by air and $\alpha = 1$ means the cell is only filled by water. The density of each cell can be calculated by

$$\rho = \alpha\rho_w + (1-\alpha)\,\rho_a \tag{7}$$

where ρ_w is the water density and ρ_a is the air density. Note that this density is the density of the mixture of air and water inside each cell.

2.2 Numerical wave flume

The two-dimensional numerical wave flume was 12 m long, 0.42 m wide and 0.8 m high. The drooping plate was placed in a position, 2 m to the end of the water flume. In order to obtain the incident and reflected wave heights using Goda's method, the free surface elevations were recorded in the position about 4.4m, 4.6m and 4.8m away from the drooping plate. As shown in Figure 1, the width of the wave chamber B were 21 cm, 23 cm, 25 cm, 27 cm and 29 cm, respectively. The immersed depth d of the drooping plate with a thickness of 4.2 cm were also 21 cm, 23 cm, 25 cm, 27 cm and 29 cm, respectively. The angles θ at the bottom of the drooping plate were 30°, 45°, 60°, 90° and -45°, respectively. The water depth h was 42 cm and the incident wave height H was 6 cm. The wave period was changed from 0.9 s to 1.8 s. The width of the leeside vertical wall was 15 cm. All the above parameters were adopted by referring to the experimental tests of Nakamura et al. (1999). The mesh near the curtain breakwater in the numerical wave flume is plotted in Figure 2.

3 Results and discussion

3.1 Verification of numerical results

In this section, the numerical results of the reflection coefficient C_r and the free surface elevation H_c inside the wave chamber are compared with the experimental data of Nakamura et al. (1999). It is noted that no less than 10 waves were taken into account to obtain the reflection coefficient and the free surface elevation. Figures 3 – 5 show comparisons between the numerical results and experimental data for the reflection coefficient C_r, where L is the incident wavelength. It can be seen from these figures that the numerical results and experimental data are in good agreement. In addition, the reflection coefficient attains a minimum value with the increasing wavelength. Figure 6 shows a comparison between the numerical results and the experimental data for the free surface elevation H_c inside the wave chamber divided by the incident wave height H. Again, the two results are in good agreement. But, the free surface elevation inside the chamber decreases with the decreasing incident wavelength. It is proved that the present numerical wave flume can well estimate the hydrodynamic performance of the curtain breakwater.
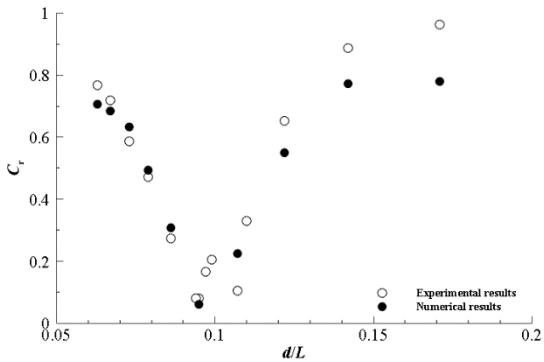
Figure 3 Variation of C_r versus d/L (B=21 cm, d=21 cm, θ=45°)
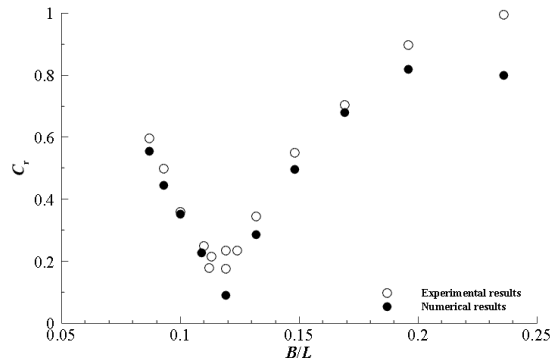
Figure 4 Variation of C_r versus B/L (B=29 cm, d=21 cm, θ=45°)
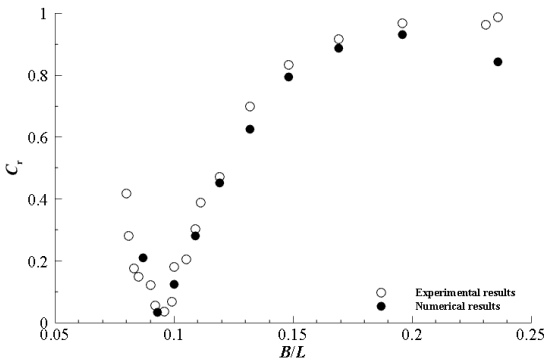
Figure 5 Variation of C_r versus B/L(B=29 cm,d=29 cm,θ=45°) Figure 6 Variation of H_c/H versus B/L(B=29 cm,d=21 cm, θ=45°)
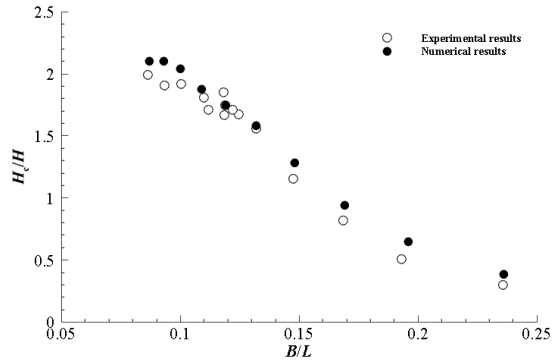
3.2 Further discussions

Numerical results are given in figures 7 and 8 to show the effects of the wave chamber width B and the immersed depth d of the drooping plate on the reflection coefficient C_r, respectively. It can be seen from these figures that for long period waves, the curtain breakwater with a larger wave chamber width B or a larger immersed depth d of the drooping plate can dissipate more incident wave energy and thus has a lower reflection coefficient. But this is just the opposite for short period waves. In addition, as the immersed depth d of the drooping plate increases in Figure 8, the minimum reflection coefficient of the breakwater occurs at longer wave period (larger wavelength L and smaller relative wave chamber width B/L).
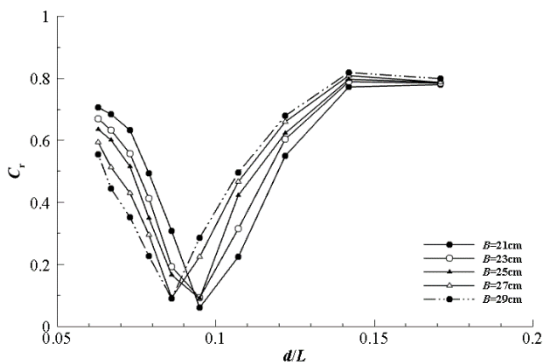
Figure 7 Variation of C_r versus d/L （d=21 cm, θ=45°)　　　Figure 8 Variation of C_r versus B/L （B=29 cm, θ=45°)
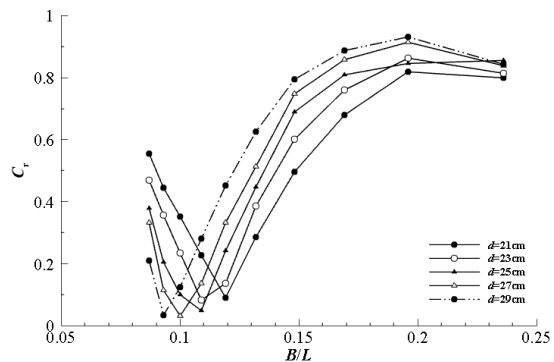
Figure 9 gives numerical results to show the effect of the wave steepness H/L on the relative wave height H_c/H inside the wave chamber. It can be seen from this figure that the value of H_c/H increases with the decreasing H/L (the increasing incident wavelength L). This is natural as more wave energy can penetrate into the wave chamber for longer period waves. Figure 10 shows the effect of angle θ at the bottom of the drooping plate on the reflection coefficient C_r. It is noted from this figure that the reflection coefficients of curtain breakwater at positive and negative angles (θ = 45° and –45°) are close. In addition, a drooping plate with a shaper corner generally can dissipate more incident wave energy (has smaller reflection coefficient).
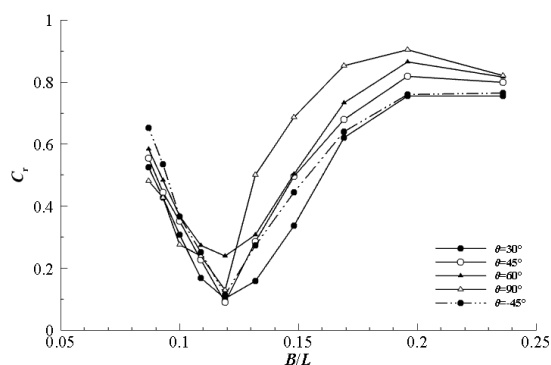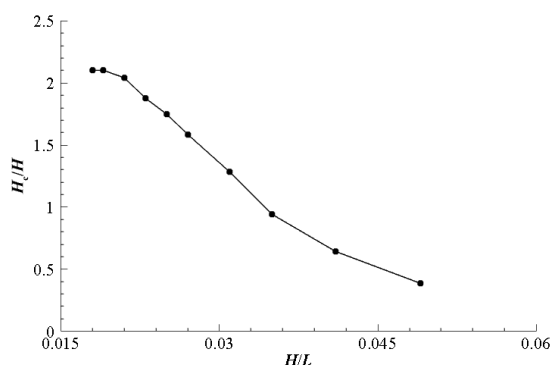
Figure 9 Variation of H_c/H versus H/L(B=29 cm, d=21 cm, $θ$=45°) **Figure 10 Variation of C_r versus B/L(B=29 cm, d=21 cm)**

In order to further examine the energy dissipation mechanism of the breakwater, the flow fields around the drooping plate with the same wave period ($T = 1.4$ s) which corresponds to the smallest reflection coefficients in Figure 10 for different angles $θ$ ($θ = 45°, –45°$ and $90°$) at the same time ($t = 35$ s) are shown in Figure 11. In this figure, vortex flows at the bottom of the drooping plate can be clearly observed, and the incident wave energy is dissipated by the vortex flows effectively. It is noted that the flow fields around the drooping plate in Figure 11 are similar, which results in close minimum reflection coefficients at about $B / L = 0.12$ for the three different cases.

$θ = 45°$ $θ = –45°$ $θ = 90°$
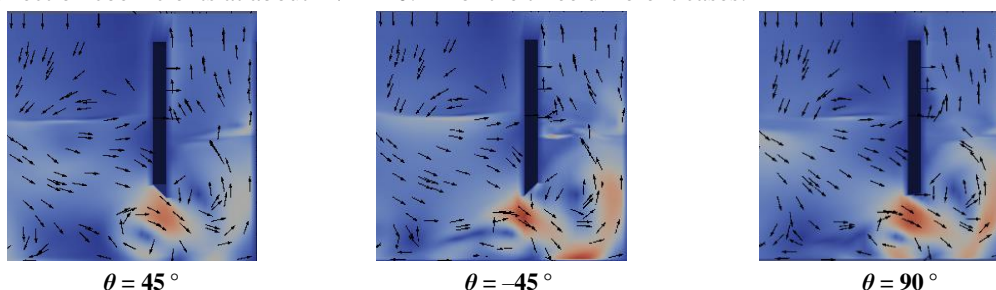
Figure 11 The flow fields around the drooping plate (B = 29 cm, d = 21 cm, t = 35 s)

4 Conclusion

In this study, the interaction between the curtain breakwater and regular waves has been studied using the numerical solution based on OpenFOAM. The numerical results of the reflection coefficient and the free surface elevation inside the wave chamber of the curtain breakwater are in a good agreement with the experimental data in literature. Numerical results have shown that for reaching a low reflection coefficient, the wave chamber width of the curtain breakwater should be designed as about one tenth of the incident wavelength. The positive and negative sloping angles at the drooping plate bottom cannot bring significant difference on dissipating incident wave energy. The present numerical solution based on OpenFOAM can well estimate the hydrodynamic performance of the curtain breakwater, and the irregular wave action on the curtain breakwater will be examined in the next study.

References
[1] F. Ursell, W.R. Dean, The effect of a fixed vertical barrier on surface waves in deep water. Mathematical Proceedings of the Cambridge Philosophical Society, 1947, 43(3):374-382.
[2] C. C. Mei, Radiation and scattering of transient gravity waves by vertical plates. Quarterly Journal of Mechanics & Applied Mathematics, 1966, 19(4):417-440.
[3] D. V. Evans, Diffraction of water waves by submerged vertical plate. Journal of Fluid Mechanics, 1970, 40(3):433-451.
[4] S. Ikeda, T. Asaeda, K. Nomoto, et al. Vortex structure and energy dissipation near a vertical plate under wave action. Proceedings of the Japan Society of Civil Engineers, 1985:87-96(in Japanese).
[5] T. Nakamura, M. Kane, Y. Nishikawa, et al. Performance of a Drooping wall reflection dissipater using the increased phenomenon of vortex flow. Proceedings of the Japan Society of Civil Engineers, 1999:796—800 (in Japanese).
[6] M. Ono, T. Nakamura, N. Takagi, et al. Vortex induced the large-scale circulation and mixing about a curtain-walled reflection dissipate in waves. Japan Annual Journal of Civil Engineering in the Ocean, 2003:559—564 (in Japanese).
[7] T. Nakamura, K. Nakahashi, Effectiveness of a chamber- type water exchange breakwater and analyzed its ability of wave power extraction by wave induced vortex flows. Japan Annual Journal of Civil Engineering in the Ocean, 2005:547—552 (in Japanese).
[8] N. G. Jacobsen, D. R. Fuhrman, J. Fredsoe, A wave generation toolbox for the open-source CFD library: OpenFoam. International Journal for Numerical Methods in Fluids, 2012, 70 (9):1073-1088.

NUMERICAL SIMULATION OF HULL PRESSURE FLUCTUATION INDUCED BY PROPELLER CAVITATION USING OPENFOAM

CHAOSHENG ZHENG[1], ZHENGQING DONG[1], DENGCHENG LIU[1], ZHIRONG ZHANG[1], FANGWEN HONG[1]

[1] *China Ship Scientific Research Center (CSSRC) national key laboratory on ship vibration & noise, Jiangsu Key laboratory of Green Ship technology, Wuxi, Jiangsu, China, zcszcs2005@163.com*

1. Introduction

The propeller cavitation, one important aspect of propeller performance, has been studied by experimental and numerical approaches. The commercial CFD software, such as ANSYS FLUENT, STARCCM+, have been widely used to study the propeller cavitation. Da-Qing Li (2012) has predicted the E779A cavitation in non-uniform wake based on RANS approach and Zwart cavitation model using ANSYS FLUENT. Kwang-Jun Paik (2013) has predicted the propeller cavitation pattern and the hull pressure fluctuation induced, using FLUENT and SchnerrSauer cavitation model.

Recently, OpenFOAM, the open-source CFD platform, has been increasingly popular in the numerical simulation of propeller cavitation. Abolfazl (2015) has predicted the PPTC propeller cavity extent within a 12°inclination of shaft using ILES method and SchnerrSauer cavitation model based on OpenFOAM. Rickard E Bensow (2015) has studied the cavity extent, flow field and forces on the propeller of a 7000 DWT chemical tanker, with ILES method and Kunz cavitation model adopted in OpenFOAM. Zheng Chaosheng (2016, 2017) has predicted the unsteady propeller cavitation and hull pressure fluctuation induced in the ship stern using RANS method and OpenFOAM, the cavitation shape and the first blade frequency (1BF) amplitudes of hull pressure fluctuation predicted resemble well with the experiment observations and measurements.

The present work aims to predict the unsteady propeller cavitation in the stern region of a 14000 TEU container vessel, with special attention to the mesh independency on the unsteady cavitation behavior and hull pressure fluctuation.

2. Numerical methods

The unsteady viscous RANS approach and SchnerrSauer cavitation model are adopted to simulate the unsteady propeller cavitation. The SST $\kappa\omega$ turbulence model is chosen to solve the turbulent viscosity, and the free surface is neglected. The computation domain is divided into two sub-regions, the ship region and propeller region, all consist of hexahedral cells generated using HEXPRESS, and the interpolation between the non-conforming interfaces of the two sub regions is accomplished by AMI, implemented in OpenFOAM.

To improve the convergence, the full wetted flow is simulated to obtain a quasi-stable flow field using MRF method, then sliding mesh is applied to mimic the rotation of propeller, and the cavitation model is activated to simulate the unsteady propeller cavitation. The scotch decomposition method is adopted for parallel computations.

3. Results and Discussions

The numerical simulation condition is summarized in Table 1.

Table 1: The numerical simulation condition

n	28rps
$\sigma n_{0.8R}$	0.2493
KT	0.1887

In order to investigate the mesh independency, three grid sizes, the coarse, medium and fine mesh are used, as shown in Table 2 and Figure 1.

Table 2: The coarse, medium and fine mesh

	Coarse	Medium	Fine
Number of cells in ship region	3253362	5516333	9783416
Number of cells in pro region	652032	1017692	1585578
Total number of cells	3905394	6534025	11368994
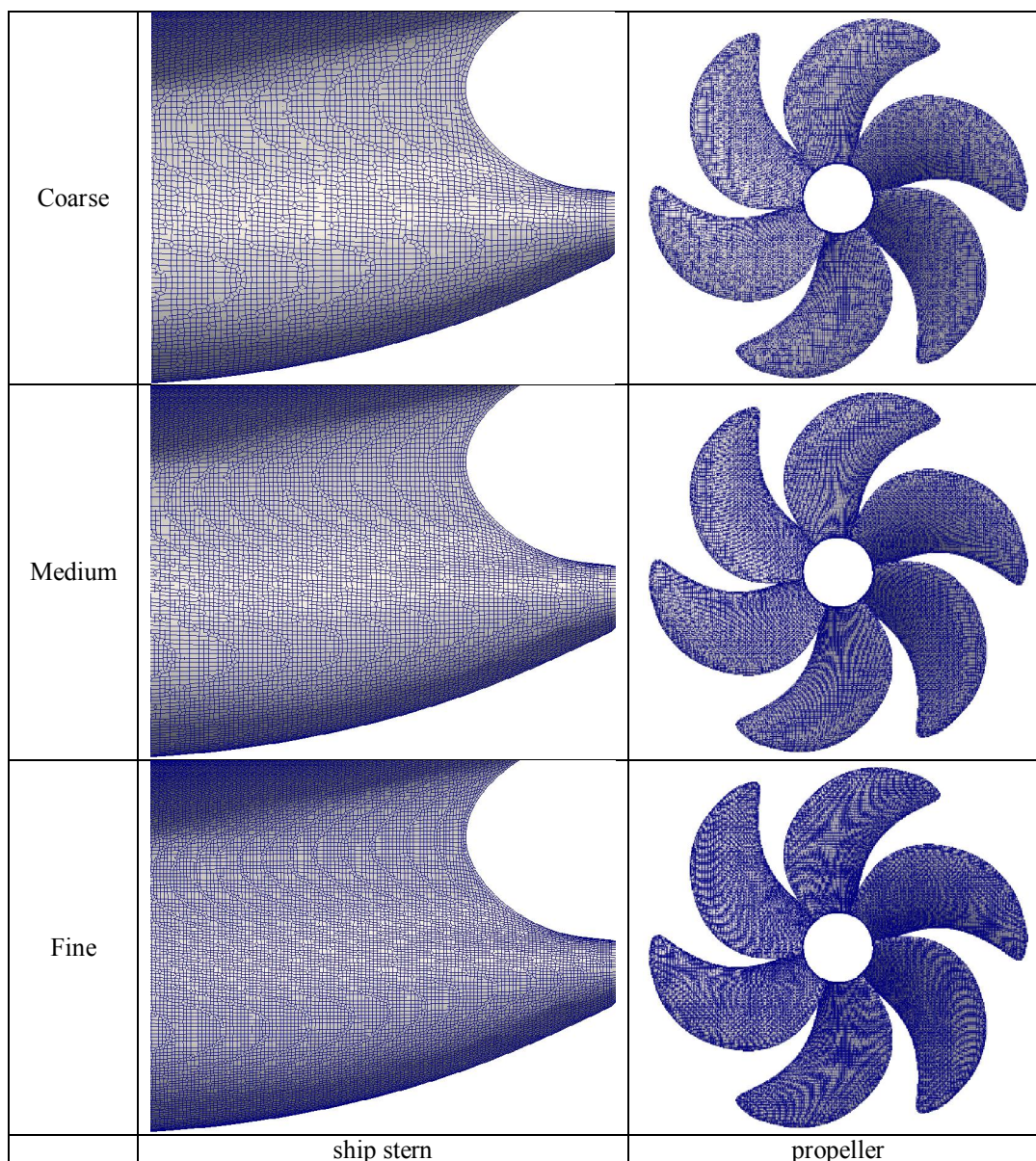
Figure 1: The surface mesh of ship stern and propeller

In the study, 300 CPU cores are utilized in the numerical simulation, and the time cost for the unsteady cavitation prediction in the coarse, medium and fine mesh is recorded in Table 3.

Table 3: The time cost for the unsteady cavitation simulation

	Coarse	Medium	Fine
Time (hours)	2.86	5.26	10.53

The predicted cavitation in the stern region is compared with the experiment sketches side-by-side in Figure 2. The predicted cavity, represented by vapour iso-surface of 0.1 shows the same behaviour as the experiment observations. The key feature, the extent change of the attached cavity with the rotation angles correlates well with the experiment, e.g. the cavity begins at about the same location $\varphi \approx -10°$, reaches the maximum area at $\varphi \approx 20°$(the rotation angle φ is defined as 0° at 12 o' clock).

In Figure 2, compared with the coarse mesh, the attached cavity predicted of the medium mesh seems closer to the outer radius, which is more accordant with the experiment observation. While, the cavity shows little difference between the medium and fine mesh. Taking the cost time into account, it implies that the medium mesh can meet the accuracy requirements of the unsteady propeller cavitation.
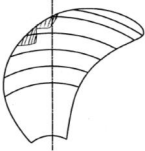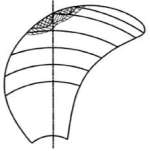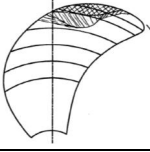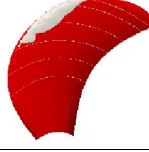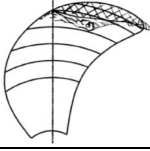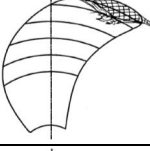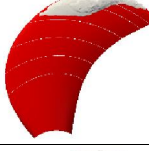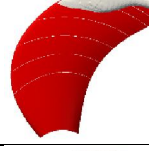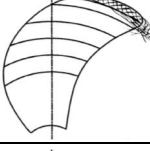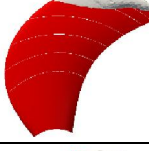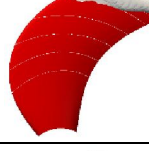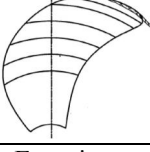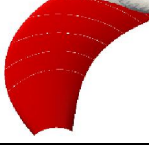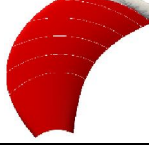
Angles	Experiment sketches	Coarse	Medium	Fine
-10°				
0°				
10°				
20°				
30°				
40°				
50°				

Figure 2: The experiment sketches vs. prediction

As to the hull pressure fluctuation induced by propeller cavitation, the monitor points are arranged on the stern surface shown in Figure 3. The pressure fluctuation predicted is compared with the experiment in Figure 4.

In Figure 4, the 1BF (1st Blade Frequency) amplitudes of hull pressure fluctuation predicted of the coarse mesh has a significant gap with the experiment, which is mainly due to the high numerical dissipation across the coarse mesh. The medium mesh obtains a dramatic improvement. The fine mesh gives more accurate results in principle, nevertheless the advancement is not as obvious as the one between the coarse and medium mesh. As a whole, it also indicates that the medium mesh can obtain more satisfactory time efficiency and precision of the hull pressure fluctuation.
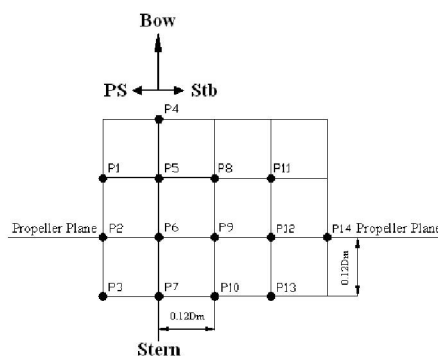
Figure 3: The arrangement of monitor points
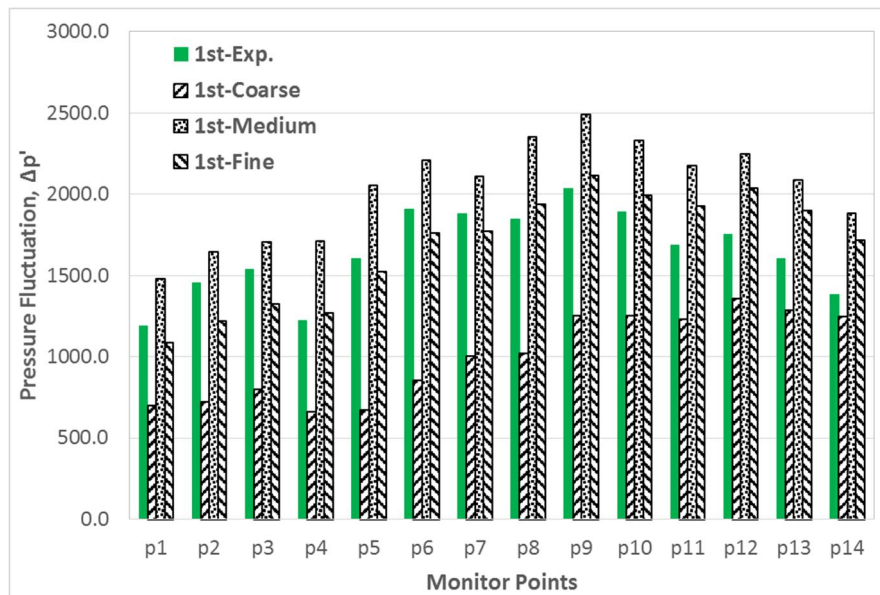
Figure 4: The 1BF of hull pressure fluctuation predicted vs. the experiment

4. Conclusions

The propeller cavitation shape and the amplitudes of the first blade frequency (1BF) of the hull pressure fluctuation predicted resemble well with the experiment observations and measurements, and the results also shows that the medium mesh can obtain more satisfactory efficiency and precision of unsteady cavitation behaviour as well as the hull pressure fluctuation.

Acknowledgements

References

[1] Kwang-Jun Paik. URANS Simulations of Cavitation and Hull Pressure Fluctuation for Marine Propeller with Hull Interaction. 3nd International Symposium on Marine Propulsors, Tasmania, pp.389-396, 2013.

[2] Abolfazl Asnaghi. Computational Analysis of Cavitating Marine Propeller Performance using OpenFOAM. 4th International Symposium on Marine Propulsors, Tesas, pp.148-155, 2015.

[3] Rickard E Bensow. Large Eddy Simulation of a Cavitating Propeller Operating in Behind Conditions with and without Pre-Swirl Stators. 4th International Symposium on Marine Propulsors, Tesas, pp.458-477, 2015.

[4] Zheng Chaosheng. The unsteady numerical simulation of propeller cavitation behind a single-screw transport ship using OpenFOAM. 2nd Conference of Global Chinese Scholars on Hydrodynamics, Wuxi, pp.117-123, 2016.

[5] Zheng Chaosheng . The numerical prediction of the propeller cavitation and hull pressure fluctuation in the ship stern using OpenFOAM . smp17, Espoo, Finland, pp.745-749, 2017.

STUDY ON REFLECTION AND TRANSMISSION COEFFICIENTS OF COMB-TYPE CAISSON BREAKWATER

XIN-YU WANG[1], YONG LIU[2]

[1]*Shandong Provincial Key Laboratory of Ocean Engineering, Ocean University of China, Qingdao 266100, China, wangxinyutykc@126.com*

[2]*Shandong Provincial Key Laboratory of Ocean Engineering, Ocean University of China, Qingdao 266100, China, liuyong@ouc.edu.cn*

Abstract: This paper presents a three-dimensional (3-D) numerical solution of nonlinear wave interactions with comb-type caisson breakwaters. The numerical solution is developed by the open-source CFD library OpenFoam® which contains a C++ toolbox called waves2Foam for solving free surface Newtonian flows using the Reynolds averaged Navier-Stokes equations with volume of fluid method (VOF) tracking the free surface. Relaxation zone technique is implemented to avoid wave reflection from marine structure and outlet boundaries by applying relaxation functions inside the relaxation zone. The second-order Stokes wave theory are adopted to generate nonlinear wave trains in the inlet relaxation zone. The numerical solution is obtained in a strip of fluid domain for the saving of computational cost by using two different boundary conditions: symmetryPlane in a planar for the front and back faces of the fluid domain and symmetry in non-planar for the wall of comb-type caissons and side plates. In order to investigate the energy dissipation from fluid viscosity, an analytical solution based on potential theory for the present problem is compared with the numerical solution. The results show that the comb-type caisson breakwater can dissipate wave energy efficiently and thus present a good sheltering for harbour basin. The present numerical model is expected to be an efficient tool for preliminary design of comb-type caisson breakwater (periodical marine structures).

Keywords: Comb-type caisson, Numerical simulation, Reflection coefficient, Transmission coefficient, Energy dissipation

1. Introduction

A comb-type caisson consisting of a rectangular caisson and two partially immersed side plates (see Figure 1) has been invented and successfully used for building a breakwater in Da-yao Bay of Dalian, China (Niu et al., 2003). Compared with traditional rectangular caissons, the comb-type caisson can save engineering investment and reduce the requirement of foundation bearing capacity, as the rectangular caisson is partially replaced by side plates (Niu et al., 2001). Most of all, the gap beneath the side plates allow the partially pass of tide current, and thus significantly reduce the flow velocity near the breakwater entrance and guarantee the navigation safety. In addition, the reflection coefficient and wave forces acting on the comb-type caisson breakwater are smaller than that of the traditional caisson breakwater, and thus the stability against sliding of the structure can be enhanced (Li et al., 2002).

The wave interactions with comb-type caisson breakwaters have been investigated by some scholars using experimental tests and numerical methods. The working mechanism of comb-type caisson breakwater and its sheltering function were summarized by Zhu et al. (2001). The hydrodynamic performance of comb-type caisson breakwaters has been examined by Li et al. (2002) and Dong et al. (2003), and an empirical formula for calculating the horizontal wave forces acting on comb-type caisson breakwaters has been developed. Wang et al. (2001) analysed the stress characteristics of side plates and carried out model tests on wave forces acting on side plates to analyse its structure and structure reinforcement design. The internal stress distribution, the natural vibration characteristics and static forces of side plates were examined by Zhang et al. (2002) using finite element method. Fang et al. (2011) developed a three-dimensional numerical wave tank using Fluent to examine the hydrodynamic performances of comb-type caisson breakwaters, and gave an empirical formula to estimate the transmission coefficient. Wang et al. (2017) developed a three-dimensional analytical solution to solve wave scattering by the comb-type caisson breakwater, and gave theoretical formulae for the reflection and transmission coefficients.

Although some studies on the comb-type breakwater have been performed, numerical analysis on comb-type caisson breakwaters are still not enough. This paper will develop an efficient 3-D numerical solution for nonlinear wave interactions with comb-type caisson breakwaters using symmetry and symmetryPlane boundary conditions. A better understanding on the hydrodynamic performance of the comb-type caisson breakwater after considering fluid viscosity and nonlinear wave may be presented by the present numerical study. In the following section, a numerical solution is presented in detail, which is capable of solving wave scattering by comb-type caisson breakwater and other periodical marine structures. In section 3, the numerical model is validated and typical numerical results are presented and discussed. Finally, the main conclusions of this study are drawn.

2. Numerical Model

2.1 Governing equations

The governing equations for the combined flow of air and water phases are given by the incompressible continuity equation and momentum equations:

$$\nabla \cdot \mathbf{U} = 0 , \tag{1}$$

$$\frac{\partial \rho \mathbf{U}}{\partial t} + \nabla \cdot (\rho \mathbf{U} \mathbf{U}^T) - \nabla \cdot (\mu \nabla \mathbf{U}) = -\nabla p^* + g \cdot (\mathbf{x} - \mathbf{x}_r) \nabla \rho , \tag{2}$$

where the bold fonts indicate a vector field. $\mathbf{U}$ is the velocity vector field; ρ is the fluid density; μ is the dynamic viscosity;

$p*$ is the dynamic pressure; $\mathbf{x}$ is the Cartesian coordinate vector, $\mathbf{x}_r$ is a reference location related to still water level.

The above governing equations for viscous fluid are simultaneously solved using waves2Foam (interFoam solver). The waves2Foam tracks the movement of the interface between air and water phases by the VOF technique (Jacobsen et al., 2015). The volume fraction α is bounded from 0 to 1 where $\alpha = 0$ means air full of cell and $\alpha = 1$ means water full of cell and any intermediate value is a mixture of air and water. The density and viscosity fields are all calculated based on the volume fraction field, which satisfies:

$$\frac{\partial \alpha}{\partial t} + \nabla \cdot \mathbf{U}\alpha + \nabla \cdot (\mathbf{U}_r \alpha(1-\alpha)) = 0 , \tag{3}$$

where, the last term at the left hand is the interface compression term to avoid the excessive diffusion of the interface, and $\mathbf{U}_r$ is a compressive velocity. The pressure and velocity fields are obtained by solving Eqs. (1) and (2), while the free surface is captured with Eq. (3).

2.2 Solving procedure

In OpenFoam, Finite volume method is employed to discretize the governing equations. In the discretization process, different interpolation schemes are adopted to discretize each term of governing equations. For instance, the implicit Euler scheme is always used for the first term of momentum equation. This scheme is a first order accuracy in time and provides relatively accurate results with small time steps. More information is introduced in Moukalled et al. (2015).

The numerical procedure for the waves2Foam is summarized as follows. First, we solve the transportation Eq. (3) equation for volume fraction field. In the process of solving the volume fraction, a numerical method called Mules (Multidimensional Universal Limiter for Explicit Solution) is applied in waves2Foam. This method is more efficiency because it introduces an artificial convection term $\nabla \cdot (\mathbf{U}_r \alpha(1-\alpha))$ developed by Weller (2002) to ensure a sharp interface rather than reconstructing the free surface in each time step. And then the values of fluid and interface properties are updated based on volume fraction field. At last, the discretized governing equations are solved using PIMPLE algorithms.

The numerical algorithm PIMPLE is adopted in numerical model combining two algorithms PISO (Pressure-Implicit Splitting of Operators) and SIMPLE (semi-implicit method for pressure-linked equations). For the implementation of PIMPLE algorithm, the transient term of solution between two time steps is solved by PISO algorithm while the steady-state flow is obtained using SIMPLE algorithm in each time step. The advantage of PIMPLE algorithm is to speed up numerical simulation by using under relaxation factor with a relative big time step. PISO and SIMPLE algorithms are thoroughly explained in Jasak (1996).

2.3 Numerical wave flume

The comb-type caisson breakwater comprised of an array of uniform comb-type caissons is plotted (only six entire caissons) in Fig. 1. It can be seen from Fig.1 that the width of a wave chamber formed by adjacent rectangular caissons and partially immersed side plates is B. The water depth is of constant d and the bottom of side plate is at a distance of b away from the seabed with a side plate height h_a ($h_a = d - b$). The composition for one unit of comb-type caisson is shown in upper left corner of Fig. 1. The length of rectangular caisson is c, and the length of side plate is a. Figure 2 shows the 3-D numerical wave flume with a model of comb-type caisson and the Cartesian coordinate system is chosen. The wave flume was set up in 25 m long, 1.5 m high and 1.6 m wide and divided into three zones: inlet relaxation zone I, zone II with one unit of comb-type caisson and inlet relaxation zone III. Waves with wave height H and wavelength L are normally incident. The origin is located at the intersection of inlet face, seabed face and front face. Thus, the x-y plane is in the seabed at $z = 0$ and y-axis points vertically upwards along the inlet surface with the still water level at $y = 1$ m.
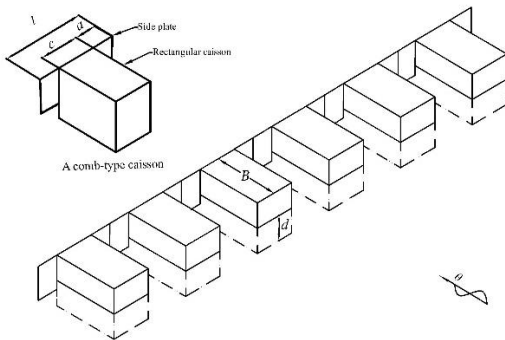
Fig. 1 Idealized sketch for wave interaction with a comb-type caisson breakwater
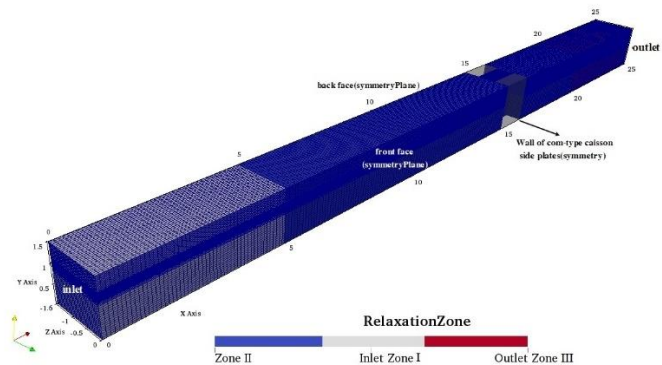
Fig. 2 The sketch of 3-D wave flume with a comb-type caisson

In Fig. 3, a 2-D sketch is plotted to present the vertical cross section created along $z = -0.8$ m of the 3-D wave flume in Fig.2. The vertical cross section is located at the middle of the side plate. Three horizontal zones with identical cell size grading have been defined. The inlet relaxation zone I represents the wave propagation and absorption area, and covers from $x = 0$ m to $x = 5$ m. The zone II is located from $x = 5$ m to $x = 20$ m. The comb-type caisson lies between 15 m and 16.25 m as show in Fig. 3. The thickness of the side plate Δx_t is set to 0.05 m. The outlet relaxation zone III covers the final 5 m where the wave energy is totally absorbed. In the y-direction the cell size is constant and equal to 1 cm throughout the flume.

2.4 Generation of mesh refinement

The mesh refinement is created with snappyHexMesh at a band from $y = 0.9$ m to 1.1 m around free surface elevation. The grid cells are refined in all directions by splitting the original cells in quarter. This mesh refinement scheme saves computational cost by having less cells. A numerical investigation without marine structure are implemented to study the effect of different mesh sizes on the numerical results at $x=15$ m in Fig. 4. It can be seen from Fig. 4 that slight wave attenuations occur in sparse grid where sparse grid spacing ($\Delta x_s = 0.05$ m) in x-direction is a fifth of refinement grid spacing (Δx_r). But, we can obtain a target wave height $H = 0.05$ m for sparse grid at breakwater area when we set an appropriate inlet wave height. Therefore, for high efficiency in computations, the mesh level Δx_s is adopted in following simulations.

The results of numerical solution can be obtained in a strip of one comb-type caisson unit instead of calculating the whole fluid domain owing to adopting two different boundary conditions: one is called symmetryPlane in a planar for the front and back face of the fluid domain and the other is called symmetry in non-planar for the wall of comb-type caissons and side plates. The numerical boundary conditions utilized in this model can improve computational efficiency considerably.

Table 1 The list of wave parameters, dimensions of comb-type caisson element and locations of wave gauges.

Dimensions of comb-type caisson		Numerical wave parameters	wave gauges points(WGP) (x, y, z) unit(m)			
A	0.3 m	wave theory: Stokes waves	0	(0, 0.9~1.1, -0.8)	4	(10, 0.9~1.1, -0.8)
C	1.0 m	wave height: 0.05 m, 0.08 m	1	(3, 0.9~1.1, -0.8)	5	(16.5, 0.9~1.1, -0.8)
B	0.5 m	water depth: 1 m	2	(8, 0.9~1.1, -0.8)	6	(22, 0.9~1.1, -0.8)
B	1.2 m	wave period: 1.2 s, 1.8 s	3	(9, 0.9~1.1, -0.8)	7	(24, 0.9~1.1, -0.8)

3. Numerical results

3.1 Validations of numerical model

The present numerical model is validated from two aspects, including the generation of linear and nonlinear wave trains and interactions between waves and comb-type caisson breakwaters. The dimensions of comb-type caisson structure, wave parameters and wave gauge points (WGP) utilized in the following calculations are listed in Table 1.

Linear wave train with $H = 0.05$ m and $T = 1.8$ s and non-linear second-order stokes wave train with $H = 0.08$ m and $T = 1.2$ s are generated in the wave flume without marine structure. The corresponding numerical results of wave surface elevations are compared with the theoretical results in Fig. 5 and Fig. 6, respectively. It is noted that the time series of free surface elevations for numerical solution are in good agreement with that of theoretical solution at $x = 0$ m and 3 m. The wave heights are reduced effectively at $x = 22$ m and almost vanished at $x = 24$ m because the wave gauge locations are inside outlet relaxation absorption zone. Thus, the effectiveness of the relaxation zones at the inlet and outlet is confirmed. It is also noted in Fig. 6 that the mean water level of the numerical solution has a slight increase at the entire time instance because of the nonlinear resonant wave interactions (Chapalain et al., 1992).

In Fig.7, the wave forms with $x = 11$ m and 13 m are also plotted to verify the nonuniformity of the numerical wave flume at $z = -0.4$ m and -0.8 m. It can be seen that the wave forms at two z-directions are in good agreement at $x = 11$ m before $t = 22$ s. But for $t > 22$ s a slight difference in the wave forms appears due to the phase shift resulting from the periodical structure along z-directions. We can also observe that at $x = 13$ m the wave forms at $z = -0.4$ m and -0.8 m do not exactly coincide after $t = 17$ s. But the difference between $x = 11$ and 13 m is that the non-overlapping phenomenon appears earlier at $x = 13$ m due to the shorter distance from the front wall of the breakwater.
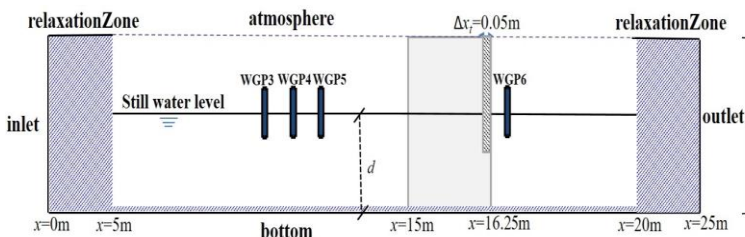
Fig. 3 A 2-D sketch of vertical cross section along $z = -0.8$ m of the 3-D wave flume.
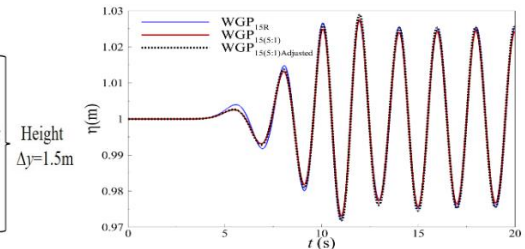
Fig. 4 Free surface elevations of linear wave at WGP ($x = 15$ m) for two different grid sizes.
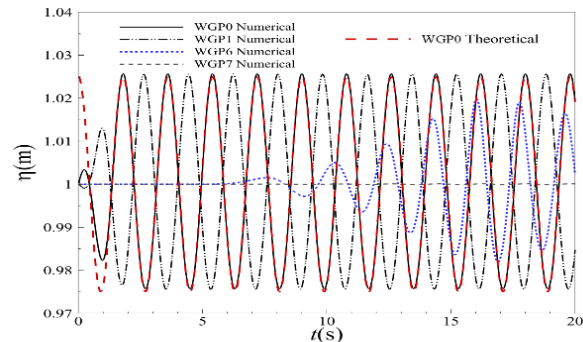
Fig. 5 Free surface elevations at the WGP of linear waves.
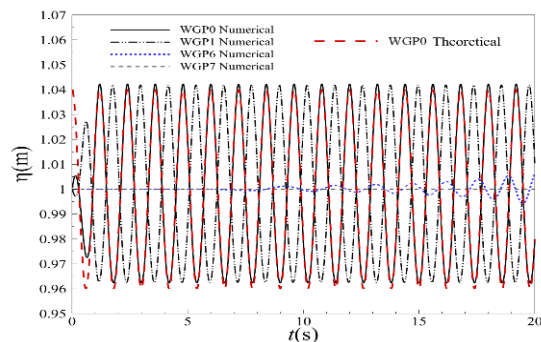
Fig. 6 Free surface elevations at the WGP of second-order Stokes waves.

3.2 Discussions

Comparisons between the present numerical results and the analytical solution (Wang et al., 2017) for the reflection coefficients C_r and the transmission coefficients C_t at different heights of side plates are plotted in Fig. 8 and Fig. 9, respectively. The reflection coefficients of numerical solution are determined by the method of Goda and Suzuki (1976). It can be seen from Figs. 8 and 9 that the curves of C_r and C_t calculated by the two different methods have the same variation trend with the increasing value of h_a. But the numerical results are smaller than that of the analytical solution as the fluid viscosity (energy dissipation) has been well considered in the numerical solution. In Fig.10, the quadratic sum of the reflection and transmission reflections ($C_r^2 + C_t^2$) for the numerical reuslts is plotted. It is noted that the value of $C_r^2 + C_t^2$ for the analtyical solution always equals to unity due to zero energy loss in analytical solution. Thus it is not plotted. For the numerical result in Fig. 10, the curve of $C_r^2 + C_t^2$ first decreases and then increases with the increasing value of h_a. In general, the side plate heights have significant effect on the hydrodynamic performance of comb-type breakwaters and should be carefully taken into account in the engineering design.
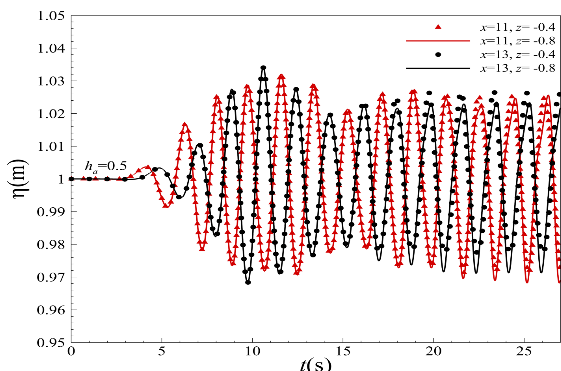
Fig. 7 Wave surface elevations at different locations.
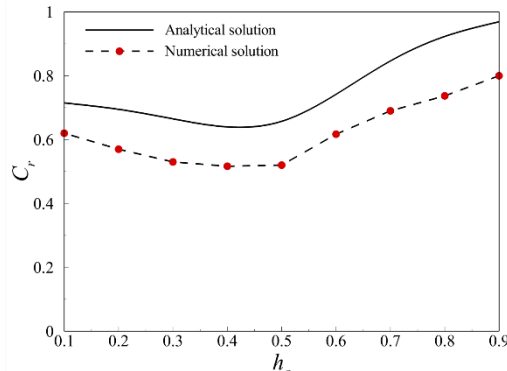
Fig. 8 Comparison between the analytical and the numerical results of C_r.
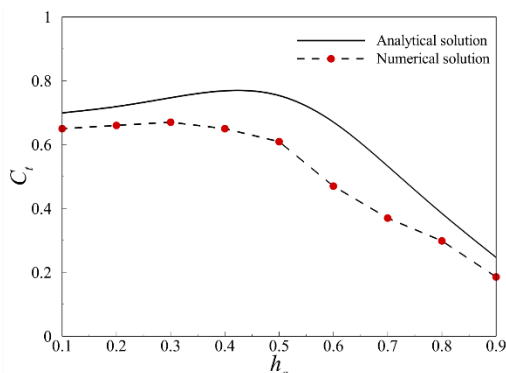
ig. 9 Comparison between the analytical and numerical results of C_t.
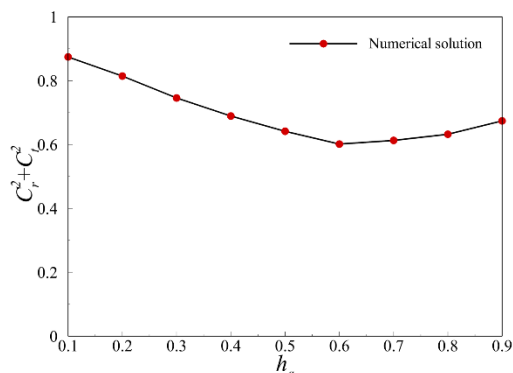
Fig. 10 Variations of the quadratic sum of C_r and C_t versus the heights of side plate.

4. Conclusion

In this study, a 3-D numerical solution for problems regarding wave generation, absorption and wave interacting with comb-type caisson breakwaters has been developed based on OpenFOAM®. The present method is very efficient to investigate water wave scattering by periodical structures because of the application of symmetry and symmetryPlane boundary conditions. The wave surface elevations generated in the numerical wave flume have been carefully examined and confirmed. The variation of the numerical results for the reflection and transmission coefficients versus the side plate height is similar to that of the analytical solution based on linear potential theory, while the value of the numerical solution is much smaller due to energy dissipation by the fluid viscosity. The reflection and transmission coefficients and the energy dissipation due to fluid viscosity are significantly affected by the height of side plate. The present numerical solution will be further validated by experimental data in the next study.

Reference

[1] Chapalain G, Cointe R, Temperville A. Observed and modeled resonantly interacting progressive water-waves. Coastal Engineering, 1992, 16(3):267-300.

[2] Dong, G. H., Li, Y. C., Sun, Z. C., Sun, Y., Niu, E. Z. and Mao, K., Interaction between waves and a comb-type breakwater. China Ocean Engineering, 2003, 17(4), 517-526.

[3] Fang, Z., Zhang, N. C., and Zang Z. P., Numerical simulations of open comb-type breakwater and research on its wave transmission coefficient. Journal of Waterway and Harbor, 2011, 32(2):86-93.

[4] Goda, Y., Suzuki, Y. Estimation of incident and reflected waves in random wave experiments. Proc. of 15th Int. Coastal Eng. Conf., 1976, 828–845.

[5] Jacobsen, N.G., Fuhrman, D. R., and Fredsøe, J. A wave generation toolbox for the open-source CFD library: OpenFoam®. International Journal for Numerical Methods in Fluids, 2012, 70(9), 1073–1088.

[6] Jasak, H. Error analysis and estimation for the finite volume method with applications to fluid flows. Ph.D. thesis, Imperial College of Science, Technology and Medicine, 1996.

[7] Li, Y. C., Sun, Z. C., Xu, S. Q., Dong, G. H., Lin, Y. Z., Niu, E. Z. and Mao, K., The hydraulic performance of comb-type vertical breakwater. Journal of Hydrodynamics, Ser. A, 2002, 17(4), 472-482. (In Chinese with English abstract)

[8] Moukalled F, Mangani L, Darwish M. The Finite Volume Method in Computational Fluid Dynamics: An Advanced Introduction with OpenFOAM and Matlab, Springer Publishing Company, Incorporated, 2015.

[9] Niu, E. Z., Ma, D. T. and Sun, S. C., The novel Comb-type breakwater. China Civil Engineering Journal, 2003, 36(10), 51-56. (In Chinese with English abstract)

[10] Niu, E. Z., Deng, L. and Ma, D. T., Experimental studies and construction of comb-type breakwater. China Harbour Engineering, 2001, 6, 5-8. (In Chinese with English abstract)

[11] Wang, Q. X., Zhang, T., Zhao, G. F. and Niu, E. Z., Structure analysis for flange plate of Comb-type caisson. China Harbour Engineering, 2001, 3, 13-17. (In Chinese with English abstract)

[12] Wang, X. Y., Liu, Y., Study on reflection and transmission characteristics of comb-type caisson breakwater. 18th Academic Symposium on the China Ocean (offshore) project, 2017. (In Chinese with English abstract)

[13] Weller, H.G., Derivation, modelling and solution of the conditionally averaged two-phase flow equations. Technical Report TR/HGW/02. Nabla Ltd., 2002.

[14] Zhu, H., Niu, E. Z. and Zheng, T. L., Mechanism and Characteristics of Comb-type Open Breakwater and Its Sheltering Effect. Port & Waterway Engineering, 2001, 10, 008. (In Chinese with English abstract)

CFD SIMULATION OF TIDAL CURRENT FARM BY USING AL MODEL

CHENG LIU[1], CHANGHONG HU[2]

[1,2] *Research Institute for Applied Mechanics, Kyushu University,* [1] *liu@riam.kyushu-u.ac.jp,*
[2] *hu@riam.kyushu-u.ac.jp*

Keywords: *Tidal current farm; Immersed boundary method; Wall function model; Adaptive mesh refinement; Actuator line model.*

Introduction

Tidal current power is one of the most potential resources for future electricity generation, corresponding investigation is attracted increasing interest. Mycek et al. [1] performed experiments for two tandem horizontal-axis tidal turbines (HATTs) in the IFREMER circulation flume tank, in which two ambient turbulence intensity (TI) rates (3% and 15%) is measured. Stallard et al. [2] carried out experiments to study the wake induced by staggered and aligned configurations, the wall effect was also under investigation.

Compared with experiment, numerical simulation has the potential to study the effect of different conditions with significantly lower cost. The Large Eddy Simulation (LES) and Reynolds-averaged Navier–Stokes (RANS) turbulence models can be used for predicting the mean performance and near-wake structure of a HATT. However, 3D blade-resolved simulation is cumbersome since a lot of time must be spent to generate mesh resolving the blade surface. Besides, the cost for adjusting the grid is also too high to perform numerous case-studies of a tidal farm.

In this study, an efficient numerical method for predicting the wake interference of multiple turbines is presented. To save the cost, the (actuator line) AL model [3] instead of the fully resolved turbine are developed. The URANS equations are solved to model the turbulent flow behind the rotor. Three turbulence models, original $k-\omega$, $k-\omega-SST$ and corrected $k-\omega$ model are implemented for comparison. The AL model with corrections to volume force calculation is introduced to represent the rotors. The moving least square (MLS) immersed boundary (IB) method [4] [5] considering the wall functions is proposed to study the hub and tower effect. The local mesh refinement is applied at the regions containing high gradient. The combination of AL model and IB method is highly efficient for case-studies of different configurations of multiple turbines. Numerical tests show the efficiency and accuracy for present solver in predicting velocity deficit and TIs. Present AL/MLS-IB method is also applicable for LES simulations. An example is given lastly for illustration of its potential in LES simulation of a tidal farm.

Numerical Method

Immersed Boundary Method

To impose the boundary conditions sharply around the surface, a MLS-IB method [4] [5] is applied to reconstruct the velocity at the forcing points adjacent to the rigid boundary. The fluid points, solid points and forcing points are shown as in Figure. 1 (a).

(a)   **(b)**   **(c)**

○ Fluid point   ● Forcing point   ● Solid point   ▢ Body surface   ⌐⌐⌐ Supporting domain   ✕ Intersecting point
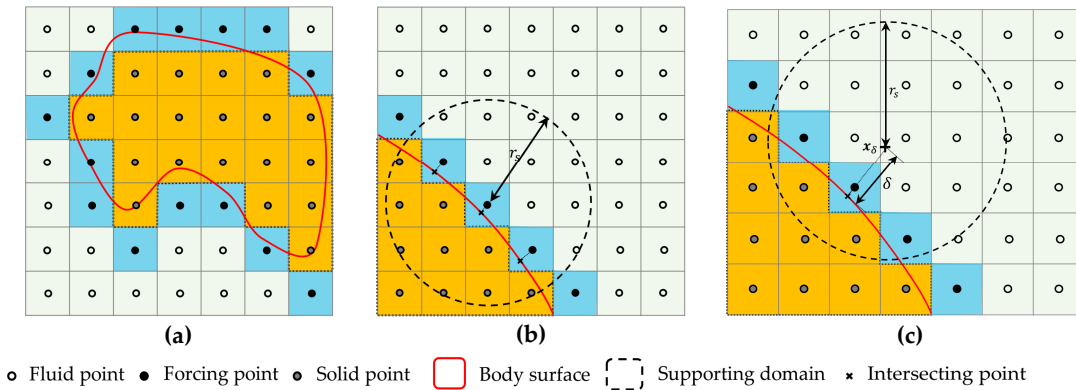
Figure 1: (a). Classification of the points in the computational domain, (b) definition of the supporting domain, (c) illustration for wall conditions of tangential velocity at the forcing points.

For present direct forcing method, the scalar quantity $\varphi(\boldsymbol{x})$ at the forcing point is determined by the moving least square approach with a supporting domain, see Fig. 1 (b),

$$\varphi(\boldsymbol{x}) = \sum_{i=1}^{m} p_i(\boldsymbol{x}) \, C_i(\boldsymbol{x}) = \mathbf{p}^{\mathrm{T}}(\boldsymbol{x})\mathbf{C}(\boldsymbol{x}), \tag{1}$$

where $\mathbf{p}^{\mathrm{T}}(\boldsymbol{x})$ is the orthogonal basis function vector. The accuracy of the interpolation depends on the vector length m. $\mathbf{C}(\boldsymbol{x})$ is the coefficient vector, which can be determined by minimizing the following weighted residual,

$$\mathcal{R} = \sum_{j=1}^{n} W(\boldsymbol{x} - \boldsymbol{x}_j) \, [\mathbf{p}^{\mathrm{T}}(\boldsymbol{x}_j)\mathbf{C}(\boldsymbol{x}) - \varphi(\boldsymbol{x}_j)]^2, \tag{2}$$

where $\boldsymbol{x}_j$ stands for the fluid point and intersecting point fall into the supporting domain. n is the number of points used for reconstruction. $W(\boldsymbol{x} - \boldsymbol{x}_j)$ is the weighed function that depends on the distance between $\boldsymbol{x}$ and $\boldsymbol{x}_j$. By solving Eq. (2),

the coefficients vector $\mathbf{C}(\mathbf{x})$ can be determined. Finally, the scalar quantity φ at the forcing point $\mathbf{x}$ can be calculated through Eq. (1). Details are described in [4] [5].

Wall Functions
When the turbulence flow approaches a solid wall, the mean and fluctuating components decrease quickly and create a large gradient near the wall. To accurately represent the near wall boundary layer, numerous grid points in the near wall region are required. For high Reynolds number turbulence models such as $k - \varepsilon$ and $k - \omega$ model, traditional IB method cannot fully resolve the boundary layers, the calculation of the shear stress in this way may result in incorrect values. In previous research, linear and quadratic interpolations are often been used in IB methods. However, they are effective only when the forcing points are located in the linear region of the boundary layer. In present research, by using the wall models, the logarithmic laws are maintained with medium fine resolution of the near wall layer.
For the implementation, first we should know whether the forcing point is applicable for using the wall model function. Here we use d_C^+ to determine whether the points lies in the viscous or inertial sub-layer.

$$d_C^+ = \frac{C_\mu^{025} k_C^{05}}{\nu} \text{dist}(\mathbf{x}_c),$$ (3)

where ν is the laminar viscosity, k_C is the near wall turbulence kinetic energy and the function $\text{dist}(\mathbf{x}_c)$ indicates the distance to the wall. It is assumed that the transition from the viscous region to inertia layer occur at d_{tr}^+, $d_{tr}^+ = 11$ is adopted according to previous research. The intersection position of the logarithmic and the linear profile can be represented by d_{tr}^+. For d_C^+ lower than d_{tr}^+, the forcing point C locates in the viscous region. In this case, the flow is assumed to be laminar and the viscosity at C is equal to the laminar viscosity μ. The turbulence kinetic energy k at the interface is zero, thus the MLS interpolation in Eq. (1) can be applied for the reconstruction of k at the forcing point. When $d_C^+ > d_{tr}^+$, the forcing point C is in the inertia boundary layer, so the logarithmic wall function is applied. The velocity profile of tangential component is given in the following formula through experimental investigations [9].

$$\frac{u^t}{u_\tau} = \frac{1}{\kappa} \ln(1 + \kappa y^+) + 78 \left[1 - e^{\left(\frac{-y^+}{d_{tr}^+}\right)} - \frac{y^+}{d_{tr}^+} e^{\left(\frac{-y^+}{3}\right)} \right],$$ (4)

here u^t is the tangential velocity, u_τ represents the friction velocity, κ is set by 0.4187. y^+ is the dimensionless wall distance. By using Eq. (4), the linear viscous sub-layer and the logarithmic layer can be replicated correctly. The wall conditions of tangential velocity at the forcing points are calculated as described in following procedure. 1. Using MLS interpolation (Eq. (1)) to obtain the tangential velocity u_δ^t at $\mathbf{x}_\delta$, here the distance (δ) from $\mathbf{x}_\delta$ to the solid surface is set by $\delta = \sqrt{2}\Delta h$, h is the grid interval, see Fig. 2. 2. Using Eq. (4) to get the friction velocity u_τ at $\mathbf{x}_\delta$. 3. Calculate the tangential velocity u^t using Eq. (4) again at the forcing point with the assumption that the friction velocity at the forcing point and $\mathbf{x}_\delta$ is identical. It is noted that in the MLS interpolation of step 1, the forcing points fall into the supporting domain should be avoided to be used. For the normal components of the velocity and other scalar qualities, the MLS interpolation is applied to reconstruct the status. In the $k - \omega$ model, the turbulence frequency ω at the forcing point can be calculated using the analytical solution. If the forcing point lies in viscous layer,

$$\omega_C = \frac{6\nu}{C_{\beta1}(d_C^+)^2}.$$ (5)

Otherwise, when the forcing points in the inertia region, the ω equation will not be solved for the first interior point and the value is set by the formula,

$$\omega_C = \frac{k_C^{05}}{\kappa C_{\beta1}^{025} d_C^+}.$$ (6)

Actuator Line Model
The AL approach is a combination of classical BEM theory and Navier–Stokes equation [3]. It is an efficient approach that can provide majority wake flow characteristics of a rotating turbine. In AL approach, the rotor is defined in Cartesian coordinate frame with three actuator lines to represent rotating blades. A series of points along each blade's axis are defined and each point is the center of an actuator element. The position of these points rotate according to the angular speed of the turbine at each time step. The critical point in implementing AL model is to add the force terms at the right side of the Navier–Stokes equation to represent the rotor effect.

Adaptive Mesh Refinement
In OpenFOAM, the adaptive mesh refinement is included in the class dynamicRefineFvMesh. By including the corresponding libraries, we can create a solver that containing AMR functions by modifying existing Foam solvers. The gradient of the velocity field is calculated to build a refinement criterion.

Numerical Solutions
URANS simulation-IFREMER rotor test
In order to validate the new developed AL model, the experimental data of the HATT model test by Mycek et al [1] is used for comparison. The experiment was carried out in the *IFREMER* flume tank, Boulogne-Sur-Mer, France in which the 1/30 scaled prototypes tidal turbine with different inlet TIs are studied. In the experiment, the upstream conditions,

$U_\infty = 0.8 m/s$, $I_\infty = 3\%$ are considered. The optimized tip speed ratio (TSR) is 3.67 for all of the *IFREMER* rotor test. Other parameters, initial conditions and boundary conditions are found in reference [1].

The results of downstream turbine under low TI ($I_\infty = 3\%$) cases are shown in Figure. 2 in which the wake profiles of 7 transects (2D~10D behind the rotor plane) are given. Since the rotor is placed in the turbulent flow generated by the upstream rotor, the actual ambient TI around the downstream is larger than single turbine case. It is observed the TI profiles predicted by the $k - \omega$ model are not consistent with experiment at x/D < 3 (Figure. 2 (a)). The corrected $k - \omega$ model seems to resolve the TI profiles better around the rotor hub (x/D=2) but still give over-predict TI. For x/D > 4, the differences of the three models are not obvious. Generally, the corrected $k - \omega$ and the $k - \omega - SST$ model shows better performance in predicting TI in the near wake region, the performance of the three models are almost identical for far wake (x/D > 3). Since $k - \omega - SST$ give the lowest TI predictions, the largest velocity deficits can also be observed. To make a clearer view of the differences among the three models, the wake profiles ($I_\infty = 3\%$, 4D) along the rotor center are given as in Figure. 2 (c-d).
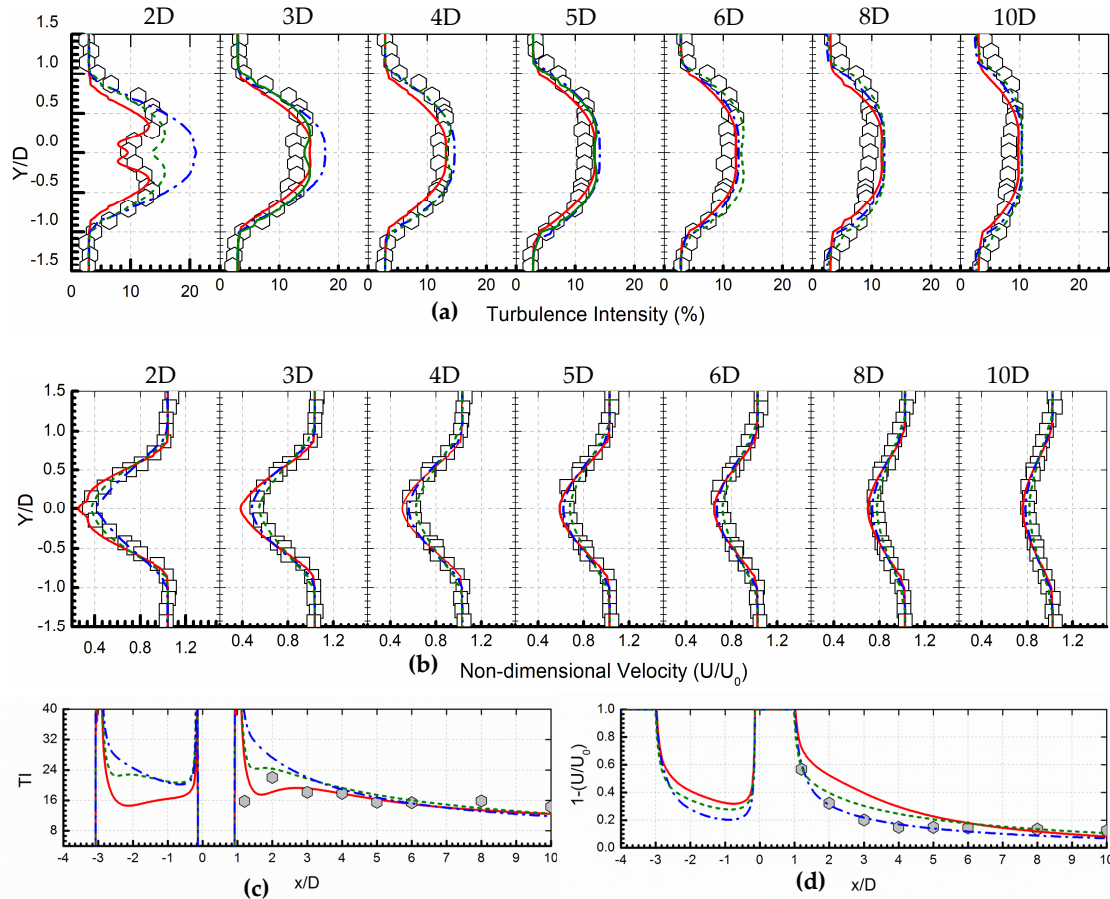
Figure 2: TI profiles (a) and velocity deficit (b) along the rotor center for the IFREMER's double rotors case TI=3% and 4D spacing, TI profiles (c) and velocity deficit (d) along the rotor center. ○: TI from the experiment [1], □: U/U_0 from the experiment [2], - - -: Corrected k-w results, - — - — : k-w model results ——: SST model results.

URANS simulation- Manchester rotor test

A group of experiments for three rotors operating in turbulent upstream are studied by Stallard et al. [2]. The experimental are carried out in the flume (test section: $5m$ width, $12m$ length, $0.45m$ depth) at University of Manchester. The turbulent inlet flow is characterized by mean velocity $U_\infty = 0.47 m/s$ and $I_\infty = 10\%$ at the rotor plane for the experiment. All of the three rotors are operated under TSR=4.7.

Figure. 3 shows the wake profiles of normalized mean velocity and TI at 6 transects (2D~12D). It is evident that the major differences of the three turbulence models are in the range of x/D < 4. The $k - \omega$ model over-predict TI and under-predict the velocity deficit from 2D to 4D. $k - \omega$ model cannot predict the double TI peak induced by the tip at $x = 2D$. The *SST* model shows the best prediction of TI, however the velocity still recovers too fast at the rotor center. For the near wake ($x \leq 2D$) prediction, the performance of corrected $k - \omega$ model is better than the $k - \omega$ but worse than the *SST* model. While for the far field wake ($12D \geq x \geq 6D$) prediction, results of all three models confirm with the experiment. For the high TI case, the wake merging can be observed evidently in the numerical and experimental tests. The differences of three wakes cannot be distinguished when $x \geq 8D$.

LES simulation-Gravity based tidal current turbine

Lastly, the AL/MLS-IB method is extended to LES simulation of a gravity based tidal turbine, as shown in Figure 4 (a).

(a) Turbulence Intensity (%)

(b) Non-dimensional Velocity (U/U_0)
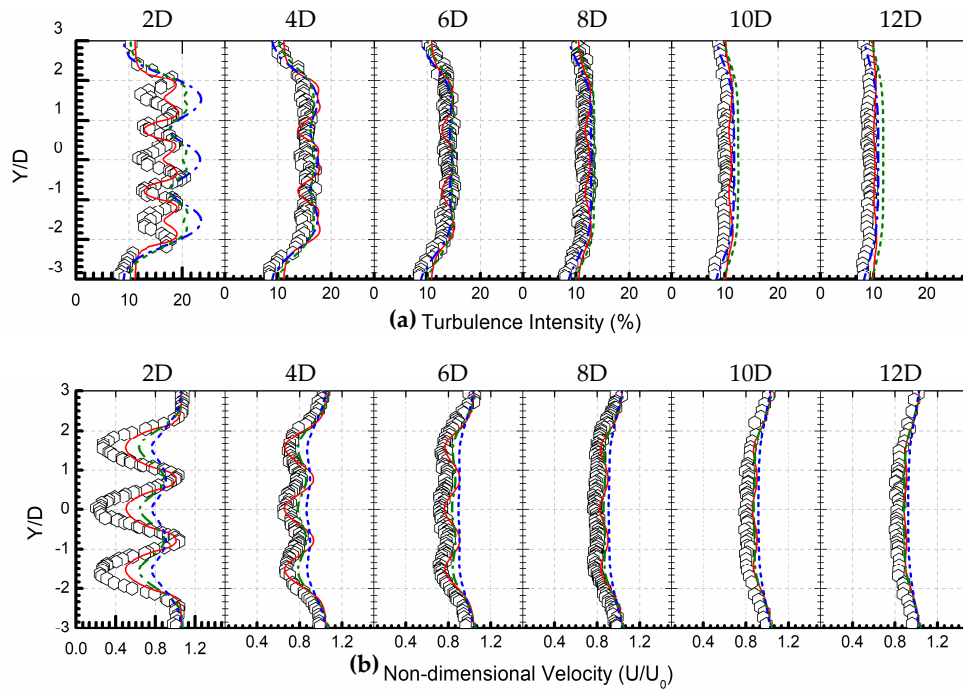
Figure 3: Wake profiles for the Manchester's triple rotors case with inlet turbulence intensity of 10%, the spacing of two rotors is 1.5D, same description of the symbols and lines can be found in Figure. 2.

The dynamically cell-based mesh refinement in OpenFOAM is utilized to resolve the regions containing solid surface and large velocity gradient. Figure 4 (b) and (c) demonstrate the mesh before or after the rotation starts, respectively. The regions adjacent to the support structure and blades as well as tip vortex are under refining (Figure. 4(d)).

(a)   **(b)**   **(c)**   **(d)**
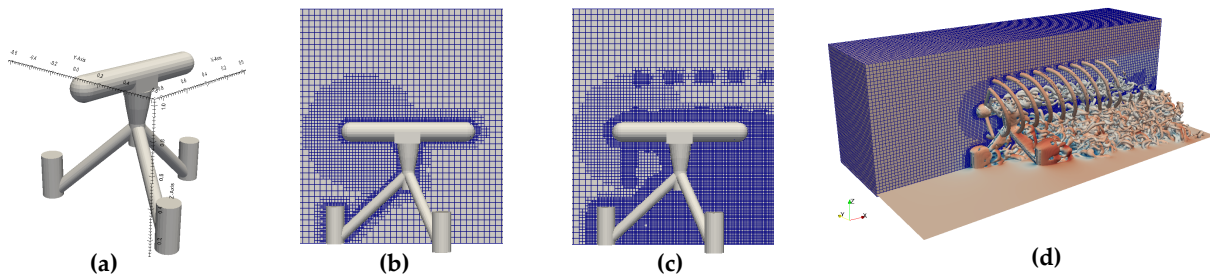
Figure 4: (a) Structure of a gravity based tidal current turbine, (b) and (c) indicate the initial and instantaneous adaptive mesh during the simulation, (d) instantaneous vortex structure and adaptive mesh.

Summary

In this manuscript, we present our numerical developments on prediction of the wake induced by the tidal turbine rotors. This study is based on our previous study on the IB method [5] [6]. Several tests show that the present AL/MLS-IB method is efficient and accurate to predict the wake of multiple tidal turbines.

References

[1] Mycek P, Gaurier B, Germain G, et al. Experimental study of the turbulence intensity effects on marine current turbines behaviour. Part II: Two interacting turbines. Renewable Energy, 2014, 68: 876-892.

[2] Stallard T, Collings R, Feng T, et al. Interactions between tidal turbine wakes: experimental study of a group of three-bladed rotors. Philosophical Transactions of the Royal Society of London A: Mathematical, Physical and Engineering Sciences, 2013, 371(1985): 20120159.

[3] Sørensen J N, Shen W Z. Numerical modeling of wind turbine wakes. Journal of Fluids Engineering, 2002, 124(2): 393-399.

[4] Vanella M, Balaras E. A moving-least-squares reconstruction for embedded-boundary formulations. Journal of Computational Physics, 2009, 228(18): 6617-6628.

[5] Liu C, Hu C. An adaptive multi-moment FVM approach for incompressible flows, Journal of Computational Physics, 2018, 359, 239-262.

[6] Liu C, Hu C. An efficient immersed boundary treatment for complex moving object. Journal of Computational Physics, 2014, 274: 654-680.

SURVIVABILITY SIMULATION OF A WAVE ENERGY CONVERTER IN A NUMERICAL WAVE TANK

BRECHT DEVOLDER[1], PETER TROCH[2], PIETER RAUWOENS[3]

[1]*Dept. of Civil Engineering, Ghent University & KU Leuven (campus Bruges), Brecht.Devolder@UGent.be*
[2]*Dept. of Civil Engineering, Ghent University, Peter.Troch@UGent.be*
[3]*Dept. of Civil Engineering, KU Leuven (campus Bruges), Pieter.Rauwoens@KULeuven.be*

Keywords: *Wave energy; Floating point absorber; Single unit; Coupled CFD–motion solver; Survivability simulation*

1 Introduction

Wave energy from ocean waves is captured by wave energy converters (WECs) and converted into electrical power. WECs of the floating point absorber (FPA) type are selected which are heaving under wave loading. In this study, the numerical simulations of a WEC under operational wave conditions [1] are extended to a survivability simulation of a WEC under extreme design load conditions. Therefore, the WEC is subjected to breaking waves in a numerical wave tank (NWT).

2 Numerical framework

CFD-modelling is performed to study the behaviour of a floating WEC unit inside a NWT implemented in OpenFOAM. The two-phase flow field is resolved by the incompressible RANS equations together with a conservation equation for the volume of fluid (VoF) method. RANS turbulence modelling is applied by using a buoyancy-modified $k - \omega\ SST$ model developed by the authors [2, 3]. Wave generation and absorption at the boundaries of the NWT are adopted from the IHFOAM toolbox. The CFD-fluid solver is coupled to a motion solver in order to simulate rigid body motions. Only the governing motion of the WEC's behaviour is considered, the heave motion, allowing a reduction from a six to a one degree of freedom motion solver. The mesh motion is organised that only the highest and lowest row of cells is distorted (compressed or expanded) to prevent undesirable mesh deformations around the air-water interface. A coupling algorithm between the fluid and the motion solver is needed to obtain a converged solution between the hydrodynamic flow field around the WEC and the WEC's kinematic motion during every time step in the transient simulation. The coupling algorithm is using implicit coupling in the sub iterations by calculating a Jacobian, based on the available solutions of previous sub iterations for the acceleration of the floating body and the force acting on it, in order to minimise the number of sub iterations and consequently the CPU time [4].

3 Results & Discussion

This section presents two numerical results obtained in the NWT. Firstly, as a preliminary simulation, a two-dimensional (2D) NWT is considered without a floating WEC unit, i.e. an empty NWT. For a survivability simulation, breaking waves on the WEC are required. In order to trigger steepness-induced wave breaking in a constant water depth $d = 1.70\ m$, irregular waves are generated at the inlet by using three wave components and the method of wave focussing is applied. The surface elevations at the inlet ($x = 0\ m$) are calculated by superposition assuming linear wave theory:

$$\eta(x, t) = \sum_{i=1}^{3} \frac{H_i}{2} \cos\left(\frac{2\pi}{L_i}x - \frac{2\pi}{T_i}t + \phi_i\right) \tag{1}$$

in which H_i is the wave height, T_i the wave period, L_i the linear wave length and ϕ_i the phase of wave component i. Breaking waves are achieved by bringing the three wave components in phase at $x_f = 5\ m$ for $t_f = 10\ s$ by calculating ϕ_i of each wave component i as: $\frac{2\pi}{L_i}x_f - \frac{2\pi}{T_i}t_f + \phi_i = 0$ (linear wave theory). The numerical values for each wave component are as follows:

- $H_1 = 0.15\ m$; $T_1 = 1.00\ s \longrightarrow L_1 = 1.56\ m \longrightarrow \phi_1 = 42.71$;
- $H_2 = 0.10\ m$; $T_2 = 1.10\ s \longrightarrow L_2 = 1.89\ m \longrightarrow \phi_2 = 40.49$;
- $H_3 = 0.05\ m$; $T_3 = 1.20\ s \longrightarrow L_3 = 2.25\ m \longrightarrow \phi_3 = 38.38$;

Note that the wave periods are around the natural period of the WEC equal to $1.136\ s$, causing resonance of the WEC's heave motion. The three wave components are non-linear and therefore linear wave theory is not applicable and a non-linear fluid solver is required. Furthermore, waves generated with different wave periods generate new wave components which do not satisfy the linear dispersion relation. This is indicated in Figure 1 by the surface elevations over the length of the NWT at $x = 1\ m$, $x = 2\ m$, $x = 3\ m$, $x = 4\ m$, $x = 5\ m$ and $x = 6\ m$ for both the linear wave theory (dashed blue lines), equation (1), and the CFD result (solid red lines) during the first 30 seconds of the simulation. Due to the large wave steepness, wave breaking is induced between $x = 2\ m$ and $x = 3\ m$. This observation stresses the need for a CFD NWT to perform survivability simulations of a WEC subjected to breaking waves.
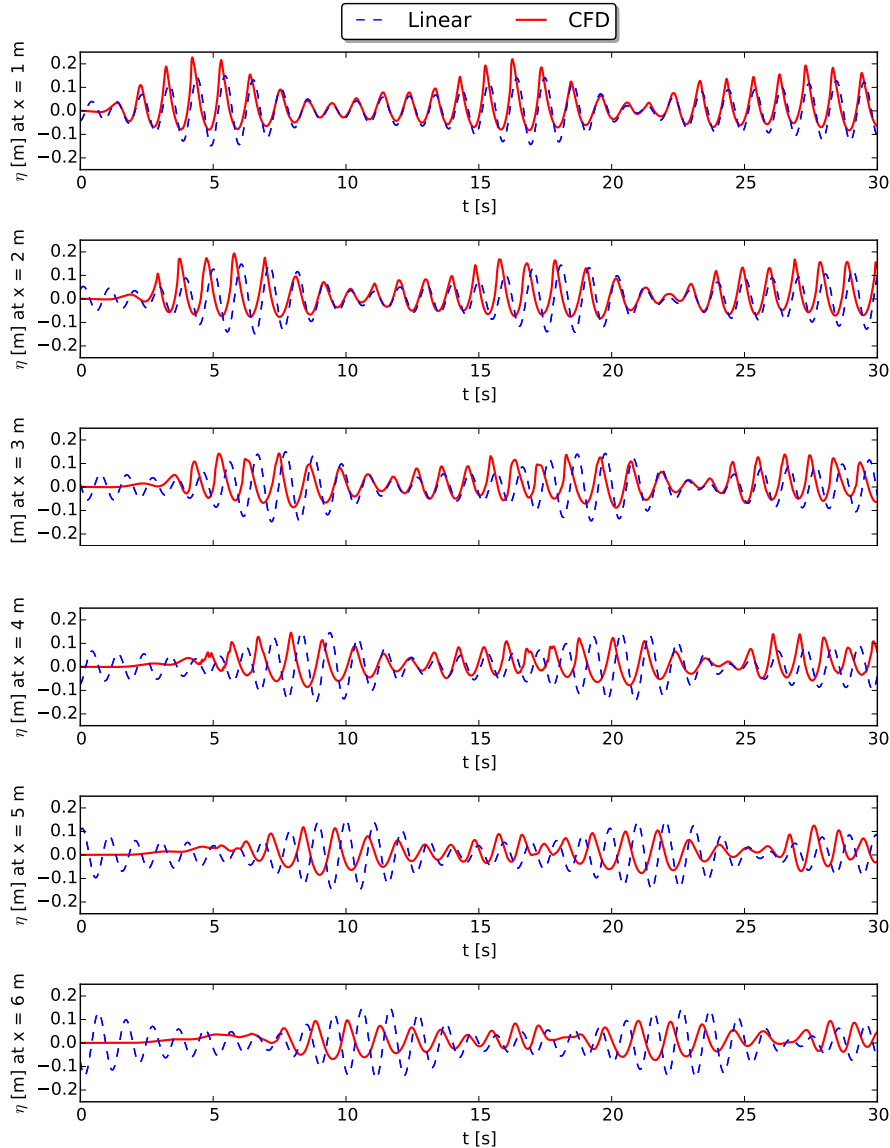
Figure 1: Surface elevations obtained with linear wave theory (equation (1), blue dashed lines) and in the empty CFD NWT (red solid lines).

For the second simulation, a WEC is installed in a three-dimensional (3D) NWT and the same irregular waves are generated. The WEC's centre is located at $x = 3\ m$, inside the wave breaking zone as found during the preliminary simulation using an empty NWT. A longitudinal symmetry plane is implemented to reduce the size of the computational domain. The NWT is $8\ m$ long, $1.6\ m$ heigh and $0.7875\ m$ wide. The computational domain has a vertical resolution of $1\ cm$ and a horizontal resolution of maximum $2\ cm$ around the free water surface. A detail of a longitudinal cross section around the WEC is visualised in Figure 2. The aspect ratio of the cells behind the WEC towards the outlet boundary on the right increases gradually which will cause numerical wave damping. This is however beneficial in order to avoid wave reflection from the absorbing outlet boundary. A maximum Courant number of 0.3 is used to limit the time step.

Figure 3 and Figure 4 visualise time series for the vertical position of the WEC z and the horizontal surge force acting on the WEC F_x respectively. Between $t = 5\ s$ and $t = 10\ s$ for example, the amplitude of the WEC's heave motion is

atmosphere

inlet

outlet

bottom
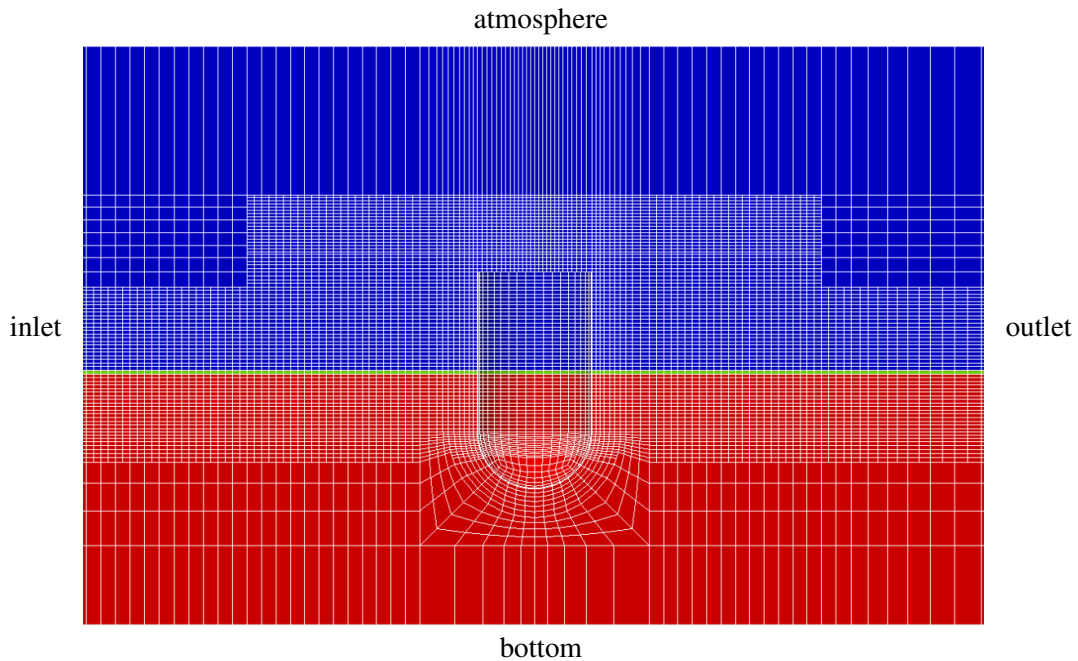
Figure 2: Cross section (XZ-plane) of the 3D computational domain in which a WEC is installed showing the initial condition for the volume fraction α at $t = 0\ s$ ($\alpha = 1$: water shown in red, $\alpha = 0$: air shown in blue).

gradually increasing due to resonance effects and the viscous damping force is important to predict correctly the WEC's heave motion. In Figure 4, the peaks observed in the time signal of the surge force on the WEC indicate the breaking wave impacts on the WEC. These forces obtained during a survivability simulation are important to quantify the design loading conditions on a WEC.
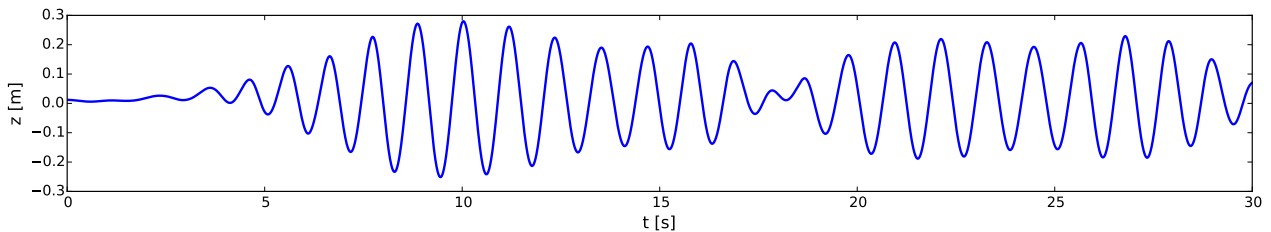
Figure 3: Vertical position z of the WEC subjected to breaking waves.
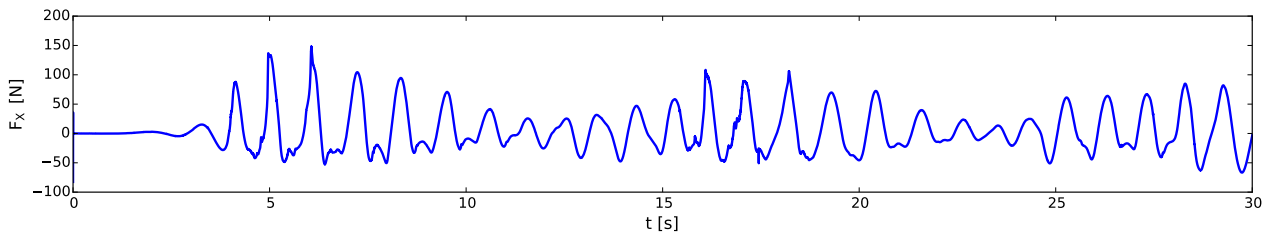
Figure 4: Horizontal surge force F_x acting on the WEC subjected to breaking waves.

Figure 5 depicts the number of sub iterations to achieve a converged fluid–motion coupling during every time step. Mostly two and occasionally three or more sub iterations are needed which indicates the successful application of the accelerated coupling algorithm for a survivability simulation of a WEC unit.

Finally, a snapshot of a breaking wave impacting on the WEC is visualised in Figure 6 at $t = 6.20\ s$. The wave starts to break in front of the WEC and the overturning volume of water is impacting on the WEC. Those highly non-linear and fully turbulent flows for breaking wave impact simulations are only possible by using a CFD NWT.
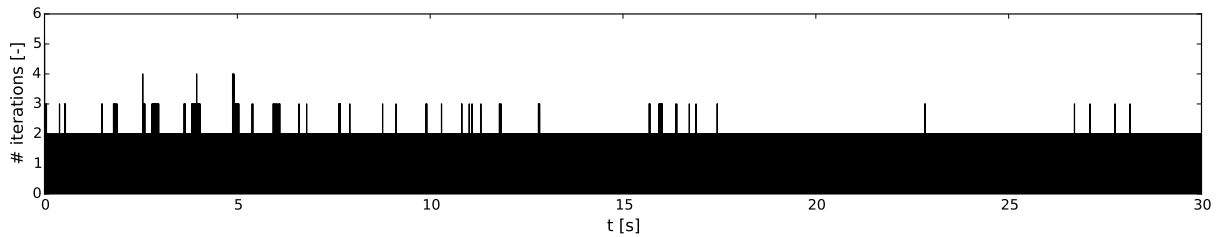
Figure 5: The number of sub iterations for every time step to have a converged fluid–motion coupling for the WEC subjected to breaking waves.
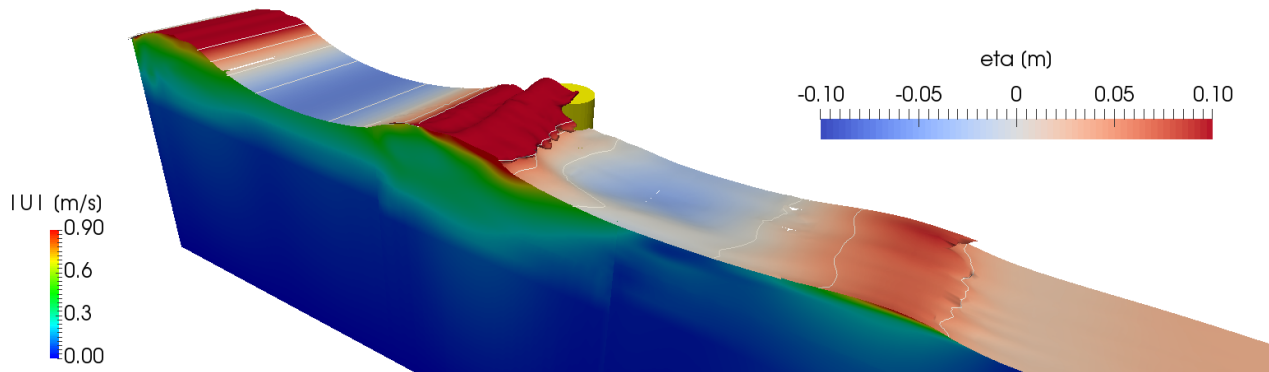
Figure 6: A snapshot at $t = 6.20\ s$ of a breaking wave impacting on the WEC in the NWT. Contour lines of the surface elevation $[m]$ are depicted on the isosurface for the volume fraction $\alpha = 0.50$. The vertical plane visualises the velocity magnitude $[m/s]$.

4   Conclusions

Based on this proof of concept study, we conclude that a CFD NWT is necessary to resolve non-linear wave–wave interactions during wave propagation and to simulate wave breaking events on a WEC for testing survivability conditions. Furthermore, it has been demonstrated that our coupling algorithm for the fluid–motion solver remains stable under extreme wave conditions and large displacements of the WEC by using few sub iterations during every time step. Future research is required to validate the numerical model for extreme wave conditions by using experimental measurements. In addition, a coupling between an accurate wave-structure interaction solver (e.g. OpenFOAM as a non-linear viscous NWT) and a fast wave-propagation solver (e.g. OceanWave3D as a non-linear potential flow NWT) will increase the efficiency of the numerical simulations by reducing the time-consuming 3D CFD domain.

Acknowledgments

References

[1] B. Devolder, P. Rauwoens, and P. Troch, "Numerical simulation of a single Floating Point Absorber Wave Energy Converter using OpenFOAM®," in *Progress in Renewable Energies Offshore*.   CRC Press, 2016, pp. 197–205.

[2] ——, "Application of a buoyancy-modified k-ω SST turbulence model to simulate wave run-up around a monopile subjected to regular waves using OpenFOAM®," *Coastal Engineering*, vol. 125, pp. 81–94, jul 2017.

[3] B. Devolder, P. Troch, and P. Rauwoens, "Performance of a buoyancy-modified k-ω and k-ω SST turbulence model for simulating wave breaking under regular waves using OpenFOAM®," *under review for Coastal Engineering*, 2018.

[4] ——, "Accelerated numerical simulations of a heaving floating body by coupling a motion solver with a two-phase fluid solver," *under review for Computers & Mathematics with Applications*, 2018.

ANALYSIS OF HYDRODYNAMIC PERFORMANCE OF A SHIP WITH PROPELLER USING OPENFOAM

ZHAI SHUCHENG[1], ZHENG CHAOSHENG[2], LIU DENGCHENG[3]

[1] *China Ship Scientific and Research Center, National Key Laboratory of Ship Vibration and Noise, Jiangsu Key Laboratory of Green Ship Technology, zsc_cssrc@163.com*

[2] *China Ship Scientific and Research Center, National Key Laboratory of Ship Vibration and Noise, Jiangsu Key Laboratory of Green Ship Technology, zsczsc2005@163.com*

[3] *China Ship Scientific and Research Center, National Key Laboratory of Ship Vibration and Noise, Jiangsu Key Laboratory of Green Ship Technology, edon_00@163.com*

Abstract

This paper analyses the resistance performance of an oil tank ship and the hydrodynamic characters of propeller behind this ship. The study was completed using an open source computational program, Open Field Operation and Manipulation (OpenFOAM), and the resistance character and propeller hydrodynamics performance were compared with experimental results. Reasonable results were produced such that the resistance, thrust, torque and efficiency trends were in good agreement with experimental data. It was found that OpenFOAM has good prediction of ship hydrodynamic performance.

Keywords: hydrodynamic performance, propeller, OpenFOAM.

This template provides a definition of the Microsoft Word styles for extended abstract submissions to the 13th OpenFOAM Workshop.

0 Introduction

The computational fluid dynamic (CFD) is more and more popular in ship and propeller design process. OpenFOAM is an established object-oriented library for Computational Continuum Mechanics, such as CFD [1], [2]. Many investigations have been done in ship and ocean engineering by this advanced tool package. Kim et al. [3] report a series of simulations on prediction of cavitation and performance of marine propellers. Simulations of propellers in open water utilizes the geometry of a single rotating frame of reference. Beaudoin et al [4] report a steady-state simulation of a Francis turbine, using the MFR model and two mixing plane interfaces. Zheng et al [5] gives the open water predictions of DTMB4119 propeller, which agree well with test data. Cha Jingjing et al[6] use interDyMFoam package with piston and flap type numerical wave makers to generate linear wave and finite amplitude waves. A damping zone function is added to the solver to absorb wave and be testified by several experiments. Li Yulong et al[7] simulated the ship motions coupled with tank sloshing in time domain based on OpenFOAM, and the simulation and experimental studied indicate that the numerical results of ship motion coupled with tank sloshing can clearly show the coupling effect of tank sloshing on the ship global motion. LV Lianli et al[8] established a numerical wave tanks to study the wave pressure field impacted on the ship. ZHOU Hu et al[9] investigated the difference between aerodynamics of two blades and three blades wind turbine under different wind conditions with different turbulence model and unstructured grid influences.

The aim for this paper is to successfully model a ship with propeller. The ship resistance and propeller thrust and torque are simulated. It will allow for good comparison between experimental results. Moreover, further analysis can be conducted in how the force is affected on ship and propeller in different conditions.

1 Model

1.1 CFD Methods

The incompressible Reynolds-Averaged Navier-Stocks equations (RANS) method is used to simulate the hydrodynamic performance of ship in this paper. See eq. (1) (2). With the RANS equations there is still a closure problem. This is solved using a turbulence model. The k-ω SST model is applied, which is using blending functions to be able to use the k-ω model near the wall and the k-ε in the free stream and to get a smooth transition between them [10]. This model is useful in ship and propeller simulation. The second order upwind scheme is used to discretize the equations and the pressure velocity coupling is solved by SIMPLE method. The Multiple Reference Frames (MRF) is used to simulate the propeller rotating. OpenFOAM version 2.3.0 is used in this paper.

$$\frac{}{\partial_i}\left(\overline{U}_i\overline{U}_J = -\frac{1}{\rho}\frac{\partial \overline{P}}{\partial x_i} + \mu \frac{\partial^2 U_i}{\partial_j \partial_j} - \frac{\partial \overline{U_i U_J}}{\partial_j} \right) \tag{1}$$

$$\frac{\partial \overline{U_J}}{\partial x_j} = 0 \qquad\qquad (2)$$

1.2 Ship Model

Oil tanker is one of the four main ship types in the shipping market. The present research model is an oil tanker with four blades propeller and rudder behind and its design speed is 14.5 kn. Main parameters of ship and propeller are shown in table 1.

Table 1 Main parameters of ship and propeller

Name		Symbol	Vale	Unit
Ship	Length of waterline	L_w	179	m
	Design draught	D_f	11	m
Propeller	Propeller diameter	D_p	7.29	m
	Pitch ratio	$(P/D_{PS})_{0.75R}$	0.835	-
	Blade area tatio	A_E/A_0	0.4	-
	Number of blades	Z	4	-
	Direction of rotation	-	Right	-
Scale		-	1:29	-

Fig 1 Oil tanker model with propeller

1.3 Mesh

The calculating domain is a rectangle with $7L_w \times 2L_w \times L_w$, The ship model position is L_w to inlet, L_w to side and $5 \times L_w$ to outlet. The boundary conditions are shown in figure 2. We use overlap model to simulate without consider the free water surface, because the Froude number of oil tanker is small, the wave resistance has little effect of propeller hydrodynamic performance, but it should be careful that some error will be put in the ship resistance. The mesh is generated by HEXPRESS software with unstructured hexahedron cell. In order to improve the spatial resolution in stern region using mesh density core, as shown in figure 3. Total mesh of resistance simulation case is about 2 million and 4 million for ship with propeller case. The personal computer with i7-3400@3.4Ghz CPU is usedto calculate and the time consume is about 10 CPU hours.
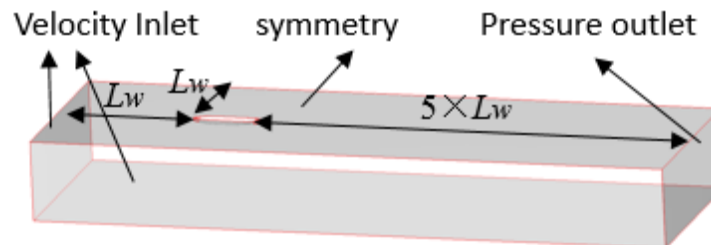
Fig 2 Calculating domain
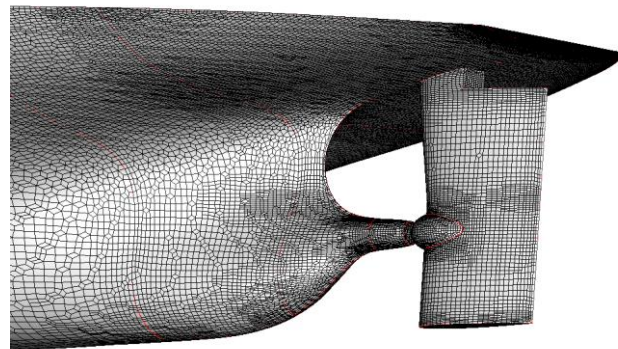
Fig 3 Mesh of the stern

2 Results and Analysis

Firstly, we calculate the ship resistance without propeller, and compare results with test data. C_{tm} is the resistance coefficient of bare hull defined as $C_{tm} = R/0.5\rho v^2 S$, where R is the resistance of ship, ρ is the water density, v is the upstream velocity, S is wet surface area. Here the commercial software Fluent simulate results are also shown in table 2. The simulation values are larger than experimental results. The error of OpenFOAM predictions is about 5.1%, a little larger than Fluent.

Table 2 Resistance of ship without propeller

V_s(kn)	F_n	Method	$C_{tm}(10^{-3})$	Δ (%)
10.5	0.129	Experiment	3.913	-
		Fluent	4.024	2.8%
		OpenFoam	3.645	-6.9%
14.5	0.178	Experiment	3.786	-
		Fluent	3.933	3.8%
		OpenFoam	3.980	5.1%

The ship self-propelled condition is a complex system, because the propeller is working in ship's wake flow field. The vortex structure generated by ship hull will flow into the propeller plane and affect the propeller hydrodynamic. In condition, the good simulation of rotating parts is also a difficult point. In this paper, the propeller rotating is simulated with MRF method, which is a quasi-steady method including centrifugal and Coriolis force in equation. The data transfer between moving region and static region is by using AMI type interface tool.

The propeller thrust and torque are calculated, as shown in Table 3. The OpenFOAM results are little better than Fluent results but both are higher than experimental results. The pressure coefficient C_p contours of the hull and propeller are shown in Figure 4 and Figure 5. The hull contour characters of pressure calculated by two softwares are almost the same. It should be noted that there are some differences at the pressure side and suction side of the propeller, which cause the thrust and torque with some differences. The oil tanker has large block coefficient and the stern geometry is plump, the water flows around these surfaces may separate when the upstream water velocity is specified. This complex separation flow is hard to simulate accurately, and leads to some simulation error.
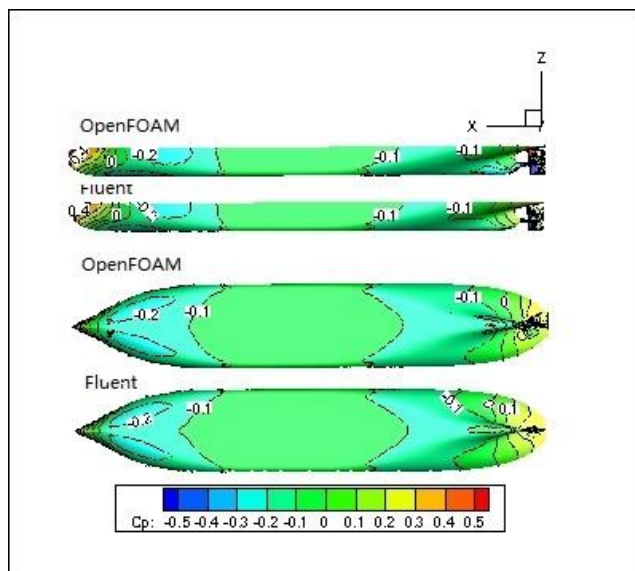
Fig 4 Pressure coefficient on ship hull
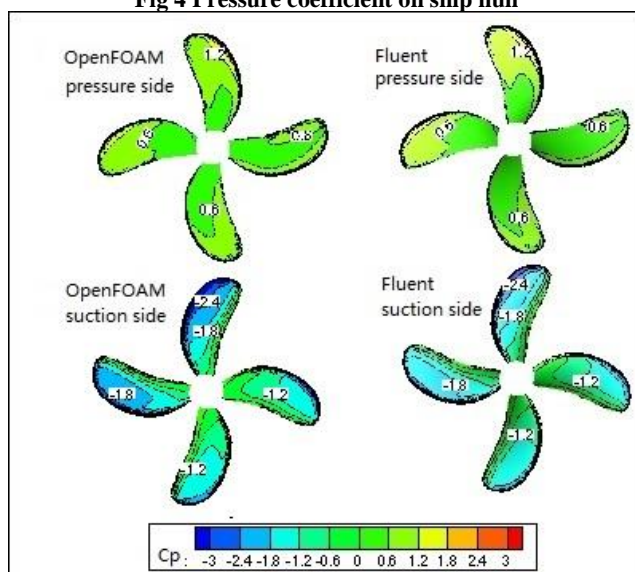
Fig 5 Pressure coefficient on propeller

Table 3 Hydrodynamics of propeller behind ship

Vm(m/s)	Nm(rps)	Method	Tm(N)	Δ (%)	Qm(N.m)	Δ (%)
1.385	6.664	Experiment	27.005	-	0.906	-
		Fluent	29.204	8.1%	0.989	9.2%
		OpenFOAM	27.449	1.6%	0.914	8.4%

3 Conclusions

The hydrodynamic performances of hull and propeller behind it are simulated by OpenFOAM in this paper. The hydrodynamic of ship model and propeller performance are calculated successfully. The errors between simulation and test data are acceptable. In further the turbulence model and some solution methods will be investigated to improve the simulation accuracy.

Reference

[1] Joris Degroote, Patrick Segers and Jan Vierendeels . CFD Challenge: Solutions Using an Open-Source Finite Volume Solver, OpenFOAM. ASME 2012 Summer Bioengineering Conference. pp. 139-140. 2012.

[2] P. Berg, G. Janiga and D. Thévenin. CFD Challenge: Solutions Using the Commercial Solver Fluent and the Open-Source Solver OpenFOAM. ASME 2012 Summer Bioengineering Conference. pp. 115-116. 2012.

[3] Kim, S.-E., Scroeder, S., and Jasak, H.: "A Multi-Phase CFD Framework for Predict-ing Performance of Marine Propulsors", InThe Thirteenth International Symposium on Transport Phenomena and Dynamics of Ro-tating Machinery (ISROMAC-13), Honolulu,Hawaii, April 2010.

[4] Page, M., Beaudoin, M., and Giroux, A.-M.: "Steady-state Capabilities for Hydroturbines with OpenFOAM", Int. J. of Fluid Machinery and Systems, 4(1):160–170, Jan-Mar 2011.

[5] ZHENG Chaosheng, ZHANG ZHirong, Prediction Method for Open-Water Perfoamance of Propeller Based on OpenFOAM.Chanese Journal of Ship Research, Vol.7 No.3, Jun.2012.

[6] CHA Jingjing, WAN Decheng. Numerical wave generation and absorption based on OpenFOAM. The Ocean Engineering, Vol. 29 No.3 Aug.2011, pp.1-12.

[7] LI Yulong, ZHU Renchuan, MIAO Guoping, FAN Jun, LU Zhimei. Simulation of ship motions coupled with tank closhing in time domain based on OpenFOAM. Journal of Ship Mechanics, Vol. 16 No.7 Jul. 2012. pp : 751-762.

[8] LV lianli, SUN Hequan, WANG Jiguang, HUANG Pengfei. Ocean Wave Impact on Ship Hydrodynamic Pressure Field Based on OpenFOAM. Ship Electronic Engineering. Vol.34, No.10, pp: 135-147.

[9] ZHOU Hu, WAN Decheng. Numerical simulation of the unsteady flow around wind turbines with different blades numbers. Chinese Journal of Hydrodynamics. Vol. 29, No.4, July, 2012, pp: 445-452.

[10] Davidsson L., an Introduction to Turbulence Models. Göteborg, Sweden, Chalmers University of Technology, Department of Thermo and Fluid Dynamics. November 2003.

NUMERICAL SIMULATION OF CAVITATING FLOWS CONSIDERING THE FLUID COMPRESSIBILITY IN OPENFOAM

CHANGCHANG WANG[1], GUOYU WANG[2], BIAO HUANG[3]

[1] *School of Mechanical Engineering, Beijing Institute of Technology, Beijing, 100081, China,*
wangchangchang@bit.edu.com

[2]*School of Mechanical Engineering, Beijing Institute of Technology, Beijing, 100081, China,*
wangguoyu@bit.edu.com

[3] *School of Mechanical Engineering, Beijing Institute of Technology, Beijing, 100081, China,*
huangbiao@bit.edu.com

Keywords: Compressible cavitating flow, Tait equation of state, Shock wave emission, OpenFOAM

Abstract
The objective of this paper is to address the simulation of transient cavitating flows with the compressibility of both water and vapour considered. The compressible phase volume fraction transport equations and compressible Pressure Possion equation with phase change are derived and a phase change algorithm is implemented into the native compressible two-phase flow solver compressibleInterFoam in OpenFOAM-4.0. The compressible governing equations together with the Tait equation of state for water and ideal gas equations of state for vapour are solved. The partial cavitating flow characterized by alternate effects of re-entrant flow and shock wave around a NACA66 hydrofoil is selected for the solver performance test. Comparisons are made between the results obtained by the native incompressible cavitation solver interPhaseChangeFoam and the present compressible cavitation solver. Results show that both the incompressiblt cavitation solver and compressible solver can predict the attached cavity growth, re-entrant flow development and large scale cloud cavity formation and shedding process, while the cloud cavity collapse induced shock wave phenomena which is highly related with the water/vapour compressibility is only captured by the implemented compressible cavitation solver. Moreover, the compressible cavitation solver can better predict cavitation evolution cycle and cavitation induced pressure fluctuations. The water compressibility is important for the wave dynamics in cavitating flows.

Introduction
Cavitation occurs when pressure drops below vapour pressure in high speed liquid flows. Cavitation is the complex multiphase flow, consisting of mass transfer, multiphase, turbulence and compressibility. Experiments have identified the shock as one of main origins of cavitation instabilities except for the re-entrant flow, which will cause large scale pressure fluctuations, strong vibrations and noise. The wave dynamics in cavitating flows is highly associated with the fluid compressibility, requiring to solve the compressible cavitation governing equations, including continuity, momentum and energy equations. Thus the development of compressible cavitation solver has great signidicance.
The purpose of this paper is to introduce an implementation of a compressible cavitation solver with transport equation cavitation in OpenFOAM and show its ability in capturing the cloud cavity collapse induced shock wave.

Methods
In the present study, the compressible Navier-Stokes equations including continuity, momentum and energy equations, along with the transport equation for void fraction, are used as governing equations. To account for the fluid compressibility, the Tait equations of state for water and ideal gas equation of state for vapour are employed. The phase change algorithm is implemented into the native pressure-based compressible two-phase flow solver compressibleInterFoam. The compressible phase volume fraction transport equation and compressible Pressure Possion equation with phase change are derived.
The Tait equation of state for water

$$\frac{p_l+B}{p_{l,sat}+B} = \left(\frac{\rho_l}{\rho_{l,sat}}\right)^N \tag{1}$$

where p_{sat}=2338.6 Pa and ρ_{sat}=998.16 kg/m^3 are the saturation pressure and saturation density of liquid water at 293.15 K according to NIST data. B=3.06×108 Pa and N=7.1 are the fitted constants.
The ideal gas equation of state for vapor

$$p_v = \rho_v R_v T_v \tag{2}$$

where subscript v denotes vapor-phase value and R_v=461.6 J/(kg.K) is gas constant. In the present study, the non-condensable gas is ignored in the gas phase.

The Saito cavitation model and SST SAS turbulence model

$$\dot{m}^- = C_c \alpha^2 (1-\alpha) \frac{max((p-p_v),0)}{\sqrt{2\pi R_g T}}, \text{ if } p > p_v \tag{3}$$

$$\dot{m}^+ = C_e \alpha^2 (1-\alpha) \frac{\rho_l}{\rho_g} \frac{max((p_v-p),0)}{\sqrt{2\pi R_g T}}, \text{ if } p < p_v \tag{4}$$

where α is the void fraction, ρ_l is the liquid density, ρ_v is the vapor density, R_g is the gas constant, T is the local fluid temperature, p_v is the saturated liquid vapor pressure and p is the local fluid pressure. C_c is the rate coefficient for reconversion of vapor back into liquid when local pressure exceeds the saturated vapor pressure. C_e is the rate coefficient for vapor generated from liquid when local pressure below the saturated vapor pressure. In the present study, $C_c=C_e=0.1$ is taken. The von Karman length-scale and the SAS term are as following

$$L_{vK} = \kappa \left| \frac{\partial U/\partial y}{\partial^2 U/\partial y^2} \right| \tag{5}$$

$$Q_{SAS} = max\left[\rho \zeta_2 S^2 \left(\frac{L}{L_{vK}}\right)^2 - C_{SAS} \frac{2\rho k}{\sigma_\Phi} max\left(\frac{1}{k^2}\frac{\partial k}{\partial x_j}\frac{\partial k}{\partial x_j}, \frac{1}{\omega^2}\frac{\partial \omega}{\partial x_j}\frac{\partial \omega}{\partial x_j}\right), 0 \right] \tag{6}$$

Where $\zeta_2=3.51$, $\sigma_\Phi=2/3$, $C_{SAS}=2.0$, $L = \sqrt{k}\left(c_\mu^{1/4} \cdot \omega\right)$ is the length scale of the modeled turbulence.
The compressible phase volume fraction transport equation with phase change is derived as following:

$$\frac{\partial \alpha_1 \rho_1}{\partial t} + \nabla \cdot (\rho_1 \alpha_1 U) = \dot{m} \tag{7}$$

$$\frac{\partial \alpha_2 \rho_2}{\partial t} + \nabla \cdot (\rho_2 \alpha_2 U) = -\dot{m} \tag{8}$$

Expanding the Eq. (7), then:

$$\frac{\partial \alpha_1}{\partial t} + \nabla \cdot (\alpha_1 U) = -\frac{\alpha_1}{\rho_1}\frac{D\rho_1}{Dt} + \frac{\dot{m}}{\rho_1} \tag{9}$$

The similar as Eq. (8):

$$\frac{\partial \alpha_2}{\partial t} + \nabla \cdot (\alpha_2 U) = -\frac{\alpha_2}{\rho_2}\frac{D\rho_2}{Dt} + \frac{\dot{m}}{\rho_2} \tag{10}$$

Add Eq. (9) and Eq. (10), then,

$$\nabla \cdot U = -\left(\frac{\alpha_1}{\rho_1}\frac{D\rho_1}{Dt} + \frac{\alpha_2}{\rho_2}\frac{D\rho_2}{Dt}\right) + \dot{m}\left(\frac{1}{\rho_1} - \frac{1}{\rho_2}\right) \tag{11}$$

Expanding Eq. (9), then

$$\frac{\partial \alpha_1}{\partial t} + \alpha_1 \nabla \cdot U + U\nabla \alpha_1 = -\frac{\alpha_1}{\rho_1}\frac{D\rho_1}{Dt} + \frac{\dot{m}}{\rho_1} \tag{12}$$

Substituting Eq. (11) into Eq. (12)

$$\frac{\partial \alpha_1}{\partial t} + \nabla(\alpha_1 U) = \alpha_1 \alpha_2 \left(\frac{1}{\rho_2}\frac{D\rho_2}{Dt} - \frac{1}{\rho_1}\frac{D\rho_1}{Dt}\right) + \dot{m}\left[\frac{1}{\rho_1} - \alpha_1\left(\frac{1}{\rho_1} - \frac{1}{\rho_2}\right)\right] + \alpha_1 \nabla \cdot U \tag{13}$$

The interface compression term is implemented, thus

$$\frac{\partial \alpha_1}{\partial t} + \nabla(\alpha_1 U) + \nabla \cdot (U_r \alpha_1 \alpha_2) = \alpha_1 \alpha_2 \left(\frac{1}{\rho_2}\frac{D\rho_2}{Dt} - \frac{1}{\rho_1}\frac{D\rho_1}{Dt}\right) + \dot{m}\left[\frac{1}{\rho_1} - \alpha_1\left(\frac{1}{\rho_1} - \frac{1}{\rho_2}\right)\right] + \alpha_1 \nabla \cdot U \tag{14}$$

Where U_r is the modelled relative velocity, defined as

$$U_r = c_\alpha |U| \tag{14}$$

Where c_α is a parameter used to adjust the strength of the compression of interface. The equation is solved explicitly with the MULES (multidimensional universal limiter with explicit solution) scheme in several sub-cycle within a time step.
The compressible Pressure Possion equation is derived as follows:
Thermodynamics equation of state:

$$\rho = \Psi p \tag{15}$$

Where ψ is the compressible coefficient. Substitute Eq. (15) into Eq. (7), then

$$\frac{\partial (\Psi_1 \alpha_1 p)}{\partial t} + \nabla \cdot (\Psi_1 \alpha_1 p U) = \Psi_1 \frac{\partial \alpha_1 p}{\partial t} + \alpha_1 p \frac{\partial \Psi_1}{\partial t} + \Psi_1 \alpha_1 p \nabla U + U\nabla(\Psi_1 \alpha_1 p) = \dot{m} \tag{16}$$

Expand Eq. (16), then

$$\Psi_1 \frac{D\alpha_1 p}{Dt} + \rho_1 \nabla U = \dot{m} \tag{17}$$

Similarly, Eq. (8) can be rearranged as

$$\Psi_2 \frac{D\alpha_2 p}{Dt} + \rho_2 \nabla U = -\dot{m} \tag{18}$$

Finally, the compressible Pressure Possion equation with phase change is as following

$$\left(\frac{\alpha_1}{\rho_1}\Psi_1 + \frac{\alpha_2}{\rho_2}\Psi_2\right)\left(\frac{\partial p}{\partial t} + U\nabla \cdot p\right) + \nabla \cdot U = \left(\frac{\alpha_1}{\rho_1} - \frac{\alpha_2}{\rho_2}\right)\dot{m} \tag{19}$$

Results
The numerical results are shown for both the present compressible cavitation solver and the native incompressible cavitation solver interPhaseChangeFoam. Fig. 1 shows the time evolution of cavity volume obtained by both the compressible and incompressible results. The comparisons of the experimentally measured and numerically predicted cavitation evolution frequency based on the cavity volume evolution are shown in Tab. 1, in which the relative error is also presented. The Saito cavitation model and the SST SAS turbulence model are used for both incompressible and compressible simulation. It can be observed that the cavity volume predicted by the present compressible solver is

larger than that the incompressible solver. The cavity evolution frequency in Tab. 1 indicates that the present compressible cavitating flow solver could predict the unsteady cavitation frequency more precisely.
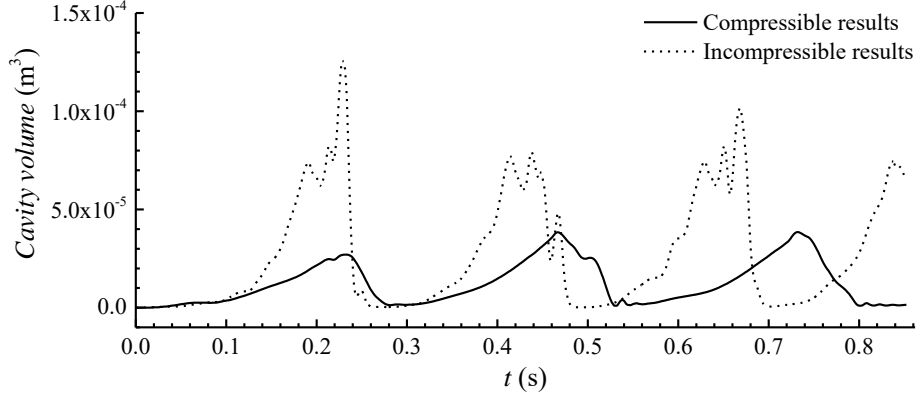
Figure 1: Comparisons of the time evolution of cavity volume based on compressible solution and incompressible solution.
Table 1: Comparisons of the measured (Exp., Leroux et al., 2014) and numerically predicted (Num.) cavity evolution frequency.

	Exp. [4]	**Num. (Incompressible)**	**Num. (Compressible)**
Mean value f (Hz)	3.625	4.504 (24.2 %)	3.867 (6.7 %)

The comparisons of the absolute pressure evolution between the compressible results, incompressible results and the experiments data at x/c=0.7 during 0.64 s are shown in Fig. 2. It can be found that the numerically predicted absolute pressure magnitude agrees well with the experiment data. However, the cavity cloud collapse induced shock wave is only captured by the compressible results. The pressure evolution frequency agrees with the cavity behaviours evolution.
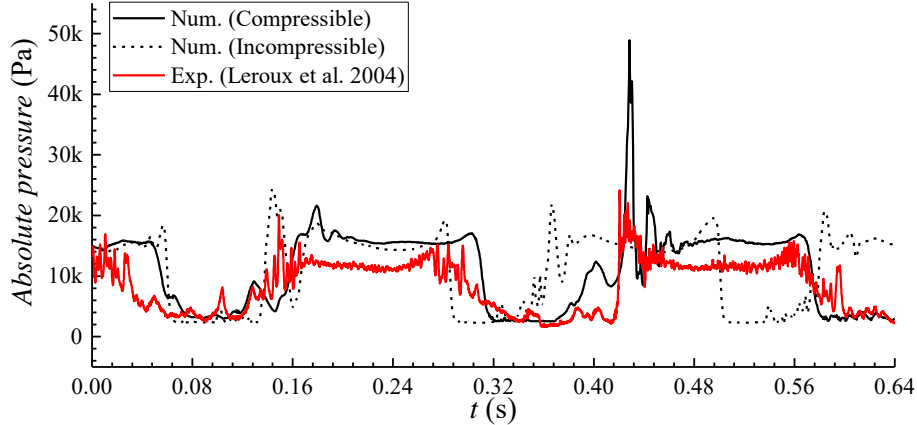
Figure 2: Comparisons of the absolute pressure evolution predicted by the compressible solver with the experiments data and incompressible solver results at x/c=0.7.

Conclusions

In this paper, a compressible cavitation solver is developed by implementing the phase change algorithm into the native compressible two-phase flow solver compressibleInterFoam in OpenFOAM-4.0, considering the compressibility of both water and vapour. The thermodynamic equations of state with Tait state equation for water and ideal gas state equation for vapour are employed. The Saito cavitation model and the SST-SAS turbulence model are applied to simulate the turbulent cavitating flow. The cloud cavity collapse induced shock wave dynamics and its interaction with the attached cavity sheet growth is well predicted by the implemented compressible cavitation solver. The attached cavity sheet growth, the re-entrant flow development and the large scale cloud cavity shedding can be simulated well by both the incompressible cavitation solver, while the cavitation dynamics associated with the compressibility, such as the shock wave dynamics, can only be predicted by the compressible cavitation solver, which considers the compressibility of both water and vapour.

References

[1] R. Issa, A. Gosman, A. Watkins, The computation of compressible and incompressible recirculating flows by a non-iterative implicit scheme, J. Comput. Phys. 62 (1986): 66-82.

[2] H. Jasak, Error analysis and estimation for the definite volume method with applications to fluid flows. University of London: 1996. Ph.D. Thesis.

[3] S. Miller, H. Jasak, D. Boger, F. Paterson and A. Nedungadi, A pressure-based, compressible, two-phase flow finite volume method for underwater explosions, Comput. Fluids 38 (2013) 132-143.

[4] J.B. Leroux, J.A. Astolfi and J.Y. Billard, An experimental study of unsteady partial cavitation, J. Fluids. Eng. 126 (2004) 94-101.

NUMERICAL SIMULATION OF WAVE PROPAGATION OVER A SLOPING BEACH USING A COUPLED RANS-NLSWE MODEL

INE VANDEBEEK[1], ERIK TOORMAN[2], PETER TROCH[3]

[1]Ghent University, Dept. of Civil Eng. & KU Leuven, Hydraulics Laboratory, Dept. of Civil Eng.,
Ine.Vandebeek@UGent.be
[2] KU Leuven, Hydraulics Laboratory, Dept. of Civil Eng., Erik.Toorman@kuleuven.be
[3] Ghent University, Dept. of Civil Eng., Peter.Troch@UGent.be

Keywords: *Two phase flow; wave propagation; coupled model; OpenFOAM; SWASH*

1.   Introduction

Northern European countries such as Belgium, are characterised by a very typical coastal defence system: a hard dike with a promenade and an almost continuous line of high-rise buildings, fronted by a mildly sloped and very shallow foreshore. The presence of this foreshore influences the wave transformation from offshore to nearshore and the interaction with coastal structures significantly. Its effect is not yet fully understood. Taken into account the role of sea dikes as both coastal defences and recreational spaces, it is essential to fully understand and predict the influence of the foreshore on for example wave overtopping on sea dikes and wave loading forces on buildings. The present research, performed in the framework of the CREST research project [1], aims at developing a reliable and accurate tool for the assessment of wave overtopping over the dike crest and wave loading forces for the specific case of a very shallow foreshore.

2.   Numerical framework

Modelling the whole process of wave propagation, transformation, breaking and wave structure interaction is a well-known challenge in the field of coastal engineering.

Non-linear shallow water (NLSW) models are widely used due to its relative simplicity. These models can be applied with good confidence to study wave transformation in the swash zone [2][3] at a limited computational cost. However, depth-averaged models are not exact forms of the governing equations of fluid motion and contain an error of some order [4]. To accurately model the very complex behaviour of the free surface near coastal structures and the associated nonlinear effects, Navier-Stokes (NS) based solvers are required. However, simulating wave propagation and wave transformation over large domains and for long durations with solely a NS solver is currently not feasible due to the requirement of (1) a large computational domain since processes on the beach are driven by waves originally generated at sea and (2) a very high spatial resolution to avoid excessive numerical damping of incoming waves and to accurately simulate wave breaking and wave structure interactions. This results in a very high computational effort.

To obtain the advantages and reduce the disadvantages of both models without loss in accuracy, the authors have investigated a coupling between depth-integrated models and NS models in space. This work describes the simultaneous use of two solvers that belong to the aforementioned categories. The first model which is used, is SWASH [5], a time domain model based on the non-linear shallow water equations. SWASH has proven to accurately reproduce surface elevations for wave transformation over a very shallow foreshore in 1D calculations with very little computational resources due to the depth-averaged assumption and parallel computation capabilities. However SWASH is not able to deal with abrupt changes in geometry e.g. due to the presence of coastal structures [6] and is not suitable to predict in great detail wave loading forces or overtopping volumes over dike crests. The second model which is used, is the CFD model OpenFOAM where the two-phase flow field is resolved by the incompressible Reynolds averaged Navier-Stokes (RANS) equations and the interface is tracked with a volume of fluid method. Contrary to SWASH, OpenFOAM has proven to be able to accurately simulate wave structure interactions [7].

The present coupling methodology is a first straightforward method and consists of a one-way coupling. The NLSW model SWASH is applied in the non-breaking zone and the RANS model OpenFOAM in the zone of high turbulence, breaking waves and wave structure interactions. The two models share a common interface for the data exchange. At this interface, SWASH provides the surface elevation and the velocity values at different levels of depth, depending on the amount of vertical layers used at the coupling location. This information is passed to OpenFOAM and imposed on the inlet OpenFOAM boundary. The coupling interface is located at a low turbulence area. More details about the coupling methodology will be presented at the workshop.

3. Results & Discussion

To test the model for validity, the coupled model is used to simulate two scenarios: (1) solitary wave propagation in a flume with constant water depth and (2) solitary wave propagation over a sloping beach.

In the first case the propagation of a solitary wave with an amplitude of 0.05 *m* in a 28.0 *m* long channel with a constant water depth of 0.5 *m* is simulated. The domain is divided in two subdomains: a subdomain with a length of 18.0 *m* occupied by the NLSW model and a subdomain of 10 *m* occupied by the RANS model. The wave is generated in the NLSW domain and propagates to the RANS model domain.

The evolution of the solitary wave as it propagates along the channel can be seen in Figure 1 (solid blue line) where several snapshots of the free surface elevations at different times are presented. The results clearly demonstrate that the solitary wave maintains its original shape and the wave height does not vary when propagating through the channel. The wave is correctly transmitted from the NLSW to the RANS domain, no disturbance takes place at the coupling interface located at $x = 18$ *m*. For comparison the simulation is also performed with the NLSW model in the complete domain. These results are shown with red dots. There is good agreement between the NLSW standalone results and the coupled model results. Figure 2 shows a snapshot of the entire computational domain modelled with the coupled model. In the left part, only the free surface calculated with SWASH is shown, the right part depicts the results obtained with OpenFOAM, where the colours represent the horizontal velocities. The coupled model saves computational time by a factor proportional to the reduction in cells in the OpenFOAM model.
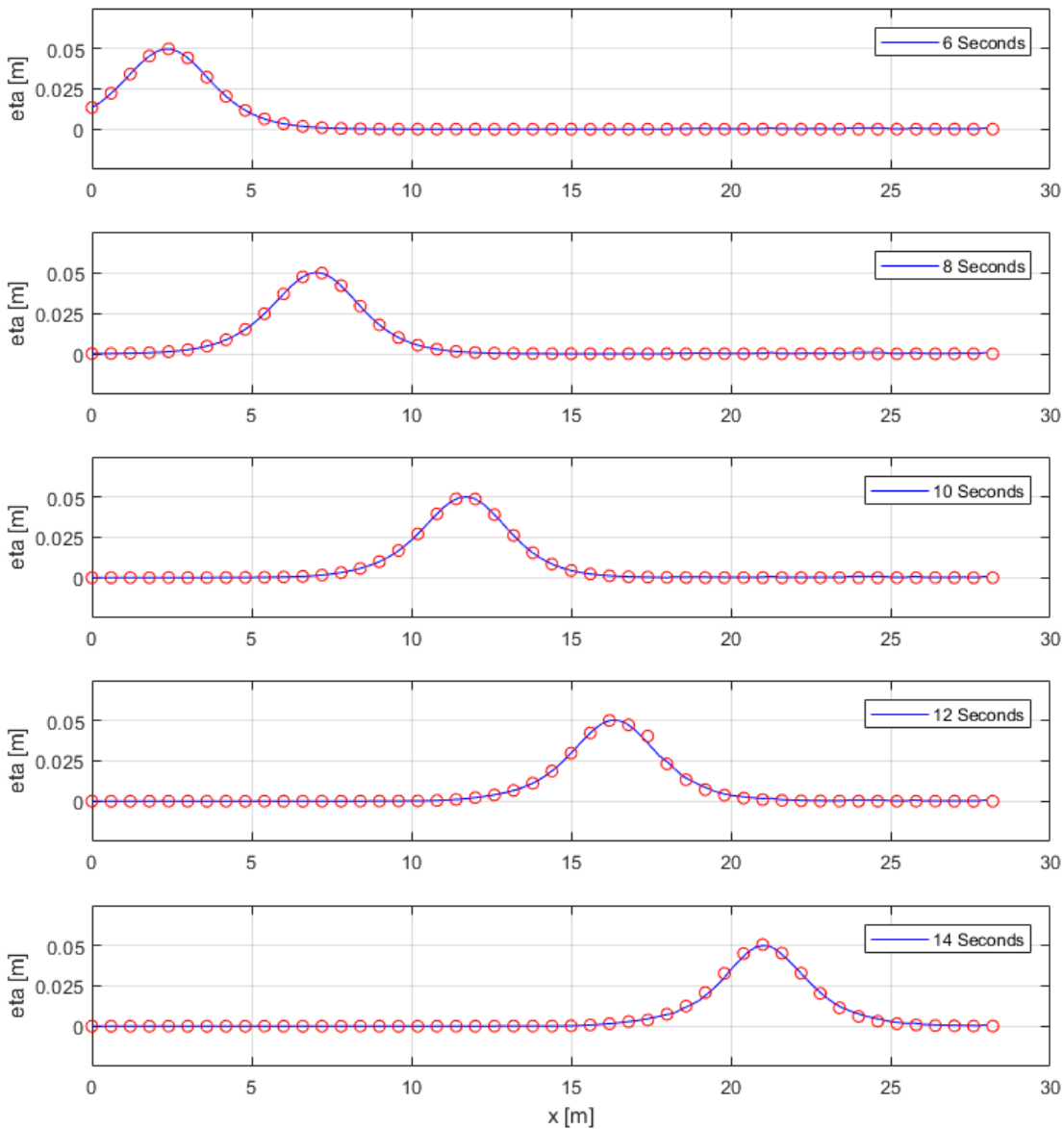
Figure 1: Surface elevation for solitary wave propagation over a flat bottom. Dots represent the results of a SWASH stand-alone simulation over the complete domain. The blue line represents the results of the coupled model (0 *m* ≤x≤ 18 *m*: SWASH, 18 *m* ≤x≤ 28 *m*: OpenFOAM).
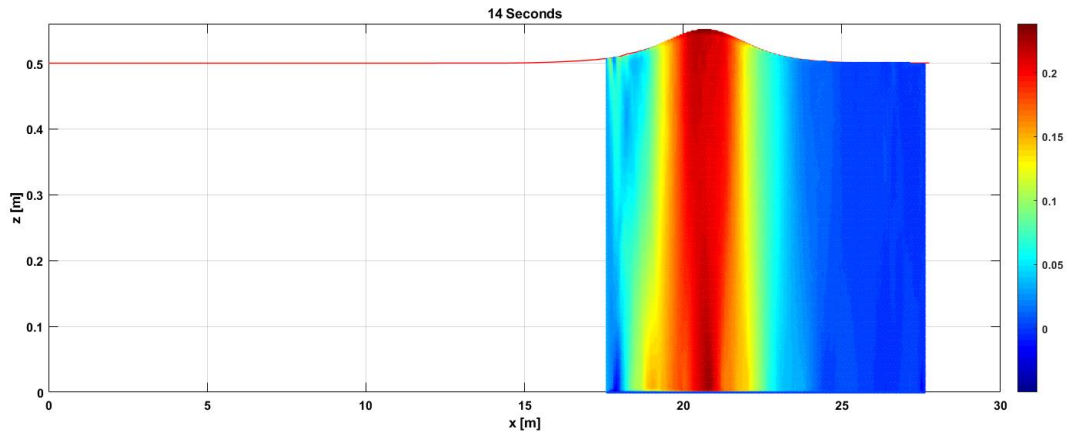
Figure 2: Snapshot of the simulation for the entire domain modelled with the coupled SWASH-OpenFOAM model. The colours represent the horizontal velocity.

A second test case simulates the propagation of a solitary wave over a sloping bottom similar to the experiment of Zelt [8]. A sketch of the simulated case is depicted in the upper corner of Figure 3. The wave is generated in the NLSW domain and propagates to the RANS model domain, respectively with a length of $10.0\ m$ and $5.0\ m$. The wave gauge is located at a distance $7.87d$ from the toe of the foreshore with d the water depth conform the experimental test. The coupling location is chosen on the horizontal part of the bottom, $0.05\ m$ before the wave gauge.

The time series of the surface elevation normalised with the water depth d at the indicated wave gauge is also shown in Figure 3. The numerical results are represented by the solid blue line. Experimental data are marked with red dots. The first peak corresponds to the incident wave, the second to the reflected wave. A good agreement is found both for the incident and the reflected wave between the experimental data and the obtained numerical results.
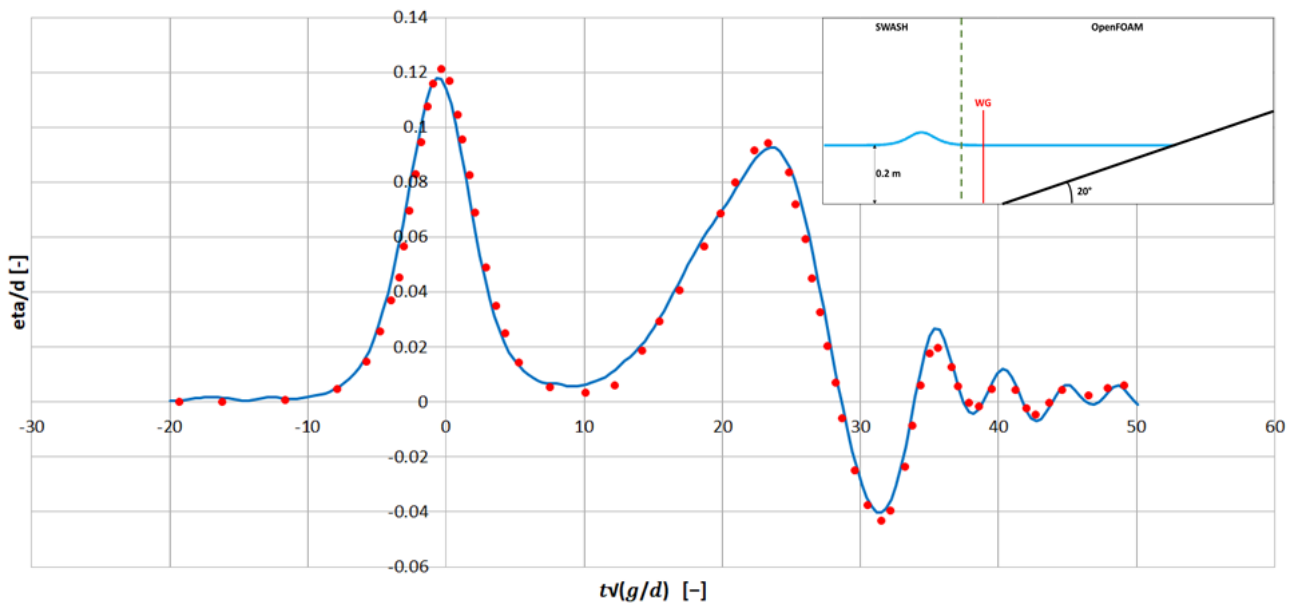
Figure 3: Normalised surface elevations at the indicated wave gauge (WG) for the case of wave propagation of a solitary wave over a sloping beach. The red dots represent experimental data of Zelt [8]. The solid blue line represents the results of the coupled numerical model.

4. Conclusions

A coupled model is developed starting from the NLSW model SWASH and the NS model OpenFOAM. The presented approach is a one-way coupling. The aim of this coupled model is to achieve the same accuracy with the coupled model as with a full RANS solution but reducing considerably the computational time.

The obtained results demonstrate the capabilities of the coupled model to generate and propagate waves. Future work will include further development of the model and the application of the model to cases with very shallow foreshores. The proposed method shows great promise to allow a realistic prediction of wave overtopping and wave loading forces with reasonable computation cost in the future.

References

[1]   VLIZ   (Flanders   Marine   Institute),   *CREST   project   webpage*,   2018.   [Online].   Available: http://www.crestproject.be/en.

[2]   D.H. Peregrine, "Equations for water waves and the approximations behind them", *Waves on Beaches and the Resulting Sediment Transport*, pp. 95-121, 1972.

[3]   S. Hibberd and D.H. Peregrine, "Surf and run-up on a beach: A uniform bore", *J. Fluid Mech.,* vol. 9, no. 2, pp. 323-345, 1979.

[4]   G. Wei and J.T. Kirby, "Time-dependent numerical code for extended Boussinesq equations", *J. Waterway. Port Coast. Ocean Eng.*, vol. 121, pp. 251-261, 1995.

[5]   M. Zijlema, G. Stelling, and P. Smit, "SWASH: An operational public domain code for simulating wave fields and rapidly varied flows in coastal waters", *Coast. Eng.*, vol. 58, pp. 992–1012, 2011.

[6]   T. Suzuki, T. Verwaest, and W. Hassan, "The applicability of SWASH model for wave transformation and wave overtopping: A case study for the Flemish coast", *Proc. 5th Int. Conf. on Advanced Computational Methods in Engineering*, vol. 2011, no. November, pp. 14–17, 2011.

[7]   P. Higuera, J.L. Lara and I.J. Losada, "Three-dimensional interaction of waves and porous coastal structures using OpenFOAM. Part I: Formulation and validation", *Coast. Eng.,* vol. 83, pp. 243-258, 2014.

[8]   J. A. Zelt, "The run-up of nonbreaking and breaking solitary waves", *Coast. Eng.*, vol. 15, no. 3, pp. 205–246, Jun. 1991.

THE NAVAL HYDRO PACK: CURRENT STATUS AND CHALLENGES

VUKO VUKČEVIĆ[1,2], INNO GATIN[1,2], HRVOJE JASAK[1,2]

[1]*University of Zagreb, Croatia,{vuko.vukcevic, inno.gatin, hrvoje.jasak}@fsb.hr*
[2]*Wikki Ltd, United Kingdom, {v.vukcevic, i.gatin, h.jasak}@wikki.co.uk*

This paper serves as an overview of the numerical modelling technology within the Naval Hydro Pack, a software package specifically designed for efficient simulations of various marine hydrodynamic problems. The Naval Hydro Pack is based on `foam-extend`, a community driven fork of the OpenFOAM software. The goal of this paper is to provide an overview of numerical models required for free surface flows in marine hydrodynamics, where we intend to openly discuss drawbacks and advantages of each of our methods.

Introduction

We start by considering the final goal of the Naval Hydro Pack: we would like to be able to reliably calculate the most complicated problem in marine hydrodynamics with reasonable computational resources and sufficient accuracy. The most difficult problem we can currently think of is a self–propelled ship performing some kind of manoeuvre in a severe storm. To add a an additional layer of complexity, imagine that the ship is an ultra large container carrier where the structural response and hydrodynamic excitation are interdependent. Let us now take a "divide–and–conquer" approach of this complicated problem and identify the underlying challenges:

1. The first obvious challenge is the modelling of the two–phase flow (water and air), where we need to accurately take into account free surface kinematics and dynamics,

2. The second challenge is the efficient modelling of gravity waves, propagation and prevention of wave reflection,

3. The third challenge is associated with the hydro–structural coupling where the ship naturally responds to hydrodynamic forces acting on it. Even if we consider the ship as a rigid body, the hydro–structural coupling is highly nonlinear and therefore efficient strategies for resolving this coupling need to be considered.

In the following text, we discuss our solutions to these challenges without going into details, while providing references to all topics.

Free Surface Modelling

In marine hydrodynamic flows, the free surface is dividing two immiscible phases: water and air. Two distinct problems arise in accurate numerical handling of the free surface: i) How to represent and transport the free surface and ii) Once the free surface location is known, how to obey the jump conditions due to different physical properties of air and water?

Interface capturing schemes

In the Naval Hydro Pack, three different interface capturing schemes can be used to advect the free surface:

1. Algebraic Volume–of–Fluid Method (A–VOF),

2. Implicitly Redistanced Level Set Method (IR–LS) [1],

3. Geometric Volume–of–Fluid Method (G–VOF) [2].

The advantages and drawbacks of these schemes are summarized in Table 1, where the reader can easily deduce that there is no "perfect" tool and some trade–off is always necessary. Here, we briefly discuss our best practice guidelines for different types of marine hydrodynamic problems. The A–VOF scheme is suitable for steady resistance and seakeeping simulations where large time–steps are required and the perfect mass conservation is desirable. In cases where unphysical numerical smearing of the interface is present with the A-VOF scheme due to complex flow field or really low–quality mesh, we tend to use the IR–LS method [1]. The method proved to be excellent in preventing numerical ventilation when considering high speed craft. Although the method is not strictly mass conservative, this does not seem to affect the results we are interested in: forces and motions. The G–VOF scheme [2] is by far the most accurate scheme and therefore we

Table 1: Comparison of different interface capturing schemes as implemented in the Naval Hydro Pack.

Advection scheme	A-VOF	IR-LS	G-VOF
Mass conservation	Machine tolerance	Discretisation error	Machine tolerance
Courant number limit	No	No	Yes, $C_o < 1$
Control of interface smearing	Poor	Excellent	Excellent

often use it for violent free surface flows where we seek accurate interface resolution, *e.g.* green water simulations [3]. The obvious drawback is that it requires a Courant number lower than 1.

Ghost Fluid Method for interface jump conditions

Once the free surface location is known, the discontinuity in density and consequently dynamic pressure needs to be taken into account in an accurate way. If one uses standard discretisation practices where the dynamic pressure and density gradient are coupled within the momentum equation, this will cause spurious velocities near the interface in the lighter phase [4] (even without surface tension). The phenomenon can also cause difficulties with advection of the interface because the velocity field is non–physical near the interface. The kinematic and dynamic boundary conditions between water and air can be taken into account with interface–corrected discretisation schemes with the Ghost Fluid Method (GFM) [4]. A similar approach is used by Queutey and Visonneau [5] in the ISIS–CFD software (the CFD solver behind NUMECA's FINE/Marine suite). Currently, our implementation handles dynamic pressure and density jumps across the interface, while the tangential stress balance is still approximated by calculating the velocity gradient using standard Finite Volume discretisation. All interface capturing schemes are used alongside the GFM method in the Naval Hydro Pack. For backward compatibility reasons, the old formulation without the GFM is still available, although we rarely use it.

There is one difficulty with the GFM that we have recently experienced. Since the GFM assumes infinitesimally discontinuous distribution of the density and dynamic pressure, the simulation becomes unstable if water entrains air in a way that the air should be compressed. This is actually the drawback of the incompressibility assumption and not the GFM method. Currently, we are working on extending the GFM for two phase flows where one phase is fully incompressible (water) and the other is compressible with isentropic equation of state (air).

It is equally important to note the indirect benefits of the GFM. As the velocity field across the free surface is continuous and there are no spurious air velocities in air, we observe two advantages: i) The advection of the free surface with all methods is much more stable since the flux is well defined across the interface and ii) The maximum Courant number is significantly lower, enabling faster simulations.

Wave Modelling

In order to efficiently model gravity water waves in the CFD domain, different strategies can be used. In the Naval Hydro Pack, we extend the relaxation zone approach by Jacobsen *et al.* [6] in order to have implicit blending during the transport [1]. The relaxation zones provide an efficient and straightforward tool that we can build upon in future to couple our CFD model with CPU time efficient potential flow models. The approach is also favourable for considering unbounded domains (*e.g.* ships sailing in ocean) and directional sea states. Since the potential flow solution has negligible cost compared to CFD, we prefer to use fully nonlinear stream function wave theory for monochromatic waves and Higher Order Spectrum (HOS) method [7] for irregular sea states. The HOS is quite favourable since it accounts for nonlinear wave modulation and wave–wave interaction, so there is no need to resolve these within CFD.

In the Spectral Wave Explicit Navier–Stokes Equations (SWENSE) method as implemented in the Naval Hydro Pack [1], the waves are introduced in the whole CFD domain. This approach gives us the possibility of calculating only the nonlinear perturbation around the explicit incident wave, instead of calculating the total fields using the standard approach and introducing waves only within the relaxation zones. Since the incident wave field is explicit in the SWENSE method, it slightly facilitates the wave propagation in CFD domain. However, for violent free surface effects such as green water, it is reasonable to expect that the flow solution will be significantly different from the incident wave, making the SWENSE method unsuitable for this type of problems.

Hydro–Structural Coupling

The previous two sections give us a variety of tools to handle the two–phase flow, while the missing bit is the coupling of the flow field with the motion of a ship or another offshore object. Two distinct challenges can be identified when considering the hydro–structural coupling: i) Coupling strategy between the fluid–flow and 6 DOF equations of motion and ii) Efficient handling of dynamic mesh.

Algorithms for hydro–structural coupling

In Finite Volume CFD, almost all hydro–structural coupling algorithms are partitioned, meaning that the flow field and 6 DOF equations of motion are solved one after another in an iterative manner. In the Naval Hydro Pack, the 6 DOF equations are strongly coupled to the fluid flow within the nonlinear (PIMPLE) loop, where a sufficient number (usually six or more for seakeeping) of nonlinear corrector steps is necessary to converge the solution within a time–step. We have implemented an enhanced strategy where the 6 DOF equations are additionally integrated after each pressure correction step. The approach provides significantly improved convergence of 6 DOF and flow field at a negligible CPU time cost. The benefit of this approach is demonstrated in Gatin *et al.* [8], where almost the same motion amplitudes are obtained by using 2, 4, 6 or 8 nonlinear correctors for the seakeeping of the KCS model. This allowed us to speed-up our seakeeping simulations up to three times without sacrificing the accuracy.

Recently, we have also developed a monolithic coupling approach, where the 6 DOF equations are solved as a constraint within the pressure equation. Similar to the enhanced coupling, the monolithic coupling improves the convergence with lower number of nonlinear correctors, as presented on Figure 1 where the heave motion for seakeeping of the KCS model is depicted. The monolithic approach proved to be quite favourable for motions with high acceleration (*e.g.* seakeeping of high speed planning hulls) and high added mass (relative to the mass of the ship). However, it should be stated that for the seakeeping of displacement ships, this approach is rather excessive: although it can be used confidently, the benefit will be minor compared to the enhanced approach [8]. The numerical details and benefits of this approach are described by Jasak *et al.* [9].
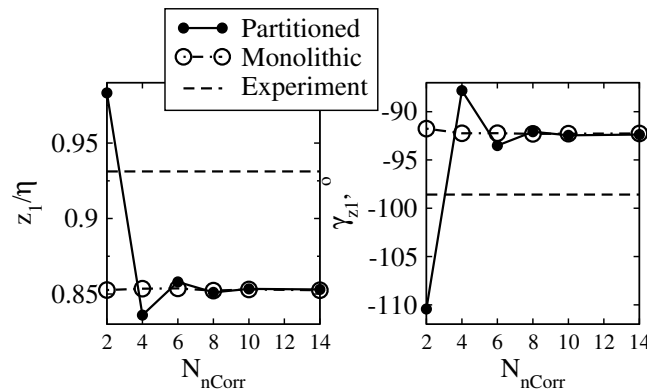
Figure 1: Heave amplitude and phase for different number of nonlinear correctors, KCS model, C5 case, Tokyo Workshop [10]

Dynamic Mesh Handling

Once the 6 DOF equations are solved and the new position of the ship is obtained, one needs to efficiently handle the dynamic mesh motion. Different approaches exist in the Naval Hydro Pack and `foam-extend`, which are summarized in Table 2. The first option is the simplest: the domain is moved as a rigid body. The method is simple to implement and robust, while it does not allow multiple bodies and is not suitable for fairly large motions. The second method is mesh deformation, where we prefer to use an algebraic approach where the mesh is moved rigidly in the vicinity of the body and the deformation slowly decays towards farfield boundaries. The approach is as efficient as the domain motion. Although it can also have difficulties with large amplitude motions, the method is suitable for most of the standard marine hydrodynamic problems. Both domain motion and mesh deformation strategies cannot handle appendages that can move relative to the moving ship. In `foam-extend-4.1`, a significant improvements to the Immersed Boundary library and Overset Mesh library have been added, making these choices more suitable for marine hydrodynamic flows. Both methods offer extreme versatility in a sense that they can handle complex relative motions. The Overset Mesh method is more suitable for flows where viscous effects are important, while the Immersed Boundary method is favourable where the pressure effects are dominant and the viscous effects are of secondary interest. In current state, both methods are efficiently parallelised and work well, although the pre–processing stage is more demanding for the Overset Mesh since it requires careful consideration of the overlapping region. Both methods are in their intermediate stages of development in `foam-extend`, which practically means that the tools are working, although a significant portion of thorough verification and validation is missing, along with some additional minor development.

Conclusion and Future Work

A single conclusion can be drawn from this discussion and our experience during the past decade: there is no single best tool which will be able to efficiently tackle all the marine hydrodynamic problems. In our opinion, it is up to

Table 2: Comparison of different dynamic mesh strategies as implemented in the Naval Hydro Pack and `foam-extend`.

	Domain Motion	**Mesh Deformation**	**Overset Mesh**	**Immersed Boundary**
Complexity	Low	Low	High	High
Development stage	Mature	Mature	Intermediate	Intermediate
Robustness	High	High	Intermediate	Intermediate
Versatility	Low	Low	High	High

the experienced researcher and engineer to determine the most suitable combination of tools to tackle a given problem. Therefore, we have focused on developing and testing various interface capturing, interface handling, hydro–mechanical coupling and dynamic mesh methods in the Naval Hydro Pack. Where one method proves to be unsuitable, it is often more natural and less time consuming to switch to another method, rather than to "improve" the original one.

Currently, our short term research and development covers the following topics: i) Improved turbulence modelling practices for marine hydrodynamics free surface flow. Ordinary turbulence models are derived and tuned for single phase flows, usually causing non–physical turbulent eddy–viscosity near the free surface [11], which needs to be reconsidered, ii) Extension of the GFM for tangential stress balance in order to more accurately calculate the velocity gradient near the free surface and iii) Extension of the GFM for incompressible/compressible two–phase flow.

In the long term, we will focus on more advanced dynamic mesh handling strategies: i) Improving the robustness of our automatic overlap assembly strategy in Overset Mesh library and ii) Further testing, verification and validation of the Immersed Boundary library for marine hydrodynamics. In order to tackle the problem discussed at the beginning of the paper, we are looking into obtaining the funding to develop a fully open–source framework for hydro–elastic computations where we would couple the Naval Hydro Pack with an open source FEM structural method.

Acknowledgments

References

[1] V. Vukčević, H. Jasak, and S. Malenica, "Decomposition model for naval hydrodynamic applications, Part I: Computational method," *Ocean Eng.*, vol. 121, pp. 37–46, 2016.

[2] J. Røenby, H. Bredmose, and H. Jasak, "A computational method for sharp interface advection," *Open Science*, vol. 3, no. 11, 2016.

[3] Gatin, I. and Vukčević, V. and Jasak, H. and Seo, J. and Rhee, S.-H., "CFD Verification and Validation of Green Sea Loads," *Ocean Engineering*, vol. 148, pp. 500–515, 2017.

[4] V. Vukčević, H. Jasak, and I. Gatin, "Implementation of the Ghost Fluid Method for Free Surface Flows in Polyhedral Finite Volume Framework," *Comput. Fluids*, vol. 153, pp. 1–19, 2017.

[5] P. Queutey and M. Visonneau, "An interface capturing method for free–surface hydrodynamic flows," *Comput. Fluids*, vol. 36, pp. 1481–1510, 2007.

[6] N. G. Jacobsen, D. R. Fuhrman, and J. Fredsøe, "A wave generation toolbox for the open-source CFD library: OpenFoam®," *Int. J. Numer. Meth. Fluids*, vol. 70, no. 9, pp. 1073–1088, 2012.

[7] I. Gatin, V. Vukčević, and H. Jasak, "A Framework for Efficient Irregular Wave Simulations Using Higher Order Spectral Method Coupled With Viscous Two Phase Model," *Journal of Ocean Engineering and Science*, vol. 2, pp. 253–267, 2017.

[8] I. Gatin, V. Vukčević, H. Jasak, and H. Rusche, "Enhanced coupling of solid body motion and fluid flow in finite volume framework," *Ocean Eng.*, vol. 143, pp. 295–304, 2017.

[9] Jasak, H. and Gatin, I. and Vukčević, V., "Monolithic Coupling of the Pressure and Rigid Body Motion Equations in Computational Marine Hydrodynamics," *J. Marine Sci. Appl.*, pp. 1–7, 2017.

[10] "Tokyo 2015: A Workshop on CFD in Ship Hydrodynamics," http://www.t2015.nmri.go.jp/, 2015, [Online; accessed 20 August 2015].

[11] B. Devolder, P. Rauwoens, and P. Troch, "Application of a buoyancy-modified $k - \omega \, SST$ turbulence model to simulate wave-run up around a monopile subjected to regular waves using OpenFOAM," *Coastal Eng.*, vol. 125, pp. 81–94, 2017.

STUDY ON SLOSHING COUPLED MOTION OF A FLNG SECTION IN WAVES USING WHOLE-FLOW-FIELD CFD METHOD

QI LI, YUAN ZHUANG, DECHENG WAN[*]

Collaborative Innovation Center for Advanced Ship and Deep-Sea Exploration, State Key Laboratory of Ocean Engineering, School of Naval Architecture, Ocean and Civil Engineering, Shanghai Jiao Tong University, Shanghai 200240, China
Corresponding author: dcwan@sjtu.edu.cn

Keywords: *sloshing tank, naoe-FOAM-SJTU solver, FLNG, sloshing coupled motion*

INTRODUCTION

To reduce the cost of long distance transport of ocean resources, ship-like structures FPSO and FLNG with liquid tanks are designed, and they are widely used in ocean engineering field. For those with partially liquid filled tanks, ship motion in waves will affect the liquid sloshing in tanks, and the sloshing will influence the ship motion and stability in return. Besides, the violent flow in tanks may create high impact pressure on bulkhead. Therefore, the coupling effect is important for ship and tank structure design. The study on sloshing coupled ship motion have been conducted by many researchers for several decades. However, the further research is required as it is still a complex phenomenon with the effect of strong non-linear characteristic.

With the help of HPC, CFD method is used to simulate sloshing coupled effects, and it soon became popular. Different from the potential-CFD combined method, this paper illustrates a whole-flow-field simulation method to solve sloshing coupled problems of a FLNG section with two liquid tanks. The internal tank sloshing and external wave flow field can be solved simultaneously using this method. Based on our in-house solver naoe-FOAM-SJTU[1] which was developed on top of the open source platform OpenFOAM, the sloshing coupled FLNG motion in waves can be effectively simulated. The validation work was done to verify the accuracy and the capability of the solver by comparing numerical results with experimental results. VOF method is used to capture the free surface of the whole flow field and waves2foam toolbox is selected to generate and absorb waves. The moment on the internal tank and the external hull induced by sloshing flow and waves can be computed respectively in this solver, and the differences of the moment phases can be obtained. Moreover, the influence of several wave frequencies and wave heights are investigated. Better than potential method, violent flow sloshing and large amplitude motion can also be simulated and shown using CFD.

NUMERICAL METHOD

The viscous flow in this paper is investigated by solving the incompressible Navier-Stocks equations. Based on dynamic deformation mesh technology, the equations are as follows.

$$\nabla \cdot U = 0 \tag{1}$$

$$\frac{\partial \rho U}{\partial t} + \nabla(\rho(U - U_g)U) = -\nabla P_d - g \cdot x \nabla \rho + \nabla(\mu \nabla U) + f_\sigma \tag{2}$$

Sloshing is a fluid motion which has properties of high nonlinear and randomness. And these properties will make the shape of the free surface more complex. For this problem, VOF method is applied to capture the water free surface by tracking the water and air fraction in each cell. With the

advantages of good mass conservation, computational efficiency, and easy implementation, this method has become one of the most popular methods [2].

Dynamic Meshes Technology

During the computation, the moving-mesh technique is needed to solve the ship motion. Dynamic meshes are used in the cases of this paper. The mesh deforms with the motion of the FLNG section. The position of mesh nodes will be solved using the Laplace's equation with variable diffusivity as following.

$$\nabla \cdot (\gamma \nabla x_g) = 0 \tag{3}$$

$$\gamma = \frac{1}{r^2} \tag{4}$$

Where x_g is the displacement of mesh node; γ is the diffusivity field, determined by r which is the distance from cell center to the moving body boundary.

Forces and Moments Calculating of Divided Patches

To investigate the relation between the moment phase difference and the coupled hull motion, the ship section is divided into two patches to get the moments from internal and external tank wall respectively. After that, the results are accumulated as a whole for the calculation of the hull motion. The calculation algorithm is shown as Figure 1.
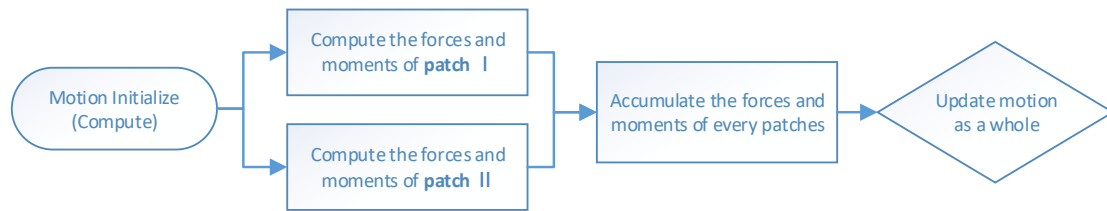
Figure 1 The algorithm of forces and moments calculating of each patch[3]

Wave Generation and Absorption

In this paper, the liquid tank will be subjected to several wave conditions. Therefore the wave generation is of vital importance. An open-source toolbox waves2foam is selected to generate and absorb waves. By modifying the velocity and phase boundary conditions, and setting the relaxation zones near the inlet and outlet boundaries, the required waves can be generated near the inlet boundary and absorbed near outlet boundary [4]. The following relaxation function and equation are applied inside the relaxation zones.

$$\alpha_R(\chi_R) = 1 - \frac{\exp(\chi_R^{3.5}) - 1}{\exp(1) - 1} \tag{5}$$

$$\phi = \alpha_R \phi_{\text{computed}} + (1 - \alpha_R) \phi_{\text{target}} \tag{6}$$

Where ϕ represent the velocity or phase value, and α_R is the relaxation function which changes along with the value of χ_R. The relation between α_R and χ_R can be seen in Figure 2.
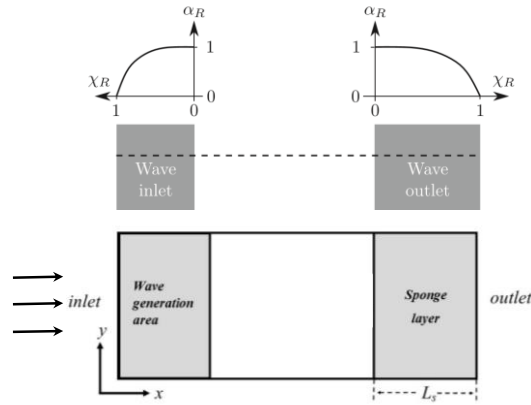
Figure 2 A variation sketch of α_R in inlet and outlet relaxation zones [4]

RESULTS AND DISCUSSIONS

Related work has been conducted by Yin and Zhuang [5][6] using whole-flow-field method to simulate a two-tank LNG ship in beam waves. Further researches are investigated in this paper. A FLNG section with two liquid tanks is made to study the sloshing coupled motion under several influence factors.

Validation of the Whole-Flow-Field Method and Solver

The naoe-FOAM-SJTU solver and the whole-flow-field method are applied and validated by the partial filling tank simulation cases under several wave excitation frequencies. The numerical results agree well with the experimental results [7], and the results are better than that of potential flow method under some wave frequencies. The comparison and the fluid flow field are shown as Figure3.
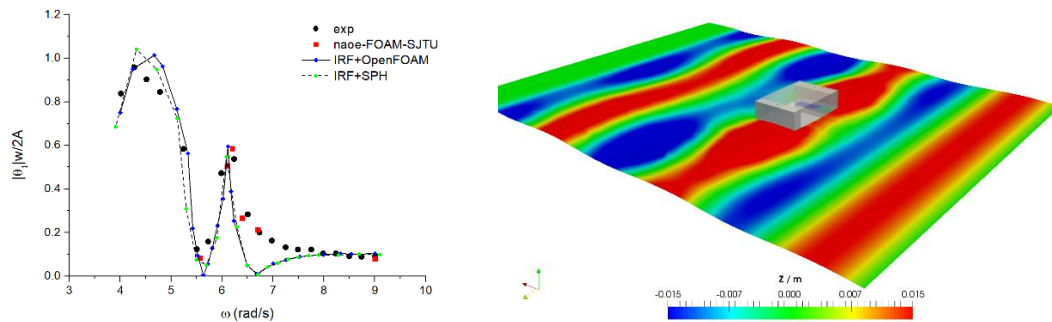
Figure 3 Results comparison and the instantaneous whole flow field

Sloshing Coupled Motion Under Different Filling Ratios

The sloshing coupled motion will be influenced by the factor of tank filling ratios. Five filling ratios are simulated in current research. Time series of tank motion, internal tank moment and external tank moment can be recorded respectively as Figure 4. The results show that the phase difference and amplitudes of sloshing coupled motion and moment can be obtained using whole-flow-field method through naoe-FOAM-SJTU solver.
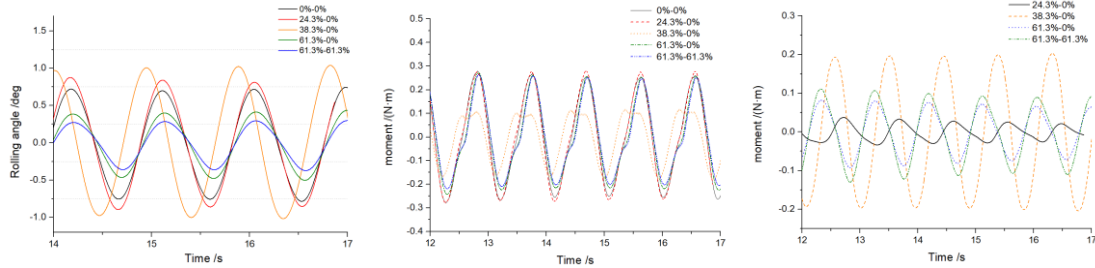
Figure 4. Time series of tank motion, external tank moment and internal tank moment

Acknowledgements

References

[1] Shen, ZR, Wan, DC, Wang, JH and Zhao, WW. "Manual of CFD solver for ship and ocean engineering flows: naoe-FOAM-SJTU," Technol Rep Solver Man, 2014, Shanghai Jiao Tong University.

[2] Cao, HJ, Wan DC, "RANS-VOF solver for solitary wave run-up on a circular cylinder," China Ocean Engineering, Volume 29, Issue 2, 183–196, 2015.

[3] Yuan Z, Wan DC, "The fully coupled effects of FPSO with different filling ratio tanks in CFD method," Proceedings of the 8th International Conference on Computational Methods (ICCM2017),25-29 July 2017, Guilin, Guangxi, China，PP.1055-1065

[4] Jacobsen, NG, Fuhrman DR and Fredsφe, "A wave generation toolbox for the open-source CFD library: OpenFoam," Int. J. Numer. Method Fluid. 2012, 70:1073–1088.

[5] Yin CH, Yuan Z, Wan DC, "Numerical Study on Liquid Sloshing in LNG Tanks Coupled with Ship Motion in Waves," Proceedings of 3rd International Conference on Violent Flows (VF-2016), 9-11, March 2016, Osaka, Japan, Paper No. 26.

[6] Yuan Z, Yin CH, Wan DC, "Numerical Study on Ship Motion Coupled with LNG tank Sloshing Using Dynamic Overset Grid Approach," Proceedings of the 7th International Conference on Computational Methods (ICCM2016), August 1-4, 2016, Berkeley, USA, paper No. ID 1503-5525-1-PB.

[7] Jiang SC, Teng B, Bai W, et al, "Numerical simulation of coupling effect between ship motion and liquid sloshing under wave action," Ocean Engineering, 2015, 108:140-154.

CFD SIMULATION OF VORTEX RING FORMATION FOR LOW SPEED IMPULSIVE PROPULSION

XIAOSONG ZHANG, DECHENG WAN*

State Key Laboratory of Ocean Engineering, School of Naval Architecture, Ocean and Civil Engineering, Shanghai Jiao Tong University, Collaborative Innovation Center for Advanced Ship and Deep-Sea Exploration, Shanghai 200240
Corresponding Author: dcwan@sjtu.edu.cn

Impulsive propulsion is a kind of bionic propulsion, whose concept comes from the squid. Squid generates an impulsive jet for thrust through its body muscle contraction. During the process of impulsive propulsion, large-scale vortex ring is generated in the near-wake, which plays an important role in the efficiency promotion. In recent years, some small underwater vehicles are equipped with Vortex Ring Thruster (VRT). In this paper, open source platform OpenFOAM is applied to numerically investigate the vortex ring behaviour during the propulsion process. A piston-nozzle apparatus is applied to simulate thruster. Mesh sensitivity study is firstly conducted. Vortex rings behaviour in calm water under different stroke ratios are simulated. The calculated vortex ring formation and pinch-off phenomenon are in good agreement with experimental results. In addition, vortex ring formation is investigated in the presence of background flow. The vortex ring is found smaller and the "pinch-off" phenomenon is delayed by the background flow. Besides, cyclic pulse simulation is carried out. The simulation indicates that there exists reverse vorticity during cyclic pulse process, which can reduce the energy of vortex rings.

Introduction

As a result of natural selection, fast moving marine animals choose impulsive modes to swim. This type of impulsive propulsion like squid has high efficiency. For ship and marine vehicle, propeller is the most commonly used propulsion device. Because of the spin of blades in water, the kinetic energy built up in water is contributed not only from the speedup water velocity in line with the thrust direction but also from the swirl velocity of water associated to the spin of the blades. Water kinetic energy due to the swirl of water doesn't contribute to the generation of thrust and therefore it is an energy waste. However, impulsive propulsion can avoid the swirl energy loss. Thus, it is very meaningful to develop impulsive propulsion.

Vortex rings are a typical phenomenon in impulsive. A great amount of experimental works have been carried out to study vortex rings through the starting flows generated from a piston-nozzle apparatus. Gharib et al.[1] proposed a universal time scale for vortex ring formation, which showed that the large-scale vortex followed by a trailing jet only occurred when stroke ratio is larger than 4. On the other hand, when stroke ratio is smaller than 4, the flow field consists of only a single vortex ring. Rosenfeld et al.[2] carried out CFD simulation of the vortex formation in calm water, the influence of three different kinds of geometric shapes were discussed. Krueger et al.[3-4] analysed the influence of vortex ring on thrust of thruster. The contribution of vortex ring was attributed to the change of fluid pressure, which was named "over-pressure". Furthermore, Krueger et al.[5] studied experimentally the vortex ring pinch-off process in the presence of a simultaneously initiated uniform background co-flow and found that the formation number was reduced by background flow. Jiang et al.[6] carried out numerical simulation to study the vortex formation in the presence of a fully developed background flow and described the interaction between vortex ring and background flow vorticity.

In this paper, CFD solver *pimpleDyMFoam* in OpenFOAM was used to solve the impulse problem and the vortex ring formation process in background flow conditions. Cyclic pulse simulations were also carried out to investigate the interaction between vortex rings.

Numerical method

In present work, the three dimensional time-dependent incompressible Navier-Stokes equations are employed for simulating the flow. The governing equations can be written as follows:

$$\nabla u_i = 0 \tag{1}$$

$$\frac{\partial u_i}{\partial t} + (u_i \cdot \nabla)u_i = -\nabla p + \nu \nabla^2 u_i \tag{2}$$

where u_i is velocity in three direction ($i = x, y, z$), ∇ is divergence operator, ∇^2 is Laplace operator, ν is the fluid kinematic viscosity.

In order to simulate piston-nozzle jet, moving mesh technology is used to control the piston motion. The mesh motion is obtained by solving a mesh motion equation, where boundary motion acts as a boundary condition and determines the position of mesh points. The motion is characterized by the spacing between nodes, which changes by stretching and squeezing.

In this study, the velocity of mesh motion u_g is obtained by solving a Laplace equation as follows:

$$\nabla \cdot \left(\gamma \nabla \boldsymbol{u_g} \right) = 0 \qquad\qquad（3）$$

By this velocity, the mesh move forward to a new position:

$$X_{new} = X_{old} + \boldsymbol{u_g} \Delta t \qquad\qquad（4）$$

The coefficient γ in Eqn. (3) is the diffusion coefficient, which is used to control the mesh spacing and quality. The definition of γ is:

$$\gamma(r) = \frac{1}{r^m} \qquad\qquad（5）$$

where r is the radius from the moving boundary, m is an integer. In this study, for x direction, m is set to 1 to obtain an appropriate mesh motion, for y direction and z direction, m is set to a very large number so that the mesh motion in these two direction are restrained.

Geometry and computational condition

A piston-nozzle apparatus was applied to simulate thruster. The computational domain consisted of nozzle and outer flow domain is shown in Figure 1. Dimension of the piston is exactly the same with previous experiments of Gharib et al.[1]. The inner diameter (D) of nozzle is 2.54cm, sharp-wedged exit nozzle shape with a tip angle of 20° is adopted. The total length of the piston is 40cm. The outer flow domain span 10D in the streamwise direction and 2.5D in the radial direction.
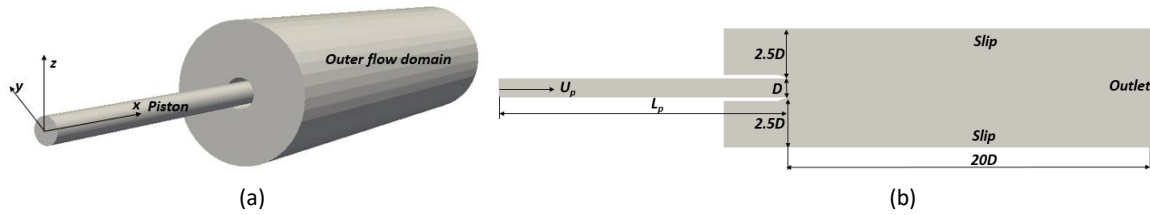
Figure 1 The computational domain. (a) Three-dimensional view of the numerical domain. (b) Domain dimension and boundary condition.

Figure 2 Details of mesh arrangement. (a) Overall mesh arrangement. (b) Local mesh around the nozzle exit

Figure2 shows the detailed mesh arrangement. Mesh in the nozzle is uniform in three directions and is gradient distribution in the radial direction for outer flow domain. According to previous literature, it is essential to accurately calculate the friction which plays an important role in the formation of vortex. Friction test has been performed by simulating pipe flow cases using the nozzle geometry with different mesh arrangements. The friction calculated with 80*50*40 meshes in the axial, radial and circumferential directions is accurate enough. This mesh arrangement is adopted for nozzle mesh. For the outer flow domain, pressure of specific point was applied for mesh sensitivity test. It avoids the problem in the previous numerical researches' mesh sensitivity test[2][6] that total circulation cannot reflect the particulars. The specific point is on the central axis of the nozzle and 2D distance away from the nozzle exit. Test results are shown as Figure 3.
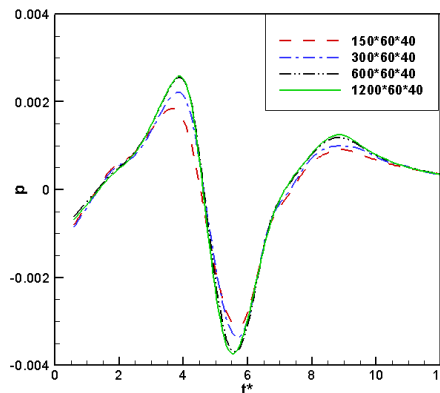
Figure 3 Mesh sensitivity test in axial and radial direction.

On the basis of results of mesh sensitivity test, 600*60*40 meshes in the axial, radial and circumferential directions is adopted in the outer flow domain.

Numerical results and analysis

In order to better represent the results of the calculation, two non-dimensional times are defined as:

$$T^* = {L_m}/{D} = {U_p T}/{D} \qquad (6)$$

$$t^* = {L}/{D} = {U_p t}/{D} \qquad (7)$$

where L_m is piston stroke, L is the distance of piston motion, D is the inner diameter of nozzle. U_p is piston velocity.

The comparison between CFD results and experimental results in calm water condition under different stroke ratios ($T^* = 2, 3.8, 14.5$) is shown in Figure 4.
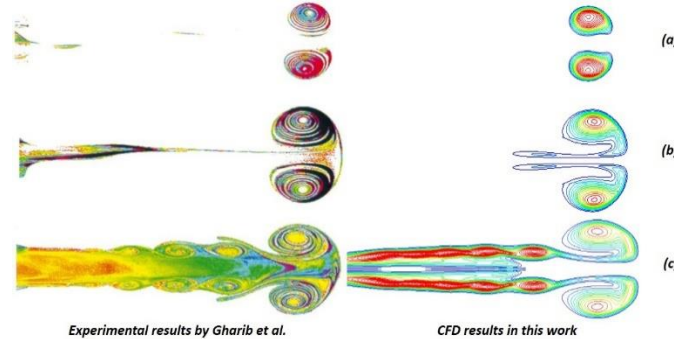
Figure.4 Comparison of vortex ring between CFD results in this work and experimental results by Gharib et al. (a) T*=2; (b) T*=3.8; (c) T*=14.5.

It is obvious that the CFD results are in good agreement with the experimental results regarding to the vortex ring formation. For the case T*<4 (a), the leading vortex is small and there is no trailing vorticity behind the vortex ring; For the case T*≈4 (b), it appears that the leading vortex ring is nearly saturated; For the case T*>4 (c), there is an obvious trailing vorticity behind the leading vortex ring and there are some small vortex in the trailing flow. It is universally accepted that the "Formation number" is nearly equal to 4 for single pulse vortex ring.

According to above phenomena, trailing vorticity flow appears when T*>4. Under this condition, another important phenomenon "pinch-off" will occur in the propagation process. The formation and propagation of the vortex ring for T*=6 is shown in Figure 5.
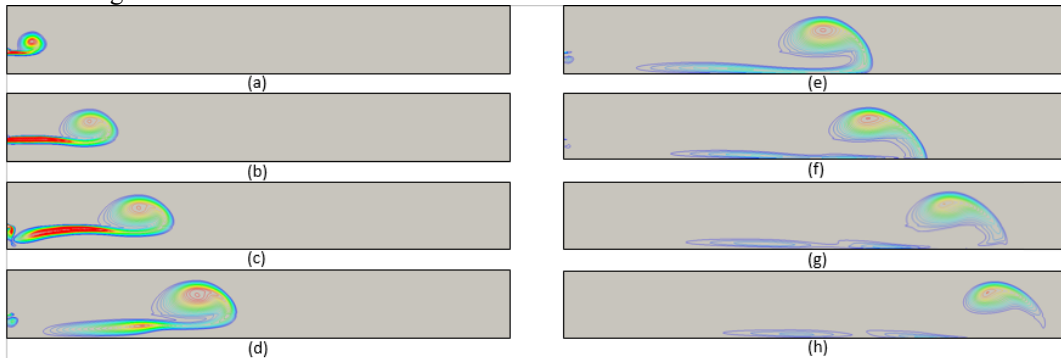
Figure.5 The formation and propagation of the vortex ring for single pulse T*=6 in calm water. The formation times are t*=1.5 (a), t*=4.5 (b), t*=6.6 (c), t*=9 (d), t*=12 (e), t*=15.6 (f), t*=19.5 (g), t*=21.6 (h).

In the case of small piston ratio, all the vorticity generated at the nozzle during the ejection is essentially entrained into the downstream propagating vortex ring. However, the situation is different for the case of large piston ratio (T*>4) as shown in Figure 5. At first, due to the action of shear layer, a large-scale vortex ring is formed at the nozzle exit. With the push of the piston, a striped wake vorticity arises behind the vortex ring. When the piston stop at time instant (c), striped wake vorticity breaks down from the nozzle. Then the leading vortex moves forward with an obvious trailing vorticity behind it. Because the energy of vortex is saturated, the trailing vorticity cannot get into the vortex, and the trailing vorticity becomes longer and longer. The large-scale leading vortex contain larger energy and move faster, then the "pinch-off" phenomenon occurs (f). The vortex ring disconnects itself from the bulk of the flow, leaving behind a noticeable tail of vorticity flow region.

For actual propulsion, the ambient fluid should not be calm water condition. Thus, it is necessary to place this apparatus into an environment with ambient flow to investigate vortex ring formation in the presence of background flow. As for CFD measure, the boundary conditions were changed as the Figure 6 to simulate the ambient flow.
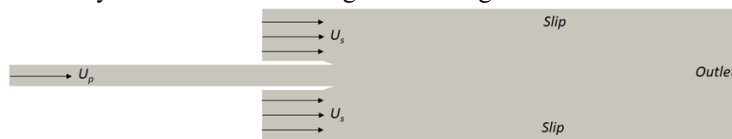
Figure 6 Boundary conditions of case with ambient flow.

where U_s is the ambient velocity. For the thruster, U_s is equivalent to advance velocity. The evolution of the vorticity field for the case of $U_s = 0.5 U_p$ is as shown in Figure 7.
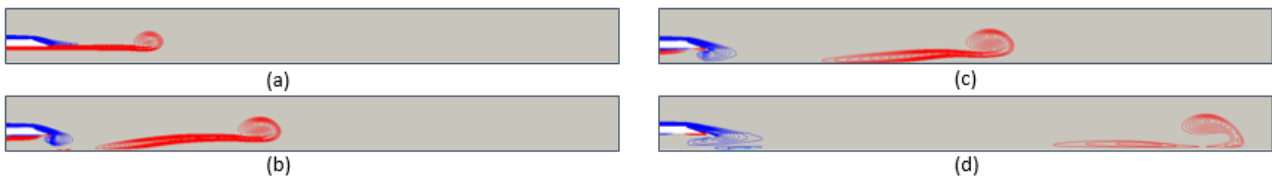
Figure.7 The formation and propagation of the vortex ring for single pulse T*=6 with background flow $U_s = 0.5U_p$. The formation times are t*=4.5 (a), t*=9 (b), t*=12 (c), t*=20.4 (d)

The influence of background flow field on vortex ring can be seen from Figure 7. Vorticity is coloured by rotation directions of vortex. At first, the vortex ring is smaller and trailing vorticity is longer obviously in contrast with the calm water condition at the same time. Besides, there is obvious reverse vorticty around the nozzle exit, which can consume the energy of vortex during the formation process. In addition, the "pinch-off" phenomenon is delayed by the background flow. It occurs at the time t*=20.4 as Figure 7 (d) shows, while it occurs at the time t*=15.6 in calm water condition as Figure 5 (f) shows.
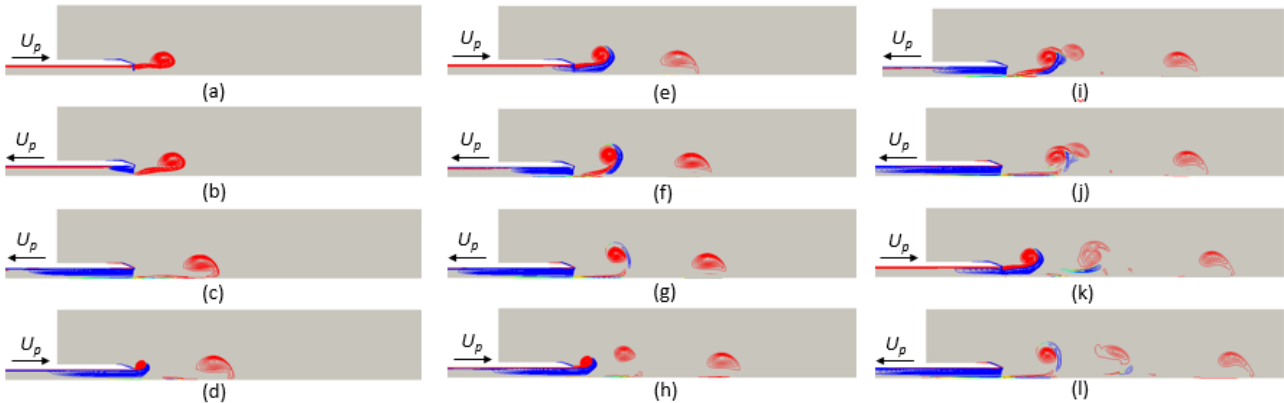
Figure.8 The formation and propagation of the vortex ring for cyclic pulse T*=3.9 in calm water. The formation times are t*=1T*(a), t*=1.2T*(b), t*=2T*(c), t*=2.3T*(d), t*=3T*(e), t*=3.5T*(f), t*=4T*(g), t*=4.5T*(h), t*=5.5T*(i), t*=6T*(j), t*=7T*(k), t*=8T*(l)

For vortex ring thruster, the thrust produced by the piston in the apparatus for reciprocating motion to breathe and remove the liquid. Since vortex ring plays an important role in the thrust production, it is significant to study the formation and propagation of the vortex ring for cyclic pulse. The detailed process is in Figure 8. T*=3.9 was selected because it is a critical saturation state for vortex ring as mentioned above. Vorticity is coloured by rotation directions of vortex. Firstly, a large-scale vortex ring generated by the first push just like the single pulse. Then the piston begin to shrink, when water is sucked into the nozzle, it will generate reverse vorticity through the nozzle exit. A long vorticity strip is formed when the piston shrinks to the limit position. Then the second pulse begins, fluid in the boundary layer is pushed pass the exit and generate a vortex ring (red in the Figure), while the vorticity strip is pushed out at the same time. During the propagation, the vortex strip is tightly attached to the vortex ring. Because of the difference of rotation direction, interaction consumes the energy of vortex ring, which contributes to volume reduction and speed reduction. Consequently, the reverse vorticity strip is exhausted, and the vortex ring becomes an isolated small vortex ring. Because the speed of the second vortex ring is very slow, it will be overtaken by the third vortex ring surrounded with vorticity strip at time instant (i), the vorticity strip is consumed by both the third vortex ring and the second vortex ring, and these two vortex rings are synthesized as one vortex ring as (k) shows. Every two pulses after will repeat the previous cycle (d-k).

It has been proposed previously that vortex ring can improve the efficiency of propulsion by the entrained fluid [3] [4]. In the present work, it is also noted that the reverse vorticity in cyclic pulse condition that can reduce the energy of vortex ring as mentioned above, which results in reduction of fluid entrainment.

References

[1] MORTEZA GHARIB, EDMOND RAMBOD, KARIM SHARIFF. A universal time scale for vortex ring formation[J]. Journal of Fluid Mechanics. 1998, 360: 121-140.

[2] MOSHE ROSENFELD, EDMOND RAMBOD, MORTEZA GHARIB. Circulation and formation number of laminar vortex rings[J]. Journal of Fluid Mechanics. 1998, 376: 297-318.

[3] PAUL S. KRUEGER. The significance of vortex ring formation and nozzle exit over-pressure to pulsatile jet propulsion[D]. California Institute of Technology Pasadena, California, 2001.

[4] PAUL S. KRUEGER, M. GHARIB. The significance of vortex ring formation to the impulse and thrust of a starting jet[J]. Physics of Fluids. 2003, 15(5): 1271-1281.

[5] PAUL S. KRUEGER, JOHN O. DABIRI, M. GHARIB. Vortex ring pinch-off in the presence of simultaneously initiated uniform background co-flow[J]. Physics of Fluids. 2003, 15: L49-L52.

[6] HOU SHOU JIANG, MARK A. GROSENBAUGH. Numerical simulation of vortex ring formation in the presence of background flow with implications for squid propulsion. Theoretical and Computational Fluid Dynamics. 2006, 20(2): 103-123.

EFFECTS OF WATER DEPTH ON STOPPING MANEUVER USING CFD NUMERICAL SIMULATION

CHENGUANG SUN[1], JIANHUA WANG[2], DECHENG WAN*

State Key Laboratory of Ocean Engineering, School of Naval Architecture, Ocean and Civil Engineering, Shanghai Jiao Tong University, Collaborative Innovation Center for Advanced Ship and Deep-Sea Exploration, Shanghai 200240
Corresponding Author: dcwan@sjtu.edu.cn

Keywords: Stopping maneuver; Shallow water; naoe-FOAM-SJTU solver; Overset grid method

As the increasingly-crowded ports and waterways, stopping ability is critical to the safety of ship maneuvering. When a ship travels in shallow water, maritime disasters such as collision and grounding occur more easily than in open waters. Therefore, it is necessary to study the behaviour of large marine vehicles in shallow water. In this paper, naoe-FOAM-SJTU solver with a hierarchy of bodies like hull, propeller and rudder using overset grid technology based on open source CFD platform OpenFOAM developed by Wan Decheng's research team in Shanghai Jiao Tong University is used to numerically investigate complex ship motion problem in stopping manuever. The simulation starts from the steady state of self-propulsion. Then the propeller is controlled to a reverse speed to carry on the stopping manuever, both in shallow and deep water. Detail information such as longitudinal and lateral distance, ship velocity and other relative parameters during stopping manuever are presented. Shallow water effects on stopping manuever is analysed through comparison of trajectory, forces, pressure distribution and flow field situation. In conclusion, several suggestions are provided to the choice of safe stopping methods in shallow water.

Introduction

In recent years, ships tend to become larger for reducing the cost of shipping and improving the transport efficiency. Since the large size worsens the manoeuvrability, accidents can easily occur in shallow water area such as crowded ports and channels. Therefore, it is significant to study the stopping ability of large ships in shallow water to prevent the ship from collision and grounding and to ensure the safety of the ship sailing near the port.

Generally, reversing the propeller is still the most common operation when a large ship needs to brake. In the procedure of the stopping manuever, the bow will turn left or right by the side forces at the aft caused by reversing propeller. The existence of the transversal force caused by reversing propeller is determined by SmittL[1] through a ship model test. Good stopping ability means minimum stopping distance, horizontal distance and yaw motion.

Among several approaches to predict ship maneuverability, direct numerical simulation is the most accurate way to reappear the real flow field during ship maneuvering motion. Using overset grid technique to solve the problem of large amplitude motion of the ship is currently the mainstream methods. Sakamoto[2] simulated the static and dynamic PMM test and gave the corresponding verification work by ship hydrodynamics software CFDShip-Iwoa Ver. 4. By solving the unsteady RANS equation, Carrica[3] carried out the numerical simulation of Z type control test of the DTMB5512 ship model. Professor Wan Decheng's research team in Shanghai Jiao Tong University developed naoe-FOAM-SJTU solver[4] based on open source CFD software OpenFOAM, which achieved great results in simulating the motion of ships and floating structures. By using the solver, Wang[5] realized the numerical simulation of the self-propulsion of ONRT in the wave.

In this paper, the author uses naoe-FOAM-SJTU solver based on overset grid technique to simulate the stopping maneuver both in shallow and deep water, predicting the vertical distance, the horizontal distance, and other parameters. Detailed analysis and comparison of the pressure distribution and the flow field around the ship are presented. The prediction can provide reference when designing a ship or choosing a stopping method.

Mathematical and numerical modelling

The computations are performed with CFD solver naoe-FOAM-SJTU. The fluid control equation is presented as an unsteady two phase incompressible RANS equation, which is as follows:

$$\nabla \cdot U = 0 \tag{1}$$

$$\frac{\partial \rho U}{\partial t} + \nabla \cdot [\rho(U - U_g)U] = -\nabla p_d - g \cdot x\nabla\rho + \nabla \cdot (\mu_{eff}\nabla U) + (\nabla U) \cdot \nabla\mu_{eff} + f_\sigma \tag{2}$$

where U is the fluid velocity field; U_g is the grid velocity; p_d is the dynamic pressure; ρ is the mixture density of the two-phase fluid; g is the gravitation acceleration; μ_{eff} is the effective dynamic viscosity; f_σ is the surface tension term.

In this paper, the SST K-W turbulence model is used to solve the RANS equation, in which k is the turbulent kinetic energy of the fluid particle and w is the characteristic dissipation rate. Turbulence model like this will not be affected by the free surface, but will also ensure the accuracy and reliability of the solution near the wall. A VOF approach with the bounded compression technique is used to capture free surface [6]. The transport equation is defined as:

$$\frac{\partial \alpha}{\partial t} + \nabla \cdot [\rho(U - U_g)\alpha] + \nabla \cdot [U_r(1 - \alpha)\alpha] = 0 \tag{3}$$

where U_r is the velocity field for the compression interface and α is the volume fraction, which is defined as:

$$\begin{cases} \alpha = 0 & \text{air} \\ \alpha = 1 & \text{water} \\ 0 < \alpha < 1 & \text{free surface} \end{cases} \tag{4}$$

The finite volume method with unstructured grid is used to transform the equations from the physical space into the computational space. The solution of the governing equations is achieved by using the pressure implicit with splitting of operator (PISO) algorithm[7].

The dynamic overset grid is the key point for direct simulation of the complex motions with a hierarchy of bodies. Generally, an overset grid comprises two or more blocks of overlapping structured or unstructured grids, and the overset grids can move independently without constraints. In the dynamic overset computation process, the grids in the computational domain are first classified into types according to their locations, such as fringe cells, hole cells and donor cells etc. After digging holes, the grid in the non-computational domain will be excluded from computation. The overlapping area can transfer the flow field information by establishing interpolation relation.

The solver naoe-FOAM-SJTU used in this paper is based on the open source CFD software OpenFOAM platform as well as overset grid technology and multistage object motion solving module. When the flow field is soluted, the Suggar++[8] program is used to calculate the domain connectivity information (DCI) between the overset grids.

Geometry and simulation design

The KVLCC2 ship model with a single propeller is used for the numerical calculations since the rudder force during the stopping manoeuver is negligible, and the main geometric characteristics are listed in table 1.

Table 1: Main parameters of the ship model

	Full scale	Model scale
Length of waterline L/m	320.00	2.909
Width of waterline B/m	58.00	0.527
Draft d/m	20.80	0.189
Propeller diameter D/m	9.86	0.080
Propeller pitch ratio P/D	0.721	0.721

The computational domain is divided into three parts: one for the background grid, one for the grid around the ship hull and one for the grid around propeller. The unstructured grids are generated by snappyHexMesh with the background grid generated by blockMesh. The overset grid arrangement and the local mesh distribution is shown in figure.1.
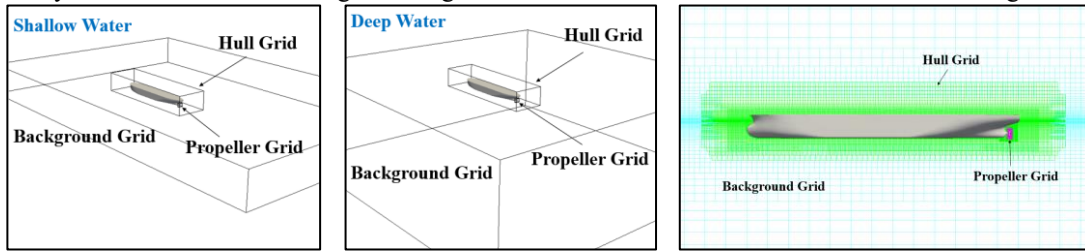
Figure 1 The overset grid arrangement and the local grid distribution

Test conditions

The simulation conditions are following the setup of experiments[9-10] performed at National Maritime Research Institute (NMRI). The simulation starts from the steady state of self-propulsion, with the speed of 0.4905 m/s in the case of model scale. Then the propeller is controlled to a reverse speed of -10.36r/s to carry on the stopping maneuver.

Numerical results and analysis

Figure 2 shows the trajectory and Figure 3 shows the speed during the simulation time.
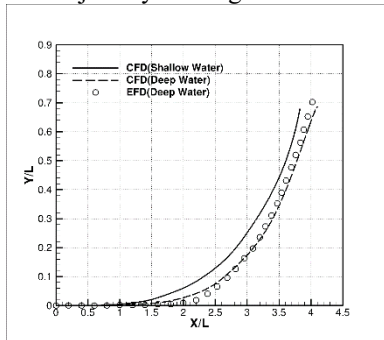
Figure 2 The ship trajectory   **Figure 3 The ship speed**
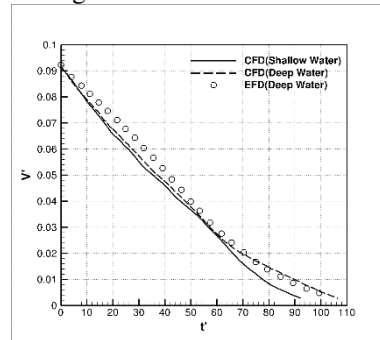
Here the dimensionless length, velocity and time are used, which is defined as: $t' = t/\sqrt{L/g}$, $V' = V/\sqrt{gL}$, where L is the length of the ship and g is the acceleration of gravity.

The figure shows that the vertical distance and the horizontal distance of ship in deep water agree well with the experimental data. The vertical distance is 0.75% more than the experimental data, which is tend to be safe. While the horizontal distance is 4.29% smaller than the experimental data, which should be paid more attention in practical application. Meanwhile, the stopping time also agrees well with the experimental data. Therefore, the numerical calculation method used in this paper can accurately forecast the parameters of stopping maneuver.

The ship in shallow water has a shorter vertical distance and a shorter stopping time in comparison with those in deep water, while the horizontal distance is almost the same.

Figure 4 shows the total longitudinal force that act on the ship. And the total longitudinal force is decomposed to the hull resistance and the propeller force, as shown in Figure 5 and Figure 6 respectively.
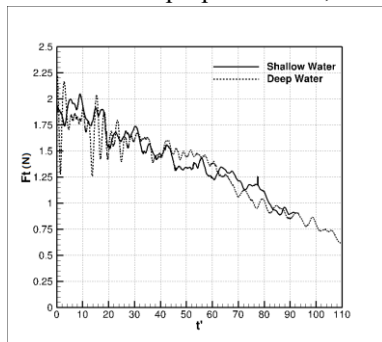
Figure 4 The total longitudinal force   **Figure 5 The hull resistance**   **Figure 6 The propeller force**
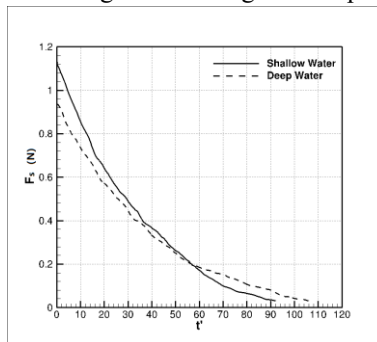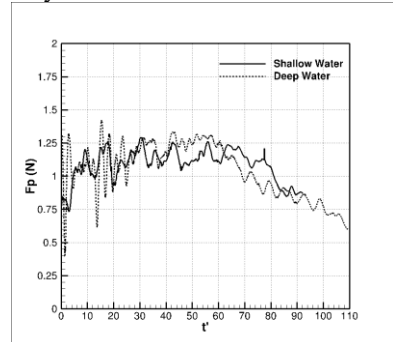
Due to the continuous rotation of the propeller, the longitudinal force curve is fluctuating. It can be seen from the figure that the total longitudinal force gradually decreases as the ship speed decreases in accordance with the anticipation.

Figure 5 indicates that hull resistance Fs decreases when the speed decreases. When the speed is higher, the resistance of the hull in shallow water is greater than that in the deep water. From Figure 6, we can see that the propeller forces in different water depth are close to each other.

Figure 7 shows the pressure distribution on the side and the bottom of the ship. While figure 8 shows the distribution of flow velocity around the ship.
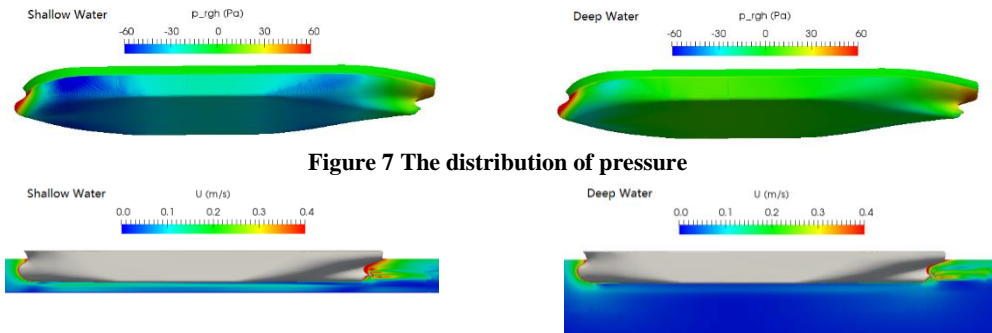
Figure 7 The distribution of pressure

Figure 8 The distribution of flow velocity

The figures indicate that when the ship is sailing in shallow water, the pressure on its side and bottom is smaller than that in deep water. Worse more, the pressure reduce will lead to the sinking of the ship, which increases the area of wetted surface, further increasing the friction resistance. Because the depth of freedom of the hull is fixed in this work, the shallow water effects is not so serious compared with the actual situation.

Figure 9 shows the time travel of bow angle, while Figure 10 shows the turning moment.
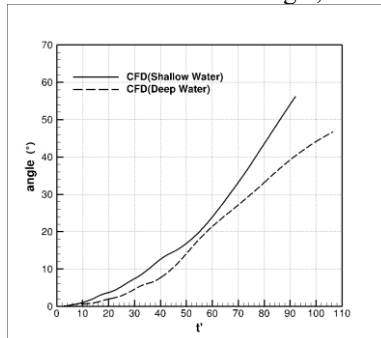
Figure 9 The bow angle   **Figure 10 The turning moment**
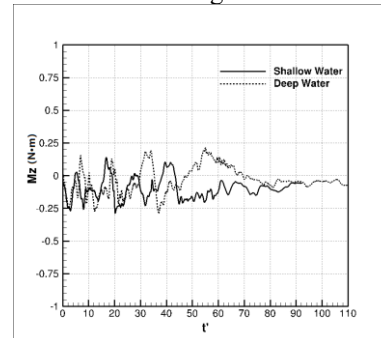
Figure 9 shows that the yaw angle in shallow water is larger through the whole process. When the ship is completely stopped, the deflection angle is 56.2 degrees. While the ship in deep water ends with the 46.3 degrees deflection angle. In shallow water, the ship model reaches a greater deflection angle with less time.

From Figure 10, it is found that the value of moment fluctuates greatly because of the dynamic working state of the propeller. The average value of moment after the propeller began to reverse in shallow water is 0.121 N·m, when it was 0.068 N·M in deep water. With the same reverse speed of propeller, the turning moment in shallow water is slightly larger, leading to greater yaw motion.

Figure 11 and Figure 12 show the distribution of pressure on the stern and velocity on horizontal section around the propeller both in shallow and deep water when the ship speed decreased to 50% initial value.

Figure 11 The distribution of pressure
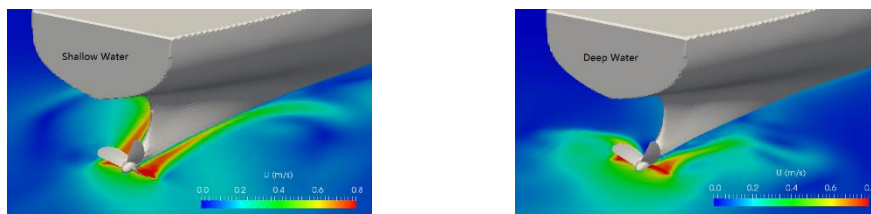
Figure 12 The distribution of flow velocity

It can be seen from Figure 11 that a high pressure area presents on the right aft of the ship because of the reversing propeller. The pressure pushes the ship tail to the left, which makes the ship turn right. In shallow water, the high pressure is more prominent, thus increasing the turning moment.

Figure 12 shows how reversing propeller works during the stopping maneuver. The water is propelled to the front, and the reaction force help the ship to decelerate. In shallow water, more liquid is propelled forward because the space below is restricted. More water pushes the hull, leading to larger lateral force and turning moment.

Although the effect of shallow water can provide some benefit to stopping maneuver as reducing the longitudinal distance, it is still very limiting. In addition, more attention is supposed to be paid to the increases of horizontal distance and yaw angle.

Acknowledgements

References

[1] CHISLETT M S, SMITT L W. A brief description of the hya large amplitude pmm system[J]. ARCHIVE Journal of Mechanical Engineering Science 1959-1982 (vols 1-23), 1972, 14(7):80-84.

[2] SAKAMOTO N, CARRICA P M, STERN F. URANS simulations of static and dynamic maneuvering for surface combatant: Part 2. Analysis and validation for local flow characteristics[J]. Journal of Marine Science and Technology, 2012, 17(4): 446-468.

[3] CARRICA P M, STERN F. DES simulations of KVLCC1 in turn and zigzag maneuvers with moving propeller and rudder[C]. Proceedings of the SIMMAN 2008 Workshop on Verification and Validation of Ship Manoeuvering Simulation Methods. Lyngby, Denmark, 2008.

[4] SHEN Z R, WAN D C. Manual of CFD solver for ship and ocean engineering flows: naoe-FOAM-SJTU. Technical Report for Solver Manual, Shanghai Jiao Tong University, 2014.

[5] WANG J H, WAN D C. Investigations of Self-Propulsion in Waves of FullyAppended ONR Tumblehome Model[J]. Applied Mathematics and Mechanics, 2016, 27(12):619-623.

[6] RUSCHE H. Computational Fluid Dynamics of Dispersed Two-Phase Flows at High Phase Fractions[D]. Imperial College London (University of London), 2003.

[7] CAO H, WAN D C. Benchmark computations of wave run-up on single cylinder and four cylinders by naoe-FOAM-SJTU solver[J]. Applied Ocean Research, 2017, 65: 327-337.

[8] NOACK R W, BOGER D A, KUNZ R F, CARRICA P M. Suggar++: An improved general overset grid assembly capability[C], Proceedings of the 47th AIAA Aerospace Science and Exhibit, San Antonio TX, 2009, 22-25.

[9] TSUKADA Y, UENO M, TANIZAWA K. Development of an Auxiliary Thruster for Free-running Model Ship Tests[J]. Journal of the Society of Naval Architects of Japan, 2014, 20:59-67.

[10] UENO M, SUZUKI R, TSUKADA Y. Estimation of stopping ability of full-scale ship using free-running model[J]. Ocean Engineering, 2017, 130:260-273.

AERODYNAMIC AND HYDRODYNAMIC OF A NEW SPAR FLOATING WIND TURBINE WITH HEAVE PLATES

YINBO SUN PEILIN DOU

Yinbo sun Jiangsu university of science and technology,imsyb@foxmail.com

Peilin Dou Jiangsu university of science and technology

Keywords: *Truss spar wind turbine; dynamic response; floating wind turbine*

This paper has described a new design of Truss spar wind turbine with heave plates. The design based on NREL 5-MW baseline wind turbine. This paper provides a description of wind turbine's properties and investigate effects of aerodynamic and hydrodynamic coupling motion response. Based on three-dimension potential flow theory, coupling dynamic response is calculated in the regular wave and wind loads. The new design RAO value is emphatically studied and compared with OC3-hywind spar turbine, and structure form is put forward for the study for offshore spar wind turbine.

Here is the structure model diagram. It has two heave plates to improve it properties.
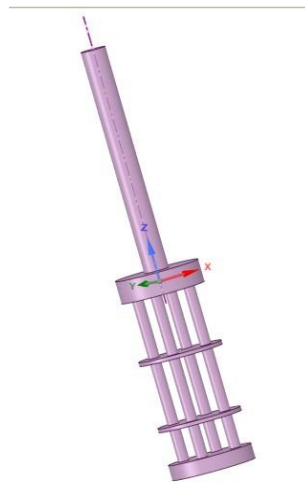
We analysis the response of structure. There are some data graphs what we found. One is the F-K force in -180 degree. Another is the free floating RAOS when frequency changed.
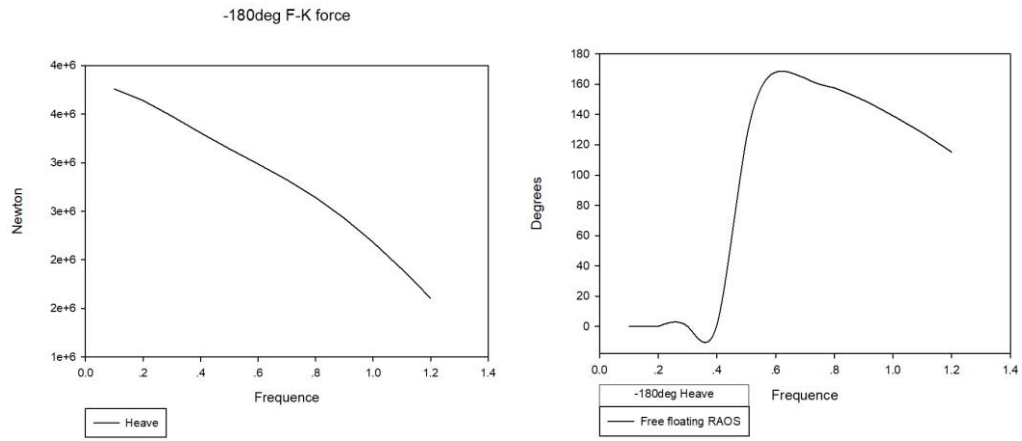
We can find that when the frequency between six and eight, the structure under F-K force, it has a max response amplitudes.

COMPARISON OF WAVE GENERATION METHODS FOR TWO-PHASE VOF SOLVERS

Zhaobin LI, Ganbo DENG*, Patrick QUEUTEY, Benjamin BOUSCASSE*
Guillaume DUCROZET, Lionel GENTAZ, David LE TOUZÉ, Pierre FERRANT
LHEEA Lab, Ecole Centrale de Nantes, France, CNRS UMR 6598
{*ganbo.deng,benjamin.bouscasse*}*@ec-nantes.fr*

Introduction

CFD solvers rely on specific methods to generate waves for realistic marine and offshore applications. In this paper, three wave generation methods for two-phase VOF solvers are presented and compared, including the relaxation zone method, the internal wave generation method and the Spectral Wave Explicit Navier Stokes Equations (SWENSE) method. The methods, implemented either in *OpenFOAM* or in *ISIS-CFD* are tested by simulating a Catenary Anchor Leg Mooring (CALM) buoy in regular waves on a series of mesh with different spatial discretizations. The experimental data obtained by our laboratory is used to validate the results. The mesh requirements of the three methods are discussed in the end.

Wave Generation Methods

The target incident waves used by CFD are often defined in prior and introduced into the computational domain with wave generation methods. The simplest wave generation method is to impose wave velocity and free-surface elevation at the wave generation boundary. Such approach suffers from wave reflection problems and is unsuitable for wave diffraction simulation as the case investigated in this paper. Two common alternatives to overcome this difficulty are the relaxation zone approach[1] and internal wave generation approach[2]. They generate target incident waves in a upstream zone to the area of interest and let the waves propagate freely in the computational domain. On the contrary, the SWENSE method[3, 4] does not define specific zones for wave generating. It imposes explicitly the incident wave solution in the entire computational domain, and solves the disturbance of the incident waves as a complementary correction. The principles of the three methods are briefly explained as follows.

Relaxation Zone

The relaxation zone technique defines regions at the boundaries of the computational domain, where the computed value is gradually blended to the target value using a space-dependent weight function ω as shown in Figure 1(a). The value in these regions is relaxed as the linear combination of the CFD solution and the target value, as follows:

$$\chi = \omega\chi_{target} + (1 - \omega)\chi_{CFD}$$

This technique is able to generate incident waves at the inlet of the CFD domain, and can also be used to prevent wave reflections at the outlet if the target value is set accordingly[5]. A fine mesh is needed from the inlet boundary to the area of interest to ensure the accuracy of the incident waves.

Internal Wave Generator

The internal wave generation method defines either mass or momentum source function in a specific region inside the computational domain, where the wave is generated according to the target value. This method is always used together with damping zones on the boundaries to prevent wave reflections. An illustration of this technique can be found in Figure 1(b). Coarse meshes can be used in the damping zone with little influence on the incident wave accuracy since the wave generation zone locates inside the pure CFD domain. However, a fine mesh is needed in the rest of the computational domain for an accurate description of the wave field.

SWENSE

Spectral Wave Explicit Navier-Stokes Equations(SWENSE) method treats the wave-structure interaction problem by decomposing the total fields into the incident waves and a complementary correction, as illustrated in Figure 2. A primitive variable χ(velocity, pressure, or free surface elevation) in the Navier-Stokes equations is considered as the sum of an incident variable χ_I and a complementary variable χ_C. The governing equations of χ_C are mathematically derived by subtracting the Navier-Stokes equations by Euler equations as follows.

$$\nabla.\mathbf{u}_C = 0 \quad ; \quad \frac{\partial\mathbf{u}_C}{\partial t} + \mathbf{u}_C.\nabla\mathbf{u}_C + \mathbf{u}_C.\nabla\mathbf{u}_I + \mathbf{u}_I.\nabla\mathbf{u}_C = -\frac{\nabla p_C}{\rho} + \nu\nabla^2\mathbf{u}_C$$

(a) Relaxation Zone (b) Internal Wave Generator
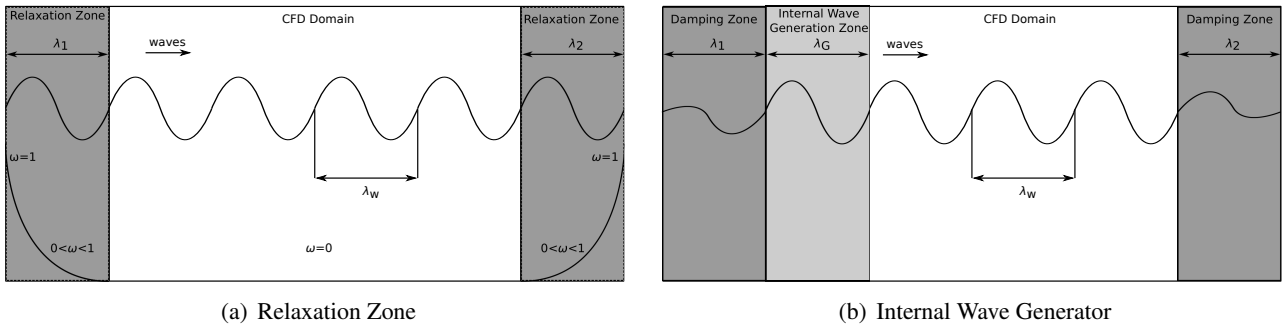
Figure 1: Wave Generation Techniques
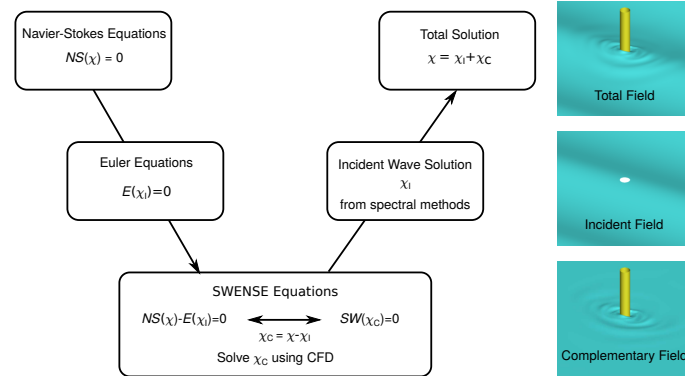
Figure 2: The SWENSE method decomposes the total field into an incident and a complementary field

With such decomposition, the mesh requirement regarding the incident wave propagation can be loosened since the incident wave information is explicitly known in the entire computational domain. A good mesh quality is only necessary near the structure to solve the wave-structure interaction with a high level of accuracy.

Test Case: CALM Buoy in regular waves

The test case reproduces an experiment carried out in the ocean wave basin of Ecole Centrale de Nantes (50m long, 30m wide and 5m deep). It deals with the interaction between regular waves and a fixed CALM buoy[6]. The buoy has a truncated cylinder form with a thin skirt near the bottom to provide additional damping forces through vortex shedding, as shown in Figure 3(a). Measurement data for the horizontal and vertical forces on the buoy and the free surface elevation at three points around it are used to validate the CFD simulation. (See Figure 3(b).)

(a) CALM Buoy Model (b) Wave Gauge Positions
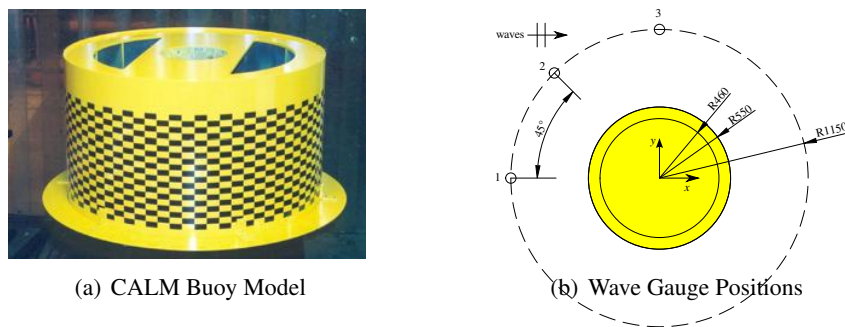
Figure 3: Experiment setup for CALM buoy in waves

Three CFD solvers, *foamStar*, *foamStarSwense* and *ISIS-CFD*, are selected for the comparison. They generate waves with the relaxation zone, the SWENSE method, and the internal wave generator respectively. *FoamStar*[7] and *foamStarSwense*[8] are solvers derived from *interDyMFOAM*, the native *OpenFOAM* solver for incompressible two-phase flow. *ISIS-CFD* is an incompressible two-phase flow solver developed at Ecole Centrale de Nantes and distributed commercially as a part of *Fine^{TM}/Marine* by NUMECA International; it uses the finite-volume method with unstructured mesh and captures the interface with the VOF technique[9].

A rectangular computational domain with a series of spatial discretization is used to test the mesh quality required by different wave generation methods. As Figure 4(a) shows, the background mesh is Cartesian; the mesh is locally refined and fitted to the body. Three configurations: 20L, 40L, and 80L are used with 20, 40, and 80 cells per wave length in the x direction. The differences between

the configurations are only in the far-field. The mesh density near the buoy is kept invariant. A cylindrical configuration, which is typically used by the SWENSE method, is added only to test *foamStarSwense* (see Figure 4(b)). The details of the different meshes are summarized in Table 1.

(a) Rectangular Computational Domain (b) Cylindric Computational Domain
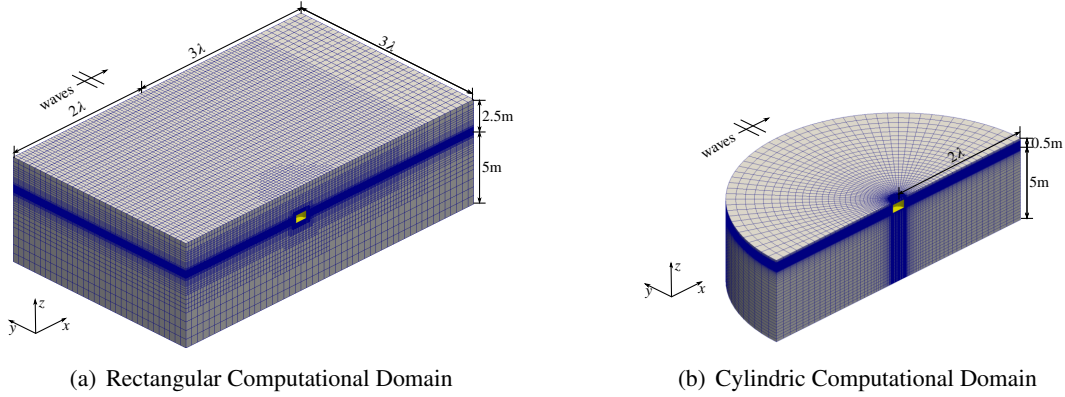
Figure 4: Mesh configuration for the test case

Table 1: Mesh configurations for CALM buoy in regular waves

Mesh	$\lambda/\Delta x$	$\lambda/\Delta y$	$H/\Delta z$	Number of cells
20L	20	10	16	1.3 M
40L	40	10	16	1.5 M
80L	80	20	16	2.5 M
Cylindrical	-	-	16	0.7 M

The CFD results and the experiment data are shown in Table 2 and summarized as follows.

- 80L: The results of the three CFD solvers are in good agreement. The difference between *foamStarSwense* and *ISIS-CFD* are inferior to 1% for the first harmonic amplitudes. *foamStar* gives slightly smaller predictions on the first harmonic amplitudes. The experiment results has a better agreement with the results of *foamStarSwense* and *ISIS-CFD*.

- 40L: According to ITTC's recommendation, 40 cells per wave length is the minimum requirement for wave simulations by CFD[10]. With this discretization, *foamStarSwense* and *ISIS-CFD* are able to predict correctly the wave force and elevation with an accuracy of 1% compared with the 80L configuration. This difference is about 3% for *foamStar* with the relaxation zone technique.

- 20L: This discretization is known to be too coarse to simulate waves in CFD. The coarse mesh causes excessive numerical diffusion and damps the incident waves. Both *foamStar* and *ISIS-CFD* give smaller predictions. However, *foamStarSwense*'s results are still within 3% different to the finest resolution.

- Cylindrical: This configuration has large cells in the far-field, and the mesh is gradually refined towards the domain center. The results of *foamStarSwense* compare well with the references, while the number of points is drastically reduced. The corresponding gain in CPU time compared to *foamStar* with the mesh 80L is a factor of 5.53 on the same hardware.

Table 2: Comparison between CFD results and experimental data

		$F_x^{(1)}$	$F_x^{(2)}$	$F_z^{(1)}$	$F_z^{(2)}$	$\eta_1^{(1)}$	$\eta_1^{(2)}$	$\eta_2^{(1)}$	$\eta_2^{(2)}$	$\eta_3^{(1)}$	$\eta_3^{(2)}$
Experiment		1.390	0.170	1.180	0.015	1.220	0.065	1.210	0.040	1.040	0.035
foamStar (Relaxation Zone)	20L	1.202	0.130	1.018	0.017	1.063	0.057	1.057	0.037	0.924	0.039
	40L	1.328	0.165	1.075	0.011	1.172	0.057	1.164	0.035	0.983	0.041
	80L	1.359	0.168	1.098	0.010	1.195	0.060	1.180	0.036	1.002	0.045
foamStarSwense (SWENSE)	20L	1.360	0.183	1.134	0.011	1.199	0.059	1.185	0.039	1.020	0.051
	40L	1.376	0.181	1.144	0.012	1.208	0.060	1.195	0.032	1.028	0.051
	80L	1.387	0.186	1.149	0.012	1.213	0.063	1.197	0.039	1.037	0.040
	Cylindrical	1.369	0.180	1.159	0.019	1.216	0.070	1.199	0.044	1.027	0.056
ISIS-CFD (Internal Wave Generator)	20L	1.314	0.150	1.094	0.014	1.169	0.065	1.155	0.038	0.997	0.042
	40L	1.369	0.171	1.133	0.013	1.216	0.070	1.199	0.043	1.032	0.049
	80L	1.378	0.173	1.141	0.014	1.224	0.064	1.208	0.040	1.041	0.050

To ensure the accuracy of the simulation, especially to validate the result of *foamStarSwense* on the coarse mesh, the flow details of the simulation are compared. Figure 5 plots the Q-criterions and the pressure fields obtained by *foamStar*, *foamStarSwense*, and *ISIS-CFD*, with 80L, 20L, and 80L respectively. The results show a good agreement and are consistent with previous numerical simulations[4].

(a) foamStar 80L	(b) foamStarSwense 20L	(c) ISIS-CFD 80L
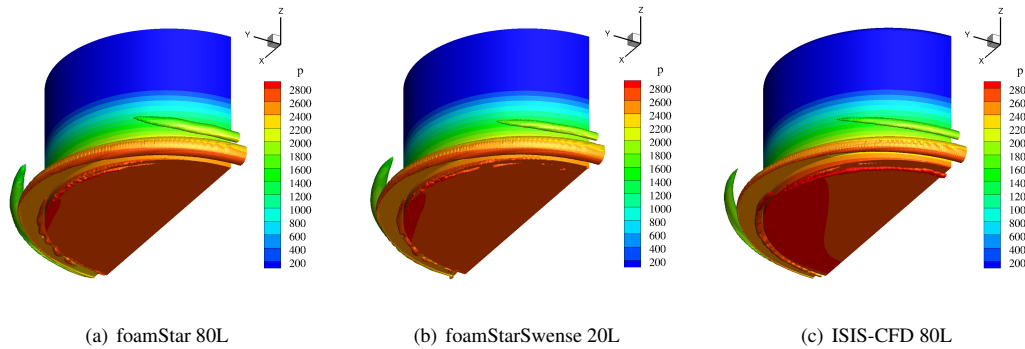
Figure 5: Comparison of the iso-surfaces of Q-criterion = 50 and pressure field when a wave crest passes the buoy

Conclusion

The present work compared three wave generation models for two-phase CFD solvers: the relaxation zone technique, the internal wave generator, and the SWENSE method. The mesh requirement of each method is studied by simulating a CALM buoy in regular waves. Results show that the relaxation zone method requires a mesh quality of at least 80 cells per wave length. The internal wave generator technique need 40 cells per wave length to keep a good accuracy of the incident waves; 80 cells per wave length should be used when a high level of accuracy is required. The SWENSE method gives good predictions even if the far-field mesh is very coarse (20 cells per wave length). The efficiency of the SWENSE method is confirmed, both in terms of mesh and CPU requirements.

Acknowledgments

References

[1] N. G. Jacobsen, D. R. Fuhrman, and J. Fredsøe, "A Wave Generation Toolbox for the Open-Source CFD Library: OpenFoam®," *International Journal for Numerical Methods in Fluids*, vol. 70, no. 9, pp. 1073–1088, 2012.

[2] Z. Hafsia, M. B. Hadj, H. Lamloumi, and K. Maalel, "Internal inlet for wave generation and absorption treatment," *Coastal Engineering*, vol. 56, no. 9, pp. 951–959, 2009.

[3] P. Ferrant, L. Gentaz, B. Alessandrini, and D. Le Touzé, "A potential/RANSE approach for regular water wave diffraction about 2-D structures," *Ship Technology Research*, vol. 50, no. 4, pp. 165–171, 2003.

[4] C. Monroy, G. Ducrozet, F. Bonnefoy, A. Babarit, L. Gentaz, and P. Ferrant, "RANS Simulations of a Calm Buoy in Regular and Irregular Seas using the SWENSE Method," *International Journal of Offshore and Polar Engineering*, vol. 21, no. 4, pp. 264–271, 2011.

[5] Y. Choi, B. Bouscasse, S. Seng, G. Ducrozet, L. Gentaz, and P. Ferrant, "Generation of regular and irregular waves in navier-stokes CFD solvers by matching with nonlinear potential wave solution at the boundary," in *OMAE*, 2018, Accepted.

[6] Rousset, J-M. and Ferrant, P., "Model tests for Principia R&D." Laboratoire de Mécanique des Fluides de l'Ecole Centrale de Nantes (UMR CNRS 6598), Tech. Rep. CTR1 - JIP Calm Buoy 2, 2005.

[7] C. Monroy, S. Seng, and S. Malenica, "Développements et validation de l'outil CFD OpenFOAM pour le calcul de tenue à la mer," in *Proceedings of the 15th Journées de l'Hydrodynamique*, 2016.

[8] Z. Li, B. Bouscasse, G. Ducrozet, L. Gentaz, and P. Ferrant, "Progress in coupling potential wave models and two-phase solvers with the SWENSE methodology," in *OMAE*, 2018, Accepted.

[9] J. Wackers, B. Koren, H. C. Raven, A. Van der Ploeg, A. Starke, G. Deng, P. Queutey, M. Visonneau, T. Hino, and K. Ohashi, "Free-surface viscous flow solution methods for ship hydrodynamics," *Archives of Computational Methods in Engineering*, vol. 18, no. 1, pp. 1–41, 2011.

[10] ITTC, *Practical guidelines for ship CFD applications ITTC Recommended Procedures and Guidelines 7.5-03-02-03*, 2014.

NUMERICAL SIMULATION ON EVOLUTION OF BOW WAVE OF KCS IN MOTION

ZHEN REN, DECHENG WAN

State Key Laboratory of Ocean Engineering, School of Naval Architecture, Ocean and Civil Engineering, Shanghai Jiao Tong University, Collaborative Innovation Centre for Advanced Ship and Deep-Sea Exploration, Shanghai, China

Keywords: Bow wave breaking, KCS, RANS, OpenFoam, surface tension

INTRODUCTION

The phenomena of wave breaking, known as white water, always occurs when ships advances in high speeds. The common issue has attracted many researchers since its complex mechanism and effects on the performance of ship. Since the shortages of towing experiments, such as expensive cost, insufficient information in flow field, et al. Computational fluid dynamics is becoming gradually a popular approach to study the overturning and breaking of ship bow wave. The advantage to provide detailed information in flow field is very helpful to understand better the mechanism of breaking wave.

The CFD solver naoe-FOAM-SJTU, which is developed on the open source software OpenFOAM, is used to investigate the wave breaking phenomena of the bow wave of KRISO Container Ship (KCS) model with sinkage and trim. URANS with high resolution VOF technique is adopted to simulate the bow wave breaking of KCS in different advance speeds, i.e. Fr=0.26, 0.35. The process of overturning and breaking of bow wave are captured clearly. The more detailed flow visualizations, such as wake profiles, vorticity and wave patterns, are presented to illustrate the hydrodynamic performance of high speed surface ship.

NUMERICAL METHOD

In the simulations, the governing equations mainly include the mass conservation equation Eqn (1) and the momentum equation Eqn (2), which can be written as:
The mass conservation equation:

$$\nabla \cdot \mathbf{U} = 0 \tag{1}$$

The moment conservation equation:

$$\frac{\partial \rho \boldsymbol{U}}{\partial t} + \nabla \cdot \left[(\rho \boldsymbol{U} - \boldsymbol{U}_g) \boldsymbol{U} \right] = -\nabla p_d - \boldsymbol{g} \cdot \boldsymbol{x} \nabla \rho + \nabla \cdot (\mu_{eff} \nabla \boldsymbol{U}) + (\nabla \boldsymbol{U}) \cdot \nabla \mu_{eff} + f_\sigma \tag{2}$$

Where $\mathbf{U}$ is fluid velocity field and $\boldsymbol{U_g}$ is the grid velocity; p_d represents the dynamic pressure; ρ is the mixture density; g is the gravity acceleration; μ_{eff} is effective dynamic viscosity, in which ν and ν_t are kinetic and eddy viscosity, respectively, and ν_t is obtained from turbulence model. f_σ is surface tension term that plays an important role in wave breaking simulation. SST k-ω model[1], is selected to solve the Reynolds stress. k denotes turbulence kinetic energy and ω denotes dissipation rate. The turbulence model combines the advantages of the standard k-ε model and k-ω model to make sure that the free surface is not influenced and ensure the accuracy and reliability of the solution at the wall.

Here the Volume of Fluid (VOF) method with artificial compression [2] is used to capture the free surface. According to the literature concerning wave breaking, small scale wave breaking is strongly influenced by surface tension. The role played by the surface tension is quite different for breaking and non-breaking waves since the surface tension pressure jump depends on the magnitude of the radius of curvature of the free surface. In order to reappear the wave patterns of the experiment, the surface tension is taken account in the present simulation and the surface tension term mentioned in Eqn(3). is expressed as:

$$f_\sigma = \sigma \kappa \nabla \alpha \tag{3}$$

Where σ stands for the surface tension, κ is the curvature of free surface and it is defined as:

$$\kappa = -\nabla \cdot \mathbf{n} = -\frac{\sum_f \mathbf{S}_f \cdot \mathbf{n}_f}{V_i} \tag{4}$$

V_i represents the volume of cell i, $\sum_f \mathbf{S}_f$ stands for the sum of value on each face of cell.

The geometry of KCS model (L_{pp}=6.0702m, with rudder) can be obtained in the workshop on CFD in ship hydrodynamics, Tokyo 2015. In the experiments, the model has two degrees of freedoms, sinkage and pitch (positive, trim by stern). In the simulation, both degrees of freedoms are considered.

VALIDATION OF NUMERICAL SCHEME

The focus of the present study is on the resolution of bow wave breaking of KCS at different speeds, i.e. Fr = 0.26, 0.35. The condition at Fr = 0.26 is selected to validate the prediction accuracy of the current numerical scheme. Table 1 shows the comparison of the predicted resistance, sinkage and pitch with the experiment data. The error of resistance, sinkage and pitch are less than 0.6%, 6%, 3%, respectively. Figure 1 shows the wave height of the three profiles (y/L = 0.0741, 0.1509, 0.4224), obtained by experiment and numerical simulations. From the near field to the far field, the calculated free surface is consistent with the experimental measurements. The wave profiles on hull surface achieved by numerical method and experiment data are shown in Figure 2. Except for the deviation of the bow and stern wave, the other results are in good agreement with the experimental measurements. The above results prove that the numerical scheme in the present work is reliable.

Table 1. Comparison of prediction and experimental data

Parameter	EFD	CFD	Error
Resistance(/N)	52.18	51.88	-0.57%
Sinkage(/m)	-0.01259	-0.01191	-5.36%
Pitch(°)	-0.1646	-0.16925	2.82%
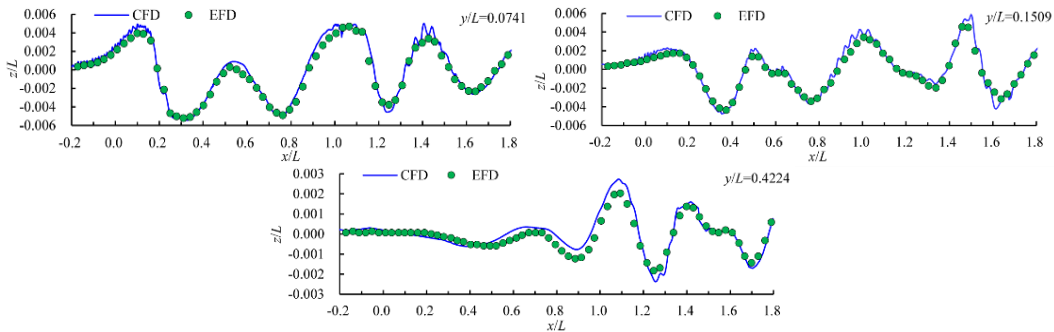
Fig 1. Comparison of Free-surface cuts between experiments (circles) and computational results(line) at different positions.
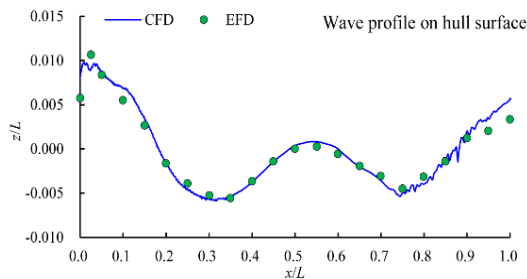
Fig 2. Wave profile on hull surface

RESULTS & ANALYSIS

Although the advance speed of KCS will not reach Fr=0.35 in the actual voyages, the phenomenon of bow wave breaking is only observed at high speeds.

Table 2 presents the prediction of resistance and motion of KCS at Fr=0.35. Compared with the values of KCS at Fr=0.26, the resistance increases rapidly and the sinkage shows the same trend. The pitch at Fr=0.35 is less than that at Fr=0.26, as presents that the trim by bow of KCS is reduced.

The velocity vector at different cutting planes in the evolution of bow wave breaking are presented in Fig.3. At x/L=0.06, the initial plunger is generated since the interaction between gravity and inertial forces. The higher velocity is concentrated at the tip of initial plunger which move downward. The initial plunger has reconnected with the below surface at x/L=0.07. At x/L=0.095, the second plunger is going to be formed. The higher velocity is concentrated near upper edges of the reconnection region.

Table 2. Prediction at Fr=0.35

Parameter	Resistance(/N)	Sinkage(/m)	Pitch(°)
Value	70.20	-0.01894	-0.07704

| x/L=0.06 | x/L=0.07 | x/L=0.095 |
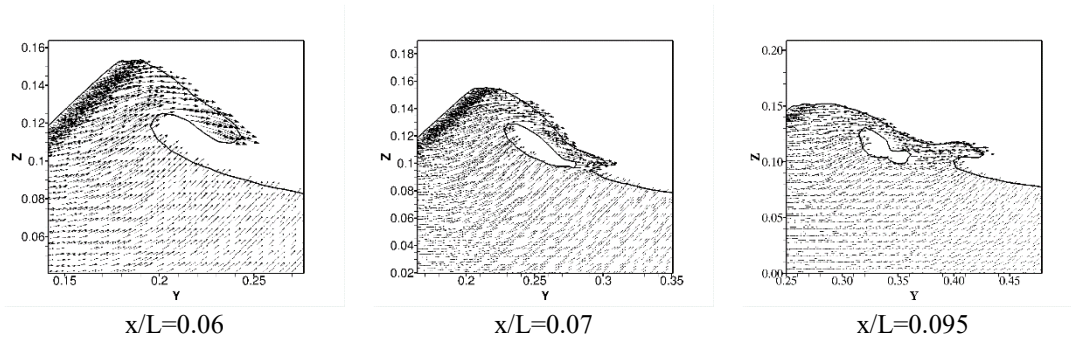
Fig.3 Velocity vector at different cutting plane

| x/L=0.06 | x/L=0.07 | x/L=0.095 |
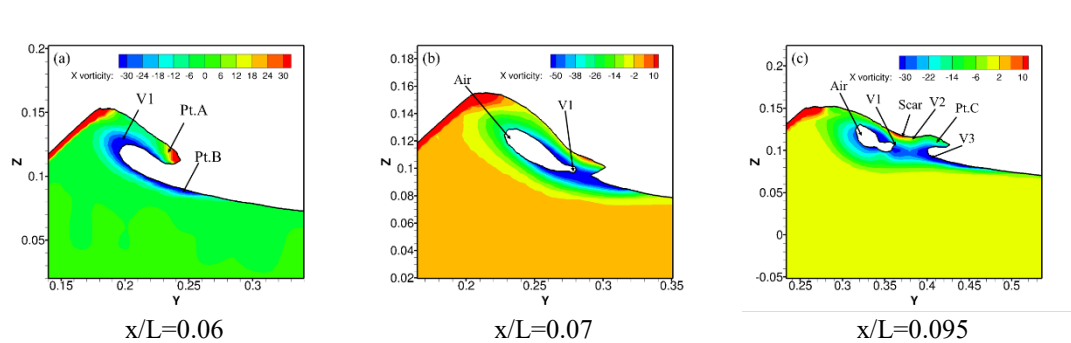
Fig.4 Axial vorticity distribution

Fig.4 presents the axial vorticity at x/L=0.06, 0.07 and 0.095, respectively. As shown in Fig.4 (a), the Pt.A represents the initial plunger that is generated due to the interaction between gravity and inertial forces. The reconnection between the initial plunger and the free surface below (represented by Pt.B) will happen along with the development of initial plunger outboard. In the high curvature region of the overturning wave, the negative axial vorticity (labeled as vortex V1) is generated in the process that the initial plunger is falling. When the tip of initial plunger reconnects with the free surface below, air will be entrained, as shown in Fig.4 (b), resulting in more complex phenomena.

The generation of the counter-rotating vortex pair (V2 and V3) at x/L=0.095 is responsible for the scar where the positive vorticity (V2) is generated and the second plunger visible at x/L=0.095. When the tip of the initial plunger reconnects with the free surface below, the interaction between the two parts causes the upward motion of fluid resulting in the positive vorticity and scar (V2, Scar in Fig4(c)) and the negative vorticity (V3) is generated at the toe. The vortex pair that has a rotating orientation pumps fluid outboard resulting in the second plunger. The air entrainment is observed at x/L=0.07, 0.095 in the process of the overturning of the initial plunger.

CONCLUSION

In the present work, an exploratory study on the wave breaking of KCS under high speed is performed. The overturning and breaking of bow wave is observed clearly and also the air entrainment and scar are noticeable. In the process of the overturning of bow wave, the variation of vorticity is concentrated near the free surface. The counter-rotating vortex generated by the reconnection of the initial plunger with the

free surface below is responsible for the second plunger and scar. In the present study, the reference of grid scale to simulate the wave breaking is provided. But the use of the present scheme does not allow for a very elaborate simulation of bow wave breaking. So, in the future work, smaller grid size may be adopted. In addition, the phenomenon of air entrainment that is captured roughly in the present study should be paid more attention, such as, the evolution downstream and outboard.

ACKNOWLEDGMENTS

REFERENCES

[1] Menter, FR, Kuntz, M, Langtry, R (2003). "Ten years of industrial experience with the SST turbulence model, Turbulence," *Turbul Heat Mass Transf*, 4(1), 625-632.

[2] Weller, H and Weller, H (2008). "A high-order arbitrarily unstructured finite-volume model of the global atmosphere: Tests solving the shallow-water equations," Int J Numer Methods Fluids, 56(8), 1589-1596.

PRELIMINARY COMPARISON BETWEEN OPENFOAM AND NON-HYDROSTATIC MODEL FOR WAVE-STRUCTURE INTERACTION

YUXIANG MA[1], CONGFANG AI[1], GUOHAI DONG[1]

[1]*State Key Laboratory of Coastal and Offshore Engineering, Dalian University of Technology,*
yuxma@126.com
aicongfang@dlue.edu.cn
ghdong_dut@yeah.net

Abstract

This study conducts comparison between the OpenFOAM and a non-hydrostatic free surface model for predicting wave-structure interactions. The non-hydrostatic model solves the incompressible Navier-Stokes equations based on a grid system, which is built from a horizontal rectangular grid by adding dozens of horizontal layers. The immersed boundary method is incorporated in the model to deal with structures. The results from the comparisons are provided for solitary wave interacting with a floating rectangular obstacle.

Keywords: Wave-structure interaction; Immersed boundary method; OpenFOAM; Non-hydrostatic model

Introduction

Wave-structure interaction has been an important issue for a very long time. For structural design and safety assessment, it is of considerable interest for researchers to present accurate predictions of wave transmission and reflection induced by structure or wave forces exerted on the structure. Offshore structures exposed to open water in coastal areas may be various types including floating, suspended and bottom-mounted structures. It would be best to develop numerical models that are capable of predicting interaction between wave and any type of structure.

The so-called non-hydrostatic models are based on Navier-Stokes equations (NSE), but they treat the free surface elevation as a single-valued function of horizontal position. With the use of a free-surface equation to track the moving water surface, non-hydrostatic models are relatively computationally efficient. They have been widely used in the predictions of short surface waves (Ai, et al., 2014; Ai and Jin, 2012; Ai, et al., 2011; Ma et al., 2012; Zijlema et al., 2011), internal waves (Ai and Ding, 2016; Lai et al., 2010; Matsumura and Hasumi, 2008; Vitousek and Fringer, 2014) and even wave-structure interactions (Ai and Jin, 2010; Ai, et al., 2016; Lin, 2006; Ma et al. 2016).

In contrast to the OpenFOAM, non-hydrostatic model is computationally efficient because it does not need to capture the moving free surface with a large number of vertical grids. However, non-hydrostatic model cannot deal with overturning flow.

Numerical models

InterFoam solver in OpenFOAM solving the NSE equations for both of the phases, water and air was used here. Details about the InterFoam solver can be referred to relating references and were not provided for brevity.

The 3D non-hydrostatic free surface flow is governed by the incompressible NSE, which can be written in the following form, by splitting the pressure into hydrostatic and non-hydrostatic ones, $p = \rho g(\eta - z) + \rho q$

$$\frac{\partial u}{\partial x} + \frac{\partial v}{\partial y} + \frac{\partial w}{\partial z} = 0 \tag{1}$$

$$\frac{\partial u}{\partial t} + \frac{\partial u^2}{\partial x} + \frac{\partial uv}{\partial y} + \frac{\partial uw}{\partial z} = -g\frac{\partial \eta}{\partial x} - \frac{1}{\rho}\frac{\partial q}{\partial x} + \frac{\partial}{\partial x}\left(\nu_t \frac{\partial u}{\partial x}\right) + \frac{\partial}{\partial y}\left(\nu_t \frac{\partial u}{\partial y}\right) + \frac{\partial}{\partial z}\left(\nu_t \frac{\partial u}{\partial z}\right) \tag{2}$$

$$\frac{\partial v}{\partial t} + \frac{\partial uv}{\partial x} + \frac{\partial v^2}{\partial y} + \frac{\partial vw}{\partial z} = -g\frac{\partial \eta}{\partial y} - \frac{1}{\rho}\frac{\partial q}{\partial y} + \frac{\partial}{\partial x}\left(\nu_t \frac{\partial v}{\partial x}\right) + \frac{\partial}{\partial y}\left(\nu_t \frac{\partial v}{\partial y}\right) + \frac{\partial}{\partial z}\left(\nu_t \frac{\partial v}{\partial z}\right) \tag{3}$$

$$\frac{\partial w}{\partial t} + \frac{\partial uw}{\partial x} + \frac{\partial vw}{\partial y} + \frac{\partial w^2}{\partial z} = -\frac{1}{\rho}\frac{\partial q}{\partial z} + \frac{\partial}{\partial x}\left(\nu_t \frac{\partial w}{\partial x}\right) + \frac{\partial}{\partial y}\left(\nu_t \frac{\partial w}{\partial y}\right) + \frac{\partial}{\partial z}\left(\nu_t \frac{\partial w}{\partial z}\right) \tag{4}$$

where t is the time; u, v and w are the velocities in the x, y, and z direction, respectively; p is the pressure; η is the free surface elevation; q is the non-hydrostatic pressure component; g is the gravitational acceleration; and ν_t is the eddy kinematic viscosity.

Here, the turbulent eddy viscosity ν_t is evaluated by using the Smagorinsky's subgrid scale model (Smagorinsky, 1963). To calculate the moving free surface, the following free surface equation is employed.

$$\frac{\partial \eta}{\partial t} + \frac{\partial}{\partial x}\int_{z=-h(x,y)}^{z=\eta(x,y,t)} u \, dz + \frac{\partial}{\partial y}\int_{z=-h(x,y)}^{z=\eta(x,y,t)} v \, dz = 0 \tag{5}$$

where $z = -h(x, y)$ is the bottom surface and $z = -\eta(x, y, t)$ is the free surface.

For the non-hydrostatic model, the overall numerical algorithm consists of the following two steps.

The first step is to solve the NSE by using an explicit projection method, which is subdivided into two stages (Ai, Jin and Lv, 2011). The first stage is to project intermediate velocities by means of solving the momentum equations that contain the non-hydrostatic pressure at the previous time level. In this stage, to get a momentum conservative scheme in the discretization of the advection terms, the Eqs. 1~4 are firstly integrated over a vertical layer. Then, the resulting

momentum equations in question are obtained by subtracting the integrated continuity equation from the integrated momentum equations. Finally, a finite volume method with a combination of first-order upwind scheme and second-order central differencing scheme is used to discretize the advection terms of the momentum equations. In the second stage, the new velocities are computed by correcting the projected values after including the non-hydrostatic pressure terms, which are obtained by solving the discretized Poisson equation. The Poisson equation is symmetric and positive definite and can be solved efficiently using the preconditioned conjugate gradient method.

In the second step, by substituting the resulting velocities into a discretized form of the free surface equation (5), we can obtain the new free surface elevation.

In the non-hydrostatic model, the immersed boundary method is used to deal with submerged structure. In this method, the structure is treated as virtual body and replaced by immersed boundary forces imposed on its boundary. Details about the immersed boundary method can be referred to Fadlun et al. (2000).

Numerical reslts: Solitary wave interacting with a floating rectangular obstacle

The first test designed by Lin (2006) concerns interactions between solitary wave and a floating structure. In the test, the still water depth is $h = 1.0$ m and the incoming solitary wave has a wave height $H_0 = 0.1$ m. The computational domain in the x direction ranges from 0 m to 100 m. A rectangular obstacle with dimensions of 5.0 m×0.6 m floats on the top of the water. The center of the obstacle is located at (32.5 m, 0.9 m). A schematic diagram showing solitary wave past a floating rectangular obstacle is depicted in Fig. 1.

In the computation, the computational domain is discretized by 1000 horizontal grids and 40 layers in the vertical direction. The time step is set to $\Delta t = 0.005$. Comparisons of time histories of the free surface elevation at $x = 1$ m and 59 m among present results and other model results are plotted in Fig. 2. In the simulations, all of the models ignored viscous effect. At the first gauging point ($x = 1$ m), the incident solitary wave and reflected waves are recorded. At the other gauging point ($x = 59$ m), the transmitted wave with reduced height is observed. The non-hydrostatic model results are in good agreement with both other model results. Fig. 3 shows comparisons of time histories of the horizontal and vertical forces exerted on the obstacle between present model results and OpenFOAM results. Good agreements can be observed for both the horizontal and vertical forces, although the present model slightly overpredicts the horizontal maximum positive and maximum negative forces. Fig. 4 shows non-hydrostatic model results of the vortex development during the process of solitary wave past the obstacle. It can be seen that a small vortex first forms near the bottom left of the obstacle, and then the other vortex is generated behind it. Both vortices persist for a very long time.
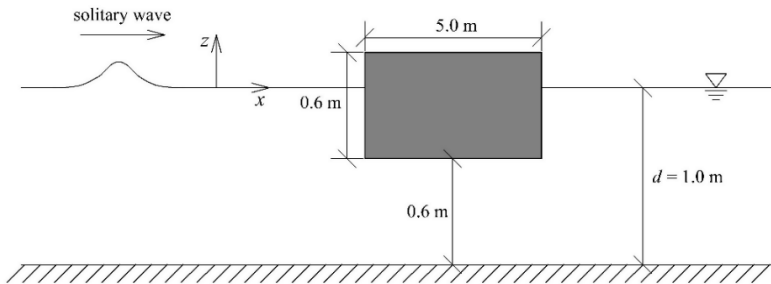
Figure 1: Schematic diagram showing solitary wave past a floating rectangular obstacle
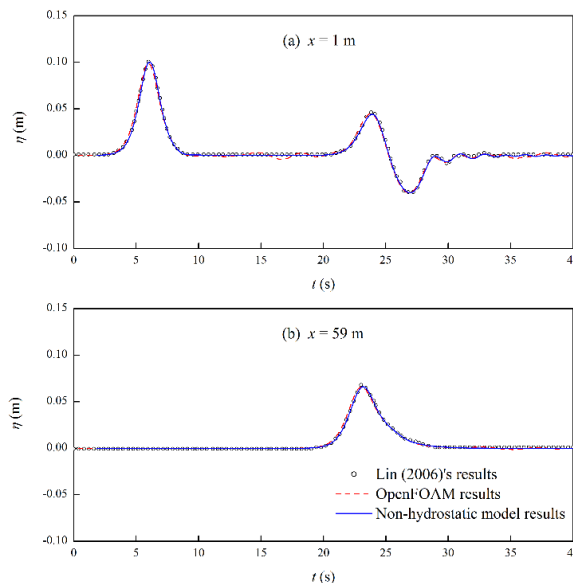
Figure 2: Comparisons of time histories of free surface elevation among non-hydrostatic model results, results published by Lin (2006) and OpenFOAM results
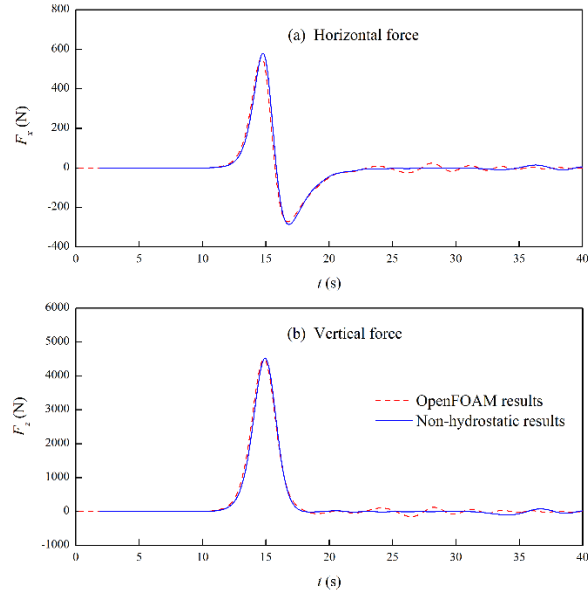
Figure 3: Comparisons of time histories of the horizontal and vertical forces exerted on the obstacle between non-hydrostatic model results and OpenFOAM results
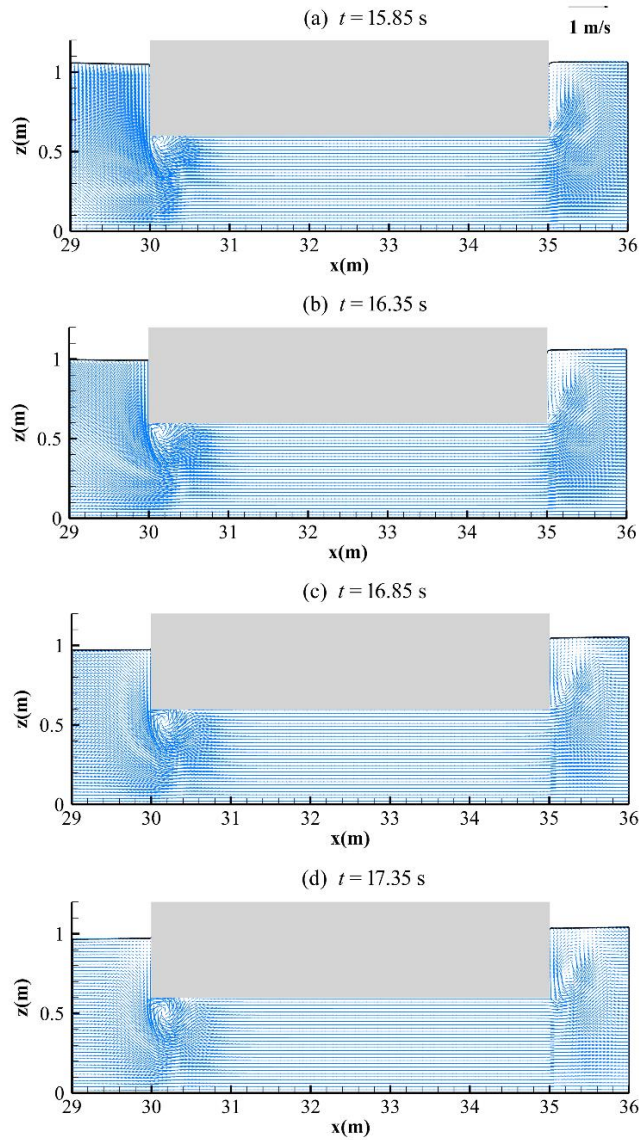
Figure 4: Velocity fields around the obstacle during solitary wave past a floating rectangular obstacle

Conclusions

This paper presents preliminary comparison between OpenFOAM and non-hydrostatic model for wave-structure interaction. It is shown that the two models show very similar results of of free surface elevation and wave force exerted on structure. It can concluded that the non-hydrostatic model is comparable to the OpenFOAM in the wave-structure interactions involving single-valued free-surface flows.

References

[1] Ai, C., Ding, W., 2016. A 3D unstructured non-hydrostatic ocean model for internal waves. Ocean Dyn. 66, 1253-1270.

[2] Ai, C., Ding, W., Jin, S., 2014. A general boundary-fitted 3D non-hydrostatic model for nonlinear focusing wave groups. Ocean Eng. 89, 134-145.

[3] Ai, C., Jin, S., 2010. Non-hydrostatic finite volume model for non-linear waves interacting with structures. Comput. Fluids 39, 2090-2100.

[4] Ai, C., Jin, S., 2012. A multi-layer non-hydrostatic model for wave breaking and run-up. Coast. Eng. 62, 1-8.

[5] Ai, C., Ding, W., Jin, S., 2017. A hybrid-grid 3D model for regular waves interacting with cylinders. J. Hydraul. Res. 55, 129-134.

[6] Ai, C., Jin, S., Lv, B., 2011. A new fully non-hydrostatic 3D free surface flow model for water wave motions. Int. J. Numer. Method Fluids 66, 1354-1370.

[7] Fadlun, E.A., Verzicco, R., Orlandi, P., Mohd-Yusof, J., 2000. Combined immersed boundary finite-difference methods for three-dimensional complex flow simulations. J. Comput. Phys. 161, 35-60.

[8] Lai, Z., Chen, C., Cowles, G.W., Beardsley, R.C., 2010. A nonhydrostatic version of FVCOM: 1. Validation experiments. J. Geophys. Res. 115, C11010.

[9] Lin, P., 2006. A multiple-layer coordinate model for simulation of wave-structure interaction. Comput. Fluids 35, 147-167.

[10] Ma, G., Farahani, A.A., Kirby, J.T., Shi, F., 2016. Modeling wave-structure interactions by an immersed boundary method in a σ-coordinate model. Ocean Eng. 125, 238-247.

[11] Matsumura, Y., Hasumi, H., 2008. A non-hydrostatic ocean model with a scalable multigrid Poisson solver. Ocean Model. 24, 15-28.

[12] OpenCFD, OpenFOAM: The Open Source CFD Toolbox. User Guide Version 1.4, OpenCFD Limited. Reading UK, Apr. 2007.

[13] Smagorinsky, J., 1963. General circulation experiments with primitive equations. Mon. Weather Rev. 91, 99-164.

[14] Vitousek, S., Fringer, O.B., 2014. A nonhydrostatic, isopycnal-coordinate ocean model for internal waves. Ocean Model. 83, 118-144.

DEVELOPMENT OF A FULLY COUPLED AERO-HYDRO-MOORING-ELASTIC TOOL FOR FLOATING OFFSHORE WIND TURBINES

YUANCHUAN LIU[1], QING XIAO[2]

[1]Department of Naval Architecture, Ocean and Marine Engineering, University of Strathclyde, Glasgow, UK, yuanchuan.liu@strath.ac.uk

[2]Department of Naval Architecture, Ocean and Marine Engineering, University of Strathclyde, Glasgow, UK, qing.xiao@strath.ac.uk

Keywords: Floating offshore wind turbine, fluid-structure interaction, blade elasticity, mooring dynamics.

Introduction

As one of the fastest growing renewable energy sources, wind energy is playing an increasingly important role in addressing the climate change and energy crisis issues the world is currently facing. The abundance of wind resource in offshore areas makes them a popular choice for turbine installation. In the past few years, several floating wind projects have emerged by installing wind turbines far offshore in deep-water sites on moored platforms. Compared to land-based or offshore fixed-bottom wind turbines, a floating offshore wind turbine (FOWT) is a fully coupled system where the wind turbine with flexible blades and the floating platform with its mooring system interact with each other in wind and waves, which makes existing design tools inadequate to accurately predict its responses. This paper presents a fully coupled high-fidelity aero-hydro-mooring-elastic analysis tool developed for FOWT applications. The numerical techniques adopted in the present tool are firstly described. Simulation results from a series of case studies are then shown to demonstrate the capabilities of the developed tool.

Numerical Methods

In the numerical tool developed in this work, OpenFOAM is coupled with an open source MultiBody Dynamics (MBD) code MBDyn (https://www.mbdyn.org) to solve the structural dynamics of an FOWT with flexible turbine blades. This is achieved by establishing an interface library to exchange data between these two codes. Additionally, a mesh motion solver is developed in OpenFOAM to tackle complex mesh movement in FOWT simulations. A mooring system analysis module is also implemented to simulate mooring lines in an FOWT. Figure 1 depicts the structure of the present FSI analysis tool, where built-in features in OpenFOAM and MBDyn are indicated in black; the wave modelling module marked in red is incorporated from the naoe-FOAM-SJTU solver [1, 2]; new functionalities implemented in this work are highlighted in blue which are described in the following sections.
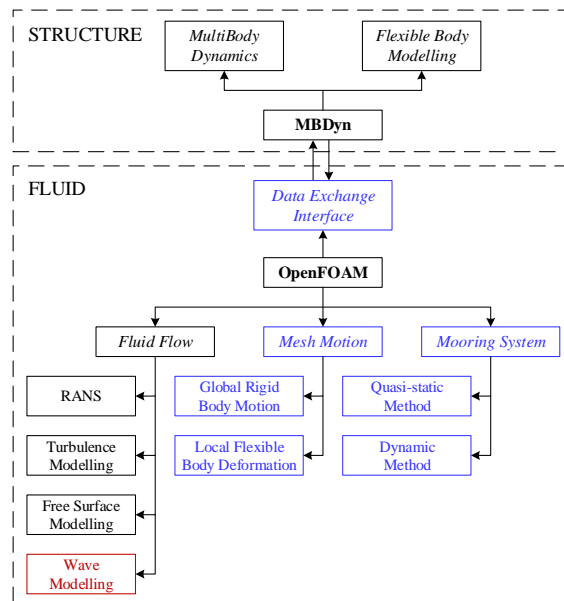
Figure 1: Structure of a fully coupled FSI analysis tool for FOWTs (Black–Built-in, Red–Incorporated, Blue–Developed)

- *Structural Dynamics*

Dynamic structural responses of an FOWT are solved using MBDyn, which adopts a Lagrange multiplier formulation for a multibody system consisting of both rigid and flexible bodies connected by kinematic constraints [3]. For each body of

the constrained system, Newton-Euler equations of motion are established in the differential-algebraic form as a set of first-order equations together with constraint equations.

MBDyn models a flexible body as a series of three-node beam elements based on a nonlinear beam theory formulated within a multibody framework [3]. As illustrated in Figure 2, a three-node beam element is divided into three portions by two evaluation points (squares). Each portion is associated with a reference point (circles), which represents the elastic axis of the beam. These reference points do not necessarily need be on a straight line and can be offset from the geometrical nodes (triangles) where equilibrium equations are established considering both external and internal forces. External forces are integrated over every beam element portion related to a reference point and later translated to its corresponding geometrical node. Meanwhile, internal forces are evaluated at cross sections of evaluation points and are related to geometrical strains and curvatures via constitutive laws.
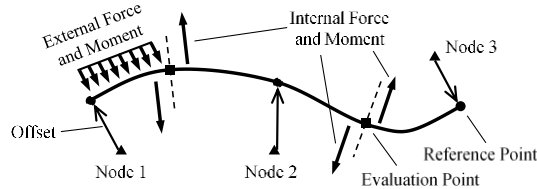
Figure 2: Illustration of a three-node beam element in MBDyn

- *CFD Mesh Motion*

One of the challenges for a fully coupled FOWT simulation with flexible blades is how to handle the motion of the CFD mesh to represent the complex structural responses of the system, including (a) global rigid body motion, i.e. platform 6DoF motion and turbine rotation; (b) local flexible body deformation, such as deflection of an aero-elastic turbine blade. The current mesh motion libraries in OpenFOAM are unable to cope with both global and local structural responses at the same time. In the present study, a customised mesh motion library is developed by incorporating features of the built-in solid body motion library into the dynamic mesh motion solver displacementLaplacianFvMotionSolver.

The implemented mesh motion library deals with global rigid body motion responses in a solid body motion manner. The computational grid is split into three separate cell zones by two pairs of Arbitrary Mesh Interface (AMI) surfaces as sketched in Figure 3. Different rigid body motions are then applied to these cell zones. When an FOWT is in motion, the outer zone only translates in surge, sway and heave directions. The middle zone experiences three rotational motion responses, i.e. roll, pitch and yaw, as well as the three translational components, while the inner zone undergoes all 6DoF platform motion responses together with prescribed turbine rotation.
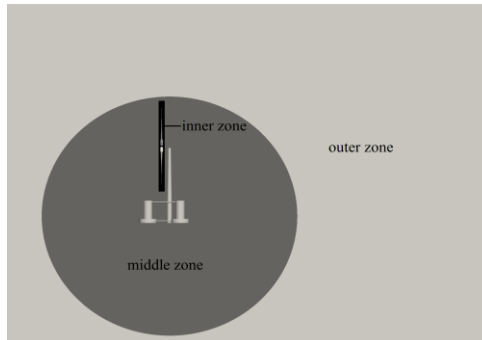
Figure 3: Cell zone decomposition of computational mesh for an FOWT

Mesh motion due to local blade deformation is handled by solving the displacement Laplacian equation for cell centres. In order to maintain grid quality, global rigid body motions are firstly subtracted from the point displacement of turbine surface mesh to obtain a temporary value, which is then used by the mesh motion solver as the boundary condition of the abovementioned Laplacian equation. When the mesh motion equation is assembled, only cells inside the inner zone shown in Figure 3 are considered while those in other zones are kept static by setting their displacement to zero. Once the displacement of cell centres is obtained, interpolation is performed to calculate the displacement of internal mesh points, which is then added to the initial position of all points to determine their updated position resulting from blade deformation. Lastly, points in the inner zone are rotated collectively to take into account global rigid body motion.

- *Mooring System*

As mooring systems are essential in station-keeping for floating structures, a mooring system analysis module is developed in OpenFOAM to calculate the mooring restoring force provided for an FOWT system. This module includes both quasi-static and dynamic methods.

In the present quasi-static method, instead of employing the analytical catenary equation, a discretised approach is utilised by dividing a mooring line into a number of segments with identical length so that lines of both catenary taut shapes can also be simulated. Equations of static equilibrium are established for each segment in horizontal and vertical directions at

each time step. By further applying the relationship between tension and segment elongation as well as geometric constraints between node coordinates and stretched segment length, tension and shape of the line can be computed in an iterative manner. The current method is also able to model mooring lines made of multiple components with different structural properties.

The mooring system analysis module is further extended by implementing a dynamic method based on a 3D lumped mass model, which discretises a mooring line into $n+1$ concentrated masses (nodes) connected by n massless springs (segments), as illustrated in Figure 4. Unlike the quasi-static method, equations of motion are applied to every node in the dynamic approach so that dynamic effects resulting from line movement are considered and tension force can be accurately predicted. The hydrodynamic loads exerted on the line are also taken into account by adopting Morison's equation. The Newmark Beta method is then employed to solve the differential equations.
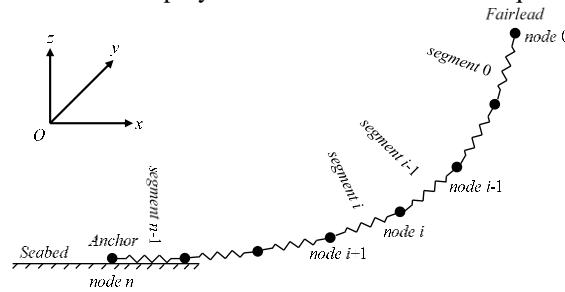
Figure 4: Sketch of a 3D lumped mass model

- *Coupling Procedure*

In MBDyn, a flexible blade is modelled as a series of three-node beam elements, while it is discretised into a surface grid comprising a large number of surface points in OpenFOAM. The gap between the level of complexity in describing the blade by the two codes leads to a pair of un-matched interfaces. A mapping scheme is therefore established to exchange data between CFD and MBD models, as illustrated in Figure 5. In the CFD model, the surface grid of the structure is decomposed into several small patches, each of which is associated with a beam node in the MBD model. A centre is defined for every patch in the CFD grid and has the same kinematics as its corresponding beam node in the MBD model via motion exchange. On the other hand, external fluid force and moment are firstly integrated over every patch of the CFD surface grid with respect to its patch centre and then transferred to MBDyn via force exchange.

In order to maintain smooth transition between patches in the CFD model, a linear interpolation scheme [4] is implemented to calculate position of surface grid points using kinematics from patch centres in the following way:

$$\mathbf{X} = \xi\left(\mathbf{X}_i + \mathbf{R}_i\mathbf{d}_i\right) + \left(1-\xi\right)\left(\mathbf{X}_{i+1} + \mathbf{R}_{i+1}\mathbf{d}_{i+1}\right) \tag{1}$$

where $\mathbf{X}$ represents position of point or patch centre; $\mathbf{R}$ denotes transformation matrix of patch centre due to rotation; $\mathbf{d}$ is distance vector pointing from patch centre to point; $\xi \in [0,1]$ stands for normalised point location between surrounding patch centres.
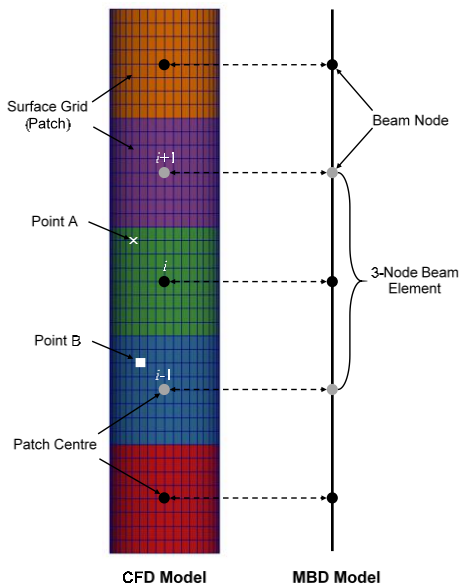
Figure 5: Diagram for mapping between CFD and MBD
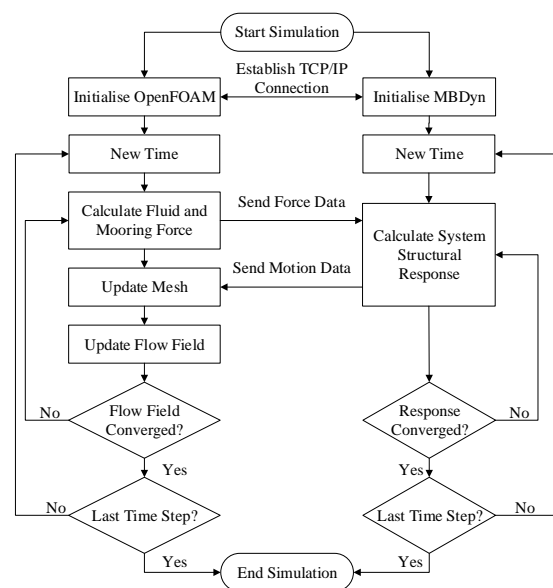
Figure 6: Flowchart for coupling OpenFOAM with MBDyn

Figure 6 shows the coupling procedure used in the present FSI analysis tool. When a fully coupled simulation is performed, both OpenFOAM and MBDyn run simultaneously as individual computer processes. Data exchange between the two codes is achieved with the help of the TCP/IP communication protocol, using a client/server model. An interface library is implemented in OpenFOAM by adopting the motion and force exchange functions provided in MBDyn, serving as the bridge connecting the flow and structural solvers.

Results

The present FSI analysis tool developed for FOWTs are applied to a series of test cases to validate its various components and features [5-7]. The NREL Phase VI wind turbine is firstly studied to validate the aerodynamic modelling feature of the tool. Turbine aerodynamic torque from present simulations agrees well with experimental results under various wind conditions, as shown in Figure 7. Hydrodynamic modelling is then validated by investigating the DeepCwind semi-submersible of the OC4 FOWT project. Figure 8 reveals good agreement between the motion RAOs of the platform predicted by the present tool and experimental data under regular incident waves. Subsequently, a dynamic analysis is conducted for a flexible hanging riser subject to prescribed surge motion at its fairlead. Figure 9 show that the present prediction of fairlead tension is in perfect agreement with previous results, demonstrating good accuracy of the dynamic mooring line method. Furthermore, the capability of the tool in modelling flexible structures is validated by comparing deflections of a turbine blade under a concentrated loading at its tip, as illustrated in Figure 10.
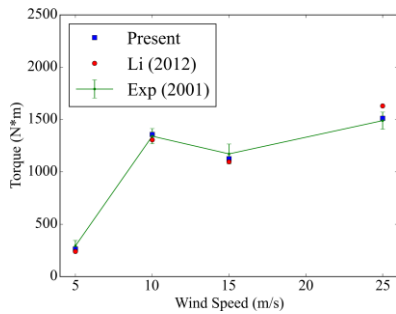
Figure 7: Aerodynamic torque of NREL Phase VI wind turbine
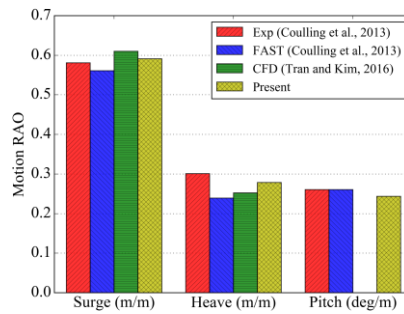
Figure 8: Motion RAO of OC4 DeepCwind semi-submersible
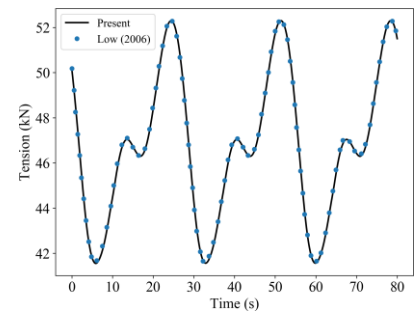
Figure 9: Fairlead tension of a hanging riser subject to surge motion
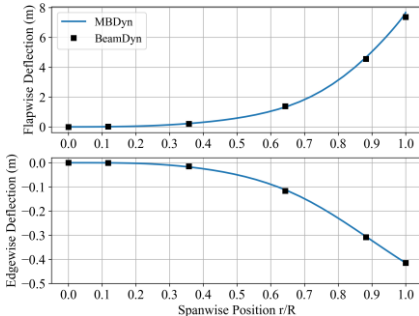
Figure 10: Blade deflections under a concentrated loading at tip
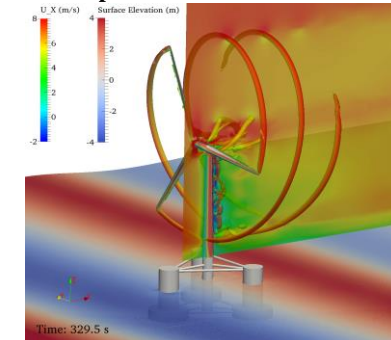
Figure 11: Fluid field around an FOWT
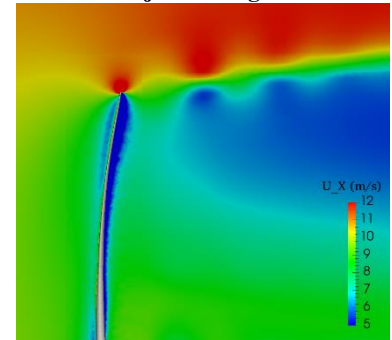
Figure 12: Blade deformation in wind

With the fully coupled CFD-MBD tool implemented in this work, high-fidelity aero-hydro-mooring-elastic analysis can be performed. Figure 11 and Figure 12 depict the complex fluid flow around the OC4 semi-submersible FOWT under combined wind/wave conditions. This tool can be utilised to better understand the underlying physics and sophisticated interaction between fluid flow and an FOWT as well as the influence of different parts of the system on each other.

Acknowledgements

References

[1]   H. Cao and D. Wan, "Development of Multidirectional Nonlinear Numerical Wave Tank by naoe-FOAM-SJTU Solver," *International Journal of Ocean System Engineering,* vol. 4, pp. 52-59, 2014.

[2]   J. Cha and D. Wan, "Numerical wave generation and absorption based on OpenFOAM," *The Ocean Engineering,* vol. 29, pp. 1-12, 2011.

[3]   G. L. Ghiringhelli, P. Masarati, and P. Mantegazza, "Multibody Implementation of Finite Volume C Beams," *AIAA Journal,* vol. 38, pp. 131-138, 2000.

[4]   M. Pierangelo and S. Jayanarayanan, "Coupled CFD/Multibody Analysis of NREL Unsteady Aerodynamic Experiment Phase VI Rotor," in *49th AIAA Aerospace Sciences Meeting including the New Horizons Forum and Aerospace Exposition*, Orlando, Florida, USA, 2011.

[5]   Y. Liu, Q. Xiao, A. Incecik, C. Peyrard, and D. Wan, "Establishing a fully coupled CFD analysis tool for floating offshore wind turbines," *Renewable Energy,* vol. 112, pp. 280-301, 2017.

[6]   Y. Liu, Q. Xiao, and A. Incecik, "A coupled CFD/Multibody Dynamics analysis tool for offshore wind turbines with aeroelastic blades," in *36th International Conference on Ocean, Offshore and Arctic Engineering*, Trondheim, Norway, 2017.

[7]   Y. Liu, Q. Xiao, A. Incecik, and D. Wan, "Investigation of the effects of platform motion on the aerodynamics of a floating offshore wind turbine," *Journal of Hydrodynamics, Ser. B,* vol. 28, pp. 95-101, 2016.

CFD SIMULATION OF AN INTEGRATION SYSTEM OF OSCILLATING BUOY WEC WITH A FIXED BOX-TYPE BREAKWATER

YANJUN MAO[1], YONG CHENG[2], GANGJUN ZHAI[1,*]

[1]Deepwater engineering research center, Dalian University of Technology,

zhai@dlut.edu.cn

maoyanjun__dut@foxmail.com

[2]School of naval architecture and ocean engineering, Jiangsu University of Science and Technology,

chengyong@just.edu.cn

Introduction

With the advancement in the renewable energy, the wave energy converter devices have been opted broad research and utilization. But the high construction cost is still a significant problem. To deal with this problem, the cost-share concept has been introduced by many researchers in recent years. Integrating the wave energy converter(WEC) into some kinds of coastal and offshore structures can share the construction cost and also enhance the stability of the devices. Among these ideas, the integration of WEC with offshore breakwaters is more feasible [1–3]. This integration design model can be used to transform the existing breakwater or promote new structural concept designs for off-shore breakwaters. Ning et al [3], introduced an experiment with a buoy-type WEC combined with the pile-restrained floating breakwater. The results showed that a high energy-conversion efficiency and good wave attenuation performance can be achieved with appropriate dimensions and power take-off (PTO) damping setting. Focusing on this kind of integration system, Zhao et al [1, 2], gave the analytical solutions based on the linear potential theory to two kinds of the integration system, respectively. One is the integration of oscillating buoy WEC and a pile-restrained floating breakwater. The other is the integration of oscillating buoy WEC with a fixed box-type breakwater. The first one is a symmetric structure which has a limited wave capture width ratio(CWR) of 0.5. The later one is a floating buoy attached to a fixed box-type breakwater which is easy to assemble and extend to a large scale. Meanwhile, the analytical solution also shows that the reflection wave energy can be absorbed by the buoy. The CWR value can reach 0.8 or even higher. Thus the later one has more excellent performance. Since the above analytical solution is based on potential-flow theory in the frequency domain. It ignores the nonlinear wave conditions, the viscous effect, and the flow separation effect. Besides, only the linear PTO model is considered in the analytical solution. However, these factors usually have strong effects on the hydrodynamic performance of the devices in real sea conditions. There are many other kinds of PTO systems with good performance. Hence, aiming at above shortages, this integrated system of oscillating buoy WEC with a fixed box-type breakwater is simulated with OpenFOAM [4] in this paper. The reflection coefficient, the transmission coefficient and the CWR of the system are investigated to show the effectiveness of the device in viscous flow. Except for the linear damping PTO model which has been presented in OpenFOAM, two other types of PTO models are developed to consider the effect of different PTO systems. The quadratic damping model is formulated as $F_{pto} = C_{pto} \times V^2$ and the coulomb damping model is formulated as $F_{pto} = C_{pto} \times sign(V)$ which is often used as a simple model of a hydraulic PTO. The author hopes this development work of PTO system in OpenFOAM can extend the capability of the six degrees of freedom solver to simulate the WEC devices.

The challenge of modeling this integration system is to deal with the dynamic mesh. When the buoy gets resonance, high vibration can be expected. As the floating buoy is too close to the fixed box-type breakwater. Therefore, Using the dynamic mesh method without topology change, the mesh deformation will be very large between the floating buoy and the fixed boundary of the box-type breakwater. The large mesh deformation can easily get the simulation collapsed or lead to inaccurate results. The overset mesh method can handle this situation properly such as the work by ShenZhirong [5]. The overset mesh functionality was presented in OpenFOAM−V1706_PLUS. It can be more convenient for the simulation of floating objects, especially for ocean engineering structures. Thus the overset mesh method is applied in this paper. Also, wave input boundary and shallow water wave damping setting are presented in OpenFOAM−V1706_PLUS which can be used to construct the numerical wave tank.

Validation and Result discussions

Validation

After the validation of wave generation, it shows that good quality waves can be generated in present numerical wave tank. Further verification work is focused on the simulation of floating object using the overset mesh method. A single 2D vertical pile-restrained box type floating breakwater model [3]is chosen for the verification work. The floating breakwater can only move freely in heave direction without any extra restraint. The dimensions of the floating breakwater model: the width 0.8m, the height 0.6m, the draft 0.8m. The water depth 1.0m, wave period $T = 1.79s$, wave height $H = 0.2m$. The heave motion response from 16s to 26s is shown in Figure1. It shows that the simulation can get a stable and reliable result compared with both the experimental data by Ref [6] and the simulation result by using the dynamic mesh without topology change.
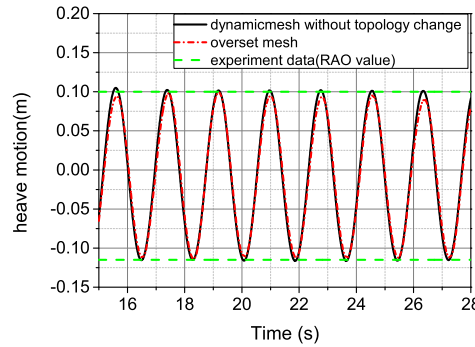
Figure 1: Heave motion response of the single bouy

The dimensions of the integrated system model are referenced from Ref [1]. The sketch of the integration of oscillating buoy WEC with a fixed box-type breakwater is shown in Figure2, the water depth $h = 10.0m$, the floating buoy $a_1/h = 0.2$, fixed breakwater $a_2/h = 0.6$, the gap between the floating buoy and the fixed breakwater $D/h = 0.1$. The total mesh number is 136050, To obtain accurate results, the meshes are refined near the free surface and around the overset zone as shown in Figure3.
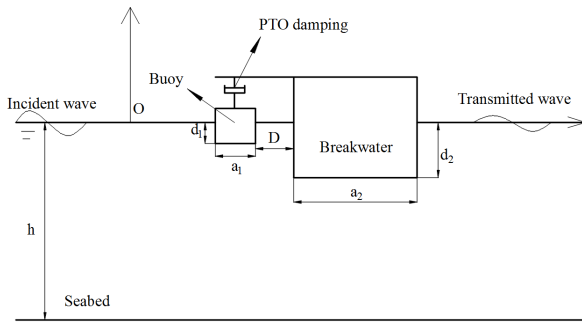
Figure 2: Sketch of the Intergated system
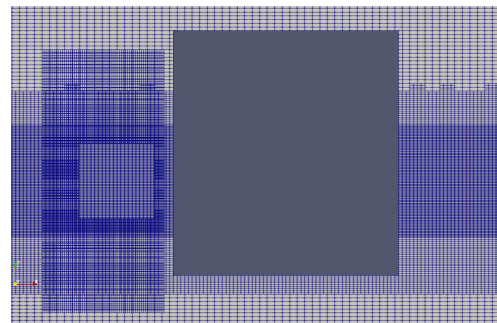
Figure 3: Refined mesh near the free surface and around the overset zone

Linear PTO damping model

The theoretical optimal linear PTO damping coefficient derived from the single floating breakwater was chosen as the PTO damping coefficient corresponding to different wave conditions in Ref [1]. However, considering the effect of viscous and the asymmetric structure which has different added mass coefficient and radiation damping coefficient compared with the single floating breakwater. The optimal PTO damping coefficient in this integrated system may have changed away from the single floating breakwater. The theoretical optimal linear PTO damping coefficients are also applied in this section. But to find out the optimal PTO damping coefficients in viscous flow, several simulations will be calculated with different times of theoretical optimal PTO damping coefficients in later work. Referencing the analytical solutions [1], several feature wave conditions are chosen in the simulation as in Table1. Figure4,5 show the reflection coefficients and the transmission coefficients obtained by present simulation compared with the analytical solution. The results are in accordance with the analytical solution except the reflection coefficient which is relatively small with the analytical solution when the

Table 1: Wave conditions

h(m)	T(s)	kh	$H_i(m)$
10.0	4.735,3.663,3.291,3.035, 2.572,2.387	7.0727 1.882	0.5

dimensionless number kh is equal to 6.09. Figure6 shows the wave CWR value of the floating buoy compared with the analytical solution. The maximum CWR value can reach 0.7 that is almost twice times higher than the single floating buoy in Ref [3]. It shows great improvement in energy conversion efficiency. From the comparison of the CWR values obtained by present simulation and the analytical solution, It shows a difference between the present simulation and the analytical solution. When the dimensionless number $kh = 2.0 \sim 5.0$, the CWR value gets a significant decrease in the present simulation where the maximum analytical CWR value can reach 1.0. The difference shows that the viscous and flow separation have a significant effect on the wave energy conversion efficiency. Further observation of the simulated flow field shows that vortex generates at the corner of the buoy as it goes up. The flow separation is different when the buoy goes up and declines. It leads to the fluctuation of the instant energy conversion power. Further research will focus on how to adjust the PTO damping coefficient to be optimal in viscous flow. While different geometry parameters also need to be simulated in viscous flow to evaluate the performance of the integrated system.
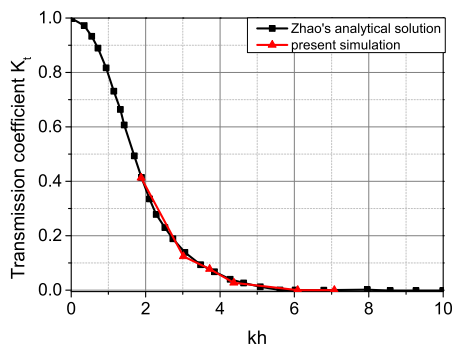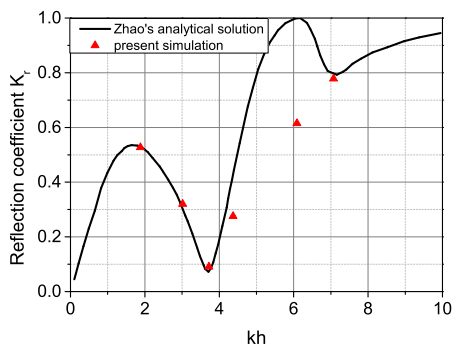
Figure 4: Comparison of the reflection coefficients obtained by present simulation and analytical solution

Figure 5: Comparison of the transmission coefficients obtained by present simulation and analytical solution
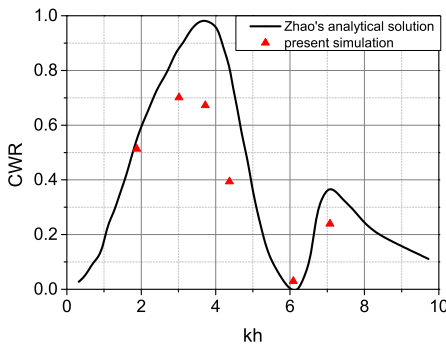
Figure 6: CWR of the intergrated system corresponding to chosen wave conditions

Nonlinear PTO damping model

The linear PTO model used in above section can obtain good results when the motion has small amplitude with a low velocity. But if the motion is strongly nonlinear, the nonlinear PTO model would be a better choice [7], the quadratic damping model and the Coulomb damping model are the typical nonlinear PTO model for WEC devices. The quadratic damping model can act as a drag force. The Coulomb damping model is a simple model of a hydraulic PTO system which is commonly used in many energy conversion devices. These two kinds of nonlinear PTO models are developed and validated in this section. The quadratic damping coefficient is $\lambda_{quadratic} = \lambda_{linear}$, the Coulomb damping coefficient is $\lambda_{coulomb} = \lambda_{linear} \times V_{max}$, the λ_{linear} value is equal to the theoretical optimal damping coefficient value$\lambda_{optimal} = 5720.91kg/s$ when the dimensionless number $kh = 3.01$. And $V_{max} = 0.48m/s$ is the maximum buoy velocity in the linear case. Figure7 shows the heave motion response of the buoy restrained by three kinds of PTO model under wave condition $T = 3.663s, H = 0.5m$. Figure8 shows the comparison of the PTO forces with three kinds of PTO model corresponding to the motion response in Figue7. From these figures, It shows that the quadratic PTO

model and the Coulomb PTO model can both get stable motion responses as the linear PTO damping model. Because the velocity of the buoy is small than $1.0m/s$. So the restraint force by the quadratic PTO model is relatively small than the linear PTO model. As a result, the motion response is larger than the linear one. On the contrary, the restraint force by the Coulomb PTO model keeps a maximum constant value for the duration of the motion response. Thus the motion response is smaller than the linear one. These differences are all reasonable and according to our expectations. So these two kinds of nonlinear PTO models developed in the paper can be used for further research work. Further work will analyze the CWR, the reflection coefficient, and the transmission coefficient with the nonlinear PTO models.

Conclusion

The simulations in this paper are calculated by OpenFOAM. The results show the motion response of the integrated system, the wave energy conversion efficiency and the wave dissipation performance. Considering the effects of viscous and the flow separation, the integrated system can still obtain a high wave energy conversion efficiency, the CWR value reaches 0.7. A good use of the reflected wave energy can be seen from the decrease of the reflection coefficient on the wave conditions that resonate the buoy. Meanwhile, the transmission coefficient can be kept below 0.5 at a wide range of wave conditions when $kh > 1.8$ which promises an ideal wave dissipation performance. The development work of nonlinear PTO models in OpenFOAM extend the functions of OpenFOAM to model the WEC devices. the optimal PTO damping coefficient in viscous flow and the character of nonlinear PTO models need more research work as concluded in the above two sections.
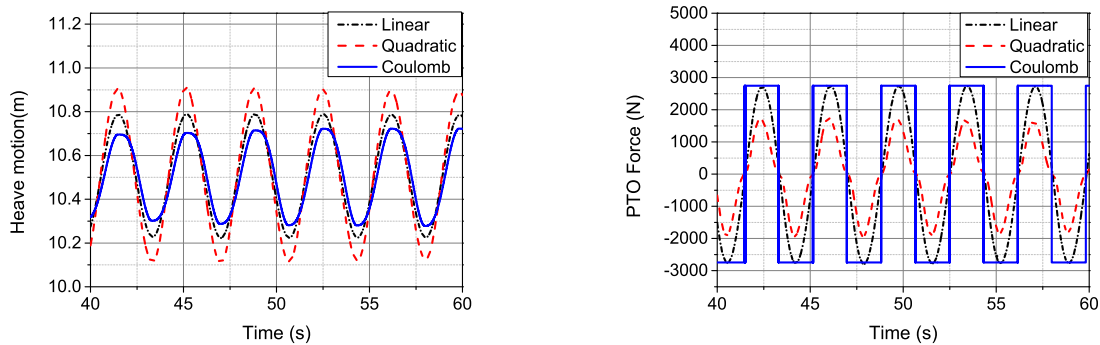
Figure 7: Motion response under three different kinds of PTO

Figure 8: Instant PTO force under three different kinds of PTO

References

[1] X. Zhao, D. Ning, C. Zhang, Y. Liu, and H. Kang, "Analytical study on an oscillating buoy wave energy converter integrated into a fixed box-type breakwater," Mathematical Problems in Engineering,2017,(2017-5-30), vol. 2017, pp. 1–9, 2017.

[2] X. Zhao, D. Ning, C. Zhang, and H. Kang, "Hydrodynamic investigation of an oscillating buoy wave energy converter integrated into a pile-restrained floating breakwater," Energies, vol. 10, no. 712, pp. 1–16, 2017.

[3] D. Ning, X. Zhao, M. Göteman, and H. Kang, "Hydrodynamic performance of a pile-restrained wec-type floating breakwater: An experimental study," Renewable Energy, vol. 95, pp. 531–541, 2016.

[4] OpenCFD, OpenFOAM: The Open Source CFD Toolbox. User Guide Version 1.4, OpenCFD Limited. Reading UK, Apr. 2007.

[5] Z. Shen, P. M. Carrica, and D.-C. Wan, "Ship motions of kcs in head waves with rotating propeller using overset grid method," vol. 2, 06 2014.

[6] M. Isaacson, J. Baldwin, S. Bhat et al., "Wave propagation past a pile-restrained floating breakwater," International Journal of Offshore and Polar Engineering, vol. 8, no. 04, 1998.

[7] L. Sjökvist, "Wave loads and peak forces on moored wave energy devices in tsunamis and extreme waves," Ph.D. dissertation, Acta Universitatis Upsaliensis, 2017.

IMPLEMENTATION OF OVERSET GRID IN OPENFOAM AND ITS VALIDATION TO PMM MODEL TEST OF A CONTAINER SHIP

CHENLIANG ZHANG[1,2], XIAOJIAN LIU[1], SHEMING FAN[1], DECHENG WAN[2], JINBAO WANG[1*]

[1]*Shanghai Key Laboratory of Ship Engineering, Marine Design and Research Institute of China*
[2]*Shanghai Jiao Tong University, Shanghai, China*
*wang_jb@maric.com.cn

Keywords: Overset grid, Ship hydrodynamics, PMM Model test, Ship manevering

Introduction

Overset grid approach is practical and elegant method in the use of computational fluid dynamics (CFD) to simulate certain complex problems that considering the flow around multiple moving bodies, deforming bodies, or bodies with complex geometries. In ship hydrodynamics, overset grid has been widely used in the simulations including self-propulsion [1, 2, 3], see-keeping [4], turning and zig-zag test [2, 3, 5] and PMM model test [6, 7, 8, 9], slamming [10] and ship maneuvering in waves [11]. In these literatures, the ships have large amplitude of motions, the geometries of propeller rudder and appendages are complex and the propeller and rudder have relative rotating motions to the ships. The results demonstrate the capability and the advatage of the overset grid methodology to deal with problems with large amplitude motions and violent flows.
In [1, 4, 5] Carrica use CFDShip-Iowa a FDM CFD solver with Suggar++ [12] and DiRTlib [13] to calculate domain connectivity information (DCI) that connect the solutions among multiple overset component grids. DiRTlib is a solver neutral library that simplifies the addition of an overset capability to a flow solver by encapsuating the required operations. In [14], Boger firstly brought overset grid mehodology in OpenFOAM. The foamedOver library stands separately from OpenFOAM and it inserts easily into solvers e.g. potentialFoam, icoFoam, interDyMFoam of OpenFOAM. foamedOver also benefits from the software packages Suggar++ and DiRTlib. Indeed, DiRTlib makes it easier for Suggar++ to be applied to different CFD solvers. As illustrated in [2], Shen implementes the overset technique into an OpenFOAM-based in-house solver naoe-FOAM-SJTU. Suggar++ is used to obtain the DCI and a lagged mode is used to allow OpenFOAM and Suggar++ to run in parallel so that shortens the waiting time of the CFD solver and Suggar++. Simillarly, Chris and Darrin in [15] developed the library Caelus also based on Suggar++. Andreas in [16] developed an Open source overset grid library Bellerophon, which extends OpenFOAM with capabilities for overset grid. This library is publicly released and can be dynamically linked to any standard OpenFOAM solver without changing the solver it self, but the low efficiency of DCI calculation limits its application to dynamic problems. In [17], Chandar described an overset grid implementation for moving grids in OpenFOAM. A dynamic library OPErA linked independently to OpenFOAM that provides DCI is developed. Flood-fill algorighm is utilized for hole cuttibg and inverse map strategy is utilized for donor search. Compared with Bellerophon, OPErA is more efficient and has been used to carry out simulations on ship hydrodynamics in [18, 19], where the overset computation results are compared with results given by StarCCM+, ANSYS Fluent and experimental measurements for validation and verification purpose. But similar with Suggar++, OPErA is not publicly released or open-source so far. The latest release version OpenFOAM-v1712 and foamextend-4.0 also include overset package but so far are not widely used and validated especially for ship maneuvering cases.
As we can see, overset grid methodology performs well for simulations with large amplitude motions and complex geometries. So far it has been widely and successfully used in ship hydrodynamics, especially for simulations of ship motion in waves, ship maneuvering, ships with full appendages. And many researchers have made their effort to extend OpenFOAM with capabilities for overset grid. Some are using commercial software like Suggar++ and DiRTlib, others are using in-house library as Bellerophon or OPErA. And the latest release version of OpenFOAM-v1712 and foamextend-4.0 also include their own overset grid package. All these codes have their own merits and limitations and most of them are not publicly released or validated. So in order to simulate ship maneuvering tests such as PMM model test, turning test, zigzag test el al, we developed a dynamically linked third party package to perform efficient Overset Grid Assembly (OGA). As with Suggar++, Bellerophon and OPErA our package will make no changes to existing standard libraries in OpenFOAM and a few changes to top-level applications. We used the existing linear solver and lduMatrix. Besides, only a few changes were made to the existing workflow.
As illustrated in [20], we extended the open-source overset grid assembly package tioga, proposed in [21], to

arbitrary polyhedral grid as generated by snappyHexMesh. And connected it to top level solvers in OpenFOAM like interDyMFoam and pimpleDyMFoam as a dynamic linked library. We have applied this package to simulate sphere water entry case, pure yaw and pure sway motion of DTMB-5415 hull , that verify the DCI calculation, flow field interpolation and multi-bodies motion control part of the program. But quantitative comparisions are still required to valid the accuracy of the solver. Considering that, in this paper, we take a container ship, which is designed by us, as an example. We have carried out resistance and PMM model test of this hull in our towing tank and the experimental measurements of hydrodynamic forces experienced by the hull together with the resulting ship motions are compared with the numerical results obtained in this paper.

Test overviews

The main dimensions of the container ship considered in current study are listed in Table 1 . The ship model used in current study does not have appendages or bilge keels but with rudder and propeller in some test cases and all the model test conditions are listed in Table 2 and 3 .

Table 1: Main dimensions of the container ship

Items	Full scale	Model scale
Waterline length (L_{wl})	389.4m	4.327m
Length between perpendicular (L_{pp})	383.0m	4.256m
Beam (B)	54m	0.6m
Fore draft (T_F)	16m	0.178m
Aft draft (T_A)	16m	0.178m
Block coefficient (C_B)	0.709	0.709

Table 2: Static PMM model test conditions

Test name	Model speed(m/s)	Drift angle(°)	Heel angle(°)	(w/o) rudder and propeller
Resistance test	1.084, 1.204, 1.356	0	0	o
Static drift test	1.204	$\pm 2, \pm 4, 6, 8, 10, 12$	released	w/o
Constant heel angle	1.204	0	$0, \pm 5, 8, -10$	o

Table 3: Dynamic PMM model test conditions of the bare hull

Test name	Model speed(m/s)	Drift angle(°)	Heel angle(°)	Frequency	Amplitude(m)
Pure sway	1.204	0	released	0.0833, 0.1, 0.125	0.4
Pure yaw	1.204	0	released	0.0833, 0.1, 0.125	0.4

Simulation design

In this study, we take grid independence study based on the resistance test case with advancing speed $V = 1.204$. Three sets of grids named as "Coarse", "Medium" and "Fine" are considered. All these three sets of grids guarantee $30 < y^+ < 80$ as required by the $k - \omega$ turbulence model when wall functions are used. Considering the fact that the flow separations will increase and result in strong side forces and moments with the growing of the drift angle β in static drift tests, a hybrid URANS/LES approach called kOmegaSSTIDDES is utilized and the grids in the wake region of the hull where flow separations may happen are refined. Table 4 presents the specific grid definition and the grid convergence verification. As is illustrated, the "Medium" grid is fine enough to capture the flow feature and yield an accurate results for the forces experienced by the ship during the resistance test with advancing speed $V = 1.204$, so the "Medium" grid is used to simulate other test cases. To summarize, this paper implement simulations of static and dynamic PMM model tests for a container ship to validate the OpenFOAM solver combined with our in-house overset grid assembly package. The numerical results together with the experimental measurements will be published in the full text.

References

[1] P. M. Carrica, A. M. Castro, and F. Stern, "Self-propulsion computations using a speed controller and a discretized propeller with dynamic overset grids," Journal of marine science and technology, vol. 15, no. 4, pp. 316–330, 2010.

Table 4: Grid description and convergence verification

Items	Coarse	Medium	Fine	Exp
Number of cells	$2.8m$	$7.8m$	$12m$	
Resistance(N)	8.23	8.53	8.56	8.75
Errors(%)	5.9	2.5	2.2	

Table 5: Numerical results of static PMM tests

Drift angle(°)	Item	CFD(N)	Errors(%)	EFD(N)
0	F_x	8.53	2.5	8.75
0	F_y	0.03	-113	-0.23
12	F_x	10.18	0.3	10.15
12	F_y	25.68	1.8	26.15
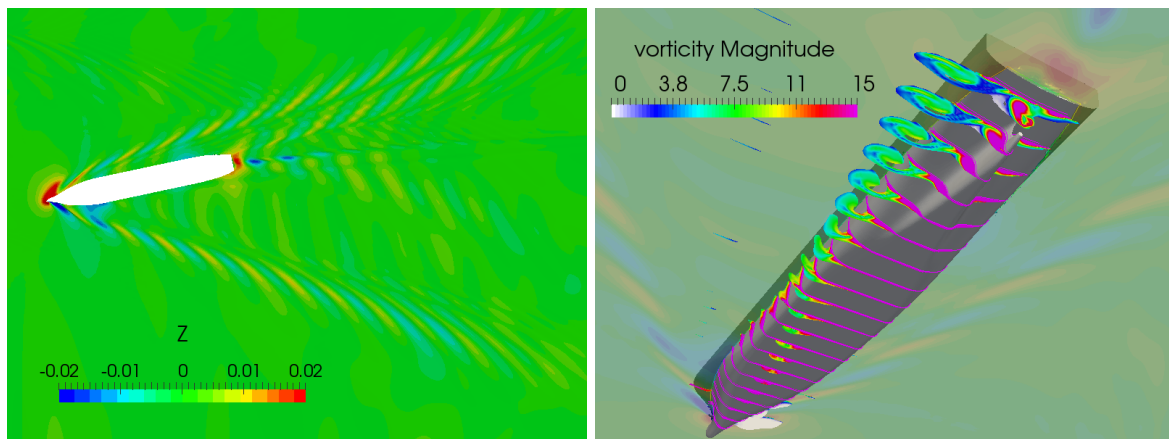
Figure 1: Numerical results of wave pattern and vortex of the container ship with drift angle $\beta = 12°$

[2] Z. Shen, D. Wan, and P. M. Carrica, "Dynamic overset grids in openfoam with application to kcs self-propulsion and maneuvering," Ocean Engineering, vol. 108, pp. 287–306, 2015.

[3] J. Wang, X. Liu, and D. Wan, "Numerical prediction of free runing at model point for onr tumblehome using overset grid method," in Proceedings of CFD Workshop 2015, 2015, pp. 383–388.

[4] P. M. Carrica, H. Fu, and F. Stern, "Computations of self-propulsion free to sink and trim and of motions in head waves of the kriso container ship (kcs) model," Applied ocean research, vol. 33, no. 4, pp. 309–320, 2011.

[5] P. M. Carrica, F. Ismail, M. Hyman, S. Bhushan, and F. Stern, "Turn and zigzag maneuvers of a surface combatant using a urans approach with dynamic overset grids," Journal of Marine Science and technology, vol. 18, no. 2, pp. 166–181, 2013.

[6] N. Sakamoto, P. M. Carrica, and F. Stern, "Urans simulations of static and dynamic maneuvering for surface combatant: part 1. verification and validation for forces, moment, and hydrodynamic derivatives," Journal of marine science and technology, vol. 17, no. 4, pp. 422–445, 2012.

[7] N. Sakamoto, P. M. Carrica, F. Stern et al., "Urans simulations of static and dynamic maneuvering for surface combatant: part 2. analysis and validation for local flow characteristics," Journal of marine science and technology, vol. 17, no. 4, pp. 446–468, 2012.

[8] H. Yoon, C. D. Simonsen, L. Benedetti, J. Longo, Y. Toda, and F. Stern, "Benchmark cfd validation data for surface combatant 5415 in pmm maneuvers–part i: Force/moment/motion measurements," Ocean Engineering, vol. 109, pp. 705–734, 2015.

[9] H. Yoon, J. Longo, Y. Toda, and F. Stern, "Benchmark cfd validation data for surface combatant 5415 in pmm maneuvers–part ii: Phase-averaged stereoscopic piv flow field measurements," Ocean Engineering, vol. 109, pp. 735–750, 2015.

[10] Z. Shen, Y.-F. Hsieh, Z. Ge, R. Korpus, J. Huan et al., "Slamming load prediction using overset cfd methods," in Offshore Technology Conference. Offshore Technology Conference, 2016.

[11] J. Wang and D. Wan, "Wave effects on free running ship in standard zigzag maneuver," in Proceedings of the 32th Workshop on Water Waves and Floating Bodies, Dalian, China 2017, 2017.

[12] R. Noack, D. Boger, R. e. Kunz, and P. Carrica, "Suggar++: An improved general overset grid assembly capability," in 19th AIAA Computational Fluid Dynamics, 2009, p. 3992.

[13] R. Noack, "Dirtlib: a library to add an overset capability to your flow solver," in 17th AIAA Computational Fluid Dynamics Conference, 2005, p. 5116.

[14] D. Boger, E. Paterson, and R. W. Noack, "Foamedover: a dynamic overset grid implementation in openfoam," in Proceedings of the 10th Symposium on Overset Composite Grids and Solution Technology. NASA Ames Research Center, Moffet Field, CA, USA, 2010.

[15] C. Sideroff and D. Stephens, "A general purpose, open-source overset library for caelus based on suggar++," in The 13th Overset Grid Symposium, Mukilteo, WA, USA, 2016.

[16] G. Andreas, "Development and application of the overset grid library bellerophon," in The 4th OpenFOAM User Conference, Cologne, Germany, 2016.

[17] D. Chandar, "Seamless integration of an overset grid framework for openfoam: The opera library," in The 3rd OpenFOAM User Conference, Stuttgart, Germany, 2015.

[18] D. Chandar and N. Vinh-Tan, "Operafoam (overset) enhancements and verification and validation," in The 4th OpenFOAM User Conference, Cologne, Germany, 2016.

[19] D. Chandar, "Development of a parallel overset grid framework for moving body simulations in open foam." Journal of Applied Computer Science & Mathematics, no. 20, 2015.

[20] C. Zhang, X. Liu, and S. Fan, "Implementation of overset grid in openfoam and its application to ship maneuvering," in 12th OpenFOAM Workshop, Exeter, UK, 2017.

[21] B. Roget and J. Sitaraman, "Robust and efficient overset grid assembly for partitioned unstructured meshes," Journal of Computational Physics, vol. 260, pp. 1–24, 2014.

[22] M. J. Brazell, J. Sitaraman, and D. J. Mavriplis, "An overset mesh approach for 3d mixed element high-order discretizations," Journal of Computational Physics, vol. 322, pp. 33–51, 2016.

AN OPENFOAM-BASED TWO-PHASE FLOW MODEL FOR SIMULATING THREE-DIMENSIONAL OSCILLATING-WATER-COLUMN DEVICES: MODEL VERIFICATION AND VALIDATION

CONGHAO XU[1], ZHENHUA HUANG[2]

[1] *Dept. of Ocean and Resources Engineering, University of Hawaii at Manoa, conghaox@hawaii.edu*

[2] *Dept. of Ocean and Resources Engineering, University of Hawaii at Manoa, zhenhua@mhawaii.edu*

Keywords: *Wave energy converter, oscillating water column, three-dimensional simulation*

1   Introduction

Wave power is one of the most promising renewable energy sources. Many types of wave energy converters (WECs) have been proposed in the past to extract energy from wave field for electricity generation, and the oscillating water columns (OWC) are one type of the promising WECs that have been widely tested and investigated. A typical OWC consists of an air chamber above the water surface with one turbine mounted to the pneumatic chamber for electricity generation; the bottom of the chamber is open and submerged so that the incident wave can cause the water column inside the chamber to oscillate. The oscillation of the water surface in side the chamber generates a fluctuation of the air pressure inside the chamber, causing the air flow to drive the turbine for electricity generation. One advantage of the OWC-type wave energy converters is its robustness in simplicity of wave energy extraction mechanism.

Many studies on the hydrodynamics and energy extraction of various OWC devices can be found in the literature; the methods used include wave-flume test, frequency-domain analysis based on potential flow theory, numerical simulations based on potential flow theory, computational-fluid-dynamics (CFD) simulations. CFD simulations of OWC devices can provide important information about the complex flow field around an OWC device and the spatial distribution of the water surface inside the OWC chamber, which is otherwise very difficult to obtain in laboratory experiments. Most of existing CFD simulations of OWC devices focused on two-dimensional configurations such as a rectangular shaped OWC [1]. OpenFOAM is an open-source CFD library for solving CFD problems using a volume of fluid method to track the free surface [2]. In this study, we introduce an OpenFOAM-based two-phase flow model developed for a circular OWC wave-energy converter integrated into a large pile. The power-takeoff is modeled using an orifice on the top cover of the OWC chamber. This study focused on the validation and verification of an OpenFOAM-based two-phase flow model using an existing set of wave-flume test results[3].

2   Model description

The relaxation-zone-based wave-generation method [2] is used for wave generation. In this method, the computational domain is divided into three sections: a wave generating relaxation section, a test section and the wave-absorbing relaxation section (numerical beach), see Fig.1 for the numerical setup and the three sections. In this study, the length of the wave generating relaxation section is 4 m long, the test section is 6 m long, and the wave absorbing section is 4 m long. Numerical tests have shown that the reflection coefficient from the wave absorbing relaxation zone is less than 0.05 for the waves examined in this study. The turbulence model used is a $k - \omega$ model. The air-water surface is tracked using a VOF method. The thin wall of the OWC chamber and the high velocity through the orifice requires very fine mesh in the vicinity of the orifice. Fig. 2 shows the quality of the waves generated in the numerical wave tank.

The oscillating-water-column device studied here is an axisymmetric oscillating-water-column (OWC) device supported by a coaxial tube-sector-shaped structure, which integrates an oscillating water column with a circular pile [3], see the right panel of Fig. 4 for a 3D view of the OWC device. The model has an overall dimension of 40 cm in total height. The distance from the lower tip of the OWC chamber to the flume bed is 24.4 cm. The inner diameter of the cylinder is 12.5 cm and the thickness of all walls is 3 mm. On the top of the tube sector an orifice of diameter 1.4 cm is used to simulate a nonlinear power takeoff (PTO) device.

3   Key Results

Representative results are presented in this section to show the agreement between the simulated and measured results. These results include surface displacements at three locations (G_1, G_2, and G_3 as shown in Fig, 1), the relative pressure of the air in the pneumatic chamber, the simulated velocity and vorticity.
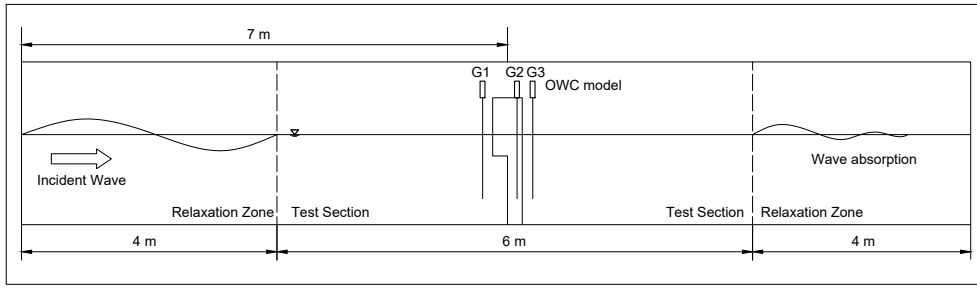
Figure 1: Numerical setup of the numerical wave tank. Not drawn to scale. G_1, G_2 and G_3 **are the three locations where waves are measured by wave gauges.**
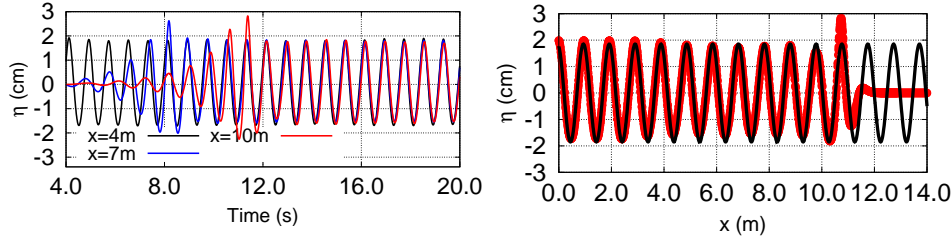
Figure 2: Left: Times series of the waves measured at three locations in the numerical wave tank with x **being the distance from the left end of the numerical wave tank. Right: A snapshot of the waves in the numerical wave tank with red line being the simulation result and the black line being the theoretical Airy wave solution.**

Comparisons between the time series of the measured and simulated relative pressure and the time series of the measured and simulated surface displacements at three locations for monochromatic waves are shown in the left panel in Fig. 3 for wave period= 0.8 s, wave height= 0.04 m and water depth=0.31 m and in the right panel of Fig. 3 for wave period = 1.3 s, wave height = 0.04 m , and water depth= 0.29 m. The simulated and measured surface displacements agree very well at all three locations. The relative pressure of the air in the pneumatic chamber, which is basically the pressure drop across the PTO, can be modeled by

$$p(t) = \frac{1}{2} c_f \rho_a |u)t)|u(t) + \rho_a L_g \frac{du(t)}{dt} \qquad (1)$$

where $u(t)$ is the air velocity, ρ_a the air density, c_f a quadratic loss coefficient, and L_g an empirical length scale related to inertia effect. For sinusoidal waves, the relative pressure in the air chamber is not sinusoidal because of the nonlinear PTO (Eq. 1) used in the study. As shown in Fig. 3, the numerical model can simulate the relative pressure of the air inside the pneumatic chamber very well, implying that the numerical stimulation can simulate the behavior of the nonlinear PTO very well.

The left panel of Fig. 4 shows an example of the simulated velocity of the air and the air-water interface. Even though the wave height is just 4 cm, the maximum velocity of the air through the PTO device can reach as high as 12 m/s. The fine mesh and high velocity speed in the vicinity of the PTO requires very small time step. Therefore, the bottleneck in the 3D simulation of an OWC device is the air flow through the PTO.

The right panel of Fig. 4 shows an example of the simulated vorticity in water. In this example, the Keulegan–Carpenter number, which can be defined by $KC = UT/D$ with D being the diameter of the OWC chamber, T the wave period and U a velocity scale. If we take $U = \omega H/2$, we have $KC = \pi H/D$. For H =0.04 m and T=1 s, KC=1.0, which means the vortex does not shed from the OWC and its support structure. This is confirmed by the computed vorticity distribution shown in right panel of Fig. 4, which shows that the vortex shedding mainly occurs at the lower tip of the OWC skirt and weak vortex shed from the sharp edge of the support structure.

4   Conclusions

An OpenFOAM-based numerical wave tank was used to study a three-dimensional OWC device supported by a C-shaped structure. The numerical results were able to reproduce the measured surface displacements around the OWC device and inside the pneumatic chamber very well. The model can also simulate the relative pressure of the air inside the pneumatic chamber very well, suggesting that numerical model can provide satisfactory modeling of the behavior of the nonlinear PTO used in the physical model tests. For the particular OWC device examined here, the vortex shedding occurs mainly at the low tip of the OWC chamber skirt. Study of how the vortex shedding affect the wave energy extraction efficiency is on the way and will be reported elsewhere.
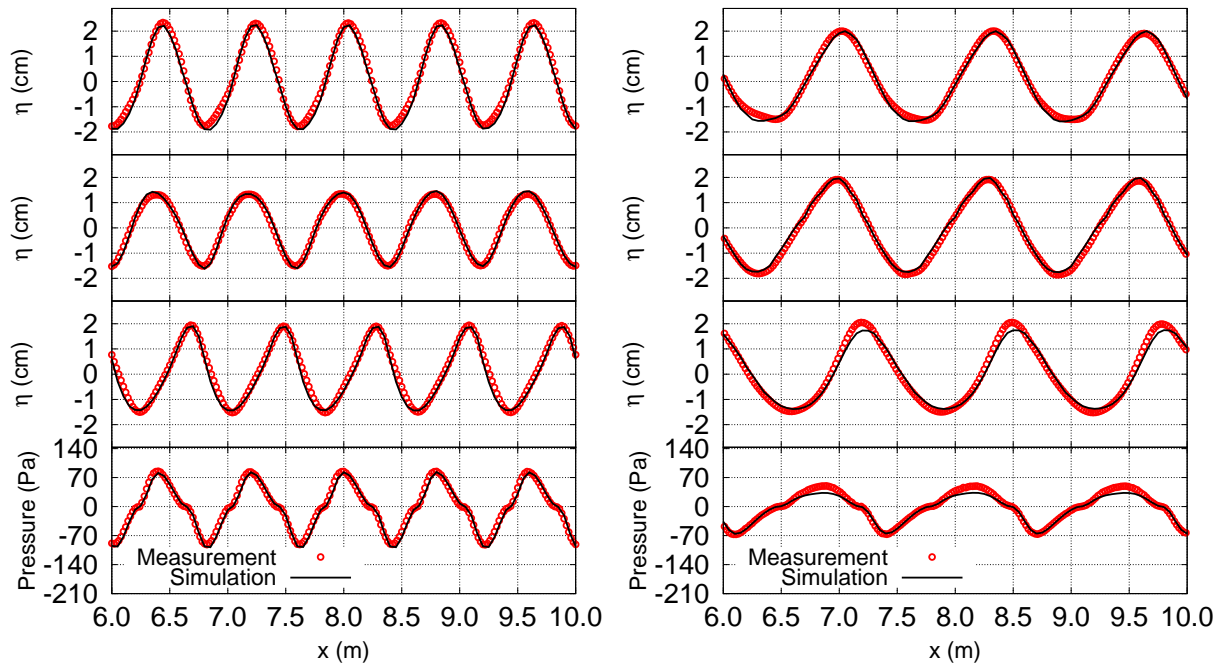
Figure 3: Comparisons between the simulated and measured surface displacements at three locations and the air pressure for T =**0.8 s (left) and** T**=1.3 s (right). From top to bottom, the plots show the measured surface displacements at the locations** G_1**,** G_2 **and** G_3**, and the relative air pressure. The circles are measurement and the solid lines are numerical simulations.**
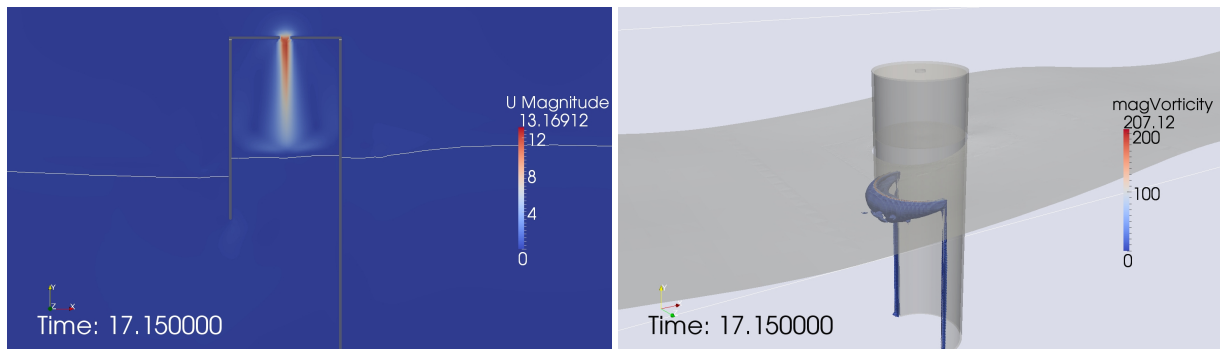
Figure 4: Left: an example of the simulated air velocity and the air-water interface. Right: An example of the simulated vorticity. For both panels. T =**1.0s,** H =**0.04 m, and** h =**0.31 m.**

Acknowledgments

References

[1] A. Iturrioz, R. Guanche, J. L. Lara, C. Vidal, and I. J. Losada, "Validation of OpenFOAM® for Oscillating Water Column three-dimensional modeling," *Ocean Engineering*, vol. 107, pp. 222–236, 2015.

[2] N. G. Jacobsen, D. R. Fuhrman, and J. Fredose, "A wave generation toolbox for the open-source CFD library: OpenFoam," *International Journal for Numerical Methods in Fluids*, vol. 70, no. 9, pp. 1073–1088, 2012.

[3] C. Xu, Z. Huang, and Z. Deng, "Experimental and theoretical study of a cylindrical oscillating water column device with a quadratic power take-off model," *Applied Ocean Research*, vol. 57, pp. 19–29, apr 2016.

APPLICATION OF STATIC LOADING TESTS TO STEEL PIPE PILES WITH LARGE DIAMETERS IN CHINA OFFSHORE WIND FARMS

XIAOJUAN LI[1,2], GUOLIANG DAI[3], WEIMING GONG[4], MINGXING ZHU[5]

[1]*School of civil engineering, Southeast University, li2942@purdue.edu*

[2]*Lyles school of civil engineering, Purdue University, li2942@purdue.edu*

[3] *School of civil engineering, Southeast University , daigl@seu.edu.cn*

[4]*School of civil engineering, Southeast University, 769301761@qq.com*

[5] *China Energy Engineering Group Jiangsu Power Design Institute Co., LTD, zhumingxing@jspdi.com.cn*

In China, wind energy is regarded to be an important source of clear energy in recent years, which will generate 17 % of renewable sources by 2030 with the existing capacity of 10.2 GW by 2015 and predicted to be 150 GW by 2030[1]. numbers of Offshore wind farms are under construction or to be built in coastal areas. steel pipe pile with large diameters (more than 1.5 m) are frequently observed in these projects. In this paper, field static loading tests results will be introduced in three offshore wind farms in China. These loading test methods include axial compression load test (test A) and uplift loading test (test B) [2]. The main information of test piles in these projects is introduced in table 1.

Table 1 parameters information of test piles in three projects field tests

Project name	Pile name	Pile length(m)	Pile diameters (m)	L/D	Test method
Project 1	ZK01	71.5	2.0	35.8	A and B
	ZK28	77.5	2.0	38.8	A and B
Project 2	1-9	46.6	1.8	25.9	A and B
	2-9	39.4	1.8	21.9	A and B
Project 3	S1	93.7	2.8	33.5	A and B
	S2	93.7	2.8	33.5	A and B

In the above three projects, both axial compression load test (A) and uplift loading test (B) were conducted at the same piles. These 6 steel pipe piles are with diameters of 1.7m to 2.8m and length of 39.4m to 93.7m, the measurements were taken to record the behaviour of these piles throughout loading test. Fibre optic sensors were used along these pile body to measure the strain change with loading steps, then the compressing and uplift ultimate shaft resistance of piles at each soil layer can be given. Vertical capacities from two kinds of loading test of each pile were compared, and soil resistance at each layer were calculated. The positive shaft resistance from top loading tests and negative ones from uplifting loading tests were given to find out the conversion factor γ (the ratio of positive shaft resistance to the negative shaft resistance) of different soil layers of each piles.

Project 1

this wind farm project is located in the coast area of Jiangsu province, the soil profile consists of marine clay and sand. the relative parameters are shown in table 1, the vertical capacity results are shown in fig.1[3] and fig.2, the shaft resistance of each layer is shown and table 2 and table 3, respectively.

(a)   **(b)**

Fig.1 ZK01 (a) the downward load-displacement of pile top from test A and (b) the uplift load-displacement of pile top from test B

| (a) | (b) |

Fig.2 ZK28 (a) the downward load-displacement of pile top from test A and (b) the uplift load-displacement of pile top from test B

From fig.1, the vertical compressing capacity of ZK01is 32800kN, the total shaft resistance is 31076kN, the uplifting capacity of ZK01 is 22800kN; the vertical compressing capacity of ZK28 is 34850kN, the total shaft resistance is 33260kN, and the uplifting capacity of ZK28 is 22000kN.the ration of total positive shaft resistance and negative one is 0.73 and 0.66.

Table 2 the shaft resistance of ZK01 from compress load test and uplifting load test

Elevation of layer top (m)	Elevation of layer bottom (m)	Thickness of layer (m)	Soil type	Compressing shaft resistance (kPa) A	Uplift shaft resistance (kPa) B	B/A
-10.1	-12.72	2.62	mud	23	11	0.48
-12.72	-20.62	7.90	Silt clay with mud	54	20	0.37
-20.62	-23.62	3.00	Silt sand	67	36	0.54
-23.62	-31.82	8.20	Silt sand	107	69	0.64
-31.82	-41.62	9.80	Silt clay with mud	105	81	0.77
-41.62	-57.92	16.30	Silt clay	94	77	0.82
-57.92	-59.62	1.70	Silt clay	95	79	0.83
-59.62	-63.70	4.08	Silt sand	128	101	0.79

Table 3 the shaft resistance of ZK28 from compress load test and uplifting load test

Elevation of layer top (m)	Elevation of layer bottom (m)	Thickness of layer (m)	Soil type	Compressing shaft resistance (kPa) A	Uplift shaft resistance (kPa) B	B/A
-10.5	-11.87	1.37	Silt sand	32	9	0.28
-11.87	-19.77	7.90	Silt clay with mud	40	12	0.30
-19.77	-23.07	3.30	Silt sand	63	31	0.49
-23.07	-30.07	7.00	Silt sand	77	44	0.57
-30.07	-40.17	10.10	Silt clay with mud	80	53	0.66
-40.17	-52.17	12.00	Silt sand	103	66	0.64
-52.17	-56.77	4.60	Silt clay	111	81	0.73
-56.77	-64.17	7.40	Silt sand	135	93	0.69
-64.17	-66.07	1.90	Silt clay	97	64	0.66
-66.07	-69.60	3.53	Silt	114	77	0.68

From table 2 and table 3, it is obvious to see that the ultimate resistance from uplift loading tests are lower than that from compressing loading test. The ration of their shaft resistance is range from 0.28 to 0.83.

Project 2

The offshore wind farm is located in the sea are of Fujian province, two piles (1-9 and 2-9 in table 1) conducted with test A and test B at each pile. The vertical capacity is shown in Fig.3 and Fig.4, and the shaft resistance from two loading methods are shown in table 4 and table 5.

(a) **(b)**

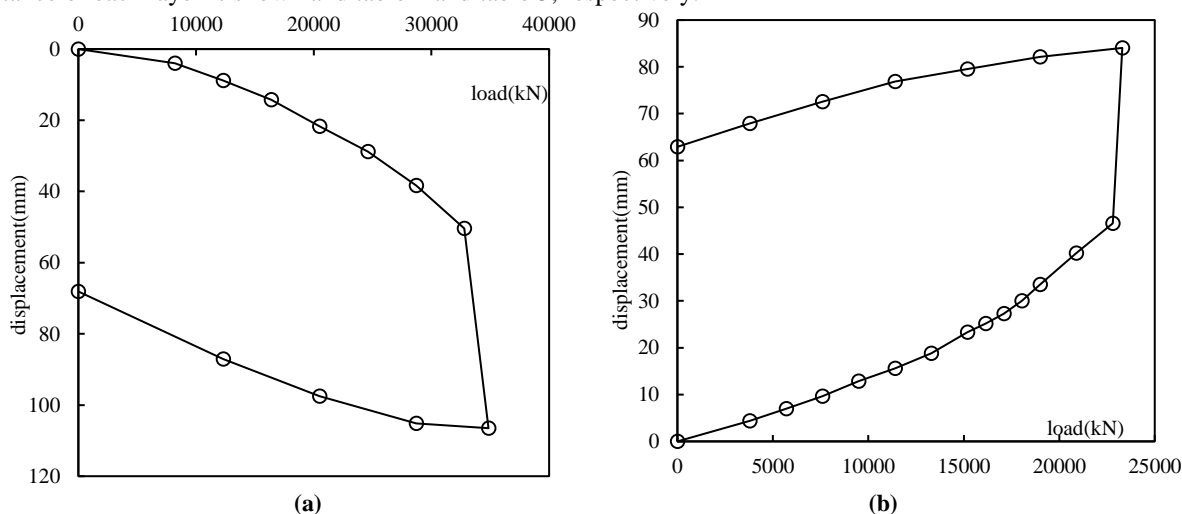**Fig.3 1-9 (a) the downward load-displacement of pile top from test A and (b) the uplift load-displacement of pile top from test B**
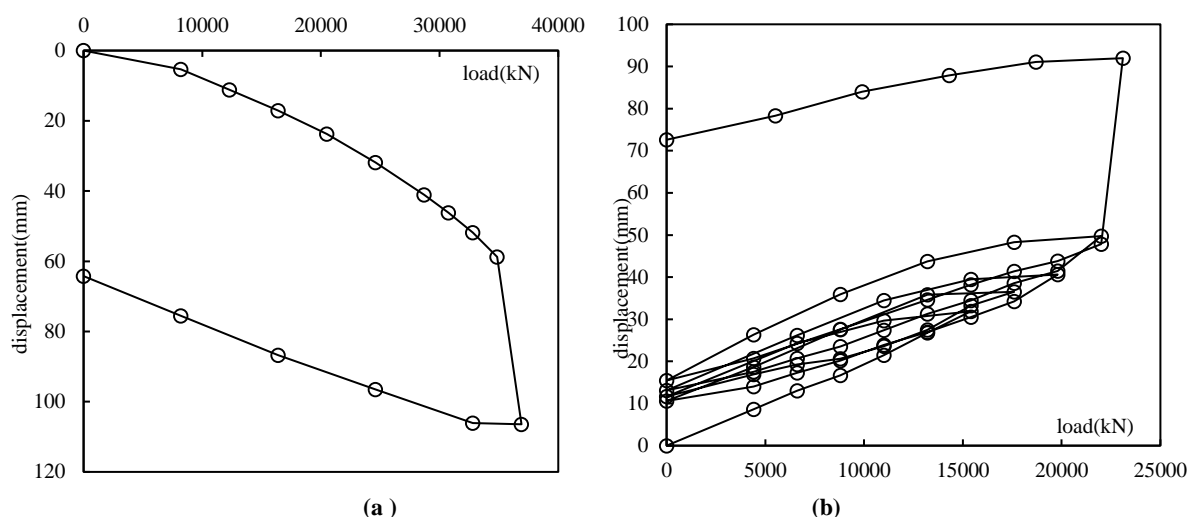

(a) **(b)**
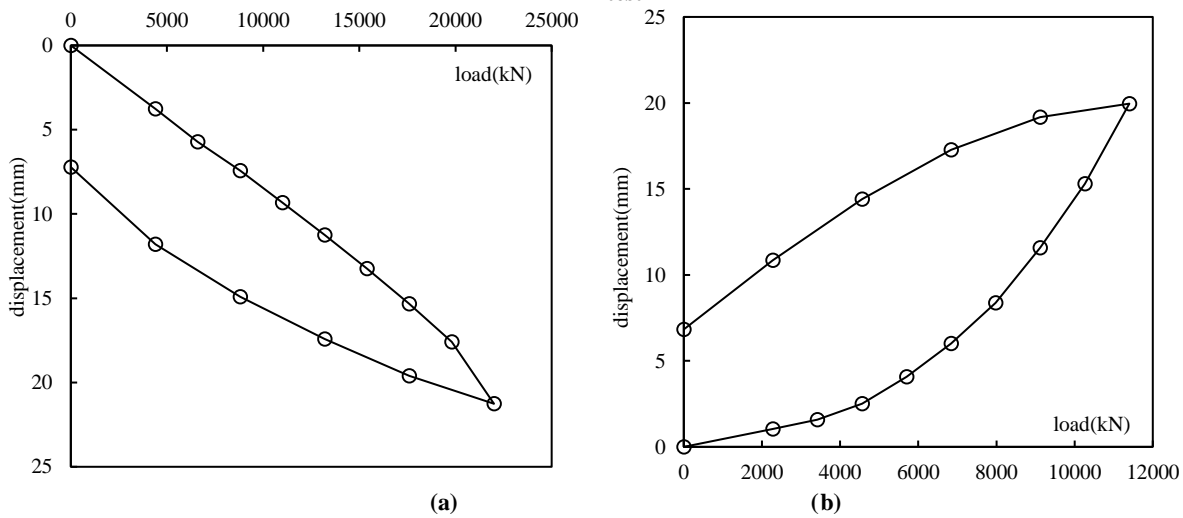
Fig.4 2-9 (a) the downward load-displacement of pile top from test A and (b) the uplift load-displacement of pile top from test B

From Fig.3, the vertical compressing capacity of 1-9 is more than 22000kN, the total shaft resistance is 17902kN, the uplifting capacity of 1-9 is 11400 kN; the vertical compressing capacity of 2-9 is more than 22000 kN, the total shaft resistance is 6941 kN, and the uplifting capacity of ZK28 is 11400kN.

Table 4 the shaft resistance of 1-9 from compress load test and uplifting load test

Elevation of layer top (m)	Elevation of layer bottom (m)	Thickness of layer (m)	Soil type	Compressing shaft resistance (kPa) A	Uplift shaft resistance (kPa) B	B/A
-4.8	-12.6	7.8	Fine sand	71.2	48.1	0.68
-12.6	-16.2	3.6	Medium sand	77.5	53.4	0.69
-16.2	-21.6	5.4	clay	63.1	44.8	0.71
-21.6	-22.6	1.0	medium coarse sand	92.9	62.1	0.67
-22.6	-27.0	4.2	Fully weathered granite	122.5	72.3	0.59
-27.0	-43.3	16.3	strongly weathered granite	145	77.4	0.53

Table 5 the shaft resistance of 2-9 from compress load test and uplifting load test

Elevation of layer top (m)	Elevation of layer bottom (m)	Thickness of layer (m)	Soil type	Compressing shaft resistance (kPa) A	Uplift shaft resistance (kPa) B	B/A
-6.1	-14.5	8.4	medium coarse sand	70.7	59	0.83
-14.5	-18.5	4.1	Fully weathered granite	116.9	86.9	0.74
-18.5	--31.00	12.5	strongly weathered granite	145	107.8	0.74

From table 4 and table 5, it is obvious to see that the ultimate resistance from uplift loading tests are lower than that from compressing loading test. The ration of their shaft resistance is range from 0.53to 0.83.

Project 3

The offshore wind project is also located in the coast area of Jiangsu province, the soil profile in this area is also sand and clay. Two test piles (S1 and S2, shown in table 1) were conducted with compression load test and uplift load test at each of same piles. The vertical capacity curves are shown in Fig.5 and Fig.6, and the shaft resistance from two loading methods are shown in table 6 and table 7.
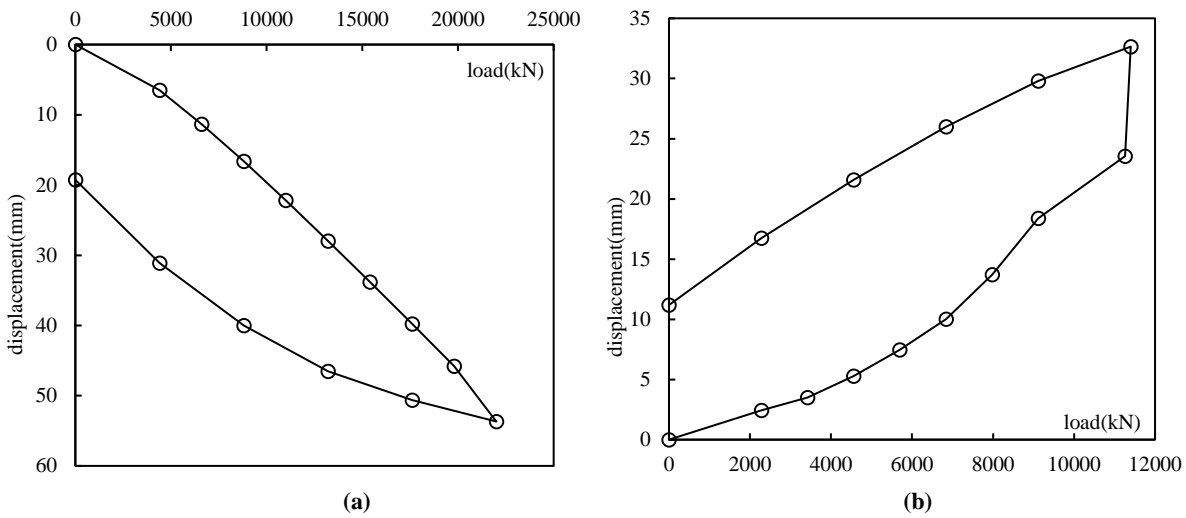

| (a) | (b) |
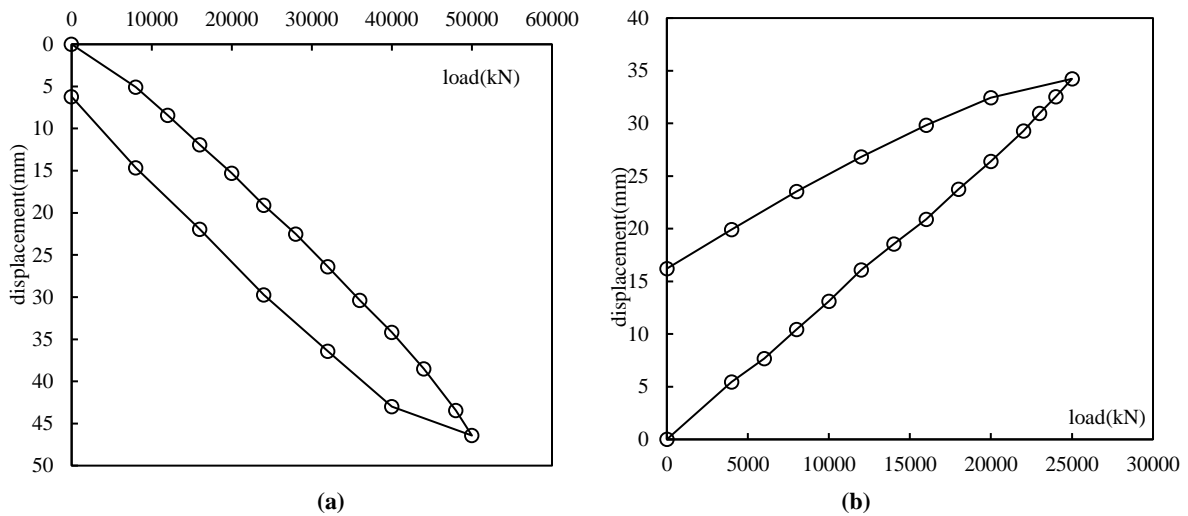
Fig.5 S1 (a) the downward load-displacement of pile top from test A and (b) the uplift load-displacement of pile top from test B

| (c) | (d) |
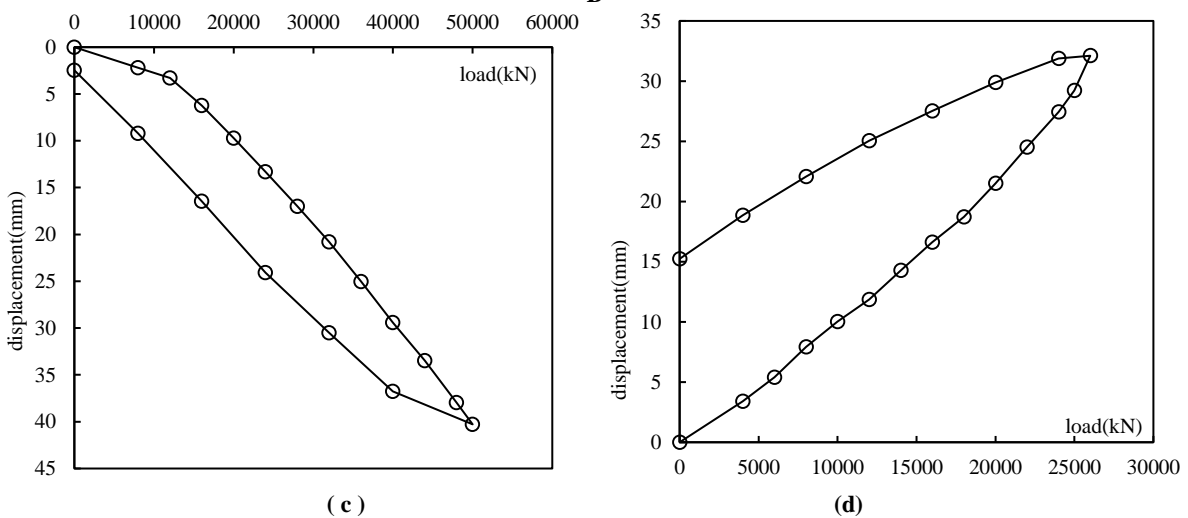
Fig.6 S2 (a) the downward load-displacement of pile top from test A and (b) the uplift load-displacement of pile top

Table 6 the shaft resistance of S1 from compress load test and uplifting load test

Elevation of layer top (m)	Elevation of layer bottom (m)	Thickness of layer (m)	Soil type	Compressing shaft resistance (kPa) A	Uplift shaft resistance (kPa) B	B/A
-13.5	-27.7	14.2	Silt clay with mud	22	11	0.50
-27.7	-31.2	3.5	Silt clay	56	28	0.50
-31.2	-60.5	29.3	Silt sand	72	36	0.50
-60.5	-73.5	13.0	Fine sand	101	50	0.49
-73.5	-85.5	12.0	Fine sand	119	60	0.50

Table 7 the shaft resistance of S2 from compress load test and uplifting load test

Elevation of layer top (m)	Elevation of layer bottom (m)	Thickness of layer (m)	Soil type	Compressing shaft resistance (kPa) A	Uplift shaft resistance (kPa) B	B/A
-13.50	-27.70	14.20	Silt clay with mud	22	11	0.50
-27.70	-31.20	3.50	Silt clay	56	28	0.50
-31.20	-60.50	29.30	Silt sand	72	36	0.50
-60.50	-73.50	13.00	Fine sand	101	51	0.50

| -73.50 | -85.50 | 12.00 | Fine sand | 121 | 61 | 0.50 |

From table 6 and table 7, it is obvious to see that the ration of their shaft resistance is range from 0.49 to 0.50.

In conclusion, the ratio of positive shaft resistance to the negative shaft resistance of different soil layers of each piles ranged from 0.45 to 0.83, which are lower than these suggested by the Code or in onshore projects [4-7]. The values of conversion factor and plugging effect coefficient in this paper can be used in offshore wind farm projects and provide reference to engineering practice.

Keywords: Static Loading Tests; Steel Pipe Piles; Large Diameters; Offshore Wind Farms

References
[1] Haiderali AE, Madabhushi, GSP : Evaluation of Curve Fitting Techniques in Deriving p–y Curves for Laterally Loaded Piles, Geotechnical and Geological Engineering, 2016, 34(5), 1453-1473.

[2] Paikowsky, SG, and Whitman RV: The effects of plugging on pile performance and design. Canadian Geotechnical Journal, 27(4), 429-440. J. D. Anderson, Jr, Modern Compressible Flow: With Historical Perspective, 3rd ed. New York: McGraw-Hill, 2003.

[3] Pan, D., A. Lucarelli, and Z. Cheng: Field Test and Numerical Analysis of Monopiles for Offshore Wind Turbine Foundations. Geotechnical and Structural Engineering Congress 2016. 2016.

[4] Code for design of ground base and foundation of highway bridges and culverts JTG D63-2007, Beijing, China Communications Press,2007.

[5] Code for soil foundations of port engineering JTS 147-1-2010, China Communications Press,2010

[6] DAI Guo-liang,GONG Wei-ming. Field test of friction resistance and negative skin friction of cast-in-situ piles .Building Structure, 2009, 39 (2):58-60.

[7] SHI Pei-dong, GU Xiao-lu.Pile and Pile foundation Handbook .China Communication Press, 2012.2:59-60.

A NUMERICAL SLOSHING ANALYSIS FOR ASSESSMENT OF LNG FUEL TANK USING OPENFOAM®

HOTAK OK[1], JIWON CHOI[2], KWANGMIN LEE[3], JINHO YANG[4]
[1]Hyundai Heavy Industries Co., Ltd., okhotak@hhi.co.kr
[2]University of Ulsan, zenith0804@ulsan.ac.kr
[3]Hyundai Heavy Industries Co., Ltd., kwangminlee@hhi.co.kr
[4]Hyundai Heavy Industries Co., Ltd., aceyang@hhi.co.kr

1. Introduction

The IMO (International Maritime Organization) has been promoting the reduction of pollutant emissions such as carbon dioxides, sulphur oxides and nitric oxides. And the environmental regulations are continuously strengthening and that makes the paradigm shift in the shipbuilding industry. Especially, there has been significant interest in the 2020 sulphur cap which means that ships will be banned from using fuel with sulphur content above 0.5% from January 1, 2020. As some shipping industries have decided to use LNG as fuel to satisfy the regulation, the needs for the LNG fuelled ships are increasing. However, in the fuel tank for LNG, the filling level changes during the ship's operation and the sloshing can be stronger at the specific filling level. As a result, the sloshing causes loads continuously on the wall of tank during the ship's lifetime.

There are several types for LNG tank and many shipowners choose the membrane type for cost effect. But the membrane tank is structurally weak because stiffeners are not installed enough to reduce costs. So, the sloshing tank is assessed strictly. For the assessment of sloshing tank, the CFD analysis is useful tool at the stage of initial tank design because experiment takes a lot of time and cost. However, there are still many difficulties in the numerical simulations since the sloshing has highly unsteady and chaotic behavior. And the effects of spatial and temporal discretization on pressure prediction are not clear. So, in the present study, we investigated numerical methods based on various versions of the OpenFOAM® to find practical procedure for sloshing CFD analysis.

2. Validation of Numerical Method

We first tested the feasibility of the current methods for the sloshing problem by comparing the predicted results with the data measured by Hinatsu[1]. The validation case has the water level of 20% and oscillating rolling motion with period 1.85 sec and 10-degree amplitude. The mesh was generated by using the blockMesh utility to form cells as close to the cube as possible. The computational domain consisted of 144,000 cells. Figure 1 shows the experimental set up and mesh arrangement.
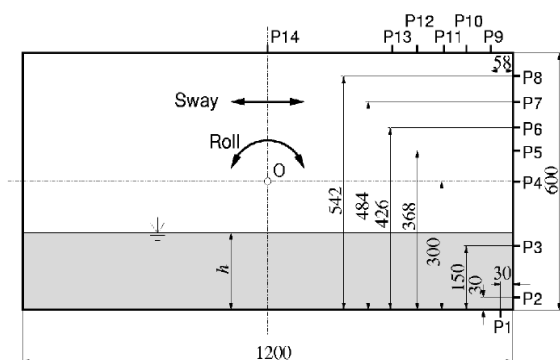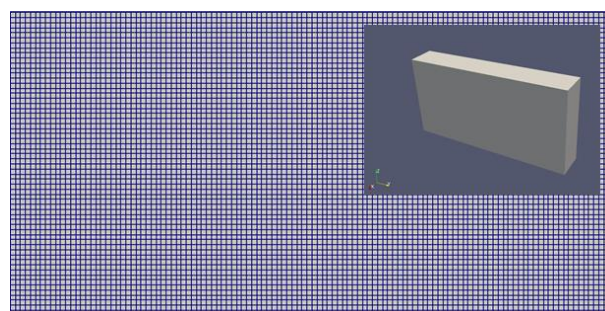
(a) Experimental setup   (b) Mesh arrangement
Figure 1: Experimental setup (left) and mesh arrangement for numerical simulations (right)

2.1. Numerical Method

We used the 2nd order schemes for spatial discretization and the Euler scheme was used for temporal discretization with adjustTimeStep. It is important to predict the free surface precisely and efficiently in sloshing simulations. To do this, we first used interDyMFoam, an incompressible interface capturing solver using VOF with dynamic mesh, which is basically provided in the OpenFOAM® where the 2.1.1 version was tested. We also employed OpenFOAM-v1712,

supported by ESI-openCFD group, to test the latest VOF scheme, isoAdvector[2] for sloshing problems. Since the OpenFOAM-v1712 does not provide on interface capturing solver with dynamic mesh using the isoAdvector yet, we created one with dynamic mesh, so called interIsoDyMFoam. Figure 2 shows predicted and measured pressure over time at the sensor P2. We can see that the present methods well predicted the periodic pressure change at corresponding position. However the 2.1.1 version tended to under-estimated the peak pressure while v1712 overly predicted. It is worthy to note it is not possible to directly compare the predicted and measured pressures in numerical simulations and experiments respectively, but statistical properties of the pressure changes are much more important information in the assessment of tank sloshing.
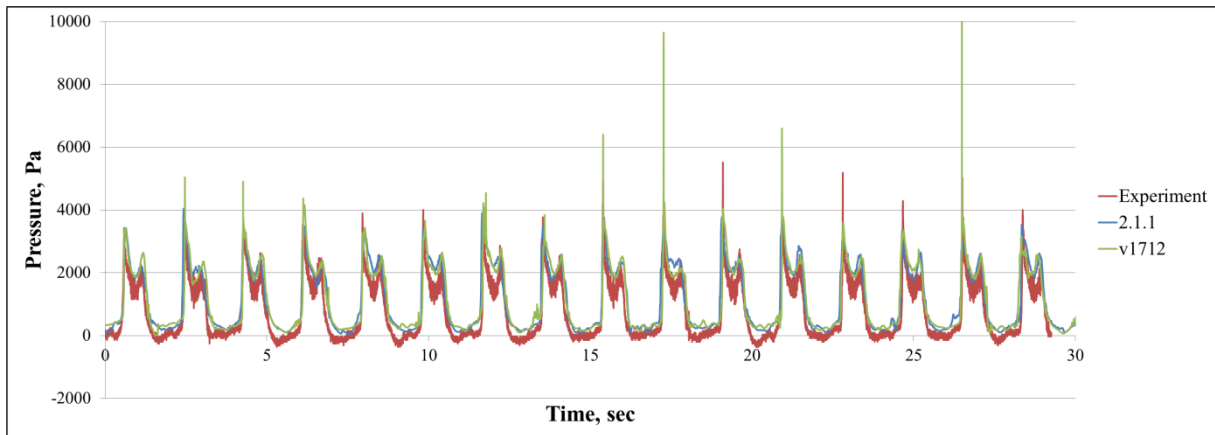
Figure 2: Comparison of predicted and measured pressure at sensor P2

We found some interesting points in a long term simulation. Figure 3 compares the predicted pressures from two different versions of the OpenFOAM. As compared, the abnormal pressure was predicted from 100 seconds. We are currently working on this part and will be presenting the results of research at the OpenFOAM Workshop.
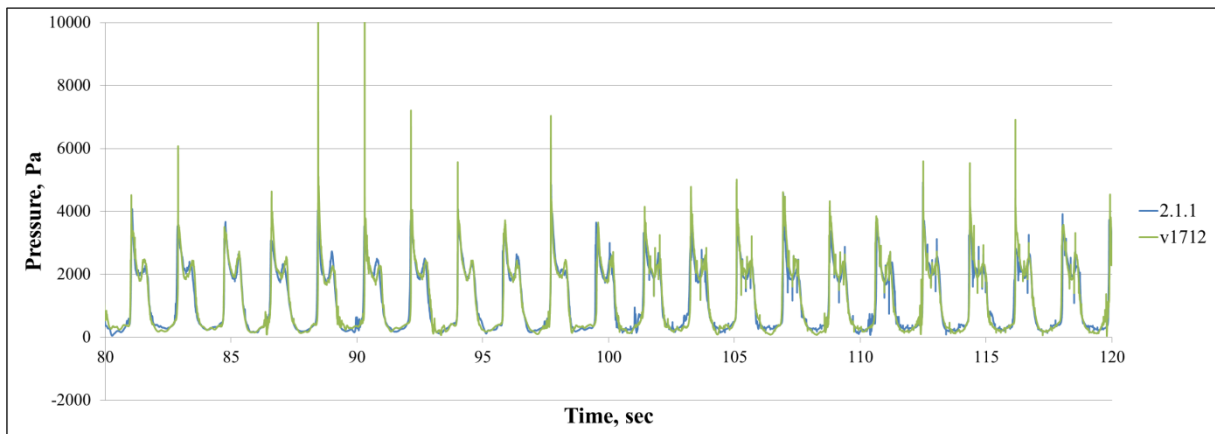
Figure 3: Comparison of predicted pressures near 100 seconds at sensor P2

2.2. Parameter Study

We compared the results with various values of the adjustTimeStep. The adjustTimeStep option adjusts the time step size to ensure the CFL number to be less than the specified value at every time step. Here, we can control the values of 'Max CFL' and 'Max Alpha CFL'. So, we compared the results by changing these two parameters. And the sloshing analysis is ambiguous to determine whether the flow itself is laminar or turbulent. We assessed the effect of the turbulence model as well. Two turbulence models were used, k-epsilon model and k-omega SST model. We will cover this study in presentation.

3. Numerical Assessment of LNG Tank

We selected a tank considered to be safe as the reference and performed an analysis on a new tank shape numerically and experimentally. Then we compare the results with the reference tank to see if the new tank will be safe. In the numerical investigation, the Aquarius has been used and the safety of the sloshing tanks has been assessed is evaluated

by means of a statistical method [3]. In the present study, we compared the statistical properties obtained from the OpenFOAM-2.1.1 and v1712 to those of Aquarius. We have selected a tank of 150K LNG Carrier as the reference tank that has been operated safely for 10 years and assessed the safety of a tank of 177K LNG Carrier. Please note that the tank shapes could not be presented due to security regulation.

Simulations were carried out on a 2D tank in model scale over the physical time corresponding to 30 hours in the real scale. We tracked the peak pressures after the simulation and compared the average of the three top peak pressures and the maximum value of the peak pressures to the reference tank. The results are shown in Table 1. As we can see, the results from 2.1.1 showed similar values and tendency to the Aquarius while the v1712 predicted overly estimated results relative to the Aquarius.

Table 1: Pressure ratio of computational results against 150K LNG Tank

Tank	Filling Level	Aquarius		2.1.1		v1712	
		Max.	Top 3 Ave.	Max.	Top 3 Ave.	Max.	Top 3 Ave.
177K LNG Tank	All	1.06	1.13	1.01	1.03	1.43	1.23
	2.75 m	0.97	0.87	0.83	0.95	0.67	0.74
	70% H	1.06	1.13	1.33	1.16	1.43	1.23
	80% H	0.75	0.93	1.01	0.98	0.62	0.84
	95% H	1.00	0.74	1.15	0.98	1.01	1.03

4. Automation System

It is a time consuming task to create a new simulation case using the OpenFOAM®. In the sloshing problems, users may have difficulties in inputting mandatory data such as filling level, motion, and locations of pressure sensors, etc. Since more than 200 cases are required to assess a LNG tank and the resultant pressure data is too huge to be directly interpreted, it will be helpful to get an automatic post-processing code. We are developing an automation program for sloshing CFD analysis. Although this is not accomplished yet, we can share some information about the automations system in the workshop.

5. Conclusion

Various OpenFOAM versions have been tested to see their feasibility for assessing sloshing tanks. The VOF solvers provided by the OpenFOAM predicted reasonable solutions of sloshing problems when they were compared to the experimental data. Due to the extremely transient and chaotic nature of the sloshing problem, the pressure predicted in a numerical simulation cannot be compared directly with the measured experimental data. Instead, we compared statistical characteristics of a tank to the reference tank. The numerical simulations for the sloshing tank assessment were compared to those of the Aquarius of Lloyd's Register, which has long been used for sloshing simulations in HHI. The 2.1.1 showed comparative solutions to the Aquarius while v1712 with isoAdvector showed quite overly estimated results. We will conduct more strict numerical tests to verify the present numerical assessment procedure of a sloshing tank and it will be discussed in the presentation.

References

[1] J. Roenby, H. Bredmose, and H. Jasak: A Computational Method for Sharp Interface Advection, Royal Society Open Science, Vol. 3, No. 11, Nov. 2016. DOI: 10.1098/rsos.160405, 2016

[2] M. Hinatsu: Experiments of two-phase flows for the joint research, in Proceedings of SRI-TUHH mini-Workshop on Numerical Simulation of Two-Phase Flows, National Maritime Research Institute & Technische Universitaet Hamburg, NMRI, 2001.

[3] Aquarius: a CFD-based software package, Lloyd's Register

NUMERICAL SIMULATION OF ADDED RESISTANCE IN HEADING AND OBLIQUE WAVES USING OPENFOAM

ZHAN JUNHUA, KUANG XIAOFENG

China Ship Scientific Research Center, zjh_702@163.com

Introduction

When a ship navigates in a seaway, the ship's forward speed decreases, compared to that in calm sea, because of added resistance due to winds, waves, rudder angle, and so forth. The magnitude of added resistance is about 15~30% of calm-water resistance. An accurate prediction of added resistance is important in the propulsion power design of a ship. Moreover, in recent years, discussions at the International Maritime Organization(IMO) have resulted in the development of an Energy Efficiency Design Index (EEDI) to measure how much greenhouse gas a ship emits, and to restrict greenhouse gas emissions from ships. For these reasons, ship designers should find optimum hull forms to minimize resistance in ocean waves, and pay more attention to the wave added resistance problem.

In the past, many predictions of the resistance and ship motions were based on potential theories, however those methods had limitations when dealing with strong nonlinear factors, such as green water on deck and breaking waves. CFD method based on the solution of RANSE may overcome the limitation of the potential flow theory based method with respect to the effects of water viscosity, wave dispersion, nonlinearity and wave breaking. Consequently, the application of RANSE based CFD method in the ship industry is increasing.

Based on the open source platform OpenFOAM, the paper used a toolbox[1] to generate and absorb free surface water waves, then coupling the regular waves with current to instead of the ship's speeds. a sixDofRigid motion solver has been implemented to predict the ship motions. For oblique wave condition, the paper used towing method to simulate the speeds of the ship model, and used the overset grid to implement the ship motions.

Ship geometry and case conditions

The YUPENG containership is a new standard model which was used by China Numerical Tank as a benchmark hull form to study ship hydrodynamics and China Ship Scientific Research Center have tested on this hull form Fig 1. The YUPENG model with a scale of47.25 is adopted for the CFD computations. Main particulars of the ships are given in Tab.1.

Table 1 YUPENG main particulars

Particular/Unit	Symbol	Model
Length between perpendiculars/m	L_{pp}	4.00
Breadth/m	B	0.5884
Draught/m	T	0.218
Displacement/kg	Δ	370.21
Pitch radius of gyration	K_{yy}/L_{pp}	0.2551
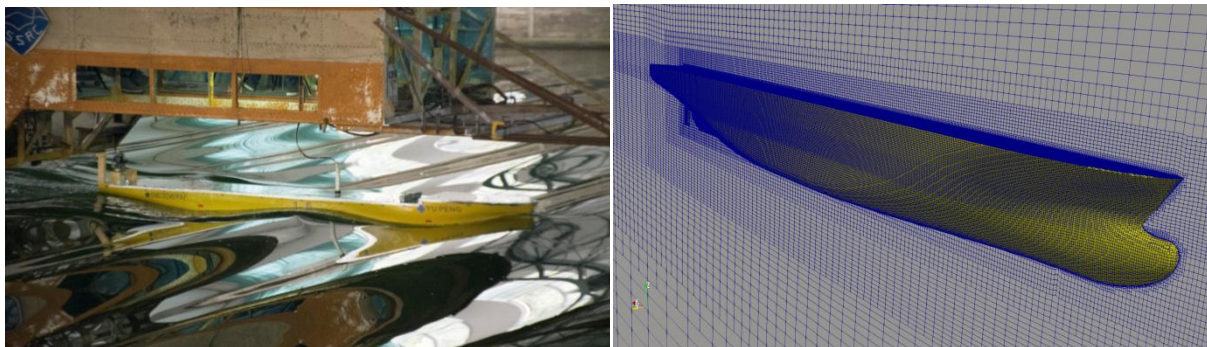
Figure 1: The YUPENG ship model test in heading wave with the speed of 18kn (left) and Mesh used for numerical computations (right).

Numerical methods

The unstructured mesh used in this paper is generated by snappyHexMesh, provided by OpenFOAM. The mesh is illustrated in Fig 1. The calculation domain is $-1.5L_{pp}<x<3.5 L_{pp}$, $0<y<1.5 L_{pp}$, $-2.0L_{pp}<z<1.0L_{pp}$. The total number of cells is around 1.5 million. It should be noted that only half of the ship hull is used in the calculations, thus a 'symmetry' boundary condition can be modified at the center plane boundary to optimize the calculations.

In the wave generation module, the inlet boundary conditions are set to generate heading waves in the research as follows:

$$\zeta(x,t) = a\cos(kx - \omega_e t) \tag{1}$$

$$u(x, y, z, t) = U_0 + a\omega e^{kz}\cos(kx - \omega_e t) \tag{2}$$

$$w(x, y, z, t) = a\omega e^{kz}\sin(kx - \omega_e t) \tag{3}$$

In which, ζ is transient wave elevation; α, ω and k are wave amplitude, wave frequency and wave number, respectively; U_0 is ship speed; $\omega_e = \omega + kU_0$ is encounter frequency in heading waves.

Relaxation zones are implemented to avoid reflection of waves from outlet boundaries and further to avoid waves reflected internally in the computational domain to interfere with the wave maker boundaries. The former obviously contaminates the results, and the latter is found to create discontinuities in the surface elevation at the wave making boundary, which leads to divergent solutions. The present relaxation technique is an extension to that of Mayer *et al*. [2]. A relaxation function:

$$\alpha_R(\chi_R) = 1 - \frac{\exp(\chi_R^{3.5}) - 1}{\exp(1) - 1} \qquad for \quad \chi_R \in [0:1] \tag{4}$$

is applied inside the relaxation zone in the following way

$$\phi = \alpha_R \phi_{computed} + (1 - \alpha_R)\phi_{target} \tag{5}$$

where φ is either **u** or γ. The variation of α_R is the same as in [3]. The definition of χ_R is such that α_R is always 1 at the interface between the non-relaxed part of the computational domain and non-relaxed part of the computational domain and the relaxation zone, as illustrated in Figure 2.
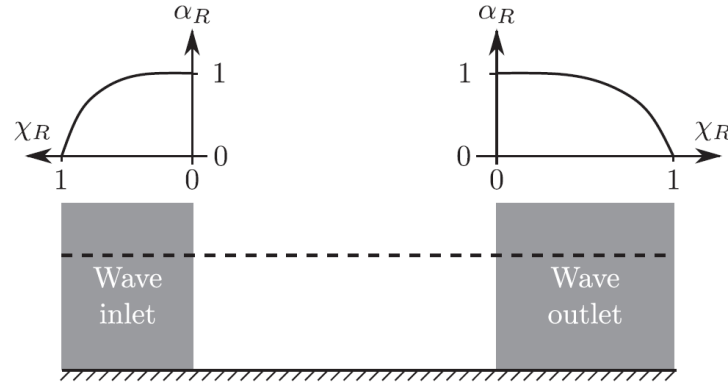
Figure 2: A sketch of the variation of $\alpha_R(\chi_R)$ for both inlet and outlet relaxation zones

Discussion of results

The added resistance is measured as the difference between the mean resistance in waves and the resistance in calm water at the same speed. The results of the added resistance are presented in a nondimensional form by the following equation:

$$C_{aw} = \frac{R_{aw}}{\rho g a^2 B^2 / L_{pp}} \tag{6}$$

in which, C_{aw} is the nondimensional added resistance, also called added resistance coefficient. R_{aw} is the added resistance. ρ is the density of water. g is the acceleration of gravity. a is the wave amplitude.
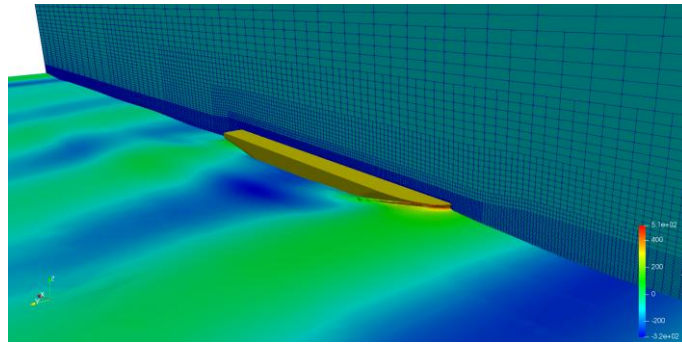
Figure 3: Free surface over an encounter period at λ/L_{pp}=1

References

[1] Niels G. Jacobsen, David Fuhrman ,A wave generation toolbox for the open-source CFD library: OpenFoam

[2] Mayer S, Garapon A. A fractional step method for unsteady free-surface flow with applications to non-linear wave dynamics. *International Journal for Numerical Methods in Fluids* 1998.

[3] Fuhrman DR, Madsen PA, Bingham HB. Numerical simulation of lowest-order short-crested wave instabilities. *Journal of Fluid Mechanics* 2006.

NUMERICAL SIMULATIONS ON THE FLOW AROUND A ROTATING WIND TURBINE

XINRU WANG[1,2], XINLIANG TIAN[1,2], LONGFEI XIAO[1,2], GANG CHEN[1]

[1]*State Key Laboratory of Ocean Engineering, Shanghai Jiao Tong University, Shanghai, China, 200240*

[2]*Collaborative Innovation Center for Advanced Ship and Deep-Sea Exploration, Shanghai, China, 200240*

The vortex–body interaction problem, which characterizes the wake meandering around a quiescent offshore wind turbine, is investigated by numerical simulations. When the blade length of a horizontal-axis wind turbine is limited, blade rotating leads to the vortices, which distributing as the spiral line downstream of the wind wheel. Vortex wake vortices exists in two main areas: the edge of the wind turbine wake and the linear path of the rotation axis (Lee, K.H., 2005). All the computations are carried out using large-eddy simulation (LES) method, based on the open source software-OpenFOAM, and the features of the wake is investigated by the typical flow variables (pressure coefficient, thrust coefficient, torque coefficient, velocity, limiting streamlines of the suction side, vertical structure and FFT) of the instantaneous flow field, all geometrical details of the full-scale turbine structure taken into account. Furthermore, the flow field around a rotating wind turbine is compared with the quiescent one to make out the difference on the tip and hub vortices evolution. Analysis of the calculated instantaneous flow field around a quiescent wind turbine reveals a detailed flow fields with complex geometry, and the vortex in the wake of the turbine behaves quite diversely, where the vortex core is relatively coherent in the wake nearby the turbine blade. A transparent distinction of flow fields is predicted between a rotating wind turbine and a quiescent one, which can be reflected by a detailed streamlined diagram and the charts on some typical flow variables parameters. The results identify for a visual description of the flow field around the offshore wind turbine with micromesh, explore the influence of the blade rotating, and then, summarize the features of the flow fields under the various motion and load status, preparing for further research.

THE HYSTERESIS PHENOMENON BETWEEN FORCE AND MOTION IN VORTEX-INDUCED MOTION OF SEMI-SUBMERSIBLE PLATFORM

SIMING LI, WEIWEN ZHAO, DECHENG WAN

Collaborative Innovation Center for Advanced Ship and Deep-Sea Exploration, State Key Laboratory of Ocean Engineering, School of Naval Architecture, Ocean and Civil Engineering, Shanghai Jiao Tong University, Shanghai, China，Corresponding Author: dcwan@sjtu.edu.cn

Keywords: *Vortex-induced motion; Semi-submersible; hysteresis phenomenon; naoe-FOAM-SJTU*

Introduction

As the increase of the depth of offshore oil and gas exploitation, semi-submersible platforms have been widely used in the field of ocean engineering because of their strong loading capacity. Compared with conventional semi-submersible platform, the Vortex-Induced Motion (VIM) increases significantly due to the increase of the effective excitation length of columns will lead to higher fluctuating pressure caused by the vortex shedding. VIM will impact the fatigue life of mooring and riser systems, therefore, many research of VIM of semi-submersible have been developed[1,2]. Compared with the single-column floating platform such as Spars, the VIMs of semi-submersibles are more complex due to the interaction of vortex shedding between the multiple columns. The VIM phenomenon is caused by periodic fluctuating pressure that arises from alternating vortex shedding from both sides of the structure. Therefore, the motion of VIM is closely related to the fluid force. Studies have shown that unlike the same trend of the lift force coefficient and the transverse motion varies with the reduced velocity of single column floating platform, at 45° current heading, the peak lift force coefficient occurs earlier than the peak transverse motion in VIM of semi-submersible platform. This phenomenon was defined as hysteresis phenomenon[3].

The aim of this paper is to explain the causes of the hysteresis phenomenon by CFD method. Therefore, numerical simulation of the VIM of a semi-submersible platform with two different column shape at 45° current heading have been carried out by an in-house CFD code naoe-FOAM-SJTU.

Numerical Method

In this paper, all numerical simulations were performed with the incompressible finite volume solver naoe-FOAM-SJTU, which is developed on the open source platform OpenFOAM[4]. It applies the Detached Eddy Simulation (DES) method to simulate the three-dimensional flow separation at high Reynolds numbers, and solves the vortex-induced motions coupled with the six-degree-of-freedom motion theory and the moving-boundary spring mesh technique.

A DDES (Delayed Detached-Eddy Simulation) based on the SST (Shear-Stress Transport) model is used to simulate the three-dimensional flow separation at high Reynolds numbers. In the SST model, the turbulent length scale is defined as:

$$l_{k-\omega} = \sqrt{k}/(\beta^*\omega) \tag{1}$$

In the SST-DDES model, the turbulent length scale is modified as follows:

$$l_{DDES} = l_{k-\omega} - f_d \max(0, l_{k-\omega} - C_{DES}\Delta) \tag{2}$$

where $C_{DES} = (1 - F_1)C_{DES}^{k-\epsilon} + F_1 C_{DES}^{k-\omega}$, $f_d = 1 - tanh[(C_{d1}r_d)^{C_{d2}}]$, $r_d = \frac{\nu_t+\nu}{\sqrt{0.5\cdot(S^2+\Omega^2)}\kappa^2 d^2}$

With this modification, the SST-DDES model controls the automatic switching of the RANS and LES methods by l_{DDES} and f_d delays the transformation of the DES model into LES model[5].

The dissipative term in the k-equation can be modified as follows:

$$D_{DES}^k = \beta^* k\omega = k^{3/2}/l_{DDES} \tag{3}$$

Details about the constants in the above equations can be referred to Zhao[6]

In this paper, the governing equations are discretized using the finite volume method. The time discretization is done using second order implicit backward scheme. The convection term is discretized using (LUST) scheme. A second order Gauss integration is used for diffusion term. The hybrid PISO-SIMPLE (PIMPLE) algorithm is used for solving the coupled pressure-velocity equations.

Numerical Simulation

To verify the hysteresis phenomenon is not an accidental, but a common phenomenon in VIM of semi-submersible platforms. A semi-submersible platform with two different column shape were chosen as the computational model in this paper. The computation model is the model in the experiment delivered by Waals et al[7]. The scale ratio λ=1:70. The characteristic dimensions of the platform are shown in Table 1.

Table 1: Parameters of the computational model

Parameter	Prototype	Model
Scale ratio (λ)	1:1	1:70
Draft (T)	35 m	0.5 m
Center-to-center column spacing (S)	56 m	0.8 m
Column width (L)	14m	0.2m
Column height (H)	24.5 m	0.35 m

Another computation model is almost the same, the difference is the column shape is rounded corner and the corner radius is selected based on the research of Chen et al[8], i.e., R=0.031m. Figure 2 shows the computational models in this paper.

(a) R=0m **(b) R=0.031m**
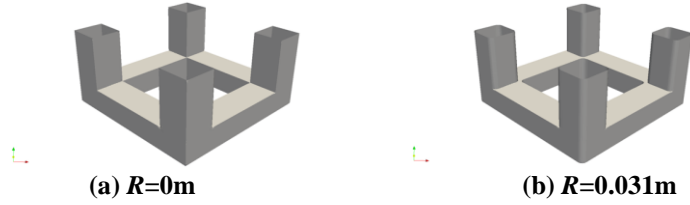
Figure 2: Computational model

Studies have shown that the hysteresis phenomenon occurs when the current heading is 45degree. Thus, the current heading is 45degree current heading and a range of reduced velocities from 4 to 20 have been carried out in this paper. Reduced velocity (Ur) is one of the most important parameters that determines the VIM response, which is defined as:

$$U_r = U/(f_n D) \tag{4}$$

Where U is the flow velocity, fn is the natural frequency of the motion in the transverse direction, D is the characteristic length of the column normal to the current. The computation durations of each test condition are the same for 600 seconds. The computational domain is shown in Figure 3. The centre of the top plane of the platform is the coordinate origin, the size of which is -15L≤x≤40L, -15L≤y≤15L, -9L≤z≤0, where L is the column width.
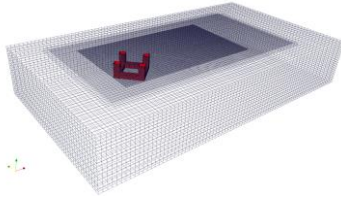
Figure 3: Computational domain   **Figure 4: Global mesh**   **Figure 5: surface mesh**
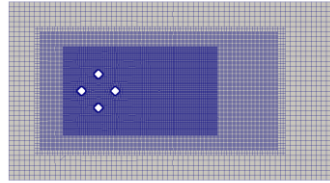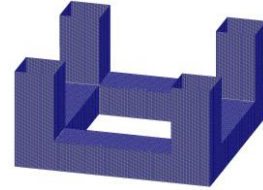
SnappyHexMesh was used to capture the model surface, refine local grid and add the boundary layer. The number of boundary layer is 8. The grid numbers of four column corner radius are about 3.3million. Figure 4 and 5 shows the global and surface mesh.

A uniform flow is set as the flow inlet boundary. For the outlet boundary, the pressure gradient is set equal to 0. The boundary condition on the platform surface is set as no-slip wall. The rest of the boundaries are set as symmetry boundary. Due to the Froude number is small, the free surface effect can be ignored, the top boundary is set as symmetry as well.

Results and Discussion

In this paper, 3 DoF motion (Surge, Sway and Yaw) coupling method is used to solve the platform motion, the effective stiffness of the mooring system is provided by four springs with linear stiffness. Figure 6 presents the time histories and spectra of free decay motions of the transverse direction. Table 2 shows the natural periods from free decay test and the results fits well with Waal et al. and Chen et al.
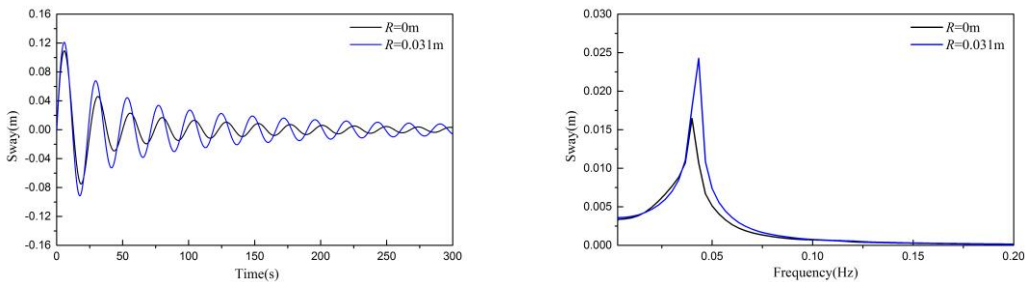
Figure 6: Time histories and spectra of free decay motions of the transverse direction

Table 2: Natural periods from free decay test

Column Corner radius (m)	Natural periods (s)	Surge	Sway	Yaw
R=0	Experiment by Waals et al.(2007)	15.77	24.50	5.85
	naoe-FOAM-SJTU(2018)	15.78	24.99	6.25
	Difference(%)	0.05%	1.97%	6.20%
R=0.031	CFD by Chen et al.(2012)	14.82	23.30	5.50
	naoe-FOAM-SJTU(2018)	14.99	23.06	5.92
	Difference(%)	1.16%	1.04%	7.12%

The motion amplitude of transverse direction is expressed as dimensionless nominal amplitude which is defined as:

$$\text{Nominal } A_y/L = \sqrt{2}\sigma(Y(t))/L \tag{5}$$

where σ(Y(t)) is the standard deviation of Y(t), Y(t) is the time histories of the sway motions.

The non-dimensional lift coefficient C_D are defined as:

$$C_L(t) = 2F_y(t)/(\rho U^2 A) \tag{6}$$

Where $F_x(t)$ and $F_y(t)$ are the time histories of the hydrodynamic forces of in-line and transverse directions, ρ is the fluid density and A is the submerged projected area of the platform normal to the current.

Figure 7 presents the comparison of the nominal amplitudes for the transverse motion of VIM of the platform with two column shapes between the numerical results and those obtained from the model tests. As shown in the figure, the numerical results fit well with the experimental data, indicating that the numerical simulations presented in this study are considered reliable. Figure 8 presents the RMS of lift force coefficient of the VIM of the platform with two column shapes. It can be seen that for the platform with square columns, the peak transverse motion occurs when the Ur=7 and the peak lift force coefficient occurs when the Ur=6, meanwhile, the peak transverse motion occurs at Ur=6 and the peak lift force coefficient occurs at Ur=5 for the platform with rounded corner columns. The peak lift force coefficient does occur earlier than the peak transverse motion. The numerical simulation results verify that the hysteresis phenomenon will occur in VIM of semi-submersible platform under 45° current heading.
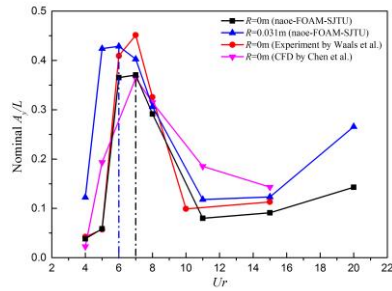
Figure 7: the nominal sway amplitudes   **Figure 8: lift force coefficient**
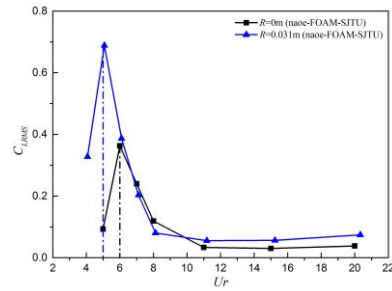
Due to the hysteresis phenomenon doesn't exist in the VIM of single-column floating platform, it may be caused by the interaction of vortex shedding between the multiple columns, therefore, the flow field is been studied by tracing vortices shedding from the upstream column. Take the platform with rounded corner column as an example. Figure 9 presents time histories of Z-vorticity contours on the z/L=-0.5 plane when Ur=5 and 6. The traced vortex is marked in the black circle. The comparison of time histories of transverse motion and lift force coefficient between Ur=5 and Ur=6 during this time period are shown in Figure 10. As shown in the Figures, when Ur=5, the amplitudes of transverse motion are lower and the traced vortex shedding from the upstream column won't impinge on the other side column. In contrast, when Ur=6, the traced vortex impinge on the side column obviously.
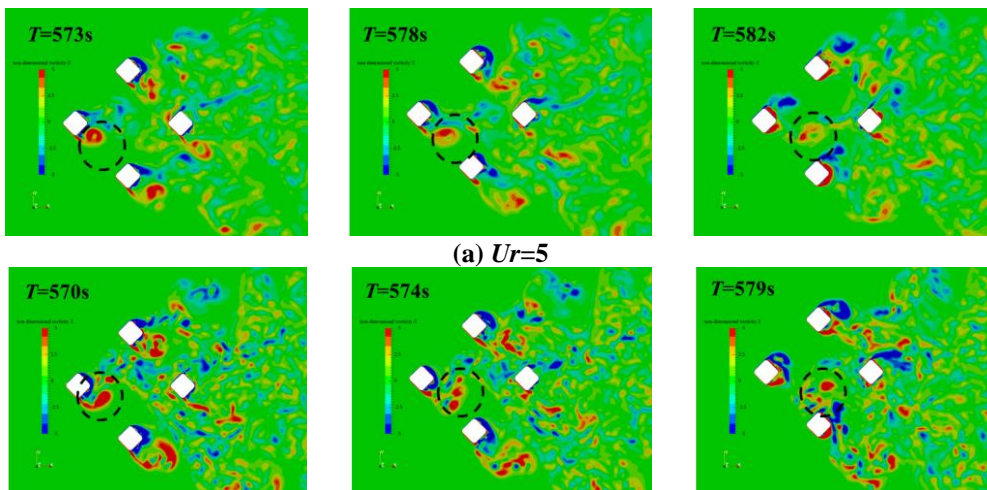
(a) Ur=5

(b) *Ur=6*
Figure 9: Time histories of Z-vorticity contours on the *z/L*=-0.5 plane
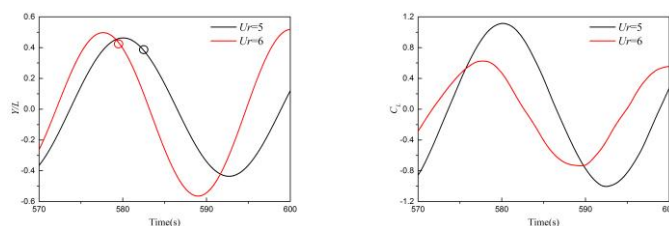
Figure 10: Comparison of time histories of transverse motion and lift force coefficient between *Ur*=5 and *Ur*=6

The impingement will lead to the change of the pressure coefficient distribution on the surface of the side column, further affecting the lift force coefficient of column and platform. The position of the platform at the impingement moment is marked in Figure 10, it can be seen that the movement tendency is the same, thus the tendency of pressure coefficient should be similarly. Figure 11 presents comparison of side column surface pressure coefficient distribution on the *z/L*=-0.5 plane at the impingement moment. As shown in the figure, the surface pressure coefficients of the impingement region decrease significantly because the opposite vortices can be cancelled out.
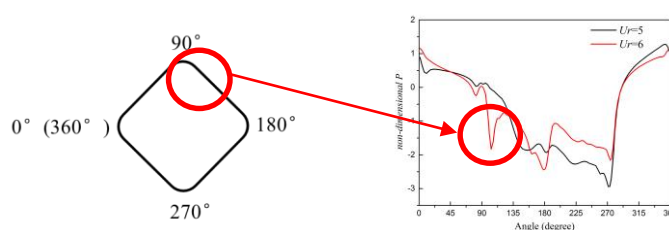
Figure 11: surface pressure coefficient distribution of side column on the z/L=-0.5 plane

Therefore, the hysteresis phenomenon is caused by the interaction of vortex shedding between the upstream and side columns. The impingement of vortices caused by the increase of the amplitudes of transverse motion will decrease the difference of the surface pressure of both column sides, thereby reducing the lift force of columns and the platform.

Acknowledgements

References

[1] J. W. Kim, A. Magee, K. Y. H. Guan. CFD Simulation of Flow-Induced Motions of a Multi-Column Floating Platform. Proceedings of the ASME 2011 30th International Conference on Ocean, Offshore and Arctic Engineering. Rotterdam, The Netherlands, 2011.

[2] M. Y. Liu, L. F. Xiao, H. N. Lu, et al. Experimental Study on Vortex-Induced Motions of a Semi-submersible with Square Columns and Pontoons at Different Draft Conditions and Current Incidences. International Journal of Naval Architecture and Ocean Engineering. 2016, 9(3): 326-338.

[3] Y. Liang, L. Tao. Interaction of Vortex Shedding Processes on Flow over a Deep-draft Semi-submersible. Ocean Engineering. 2017, 141: 427-449.

[4] Z. Shen, H. Cao, H. Ye, et al. The Manual of CFD Solver for Ship and Ocean Engineering Flows: naoe-FOAM-SJTU. Shanghai, China, Shanghai Jiao Tong University, 2012.

[5] P. R. Spalart, S. Deck, M. Shur, et al. A New Version of Detached-Eddy Simulation, Resistant to Ambiguous Grid Densities. Theoretical and Computational Fluid Dynamics, 2006, 20: 181-195.

[6] ZHAO W W, WAN D C. Detached-Eddy Simulation of Flow Past Tandem Cylinders. Applied Mathematics and Mechanics. 2016, 37(12): 1272-1281.

[7] O. J. Waals, A. C. Phadke, S. Bultema. Flow Induced Motions of Multi Column Floaters. Proceedings of the 26th International Conference on Offshore Mechanics and Arctic Engineering. California, USA, 2007.

[8] C. R. Chen, H. C. Chen. Simulation of Vortex-Induced Motions of a Deep Draft Semi-submersible in Current. Ocean Engineering, 2016, 118: 107-116.

POD-DEIM BASED MODEL ORDER REDUCTION FOR SPEED-UP OF FLOW PARAMETRIC STUDIES

MARTIN ISOZ[1]

[1]*Institute of Thermomechanics of the Czech Academy of Sciences,*
Dolejskova 5, 182 00 Prague, Czech Republic,
isozm@it.cas.cz

Current progress in numerical methods and available computational power combined with industrial needs promote the development of more and more complex CFD simulations. However, such models are expensive from the point of view of the data storage and the time necessary for their evaluation. Nevertheless, industrial practice often calls for parametric studies and optimizations performed using these models.

The model order reduction (MOR) is a useful tool for accelerating calculations connected to parametric studies or optimizations of complex systems. In this paper, we consider MOR based on the proper orthogonal decomposition (POD) with Galerkin projection, which is well described for example by Pinnau [1] or Volkwein [2]. The problems arising from the nonlinearities present in the original model are addressed within the framework of the discrete empirical interpolation method (DEIM) of Chaturantabut and Sorensen [3].

The presented reduced order model (ROM) creation technique represents an *a posteriori* approach to MOR [4]. Hence, the solution of the full order model (FOM) has to be available for the ROM creation. Moreover, not only the solution of the system is necessary for the POD-DEIM based model order reduction, the method also needs access to several other data structures, which are internal to the CFD solver and which are usually not readily available.

The open-source CFD library OpenFOAM [5] provides an easy access to the internal data structures needed for the ROM construction. Furthermore, OpenFOAM has been successfully applied to the solution of industrial scale problems in various fields of CFD. In this paper, we provide a link between POD-DEIM based MOR and the OpenFOAM library. Then, we use POD-DEIM based MOR to reduce the computational time necessary for evaluation of parametric studies in OpenFOAM.

Link between POD-DEIM based MOR and OpenFOAM

In order to outline the link between POD-DEIM based model order reduction and the OpenFOAM CFD library, we concentrate solely on the steady-state incompressible Navier-Stokes equations for laminar flow,

$$\nabla \cdot (\mathbf{U} \otimes \mathbf{U}) - \nabla \cdot (\nu \nabla \mathbf{U}) = -\nabla p + \boldsymbol{f}, \quad \nabla \cdot \mathbf{U} = 0, \tag{1}$$

defined on a simply connected bounded domain $\Omega \subset \mathbb{R}^3$ and supplemented with appropriate boundary data. We study the dependence of the solution $[\mathbf{U}, p]$ to the system (1) on some parameter $\mu \in D \subset \mathbb{R}$, i.e. $\mathbf{U} : D \times \Omega \to \mathbb{R}^3$, $p : D \times \Omega \to \mathbb{R}$. To be able to apply the proper orthogonal decomposition and discrete empirical interpolation to construct a reduced order model, the full order model has to have the form of

$$\mathbf{0} = A\boldsymbol{y} + \boldsymbol{b}(\mu, \boldsymbol{y}), \quad \forall \mu \in D, \tag{2}$$

where A is the system matrix, $\boldsymbol{b}(\mu, \boldsymbol{y})$ is the vector of nonlinearities and $\boldsymbol{y}$ is the vector of unknowns.

After the projection of the full order model solution space V on the ℓ-dimensional subspace V^ℓ spanned by the POD basis $\{\boldsymbol{\psi}\}_{j=1}^\ell$ we obtain the following reduced order system,

$$\mathbf{0} = A^\ell \boldsymbol{\eta}^\ell + \boldsymbol{f}^\ell(\mu, \boldsymbol{\eta}^\ell), \tag{3}$$

where we defined the vector-valued mapping

$$\boldsymbol{\eta}^\ell := (\eta_i^\ell)^{\mathrm{T}} : D \to \mathbb{R}^m, \quad i = 1, \dots, \ell, \tag{4}$$

the reduced system matrix

$$A^\ell := (a_{ij}^\ell) \in \mathbb{R}^{\ell \times \ell}, \quad a_{ij}^\ell = \langle A\boldsymbol{\psi}_j, \boldsymbol{\psi}_i \rangle, \tag{5}$$

and the ROM nonlinearities

$$\boldsymbol{f}^\ell := (f_i^\ell)^{\mathrm{T}} : D \to \mathbb{R}^\ell, \quad f_i^\ell(\mu, \boldsymbol{\eta}) = \left\langle \boldsymbol{b}\left(\mu, \sum_{j=1}^\ell \eta_j \boldsymbol{\psi}_j\right), \boldsymbol{\psi}_i \right\rangle . \tag{6}$$

In the above, we denote by $\langle \cdot, \cdot \rangle$ an inner product. The costs connected to the evaluation of the nonlinearities (6) are mitigated via DEIM, see [3].

The continuity equation $(1)_2$ is pressure free. Thus, the linearization and discretization of (1) on a finite volume mesh Ω^h with m cells leads to a saddle point problem,

$$\begin{pmatrix} M & N^T \\ N & 0 \end{pmatrix} \begin{pmatrix} \mathbf{U}^h \\ p^h \end{pmatrix} = \begin{pmatrix} \boldsymbol{f}^h \\ 0 \end{pmatrix}, \tag{7}$$

where we denoted the discrete representations of the considered functions by the superscript h. The matrix $N \in \mathbb{R}^{m \times 3m}$ coincides with a discrete representation of the ∇ operator. The matrix $M \in \mathbb{R}^{3m \times 3m}$ is slightly more difficult. The Navier-Stokes equations for an incompressible isothermal flow are nonlinear. Hence, the nonlinear convective term $\nabla \cdot (\mathbf{U} \otimes \mathbf{U})$, needs to be linearized during the construction of the matrix M. If we apply the Newton linearization to the nonlinear convective term,

$$\nabla \cdot (\mathbf{U}^n \otimes \mathbf{U}^n) \approx \mathbf{U}^o \cdot \nabla \mathbf{U}^n + \mathbf{U}^n \cdot \nabla \mathbf{U}^o =: \mathcal{P}(\mathbf{U}^o, \mathbf{U}^n), \quad n \ldots \text{current time step/iteration}, \, o \ldots \text{previous iteration}, \tag{8}$$

we can define a linear operator

$$\mathcal{M}(\mathbf{U}^o, \mathbf{U}^n) := \nabla \cdot (\nu \nabla \mathbf{U}^n) + \mathcal{P}(\mathbf{U}^o, \mathbf{U}^n), \tag{9}$$

and the matrix M is a discrete representation of the operator $\mathcal{M}$.

The matrices M and N are, as results of the FV discretization, large and sparse. The system (7) cannot be directly solved by the available methods of numerical linear algebra [6, 7]. However, if one assumes the matrix M to be regular, it is possible to explicitly express the velocity from the first row of the system (7) and to substitute for it in the second row. Doing so, the following system for one unknown $p^h \in \mathbb{R}^m$ is obtained

$$NM^{-1}N^{\mathrm{T}}p^h = NM^{-1}\boldsymbol{f}^h, \quad \mathbf{U}^h = M^{-1}\left(\boldsymbol{f}^h - N^{\mathrm{T}}p^h\right). \tag{10}$$

Unfortunately, because M is a large sparse matrix, its inverse is usually not obtainable.

The issue of calculation of the inverse M^{-1} is mitigated by splitting the matrix M as $M = D + L + U$, where D, L and U are a diagonal, and lower and upper triangular matrix, respectively. The inverse M^{-1} is approximated as $M^{-1} \approx D^{-1}$ and the following iterations are constructed,

$$ND^{-1}N^{\mathrm{T}}p^{h,n} = ND^{-1}(\boldsymbol{f}^h - (U+L)\mathbf{U}^{h,o}), \quad \mathbf{U}^{h,n} = D^{-1}\left(\boldsymbol{f}^h - (U+L)\mathbf{U}^{h,o} - N^{\mathrm{T}}p^h\right) \tag{11}$$

The reduced order model generated from the solution to (1) computed by a SIMPLE-based OpenFOAM solver (e.g. simpleFoam) must take into account the above outlined solution procedure. The natural variable for solution techniques for the incompressible Navier-Stokes equations based on the solution of the system (11) is the pressure. Thus, it would seem reasonable to base the reduced order model directly on the relations (11). We propose to rewrite the system $(11)_1$ as

$$\mathbf{0} = A(\mu)p^h + \boldsymbol{b}(\mu, p^h), \quad A(\mu) := ND^{-1}N^{\mathrm{T}}, \quad \boldsymbol{b}(\mu, p^h) := ND^{-1}(\boldsymbol{f}^h - (U+L)\mathbf{U}^h), \tag{12}$$

where $\mathbf{U}^h$ is the solution for the velocity obtained from the SIMPLE iterations. The system (12) is in the form (3) and can be processed by POD and DEIM.

Remark 1 *The iterations (11) do not exactly correspond to the solution procedure applied in the OpenFOAM solvers. For example, the influence of the mesh non-orthogonality on the solution procedure is not mentioned. Consequently, the matrix A and vector b in (12) are not actually constructed via the given formulas. Instead, they are obtained from* `fvm::laplacian(rAtU(), p)` *and* `fvc::div(phiHbyA)`*, respectively. Still, the overal structure of A and b is as described above.*

To reduce the order of (12) via the proper orthogonal decomposition and the discrete empirical interpolation, we need to have available the following data (full order system snapshots),

$$\boldsymbol{S} = \left\{ p_i^h := p^h(\mu_i), \mathbf{U}_i^h := \mathbf{U}^h(\mu_i) \right\}_{i=1}^n . \tag{13}$$

Note that the matrix A in (12) depends on the value of the parameter μ. Hence, only matrices $A(\mu)$ for $\mu \in \{\mu_i\}_{i=1}^n$ are available during the reduced order model construction. The matrix $A(\mu)$ for $\mu \notin \{\mu_i\}_{i=1}^n$ has to be approximated via interpolation. Let us denote $[A]_i$ the interpolated matrix. If the linear interpolation is applied to compute $[A]_i(\mu)$, then $\langle [A]_i \boldsymbol{\psi}_j, \boldsymbol{\psi}_i \rangle = [\langle A\boldsymbol{\psi}_j, \boldsymbol{\psi}_i \rangle]_i$ and it is possible to pre-compute the reduced system matrices during the reduced order model construction.

Remark 2 *The linear interpolation is used to evaluate $[A^\ell]_i(\mu)$ for $\mu \notin \{\mu_i\}_{i=1}^n$. Let us order the values of μ at which we saved the snapshots $\boldsymbol{S}$ as $\mu_1 < \mu_2 < \cdots < \mu_n$. Because of the applied linear interpolation, the generated reduced order model can be used only for $\mu \in [\mu_1, \mu_n]$.*

Optimal FOM snapshot selection

We study the dependence of the solution $[\mathbf{U}, p]$ to the system (1) on the parameter $\mu \in D \subset \mathbb{R}$. Let us assume that we have a prepared reduced order model. Now, let us introduce $\boldsymbol{\mu}_{\mathrm{u}}$, the vector of parameter values for which the full order model was already evaluated. Mind that the current ROM is based on snapshots of the full order model solution computed for $\mu \in \boldsymbol{\mu}_{\mathrm{u}}$. Let $\boldsymbol{\mu}$ denote the vector of parameter values of interest for which the FOM was not yet evaluated. We want to find the best possible $\tilde{\mu} \in \boldsymbol{\mu}$ to include in $\boldsymbol{\mu}_{\mathrm{u}}$. In other words, we seek such $\tilde{\mu} \in \boldsymbol{\mu}$ that expansion of the current matrix of snapshot by the FOM snapshot computed for $\tilde{\mu}$ will improve the most possible the quality of the resulting ROM.

We propose to use the discretized continuity error and define a cost function

$$S_{\mathrm{cont}} = \sum_{P \in \Omega^h} \left| \sum_f \Phi_f^{\mathrm{rom}} \right|, \quad \Phi_f^{\mathrm{rom}} = \mathbf{S}_f \cdot \mathbf{U}_{\mathrm{rom}}, \qquad (14)$$

where $\mathbf{S}_f$ is the face-area vector of the face f. Note that (14) corresponds to a sum of all the local continuity errors in the finite volume mesh Ω^h. Based on numerical experiments, we found that it is suitable to incorporate into the cost function the distance of the current tested parameter to the nearest parameter already included in the snapshots. The modified cost function is

$$S_{\mathrm{cont}}^{\mathrm{nn}} = d_{\mathrm{nn}}^q S_{\mathrm{cont}}, \qquad (15)$$

where d_{nn} marks the distance of the tested parameter $\tilde{\mu}$ to its nearest neighbor in $\boldsymbol{\mu}_{\mathrm{u}}$. The power q may be used to adjust the importance of d_{nn} for the final value of $S_{\mathrm{cont}}^{\mathrm{nn}}$.

The next value of the parameter to evaluate the full order model for, $\tilde{\mu} \in \boldsymbol{\mu}$, can be found as,

$$\tilde{\mu} := \underset{\mu \in \boldsymbol{\mu}}{\operatorname{argmax}}\, S_{\mathrm{cont}}(\mu) \quad \text{or} \quad \tilde{\mu} := \underset{\mu \in \boldsymbol{\mu}}{\operatorname{argmax}}\, S_{\mathrm{cont}}^{\mathrm{nn}}(\mu) \qquad (16)$$

The reduced order model may be used to predict the initial guess for p and $\mathbf{U}$ for SIMPLE iterations. The proposed approach to the evaluation of a parametric study with ROM predictor is summarized in Algorithm 1.

Algorithm 1 Parametric study evaluation with POD-DEIM based predictor

---

Require: Vector of parameters of interest $\boldsymbol{\mu} = [\mu_1, \ldots, \mu_d]^{\mathrm{T}}$, $\mu_1 < \mu_2 < \cdots < \mu_d$, target value of the cost function, ε_S

  1: Evaluate FOM at μ_1 and μ_d;
  2: Set $\boldsymbol{\mu}_{\mathrm{u}} := [\mu_1, \mu_d]$;
  3: Set $\boldsymbol{\mu} := \boldsymbol{\mu} \backslash \boldsymbol{\mu}_{\mathrm{u}}$;
  4: **while** $\boldsymbol{\mu} \neq \emptyset$ **do**
  5:      Construct ROM from snapshots available for $\boldsymbol{\mu}_{\mathrm{u}}$;
  6:      **for each** $\mu \in \boldsymbol{\mu}$ **do**
  7:          Evaluate ROM at $\mu \rightsquigarrow p_{\mathrm{rom}}(\mu)$ and $\mathbf{U}_{\mathrm{rom}}(\mu)$;
  8:          Evaluate $S_{\mathrm{cont}}(\mu)$ from (14);
  9:      **end for**
10:      **if** $\max_{\tilde{\mu} \in \boldsymbol{\mu}}\{S_{\mathrm{cont}}(\tilde{\mu})\} < \varepsilon_S$ **then** BREAK; **end if**
11:      Set $\tilde{\mu} := \operatorname{argmax}_{\tilde{\mu} \in \boldsymbol{\mu}}\{S_{\mathrm{cont}}(\tilde{\mu})\}$;
12:      Evaluate FOM at $\tilde{\mu}$;
13:      Set $\boldsymbol{\mu}_{\mathrm{u}} := [\boldsymbol{\mu}_{\mathrm{u}}, \tilde{\mu}]$;
14:      Set $\boldsymbol{\mu} := \boldsymbol{\mu} \backslash \{\tilde{\mu}\}$;
15: **end while**
16: **for each** $\mu \in \boldsymbol{\mu}$ **do**
17:      Evaluate ROM at $\mu \rightsquigarrow p_{\mathrm{rom}}(\mu)$ and $\mathbf{U}_{\mathrm{rom}}(\mu)$;
18:      Evaluate FOM at μ with $p_{\mathrm{rom}}(\mu)$ and $\mathbf{U}_{\mathrm{rom}}(\mu)$ as initial guess;
19: **end for**
20: **return** Parametric study of FOM

Numerical example

The proposed approach was tested on the `cavity tutorial` distributed with the core OpenFOAM installation [5]. The changed parameter was the flow Reynolds number Re, which was alternated via the changes in the viscosity of the considered fluid. The tested Reynolds numbers ranged from 1 to 10000.

In Figure 1, we depict a comparison of the number of SIMPLE iterations needed to obtain a FOM solution with the same level of accuracy. The compared cases are (i) a CFD simulation without any a-priori pressure and velocity fields initialization, (ii) a simulation with the initial guess predicted by a ROM of dimension $\ell = 6$ and the snapshots selected
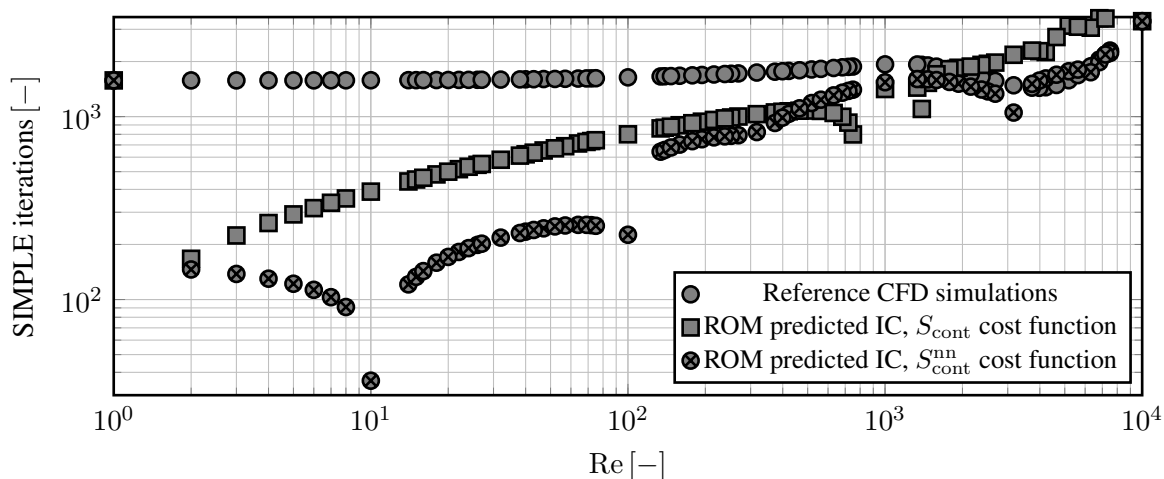
Figure 1: Comparison of the number of SIMPLE iterations needed for the simulation to converge from ROM predicted initial guess of pressure and velocity fields and from a uniform fields initialization. The total number of SIMPLE iterations performed is either 68677 **or** 99637 **in the case of ROM predicted initial guess (it depends on the used cost function) and** 126571 **otherwise.**

via Algorithm 1 and the cost function (14), and (iii) a simulation with the initial guess predicted by a ROM of dimension $\ell = 6$ and the snapshots selected similarly as in (ii), but with the cost function (15).

As it may be seen from Figure 1, when the cost function $S_{\text{cont}}^{\text{nn}}$ was applied, we were able to achieve speed-up of almost two. However, we would like to mention two things. First, the selected range of Reynolds numbers to be simulated is rather large – the studied parameter changes by four orders of magnitude. For most of the practical applications, the range of parameters of interest will be significantly more narrow and the results of the POD-DEIM predictor might be better. Second, using the cost function $S_{\text{cont}}^{\text{nn}}$ defined by (15) instead of S_{cont} introduced in (14) might seem beneficial from the point of view of the final computation speed up. Nevertheless, it seems that the optimal value of the power q in (15) is problem-dependent and we do not have any universally valid estimate for it. In practice, we are not interested in the maximal possible speed up of the calculation but in the actual results of the parametric study. Hence, it does not make much sense to find the optimal value of q for each studied case.

Acknowledgments

References

[1] R. Pinnau, "Model reduction via Proper Orthogonal Decomposition," in *Model order reduction: theory, research aspects and applications*, W. H. A. Schilders, H. A. van der Vorst, and J. Rommes, Eds. Berlin, Germany: Springer Berlin Heidelberg, 2008, ch. 2, pp. 95–109.

[2] S. Volkwein, *Proper orthogonal decomposition: theory and reduced-order modelling*, 1st ed. Konstanz, Germany: Universtity of Konstanz, 2013.

[3] S. Chaturantabut and D. C. Sorensen, "Nonlinear model reduction via discrete empirical interpolation," *SIAM J. Sci. Comp.*, vol. 32, pp. 2737–2764, 2010.

[4] A. Cosimo, A. Cardona, and S. Idelsohn, "General treatment of essential boundary conditions in reduced order morels for non-linear problems," *Adv. Model. and Simul.*, vol. 3, p. 14, 2016.

[5] OpenCFD, *OpenFOAM: The Open Source CFD Toolbox. User Guide Version 1.4, OpenCFD Limited*. Reading UK, 2007.

[6] M. Benzi, G. H. Golub, and J. Liesen, "Numerical solution of saddle point problems," *Acta Numerica*, vol. 14, pp. 1–137, 2005.

[7] H. C. Elman and G. H. Golub, "Inexact and preconditioned Uzawa algorithms for saddle point problems," *SIAM J. Num. Anal.*, vol. 31, pp. 1645–1661, 1994.

DRAFT-TUBE INLET VELOCITY PROFILE OPTIMIZATION

Xin Lin Li[1], François Guibault[2], Christophe Devals[3]

[1]*Mech. Eng. Department, École Polytechnique de Montréal, xinlinli170@gmail.com*
[2]*Comput. Eng. Department, École Polytechnique de Montréal, francois.guibault@polymtl.ca*
[3]*Comput. Eng. Department, École Polytechnique de Montréal, christophe.devals@polymtl.ca*

This paper describes a methodology to formulate and solve an inlet velocity profile optimization problem to minimize hydraulic turbine draft-tube losses. The proposed approach is based on the Mesh Adaptive Direct Search (MADS) optimization algorithm coupled to an incompressible RANS CFD simulation, using OpenFOAM and the standard $k - \epsilon$ turbulence model. Sample results for the Porjus U9 draft-tube are presented. The results show that the energy loss factor was reduced by more than 60% in optimization cases compared with the best efficiency point found using a solid body rotation test. These optimization results can be used as a design reference for turbine designers working on rehabilitation projects of hydraulic power plants.

Introduction

Although global demand for renewable energy is growing steadily and hydropower plays a vital role in this growth, the number of dams built annually tends to decrease. This contradiction has prompted engineers to find ways to extract more energy from existing hydroelectric plants instead of building new ones. The rehabilitation of existing hydropower plants - thus increasing energy production while extending their life - is becoming increasingly important. This work finds its motivation in the needs of engineers for design tools adapted to the rehabilitation of the hydroelectric plants.

The hydraulic turbine is the central technological element involved in the conversion of hydraulic energy. Among the different types of hydraulic turbines, the Kaplan turbine is the most widely used axial turbine in the world. This type of turbine allows efficient hydropower generation in the case of high flow conditions and low head. The draft-tube is one of the most important components of axial turbines. It converts the dynamic pressure of the flow into static pressure by decelerating the flow before it returns into the downstream river. It accounts for 20% to 50% of the total energy that can be recovered from a low-head power plant [1]. The performance of the draft-tube depends on speed distribution at the inlet of the turbine and other factors such as cavitation, downstream water depth, turbine operating point, drag, detachments and secondary flows. All of these factors depend not only on the geometrical shape of the draft-tube, but also strongly on the design of the turbine runner.

In a project to rehabilitate a hydroelectric plant, the spiral casing and draft-tube are usually retained because they are part of the dam and are usually constructed of concrete. Some components such as the generator, the guide vanes and the runner are replaced. Therefore, installing a newly designed runner that better matches the existing draft-tube is the most practical and effective way to improve the overall efficiency of power generation for the entire turbine.

Traditionally, to get the best fit between runner and draft-tube, tests on several models were conducted to check runner designs. However, these model tests are very expensive, so that turbine designers can not explore the optimization space in a thorough and systematic way. The final design of the turbine runner is therefore generally a practical design rather than an optimal one.

Nowadays, with the rapid development of high-performance computing and high-fidelity CFD models, designers are able to obtain accurate low-cost predictions about draft-tube flow and predict the performance of the draft-tube without performing expensive tests. An improved design of the turbine runner, corresponding best to the existing draft-tube, can thus be obtained on the basis of these new techniques. Previous results have shown that the replacement of the turbine runner, achieved by modern technologies, while keeping other existing turbine structures, made it possible to increase the power output of a hydroelectric plant by a factor that could reach from 10 to 30% [2, 3]. However, current studies on the optimization of hydraulic turbines are still mainly focused on optimizing the shape of the turbine blade and geometric optimization of the draft-tube, of which only future hydroelectric plants will benefit. More efforts should be devoted to improving the design of hydraulic turbines for existing installations.

In a rehabilitation project, the first step is to determine what type of flow downstream of the turbine runner can reduce the energy loss in the existing draft-tube and maximize its recovery efficiency. This analysis is also known as optimizing the inlet speed profile for the draft-tube. The results of solving this optimization problem will be used as a design goal for the new turbine runner.

In a recent study, Galván presented an optimization methodology for draft-tube inlet speed profiles based on an analytical

specification of speed limit conditions at the inlet of a draft-tube cone [4], using a series of commercial softwares. The present paper aims to improve the optimization methodology proposed by Galván, by integrating a more flexible method of representation of the velocity profiles in order to widen the optimization space and by using a more efficient numerical optimization algorithm to speed up the process. Instead of commercial software, this new optimization methodology is implemented with open source counterparts to avoid costly licensing fees. Therefore, the optimization problem can be solved on a larger scale and should be solved faster than before since the maximum number of simulation cases is no longer limited by commercial software licenses.

Method

The flow inside a draft-tube is complex and involves large vortices, recirculation and detachment zones. The solution presented in Fig. 1(left) is for the Porjus U9 draft-tube, which was experimentally and numerically investigated by Mulu et al. [5], and to which the present flow simulations were compared. In order to minimize losses inside such a complex system, the proposed methodology comprises three main components, namely 1) the inlet velocity profiles representation model, 2) the evaluation of the draft-tube performance through CFD simulations, which was validated through comparison with experimental results and 3) the optimization algorithm that modifies inlet velocity to minimize flow losses in the draft-tube. This global process is illustrated in Fig. 1(right), and each component is described below.
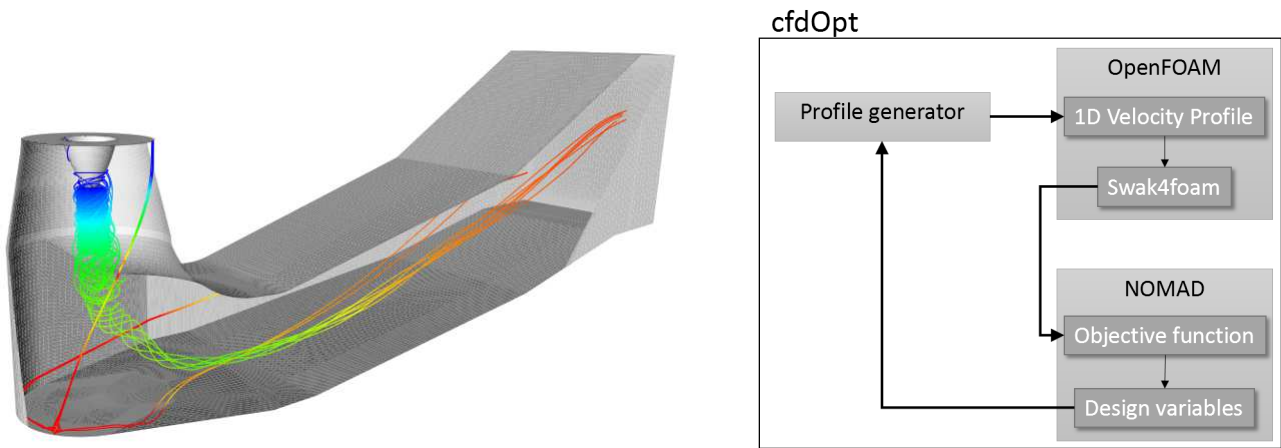

Figure 1: Draft-tube geometry and flow (left) and global optimization process (right)

Velocity Profile Representation

The three-dimensional velocity is represented in a cylindrical coordinate frame, as shown in Fig. 2(left). A typical inlet velocity profile consists of 3 different segments, namely the main profile segment, the inner boundary layer, near the runner hub, and the outer boundary layer, near the draft-tube cone. The main segment is defined as an cubic hermite curve controlled by a sequence of interpolated points. The axial velocity is controlled by five points and the tangential velocity controlled by four points, distributed uniformly along the radius. To reduce the number of free parameters, only y coordinates of the control points are considered as free, the x coordinates being fixed, as illustrated in Fig. 2(right). The radial velocity is given by the following equation:

$$V_r = V_a \cdot \sin(\Theta(r)), \tag{1}$$

where $\Theta(r)$ is the linear combination of the inner hub angle and draft-tube cone opening angle. When the inner hub presence is not considered, the center angle is zero. Both the inner boundary layer segment, near the hub (when present), and the outer boundary layer segment, near the draft-tube wall, are controlled through an analytical power law with a $1/7$ exponent. Boundary layer thickness is fixed explicitly in accordance with flow Reynolds number.

Flow simulations

The Navier-Stokes equations for a Reynolds-averaged incompressible flow is solved with the standard k-ϵ turbulence model, using the simpleFoam flow solver. While the inlet velocity boundary conditions are directly determined through the optimization process, all other boundary conditions are fixed and defined as follows: on walls, no-slip conditions are imposed for velocity, zero-gradient is imposed for pressure and evolutionary wall functions are used for both turbulent kinetic energy and turbulent energy dissipation. At the inlet, a zero-gradient is imposed for pressure, a 5% turbulence intensity is used to compute turbulent kinetic energy and a mixing length of $8, 22 \times 10^{-4}$m is used to compute turbulent energy dissipation. At the outlet, a fixed pressure average is imposed, and zero-gradients for all other variables.
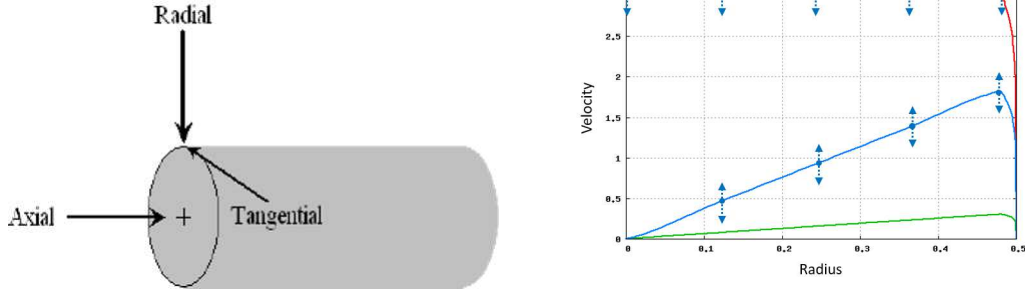
Figure 2: Velocity components in cylindrical coordinates (left) and profile representation (right)

This numerical problem definition allows computing energy losses through the draft-tube, according to the following equation:

$$\zeta = \frac{\frac{1}{A_{in}} \int_{in} P_t dA - \frac{1}{A_{out}} \int_{out} P_t dA}{\frac{1}{2} \rho (\frac{Q}{A_{in}})^2} \tag{2}$$

where P_t represents the total pressure across the inlet A_{in} and outlet A_{out} sections, ρ is the fluid density and Q is the mass flow rate. The energy loss ζ is the objective function that is minimized by the optimization algorithm.

To speed up computations, two criteria are used to determine convergence of the simulations. First, a criterion on pressure and velocity residuals is verified, and second, the energy loss factor must be stabilized.

Optimization algorithm

The optimization algorithm selected in this work is the Mesh Adaptive Direct Search (MADS) algorithm, implemented in the NOMAD open-source software [6]. This algorithm is a generalization of the Generalized Pattern Search (GPS) approach [7], which is a popular gradient-free optimization method that combines a global search step with local polling to refine good candidates and efficiently reach an optimum.

Several parallelization approaches may be used with NOMAD. In the present work, block evaluation mode has been used, where NOMAD executes sequentially, and generates several sets of design variables that can be simultaneously evaluated (see Fig. 3), thereby providing several simultaneous evaluations of the objective function. This execution mode allows taking full advantage of parallelization capacities of the function evaluations, which, in the present case, are performed through OpenFOAM simulations.
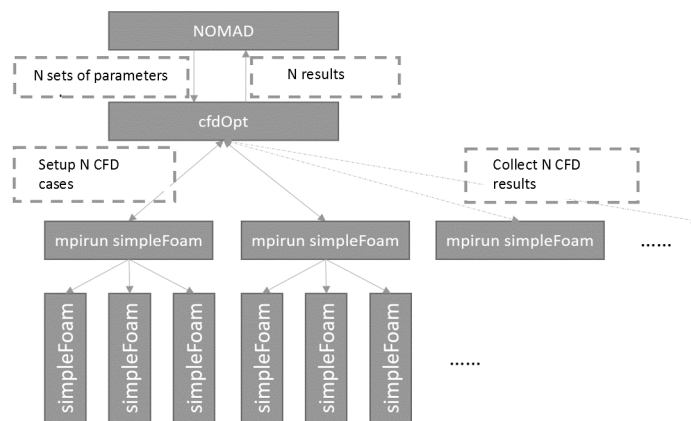
Figure 3: Optimization problem parallelization approach using NOMAD

Optimization results

Several verification and validation cases have been performed to assess the quality of flow solutions and convergence of the optimization algorithm. We only present here a sample of the optimization results obtained for the Porjus U9 test case. A preliminary optimization step consisted in determining an optimal inlet boundary condition based on a solid body rotation

profile. This initial profile, illustrated in Fig. 2(right) yielded an energy recovery factor of 0,1585, which constitutes an initial loss reference to compare the optimization results with. Figure 4 illustrates the computational mesh used (top left) and the pressure distribution across the domain (bottom left) for the optimal inlet boundary condition reached, which is illustrated in Fig. 4(right). The energy recovery factor for this optimal profile is 0,0565, which is a 64.3% reduction of draft-tube losses.
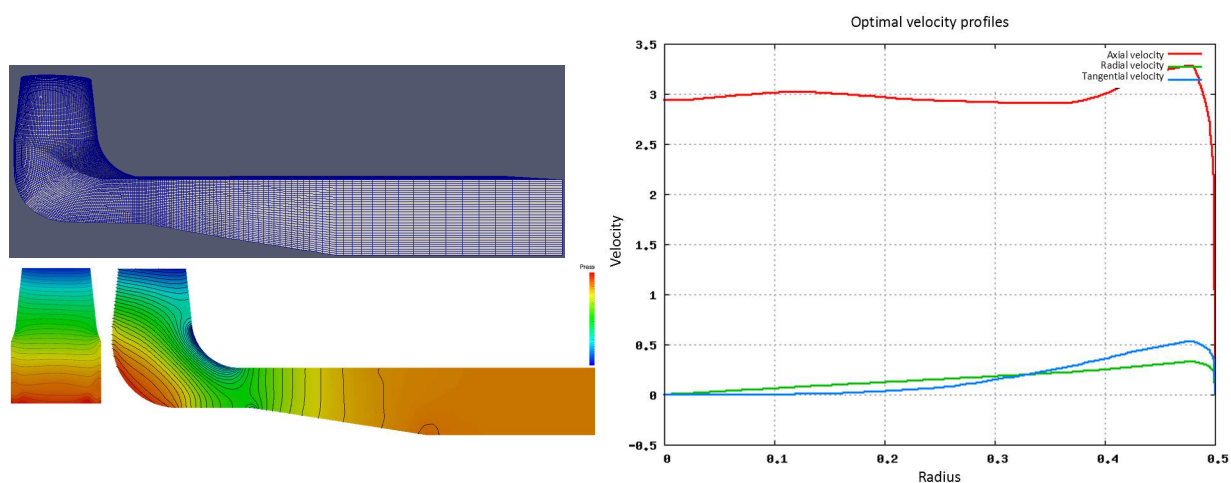

Figure 4: Draft-tube mesh (top-left), optimal pressure field (bottom-left) and optimal velocity profile (right)

Conclusion

This paper has presented a methodology to formulate and solve an inlet velocity profile optimization problem to minimize hydraulic turbine draft-tube losses. The proposed approach, based on the Mesh Adaptive Direct Search (MADS) optimization algorithm coupled to an incompressible RANS CFD simulation, uses OpenFOAM and the standard $k - \epsilon$ turbulence model. The methodology was tested on several test cases, and results are presented for one condition of the Porjus U9 draft-tube. The results show that the energy loss factor was reduced by more than 60% in optimization cases compared with the best efficiency point found using a solid body rotation test. These optimization results can be used as a design reference for turbine designers working on rehabilitation projects of hydraulic power plants.

References

[1] U. Andersson and N. Dahlbäck, "Experimental evaluation of draft tube flow. A test case for CFD simulations," in *XIX IAHR Symposium on Hydraulic Machinery and Systems*, 1998.

[2] S. Galván, M. Reggio, and F. Guibault, "Optimization of the inlet velocity profile in a conical diffuser," in *ASME 2012 Fluids Engineering Division Summer Meeting*. American Society of Mechanical Engineers, 2012, pp. 125–134.

[3] S. Bahrami, C. Tribes, S. von Fellenberg, T. C. Vu, and F. Guibault, "Physics-based surrogate optimization of Francis turbine runner blades, using mesh adaptive direct search and evolutionary algorithms," *International Journal of Fluid Machinery and Systems*, vol. 8, no. 3, pp. 209–219, 2015.

[4] S. Galván, M. Reggio, and F. Guibault, "Numerical optimization of the inlet velocity profile ingested by the conical draft tube of a hydraulic turbine," *Journal of Fluids Engineering*, vol. 137, no. 7, pp. 071 102–071 102–15, 2015, 10.1115/1.4029837.

[5] B. Mulu and M. Cervantes, "Experimental investigation of a Kaplan model with LDA," in *Proceedings of the Water Engineering for a Sustainable Environment Congress: 33rd IAHR Congress, Vancouver, Canada*, 2009, pp. 155–162.

[6] M. A. Abramson, C. Audet, J. E. Dennis Jr, and S. Le Digabel, "OrthoMADS: A deterministic MADS instance with orthogonal directions," *SIAM Journal on Optimization*, vol. 20, no. 2, pp. 948–966, 2009.

[7] C. Audet and J. E. Dennis Jr, "Analysis of generalized pattern searches," *SIAM Journal on Optimization*, vol. 13, no. 3, pp. 889–903, 2002.

APPLICATION OF CFD-BASED EFFICIENT GLOBAL OPTIMIZATION METHOD TO SHIP HULL DESIGN

AIQIN MIAO, DECHENG WAN*

School of Naval Architecture, Ocean and Civil Engineering, Shanghai Jiao Tong University, Collaborative Innovation Center for Advanced Ship and Deep-Sea Exploration, China
Corresponding author: dcwan@sjtu.edu.cn

Keywords: *Efficient global optimization, ship optimization, CFD*

With the growth in computing power of computers and the advances in computational techniques, computational fluid dynamics (CFD) has become an invaluable tool for ship hull form optimization design. However, in the process of ship optimization design, the number of objective function (certain hydrodynamic performances to be improved) evaluations using high-fidelity numerical analysis solvers, is enormous but severely limited by computational time and cost, even with the aid of supercomputers. One alternative is to construct surrogate models based on finite sample points instead of direct numerical evaluations one by one [1]. In this paper, The Efficient Global Optimization method (EGO) is used in ship optimization design based on our in-house solver OPTShip-SJTU. It is a sequential design of experiments aiming at gaining as much information as possible from as few sample points as possible by a skillful choice of adding new sample points in a sequential way

Approach

In classical ship optimization design [2-4], the surrogate model may need a bigger design of experiments like a space filling design or the like, directly evaluated by experiments of numerical simulations. The results would be evaluated by means of a regression model (such as Kriging model), estimating the unknown points in the design space. Finally, the optimal solution would be determined regarding the surrogate model. Unfortunately, this procedure has at least two significant drawbacks: the time for carrying-out of many experiments and the need to repeat the whole procedure in case of a poor fit to sample data.

The EGO method mentioned herein is a Kriging-based global optimization method considering the uncertainty of the surrogate prediction [5, 6] The key to the EGO method lies in balancing the need to fully exploit the surrogate model (by sampling where it is minimized) with the need to improve the accuracy of surrogate model (by sampling where prediction error may be high). The concept is expressed in the infill criterion of Expected Improvement (EI). The EI of optimization problem can be calculated as:

$$E[I(x)] = (f_{\min} - \hat{y})\Phi[(f_{\min} - \hat{y})/s] + s\phi[(f_{\min} - \hat{y})/s] \qquad (1)$$

Where $f_{\min}$ is the minimum value among n sampled values, Φ and ϕ being the standard distribution and normal density, respectively, $\hat{y}$ the prediction of surrogate model, and s the root mean squared error of the surrogate prediction

A simple flow chart of the EGO method applied for a simple mathematical function is shown in Fig. 1. The EGO method is added to our in-house solver OPTShip-SJTU for ship optimization design based on CFD.
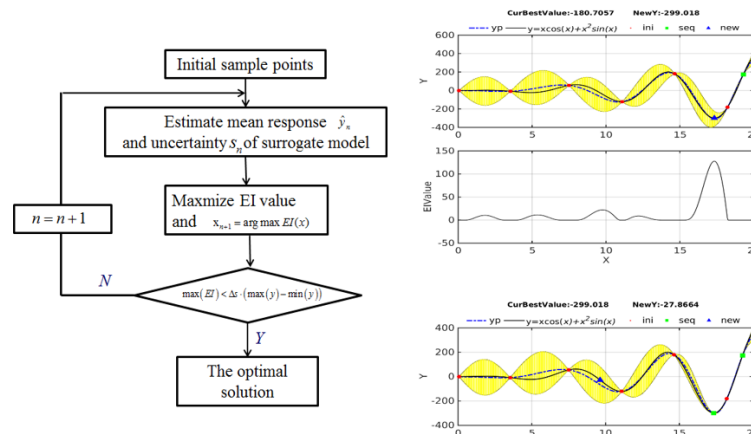

Figure 1: The flow chart of efficient global optimization: on the left, the steps are briefly described; on the right, an example is given (predetermined design points as red dots, the added new points as green squares and the next new point as a blue triangle).

In this paper, two optimization cases of Wigley and KCS ship model sailing in calm water are studied. One is ship hull form optimization of Wigley with the minimum wave-making resistance, while the other one is ship hull form optimization of KCS with the minimum total resistance. The EGO method also starts with an initial ship design which is evaluated directly by the CFD simulation[7]. The classical Kriging surrogate model is then established. The resistance of any new ship on the optimization process is analyzed by means of Kriging model, instead of a CFD-based simulation. A new design sample point is found through optimizing an infill criterion based on the surrogate model. This new design point is the next new ship directly evaluated by CFD method. The surrogate model will be rebuilt by the total sample points. This step of model reconstruction and generation of additional new design point is not iterated until a stop criterion is fulfilled.
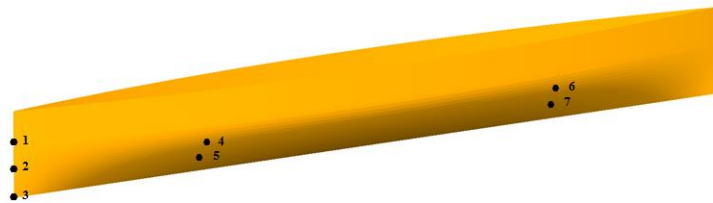
Results

Figure 2: The control points distributed on Wigley hull by RBF method

At the early stage of optimization design, 35 sample points are spread over the design space and selected by Optimal Latin Hypercube Sampling (OLHS) to obtain a Kriging model. The wave-making resistance coefficients of 35 sample hull form and additional sample points are all evaluated using a potential flow theory, Neumann-Michell method [8]. After EGO search, the total number of sample points reached 45 after adding 10 more sample points. The objective function converges to the minimum value, 1.046E-03, a larger reduction of 18.46% than the initial value. Details are shown in Fig. 3-6.
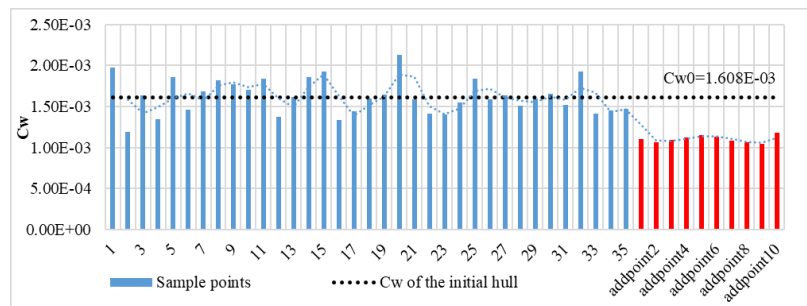

Figure 3: The initial sample hulls and the additional new hulls used in the EGO method
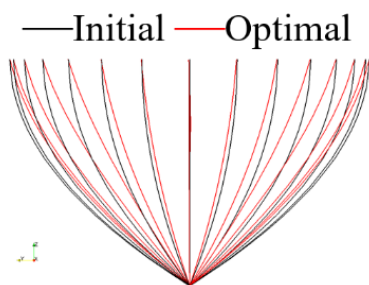

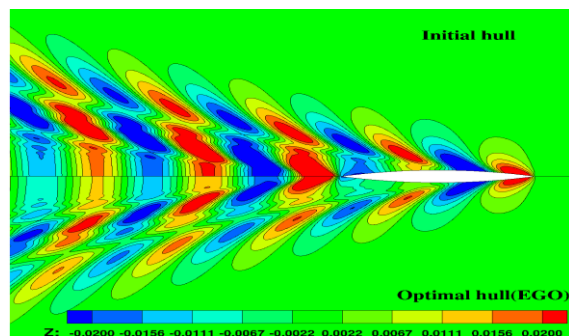**Figure 4: Comparisons of the body lines between the initial and optimal ships**

Figure 5: Comparison of free surface elevation between the initial and optimal ships

P_rgh: -400 -278 -156 -33 89 211 333 456 578 700
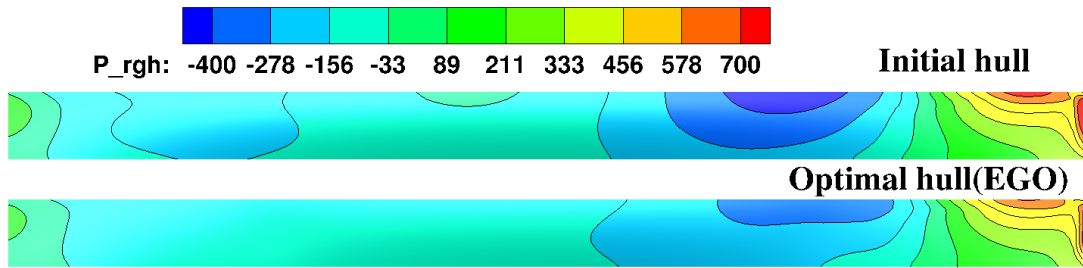
Initial hull

Optimal hull(EGO)

Figure 6: Comparison of pressure distribution between the initial and optimal hulls

The second design problem is to minimize the total resistance of KCS at the design speed. The Free-form Deformation (FFD) method (Thomas W. S. et al.,1986) is applied to modify ship hull form locally. In this study, a total of 5 design variables are used to define the modification of ship hull form. Originally, the total resistance of 30 sample ships are evaluated using a RANS-based CFD method. The objective function R_t is transformed to the corresponding EI to find the global optimum point robustly. By the EGO iterative approach with 10 added new sample ships, not only is the accuracy of the Kriging model improved but also the optimal solution is obtained. In this case, the total resistance reduces by about 4%. The differences of the initial and optimal ships are shown in Fig.7-9 from different point of view.
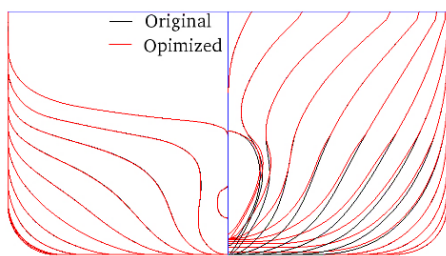
Figure 7: Comparison of the body lines of the initial and optimal hull forms
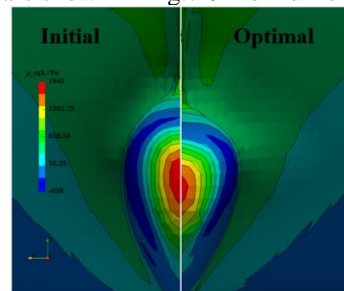
Figure 8: Contour plot of the pressure distribution of the initial and the optimal hull forms (Fr=0.26)
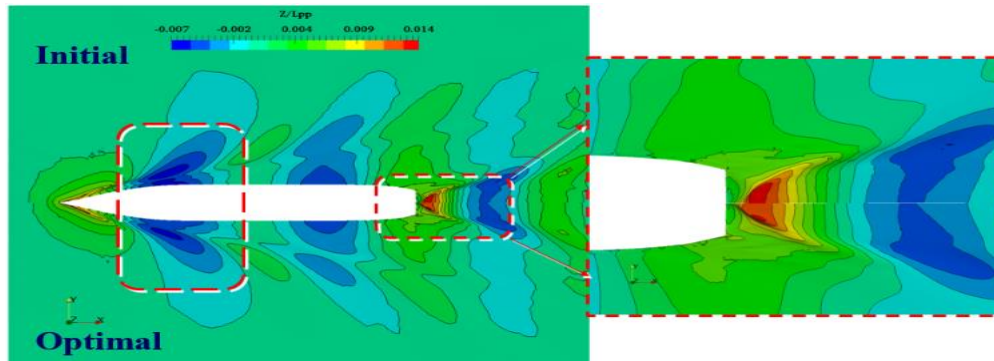
Figure 9: Contour plot of the wave patterns of the initial and the optimal hull forms (Fr=0.26)

Acknowledgements

References

[1] Simpson, T.W., 1998, "Comparison of response surface and kriging models in the multidisciplinary design of an aerospike nozzle," *Institute for Computer Applications in Science and Engineering (ICASE)*.

[2] Campana, E. F., Peri, D., Tahara, Y., and Stern, F. 2006, "Shape optimization in ship hydrodynamics using computational fluid dynamics," *Computer methods in applied mechanics and engineering*, Vol. 196, No. 1, pp 634-651.

[3] Peri, D., and Campana, E. F., 2003, "Multidisciplinary design optimization of a naval surface combatant," Journal of Ship Research, Vol. 47, No. 1, pp 1-12.

[4] Wu, J., Liu, X., Zhao, M., and Wan, D., 2017, "Neumann-Michell theory-based multi-objective optimization of hull form for a naval surface combatant," *Applied Ocean Research*, 63, pp 129-141.

[5] Jeong, S., Murayama, M., and Yamamoto, K., 2005, "Efficient optimization design method using kriging model," *Journal of aircraft*, Vol. 42, No.2, pp 413-420.

[6] Jones, D.R., Schonlau, M., and Welch, W.J., 1998, "Efficient global optimization of expensive black-box functions," *Journal of Global optimization*, Vol. 13, No. 4, pp 455-492.

[7] OpenCFD, OpenFOAM: The Open Source CFD Toolbox. User Guide Version 1.4, OpenCFD Limited. Reading UK, Apr. 2007.

[8] Noblesse, F., Huang, F. X. and Yang, C., 2013, "The Neumann-Michell theory of ship waves," *Journal of Engineering Mathematics*, Vol. 79, pp 51-71.

INDUSTRIAL OPTIMISATION WITH MULTIOBJECTIVE BAYESIAN METHODS AND OPENFOAM

G.R. TABOR[1], S.J.DANIELS[1], A.A.M. RAHAT[1], J.E. FIELDSEND[1], R.M. EVERSON[1],
S.GROSSBERG[2] AND D.JARMAN[2]

[1]*CEMPS, University of Exeter, Exeter, UK*
[2]*Hydro International LTD, UK*

Keywords: Bayesian Optimisation, Industrial Applications, Meshing

Introduction

Design optimisation often requires optimising multiple (and often conflicting) objectives simultaneously. As an example, a heat exchanger design will attempt to maximise the heat transfer while minimising the pressure drop across the system. In such cases there will be a range of solutions, the Pareto set, which represents a trade-off between the design objectives. Genetic Algorithms perform well in exploring the design space and determining the Pareto set, but typically require thousands of function evaluations, which is impractical with CFD even with modern computing power. An alternative is to use Bayesian Optimisation methods which iteratively seek to improve an approximation of the cost function for the system. Bayesian optimisation operates on two functions, an Objective function which is the approximation to the true cost function, and an Acquisition function which identifies the best location for the next sample. Note that this is not necessarily at the optimum solution but may indicate a location in parameter space to investigate to improve the overall quality of the objective function. Bayesian optimisation has been proved to be an effective approach to find optimal solutions with the minimum number of direct evaluations of the (expensive) cost function [1], which makes it an ideal choice to use with CFD.

Integration with OpenFOAM

In this work, we demonstrate the application of Bayesian methods to the optimisation of real engineering problems. We have developed a general Machine Learning Optimisation framework in Python with a link to use OpenFOAM through the PyFoam library as the CFD engine (other CFD packages could also be used). On the Optimisation side, we have implemented Genetic Algorithm and Bayesian Optimisation methods in Python into this framework.
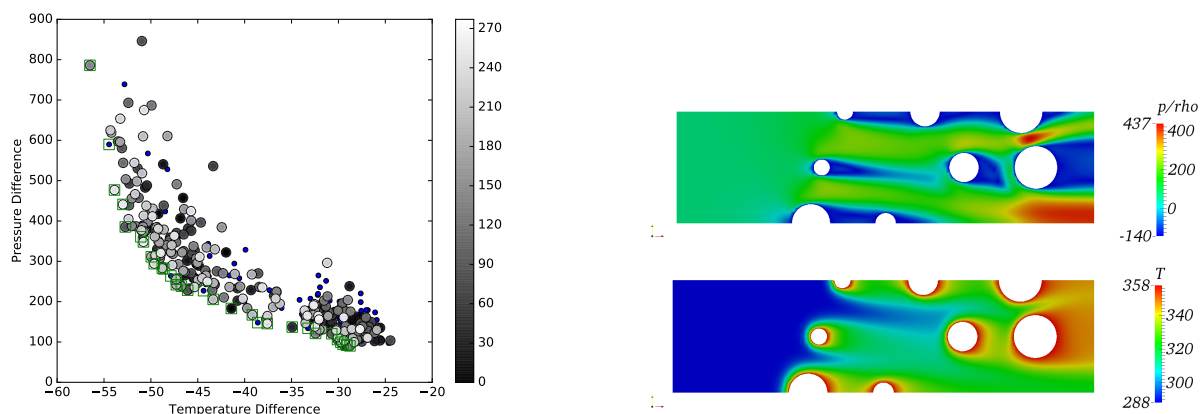
Figure 1: Left; Pareto front for heat exchanger problem. Right; Optimised (non-dominated) solution

Industrial applications

The Bayesian Optimisation algorithms have been applied to a range of including heat exchangers, draft tubes and vortex separators. The heat exchanger case is a 2d heat transfer problem at $Re = 100$, with position and size of the tube surfaces varied through the use of Chebyshev polynomial functions. The problem involves two separate, competing

objectives; enhancing heat transfer from the tubes involves increasing the contact area and slowing the flow; whilst reducing the pressure drop would require the exact opposite. The problem has been optimised using both GA and Bayesian approaches, generating a clear Pareto front; a non-dominated solution example is shown in figure 1.

The draft tube is a standard CFD optimisation problem with significant industrial interest. Hydroelectric power generation involves supplying water at high pressure head to a turbine; the water leaving the turbine is then directed through the draft tube back to the natural environment (a river or lake). Optimising the system involves minimising the pressure at the exit from the turbine/entry to the draft tube. The basic geometry (figure 2) known as the Hölleforsen draft tube was originally used for an ERCOFTAC workshop [2] on modelling and optimisation, and has been extensively studied since [3, 4, 5]; there is therefore an extensive literature of experimental and computational results to validate the basic CFD simulations against, as well as a great deal of literature on optimising the design. The problem is complicated by being fully 3d and by the swirling motion at the inlet (from the upstream Kaplan turbine) which has to be included for full acuracy. We have validated our modelling on the base case (figure 2) and then used Bayesian optimisation to find optimal solutions for this important test case.

The third example is an actual industrial problem provided by Hydro International; a Vortex Separator for wastewater treatment. Vortex separators use conical plates to encourage the formation of a vortex in the tank; particles in the flow interact with the plate boundary layers and drop out of suspension, collecting at the base of the tank for removal; whilst the cleaned water is removed at the top of the tank. This is the most challenging of the three examples as it involves a 2-stage simulation process, with an initial single phase flow simulation using `simpleFoam` to determine the system hydrodynamics followed by particle tracking to determine the separation. The simulations for this have been validated for the existing geometry and Bayesian optimisation used to determine an optimal design for the plates.
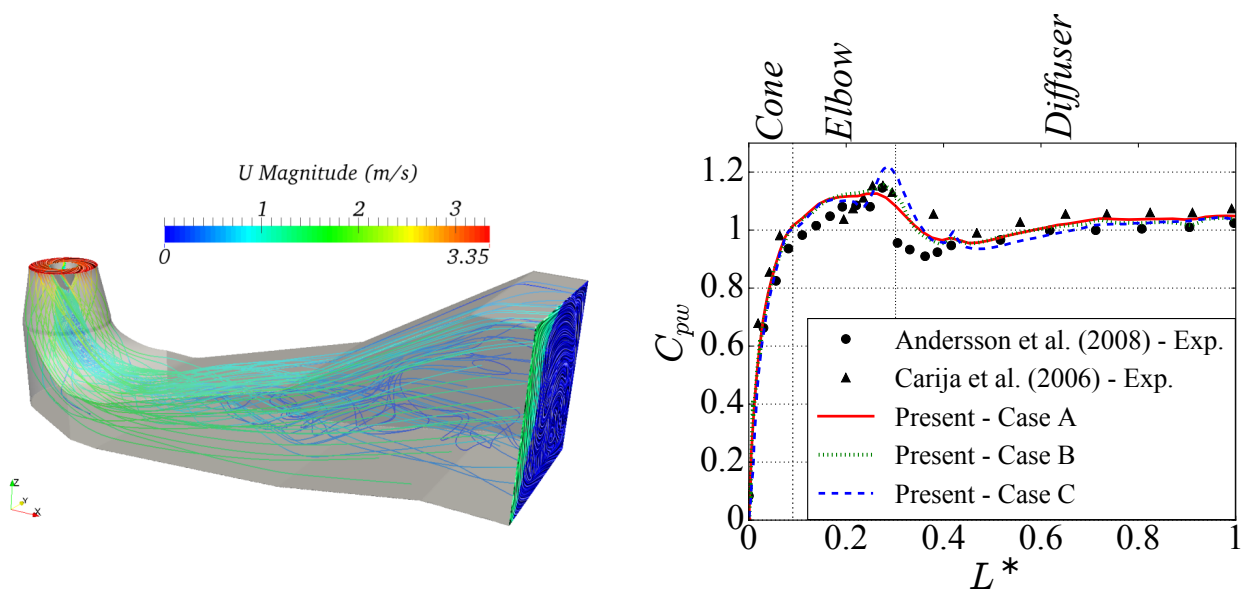
Figure 2: Hölleforsen draft tube; original geometry. Left; streamlines for flow. Right; validation of pressure coefficient along underside of the draft tube.

Mesh optimisation

Development of a high quality mesh is obviously of critical importance for any CFD simulation. However this is a very challenging problem which typically absorbs most of the human effort in developing a CFD model of a problem. This is even true for automated meshers such as `snappyHexMesh` or `cfMesh` which have input parameters controlling the meshing process whose values have to be set, typically through trial and error. This has all the hallmarks of an optimisation problem with several input parameters (the mesher settings) and a limited number of mesh quality parameters such as skewness to be optimised. This problem has been investigated using Genetic Algorithms [6]; here we apply our Bayesian Optimisation techniques to mesh a swirl flow separator using `cfMesh`.

Conclusions

Evolutionary algorithms have benefits for optimisation including their relative simplicity (there is no need to evaluate function derivatives as there is for Adjoint Optimisation) and the fact that they explore the whole of parameter space and

reliably identify global optima. However they require the evaluation of 10's of thousands of variants of the design, and this can be prohibitively expensive if each of these evaluations requires a full CFD simulation. Bayesian optimisation iterates improvements in an Objective function which is an approximation to the true cost function, and for which the optimal solution(s) can be found relatively cheaply and easily. This represents a cost-effective optimisation process based on CFD which can realistically be applied to real, complex engineering problems. We have developed a machine learning library in Python for optimisation of flow problems using CFD which integrates well with OpenFOAM; and demonstrate its utility by applying this to optimise three different industrial flow problems. We have also applied the same strategy to optimise the construction of a mesh for a vortex flow separator.

Acknowledgments

References

[1] A. A. M. Rahat, R. M. Everson, and J. E. Fieldsend, "Alternative infill strategies for expensive multi-objective optimisation." in *Proceedings of the Genetic and Evolutionary Computation Conference, GECCO'17*, 2017, pp. 873 – 880.

[2] M. J. Cervantes, T. F. Engström, and L. H. Gustavsson, Eds., *Turbine-99 III*, 2005.

[3] S. Galvan, M. Reggio, and F. Guibault, "Assessment study of k-e turbulence models and near-wall modelling for steady state swirling flow analysis in draft tube using Fluent," *Eng. App. CFD*, vol. 5, no. 4, pp. 459 – 478, 2011.

[4] Z. Krzemianowski, M. Banaszek, and K. Tesch, "Experimental validation of numerical model within a flow configuration of the model kaplan turbine," *Mechanics and Mechanical Engineering*, vol. 15, pp. 297 – 307, 2011.

[5] H. Nilsson and M. J. Cervantes, "Effects of inlet boundary conditions on the computed flow in the turbine-99 draft tube uing OpenFOAM and CFX," in *IOP Conference Series:Earth and Environmental Science*, vol. 15, no. 3, 2012, p. 03202.

[6] B. Fabritius and G. Tabor, "Improving the quality of finite volume meshes through genetic optimisation," *Engineering with Computers*, vol. 32, no. 3, pp. 425 – 440, 2015.

HULL FORM OPTIMIZATION OF JBC BASED ON RESISTANCE AND PROPULSION PERFORMANCES

XINWANG LIU[1], DECHENG WAN[2]

[1]*Collaborative Innovation Center for Advanced Ship and Deep-Sea Exploration, State Key Laboratory of Ocean Engineering, School of Naval Architecture, Ocean and Civil Engineering, Shanghai Jiao Tong University, huhgf670@163.com*

[2] *Collaborative Innovation Center for Advanced Ship and Deep-Sea Exploration, State Key Laboratory of Ocean Engineering, School of Naval Architecture, Ocean and Civil Engineering, Shanghai Jiao Tong University, dcwan@sjtu.edu.cn*

Introduction

In the ship design process, hull form design is of vital importance. In recent years, with the huge development of computer technology and calculation theories, the Simulation-Based-Design (SBD) technology is becoming possible rather than empirical or semi-empirical formulas. It is a new design way which integrates hull form transformation method, optimization technology and numerical simulation module.

If we consider viscosity, Navier-Stokes equations are the fundamental equations to solve using numerical methods. OpenFOAM is the leading free, open source software for computational fluid dynamics (CFD) including a lot of standard solvers, for example, *pimpleDyMFoam* solver is a transient solver for incompressible, turbulent flow of Newtonian fluids on a moving mesh while *interDyMFoam* solver is a solver for 2 incompressible, isothermal immiscible fluids using a VOF (volume of fluid) phase-fraction based interface capturing approach [1].

In this study, we focus on the resistance and propulsion performances of the hull. Although we can simulate the new hulls sailing in calm water including free surface using *interDyMFoam* solver, we finally decide to use *pimpleDyMFoam* solver and double model instead of the whole ship model. The reasons are as follows: One is that the wave-making resistance represents too small a percentage of the total resistance when the Froude number is small, the other is that the propeller disk has a relatively big distance to the still water level, so the wake field cannot be much affected by the free surface. As a result, it can save most of computational time with relatively high fidelity.

Furthermore, in order to do the efficient optimization, one method is to construct a relatively simple surrogate model instead of the simulations of a large number of sample points to find the relationship, which is often with strong nonlinearity, between the design variables (input) and the objective functions (output). The model requires very little time to evaluate the objective function. The most widely used surrogate models are the polynomial-based models: the response surface model and the Kriging model.

In this paper, the Japan Bulk Carrier (JBC) is considered as the initial hull. The hull form can be globally or locally deformed while the wetted surface area and displacement are constrained within a certain range. A practical hydrodynamic optimization tool OPTShip-SJTU [2] are applied for the hull form optimization. Here, the free-form deformation (FFD) method and shifting method are used as parametric hull surface modification techniques in order to generate a series of hull forms subjected to geometric constraints. The parameters of the sample deformed hull forms are generated by the OLHS approach and their hydrodynamic performances are calculated by *pimpleDyMFoam* solver.

Hull form optimization is comprehensive technology. The OPTShip-SJTU solver is a self-developed tool based on C++ language for the ship hull form optimization, which has obtained national software copyright. The framework of OPTShip-SJTU is shown in Figure 1.
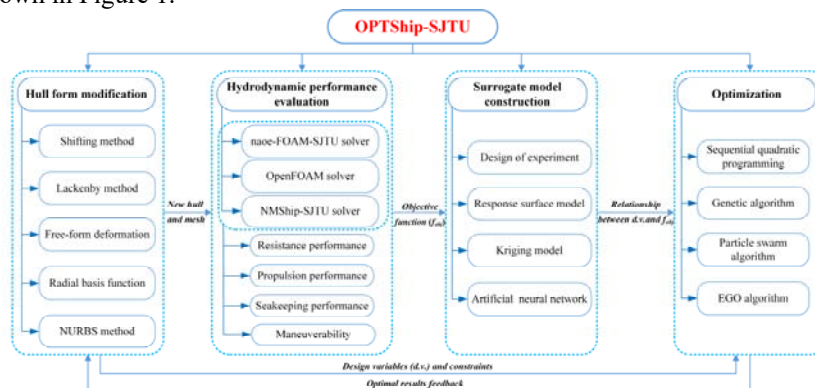
Figure 1: Framework diagram of OPTShip-SJTU

Optimization methods

Ship hull form transformation module is a bridge connecting ship performance evaluation module and optimization module. Once a series of design variables values are selected, ship transformation module needs to make rapid response to the certain set of design variables, that is, to modify the initial model to the new ones, and send them to the ship hydrodynamic performance evaluation module. The free form deformation method is proposed by Sederberg and Parry [3] that has been widely used in various fields including hull geometry reconstruction and other transportation tools. By changing the location of the control points, different new meshes of the hulls can be obtained easily. Furthermore, the shifting method can be applied to the global transformation of the hull form.

Hydrodynamic Performance Evaluation

Taking the initial hull as an example, the transformed hulls are evaluated similarly.

For pre-processing involving mesh generation, we use the utility *blockMesh*, supplied in OpenFOAM, to generate a rectangular background mesh for a cubic domain. In this study, it was set to $-L_{wl} \le x \le 4L_{wl}, 0 \le y \le L_{wl}, -L_{wl} \le z \le 0$, and the origin of the region is at the intersect of the still water level, central longitudinal section, and the bow part of the hull. Furthermore, and numbers of cells in each direction is $(n_x, n_y, n_z) = (42,9,30)$. Then, we can use *snappyHexMesh* utility to do the 'castellatedMesh', 'snap', and 'addLayers' steps.

The boundary condition settings, calculation region and mesh are shown below.

Table 1: Boundary conditions of the case

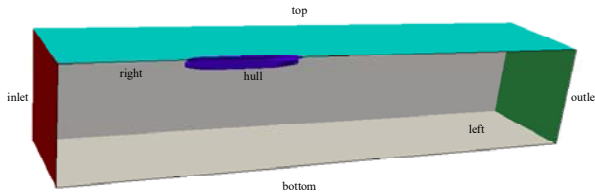| Boundary	Velocity	Pressure
inlet	fixedValue	zeroGradient
outlet	zeroGradient	fixedValue
left	symmetryPlane	symmetryPlane
right	fixedValue	slip
top	symmetryPlane	symmetryPlane
bottom	fixedValue	slip
hull	fixedValue	zeroGradient

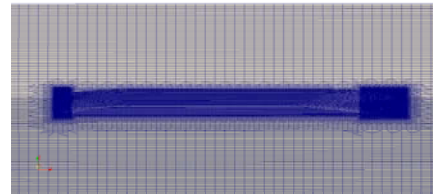Figure 2: Calculation region of the case

Figure 3: Mesh around the hull of the case

Surrogate Model Construction

As a kind of regression model, Kriging model is able to exploit the spatial correlation of data in order to predict the shape of the objective function based only on limited information. [4] Kriging exploits the spatial correlation of data in order to build interpolation; therefore, the correlation function is a critical element. The accuracy of the prediction value largely depends on the distance from sample points.

Optimization Method

At the stage of computing optimization, we first select 50 sample points in the design space by Optimal Latin Hypercube Sampling method (OLHS) design [5], and use the Kriging model instead of huge numerical calculation to make quick evaluations. Finally, the genetic algorithm NSGA-II [6] is selected as the optimization method, and after 300×200 individual evolutions, the ideal optimal hull forms can be obtained.

Objective Function

The optimization problem in this paper takes the JBC as the initial ship, which has the ship main dimensions of L_{wl}=7.125m, B=1.125m, D=0.625m, T=0.4125m in model scale, and the model can be seen in Figure 4.

Figure 4: Ship hull form of JBC

In this study, the objective functions are shown below,

$$\min \quad F_t \tag{1}$$

$$\min \quad w = \sqrt{\frac{\sum_{i=1}^{N}\left(u_{x,i} - \bar{u}_x\right)^2}{N\bar{u}_x^{\,2}}} \tag{2}$$

where F_t is the total resistance of the hull without considering free surface, and w is the normalized standard deviation of the velocity distribution in direction x at the propeller disk.

Design Variables

Optimization variables are used to control the free variation of the ship form in the design space. Ship transformation method in this paper is FFD and shifting method, involving one lattice (shown in Figure 5) at the bulbous bow. Red points are movable while green points are fixed.

Five optimization design variables, including alpha1, alpha2, X1, Y1, Z1, are summed up. The first 2 variables are for the shifting method, and the latter three control the change of the bulbous bow surface in three directions: x, y and z. In order to ensure that the hull form is within a reasonable range, the range of the design variables is specified in Table 2. For instance, if X1=+0.005, then all the red points in Figure 5(a) move along the x-axis with a distance of +0.005m at the same time.

Table 2: The range of the 5 variables

Method	Variables	Min	Max
Shifting method	alpha1	0	0.06
	alpha2	0	0.06
FFD method	X1	-0.01	0.01
	Y1	-0.01	0.001
	Z1	-0.005	0.005

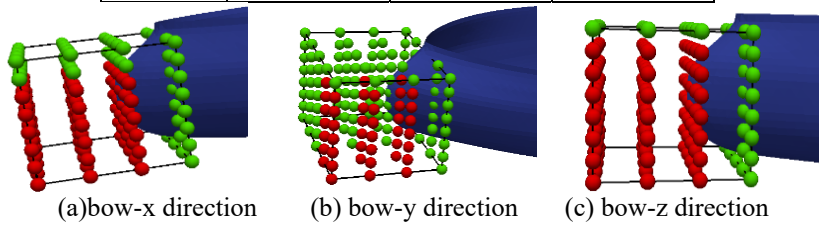(a)bow-x direction   (b) bow-y direction   (c) bow-z direction

Figure 5: Schematic diagram of FFD method (Lattice and layout of control points)

Optimization result and analysis

We can finally use NSGA-II to get the Pareto front shown in Figure 6 and the corresponding values of the design variables are shown in Table 3.
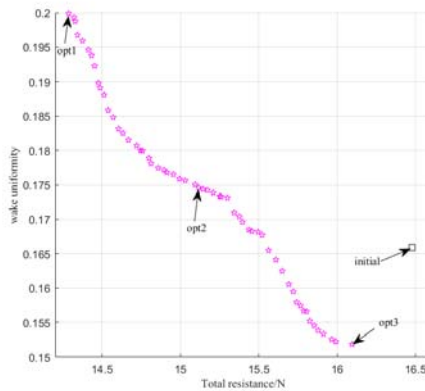
Figure 6: Pareto front of the optimization problem

Table 3: The comparisons of the design variables and the objective functions of initial and optimal hulls

Ship	alpha1	alpha2	X1	Y1	Z1	F_t/N	w	$\triangle F_t$/%	$\triangle w$/%
initial	0	0	0	0	0	16.4819	0.1660	0	0
opt1	0.0348	0.0600	-0.0023	-0.0003	-0.0007	14.2856	0.1999	-13.33%	20.39%
opt2	0.0547	0.0246	-0.0067	-0.0045	-0.0017	15.1159	0.1746	-8.29%	5.16%
opt3	0.0066	0.0008	-0.0100	0.0079	0.0032	16.0953	0.1519	-2.35%	-8.52%

The hull lines comparisons are shown in Figure 7. We can see from Figure 7 that the bulbous of the optimal hulls are fatter in the y direction than the initial one, and the fore part after the bulbous and also stern parts of the optimal hulls are a bit thinner than the initial one.
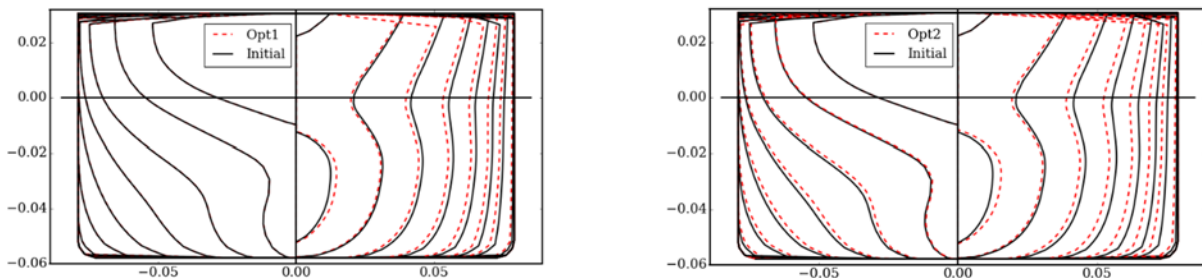
Figure 7: Hull line comparisons

We might as well compare the initial and some certain hull forms through their pressure and wake field information.

(a)	(b)

Figure 8: Pressure distribution comparisons   **Figure 9: Wake field comparisons**

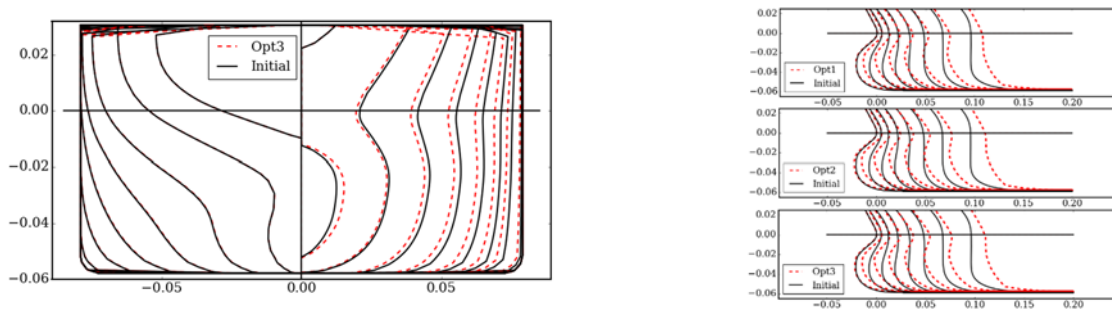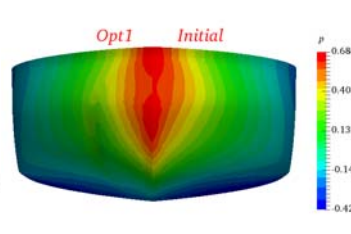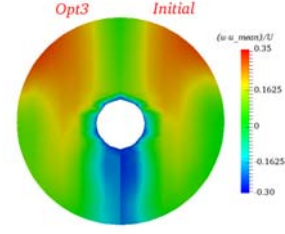Seen from Figure 8, the fore part of the optimal hull Opt1 has smaller high pressure and low pressure regions, which results in the lower resistance.

We can also know from Figure 9 that the velocity distribution in direction x at the propeller disk of the optimal hull Opt3 is more uniform than that of the initial one, which is good for the propulsion performance.

Conclusions

In this paper, the JBC is considered as the parent ship. The hull form can be globally and locally deformed while the wetted surface area and displacement are constrained within a certain range. Kriging approximate model is constructed which can reduce the computational cost. Finally, the multi-objective genetic algorithm is taken as the optimization technique leading to the optimal hull forms which have better resistance and propulsion performances.

The whole optimization process is implemented based on OpenFOAM and in-house optimization solver OPTShip-SJTU. It turns out that it's convenient to use OpenFOAM to consider the hydrodynamic performances of the ship in the design period and OPTShip-SJTU has practical applications in the aspect of the optimization of ship hydrodynamic performances.

References

[1] The OpenFOAM Foundation, OpenFOAM v5 User Guide[EB/OL]. https://cfd.direct/openfoam/user-guide, Mar. 2018.

[2] J. W. Wu, X. Y. Liu, D. C. Wan, The Manual of ship hull optimization software OPTShip-SJTU[R]. Technical Report No.2016SR094162, Shanghai Jiao Tong University, 2016.

[3] T.W. Sederberg, S. R. Parry, Free-form deformation of solid geometric models[J]. ACM Siggraph Computer Graphics, 1986, 20(4): 151-160.

[4] T.W. Simpson, T. M. Mauery, J. J. Korte, F. Mistree, Kriging models for global approximation in simulation-based multidisciplinary design optimization[J]. AIAA Journal, 2001, 39(12): 2233-2241.

[5] R. Jin, W. Chen, A. Sudjianto, An efficient algorithm for constructing optimal design of computer experiments[J]. Journal of Statistical Planning and Inference, 2005, 134: 268-287.

[6] N. Srinivas, K. Deb, Multi objective optimization using non-dominated sorting in genetic algorithms[J]. Evolutionary Computation, 1994, 2(3): 221-248.

TRANSPLANT AND OPTIMIZE OPENFOAM ON SUNWAY TAIHULIGHT SUPERCOMPUTER

HU REN[1], HANFENG GU[1], FEI GAO[1], XIN LIU[1,2], WEI XUE[1,3]

[1]*National Supercomputing Center in Wuxi, Wuxi 214072, China,* renhu@mail.nsccwx.cn
[2]*Wuxi Jiangnan Institute of Computing Technology, Wuxi 214000, China*
[3]*TsingHua University, Beijing 100084, China*

Keywords: *Supercomputing, Optimization, Sunway TaihuLight, OpenFOAM, CFD, many-core*

Sunway TaihuLight is the world's first supercomputer with peak performance over 100PFlop/s. It was composed with over 40K "SW26010" chips. "SW26010" is a novel architected many-core processor, with 4 managing cores (MPE) and 256 computing cores (CPE) all integrated on a single chip. OpenFOAM is one of the most popular open CFD softwares, but written with millions C++ lines and based on an unstructured mesh and data layout. Transplanting and Optimizing OpenFOAM on Sunway TaihuLight was necessarily valuable and challengeable.

The present work reports the porting and comprehensive optimization of OpenFOAM on the Sunway TaihuLight supercomputer. The most important problem while transplanting is that the "wmake" build tool was found to some extent only suitable for shared-library type compiling. Since it is more reliable on Sunway system using static-library type building, a script-based archiving method was used to enable static library support. The optimizations were carried out from two levels – the process level using MPI and the sub-process level many-core parallelization, in which architecture aware acceleration technics, problem oriented strategies, as well as algorithm upgrades were involved.
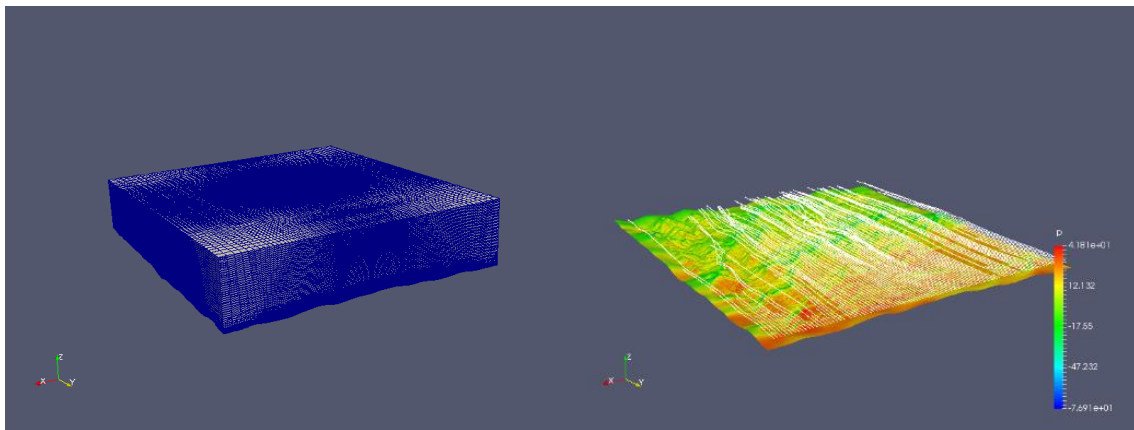

Figure 1: The test case
A wind field, with an about 30 km × 30 km square terrain and an about 7.5 km vertical height to the atmosphere, was under consideration. The domain was discretized with about 50 million unstructured mesh (left). A steady velocity and pressure distribution is to be calculated (right).

Table 1: Test case solving setup

Governing equation	Incompressible Navier-Stokes
Algorithm	SIMPLE family
Variables	ux, uy, uz, p
Orthogonality correction number	1
Velocity equation solver	ILU preconditioned PBiCG
Pressure equation solver	GAMG with Gauss smoother
Turbulence model	k-epsilon

The case used for performance test was a wind field shown as **Figure 1**, and the key solving configurations were listed in **Table 1.** Boundary conditions are obtained from meteorological observations and weather simulations in real applications. **Figure 2** shows the main measures taken in optimization, and corresponding accumulated effects. First, a problem oriented mesh partition was implemented in place of the default "scotch" partition method for unstructured meshes. Then, in order to achieving more efficient memory access, the whole-chip memory was disabled after getting rid of data gathering to main process by post-processing function objects. Manual caching with pre-calculated array stamps was used in the flux and source term computations in the finite volume discretization and the algebra equation formations. For the

sparse matrix-vector multiplication (SpMV) kernel "Amul" and "ATmul", matrix reordering strategies was taken to reduce the random data fetching. Despite the flux and matrix related calculations, there are still a large number of vector operations along the execution process. Manual coding respectively would be time consuming and prone to bugs. A series of vector acceleration interfaces were developed, with which a single vector kernel can be accelerated by no more than several dozens of lines, about 10 to 100 times less than respective coding. Apart from accelerations and optimizations on codes itself, algorithms for linear system solver were also upgraded. In the "GAMG" solver of OpenFOAM, the Gauss iteration is mostly used for smoothing, and the ILU preconditioner is frequently adopted together with the "PBiCG" solver. However, Gauss iteration and ILU are algorithmically of a limited degree of parallelism. By extending a new Chebyshev smoother and matching a diagonal preconditioner to a new stabilized conjugate gradient (CG) solver, the degree of parallelism was released with little overhead and similar convergence.
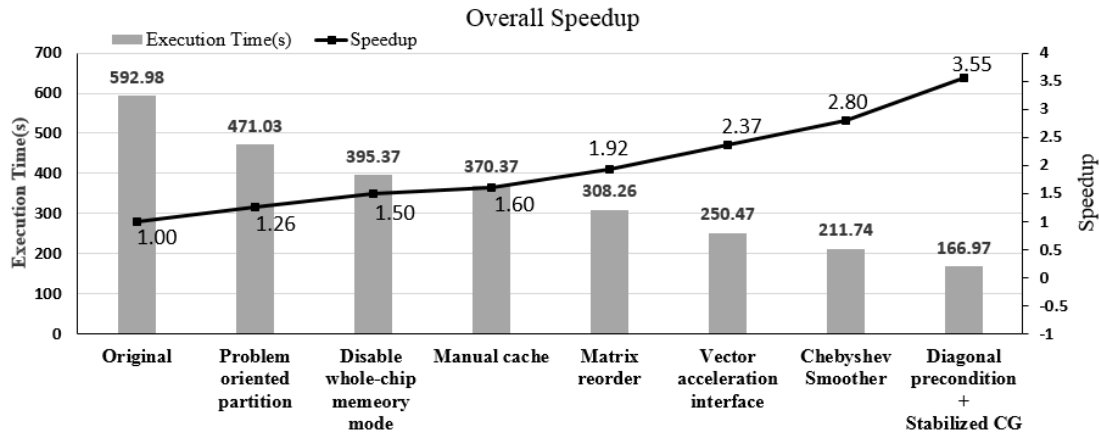
Figure 2: The overall speedup

The speedup is observed in steady wind field case, configured with 50 million unstructured mesh, using 256 core groups on Sunway TaihuLight. Detailed case setups can be found in **Table 1**. The pillars illustrate the "Execution Time" reported by OpenFOAM after 40 SIMPLE iterations. Effects are accumulated. The solid line shows the speedup converted from the "Execution Time" result.

Finally upto 3.55 times' overall speed up was achieved compared to the original version. The performance per one core group on Sunway - there are 4 core groups on a single SW26010 processor - is about 1.18 times of that on a prevailing Intel x86 core at present state. CFD simulations with OpenFOAM are now routines on Sunway system, helping best-in-class companies select wind fun location and predict wind power generation.

Acknowledgements

A PARALLEL MULTI-SELECTION GREEDY METHOD FOR THE RBF MESH DEFORMATION IN OPENFOAM

CHAO LI[1,2], XIAOWEI GUO[1,3], CHENGKUN WU[1], XIANG ZHANG[1],
YI LIU[1], LIHUAN YUAN[1], SIJIANG FAN[1], CANQUN YANG[1]

[1]*College of Computer, National University of Defense Technology, Changsha 410073, China*
[2]*Email: dirk911@nudt.edu.cn*
[3]*Email: guoxiaowei@nudt.edu.cn*

Keywords: *CFD Mesh deformation; Radial basis function; Greedy algorithm; Multi-selection; Parallelization*

For a general CFD simulation with moving boundaries, the mesh deformation procedure could be logically divided into two steps. In the first step, the deformation of the mesh on the surface is performed based on a predefined equation or coupled iterative calculations. In the second step, the volume mesh is deformed to coordinate with the surface mesh using a specific method. The radial basis function(RBF) based mesh deformation is a point-by-point mesh movement scheme, which interpolates the displacement of the surface mesh to all the nodes of the flow mesh. The whole mesh points could be grouped into three categories: moving boundary points(x_m), static boundary points(x_s) and internal points(x_{in}). Based on a given basis function, the motion of any of these points could be calculated by:

$$s(x) = \sum_{j=1}^{N_b} \lambda_j \phi\left(\left\|x - x_j\right\|\right) \qquad (1)$$

where x_{bj} is the coordinate of the jthboundary point, φ is the radial basis function as function of the Euclidean distance $\left\|x\right\|$, N_b is the number of the boundary points and λ_j is the weight coefficients. The conventional RBF mesh deformation would use all the boundary points to calculate the weight coefficients, which results in an interpolation scale of N_b^3. During the interpolation for the motion of the internal points, a time scale of $N_{in} \times N_b$ (N_{in} is the number of internal points) is introduced. Considering the whole mesh deformation procedure, it may be observed that the number of the boundary points N_b is the dominant factor in the cost of the method. Therefore, for large-scale 3D simulations with complex moving boundaries, N_b may reach to a very high value, which will result in a huge RBF system to be solved. In addition, if the mesh deformation is performed at each time step, the computational cost will be unacceptable.

An effective solution is to select a reduced subset from the boundary points to represent the surface meshes. These selected points, labeled as control points(x_c), then could be used instead to interpolating the motion of the internal points. Then new problems arises: how many control points should be selected and how to determine them. An ideal criterion is that the selected control points should be the minimum subset which could represent the geometry and motion of the boundary to a given degree of accuracy. This means N_c (number of the control points) should not be too large, which would influence the efficiency of the computation, nor too small, which might reduce the accuracy of the interpolation. Considering this appealing criterion, a real surface error based greedy algorithm is proposed by Rendall and Allen and the detailed procedure could refer to [1].
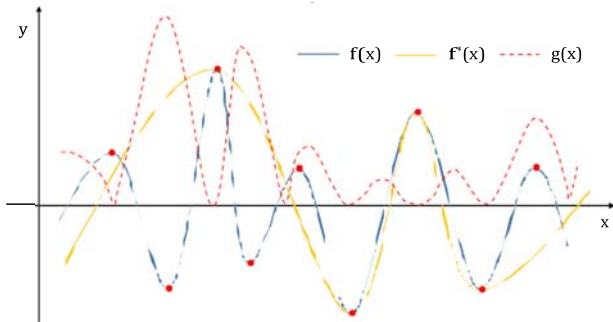

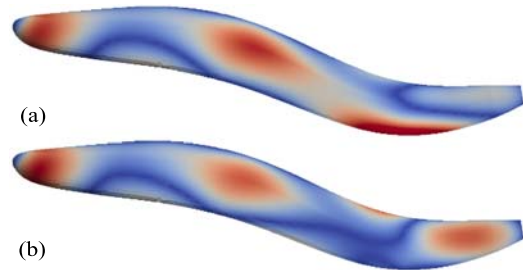**Figure 1: Illustration for the curve fitting.**

Figure 2: Distributions of the normalized boundary error when (a) $N_c = 10$ and (b) $N_c = 11$.

From the results discussed by Rendall and Allen, the greedy algorithm could effectively reduce the number of boundary points used to interpolating the motion of the volume mesh. But the time cost is reasonable only when the

final value of N_c is smaller than 400. The grey curve in Fig. 5 shows the time cost of the original greedy algorithm as a function of N_c. We could see the cost is in an exponential growth when N_c increases. Especially when N_c is larger than $1,000$, it will take several hours for the point selection procedure, which is unacceptable even for cases that only perform the greedy procedure once at the beginning. Consequently for large-scale $3D$ simulations with complex deformations, when the required N_c is large, the greedy procedure will become a bottleneck for the mesh deformation. To accelerate this procedure, a multi-selection method and a hybrid decomposition parallel algorithm are proposed and implemented respectively in OpenFOAM.

In the original greedy algorithm, only one point is added to the subset at each loop step, which will then lead to an inefficiency problem. It is easy to imagine that if multiple points are selected at each step, the loop times should be reduced accordingly. The abstract of the greedy algorithm is to select a small subset to represent a large data set, which is similar to the idea of curve fitting. As illustrated in Fig. 1, $f(x)$ is a curve with 9 peaks or valleys(red points), $f^*(x)$ is the fitting curve, $g(x)$ represents $|f(x) - f^*(x)|$. It is obvious that for $f^*(x)$, the fastest way to approaching to $f(x)$ is to select the 9 feature points as its sample data and currently 4 of them have already been included. For the remaining 5 unselected points, we could see they are generally located in the similar positions(x axis) as the points of $g(x)$ that contain the largest local maximum values(except for the far left one). That is to say, the largest local maximums of $g(x)$ are probably(not absolutely) corresponding to the feature points. As an analogy, we could take the actual boundary displacements as $f(x)$, the interpolated displacements as $f^*(x)$ and the displacement errors as $g(x)$. Thus, in a similar way, the points that contain the local maximum errors may correspond to the feature points to be selected. To validate this idea, the distributions of the surface error with $N_c = 10$ and $N_c = 11$ is plotted in Fig. 2. It could be clearly noted there are several local maximum errors scattered on the surface. This demonstrates that we could select multiple points that contain the local maximum errors at each step in the greedy algorithm.

Algorithm 1 The multi-selection greedy algorithm

Require: $\boldsymbol{x}_b, \Delta\boldsymbol{x}_b, \xi_{tol}$
Ensure: $\boldsymbol{x}_c, \Delta\boldsymbol{x}_c$
1: neighbors$[][] = ConstructBdyNeib(\boldsymbol{x}_b)$
2: $\boldsymbol{x}_c = \boldsymbol{x}_b[0] \qquad \Delta\boldsymbol{x}_c = \Delta\boldsymbol{x}_b[0]$
3: **repeat**
4: $\quad \varepsilon_{pre} = \parallel \boldsymbol{\varepsilon} \parallel_2 / \parallel \Delta\boldsymbol{x}_b \parallel_2$
5: $\quad \boldsymbol{\lambda}_c = \boldsymbol{\Phi}_{c,c}^{-1} \Delta\boldsymbol{x}_c$
6: $\quad \Delta\boldsymbol{x}_b^* = \boldsymbol{\Phi}_{b,c} \boldsymbol{\lambda}_c$
7: $\quad \boldsymbol{\varepsilon} = \Delta\boldsymbol{x}_b^* - \Delta\boldsymbol{x}_b$
8: $\quad \varepsilon_{cur} = \parallel \boldsymbol{\varepsilon} \parallel_2 / \parallel \Delta\boldsymbol{x}_b \parallel_2$
9: $\quad \boldsymbol{\varepsilon}_{mxm}[] = 0 \qquad \text{indices}_{mxm}[] = 0$
10: $\quad$ **for** $i = 0$ to $N_b - 1$ **do**
11: $\quad\quad$ **if** $\parallel \boldsymbol{\varepsilon}[i] \parallel > \parallel \boldsymbol{\varepsilon}[\text{neighbors}[i][0]] \parallel$ && ... && $\parallel \boldsymbol{\varepsilon}[i] \parallel > \parallel \boldsymbol{\varepsilon}[\text{neighbors}[i][end]] \parallel$ **then**
12: $\quad\quad\quad \boldsymbol{\varepsilon}_{mxm} = (\boldsymbol{\varepsilon}_{mxm}, \boldsymbol{\varepsilon}[i]) \qquad \text{indices}_{mxm} = (\text{indices}_{mxm}, i)$
13: $\quad\quad$ **end if**
14: $\quad$ **end for**
15: $\quad$ Select multiple control points based on $\boldsymbol{\varepsilon}_{mxm}$ and indices$_{mxm}$
16: **until** $\varepsilon_{cur} < \xi_{tol}$

Based on the above idea, we have proposed a multi-selection greedy algorithm as presented in Algorithm 1. Step 1 is to construct a $2D$ array which contains the neighbors of each boundary point. After the initialization, the greedy loop is performed from Step 3 to 16. In Steps 5-7, the boundary displacement errors are firstly calculated. Then a loop is executed to calculate the local maximum errors in Steps 10-14. The arrays $\boldsymbol{\varepsilon}_{mxm}$ and indices$_{mxm}$ respectively contain the specific values and indices of current local maximum errors. In step 15, multiple points with local maximum errors will be selected. A remaining question to consider is how many exactly control points should be selected. Here we implemented tow different strategies. Strategy 1 is to select a constant number(N_{cst}) of control points at each loop step and Strategy 2 is an adaptive strategy based on the gradient of the error reduction. For either Strategy 1 or Strategy 2, multiple points will be selected at each loop step, thus compared to the original greedy algorithm, Algorithm 1 is thought to have a faster convergence speed.

The RBF mesh deformation with data reduction could be divided into two major steps: (1) Reduce the number of control points by the greedy algorithm; (2) Interpolate the motion of the internal points based on the selected control points. Our parallelization work is mainly focused on $\boldsymbol{\Phi}_{b,c}$(a matrix to calculate the interpolated displacements of the boundary points) in the greedy procedure and $\boldsymbol{\Phi}_{in,c}$(a matrix to calculate the motion of the internal points) in the interpolation procedure. At present, most CFD tools employ parallel algorithms based on the mesh decomposition. The mesh points are decomposed into multiple parts at beginning of the simulation, and each processor reads a portion of the
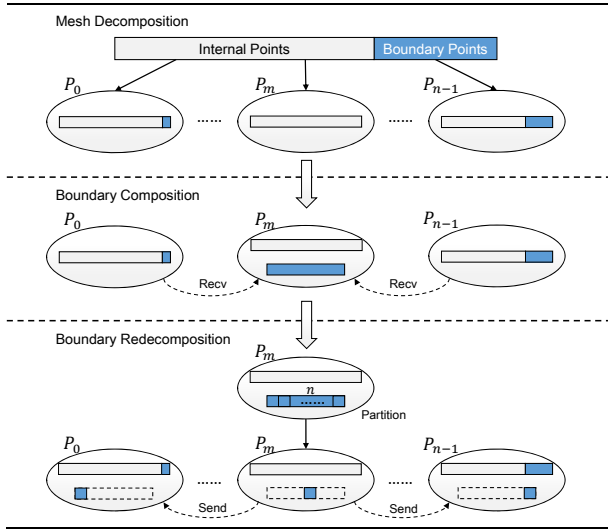
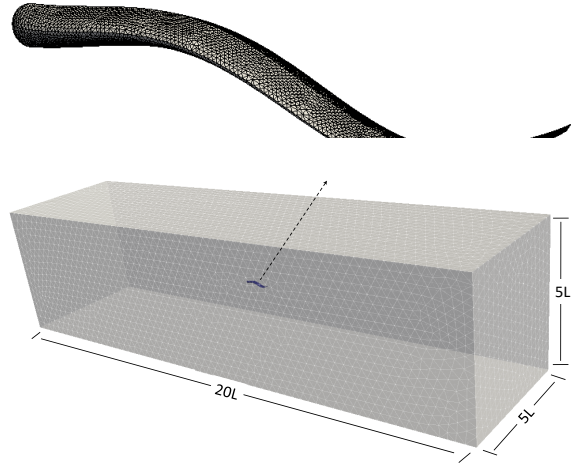**Figure 3: The hybrid decomposition parallel method.**

Figure 4: Computational mesh for the $3D$ undulating fish.

points and then begins the computation. In most cases the graph partition algorithm is used based on the relations between mesh cells. Generally when the degree of parallelism is small, both the boundary points and the internal points could be evenly allocated to each processor. However, when the degree of parallelism increases, it's hard to ensure all processors be allocated with the boundary points. This will then lead to a load imbalance problem.

To address the problem above, we proposed a hybrid decomposition parallel method as illustrated in Fig. 3. The arrays of the coordinates of internal points and boundary points are separately colored by grey and blue. Firstly in the mesh decomposition procedure, all the mesh points are allocated to n processors. We could see the boundary points are unevenly distributed. Then in the following step, a boundary composition procedure is performed. All the processors send their local arrays of the boundary points to a specific processor P_m. By assembling these scattered data, a global array containing the coordinates of all the boundary points is constructed on P_m. At last in the boundary re-decomposition procedure, P_m partitions the global array into n uniform portions and then evenly sends them to other processors according to their ranks. Thus each processor will obtain a same-size portion of the boundary points and then could perform the computations for $\Phi_{b,c}$ in parallel without any load imbalance.
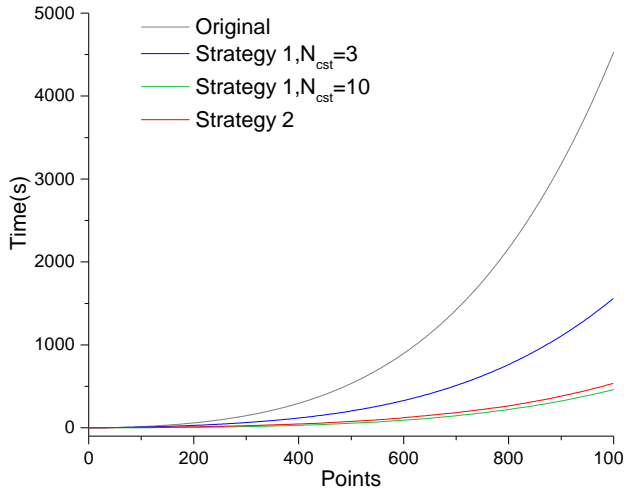

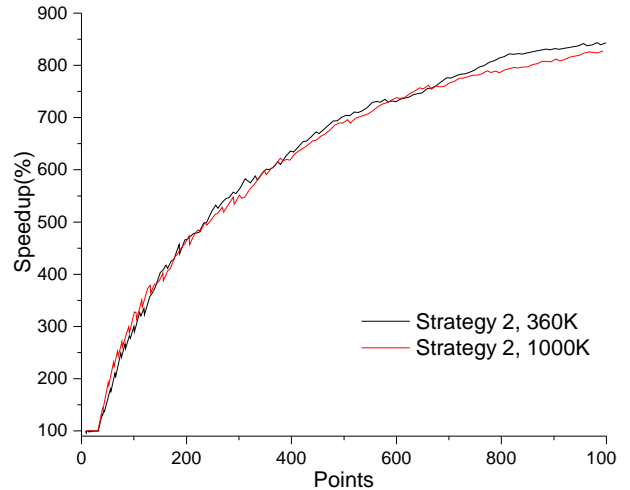**Figure 5: Greedy time cost vs. number of selected points.**

Figure 6: Speedup of 360×10^3 and 10^6 cell meshes.

To assess the effectiveness and efficiency of our method, a $3D$ moving fish test case is considered. As illustrated in Fig. 4, a fish with length L is undulating in the middle of a $20L \times 5L \times 5L$ cubic tank. In terms of the convergence speed, Fig. 5 plots the greedy time as a function of the number of selected control points. We could see as N_c increases, the cost of the original greedy method is in a very fast exponential growth. For our multi-selection method, using Strategy 1 with $N_{cst} = 3$, the cost could obtain a reduction of more than 50%. Further more, using either Strategy 1 with $N_{cst} = 10$ or Strategy 2, the cost could be reduced almost to a linear growth. This verifies the high efficiency of our multi-selection method. Comparison of Strategy 2 applied on different meshes is illustrated in Fig. 6. It can be seen that the speedup of Strategy 2 is mesh independent. For both two meshes, as the number of selected points increases, the speedup will

accordingly grow up and gradually approach to a limit value. Fig. 8 illustrates with contours the manner in which the surface errors decay as more points are added using Strategy 2. Typically, it is possible to achieve maximum errors less than 0.025% of the undulating amplitude($0.125L$) with 683 control points on the 10^6 cell meshes.

(a) Normalized cost for the greedy procedure

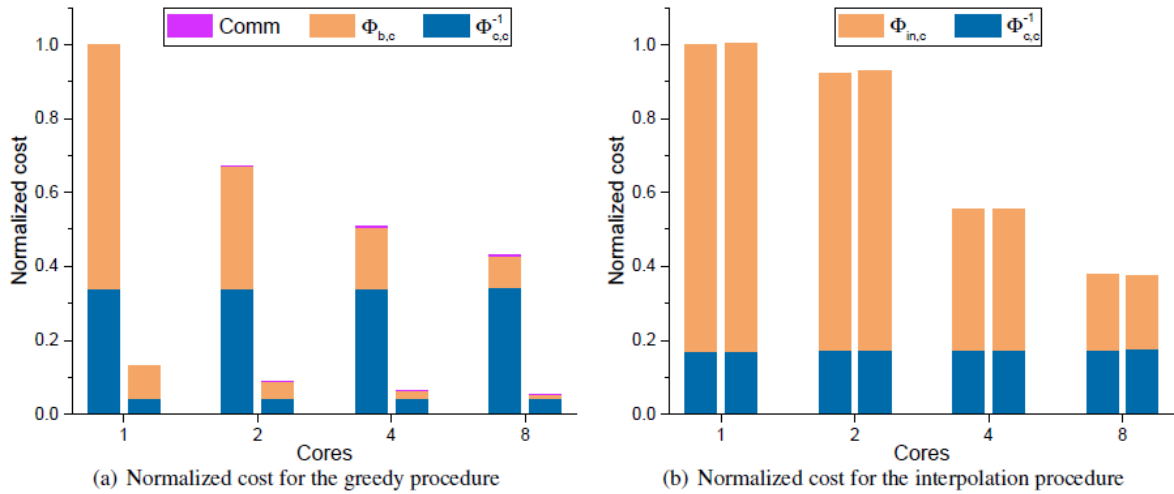(b) Normalized cost for the interpolation procedure

Figure 7: Time Cost versus degree of parallelism for each part of the RBF mesh deformation using the original greedy method(left columns) and the multi-selection greedy method(right columns) on the 10^6 cell mesh with error tolerance of 1e–4.

The time cost of each part of the RBF based mesh deformation procedure on the 10^6 cell mesh is illustrated against the degree of parallelism in Fig. 7. For the greedy procedure, the cost is reduced completely due to the reduction of $\Phi_{b,c}$, while $\Phi_{c,c}^{-1}$(a matrix calculation that could not be parallelized) remains unchanged at all parallelism. In addition, as the parallelism increases, the communication cost will increase and thus lead to a decrease of the parallel efficiency. Similarly for the interpolation procedure, the cost is reduced completely due to the reduction of $\Phi_{in,c}$ and $\Phi_{c,c}^{-1}$ also remains the same at all parallelism. As shown in Fig. 9, the total speedup of Strategy 2 for both meshes is illustrated against the degree of parallelism. The parallel speedup using the original greedy algorithm is also plotted as a comparison. We could see using our multi-selection method at parallelism of 72, a total speedup near to 12 and 20 will be obtained respectively for the 360×10^3 cell mesh and the 10^6 cell mesh at last.
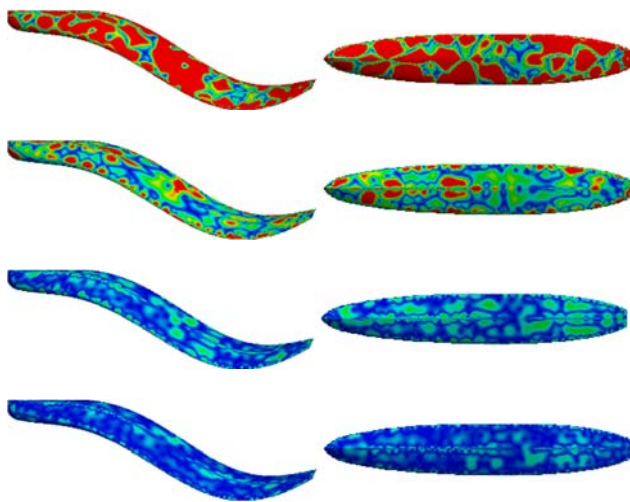

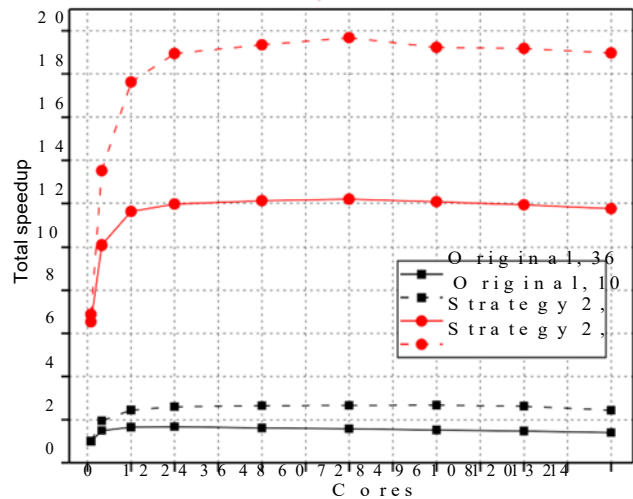**Figure 8: Evolution of the surface errors on the 10^6 cell mesh.**

Figure 9: Total speedup vs. degree of parallelism.

References

[1]T. C. Rendall and C. B. Allen, "Efficient mesh motion using radial basis functions with data reduction algorithms," *Journal of Computational Physics*, vol. 228, no. 17, pp. 6231–6249, 2009.

DEVELOPMENT OF NEW FUNCTION OBJECT
FOR SLOSHING IMPACT ASSESSMENT

WOOYOUNG JEON[1], SEONGJIN SONG[2], SUNHO PARK[3]

[1]Korea Maritime and Ocean University, jwy17@kmou.ac.kr
[2]Korea Maritime and Ocean University, ssong@kmou.ac.kr
[3]Korea Maritime and Ocean University, spark@kmou.ac.kr

Keywords: OpenFOAM, function object, source code, sloshing

The most important parameter for sloshing impact load assessment is impact pressure on the tank wall. Since analytically predicted tank wall pressures were not acceptable to large amplitude sloshing, scale model experiments are carried out [1]. In model experiment, to measure impact pressure on the tank wall, pressure sensors were mounted along the tank boundary [2][3]. Moreover, CFD simulations were carried out and validated against experimental result [4], [5]. Nevertheless, evaluation of impact pressures by numerical CFD analysis not reliable because of high impact pressure is strictly localized in the space and the time, being very sensitive to the local effect and depends on many physical parameters of liquid, gas and structure involved in the impact e.g. density, viscosity, ullage pressure, surface tension, compressibility, hydroelasticity, viscoelasticity, etc. [4][5][6]. Bureau Veritas guidance note suggested the impact normal velocity with respect to the wall based CFD analysis [7]. The impact normal velocity could evaluate kinetic energy of the liquid and thus quantify the sloshing impact. Therefore, the objectives of this paper are describing new function object called *sloshingDynamicProbe* plugged in *interDyMFoam* and its application. For the development of new function object, OpenFOAM-5.0 was used.

In case of model experiment, it is possible to gather only limited position's data where pressure sensors are mounted on model tank's boundary. On the other hand, the new function object considers all fluid field and wall boundaries. If it stores time series data entire simulation, too much data has stored so huge storage space are required and post-process would be difficult. Therefore, defining a state where normal velocity exceeds threshold velocity (user-defined value) as sloshing event, *sloshingDynamicProbe* store data for a specific time (also user-defined value) before (pre-trigger) and after (post-trigger) the event. Through this, it is possible to reduce the storage and store only impact relevant data.

The *sloshingDynamicProbe*s working in *interDyMFoam* is schematically showed in Figure 1. The function object consists of three parts those are input, process and output. The input part is operated only once when a solver initializing. After the solver has executed, the solver create *sloshingDynamicProbe* object, *sloshingDynamicProbe*'s constructor call *read* member function of *sloshingDynamicProbe* class. It reads the dictionary where the user defined variables are defined. The variables are wall patch names of the sloshing tank, threshold velocity, offset, pre-trigger and post-trigger. Then it initializes member data defined in the header file. The process part is operated at the end of every time loop. It calculates a liquid normal velocity at every probe location, which is offset in the vertical direction from the tank wall. The liquid normal velocity is expressed

$$(\alpha \vec{v})_{p.o.} \cdot \vec{n} \qquad (1)$$

where α is the liquid volume fraction (1 for the liquid, 0 for the gas), $\vec{v}$ is the velocity vector, the subscript $p.o.$ means probe offset location from the tank wall, and $\vec{n}$ is the normal vector from the tank wall. It updates buffer to write the relevant sloshing data before the event after calculation. The buffer size is determined by pre-trigger and time step size. When the normal velocity exceeds threshold velocity, the probe is activated. The data for the pre-trigger time are written to the file and then the probe writes the data before the normal velocity is less than the threshold velocity. After the threshold velocity exceeds the normal velocity, the probe is deactivated after the post-trigger time. Figure 2 describes algorithm for activate or deactivate probe as shown is Figure 3. In output part the data of the activated probe are written to the file.
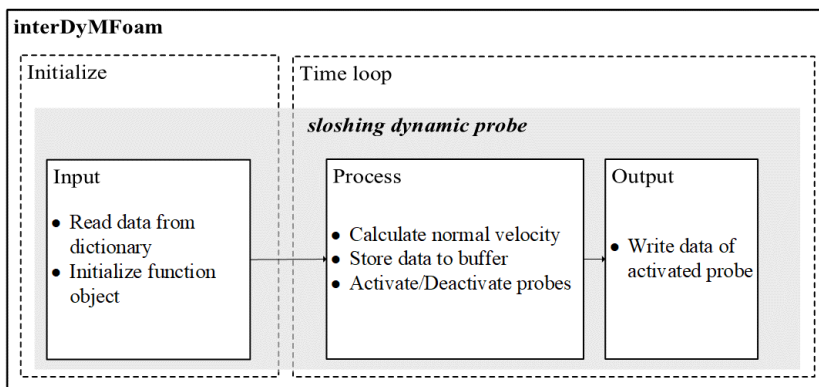
Figure 1: Three parts of *sloshingDynamicProbe* working with *interDyMFoam*.
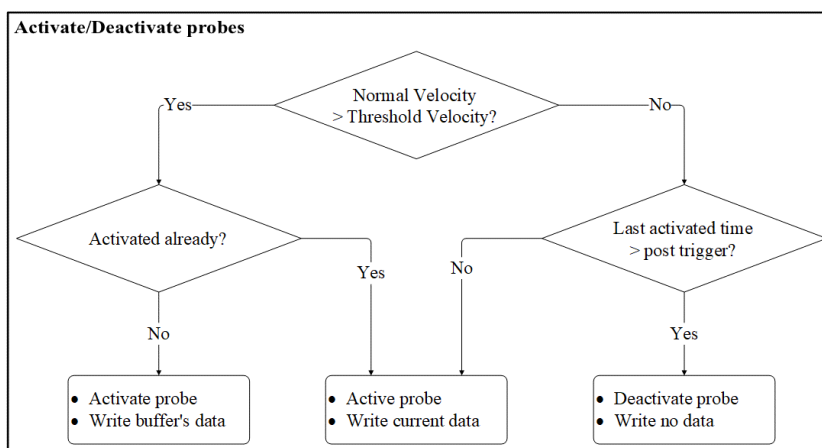
Figure 2: Algorithm for activating/deactivating dynamic probe.

The *sloshingDynamicProbe* has been tested with *sloshingTank3D* tutorial of OpenFOAM-5.0. Figure 3 are example of the output data. It shows the new function object can store relevant data before and after sloshing event without data loss or overlap. When the velocity exceeds the threshold velocity the impact count is increased by one.

Figure 3: Example of extracted normal velocity at an offset location using the *sloshingDynamicProbe*.

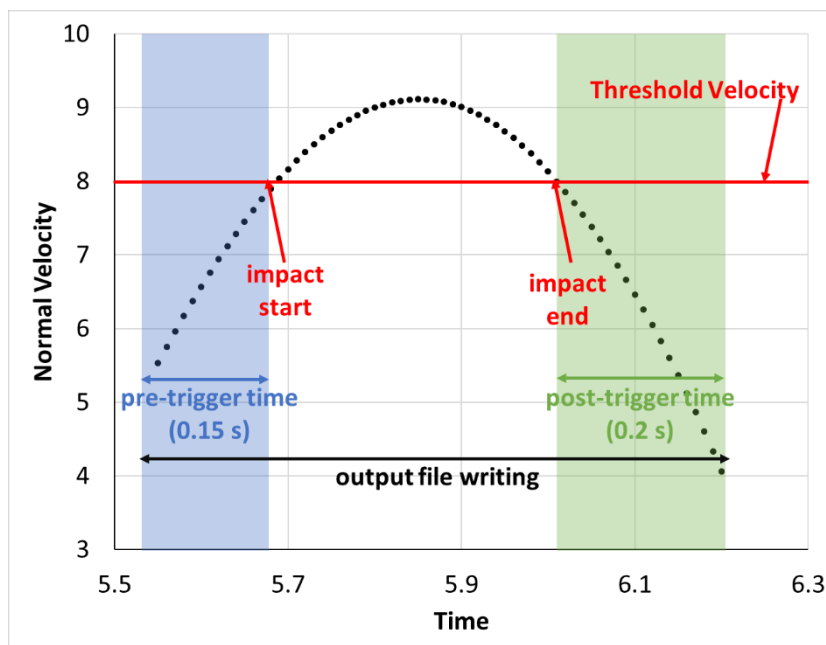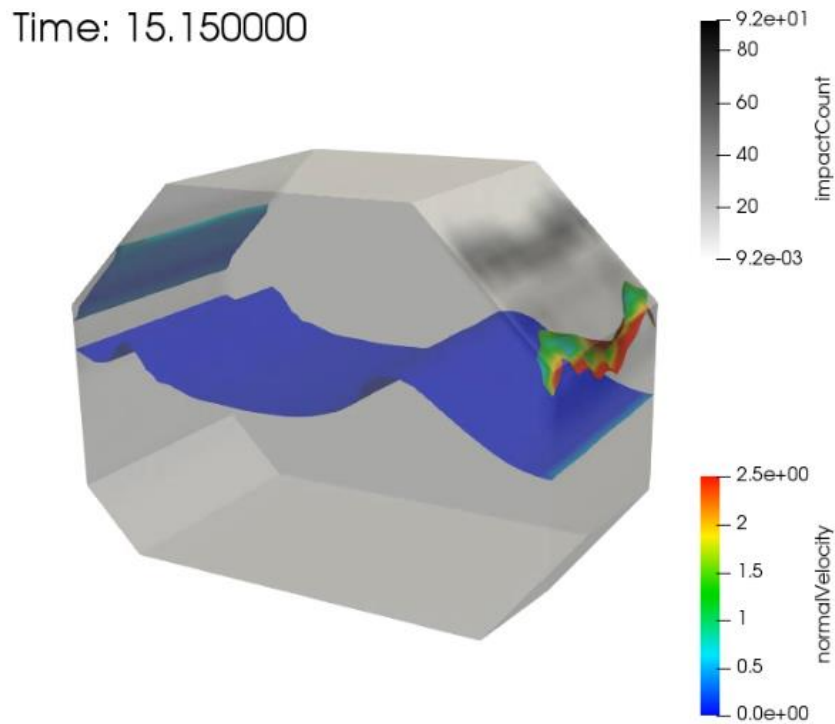**Figure 4: Example of extracted sloshing impact count and normal velocity using the *sloshingDynamicProbe*.**

Acknowledgement

References

[1] R. Bass, E. Bowles, R. Trudell, J. Navickas, J. Peck, N. Yoshimura, S. Endo and B. Pots, "Modeling Criteria for Scaled LNG Sloshing Experiments", *Journal of Fluids Engineering*, vol. 107, no. 2, pp. 272-280, 1985.

[2] S.-Y. Kim, K.-H. Kim, Y. Kim, "Comparative study on pressure sensors for sloshing experiment," *Ocean Engineering*, Vol. 94, pp. 199-212, 2015

[3] M.-A.Xue, J. Zheng, P. Lin, X. Yuan, "Experimental study on vertical baffles of different configurations in suppressing sloshing pressure," *Ocean Engineering*, Vol. 136, pp. 178-189, 2017

[4] D. Lee, M. Kim, S. Kwon, J. Kim and Y. Lee, "A parametric sensitivity study on LNG tank sloshing loads by numerical simulations", *Ocean Engineering*, vol. 34, no. 1, pp. 3-9, 2007.

[5] B. Godderidge, S. Turnock, M. Tan and C. Earl, "An investigation of multiphase CFD modelling of a lateral sloshing tank", *Computers & Fluids*, vol. 38, no. 2, pp. 183-193, 2009.

[6] NI 554. "Design Sloshing Loads for LNG Membrane Tanks", *Guidance note NI 554 DT R00 E*, 2011.

[7] T. Gazzola and L. Diebold. "Dynamic Probes: an on-the-fly CFD Plug-in for Sloshing Impact Assessment." .", in *Proc. 23rd International Offshore and Polar Engineering*, 2013, pp. 268-275.

HELYX-OS V3, THE NEXT-GENERATION GUI FOR OPENFOAM®

PAOLO GEREMIA[1], STEFANO VALERI[1], DAVIDE CIANI[1]

[1]ENGYS, info@engys.com

Keywords: *HELYX-OS, Pre-Processing, OpenFOAM® GUI, HPC*

One of OpenFOAM®'s main shortcomings has always been its lack of a Graphical User Interface (GUI). This has created a barrier to entry, especially for those new to CFD, and made many simple tasks error prone. HELYX-OS [1] is a product from ENGYS that attempts to remedy this shortcoming by providing an intuitive interface for creating and managing OpenFOAM® cases. Although there are already working examples of GUIs for OpenFOAM® the main objective of HELYX-OS is to make available an easy-to-use software for both new users approaching the software for the first time and advanced users which might want to use the GUI for daily work to quickly mesh, setup and run a case or testing different solution settings, different geometries, etc.

The GUI has been developed and maintained by ENGYS using both Java and VTK libraries since from 2012 when the first version of the software was released for Linux 64-bit distributions. All the installation files instructions are available from the GitHub website which also hosts a ticketing system for bug report and a dedicated forum for technical discussions.
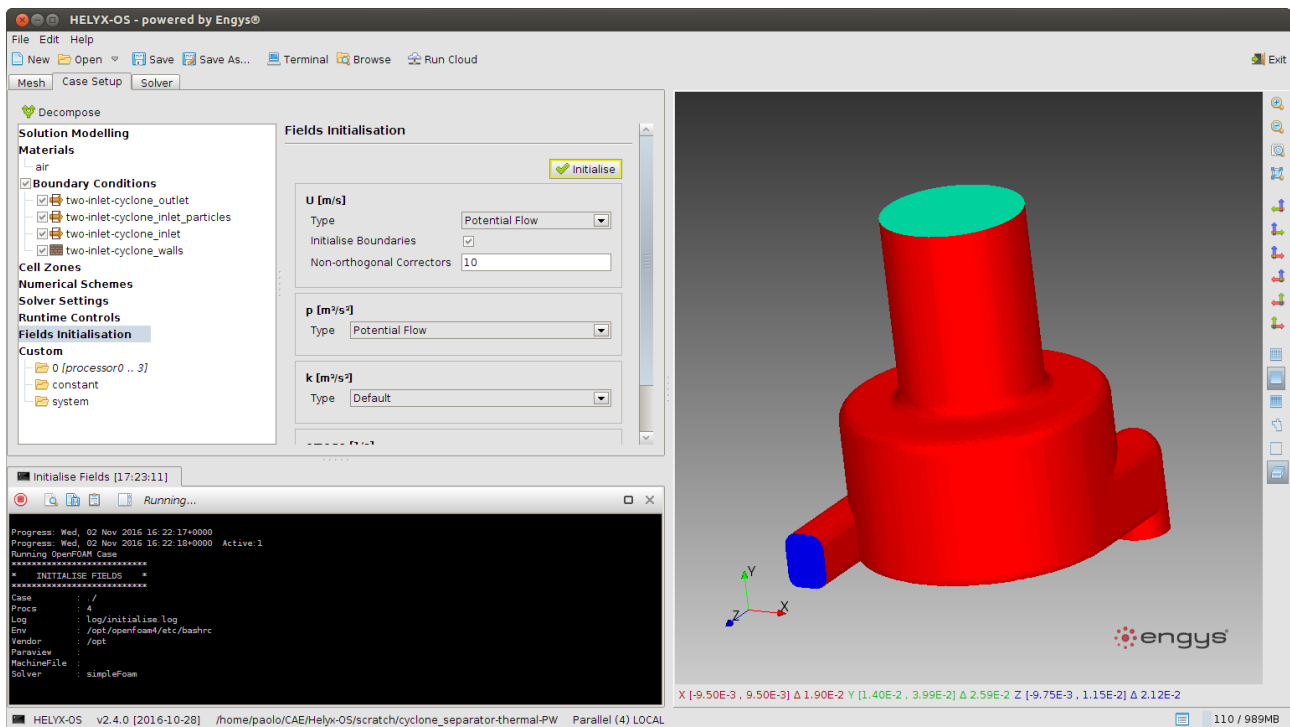

Figure 1 – HELYX-OS graphical user interface for OpenFOAM®

HELYX-OS layout (see **Error! Reference source not found.**) consists of three main components called Mesh, Case Setup and Solver which allows easy mesh creation, case setup, run and solution monitoring of an existing case. A 3D window for direct user interaction is available from within the Mesh and Case Setup components whose settings are defined in specific panels accessible by the users via specific buttons. In addition, the presence of a tree allows the grouping of both the geometrical entities (including surfaces and volumes) in the Mesh tab and the patches and cell zones in the Case Setup tab.

The key-features of HELYX -OS are as follows:

- Create a new case or load an existing case
- Support of serial and parallel cases
- Create a mesh using blockMesh and snappyHexMesh utilities
- Setup a case including turbulence model, boundary conditions, etc.
- Run and monitoring of a case in the Solver tab

HELYX -OS is designed to reproduce the typical user workflow starting from the case creation till the run execution through an intuitive user interface. In fact the presence of a series of buttons accessible by the user to specify the case settings has been designed to meet the requirements of both a wizard-based to follow each intermediate step from the case creation to the run execution in a serial mode and an advanced usage to quickly jump from one panel to another with necessarily going through all the steps required to setup and a case from scratch.

In the work detailed here we present the new version 3 of HELYX-OS, which brings considerable improvements with respect to the previous v2 framework, including the following features:

- New multi-region cases handling, e.g. for Conjugate Heat Transfer (CHT) cases
- A more consistent and intuitive ribbon-based design layout of both tasks and objects workflow
- Enhanced performance for handling of larger parallel cases
- New Run Mode pre-set for custom running scripts
- HPC and cloud-ready interface for execution of OpenFOAM® jobs
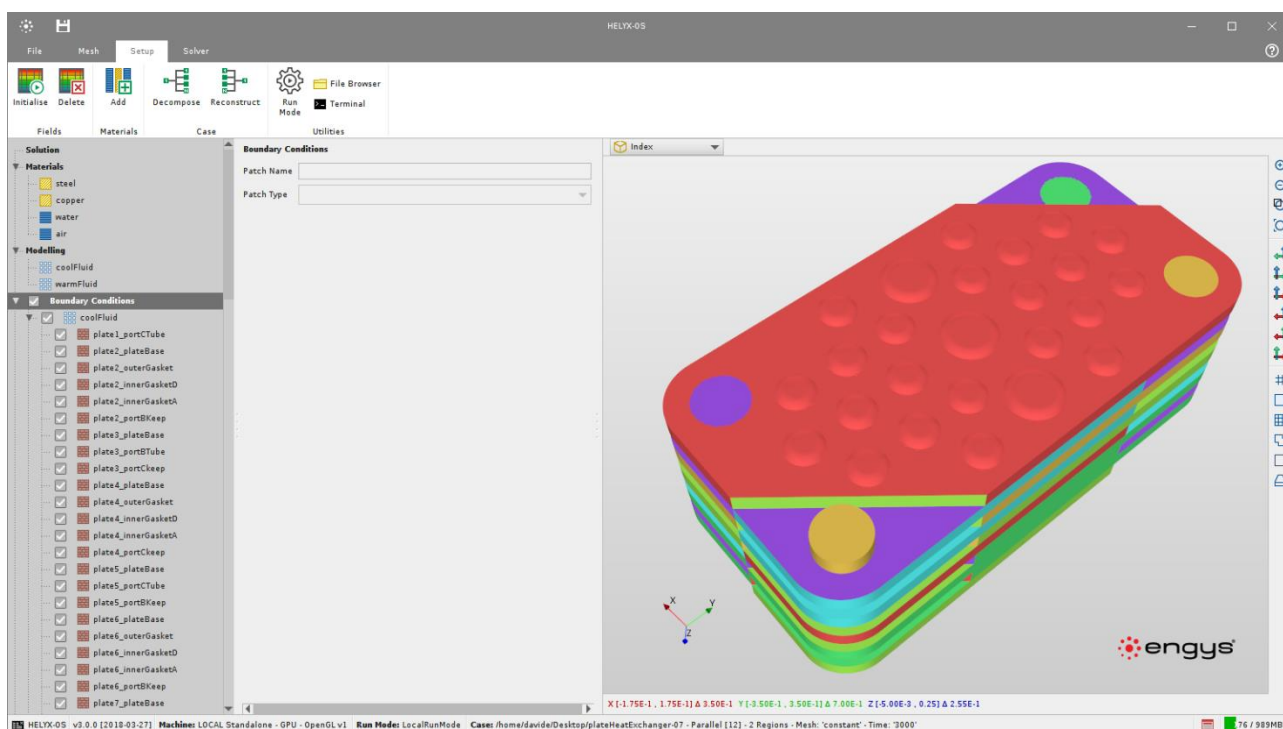
Figure 2 – New interface available in HELYX-OS v3

In addition to the features added to the new v3 version the authors will also share plans regarding the release roadmap to make sure that the continuous development process that ENGYS has been providing for HELYX-OS in the last years will help the community to use OpenFOAM® in a more efficient and productive way.

References

[1]   HELYX-OS website: http://engys.github.io/HELYX-OS/

THE HIGHLY-EFFICIENT CAE PRE-AND POST-PROCESSING SOLUTIONS BASED ON OPENFOAM

FIRST BINTANG, SECOND BAOJUNLI, THIRD PENGJI

[1] *BinTang Institutional Affiliation, michaeltangbin@163.com*
[2] *Baojun Li Institutional Affiliation, libaojunqd@foxmail.com*
[3] *Peng Ji Institutional Affiliation, love_peng20@163.com*

Keywords: *FastCAE, OpenFOAM, pre-processing, post-processing, Designer, GUI*

Abstract — As a widely used open source computational fluid dynamics software, OpenFoam has many advantages, such as the diversity of the pre-and post-processing interfaces, the stable fundamental class library, and the outstanding capability of large-scale parallel computing. Due to the deficiency of visualization window interface of this open source software, user learning is costly. Therefore, an interfacial interaction system based on the FastCAE platform contains OpenFOAM pre-processing, parameter configuration, solution calculation and post-processing is developed. The platform also capable of design specific interactive interface based on the integration of the two preprocessing meshes, the BlockMesh and SnappyHexMesh, from OpenFOAM. It also can automatically map different dictionary files, and provide users with parameter configuration entries when calculation parameters of solver are importing to the platform. The post-processing uses independently developed visual software to analyze the result files generated by the OpenFOAM calculation and support the functions of two-dimensional curves, contour graphs, vector graphs and animation. The OpenFOAM GUI based on the FastCAE platform, can greatly reduce user's use-cost and improve its application efficiency.
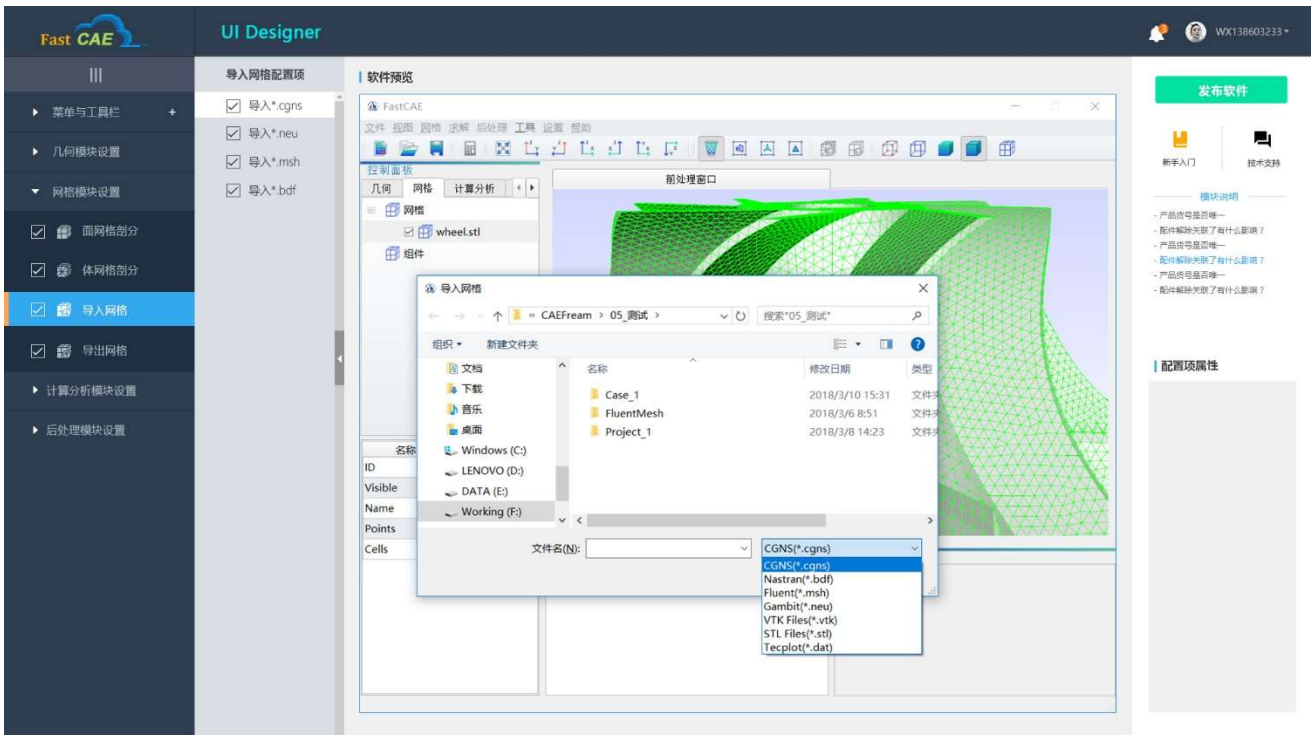
Figure 1: Designer pre-processing
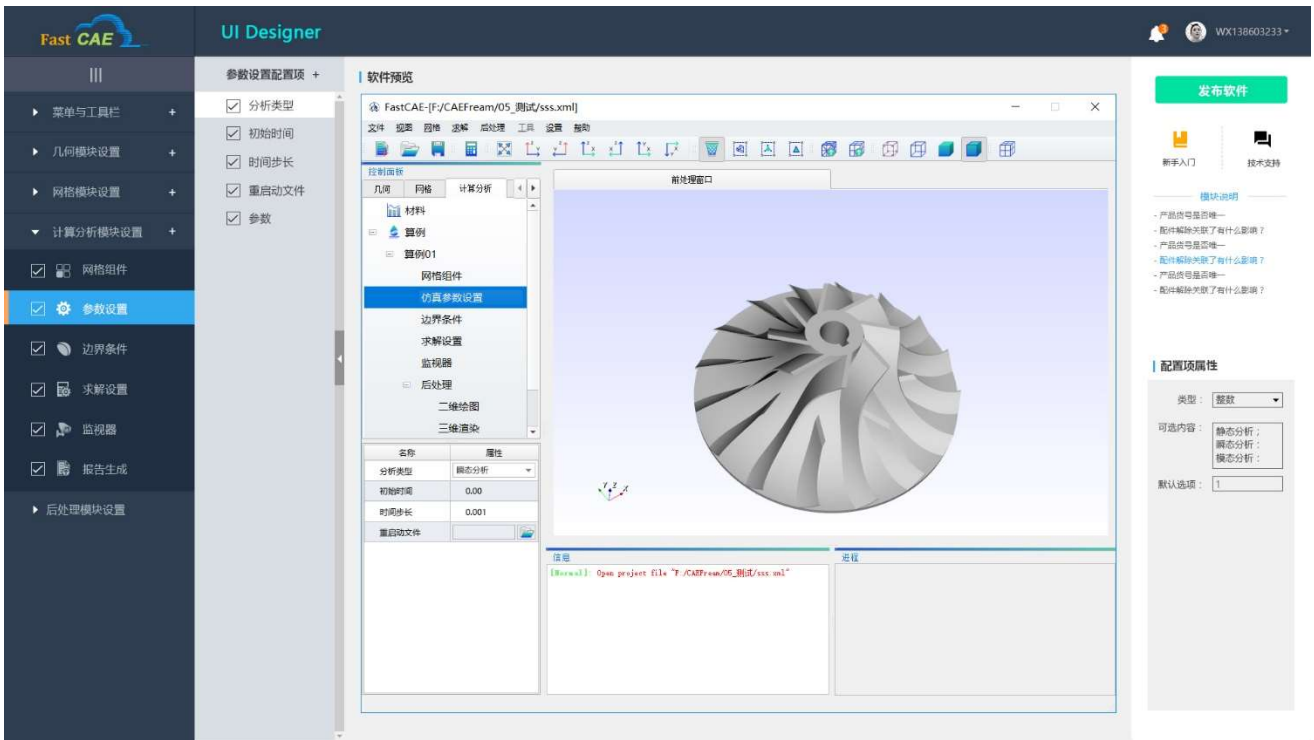
Figure 2: Designer parameter configuration
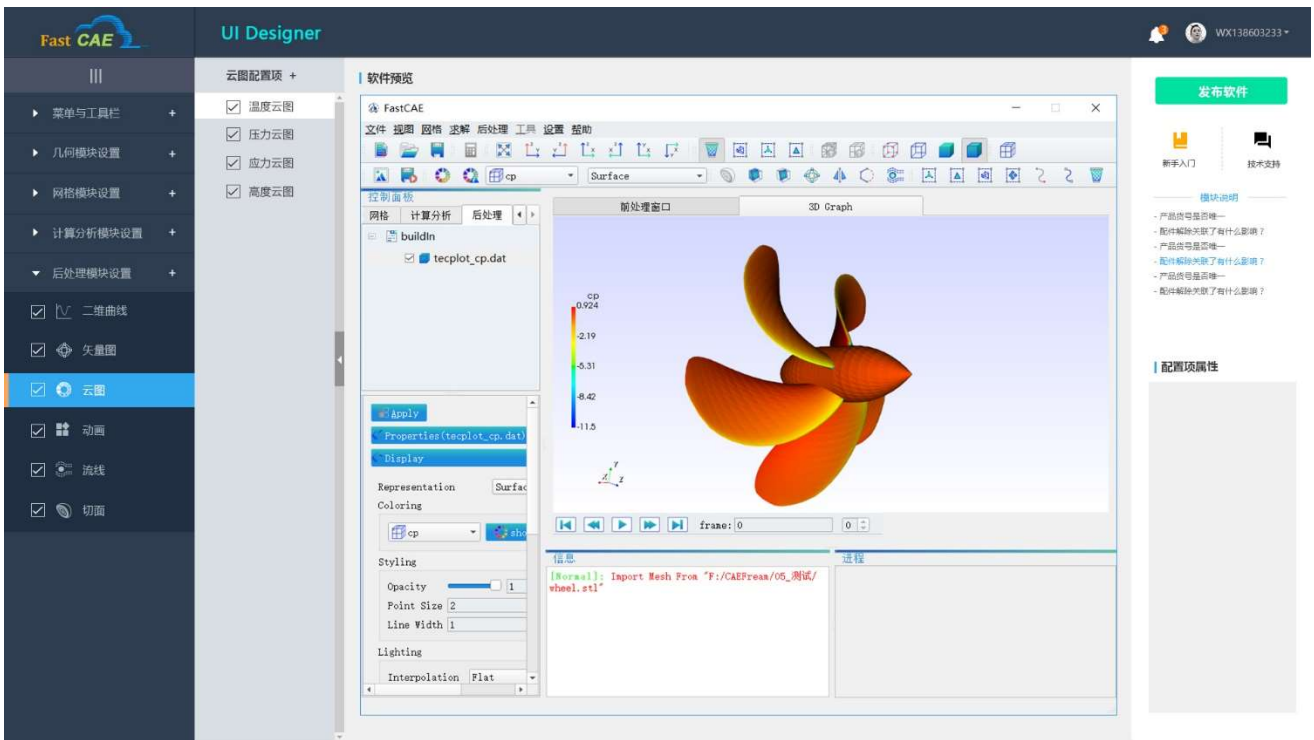
Figure 3: Designer post-processing

Acknowledgements

The authors thank all those involved in the organisation of OFW13 and to all the contributors that will enrich this event.

References

[1] Ye Donghui: The Analysis of Key Technology Application in Ship Hydrodynamics Based on Open FOAM：Huazhong University of Science & Technology Wuhan 430074, P. R. China May, 2013.

COUPLING OPENFOAM WITH FENICS FOR MULTIPHYSIS SIMULATION

QINGFENG XIA[1], DAVID GILLESPIE[2]

[1]*Oxford Thermofluids Institute, Department of Engineering Science, University of Oxford,*
qingfeng.xia@eng.ox.ac.uk
[2]*Department of Engineering Science, University of Oxford, David.Gillespie@eng.ox.ac.uk*

Keywords: *Multiphysics, FSI, FenicsSolver, FreeCAD, design automation*

There is a trend of tight integration of Computer-aided Design (CAD) and Computer-aided Engineering (CAE) for both commercial and open source software packages. CAD platforms not only create geometry, but also provide functions of computational engineering and product life management. Meanwhile, CAE software for physical system simulation, has strengthened the geometry creation and meshing capability for a smoother engineering process. However, there are gaps for an automated engineering design/optimisation process from geometry prototyping to Computer-aided Manufacturing (CAM). In particular, the changed geometry topology, i.e. the way surfaces forming a solid geometry, will invalidate meshing and boundary condition setup in CAE, because the boundary setting is linked with volatile surface identifier integer, not the spatial coordinates. This suggests understanding geometry topology is the key to optimisation and simulation automation.

In this paper, the process of automated engineering design using Python is demonstrated, based on open source CAE modules. Built on top of the meshing functions in FEM module of FreeCAD [1], the authors developed a CFD module [2] as a graphical pre-processor for meshing, solver input setup. Open source CAE solvers such as OpenFOAM [3] (FVM) and FenicsSolver (FEM) [4], are integrated into FreeCAD, to solve multi-physics partial differential equations. The graphic user interface eases the setup of open source solver, and enables modelling complicate geometry in real-world engineering problem. User operation in FreeCAD GUI can be recorded into Python code, which assists experienced engineers in building up automatic design pipeline in a later stage. Thereby, a one-stop design process from geometry building to analysis is provided for both GUI and scripting users.

Furthermore, coupling OpenFOAM with external solver can be achieved by mesh and data exchange via files or code insertion. preCICE [5] is an emerging open source library for rapid source code integration, while MpCCI [6] is a commercial framework of file-based data exchange without modifying OpenFOAM or other external solvers. In order to be compatible with current Fem and Cfd modules of FreeCAD, the mpCCI style coupling strategy is adopted and flow-structure coupling with FenicsSolver is demonstrated. This Fluid-Structure Interaction, with large deformation nonlinear solid solver and non-Newtonian fluid solver, can be used to numerically study turbomachinery sealing, and journal bearing lubrication.

The automated process from CAD to CAM can dramatically reduce engineer's time on design prototyping and optimisation. Multiphysics solvers can be further coupled with system modelling tools, such as open standard of Modelica and Simscape of Mathworks, for multi-component system validation. In the future, artificial intelligence will be introduced into engineering design, once design automation is achieved. The target function will be a comprehensive evaluation of production cost, performance, reliability weight, etc, maintenance cost, depending on engineering sectors. For example, product design in aerospace engineering emphasizes maintenance cost, safety margin, performance for unit weight, in addition to manufacturing cost.
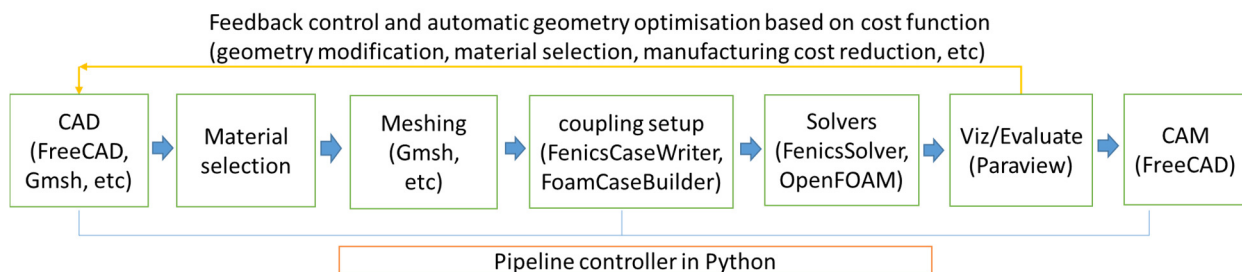

Figure 1: Pipeline of automated Multiphysics design using open source packages

References

[1] R. Jürgen, W. Mayer and Y. van Havre. About FreeCAD: an open source CAx platform. https://www.freecadweb.org/, 2012.

[2] Q. Xia, CFD module for FreeCAD. https://github.com/qingfengxia/Cfd, 2016.

[3] OpenCFD, OpenFOAM: The Open Source CFD Toolbox. User Guide Version 1.4, OpenCFD Limited. Reading UK, Apr. 2007.

[4] Q. Xia and D. Gillespie, Automated Mechanical Engineering Design using Open Source CAE Software Packages, Fenics'18, Oxford, March 2018. https://github.com/qingfengxia/FenicsSolver

[5] H.-J. Bungartz, F. Lindner, B. Gatzhammer, M. Mehl, K. Scheufele, A. Shukaev, and B. Uekermann: preCICE - A Fully Parallel Library for Multi-Physics Surface Coupling. Computers and Fluids, 141, 250–258, 2016.

[6] W. Joppich, M. Kürschner. MpCCI—a tool for the simulation of coupled applications. Concurrency and computation: Practice and Experience. 2006, 18(2):183-92.

A PRE-PROCESSING UTILITY FOR COUPLING WRF AND OPENFOAM

JIAHUI LI, XI ZHANG[*], YING ZHONG, NINGNING WU

National Supercomputer Center in Guangzhou, Sun Yat-sen University, xi.zhang@nscc-gz.cn

Keywords: Pre-processing, WRF, OpenFOAM, coupling

The prediction of wind resource is the initial step for the construction of wind farm, which plays a crucial role in making good use of wind energy. Numerical simulation is a useful tool for the prediction of wind resource. However, mesh in large resolution is required for complex terrain, which leads to large computational resource consumption. Thus, more efficient numerical model is necessary. Furthermore, precise boundary condition is also important, which depends on observation or weather report. As a matter of fact, some coupled numerical models [1] have been developed. In those coupled models, Weather Research and Forecasting (WRF) [2] is often used in a mesoscale computational domain for providing boundary conditions of Computational Fluid Dynamics (CFD) software. CFD software is used in a micoscale domain for prediction wind resource. In this paper, OpenFOAM is applied for simulating wind field with the boundary conditions supplied by WRF. Due to different mesh resolutions and computational domains, the WRF results should be transferred into boundaries and internal field of OpenFOAM domain. Hence, a utility is developed for data transfer. The process of data transfer contains three steps. Firstly, coordinates of face centres of boundaries and cell centres of internal field in OpenFOAM are transformed from Cartesian coordinate into Geographic coordinate. Then, both velocity and kinetic turbulence energy should be interpolated from WRF results. In the third place, the necessary files including U and k are output with prescribed values on the boundaries. Finally, the steady incompressible solver simpleFoam is used to simulate wind field coupled with WRF. Proper boundaries conditions prescribed by WRF are used. A probe location shown in Figure 1 is used for recording velocity, which shows the iterative process of the simulation in Figure 2.
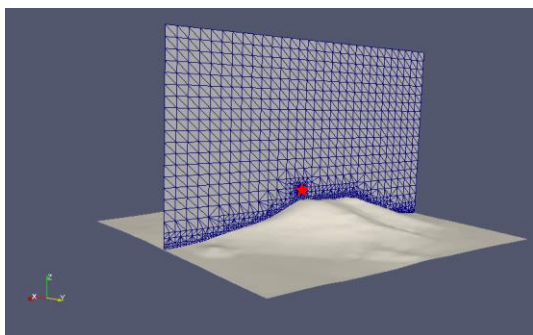
Figure 1: The probe location in OpenFOAM domain (red star)
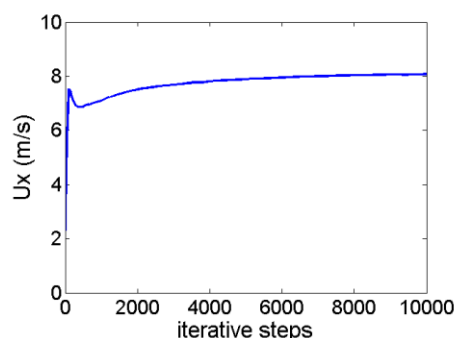
Figure 2: The x component of velocity in probe location

Acknowledgements

References

[1] E. Leblebici, H.I. "Tuncer. Development of OpenFOAM-WRF Coupling Methodolgy for Wind Power Production Estimations," presented at the 5th Symposium on OpenFOAM in Wind Energy. Pamplona, Spain, 2016.

[2] W.C. Skamarock, J.B. Klemp, J. Dudhia, D.O. Gill, D.M. Barker, M.G. Duda, X.Y. Huang, W. Wang, and J.G. Powers. "A Description of the Advanced Research WRF Version 3." Internet: http://www2.mmm.ucar.edu/wrf/users/citing_wrf.html 2008 [May. 16, 2018]

IMPACT OF DYNAMIC SUBGRID SCALE MODELING IN DDES SIMULATION OF MASSIVELY SEPARATED FLOWS

DI WU[1], WEIWEN ZHAO[2], DECHENG WAN[3]

[1,2,3]Collaborative Innovation Center for Advanced Ship and Deep-Sea Exploration, State Key Laboratory of Ocean Engineering, School of Naval Architecture, Ocean and Civil Engineering, Shanghai Jiao Tong University, Shanghai, China, [3]Corresponding Author: dcwan@sjtu.edu.cn

Keywords：*DDES; dynamic DDES; square cylinder; flow separation*

Massively separated flow is of great interest in academic researches of turbulence for its highly frequent appearance in industry applications such as deep sea platforms. For the balance of accuracy and economy, hybrid RANS/LES combines the advantages of RANS and LES by simulating the near wall flow region with RANS and the separated flow region with LES. It stands to reason that hybrid RANS/LES methods become an ideal choice to predict massively separated flows in current engineering applications. Detached-eddy simulation (DES) is one of the mostly used hybrid RANS/LES method due to its simplicity in formulation and adaptation in complex geometry. However, one of the most serious problem faced by DES is the modeled stress depletion (MSD) problem. MSD occurs when the grid is fine enough for activating LES branch of DES but not fine enough to resolve the turbulence fluctuations internal to boundary layers. Delayed detached-eddy simulation (DDES) is the remedied version of detached-eddy simulation (DES) by optimizing the character turbulence length scale to protect the RANS region from being prematurely switched into LES region. But DDES should be hardly declared as perfect, and there still remains a rather large space for the improvement of DDES. Since the investigation of improving LES is going on by many scholars at the same time, it is a natural idea to introduce the research achievement of LES into DDES for better performance. One of the most remarkable concept in LES modeling is the dynamic model. Recently, a few researches of deriving the dynamic version of DDES, in which the model constant is dynamically determined, have been carried out by Z.Yin, et al[1] and He, et al[2] independently.

The main purpose of this paper is to study the impact that how dynamic procedure can influence the performance of DDES in simulating massively separated flow around bluff-bodies which is a research hotspot in ocean engineering. Since the concept of dynamic DDES is quite brandnew and very few relevant researches have been carried out, it is very meaningful to examine the capability of dynamic DDES model to be industrial. In the current work, flow around a square cylinder at Reynold number Re =22000 is simulated. Here the two-equation SST model are operated in RANS mode both in DDES and dynamic DDES models.

The main idea of DES is redefining the turbulence length scale which is contained in the dissipative term of the turbulence kinetic energy transport equation. The turbulence length scale defined in the SST-DES model[3] is as follows:

$$L_{DES} = \min(L_{RANS}, L_{LES}) \tag{1}$$

where $L_{RANS} = \sqrt{k}/(C_\mu \omega)$ is the RANS turbulence length scale, and $L_{LES} = C_{DES}\Delta$ is the LES length scale, i.e. local grid scale.

To protect RANS region from being invaded by LES region, DDES modified the character turbulence length scale by introducing the delay function. The delay function proposed by Spalart[4] takes the form:

$$f_d = 1 - \tanh((8r_d)^3) \tag{2}$$

where $r_d = \frac{\nu_t + \nu}{\sqrt{u_{ij}u_{ij}}\kappa^2 d^2}$ is the delay factor. In the near wall boundary layer, f_d is equal to 0. While in the separated region far from wall, f_d approaches 1. The RANS turbulence length scale of DDES version is defined as

$$L_{DDES} = L_{RANS} - f_d \max(0, L_{RANS} - L_{LES}) \tag{3}$$

One can see that L_{DDES} is promised to be L_{RANS} in the boundary layer where is supposed to be covered by RANS region.

The dynamic k-equation subgrid LES model proposed by Kim, et al[5] can be chosen as the chief source, which is as follows:

$$\frac{\partial \rho k}{\partial t} + \nabla \cdot (\rho U k) = \nabla \cdot \left[\left(\mu + \frac{\mu t}{\sigma_{K3}}\right)\nabla k\right] + P_k - \frac{\rho k^3}{\Delta/C_e} \tag{4}$$

Where we can define the LES length scale

$$L_{LES} = C_k \Delta \tag{5}$$

and the subgird eddy viscosity is read as

$$\mu_{sgs} = L_{LES}\sqrt{k} \tag{6}$$

In the dynamic subgird k-equation LES model, the model coefficients C_k and C_e are dynamically determined during computation as

$$C_k = \frac{1}{2}\frac{L_{ij} \cdot M_{ij}}{M_{ij} \cdot M_{ij}} \tag{7}$$

where

$$L_{ij} = \overline{\widehat{U_i U_j}} - \widehat{U_i}\widehat{U_j} \tag{8}$$

$$M_{ij} = -2\Delta\sqrt{K}\widehat{S_{ij}} \tag{9}$$

Back to DDES model, the LES subgrid length scale L_{LES} is defined in eq (5). Apparently, one can substitute it with the L_{LES} of the dynamic subgird k-equation LES model which is described above and dynamic DDES is obtained. What should be noticed is that the coefficient C_e is unused in the derivation of dynamic DDES in this paper. It is for the reason that C_e is responsible for the construction of the dissipation term in the dynamic k-equation LES model, while the dissipation term of DDES is explicitly constructed by the form of ω-transport equation. Hence, it is unnecessary to reconstruct the dissipation term of DDES using the form which is defined in the dynamic subgrid LES model. For more details of dynamic DDES model, one can read the paper[2] for reference.

All the computations presented in this paper is carried out on the open source platform OpenFOAM. The Naiver-Stokes equations are discretized by using a cell-centered finite-volume method based on block-structured grids. The implicit Euler scheme is adopted to discretize the unsteady time integration. The convective term is discretized by linear TVD scheme with a limiter, while the diffusive term is discretized by Gauss linear conservation scheme. The coupled velocity and pressure is dealt by applying the PIMPLE algorithm.

The diameter of the square cylinder is set to be $D = 0.01$m, and the height is set to be 4D. The origin of coordinates is set at the center of the square cylinder. The length of the computational domain in the flow direction is arranged as 36D, while 20D is set for the vertical direction. This form of domain arrangement is to ensure the full characteristics of flow past a square cylinder can be completely captured.

According to the physics feature of the computation domain, the boundary is marked as the inlet, the outlet, the sides, the bottom and the top. The surface of the cylinder is considered as a no-slip wall. At the inlet boundary, a uniform incoming flow with velocity equal to the free stream velocity $U_\infty = 2.2 m \cdot s^{-1}$ is defined. At the outlet boundary, the pressure gradient is set equal to 0. The rest of the boundaries is defined as symmetry boundary, assuming that the height of the cylinder is infinite.

As can be seen in Figure 1, Structured mesh generation is chosen in this case because of the simple geometry of the cylinder. the mesh domain of $5D$ around the cylinder is generated with the O block grids. While the rest of mesh domain is generated with orthogonal hexahedral grids. The thickness of the first grid near the wall of the cylinder is set as $\Delta = 0.005D$ with time step being $0.003D/U_\infty$ to ensure that $y^+ \leq 1$. The grid nodes distributed in the span-wise direction is set to be $n_z = 80$.
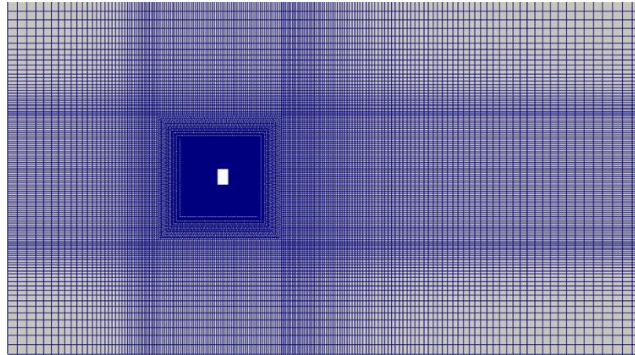

Figure 1: Computation Mesh

Some typical values of the overall flow parameters such as the drag coefficient C_d and the period of shedding S_t are presented together with experimental values[5] and LES predictions[6] in Table 1. The total averaged time is about 100 periods of vortex shedding, which is considered to be long enough for the average operations. Compared with the experiments data, one can see that the overall flow parameters predicted by both DDES and dynamic DDES are admirably accuracy. It means that the dynamic procedure can barely improve the performance of DDES in predicting time averaged overall parameters. This observation is also obtained by Carine, et al[7] when studying the impact of the dynamic procedure in the performance of VMS subgrid LES model.

Table 1: Overall flow parameters of the flow past a square cylinder

Data Source	C_d	St	l_r/D
DDES	2.40	0.126	1.14
dynamic DDES	2.38	0.128	1.10
Experiment[5]	2.35	0.135	-
LES[6]	2.18	0.130	1.07

The distribution of normalized mean horizontal velocity in the centerline of the wake compared with the experiment value is shown in Figure 2. It can be seen that the prediction of both these two model is quite close in the near wall regime where RANS model is supposed to be activated. While dynamic DDES shows better congruency with

experiment data than DDES in regime $2 \leq x/D \leq 6$. It could be speculated that dynamic DDES resolves more abundant turbulence motions than DDES, i,e the dynamic procedure helps DDES to reach wider range of turbulence scales. This deduction is supported by the distribution of horizontal velocity fluctuations in the centerline which is shown in Figure 5. It can be seen that the horizontal velocity fluctuations predicted by dynamic DDES is apparently smaller than DDES, as a result of more turbulence motion resolved by dynamic DDES. Moreover, as can be seen in Figure 6, dynamic DDES is also thought to be better than DDES in predicting the distribution of vertical velocity fluctuations in regime $2 \leq x/D \leq 6$ which is mentioned above.

The distribution of mean horizontal velocity and mean vertical velocity is also shown in Figure 3-4. It could be seen that the predictions of dynamic DDES and DDES are both quite close to the experiment data. While in the regime y/D >=1.5 away from the wall, dynamic DDES shows slightly superior than DDES in predicting the mean vertical velocity. It has been reported by Matthieu, et al[8] that the predictions of mean velocity at section x/D=1 by RANS and DDES is nearly the same. Hence, it is not surprising that dynamic DDES shows barely improvement of DDES.
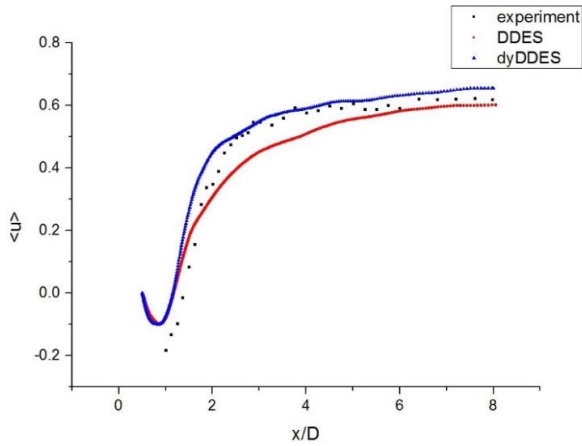

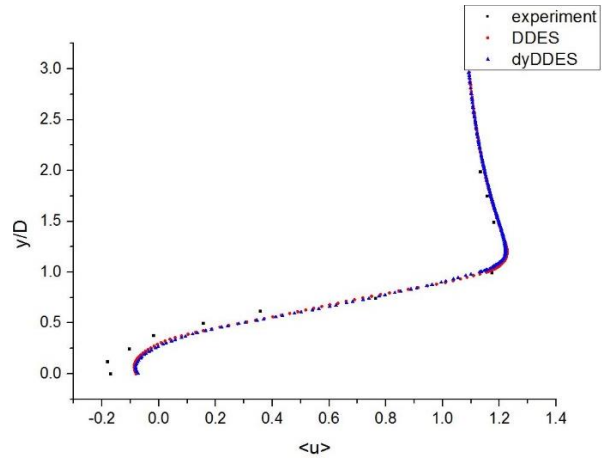**Figure 2: Mean horizontal velocity in the centerline**

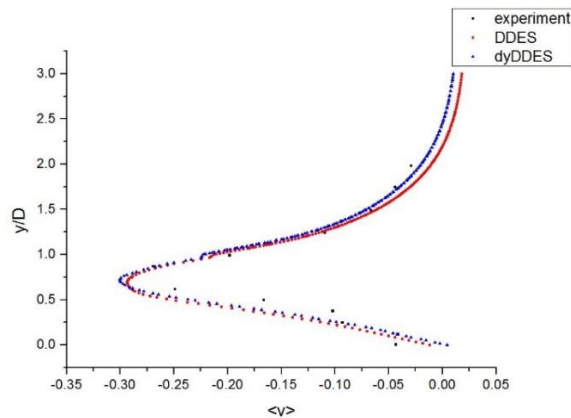**Figure 3: Mean horizontal velocity at x/D=1**

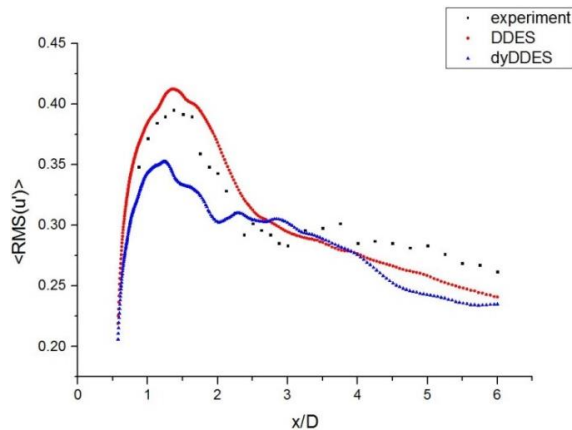**Figure 4: Mean vertical velocity at x/D=1**

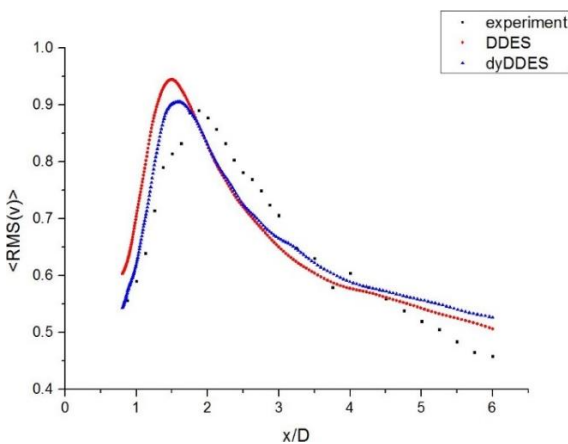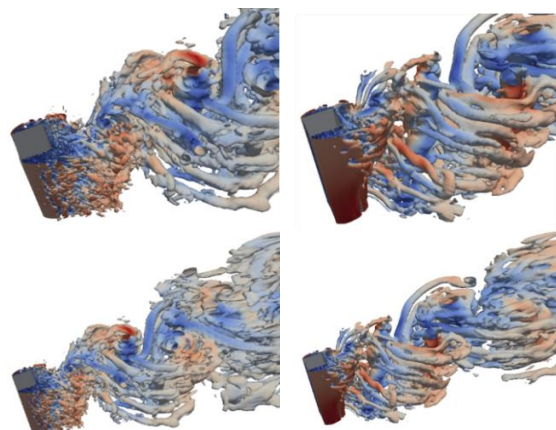**Figure 5: Horizontal velocity fluctuations in the centerline**

Figure 6: Vertical velocity fluctuations in the centerline

(a) Dynamic DDES   (b) DDES
Figure 7: Iso-surface of the Q-criterion

Figure 7 depicts the instantaneous flow structures predicted by SST-SAS and SST-DDES. The visualization of the vortices is realized by displaying the iso-surface of the Q-criterion recommended by Hunt[9]. Surprisingly, dynamic DDES apparently catches much finer vorticity structures than DDES, especially in the transition region. It can be seen that the transition predicted by DDES is a bit later and rougher than dynamic DDES, whose performance is rather close to LES. From this figure one can clearly observe that dynamic DDES indeed resolves more abundant turbulence motions than DDES by visualization.

Acknowledgements

References

[1] Yin. Z, Reddy. K. R, Durbin. P. A. On the dynamic computation of the model constant in delayed detached eddy simulation. Physics of Fluids, 2015, 27(2):4-8.

[2] Chuangxin. He, Liu. Y, Yavuzkurt. S. A dynamic delayed detached-eddy simulation model for turbulent flows. Computers & Fluids, 2017, 146:174-189.

[3] Strelets. M. Detached eddy simulation of massively separated flows. AIAA 2001-0879. Reno: AIAA, 2001.

[4] P. R. Spalart, S. Deck, M. Shur, et al. A New Version of Detached-Eddy Simulation, Resistant to Ambiguous Grid Densities. Theoretical and Computational Fluid Dynamics, 2006, 20: 181-195.

[5] Norberg. C. Flow around rectangular cylinders: Pressure forces and wake frequencies. Wind Eng. Ind. Aerodyn. 1993, 49: 187–196.

[6] Schmidt. S. Grobstruktursimulation Turbulenter Strömungen in Komplexen Geometrien und bei Hohen Reynoldszahlen;Mensch Mensch & Buch-Verlag: Berlin, Germany, 2000.

[7] Moussaed. C, Wornom. S, Salvetti. M. V, et al. Impact of dynamic subgrid-scale modeling in variational multiscale large-eddy simulation of bluff-body flows. Acta Mechanica, 2014, 225(12):3309-3323.

[8] Boudreau. M, Dumas. G, Veilleux. J. C. Assessing the Ability of the DDES Turbulence Modeling Approach to Simulate the Wake of a Bluff Body. 2017, 4(3):41.

[9] Hunt. J. C. R, Wray. A. A, Moin P. Eddies, streams, and convergence zones in turbulent flows. Center for Turbulence Research Report CTR-S88, Stanford University, USA, 1988.

IMPLEMENTATION AND VALIDATION OF A METHOD TO INTRODUCE SYNTHETIC TURBULENCE BY VOLUME FORCES

EIKE TANGERMANN[1], MARKUS KLEIN[2]

[1]*Universität der Bundeswehr München, eike.tangermann@unibw.de*
[2]*Universität der Bundeswehr München, markus.klein@unibw.de*

Keywords: Synthetic turbulence, turbulence-resolving methods, LES, DES

In CFD simulations from the field of external aerodynamics the usage of boundaries of the farfield type is very common. In such configurations the boundary is located far away from the region of interest in order to decouple the boundary conditions from the phenomena in the vicinity of the geometry under investigation. Grid cells outside of the focus region are usually significantly increasing in size since small flow structures are either not present or not desired. This method is suitable for both steady and unsteady investigations.

However, when investigating the interaction of the flow field with perturbations in the approaching flow the problem arises to transport the perturbation towards the focus region. Such perturbations can for example represent a gust of larger scale or resolved turbulent fluctuations of several, usually smaller, scales. The convective transport from the inflow boundary requires a significantly higher grid resolution in order to resolve the perturbations and also a long span of computed time at a time step size sufficiently low to preserve details of the fluctuations.

Several approaches have been introduced to circumvent this issue by introducing the perturbations closer to the focus region. Recently Schmidt and Breuer [1] have proposed a method based on applying a volume force to superimpose synthetic turbulence at arbitrary locations of the computational domain.

The present work features the implementation of a method, which adapts the approach by Schmidt and Breuer, in the pimpleFoam solver. As in the original publication a source term F^{syn} representing a volume force is added to the momentum equation. It is present only in those regions, where the fluctuations are to be superimposed to the mean velocity field. Schmidt and Breuer propose to generate the fluctuation field according to Klein et al. [2] from digital filtering of a random field. However, other methods might also be used. Here a similar approach has been selected and implemented in OpenFOAM, in which the filtering is achieved by solving a diffusion equation [3].

With the force term the momentum equation becomes

$$\frac{\partial \vec{u}}{\partial t} + \nabla \cdot (\vec{u}\vec{u}) - \nabla \cdot (\nu \nabla \vec{u}) = -\nabla p + \vec{F}^{syn}. \tag{1}$$

The force needs to be set appropriately in order to achieve the desired velocity fluctuations. The location of a forcing zone upstream of an airfoil is shown in Figure 1. As in the original publication the force field is not moving continuously with the convection velocity. Instead one slice from the fluctuation field is used for the entire forcing region being updated every time step.

The volume force depends primarily on the transition time T a fluid element spends travelling across the influence region. To facilitate the numerical solution the force should not introduce sudden jumps into the equation. Therefore a Gaussian bell-shaped function G is introduced to smoothen the force field towards its boundaries. To preserve the total force effect G ist normalized by its mean value $\overline{G}$. Assuming that the undisturbed flow primarily is pointing in the x-direction, the force term superimposing a fluctuation velocity $(u')^{syn}$ is calculated by

$$F_{syn} = \frac{(u')^{syn}}{T} \cdot G(x,y,z)/\overline{G} = \frac{(u')^{syn}}{L_x/u_0} \cdot G(x,y,z) \cdot \left(1/L_x \int_{-L_x/2}^{L_x/2} G(x)\,dx\right)^{-1}. \tag{2}$$

At weak levels of turbulence intensity the bell function primarily acts in the flow direction. For stronger turbulence it can become necessary to smoothen the force field towards all edges of the forcing region. Thus a three-dimensional function is applied.

$$G = \exp\left(-\frac{\pi}{2}\left(\frac{(x-x_0)^2}{(L_x/2)^2} + \frac{(y-y_0)^2}{(L_y/2)^2} + \frac{(z-z_0)^2}{(L_z/2)^2}\right)\right) \tag{3}$$

This modification of the momentum equation needs to be taken into account in the pressure equation. In the semi discretized form according to Jasak [4] an additional term arises.

$$\nabla \cdot \left(\frac{1}{a_p}\nabla p\right) = \nabla \cdot \left(\frac{H(\vec{u})}{a_p}\right) + \nabla \cdot \vec{F}^{syn} \tag{4}$$
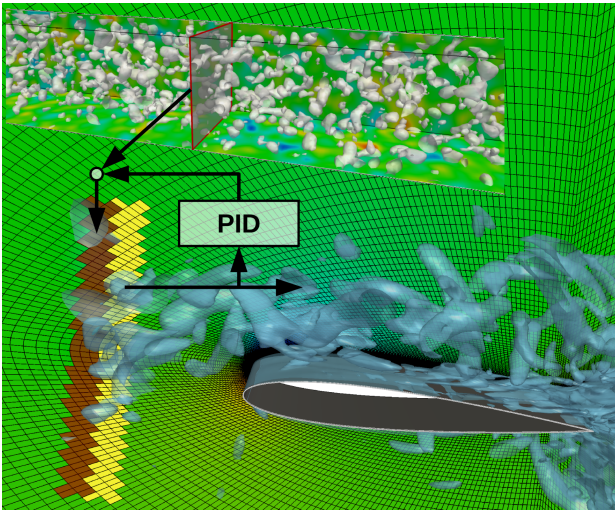
Figure 1: Setup of forcing and controller. The synthetic fluctuations are introduced in the red forcing region, the resulting fluctuation velocity is then determined in the yellow control region and looped back via the PID controller.
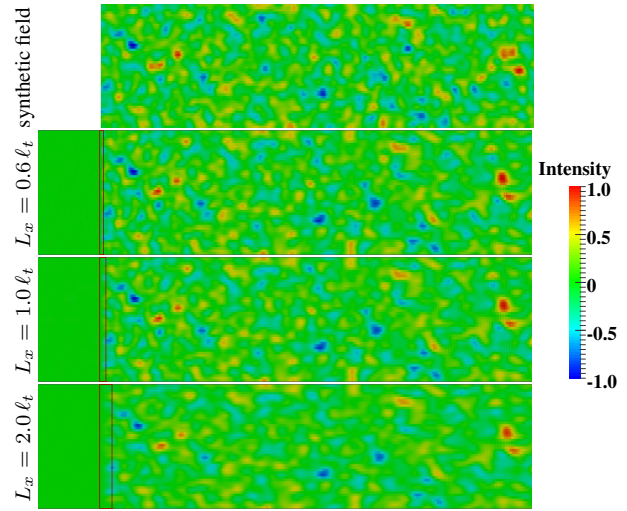

Figure 2: Original fluctuation field (top) and transport as a passive scalar with variations of L_x. Decreasing intensity of small scale fluctuations with increasing width.

a_p denotes the matrix coefficient for the central cell and $H(\vec{u})$ represents the neighbour cells and the temporal derivative. It needs to be mentioned that, if the forcing term in the momentum equation is implemented correctly in OpenFOAM, $H(\vec{u})$ will also incorporate it as a source term. However, this has been prevented here for the sake of demonstration.

As mentioned before one slice of the fluctuation field is spread along the forcing region. This means, that the local force changes, while a fluid element is passing. This changes the amount of force applied depending on the ratio of the length scale of each fluctuation to the forcing region length. The wider the forcing zone is selected the lower the fluctuation amplitude will become. This is illustrated in Figure 2 with fluctuations of a passive scalar field, for which a convection equation with constant convection velocity has been solved. It shows the field of synthetic fluctuations in the upper image and below the field for different widths of the forcing region. While the length scale of the fluctuations is produced very well, the magnitude especially of the smaller eddies decays with increasing width of the forcing region.

To overcome this a control loop is used inspired by the mechanism proposed in [5]. An amplification factor is introduced in Equation 2, which scales the force field globally. Downstream of the forcing region a control region needs to be placed, in which the resulting fluctuation velocity or turbulent kinetic energy is calculated. In order to reduce local variations of turbulence intensity the control region should be set sufficiently wide, then the mean value of u'_{rms} is calculated inside.

The difference between the actual and desired fluctuation velocity, the error variable $e = u'_{target} - u'_{rms}$, is determined. The calculated error is then processed in a common PID control function in a discrete formulation.

$$u_{c,n} = K_p \cdot e_n + K_i \sum_0^n e_n \Delta t_n + K_d \frac{e_n - e_{n-1}}{\Delta t_n}. \tag{5}$$

The controller output u is then added to the amplification factor. For the calculations in the present study a set of $K_p = 1.0$, $K_i = 0.0001$ and $K_d = 0.1$ has been selected for the controller coefficients ensuring stability and sufficiently fast reaction time. However, these values depend strongly on the dead time in the control loop.

With this controller mechanism the magnitude of the input fluctuation field becomes irrelevant. Only the length scale and, if required, the cross correlation of the Reynolds stresses need to be prescribed correctly. The magnitude of the fluctuations can then be amplified to an arbitrary value.

To demonstrate this capability the two-dimensional flow around a cylinder with synthetic fluctuations in the approaching flow has been calculated with different settings for the turbulence intensity. The setup is shown in Figure 3, the forcing zone is located one diameter upstream of the cylinder and 1.5 times the diameter downstream of the inlet boundary. It extends up to five cells in stream-wise direction. The measuring region of the controller is located immediately downstream of the forcing.

From one field of synthetic fluctuations calculations at four different turbulence levels have been performed. They range from from almost undisturbed flow ($u'_{rms}/u_\infty = 0.01$) to high turbulence ($u'_{rms}/u_\infty = 1$). At a Reynolds-number of $2 \cdot 10^5$ based on the undisturbed flow velocity and diameter the cylinder wake flow forms a characteristic Karman vortex street, which is perturbed by the approaching fluctuations. An instantaneous view to the flow field is given by Figure 4 for two settings of turbulence intensity after sufficient computed time to achieve a quasi-steady state. The smaller scale eddies become dissipated quickly downstream of the cylinder because of dissipation and coarser mesh resolution.

The controller reaches the prescribed turbulence level approximately within five characteristic time units (CTU). As illustrated in Figure 5 an overshoot occurs and around fifteen CTU the final level of amplification is reached. In the case
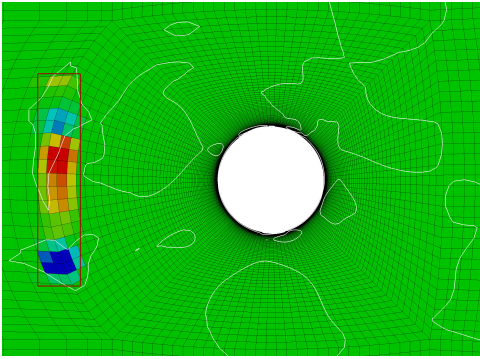
Figure 3: Instantaneous volume force field F_x^{syn} and isolines of Q.
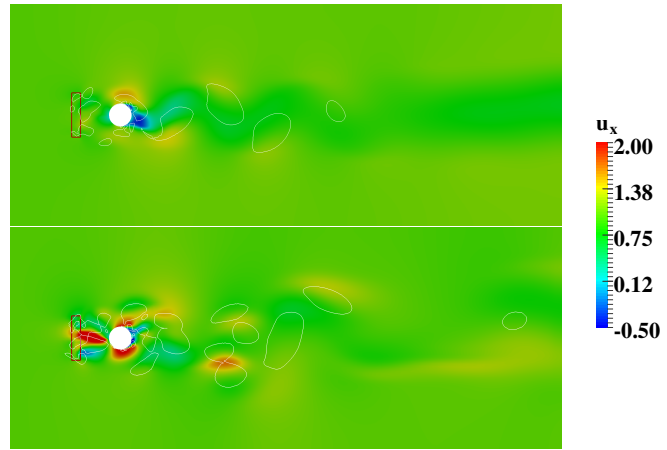

Figure 4: Cylinder flow with synthetic turbulence. $u'/u_\infty = 0.1$ (top) and $u'/u_\infty = 0.5$ (bottom). White isolines from Q-criterion.

with lowest turbulence intensity the setup fails, the amplification factor drops to zero (where it is bounded) after fifteen CTU. The reason is, that the vortex street induces very small variations of the velocity upstream of the cylinder. These are recorded by the controller and in this case they are sufficient to pretend the presence of enough synthetic fluctuations. To overcome this, the mechanism would have to be placed further upstream of the cylinder, where no influence of the vortex street is measurable. This means, that this case is almost identical with a case without perturbation.

The effect of turbulence in the approaching flow is, that the vortex street forms sooner. Figure 6 shows the temporal evolution of the lift coefficient. In the case with the lowest turbulence the longest time is needed to achieve the final amplitude of the alternating vortex separation. In the second case the development of the vortex street happens sightly sooner and it then reaches its final amplitude after a short time. The appearance of the lift curve still is regular with only slight perturbations.

In the third case the separation starts almost immediately compared to the previous two cases. The influence of the perturbation is clearly visible but also the characteristic of the alternating separation remains visible in the lift plot. In the case of highest turbulence intensity the alternating pattern almost vanishes while the force is dominated by the perturbations. The coefficient reaches values far higher than those seen purely from the vortex street. The velocity field shows, that the vortex street is still present but it is strongly deformed by the perturbations.

In order to determine the significance of the changes to the pressure equation the same set of cases has been calculated again with the original pressure equation and the forcing term only being present in the momentum equation. As long as the iterative procedure of the PIMPLE algorithm converges, this is supposed to reach the same converged state for each time step as in the previous setup but might need more corrective iteration steps for the pressure equation. The result of the comparison is presented in Table 1.

For all four cases the computing time and the number of pressure equations are compared. The data is taken from a calculation at quasi-steady state simulating a range of five CTU starting after the first twenty CTU. In the first case it needs to be reminded, that the controller mechanism has faded out the turbulent forcing for most of the time. This still produces overhead to handle the zero-forcing in the pressure equation and leads to an increase of computing time. However, the number of pressure iterations decreases during the short phases, when the amplification becomes greater than zero. This resuts in a slight decrease in total pressure iterations.

For the three cases with significant perturbation level the result changes considerably. The number of pressure iterations decreases by more than ten percent and up to thirteen percent. The reduction of computing time is not as big as the
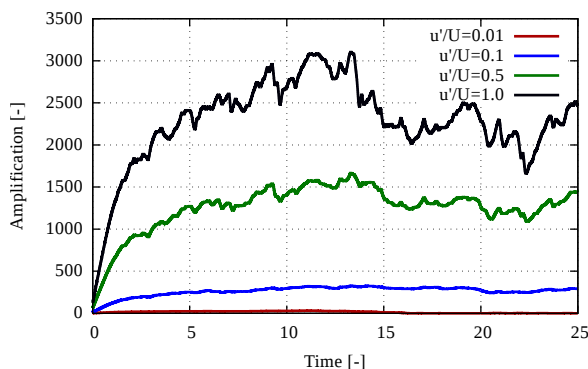

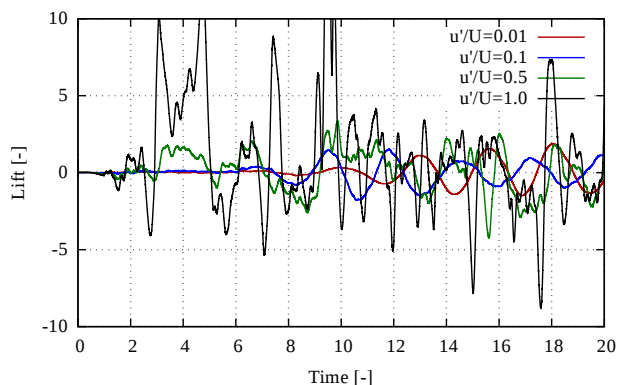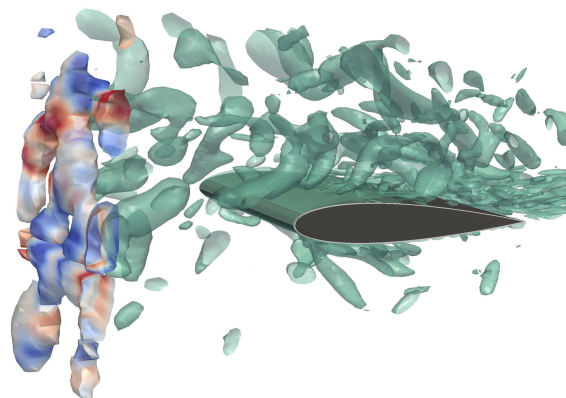**Figure 5: Amplification factor from the controller for different turbulence intensities.**

Figure 6: Cylinder lift coefficient.

Table 1: Relative change in computational effort with corrected pressure equation.

u'_{rms}/u_∞	Computing Time	Pressure Iterations
0.01	+3.5%	−0.63%
0.1	−6.0%	−13.3%
0.5	−7.8%	−11.5%
1.0	−7.0%	−10.4%

Figure 7: Flow around a NACA0012 airfoil. Q isosurfaces (green) and volume force (red/blue).

decrease of pressure iterations but still significant. It ranges from six to almost eight percent. It appears to be independent of the fluctuation magnitude. However, the difference for each case certainly has a strong dependence on the solver settings and can vary for different applications.

The two-dimensional cases presented here have been selected to reduce computational effort for validation and demonstration. Actual turbulence needs to be studied in three-dimensional applications to resolve the three-dimensional aspect of turbulent motion correctly. Such turbulence-resolving computations require parallelisation to achieve results within reasonable computing wall time. It should be noted, that in a parallel computation the controller needs intercommunication to produce one uniform amplification factor.

As a three-dimensional test case the flow around a NACA0012 airfoil is shown here. It is a hybrid RANS LES simulation featuring the kωSST-DDES model. The Reynolds-number is 50000 and the flow is approaching the airfoil at an angle of attack of six degrees. The mesh of 2.5 million hexahedral cells extends half the chord length in span-wise direction with a periodic boundary condition and has a structured C topology. The computational domain extends 20 times the chord length from the leading edge, on the outer side it features a farfield boundary condition. Here it would not be possible to prescribe turbulence at the inflow boundary. Instead perturbations are introduced half a chord length upstream of the leading edge.

The prescribed turbulence features an intensity of $u'/u_\infty = 0.1$ and its integral length scale is one tenth of the chord length. The initial amplification is set too high and after one CTU the correct level of amplification is reached. In case of laminar inflow this simulation will not show any resolved turbulent motion. The turbulence model acts in RANS mode along the wall not resolving boundary layer turbulence. This leads to a steady and smooth flow. With turbulence in the approaching flow the vortices reaching the airfoil produce fluctuations of the aerodynamic forces and moments. The isosurfaces of Q in Figure 7 illustrate the vortices passing around the airfoil and perturbing the boundary layer.

Under circumstances, where the flow tends to separate, the approaching turbulence can significantly affect the separation behaviour of the flow. This will be subject of forthcoming investigations within the field of laminar separation.

Concluding the presented work, the implementation of the method to introduce synthetic turbulence at arbitrary locations within the computational domain can be considered validated. By considering the volume force in the pressure equation a significant reduction of computational effort has been achieved. Finally a controller mechanism has been introduced to compensate the distortion of the perturbation amplitude. This further allows to easily scale a field of synthetic fluctuations to other levels of turbulence intensity. The method has been shown to be working in two- and three-dimensional cases as well as in parallel computations.

References

[1] S. Schmidt and M. Breuer, "Source term based synthetic turbulence inflow generator for eddy-resolving predictions of an airfoil flow including a laminar separation bubble," *Computers & Fluids*, vol. 146, pp. 1–22, 2017.

[2] M. Klein, A. Sadiki, and J. Janicka, "A digital filter based generation of inflow data for spatially developing direct numerical or large eddy simulations," *Journal of computational Physics*, vol. 186, no. 2, pp. 652–665, 2003.

[3] A. Kempf, M. Klein, and J. Janicka, "Efficient generation of initial-and inflow-conditions for transient turbulent flows in arbitrary geometries," *Flow, Turbulence and combustion*, vol. 74, no. 1, pp. 67–84, 2005.

[4] H. Jasak, "Error analysis and estimation for finite volume method with applications to fluid flow," 1996.

[5] M. Klein, N. Chakraborty, and S. Ketterl, "A comparison of strategies for direct numerical simulation of turbulence chemistry interaction in generic planar turbulent premixed flames," *Flow, Turbulence and Combustion*, vol. 99, no. 3-4, pp. 955–971, 2017.

IMPLEMENTATION OF VLES TURBULENCE MODELING IN OPENFOAM FOR SEPARATED FLOW SIMULATION

ZHAOYANG XIA[1], ZHONGYU CHENG[1], XINGSI HAN[1,2] JUNKUI MAO[1]

[1] *College of Energy and Power Engineering, Nanjing University of Aeronautics and Astronautics,*
Aero-engine Thermal Environment and Structure Key Laboratory of Ministry of Industry and
Information Technology, Nanjing 210016, China
[2] *Corresponding author, email: xshan@nuaa.edu.cn*

1. Introduction

Most of the fluid flows in engineering applications are in the turbulent regime. Turbulence modelling is thus the hot research topics for many years. However, for the complex nature of turbulence, the high-fidelity modelling is still challenging even now. In the past decades, turbulence modelling has developed rapidly with the development of several disciplines.

Turbulence modelling can be generally divided into three main groups, RANS (Reynolds-Averaged Navier-Stokes), LES (Large Eddy Simulation) and DNS (Direct Numerical Simulation). In recent years, LES is becoming more and more popular as it can resolve the large turbulent structures directly. The computation grid is directly related to the resolved turbulence scale in LES. In high Reynolds turbulent flow, the small turbulence scale becomes smaller, and thus it needs very fine mesh to resolve the small turbulence scales, especially in the near-wall region. The high computation cost has become one of the barriers to limit the application of LES for high Re number flow simulation.

In the past two decades, hybrid turbulence modelling, i.e. combing different turbulence approaches, are becoming more and more popular as it uses the advantages of different methods. Hybrid RANS-LES method is supposed to be the main method which can make LES applicable for high Re flow in engineering problems [1]. Among them, various hybrid methods are proposed. The DES (Detached Eddy Simulation) method [2] is one of the most widely used and it has been applied for various turbulent flows. In recent years, several unified turbulence modelling are proposed and they attract intensive interests, such as VLES (Very-Large Eddy Simulation) [3, 4], PANS (Partially-Averaged Navier-Stokes) [5], PITM (Partially-Integrated Transport Method) [6]. The present study focuses on the VLES modeling. The main idea of unified turbulence modelling is that, based on the resolution mesh scale and the local turbulence scales, the turbulence modelling can gradually evolve from RANS to LES, finally to DNS. It means that there is no boundary between different turbulence methods, and the one modelling method can cover the three traditional modelling methods of RANS, LES and DNS in a unified framework. The main advantage is that it can be applied for various turbulent flow simulations, especially for high Re turbulent flow in engineering applications.

The research of separated turbulent flow has attracted extensive interests in both academia and industry for decades. It is encountered in various applications, such as flow around various bluff bodies, internal flows with large pressure gradients, etc. However, the accurate prediction of separated flow is still challenging for turbulence modelling. Thus, the present study aims to investigate the performance of VLES modelling for separated flow based on the open source toolbox, OpenFOAM. The main objectives are two aspects: firstly, to validate the relatively new VLES modelling for separated flow simulation; and secondly, to assess the OpenFOAM toolbox for complex flow simulations.

2. Numerical methods

In the present study, two versions of VLES modelling [3, 4] are applied, i.e. based on the standard k-ε turbulence model and the Wilcox k-ω model (referred to as *VLES_ke* and *VLES_kw*), respectively. In the VLES modelling, the form of the underlying RANS modelling is not changed, and only the turbulent viscosity is modified by scaling with a resolution control function *Fr*. The parameter, *Fr*, is the core of VLES modelling. It has the form as shown in Eq. (1), where L_c, L_i and L_k are the cut-off length scale, integral length scale and Kolmogorov length scale, respectively.

$$Fr = \min\left[1.0, \left(\left(1.0 - \exp(-\beta L_c / L_k)\right)/\left(1.0 - \exp(-\beta L_i / L_k)\right)\right)^2\right] \tag{1}$$

With the mesh resolution changing, the control function *Fr* has a value between 0 and 1.0, which determines how much of the turbulence is modelled. Thus, with different mesh resolution, it can work in different turbulence modelling modes, ranging from the RANS, LES to DNS. More details can be found elsewhere [3, 4].

On the basis, the *VLES_ke* modelling can be shown as in Eqs. (2) - (4), where the governing equations of turbulent kinetic energy k and its dissipation rate ε is the same as in the standard k-ε turbulence model. The turbulent viscosity is scaled by the resolution control function *Fr*.

$$D\rho k / Dt = P_k - \rho\varepsilon + \partial\left[\left(\mu + \mu_t / \sigma_k\right)\partial k / \partial x_j\right]/\partial x_j \tag{2}$$

$$D\rho\varepsilon / Dt = (\varepsilon / k)(C_{\varepsilon 1}P_k - C_{\varepsilon 2}\rho\varepsilon) + \partial\left[(\mu + \mu_t / \sigma_\varepsilon)\partial\varepsilon / \partial x_j\right] / \partial x_j \tag{3}$$

$$\mu_t = Fr \cdot \rho C_\mu k^2 / \varepsilon \tag{4}$$

Similarly, the *VLES_kw* modelling can be written as in Eqs. (5) - (7), where the control function *Fr* has the same form as in the *VLES_ke* model (refer to Eq. (1)).

$$D\rho k / Dt = P_k - \beta_1^* \rho k\omega + \partial\left[(\mu + \sigma_k^*\mu_t)\partial k / \partial x_j\right] / \partial x_j \tag{5}$$

$$D\rho\omega / Dt = (\gamma\omega P_k / k - \beta_2^* \rho\omega^2) + \partial\left[(\mu + \sigma_\omega^*\mu_t)\partial\omega / \partial x_j\right] / \partial x_j \tag{6}$$

$$\mu_t = Fr \cdot \rho k / \omega \tag{7}$$

The present VLES methods have been implemented in the OpenFOAM toolbox [7]. The unsteady simulations are performed using the modified pimpleFOAM solver. For high-fidelity simulations, the convective terms are discretized using a second-order central differencing scheme coupled with a small fraction of first order upwind scheme in order to minimize the numerical dissipation. A second-order implicit Crank-Nicolson scheme (with a small fraction of first order implicit scheme) is used for the temporal discretization.

Two separated flow test cases are selected, i.e. the flow past a backward facing step flow and the periodic hill flow. Based on the previous studies, there are generally two kinds of flow separation. The first one is triggered by the sharp geometry changes and the separation point is fixed, such as sharp edges. The second one corresponds to smooth flow separation, where the separation point changes in the flow. Thus, the selected backward facing step flow corresponds to the first kind of separation and the periodic hill flow to the second kind.
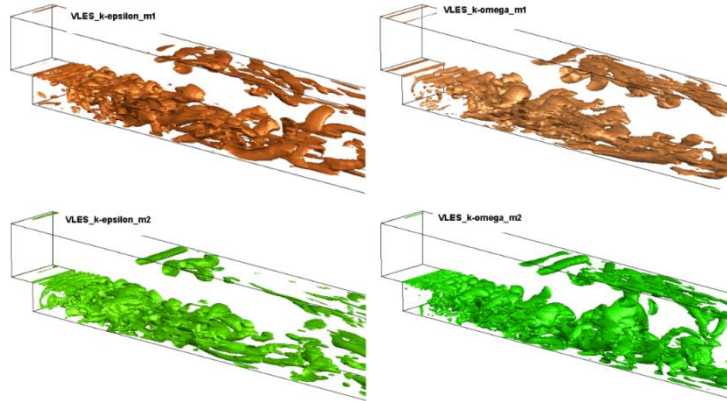
3. Backward facing step flow case with Re=40000

Figure 1: Iso-surface of the second invariant of the velocity gradient (Qh^2/U_0=0.2) for backward facing step flow with different VLES modelling.

The test case deals with a channel flow which separates from a downstream backward-facing step. It is a typical flow separation case and has been widely studied. The Reynolds number is 40000 based on the height of the step (*h*), i.e. Re = $U_0 h / v$ =40000. There is a thick boundary layer at the inlet, which is around 0.37 times of the step height. In the present VLES simulations, two quite coarse meshes are applied, which contains about 0.6 million and 2.0 million cells (denote as m1 and m2), respectively. The simulation results are compared with available experimental data [8].
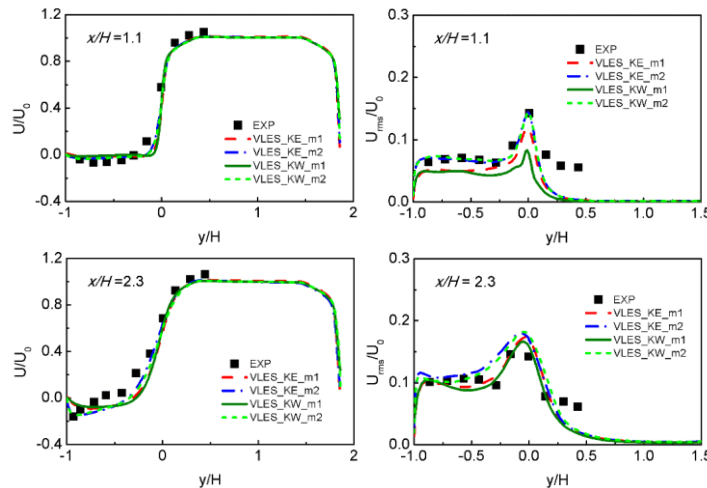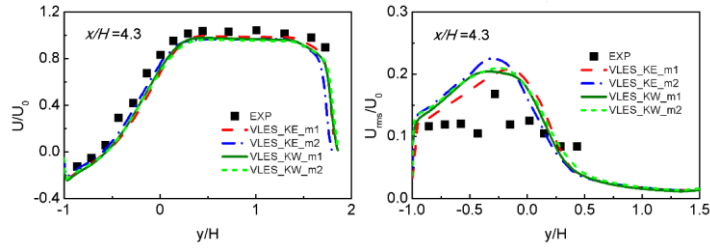
Figure 2: Comparisons of the mean (left) and RMS velocities by the present VLES modelling with experiments [8] in the backward facing step flow, at different downstream locations.

Figure 1 shows the Q criteria of turbulent structures by VLES method for backward step flow. It shows that the two VLES method gives quite close predictions. With increasing the mesh resolution, more turbulent structures can be observed. The mean and RMS velocities at three downstream locations are presented in Fig. 2, accompanying with the experimental data [8]. The comparisons show that the two VLES methods both give satisfactory results and they agree well with experiments. Also, with decreasing the mesh resolution, the predictions just slightly become less good. The test case demonstrates that the present VLES modelling can accurately predict the backward facing step flow on the basis of OpenFOAM toolbox.
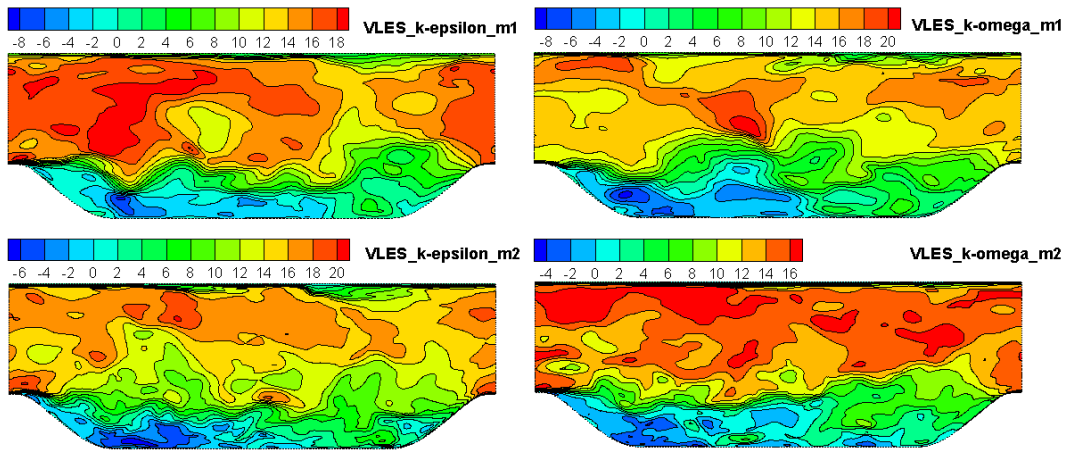
4. Periodic hill flow case with Re=10595

Figure 3: Instantaneous velocity distributions for periodic hill flow with different VLES modelling.
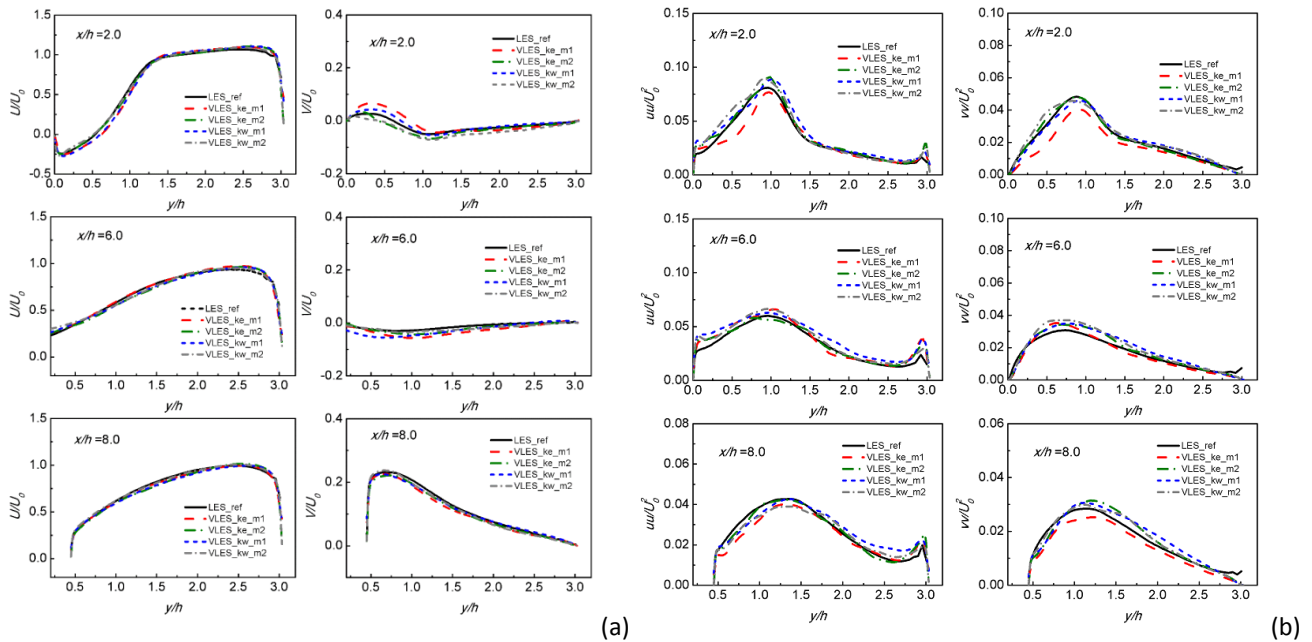

(a)

(b)

Figure 4: Comparisons of the mean velocities (left) and Reynolds stresses by the present VLES modelling with reference LES results [9] in the periodic hill flow, at different downstream locations.

The periodic hill flow test case represents a flow separation in a channel with periodic smoothly curved hills on the bottom wall. The test case involves complex flow phenomena, such as smooth flow separation, recirculation, vortex movement, reattachment, etc. The Reynolds number is $Re_h = 10595$, based on the hill height h, and the bulk velocity U_0 above the hill crest. It has been numerically studied using a well-resolved LES [9] and the LES results are used here as the reference data. In the present VLES simulations, two quite coarse meshes are applied, which contains about 0.6 million and 1.8 million cells (denote as m1 and m2), respectively.

Figure 3 shows the instantaneous streamwise velocity predicted by the present VLES. It shows that complex flow revolution can be observed. With increasing the mesh resolution, smaller turbulent structures can be observed. Figure 4 presents the results of the mean velocities and the normal Reynolds stresses by the VLES method. The first observation is that the present VLES modelling gives quite good results compared with reference LES results, for both the mean velocity and Reynolds stress. With increasing the mesh resolution, the results can be improved. However, on the coarser mesh m1, the predictions by VLES method are still satisfactory, considering the computation mesh used (about 0.6 million cells). The results also show that on the coarser m1, the VLES modelling based on the k-ε model gives the worst predictions, compared with other three sets of results. It implies that the VLES modelling based on the k-ω model performs better than the VLES modelling based on the k-ε model for the periodic hill case.

The present results demonstrate that the present VLES modelling based on k-ε model and k-ω model both can give satisfactory results for the complex separated flow simulations, and quite coarse meshes can be used in the simulations. The study also shows that the OpenFOAM software can provide a very good platform for high-fidelity simulation of complex separated flow. The accuracy and reliability are both quite satisfactory.

More simulation results, comparisons and detailed analysis will be given in the full length paper.

References

[1] P. Sagaut, S. Deck, M. Terracol, Multiscale and Multiresolution Approaches in Turbulence, LES, DES and Hybrid RANS/LES Methods: Applications and Guidelines, 2nd ed., Imperial College Press, London, 2013.

[2] P.R. Spalart, Detached-eddy simulation, Annual Review of Fluid Mechanics, 41: 203-229, 2009.

[3] X. Han, S. Krajnovic, An efficient very large eddy simulation model for simulation of turbulent flow, International Journal for Numerical Methods in Fluids, 71(11):1341-1360, 2013.

[4] X. Han, S. Krajnovic, Very-Large Eddy Simulation Based on k-ω Model. AIAA Journal, 53: 1103-1108, 2015.

[5] E. Jeong, S.S. Girimaji. Partially Averaged Navier–Stokes (PANS) Method for Turbulence Simulations – Flow past a Square Cylinder. ASME Journal of Fluids Engineering, 132: 121203, 2010.

[6] B. Chaouat, R. Schiestel. Hybrid RANS/LES simulations of the turbulent flow over periodic hills at high Reynolds number using the PITM method. Computers & Fluids, 84: 279-300, 2013.

[7] OpenFOAM: The Open Source CFD Toolbox. User Guide Version 4.0, the OpenFOAM Foundation, 2017.

[8] B. Sainte-Rose, N. Bertier, S. Deck, F. Dupoirieux, A DES method applied to a backward facing step reactive flow, Comptes Rendus Mecanique, 337:340–351, 2009.

[9] J. Frohlich, C.P. Mellen, W. Rodi, L. Temmerman, M. Leschziner, Highly resolved large-eddy simulation of separated flow in a channel with streamwise periodic constrictions, Journal of Fluid Mechanics, 526:19–66, 2005.

FINU TUNING OF THE γ - $\tilde{Re}_\theta$ TURBULENCEMODEL USING HISTORICAL DATA SETS

G.ERFORT[1], T.W von BACKSTROM, G. VENTER

[1]*Mechanical and Mechatronic Engineering, Stellenbosch University. erfort@sun.ac.za*

The use of empirical turbulence models has been well documented in computational fluid dynamic simulations. The γ - $\tilde{Re}_{\theta_t}$ model, also known as the SST-transition model, proposed by Langtry and Menter, in particular has received much attention for being able to more closely replicate the pressure values on an airfoil surface as seen in experiments. The original empirical relations were based on observations by the authors, but the published relationships were developed to capture multiple geometries and experimental set-ups. This paper discusses an optimisation approach used to alter the empirical formula to match an existing data set, captured prior to the models' development. Simulations were carried out using open source CFD package openFOAM [1]. The new model coefficients are then compared to the standard formulation as well as the shear stress transport $k - \omega$ model ($k - \omega\ SST$). This work aims to show how the SST-transition model can be adapted for specific geometries using historical data sets.

Introduction

The modelling of transition from laminar to turbulent flow is a complicated task and is closely linked to aerodynamic stall. Reynolds Averaged Navier Stokes equations are not capable of fully capturing this phenomenon, while the more computationally expensive methods like Large Eddy Simulations come closer to accurate predictions. Intermittentcy models attempt to describe the transition process and are usually coupled to existing turbulence models.

Intermittentcy transport models are not new in the field of CFD, having being reported as early as the 1990s. In 2004 Vicedo et al proposed one such transport model that was applied in the modelling of separation bubbles [2]. At the time of publication the trend was to have mathematical models that were specific to certain geometries and flow parameters, thus limiting their applicability. Vicedo et al instead developed a model that required no normal-to-wall distance and related transition onset to the local momentum thickness Reynolds number. In 2005 Langrty and Menter authored a paper outlining a correlation based transition model which is based entirely on local variables[3], namely a transition momentum thickness Reynolds number ($\tilde{Re}_{\theta_t}$) and intermittentcy (γ). The model uses two transport equations for intermittentcy and transition onset criteria. Since the model is based entirely on local variables, it is compatible with unstructured meshes and well suited for parallelization. The model does not try to describe the physical process but instead is based on experimental observations and relations. Upon publication the Langtry and Menter did not release their original correlations but subsequent authors using their framework have presented their findings while using the SST-transition model.

Misaka and Obayashi applied their own correlations, based on flat plate boundary layer tests, in modelling flow around wings [4].

In 2007 Toyoda et al made use of the correlation model to predict boundary layer transition on the JAXA high-lift configuration model [5]. The authors applied their own empirical correlations to compare the lift and drag results as well as the skin friction for identifying the start of intermittentcy. Their results indicated that the model was not able to handle a large cross flow velocity. Sorensen attempted to determine the empirical relationships for the correlation model and verified the results with tests on two different aerofoils and a wind turbine rotor [6]. However the correlations supplied were also not in agreement with those previously disclosed by other authors.

In 2009 Langrty and Menter released their empirical relationships for the length of transition region (F_{length}), critical Reynolds number (Re_{θ_c}) indicating where intermittentcy first increases within the boundary layer and transition onset Reynolds (Re_{θ_t}), which is a function of pressure gradient and turbulence intensity [7]. Using previously published empirical relations, a reasonable assumption could be made on the expected relationship between all empirical relationships. Optimization was then undertaken to match the experimental values for lift and drag over a range of angles of attack, at a fixed Reynolds number. The NACA0012 airfoil was selected as it has an extensive collection of public data sets previously corroborated experimentally [8].

$\gamma - \tilde{R}e_\theta$ **model**

The $\gamma - \tilde{R}e_\theta$ model is coupled to the shear stress transport $k - \omega$ model. It brings in two more transport equations for intermittentcy (γ)and transition momentum thickness Reynolds number ($\tilde{R}e_{\theta_t}$). The equation for intermittentcy is

$$\frac{\partial(\rho\gamma)}{\partial t} + \frac{\partial\rho U_j\gamma}{\partial x_j} = P_\gamma - E_\gamma + \frac{\partial}{\partial x_j}\left[(\mu + \frac{\mu_t}{\sigma_f})\frac{\partial\gamma}{\partial x_j}\right] \tag{1}$$

where transition source is P_γ and the destruction source is E_γ. The transport equation for transition momentum thickness Reynolds number is

$$\frac{\partial(\rho\tilde{R}e_{\theta_t})}{\partial t} + \frac{\partial\rho U_j\tilde{R}e_{\theta_t}}{\partial x_j} = P_{\theta_t} + \frac{\partial}{\partial x_j}\left[\sigma_{\theta_t}(\mu + \mu_t)\frac{\partial\tilde{R}e_{\theta_t}}{\partial x_j}\right] \tag{2}$$

The source term P_{θ_t} is used to ensure the transport variable $\tilde{R}e_{\theta_t}$ matches the locally determined Re_{θ_t}. γ is used as a trigger for transition while $\tilde{R}e_\theta$ takes into account the non local effects of turbulence intensity. These non local effects include the decay of turbulence kinetic energy in the freestream and changes in velocity outside of the boundary layer. This equation is important as it brings together the empirical relationships which are used in the γ equation. Full details of the model are provided in [7], where the empirical relationships are given a piecewise definition. Re_{θ_t} is a function of turbulence intensity (Tu) and pressure gradient (λ_θ), while F_{length} and Re_{θ_c} are functions $\tilde{R}e_{\theta_t}$

Optimisation process

The aim of this work is to utilise the SST-transition model in CFD code such that the results for Lift and Drag match previously documented experimental results. These results were for various angles of attack and Reynolds numbers. It was decided to focus on a single Reynolds number and to tune the model to fit a single angle of attack. This work used the angle of attack with the minimum lift coefficient (C_L) found post stall for optimisation. The parameters available for optimisation are the empirical relationships. However their definition as per [7] would require the simultaneous optimisation of 37 coefficients. While the open source nature of openFOAM allows for direct coupling with outside code, coupling the CFD runs to an optimiser was not feasible due to the run time. As such a meta model was chosen to replace the CFD during optimisation. A breeder genetic algorithm (BGA) was used for optimisation. The objective function being minimized during optimisation was the difference between the experimental data sets' C_L and that reported by the simulation.

Approximating empirical relationships

An effective meta model requires a good training set. When fitting a quadratic polynomial to data, at least 1.5 times the number of coefficients are required in terms of training samples. As we increase the dimensions of the problem we expect an increased complexity. For 37 coefficients a conservative approach would be to require a minimum of 55 samples to fit a simple polynomial. The relationship being modelled, our empirical parameters versus C_L, are assumed to be more complex thus an effort was made to reduce the number of coefficients. The parametric curves described by Langrty and Menter were replaced with more complex mathematical functions with reduced coefficients. Looking at [6] and [7] it was determined that the transition length was approximated by a Gaussian curve:

$$F_{length} = \frac{A}{\sqrt{2\pi B^2}} \cdot e^{\frac{-\tilde{R}e_{\theta_t}^2}{2\sigma^2}} + C \tag{3}$$

while the critical Reynolds number, should more closely follow the blended function as laid out by [6]:

$$\beta = \tanh(\tilde{R}e_{\theta_t}/D)^E$$
$$Re_{\theta_c} = \beta \cdot F + (1 - \beta) \cdot (0.68 \cdot \tilde{R}e_{\theta_t}) \tag{4}$$

In equation 4 the gradient of the straight line portion is equal to the gradient of a straight line fit to [7] definition. This allowed the capture of both types of relationships. Transition onset Reynolds number was represented as a hyperbolic tangent overlaid on an exponential function for λ_θ and an exponential function for Tu.

$$Re_{\theta_t} = G\exp(-H \cdot Tu)\tanh(I \cdot \lambda_\theta \cdot 900 - J) + K \tag{5}$$

The new mathematical functions are plotted in figure 1 along with the original formulations. These equations were tested on the flat plate example, used by Langtry and Menter in the model development, and showed a good correlation with expected results thus the number of variables was reduced from 37 to 16.
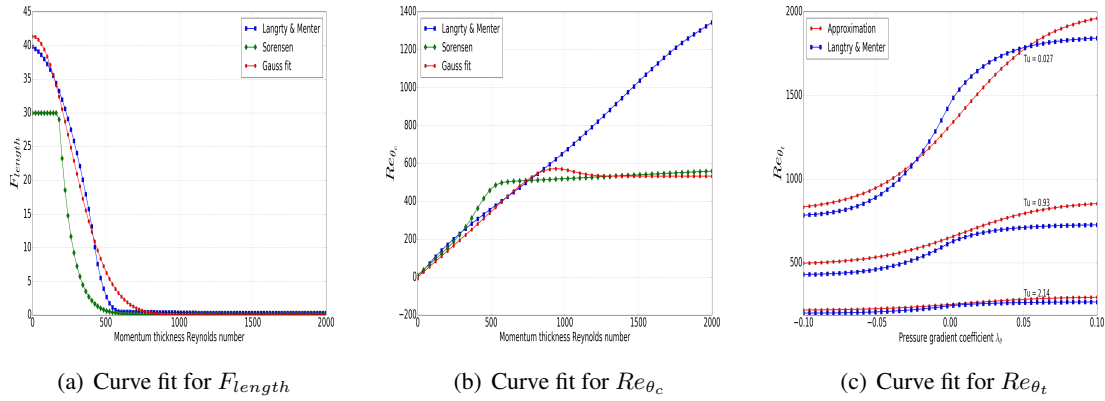
(a) Curve fit for F_{length} (b) Curve fit for Re_{θ_c} (c) Curve fit for Re_{θ_t}

Figure 1: The simplified curves used in the meta mode compared with the original formulation

Meta Model

Having reduced the number of variables, latin hyper cube sampling was used to generate testing and training data points. The relationships being modelled were not linear so various regression techniques were tested. Support vector regression (SVR), multi-layered perceptons (MLP) and random forest (RF) methods were all tested with an increasing number of sample points.The random forest approach showed the most promise, as the number of samples increased the in and out of sample error decreased and levelled off at the lowest error out of the 3 models. Hyper tuning the RF model achieved a coefficient of determination (R^2) value for in sample training of 0.92 and out of testing sets value of 0.45.

Results

Figure 2 shows C_L as reported by Sheldahl and Klimas [8] at a Reynolds number of 1e6 over a range of angles of attack. The figure also shows the results of various turbulence models for the same conditions. The standard $k - \omega$ SST model captures the trend with a noticeable delay. The original $\gamma - \tilde{Re}_\theta$ model is the worst performing with large over predictions in lift after separation has occurred. Finally the optimised $\gamma - \tilde{Re}_\theta$ is plotted showing an improvement. Table 1
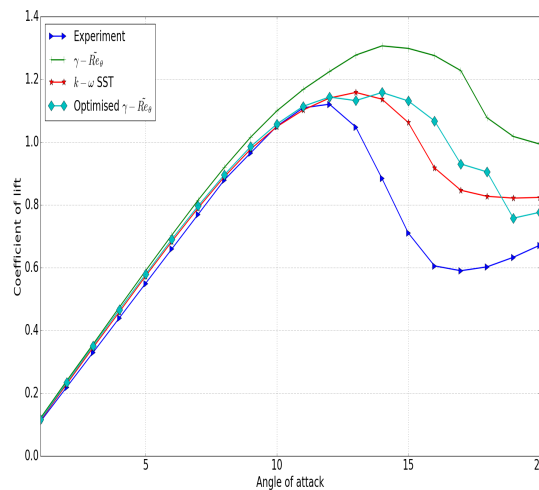

Figure 2: NACA 0012 lift coefficients at Reynolds number of 1e6 for various turbulence models

compares each model using the Pearson correlation coefficient (r). each turbulence model was evaluated for correlation to the data set. The optimisation started with a seed vector that had the coefficients approximating the original formulation, producing an objective function value of 0.58. The meta model reported the value as 0.57. Optimisation was complete after 75 generations with a final value of 0.37. The new coefficients were then run through CFD for all angles of attack and a final check of the difference between C_L showed a value of 0.34. This tells substantiated that the meta model was built correctly and provided accurate predictions.

Table 1: Pearson correlation coefficient, r, for reported lift coefficient versus experimental data set

Model	r
$\gamma - \tilde{Re}_\theta$	0.78
$k - \omega$ SST	0.92
Opt. $\gamma - \tilde{Re}_\theta$	0.88

Conclusion

This paper presented an approach to adjusting empirical relationships in a turbulence model. The adjustments were made in an attempt to correlate CFD reported lift coefficients with historical experimental data sets. The phenomena being modelled is unsteady but due to time constraints steady state simulations were used. The building of a surrogate model was important to reduce computational cost and the time needed for data collection. The reduction in number of variables for these relationships has proven effective and valid. The optimised model did not outperform the standard $k - \omega$ SST model in lift predictions, however further testing will be conducted to see if the location of transition point has been improved through this work. It is recommended to adjust the boundaries for the 16 variables and run the optimisation again.

Acknowledgments

References

[1] H. G. Weller, G. Tabor, H. Jasak, and C. Fureby, "A tensorial approach to computational continuum mechanics using object-oriented techniques," *Computers in physics*, vol. 12, no. 6, pp. 620–631, 1998.

[2] J. Vicedo, S. Vilmin, W. Dawes, and A. Savill, "Intermittency transport modeling of separated flow transition," *Journal of turbomachinery*, vol. 126, no. 3, pp. 424–431, 2004.

[3] R. Langtry and F. Menter, "Transition modeling for general cfd aapplication in aeronaurics," in *43rd AIAA Aerospace Sciences Meeting and Exhibit*, 2005.

[4] T. Misaka and S. Obayashi, "Application of local correlation-based transition model to flows around wings," in *44th AIAA Aerodspace Sciences Meeting and Exhibit*, 2006.

[5] A. Toyoda, T. Misaka, and S. Obayashi, "Anapplicmodel of local correlation-based transition mode to jaxa high lift configuration model," in *25th AIAA Applied Aerodynamics Conference*, 2007.

[6] N. N. Sorensen, "Cfd modemodel of laminar-turbulent transition for airfoils and rotors using the γ - re model," *Wind energy*, vol. 12, no. 8, pp. 715–733, 2009.

[7] R. B. Langtry and F. R. Menter, "Correlation-based transition modmodel for unstructred parallelized computational fluid dynamics codes," *AIAA journal*, vol. 47, no. 12, pp. 2894–2906, December 2009.

[8] R. E. Sheldahl and P. C. Klimas, "Aerodynamic characteristics of seven symmetrical airfoil sections through 180-degree angle of attack for use in aerodynamic analysis of vertical axis wind turbines," Sandia National Labs., Albuquerque, NM (USA), Tech. Rep., 1981.

IMPLEMENTATION AND VALIDATION OF A NOVEL TABULATED CHEMISTRY TURBULENT COMBUSTION MODLE IN OPENFOAM

YIFAN DUAN[1], ZHIXUN XIA[2], LIKUN MA[3], JIARUI ZHANG[4], XIANGYU CAO[5]

[1]*College of Aerospace Science and Technology, National University of Defense Technology,*
duanyifan12@nudt.edu.cn

[2]*College of Aerospace Science and Technology, National University of Defense Technology,*
zxxia@nudt.edu.cn

[3]*College of Aerospace Science and Technology, National University of Defense Technology,*
malikun@nudt.edu.cn

[4]*College of Aerospace Science and Technology, National University of Defense Technology,*
zhangjiarui@nudt.edu.cn

[5]*College of Aerospace Science and Technology, National University of Defense Technology,*
caoxiangyu12@nudt.edu.cn

In recent years, Flamelet-Generated Manifolds (FGM) proposed by **Van Oijen** et al. has been widely used in the numerical simulation of various turbulent combustion flames and obtained encouraging results[1-3]. The FGM model builds a look-up table by computing a series of 1D laminar flamelet that takes into account the detailed chemical reaction mechanism. By considering the interaction between turbulence and chemical reaction by the Presumed-PDF (P-PDF) method, laminar flamelet look-up table expanded into a turbulent flamelet look-up table. Due to the limitations of P-PDF assumption itself, for example, the model assumes that the control variables are independent of each other, which is a strong assumption in many cases. And also, with increase of control variables or the reaction mechanism, the size of the look-up table increases exponentially and the memory requirements are huge. With the development and application of FGM model, more and more simulation results prove the limitation of P-PDF method. **Bray** et al. [4] studied the sensitivity of average chemical reaction rates to three P-PDF methods in Sandia Flame D and compared the P-PDF method to DNS data. The results show that there is a remarkable gap between the three most widely used β-PDFs and the actual DNS data, and the assumed shape factors in the P-PDF method greatly affect the chemical reaction rate prediction. In a study of turbulent spray combustion models, **Ge** et al.[5] found that the actual PDFs of the mixture fraction, gas temperature and enthalpy in the model was significantly different from the standard β-PDF. Based on the FGM model, this paper abandon the P-PDF method and combine the ESF model with the FGM model to directly consider the probability density function of the control variables. The new ESF-FGM model has been developed in this study and implemented in OpenFOAM.

In FGM models, there is no need to solve the transported equation for all components and energies, and the chemical reactions in turbulent combustion are thought to occur in low-dimensional manifolds, which means that only a few independent variables are required in the entire component space to characterize Chemical reaction in turbulent combustion. In the model, the "mixture fraction", Z, that characterizes the mixed state of fuel and oxidant and the "progress variable", C, that characterizes the progress of chemical reaction are usually selected as independent variables. Of course, depending on the physical model being simulated, variables such as pressure and enthalpy loss can be added as supplementary independent variables[6]. The FGM turbulent combustion model under the LES method can be expressed as follows:

$$\frac{\partial \overline{\rho}}{\partial t} + \frac{\partial \overline{\rho}\tilde{u}_j}{\partial x_j} = \overline{S}_\rho \tag{1}$$

$$\frac{\partial \overline{\rho}\tilde{u}_j}{\partial t} + \frac{\partial \left(\overline{\rho}\tilde{u}_i\tilde{u}_j\right)}{\partial x_j} = -\frac{\partial \overline{p}}{\partial x_i} + \frac{\partial}{\partial x_j}\left(\overline{2\mu}\tilde{S}_{ij}^D - \tau_{ij}\right) + \overline{S}_{u_i} \tag{2}$$

$$\frac{\partial \overline{\rho}\tilde{Z}}{\partial t} + \frac{\partial \overline{\rho}\tilde{u}_j\tilde{Z}}{\partial x_j} = \frac{\partial}{\partial x_j}\left[\overline{\rho}\left(\tilde{D}+D_t\right)\frac{\partial \tilde{Z}}{\partial x_j}\right] + \overline{S}_Z \tag{3}$$

$$\frac{\partial \overline{\rho}\tilde{Y}_C}{\partial t} + \frac{\partial \overline{\rho}\tilde{u}_j\tilde{Y}_C}{\partial x_j} = \frac{\partial}{\partial x_j}\left[\overline{\rho}\left(\tilde{D}+D_t\right)\frac{\partial \tilde{Y}_C}{\partial x_j}\right] + \overline{\dot{\omega}}_{Y_C} \tag{4}$$

$$S_{ij} = \frac{1}{2}\left(\frac{\partial u_i}{\partial x_j} + \frac{\partial u_j}{\partial x_i} \right) \tag{5}$$

$$S_{ij}^D = S_{ij} - \frac{1}{3}\delta_{ij}S_{KK} \tag{6}$$

Where τ_{ij} is the sub-grid scale (SGS) stress. It is closed with HybridSGS model in the LES. Z is mixture fraction, and defined by **Bilger's** method of element definition with the same diffusion coefficient of all components; Y_C is an un-normalized progress variable, and it's definition in this study is as follows:

$$Y_C = \frac{Y_{CO2}}{W_{CO2}} + \frac{Y_{H2O}}{W_{H2O}} + \frac{Y_{H2}}{W_{H2}} \tag{7}$$

Where Y is molar mass and W is mass fraction, respectively. Export Y_C normalization as progress variable C:

$$C = \frac{Y_C - Y_C^u}{Y_C^b - Y_C^u} \tag{8}$$

Superscripts b and u respectively represent the burned and unburned state. The sum of the equations for Z and C is the independent variable of the look-up table.

Considering the influence of turbulent fluctuation on the chemical reaction, the original FGM model uses the P-PDF method to describe its distribution through the first moment and the second moment of two independent variables. At the same time, the original 2D laminar flamelet look-up table expanded into 4D turbulent flamelet look-up table. In this paper, we abandon this method and choose real-time solutions to components jointing probability density function of two independent variables transported equation and integrate them in the sample space to obtain all the single-point statistics of all the space and time of two independent variables in real time. In this paper, Eulerian Stochastic Field (ESF) model in the transported probability density function class model is used to accomplish this task, and then the ESF model is introduced.

In solving the transported equation of probability density function, when there are many components, the dimension of transported equation is quite high. In this situation, it is difficult to solve the equation with finite volume, finite difference or finite element method. This paper adopts Eulerian Stochastic Field (ESF) model, using a series of stochastic fields N_F to represent joint-composition PDF required by this model. In this N_F stochastic fields, each field contains each component value at each position in the entire flow field. It can be expressed as[7]:

$$f_\varphi(\psi; \vec{x}, t) \approx \frac{1}{N_F}\sum_{n=1}^{N_F}\prod_{\alpha=1}^{N_s}\delta(\psi_\alpha - \varphi_{\alpha,n}) \tag{9}$$

$\varphi_{\alpha,n}$ is the value of scalar α under $\vec{x}$ position under t time in n field. In this model, $\varphi_\alpha = [Z, C]$, each stochastic field evolvesaccording to the stochastic partial differential equations (SPDE) derived from transport equation of the joint-composition PDF. These SPDE can be expressed as[8]:

$$d(\bar{\rho}\varphi_{\alpha,n}) = -\frac{\partial}{\partial x_j}\left(\bar{\rho}\tilde{u}_j\varphi_{\alpha,n}\right)dt + \frac{\partial}{\partial x_j}\left[\left(\frac{\mu}{S_C} + \frac{\mu_t}{S_{Ct}}\right)\frac{\partial\varphi_{\alpha,n}}{\partial x_j}\right]dt + \dot{\omega}_\alpha^n dt -$$
$$\frac{\bar{\rho}}{2\tau_{sgs}}\left(\varphi_{\alpha,n} - \tilde{\phi}_\alpha\right)dt + \left(2\bar{\rho}^2\frac{\mu_t}{S_{Ct}}\right)^{1/2}\frac{\partial\varphi_{\alpha,n}}{\partial x_j}dW_{j,n}, \quad for \quad n = 1, \cdots N_F \ and \quad \alpha = 1, \cdots N_s \tag{10}$$

The first three items on the right side of the equation correspond to convection term, turbulence diffusion term, and source term of the mean flow, respectively. The fourth term indicates micro-mixing due to the attenuation of scalar fluctuations. The last term is the Wiener term, which denotes a random term caused by turbulence, which varies over time but not with spatial location. In a given stochastic field, all scalars use the same $dW_{j,n}$ value, it denotes increments of a vector Wiener process, independent of the spatial location and different for each stochastic field. The turbulent mixing time τ_{sgs} is determined according to the mixing time model proposed by [9]and reads

$$\Omega_{sgs} = \frac{1}{\tau_{sgs}} = C_{\Omega} \frac{\bar{\nu} + \nu_t}{\Delta^2}$$
(11)

Where the suitable value for the micro-mixing constant is proposed in the same work as $C_{\Omega} = 2$ and ν denotes the kinematic viscosity.

By solving the stochastic differential equations of each stochastic field, the evolution law of the mixture fraction and the progress variables over time in each stochastic field considering the influence of turbulence is obtained. A statistical average is then used to find the control variables for the flamelet look-up table.

According to the established theoretical model, using OpenFOAM solver that developed in this study, the simulation of flame Sandia Flame (D-F) was carried out under a variety of stochastic fields. This paper first verifies the correctness of the model in the RANS.
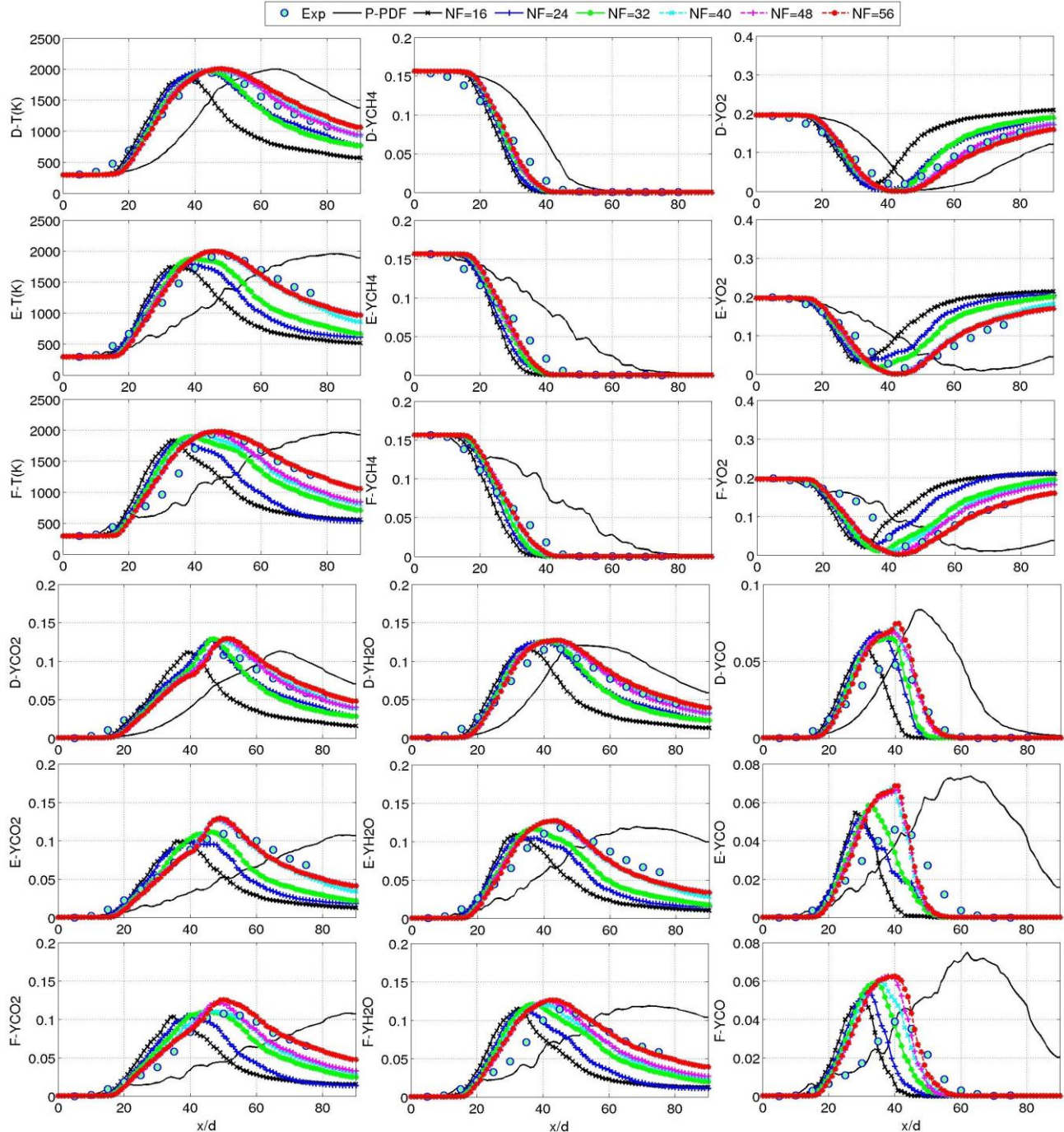
Figure 1: Comparison of predicted and measured mean axial temperature and main components mass fraction in Sandia Flame (D-F) (RANS)

Fig. 1 shows the comparison of predicted and measured mean axial temperature and main components mass fraction between the ESF / FGM model and the original FGM model. Overall, the ESF / FGM model predicts better the

distribution of temperature and main components than the original FGM model using the P-PDF method. For axial components, the ESF / FGM model achieves a more accurate prediction, and as the number of stochastic fields increases, the simulation accuracy is better. With the increase of the number of stochastic fields, the simulation accuracy of the new turbulent combustion model has been continuously improved. However, when the number of stochastic fields is higher than a certain value, the simulation results have little change and tend to be stable. This phenomenon is consistent with the conventional statistical thinking. However, ESF / FGM models were found to simulate the location of the flame ignition later in the experiment, while the position where the axial CH_4 and O_2 mass fractions began to decline, as well as the positions where other products started to appear, were behind the actual flame positions. It shows that the model simulates the effect of turbulent mixing before flame ignition is weaker than the actual one and the ignition position is further away from the fuel inlet. The rate of temperature rise is also faster than the experiment, and both the rate of fuel consumption and the product formation rate are faster than the experiment. The reason may be that laminar flamelet building does not consider the effect of flow on the flamelet stretching and bending. For the simulation of both CO and CO_2 components, the peak position coincides with the experiment, but the simulated value is slightly higher than the experimental value.

So, we use the large eddy simulation to improve the simulation accuracy of the fuel and oxidant mixing process, so as to further improve the accuracy of the simulation results of the new turbulent combustion model.

References

[1]   C. Bekdemir, L. M. T. Somers, and L. P. H. D. Goey, "Modeling diesel engine combustion using pressure dependent Flamelet Generated Manifolds," *Proceedings of the Combustion Institute,* vol. 33, pp. 2887-2894, 2011.

[2]   A. Donini, R. Bastiaans, J. A. V. Oijen, and P. D. Goey, "Numerical Simulations of a Turbulent High-Pressure Premixed Cooled Jet Flame with the Flamelet Generated Manifolds Technique," *Journal of Engineering for Gas Turbines & Power,* vol. 137, 2015.

[3]   L. Ma and D. Roekaerts, "Modeling of spray jet flame under MILD condition with non-adiabatic FGM and a new conditional droplet injection model," *Combustion & Flame,* vol. 165, pp. 402-423, 2016.

[4]   K. N. C. Bray, M. Champion, P. A. Libby, and N. Swaminathan, "Finite rate chemistry and presumed PDF models for premixed turbulent combustion," *Combustion & Flame,* vol. 146, pp. 665-673, 2006.

[5]   H. W. Ge and E. Gutheil, "Simulation of a turbulent spray flame using coupled PDF gas phase and spray flamelet modeling," *Combustion & Flame,* vol. 153, pp. 173-185, 2008.

[6]   L. Ma and D. Roekaerts, "Numerical study of the multi-flame structure in spray combustion," *Proceedings of the Combustion Institute,* vol. 36, 2016.

[7]   F. Nmira, D. Burot, and J. L. Consalvi, "Stochastic Eulerian field method for radiative heat transfer in a propane oxygen-enhanced turbulent diffusion flame," *Combustion Theory & Modelling,* vol. 21, pp. 62-78, 2016.

[8]   A. Avdić, G. Kuenne, and J. Janicka, "Flow Physics of a Bluff-Body Swirl Stabilized Flame and their Prediction by Means of a Joint Eulerian Stochastic Field and Tabulated Chemistry Approach," *Flow Turbulence & Combustion,* vol. 97, pp. 1-26, 2016.

[9]   W. P. Jones, S. Navarro-Martinez, and O. Röhl, "Large eddy simulation of hydrogen auto-ignition with a probability density function method," *Proceedings of the Combustion Institute,* vol. 31, pp. 1765-1771, 2007.

WALL-MODELLED LARGE-EDDY SIMULATION OF THE FLOW OVER A BACKWARD-FACING STEP

TIMOFEY MUKHA[1], SALEH REZAEIRAVESH[2], MATTIAS LIEFVENDAHL[3,4]

[1]*Department of Information Technology, Uppsala University, Sweden, timofey.mukha@it.uu.se*
[2]*Department of Information Technology, Uppsala University, Sweden, saleh.rezaeiravesh@it.uu.se*
[3]*Department of Information Technology, Uppsala University, Sweden, mattias.liefvendahl@it.uu.se*
[4]*Swedish Defence Research Agency, FOI, mattias.liefvendahl@foi.se*

Introduction

Wall-modelled Large-Eddy Simulation (WMLES) is a turbulence modelling technique that allows to drastically reduce the computational requirements for LES of wall-bounded turbulent flows. This is achieved by introducing special near-wall treatment that accounts for the dynamics of the inner region of turbulent boundary layers (TBLs), thus alleviating the necessity to resolve it with the LES grid. Various approaches to WMLES exist, a review of which can be found in [1]. Here, wall-stress modelling is considered, which aims at incorporating the effect of the processes in the inner layer by predicting and enforcing the correct local value of the wall shear stress, τ_w. A detailed discussion of how a wall-stress model can be formulated in the framework of a collocated finite volume solver can be found in [2].

In this work, WMLES is applied to the flow over a backward-facing step (BFS). In particular, the simulations aim at reproducing the experiment of Jovic [3], the data of which are used as a reference. The study focuses on the influence of several simulation parameters on the accuracy of the flow prediction. This includes the grid resolution, the interpolation scheme used for computing convective cell-face fluxes, and the distance to the sampling (matching) point of the wall model, h.

Computational fluid dynamics methods

The conducted simulations are performed using a library for WMLES based on `OpenFOAM` technology developed by the authors, see [4]. The collocated finite volume method is used for discretisation of the LES equations. Linear interpolation is employed for computing the diffusive cell-face fluxes. For the convective fluxes, two options are considered. One is, again, linear interpolation, which is referred to as using the "*linear* scheme" below. The other is employing the *LUST* scheme, which computes the fluxes using a weighted average of the corresponding values obtained using the *linear* scheme (75%) and a second-order accurate upwind scheme (25%), see [5]. For discretisation in time, a second-order backward-differencing scheme is used (see e.g. [6]). The PISO algorithm [7] with three corrector steps is used for pressure-velocity coupling. The WALE model [8] is used for modelling the subgrid stresses in the interior of the domain. For wall-modelling, an algebraic wall-stress model based on Spalding's law of the wall [9] is employed.

Numerical experiments

Case set-up

The set-up of the simulation aims at matching the settings in the experiment of Jovic [3]. The computational domain is shown in Figure 1. A Cartesian coordinate system x, y, z is introduced, with the origin placed in the top-left corner of the step. The three axes correspond to the streamwise, wall-normal and spanwise directions, respectively. The length of the plate upstream of the step, $L_{x,1}$ is $8H$, where $H = 1.0625$ m is the height of the step. This is deemed large enough to remove the inaccuracies associated with the inflow generation procedure, see below. The length of the post-expansion region is $\approx 32H$, which is enough to analyse the recovery of the TBL and how it is affected by the simulation parameters. The height of the domain upstream of the step is $L_y \approx 5.3H$, which leads to an expansion ratio of 1.19, which matches that used in the experiment [3]. In the spanwise direction, the domain size is $L_z \approx 7.5H$, which ensures the absence of spurious periodicity effects.

The boundary conditions are as follows. At the walls, the no-slip condition is prescribed. Wall-modelling is applied at the two horizontal walls. The top boundary is treated as a symmetry plane, which reflects the set-up of the experiment in [3]. A pressure outlet is used at the outflow. In the spanwise direction, periodic boundaries are used. The velocity values at the inflow are generated using precursor fully-developed turbulent channel flow simulations, using the method described in [10].

The Reynolds number Re_H, based on the step-height and the free-stream velocity at the inlet, $U_0 = 1.12$ m/s, is $37\,000$. The upstream TBL is characterised by the δ_{99}-based Reynolds number, $Re_{\delta_{99}} \approx 30\,500$. Here, following [3], the value of $\delta_{99} \approx 0.87$ m is computed at $x = -1.05H$. This entails $\delta_{99}/H \approx 0.82$. It should be noted that the value of δ_{99} at this station varies within the range 0.82-0.88 m depending on the choice of modelling parameters. In [3], the separating TBL is also characterised by the value of the momentum-thickness based Reynolds number, $Re_\theta \approx 3\,600$. In the simulations presented here this value is under-predicted and lies in the range 2650-3100. Due to the level of accuracy of mean velocity profiles produced by WMLES, it is not possible to match both $Re_{\delta_{99}}$ and Re_θ with the experiment, and here the choice was made to match the former.
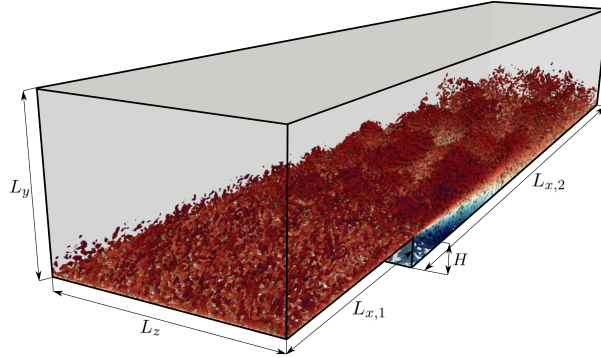
Figure 1: The computational domain. Resolved turbulent structures are visualised by iso-surfaces of the second invariant of the velocity gradient, coloured by mean streamwise velocity

The simple geometry of the computational domain allows constructing the mesh using hexahedral cells. Let δ be the height of the TBL at the inlet of the domain. Below $y = \delta$ the domain is meshed using cubic cells of equal size. The resolution of this part of the mesh can be characterised by the number of cells used to discretise the thickness of the upstream TBL, n/δ. Here, two resolutions are considered, $n/\delta = 15$ and 20. This corresponds to $3\,375$ and $8\,000$ cells per δ^3-cube, respectively. Both values are in line with the recommendations found in the literature, see e.g. [1]. Above $y = \delta$, the size of the cells in the wall-normal direction is increased towards the upper boundary, leading to coarse cells in the region occupied by the free stream. The total number of cells in the two meshes are ≈ 4.1 and ≈ 8.6 million, respectively.

All simulations were first run for $\approx 8T_{ft}$, where $T_{ft} = 37.8$ s is the flow-through time. Afterwards, time-averaging was started and continued for another $\approx 45T_{ft}$. The time-step used was $\Delta t = 0.01$ s, which resulted in the maximum CFL number of ≈ 0.4 on the densest employed grid and corresponds to $\approx 0.01H/U_0$.

The simulation campaign consists of eight WMLES and aims to assess the influence of the following modelling choices. Firstly, that of the density of the mesh, n/δ, which is taken to be either 15 or 20. Secondly, that of the scheme employed for computing the convective cell-face fluxes, taken to be either *linear* or *LUST*. Finally, the effect of the prescribed distance to the sampling point of the wall model, h, is also investigated. For the plate downstream of the step two alternatives are considered: using the distance to the centre of the wall-adjacent cell or to that of the second consecutive off-the-wall cell. For brevity, this will be from here on referred to as using $h = $ 1st and $h = $ 2nd, respectively. At the plate upstream of the step, $h = $ 2nd is always employed, as this has been shown to lead to more accurate results in simulations of attached TBLs, see e.g [1, 4].

Results

This section examines the obtained results. The focus of the analysis is on the influence of the different modelling choices on the flow prediction, whereas definitive conclusions regarding accuracy are avoided. The latter is motivated by the uncertainties associated with the experimental data. Also, the accuracy of a direct comparison between the WMLES and the experimental data in the post-separation region is somewhat undermined by the discrepancies in the characteristics of the separating TBL discussed above.

The plots in Figure 2 show the obtained values of the skin friction coefficient downstream of the step. It is observed that all the simulations predict a shorter recirculation region as compared to the experiment for which the mean reattachment point is, $x_r \approx 6.8H$. The under-prediction is systematically larger in simulations that employ the *LUST* scheme (dashed lines). Examining the recirculation region (see right plot in Figure 2), it is observed that $h = $ 1st (red-yellow lines) leads to a negative peak value that is closer to the experimental data. The small positive peak of c_f immediately downstream of the step corresponds to the secondary recirculation bubble. All simulations using the *LUST* scheme capture the bubble and give similar c_f predictions in that region. In the case of the *linear* scheme, the results are strongly dependent on the mesh and choice of h. It is speculated that this is due to the typical numerical instabilities associated with this scheme, which dominate over small flow features when a coarser grid is used. Downstream of reattachment, the simulations using $h = $ 2nd (blue-green lines) exhibit behaviour that is in better agreement with the reference data. This is particularly clear
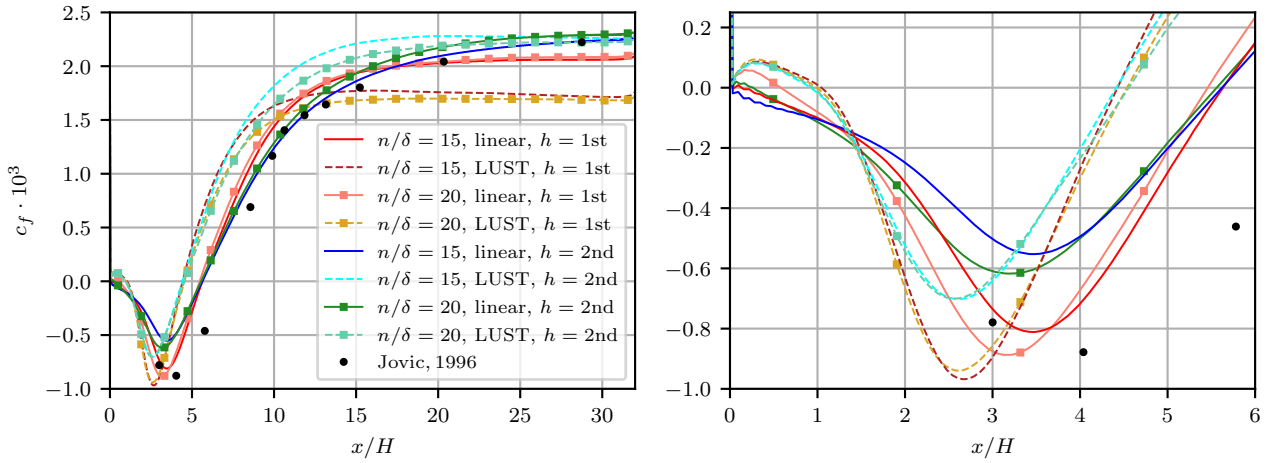
Figure 2: Values of the skin friction coefficient, c_f, on the wall downstream of the step. A zoom into the recirculation region is shown on the right.

in the case of simulations using the *LUST* scheme. The optimal choice of h thus appears to be using $h = 1^{st}$ upstream of reattachment and $h = 2^{nd}$ further downstream.

Figure 3 shows the profiles of the mean streamwise velocity in the detached shear layer at three selected locations. The mesh resolution does not seem to have a significant effect, and the most influential modelling choice is the employed numerical scheme. At $x/H = 0.26$, the profiles still resemble that of a flat-plate TBL. The profiles from the simulations using the *LUST* scheme are flatter, reflecting the larger amount of numerical diffusion. In general, all WMLES show acceptable agreement with the experiment. A similar conclusion can be drawn regarding the results at $x/H = 2.10$. The last station, $x/H = 6.58$, is located past the predicted reattachment point for all the simulations. In the reference experiment, on the other hand, the station lies in close proximity of the reattachment point. This is the main reason for the disagreement between the obtained profiles and the reference, which is particularly stark in the case of simulations using the *LUST* scheme. It is interesting to note that the choice of h seems to have a negligible effect on the form of the $\langle u \rangle / U_0$ profiles, even close to the wall.
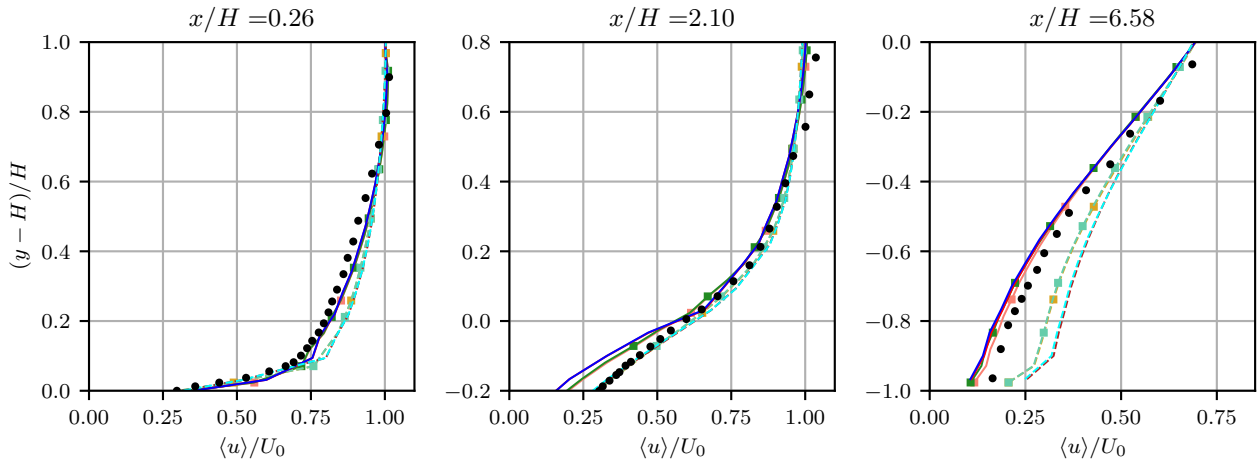
Figure 3: The outer-scaled mean streamwise velocity profiles in the detached shear layer. Line colour and style as in Figure 2.

Figure 4 shows the inner-scaled profiles of the streamwise velocity at three locations downstream of the reattachment point. The development of the logarithmic layer is clearly observed, but the overall profile shape still differs from that of an equilibrium zero-pressure-gradient TBL. The effect of h is significant here, in particular in the case of the simulations using *LUST*. Sampling from the wall-adjacent cell leads to an under-prediction of u_τ, whereas sampling from the second consecutive cell improves the results. This is consistent with the results obtained for c_f, and previous studies on equilibrium TBLs, e.g. [11]. Regarding the shape of the profiles, the agreement with the reference data is good in the log layer, but significant deviation is observed at $y^+ > 1000$ in some of the cases.

Conclusions

This work presents and analyses the results from a series of WMLES of the flow over a BFS. Different combinations of mesh density, numerical schemes and wall-treatments are considered. All simulations resulted in predictions that agree
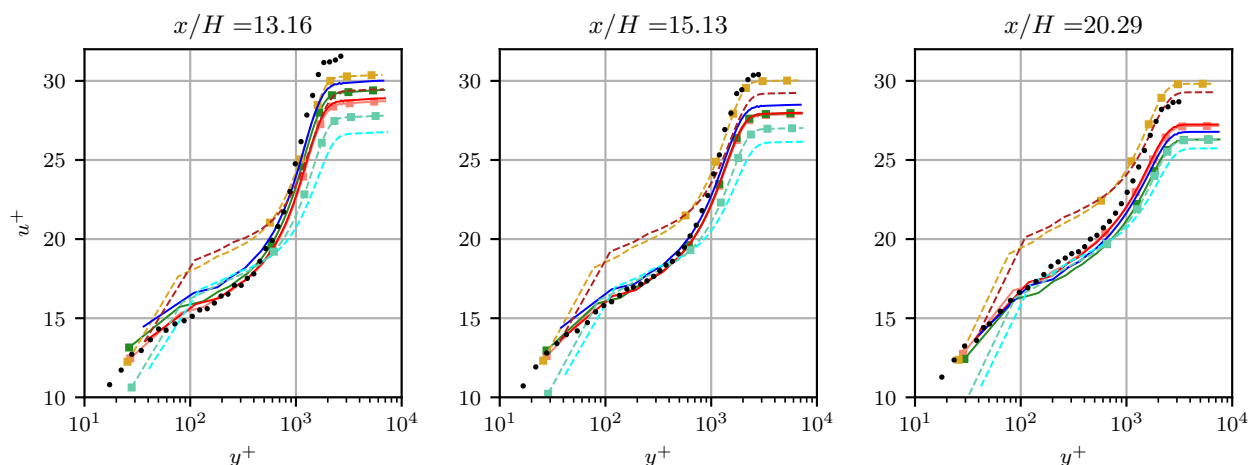
Figure 4: The inner-scaled mean streamwise velocity profiles in the recovering TBL. Line colour and style as in Figure 2.

reasonably well with the reference experimental dataset [3]. However, an $\approx 35\%$ error in the obtained location of the mean reattachment point was observed when using the *LUST* scheme. Using a denser mesh consistently leads to improved results, but the increase in computational costs is very significant. The choice of h is shown to significantly affect the prediction of the wall shear stress. In the post-reattachment region, using a larger value of h is beneficial. By contrast, in the recirculation region using the wall-adjacent cell for sampling gives better results. Thus, optimally, h should be selected depending on the flow region. The choice of numerical scheme is observed to have the largest effect on the obtained solution. Further studies are needed to judge definitely which scheme leads to better accuracy. What can be concluded is that *LUST* makes the wall model more sensitive to the choice of h, whereas the *linear* scheme is more sensitive to the resolution of the grid.

Acknowledgements

References

[1] J. Larsson, S. Kawai, J. Bodart, and I. Bermejo-Moreno, "Large eddy simulation with modeled wall-stress: recent progress and future directions," *Mechanical Engineering Reviews*, vol. 3, no. 1, pp. 1–23, 2016.

[2] M. Liefvendahl, T. Mukha, and S. Rezaeiravesh, "Formulation of a wall model for LES in a collocated finite-volume framework," Uppsala University, Department of Information Technology, Tech. Rep. 2017-001, 2017.

[3] S. Jovic, "An Experimental Study of a Separated/Reattached Flow Behind a Backward-Facing Step. $Re_h = 37\,000$," NASA Ames Research Center, Tech. Rep., 1996.

[4] T. Mukha, S. Rezaeiravesh, and M. Liefvendahl, "An OpenFOAM library for wall-modelled large-eddy simulation," in *12th OpenFOAM Workshop*, 2017.

[5] H. Weller, "Controlling the computational modes of the arbitrarily structured C grid," *Monthly Weather Review*, vol. 140, no. 10, pp. 3220–3234, 2012.

[6] H. Jasak, "Error Analysis and Estimation for the Finite Volume Method with Applications to Fluid Flows," Ph.D. dissertation, Imperial College of Science, Technology and Medicine, 1996.

[7] R. I. Issa, "Solution of the implicitly discretised fluid flow equations by operator-splitting," *Journal of Computational Physics*, vol. 62, no. 1, pp. 40–65, 1986.

[8] F. Nicoud and J. Baggett, "On the use of the optimal control theory for deriving wall models for LES," *Annual Research Briefs, Center for Turbulence Research, Stanford University*, pp. 329–341, 1999.

[9] D. B. Spalding, "A single formula for the "law of the wall"," *Journal of Applied Mechanics*, vol. 28, no. 3, pp. 455–458, 1961.

[10] T. Mukha and M. Liefvendahl, "The generation of turbulent inflow boundary conditions using precursor channel flow simulations," *Computers and Fluids*, vol. 156, pp. 21–33, 2017.

[11] S. Kawai and J. Larsson, "Wall-modeling in large eddy simulation: Length scales, grid resolution, and accuracy," *Physics of Fluids*, vol. 24, no. 1, p. 015105, 2012.

NUMEIRICAL SIMULATION OF SAJBEN DIFFUSER WITH A TURBULENCE MODEL

GAO LIN[1]

[1]*Gao Lin, College of Mechanical Engineering, Xi'an Shiyou University, gldut@126.com*

To avoid the separation in the flow field, the requirement of designing is always to reduce the size of subsonic diffuser. Therefore, it is very difficult to choose from meeting the requirements of length and size of diffuser and avoiding of separation. Sajben diffuser is a typical transonic nozzle, which is very fit for verifying the turbulence model for separated flow. In this paper, a turbulence model k-ξ model is adopted, with which better results are expected. For comparison, experimental data and several results of other turbulence models are given.

1. Governing equations and computational methods

There are two transport equations solved for two turbulent quantities in two-equation models, which are the turbulent kinetic energy k and the other variable to derive a turbulent length scale. Thus the eddy viscosity can be expressed as:

$$\nu_t = C_\mu \cdot k^m \cdot \psi^n \tag{1}$$

In which, C_μ, m, n are constants, ψ is considered as a generic length-scale variable. Based on numerical analysis, the second length-scale variable in turbulence modeling is very important, especially in prediction of separated flows. The larger the value of the sum of m and n, the larger the eddy viscosity since most turbulence variables are proportional to rate of strain in strong shear boundary layer regions. This will affect the ability of models to predict separated flows. Table 1 presents the comparison of the sum of m and n of commonly used two-equation models.

Table 1 *m* and *n* value of different models

Turbulence model	ψ	*m*	*n*	$\Sigma = m + n$
$k - \varepsilon$ (Launder and Sharma)	ε	2	-1	1
$k - \omega$ (Wilcox)	α	1	-1	0
$k - \zeta$ (Jiang)	ξ	1	-2	-1

In this paper, a new eddy viscosity turbulence model, k-ξ model, has been adopted. It is directly derived from standard k-ε and k-ω models based on a new standpoint.

The k-ξ model base on the standard model and a new variable ξ is introduced, which is the square root of specific dissipation $\xi = \sqrt{\omega} = \dfrac{\sqrt{\varepsilon}}{\sqrt{k}}$. Space lacks for a detailed description of the detailed deducing process.

The transport equations of k and ξ are as below:

$$\frac{\partial \xi}{\partial t} + U_j \frac{\partial \xi}{\partial x_j} = \alpha \frac{\xi}{k} P_k - \beta \xi^3 + \frac{\partial}{\partial x_j}\left[(\nu + \sigma_\xi \nu_t)\frac{\partial \xi}{\partial x_j}\right] + \sigma_c \frac{1}{\xi^2} \frac{\partial k}{\partial x_j} \frac{\partial \xi}{\partial x_j} \tag{2}$$

$$\frac{\partial k}{\partial t} + U_j \frac{\partial k}{\partial x_j} = P_k - k\xi^2 + \frac{\partial}{\partial x_j}\left[(\nu + \sigma_k \nu_t)\frac{\partial k}{\partial x_j}\right] \tag{3}$$

Where the production rate P_k is $P_k = \nu_t S_{ij}^2$. With the strain rate S_{ij} is $S_{ij} = \dfrac{1}{2}\left(\dfrac{\partial u_i}{\partial x_j} + \dfrac{\partial u_j}{\partial u_i}\right)$.

The eddy-viscosity is defined as

$$\nu_t = C_\mu \frac{k}{\xi^2} \tag{4}$$

The constants for turbulence model used in this paper are given in Table2.

Table2 Constants for k-ξ turbulence model

α	β	σ	σ	C_μ	σ_c (to ensure to be non-negative)
0.26	0.4	1.0	1.0	0.09	0,if $\dfrac{\partial k}{\partial x_j}\dfrac{\partial \xi}{\partial x_j}\leq 0$; 1.5,if $\dfrac{\partial k}{\partial x_j}\dfrac{\partial \xi}{\partial x_j}> 0$

In this paper numerical results obtained with k-ξ model had compared with experimental data to test and verify the new eddy viscosity turbulent model.

For both cases, the inlet condition of k and ξ can be set as followed:

$$k = \frac{3}{2}(U \cdot i)^2 \tag{5}$$

$$\xi = \sqrt{C_\mu k / \nu_t} \tag{6}$$

The eddy viscosity is nearly ten times of fluid viscosity ν_t =10 ν , and outlet variables can be set as zero gradients. No-slip wall conditions are used on the airfoils surface. If the mesh is coarse (y^+ ≥30), standard wall-functions for the turbulent variables are adopted. When the mesh is fine enough ($y^+ \approx$ 1), turbulent kinetic energy is set to zero and

$$\xi = \sqrt{\frac{6\nu}{0.075 y^2}}$$

are directly derived from the wall boundary condition for ω with a fine mesh .An under-relaxation method is used for stability and faster convergence. The pressure under-relaxation factor is 0.3 and a value of 0.7 is used for the other equations.

In this paper, all calculation and simulation are implemented on OpenFOAM 1.7.1. OpenFOAM is an Open Source library written in C++. It is a well-structured code, mostly used to implement CFD solvers, although it is also used in other applications. OpenFOAM is based on the finite volume method, but there are also implementations of the finite area and finite element methods. With regards to basic features, such as turbulence models and discretization schemes, OpenFOAM is a serious and high quality CFD tool that is constantly evolving. The solution is affected by an iterative pressure-correction (semi-implicit method for pressure-linked equations）SIMPLE algorithm for incompressible flow. The advective volume-face fluxes are approximated using second-order（total variation deminishing）TVD-limited linear differencing. Preconditioned (bi-) conjugate gradient matrix solver methods are used to solve the discretised matrix equations.

2.Numerical results and discussions

During 1979 to 1986, experiments and theoretical studies have been carried by several researchers. The flow-field in sajben diffuser with weak shock have been analyzed. Figure 1 is the geometric diagram of sajben diffuser, which is a kind of a converging-diverging diffuser.
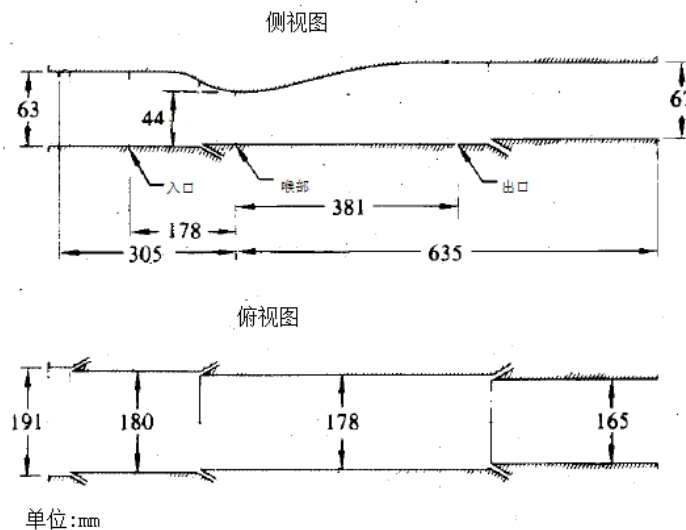

Figure 1: sajben diffuser

As seen, the ratio of the inlet width of the diffuser passage to the throat width (that is, the narrowest part of the pipe) is 1.4, and the ratio of inlet to throat is 1.5. The distance between throat and inlet is four times as long as the width of throat. In the experiment, in order to ensure the two-dimensional characteristics of the flow, suction joints are installed at the corners of the wall and the upper surface perpendicular to the flow direction.

In this case, mach number is 0.46 with uniform inflow and 1% turbulence. The conditions of fluid flows are subsonic inlet and 16.937pisa outlet pressure. The case is meshed as 307*51 hexahedron unstructured mesh, with proper enciphering of wall boundary layer. The simulated results are shown as below. The fluid flows into the diffuser from inlet with uniform condition, and the fluid pressure is varied as the pipeline shape changing. First, the flow pressure reduces and the velocity increases as the pipe constriction. And then the flow velocity decreases and the pressure rise after the throat. At last the flow is tending to balance gradually. It is experimental data that the mach number is 0.46 at inlet, 0.78 after weak shock, and 0.51 at outlet. Its highest value can be 1.3 around throat. The pressure distributions on upper and lower walls are shown in Figure 2 and 3. As seen it is got the nearly results with different turbulence models. But the k-ξ model gives the better pressure distribution and location of the weak shock near throat. The k-ε turbulence model has the late shock separation, compared with the experimental data. At the beginning of balance stage, k-ε turbulence model gives the higher pressure. The trend of fluid flow is better predicted with the k-ξ model. The results of it is closer to experimental data, especially on upper wall.
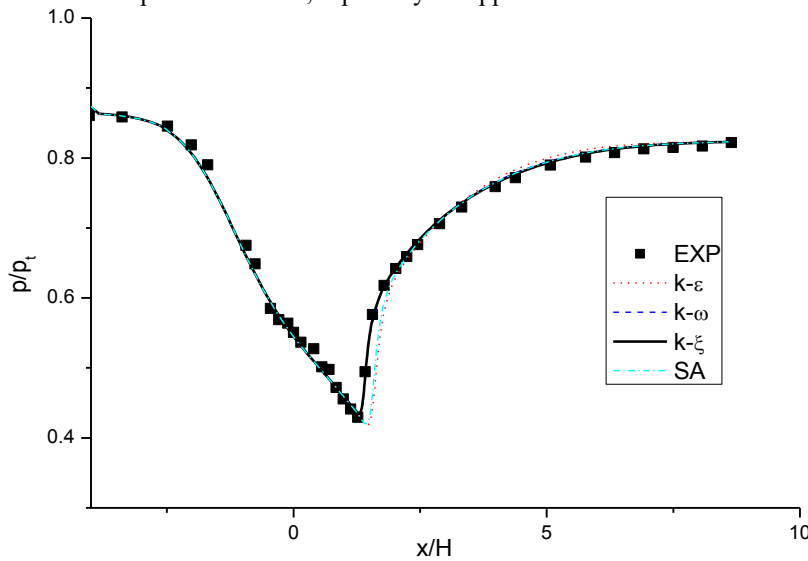
Figure 2: ma=0.46，pressure distributions on lower wall
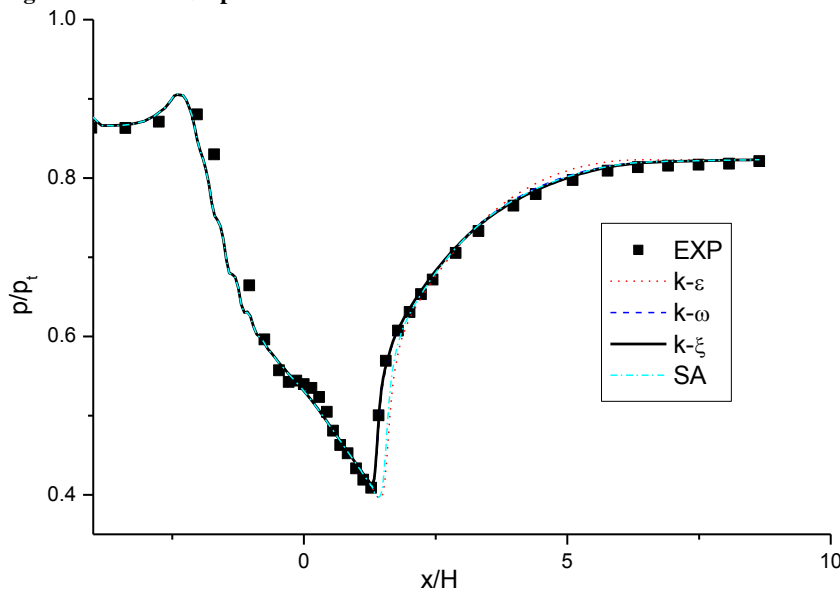
Figure 3:.ma=0.46，pressure distributions on upper wall

Diffuser wall pressure depends more on shape of wall and initial condition, so all pressure results with different model are close. The velocity profile on the cross section of the diffuser is more persuasive, it is shown the details inside flow field. The figures below show us the velocity profile on the different cross section, x/H=1.729，2.882，4.611，6.340. H is the height of throat of diffuser. It is seen that results with k-ε model have got the higher value on cross section 1 and lower value on cross section 3 and 4. Compared to other models, the results with k-ξ model are closer to experimental data and more in line with physical reality.
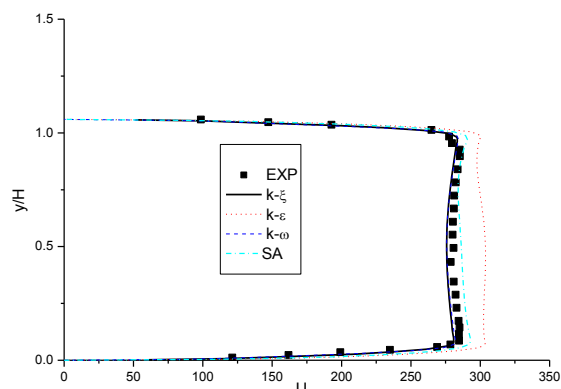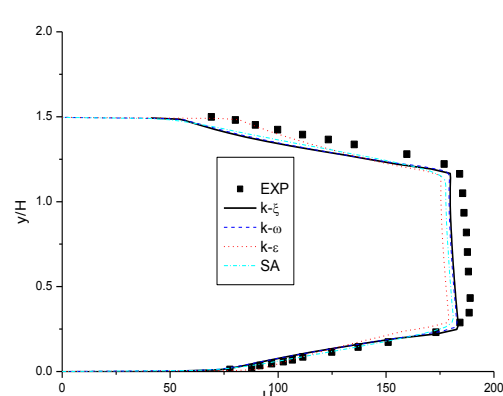
(a) velocity profile on the different cross section, x/H=1.729
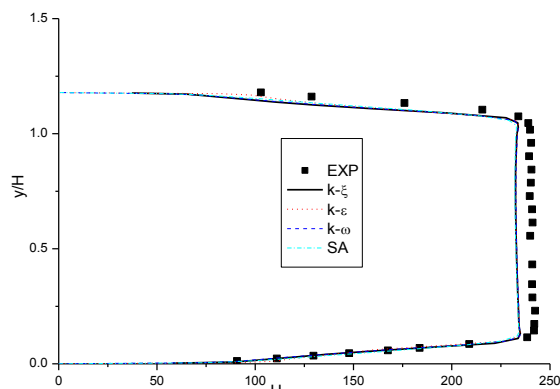
(c) velocity profile on the different cross section, x/H=4.661
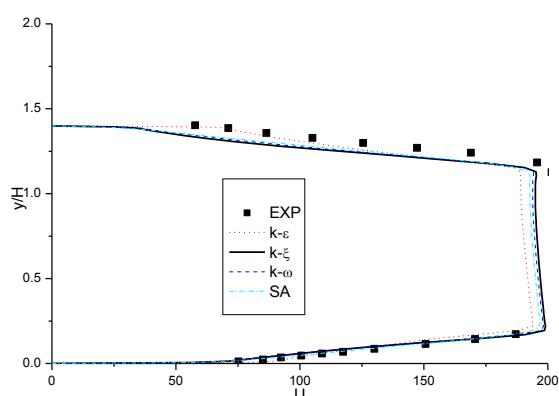
(b) velocity profile on the different cross section, x/H=2.882

(d) velocity profile on the different cross section, x/H=6.340

Figure 4:ma=0.46，velocity profile on the different cross section, x/H=1.729，2.882，4.611，6.340.

References

[1] W.Mayer, D. and W.D. kneeling, Evaluation of Two Flow Analyses for Subsonic Diffuser Design, in 30th Aerospace Sciences Meeting & Exhibit, A. 92-0273, Editor. 1992: Reno, Nevada.

[2] Bogar, T.J., Structure of Self-Excited Oscillations in Transonic Diffuser Flows. AIAA JOURNAL, 1986. 24(1): p. 54-61.

[3] Chen, C.P., M. Sajben, and J.C. Kroutil, Shock Wave Oscillations in a Transonic Diffuser Flow. AIAA JOURNAL, 1979. 17(10): p. 1076-1083.

[4] Hsieh, T., T.J. Bogar, and T.J. Coakley, Numerical Simulation and Comparison with Experiment for Self-Excited Oscillations in a Diffuser Flow. AIAA JOURNAL, 1987. 25(1): p. 75-81.

[5] Hsieh, T., et al., Numerical Investigation of Unsteady Inlet Flowfields. AIAA JOURNAL, 1987. 25(1): p. 81.

[6] Sajben, M., T.J. Bogar, and J.C. Kroutil, Forced Oscillation Experiments in Supercritical Diffuser Flows. AIAA JOURNAL, 1984. 22(4): p. 474.

[7] Salmon, J.T., T.J. Bogar, and M. Sajben, Laser Doppler Velocimeter Measurements in Unsteady, Separated Transonic Diffuser Flows. AIAA JOURNAL, 1983. 21(12): p. 1697.

[8] Liou, M.S. and T.J. Coakley, Numerical Simulations of Unsteady Transonic Flow in Diffusers, in AIAA/ASME 3rd Joint Thermophysics,Fluids, Plasma and Heat Transfer Conference. 1982: St. Louis, Missouri.

[9] Xiao, Q., H.M. Tsai, and F. Liu, Viscous Computation of Steady/Unsteady Transonic Diffuser Flows, in 32nd AIAA Fluid Dynamics Conference and Exhibit. 2002: St. Louis, Missouri.

[10] Bogar, T.J. and M. Sajben, Characteristic Frequencies of Transonic Diffuser Flow Oscillations. AIAA Journal, 1983. 21(9): p. 1240.

THE EFFECT OF SUB-GRID SCALE MODELS ON THE LARGE EDDY SIMULATION OF A CORRUGATED CHANNEL FLOW

YERU SHANG[1], ESRA SORGUVEN[2]

[1]*The University of Sussex, Yeru.Shang@sussex.ac.uk*
[2]*The University of Sussex, E.sorguven@sussex.ac.uk*

Introduction

Corrugated channels or multiple cavities, are widely appeared in numerous applications from gas turbine, ship to ship fuel transfer, to heat exchangers in solar energy systems, due to their flexibility, ease of manufacturing and increased heat transfer coefficients. Although devices with such geometry are frequently used for last few decades, its associated flow dynamics, including the flow separation and reattachment on the corrugated surface, momentum exchange between bulk flow and the flow in the corrugation, and the transition from boundary layer to separated shear layer, are still not properly understood. The combination of these effects lead to a minor modification in corrugation geometry triggering a significant change in flow structures and heat transfer characteristics.

Such an interesting and challenging subject has been attracting researchers' interests for almost a century. Its earliest experimental study can be traced back to 1928 when Fritsch ([1] of [2]) investigated the velocity distribution along the mid-plane of various rough surfaces including a corrugated (wavy) channel. It was reported that the velocity distribution depends only on the shearing stress, no matter the stress is changed by different roughness or Re, indicating turbulence plays an important role in corrugated channels. Some pioneer works by Perry et al. [3] and other researchers [4, 5] on square cavities reported when the length-to-height ratio of the cavity is greater than 4, the vertices inside the cavity become unstable and reattachment appear at the bottom of the cavity, and increasing the cavity length and Re will intensify the interaction between bulk flow and cavity flow, but changing of the cavity height did not affect the flow behaviours. Subsequent numerical analysis on this geometry [6] indicated even Reynolds Averaged Navier Stokes (RANS) solution can have a good agreement with experimental data. Nevertheless, numerical prediction of the flow on curved cavities has been proved to be more challenging [7]. Current research of curved wavy corrugated geometry are divided into two categories, i.e. the corrugation with a shape of sinusoidal wave and of periodic hill. Extensive experimental and numerical studies have been conducted for both categories. Results suggest flow separation and reattachment on curved surfaces are very unstable. The flow field can be turbulent around the curved surfaces at a Reynolds number, Re, of as low as 100 as suggested by Direct Numerical Simulation (DNS) of Krettenauer and Schumann [8]. Various studies [9, 10, 11] also demonstrated that the flow separation and reattachment, thereby the entire flow, are profoundly influenced by the modelling approximation, i.e. the wall treatment, SGS modelling and grid density. Therefore, RANS, under resolved Large Eddy Simulation (LES), and improper selection of wall modelling will fail to capture the main characteristics of the flow.

Despite of the fact that extensive studies have been carried out on simple wavy geometry and some best practices have been identified, studies on realistic geometry used in industry which resembles the configuration of the curved wavy corrugated flow have not been systematically performed. Those geometries, such as the flexible pipes and secondary flow system in gas turbine engine, tend to have less (or even no) post-reattachment-recovery region than the case in the periodic hill and much smaller length-height ratio of cavity than those corrugations with a shape of sinusoidal wave. Jaiman et al. [12] performed a numerical simulation on cryogenic flexible pipe for LNG transformation by a RANS and Delayed Detached Eddy Simulation (DDES), and observed a steady solution for RANS and unsteady one for DDES. Unal et al. [7] conducted Unsteady RANS and LES on a corrugation geometry of flexible pipes, and found LES can capture the unstable motion of the separation and reattachment points, and the strong mixing effect between flow in the corrugation and the bulk flow, while URANS fails to do so. But the study also pointed out the time-averaged values predicted by LES are not in good agreement with the experimental data. So the objective of current research is to study the sensitivities of the solution to SGS models on the realistic geometry.

Case Configuration

The corrugated channel investigated in present work is a 2D representation of a widely used commercial stainless steel flex pipe (heat exchanger) with a circular cross section. The geometry has a rectangular cross section, as shown in Fig. 1a, the bottom wall has a wavy shape with periodic grooves, whereas top wall and two sidewalls are both flat plates. A experiment with identical geometry and dimension is carried out by using Particle Image Velocimetry (PIV) technique [13], the dimensions of the geometry is shown in Fig. 1b.

Variables	Description	Value (mm)
H	channel height	15.85
h	corrugation height	4.15
λ	wavelength of the corrugation	6.6
d_1	diameter of the groove	3.0
d_2	corrugation diameter	3.6
b	channel width	20

(a)   **(b)**   **(c)**
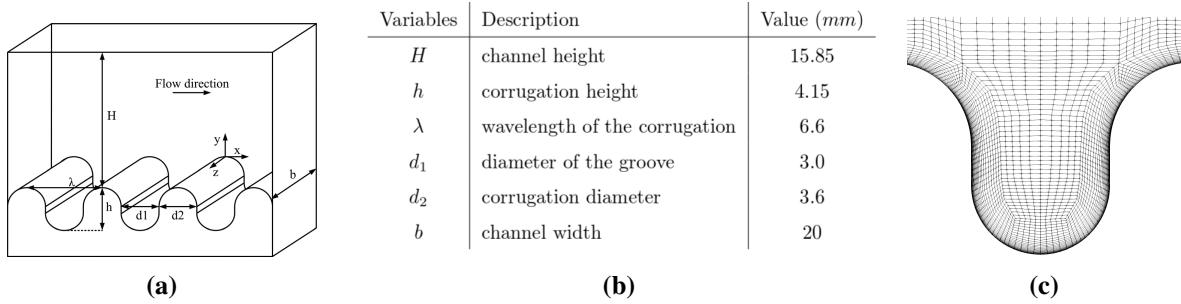
Figure 1: (a). Schematic Representation of Corrugated Channel; (b). Dimentions of the corrugated channel; (c). Mesh used in current LES.

The structured hexahedral mesh used in current study is shown in Fig. 1c. The mesh density increases as approaching the wall. The first layer distance on corrugated wall is less than 0.005 mm, on top wall is less than 0.006 mm and on side walls is less than 0.06 mm. A posterior analysis shows that y^+ value for corrugated wall is less than 0.25 with mean value of 0.04, for top wall it is less than 0.16 with mean value of 0.11, for side walls it is less than 2.4 with average value of 0.72, justifying the use of no-slip wall boundary condition. The total number of mesh cells for each corrugations is 0.9 million.

SGS Models

The SGS models studied in current research are listed in Table 1, which are all the standard implementations in OpenFOAM v1612+.

Table 1: Summary of SGS models tested in current channel flow case.

SGS Models	Model Description
SMAG+VD	Smagorinsky SGS model ($C_s = 0.2$) with van-Driest wall damping function
KEQ+VD	k-equation SGS model with van-Driest wall damping function
DyK	Dynamic k-equation SGS model
WALE	Wall-adapting local eddy-viscosity (WALE) SGS model

Numerical Setup

Re, based on bulk velocity, U_b, and hydraulic diameter of the channel is 5300. The density and laminar viscosity of the fluid is $\rho = 998.2 kg/m^3$ and $\mu = 0.001\ Pa\ s$ respectively, leading to U_b = 0.3 m/s. Periodic Boundary Condition (BC) is applied on both inlet and outlet, i.e. the two plane normal to x direction. The corrugated wall, two side walls, and the top walls are set to be no-slip, matching the BC used in experiment. Due to the shape of the corrugated wall, U_b for the whole computational domain must be carefully adjusted to ensure the desired bulk velocity at the inlet. Spatial interpolation of convection and diffusion terms are based on second order central differencing scheme. Time marching is approximated by second order backward differencing implicit scheme with a time step size $\Delta t = 5 \times 10^{-5} s$. The decoupling of velocity and pressure in the equation is obtained by Pressure Implicit with Splitting of Operators (PISO) algorithm. Velocity components are calculated by one momentum predictor step using smooth solvers with symmetric Gauss-Seidel smoother. While pressure field is corrected twice by generalised geometric-algebraic multi-grid (GAMG) solver with Gauss-Seidel smoother for the first corrector step and diagonal incomplete-Cholesky/LU with Gauss-Seidel (DICGaussSeidel) for the second one. A fully developed flow field with SMAG+VD are used as initial condition for all cases with other SGS models. All cases are allowed for a further 1s simulation to ensure the fluctuation induced by change of SGS model to be settled, followed by an averaging window of 8s. Flow field became statistically steady before data processing.

Results and Discussion

Despite of not showing here, all SGS models tested in current study are able to predict a chaotic, 3-dimensional and unstable flow field. Fig. 2a and Fig. 2b show the effect of various corrugation lengths and grid density on the normalised mean stream-wise velocity $\langle u \rangle / U_{mean}$, at mid-plane predicted by SMAG+VD. They suggest the suitable channel length for performing the simulation is $L = 16\lambda$ and current grid (referred to as Grid 1 in Fig 2b) is adequately fine, since further increase of channel length and grid density (Grid 2 in Fig 2b) have almost no effect on result. The adequacy of the grid density are also confirmed by the energy spectrum analysis (Fig. 2d) for a point close to the rising slope of the corrugation, as the spectrum is continuous and largely follow the slope of $\kappa^{-5/3}$. So all simulation are carried out with $L = 16\lambda$ on Grid 1.

The $\langle u \rangle / U_{mean}$ at mid-plane predicted by various SGS models are shown in Fig. 2c. It suggests that the simulation is insensitive to the selected SGS models, since all models predict a similar magnitude of $\langle u \rangle_{max}$ which locate at $y/h = 1.93$, slightly above the centreline ($y/h = 1.91$), suggesting the effect of corrugated wall on bulk flow is captured by different SGS models to a certain extent. The profile of time-averaged Reynolds stresses which is presented in Fig. 3 also demonstrate the insensitivity of the result on different SGS models. The magnitude and location of the maximum turbulent intensity obtained by different models are very similar for both top and corrugated wall with only marginally difference being observed on DyK. The CPU time is also compared between different models, it is found WALE is around 4% faster than SMAG+VD, whereas KvD and DyK are respectively 27% and 20% more time consuming than SMAG+VD.

Conclusion

The effect of SGS models on the prediction of a corrugated channel flow is investigated. A grid independence study was conducted prior to the main simulation, which found a total channel length of $L = 16\Lambda$ and Grid 1 are suitable for current study. Simulation outcome for SGS models of SMAG+VD, KvD, DyK and WALE are studied. It is learned that both time-averaged stream-wise velocity and turbulent intensity results are insensitive to SGS models. CPU time required for different SGS models is also compared, which shows the simulation of WALE are slightly (4%) faster than SMAG+VD, and KvD and DyK are over 20% slower than SMAG+VD. Therefore, WALE with $L = 16\lambda$ and Grid 1 will be used for further study on the corrugated channel flow.

References

[1] W. Fritsch, "Der einfluss der wandrauhigkeit auf die turbulente geschwindigkeitsverteilung in rinnen," *Z. angew. Math. Mech*, pp. 199–216, 1928.

[2] J. Nikuradse, "Laws of flow in rough pipes," *VDI Forschungsheft*, p. 361, 1933.

[3] A. E. Perry, W. H. Schofield, and P. N. Joubert, "Rough wall turbulent boundary layers," *Journal of Fluid Mechanics*, vol. 37, no. 2, p. 383413, 1969.

[4] L. DJENIDI, R. ELAVARASAN, and R. A. ANTONIA, "The turbulent boundary layer over transverse square cavities," *Journal of Fluid Mechanics*, vol. 395, p. 271294, 1999.

[5] J. Jimnez, "Turbulent flows over rough walls," *Annual Review of Fluid Mechanics*, vol. 36, no. 1, pp. 173–196, 2004.

[6] H. Stel, R. Morales, A. Franco, S. Junqueira, R. H. Erthal, and M. A. L. Goncalves, "Numerical and experimental analysis of turbulent flow in corrugated pipes," vol. 132, 07 2010.

[7] E. Unal, E. Sorguven, and H. Ahn, "Computational investigation of vortex structure in the corrugated channel," vol. 7A: Fluids Engineering Systems and Technologies, 2013.

[8] K. Krettenauer and U. Schumann, "Numerical simulation of turbulent convection over wavy terrain," *Journal of Fluid Mechanics*, vol. 237, p. 261299, 1992.

[9] L. Temmerman and M. A. Leschziner, "Large eddy simulation of separated flow in a streamwise periodic channel constriction," in *TSFP Digital Library Online*. Begel House Inc., 2001.

[10] L. Temmerman, M. A. Leschziner, C. P. Mellen, and J. Frhlich, "Investigation of wall-function approximations and subgrid-scale models in large eddy simulation of separated flow in a channel with streamwise periodic constrictions," *International Journal of Heat and Fluid Flow*, vol. 24, no. 2, pp. 157 – 180, 2003.

[11] M. Breuer, N. Peller, C. Rapp, and M. Manhart, "Flow over periodic hills numerical and experimental study in a wide range of reynolds numbers," *Computers Fluids*, vol. 38, no. 2, pp. 433 – 457, 2009.

[12] R. Jaiman and O. Oakley, "Cfd modeling of corrugated flexible pipe," vol. 6, 01 2010.

[13] E. Ünal, H. Ahn, and E. Sorguven, "Experimental investigation on flows in a corrugated channel," *Journal of Fluids Engineering*, vol. 138, no. 7, p. 070908, 2016.
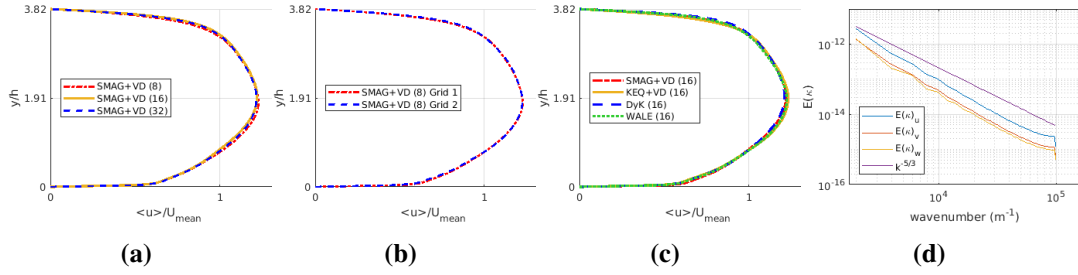
Figure 2: Predicted normalised mean stream-wise velocity, $\langle u \rangle / U_{mean}$, at mid-plane: (a). by SMAG+VD on different lengths of computational domain; (b). by SMAG+VD on different grid densities; (c). by different SGS models under 16 corrugations case. Also, (d). Energy spectrum, $E(\kappa)$, as a function of wavenumber recorded for a point close to the rising slope of the corrugation.
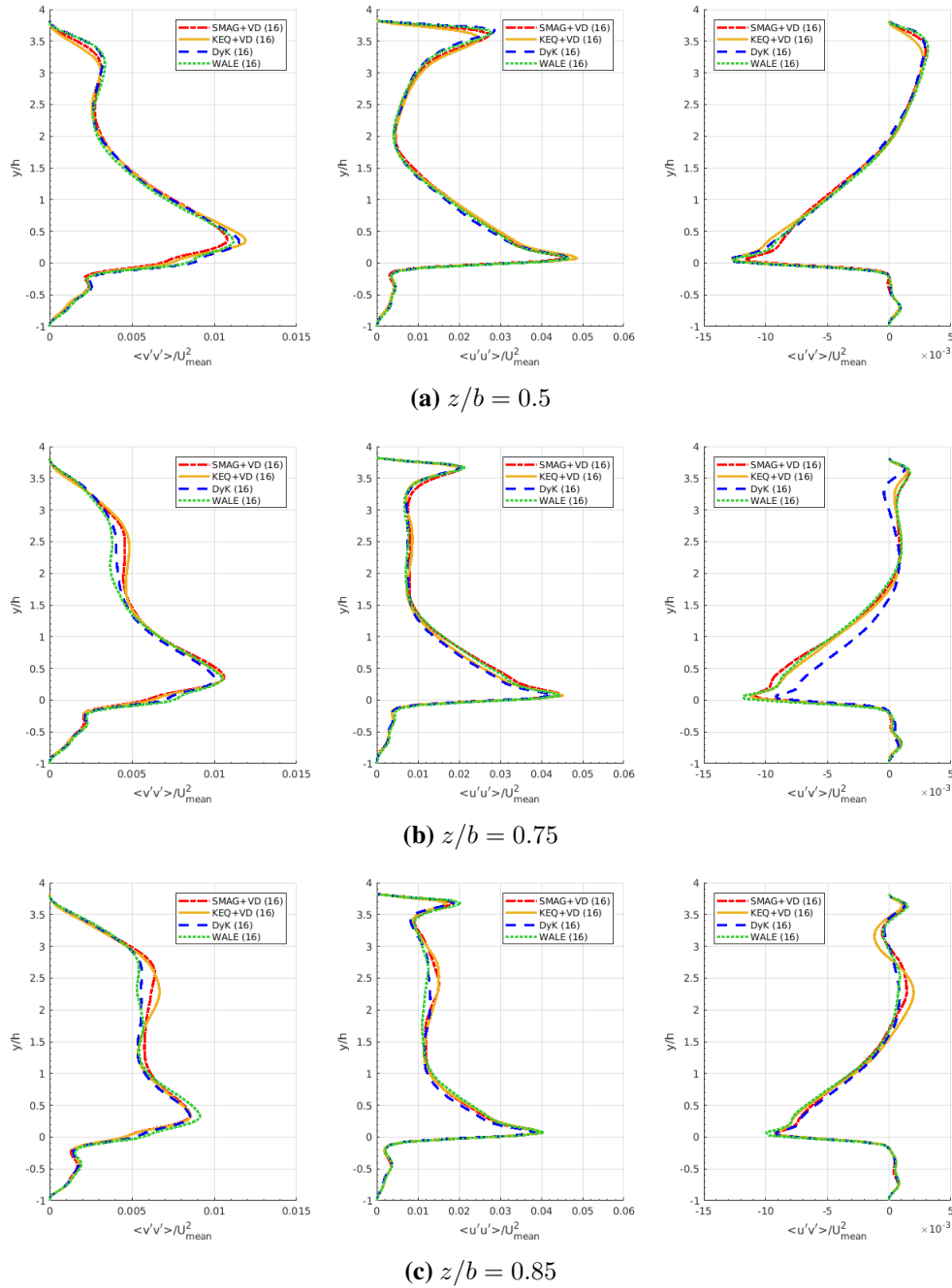

(a) $z/b = 0.5$

(b) $z/b = 0.75$

(c) $z/b = 0.85$

Figure 3: Profile of resolved Reynolds stresses, $\langle u'u' \rangle$, $\langle v'v' \rangle$ and $\langle u'v' \rangle$, normalised by mean velocity square at different location along z direction predicted by different SGS models.

Research of Gas Flowing Characteristics in Knudsen Pump

Xiaowei Wang, Zhijun Zhang*, Piaopiao Zhang, Shiwei Zhang

Institute of Chemical Process Machinery, School of Mechanical Engineering and Automation,

Northeastern Uinversity, Liaoning Shenyang 110819, Chain

*Email:Zhjzhang@mail.neu.edu.cn

Introduction

Micro Electro Mechanical System(MEMS) is a popular interdisciplinary study, with its miniaturization, low-cost mass production, highly integration, easy expansion and other advantages, which can be widely used in information, electronics, communication, military, biomedical, aerospace and other fields. Therefore, the drive and control of fluid in MEMS is one of the problems that must be solved when researching microfluidic devices. For developing and improving the microfluidic devices, micro-pumps, the drive control engine, are the most important point. The Knudsen pump was first proposed by Danish physicist Martin Knudsen in 1909. Compared to other micro-pumps, it is highly favored in the microfluidic devices application because of the advantages: no complex moving parts, simple structure, long service life, easy mass production, easy expansion, wide energy sources and low energy consumption.

Gas can flow in the channel since the gradient temperature field in the dilute gas, and the functional mechanism of the Knudsen pump is thermal induction flow. The classic Knudsen pump consists of a series of connecting fat and thin channels. Thermal creep effect is based on the gradient temperature which parallels to the wall of channel, which can drive gas flow from the low temperature to the high temperature side.

Methods

In this paper, the classical Knudsen Pump in rectangular channel model is studied. We analyze the flow characteristics of single gas (Ar, N_2, O_2) respectively and mixed gas (N_2 and O_2) in the pump channels by using Direct Simulation Monte Carlo (DSMC) method based on dsmcFoam solver of OpenFOAM . In addition, how these three different molecular models (Hard-Sphere (HS) model, Variable Hard Sphere (VHS) model, and Variable Soft Sphere (VSS) model) affect the gas flow is also researched by applying self compiling code of Binary Collision Model.

Results & Discussion

Fig.1
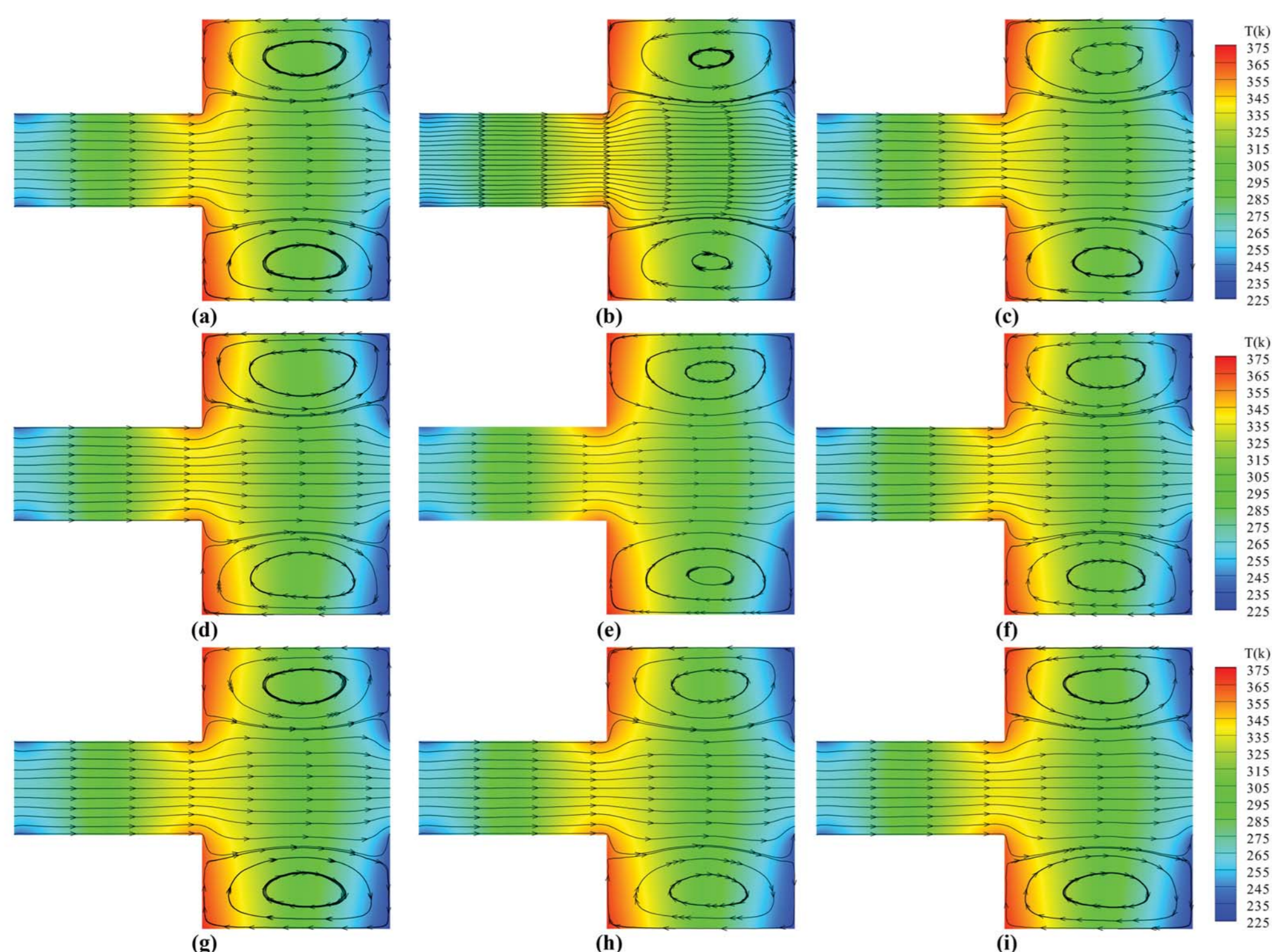
Fig.1.Streamlines and temperature contours for different gas compositions : (a)Ar; (b)N_2; (c)O_2; (d)N_2&O_2=4:1;(e)N_2&O_2=1:1; (f)N_2&O_2=1:4 and different molecular models: (g)HS model; (h)VHS model; (i)VSS model under atmospheric pressure.

The results indicate that changes in gas compositions, species, and molecular models do not affect the overall distribution and variation of the field in the channels.

Fig.2
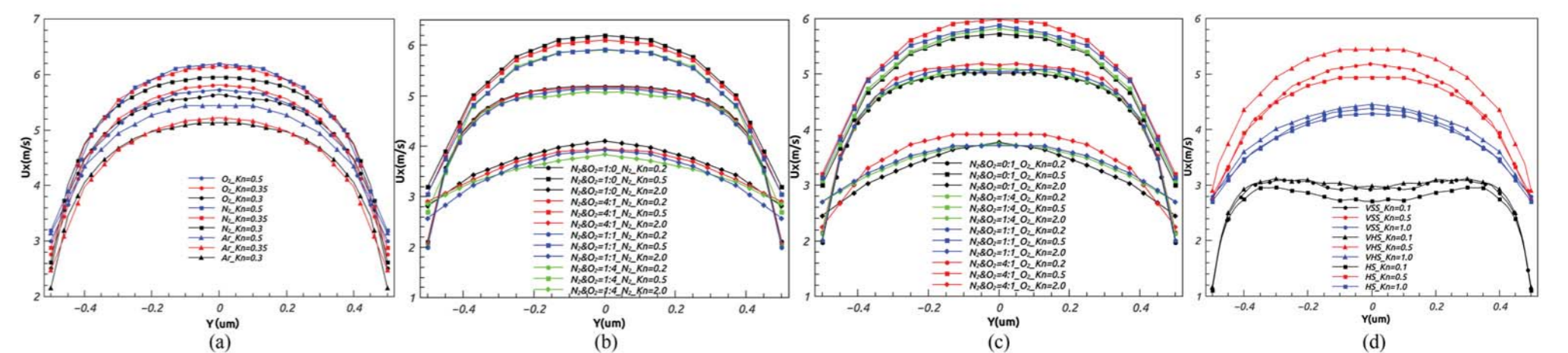
Fig.2.Velocity of different gas flow at X=1um. The thermal creep effect shows a trend of increasing first and then decreasing as the increasing of Kn number; gas N_2 has the strongest thermal creep effect; when the proportion of N_2 increases in the mixed gas, it can not only enhance the thermal creep effect but also promote the forward movement of the heavier gas; Variable Hard Sphere (VHS) model shows the strongest thermal creep effect among these three molecular models.

Fig.3
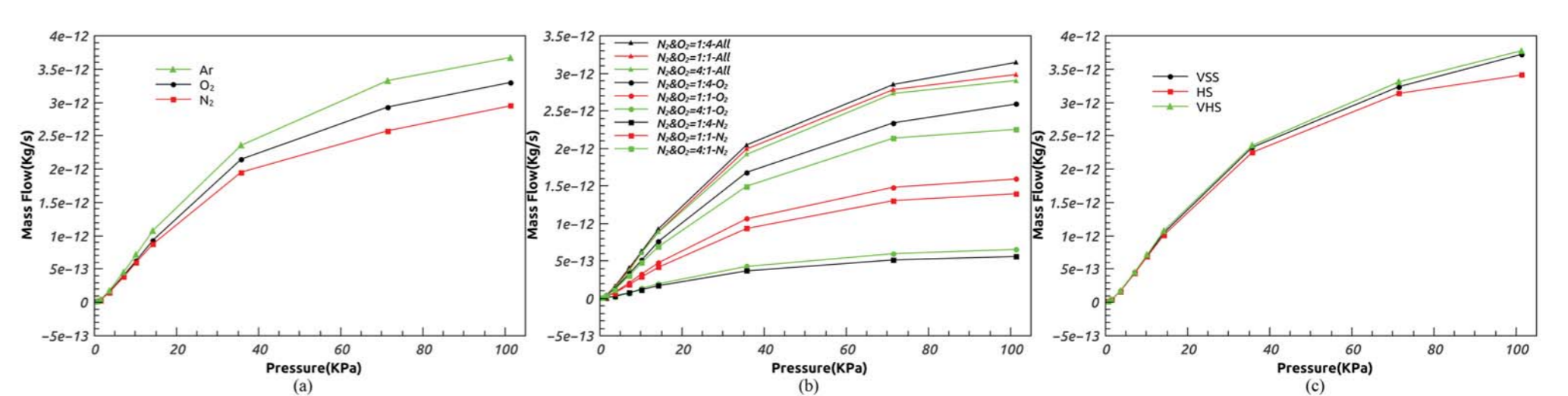
Fig.3.Mass flow versus pressure for different gas flows. Mass flow increases with the increasing of gas molecular weight; compared with the VSS model that can more practically reflect the movement of gas, the HS model will underestimate the actual performance of the pump, while the VHS model will overestimate the actual performance. When the Kn number is larger, the movement rule of the VSS model is more consistent with that of HS model. On the contrary, while the pressure is higher, the VSS model movement rule is closer to that of VHS model.

Conclusions

1.Changes of physical properties of the gas flow do not affect the overall distribution and variation of the field in the channels;

2.The lighter the gas molecular weight is, the stronger the thermal creep effect is;

3.The lighter gas can promote the forward movement of the heavier one;

4.Thermal creep effect increases with the increasing of gas molecular diameter.

Bibliography

[1] M.Knudsen, Eine revision der gleichgewichtsbedingung der gase. Thermische Molekularströmung, Ann. Phys. 336 (1) (1909) 205–229.

[2] Scanlon T J, Roohi E, White C, et al. An open source, parallel DSMC code for rarefied gas flows in arbitrary geometries[J]. Computers & Fluids, 2010, 39(10):2078-2089.

[3] Nakaye S, Sugimoto H, Gupta N K, et al. Thermal method of gas separation with micro-pores[C]// Sensors. IEEE, 2014:815-818.

[4] Szalmas L, Valougeorgis D, Colin S. DSMC Simulation of Pressure Driven Binary Rarefied Gas Flows Through Short Microtubes[C]// ASME 2011, International Conference on Nanochannels, Microchannels, and Minichannels. 2011:279-288.

[5] Vargas M, Naris S, Valougeorgis D, et al. Time-dependent rarefied gas flow of single gases and binary gas mixtures into vacuum[J]. Vacuum, 2014, 109(2):385-396.

[6] Bird G A. Monte Carlo Simulation of Gas Flows[J]. Annual Review of Fluid Mechanics, 2003, 10(8):11-31.

[7] G.A. Bird, Molecular Gas Dynamics and the Direct Simulation of Gas Flows,Clarendon Press, Oxford, 1994.

[8] Han Y L. Thermal-Creep-Driven Flows in Knudsen Compressors and Related Nano/Microscale Gas Transport Channels[J]. Journal of Microelectromechanical Systems, 2008, 17(4):984-997.

Improved Pressure-Velocity Coupled Algorithm For Compressible Flow

Taewoo Kim[1]; Jaeheung Gill[1]; Jaeryul Shin[1]

[1]NEXTfoam Co. LTD., Republic of Korea

Abstract

In this research, an improved pressure-velocity coupled computational fluid dynamics algorithm for numerical analysis of compressible flow with the discontinuous phenomena as like shock waves was described.

Introduction

The pressure-velocity coupled algorithm to analyze at various flow speeds was studied by Drawish[1]. In that paper, they demonstrated that the developed algorithm works well in flow fields at various speeds. The other hand, the pressure-enthalpy coupling scheme for the simulation with high change of enthalpy was performed Emans[2]. This algorithm was adapted to analyse for engine flow problems.

Kraposhin[3] has applied the Kurganov-Tadmor flux splitting scheme, which is mainly used in density-based solvers, to the pressure-based algorithm of OpenFOAM. In that study, they proved that flux splitting schemes are appropriate to interpret the discontinuous flow phenomena as a pressure-based algorithm.

In this study, the Kurganov-Tadmor flux splitting scheme, developed by Kraposhin[3], was applied to a developed coupled algorithms and a verification analysis of compressible flow problems were performed using the developed solver.

Methods

The Original pressure-velocity & pressure-enthalpy coupled algorithm
- The coupled algorithm in pressure based solver is a way of simultaneously updating the flux on cell faces and the pressure gradient in iterative calculation
- The pressure based coupled solver has than the segregated pressure based solvers but this way is required more computation resources
- To analyze the flow with a large change in density induced by enthalpy in the pressure-velocity coupled algorithm, an internal iterations has to be performed for density convergence
- The pressure-enthalpy coupled algorithm was employed for the phenomena that has large density change induced by energy change

An improved pressure-velocity-enthalpy coupled algorithm
- The two coupled algorithms have some disadvantages to perform analysis the flow with high energy and velocity change as like shock tube and nozzle problem
- To solve this problem, an improved algorithm by combining the above two methods with flux splitting method studied by Kraposhin[3] was developed
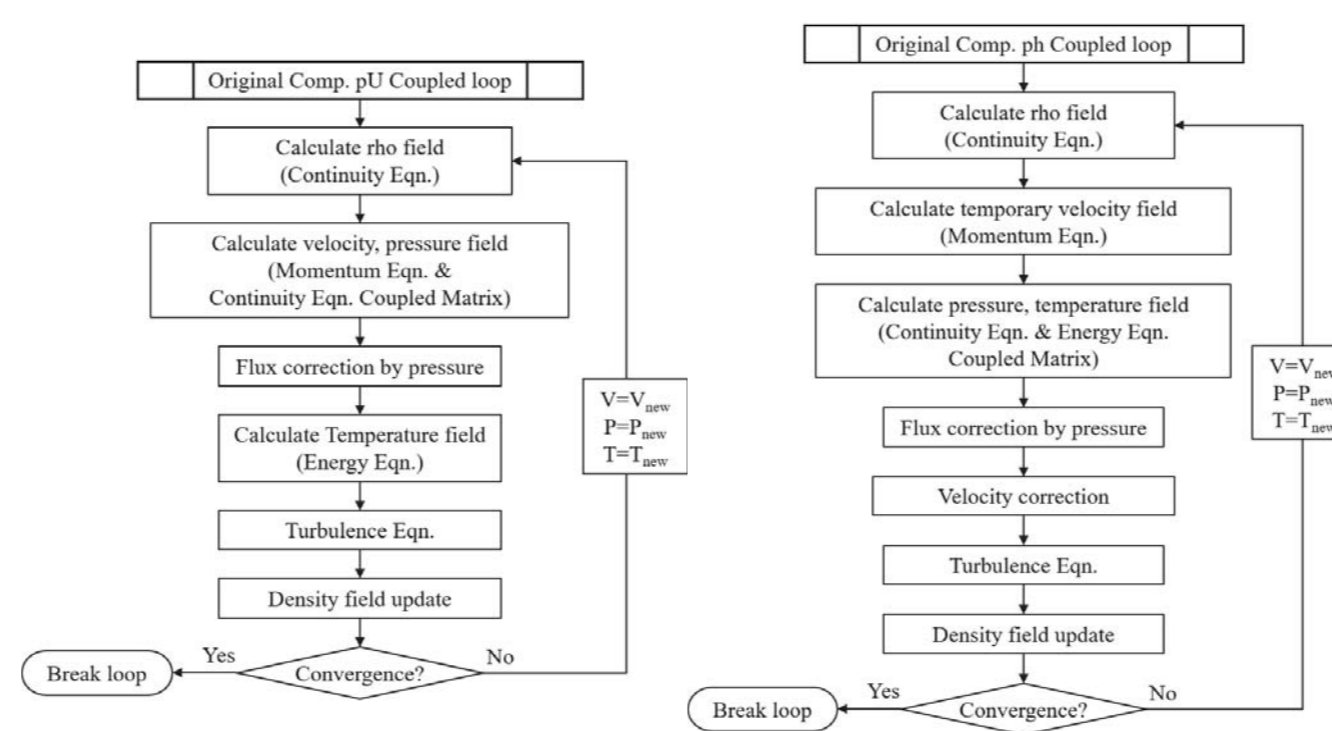
Figure 1. The original algorithms of coupled numerical analysis.
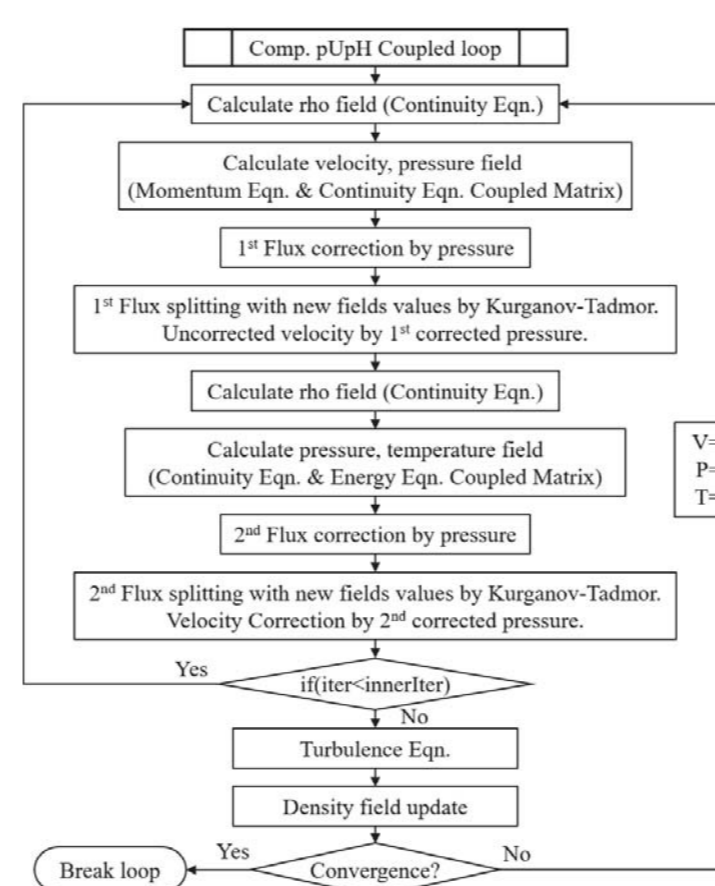
Figure 2. The developed algorithm of coupled numerical analysis.

Results

Some flow cases was employed to verify the developed solver.

1D Shock problems
- There is 3 shock problem – Sod(Figure 3), Lax(Figure 4), Shu & Osher(Figure 5) cases
- The analyzed results by developed solver are comparatively similar to other in-house and experimental results
- Through the analysis of the these cases, the analytical ability of the developed solver by improved algorithm for the flow with discontinuous flow phenomenon can be verified

JPL nozzle Problem
- Over-expended nozzle case was employed(Figure 6)
- Various mach number region was appeared through in converging-diverging regions
- Through the JPL over-expended nozzle case, the analytical ability of the developed solver by improved algorithm for the flow with wide mach number range can be validated
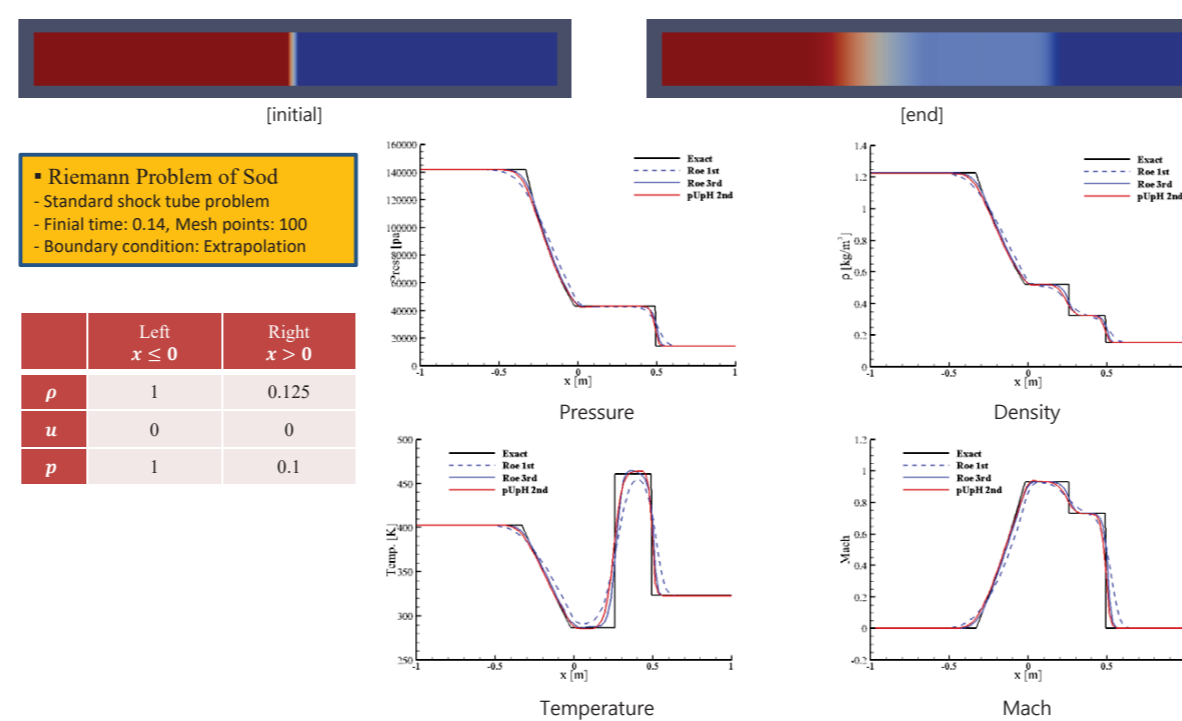

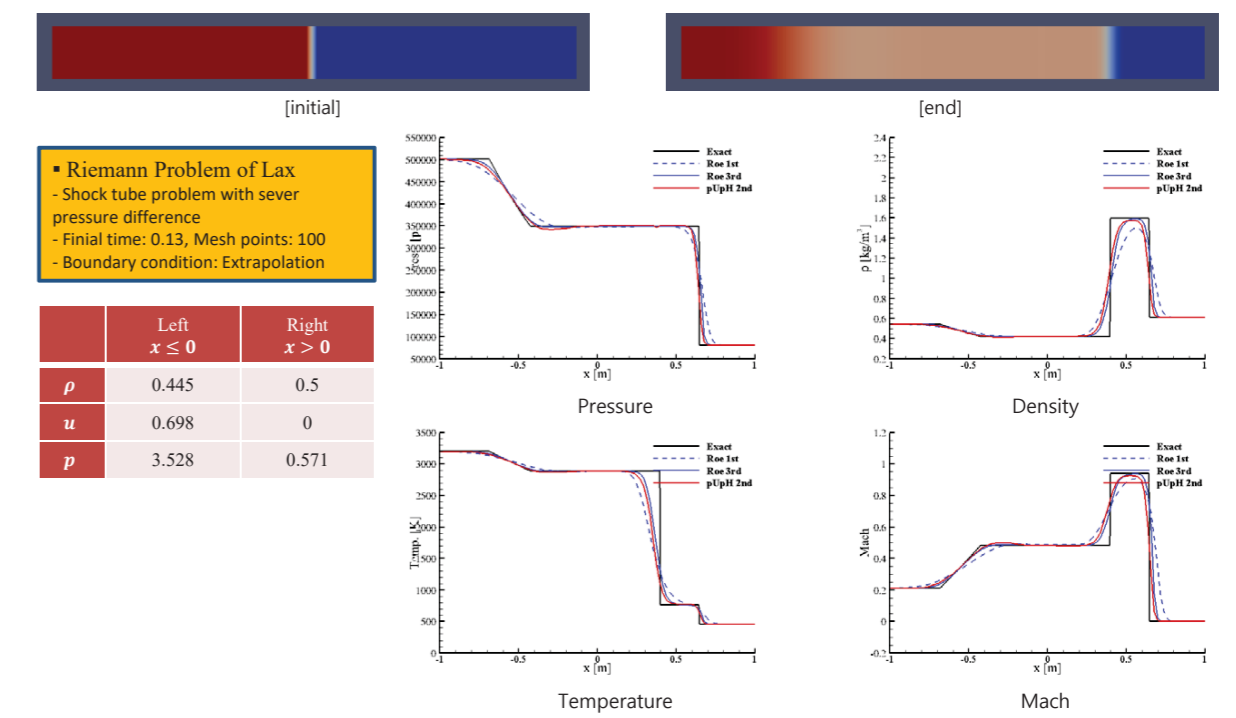**Figure 3.** 1D Sod problem conditions and results.

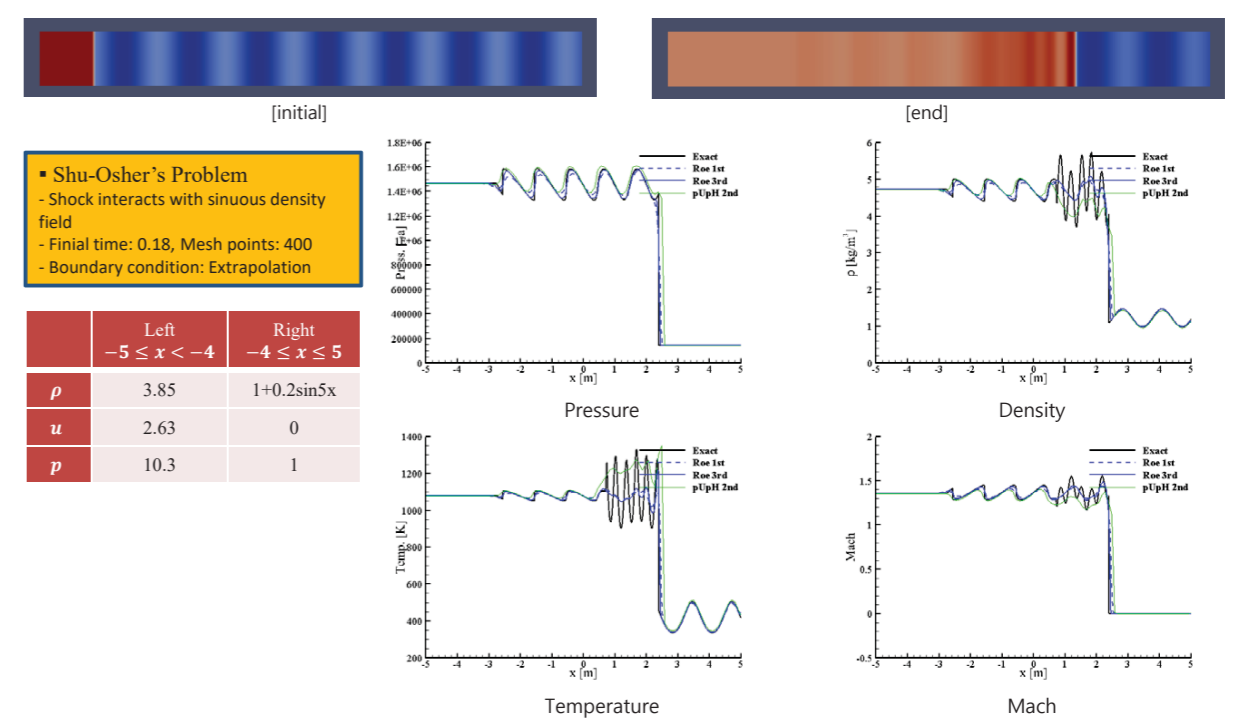**Figure 4.** 1D Lax problem conditions and results.

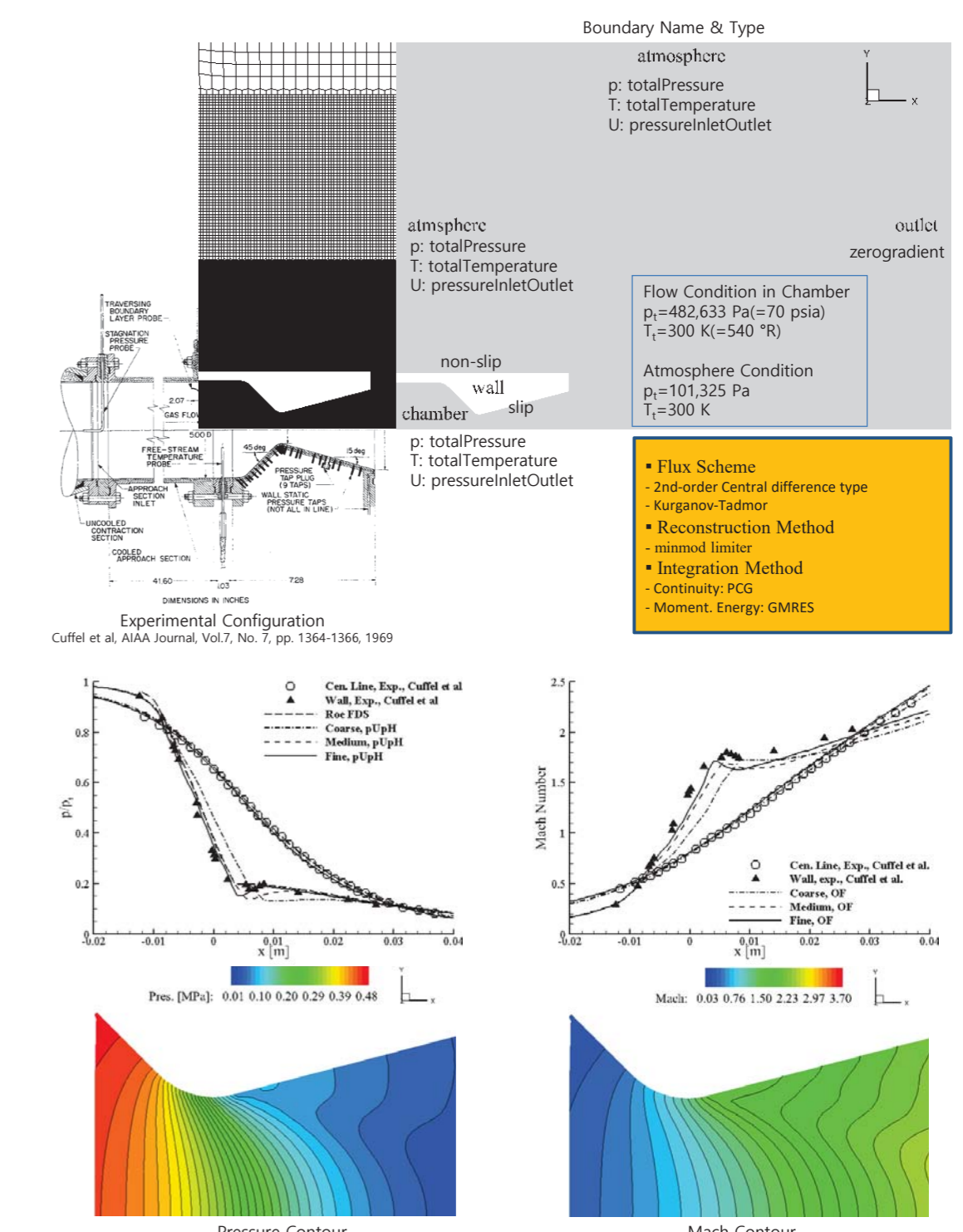**Figure 5.** 1D Shu & Osher problem conditions and results.

Figure 6. JPL Nozzle conditions and results.

Conclusions

It was confirmed that the developed solver had the similar analytical ability with that of the other numerical codes through the analysis of the shock wave induced problems in the supersonic flow region.

In order to verify the analytical ability for the all mach number flow region of the developed solver, the nozzle flow problems were analyzed and compared with results of experiments and other numerical analysis codes. It is confirmed that the analytical ability of developed solver in the high speed flow region such as supersonic and transonic is similar to the other density based in-house codes.

Contact

Taewoo Kim, Ph.D.
NEXTFoam Co. LTD.
Email: truepray@nextfoam.co.kr
        truepray@nate.com
Website: http://www.nextfoam.co.kr

References

1. M. Drawish and F. Moukalled, OpenCFD, A Fully Coupled Navier-Stokes Solver For Fluid Flow at All Speeds, Numerical Heat Transfer, Part B, 45: 410-444, 2014.
2. M. Emans, Z. Zunic, B. Basara, S. Frolov, A Novel SIMPLE-Based Pressure-Enthalpy Coupling Scheme for Engine Flow Problems, Mathematical Modelling and Aanalysis, Vol. 17, No. 1, pp. 1-20, 2012.
3. M. Kraposhin, A. Bovtrikova, S. Strijhak, Adaptation of Kurganov-Tadmor Numerical Scheme For Applying in Combination With the PISO Methodin Numerical Simulation of Flows in a Wide Range of Mach Numbers, Procedia Computer Science, Vol. 66, pp. 43-52, 2015.

The OpenFOAM Calculation of Subsonic-Supersonic Shear Mixing Layer

Yang Liu, Ben-shuai FU

Northwestern Polytechnical University, Xi'an, China, 710072

Introduction

Subsonic-supersonic shear mixing flow is one of important research field in turbulence research. In the rocket ramjet combustion chamber, the mixing of main rocket gas and air is a typical large gradient subsonic-supersonic shear mixing flow, which has characteristics of high convective Mach number (Mc) and large flow parameter gradient. It is of great significance to study the development rule and flow structure of the large gradient subsonic-supersonic shear mixing flow, which is of great significance to enhance the blending and enhance the working performance of the ramjet engine.

Numerical simulation

Figure 1: Schematic diagram of flow area
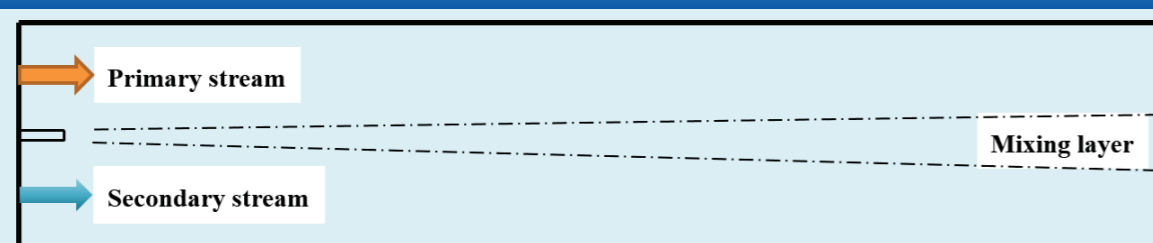
The numerical simulation work of subsonic-supersonic shear mixing flow is carried out based on OpenFOAM computing platform, and using rhoCentralFoam compressible solver, which is a compressible density solver, based on Kurganov & Tadmor center windward format, and has good adaptability for compressible flow.

Velocity and static temperature are given at high speed and low speed inlet. Given static pressure at the high speed inlet, the low speed inlet pressure is obtained by extrapolation. The export condition is zero-gradient boundary condition. The split board is non-slip boundary condition, and the upper and lower wall is sliding wall surface.

Table 1: Numerical calculation parameters

	U1(m/s)	U2(m/s)	Ma1	Ma2	Mc
Case1	517.61	103.24	2	0.3	0.69
Case2	517.61	201.22	2	0.6	0.53
Case3	517.61	289.90	2	0.9	0.39

In this paper, the range of convection Mach number (Mc) was 0.39-0.69. The subsonic-supersonic shear mixing flow of normal temperature is studied. Keeping the other parameters constant and changing Ma of the secondary flow of Case1-Case3, study the effect of Mc on compressibility of shear mixing layer.

Figure 2: Comparison of shear mixing layer velocity profile between numerical result and experimental data.
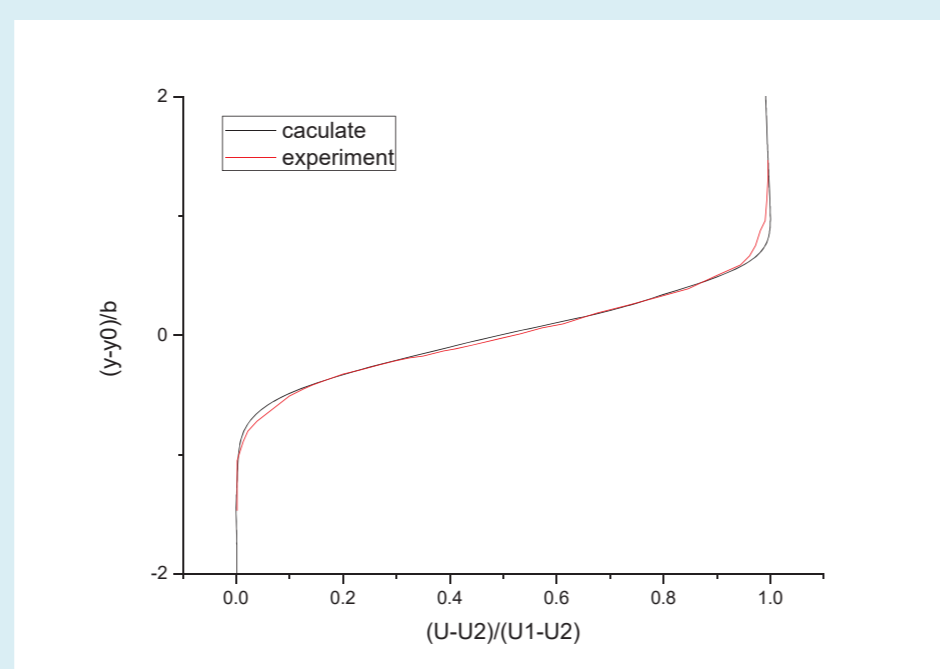
Experimental data of normal temperature subsonic-supersonic shear mixing layer carried out by Goebel is adopted for numerical validation LES model using in this paper. Figure 2 shows the shear mixing layer velocity profile expressed in self-similar form, and it can be found that numerical result is in good agreement with experiment data.

In the calculation process, when the shear mixing flow reaches the quasi-steady state, the data of a certain moment is selected to obtain the temperature contour. Figure 3 (a) - (c) is the temperature contour of each group of Case1-Case3.

(a) Static temperature distribution contour of Case1.
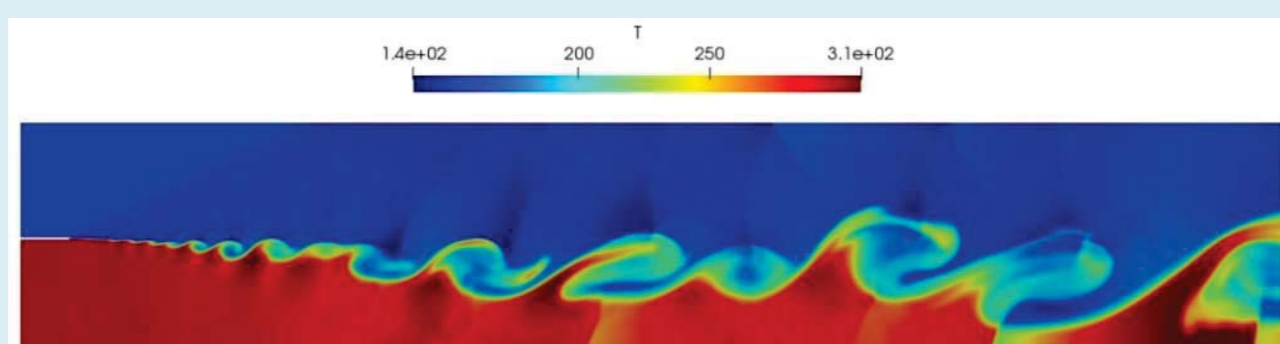
(b) Static temperature distribution contour of Case2.
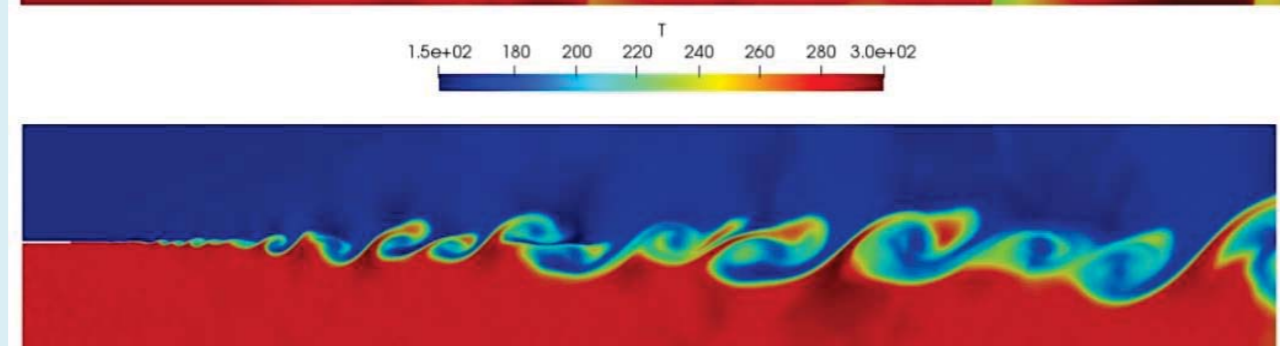
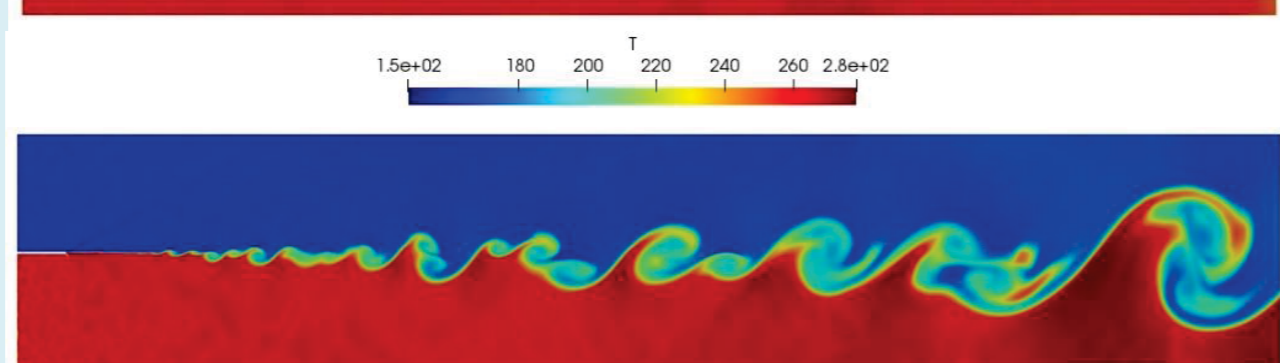**(c) Static temperature distribution contour of Case3.**

Figure 3: Static temperature distribution contours of Case1-Case3.

$$U^*(y) = \frac{U(y) - U_2}{U_1 - U_2}$$

$$\delta_{nor} = \frac{(d\delta/dx)}{(d\delta/dx)_{inc}} = f(M_c)$$

$$\left(\frac{d\delta}{dx}\right)_{inc} = C_\delta \frac{(1-r)(1+\sqrt{s})}{2(1+r\sqrt{s})}\{1 - \frac{(1-\sqrt{s})/(1+\sqrt{s})}{1+2.9(1+r)/(1-r)}\}$$

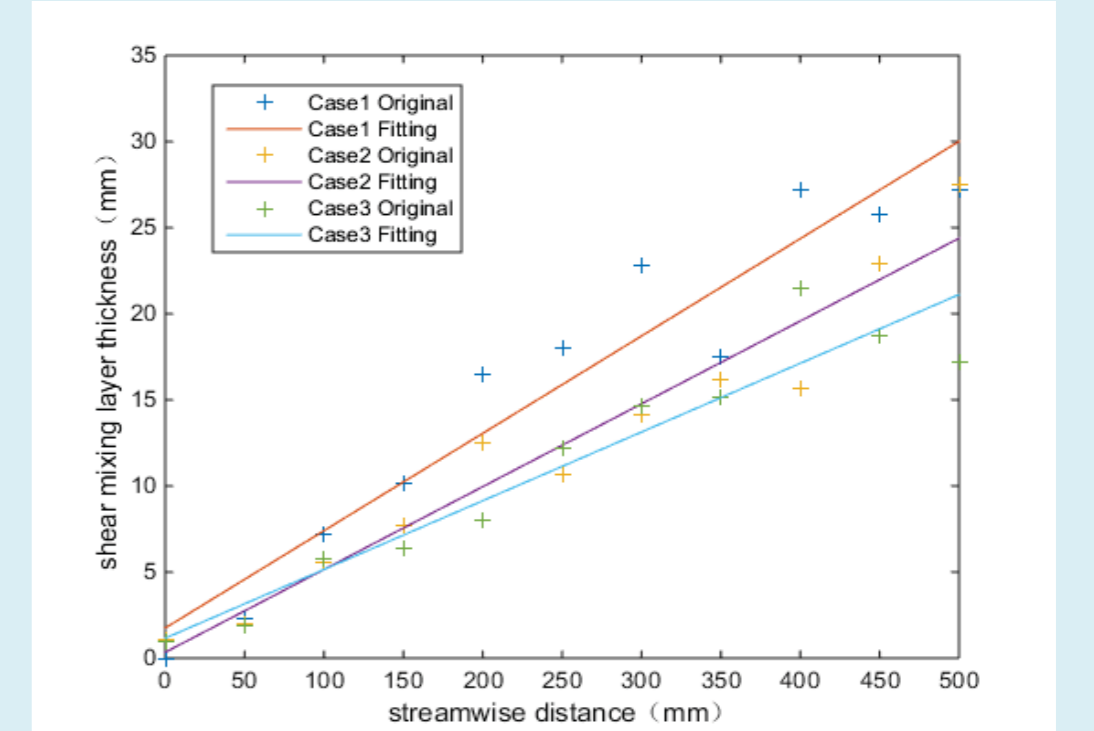**Figure 4: Thickness of shear mixing layer of Case1-Case3.**

Using the incompressible shear layer thickness growth rate δ_0' to make the compressible shear layer thickness growth rate δ' nondimensionalize, then get the shear layer thickness growth rate δ'/δ_0', and give the corresponding Mc, shown in the following table.

|	Case1	Case2	Case3
δ'	0.0565	0.0481	0.0399
δ_0'	0.2078	0.1433	0.0948
δ'/δ_0'	0.2720	0.3356	0.4209
Mc	0.69	0.53	0.39

Table 2: Shear layer thickness growth rate and corresponding Mc of Case1-Case3.

It can be seen from the above table, the dimensionless thickness growth rate of shear mixing layer decreases with the increase of Mc.

Calculation results of Changing parameters

Based on Case3, the boundary conditions of the upper and lower wall surfaces were changed to compare the thickness growth rate of subsonic-supersonic shear mixing layer under different boundary conditions.

	Ma1	Ma2	Mc	boundary conditions of the upper and lower wall surfaces
A1	2	0.3	0.39	Slid
A2	2	0.3	0.39	No slid
A3	2	0.3	0.39	Speed entrance

	A1	A2	A3
δ'	0.0399	0.0877	0.0323
δ_0'	0.0948	0.0948	0.0948
δ'/δ_0'	0.4209	0.9251	0.3407
boundary conditions of the upper and lower wall surfaces	Slid	No slid	Speed entrance
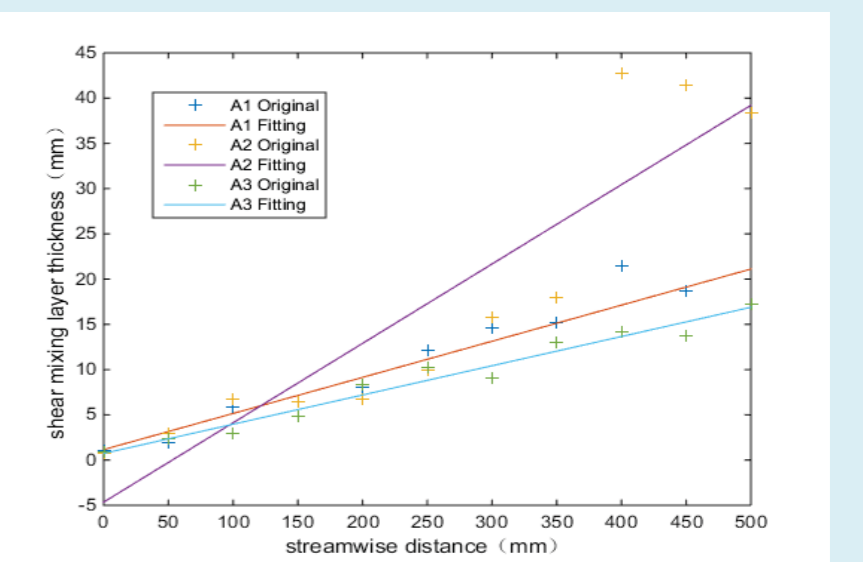
It can be seen from the above table that the dimensionless thickness growth rate and thickness growth rate of the shear mixing layer have great changes with the change of boundary conditions of the upper and lower wall surfaces.

Based on Case3, the static pressure of the incoming flow was changed to compare the thickness growth rate of subsonic-supersonic shear mixing layer under different static pressure conditions.

	Ma1	Ma2	Mc	static pressure (kPa)
B1	2	0.3	0.39	36
B2	2	0.3	0.39	60
B3	2	0.3	0.39	100

	B1	B2	B3
δ'	0.0323	0.0311	0.0302
δ_0'	0.0948	0.0948	0.0948
δ'/δ_0'	0.3407	0.3281	0.3183
static pressure (kPa)	36	60	100
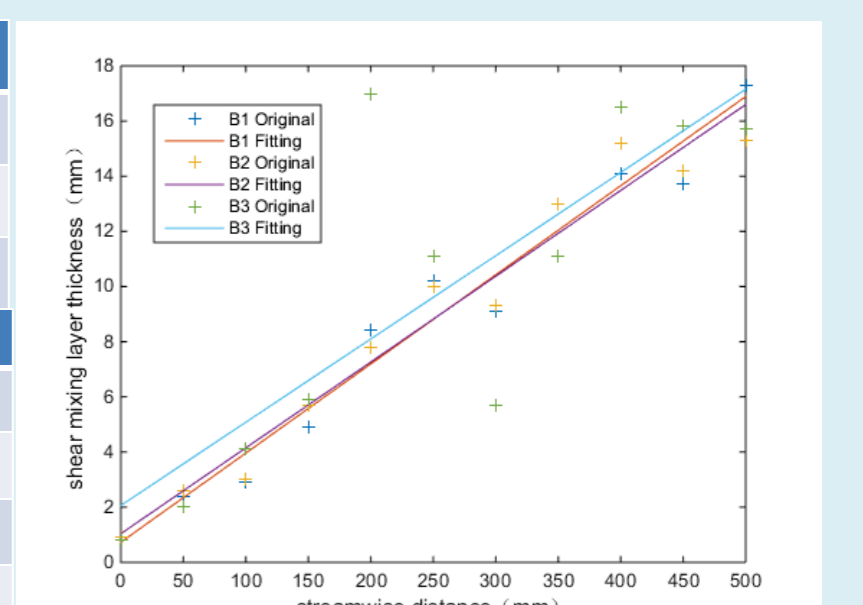
It can be seen from the above table, both dimensionless thickness growth rate and thickness growth rate of shear mixing layer decrease with the increase of static pressure.

Conclusions

In view of the subsonic-supersonic shear mixing flow, this paper uses the software of OpenFOAM to carry out large eddy simulation study, and the results show that the development process of the subsonic-supersonic shear mixing layer has the following rules:
(1) With the increase of compressibility, the dimensionless thickness growth rate of the shear mixing layer decreases.
(2) With the change of boundary conditions of the upper and lower wall surfaces, the dimensionless thickness growth rate and thickness growth rate of shear mixing layer have great changes.
(3) With the increase of static pressure, both dimensionless thickness growth rate and thickness growth rate of shear mixing layer decrease.

Simulation of Gas-Solid Flow in a Transfer Chute Based on CFD-DEM Coupling Method

Shan Zhang[a], **Xiaoling Chen[a]**, Fanhao Deng[a], Zekun Wang[b]

[a] *Beijing Key Laboratory of Process Fluid Filtration and Separation, China University of Petroleum - Beijing, Beijing, China*
[b] *BIC-ESAT & State Key Laboratory for Turbulence and Complex Systems, College of Engineering, Peking University, Beijing , China*

Introduction

Bulk solids handling is a crucial stage during coal, ore processing and chemical engineering in various industrial fields. Typically, dust is generated when the bulk materials loaded, dumped and transferred. In the case of belt conveyors, an area of particular concern for dust control occurs during transfer of bulk material from one conveyor to another, namely, transfer point. Usually, a chute is employed at a transfer point to make sure that the loads be discharged in a centralized stream and in the same direction as the receiving conveyor. Therefore, the performance of transfer chutes has a significant impact on not only the efficiency of conveyor belt systems, but also on the level of fugitive dust emissions. In this paper, the CFD-DEM coupling method is used to study dust generation and discharge mechanism in a transfer chute.

Method

There are two different substances in the flow of the transfer chute, air and particles. From a mesoscopic point of view, the gas can be treated as a continuous medium, the particles flow can be treated as discrete phase since it is composed of a large number of discrete particles. This paper uses the CFD-DEM coupling method to solve the gas-solid flow by coupling open source codes OpenFOAM and Liggghts. This method not only considers the complex flow of gas, but also simulates the complex interaction between gas-particle, particle-particle and particle-wall.

The step-by-step CFD-DEM implementation route is shown as follows:

1. Predict momentum exchange in CFD
2. Obtain particle velocity position information by solving Newton's Law in DEM
3. Obtain the particle information in the DEM, identify the grid ID of the particle and set the porosity in CFD
4. Select the reasonable force model in CFD to carry out momentum exchange and transfer to DEM to continue solving
5. Solve the whole flow field based on the Finite Volume Method (FVM) in CFD

Simulation

According to the previous experimental conditions, the iron ore particles with diameter of 4mm were selected, and the shape of the particles was assumed to be spherical. Hertz-Mindlin soft sphere model is adopted as the contact model. Potapov verified the influence of different turbulence models on gas-solid two-phase flow, the results show that the turbulence model has no great effects on the simulation result [1]. In this simulation, the k-ε turbulence model and the KochHill drag model were adopted to conduct the simulation study. The geometric model and mesh as shown in Figure 1, Figure 2.
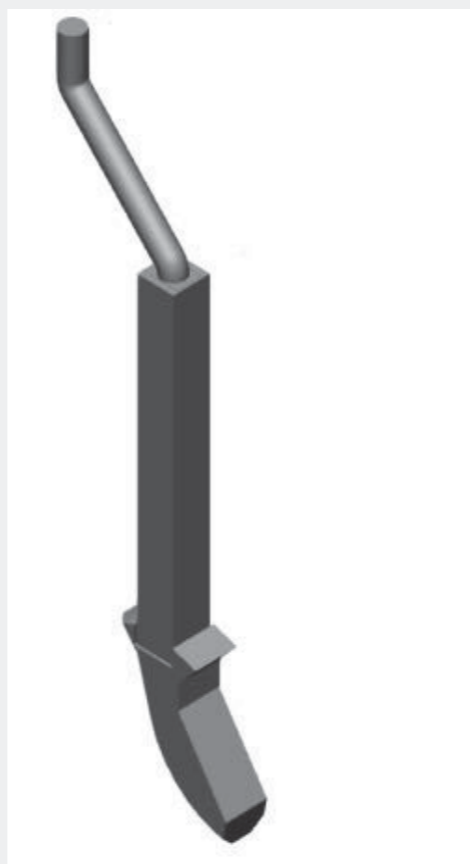
Figure 1: Geometric Model   Figure 2: Mesh
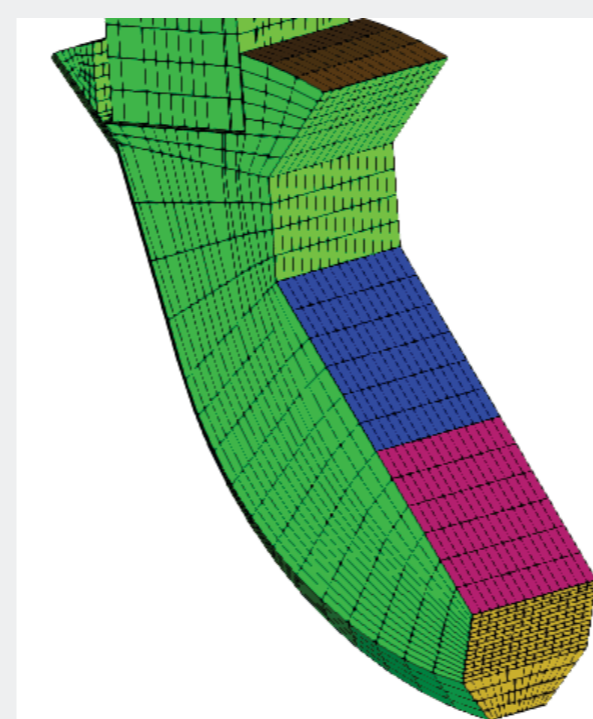
Results and discussion

The gas velocity distribution in the transfer chute were obtained from CFD-DEM coupling. To verify the simulation method, the air velocity distribution at the outlet of the transfer chute obtained from CFD-DEM coupling were compared with the previous experimental results[2], as shown in Fig. 3. It shows that the simulation results have the same trend as the experimental results. It is proved that the gas-solid two-phase flow in the transfer chute can be well predicted by using the CFD-DEM coupling method. It can be used as a powerful tool to evaluate the effect of transfer chute on the particulate flow.
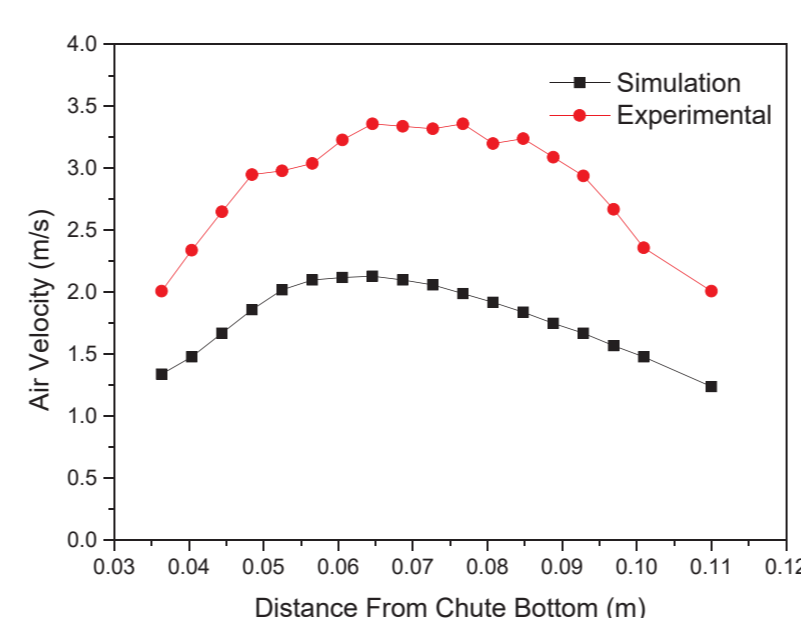

Figure 3: Comparison Between Simulated and Experimental

The turbulent motion of the gas will entrainment the dust, reducing the gas velocity will reduce the dust entrainment. Figure 4 and Figure 5 show the flow conditions of the gas in the chute, and the dust generation can be predicted based on the gas velocity and flow direction. In addition, the particle velocity and gas volume fraction are shown in Figure 6, Figure 7.
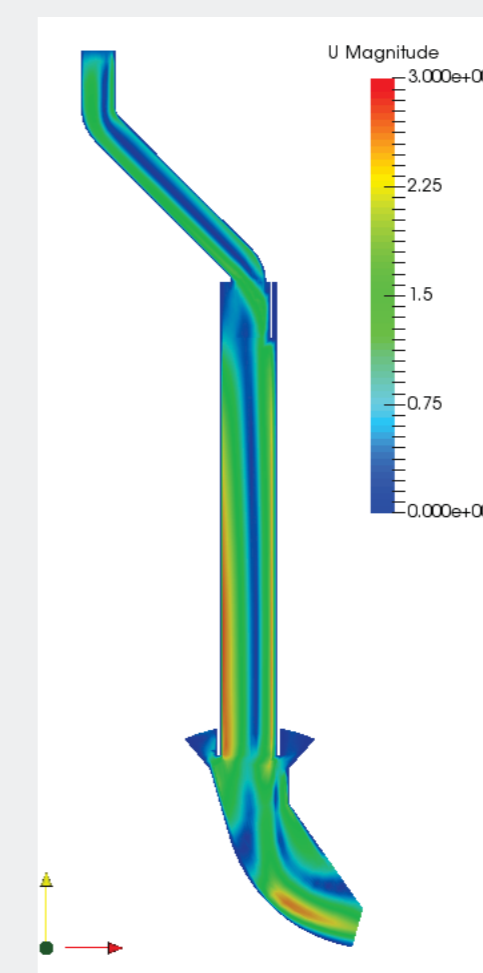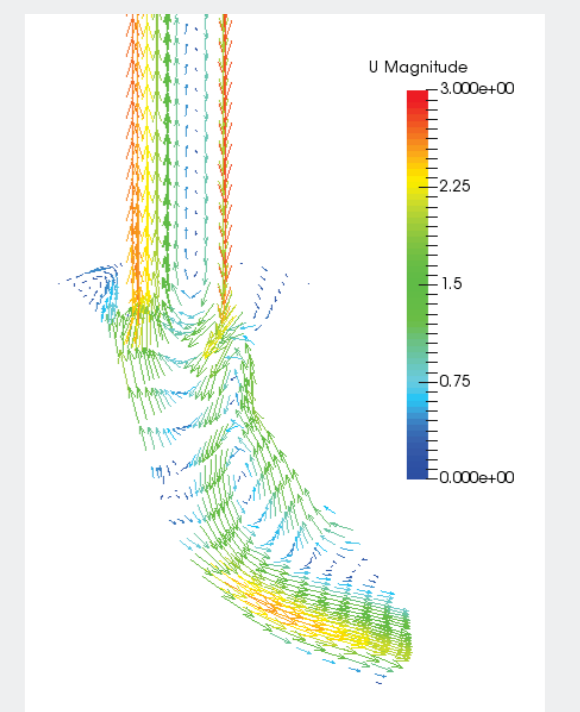

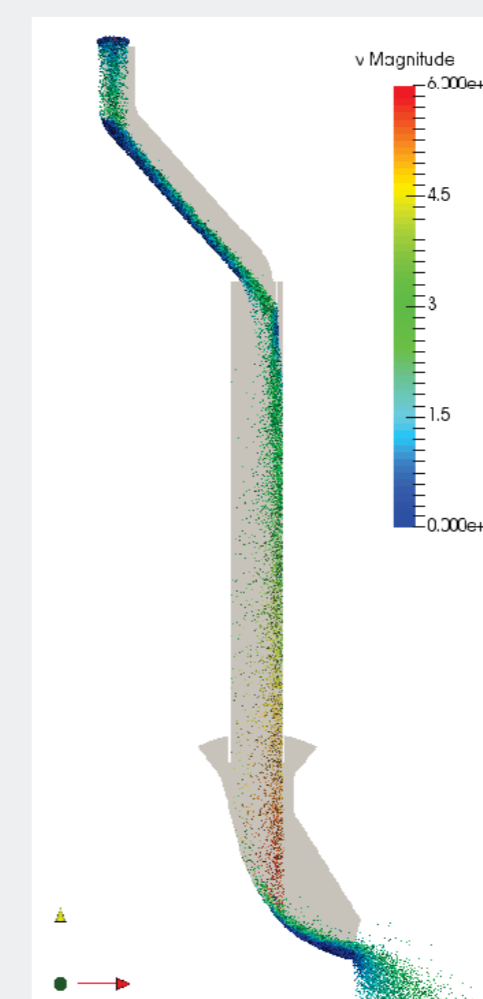**Figure 4: Gas Velocity**   **Figure 5: Gas Velocity Vector**

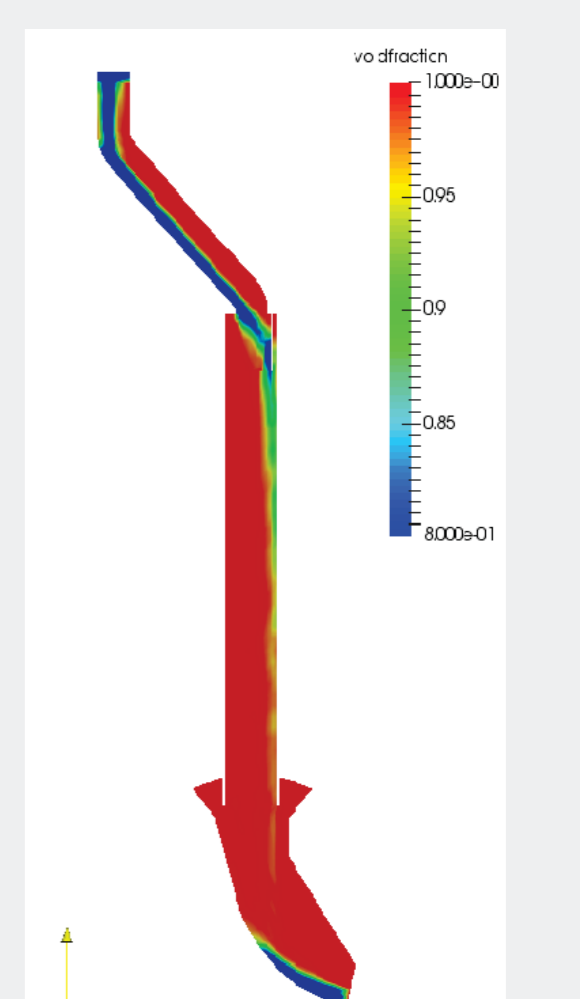**Figure 5: Particle Velocity**   **Figure 6: Gas Volume Fraction**

References

[1] A. Potapov, X.L. Chen, T.J. Donohue and C.A. Wheeler. Computer Simulation of Airflow around Transfer Chutes via Linked Discrete Element Method - Computational Fluid Dynamics Approach. 11th International Congress on Bulk Materials Storage, Handling and Transportation 2013.

[2] Chen X, Wheeler C. Computational Fluid Dynamics (CFD) modelling of transfer chutes: A study of the influence of model parameters[J]. Chemical Engineering Science, 2013, 95(3):194-202.

Acknowledgements

Simulating the interaction between waves and a fixed rectangle with OpenFOAM

Weiye Ding, Congfang Ai, Yuxiang Ma, Guohai Dong
State Key Laboratory of Coastal and Offshore Engineering, Dalian University of Technology

Introduction

The interaction between waves and structures is always a hot topic for researchers. Wave passed through a fixed rectangle, based on VOF method to track the free surface, using the open source computational fluid dynamics solver OpenFOAM had been simulated and validated in both two dimensional and three dimensional in this paper. The nonlinear (NL) k-ε turbulence model was established to solve the incompressible Reynolds-Average Navier-Stokes equation. The results show that OpenFOAM can be used to simulate the interaction between waves and structure.

Governing Equations

Continuity equation

$$\nabla \cdot u = 0$$

Navier-Stokes equation

$$\frac{\partial \rho u}{\partial t} + \nabla \cdot [\rho u u^{\mathrm{T}}] = -\nabla p^* - g \cdot x \nabla \rho + \nabla \cdot [\mu \nabla u + \rho \tau_{\mathrm{NL}}] + \sigma_{\mathrm{T}} \kappa_\alpha \nabla \alpha$$

k equation

$$\frac{\partial \rho k}{\partial t} + \nabla \cdot (\rho u k) = \nabla \left[\rho \left(\nu + \frac{\mu_t}{\sigma_k}\right) \nabla k\right] + \rho (P_k - \varepsilon)$$

ε equation

$$\frac{\partial \rho \varepsilon}{\partial t} + \nabla \cdot (\rho u \varepsilon) = \nabla \left[\rho \left(\nu + \frac{\mu_t}{\sigma_\varepsilon}\right) \nabla \varepsilon\right] + \rho \left(C_1 \frac{\varepsilon}{k} P_k - C_2 \frac{\varepsilon^2}{k}\right)$$

Transport equation for α

$$\frac{\partial \alpha}{\partial t} + \nabla \cdot (u\alpha) + \nabla [u_r \alpha(1-\alpha)] = 0$$

Conclusions

This study focuses on the interaction between wave and a fixed rectangle. In this paper, both two-dimensional and three-dimensional cases are given to study the elevations of wave surface and the distribution of forces. The numerical model solve the incompressible Navier-Stokes equations in combination with VOF method, which is based on an open source CFD toolbox OpenFOAM. And NLk-ε turbulence model is also adopted. Not only the elevations of free surface and forces on rectangle, but also the complex flow field evolution process are given. The results show that the model in OpenFOAM can simulate wave field with a fixed rectangle accuracy.

References

[1]   Bredmose, H., & Jacobsen, N. G. (2010). Breaking wave impacts on offshore wind turbine foundations: focused wave groups and cfd.
[2]   Bredmose, H., & Jacobsen, N. G. (2011). Vertical Wave Impacts on Offshore Wind Turbine Inspection Platforms. ASME 2011, International Conference on Ocean, Offshore and Arctic Engineering (pp.645-654).
[3]   Hirt, C. W., & Nichols, B. D. (1981). Volume of fluid (vof) method for the dynamics of free boundaries ☆. J.comput.phys, 39(1), 201-225.
[4]   Huang, Z. (2006). Wave interaction with one or two rows of closely spaced rectangular cylinders. Ocean Engineering, 34(11), 1584-1591.
[5]   http://www.openfoam.org/version2.3.0/multiphase.php.
[6]   Jasak, H. and Vukčević, V. (2014). Simulation of Wave Impact Loads in OpenFOAM. 21st Symposium on Theory and Practice in Shipbuilding. Hrvatska znanstvena bibliografija i MZOS-Svibor.
[7]   OpenCFD, OpenFOAM: The Open Source CFD Toolbox. User Guide Version 1.4, OpenCFD Limited. Reading UK, Apr. 2007.
[8]   Paulsen, B. T., Bredmose, H., and Bingham, H. B. (2012). Accurate computation of wave loads on a bottom fixed circular cylinder.
[9]   Pengzhi Lin. (2006). A multiple-layer σ-coordinate model for simulation of wave structure interaction. Computers & Fluids, 35, 147-167
[10]   Shih, T. H., Zhu, J. and Lumley, John L. (1996). Calculation of wall-bounded complex flows and free shear flows. International Journal for Numerical Methods in Fluids, 23(11), 1133-1144.
[11]   Sue, Y. C., Chern, M. J., & Hwang, R. R. (2005). Interaction of nonlinear progressive viscous waves with a submerged obstacle. Ocean Engineering, 32(8–9), 893-923.
[12]   Teng, T. L., Pizer, D., Simmonds, D., Kyte, A., Greaves, D., & Teng, T. L., et al. (2017). Simulation and analysis of wave-structure interactions for a semi-immersed horizontal cylinder. Ocean Engineering.
[13]   Venugopal, V., Varyani, K. S., & Barltrop, N. D. P. (2006). Wave force coefficients for horizontally submerged rectangular cylinders. Ocean Engineering, 33(11–12), 1669-1704.
[14]   Wang Daguo. (2011). A 3D Time domain coupled model for nonlinear waves acting on a box-shaped ship fixed in a harbor. China Ocean Engineering, 25(3), 441-456.

Results

Solitary past a fixe rectangle of different depths

η_0=0.1m   Water depth: 1.0m

Rectangle: 0.5m*0.6m and its front face is deployed at x=30m

Submerged case: still water depth above the obstacle is 0.4m;

Immersed case: the still water depth above the obstacle to be 0.25m;

Floating case: the obstacle is lifted 0.2m above the still water level.
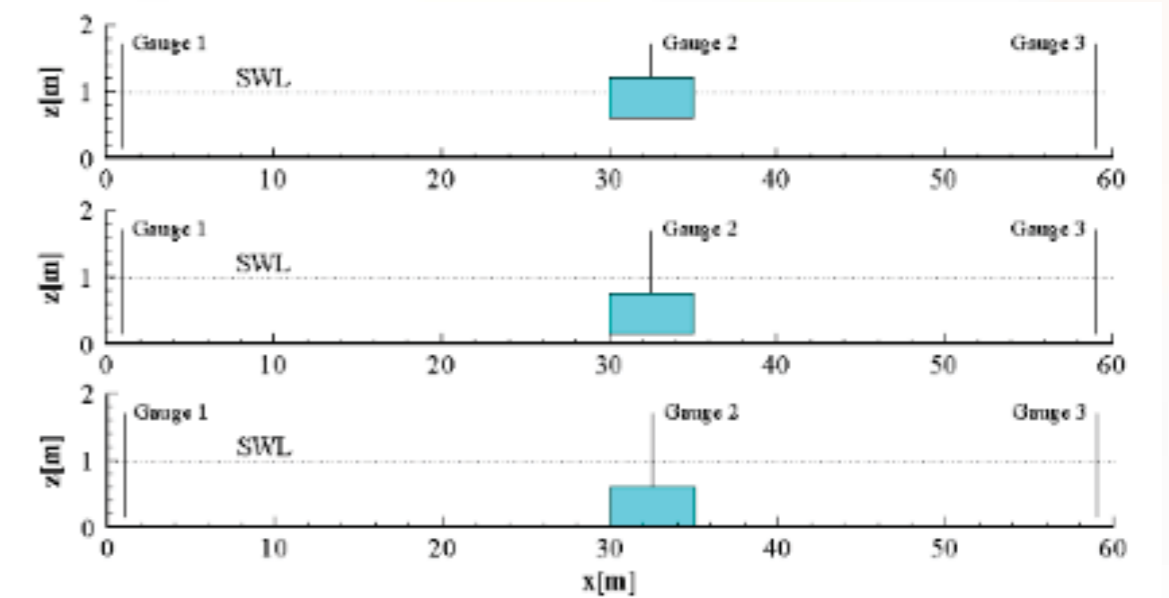
Figure 1 Schematic illustration of a solitary past a submerged, immersed, or floating rectangle
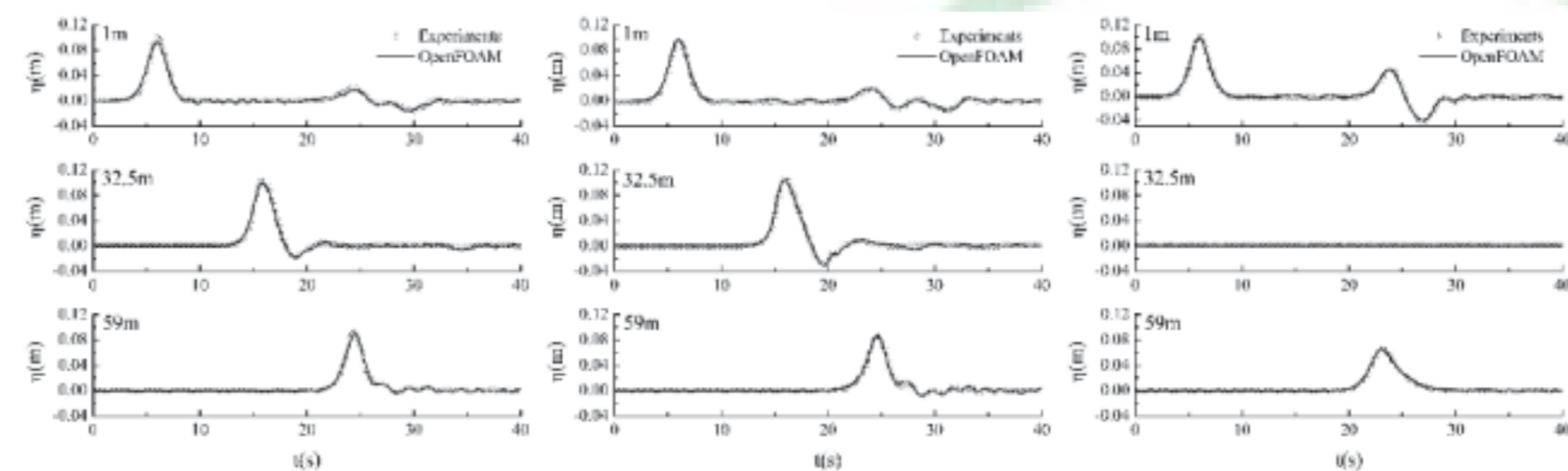
Figure 2 The comparisons of time histories of free surface displacement at x = 1 m, 32.5 m and 59 m between experiments and OpenFOAM (left panel: submerged; middle panel: immersed; right panel: floating)

Figure 3 Temporal and spatial variations for the velocity field calculated using numerical mode (left panel: submerged; middle panel: immersed; right panel: floating)
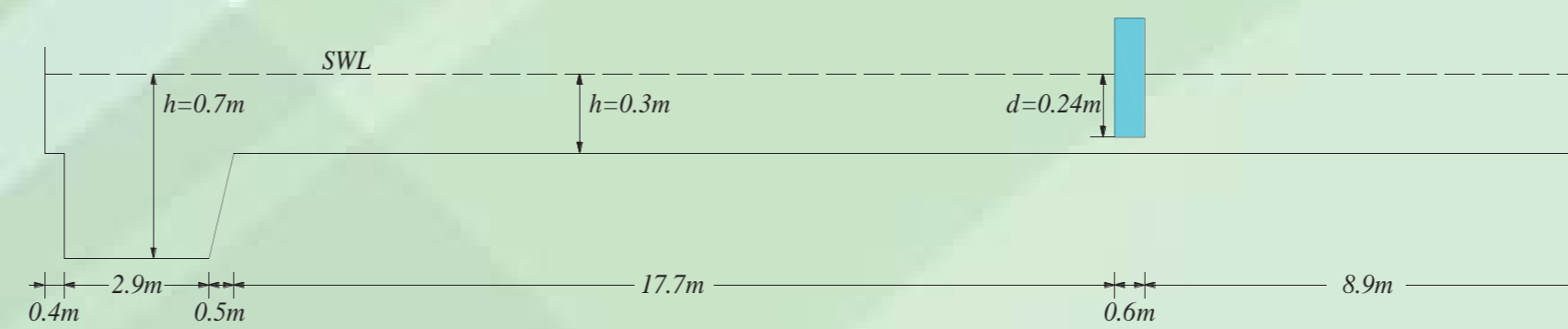
Regular wave past an immersed rectangle

Figure 4 Schematic illustration of a regular wave past an immersed rectangle

Wave tank wide: 14m

Rectangle:

Width B=2m,

Length L=0.6m,

Height H=0.45m

Draft 0.24m

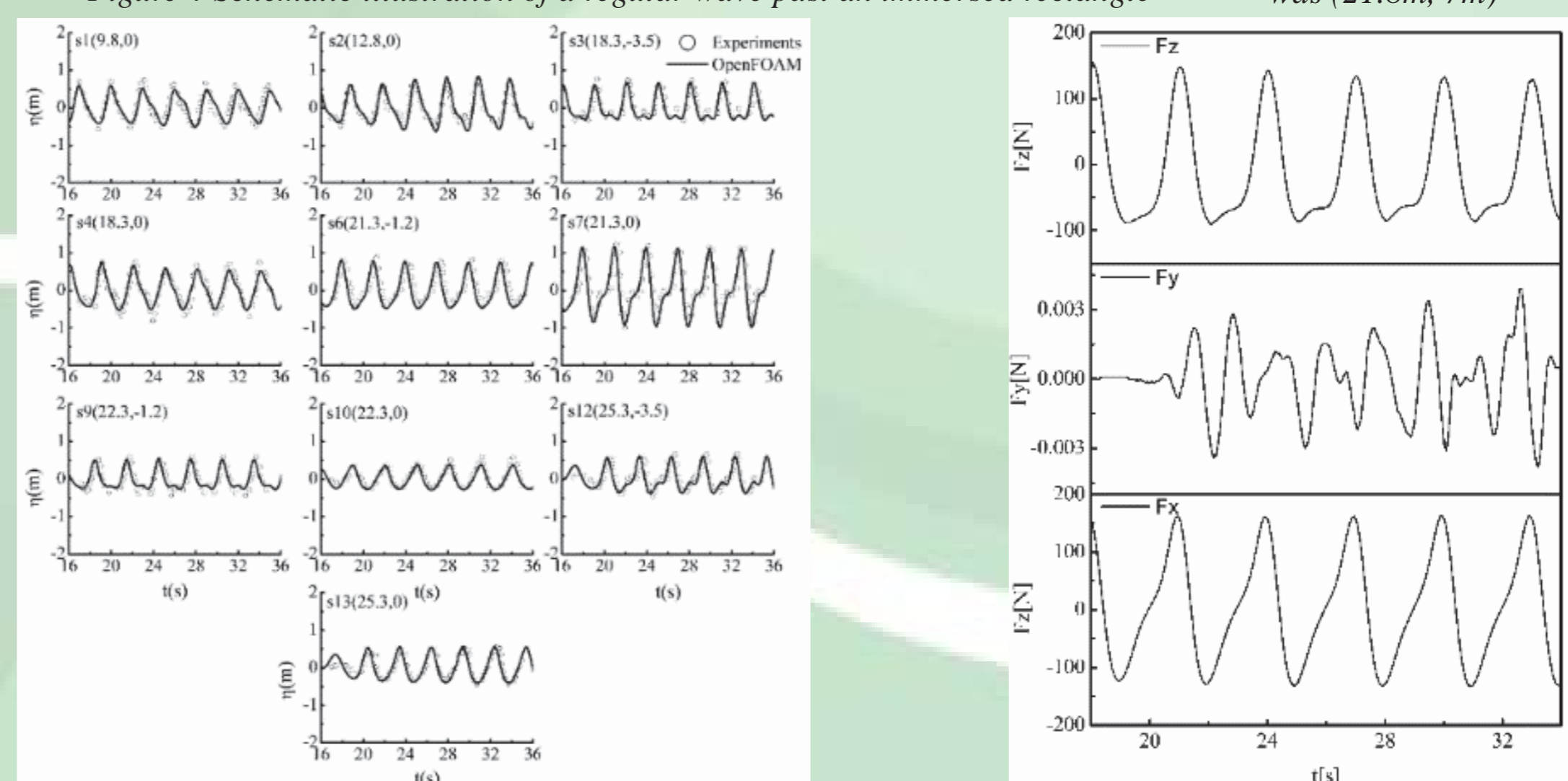Mid-point coordinates of rectangle was (21.8m, 7m)[9]

Figure 5 Time series of wave elevations (left panel) and forces on rectangle (right panel)

# The 13th OpenFOAM Workshop (OFW13)
Numerical investigation on the performance of a 'V' type breakwater

AO GANG, YUXIANG MA, GUOHAI DONG
State Key Laboratory of Coastal and Offshore Engineering,
Dalian University of Technology

Introduction

In this paper, the character of a 'V' type breakwater will be discussed. Using the VOF model in OpenFOAM, numerical simulation of regular waves through a 'V' type breakwater is carried out. In the present research, the performance of the breakwater is evaluated by measuring reflection and transmission coefficient.
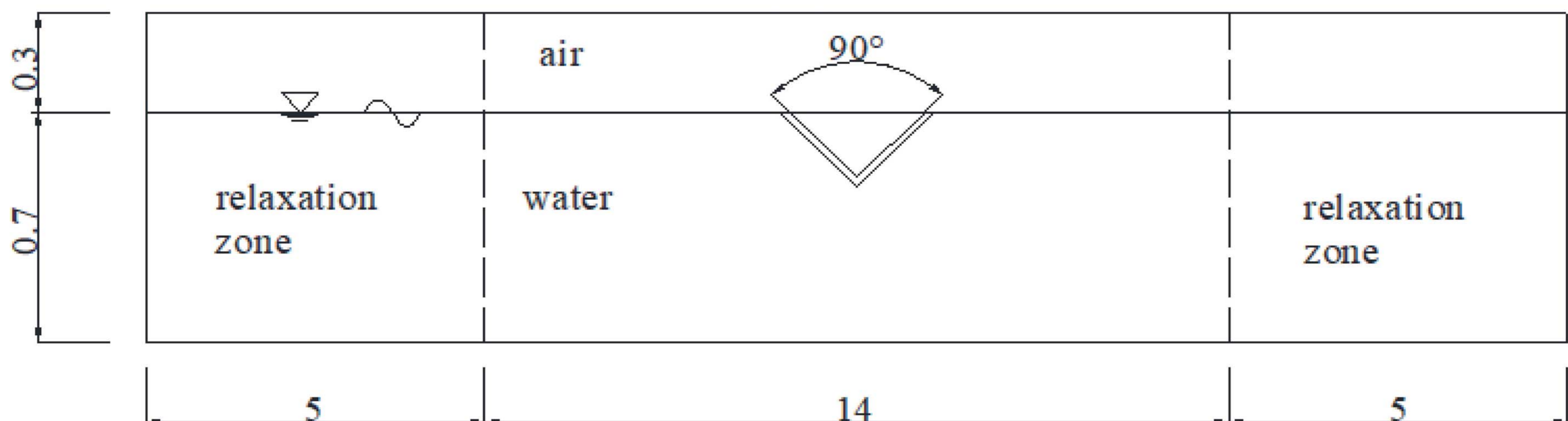
Results

Three different angles are chosen in the study, 60°, 90° and 120°. In the simulation, the bubbles are generated between the two plates, causing wave energy dissipation of wave energy.
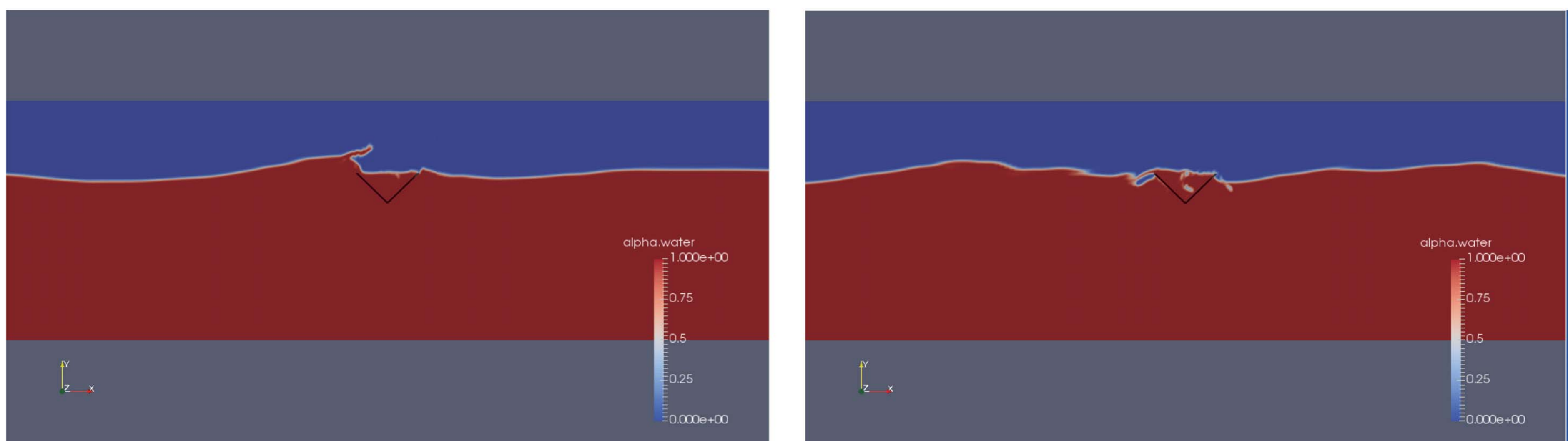
Discussion
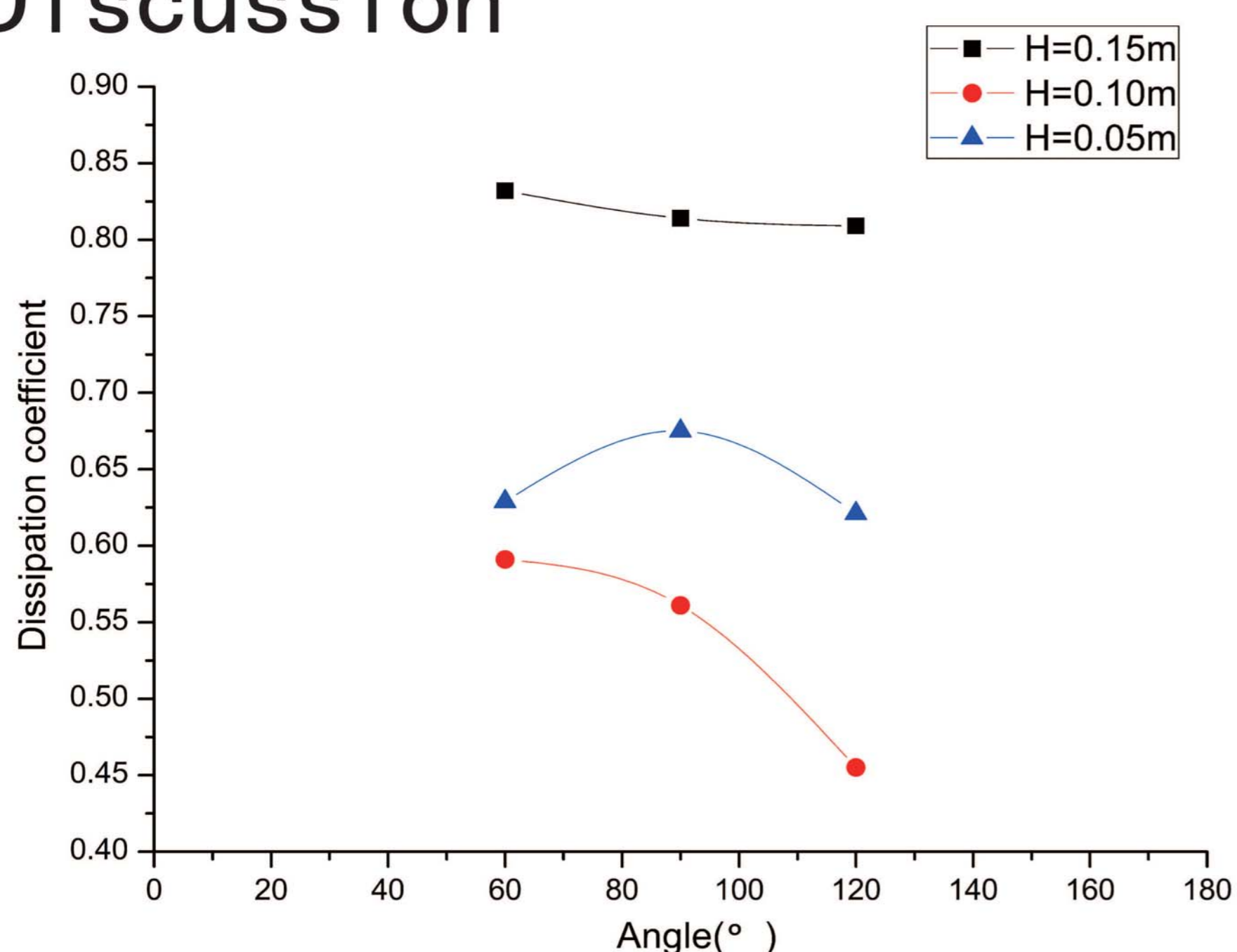
The distance of two plates is shorter, namely the angle is smaller, the appearance of reverse jet is earlier and more frequent, so the dissipation coefficient is larger. With the increasing of angle, the dissipation coefficient decreases.

Regular and Irregular Wave Generation In OpenFOAM Using High Oder Spectral Method

YUAN ZHUANG[1], DECHENG WAN[1], BENJAMIN BOUSCASSE[2], PIERRE FERRANT[2]

[1] *Collaborative Innovation Center for Advanced Ship and Deep-Sea Exploration, State Key Laboratory of Ocean Engineering, School of Naval Architecture, Ocean and Civil Engineering, Shanghai Jiao Tong University, Shanghai, China.*
2 *Ecole Centrale de Nantes, LHEEA Lab. (ECN) Nantes, France*

Introduction

On engineering applications involving wave-structure interactions [1], the use of CFD is essential to account for viscous effects and non-linear deformations and breaking of the free surface. Solving Navier-Stokes equations in a viscous numerical wave tank is of low efficiency, in particular the target is a fully developed sea state. The High Order Spectral (HOS) method solving the nonlinear inviscid problem is therefore applied for outer field wave generation. This reduces the computational cost, by reducing the size of the viscous domain.

The spatial discretization needed for the solution of the Euler equations with HOS and the Navier-Stokes equations is very different. Grid2Grid [2] is a wrapper program of HOS developed to exchange the information between the two solvers. The plug-in toolbox of OpenFOAM waves2Foam [3] can generate fully developed wave fields. Therefore we combine these two methods and this new method is implemented to do the simulations.

Major Work

Inlet and outlet can be imposed in waves2Foam through the relaxation zones which can be seen as coupling zones. At each time step the flow velocity (u,v,w) and the volume fraction of the fluid (α) in coupling zone is computed with equation 1. The value of Φ_{target} is obtained from HOS results. Through the relaxation zone, the values of wave fields from HOS can be transferred into inner CFD zone and the scattered wave in CFD zone can be mapped in target (incident) wave components when spreading outside. The sketch of the coupling method is shown in Figure 1.

$$\Phi = \alpha_R \Phi_{computed} + [1 - \alpha_R]\Phi_{target} \tag{1}$$
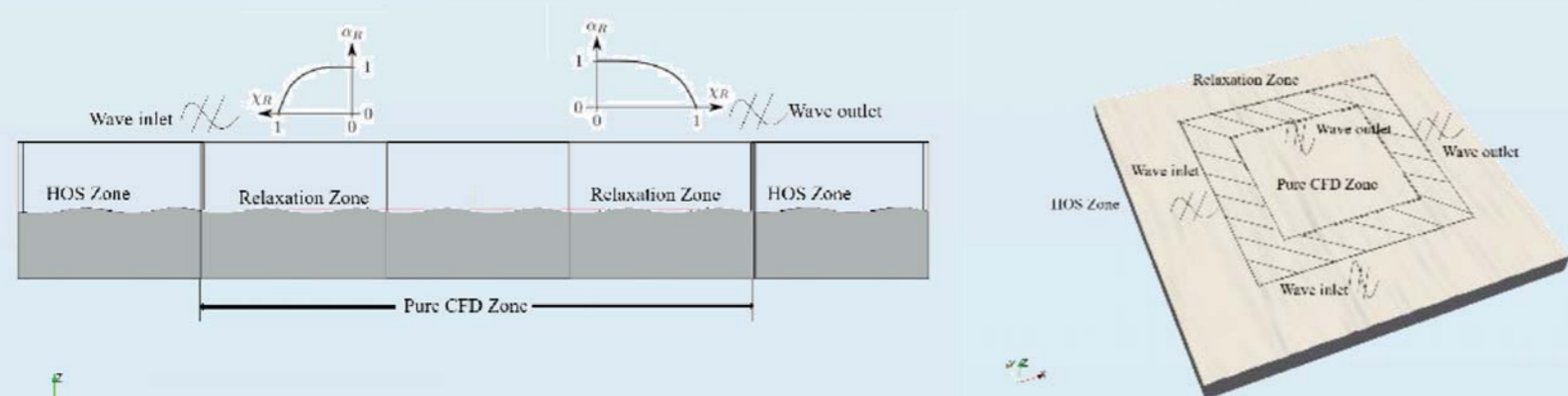
Figure 1 Sketch of the coupling method to compute the propagation wave in 2D and 3D

Results and Conclusions

To validate the effectiveness and accuracy of the coupling method, 6 cases are considered to compare the HOS solution to the CFD solution, shown in table 1. These tests have been computed [2], [4] in coupled method with HOS and foamStar, which is developed by Bureau Veritas and based on OpenFOAM. Therefore, we include the results from foamStar to compare. The wave elevation is analyzed based on the wave probe which is put in the middle of the computational domain. The wave probe is set in the same place both in HOS zone and in CFD zone. Figure 3 shows the comparison of wave elevation results from three methods.

The time history of wave elevation from CFD zone fairly agree with that from HOS zone, which shows the coupling method has the ability to simulate identical wave elevation which is generated by HOS

Table 1 HOS wave conditions

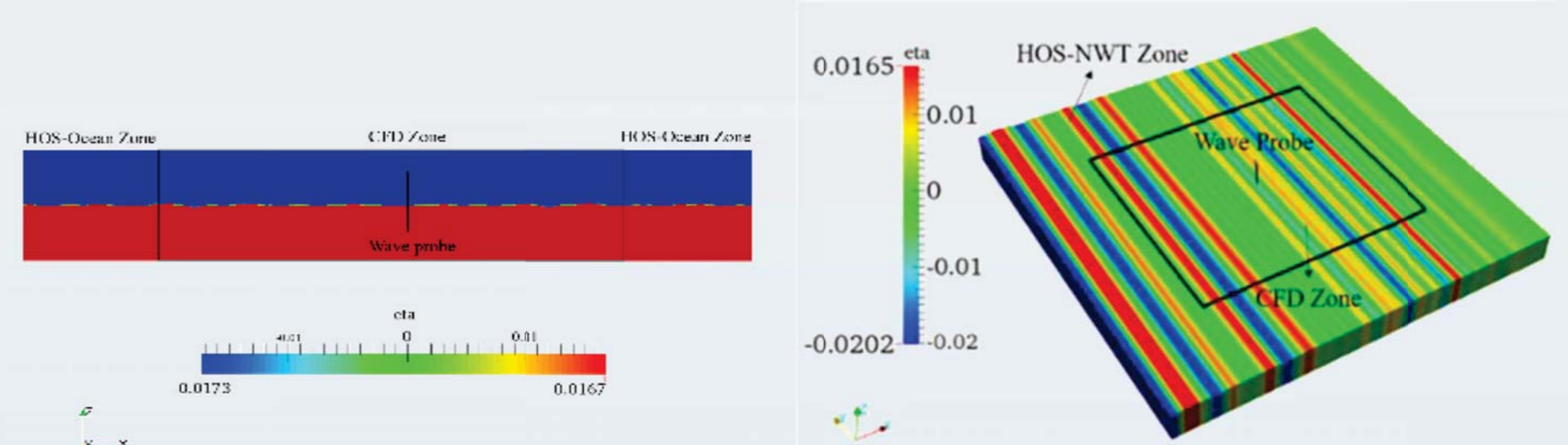| Wave type	Value	HOS-Ocean		HOS-NWT	
		2D	3D	2D	3D
Regular wave	T (s)	-	-	0.702	0.702
	H (m)	-	-	0.0431	0.0288
Irregular wave	Tp (s)	0.702	1.0	1.0	0.702
	Hs (m)	0.0288	0.10	0.05	0.0384
γ		3.3	3.3	3.3	3.3

Figure 2 Wave elevation of coupled methods with HOS and waves2Foam.

The contour of wave elevation indicates that the CFD zone can simulate in arbitrary space. The coupling method can do the simulation in naval and offshore wave-structure interaction effectively in the future.
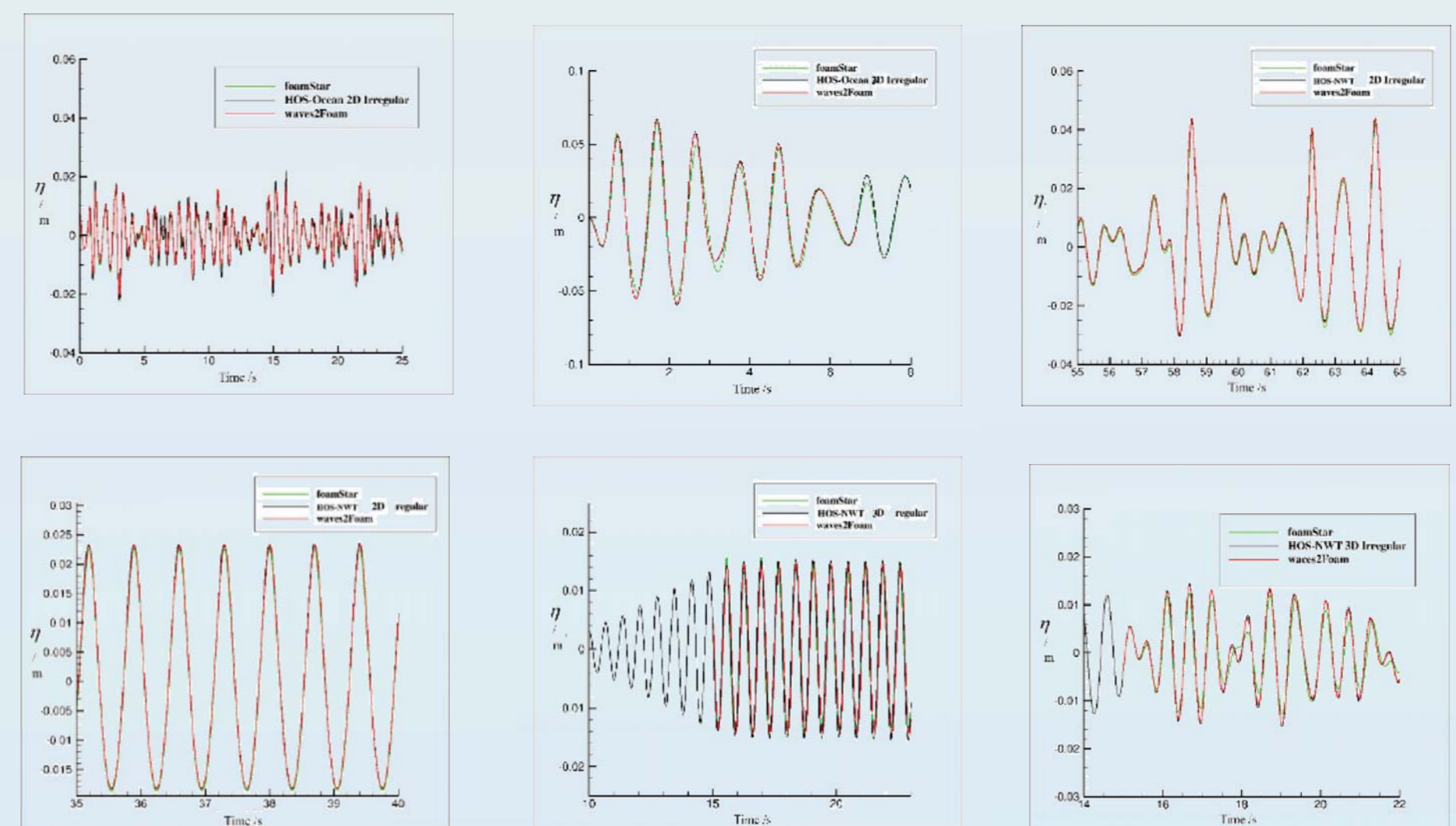

Figure 3 Validation and comparison of coupled methods with HOS and waves2Foam.

Reference

[1].Y. Zhuang, D. C. Wan, Numerical study on coupling effects of FPSO ship motion and LNG tank sloshing in low-filling condition, Applied Mathematics and Mechanics, vol. 37, pp. 1378-1393, 2016.

[2].Y. M. Choi et al. Grid2Grid: HOS Wrapper Program for CFD solvers. arXiv preprint arXiv:1801.00026, 2017.

[3].N. G. Jacobsen et al. A wave generation toolbox for the open-source CFD library: OpenFoam®. International Journal for Numerical Methods in Fluids, vol. 70, pp.1073-1088, 2012.

[4].Y. M. Choi et al. Generation of regular and irregular waves in Navier-Stokes CFD solvers by matching with the nonlinear potential wave solution at the boundaries. In Proceedings of the ASME International Conference on Ocean, Offshore and Arctic Engineering, Madrid, 2018. (Accepted)

Application of CFD-based efficient global optimization method to ship hull design

Aiqin Miao, Decheng Wan*

School of Naval Architecture, Ocean and Civil Engineering, Shanghai Jiao Tong University, Collaborative Innovation Center for Advanced Ship and Deep-Sea Exploration, China

*Corresponding author: dcwan@sjtu.edu.cn

Introduction

➢ Computational fluid dynamics (CFD) has become an invaluable tool for ship hull form optimization design.

➢ In the process of ship optimization design, the number of objective function (certain hydrodynamic performances to be improved) evaluations using high-fidelity numerical analysis solvers, is enormous but severely limited by computational time and cost, even with the aid of supercomputers.

➢ One alternative is to construct surrogate models based on finite sample points instead of direct numerical evaluations one by one.

➢ In this paper, The Efficient Global Optimization method (EGO) is used in ship optimization design based on our in-house solver OPTShip-SJTU.

Numerical methods

The EGO method mentioned herein is a Kriging-based global optimization method considering the uncertainty of the surrogate prediction. The key to the EGO method lies in balancing the need to fully exploit the surrogate model (by sampling where it is minimized) with the need to improve the accuracy of surrogate model (by sampling where prediction error may be high). The concept is expressed in the infill criterion of Expected Improvement (EI). The EI of optimization problem can be calculated as:

$$E[I(x)] = (f_{min} - \hat{y})\Phi[(f_{min} - \hat{y})/s] + s\phi[(f_{min} - \hat{y})/s]$$

A simple flow chart of the EGO method applied for a simple mathematical function is shown in Fig. 1. The EGO method is added to our in-house solver OPTShip-SJTU for ship optimization design based on CFD.

Figure 1: The flow chart of efficient global optimization: on the left, the steps are briefly described; on the right, an example is given (predetermined design points as red dots, the added new points as green squares and the next new point as a blue triangle).

Results

The EGO method is applied for ship optimization of Wigley to minimize the wave-making resistance in the calm water.
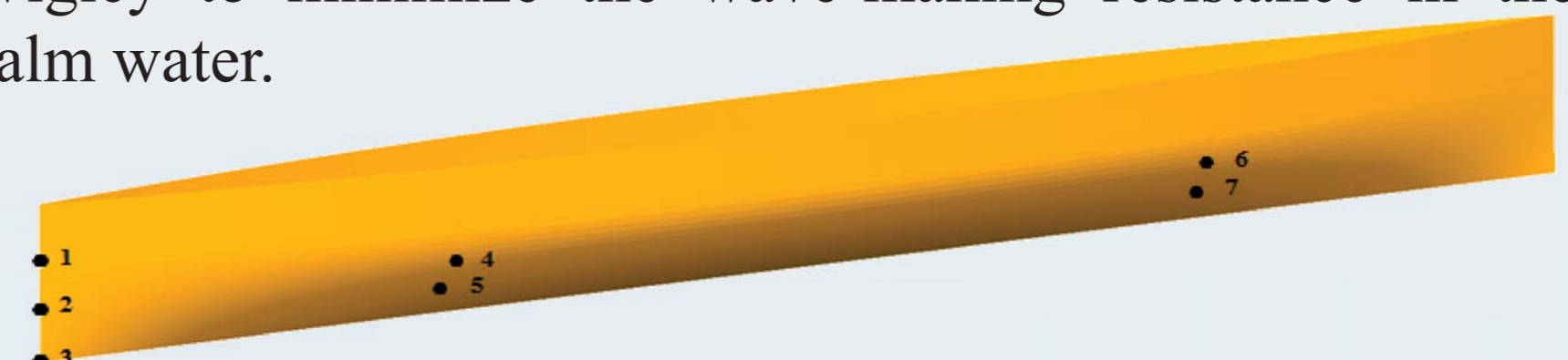

Figure 2: The control points distributed on Wigley hull by RBF method

It also starts with the classical Kriging surrogate model. A new design sample point is found through optimizing an infill criterion based on the surrogate model. This new design point is the next new ship directly evaluated by CFD method. The surrogate model will be rebuilt by the total sample points. This step of model reconstruction and generation of additional new design point is not iterated until a stop criterion is fulfilled. At last, the optimal ship will be obtained with the minimum wave-making resistance. The *Cw* converges to the minimum value, 1.046E-03, a larger reduction of 18.46% than the initial value. Details are shown in Fig. 3-6.
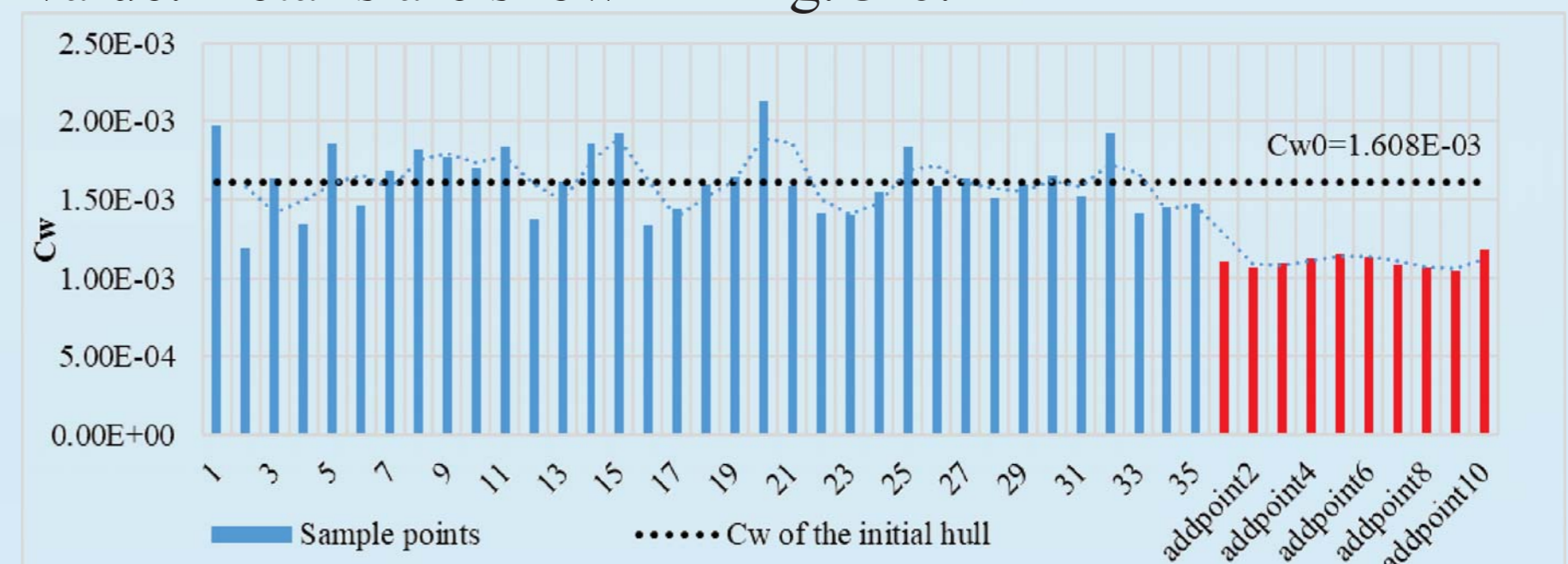

Figure 3: The initial sample hulls and the additional new hulls used in the EGO method
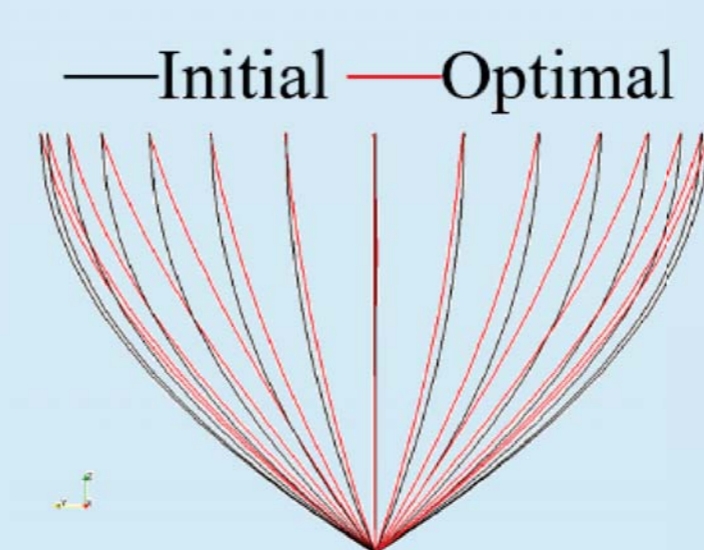

Figure 4: Comparisons of the body lines between the initial and optimal ships
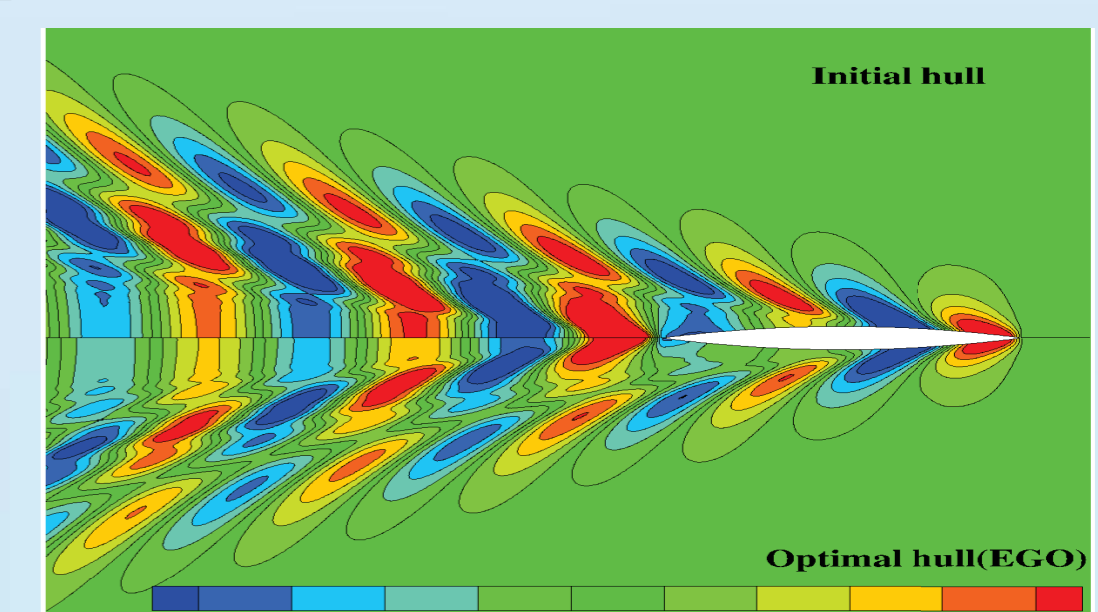
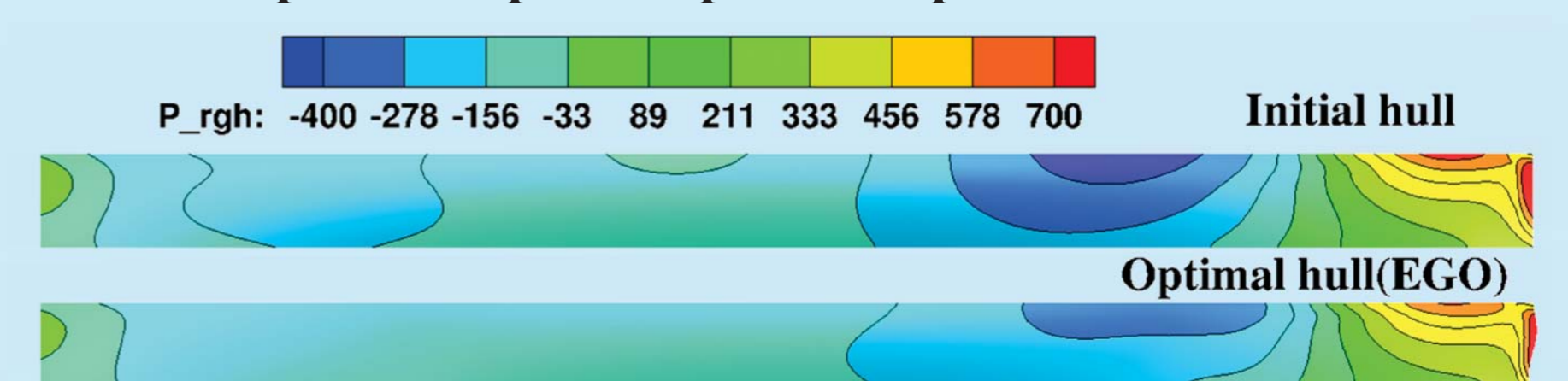Figure 5: Comparison of free surface elevation between the initial and optimal ships

Figure 6: Comparison of pressure distribution between the initial and optimal hulls

Conclusions

This paper presents a Kriging-based global optimization method, efficient global optimization (EGO), different from the ordinary optimization method. It combines the surrogate modeling with the optimization algorithm. In the future, it will be used to the more complex ship optimization problem, such as the ship hull form design to improve comprehensive hydrodynamic performance, based on entire CFD.

Transplant and Optimize OpenFOAM On Sunway TaihuLight Supercomputer

HU REN, HANFENG GU, FEI GAO, XIN LIU, WEI XUE

1. Introduction

"SW26010" processor characteristics:

- 4 core-groups (CGs) in a processor
- one management core (MPE) and one 8x8 computing core (MPE) mesh in a CG
- Every 64 MPEs share a 4M local device memory (LDM).
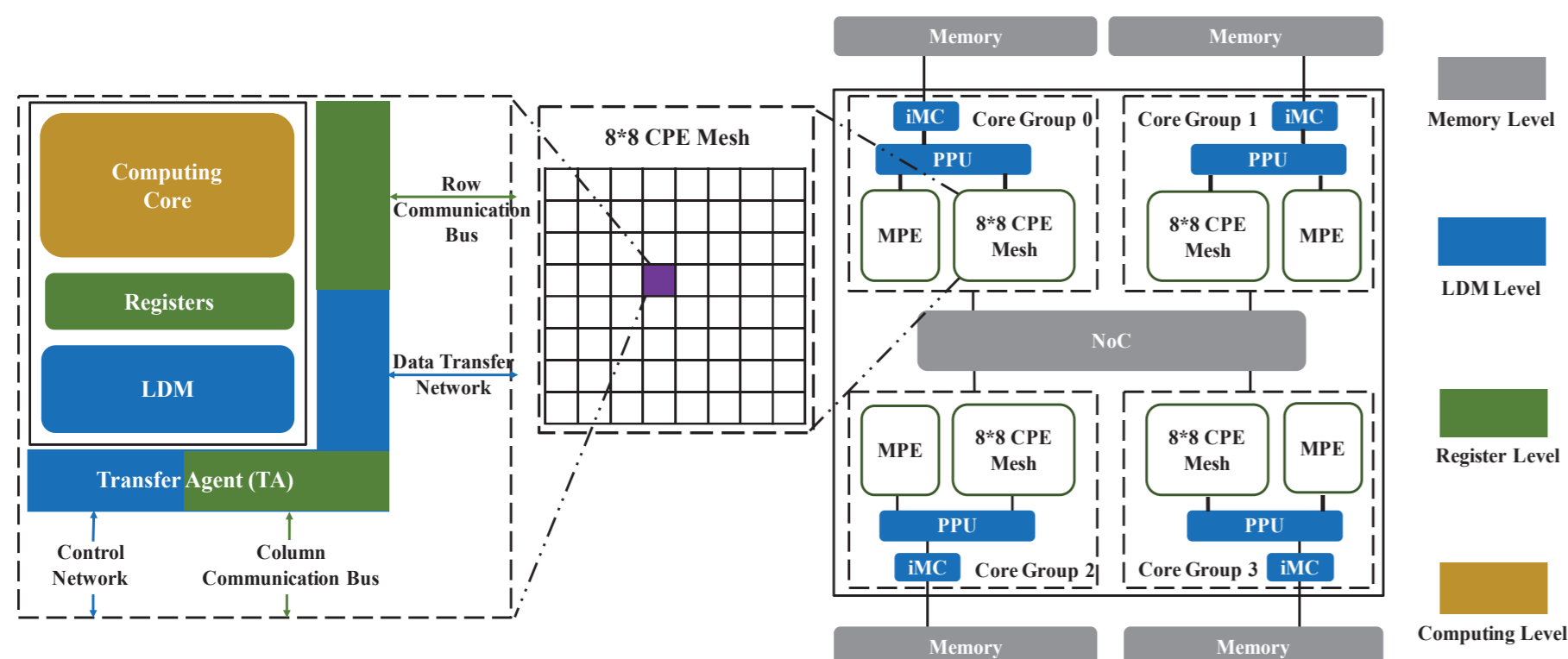

Challenges to transplant and optimize OpenFOAM:

- unstructured mesh and data layout (irregular memory fetching)
- relatively limited memory bandwidth (38GB/s to 3TFlops)
- restrictions on parallelism in algorithms (Gauss Seidel etc.)
- templated and polymorphic coding
- shared-library-oriented build system

2. Applications

CFD simulations with OpenFOAM on Sunway TaihuLight:
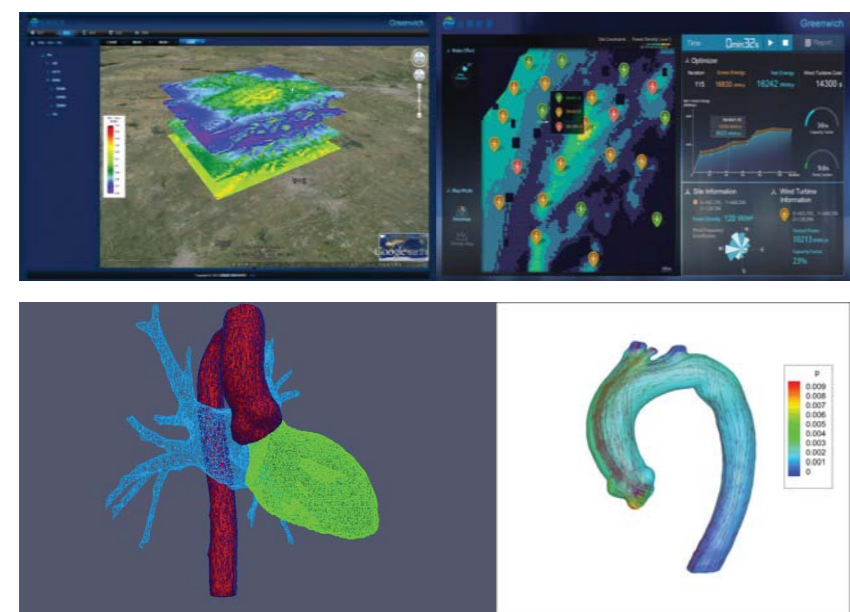
Wind power companies use OpenFOAM on Sunway TaihuLight to optimize wind fun locations and predict the daily power generation.
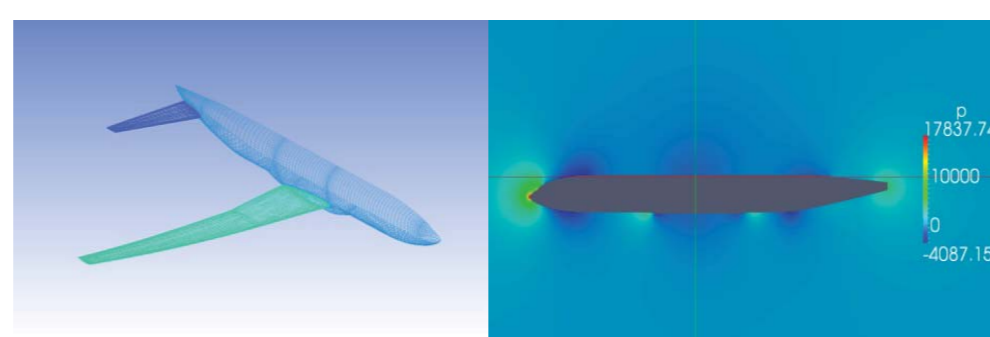
3. Acceleration Overview
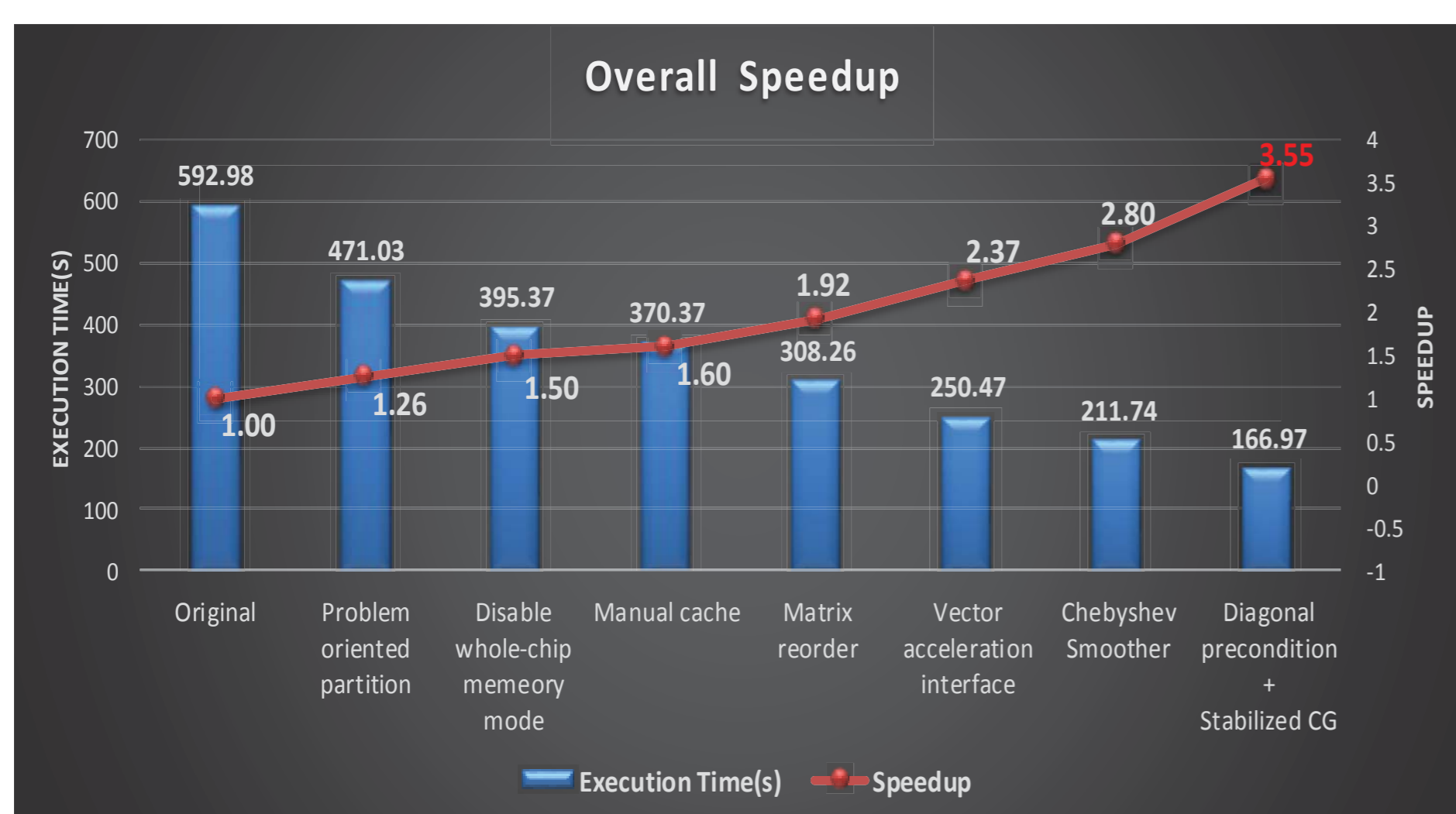
Component	Optimization	Maximum Speedup
ATmul	Matrix reorder	12x
gaussGrad	Manual cache	7x
surfaceInterpolationScheme	Manual cache	8.6x
surfaceIntegrate	Manual cache	6.5x
GAMG	Chebyshev Smooth	5x
PBiCG	Diagonal precondition + Stabilized CG	5x
Array Operations	Vector acceleration interface	18x

National Super-Computing Centre in Wuxi (NSCCWX), is located in Wuxi China. and co-operated by local government and Tsinghua University. It has the world's first supercomputer with peak performance over 100PFlop/s—Sunway TaihuLight . Sunway TaihuLight is composed with over 40K "SW26010" chips, and integrates in total over 10 million cores. Sunway TaihuLight is also the first computer that uses China homegrown processors and occupies the first place on Top500 list for successive 4 times.

Since June, 2016, over 70 large-scale applications from over 100 research institutes were done, covering 19 application domains, 16 full-scale applications, 18 half-scale, 22 million-core-scale, 5 Gordon Bell Finals, and 2 Gordon Bell Prize.
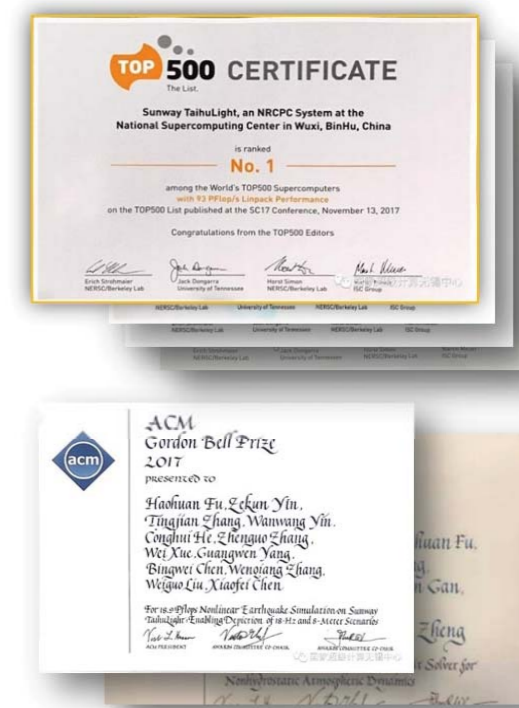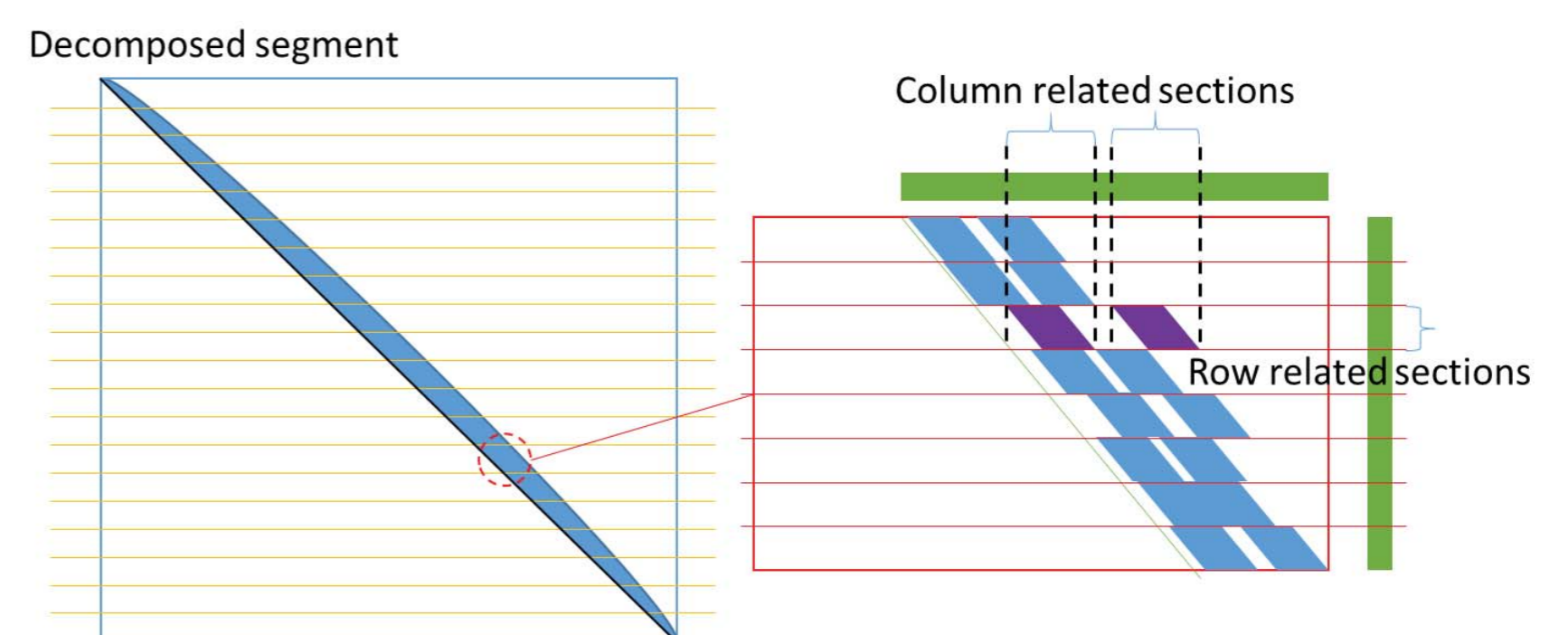

4. Optimizations (parts of all)

Matrix Reorder :

Non-zeros were reordered to form box, make sure the row and column related array is located in localized sections
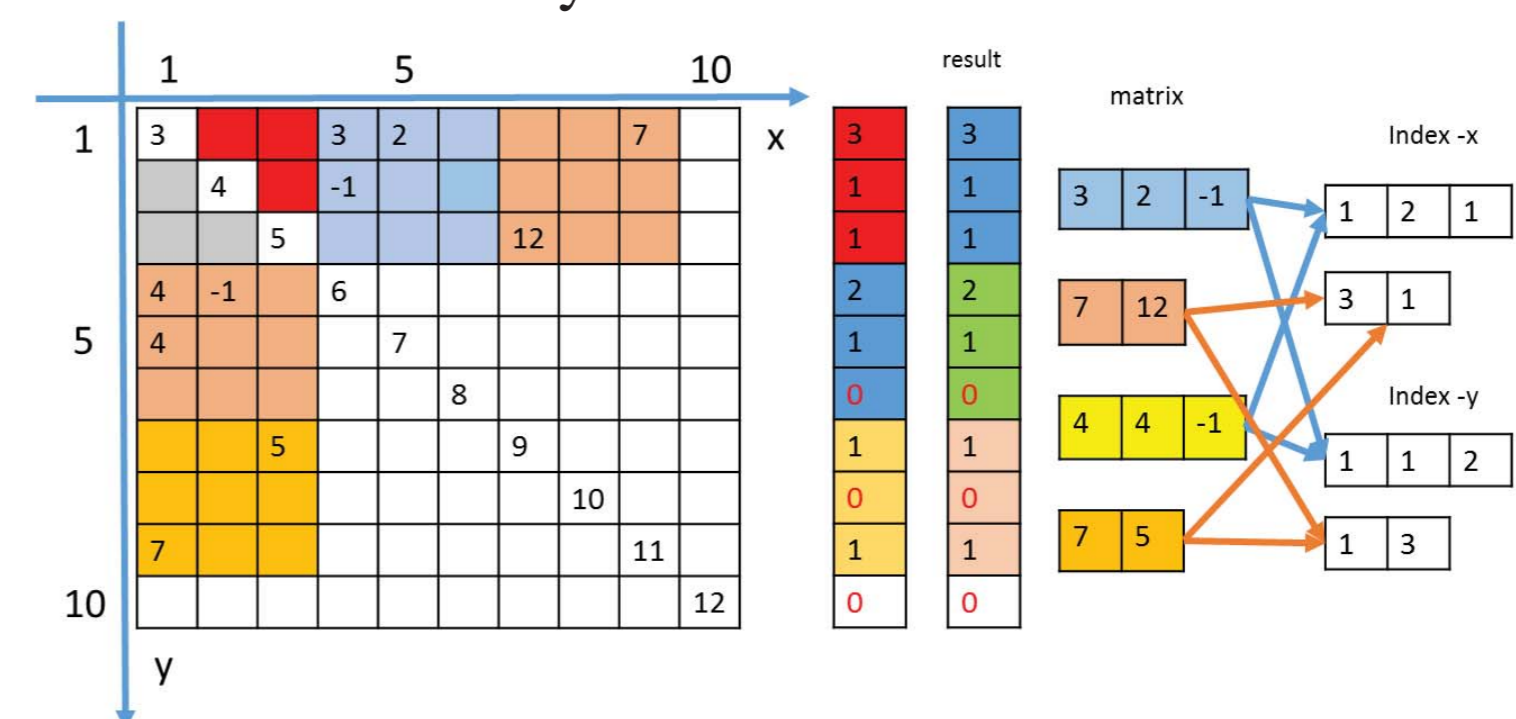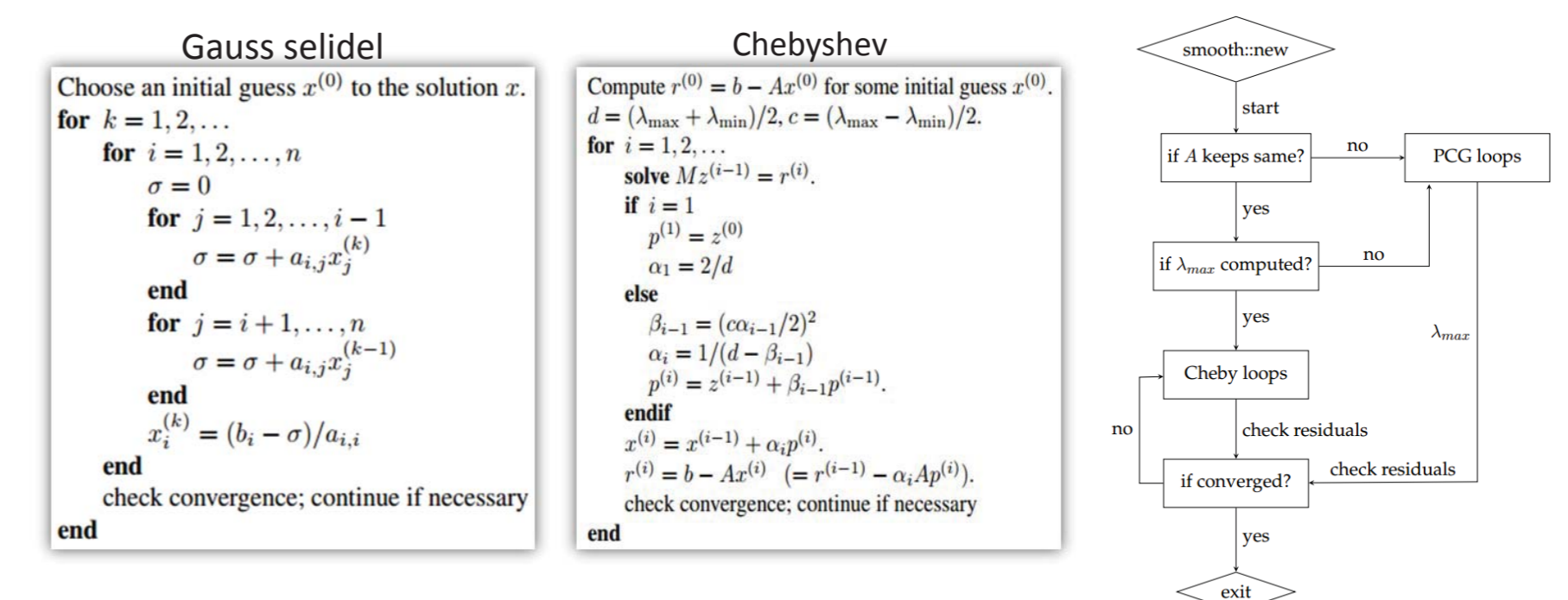

Manual Cache:

The non-zeros were lumped into sections for each row section, and the array section starts and ends were recorded for manual caching
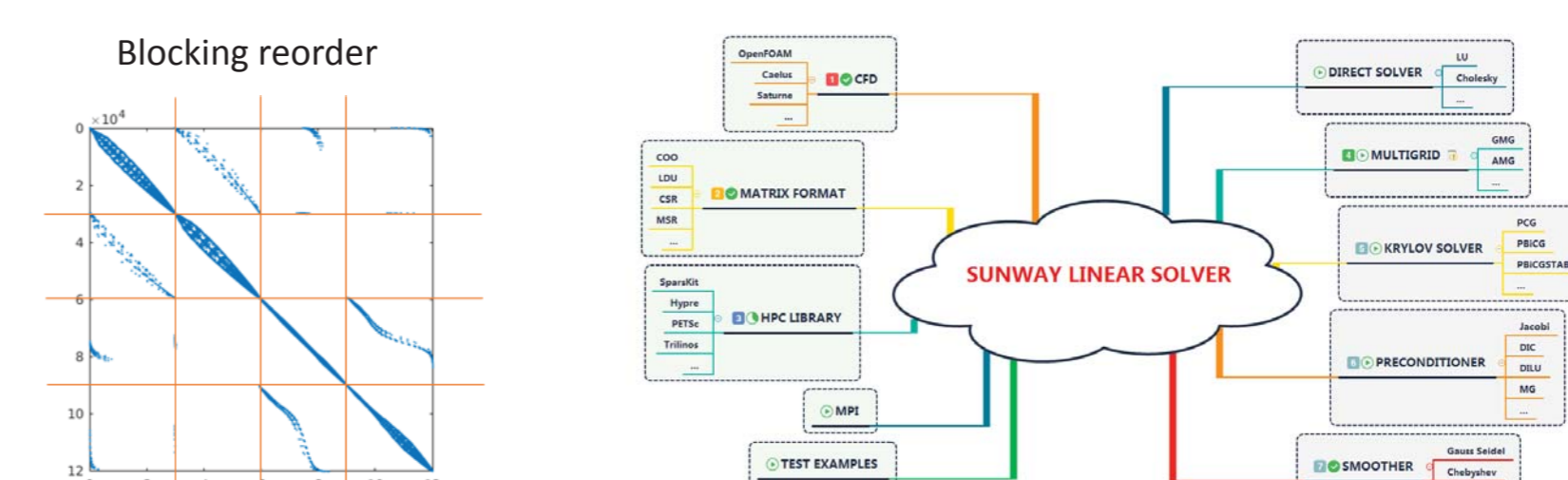

Chebyshev smoother:

Gauss Seidel was replace by Chebyshev in GAMG Solver to release parallelism, and a new procedure was proposed

5. Coming soon

- **Sophisticated reordering** for unstructured mesh and data structure
- **Overall acceleration** for a series of Solvers
- **High performance stand-alone linear solvers** on Sunway
- **Web base GUI** for SW-OpenFOAM and services

IMPLEMENTATION AND VALIDATION OF A NOVEL TABULATED CHEMISTRY TURBULENT COMBUSTION MODLE IN OPENFOAM

Y.F. Duan, L.K. Ma*, X. Huang and Z.X. Xia

College of Aerospace Science and Technology, National University of Defense Technology

*Email: malikun@nudt.edu.cn

1. Introduction

Objectives:

- To aviod the limitations of the presumed PDF (PPDF) method, e.g. assumption on the statistic independence of the controlling variables and expensive storage requirement due to large lookup tables, that is used in the conventional flamelet-based models, a novel turbulent combustion model was developed by combining of the Flamelet Generated Manifolds (FGM) model and Eulerian Stochastic Field (ESF) mehtod.

2. Validation Dataset

Burner details:

- **Main jet inner diameter:** 7.2mm
- **Pilot annulus inner diameter:** 7.7mm
- **Pilot annulus outer diameter:** 18.2mm
- **Burner outer wall diameter:** 18.9mm
- **Wind tunnel exit:** 30cm by 30cm
- **Coflow velocity:** 0.9m/s(+/- 0.05 m/s)
- **Main jet composition;** 25%CH4, 75% dry air
- **Main jet kinematic viscosity:** 1.58e-05 m^2/s
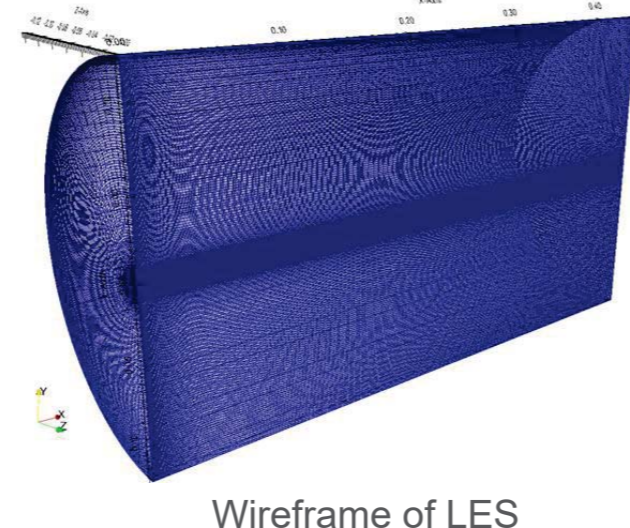- **Main jet velocity:** U_D = 49.6 m/s

Model details:

- **RANS Model:** standard k-ε
- **RANS Grid:** 51,957
- **LES Model:** *HybridSGS*
- **LES Grid:** 3,477,600

Sandia D flame
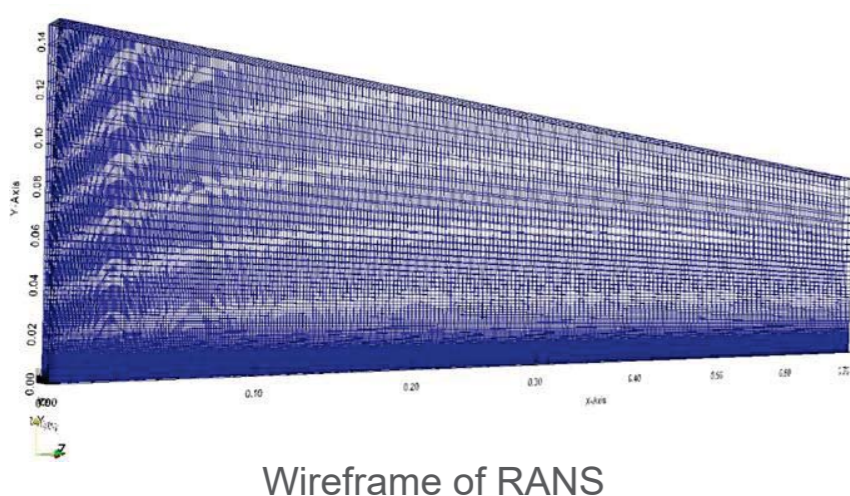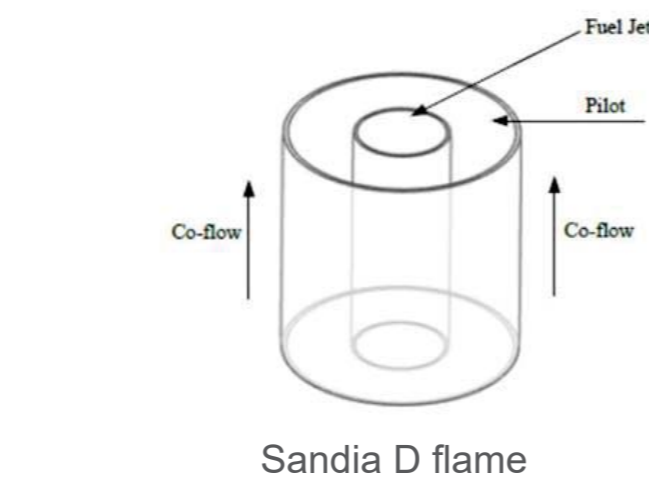
Wireframe of RANS

Wireframe of LES

3. Numerical method (1)

FGM Model: select two control variables to characterize Chemical reaction in turbulent combustion. The "mixture fraction", Z, that characterizes the mixed state of fuel and oxidant and the "progress variable", C, that characterizes the progress of chemical reaction are usually selected as independent variables.

Innovation : abandon the P-PDF method (the original FGM model) and choose real-time solutions to components jointing probability density function of two independent variables transported equation and integrate them in the sample space to obtain all the single-point statistics of all the space and time of two independent variables in real time. The Eulerian Stochastic Field (ESF) model in the transported probability density function class model is used to accomplish this task.

ESF Model: use a series of stochastic fields N_F to represent joint-composition PDF required by this model. In this N_F stochastic fields, each field contains each component value at each position in the entire flow field. It can be expressed as

$$f_\varphi\left(\psi;\vec{x},t\right) \approx \frac{1}{N_F}\sum_{n=1}^{N_F}\prod_{\alpha=1}^{N_s}\delta\left(\psi_\alpha - \varphi_{\alpha,n}\right)$$

$\varphi_{\alpha,n}$ is the value of scalar α under $\vec{x}$ position under t time in n field. In this model, $\varphi_\alpha = [Z,C]$, each stochastic field evolves according to the stochastic partial differential equations (SPDE) derived from transport equation of

3. Numerical method(2)

the joint-composition PDF. These SPDE can be expressed as

$$d\left(\bar{\rho}\varphi_{\alpha,n}\right) = -\frac{\partial}{\partial x_j}\left(\bar{\rho}\tilde{u}_j\varphi_{\alpha,n}\right)dt + \frac{\partial}{\partial x_j}\left[\left(\frac{\mu}{S_C}+\frac{\mu_t}{S_{Ct}}\right)\frac{\partial\varphi_{\alpha,n}}{\partial x_j}\right]dt + \dot{\omega}_\alpha^n dt -$$

$$\frac{\bar{\rho}}{2\tau_{sgs}}\left(\varphi_{\alpha,n}-\tilde{\phi}_\alpha\right)dt + \left(2\bar{\rho}^2\frac{\mu_t}{S_{Ct}}\right)^{1/2}\frac{\partial\varphi_{\alpha,n}}{\partial x_j}dW_{j,n}, \quad for \quad n=1,\cdots N_F \quad and \quad \alpha=1,\cdots N_s$$

By solving the stochastic differential equations of each stochastic field, the evolution law of the mixture fraction and the progress variables over time in each stochastic field considering the influence of turbulence is obtained. A statistical average is then used to find the control variables for the flamelet look-up table.
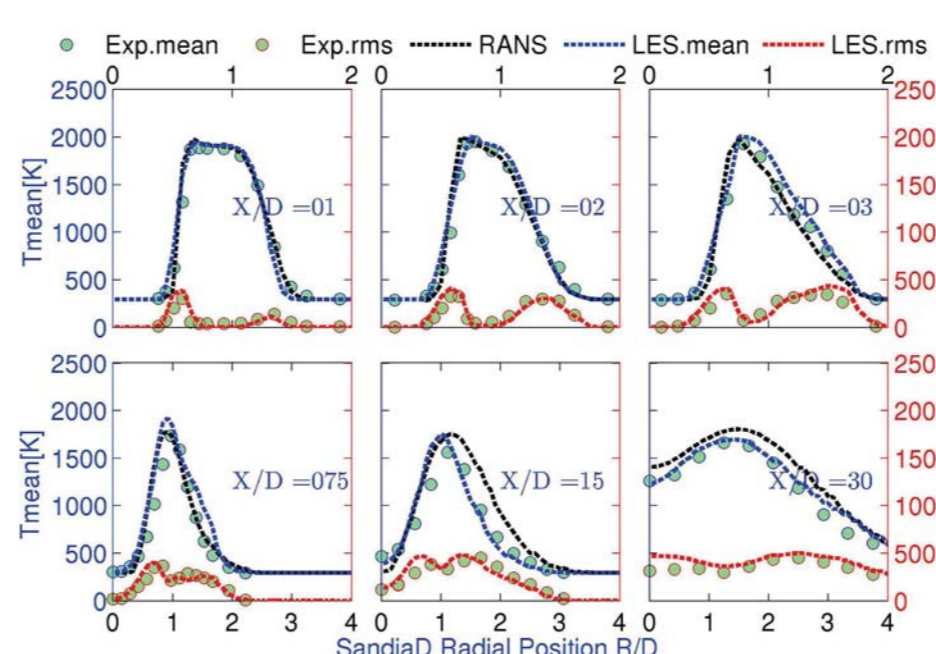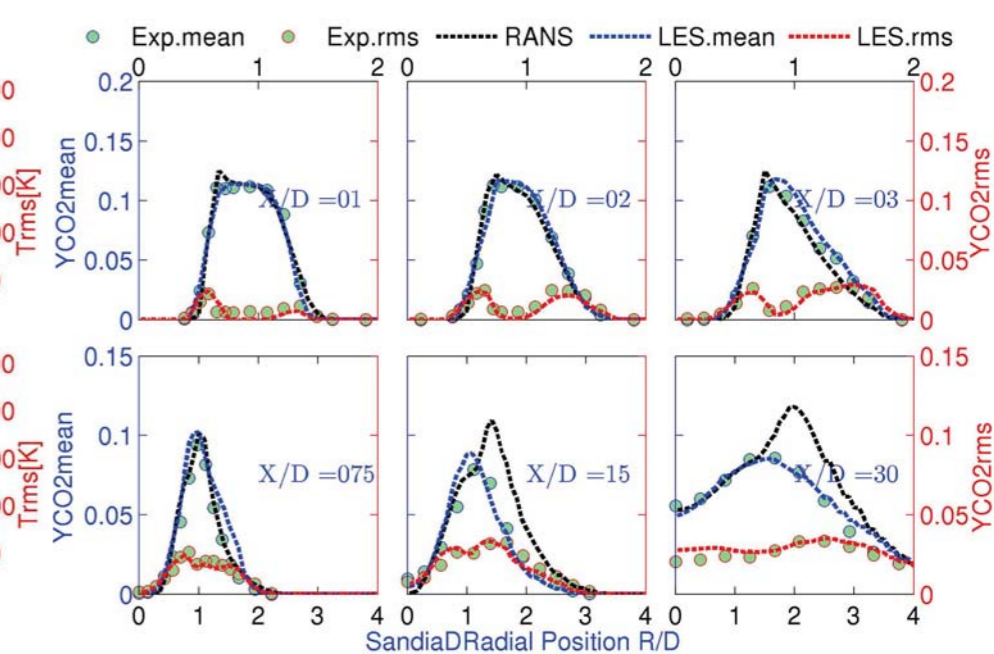
4. Results
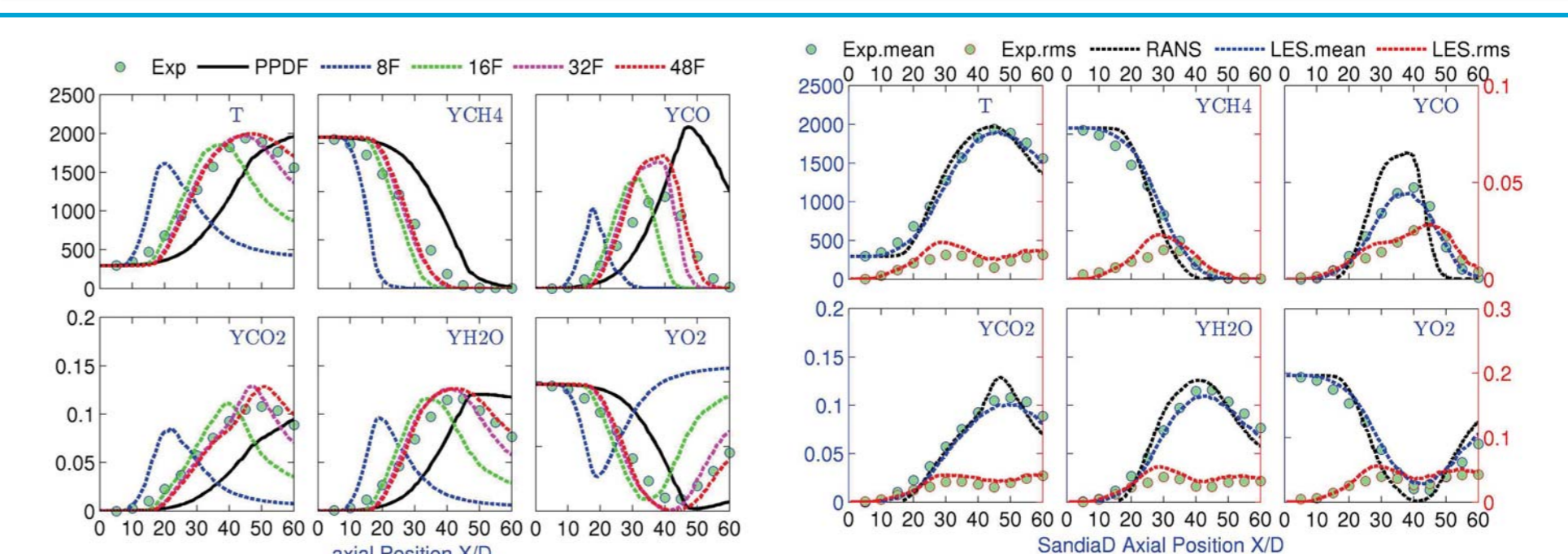
Mean plot of temperature and main components along the centreline of SandiaD flame **[RANS]**
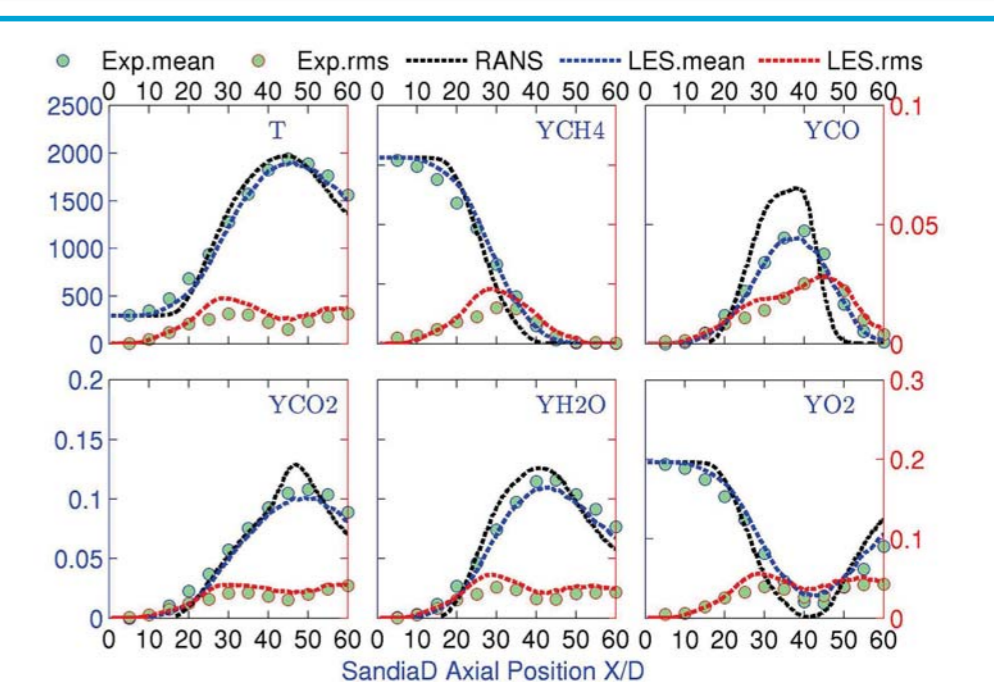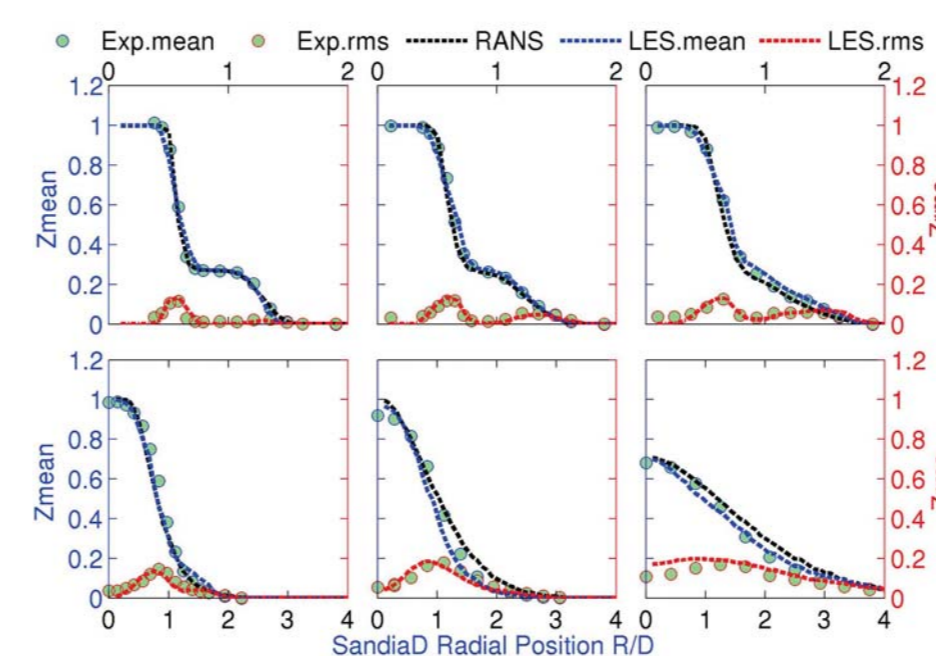

Mean and rms plot of temperature and main components along the centreline of SandiaD flame **[LES&RANS]**
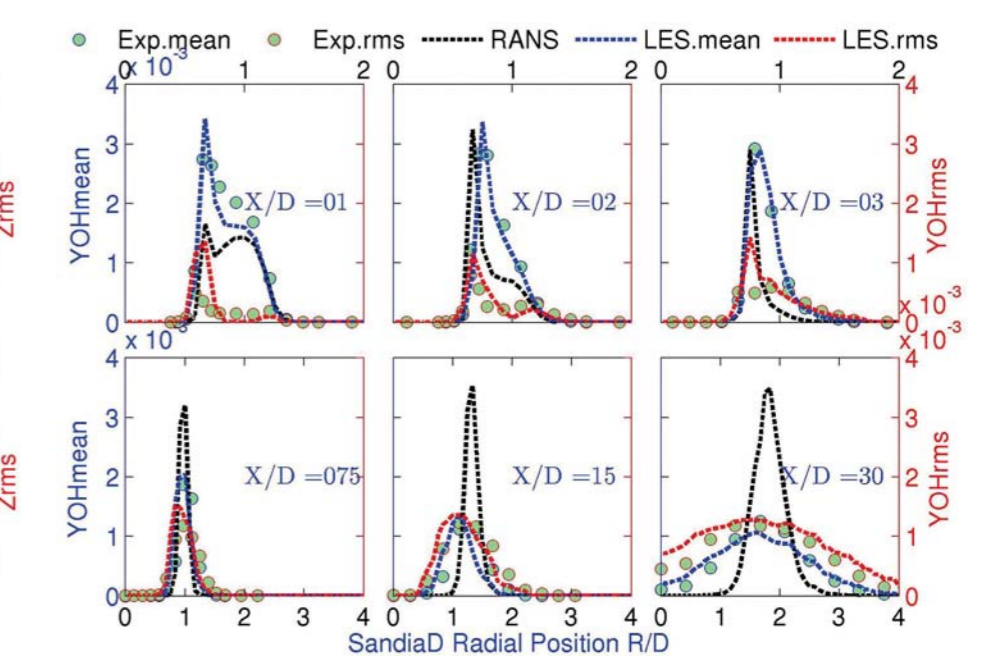

Radial profiles of mean and rms plot of temperature at six axial location of SandiaD flame **[LES&RANS]**

Radial profiles of mean and rms plot of CO2 mass fraction at six axial location of SandiaD flame **[LES&RANS]**

Radial profiles of mean and rms plot of Z at six axial location of SandiaD flame **[LES&RANS]**

Radial profiles of mean and rms plot of OH mass fraction at six axial location of SandiaD flame **[LES&RANS]**

5. Conclusions

- For the simulated case, the accuracy of the proposed model in terms of the predicted temperature and species distribution is higher than the FGM model with PPDF.

- With the increase of the number of stochastic fields, the simulation accuracy of the **ESF/FGM** turbulent combustion model has been continuously improved.

- **LES** model improved the simulation accuracy of the fuel and oxidant mixing process, the results is better than the **RANS** model's.

References:

1. F. Nmira, D. Burot, and J. L. Consalvi, "Stochastic Eulerian field method for radiative heat transfer in a propane oxygen-enhanced turbulent diffusion flame," Combustion Theory & Modelling, vol. 21, pp. 62-78, 2016.

Contact:

Mr Yeru Shang

PhD Student and Associate Tutor

Thermo-Fluid Mechanics

Research Centre (TFMRC)

University of Sussex

+44 (0) 1273 876 706

Yeru.shang@sussex.ac.uk

The Effect of SGS Models on the Large Eddy Simulation of a Corrugated Channel Flow

University of Sussex

GOAL:

Analyse the effect of different Sub-grid Scale (SGS) models on the Large Eddy Simulation (LES) of the realistic corrugated channel flow.

MOTIVATION:

The existing researches in academia on multiple cavities or corrugated wall are focusing on simplified/idealised geometry. Although reports show many SGS models perform well on these idealised geometries, their accuracy of prediction on more realistic corrugated geometry has not been systematically evaluated.
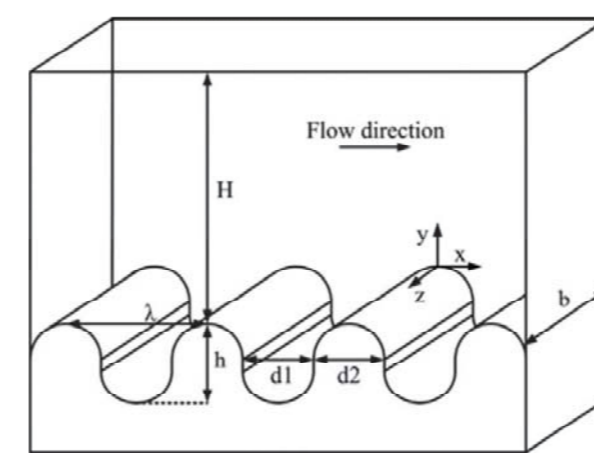
Realistic

Academia

VS

Current Research

Variables	Description	Value (mm)
H	channel height	15.85
h	corrugation height	4.15
λ	wavelength of the corrugation	6.6
d_1	diameter of the groove	3.0
d_2	corrugation diameter	3.6
b	channel width	20

CASE INTRODUCTION:

The geometry is a 2D representation of a widely used commercial stainless steel flex pipe (heat exchanger) with a circular cross-section. the bottom wall has a wavy shape with periodic grooves, whereas top wall and two sidewalls are both flat plates.

NUMERICAL SETUPS:

$Re_b = 5300 \quad U_b = 0.3 m/s \quad \rho = 998.2 kg/m^3 \quad \mu = 0.001 \, Pa \cdot s \quad \Delta t = 5 \times 10^{-5} s$

Periodic Boundary Condition (BC) is applied to both inlet and outlet. Spatial interpolation of convection and diffusion terms is based on 2nd order central differencing scheme. Time marching is approximated by 2nd order backwards differencing implicit scheme. The decoupling of velocity and pressure in the equation is obtained by PISO algorithm, i.e. velocity components are calculated by one momentum predictor step (using smooth solvers with symmetric Gauss-Seidel smoother) and pressure field is corrected twice (by generalised geometric-algebraic multi-grid (GAMG) solver) with Gauss-Seidel smoother for the first corrector step and diagonal incomplete-Cholesky/LU with Gauss-Seidel (DICGaussSeidel) for the second one.

MESH DETAILS:

The structured hexahedral mesh is used in current study. The mesh density increases as approaching the wall. The first layer distance on the corrugated wall is less than 0.005 mm, on top wall is less than 0.006 mm and on sidewalls is less than 0.06 mm. A posterior analysis shows that y+ value for the corrugated wall is less than 0.25 with a mean value of 0.04, for top wall it is less than 0.16 with a mean value of 0.11, for sidewalls it is less than 2.4 with a mean value of 0.72, justifying the use of no-slip wall boundary condition. The total number of mesh cells for each corrugation is 0.9 million.
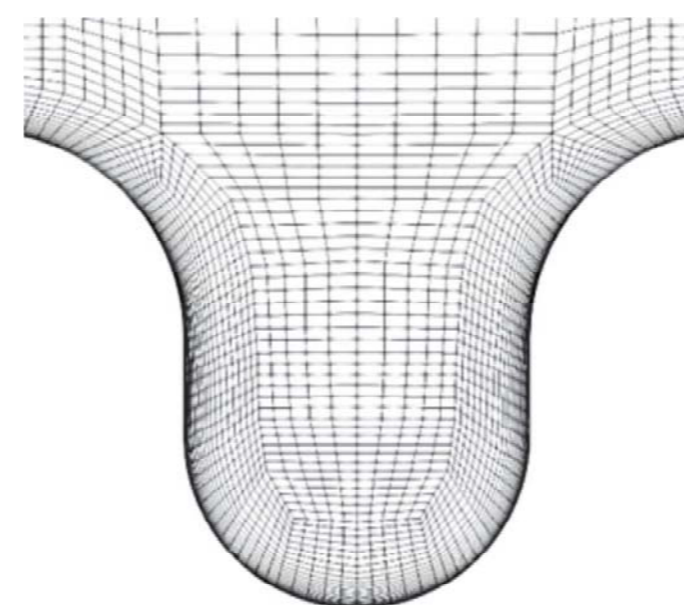

CALCULATION PROCEDURE:

A fully developed flow field with SMAG+VD is used as initial condition for all cases with other SGS models. All cases are allowed for a further 1s simulation to ensure the fluctuation induced by the change of SGS model to be settled, followed by an averaging window of 8s. Flow field became statistically steady before data processing.

RESULTS AND FUTURE STUDIES:

All SGS models tested in the current study can predict a chaotic, 3-dimensional and unstable flow field (Fig. a). Vortex Evolution and hydrodynamics observed in the experiment can be reproduced by all SGS models in LES (Fig. b). The suitable channel length is 16 corrugations (Fig. c) and the current grid is adequately fine (Fig. d). The results suggest that the simulation is insensitive to the selected SGS models for both mean velocity profile (Fig. e) and turbulence intensity (Fig. f-h). In next stage, different inlet turbulence BCs will be tested.
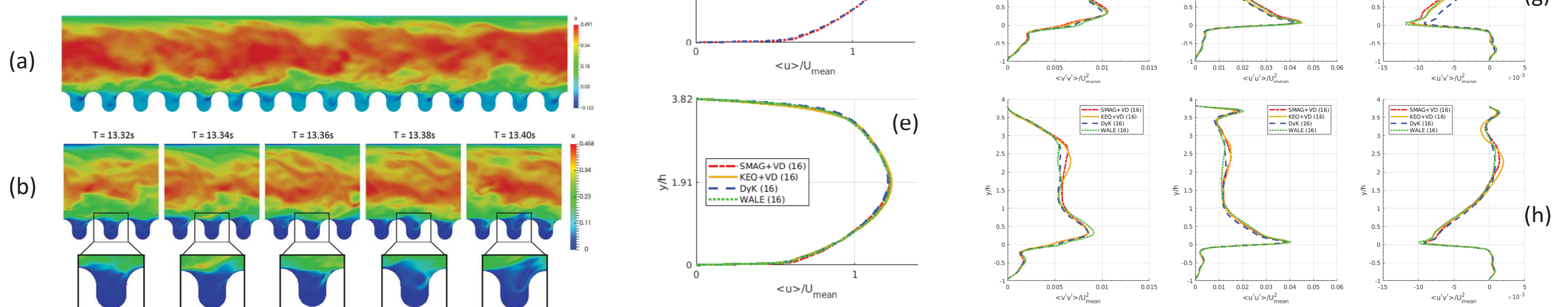
ParaView

A **ParaView basic and advanced course** will take place in **Hong Kong** during **winter of 2018**.

Please write your name and email address to be kept informed on this event.

2018年冬季，在香港将会举办ParaView的基础以及进阶课程，请留下您的姓名以及电子邮箱地址以让我们能及时通知您。

Kitware

ParaView In 2018
Features Quick Peek

About Kitware

- Software Development Company
- Primarily work in Open Source
- Founded in 1998
- 140+ employees and growing
  - 3 offices in the US
  - 1 in Europe founded in 2010
- Focus in
  - Scientific computing
  - Large data visualization
  - Medical image processing
  - Informatics
  - Computer vision
  - Scientific data publishing
  - Quality software processes
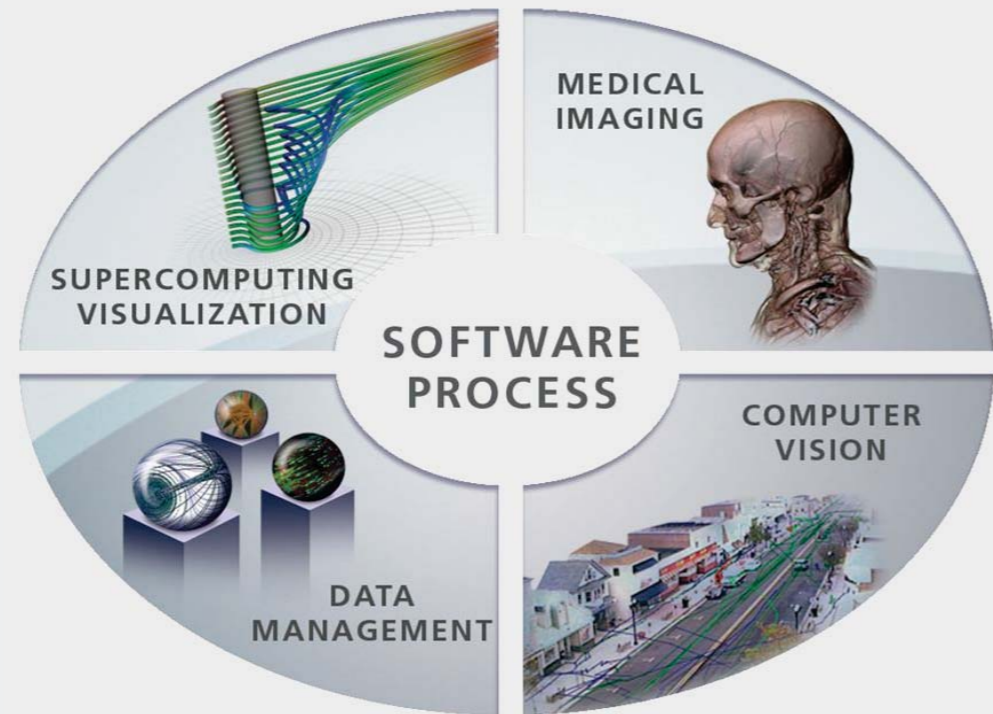
What is ParaView ?   www.paraview.org

An **application** and **architecture** for **display** and **analysis** of **massive** scientific datasets:

- **Application** - you don't have to write any code to analyze your data
- **Architecture** - designed to be extensible if you want to code
  - Notably custom apps (ParaViewWeb), plugins and python scripting
- **Display** - excels at traditional sci vis qualitative 3D rendering
- **Analysis** - data drill down through charts, stats, all the way to values
- **Massive** - scales from netbooks to worlds largest supercomputers

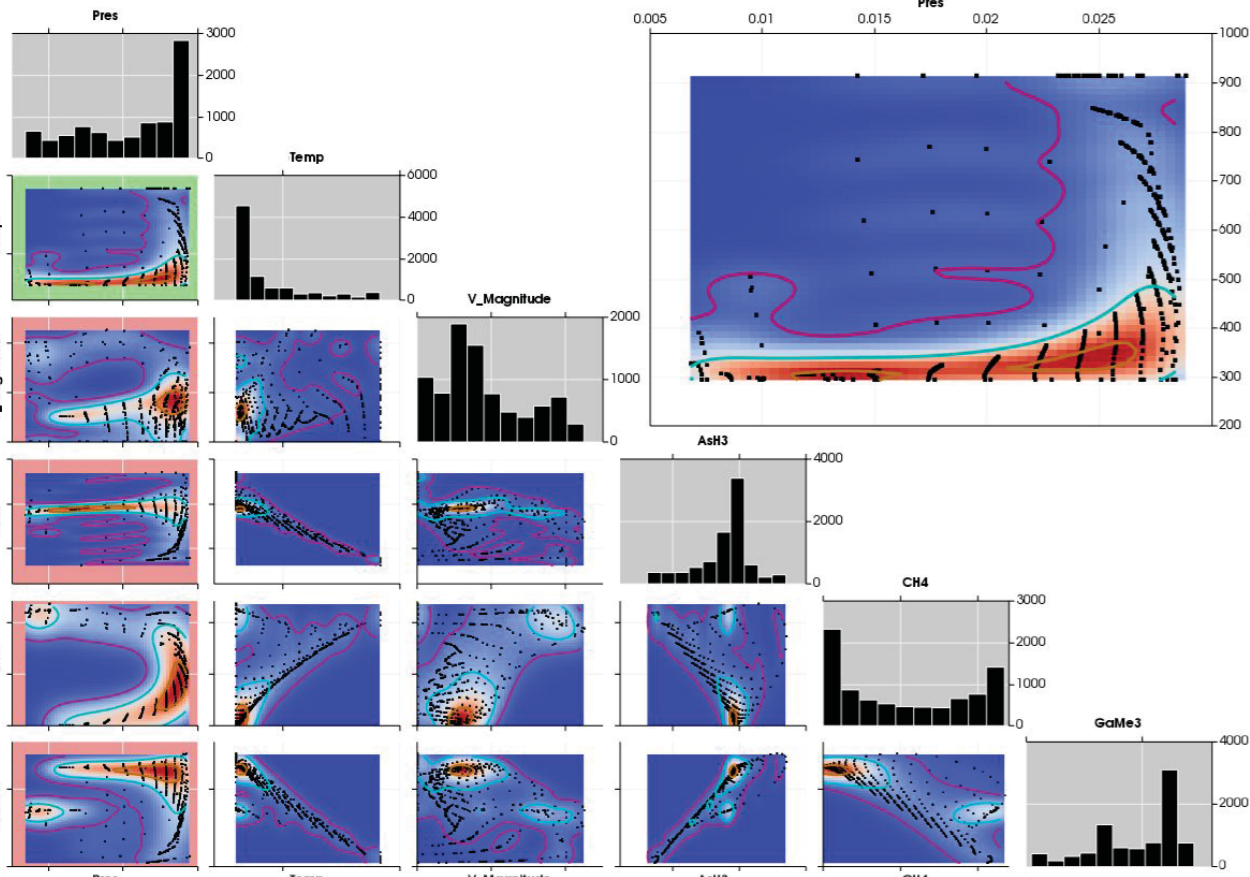Strength is its flexibility - *you create arbitrary pipelines with it*.

OpenTURNS : Stats and Uncertainty tools

ParaView is always been great for 3D Analysis, but is was not the de-facto choice for statistical analysis. Thanks to EDF funding, new capabilities for data analysis is making its debut in ParaView and VTK based on OpenTURNS. OpenTURNS is an open source initiative for the Treatment of Uncertainties, Risks'N Statistics, and is now an optional dependency of VTK. It takes the form of an optional VTK module that can be requested to be built in ParaView by turning ON the CMake option `PARAVIEW_USE_OPENTURNS`.

Two new filters, **OT Kernel Smoothing** and **OT Density Map** are now available, and the OT Density Map is even integrated into the Plot Matrix View in order to show the density map of the first and last decile as well as the median, which results can be seen on Fig. 1 and on Kitware blog article : *"OpenTURNS Integration in ParaView : Stats and Uncertainty tools"*.

Figure 1: Improvement of the Plot Matrix view to display density map computed with OpenTURNS.

Major Improvements on the Point Gaussian Representation

The new **Point Gaussian Representation** was supposed to replace the deprecated Point Sprite Representation and be supported for a long time as an official representation and not "just a plugin" as before. However Point Sprite users were not very happy with it: the new feature was not easy to use and lot slower when rendering big number of points.
This issue comes to an end with some new features and bug fixes which are now merged into ParaView, as show on Fig. 2 and on Kitware blog article *"Major Improvements on the Point Gaussian Representation"*:

- Possibility to write Custom Shader from within ParaView UI, as seen on Fig. 2.
- Possibility to use Opacity and Scaling not only with a Scalar Array but also with a Vector Array by selecting the component to use or the magnitude;
- Opacity and Scale transfer functions are now dynamic and automatically adjusted;
- Enable Point Gaussian Representation for every DataSet type;
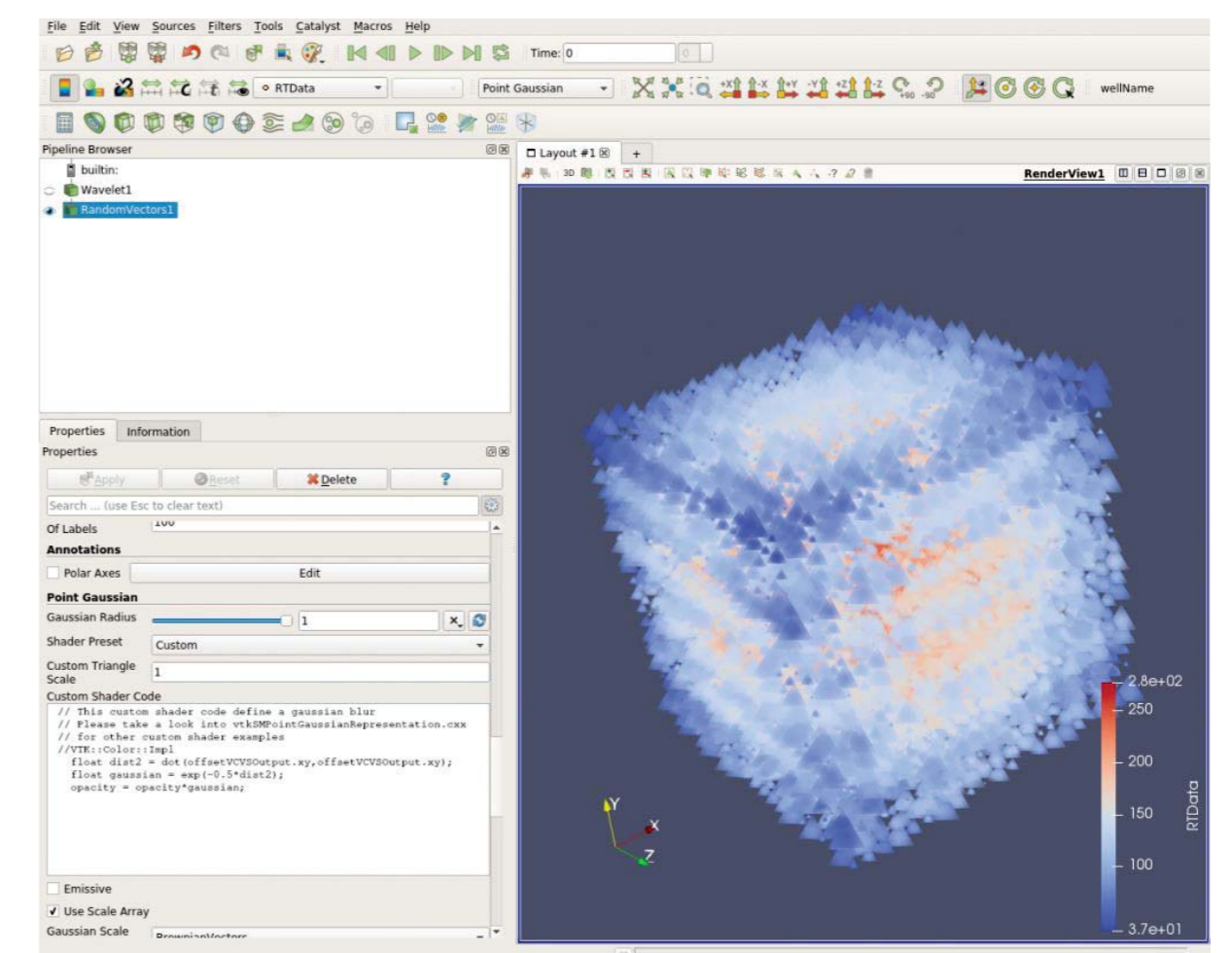- Support for point selection and point picking with "Hover Point".

Figure 2: Custom Shader for Point Gaussian Representation.

Separate Color Map and Multi Component volume rendering

By default, ParaView share color map by the name of the colored array. We have now introduced a way to "separate" a color map, insuring it is not shared. This enabled the implementation of a new feature, Multi Component Volume Rendering.

When this new feature is enabled and the **Multi Component Mapping** checkbox checked:
- For a two-components array, the first component is mapped to the color, the second component is mapped to the opacity, see Fig. 3;
- For a four-components array, the first, second and third components are used as RGB values and the fourth component is mapped to the opacity.

The color map for current array and representation is automatically separated when this feature is enabled to avoid conflicts with other representations..
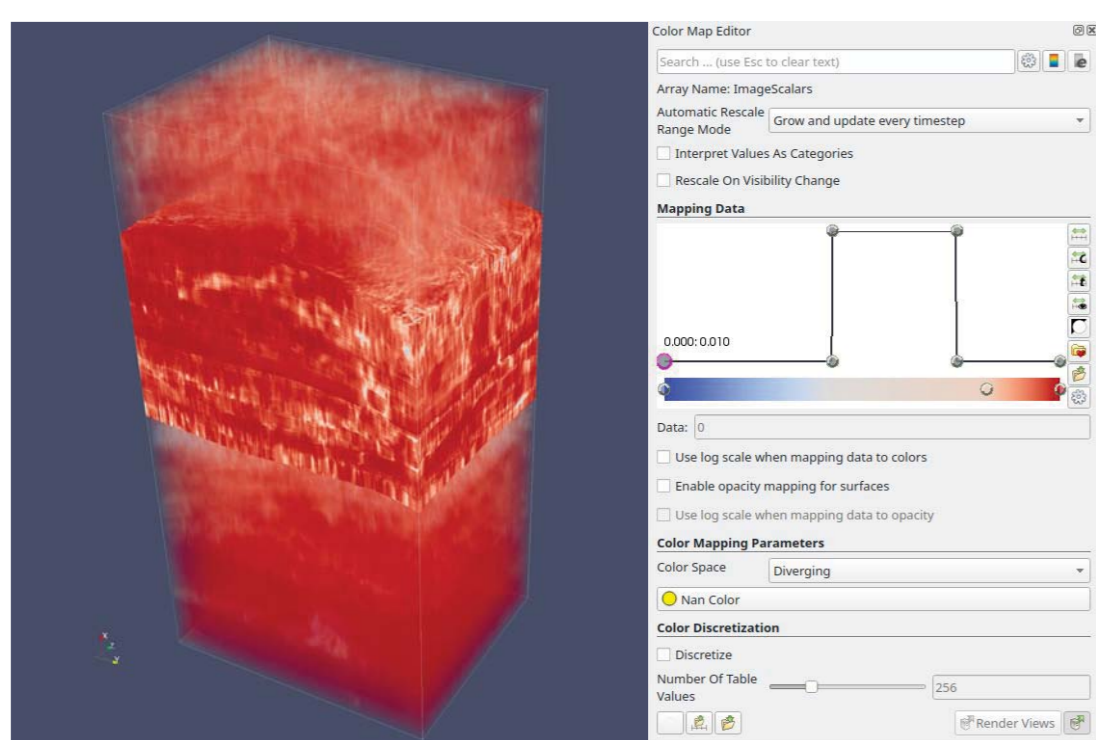

Figure 3: Volume rendering of a geological model using a two components array: the first is used for the color, the second for the opacity - dataset by TOTAL.

The Embossing Representations Plugin

Besides being large, climate simulations are usually comprised of many different variables and quantities that often need to be visualized side by side. The two new representations included in a new plugin have been explicitly developed with this idea in mind, and as climate simulations tend to be based on all kind of different grids, special attention was paid that all major ones are supported. Both representations have been tested with rectilinear grids, tri-polar curvilinear grids, as well as semi-irregular grids such as ICON/MPAS. Those 2 representations take full advantage of the GPU to perform the rendering at high frame rates.

- The new **Bump Mapped Surface** representation works only with point data and does not modify at all the current geometry. The GPU uses the gradient of the data to alter surface normals and creates a shade effect. When selected, the data array and a scaling factor can be chosen by the user.
- The new **Extrusion surface** is mainly designed to work with cell data and behaves like an extruded "city map". The cells are extruded based on their value in the selected array and a user defined factor. Optionally, it is possible to normalize values with an auto-scaling based on the range of the data or a manual range. See Fig. 4 and our Kitware blog article : *"A new Embossing Representations Plugin for ParaView"*.
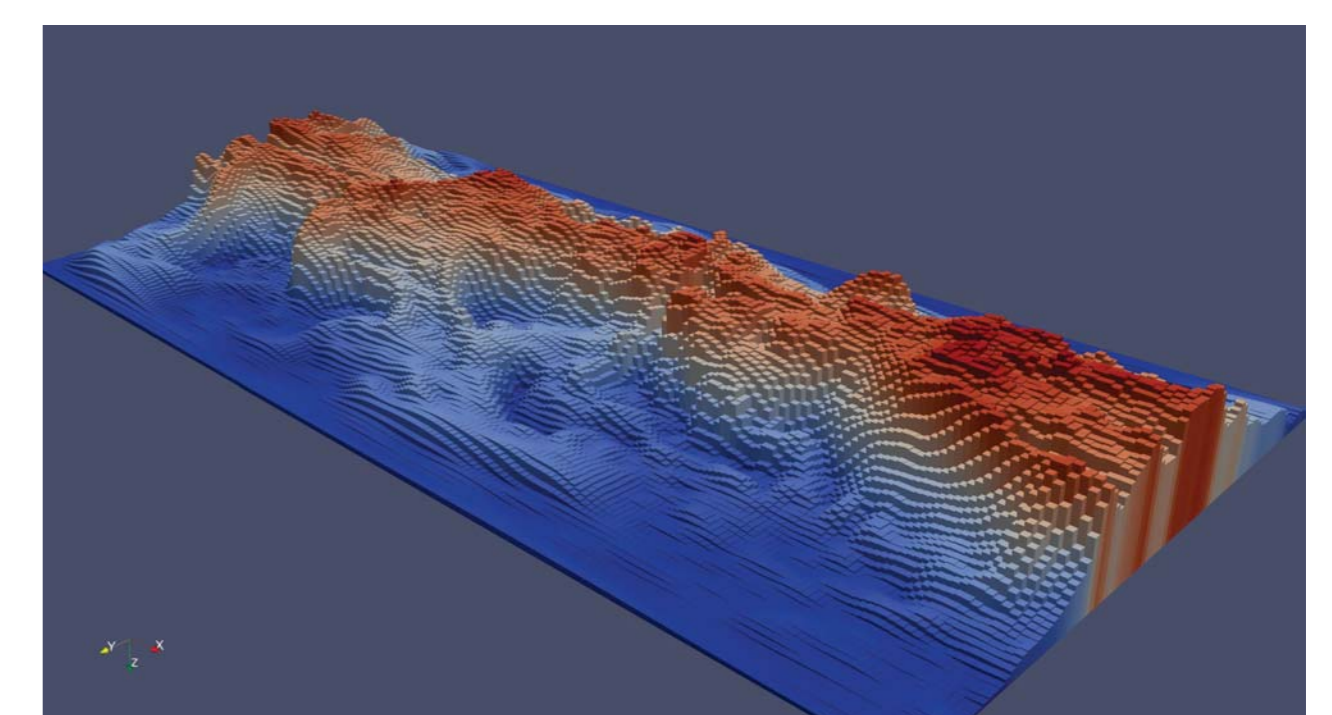
Figure 4: Results of using the Extrusion Surface representation. Dataset by DKRZ.

Mathieu Westphal   mathieu.westphal@kitware.com
Joachim Pouderoux   joachim.pouderoux@kitware.com
Michael Migliore   michael.migliore@kitware.com

Kitware SAS
26 rue Louis Guérin, 69100 Villeurbanne, France
www.kitware.eu

Host and Organizers

上海交通大学
SHANGHAI JIAO TONG UNIVERSITY

COMPUTATIONAL MARINE HYDRODYNAMICS LAB
SHANGHAI JIAO TONG UNIVERSITY

Co-Organizers

水动力学研究与进展
Journal of Hydrodynamics

上海市船舶工程重点实验室
Shanghai Key Laboratory of Ship Engineering

航运技术与安全国家重点实验室
State Key Laboratory of Navigation and Safety Technology

Sponsors

船舶海洋与建筑工程学院
School of Naval Architecture, Ocean and Civil Engineering

中船重工第七〇二研究所
China Ship Scientific Research Center

engys

CALCNEXT
计算未来

CAE Solutions

Email: dcwan@sjtu.edu.cn

Homepage: http://dcwan.sjtu.edu.cn/